DEBRIS-COVERED GLACIERS: FORMATION, GOVERNING PROCESSES, PRESENT STATUS AND FUTURE DIRECTIONS

EDITED BY: Aparna Shukla, Argha Banerjee, Koji Fujita,
Lindsey Isobel Nicholson and Duncan Joseph Quincey

PUBLISHED IN: Frontiers in Earth Science

frontiers Research Topics

frontiers

ISSN 1664-8714
ISBN 978-2-83250-405-5
DOI 10.3389/978-2-83250-405-5

About Frontiers

Frontiers is more than just an open-access publisher of scholarly articles: it is a pioneering approach to the world of academia, radically improving the way scholarly research is managed. The grand vision of Frontiers is a world where all people have an equal opportunity to seek, share and generate knowledge. Frontiers provides immediate and permanent online open access to all its publications, but this alone is not enough to realize our grand goals.

Frontiers Journal Series

The Frontiers Journal Series is a multi-tier and interdisciplinary set of open-access, online journals, promising a paradigm shift from the current review, selection and dissemination processes in academic publishing. All Frontiers journals are driven by researchers for researchers; therefore, they constitute a service to the scholarly community. At the same time, the Frontiers Journal Series operates on a revolutionary invention, the tiered publishing system, initially addressing specific communities of scholars, and gradually climbing up to broader public understanding, thus serving the interests of the lay society, too.

Dedication to Quality

Each Frontiers article is a landmark of the highest quality, thanks to genuinely collaborative interactions between authors and review editors, who include some of the world's best academicians. Research must be certified by peers before entering a stream of knowledge that may eventually reach the public - and shape society; therefore, Frontiers only applies the most rigorous and unbiased reviews.
Frontiers revolutionizes research publishing by freely delivering the most outstanding research, evaluated with no bias from both the academic and social point of view. By applying the most advanced information technologies, Frontiers is catapulting scholarly publishing into a new generation.

What are Frontiers Research Topics?

Frontiers Research Topics are very popular trademarks of the Frontiers Journals Series: they are collections of at least ten articles, all centered on a particular subject. With their unique mix of varied contributions from Original Research to Review Articles, Frontiers Research Topics unify the most influential researchers, the latest key findings and historical advances in a hot research area! Find out more on how to host your own Frontiers Research Topic or contribute to one as an author by contacting the Frontiers Editorial Office: frontiersin.org/about/contact

DEBRIS-COVERED GLACIERS: FORMATION, GOVERNING PROCESSES, PRESENT STATUS AND FUTURE DIRECTIONS

Topic Editors:
Aparna Shukla, Ministry of Earth Sciences, India
Argha Banerjee, Indian Institute of Science Education and Research, Pune, India
Koji Fujita, Nagoya University, Japan
Lindsey Isobel Nicholson, University of Innsbruck, Austria
Duncan Joseph Quincey, University of Leeds, United Kingdom

Citation: Shukla, A., Banerjee, A., Fujita, K., Nicholson, L. I., Quincey, D. J., eds. (2022). Debris-Covered Glaciers: Formation, Governing Processes, Present Status and Future Directions. Lausanne: Frontiers Media SA.
doi: 10.3389/978-2-83250-405-5

Table of Contents

frontiers | Frontiers in Earth Science

TYPE Editorial
PUBLISHED 21 September 2022
DOI 10.3389/feart.2022.1021292

OPEN ACCESS

EDITED AND REVIEWED BY
Michael Lehning,
Swiss Federal Institute of Technology Lausanne, Switzerland

*CORRESPONDENCE
Aparna Shukla,
aparna.shukla22@gmail.com

SPECIALTY SECTION
This article was submitted to Cryospheric Sciences, a section of the journal Frontiers in Earth Science

RECEIVED 17 August 2022
ACCEPTED 29 August 2022
PUBLISHED 21 September 2022

CITATION
Shukla A, Nicholson L, Banerjee A, Fujita K and Quincey DJ (2022), Editorial: Debris-covered glaciers: Formation, governing processes, present status and future directions. *Front. Earth Sci.* 10:1021292. doi: 10.3389/feart.2022.1021292

Editorial: Debris-covered glaciers: Formation, governing processes, present status and future directions

Aparna Shukla[1]*, Lindsey Nicholson[2], Argha Banerjee[3], Koji Fujita[4] and Duncan J. Quincey[5]

[1]Ministry of Earth Science (MoES), New Delhi, India, [2]Institute of Atmospheric and Cryospheric Sciences, University of Innsbruck, Innsbruck, Austria, [3]Indian Institute of Science Education and Research (IISER), Pune, India, [4]Graduate School of Environmental Studies, Nagoya University, Nagoya, Japan, [5]School of Geography, University of Leeds, Leeds, United Kingdom

KEYWORDS

debris-covered glacier (DCG), debris transport, ablation hotspots, sub-debris ablation, glacier evolution

Editorial on the Research Topic
Debris-Covered Glaciers: Formation, Governing Processes, Present Status, and Future Directions

Introduction

Considerable parts of the ablation zone of many high mountain glaciers are covered with supraglacial debris. The presence of supraglacial debris complicates the interplay of processes linking climate change, topography, and glacier dynamics. Debris-covered glaciers (DCGs) thus differ significantly from their clean-ice counterparts, as they form a more complex system of forcing factors, couplings, and feedback mechanisms that are yet to be fully understood. Resolving the uncertain response and evolution of debris-covered glaciers is vital for devising sustainable management strategies for freshwater availability, glacier-related hazards, hydro-power generation, and also for more precise estimation of their contribution to eustatic sea level changes. The articles in this Research Topic cover conceptual, modelling, and observational approaches to study DCGs at point to glacier and regional scales.

Exploring differences with clean ice glaciers

Several contributions in this Research Topic include summaries of the processes and response characteristics of DCGs and the conceptual ways they differ from their clean-ice

counterparts. Using Baltoro Glacier in the central Karakoram as an example, Huo et al. review several key DCG processes and recognise climate forcing, the properties and transport of debris, topography and cryokarst features as key factors controlling glacier behaviour and conclude that their integrated effects govern the ice loss from DCGs. Nicholson et al. highlight the fundamental ways in which debris partially decouples the glacier behaviour from climate forcing and the open challenges that need to be addressed in order to couple these time-dependent feedbacks within a modelling system to fully capture DCG development over time. Nicholson et al. and Mayer and Licciulli both argue that DCGs should not be expected to achieve a steady state in response to constant climatic forcing, making it difficult to interpret modern observations of the fluctuation of debris-covered glaciers on the basis of a changing climate alone.

DC thermal properties

Thermal properties (surface temperature, thermal inertia/resistance, diffusivity and conductivity) of the debris layer are valuable for understanding multiple DCG issues, particularly melting of the underlying ice. Patel et al. determine spatio-temporal variations in the *in situ* thermal properties of three glaciers in the Chandra basin of the Western Himalaya and find that debris-surface temperature correlated well with sub-debris temperature, and that both were directly related to near-surface air temperature. Field experiments such as these add to a growing database of empirical measurements of sub-debris melt rates and the effects of altitude and debris-thickness, and measurements of thermal resistance with debris layers of variable thickness. Indeed, Boxall et al. exploit data such as these alongside *in situ* debris thickness measurements and satellite-derived surface temperature to estimate the supraglacial debris thickness across High Mountain Asia. In contrast to some other regional studies they find at the mountain range scale that elevation and surface velocity are stronger predictors of debris thickness than slope or aspect. Herreid explores the usage and value of thermal data (acquired in field and remotely) for investigating DCG processes on Canwell Glacier, Alaska. He proposes methods for estimating the debris-thickness and bare-ice and sub-debris melt, and then compares results with other published models. This study recommends using thermal images acquired during cloudy conditions and sub-pixel correction of ASTER thermal imagery for enhancing their spatial resolution. Beneath the debris, there are very few measurements of ice thermal properties, but Miles et al. present measurements from several near-surface boreholes (1.5–7.0 m depth) and report the propagation of the winter season cold wave into Khumbu Glacier, Nepal, refining the knowledge on equilibrium line altitude and timings of onset/end of the ablation season in this high elevation Himalayan site, as well as providing more accurate information for thermo-mechanical models of ice-deformation.

Debris transport

Investigating the processes governing debris-transport within, on, and off the glacier surface is important for the extent and spatial distribution of the debris cover, and its evolution, which controls the magnitude of ablation, the genesis of glacier surface morphology, and the long-term glacier geometry (Huo et al.; Moore; Mayer and Licciulli). Huo et al. remind us that supraglacial debris moves due to advective-diffuse processes governed by ice-flow (operational on larger and longer spatio-temporal scales), gravitational movement (applicable at smaller and shorter spatio-temporal scales), and fluvial processes. Moore simulates the evolution of an idealized DCG on the timescale of complete de-glaciation with a model of coupled ablation and downslope debris transport, and finds that debris mobility can hasten ice mass loss compared to immobile debris. Highly mobile debris causes rapid topographic inversions and produces subdued supra- and post-glacial reliefs, whereas low debris mobility is characterised by more pronounced supra- but subdued post-glacial reliefs. Further, an intermediate debris mobility optimizes both postglacial relief and the rate of de-icing, and this novel realization may be an important component of the unexpectedly high mass loss rates of DCGs.

Ablation hotspots: Observations and modelling

The uneven and hummocky topography of DCGs, which results from differential ablation, is adept at storing melt/rainwater and results in the formation of supraglacial ponds. Surface heterogeneities may also cause pronounced relief changes resulting in debris-slumping, which often expose ice-cliffs covered by a thin veneer of debris. Considered as glacier "*melt hotspots*," the dynamics of these cryokarst features and eventually their contribution to glacier ablation are vital for processes governing the evolution of DCGs. Wendleder et al. (Baltoro Glacier, Karakoram; 2016-20), Sato et al. (Trakarding Glacier, Nepal; 2007-2018-2019) Loriaux and Ruiz (Verde Glacier, Chile; 2009-19) and Guo et al. (Halong Glacier, Tibet; August and September 2019) all use high resolution remotely sensed data (*via* aerial and spaceborne sensors) to monitor the characteristics and dynamics of supraglacial ponds and ice-cliffs. Important observations from these studies which further the existing knowledge about supraglacial ponds and ice-cliffs include:

1. newly formed ice-cliffs have gentle slopes and random aspects as compared to perennial ones, which are relatively steeper

and with certain predominant aspect (north-west and south facing),
2. count and areas covered by these cryokarst features are maximum at the beginning of the ablation season and minimum at the end of ablation. Additionally, Wendleder et al. report that the supraglacial ponds fill between mid-April to mid-June and drain between mid-June to mid-September,
3. supraglacial ponds usually occupy gentle and stagnant regions, however, ice-cliffs appear less controlled by flow velocity and gradient,
4. areas surrounding these features are characterised by low surface ice velocities, high surface elevation changes (>2 m yr^{-1}) and high mass loss (1.36 and 1.22 m.w.e.). Ice-cliff backwasting of 7.8 m/month to 24 m yr^{-1} is reported,
5. ice-cliff edge length strongly correlates with the ice-cliff inclined area, which will enable estimation of the ice cliff inclined area from coarser satellite-based images even without high-resolution DEMs.

Overall, these studies suggest that, besides regional meteorology and surface gradients, the occurrence and seasonality of cryokarst features is significantly related with the englacial and supraglacial hydrological processes, and the new insights will allow further assessment of their overall contribution to DCG mass loss and long term behaviour.

On the glacier-scale, Anderson et al. explore the role of dynamic thinning in DCG mass loss and evolution. They firstly assess the inter-relationship between melt-hotspots, debris-thickness, and ice-dynamics of Kennicott Glacier, Alaska, and subsequently simulate their changes over decadal timescales to understand the pathways of glacier evolution. Glacier bed topography is found to control ice-flow and thus debris expansion, which follows the changes in flow direction. Feedbacks involving supraglacial pond positions, relief, debris characteristics and ice-cliff locations are shown to be instrumental in governing thinning rates, with ice ablation at high-elevation feeding through into decreased ice-flux (and thus emergence) down-glacier. Similar studies on other glaciers will help determine if these relationships are site specific or generalised.

Suitable sub-debris melt and DCG runoff modelling underpins all assessments of downstream hydrological influences of DCGs. Steiner et al. integrate field and remotely acquired data within a distributed energy balance model for estimating the melt rates of Lirung Glacier, Nepal at an hourly scale. They test the sensitivity of their results towards thermal conductivity and debris thickness. They also validate their results with the surface lowering rates from field-derived DEMs. A key finding is that simple modelling approaches do not accurately simulate the diurnal melt pattern, but are capable of quantifying total melt, and therefore have merit for application at catchment scale. Similarly, Billington et al. implement a new 1-D model based on the simultaneous heat and water transfer model on North Changri Nup Glacier, Nepal Himalaya for estimating DCG ablation. The model results simulate the characteristic pattern of decreasing ablation with increasing debris thickness. However, the observed melt rates show little dependence on the debris thickness, possibly due to the influence of a patchy snow-cover at the study site. The study highlights the patchy snow-cover during the ablation season as a possible unquantified source of uncertainty in estimating sub-debris ice melt.

Large-scale observed changes

The unique character of DCGs means they respond differently to clean ice glaciers under the same climatic forcing, and observations of these changes are useful in disentangling the primary controls. Racoviteanu et al. (glaciers in the Manaslu region, Nepal; 1970-2019), Majeed et al. (87 glaciers in the Pangong region, Ladakh, Himalaya; 1990-2019) and Falaschi et al. (three glaciers in the Patagonian Andes; 1958–2020) use aerial and satellite remote sensing and limited field data (Racoviteanu et al.), and report recent snapshots (shorter timescale) of climate driven response of debris-covered glaciers in different regions. Key findings from these studies include:

1. DCGs mostly show an increase in debris extent and thickness downglacier, ice deceleration, decrease in slope, persistent negative mass balance, ascending equilibrium line altitude, and open crevasses,
2. spatio-temporal predominance of the cryokarst features and high mass loss around these features,
3. retreat and surface thinning rates on DCGs exceed those on clean-ice counterparts,
4. formation of new proglacial lakes in the vicinity of DCGs are prevalent and that the lake-terminating glaciers experience twice as much thinning compared to land-terminating ones.

Further, based on the analysis of 975 DCGs across HMA, Shea et al. propose a new metric termed as the *Debris Emergence Elevation (DEE)* for ascertaining the regional debris-covered glacier changes over decadal time scales, which could be used to reconstruct their relative mass changes. This metric appears to have potential for acting as a reliable proxy of DCG status as their geometric response is known to be sensitive to the location at which debris is added to the system or emerges at the surface (Nicholson et al.).

Glacier evolution modelling

While findings of these shorter-timeframe studies create a base-line dataset for understanding of DCG behaviour and response, they do not elucidate the details of the theory of

formation and long-term evolution of DCGs and the relevant controlling processes (Huo et al.; Nicholson et al.). This requires a well-validated and adequately parametrized numerical model that integrates the primary forcing factors, feedbacks and couplings (Huo et al.; Anderson et al.; Nicholson et al.; Mayer and Licciulli). To this end, Nicholson et al. provide a detailed review of the fundamental processes and concepts that control the evolution of DCGs and numerical modelling attempts to simulate the same together with their limitations. They explain the key ways in which debris-cover decouples a glacier system from climate forcing and that development of debris-cover over time should prevent the glacier from achieving a steady state. They also discuss existing bottle-necks of realistic representation of DCGs through modelling approaches. Mayer and Licciulli investigate these aspects in some depth, demonstrating that they have an inherent tendency to switch to an oscillating state (retreat and advance cycles) that would occur even without any variations in climate. The advance phase of such oscillations would end with the separation of the heavily debris-loaded lowermost glacier tongue, at time scales of decades to centuries.

This compendium primarily consolidates the state-of-art knowledge about the processes governing DCG behaviour, highlights the recent insights regarding their evolution, and identifies critical future research directions. This is still a rapidly evolving field, and further research is needed on aspects such as debris-production (variability and emergence), multi-scale hydrological processes, and the long-term coupling that supraglacial debris provides between landscapes, their climate, and DCGs themselves over geological timescales.

Author contributions

AS wrote the first draft of the manuscript. All authors contributed to manuscript revision, read, and approved the submitted version.

Conflict of interest

The authors declare that the research was conducted in the absence of any commercial or financial relationships that could be construed as a potential conflict of interest.

Publisher's note

frontiers in Earth Science

ORIGINAL RESEARCH
published: 24 May 2021
doi: 10.3389/feart.2021.652279

Understanding Complex Debris-Covered Glaciers: Concepts, Issues, and Research Directions

Da Huo[1]*, *Michael P. Bishop*[1] *and Andrew B. G. Bush*[2]

[1] Department of Geography, Texas A&M University, College Station, TX, United States, [2] Department of Earth and Atmospheric Sciences, University of Alberta, Edmonton, AB, Canada

Understanding the climate-glacier dynamics of debris-covered glaciers is notoriously difficult given a multitude of controlling factors and feedback mechanisms involving climate forcing, debris-load properties, supraglacial water bodies, and multi-scale topographic effects. Recent studies have provided insights into controlling factors, and have reported the presence of anomalies that contradict the general consensus of the protective influence of debris loads on ablation dynamics. Nevertheless, numerous processes that regulate glacier dynamics at various spatial and temporal scales have not been adequately accounted for in statistical and numerical modeling studies. Furthermore, important feedbacks involving ablation, topography, irradiance, gravitational debris flux, and supraglacial ponding are often neglected or oversimplified in existing models, which poses a challenge to our understanding of conflicting field observations such as the accelerated mass loss of many Himalayan glaciers, and glacier-subsystem responses (ice-flow, debris flux, surface morphology, and supraglacial water bodies) to climate forcing. This paper provides insights into the complexity of debris-covered glacier systems by addressing concepts and issues associated with forcing factors and glacial processes, and highlights the importance of understanding system couplings and feedbacks. Specifically, we review recent studies on debris-covered glaciers and utilize simulation results based on the Baltoro Glacier in the central Karakoram to discuss important concepts and issues. Our results demonstrate that climate forcing, the properties and transport of debris, topography and supraglacial water bodies are the key controlling factors in a debris-covered glacier system, and that their coupled effects and positive feedbacks may increase the ice loss of a debris-covered glacier. We also recommend new research directions for future studies.

Keywords: debris-covered glaciers, climate-glacier dynamics, debris load, supraglacial water bodies, glacier model, Baltoro glacier

OPEN ACCESS

Edited by:
Duncan Joseph Quincey, University of Leeds, United Kingdom

Reviewed by:
Leif S. Anderson, University of Lausanne, Switzerland
Christoph Mayer, Bavarian Academy of Sciences and Humanities, Germany

***Correspondence:**
Da Huo
dh21@tamu.edu

Specialty section:
This article was submitted to Cryospheric Sciences, a section of the journal Frontiers in Earth Science

Received: *12 January 2021*
Accepted: *23 April 2021*
Published: *24 May 2021*

Citation:
Huo D, Bishop MP and Bush ABG (2021) Understanding Complex Debris-Covered Glaciers: Concepts, Issues, and Research Directions. Front. Earth Sci. 9:652279. doi: 10.3389/feart.2021.652279

1. INTRODUCTION

Debris-covered glaciers (DCGs) present a series of unique and complex challenges to those investigating climate-glacier dynamics and their role in downstream impacts such as freshwater availability, hydroelectric power generation, natural hazards and landscape evolution (Bishop et al., 2002; Seong et al., 2009; Immerzeel et al., 2010; Reid and Brock, 2010; Bush et al., 2020). While

debris-free glaciers are relatively well-understood and modeled, DCGs introduce a number of additional complex dynamical and thermodynamical feedbacks between the underlying glacier ice, the debris cover, the adjacent-terrain geomorphological conditions, and the overlying atmosphere. The thermal and radiative characteristics of the debris cover itself depend on geographic location and the surrounding lithology. The thickness of the debris cover, which so critically determines whether the debris acts as an insulator for the ice or accelerates ice ablation, depends on the steepness of the surrounding topography, regional erosion characteristics, and glacier dynamics, which in turn depend on atmosphere-glacier interactions that have not yet been fully quantified (Bolch et al., 2012; Dobreva et al., 2017; Farinotti et al., 2020).

Currently, we have not achieved an agreement on the state and fate of many DCGs in High-Mountain Asia due to uncertainties related to climate, topographic evolution, debris-load forcings, and the development of supraglacial water bodies and ice-cliffs. Most researchers agree that debris insulation makes a glacier less sensitive to climate change (e.g., Reid and Brock, 2014; Pratap et al., 2015; Anderson and Anderson, 2016; Vincent et al., 2016). Recent observations and simulations, however, show that many DCGs exhibit comparable ice-loss to debris-free glaciers despite the presence of supraglacial debris (Kääb et al., 2012; Immerzeel et al., 2013; Fujita et al., 2014; Salerno et al., 2017). Therefore, it appears that DCGs may be more sensitive to climate change than previously thought, as a multitude of processes and feedbacks have not been accurately characterized. Existing DCG models do not provide a satisfactory explanation to these conflicting interpretations of climate-glacier dynamics, which is partially due to the over-simplified assumptions of important processes and feedbacks that involve ablation dynamics, debris flux and property variation, surface ponding, and topographic evolution.

Mountains that exhibit DCGs typically have substantial vertical relief and erosional forces that produce significant mass flux from the sidewalls onto the glacier. In the central Karakoram in Pakistan, extreme relief and complex climate systems generate some of the largest DCGs in the world (Bishop et al., 2001; Hewitt, 2005; Copland et al., 2009). Precipitation rates can be highly variable in space and time caused by the dominance of regional climate systems and topography. A particular system such as the Westerlies or the Monsoon could dominate over an area over a specific time frame, and it is also possible that an area could receive precipitation from both systems for a period. Furthermore, topographic variation partially controls the degree of orographic precipitation and this would also vary depending upon which system dominants over an area (i.e., moisture conditions, wind velocity and direction). This very high degree of coupled climate-topographic interactions presents a challenge to the numerical modeling of climate-glacier dynamics.

The surface-energy balance determines the ablation rates on DCGs, and net long-wave and short-wave fluxes play a major role in that balance, but the atmospheric conditions through which that radiation must pass play an equally important role: if the atmosphere is cloudy then the incoming short- and long wave radiations are fundamentally altered. Additionally, atmospheric temperature above the surface is critical to determining precipitation type (rain, snow, or some combination of frozen/liquid water). For example, debris cover can provide a surface heat source that drives convection and precipitation in the overlying atmosphere (e.g., Collier et al., 2015); depending on the temperature, that precipitation may fall as snow which would accumulate on the glacier ice in the absence of the debris, but given the presence of the warm debris the snow may melt and percolate down to the glacier surface, thereby enhancing ablation.

Supraglacial ponding is another critical process on DCGs. Supraglacial ponds and lakes play an important role in glacier ice-loss as well as glacial hydrology (Fountain and Walder, 1998; Sakai et al., 2000; Wessels et al., 2002; Miles et al., 2016, 2018). Researchers have identified an increasing number of ponds on some large DCGs (Gibson et al., 2017). Studies have also indicated that the increase in spatial density of supraglacial ponds can be facilitated by localized thinning, insufficient drainage, collapse of water channels, and overall lowering that decreases the slope of the glacier altitude profile in the ablation zone (Sakai et al., 2000). Unfortunately, many of these important mechanisms have not been adequately studied and are often neglected in existing glacier models and simulations.

Such complexities are only now beginning to be understood through the use of numerical models (e.g., Collier et al., 2013; Rowan et al., 2015; Anderson and Anderson, 2016; Miles et al., 2018). Field observations of en-debris and sub-debris processes can be difficult to obtain given time, economic, and logistic constraints. Nevertheless, field observations are essential for understanding the magnitude of specific properties and processes, providing constraints for input into numerical models, and for validation and accuracy assessment of numerical modeling efforts. However, many mechanisms that govern glacier dynamics can not be fully understood through field observations and remote sensing data. Consequently, numerical modeling that evaluates new parameterization schemes to account for processes and important feedback is sorely needed to better understand complex climate-glacier dynamics of DCGs.

The objectives of this paper are therefore to discuss a multitude of complex interactions and uncertainties that limit our understanding of how DCGs may be responding to climate change. We review our current understanding of debris-covered glaciers and identify gaps in knowledge about some processes and feedbacks that appear to play important roles with respect to ablation dynamics. We also utilize numerical simulations to demonstrate various concepts and processes. We specifically discuss various issues and use our simulation results to identify future research pathways that can help eliminate uncertainty and promote new empirical and numerical-modeling research. We acknowledge that we cannot account for all processes, nor utilize fully comprehensive parameterization schemes that accurately predict process rates (an objective of numerical modeling research). Rather, we attempt to provide for a first-order characterization and understanding of processes and feedbacks based upon the simulations that we have incorporated into our discussion. Furthermore, it should be noted that this work should not be viewed as a formal modeling paper, complete with parameter sensitivity

and uncertainty analyses, as this is beyond the scope of our objectives.

We synthesize our treatment of this complex topic by organizing the paper based upon concepts related to climate-glacier system components. We first address climate forcing and specifically address radiative and precipitation forcing, where we identify some processes that should be considered regarding the surface energy balance in high relief mountains. We then discuss debris load properties and debris transport dynamics. We finally address various feedback mechanisms and system couplings on the glacier surface with respect to ablation, supraglacial water bodies, ice cliffs, and surface topography.

2. CLIMATE FORCING

Radiative and precipitation forcing govern glacier dynamics, although the partitioning of these forcing components in any particular geographic area is not well-known with any degree of certainty, given a multitude of multi-scale topographic effects and our inability to accurately characterize and account for radiative and precipitation processes (Bishop et al., 2019; Bush et al., 2020). For example, it is thought that radiative forcing dominates in the Eastern Himalaya, while precipitation forcing has the biggest influence in the western Himalaya (Bolch et al., 2012). Nevertheless, we require a much more detailed understanding of climate-glacier dynamics from an internal and external scale-dependent forcing perspective, as various aspects of climate, glacial, and geomorphological systems need to be accounted for. Unfortunately, we lack basic data regarding radiation transfer and precipitation components that govern glacier states, and we do not know the responses and sensitivity to climate change for many regions of the world (Bolch et al., 2012; Dobreva et al., 2017; Bishop et al., 2019; Bush et al., 2020; Farinotti et al., 2020). Furthermore, the data sets that we tend to rely upon for such information (e.g., climate simulations and re-analysis data) do not accurately characterize local-scale radiative and precipitation fluxes due to inadequate representation of topography and/or processes (Bush et al., 2020).

Energy balance calculation at the glacier surface (with or without debris) is the first step toward determining the low-level air temperature above the glacier, but it neglects potential temperature advection by atmospheric circulations (e.g., anabatic, katabatic, or frontal winds, which all advect temperature). Furthermore, during the daytime, heating of the debris cover itself can generate atmospheric convection above the debris leading to strong converging surface winds and potential precipitation, which can further alter the surface energy balance. Consequently, numerous radiative-transfer (RT) parameters, circulation dynamics and cloud properties, and convective, cyclonic and orographic precipitation mechanisms must be considered to understand glacier response and sensitivity to forcings.

2.1. Irradiant Fluxes

The short-wave and long-wave radiant energy components of the surface-energy balance strongly regulate ablation dynamics. The short-wave surface irradiance (E) components include the direct irradiance from the sun (E_b), the diffuse-skylight irradiance due to atmospheric scattering (E_d) and the adjacent-terrain irradiance (E_t). All of these components are space-time-topography-wavelength dependent, and numerical modeling is the only way to account for the inherent scale-dependent operation of orbital, atmospheric and lithospheric processes that govern the variability of the magnitude of these RT parameters over glaciers (Bishop et al., 2019). These radiation fluxes significantly contribute to ablation at a particular location depending upon the surrounding land cover and topographic conditions. Studies have estimated that the shortwave radiation usually accounts for 75% or more of total irradiance on glacier surfaces (Oerlemans and Klok, 2002).

2.1.1. Short-Wave Direct Irradiance

The direct irradiance is the dominant short-wave irradiance component (Proy et al., 1989; Olson and Rupper, 2019). It is strongly controlled by local and meso-scale topographic effects. It can be represented as:

$$E_b(\lambda) = \int_{\lambda_1}^{\lambda_2} E^0(\lambda) T^{\downarrow}(\theta_s, \lambda) \cos i S d\lambda, \tag{1}$$

where λ_l is wavelength, E^0 is the exo-atmospheric irradiance adjusted for Earth-Sun distance, $T^{\downarrow}$ is the downward atmospheric transmittance of radiation governed by atmospheric absorption and scattering, and θ_s is the solar zenith angle. Transmittance also accounts for the atmospheric optical depth that is partially governed by the relief structure of the landscape (i.e., altitude).

The cosine of the incidence angle ($\cos i$) characterizes the local topographic effects on irradiance given solar and terrain geometry relationships. Specifically, the incidence angle of illumination (i) between the sun and normal to the ground surface is defined as:

$$\cos i = \cos\theta_s \cos\theta_t + \sin\theta_s \sin\theta_t \cos(\phi_s - \phi_t), \tag{2}$$

where θ_s is the apparent solar zenith angle that accounts for altitude variations and atmospheric refraction given the atmospheric temperature and pressure profiles, θ_t represents the terrain slope angle, ϕ_s is the solar azimuth angle, and ϕ_t is the terrain slope-azimuth angle. Calculation of $\cos i$ is possible with the use of a digital elevation model, and negative values must be corrected to 0.0. Local topographic properties can have a significant effect on the magnitude of the direct irradiance that reaches the surface of a glacier. Ablation and meltwater transport, and gravitational sediment fluxes all alter the altitude, slope and slope azimuth of the ice and sediment surfaces of a glacier. A feedback between ablation-topography and surface irradiance controls the topographic evolution of a glacier surface (Huo et al., 2020). The importance of the local topographic conditions on the direct irradiance cannot be overlooked. The cosine of the incidence angle can range from 0 to 1 based upon slope angle and slope-azimuth angle variations caused by sediment transport and ablation processes. Based upon our simulations in the Karakoram (see **Figure 1**), direct irradiance values can be greater than 1,000

Wm^{-2}. Consequently, rapidly evolving topography should be accounted for as this sub-parameter strongly regulates ablation, all other factors such as debris properties being equal.

For many valley glaciers, the topographic shading on the direct solar radiation can be significant due to complex topography (Olson and Rupper, 2019). The S parameter in Equation (1) accounts for the meso-scale relief structure of the topography that governs the presence of cast shadows on the landscape. Cast shadows on the landscape are governed by the size of the solar disk and the Earth-Sun distance. More specifically, the solar angular width ($\alpha_s(t)$,[degrees]) in relation to topographic relief, will govern the overall length of a cast shadow in the direction of ϕ_s. This angle and other geometry parameters can be used to compute the planimetric length of the umbra and penumbra subregions that collectively represent the total cast-shadow region. The umbra is the region over the landscape where E_b is totally obstructed by the topography. Conversely, the penumbra region receives a fraction of E_b because a portion of the solar disk is obstructed by the topography. In the penumbra region, the fraction of E_b is governed by the pixel location. Consequently, a location in the umbra region would exhibit a shadow coefficient of 0.0, while a location in the penumbra region would exhibit a coefficient value ranging from $0.0 < S < 1.0$. Therefore, cast shadow locations can also include irradiance from E_b. Furthermore, because of the eccentricity of the Earth's orbit around the sun, the length of the cast shadow region varies non-linearly with time. Given the extreme relief in many mountain environments, cast shadows can significantly modulate direct irradiance over the course of a day, let alone over the course of an ablation season. The importance of cast shadows should also not be underestimated, as the S parameter strongly regulates the direct irradiance during the early morning and late afternoon, as governed by basin relief and solar geometry. Large areas of a glacier's surface can be in cast shadow (umbra) for hours during the day, thereby blocking the direct irradiance and decreasing the surface irradiance and ablation potential. It is more difficult to evaluate the significance of the penumbra on ablation, other than to say that the length of the penumbra in the direction of the solar azimuth angle causes a direct irradiance gradient that influences ablation depending upon its length. Numerical modeling and sensitivity analysis are required to have a better understanding of the entire S parameter. Consequently, the S parameter can have a significant to insignificant influence on glacier ablation depending upon environmental conditions and the total length of the umbra and penumbra and time that cast shadows are found over the glacier surface. Its modulating effects on ablation will increase during the ablation season as solar zenith angles increase.

Simulating the magnitude and distribution of E_b on a glacier surface is relatively straight-forward, given that topographic evolution resulting from ablation dynamics is accounted for with respect to local topographic properties and relief. We demonstrate relatively accurate simulated estimates of diurnal direct irradiance (1 day; July 24, 2004) using a SRTM 30 m DEM, and compared our simulation to field-based surface irradiance measurements collected on the same day by Mihalcea et al. (2008) for the same location on the Baltoro Glacier (**Figure 1**). We

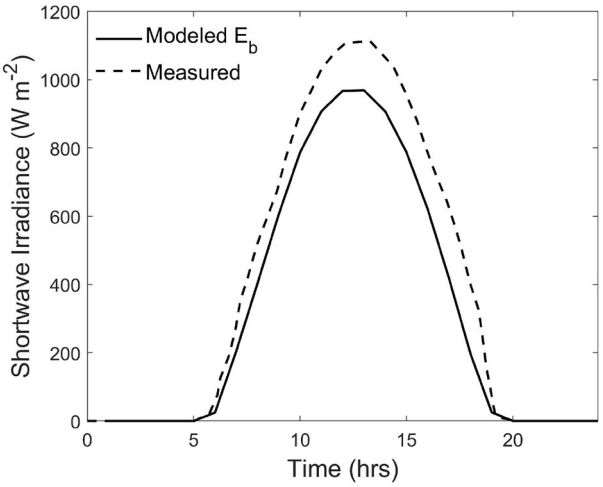

FIGURE 1 | Simulated short-wave direct-beam irradiance (E_b) component (wavelength range: 0.3 μm to 3 μm) for the Baltoro Glacier, compared to field measurements of short-wave irradiance at the same location on July 24th 2004. The discrepancy in magnitude is mainly caused by the diffuse-skylight irradiance and the adjacent-terrain irradiance.

accounted for orbital parameters based upon Berger (1978) and used the apparent solar zenith angle accounting for parallax and atmospheric refraction, assuming the temperature and pressure profiles of the atmosphere. In this simulation, however, we did not utilize ray-tracing to account for cast shadows. The simulation results are reasonable, the modeled E_b is less than measured E values in the field, as we did not account for E_d and E_t that is represented in the E values. Perhaps it is more important to notice the discrepancy in magnitude in the early morning and late afternoon, caused by cast shadows (i.e., shape at the base of the distribution is different). Rapidly changing magnitudes at these times clearly reveals the influence of cast shadows in E, vs. simulated E_b values. We would expect these differences to become more pronounced during the later stages of the ablation season as the solar zenith angles increases.

Challenges in estimating this dominant component more accurately involve better characterization of atmospheric conditions, use of higher-resolution DEMs for establishing initial conditions, and the development and evaluation of different parameterization schemes to account for those controlling parameters that govern the energy-balance at the glacier surface.

2.1.2. Short-Wave Diffuse-Skylight Irradiance

Atmospheric scattering will produce a hemispherical source of irradiance that contains isotropic and anisotropic components (Perez et al., 1986; Proy et al., 1989). The anisotropic nature of E_d has been the largest source of error for estimating this component, as it is governed by circumsolar brightening due to forward scattering by aerosols, and horizontal brightening due to Rayleigh scattering (Perez et al., 1986). A Two-stream approximation model assumes that there is a Rayleigh-scattering component (E_r), an aerosol-scattering component (E_a), and a secondary ground/sky-backscattering component (E_g) caused

by multiple interactions between the ground surface and the atmosphere (Proy et al., 1989; Gueymard, 1995; Zhang et al., 2015). One can account for single-scattering or a multiple-scattering Rayleigh atmosphere. The single-scattering albedo is required to account for aerosol scattering which is a function of both wavelength and humidity. Aerosol type and models such as rural, urban, maritime or tropospheric can also be accounted for Gueymard (1995). The ground backscatter component can be modeled by accounting for the zonal ground reflectance from the overall ground and sky reflectance (Gueymard, 1995). Numerous parameterization schemes are available that enable a reasonable characterization of this irradiance component for a horizontal surface (e.g., Bird and Riordan, 1986; Gueymard, 1995). Multi-scale topographic effects, however, need to be considered at each location on the landscape (Proy et al., 1989; Bishop et al., 2019).

Both local and meso-scale topographic properties govern E_d and Proy et al. (1989) provides a computation solution such that:

$$E_d(\lambda) = \int_{\phi_i=0}^{2\pi} \int_{\theta_i=0}^{\pi/2} L^{\downarrow}(\alpha_s, \theta_i, \phi_i) \cos I \sin\theta_i d\theta_i d\phi_i, \quad (3)$$

where $L^{\downarrow}$ is the downward radiance from sky-hemispherical incident directions θ_i and ϕ_i, and θ_i and ϕ_i are the zenith and azimuth angles from the hemisphere, α_s is the solar-elevation angle ($\alpha_s = \pi/2 - \theta_s$), and I is the incidence angle of the direction defined by sky-hemisphere and terrain geometry, similar to Equation (2) using incident geometry. Such a computation is computationally expensive given that E_d is wavelength dependent, and hemispherical topographic shielding must be accounted for by limiting the integration based upon the maximum relief angle for all hemispherical azimuth directions.

Basin relief production is primarily governed by paleo-glacier erosion and uplift history. There is a time disconnect such that the majority of the relief production occurred in the past, however the resulting relief (i.e., topographic shielding) partly influences the modern-day diffuse-skylight irradiance. Its altitudinal spatial variability can therefore govern the spatial variability in ablation. We demonstrate this topographic control using radiative and ablation simulations over the Baltoro Glacier in the central Karakoram (**Figure 2**). For this simulation, we did not perform the full integration of E_d because of the computational intensity of doing so over all wavelengths. Rather we used the algorithms from Bird and Riordan (1986) to estimate E_d on a horizontal surface, and then multiplied the results by the so-called skyview-factor coefficient that represents the relative magnitude of topographic shielding. The computation of this topographic parameter is highly scale dependent, and Bishop and Dobreva (2017) demonstrated that it is highly variable across mountain environments given the polygenetic nature of erosion dynamics and topographic evolution (for more parameter details see Dozier et al., 1981; Wilson and Bishop, 2013). Regarding the ablation simulations, we account for debris thickness distribution over the Baltoro Glacier from Mihalcea et al. (2008) and meltwater ponds to generate a temporally-averaged ablation rate over the glacier. We then compared the skyview-factor coefficient to simulated ablation over the glacier (**Figure 2**). Clearly there is a decrease in the ablation rate with altitude that accounts for the collective influence of cooler atmospheric temperatures and an increase in topographic shielding (lower skyview coefficient). At about $4,400 - 4,500$ m (below Concordia; Concordia is at about 4,691 m) topographic shielding begins to decrease and is associated with the confluence of glacier tributaries. It then abruptly increases with maximum topographic shielding being spatially coincident with the minimum ablation rate for the profile. These simulation results suggest that meso-scale topographic effects also play an important role governing the magnitude of E_d and ablation depending upon paleo-glacier erosion dynamics and basin relief production (i.e., erosion-uplift dynamics).

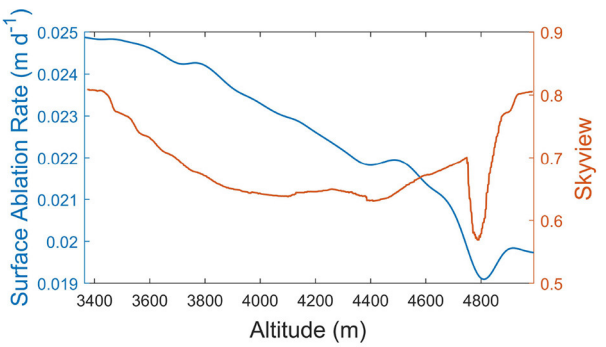

FIGURE 2 | Topographic shading effect on the simulated surface ablation rates for the Baltoro Glacier in 2004. The ablation rates are averaged over 30 m altitude bins. The skyview factor represents the topographic shielding that governs the diffuse-skylight irradiance. The abrupt drop in the skyview is associated with the minimum ablation along the profile, which highlights this meso-scale topographic effect on glacier surface ablation.

The significance of this secondary surface-irradiance parameter on ablation is difficult to ascertain, as numerical simulation sensitivity analysis focused on irradiance partitioning is sorely needed. We have demonstrated, however, that mesoscale topographic effects on the diffuse irradiance potentially regulate ablation rates based upon glacier erosion histories (i.e., relief production). Simulation results indicate that the magnitude of this parameter can range from relatively low or moderate energy levels in the visible portion of the spectrum (generally 5–200 Wm^{-2}) depending upon topographic conditions. Spatial distribution patterns of higher diffuse energy are most likely found at higher altitudes where basin relief significantly decreases. Furthermore, the influence of landcover conditions can also increase the magnitude of this component given high albedo surfaces (i.e., snow) and secondary scattering back to the surface.

2.1.3. Short-Wave Adjacent-Terrain Irradiance

The aforementioned irradiance components and surface Bi-Directional Reflectance Distribution Function (BRDF) interact with the surrounding terrain geometry to produce the adjacent-terrain irradiance (E_t). This irradiance component is extremely complicated but important to characterize, because variations in land cover and topographic complexity strongly regulate its

magnitude. Highly reflective materials such as felsic minerals, vegetation, and ice and snow coupled with steep slopes can cause significant irradiance that impacts ablation dynamics, and especially the retreat of ice-cliffs (Sakai et al., 2002; Buri et al., 2016).

The characteristics of surface reflectance properties can range between diffuse and specular (Iqbal, 1983; Zhang et al., 2015). We know, however, that the isotropic assumption of reflectance is not valid in mountains, and the surface BRDF (ρ_{brdf}) must be accounted for at each location on the landscape, as reflectance from the surrounding terrain and other glacier surface locations can contribute to E_t. The BRDF is used to describe the anisotropic nature of surface reflectance characteristics. It is a scattering function that describes anisotropic reflectance given all input-output angles. It is characterized as:

$$\rho_{brdf}(\theta_i^e \phi_i^e \theta_v^e \phi_v^e \lambda) = \frac{L(\lambda)}{E(\lambda)}, \tag{4}$$

where, L is the surface radiance and E is the surface irradiance ($E = E_b + E_d + E_t$). The effective illumination (θ_i^e, ϕ_i^e) and viewing directions (θ_v^e, ϕ_v^e) are a function of solar geometry and terrain geometry. Consequently, the topography has a significant affect on the BRDF (Zhang et al., 2015), and the intimate mixture of materials and structure of the surface also influence scattering direction. The BRDF, however, is difficult to measure accurately, and is also the basis for the computation of surface albedo, another important RT parameter that is difficult to estimate.

The irradiance component E_t can be characterized in the following fashion:

$$E_t(\lambda) = \int_{\phi_i=0}^{2\pi} \int_{\theta_i=0}^{\pi} L_s\left(\theta_i^e, \phi_i^e, \theta_v^e, \phi_v^e, \lambda\right) T_t^{\downarrow\uparrow}(\theta_v) \cos I_t S_t d\theta_i d\phi_i, \tag{5}$$

where L is the adjacent surface reflected radiance coming from the effective incident direction, ϕ_i is the hemispherical incident azimuth angle, θ_i is the incident vertical hemispherical zenith angle to account for terrain radiance above and below a pixel location, $T^{\downarrow\uparrow}$ is the atmospheric transmittance given the optical depth of the atmosphere due to relief and propagation zenith angle through the atmosphere (θ_v) between two locations, $\cos I_t$ represents the terrain incidence angle given the influence of the local terrain geometry in relation to the incident directional geometry, and S_t representing terrain blocking of the adjacent surface radiance between any two points of the surrounding terrain. As a general rule-of-thumb, the computation of E_t should account for the terrain conditions extending out to some distance (e.g., 5 km) from each pixel location (Proy et al., 1989). However, the appropriate distance in any direction can vary as a function of the anisotropic nature of the topography, given the orientation of the structural fabric of the topography related to differential erosion and tectonics. As such, the adjacent hemispherical distribution of locations that can contribute to E_t for any particular location can be extremely scale dependent, given that it is also a function of altitude, such that the contributing zones of adjacent-terrain irradiance may be spatially contiguous or spatially fragmented. To our knowledge, this level of complexity has not been evaluated with respect to determining its impact on ablation dynamics, although it most likely plays a role in ice-cliff retreat when considering the coupled influence of the long-wave adjacent-terrain irradiance term.

The short-wave adjacent-terrain irradiance is thought to be a tertiary surface irradiance component that does not significantly affect ablation. However, given our parameterization scheme and the nature of highly directional and diffuse reflectance components associated with the BRDF, coupled with changing glacier surface topography, solar zenith and solar azimuth angles, the E_t component is likely to be highly variable in space and time, and facilitate ablation in general. The significance of this component could be greater than the diffuse irradiance given specific topographic and adjacent land cover conditions, such as at depression areas that are surrounded by highly reflective felsic minerals and snow.

2.2. Precipitation

Precipitation in mountainous regions is partly modified by avalanche redistribution of snow, and is determined by uplift in traveling frontal zones or by orographic uplift. The former will move spatially with the frontal system while the latter will remain stationary given the topography and the wind direction. Determining where near-constant orographically-forced precipitation occurs may lead to an explanation of why a particular glacier exists at one location but not in another nearby location.

Separating orographic precipitation from frontal precipitation is difficult from observations (in which all precipitation is combined). For orographic precipitation one needs to know the wind direction, the atmospheric moisture content, and the topography itself but one also has to track the properties of the air parcels along their trajectories to keep track of the amounts of condensation, evaporation, and precipitation as the air travels up and perhaps over multiple peaks, potentially losing all of its water content along the way. Some attempts at quantifying this process have been made using a combination of a high resolution DEM and downscaled reanalysis climate data (e.g., Dobreva et al., 2017).

Regardless of the driving mechanism behind mountain precipitation, the precipitate-formation process is mostly a cold-based one given typical surface temperatures at high elevations and the adiabatic lapse rate, i.e., the precipitate-formation process occurs at temperatures below freezing and so is governed by the Bergeron-Findeisen process. According to this process, in a cloud that has a mix of ice crystals and supercooled water droplets, water vapor in the cloud preferentially deposits on the ice crystals because of the lower saturation vapor pressure over ice than over water. As the water vapor decreases through deposition on the ice, the supercooled droplets evaporate and lose their water to the growing ice crystals, which may then grow large enough to overcome any updrafts and fall to the surface. This process dominates mid-latitude precipitation (even during the summer) and at high altitudes.

Most precipitation in mountainous regions therefore begins frozen; whether it remains frozen on its way down to the surface is dependent on the atmospheric temperatures through which it

falls. At high altitudes, it is more likely to remain frozen than, for example, at sea level in mid-latitudes, but if conditions are warm enough then it will melt completely and fall as rain (or, if the precipitate does not have enough time to melt completely it will fall as graupel, sleet, or freezing rain).

Snowfall above the equilibrium line altitude (ELA) is paramount for a glacier's survival. Climate change can alter the ELA up or down, depending on local conditions, but with a general warming trend ELAs on average are rising. If the ELA rises above the peak of the mountain then no glacier can exist. If atmospheric conditions above the ELA become conducive to rain then glacier ablation will be accelerated.

When debris cover is present additional factors must be taken into account. If the debris temperature is below freezing, snowfall would accumulate as on a debris-free glacier. If the debris cover is above freezing, however, then it will melt the snow leading to percolation of liquid water onto the glacier surface that can enhance ablation. Refreezing of the percolated water at the glacier surface is possible, with the release of latent heat into the interstitial spaces of the debris cover (Collier et al., 2014, 2015). The debris cover fundamentally alters the fluxes of sensible and latent heat to the overlying atmosphere (Collier et al., 2014). In addition, a relatively warm debris cover (through daytime solar heating) can trigger convection in the atmosphere above and produce precipitation that melts on contact and increases surface ablation (Collier et al., 2015). So DCGs have the potential to increase their own ablation rates through dynamic interactions with the overlying atmosphere as well as the underlying glacier.

TABLE 1 | Debris-cover physical and radiative-transfer properties that regulate ablation in space and time.

Physical properties	Symbol [SI units]	Relevance
Debris thickness	h_d [m]	Governs distribution and magnitude of ablation and thermal gradient
Mineralogical/rock composition		Governs radiation transfer properties and thermal gradient
Porosity/particle size	φ [dimensionless]	Governs thermal gradient and bulk thermal conductivity
Moisture content	w [dimensionless]	Governs thermal properties and temperature profiles
Slope	θ_t [rad]	Governs surface irradiance and sediment transport
Slope Azimuth	ϕ_t [rad]	Governs surface irradiance and sediment transport
Temperature	T_d [K]	Governs long-wave irradiant flux and convective atmospheric motion
Radiative-Transfer Properties		
Albedo	α [dimensionless]	Governs irradiance
Emissivity	ε [dimensionless]	Governs irradiance

3. SUPRAGLACIAL DEBRIS LOAD

3.1. Composition and Properties

Investigators are increasingly recognizing the significance of the supraglacial debris load as a major controlling factor in regulating ablation and the morphological evolution of DCGs (Adhikary et al., 2000; Nicholson and Benn, 2006; Reid et al., 2012; Rowan et al., 2015; Anderson and Anderson, 2016; Zhang et al., 2016; Gibson et al., 2017). Field data and numerical-modeling efforts (given various assumptions) demonstrate the general relationship between debris thickness and ablation rate, as thicker debris loads decrease the thermal energy available for ablation at the debris/ice interface, while thin and moisture laden debris can significantly accelerate ablation beyond that of debris-free conditions (Mattson, 1993; Kayastha et al., 2000; Reznichenko et al., 2010). This general relationship, however, does not account for a variety of debris-load properties, processes, and feedbacks regarding ablation dynamics, as supported by findings related to the "debris-covered glacier anomaly" (Salerno et al., 2017) and numerical modeling efforts (Anderson and Anderson, 2016; Zhang et al., 2016; Gibson et al., 2017; Huo et al., 2020). Consequently, the multi-faceted nature of this controlling factor is not adequately understood, as there are many unknowns with regard to properties and processes that govern ablation dynamics, and research clearly reveals the relatively high spatio-temporal variability in debris properties and processes that should be accounted for Scherler et al. (2011b); Reid et al. (2012); Rowan et al. (2015); Yue et al. (2017). The complexity of the problem is highlighted by the relatively large number of debris, near-surface and scale-dependent topographic parameters that partially govern ablation. **Table 1** lists various physical and radiative-transfer properties that all contribute toward regulating the magnitude of ablation in space and time. It is also important to realize that location/scale specific parameters related to the topography and lithology beneath and surrounding a glacier also contribute to spatial and property variations in the debris load, as debris sources and mineralogical composition of debris and rocks is governed by the nature of the geological setting, and the geomorphological system within the glacial basin.

An important first-order property that requires consideration is the particle size/distribution of the debris load. This property can be highly spatio-temporally variable over a glacier, and is regulated by source and sediment-transport dynamics. It can have a significant impact on ablation dynamics, as "particles" can include dust, fines, gravel, cobbles, rocks, isolated boulders, and boulder fields (**Figure 3**; the full range of debris particle sizes). Such heterogeneous conditions are common on many glaciers around the world, and "particle" distributions can be significantly different on glaciers within a region, depending upon paleo-climate-glacier dynamics (Bush et al., 2020). Such variations are the result of polygenetic sediment-transport dynamics involving mass movements, aeolean, suprafluvial, englacial, gravitational, and ice-flow transport mechanisms. Spatio-temporal variations of this aspect of the debris load are usually not considered, and homogeneous unconsolidated debris conditions are assumed, which causes uncertainties in ablation estimates.

The composition of the debris load is another important property. It is rarely accounted for, although it can be taken into consideration by using estimates of the debris bulk conductivity. It not only governs the bulk thermal

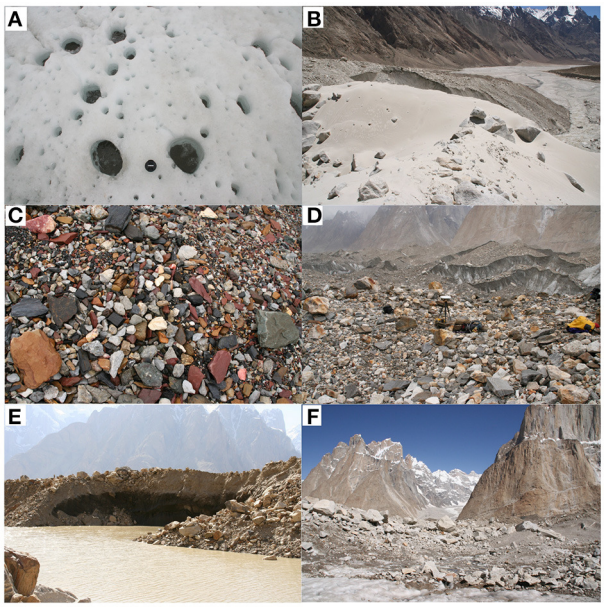

FIGURE 3 | Supraglacial debris cover conditions on the Baltoro Glacier during the summer of 2005. The nature of the supraglacial debris load can vary significantly with respect to particle size, composition, and debris thicknesses. **(A)** Cryoconite holes at Concordia at 4,500 m. These features form as wind blown dust, soot and particles that absorb radiation generate holes that contain water that contributes further to increase ablation and the depth and width of the hole. **(B)** Wind blown silt and sand deposits at the terminus of the glacier. Wind turbulence caused by up valley winds and altitude variations between the pro-glacial valley floor and the glacier surface results in wind-sorted supraglacial debris. **(C)** Supraglacial debris load consisting of gravel, pebbles, and cobble-sized particles. Notice the felsic and mafic compositional variations of particles. **(D)** Supraglacial debris dominated by larger rocks over the glacier surface. Rock spatial density greatly governs the spatial variation in ablation dues to shadowing and rock mass influence on the vertical debris load thermal gradient. **(E)** Debris load consisting of sediment, rocks, and boulders. Debris thickness is about 5 m. Debris thickness can be highly variable over a glacier surface depending upon a multitude of controlling factors. **(F)** Debris loads in the Himalaya frequently consist of boulder fields, that make it difficult to accurately assess or model thermal gradients, given shadowing and alternation of the wind field. Photo credit: Michael P. Bishop.

properties of the debris, but also the surface reflectance properties and the surface energy balance of the short-wave irradiance (i.e., albedo). Consequently, remote sensing analysis and absorption-feature modeling can be used for mineral detection and determining the composition of the debris using hyperspectral data. This approach can provide more explicit estimates of the surface composition and distribution of moisture-laden debris. Such data regarding the debris load are too logistically difficult to acquire in the field, but high-resolution hyperspectral remote-sensing capabilities are now available using uncrewed aerial systems (UAS) to better assess "particle" distributions, surface mineralogy and other parameters that are not usually accounted for (e.g., Fyffe et al., 2020).

Debris load thickness has been shown to be highly variable (Mihalcea et al., 2008; Fyffe et al., 2020). Many glaciers exhibit low-frequency debris thickness variation (the generally thicker debris toward the terminus) controlled by surface ice-flow transport dynamics and englacial transport of sediment and rocks into the terminus region (Anderson and Anderson, 2016; Wirbel et al., 2018). Higher-frequency debris thickness variations must also be considered, as the debris load is modulated by supra-fluvial transport, topography-driven gravitational transport, and other ablation dynamics including supraglacial lake development and evolution. Furthermore, a high percentage of debris cover lowers the glacier surface albedo that partially counters the debris insulation effect (Fyffe et al., 2020). Such complexities have not been adequately investigated, and it is essential to note that complex feedbacks exist between sediment fluxes, ablation, topography and the surface-energy balance (Huo et al., 2020). Although several approaches have been developed to estimate the distribution of debris thickness (e.g., Mihalcea et al., 2008; Zhang et al., 2011; Reid et al., 2012; Rounce et al., 2018), higher-frequency variations in debris thickness and the spatial variability of ablation is not known with any degree of certainty on most DCGs.

Field measurements suggest that debris temperature gradients are approximately stable and linear with depth during the ablation season (Rowan et al., 2021), although the linearity and stability depend on the time scale, and linearity is also dependent upon the debris thickness. Assuming linearity, debris surface temperature can be used to estimate sub-debris ablation, which is also controlled by debris thickness, and thermal conductivity (Nakawo and Young, 1981; Nicholson and Benn, 2006). Given shallow debris thicknesses, relative homogeneity in particle distribution, and lack of moisture-laden sediment, this first-order approximation assumes isotropic conditions with respect to various properties. With greater debris load thicknesses, however, porosity variation has the potential to alter the thermal gradient given the translocation of the fine size-fraction of particles and presence of moisture-laden sediment. Therefore, the thermal conductivity of debris can be difficult to determine given the complex composition and pore-space conditions. Nicholson and Benn (2006) presented an approach to address this issue using measured temperature profiles. Based on this model, the bulk thermal conductivity of the debris layer (k_d) can be written as:

$$k_d = \left(c_d \rho_d (1-\varphi) + c_v \rho_v \varphi\right) \kappa, \tag{6}$$

where c_d, ρ_d, c_v, ρ_v are the specific heat capacity and density of debris, and specific heat capacity and density of the pore-space filler, respectively. φ is the porosity, and κ is the apparent thermal diffusivity of the debris, which can be determined using the thermal diffusion equation:

$$\frac{\partial T_d(z,t)}{\partial t} = \kappa \frac{\partial^2 T_d(z,t)}{\partial z^2}, \tag{7}$$

where T_d is the debris temperature, which is a function of depth (z) and time (t). κ can then by determined from the measured temperatures-time and temperatures-depth variations. Another method was presented by Reid and Brock (2010), based on which,

the debris was broken down to multiple thin layers to estimate the thermal conductivity and internal temperature profiles:

$$\rho_d c_d \frac{\partial T_d(z,t)}{\partial t} = \frac{\partial}{\partial z}\left(k_d \frac{\partial T_d(z,t)}{\partial z}\right), \quad (8)$$

Debris moisture conditions, mineral mixing, debris surface structure, and surface topography can also significantly influence the surface albedo that regulates debris temperature and ablation (Pelto, 2000; Nicholson and Benn, 2006). Accurate estimation of the albedo based upon the surface BRDF is difficult to compute, and rapidly changing glacier-surface dynamics should cause the surface albedo to exhibit relatively high spatio-temporal variability (Takeuchi and Li, 2008; Yue et al., 2017). Therefore, better estimates of debris surface reflective parameters are required using more reliable parameterization schemes.

We demonstrate this using numerical simulations and accounting for the spectral reflectance of minerals that make of the debris load of the Baltoro Glacier. Specifically, we utilize a radiation-transfer approach (Coakley, 2003) to compute the broadband surface albedo (α) based on the mixing of sediments and water at each grid cell, such that:

$$\alpha = \frac{\int_{\lambda_1}^{\lambda_2} L(\lambda)}{\int_{\lambda_1}^{\lambda_2} E(\lambda)}, \quad (9)$$

where E is the total short-wave irradiance and L is the reflected surface radiance, which, based on an isotropic (Lambertian) assumption, can be written as (Bishop and Colby, 2011):

$$L(\lambda) = r_{mc}(\lambda)\frac{E(\lambda)}{\pi}, \quad (10)$$

where r_{mc} is the spectral reflectance of the mineralogical composite representing the debris, which is considered as a composite reflectance of different types of minerals. The debris lithological distribution over the Baltoro Glacier was based on Gibson et al. (2017), which indicates that the surface is mostly covered by a composite of gneiss (about 53%), granite (about 30%), and schist metasediment (about 17%). Simulated results in **Figure 4** reveal significant spatial variations in the surface albedo over the lower ablation zone of the Baltoro Glacier caused by mineralogical and moisture variations. We performed the narrow-band to broad-band conversion of surface albedo using ASTER imagery based on the work of Liang (2001), and confirmed that our simulated values are very close to the remote-sensing approach. In the future, the use of semi-empirical BRDF models should be used with multi-angle reflectance imagery to generate higher quality albedo estimates for glacier surfaces.

3.2. Debris Transport

Debris loads are mobile due to ice-flow, gravitational movement, and fluvial processes (Anderson, 2000; Benn and Evans, 2014; Anderson and Anderson, 2016, 2018; Zhang et al., 2016; van Woerkom et al., 2019; Fyffe et al., 2020). Although the exact glacial debris production mechanisms have not been fully understood, most investigators consider the main sources are from headwalls, sidewalls, basal erosion and moraines (Anderson, 2000; Benn and Owen, 2002; Anderson and Anderson, 2016; van Woerkom et al., 2019). Studies have observed mass transport from landslides (Benn and Evans, 2014), avalanches (Benn and Lehmkuhl, 2000), and rockfalls from valley walls (Benn and Evans, 2014). Englacial debris loads and rock encapsulated by basal erosion also contribute to the total debris mass balance, and several models have been developed to investigate the transport of englacial debris loads (Anderson and Anderson, 2016; Wirbel et al., 2018).

One of the first models of supraglacial debris flux was developed by Anderson (2000), which describes the diffusive debris flux originated from medial moraines in valley glaciers. Anderson and Anderson (2016) and Anderson and Anderson (2018) developed a similar model that couples with ice dynamics to investigate the longer-term evolution of debris cover. Moore (2018) presented a comprehensive study on the gravitational debris transport across the ice surface, as the topography evolves due to melt. A theoretical framework was developed for assessing slope stability and gravitational mass transport accounting for meltwater balance on ablating ice. Modeled results provided insights into the geometry of stable slopes as a function of debris thickness and texture. Another recent study by Fyffe et al. (2020) provides valuable field observations on the rates and forms of debris transport. van Woerkom et al. (2019) studied the debris transport from lateral moraines using high resolution DEMs and found that the lateral moraines contribute to debris thickening along the margin of the glacier surface.

Here we discuss two dominant processes that govern debris movement on a glacier at different spatio-temporal scales: the gravitational process that operates at smaller spatio-temporal scales given complex glacier topography, and the advective-diffusive processes that control debris flux over larger spatio-temporal scales governed by the ice-flow .

3.2.1. Gravitational Debris Fluxes

Gravitational debris movement (such as sliding and slumping) occurs on hillslopes and on glacier surfaces (Benn and Evans, 2014; Fyffe et al., 2020). Gravity-driven debris flux regulates the local thickness distribution of supraglacial debris during the ablation season when the surface topography is constantly changing under rapid melting, especially around melt hotspots such as supraglacial ponds and ice-cliffs. Field observations have identified sediment sliding or slumping off steepening ice-cliffs due to ice-cliff retreat and supraglacial lake expansion (Buri et al., 2016; Miles et al., 2017).

Gravity, internal friction and basal resistance force govern the gravitational movement of debris. Based on the debris flow model by Chen and Lee (2000), the unit net force acting on a debris column, F, can be written as:

$$F_x = \rho_d g[\frac{z_x}{z_x^2+z_y^2+1} - k\frac{dh_d}{dx} - \frac{1}{\sqrt{z_x^2+z_y^2+1}}\frac{u_x}{\sqrt{u_x^2+u_y^2+1}}(1-r_u)tan\phi], \quad (11)$$

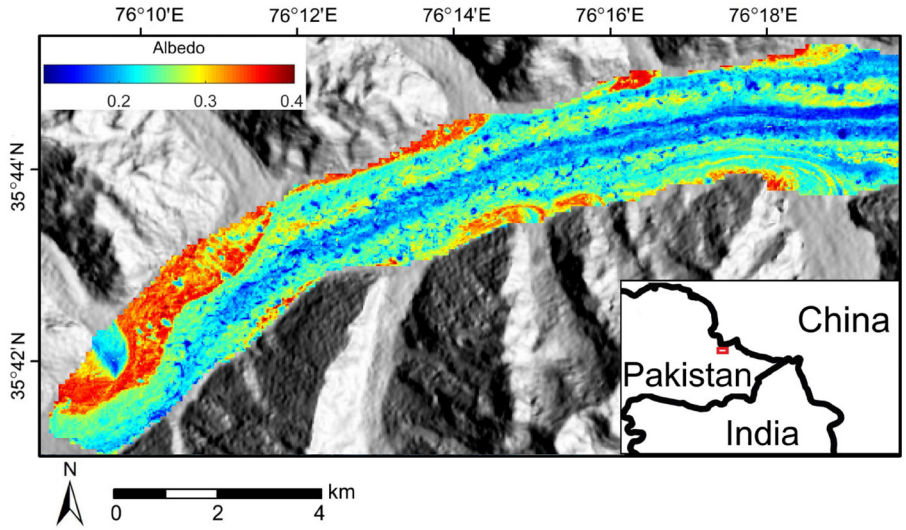

FIGURE 4 | Modeled surface albedo over the lower ablation zone of the Baltoro Glacier. The geomorphological conditions were estimated from an ASTER scene acquired on August 14th, 2004 (AST_08_00308142004054614).

$$F_y = \rho_d g[\frac{z_y}{z_x^2 + z_y^2 + 1} - k\frac{dh_d}{dy} - \frac{1}{\sqrt{z_x^2 + z_y^2 + 1}}\frac{u_y}{\sqrt{u_x^2 + u_y^2 + 1}}(1 - r_u)tan\phi], \quad (12)$$

where ρ_d is debris density, g is the gravitational acceleration, z_x and z_y are the first derivatives of ice-surface elevation in the horizontal and vertical directions, respectively, k is the pressure ratio as defined by Chen and Lee (2000), u_x and u_y are debris velocity components, r_u is the constant pore-pressure ratio, and ϕ is the dynamic internal friction angle of the debris. The first term on the right represents the gravitational force, the second term describes the internal friction of debris particles, and the third term represents the resistance force at the base of the debris column. Gravitational debris flux governs the local redistribution of debris thickness during the ablation season when the ice surfaces topography changes rapidly due to melt. The transport of a thin debris cover, however, is strongly controlled by more complex processes such as fluvial transport and rain wash (Fyffe et al., 2020).

3.2.2. Ice-Flow and Debris Advection

Ice-flow describes the glacier motion that governs the advective debris transport from the production zone to the terminus (Benn et al., 2012; Rowan et al., 2015; Anderson and Anderson, 2016; Wirbel et al., 2018). Therefore, ice-flow dynamics play a fundamental role in debris transport as demonstrated by recent numerical simulations (e.g., Anderson and Anderson, 2016; Wirbel et al., 2018).

Ice-flow velocity is governed by multiple factors such as the ice thickness and basal water pressure, and many DCGs exhibit high flow velocities even though they have stable termini (Copland et al., 2009; Quincey et al., 2009, 2011). The surface velocity field can be determined from remote sensing analysis, estimating englacial ice-flow velocities can be challenging, although estimates are usually sufficient for computing particle trajectories if far enough away from the bed (about 80% of the ice depth). Therefore, most studies use ice-flow models (such as the shallow ice approximation) to solve the englacial velocity field (Herman and Braun, 2008; Bueler and Brown, 2009; Anderson and Anderson, 2016), which usually requires ice thickness measurements from geophysical surveys using seismic or radio sounding (McNabb et al., 2012). Modeled ice-flow velocities often suffer from high uncertainty (Farinotti et al., 2017), however, more accurate models have been developed to account for basal melt, temperature-adjusted ice properties and rugged bed topography (e.g., Bueler and Brown, 2009; Egholm et al., 2011).

Debris advection is governed by the ice-flow velocity field (Benn and Evans, 2014; Anderson and Anderson, 2016; Wirbel et al., 2018). A recent model was developed by Anderson and Anderson (2016), in which the englacial and supraglacial debris advection were modeled under a steady debris input to understand the mechanisms in the debris-glacier-climate system. Simulations indicated that debris has significant control on glacier length and gradients of ice discharge, ice thickness, and surface velocities. Their model demonstrated that high debris flux slows down the glacier and contributes to extending its length. Based on this , the rate of change of supraglacial debris thickness in the ablation zone can be written as (Anderson, 2000; Anderson and Anderson, 2016, 2018):

$$\frac{\partial h_d}{\partial t} = \frac{c_s M_s}{(1 - \varphi)\rho_d} - \nabla \cdot (h_d \mathbf{u_s}), \quad (13)$$

where h_d is the surface debris thickness, t is time, c_s is the near-surface debris concentration, M_s is surface ablation rate, and $\mathbf{u_s}$

is surface ice velocity. The use of advection is valid for glacial debris transport because advection is defined as the transport of materials due to the bulk motion of a fluid, and glacier ice is a form of a viscoelastic fluid that is the basis for all modern ice-flow models. **Figure 5D** shows the simulated supraglacial debris advection based on Equation (13) given the initial debris thickness (**Figure 5A**) and surface velocity (**Figure 5C**).

The transport of englacial debris and its contribution to the surface debris load is controlled by ice-flow dynamics, given that the vertical component of ice velocity usually points upward in the lower glacier where ice thickness increases toward the terminus. These processes have been described by Anderson (2000), and demonstrated in the simulations by Anderson and Anderson (2016) and Wirbel et al. (2018). The contribution of englacial debris load may explain the debris mass balance issue discussed by van Woerkom et al. (2019). The most recent englacial debris transport model was presented by Wirbel et al. (2018), in which both the advection and diffusion of englacial debris are accounted for:

$$\frac{\partial c_e}{\partial t} = \nabla \cdot (D \nabla c_e) - \nabla \cdot (c_e \mathbf{u_e}) + r, \tag{14}$$

where c_e is the concentration of englacial debris, D is the diffusion coefficient, $\mathbf{u_e}$ is englacial ice velocity, and r represents englacial debris sources or sinks.

Remote-sensing approaches have been used to map debris thickness distributions (Mihalcea et al., 2008; Juen et al., 2014; Gibson et al., 2017; Rounce et al., 2018); the results, however, suffer from high uncertainties due to the instantaneous nature of satellite imagery and the complex properties of debris. Further investigations on debris production and transport modeling are required to better address the spatial patterns of surface melt and supraglacial morphological conditions.

4. ABLATION DYNAMICS

Surface melt dominates the ablation of a DCG (Hambrey et al., 2008; Reid and Brock, 2014; Rowan et al., 2015). The melt rate is strongly affected by the properties of debris loads and the presence of supraglacial water bodies due to their strong impact on the energy transfer dynamics (Sakai et al., 2000; Nicholson and Benn, 2006; Reid and Brock, 2010; Fyffe et al., 2014; Miles et al., 2016).

Field measurement of ablation is usually conducted through monitoring ablation stakes at multiple locations on the glacier surface. Ablation rates at locations with different debris thickness are measured by several studies, and field data showed that debris thickness is a predominant factor that governs the sub-debris ablation rate (Mattson, 1993; Kayastha et al., 2000; Rounce et al., 2015). Given the complex debris effects, empirical approaches such as the degree-day method for estimating ablation may be highly unreliable for DCGs (Braithwaite and Olesen, 1990; Nicholson and Benn, 2006). Therefore, physics-based surface energy balance models are widely used for estimating sub-debris ablation (e.g., Nicholson and Benn, 2006; Reid and Brock, 2010, 2014; Fyffe et al., 2014; Miles et al., 2016), and several remote-sensing approaches have been developed to estimate the key parameters, such as the thickness and thermal properties of debris (e.g., Mihalcea et al., 2008; Zhang et al., 2011; Foster et al., 2012; Juen et al., 2014).

Several recent studies have successfully used the surface energy balance model to estimate ablation on DCGs. For example, Fyffe et al. (2014) used a distributed model to compute melt rate on the Miage glacier in Alps. Rounce et al. (2015) compared the influences of debris thermal conductivity, albedo, and surface roughness on the surface energy balance of the Imja-Lhotse Shar glacier in Nepal. These results highlighted that: (1) Unlike the thick debris layer, a thin debris is sensitive to air temperature variation and water content, therefore areas with wet thin debris must be identified. (2) Subdebris ablation is more sensitive to the changes in thermal conductivity than surface roughness and albedo. (3) It is important to account for the realistic topographic shielding and wind speed over the glacier surface in the energy balance model. (4) Many model parameters need to be calibrated using field measurements or remote sensing data as they can be highly site-specific. The energy balance model at the debris/air interface can be written as (Nakawo and Young, 1981; Nicholson and Benn, 2006; Zhang et al., 2011; Rounce et al., 2015):

$$Q_s + Q_l + Q_h + Q_e + Q_c = 0, \tag{15}$$

where Q_s is the net shortwave radiation flux, Q_l is the net long-wave radiation flux, Q_h is the net sensible-heat flux, Q_e is the net latent-heat flux, and Q_c is the conductive heat flux into the debris which governs the ablation rate. Net radiation fluxes dominate glacier surface energy balance and significantly control surface ablation rates (Nicholson and Benn, 2006; Cuffey and Paterson, 2010). The net shortwave radiation flux and the net long-wave radiation flux can be computed as:

$$Q_s = (E_b + E_d + E_t)(1 - \alpha), \tag{16}$$

$$Q_l = \varepsilon_a \sigma T_0^4 - \varepsilon_s \sigma T_s^4 + \varepsilon_t \sigma T_t^4, \tag{17}$$

where E_b is the direct-beam irradiance from the sun, E_d is the diffuse-skylight irradiance, E_t is the adjacent-terrain irradiance, and α is the surface albedo. For the long-wave radiation fluxes, ε_a, ε_s and ε_t are the emissivity for the air, glacier surface and adjacent terrain, respectively, σ is the Stefan-Boltzmann constant, T_0 is the air temperature which is a function of altitude, T_s is the glacier surface temperature, and T_t is the surface temperature of the surrounding terrain, which is responsible for the long-wave adjacent-terrain irradiance.

The energy balance at the debris/ice interface can be written as (Nakawo and Young, 1981):

$$Q_m = Q_c^{\downarrow} - Q_c^{'}, \tag{18}$$

where Q_m is the heat flux used for sub-debris ice ablation, $Q_c^{\downarrow}$ is the conductive heat flux from the debris, and $Q_c^{'}$ is the

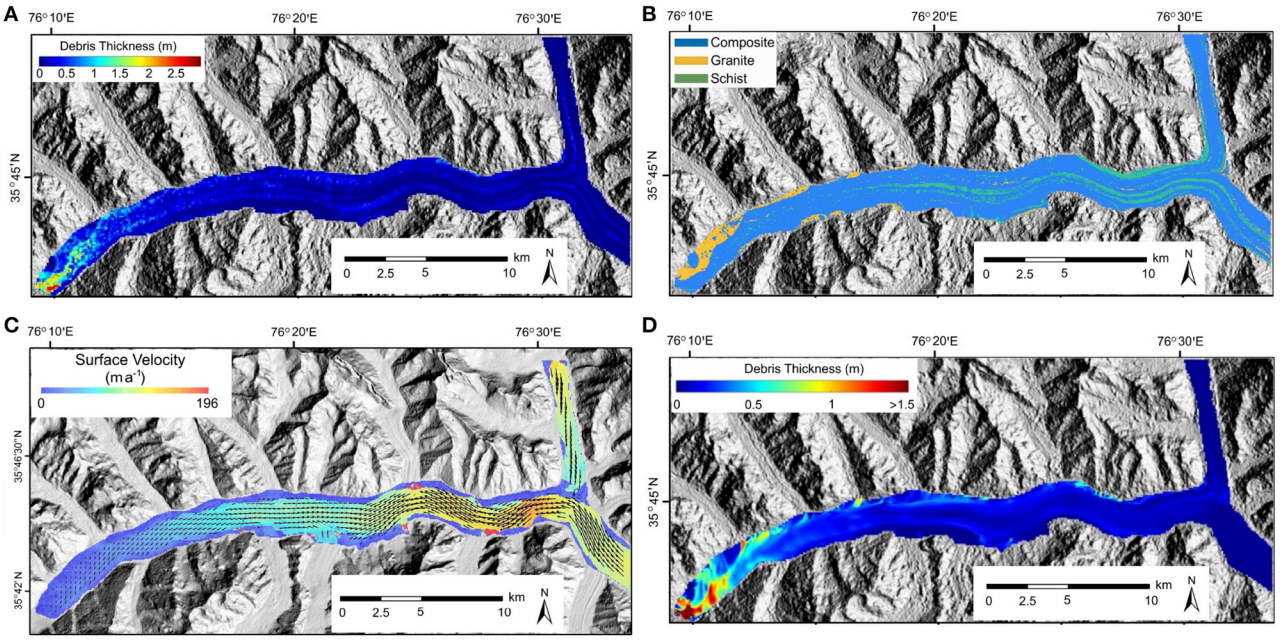

FIGURE 5 | Supraglacial debris conditions for the Baltoro Glacier. **(A)** The debris-thickness distribution over the Baltoro glacier in summer 2004 computed from ASTER surface kinetic temperature data following the approach by Mihalcea et al. (2008). **(B)** Debris rock type distribution over the Baltoro Glacier in 2004 based on the remote-sensing analysis by Gibson et al. (2017). **(C)** Surface ice-flow velocity of the Baltoro Glacier estimated from a Landsat-8 OLI panchromatic image pair acquired on September 15, 2004 and September 2, 2005. **(D)** Simulated debris transport due to ice-flow (advection process) over a 50-year period. Result represents the debris thickness distribution for year 50..

heat flux toward the ice that is not used for ablation, which is often negligible under a temperate ice assumption (Cuffey and Paterson, 2010).

Most models assume constant heat storage and a linear debris-temperature gradient, then Q_m during the ablation season can be computed using the simplified heat-flux approach based on daily mean values at a minimum 24 h timescale (Nakawo and Young, 1981; Nicholson and Benn, 2006):

$$Q_m = k_d \frac{(T_s - T_i)}{h_d}, \tag{19}$$

where k_d is the bulk thermal conductivity of the debris layer accounting for water in pore-spaces, T_i is the ice temperature. The sub-debris melt rate (M_s) can then be computed as (Nakawo and Young, 1981; Nicholson and Benn, 2006):

$$M_s = \frac{Q_m}{\rho_i L_f}, \tag{20}$$

where L_f is the latent heat of fusion for ice, and ρ_i is the density of ice.

Precipitation can also contribute to surface melt (Fujita et al., 2014; Fyffe et al., 2014; Miles et al., 2016), and several methods have been used to account for this process (e.g., Reid and Brock, 2010; Fujita et al., 2014; Miles et al., 2016). Although more complicated processes have not been accounted for, such as the energy exchange between rainfall and heated debris that could eventually lead to additional ice melt. The latent and sensible heat fluxes have been found to be less significant with respect to melt variability compared to the shortwave and longwave fluxes in different climates (Sicart et al., 2008).

Using the aforementioned equations, **Figure 6A** shows the simulated ablation rates on the Baltoro Glacier in the Karakoram, using surface conditions presented by Mihalcea et al. (2008). Note that the modeled values are reasonably similar to field measurements on several Himalayan glaciers (Nicholson and Benn, 2006), including Barpu Glacier (Khan, 1989), Khumbu Glacier (Kayastha et al., 2000), and Rakhiot Glacier (Mattson, 1993). **Figure 6B** is an example of the temporal variation in ablation rate as a function of debris thickness over an ablation season, which highlights the important role of the dynamics involving debris redistribution in regulating local ablation rates on the glacier surface, especially for areas with water bodies and ice-cliffs. **Figure 7** depicts simulated surface ablation rates compared to the remote-sensing-based estimates (Mihalcea et al., 2008). Both results show suppressed ablation in the terminus region and higher ablation around inter-moraine valleys corresponding to the difference in debris thickness (**Figure 5A**).

5. SUPRAGLACIAL WATER BODIES AND ICE CLIFFS

Supraglacial water bodies and ice-cliffs elevate the ice loss of DCGs (Anderson, 2014; Reid and Brock, 2014; Steiner et al., 2015;

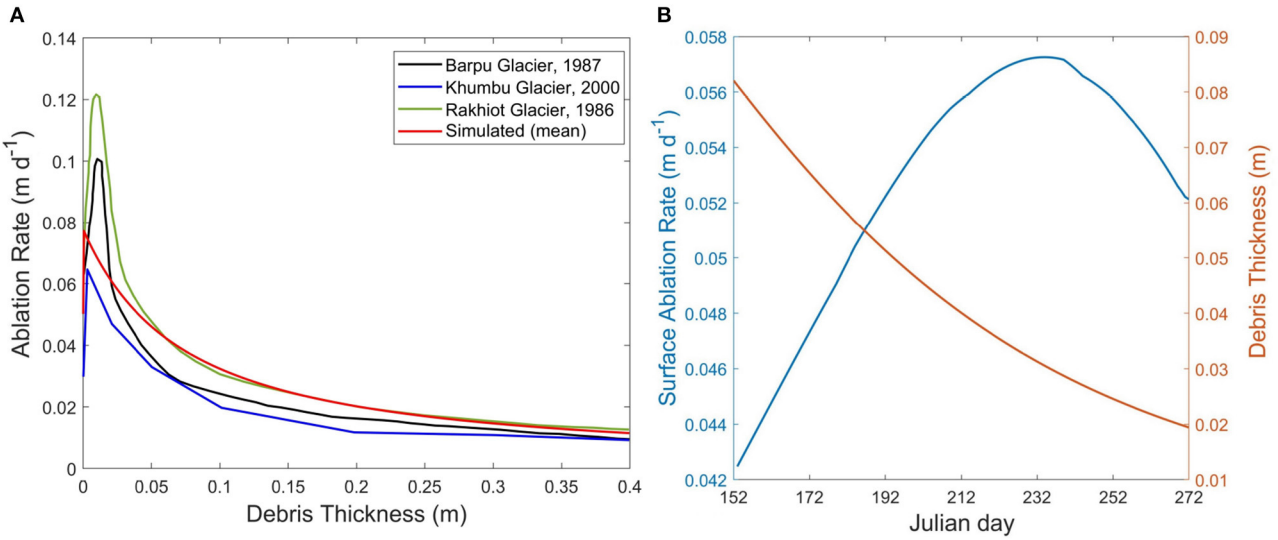

FIGURE 6 | The debris-thickness control on surface ablation rates. **(A)** June-averaged ablation rate as a function of debris thickness on the Baltoro Glacier (red) compared to *in-situ* measurements in the ablation season on other Himalayan glaciers (replotted), including Barpu Glacier (Khan, 1989), Khumbu Glacier (Kayastha et al., 2000), and Rakhiot Glacier (Mattson, 1993). Note that the melt-enhancing effect of thin-debris is observed on all glaciers. **(B)** An example of the temporal variation in ablation rate vs. debris thickness around a supraglacial lake on the Baltoro Glacier. The debris layer is getting thinner as sediments are gradually sliding into the lake, which leads to an increase in ablation rate (the decrease of ablation rate in late ablation season is due to the decreasing irradiance).

Buri et al., 2016; Miles et al., 2016, 2018; Thompson et al., 2016; Dobreva et al., 2017; Mertes et al., 2017; Huang et al., 2018). The number of supraglacial ponds and lakes have been found to be increasing on many DCGs, which is related to the glacier morphological changes such as differential surface lowering and collapse of englacial channel roofs (Sakai et al., 2000, 2002; Benn et al., 2001; Quincey and Glasser, 2009; Gibson et al., 2017). These water bodies also play an important role in regulating water storage and drainage in a glacier system (Cuffey and Paterson, 2010; Benn and Evans, 2014), and cause englacial ablation via efficient heat transfer (Sakai et al., 2000; Gulley and Benn, 2007; Benn et al., 2012; Miles et al., 2016; Mertes et al., 2017).

Supraglacial lakes can be relatively large to moderate-sized water bodies (lake azimuthal distances have been observed to be up to 0.6 km in length on the Baltoro Glacier) that can be relatively short lived or exist over multiple years, and supraglacial ponds are smaller but more common water bodies that usually only appear during the ablation season. These water bodies are typically abundant in the ablation zone where the surface slope is gentle and heterogeneous surface lowering occurs (Reynolds, 2000; Sakai et al., 2002; Reid and Brock, 2014). The evolution of many supraglacial lakes and ponds are governed by filling and draining cycles, and hydrological connectivity that are controlled by glacier surface and internal structures (Benn et al., 2001, 2017; Wessels et al., 2002; Miles et al., 2017). Studies also found that proglacial lakes also have a significant control on the glacier dynamics (Sutherland et al., 2020). These processes have only been studied on a handful of glaciers in the field, and there are still many processes and feedbacks that need to be investigated.

Supraglacial ponds and lakes are efficient in transferring heat into glacier ice due to their low surface albedo and active convection (Lüthje et al., 2006; Miles et al., 2016). Studies have estimated that the ablation rates around the lakes can be much higher than that of most debris-covered areas (Sakai et al., 2000; Thompson et al., 2016). The simulations by Miles et al. (2018) revealed that ponds may be responsible for 1/8 of total ice loss in the Langtang valley, Nepal. Furthermore, supraglacial water bodies will most likely exhibit accelerated growth on Himalayan glaciers given current atmospheric temperature trends (Benn et al., 2001). For example, Gibson et al. (2017) estimated that the number of water bodies on the Baltoro Glacier has increased from 234 in 2001 to 570 in 2012, and the area has tripled, which suggests that supraglacial water bodies can expand quickly on DCGs.

One of the first energy-balance models for supraglacial ponds on DCGs was developed by Sakai et al. (2000), which was used to address field observations on the Lirung Glacier in the Langtang Valley, Nepal. The core of this model is the energy-balance of a supraglacial lake that accounts for heat flux input and output due to meltwater, heat storage of the lake, and the bare-ice vs. debris covered areas beneath the lake surface:

$$Q + Q_{in} - Q_{out} - \Delta Q_t - Q_i - Q_d = 0, \tag{21}$$

where Q is the net radiation heat flux on the lake surface, Q_{in} is the input heat flux from meltwater inflow into the lake, which in most cases, can be neglected (Sakai et al., 2000), Q_{out} is the output heat flux from the water outflow from the lake, which dominates the englacial ablation such as the expansion of conduits (Sakai et al., 2000), ΔQ_t is the change in heat storage of the lake, Q_i is

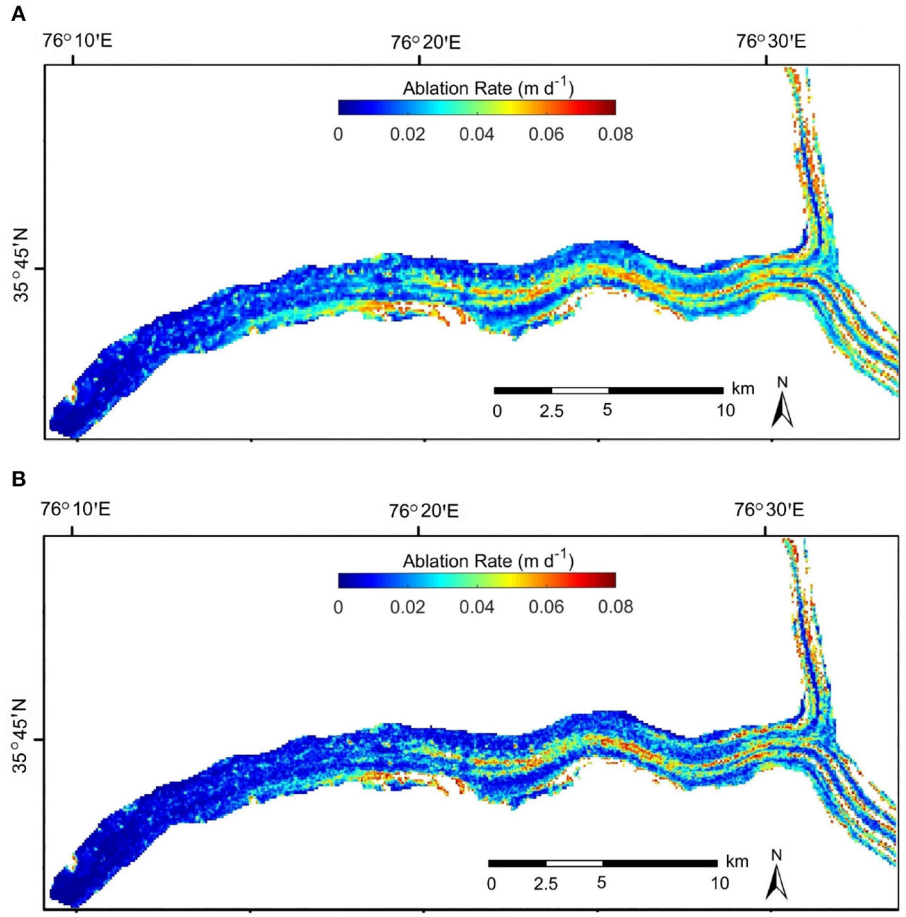

FIGURE 7 | Surface ablation rates for the Baltoro Glacier modeled with two different methods: **(A)** The remote-sensing based approach (Mihalcea et al., 2008), which uses surface temperature data acquired by satellite. **(B)** The surface energy balance based approach, which uses modeled surface irradiance. Both results are based on the same debris thickness distribution, assuming no water bodies and were produced to represent rates on August 14 2004. Note the high spatial variability in ablation rate caused by the debris thickness distribution (**Figure 5A**).

the heat flux for ice melt at subaqueous ice-cliff, and Q_d is the heat flux for ice melt beneath the subaqueous debris layer.

A more recent model was presented by Miles et al. (2016), which improves the Sakai et al. (2000)'s model in several aspects, such as the energy flux due to rainfall, more accurate turbulent fluxes, and the free convection of water that may circulate within the pond. In addition to the energy-balance, Miles et al. (2016) used a mass balance model to account for the changes in pond volume (ΔV):

$$\Delta V = V_{in} + V_i + V_d + V_{le} + V_r - V_{out}, \qquad (22)$$

where V_{in} and V_{out} are the inflows and outflows, V_i is the subaqueous bare ice melt volume, V_d is the subaqueous subdebris melt volume, V_{le} is the volume of vapor exchanges, and V_r is the volume gained from rain. All terms in the energy-balance model and the mass-balance model have been discussed. Although some parameters are based on empirical relationships, this work provides the most comprehensive physics-based pond model to date. **Figure 8** depicts the large number of supraglacial water bodies identified in the terminus region of the Baltoro Glacier. Our simulation results (**Figures 8C,D**) based on the above model suggest that supraglacial water bodies make a significant contribution to the total ice loss and surface lowering in the ablation zone, and exhibit a non-linear seasonal trend toward the end of the ablation season, as the extent and amount of lakes and ponds gradually expand to yearly maximum.

The dynamics of supraglacial lakes and ponds is often coupled with the evolution of ice-cliffs around them. Studies have suggested that this cliff/lake system plays an important role in governing the mass balance of DCGs, and most field observations and modeling results confirmed that ice-cliffs can make a significant contribution to the total ice mass loss on a DCG (Sakai et al., 2002; Anderson, 2014; Steiner et al., 2015; Buri et al., 2016), although many questions remain unresolved (Sakai et al., 2002; Buri et al., 2016; Miles et al., 2016). Several forms of interactions exist between ice-cliffs and ponds/lakes. For example, lake undercut can cause the steepening of some ice-cliffs

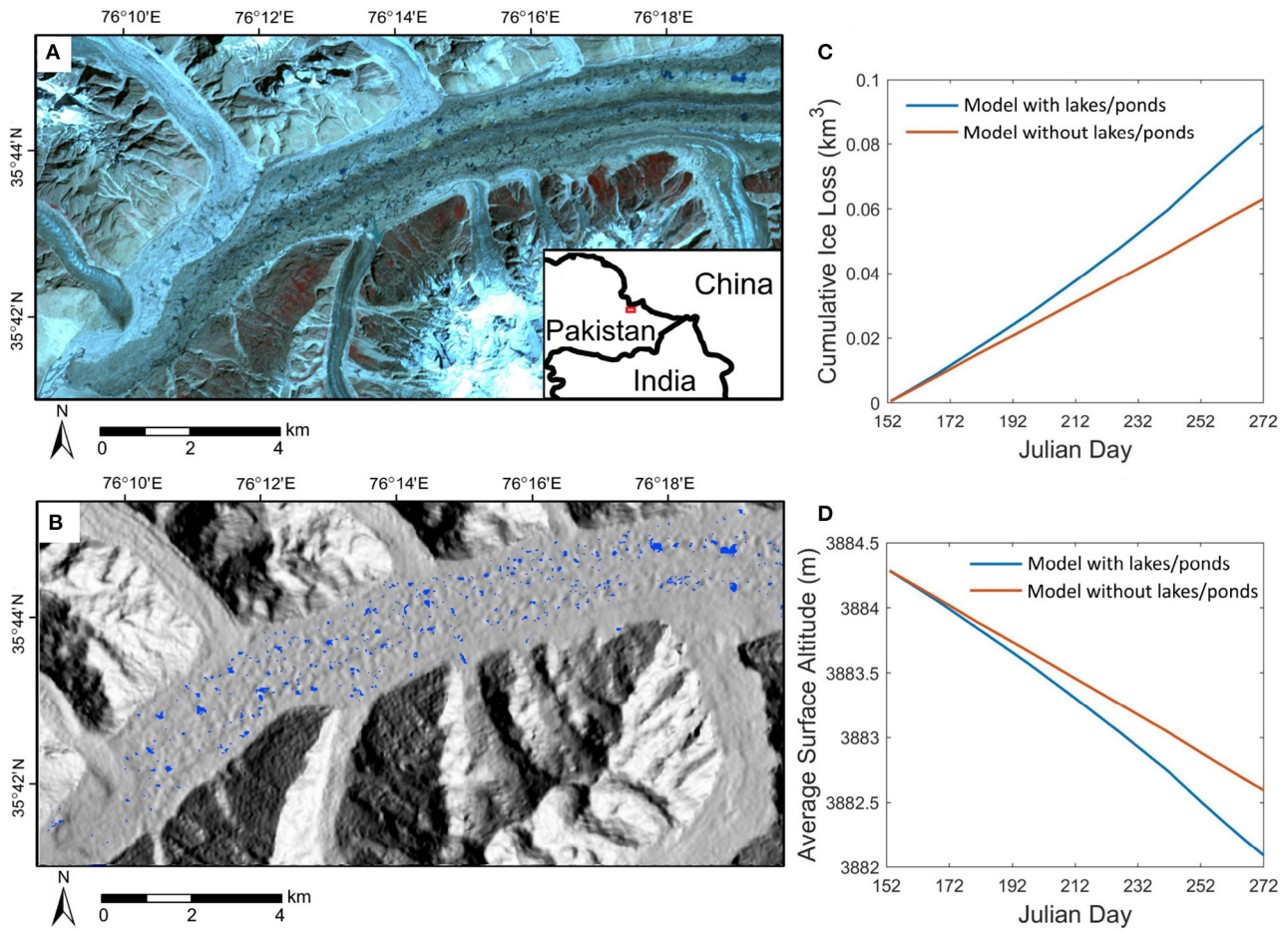

FIGURE 8 | (A) ASTER false-color composite imagery (VNIR bands) of the lower ablation zone of the Baltoro Glacier acquired on August 14, 2004. **(B)** A large number of supraglacial ponds and lakes mapped from the satellite data using the normalized difference water index. **(C)** Temporal variation in the simulated cumulative ice-volume loss for this area over the ablation season of 2004. Two scenarios (with and without lakes/ponds) are compared. **(D)** Comparison of the mean surface altitude variations for the two simulations. Note the increased non-linearity in ice loss and surface lowering when supraglacial lakes/ponds are present.

(Sakai et al., 2000, 2002), and the melt of ice-cliff below the water surface is strongly affected by water fluctuations (Miles et al., 2016).

Sakai et al. (2002) found that the orientation and inclination of ice-cliffs significantly control the evolution of ice cliffs given the solar geometry and cast shadows. The geometry of the ice-cliff also controls the thickness distribution of debris cover which regulates meltwater production. Ice-cliffs are also controlled by englacial processes, and studies have attributed the formation of some ice-cliffs to the collapses of englacial conduits (Sakai et al., 2000, 2002). Some recent simulations (Steiner et al., 2015; Buri et al., 2016) confirmed that the complex terrain around the cliff has a non-negligible effect on ice-cliff evolution due to the local shading and the adjacent terrain irradiance. Furthermore, ice-cliff evolution can also be governed by pond-water ablation that undercuts adjacent lake slopes. In addition, the ice topographic load coupled with the debris load causes significant variations in the ice stress fields, that partially control the process of calving. We have observed this process on a very large supraglacial lake near the terminus of the Liligo Glacier during the summer of 2005. Significant water depths coupled with wind and wave action can cause significant undercutting, thereby altering the ice stress fields which enables calving and the production of icebergs in glacial lakes. The ice cliffs that are generated from these processes typically have very steep slopes, and the debris loads above them are quickly transported. Collectively, various feedbacks promote ice-cliff retreat and rapid supraglacial lake expansion, that most likely represents a non-linear ablation response to climate forcing.

Understanding supraglacial water bodies and ice-cliff dynamics is critical to assessing DCG sensitivity to climate change, and valuable knowledge has been gained from the aforementioned studies. However, there are still many issues that need to be investigated including the filling and draining cycles that control the evolution of many supraglacial ponds, the connectivity between surface water bodies and englacial

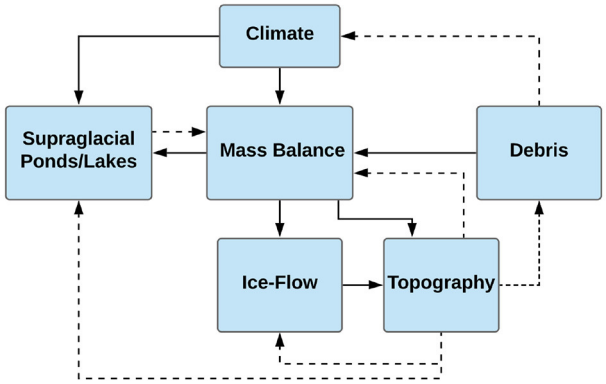

FIGURE 9 | Diagram illustrating the interactions between key controlling factors discussed in this paper that govern the dynamics of a debris-covered glacier. The feedbacks (dashed lines) are important to the system as they may increase a glacier's sensitivity to climate change over time.

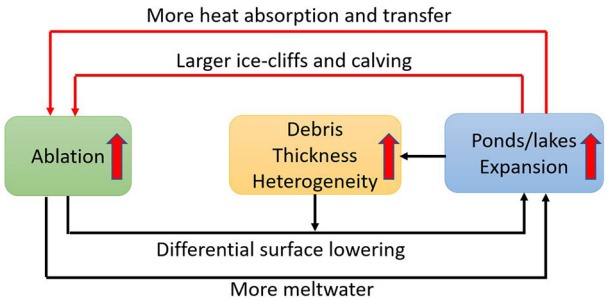

FIGURE 10 | Conceptual diagram that illustrates the positive feedbacks between ablation, surface ponding and the spatial distribution of debris thickness.

conduits, englacial ablation due to warm water outflow, rockfall from ice-cliffs, and modeling the edge effects and temperature gradients in ponds (Benn et al., 2001, 2017; Miles et al., 2016, 2017).

6. FEEDBACK AND SYSTEM COUPLINGS

The dynamics of a DCG system is controlled by the complex interactions between climate, debris load, ice dynamics, hydrologic conditions and topography (Scherler et al., 2011a,b; Dobreva et al., 2017; Gibson et al., 2017). Unfortunately, few studies have investigated the couplings and feedback mechanisms in a DCG system, which is a major issue in characterizing DCGs, because isolating a small number of processes out of the full system increases uncertainty in results, as system couplings and feedbacks can significantly affect glacier dynamics (Rowan et al., 2015; Anderson and Anderson, 2016). Studies are often limited in spatio-temporal scale (Anderson, 2014; Anderson et al., 2021), because they rely on instantaneous remote-sensing data or field measurements at limited sites that do not describe multi-year or longer-term variations in glacier conditions (such as ice thickness, debris distribution and topography). Furthermore, many system couplings and feedbacks operate at very different spatio-temporal scales, making them difficult to investigate in the field. Therefore, numerical modeling is required to address the feedbacks and non-linear relationships between major glacier components. **Figure 9** is a conceptual diagram showing the major systems couplings we identified between climate, mass balance, supraglacial water bodies, debris load, ice flow, and topography that govern the dynamics of a DCG.

6.1. Feedbacks on Glacier Surface

Figure 10 is a conceptual diagram that illustrates the feedbacks we identified between ablation, surface ponding and debris thickness. The most obvious positive feedback describes the relationship between meltwater production and supraglacial pond expansion: as a pond grows, its surface area and surrounding ice-cliff area get larger, they absorb more solar energy due to the lower albedo, causing enhanced melt and calving, which in turn, leads to further expansion of the pond. Another feedback involves the differential lowering of the glacier surface, the distribution of debris and the increased ponding of surface water: the spatially heterogeneous distribution of supraglacial water bodies and ice-cliffs governs the differential elevation change, which in turn, facilities the expansion of existing ponds and the formation of new ponds as suggested by multiple studies (Benn and Owen, 2002; Benn et al., 2012; Reid and Brock, 2014; Rowan et al., 2015; Salerno et al., 2017; Miles et al., 2018). The presence of supraglacial ponds and lakes also increases the spatial heterogeneity of debris thickness. Rounce et al. (2018) found that debris thinning is usually associated with the formation of supraglacial lakes and ice-cliffs, then the heterogeneous distribution of debris thickness further enhances the differential surface lowering which creates more depression zones for new ponds.

Positive feedbacks also exist between the lowing of surface albedo and enhanced melt, as a wet surface often exhibits lower albedo. Pritchard et al. (2008) showed that this mechanism has significant influence on millennial-scale mass-loss of ice sheets. For certain locations on the glacier surface, such as on ice-cliffs, the decrease in albedo is more significant due to the thinner debris and high moisture content, i.e., the "dirty ice" that causes more ablation (Fyffe et al., 2020), which is also coupled with the topographic factors (such as the orientation of the cliff wall and the high adjacent terrain irradiance on the cliffs) to form positive feedback that accelerates melting, causing faster ice-cliff backwasting than previously thought (Sakai et al., 2000; Benn and Owen, 2002; Reid and Brock, 2014).

6.2. The Role of Glacier Surface Topography

Surface topography is an important factor that acts as a bridge between multiple components of a DCG, and studies have identified the following topographic effects on DCGs:

1. Surface topography has a direct impact on glacier surface ablation because slope, slope azimuth, and basin topographic shielding directly control the total amount of shortwave radiation

received by the glacier surface (Arnold et al., 2006; Garg et al., 2017; Olson and Rupper, 2019).

2. Surface topographic conditions control supraglacial hydrology, especially the development of ponds and lakes (Huo et al., 2021). Water transport is enhanced with steeper gradients, while ponding is enhanced with lower gradients, therefore supraglacial water bodies are more abundant where the glacier surface is flatter (Reynolds, 2000; Sakai et al., 2002; Immerzeel et al., 2014; Reid and Brock, 2014). Topographic depressions caused by differential ablation and debris loading are also important, as they provide topographic sinks for meltwater to accumulate.

3. Topography also affects the distribution and transport of supraglacial debris. Observations and simulations have shown that the morphometric conditions of the sidewalls and headwalls of the glacial valley control sediment input to the glacier (Benn and Evans, 2014; Anderson and Anderson, 2016).

4. The adjacent-terrain irradiance due to complex topography coupled with debris cover contributes to the surface melt, and especially the retreat of ice-cliffs (Sakai et al., 2002; Wessels et al., 2002).

6.3. Basal Processes

The glacier bed is slowly evolving due to differential glacier erosion caused by variations in ice-flow dynamics, such that erosion is most likely at a maximum near the ELA due to relatively thick ice and high flow velocities (Herman et al., 2011; Steer et al., 2012). Another complexity is the basal hydrological conditions that govern sliding velocity, as high basal water pressure may lubricate the ice-bedrock interface (Cuffey and Paterson, 2010; Quincey et al., 2011). The higher sliding velocity leads to more frictional heating that further increases basal water pressure, which forms a positive feedback (Benn and Evans, 2014). Many details about the interactions between basal sliding, erosion, subglacial ablation, basal hydrology, and subglacial debris transport need to be investigated in future studies.

Collectively, the DCG system is complicated by interactions and feedbacks between debris load, ablation, topography, ice-flow, basal processes, and supraglacial water bodies. An integrated modeling of these processes may help explain field observations over High-Mountain Asia, such as the rapid lowering on Himalayan DCGs (Kääb et al., 2012; Immerzeel et al., 2013; Fujita et al., 2014) and the advancement of many glaciers in the Karakoram (Bolch et al., 2012; Bishop et al., 2014; Dobreva et al., 2017; Farinotti et al., 2020). Furthermore, it is also important to account for ice-flow dynamics being a potential cause of glacier thinning, as the re-distribution of ice mass, especially the declining ice discharge plays a dominant role in setting the thinning patterns on debris-free glaciers (e.g., Cuffey and Paterson, 2010), and has also been shown to be important for DCGs (Vincent et al., 2016; Brun et al., 2018; Anderson et al., 2021).

Improved parameterization schemes (more parameters and processes) suggest that climate glacier dynamics for DCGs are more complex than debris-free glaciers and that DCGs may be more sensitive to climate change than previously thought.

We recommend that more energy input components (e.g., the adjacent-terrain irradiance) and multi-scale topographic effects be accounted for in improved parameterization schemes. Our simulations indicate that scale dependent processes such as the gravitational debris transport and supraglacial ponding must also be accounted for given the coupling of climate and surface process and the non-linear responses in ablation and ice-mass loss. In all likelihood, our simulations probably underestimate the magnitude of non-linear responses due to these coupled processes/systems, as other processes such as calving were not accounted for. Furthermore, it is essential that future research focus on addressing questions about the significance of missing and existing processes so that we have an improved understanding of the degree of dominance and partitioning of key parameters and processes/systems that need to be incorporated into DCG models. This will require important comparative analysis of parameterization schemes and parameter sensitivity analysis to account for uncertainty in so many parameters and processes that govern climate-glacier dynamics.

More remote sensing and field-based studies are required to validate numerical modeling results. Further research is also required to determine if DCGs in different geographic locations exhibit similar or different sensitivity to climate change given variations in internal and external forcing factors. We speculate that such complex non-linear systems have the potential to reach tipping points based upon changing climate and geomorphological conditions within glacierized basins.

7. CONCLUSIONS

Debris-covered glaciers represent complex non-linear systems that operate given the coupling of climate, geomorphological and glaciological processes and feedbacks. Many important processes and systems have not been adequately characterized. Consequently, our current understanding of DCG sensitivity to climate change is most likely oversimplified, as numerous processes and scale dependencies have not been accounted for. This has resulted in conflicting views about these glaciers, such as the Karakoram anomaly and the "debris-covered glacier anomaly," where the lack of data and information about climate forcing and ablation dynamics force us to rely on empirical measurements that represent a static snapshot in space and time. This paper and our simulations have attempted to provide a more integrated synthesis into the complexity of DCG systems by addressing important concepts associated with the key external and internal forcing factors and glacial processes, highlighting the importance of feedback mechanisms, system couplings, and recognition of the high degree of uncertainty related to numerous properties and parameters that need to be taken into consideration. Our simulation results based on the Baltoro Glacier in the central Karakoram combined with a review of literature reveal that climate-DCG dynamics and responses can be significantly attributed to the following factors:

1. Climate forcing: solar radiation and precipitation are the main driving forces for ice loss or gain. An accurate surface energy balance model for debris-covered glaciers needs

to account for short-wave and long-wave irradiance. Our simulations showed that multi-scale topographic effects on surface ablation can be significant for debris-covered glaciers, given glacier surface topographic evolution and differential sky-view conditions in the glacier valley. Other meso-scale topographic effects such as cast shadows and adjacent-terrain influences should also be considered.

2. Supraglacial debris: physical properties of debris, such as thickness, lithology, grain size, moisture content and thermal conductivity strongly govern the surface ablation rates on debris-covered glaciers. Many of these factors, however, have not been adequately characterized or studied. We showed that there are significant spatial variability in debris thickness, albedo, particle size and composition, which are also coupled with the dynamic movement of debris due to gravity and ice-flow. Such complexity needs to be accounted for in models and field studies to better assess debris-related effects on glacier mass balance.

3. Supraglacial water bodies and ice-cliffs: supraglacial ponds, lakes, and surrounding ice-cliffs are melt hotspots on debris-covered glaciers and are expanding in size on many glaciers. Our simulations based on the Baltoro Glacier suggest that supraglacial water bodies make a significant contribution to the total ice-mass loss over the ablation season. Further investigations are needed to address the evolution of supraglacial water bodies and ice-cliffs, and their interactions with debris load, topography and englacial processes.

4. System coupling and feedback: positive feedbacks on debris-covered glaciers have been identified in numerical simulations, such as the surface melt-lowering-ponding feedback, and the atmospheric convection feedback. These couplings and especially the positive feedbacks may govern the non-linearity of the glacier's response to climate forcing, which are represented as an acceleration in ice-mass loss and heterogeneous surface lowering. The combined effect of these processes may lead to the beginning of a critical transition of the glacier system that signifies an increasing level of glacier sensitivity to climate change.

DATA AVAILABILITY STATEMENT

The original contributions presented in the study are included in the article/supplementary material, further inquiries can be directed to the corresponding author/s.

AUTHOR CONTRIBUTIONS

DH conducted the model simulations, made the figures, and wrote the sections 3.2–6. MB proposed and designed the research, developed the parameterization schemes, wrote the sections 2.1 and 3.1, and edited the manuscript. AB wrote the section 2.2 and edited the manuscript. All authors contributed to the writing of the introduction and conclusions and the final editing.

ACKNOWLEDGMENTS

We would like to thank Dr. Zhaohui Chi and Brennan Young at Texas A&M University for discussion. AB recognizes support from the Canadian Natural Sciences and Engineering Research Council and the computational resources of Compute Canada.

REFERENCES

Adhikary, S., Masayoshi, N., Seko, K., and Shakya, B. (2000). "Dust influence on the melting process of glacier ice: experimental results from Lirung glacier, Nepal Himalayas, in *Debris-Covered Glaciers: Proceedings of an International Workshop* (Seattle, WA: IAHS), 43.

Anderson, L. S. (2014). *Glacier response to climate change: modeling the effects of weather and debris-cover* (Doctoral dissertation), University of Colorado at Boulder, Boulder, CO.

Anderson, L. S., and Anderson, R. S. (2016). Modeling debris-covered glaciers: response to steady debris deposition. *Cryosphere* 10:1105. doi: 10.5194/tc-10-1105-2016

Anderson, L. S., and Anderson, R. S. (2018). Debris thickness patterns on debris-covered glaciers. *Geomorphology* 311, 1–12. doi: 10.1016/j.geomorph.2018.03.014

Anderson, L. S., Armstrong, W. H., Anderson, R. S., and Buri, P. (2021). Debris cover and the thinning of Kennicott glacier, Alaska: *in situ* measurements, automated ice cliff delineation and distributed melt estimates. *Cryosphere* 15, 265–282. doi: 10.5194/tc-15-265-2021

Anderson, R. S. (2000). A model of ablation-dominated medial moraines and the generation of debris-mantled glacier snouts. *J. Glaciol.* 46, 459–469. doi: 10.3189/172756500781833025

Arnold, N. S., Rees, W. G., Hodson, A. J., and Kohler, J. (2006). Topographic controls on the surface energy balance of a high arctic valley glacier. *J. Geophys. Res. Earth Surface* 111. doi: 10.1029/2005JF000426

Benn, D., Bolch, T., Hands, K., Gulley, J., Luckman, A., Nicholson, L., et al. (2012). Response of debris-covered glaciers in the Mount Everest region to recent warming, and implications for outburst flood hazards. *Earth Sci. Rev.* 114, 156–174. doi: 10.1016/j.earscirev.2012.03.008

Benn, D., and Evans, D. J. (2014). *Glaciers and Glaciation*. London: Routledge. doi: 10.4324/9780203785010

Benn, D., Wiseman, S., and Hands, K. (2001). Growth and drainage of supraglacial lakes on debris-mantled Ngozumpa glacier, Khumbu Himal, Nepal. *J. Glaciol.* 47, 626–638. doi: 10.3189/172756501781831729

Benn, D. I., and Lehmkuhl, F. (2000). Mass balance and equilibrium-line altitudes of glaciers in high-mountain environments. *Quat. Int.* 65, 15–29. doi: 10.1016/S1040-6182(99)00034-8

Benn, D. I., and Owen, L. A. (2002). Himalayan glacial sedimentary environments: a framework for reconstructing and dating the former extent of glaciers in high mountains. *Quat. Int.* 97, 3–25. doi: 10.1016/S1040-6182(02)00048-4

Benn, D. I., Thompson, S., Gulley, J., Mertes, J., Luckman, A., and Nicholson, L. (2017). Structure and evolution of the drainage system of a Himalayan debris-covered glacier, and its relationship with patterns of mass loss. *Cryosphere* 11, 2247–2264. doi: 10.5194/tc-11-2247-2017

Berger, A. (1978). Long-term variations of daily insolation and quaternary climatic changes. *J. Atmos. Sci.* 35, 2362–2367. doi: 10.1175/1520-0469(1978)035<2362:LTVODI>2.0.CO;2

Bird, R. E., and Riordan, C. (1986). Simple solar spectral model for direct and diffuse irradiance on horizontal and tilted planes at the Earth's surface for cloudless atmospheres. *J. Climate Appl. Meteorol.* 25, 87–97. doi: 10.1175/1520-0450(1986)025<0087:SSSMFD>2.0.CO;2

Bishop, M. P., Bonk, R., Kamp, U. Jr., and Shroder, J. F. Jr. (2001). Terrain analysis and data modeling for alpine glacier mapping. *Polar Geogr.* 25, 182–201. doi: 10.1080/10889370109377712

Bishop, M. P., and Colby, J. D. (2011). Topographic normalization of multispectral satellite imagery. *J. Glaciol.* 55, 131–146. Available online at: http://citeseerx.ist.psu.edu/viewdoc/download?doi=10.1.1.727.9345&rep=rep1&type=pdf

Bishop, M. P., and Dobreva, I. D. (2017). "Geomorphometry and mountain geodynamics: issues of scale and complexity," in *Integrating Scale in*

Remote Sensing and GIS, eds D. A. Quattrochi, E. Wentz, N. S.N. Lam, and C. W. Emerson (Boca Raton, FL: Taylor and Francis), 189–228. doi: 10.1201/9781315373720-8

Bishop, M. P., Shroder, J. F., Ali, G., Bush, A. B. G., Haritashya, U. K., Roohi, R., et al. (2014). "Remote sensing of glaciers in Afghanistan and Pakistan," in *Global Land Ice Measurements from Space*, eds J. S. Kargel, G. J. Leonard, M. P. Bishop, A. Kääb, and B. Raup (Berlin; Heidelberg: Springer), 509–548. doi: 10.1007/978-3-540-79818-7_23

Bishop, M. P., Shroder, J. F. Jr., Bonk, R., and Olsenholler, J. (2002). Geomorphic change in high mountains: a western himalayan perspective. *Glob. Planet. Change* 32, 311–329. doi: 10.1016/S0921-8181(02)00073-5

Bishop, M. P., Young, B. W., Colby, J. D., Furfaro, R., Schiassi, E., and Chi, Z. (2019). Theoretical evaluation of anisotropic reflectance correction approaches for addressing multi-scale topographic effects on the radiation-transfer cascade in mountain environments. *Remote Sens.* 11:2728. doi: 10.3390/rs11232728

Bolch, T., Kulkarni, A., Kääb, A., Huggel, C., Paul, F., Cogley, J. G., et al. (2012). The state and fate of Himalayan glaciers. *Science* 336, 310–314. doi: 10.1126/science.1215828

Braithwaite, R. J., and Olesen, O. B. (1990). Response of the energy balance on the margin of the greenland ice sheet to temperature changes. *J. Glaciol.* 36, 217–221. doi: 10.3189/S0022143000009461

Brun, F., Wagnon, P., Berthier, E., Shea, J. M., Immerzeel, W. W., Kraaijenbrink, P. D. A., et al. (2018). Ice cliff contribution to the tongue-wide ablation of Changri Nup glacier, Nepal, central Himalaya. *Cryosphere* 12, 3439–3457. doi: 10.5194/tc-12-3439-2018

Bueler, E., and Brown, J. (2009). Shallow shelf approximation as a "sliding law" in a thermomechanically coupled ice sheet model. *J. Geophys. Res. Earth Surface* 114. doi: 10.1029/2008JF001179

Buri, P., Miles, E. S., Steiner, J. F., Immerzeel, W. W., Wagnon, P., and Pellicciotti, F. (2016). A physically based 3-D model of ice cliff evolution over debris-covered glaciers. *J. Geophys. Res. Earth Surface* 121, 2471–2493. doi: 10.1002/2016JF004039

Bush, A. B. G., Bishop, M. P., Huo, D., Chi, Z., and Tiwari, U. (2020). "Issues in climate analysis and modeling for understanding mountain erosion dynamics," in *Reference Module in Earth Systems and Environmental Sciences* (Amsterdam: Elsevier). doi: 10.1016/B978-0-12-818234-5.00022-5

Chen, H., and Lee, C. (2000). Numerical simulation of debris flows. *Can. Geotech. J.* 37, 146–160. doi: 10.1139/t99-089

Coakley, J. (2003). "Reflectance and albedo, surface," in *Encyclopedia of the Atmosphere Sciences* eds. J. Holton, J. Curry (Amsterdam: Elsevier), 1914–1923. doi: 10.1016/B0-12-227090-8/00069-5

Collier, E., Maussion, F., Nicholson, L. I., Mölg, T., Immerzeel, W. W., and Bush, A. B. G. (2015). Impact of debris cover on glacier ablation and atmosphere-glacier feedbacks in the Karakoram. *Cryosphere* 9, 1617–1632. doi: 10.5194/tc-9-1617-2015

Collier, E., Mölg, T., Maussion, F., Scherer, D., Mayer, C., and Bush, A. B. G. (2013). High-resolution interactive modelling of the mountain glacier-atmosphere interface: an application over the Karakoram. *Cryosphere* 7, 779–795. doi: 10.5194/tc-7-779-2013

Collier, E., Nicholson, L. I., Brock, B. W., Maussion, F., Essery, R., and Bush, A. B. G. (2014). Representing moisture fluxes and phase changes in glacier debris cover using a reservoir approach. *Cryosphere* 8, 1429–1444. doi: 10.5194/tc-8-1429-2014

Copland, L., Pope, S., Bishop, M. P., Shroder, J. F., Clendon, P., Bush, A. B. G., et al. (2009). Glacier velocities across the central Karakoram. *Ann. Glaciol.* 50, 41–49. doi: 10.3189/172756409789624229

Cuffey, K. M., and Paterson, W. S. B. (2010). *The Physics of Glaciers*. Oxford: Academic Press.

Dobreva, I. D., Bishop, M. P., and Bush, A. B. G. (2017). Climate-glacier dynamics and topographic forcing in the Karakoram Himalaya: concepts, issues and research directions. *Water* 9:405. doi: 10.3390/w9060405

Dozier, J., Bruno, J., and Downey, P. (1981). A faster solution to the horizon problem. *Comput. Geosci.* 7, 145–151. doi: 10.1016/0098-3004(81)90026-1

Egholm, D. L., Knudsen, M. F., Clark, C. D., and Lesemann, J. E. (2011). Modeling the flow of glaciers in steep terrains: the integrated second-order shallow ice approximation (isosia). *J. Geophys. Res. Earth Surface* 116. doi: 10.1029/2010JF001900

Farinotti, D., Brinkerhoff, D. J., Clarke, G. K. C., Fürst, J. J., Frey, H., et al. (2017). How accurate are estimates of glacier ice thickness? Results from ITMIX, the Ice Thickness Models Intercomparison experiment. *Cryosphere* 11, 949–970. doi: 10.5194/tc-11-949-2017

Farinotti, D., Immerzeel, W. W., de Kok, R. J., Quincey, D. J., and Dehecq, A. (2020). Manifestations and mechanisms of the Karakoram glacier anomaly. *Nat. Geosci.* 13, 8–16. doi: 10.1038/s41561-019-0513-5

Foster, L., Brock, B., Cutler, M., and Diotri, F. (2012). A physically based method for estimating supraglacial debris thickness from thermal band remote-sensing data. *J. Glaciol.* 58, 677–691. doi: 10.3189/2012JoG11J194

Fountain, A. G., and Walder, J. S. (1998). Water flow through temperate glaciers. *Rev. Geophys.* 36, 299–328. doi: 10.1029/97RG03579

Fujita, K., Sakai, A., et al. (2014). Modelling runoff from a himalayan debris-covered glacier. *Hydrol. Earth Syst. Sci.* 18, 2679–2694. doi: 10.5194/hess-18-2679-2014

Fyffe, C. L., Reid, T. D., Brock, B. W., Kirkbride, M. P., Diolaiuti, G., Smiraglia, C., et al. (2014). A distributed energy-balance melt model of an alpine debris-covered glacier. *J. Glaciol.* 60, 587–602. doi: 10.3189/2014JoG13J148

Fyffe, C. L., Woodget, A. S., Kirkbride, M. P., Deline, P., Westoby, M. J., and Brock, B. W. (2020). Processes at the margins of supraglacial debris cover: quantifying dirty ice ablation and debris redistribution. *Earth Surface Process. Landforms* 45, 2272–2290. doi: 10.1002/esp.4879

Garg, P. K., Shukla, A., and Jasrotia, A. S. (2017). Influence of topography on glacier changes in the central Himalaya, India. *Glob. Planet. Change* 155, 196–212. doi: 10.1016/j.gloplacha.2017.07.007

Gibson, M. J., Glasser, N. F., Quincey, D. J., Mayer, C., Rowan, A. V., and Irvine-Fynn, T. D. (2017). Temporal variations in supraglacial debris distribution on Baltoro glacier, Karakoram between 2001 and 2012. *Geomorphology* 295, 572–585. doi: 10.1016/j.geomorph.2017.08.012

Gueymard, C. (1995). *SMARTS2, A Simple Model of the Atmospheric Radiative Transfer of Sunshine: Algorithms and Performance Assessment*. Florida Solar Energy Center, Cocoa, FL.

Gulley, J., and Benn, D. (2007). Structural control of englacial drainage systems in himalayan debris-covered glaciers. *J. Glaciol.* 53, 399–412. doi: 10.3189/002214307783258378

Hambrey, M. J., Quincey, D. J., Glasser, N. F., Reynolds, J. M., Richardson, S. J., and Clemmens, S. (2008). Sedimentological, geomorphological and dynamic context of debris-mantled glaciers, Mount Everest (Sagarmatha) region, Nepal. *Quat. Sci. Rev.* 27, 2361–2389. doi: 10.1016/j.quascirev.2008.08.010

Herman, F., Beaud, F., Champagnac, J.-D., Lemieux, J.-M., and Sternai, P. (2011). Glacial hydrology and erosion patterns: a mechanism for carving glacial valleys. *Earth Planet. Sci. Lett.* 310, 498–508. doi: 10.1016/j.epsl.2011.08.022

Herman, F., and Braun, J. (2008). Evolution of the glacial landscape of the southern Alps of New Zealand: insights from a glacial erosion model. *J. Geophys. Res. Earth Surface* 113. doi: 10.1029/2007JF000807

Hewitt, K. (2005). The Karakoram anomaly? Glacier expansion and the "elevation effect," Karakoram Himalaya. *Mountain Res. Dev.* 25, 332–340. doi: 10.1659/0276-4741(2005)025[0332:TKAGEA]2.0.CO;2

Huang, L., Li, Z., Han, H., Tian, B., and Zhou, J. (2018). Analysis of thickness changes and the associated driving factors on a debris-covered glacier in the tienshan mountain. *Remote Sens. Environ.* 206, 63–71. doi: 10.1016/j.rse.2017.12.028

Huo, D., Bishop, M. P., Young, B. W., Chi, Z., and Haritashya, U. K. (2020). "Numerical modeling issues for understanding complex debris-covered glaciers," in *Reference Module in Earth Systems and Environmental Sciences* (Elsevier). doi: 10.1016/B978-0-12-818234-5.00019-5

Huo, D., Chi, Z., and Ma, A. (2021). Modeling surface processes on debris-covered glaciers: a review with reference to the high mountain asia. *Water* Amsterdam, 13:101. doi: 10.3390/w13010101

Immerzeel, W., Kraaijenbrink, P., Shea, J., Shrestha, A., Pellicciotti, F., Bierkens, M., et al. (2014). High-resolution monitoring of Himalayan glacier dynamics using unmanned aerial vehicles. *Remote Sens. Environ.* 150, 93–103. doi: 10.1016/j.rse.2014.04.025

Immerzeel, W., Pellicciotti, F., and Bierkens, M. (2013). Rising river flows throughout the twenty-first century in two Himalayan glacierized watersheds. *Nat. Geosci.* 6, 742–745. doi: 10.1038/ngeo1896

Immerzeel, W. W., Van Beek, L. P., and Bierkens, M. F. (2010). Climate change will affect the asian water towers. *Science* 328, 1382–1385. doi: 10.1126/science.1183188

Iqbal, M. (1983). *An Introduction to Solar Radiation*. Toronto, ON: Academic Press.

Juen, M., Mayer, C., Lambrecht, A., Han, H., and Liu, S. (2014). Impact of varying debris cover thickness on ablation: a case study for KOXKAR glacier in the Tien Shan. *Cryosphere* 8:377. doi: 10.5194/tc-8-377-2014

Kääb, A., Berthier, E., Nuth, C., Gardelle, J., and Arnaud, Y. (2012). Contrasting patterns of early twenty-first-century glacier mass change in the Himalayas. *Nature* 488, 495–498. doi: 10.1038/nature11324

Kayastha, R. B., Takeuchi, Y., Nakawo, M., and Ageta, Y. (2000). Practical prediction of ice melting beneath various thickness of debris cover on Khumbu glacier, Nepal, using a positive degree-day factor. *IAHS Publ*. 264, 71–81.

Khan, M. I. (1989). *Ablation on Barpu glacier, Karakoram Himalaya, Pakistan a study of melt processes on a faceted, debris-covered ice surface* (Master thesis), Wilfrid Laurier University, Waterloo, ON.

Liang, S. (2001). Narrowband to broadband conversions of land surface albedo I: algorithms. *Remote Sens. Environ*. 76, 213–238. doi: 10.1016/S0034-4257(00)00205-4

Lüthje, M., Pedersen, L., Reeh, N., and Greuell, W. (2006). Modelling the evolution of supraglacial lakes on the west Greenland ice-sheet margin. *J. Glaciol*. 52, 608–618. doi: 10.3189/172756506781828386

Mattson, L. (1993). Ablation on debris covered glaciers: an example from the Rakhiot glacier, Punjab, Himalaya. *Intern. Assoc. Hydrol. Sci*. 218, 289–296.

McNabb, R., Hock, R., O'Neel, S., Rasmussen, L. A., Ahn, Y., Braun, M., et al. (2012). Using surface velocities to calculate ice thickness and bed topography: a case study at Columbia glacier, Alaska, USA. *J. Glaciol*. 58, 1151–1164. doi: 10.3189/2012JoG11J249

Mertes, J. R., Thompson, S. S., Booth, A. D., Gulley, J. D., and Benn, D. I. (2017). A conceptual model of supra-glacial lake formation on debris-covered glaciers based on GPR facies analysis. *Earth Surface Process. Landforms* 42, 903–914. doi: 10.1002/esp.4068

Mihalcea, C., Mayer, C., Diolaiuti, G., D'agata, C., Smiraglia, C., Lambrecht, A., et al. (2008). Spatial distribution of debris thickness and melting from remote-sensing and meteorological data, at debris-covered Baltoro glacier, Karakoram, Pakistan. *Ann. Glaciol*. 48, 49–57. doi: 10.3189/172756408784700680

Miles, E. S., Pellicciotti, F., Willis, I. C., Steiner, J. F., Buri, P., and Arnold, N. S. (2016). Refined energy-balance modelling of a supraglacial pond, Langtang Khola, Nepal. *Ann. Glaciol*. 57, 29–40. doi: 10.3189/2016AoG71A421

Miles, E. S., Steiner, J., Willis, I., Buri, P., Immerzeel, W. W., Chesnokova, A., et al. (2017). Pond dynamics and supraglacial-englacial connectivity on debris-covered Lirung glacier, Nepal. *Front. Earth Sci*. 5:69. doi: 10.3389/feart.2017.00069

Miles, E. S., Willis, I., Buri, P., Steiner, J. F., Arnold, N. S., and Pellicciotti, F. (2018). Surface pond energy absorption across four Himalayan glaciers accounts for 1/8 of total catchment ice loss. *Geophys. Res. Lett*. 45, 10–464. doi: 10.1029/2018GL079678

Moore, P. L. (2018). Stability of supraglacial debris. *Earth Surface Process. Landforms* 43, 285–297. doi: 10.1002/esp.4244

Nakawo, M., and Young, G. J. (1981). Field experiments to determine the effect of a debris layer on ablation of glacier ice. *Ann. Glaciol*. 2, 85–91. doi: 10.3189/172756481794352432

Nicholson, L., and Benn, D. I. (2006). Calculating ice melt beneath a debris layer using meteorological data. *J. Glaciol*. 52, 463–470. doi: 10.3189/172756506781828584

Oerlemans, J., and Klok, E. J. (2002). Energy balance of a glacier surface: analysis of automatic weather station data from the morteratschgletscher, switzerland. *Arctic Antarct. Alpine Res*. 34, 477–485. doi: 10.1080/15230430.2002.12003519

Olson, M., and Rupper, S. (2019). Impacts of topographic shading on direct solar radiation for valley glaciers in complex topography. *Cryosphere* 13, 29–40. doi: 10.5194/tc-13-29-2019

Pelto, M. S. (2000). Mass balance of adjacent debris-covered and clean glacier ice in the north Cascades, Washington. *IAHS Publ*. 35–42.

Perez, R., Stewart, R., Arbogast, C., Seals, R., and Scott, J. (1986). An anisotropic hourly diffuse radiation model for sloping surfaces: description, performance validation, site dependency evaluation. *Solar Energy* 36, 481–497. doi: 10.1016/0038-092X(86)90013-7

Pratap, B., Dobhal, D., Mehta, M., and Bhambri, R. (2015). Influence of debris cover and altitude on glacier surface melting: a case study on Dokriani glacier, central Himalaya, India. *Ann. Glaciol*. 56, 9–16. doi: 10.3189/2015AoG70A971

Pritchard, M. S., Bush, A. B. G., and Marshall, S. J. (2008). Neglecting ice-atmosphere interactions underestimates ice sheet melt in millennial-scale deglaciation simulations. *Geophys. Res. Lett*. 35. doi: 10.1029/2007GL031738

Proy, C., Tanré, D., and Deschamps, P. Y. (1989). Evaluation of topographic effects in remotely sensed data. *Remote Sens. Environ*. 30, 21–32. doi: 10.1016/0034-4257(89)90044-8

Quincey, D., Braun, M., Glasser, N. F., Bishop, M., Hewitt, K., and Luckman, A. (2011). Karakoram glacier surge dynamics. *Geophys. Res. Lett*. 38. doi: 10.1029/2011GL049004

Quincey, D., Copland, L., Mayer, C., Bishop, M., Luckman, A., and Belo, M. (2009). Ice velocity and climate variations for Baltoro glacier, Pakistan. *J. Glaciol*. 55, 1061–1071. doi: 10.3189/002214309790794913

Quincey, D. J., and Glasser, N. F. (2009). Morphological and ice-dynamical changes on the Tasman glacier, New Zealand, 1990-2007. *Glob. Planet. Change* 68, 185–197. doi: 10.1016/j.gloplacha.2009.05.003

Reid, T., and Brock, B. (2014). Assessing ice-cliff backwasting and its contribution to total ablation of debris-covered miage glacier, Mont Blanc Massif, Italy. *J. Glaciol*. 60, 3–13. doi: 10.3189/2014JoG13J045

Reid, T., Carenzo, M., Pellicciotti, F., and Brock, B. (2012). Including debris cover effects in a distributed model of glacier ablation. *J. Geophys. Res. Atmos*. 117. doi: 10.1029/2012JD017795

Reid, T. D., and Brock, B. W. (2010). An energy-balance model for debris-covered glaciers including heat conduction through the debris layer. *J. Glaciol*. 56, 903–916. doi: 10.3189/002214310794457218

Reynolds, J. M. (2000). On the formation of supraglacial lakes on debris-covered glaciers. *IAHS Publ*. 153–164.

Reznichenko, N., Davies, T., Shulmeister, J., and McSaveney, M. (2010). Effects of debris on ice-surface melting rates: an experimental study. *J. Glaciol*. 56, 384–394. doi: 10.3189/002214310792447725

Rounce, D., Quincey, D., and McKinney, D. (2015). Debris-covered energy balance model for Imja-Lhotse Shar glacier in the Everest region of Nepal. *Cryosphere Discuss* 9, 3503–3540. doi: 10.5194/tcd-9-3503-2015

Rounce, D. R., King, O., McCarthy, M., Shean, D. E., and Salerno, F. (2018). Quantifying debris thickness of debris-covered glaciers in the Everest region of Nepal through inversion of a subdebris melt model. *J. Geophys. Res. Earth Surface* 123, 1094–1115. doi: 10.1029/2017JF004395

Rowan, A., Nicholson, L., Quincey, D., Gibson, M., Irvine-Fynn, T., Watson, C., et al. (2021). Seasonally stable temperature gradients through supraglacial debris in the Everest region of Nepal, Central Himalaya. *J. Glaciol*. 67, 170–181. doi: 10.1017/jog.2020.100

Rowan, A. V., Egholm, D. L., Quincey, D. J., and Glasser, N. F. (2015). Modelling the feedbacks between mass balance, ice flow and debris transport to predict the response to climate change of debris-covered glaciers in the Himalaya. *Earth Planet. Sci. Lett*. 430, 427–438. doi: 10.1016/j.epsl.2015.09.004

Sakai, A., Nakawo, M., and Fujita, K. (2002). Distribution characteristics and energy balance of ice cliffs on debris-covered glaciers, Nepal Himalaya. *Arctic Antarct. Alpine Res*. 34, 12–19. doi: 10.1080/15230430.2002.12003463

Sakai, A., Takeuchi, N., Fujita, K., and Nakawo, M. (2000). Role of supraglacial ponds in the ablation process of a debris-covered glacier in the nepal himalayas. *IAHS Publ*. 119–132.

Salerno, F., Thakuri, S., Tartari, G., Nuimura, T., Sunako, S., Sakai, A., et al. (2017). Debris-covered glacier anomaly? Morphological factors controlling changes in the mass balance, surface area, terminus position, and snow line altitude of Himalayan glaciers. *Earth Planet. Sci. Lett*. 471, 19–31. doi: 10.1016/j.epsl.2017.04.039

Scherler, D., Bookhagen, B., and Strecker, M. R. (2011a). Hillslope-glacier coupling: the interplay of topography and glacial dynamics in high Asia. *J. Geophys. Res. Earth Surface* 116. doi: 10.1029/2010JF001751

Scherler, D., Bookhagen, B., and Strecker, M. R. (2011b). Spatially variable response of Himalayan glaciers to climate change affected by debris cover. *Nat. Geosci*. 4, 156–159. doi: 10.1038/ngeo1068

Seong, Y. B., Owen, L. A., Yi, C., and Finkel, R. C. (2009). Quaternary glaciation of Muztag Ata and Kongur Shan: evidence for glacier response to rapid climate changes throughout the late glacial and holocene in westernmost tibet. *Geol. Soc. Am. Bull*. 121, 348–365. doi: 10.1130/B26339.1

Sicart, J.-E., Hock, R., and Six, D. (2008). Glacier melt, air temperature, and energy balance in different climates: the Bolivian Tropics, the French Alps, and northern Sweden. *J. Geophys. Res. Atmos*. 113. doi: 10.1029/2008JD010406

Steer, P., Huismans, R. S., Valla, P. G., Gac, S., and Herman, F. (2012). Bimodal plio-quaternary glacial erosion of fjords and low-relief surfaces in scandinavia. *Nat. Geosci*. 5, 635–639. doi: 10.1038/ngeo1549

Steiner, J. F., Pellicciotti, F., Buri, P., Miles, E. S., Immerzeel, W. W., and Reid, T. D. (2015). Modelling ice-cliff backwasting on a debris-covered glacier in the Nepalese Himalaya. *J. Glaciol*. 61, 889–907. doi: 10.3189/2015JoG14J194

Sutherland, J. L., Carrivick, J. L., Gandy, N., Shulmeister, J., Quincey, D. J., and Cornford, S. L. (2020). Proglacial lakes control glacier geometry and behavior during recession. *Geophys. Res. Lett*. 47:e2020GL088865. doi: 10.1029/2020GL088865

Takeuchi, N., and Li, Z. (2008). Characteristics of surface dust on Ürümqi glacier no. 1 in the tien Shan mountains, China. *Arctic Antarct. Alpine Res*. 40, 744–750. doi: 10.1657/1523-0430(07-094)[TAKEUCHI]2.0.CO;2

Thompson, S., Benn, D. I., Mertes, J., and Luckman, A. (2016). Stagnation and mass loss on a himalayan debris-covered glacier: processes, patterns and rates. *J. Glaciol*. 62, 467–485. doi: 10.1017/jog.2016.37

van Woerkom, T., Steiner, J. F., Kraaijenbrink, P. D., Miles, E., and Immerzeel, W. W. (2019). Sediment supply from lateral moraines to a debris-covered glacier in the Himalaya. *Earth Surface Dyn*. 7, 411–427. doi: 10.5194/esurf-7-411-2019

Vincent, C., Wagnon, P. W., Shea, J. M., Immerzeel, W. W., Kraaijenbrink, P., Shrestha, D., et al. (2016). Reduced melt on debris-covered glaciers: investigations from Changri Nup Glacier, Nepal. *Cryosphere* 10, 1845–1858. doi: 10.5194/tc-10-1845-2016

Wessels, R. L., Kargel, J. S., and Kieffer, H. H. (2002). Aster measurement of supraglacial lakes in the Mount Everest region of the Himalaya. *Ann. Glaciol*. 34, 399–408. doi: 10.3189/172756402781817545

Wilson, J. P., and Bishop, M. P. (2013). "Geomorphometry," in *Remote Sensing and GIScience in Geomorphology*, ed J. S. Bishop (Waltham, MA: Academic Press), 162–186. doi: 10.1016/B978-0-12-374739-6.00049-X

Wirbel, A., Jarosch, A. H., and Nicholson, L. (2018). Modelling debris transport within glaciers by advection in a full-stokes ice flow model. *Cryosphere* 12, 189–204. doi: 10.5194/tc-12-189-2018

Yue, X., Zhao, J., Li, Z., Zhang, M., Fan, J., Wang, L., et al. (2017). Spatial and temporal variations of the surface albedo and other factors influencing Urumqi glacier no. 1 in Tien Shan, China. *J. Glaciol*. 63, 899–911. doi: 10.1017/jog.2017.57

Zhang, Y., Fujita, K., Liu, S., Liu, Q., and Nuimura, T. (2011). Distribution of debris thickness and its effect on ice melt at Hailuogou glacier, southeastern Tibetan plateau, using *in situ* surveys and aster imagery. *J. Glaciol*. 57, 1147–1157. doi: 10.3189/002214311798843331

Zhang, Y., Hirabayashi, Y., Fujita, K., Liu, S., and Liu, Q. (2016). Heterogeneity in supraglacial debris thickness and its role in glacier mass changes of the mount Gongga. *Sci. China Earth Sci*. 59, 170–184. doi: 10.1007/s11430-015-5118-2

Zhang, Y., Li, X., Wen, J., Liu, Q., and Yan, G. (2015). Improved topographic normalization for landsat tm images by introducing the MODIS surface BRDF. *Remote Sens*. 7, 6558–6575. doi: 10.3390/rs70606558

Conflict of Interest: The authors declare that the research was conducted in the absence of any commercial or financial relationships that could be construed as a potential conflict of interest.

frontiers in Earth Science

ORIGINAL RESEARCH
published: 04 June 2021
doi: 10.3389/feart.2021.623623

Ice Cliff Dynamics of Debris-Covered Trakarding Glacier in the Rolwaling Region, Nepal Himalaya

Yota Sato[1], Koji Fujita[1], Hiroshi Inoue[2], Sojiro Sunako[3], Akiko Sakai[1], Akane Tsushima[1,4†], Evgeny A. Podolskiy[5,6], Rakesh Kayastha[7] and Rijan B. Kayastha[7]*

[1]Graduate School of Environmental Studies, Nagoya University, Nagoya, Japan, [2]National Research Institute for Earth Science and Disaster Resilience (NIED), Tsukuba, Japan, [3]Snow and Ice Research Center, National Research Institute for Earth Science and Disaster Resilience (NIED), Nagaoka, Japan, [4]Japan Meteorological Agency, Meteorological Research Institute, Tsukuba, Japan, [5]Arctic Research Center, Hokkaido University, Sapporo, Japan, [6]Global Station for Arctic Research, Global Institution for Collaborative Research and Education, Hokkaido University, Sapporo, Japan, [7]Himalayan Cryosphere, Climate, and Disaster Research Center (HiCCDRC), Department of Environmental Science and Engineering, School of Science, Kathmandu University, Dhulikhel, Nepal

OPEN ACCESS

Edited by:
Timothy C. Bartholomaus, University of Idaho, United States

Reviewed by:
Leif S. Anderson, University of Lausanne, Switzerland
Qiao Liu, Chinese Academy of Sciences (CAS), China
Eric Petersen, University of Alaska Fairbanks, United States

***Correspondence:**
Yota Sato
yota.sato@nagoya-u.jp

†Present address:
Akane Tsushima, Graduate School of Sciences, Chiba University, Chiba, Japan

Specialty section:
This article was submitted to Cryospheric Sciences, a section of the journal Frontiers in Earth Science

Received: *30 October 2020*
Accepted: *05 May 2021*
Published: *04 June 2021*

Citation:
Sato Y, Fujita K, Inoue H, Sunako S, Sakai A, Tsushima A, Podolskiy EA, Kayastha R and Kayastha RB (2021) Ice Cliff Dynamics of Debris-Covered Trakarding Glacier in the Rolwaling Region, Nepal Himalaya. Front. Earth Sci. 9:623623. doi: 10.3389/feart.2021.623623

Ice cliffs can act as "hot spots" for melt on debris-covered glaciers and promote local glacier mass loss. Repeat high-resolution remote-sensing data are therefore required to monitor the role of ice cliff dynamics in glacier mass loss. Here we analyze high-resolution aerial photogrammetry data acquired during the 2007, 2018, and 2019 post-monsoon seasons to delineate and monitor the morphology, distribution, and temporal changes of the ice cliffs across the debris-covered Trakarding Glacier in the eastern Nepal Himalaya. We generate an ice cliff inventory from the 2018 and 2019 precise terrain data, with ice cliffs accounting for 4.7 and 6.1% of the debris-covered area, respectively. We observe large surface lowering (>2.0 m a^{-1}) where there is a denser distribution of ice cliffs. We also track the survival, formation, and disappearance of ice cliffs from 2018 to 2019, and find that ~15% of the total ice cliff area is replaced by new ice cliffs. Furthermore, we observe the overall predominance of northwest-facing ice cliffs, although we do observe spatial heterogeneities in the aspect variance of the ice cliffs (ice cliffs face in similar/various directions). Many new ice cliffs formed across the stagnant middle sections of the glacier, coincident with surface water drainage and englacial conduit intake observations. This spatial relationship between ice cliffs and the glacier hydrological system suggests that these englacial and supraglacial hydrological systems play a significant role in ice cliff formation.

Keywords: ice cliff, high mountain asia, debris-covered glacier, unmanned aerial vehicles, Himalaya

INTRODUCTION

Glaciers in High Mountain Asia have been shrinking in recent decades (e.g., Bolch et al., 2012; Brun et al., 2017; Shean et al., 2020). Around 10–19% of the glacier area in High Mountain Asia is debris-covered (Herreid and Pellicciotti, 2020), with this debris cover contributing to complex melting processes (e.g., Zhang et al., 2011). A debris mantle thicker than ~5 cm has an insulating effect, whereas a debris layer that is only a few centimeters thick can enhance ice ablation (e.g., Mattson et al., 1993; Østrem, 1959; Nicholson and Benn, 2006). Conversely, several studies have revealed that debris-covered and clean glaciers possess comparable thinning rates (e.g., Kääb et al., 2012; Nuimura

et al., 2012; Gardelle et al., 2013; Lamsal et al., 2017; Brun et al., 2019), and have called this phenomenon a "debris-covered anomaly" (Pellicciotti et al., 2015; Vincent et al., 2016; Salerno et al., 2017). It has been suggested that the local facilitation of debris-cover-driven glacier melting can be caused by ice cliffs and ponds, which are considered "hotspots" of melt (e.g., Sakai et al., 1998; Sakai et al., 2002; Han et al., 2010; Steiner et al., 2015; Buri et al., 2016; Thompson et al., 2016; Brun et al., 2018; Anderson et al., 2019a).

Several ice cliff studies have analyzed field observations and employed remote-sensing methods to elucidate ice cliff processes. Sakai et al. (1998) first observed the ice cliff backwasting rate across Lirung Glacier, Nepal. Subsequent studies have attempted to quantify the amount of ice cliff ablation using high-resolution remote-sensing data. Thompson et al. (2016) computed the thinning rate of Ngozumpa Glacier, Khumbu region, Nepal, using high-resolution (1.0 m) digital elevation models (DEMs), and found that ice cliff wasting contributed to ~40% of the total surface lowering, even though ice cliffs occupied only 5% of the total debris-covered area. Recent developments in photogrammetry-based terrain data processing and unmanned aerial vehicle (UAV) technology have greatly advanced ice cliff research (e.g., Immerzeel et al., 2014). Brun et al. (2018) combined *in situ* measurements, UAV photogrammetry, and satellite data to estimate the ice cliff mass loss across the debris-covered area of the Changri Nup Glacier in the Khumbu region, Nepal. They estimated that ice cliff ablation contributed to ~23% of the total glacier mass loss, even though the ice cliff area accounted for only ~8% of the debris-covered area. Studies on the spatial distribution and temporal changes of ice cliffs have also been conducted at the regional scale to elucidate ice cliff processes. Watson et al. (2017a) extracted ice cliffs and supraglacial ponds across 14 glaciers in the Khumbu region, Nepal, using Google Earth Pro, and found that the ice cliffs were primarily north-facing, regardless of the glacier-flow direction, with supraglacial ponds often forming adjacent to the ice cliffs. Steiner et al. (2019) analyzed the spatiotemporal variability of ice cliffs during the 1974–2015 period by combining multiple satellite images in the Langtang catchment of Nepal, and revealed that 17% of the ice cliffs at the Langtang Glacier have persisted for nearly a decade.

Only a few high-resolution (decimeter scale) annual ice cliff monitoring studies have been conducted to date, although these previous studies have extended our understanding of ice cliff processes on debris-covered glaciers (e.g., Immerzeel et al., 2014; Brun et al., 2018). Therefore, the morphology (i.e., size, slope, and aspect), spatial distribution, and dynamics (formation and decay processes) of ice cliffs across debris-covered glaciers remain largely unknown. Here we employ high-resolution photogrammetry to (1) generate an ice cliff inventory, (2) characterize the morphology and spatial distribution of ice cliffs, and (3) observe ice cliff persistence, decay, and formation at the annual scale across the debris-covered Trakarding Glacier in the eastern Nepal Himalaya.

STUDY SITE, DATA, AND METHODS

Study Site

Debris-covered Trakarding Glacier (27.9°N, 86.5°E) is located in Rolwaling Valley in the eastern Nepal Himalaya (**Figure 1A,B**); the debris-free Trambau Glacier is situated above (Sunako et al., 2019), and has been disconnected from Trakarding Glacier since the 1970s. Previous studies have treated the two glaciers as the "Trakarding–Trambau Glacier system" (Podolskiy et al., 2018; Podolskiy et al., 2019; Sunako et al., 2019). The total area of the system is 31.7 km^2 (Nuimura et al., 2015), and spans elevations of 4,500–6,690 m above sea level (a.s.l.). Trakarding Glacier is surrounded by steep valley sides, with snow accumulation occurring largely through avalanches from the eastern headwall (Sunako et al., 2019). A negative mass balance has been confirmed via stake measurements (Sunako et al., 2019). It is a lake-terminating glacier, with Tsho Rolpa, one of the largest glacial lakes in Nepal, at its terminus. Tsho Rolpa has been expanding since the 1950s (Sakai et al., 2000a; Fujita et al., 2013). Trakarding Glacier has a debris-covered area of 2.9 km^2 and extends 4.7 km along the glacier centerline, with flow to the northwest (~310°), based on its 2018 terminus position. We have divided the study area into nine sections, labeled sections A–I (500 m intervals from the 2018 terminus), to analyze the spatial characteristics of the ice cliff distribution (**Figure 1C**).

Field Observations

We have conducted five field campaigns across Trakarding Glacier since 2016. We first deployed mass-balance stakes across the glacier in May 2016, which have been resurveyed every October from 2016 to 2019. The stake positions were measured using a differential global positioning system (DGPS, GEM-1/-2, Enabler Inc.). We also conducted a kinematic DGPS survey across both the on- and off-glacier terrain in May 2016 and October to November 2019 to obtain validation points for the photogrammetry-based DEMs (**Figure 1C**). The base station for this survey was installed beside the automatic weather station at 4,806 m a.s.l. on the lateral moraine (**Figure 1C**).

Aerial Photogrammetry Survey

We used three aerial photogrammetry datasets to monitor the surface elevation changes, surface flow velocity, and ice cliff distribution across the debris-covered area of Trakarding Glacier (**Table 1**). We conducted two of the photogrammetry surveys during the 2018 and 2019 field campaigns; we also analyzed the data from a 2007 photogrammetry survey to identify any decadal-scale changes. We chartered a helicopter on October 18, 2018, and mounted three cameras (Richo GR and GRII) on the skid and lower pilot's window (**Supplementary Figure S1A**), with images acquired at a 2-s interval. We then mounted a Richo GRII camera (1-s interval time-lapse mode setting) onto a fixed-wing UAV (Hobbyking Sky Walker X-5; **Supplementary Figure S1B**), which had a 1.8 m wingspan and 1.4 kg body (including camera), for four flights on 18 and October 19, 2019. The mean flight speed was ~60 km h^{-1}, with a maximum flight time of ~60 min. The UAV details are available in Fujita et al. (2017). The flight path was set to obtain an alongside overlap of ~80%, side overlap of ~60%, and <0.2 m ground resolution.

We analyzed the aerial photogrammetry dataset taken from a private jet in 2007 (**Figure 1B**) to estimate the decadal change in debris-covered area. The flight altitude was estimated as ~6,700 m above ground level (a.g.l.; **Table 1**), and Canon EOS-5D and

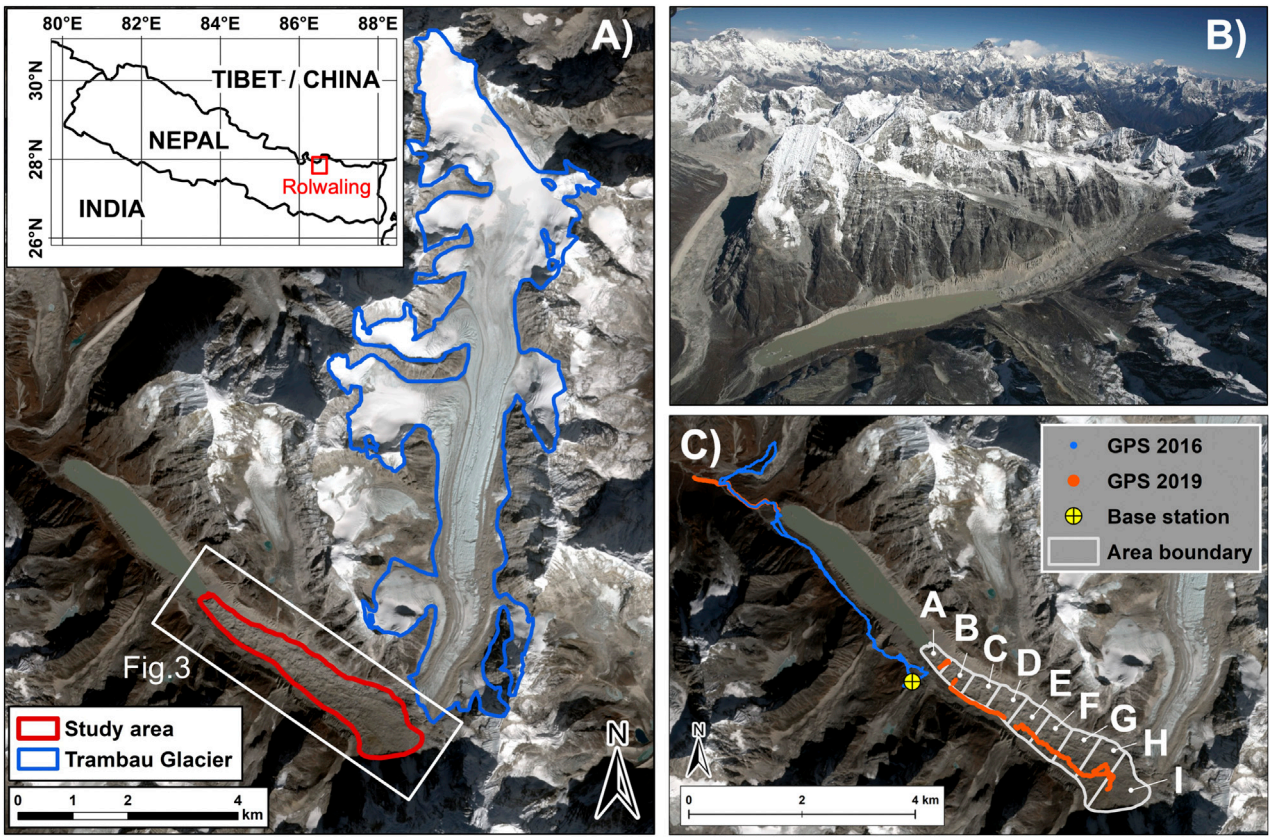

FIGURE 1 | Details of the study area. **(A)** Location of the Rolwaling region and overview of the Trakarding-Trambau Glacier system. **(B)** Aerial photograph of the study area, taken from a business jet plane during the photogrammetry survey on November 24, 2007. **(C)** Outline of the study section boundaries along the debris-covered Trakarding Glacier and GPS tracks. The white box in **(A)** denotes the domain of **Figure 3**. The background image in **(A)** and **(C)** is a Sentinel-2 satellite image (acquired on November 24, 2017). Glacier boundaries are modified from the GAMDAM Glacier Inventory (Nuimura et al., 2015; Sakai, 2019).

TABLE 1 | Details of the aerial photogrammetry survey and structure from motion data processing.

	November 24, 2007	October 18, 2018	October 18–19, 2019
Platform	Business jet plane	Helicopter	Fix-wing UAV
Camera	Canon EOS-1Ds MarkII CanonEOS-5D	Ricoh GR Ricoh GR II	Ricoh GR II
Number of flights	1	1	4
Number of images	242	986	1,644
Flying altitude (m a.g.l.)*	6,690	686	449
Coverage area (km^2)*	401	80	121
Ground resolution (m)*	1.49	0.18	0.11
Number of GCPs	33	78	174
SfM-DEM size (pixel)*	18,736 × 17,671	71,988 × 62,360	208,277 × 208,662
Ortho/DEM resolution (m)	2.0/2.0	0.2/0.2	0.2/0.2

**Calculated values in agisoft metashape.*

Canon EOS-1Ds cameras were used for the image acquisition. However, the ground resolution was rather coarse due to the high flight altitude, such that delineation of the ice cliffs and supraglacial ponds was not possible. Therefore, these data were only used for our surface elevation change analysis. We successfully obtained images of the off-glacier terrain in 2007 and 2018, whereas the 2019 images mainly covered the main body of Trakarding Glacier, with limited off-glacier terrain coverage (**Supplementary Figure S2**).

Ground Control Points

We extracted ground control points (GCPs) for the photogrammetry data processing (*Structure From Motion Data Processing*) using ortho-images and a DEM derived from the

Pléiades satellite imagery. The Pléiades image was acquired on December 1, 2017. The ortho-image and DEM resolutions are 0.5 and 2.0 m, respectively (Berthier et al., 2014). We assessed the vertical accuracy of the Pléiades-derived DEM (hereafter Pléiades-DEM) using *in-situ* DGPS measurements obtained at off-glacier sites in 2016. The GPS data points that were acquired during the 2016 field campaign were projected to Universal Transverse Mercator coordinates (UTM, zone 45 north, WGS84). The GPS points were then interpolated in ArcGIS using the inverse distance weighted method to create a GPS-derived DEM (hereafter GPS-DEM) with the same grid size as the Pléiades-DEM. Grid cells with no GPS points were then excluded (Tshering and Fujita, 2016).

Berthier et al. (2014) reported that the vertical accuracy of Pléiades-DEMs can be improved by shifting the DEMs horizontally. The elevation difference relative to the GPS-DEM was calculated by shifting the Pléiades-DEM horizontally in 0.5 m increments (one pixel of the Pléiades panchromatic ortho-image). We estimated the most suitable shifting position that minimized the standard deviation (SD) of the elevation difference between the Pléiades- and GPS-DEMs (Berthier et al., 2007). Grid cells containing surface slopes steeper than 30° were not used for the accuracy assessment (Fujita et al., 2008; Nuimura et al., 2012). The minimum SD of the elevation difference (0.97 m) was found when the Pléiades-DEM was shifted horizontally by +3.5 m in the easting direction and −3.0 m in the northing direction (N = 17,047 GPS-DEM grid cells). The mean vertical residual (0.88 m) was then corrected after the Pléiades-DEM shift. The GCPs were extracted (locations and elevations) from the panchromatic ortho-image after the Pléiades-DEM shift, which also shifted with the DEM. The topographic features (e.g., boulders or rock cracks) of these GCPs were located on the stable off-glacier terrain.

Structure From Motion Data Processing

Structure from Motion (SfM) was used to generate ortho-images and DEMs from the aerial photographs. We used Agisoft Metashape Professional Edition 1.5.1 (Agisoft LLC, 2020) for the data processing, and followed the analysis workflow outlined in Lucieer et al. (2014), Wigmore and Mark (2017), and the Agisoft Metashape Professional User manual (2020). We initially focused on the 2018 photogrammetry dataset since the aerial photogrammetry coverage area in 2018 extended to the off-glacier terrain; we extracted 78 GCPs from the shifted Pléiades-DEM and ortho-image (*Ground Control Points*) to create the 2018 ortho-image and DEM (hereafter SfM-DEM-2018). We corrected the SfM-DEM-2018 by the mean elevation difference relative to the GPS-DEM. We further extracted GCPs on the off-glacier terrain from the SfM-DEM/ortho-image-2018 and used these GCPs for the other photogrammetry datasets. The SfM data processing workflow is shown in **Figure 2A**, and the GCP locations are shown in **Supplementary Figure S2**. The SfM-DEM vertical biases (mean elevation difference ± SD) relative to the GPS-DEMs were 1.21 ± 2.32 m (2007), −1.58 ± 1.82 m (2018), and 4.64 ± 2.35 m (2019; **Table 2**; **Supplementary Figure S3**). Each SfM-DEM bias was corrected using these mean elevation differences. We could not compute the stable-ground elevation differences because the UAV photogrammetry area obtained in 2019 was spatially limited. Therefore, we estimated the relative GCP vertical error (**Supplementary Table S1**) and GCP placement error that was calculated in Agisoft Metashape (**Supplementary Table S2**) for additional error assessments.

Ice Cliff Analysis

Delineation

We delineated the ice cliffs on the debris-covered area to characterize the ice cliff morphology and spatial distribution. The ortho-image and processed SfM-DEM data (hillshade, aspect, and slope) were analyzed in ArcGIS, with edge polylines and slope polygons manually created on the ridges and slope sections of the ice cliffs, respectively (**Supplementary Figure S4**). We calculated the ridge length, ice cliff height, mean slope of the cells within each ice cliff polygon, horizontal footprint of the slope (map-view area), ice cliff inclined area (actual slope area; **Supplementary Figure S4E**), and ice cliff orientation, which is the vector mean of all of the grid cells contained in the slope polygons, from the ice cliff inventory. We also delineated the supraglacial ponds on the debris-covered area and analyzed their spatial adjacency with ice cliffs by checking the relative positions of the ponds and cliffs polygons in the ArcGIS environment.

One main operator (researcher) delineated all of the ice cliffs to ensure that the ice cliffs were selected and delineated in a consistent manner. We then evaluated the delineated ice cliffs independently to estimate the delineation uncertainty due to subjective bias. Specifically, five operators (including the main operator) generated ridge lines and slope polygons for 20 randomly selected ice cliffs of various size and shape. We then calculated the standard deviations of the edge length and map-view area for these 20 ice cliffs. The ice cliff inclined area is strongly affected by the cliff slope, which depends on the DEM quality. Therefore, we also tested the inclined area's sensitivity to a slope angle change of ±1° for all of the ice cliffs.

The ice cliff inclined area strongly relates to mass loss; therefore, we defined "ice cliff density ($m^2\ m^{-2}$)" as an indicator of the spatial density of ice cliffs. The total ice cliff inclined area in each section was divided by the section map-view area. We also estimated the ice cliff length density, which is defined as the ice cliff edge length per square meter, for comparison with a previous study in the neighboring Khumbu region (Watson et al., 2017a). We calculated the circular variance of the ice cliff orientation (Fisher, 1995), which is defined by the following equation:

$$V = 1 - \overline{R} \tag{1}$$

where V is the circular variance and $\overline{R}$ is the mean resultant length of the target ice cliff orientation, which ranges from 0 to 1. The mean resultant length is $\overline{R}$ calculated as:

$$\overline{R} = \left[\left(\frac{1}{N} \sum_{i=1}^{N} \cos \theta_i \right)^2 + \left(\frac{1}{N} \sum_{i=1}^{N} \sin \theta_i \right)^2 \right]^{1/2} \tag{2}$$

where N is the number of target ice cliffs and θ_i is the individual ice cliff aspect. A lower circular variance implies that the ice cliff target group faces a uniform direction, whereas an ice cliff group that faces multiple directions has a higher circular variance.

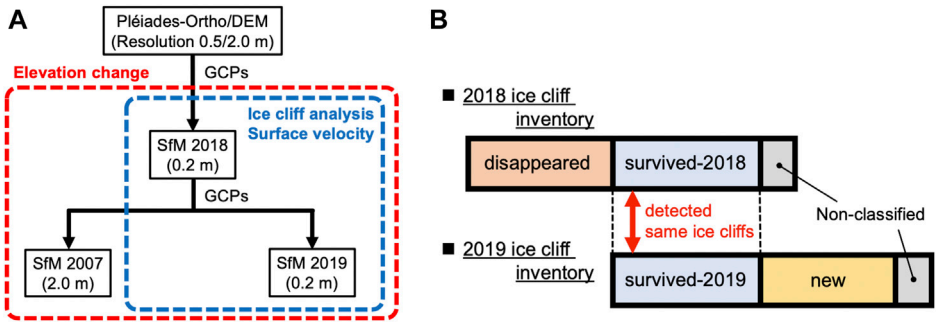

FIGURE 2 | (A) Structure from Motion data processing workflow and **(B)** conceptual diagram of the ice cliff annual tracking and classification.

TABLE 2 | Accuracy of the SfM-DEMs.

SfM-DEM minus GPS-DEM			
Year	**Mean (m)**	**SD (m)**	**Pixel count**
2007	2.43	2.18	8,693
2018	−1.58	1.82	26,142
2019	4.64	2.35	8,790

Tracking Temporal Changes in Ice Cliffs

We tracked the evolution, persistence, and decay of ice cliffs by comparing the 2018 and 2019 ice cliff inventories. **Figure 2B** shows ice cliff classification, whereby the ice cliffs are defined as either "survived", "new", or "disappeared". The survived-2018 and -2019 cliffs are those that have been identified in both inventories. Conversely, the new cliffs are those in the 2019 inventory that could not be detected in the 2018 inventory, and the disappeared cliffs are those in the 2018 inventory that could not be detected in the 2019 inventory. Some survived-2018 ice cliffs either merged or split after one year, resulting in slight variations between the number of survived cliffs in 2018 and 2019. We defined the remaining ice cliffs that could not be clearly categorized as "non-classified" cliffs.

Surface Elevation Change, Surface Flow Velocity, and Water Flow Analyses

We estimated the decadal (2007–2018) and annual (2018–2019) surface elevation changes of the debris-covered area by differentiating the generated SfM-DEMs. We modified the glacier area from the GAMDAM Glacier Inventory (Nuimura et al., 2015; Sakai, 2019) using the glacier boundary and calving front that were derived from the ortho-images for the surface elevation change analysis. All of the SfM-DEMs were acquired in the post-monsoon season, which meant that a seasonal correction was unnecessary. We evaluated the surface elevation change of the terminus portion that was lost by calving and/or retreat as the elevation difference between the glacier surface in a pre-DEM and the lake level in a post-DEM since Tsho Rolpa grew during the study period; the lake level was determined by averaging the shoreline elevation of the SfM-DEM (Fujita et al., 2013).

The surface flow velocities were calculated using a manual feature tracking method (Immerzeel et al., 2014; Kraaijenbrink P. et al., 2016). We calculated the displacements of the same boulders that were detected in the 2018 and 2019 ortho-images. We excluded any boulders on steep slopes (>20°) to eliminate irregular displacements (e.g., overturning or slipping boulders). Boulder displacements were calculated for 394 points (out of 446 initial candidates), and the spatial distribution of the surface velocities was obtained via an ordinary kriging interpolation method (Immerzeel et al., 2014; Kraaijenbrink P. et al., 2016).

The SfM-DEM-2019 was analyzed using the hydrological analysis tool in ArcGIS to identify potential supraglacial drainage paths since they may affect ice cliff generation (Sakai et al., 2000b; Benn et al., 2017). We employed the D8 algorithm (O'Callaghan and Mark, 1984) to determine the potential surface flow direction using the SfM-DEM-2019, which was resampled from 0.2 to 3.0 m resolution to avoid microtopography-generated noise. We estimated the englacial conduit network from field observations of intake and outlet holes, aerial oblique movies taken from multi-copter UAV Phantom4 (DJI), and aerial photographs from the fixed-wing UAV during the 2019 field campaign. The glacier surface slope was also calculated from the SfM-DEM-2019, with the surface elevations broken into 500 m long sections along the glacier centerline.

The debris thickness distribution across a glacier may potentially affect ice cliff formation; however, there is no direct method to measure its distribution. Therefore, we employed thermal resistance, a proxy for debris thickness that is defined as the thickness divided by the thermal conductivity of the debris (Nakawo and Young, 1982). We adopted the spatial distribution of the thermal resistance across the surface of Trakarding Glacier using nine ASTER images that were acquired between October 2004 and February 2008 (Fujita and Sakai, 2014).

RESULTS

Surface Elevation Change and Flow Velocity

Surface elevation change rates (dh/dt) were calculated from the three SfM-DEMs (**Figures 3A,B**; **Supplementary Figure S6**), with mean dh/dt values of −1.7 and −4.7 m a^{-1} obtained for the 2007–2018 and 2018–2019 periods, respectively. Large surface

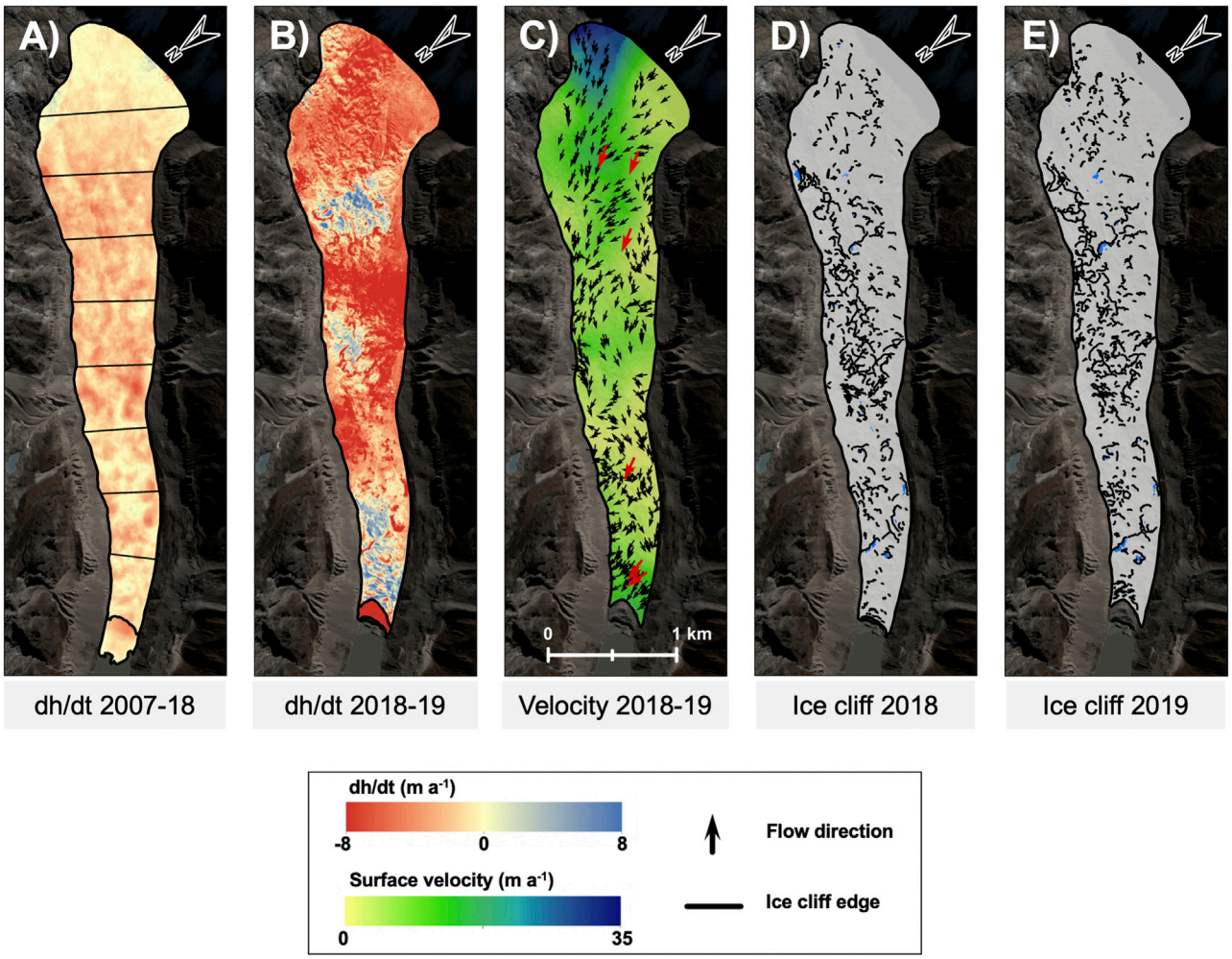

FIGURE 3 | Spatial distribution of surface elevation change (dh/dt) for the **(A)** 2007–2018 and **(B)** 2018–2019 periods. **(C)** 2018–2019 surface flow velocity field. Ice cliff distributions (cliff edges highlighted) and supraglacial ponds in **(D)** October 2018 and **(E)** October 2019. The section boundaries are indicated in **(A)**. Both the pre- and post-terminus positions are shown in **(A)** and **(B)**. Red arrows in **(C)** are the stake-measured surface flow vectors.

lowering (>2.0 m a^{-1}) was observed across the middle sections (sections D–F) at the decadal timescale (2007–2018; **Figure 4A**). The largest elevation lowering during the 2018–2019 period occurred across Section F (section mean: −7.6 m a^{-1}), followed by the calving front (Section A, section mean: −6.0 m a^{-1}; **Figure 4A**). The spatially averaged surface flow velocity was 6.7 m a^{-1} for the 2018–2019 period (**Figure 3C**), with a maximum surface flow velocity of 30.2 m a^{-1} observed across the uppermost reaches of Section I. A general up-glacier to down-glacier decrease in surface flow velocity was observed, with a stagnation in flow observed in the down-glacier sections (Section C; **Figure 4B**); however, an increase in surface flow velocity was observed near the glacier terminus (Section A).

Uncertainty in Ice Cliff Delineation

We calculated the standard deviations of the edge length and map-view area of each ice cliff that was delineated by the five operators (**Supplementary Figure S5**), and employed the mean standard deviations (6.0 m for the cliff edge length and 24 m^2 for map-view area of a cliff) as the delineation uncertainty. The corresponding uncertainties are estimated to be ±12.5% (2018) and ±11.4% (2019) for the edge length, and ±8.3% (2018) and ±6.9% (2019) for the map-view area, respectively. The cliff inclined area uncertainties that are associated with the map-view area uncertainties are ±8.1% (2018) and ±6.7% (2019). The additional uncertainty of the inclined area, which is associated with a slope angle uncertainty of ±1°, does not exceed ±2%.

Ice Cliff Characteristics

We extracted 481 and 505 ice cliffs from the 2018 and 2019 ortho-images, respectively (**Figures 3D,E**). The total ice cliff map-view areas were 138 × 103 m^2 (4.7% of the study area) and 176 × 103 m^2 (6.1%) in 2018 and 2019, respectively. The ice cliff length densities for the entire study area were 7.9×10^{-3} and 9.1×10^{-3} m m^{-2} in 2018 and 2019, respectively. The average ice cliff aspects were 335° (2018) and 325° (2019), which clearly suggested the

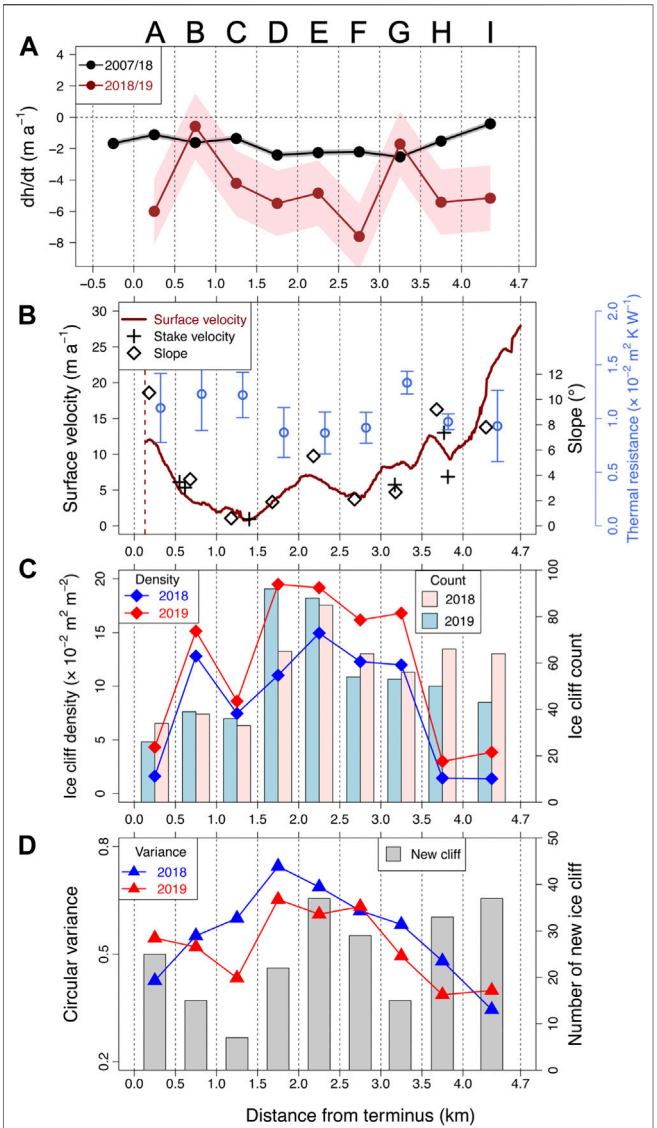

FIGURE 4 | Section means of the **(A)** surface elevation change rate (dh/dt), **(B)** longitudinal surface flow velocity profile, stake displacement rate, thermal resistance (Fujita and Sakai, 2014), and section slopes in 2019, **(C)** ice cliff density and ice cliff count, and **(D)** circular variance of the ice cliff aspect and number of new ice cliffs in 2019. Glacier-wide segments A–I are 500-m-long segments that extend up-glacier from the terminus. The distance on the *x*-axis refers to the terminus position in October 2018 (0.0 km); the dashed line in **(B)** indicates the terminus position in 2019. The shaded region in **(A)** denotes the elevation change uncertainties (standard deviation of the SfM-DEMs pair; **Table 2**).

predominance of northwest-facing ice cliffs (**Figure 5A**). We also calculated the morphological characteristics of the ice cliffs (**Table 3**). We found a strong positive correlation (r = 0.87, $p < 0.001$) between the ice cliff edge length and inclined area, with a power-law fit confirming the strong relationship between these ice cliff characteristics (R^2 = 0.85, $p < 0.001$; **Figure 5B**). The power-law fit makes it possible to estimate the cliff inclined area from cliff edge length, which can be delineated from rather lower-resolution images. Supraglacial ponds covered 113 × 102 m^2 (0.4% of the study area) in 2018 and 130 × 102 m^2 (0.5%) in 2019. Approximately 83 and 74% of the total pond areas in 2018 and 2019, respectively, were adjacent to ice cliffs. Conversely, 15% (2018) and 8% (2019) of ice cliffs in the map-view area were adjacent to supraglacial ponds.

Spatial Distribution of Ice Cliffs

The ice cliff density and ice cliff count were analyzed across the nine sections (**Figure 4C**), with both the highest ice cliff density and ice cliff count observed across the middle section (Section E) during both years. The section means of the long-term elevation change (2007–2018) and ice cliff density in 2018 exhibit a strong negative correlation (r = −0.80, $p < 0.05$), whereas no correlation between the annual surface elevation change (2018–2019) and ice cliff density is observed. The ice cliff densities tend to decrease from the middle to both the terminus and up-glacier sections of the study area. High ice cliff counts were observed in the middle section (Section E) and up-glacier sections (sections H and I). The high ice cliff numbers and low ice cliff densities observed in the up-glacier sections (sections H and I) indicate that this area generally has smaller ice cliffs (**Figure 4C**).

The circular variance is high across the middle sections (sections D–F: >0.6) and low across the up-glacier and terminus sections (sections A, H, and I; **Figure 4D**). The ice cliff orientations show that north-facing ice cliffs (northeast and northwest) are predominant across all of the sections, whereas the aspect proportions vary among the sections (**Figure 6**). The south-facing ice cliffs (southwest and southeast) possess higher aspect proportions (>30%) across the middle sections (sections D–F) than across the terminus and up-glacier sections, which explains the large ice cliff variance across the middle sections (**Figure 4D**).

Temporal Changes in Ice Cliffs and Supraglacial Streams

Our ice cliff tracking analysis shows that 45% of the ice cliffs and 14% of their inclined area disappeared between 2018 and 2019 (**Table 4**). The ice cliff aspect is summarized for each ice cliff type in **Figure 7**. Most of the survived-2018 and -2019 ice cliffs are north-facing (~80%; **Figures 7B,C**), with the disappeared and new ice cliffs consisting of more south-facing cliffs (~35%) than the survived ice cliffs (~20%; **Figure 7**). The circular variance for each ice cliff type also supports the aspect alignment of the survived ice cliffs and the aspect heterogeneity of the disappeared and new ice cliffs (**Figure 7**).

The ice cliff inclined area and slope also exhibit significant differences among the four ice cliff types (**Table 5**). The mean inclined area of the survived-2018 ice cliffs was significantly larger than that of the disappeared ice cliffs ($p < 0.001$ *via* Welch's *t*-test), and the survived-2019 ice cliffs had a larger inclined area than the new ice cliffs ($p < 0.001$). Furthermore, the disappeared cliffs had gentler slopes than the survived-2018 ice cliffs ($p < 0.05$), and the survived-2019 ice cliffs had significantly steeper slopes than the new ice cliffs ($p < 0.001$). A comparison of the survived-2018 and -2019 ice cliff morphologies revealed that the survived-2018 ice cliffs became significantly larger ($p < 0.05$) and steeper ($p < 0.001$) over time (**Table 5**). The aspect dependency of

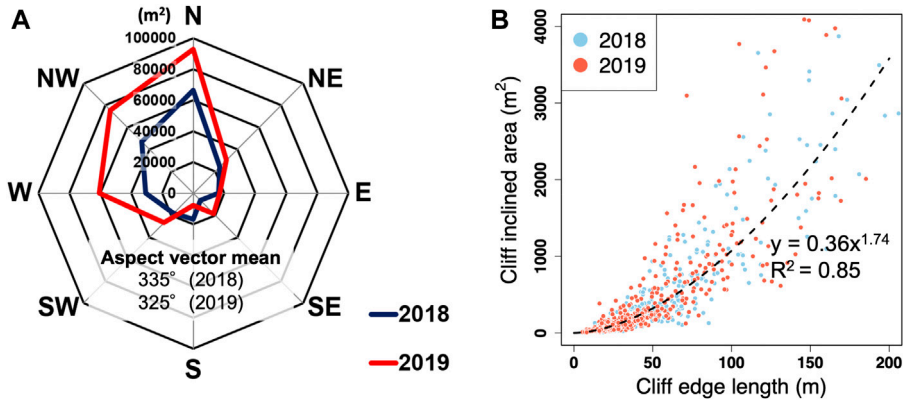

FIGURE 5 | (A) Ice cliff aspect chart for the cliff inclined area (m^2) and **(B)** the relationship between ice cliff edge length and inclined area. The dashed line in **(B)** is a power-law fit curve based on the ice cliff edge length and inclined area.

TABLE 3 | Morphological characteristics of the analyzed ice cliffs. The maximum (Max.), minimum (Min.), and median (Med.) values are provided.

	Edge length (m)			Inclined area (m^2)			Height (m)			Slope (°)		
	Min.	Med.	Max.	Min.	Med.	Max.	Min.	Med.	Max.	Min.	Med.	Max.
2018	4	33	334	1	167	8,399	1	9	53	10	42	62
2019	5	32	438	7	159	11,706	1	10	71	21	43	60

the survived ice cliffs shows that the northwest-facing cliffs mostly expanded (170% increase in the inclined area) from 2018 to 2019 (**Supplementary Table S3**). We plotted the new ice cliffs and counted the number in each section (**Figures 4D**, **8A**). More new ice cliffs formed across the middle (sections E and F), terminus (Section A), and up-glacier sections (sections H and I). Our supraglacial water flow analysis with the observed conduits is shown in **Figure 8**, which used nine exposed conduits that were identified from the aerial and terrestrial observations in 2019. The thermal resistance is relatively high in the terminus sections (sections A–C) and low in the middle to upper sections (sections D–I; **Figure 4B**).

DISCUSSION

Ice Cliff Distribution and Morphology

The ice cliffs across Trakarding Glacier cover 4.7 and 6.1% of the debris-covered area, with ice cliff length densities of 7.9 and 9.1 × 10^{-3} m m^{-2} in 2018 and 2019, respectively. Our ice cliff coverage ratios are larger than the 0.2–3.9% values obtained for individual glaciers in the Langtang catchment (the maximum ratio was observed on Langtang Glacier, May 2015, Steiner et al., 2019), and our ice cliff length densities are higher than the highest ice cliff length density of 7.4 × 10^{-3} m^{-1} on Lhotse Shar Glacier, Khumbu region, in May 2009 (out of 14 glaciers, Watson et al., 2017a). Trakarding Glacier has a denser ice cliff distribution than other glaciers in the Nepal Himalaya, although we note that these previous analyses were conducted at coarser spatial resolutions. We also confirmed the remarkable spatial adjacency of supraglacial ponds to ice cliffs (83% of total pond area in 2018 and 74% in 2019) that has been reported in previous studies (Thompson et al., 2016; Watson et al., 2017a; Steiner et al., 2019), with our analysis obtaining a similar value to that reported by Watson et al. (2017a) for the Khumbu region (77% of the total pond area). It has been suggested that this spatial relationship generates thermal undercutting of the ice cliff, and further enhances cliff ablation (Kraaijenbrink P. D. A. et al., 2016; Miles et al., 2016; Watson et al., 2017b). In the present study, we conducted annual monitoring of the spatial distribution of supraglacial ponds and ice cliffs to investigate their spatial adjacency. However, Steiner et al. (2019) reported that seasonal variations can exist in areas occupied by ice cliffs and ponds. Therefore, a better understanding of the spatial relationship between ice cliffs and supraglacial ponds can be obtained by increasing the temporal resolution of the monitoring observations.

We find a strong correlation between the ice cliff edge length and inclined area (**Figure 5B**). Previous studies have delineated the ice cliff edge from high-resolution satellite imagery and DEMs (Thompson et al., 2016; Watson et al., 2017a). However, Steiner et al. (2019) mentioned the difficulty in estimating the inclined area of steep ice cliffs from satellite DEMs with meter-scale resolution. Combining aerial photogrammetry with the SfM method can generate super-high-resolution DEMs that enable the effective analysis of ice cliff slope morphology; however, we note that the UAV acquisition method has coverage and cost limitations. Our results suggest that the ice cliff inclined area can be inferred from the ice cliff edge length, which can be extracted from high-resolution satellite images when UAV-based DEMs are not available.

The ice cliff slope distribution peaked at 40°–45° (32% of all ice cliffs; **Supplementary Figure S7**; Kraaijenbrink P. D. A. et al. (2016)) analyzed the ice cliff slopes in the terminus area of Langtang Glacier using UAV-based DEMs, where they

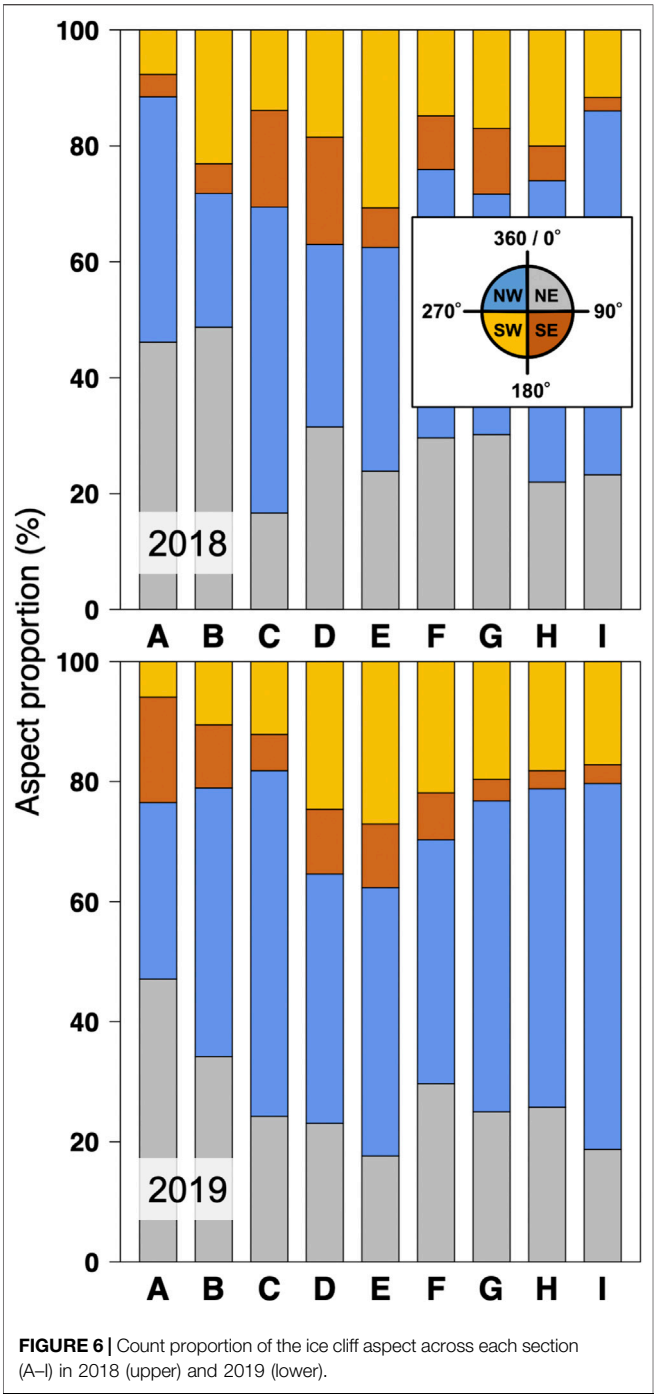

FIGURE 6 | Count proportion of the ice cliff aspect across each section (A–I) in 2018 (upper) and 2019 (lower).

determined a mean slope of 45°, with 50% of the exposed ice cliff slopes in the 35°–42° range. Buri and Pellicciotti (2018) also reported that the mean ice cliff slope on Lirung Glacier was 40°, using a UAV-based DEM. These similar results suggest that ice cliff slopes are commonly in the 35°–45° range in the Nepal Himalaya. Sakai et al. (2002) reported that there were no ice cliffs with <30° slopes, and estimated the angle of repose for the debris mantle to be 30°–35° on Lirung Glacier. We find that ice cliffs with gentler slopes (<30°) comprised only 3.5% of the total ice cliff area. The median inclined area of these gently sloping ice cliffs (64 m^2) was smaller than that of all the ice cliffs (162 m^2). Furthermore, the disappeared ice cliffs had smaller inclined areas and gentler slopes than the survived-2018 ice cliffs (**Table 5**). These results suggest that most gently sloping ice cliffs are in the process of being buried by debris, which is in agreement with a previous study (Sakai et al., 2002), and are therefore disappearing.

Ice Cliff Orientation and Temporal Changes

The north-facing ice cliffs are more predominant than the south-facing ice cliffs across the studied debris-covered area (**Figure 5A**). Previous studies have hypothesized that the north-facing ice cliffs tended to persist, whereas the south-facing ice cliffs would often decay in the Nepal Himalaya since they receive direct shortwave radiation along their clifftops (e.g., Sakai et al., 2002; Buri and Pellicciotti, 2018). The different melting rates at the top and base of the ice cliffs lead to a gentler slope, such that the cliffs will eventually become debris-covered (Sakai et al., 1998). Conversely, the north-facing ice cliffs provide their own shade, such that ice cliff melting is controlled by longwave radiation from the warm debris mounds beside the ice cliffs (Sakai et al., 2002; Steiner et al., 2015; Buri et al., 2016). Therefore, the north-facing ice cliffs could retreat while preserving their steep slopes. The ablation season in High Mountain Asia coincides with the monsoon season, especially in the Himalayan region. Therefore, the glaciers are often shaded by cloud in the afternoon, such that they are protected from solar radiation from the southwest. Therefore, these glaciers suffer from stronger solar radiation from the southeast, with this energy flux leading to the survival of northwest-facing ice cliffs and the disappearance of southeast-facing ice cliffs (Sakai et al., 1998; Buri and Pellicciotti, 2018). The predominance of north-facing ice cliffs has also been observed in the Khumbu and Langtang regions via high-resolution satellite image analysis (Thompson et al., 2016; Watson et al., 2017a; Steiner et al., 2019). Our results are consistent with those presented in these previous studies, with the predominance of north-facing ice cliffs observed in remote-sensing data.

We find that the number of survived-2018 ice cliffs is higher than the number of disappeared ice cliffs (**Table 4**), whereas Steiner et al. (2019) reported that 50% of the ice cliffs survived between 2014 and 2015 across Langtang Glacier. However, the inclined areas of the new and disappeared ice cliffs are <15% of the total area in both 2018 and 2019 (**Table 4**). This result suggests the importance of estimating the melting of survived ice cliffs to determine the melting contribution of ice cliffs to glacier ablation. We also confirm a significant change in the survived ice cliffs, which became steeper and extended between 2018 and 2019 (**Table 5**). This suggests that the survived ice cliffs tend to evolve into more suitable forms for survival. Approximately 17% of the ice cliffs across Langtang Glacier, central Himalaya, survived during their decade-long study period (2006–2015, Steiner et al., 2019). It is therefore necessary to also conduct annual tracking of the ice cliffs for an extended period to better capture the survival of ice cliffs across Trakarding Glacier. We also note that the four ice cliff types possess different aspect proportions. The south-facing cliffs (southeast to southwest) are dominated by disappeared- and survived-2018 ice cliffs, with the disappeared ice cliffs possessing 12% higher south-facing aspect proportions than the survived-2018 ice cliffs (**Figures 7A,B**). This

TABLE 4 | Number and inclined area of each ice cliff type (disappeared, survived-2018, survived-2019, new, and non-classified). The corresponding percentages are shown in parentheses.

2018 ice cliff			2019 ice cliff		
	Count	Incl. area (m^2)		Count	Incl. area (m^2)
Disappeared	216 (45)	307×10^2 (14)	New	235 (47)	426×10^2 (13)
Survived-18	239 (50)	184×10^3 (81)	Survived-19	220 (44)	262×10^3 (80)
Non-class	26 (5)	111×10^2 (5)	Non-class	50 (9)	229×10^2 (7)
Total	481	226×10^3	Total	505	327×10^3

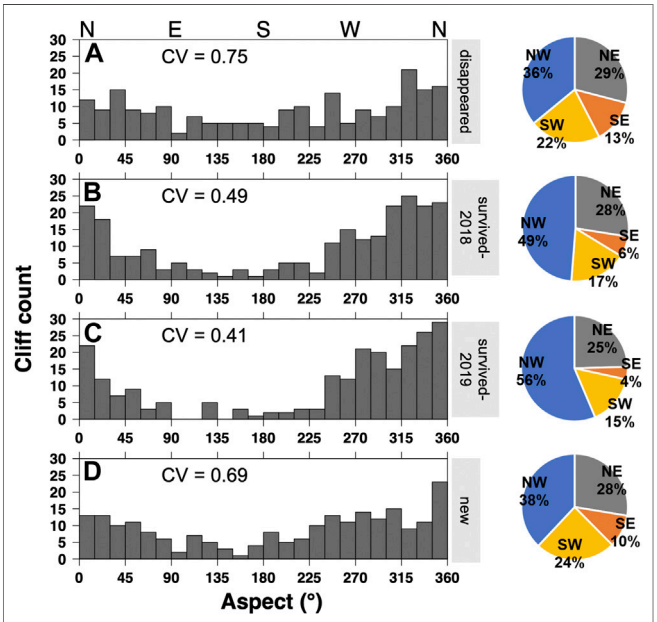

FIGURE 7 | Histogram of each type of ice cliff aspect: **(A)** disappeared, **(B)** survived-2018, **(C)** survived-2019, and **(D)** new. CV is the circular variance of each type of ice cliff aspect. Pie charts show each ice cliff type's aspect percentage (cliff count).

TABLE 5 | Mean inclined area and slope angle of each ice cliff type.

	Disappeared	Survived-18	Survived-19	New
Inclined area (m^2)	142	771	1,117	194
Slope angle (°)	40	42	44	42

result also supports the survival hypothesis of north-facing ice cliffs. The new ice cliffs possess higher south-facing proportions and circular variances than the survived-2019 ice cliffs (**Figure 7C, D**). This is the first documented instance of observing and documenting the randomness of the new ice cliff aspects across a debris-covered glacier.

Ice Cliff Formation and Dynamics Across Trakarding Glacier

A large number of new ice cliffs are distributed across the up-glacier (sections H and I), middle (sections D–F), and terminus (Section A) sections of Trakarding Glacier (**Figures 4D**, **8A**). The formation mechanisms of these ice cliffs may vary by section, owing to spatial differences in glacier dynamics and morphology. The up-glacier sections (sections H and I) are covered by a thin debris layer and possess a steeper slope (~8°) than the other sections (**Figure 4B**). This condition would enhance ice melting, even at the higher elevations, which is evidenced by recent stake measurements (Sunako et al., 2019). Spatially heterogeneous melting rates increase the potential for the mass wasting of debris from the debris mound. The ice cliffs that form *via* this mechanism are likely to be small, as suggested by the coincidence of high cliff count and low cliff density in the up-glacier section (**Figure 4C**). Such small cliffs are unlikely to grow into large ice cliffs because they are easily buried by debris. A high cliff count, large number of new ice cliffs, and low ice cliff density are therefore observed across the up-glacier sections (sections H and I; **Figures 4C,D**).

The surface slope is gentle (~2°) and the surface velocity decreases from the up-glacier to middle sections (sections F and G; **Figure 4B**). Previous studies have indicated that large supraglacial ponds tend to form under these topographic characteristics (e.g., Quincey et al., 2007; Sakai and Fujita, 2010; Salerno et al., 2012; Miles et al., 2017a). The up-glacier supply of meltwater pools is supraglacial ponds that form along the gentle slope and hummocky sections of sections F and G. These ponds could be heated by thermal exchange with the atmosphere, enhancing the potential for heated pond water to expand the englacial conduits when it flows through the englacial hydrological system (e.g., Benn et al., 2001; Röhl, 2008; Watson et al., 2016; Watson et al., 2018; Narama et al., 2017). Several exposed conduit holes have been observed across Section G, and are considered the intake points of englacial conduits (**Figures 8A–C**). The up-glacier supply of supraglacial water would pour into the englacial hydrological system along the middle sections (sections G and F; **Figure 8A**), even after these large supraglacial ponds have disappeared, further expanding the englacial conduits. Such a hydrological system with supraglacial water flow into englacial channels has also been observed along Ngozumpa (Benn et al., 2012; Benn et al., 2017) and Khumbu (Gulley et al., 2009; Miles et al., 2019) glaciers. A dense englacial conduit network is therefore inferred to exist along the gently sloping middle sections (sections F and G) of Trakarding Glacier.

A large number, high density, and high circular variance (randomness of aspect orientation) of the ice cliffs observed across the middle sections (sections D–F; **Figures 4C,D**, **6**) are considered to have a strong relationship with supraglacial and englacial hydrological systems. Previous studies have suggested

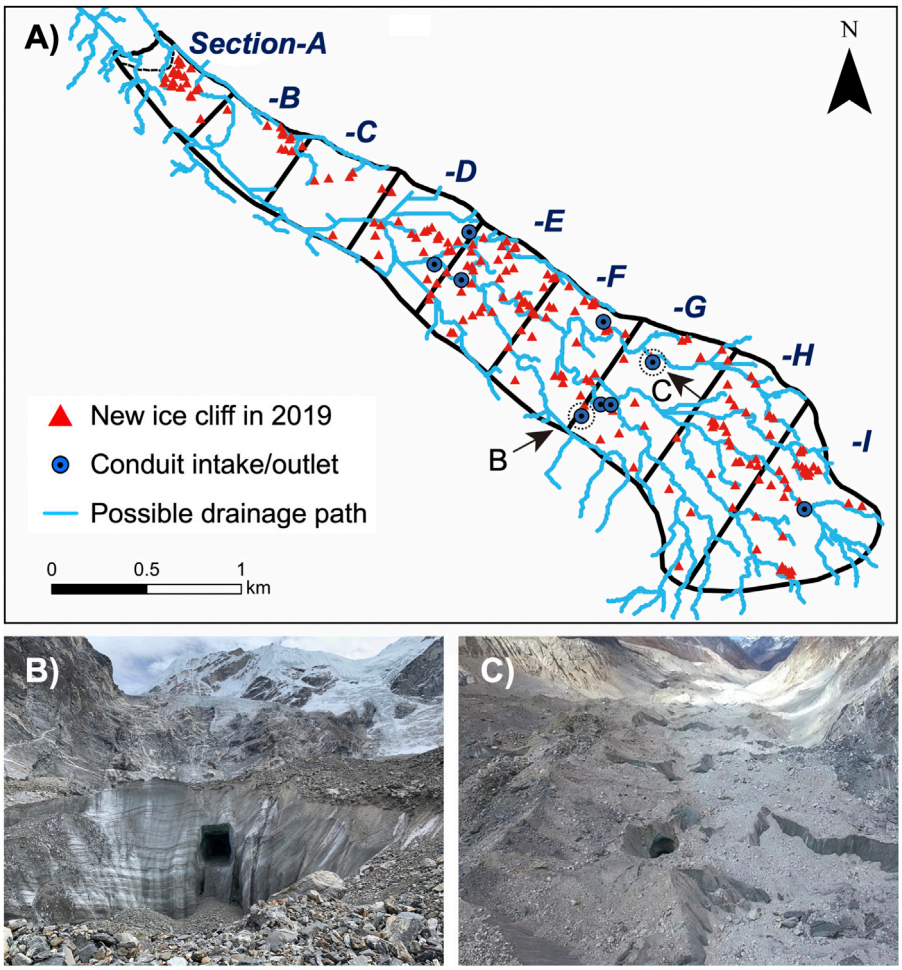

FIGURE 8 | (A) Locations of the new ice cliffs, conduit intakes or outlets, and possible drainage paths in 2019. **(B)** and **(C)** Photographs of a conduit intake or outlet hole. The arrows on panel **(A)** show the directions from which the photographs were taken; the conduit holes in **(B)** and **(C)** are circled in **(A)**. **(B)** is a terrestrial photograph, and **(C)** was acquired by UAV (Phantom 4) oblique movie.

that ice cliffs can form via (1) the incision of supraglacial streams (e.g., Anderson et al., 2019b; Mölg et al., 2020) and/or (2) the collapse of englacial conduits on debris-covered glaciers (e.g., Sakai et al., 2000b; Gulley and Benn, 2007; Benn et al., 2012; Miles et al., 2017b). The spatial coincidence of the potential drainage pathways and newly formed ice cliffs are confirmed in the gentle upper-middle sections (sections F and G; **Figure 8A**). Such a spatial coincidence between supraglacial streams and ice cliffs has also been observed in Alaska (Anderson et al., 2019b) and the European Alps (Mölg et al., 2020). Supraglacial streams could be a potential source of new ice cliffs through incision and erosion of the flat glacier surface (Mölg et al., 2020). Supraglacial streams tend to meander across the glacier surface and undercut it, especially on gentle surface slopes, promoting the formation and persistence of ice cliffs (Anderson et al., 2019b). The middle sections are also likely to possess a dense englacial hydrological network, such that new ice cliffs may form via the collapse of these conduits (**Supplementary Figure S8A**). The collapse of a conduit leads to the formation of multiple new ice cliffs with random orientations, resulting in the observed high circular variance of the ice cliffs across the middle sections (**Figures 4D**, **6**). These new ice cliffs are inferred to have aspect inhomogeneity, owing to their ice cliff formation mechanism (*Temporal Changes in Ice Cliffs and Supraglacial Streams*; **Figure 7D**). The newly formed ice cliffs would promote local ice ablation after the collapse of the englacial conduit, such that the up-glacier supply of meltwater may then form supraglacial ponds adjacent to the ice cliffs. Such a cliff-pond system creates a positive feedback for the expansion of the englacial hydrological system and new ice cliff formation. Therefore, a high ice cliff density, large number of new ice cliffs, and high aspect variance are observed along the middle sections (sections D–F), coincident with rapid surface lowering (**Figures 4A,C,D**). We identify a strong negative correlation between the ice cliff density and long-term surface elevation change ($r = -0.80$, $p < 0.05$), which suggests that the newly formed ice cliffs along the middle sections and conduit collapse have contributed to glacier thinning at the decadal scale (2007–2018). A similar relationship between the ice cliff distribution and surface lowering has been reported across the Langtang region (Ragettli et al., 2016) and the Khumbu region (Watson et al., 2017a).

The surface flow velocity decreases across the middle section (Section D; **Figure 4B**), suggesting the prevalence of longitudinal compression, which could promote closure of the englacial conduit network. Ice cliff formation owing to the collapse of englacial conduits would therefore decrease, resulting in lower ice cliff densities across Section D. Such a closure of the englacial conduit network in a compressive regime has been suggested in a previous study on Langtang Glacier (Kraaijenbrink P. D. A. et al., 2016). The surface flow velocity then increases again toward the terminal sections (sections A and B; **Figures 4B,D**), with the new ice cliffs in these sections likely forming as a result of crevassing (**Supplementary Figure S8B**). The low circular variances of these new cliffs are primarily north-facing, which is consistent with the glacier flow direction (**Figures 4D**, **6**).

New ice cliffs have formed across the up-glacier, middle, and terminus sections of Trakarding Glacier; however, the ice cliff number and formation processes are different across each section. A large number of new and survived ice cliffs are distributed across the stagnant middle section, thereby contributing to the relatively large decadal-scale surface lowering across this section. We identify the spatial heterogeneity of the ice cliff aspect as a potential indicator of the ice cliff formation mechanism (e.g., conduit collapse or incision). However, we have not directly detected the ice cliff formation processes *via* an analysis of our high-resolution imagery over a one-year interval. Additional seasonal or monthly aerial photogrammetry surveying has the potential to identify the formation mechanism of individual ice cliffs. Previous studies have evaluated the contribution of ice cliff mass loss to glacier-scale mass balance (Brun et al., 2018; Anderson et al., 2019b). It is important to obtain such data sets to discuss the relationship between ice cliff dynamics and glacier mass balance, and quantify the mass loss contribution due to ice cliffs.

CONCLUSION

Here we presented the decadal and annual surface elevation changes and recent ice cliff dynamics across the debris-covered Trakarding Glacier, eastern Nepal Himalaya, using high-resolution aerial photogrammetry. We analyzed the remote-sensing data from three aerial photogrammetry surveys that were conducted during the 2007, 2018, and 2019 post-monsoon seasons, and generated DEMs *via* SfM. We also manually generated ice cliff inventories from the 2018 and 2019 SfM-DEMs and ortho-images. The morphology, spatial distribution, and temporal changes of the ice cliffs were analyzed using these high-resolution inventories. Ice cliffs covered 4.7 and 6.1% of the debris-covered area in 2018 and 2019, respectively. The ice cliff edge length correlates strongly with the ice cliff inclined area, which enables us to estimate the ice cliff inclined area from coarser satellite-based images when very-high-resolution DEMs are lacking. Our annual tracking of ice cliffs indicates that the disappeared ice cliff inclined area occupied 14% of the total ice cliff inclined area in 2018, with the newly formed ice cliff inclined area accounting for almost the same percentage in 2019. The new ice cliffs that formed in 2019 generally possessed a random aspect, smaller inclined area, and gentler slope than the survived ice cliffs. The survived ice cliffs generally have predominantly northwest-facing, steep slopes, and large inclined areas. The disappeared ice cliffs have a higher south-facing aspect count proportion than the survived ice cliffs. Our results support the hypothesis of persisting north-facing ice cliffs that has been suggested by previous studies. Greater circular variance is observed in the middle and terminus sections of the glacier, which indicates the formation of new ice cliffs with random aspects.

We could elucidate the factors potentially controlling ice cliff dynamics (e.g., glacier flow velocity field, off glacier terrain, and meteorological conditions) by applying the ice cliff classification demonstrated in this study to glaciers in other regions. Although we only focused on the surface elevation changes in this study, it is important to quantify the mass loss contribution of ice cliffs to the total glacier mass balance. Ice thickness and flow velocity distributions are required to estimate the emergence velocity, which is an upward motion of the ice that compensates the glacier ablation. Evaluating both the dynamics and mass loss of ice cliffs will allow us to elucidate the quantitative impact of ice cliffs on the ablation of debris-covered glaciers.

DATA AVAILABILITY STATEMENT

The raw data supporting the conclusions of this article will be made available by the authors, without undue reservation.

AUTHOR CONTRIBUTIONS

KF designed the study. YS, KF, SS, HI, AT, AS, EP, and RK conducted the field observations with the support of RK, YS processed the photogrammetry data, and SS and KF analyzed the GPS data. YS, KF, AS, and EP wrote the manuscript. All of the authors contributed to the discussion.

FUNDING

This study was supported by JSPS-KAKENHI (grant numbers 17H01621 and 18KK0098), and JSPS and SNSF under the Joint Research Projects (JRPs; grant number 20191503).

ACKNOWLEDGMENTS

We thank Etienne Berthier for providing the Pléiades satellite data. We are indebted to Guide For All Seasons Trek for logistical support during the fieldwork. The Asahi Shimbun Company supported the aerial photogrammetry survey in 2007. We acknowledge three reviewers for their constructive and insightful comments.

SUPPLEMENTARY MATERIAL

The Supplementary Material for this article can be found online at: https://www.frontiersin.org/articles/10.3389/feart.2021.623623/full#supplementary-material

REFERENCES

Agisoft LLC (2020). *Agisoft Metashape User Manual Professional Edition, Version 1.6*. Available at: https://www.agisoft.com/pdf/metashape-pro_1_6_en.pdf. (Accessed April 1, 2020)

Anderson, L. S., Armstrong, W. H., Anderson, R. S., and Buri, P. (2019a). Debris Cover and the Thinning of Kennicott Glacier, Alaska, Part B: Ice Cliff Delineation and Distributed Melt Estimates. *Cryosphere Discuss.* doi:10.5194/tc-2019-177

Anderson, L. S., Armstrong, W. H., Anderson, R. S., and Buri, P. (2019b). Debris Cover and the Thinning of Kennicott Glacier, Alaska, Part C: Feedbacks between Melt, Ice Dynamics, and Surface Processes. *Cryosphere Discuss.* doi:10.5194/tc-2019-178

Benn, D. I., Wiseman, S., and Hands, K. A. (2001). Growth and Drainage of Supraglacial Lakes on Debris-Mantled Ngozumpa Glacier, Khumbu Himal, Nepal. *J. Glaciol.* 47, 626–638. doi:10.3189/172756501781831729

Benn, D. I., Bolch, T., Hands, K., Gulley, J., Luckman, A., Nicholson, L. I., et al. (2012). Response of Debris-Covered Glaciers in the Mount Everest Region to Recent Warming, and Implications for Outburst Flood Hazards. *Earth-Science Rev.* 114, 156–174. doi:10.1016/j.earscirev10.1016/j.earscirev.2012.03.008

Benn, D. I., Thompson, S., Gulley, J., Mertes, J., Luckman, A., and Nicholson, L. (2017). Structure and Evolution of the Drainage System of a Himalayan Debris-Covered Glacier, and its Relationship with Patterns of Mass Loss. *The Cryosphere* 11, 2247–2264. doi:10.5194/tc-11-2247-2017

Berthier, E., Arnaud, Y., Kumar, R., Ahmad, S., Wagnon, P., and Chevallier, P. (2007). Remote Sensing Estimates of Glacier Mass Balances in the Himachal Pradesh (Western Himalaya, India). *Remote Sensing Environ.* 108, 327–338. doi:10.1016/j.rse.2006.11.017

Berthier, E., Vincent, C., Magnússon, E., Gunnlaugsson, Á. Þ., Pitte, P., Le Meur, E., et al. (2014). Glacier Topography and Elevation Changes Derived from Pléiades Sub-meter Stereo Images. *The Cryosphere* 8, 2275–2291. doi:10.5194/tc-8-2275-2014

Bolch, T., Kulkarni, A., Kääb, A., Huggel, C., Paul, F., Cogley, J. G., et al. (2012). The State and Fate of Himalayan Glaciers. *Science* 336, 310–314. doi:10.1126/science.1215828

Brun, F., Berthier, E., Wagnon, P., Kääb, A., and Treichler, D. (2017). A Spatially Resolved Estimate of High Mountain Asia Glacier Mass Balances from 2000 to 2016. *Nat. Geosci* 10, 668–673. doi:10.1038/NGEO2999

Brun, F., Wagnon, P., Berthier, E., Shea, J. M., Immerzeel, W. W., Kraaijenbrink, P. D. A., et al. (2018). Ice Cliff Contribution to the Tongue-wide Ablation of Changri Nup Glacier, Nepal, Central Himalaya. *The Cryosphere* 12, 3439–3457. doi:10.5194/tc-12-3439-2018

Brun, F., Wagnon, P., Berthier, E., Jomelli, V., Maharjan, S. B., Shrestha, F., et al. (2019). Heterogeneous Influence of Glacier Morphology on the Mass Balance Variability in High Mountain Asia. *J. Geophys. Res. Earth Surf.* 124, 1331–1345. doi:10.1029/2018JF004838

Buri, P., and Pellicciotti, F. (2018). Aspect Controls the Survival of Ice Cliffs on Debris-Covered Glaciers. *Proc. Natl. Acad. Sci. USA* 115, 4369–4374. doi:10.1073/pnas.1713892115

Buri, P., Miles, E. S., Steiner, J. F., Immerzeel, W. W., Wagnon, P., and Pellicciotti, F. (2016). A Physically Based 3-D Model of Ice Cliff Evolution over Debris-covered Glaciers. *J. Geophys. Res. Earth Surf.* 121, 2471–2493. doi:10.1002/2016JF004039

Fisher, N. I. (1995). *Statistical Analysis of Circular Data*. Cambridge: Cambridge University Press.

Fujita, K., and Sakai, A. (2014). Modelling Runoff from a Himalayan Debris-Covered Glacier. *Hydrol. Earth Syst. Sci.* 18, 2679–2694. doi:10.5194/hess-18-2679-2014

Fujita, K., Suzuki, R., Nuimura, T., and Sakai, A. (2008). Performance of ASTER and SRTM DEMs, and Their Potential for Assessing Glacial Lakes in the Lunana Region, Bhutan Himalaya. *J. Glaciol.* 54, 220–228. doi:10.3189/002214308784886162

Fujita, K., Sakai, A., Takenaka, S., Nuimura, T., Surazakov, A. B., Sawagaki, T., et al. (2013). Potential Flood Volume of Himalayan Glacial Lakes. *Nat. Hazards Earth Syst. Sci.* 13, 1827–1839. doi:10.5194/nhess-13-1827-2013

Fujita, K., Inoue, H., Izumi, T., Yamaguchi, S., Sadakane, A., Sunako, S., et al. (2017). Anomalous Winter-Snow-Amplified Earthquake-Induced Disaster of the 2015 Langtang Avalanche in Nepal. *Nat. Hazards Earth Syst. Sci.* 17, 749–764. doi:10.5194/nhess-17-749-2017

Gardelle, J., Berthier, E., Arnaud, Y., and Kääb, A. (2013). Region-wide Glacier Mass Balances over the Pamir-Karakoram-Himalaya during 1999-2011. *The Cryosphere* 7, 1263–1286. doi:10.5194/tc-7-1263-2013

Gulley, J., and Benn, D. I. (2007). Structural Control of Englacial Drainage Systems in Himalayan Debris-Covered Glaciers. *J. Glaciol.* 53, 399–412. doi:10.3189/002214307783258378

Gulley, J. D., Benn, D. I., Screaton, E., and Martin, J. (2009). Mechanisms of Englacial Conduit Formation and Their Implications for Subglacial Recharge. *Quat. Sci. Rev.* 28, 1984–1999. doi:10.1016/j.quascirev.2009.04.002

Han, H., Wang, J., Wei, J., and Liu, S. (2010). Backwasting Rate on Debris-Covered Koxkar Glacier, Tuomuer Mountain, China. *J. Glaciol.* 56, 287–296. doi:10.3189/002214310791968430

Herreid, S., and Pellicciotti, F. (2020). The State of Rock Debris Covering Earth's Glaciers. *Nat. Geosci.* 13, 621–627. doi:10.1038/s41561-020-0615-0

Immerzeel, W. W., Kraaijenbrink, P. D. A., Shea, J. M., Shrestha, A. B., Pellicciotti, F., Bierkens, M. F. P., et al. (2014). High-resolution Monitoring of Himalayan Glacier Dynamics Using Unmanned Aerial Vehicles. *Remote Sensing Environ.* 150, 93–103. doi:10.1016/j.rse.2014.04.025

Kääb, A., Berthier, E., Nuth, C., Gardelle, J., and Arnaud, Y. (2012). Contrasting Patterns of Early Twenty-First-Century Glacier Mass Change in the Himalayas. *Nature* 488, 495–498. doi:10.1038/nature11324

Kraaijenbrink, P., Meijer, S. W., Shea, J. M., Pellicciotti, F., De Jong, S. M., and Immerzeel, W. W. (2016). Seasonal Surface Velocities of a Himalayan Glacier Derived by Automated Correlation of Unmanned Aerial Vehicle Imagery. *Ann. Glaciol.* 57, 103–113. doi:10.3189/2016AoG71A072

Kraaijenbrink, P. D. A., Shea, J. M., Pellicciotti, F., Jong, S. M. d., and Immerzeel, W. W. (2016). Object-based Analysis of Unmanned Aerial Vehicle Imagery to Map and Characterise Surface Features on a Debris-Covered Glacier. *Remote Sensing Environ.* 186, 581–595. doi:10.1016/j.rse.2016.09.013

Lamsal, D., Fujita, K., and Sakai, A. (2017). Surface Lowering of the Debris-Covered Area of Kanchenjunga Glacier in the Eastern Nepal Himalaya since 1975, as Revealed by Hexagon KH-9 and ALOS Satellite Observations. *The Cryosphere* 11, 2815–2827. doi:10.5194/tc-11-2815-2017

Lucieer, A., Jong, S. M. d., and Turner, D. (2014). Mapping Landslide Displacements Using Structure from Motion (SfM) and Image Correlation of Multi-Temporal UAV Photography. *Prog. Phys. Geogr. Earth Environ.* 38, 97–116. doi:10.1177/0309133313515293

Mattson, L. E., Gardner, J. S., and Young, G. J. (1993). Ablation on Debris Covered Glaciers: an Example from the Rakhiot Glacier, Punjab, Himalaya. *IAHS Publ.* 218 (Symposium at Seattle 2000 – Debris-Covered Glaciers), 289–296.

Miles, E. S., Pellicciotti, F., Willis, I. C., Steiner, J. F., Buri, P., and Arnold, N. S. (2016). Refined Energy-Balance Modelling of a Supraglacial Pond, Langtang Khola, Nepal. *Ann. Glaciol.* 57, 29–40. doi:10.3189/2016AoG71A421

Miles, E. S., Willis, I. C., Arnold, N. S., Steiner, J., and Pellicciotti, F. (2017a). Spatial, Seasonal and Interannual Variability of Supraglacial Ponds in the Langtang Valley of Nepal, 1999-2013. *J. Glaciol.* 63, 88–105. doi:10.1017/jog.2016.120

Miles, E. S., Steiner, J., Willis, I., Buri, P., Immerzeel, W. W., Chesnokova, A., et al. (2017b). Pond Dynamics and Supraglacial-Englacial Connectivity on Debris-Covered Lirung Glacier, Nepal. *Front. Earth Sci.* 5, 69. doi:10.3389/feart.2017.00069

Miles, K. E., Hubbard, B., Quincey, D. J., Miles, E. S., Irvine-Fynn, T. D. L., and Rowan, A. V. (2019). Surface and Subsurface Hydrology of Debris-Covered Khumbu Glacier, Nepal, Revealed by Dye Tracing. *Earth Planet. Sci. Lett.* 513, 176–186. doi:10.1016/j.epsl.2019.02.020

Mölg, N., Ferguson, J., Bolch, T., and Vieli, A. (2020). On the Influence of Debris Cover on Glacier Morphology: How High-Relief Structures Evolve from Smooth Surfaces. *Geomorphology* 357, 107092. doi:10.1016/j.geomorph.2020.107092

Nakawo, M., and Young, G. J. (1982). Estimate of Glacier Ablation under a Debris Layer from Surface Temperature and Meteorological Variables. *J. Glaciol.* 28, 29–34. doi:10.3189/S002214300001176X

Narama, C., Daiyrov, M., Tadono, T., Yamamoto, M., Kääb, A., Morita, R., et al. (2017). Seasonal Drainage of Supraglacial Lakes on Debris-Covered Glaciers in the Tien Shan Mountains, Central Asia. *Geomorphol.* 286, 133–142. doi:10.1016/j.geomorph.2017.03.002

Nicholson, L., and Benn, D. I. (2006). Calculating Ice Melt beneath a Debris Layer Using Meteorological Data. *J. Glaciol.* 52, 463–470. doi:10.3189/172756506781828584

Nuimura, T., Fujita, K., Yamaguchi, S., and Sharma, R. R. (2012). Elevation Changes of Glaciers Revealed by Multitemporal Digital Elevation Models Calibrated by GPS Survey in the Khumbu Region, Nepal Himalaya, 1992-2008. *J. Glaciol.* 58, 648–656. doi:10.3189/2012JoG11J061

Nuimura, T., Sakai, A., Taniguchi, K., Nagai, H., Lamsal, D., Tsutaki, S., et al. (2015). The GAMDAM Glacier Inventory: a Quality-Controlled Inventory of Asian Glaciers. *The Cryosphere* 9, 849–864. doi:10.5194/tc-9-849-2015

O'Callaghan, J. F., and Mark, D. M. (1984). The Extraction of Drainage Networks from Digital Elevation Data. *Comput. Vis. Graph. Image Process.* 28, 323–344. doi:10.1016/S0734-189X(84)80011-0

Østrem, G. (1959). Ice Melting under a Thin Layer of Moraine, and the Existence of Ice Cores in Moraine Ridges. *Geografiska Annaler* 41, 228–230. doi:10.1080/20014422.1959.11907953

Pellicciotti, F., Stephan, C., Miles, E., Herreid, S., Immerzeel, W. W., and Bolch, T. (2015). Mass-balance Changes of the Debris-Covered Glaciers in the Langtang Himal, Nepal, from 1974 to 1999. *J. Glaciol.* 61, 373–386. doi:10.3189/2015JoG13J237

Podolskiy, E. A., Fujita, K., Sunako, S., Tsushima, A., and Kayastha, R. B. (2018). Nocturnal Thermal Fracturing of a Himalayan Debris-Covered Glacier Revealed by Ambient Seismic Noise. *Geophys. Res. Lett.* 45, 9699–9709. doi:10.1029/2018GL079653

Podolskiy, E. A., Fujita, K., Sunako, S., and Sato, Y. (2019). Viscoelastic Modeling of Nocturnal Thermal Fracturing in a Himalayan Debris-Covered Glacier. *J. Geophys. Res. Earth Surf.* 124, 1485–1515. doi:10.1029/2018JF004848

Quincey, D. J., Richardson, S. D., Luckman, A., Lucas, R. M., Reynolds, J. M., Hambrey, M. J., et al. (2007). Early Recognition of Glacial Lake Hazards in the Himalaya Using Remote Sensing Datasets. *Glob. Planet. Change* 56, 137–152. doi:10.1016/j.gloplacha.2006.07.013

Ragettli, S., Bolch, T., and Pellicciotti, F. (2016). Heterogeneous Glacier Thinning Patterns over the Last 40 Years in Langtang Himal, Nepal. *The Cryosphere* 10, 2075–2097. doi:10.5194/tc-10-2075-2016

Röhl, K. (2008). Characteristics and Evolution of Supraglacial Ponds on Debris-Covered Tasman Glacier, New Zealand. *J. Glaciol.* 54, 867–880. doi:10.3189/002214308787779861

Sakai, A., and Fujita, K. (2010). Formation Conditions of Supraglacial Lakes on Debris-Covered Glaciers in the Himalaya. *J. Glaciol.* 56, 177–181. doi:10.3189/002214310791190785

Sakai, A., Nakawo, M., and Fujita, K. (1998). Melt Rate of Ice Cliffs on the Lirung Glacier, Nepal Himalayas, 1996. *Bull. Glacier Res.* 16, 57–66.

Sakai, A., Chikita, K., and Yamada, T. (2000a). Expansion of a Moraine-Dammed Glacial Lake, Tsho Rolpa, in Rolwaling Himal, Nepal Himalaya. *Limnol. Oceanogr* 45 (6), 1401–1408. doi:10.4319/lo.2000.45.6.1401

Sakai, A., Takeuchi, N., Fujita, K., and Nakawo, M. (2000b). Role of Supraglacial Ponds in the Ablation Process of a Debris-Covered Glacier in the Nepal Himalayas. IAHS Publ., no. 264.

Sakai, A., Nakawo, M., and Fujita, K. (2002). Distribution Characteristics and Energy Balance of Ice Cliffs on Debris-Covered Glaciers, Nepal Himalaya. *Arctic, Antarctic, Alpine Res.* 34, 12–19. doi:10.2307/1552503

Sakai, A. (2019). Brief Communication: Updated GAMDAM Glacier Inventory over High-Mountain Asia. *The Cryosphere* 13, 2043–2049. doi:10.5194/tc-13-2043-2019

Salerno, F., Thakuri, S., D'Agata, C., Smiraglia, C., Manfredi, E. C., Viviano, G., et al. (2012). Glacial Lake Distribution in the Mount Everest Region: Uncertainty of Measurement and Conditions of Formation. *Glob. Planet. Change* 92-93, 30–39. doi:10.1016/j.gloplacha.2012.04.001

Salerno, F., Thakuri, S., Tartari, G., Nuimura, T., Sunako, S., Sakai, A., et al. (2017). Debris-covered Glacier Anomaly? Morphological Factors Controlling Changes in the Mass Balance, Surface Area, Terminus Position, and Snow Line Altitude of Himalayan Glaciers. *Earth Planet. Sci. Lett.* 471, 19–31. doi:10.1016/j.epsl.2017.04.039

Shean, D. E., Bhushan, S., Montesano, P., Rounce, D. R., Arendt, A., and Osmanoglu, B. (2020). A Systematic, Regional Assessment of High Mountain Asia Glacier Mass Balance. *Front. Earth Sci.* 7, 363. doi:10.3389/feart.2019.00363

Steiner, J. F., Pellicciotti, F., Buri, P., Miles, E. S., Immerzeel, W. W., and Reid, T. D. (2015). Modelling Ice-Cliff Backwasting on a Debris-Covered Glacier in the Nepalese Himalaya. *J. Glaciol.* 61, 889–907. doi:10.3189/2015JoG14J194

Steiner, J. F., Buri, P., Miles, E. S., Ragettli, S., and Pellicciotti, F. (2019). Supraglacial Ice Cliffs and Ponds on Debris-Covered Glaciers: Spatio-Temporal Distribution and Characteristics. *J. Glaciol.* 65, 617–632. doi:10.1017/jog.2019.40

Sunako, S., Fujita, K., Sakai, A., and Kayastha, R. B. (2019). Mass Balance of Trambau Glacier, Rolwaling Region, Nepal Himalaya: In-Situ Observations, Long-Term Reconstruction and Mass-Balance Sensitivity. *J. Glaciol.* 65, 605–616. doi:10.1017/jog.2019.37

Thompson, S., Benn, D. I., Mertes, J., and Luckman, A. (2016). Stagnation and Mass Loss on a Himalayan Debris-Covered Glacier: Processes, Patterns and Rates. *J. Glaciol.* 62, 467–485. doi:10.1017/jog.2016.37

Tshering, P., and Fujita, K. (2016). First In Situ Record of Decadal Glacier Mass Balance (2003-2014) from the Bhutan Himalaya. *Ann. Glaciol.* 57, 289–294. doi:10.3189/2016AoG71A036

Vincent, C., Wagnon, P., Shea, J. M., Immerzeel, W. W., Kraaijenbrink, P., Shrestha, D., et al. (2016). Reduced Melt on Debris-Covered Glaciers: Investigations from Changri Nup Glacier, Nepal. *The Cryosphere* 10, 1845–1858. doi:10.5194/tc-10-1845-2016

Watson, C. S., Quincey, D. J., Carrivick, J. L., and Smith, M. W. (2016). The Dynamics of Supraglacial Ponds in the Everest Region, Central Himalaya. *Glob. Planet. Change* 142, 14–27. doi:10.1016/j.gloplacha.2016.04.008

Watson, C. S., Quincey, D. J., Carrivick, J. L., and Smith, M. W. (2017a). Ice Cliff Dynamics in the Everest Region of the Central Himalaya. *Geomorphology* 278, 238–251. doi:10.1016/j.geomorph.2016.11.017

Watson, C. S., Quincey, D. J., Smith, M. W., Carrivick, J. L., Rowan, A. V., and James, M. R. (2017b). Quantifying Ice Cliff Evolution with Multi-Temporal Point Clouds on the Debris-Covered Khumbu Glacier, Nepal. *J. Glaciol.* 63, 823–837. doi:10.1017/jog.2017.47

Watson, C. S., Quincey, D. J., Carrivick, J. L., Smith, M. W., Rowan, A. V., and Richardson, R. (2018). Heterogeneous Water Storage and Thermal Regime of Supraglacial Ponds on Debris-Covered Glaciers. *Earth Surf. Process. Landforms* 43, 229–241. doi:10.1002/esp.4236

Wigmore, O., and Mark, B. (2017). Monitoring Tropical Debris-Covered Glacier Dynamics from High-Resolution Unmanned Aerial Vehicle Photogrammetry, Cordillera Blanca, Peru. *The Cryosphere* 11, 2463–2480. doi:10.5194/tc-11-2463-2017

Zhang, Y., Fujita, K., Liu, S., Liu, Q., and Nuimura, T. (2011). Distribution of Debris Thickness and its Effect on Ice Melt at Hailuogou Glacier, Southeastern Tibetan Plateau, Using In Situ Surveys and ASTER Imagery. *J. Glaciol.* 57, 1147–1157. doi:10.3189/002214311798843331

Conflict of Interest: The authors declare that the research was conducted in the absence of any commercial or financial relationships that could be construed as a potential conflict of interest.

frontiers in Earth Science

ORIGINAL RESEARCH
published: 08 June 2021
doi: 10.3389/feart.2021.681071

Spatio-Temporal Distribution of Supra-Glacial Ponds and Ice Cliffs on Verde Glacier, Chile

Thomas Loriaux[1]* *and Lucas Ruiz*[2]

[1]Centro de Estudios Científicos, Valdivia, Chile, [2]Instituto Argentino de Nivología, Glaciología y Ciencias Ambientales (IANIGLA), Gobierno de Mendoza, Universidad Nacional de Cuyo, CONICET, Mendoza, Argentina

Known for their important role in locally enhancing surface melt, supraglacial ponds and ice cliffs are common features on debris-covered glaciers. We use high resolution satellite imagery to describe pond-cliff systems and surface velocity on Verde debris-covered glacier, Monte Tronador, and Southern Chile. Ponds and ice cliffs represent up to 0.4 and 2.7% of the glacier debris-covered area, respectively. Through the analyzed period and the available data, we found a seasonality in the number of detected ponds, with larger number of ponds at the beginning of the ablation season and less at the end of it. Using feature tracking, we determined glacier surface velocity, finding values up to 55 m/yr on the upper part of the debris-covered area, and decreasing almost to stagnation in the terminus. We found that larger ponds develop in glacier zones of low velocity, while zones of high velocity only contain smaller features. Meanwhile, ice cliffs appeared to be less controlled by surface velocity and gradient. Persistent ice cliffs were detected between 2009 and 2019 and backwasting up to 24 m/yr was measured, highlighting significant local glacier wastage.

Keywords: debris-covered glacier, chile, supraglacial ponds, ice cliffs, glacier velocity, Southern Andes

OPEN ACCESS

Edited by:
Aparna Shukla,
Ministry of Earth Sciences, India

Reviewed by:
Purushottam Kumar Garg,
Wadia Institute of Himalayan Geology, India
Benjamin Brock,
Northumbria University, United Kingdom

***Correspondence:**
Thomas Loriaux
thomas@cecs.cl

Specialty section:
This article was submitted to Cryospheric Sciences, a section of the journal Frontiers in Earth Science

Received: *15 March 2021*
Accepted: *20 May 2021*
Published: *08 June 2021*

Citation:
Loriaux T and Ruiz L (2021) Spatio-Temporal Distribution of Supra-Glacial Ponds and Ice Cliffs on Verde Glacier, Chile. Front. Earth Sci. 9:681071. doi: 10.3389/feart.2021.681071

INTRODUCTION

Interest has been recently growing about debris-covered glaciers (DCGs) in mountain areas worldwide (e.g., Fyffe et al., 2012; Janke et al., 2015; Bhushan et al., 2018; Miles et al., 2019). Main objectives generally consist in assessing the effect of the debris layer on the mass balance (Brock et al., 2007; Hagg et al., 2008; Collier et al., 2015) and their hydrological role in glacierised landscapes (Ayala et al., 2016; Burger et al., 2019; Fyffe et al., 2019; Immerzeel et al., 2020; Miles et al., 2020).

Supraglacial ponds are common features on DCGs, where they have been observed for decades (Iwata et al., 1980; Kirkbride, 1993). Studies about supraglacial ponds on DCGs are mostly centered in High Mountain Asia (e.g., Sakai and Fujita, 2010; Miles et al., 2018; Watson et al., 2018a; Chand and Watanabe, 2019), where they can locally represent significant portion of the DCGs. Seasonal and interannual variations in ponds count and area have been observed (Steiner et al., 2019), as well as rapid filling and draining (Miles et al., 2017b), associated with englacial hydrological networks (Miles et al., 2017a; Miles et al., 2019; Watson et al., 2018b). Ponds also regulate DCGs runoff, as they act as buffer reservoirs (Irvine-Fynn et al., 2017). Exposed ice cliffs often appear at the ponds margins and can help identify the emplacement of drained features (Miles et al., 2017a).

Ponds and ice cliffs are known for their important role in locally enhancing surface melt (Sakai et al., 2000; Benn et al., 2012; Salerno et al., 2012; Maurer et al., 2016), as they absorb and transfer atmospheric energy into the glacier ice (Sakai et al., 2002; Steiner et al., 2015; Brun et al., 2018; Miles

et al., 2018). This induces the DCGs to lose as much mass as debris-free glaciers despite the debris layer, which is known as the "debris-cover anomaly" (Pellicciotti et al., 2015; Brun et al., 2018; Bisset et al., 2020). Based on energy balance modeling and satellite-based pond distribution, Miles et al. (2018) estimate that supraglacial ponds contribute to 12 ± 2% of the total ice mass loss in Langtang catchment, Nepal. Thompson et al. (2016) and Reid and Brock (2014) found that ice cliff covering only 5 and 1.3% of glacier surface contribute to 40 and 7.4% of the ablation on DCGs, respectively, in the Himalaya and Alps. Similarly, Brun et al. (2018) found that ice cliffs have a net ablation rate 3.1 ± 0.6 times higher than the average glacier tongue surface. Also, ponds are likely to coalesce and form large glacial lakes, enhancing glacier calving (Chikita et al., 1998; Röhl, 2008; Sakai and Fujita, 2010) and increasing glacial lake hazards (Quincey et al., 2007).

Mapping and inventorying supraglacial ponds and ice cliffs is therefore important due to their role as ablation hotspot and their link with the englacial hydrological network. Understanding of their magnitude and spatio-temporal variation will become increasingly significant on glaciers with negative mass balances (Deline, 2005; Stokes et al., 2007; Benn et al., 2012; Thakuri et al., 2014; Tielidze et al., 2020). In this context of glacier shrinking, mountain ranges are thought to show some transition from debris-free to debris-covered and rock glaciers, with an increase of their relative importance on the freshwater availability, quality and timing (Anderson et al., 2018; Knight et al., 2019).

The present study depicts the first assessment of supraglacial ponds and ice cliffs distribution on a DCG in Chile. Our objectives are to: 1) Document interannual changes in ponds and ice cliffs distribution using Google Earth historical imagery. 2) Analyse the inventory by determining horizontal velocity through feature tracking and extracting surface gradient from digital elevation model (DEM). 3) Detect persistent ice cliffs and measure the associate backwasting.

REGIONAL CONTEXT AND AREA OF INTEREST

The Southern Andes cover more than 4,500 km from northernmost Chile to the southern tip of South America in Tierra del Fuego. The extensive latitudinal range from subtropical to subantarctic domains (20°–55°S), steep elevation gradients, and the north-south orientation perpendicular to the prevalent atmospheric circulation cause significantly different climatic conditions, and consequently, a great variety of ice mass types along the Southern Andes (Lliboutry, 1998). North of 35 S, knows as the Dry Andes, encompasses a high (3,500–6,900 m a.s.l.) mountain range with arid (<500 mm/yr) condition to the north and modest annual precipitation amounts (1,000 mm/yr) to the south (Viale et al., 2019). Due to the topographic relief, geological context, and climatic setting, this region hosts the largest debris-covered glacier area of the Southern Andes (Barcaza et al., 2017; Zalazar et al., 2020). This region also contains the largest concentration of rock glaciers in the Andes (Barcaza et al., 2017), and includes many complex units that start as clean-ice glaciers at high elevations, gradually turn into debris-covered glaciers further down, and finally end as rock glaciers at the lowest sectors (Monnier and Kinnard, 2015, Monnier and Kinnard, 2017; Zalazar et al., 2020). Recent inventories of the Argentina side of this region found that between 60 and 70% of the glacierised area (1,200 km^2; excluding rock glaciers) are partially (10%) to totally (˃90%) debris-covered (Ferri et al., 2020).

TABLE 1 | Characteristics of Verde glacier, including the area of the whole glacier and the debris cover.

Area (km^2)		Elevation (m a.s.l.)		
Glacier	Debris	Minimum	Debris upper limit	Maximum
8.15	3.05	980	1,400	3,475

South of the 35°S, in the Wet Andes, where the elevation of most peaks usually does not exceed 4,000 m a.s.l., the precipitation amounts increase considerably, exceeding 2,000 mm/yr (Viale et al., 2019). Although, at the southern part of this regions the topographic and climatological conditions allow the development of numerous and extensive glacierized areas, which constitute the largest glacierized surface in South America. In the north part, also known as the North Patagonian Andes (35° to 45°S), glaciers are smaller than those located further south. Although glaciers along this region are mainly clean ice or debris free (98% of the glaciated area), debris-covered glaciers can still be found due to local conditions such as rock-fall and stagnation. This is the case of Verde and other valley glaciers at Monte Tronador, where rock-falls and avalanches below a massive bedrock cliff present between 1,700 and 1,400 m a.s.l., allow the concentration of debris over the glaciers tongues (Ruiz et al., 2017).

The seasonal variation in the North Patagonian Andes is driven by the location and intensity of the southern hemisphere westerlies (Garreaud et al., 2009), which bring abundant precipitations between April and September (Aravena and Luckman, 2009). At these latitudes, orographic effect induces an increase of the annual mean precipitation from the Pacific coast to the western slopes of Chile, where it reaches more than 3,000 mm (Viale and Garreaud, 2015). Ruiz et al. (2015) measured more than 3,000 mm w.e. between May and September 2013 on a stake located close to the ice divide between Alerce and Castaño Overa glaciers, and close to the equilibrium-line altitude (ELA), which lies at 2000 m a.s.l. (Carrasco et al., 2005; Condom et al., 2007).

Verde glacier (8.15 km^2, 41.21°S, 71.91°W, **Table 1**) lies on the southern flank of Monte Tronador (3,475 m a.s.l.), an extinct stratovolcano located in the North Patagonian Andes on the Chile-Argentina border (**Figure 1**). The glacier is divided into three distinct parts: the accumulation zone on the upper slope of the Monte Tronador between 2,500 and 3,475 m a.s.l. an icefall between 1,400 and 2,500 m a.s.l. and a debris-covered tongue down to 980 m a.s.l. The debris-covered tongue is about 3.05 km^2, which makes Verde glacier one of the most extended DCGs in Chile (Barcaza et al., 2017).

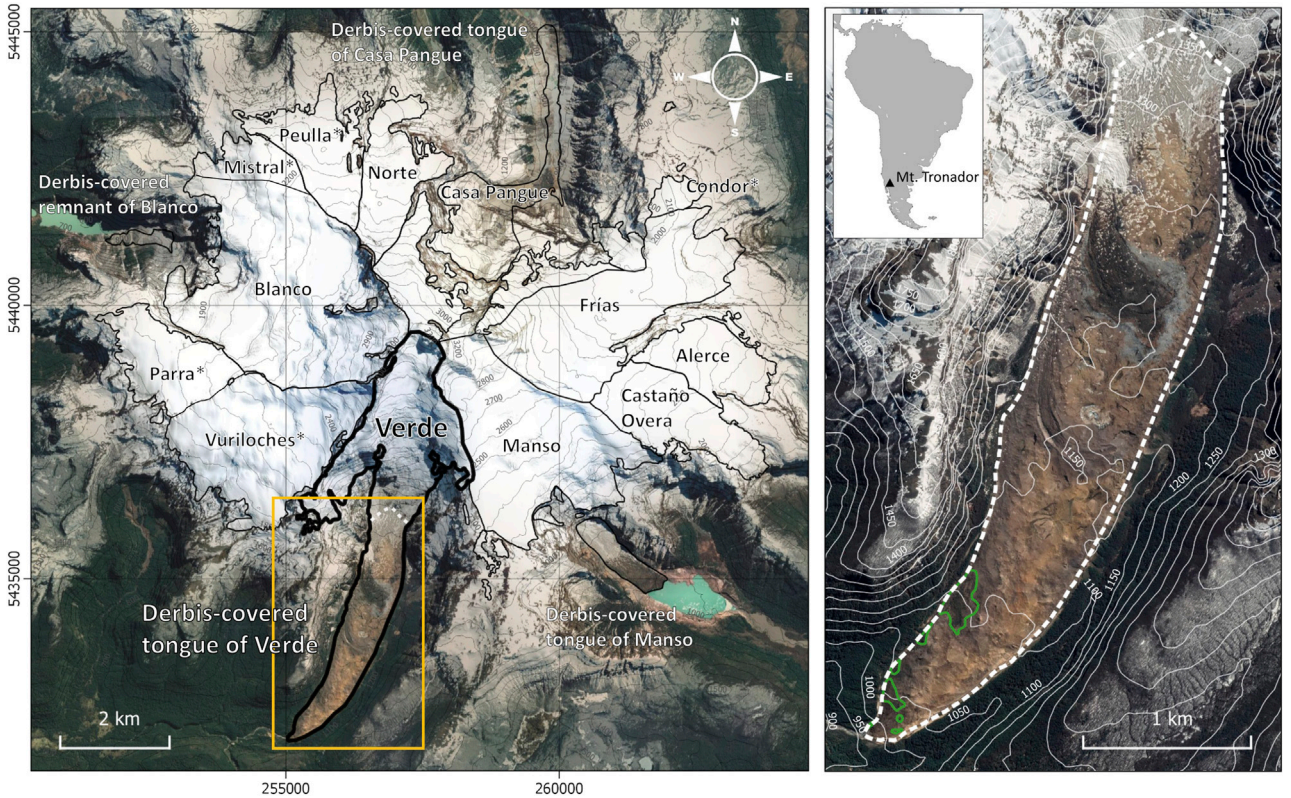

FIGURE 1 | Optical CNES/Airbus image of Monte Tronador from October 17, 2019. Verde glacier is delimited by the thick black line while other individual glaciers are delineated by thin black lines. White dotted line on Verde tongue marks the upper limit of the debris cover. Orange rectangle corresponds to the right panel, zooming in the debris-covered tongue of Verde glacier. The presence of some vegetation at the glacier lower part is indicated by green outline polygons. Coordinates in meters, universal transverse mercator (UTM) projection, zone 19, World Geodetic System (WGS84) datum.

Verde glacier has not shown significant retreat or advance over the last decades (Reinthaler et al., 2019), and its terminus is still in contact with the Little Ice Age moraines (Ruiz et al., 2015), which contrasts with the fast retreating behaviour of the glaciers in the region (Paul and Mölg, 2014). Between 2000 and 2012, the Verde glacier has a neutral mass balance (−0.08 ± 0.09 m w.e./yr), which contrast with the negative mass balance of Manso (−0.5 ± 0.1°m w.e./yr) and Casa Pangue (−0.29 ± 0.1 m w.e./yr), the other debris-covered valley glaciers at Monte Tronador (**Figure 1**). Meanwhile, the most considerable ice thickness changes of the Manso and Casa Pangue glaciers are concentrated in their lower debris-covered tongues. The Verde glacier's lower part does not show significant elevation change between 2000 and 2012 (mean elevation change of −0.6 ± 0.5 m; Ruiz et al., 2017). By applying cross-correlation to Pléiades satellite images, Ruiz et al. (2015) measured surface displacements over Monte Tronador glaciers between March and June 2012. They found that these glaciers follow a radial flow pattern. At Verde glacier, maximum surface speeds of <390 m/yr were estimated on the steep icefall area. Meanwhile, the lower reaches of the debris-covered tongues of Verde and Casa Pangue glaciers are almost stagnant. They found that low-elevation debris-covered glacier tongues show increasing velocities at the beginning of the accumulation season, probably in response to an increase in water input to the subglacial system from winter rainfall events at low elevations and a decrease in meltwater production at higher elevations.

Recently, Zorzut et al. (2020) calculated the ice thickness distribution of Monte Tronador glaciers and found that the gently sloped debris-covered tongue of the Verde glacier is one of the thicker parts of the whole glaciers of Monte Tronador, with a maximum estimated thickness of around 180 ± 60 m and a total volume of 0.59 ± 0.2 km^3.

MATERIAL AND METHODS

Google Earth Imagery

The Google Earth platform freely gives access to optical imagery of high spatial resolution, from SPOT and DigitalGlobe (e.g., QuickBird, Worldview-1 and 2, and IKONOS), and orthorectified based on the DEM from the Shuttle Radar Topography Mission–SRTM (Schmid et al., 2015). Moreover, Google Earth provides an historical catalogue with sufficient temporal resolution to enable investigation of interannual processes. Google Earth has thus been widely used as a main or supporting tool when performing cryosphere-related inventories, mainly of rock glaciers (Rangecroft et al., 2014; Schmid et al., 2015; Nagai et al., 2016; Charbonneau and

TABLE 2 | Ponds and ice cliffs observations for the 3.05 km^2 debris-covered tongue of Verde glacier.

Acquisition date	Image provider	Ponds		Ice cliffs	
		Count	Area (%)	Count	Area (%)
25-11-2009	Maxar	29	0.40	183	2.70
30-03-2012	Maxar	16	0.44	100	1.95
26-12-2012	Maxar	28	0.33	160	2.51
18-11-2013	CNES/Airbus	25	0.11	143	2.23
02-09-2015	Maxar	9	0.33	59	1.78
18-03-2016	CNES/Airbus	7	0.02	70	1.29
04-03-2018	CNES/Airbus	20	0.24	76	1.32
17-10-2019	CNES/Airbus	17	0.07	149	1.92

Smith, 2018; Jones et al., 2018; Pandey, 2019), but also debris-free (Tielidze et al., 2020) and debris-covered glaciers (Alifu et al., 2016a,b), as well as glacial lakes (Wilson et al., 2018).

In the present study, the debris-covered tongue of Verde glacier is analysed with eight high resolution scenes (<0.5 m), whose acquisition dates range from November 2009 to October 2019 (**Table 2**). Although the image distribution is uneven over the year, the dataset contains three images from end of summer (March 2012, March 2016, and March 2018), one from end of winter (September 2015), as well as four from spring and start of summer (November 2009, December 2012, November 2013, and October 2019). The scenes present clear atmospheric conditions, mostly snow-free, and show limited areas of shadow. Error in horizontal positioning between images will be assessed by marking non-moving features, such as outcrops and trees, outside of the glacier area. No image processing was performed for interpretation.

Ponds and Ice Cliffs Inventory

The inventory was conducted following the method employed by Bhushan et al. (2018), who analysed high-resolution imagery from Google Earth to identify supraglacial ponds and ice cliffs for 10 DCGs in the Zanskar Basin of Western Himalaya. By-eye ponds and ice cliffs identification and manual digitisation were realised directly in the Google Earth platform through the built-in geographic information system. The ponds and ice cliffs polygons were then exported into the QGIS geographic information system software where their distribution and geometric properties were assessed. Regarding the ice cliffs, the inventory records the planimetric area. Error in area determination was estimated by multiplying feature perimeter by the spatial resolution (Casassa et al., 2014), here rounded at 0.5 m.

The inventory allowed the tracking of persistent ice cliffs over the study period to assess retreat, which is defined here, as the observed distance between the same ice cliff between the initial and the final satellite scenes, divided by the time interval. In order to remove the displacement due to glacier flow and to only assess backwasting due to ablation, the observed ice cliff retreat was corrected for the local mean surface velocity (Steiner et al., 2019). Discriminating between the observed retreat and the assessed backwasting is particularly important for ice cliff retreat occurring parallel to flow direction, in which case the difference is maximum.

Glacier Characteristics

Horizontal surface velocity was determined following the method described by Immerzeel et al. (2014) and Wigmore and Mark (2017), who manually tracked topographic features on high-resolution photographs acquired using unmanned aerial vehicles. In the present study, this approach was adapted by tracking evenly spaced and clearly distinguishable boulders, at the glacier surface using the Google Earth historical imagery (**Figure 2**). For each identified boulder, a vector was drawn using the Google Earth path tool, which each node corresponded to the boulder position at the respective imagery date. These vectors were exported into QGIS to calculate horizontal displacement for each mapped boulder, which was then converted to surface velocity using time delay between images. Finally, velocity was interpolated to the tongue surface, using spline and kriging interpolation methods, both techniques having been applied on feature tracking on DCGs (Immerzeel et al., 2014; Wigmore and Mark, 2017). Interpolations were performed using the respective QGIS built-in tools. Error in distance calculation was rounded at the pixel size (0.5 m). Error due to image displacement was assessed by tracking non-moving features, such as trees and outcrops, outside of the glacier area.

Surface gradient was extracted from the SRTM DEM. However, this is made difficult due to the topography of DCGs being generally very coarse (Nicholson and Benn, 2012), and the SRTM showing random speckle noises (Stevenson et al., 2010), also referred as coherent multiplicative noises, that inherently exist in these products. Into QGIS, a low pass filter was thus initially applied, which is a common method to smooth SRTM DEMs (Wendi et al., 2016). Surface gradients were then grouped into four classes (0–2, 2–6, 6–10, and >10), as proposed by Reynolds (2000), and applied by Quincey et al. (2007) and Miles et al. (2017b) to analyse ponds and ice cliffs distribution. Root Mean Square Error (RMSE) was applied to compute the uncertainty of the two interpolation methods in comparison with the observations.

RESULTS

Ponds and Ice Cliffs Inventory

Over the 2009–2019 period, a total of 151 ponds and 940 ice cliffs were identified (**Table 2** and **Figure 3**). An example of mapped

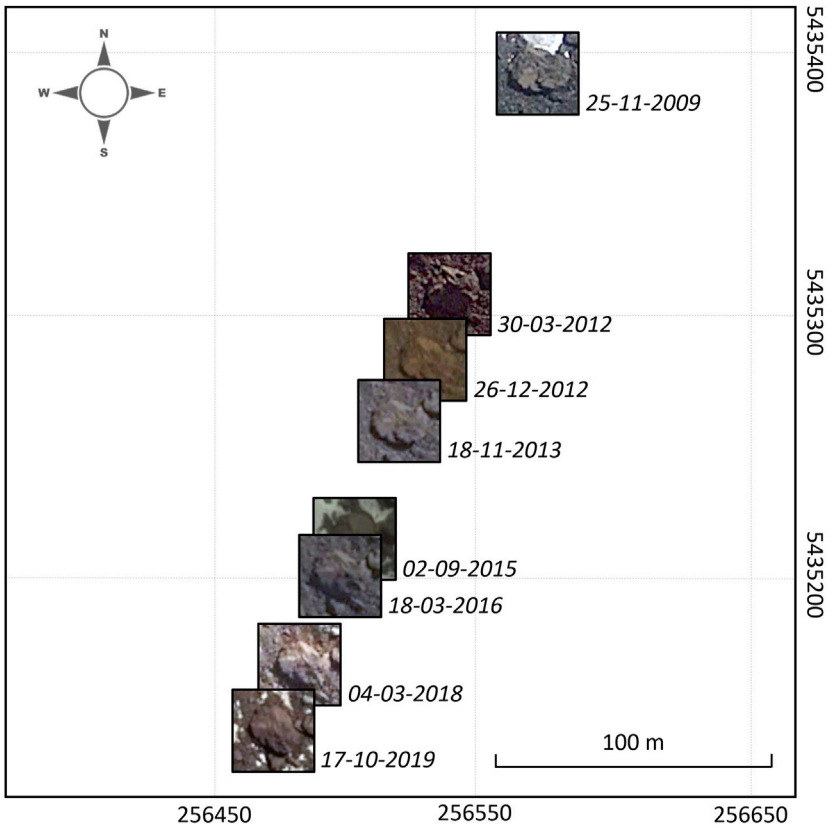

FIGURE 2 | Tracking of a boulder located at the surface of the Verde glacier. Each dated square represent the same boulder on distinct cropped images from Google Earth. Red arrow on **Figure 6A** indicates the path of the present boulder. Coordinates in meters, universal transverse mercator (UTM) projection, zone 19, World Geodetic System (WGS84) datum.

pond and ice cliff are shown on **Figure 4**. Both the ponds and the ice cliffs cover most of the tongue area, with highest density in the middle part. It is important to note that most of the ice cliffs located in the upper part of the tongue (**Figure 3B**) are associated with supraglacial channels.

The most extensive pond coverage was observed on March 30, 2012 (13,517 ± 649 m^2), which represents 0.44 ± 0.02% of the debris-covered area. Regarding the maximum ice cliff cover (82,364 ± 9,355 m^2), it occurs on November 25, 2009 and represents 2.70 ± 0.30% of the glacier tongue. Most of the ice cliffs (866 of 940) were not in contact with ponds at the moment of their mapping. High interannual variability is observed in both ponds and ice cliffs coverage (**Figure 5**).

Surface Velocity

A total of 191 boulders were tracked at the glacier surface, allowing velocity measurements over most of the debris-covered tongue (**Figure 6A**). Some boulders show displacements not concordant with the flow line direction between two dates, which is likely due to topography effects and roll overs. Ten control points were tracked around the glacier tongue (**Figure 6A**), allowing to determine a maximum total displacement error of 0.3 m/yr along the flowline.

Both spline and kriging interpolations methods (**Figures 6B,C**) show statistically similar results (**Table 3**). Highest velocities are found in the upper part of the glacier tongue, just below the steep icefall, with a regular decrease towards the glacier terminus, which is almost stagnant. This is consistent with the surface slope becoming gradually shallower towards the snout (**Figure 6D**). Low velocities are also found on the margins of the glacier. Our results are concordant with findings from Ruiz et al. (2015) which shown that higher velocities are associated with the ice fall and found almost stagnant conditions in the lower reach and lateral margins of the debris-covered tongue (**Figure 6D**). Otherwise, some discrepancies appear in the upper limits of the covered-tongue, likely associated with a lack of mapped boulders in this area of the glacier and a greatest uncertainty while applying interpolation techniques.

Ice Cliff Backwasting

Eleven ice cliffs were identified to persist over at least two scenes of the period of interest. Retreat varies from a few meters to a maximum distance of 201 m between November 2009 and October 2, 2019 for a ~200 m wide ice cliff (**Figure 7B**). After correction for local surface velocity, the highest backwasting rate was assessed to 24 m/yr for a south-facing ice cliff (third arrow

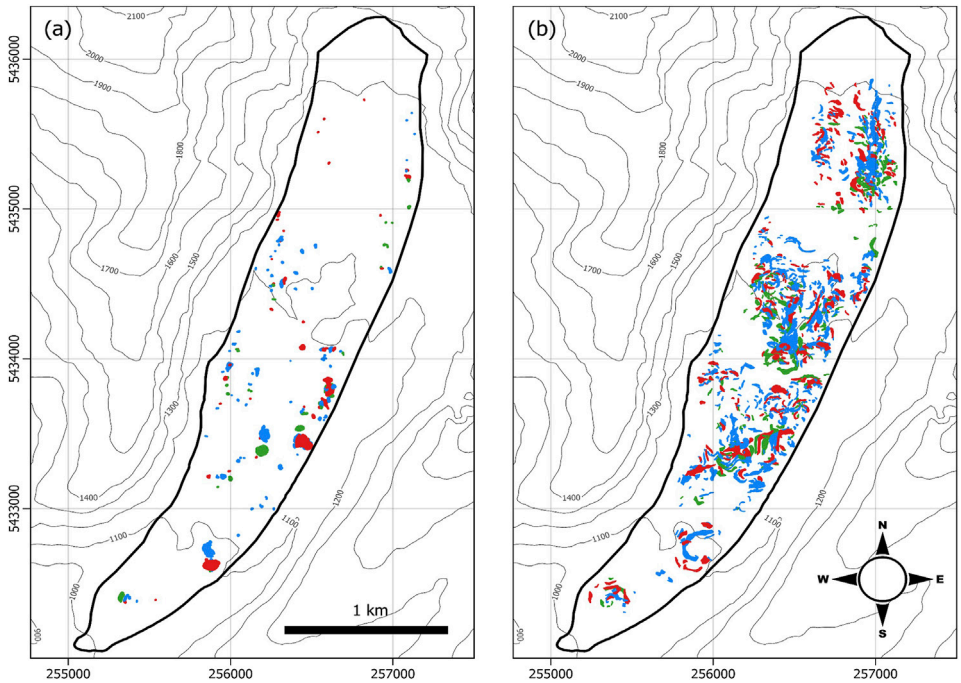

FIGURE 3 | (A) Ponds and **(B)** ice cliffs observed over the 2009–2019 period on the debris-covered tongue of Verde glacier. Features are colour-coded in function of the period of the year they were mapped, blue corresponding to November 2009, December 2012 and November 2013; red to March 2012, March 2016, March 2018; and green to September 2015 and October 2019. Elevation data are based on SRTM DEM. Coordinates in meters, Universal Transverse Mercator (UTM) projection, zone 19, World Geodetic System (WGS84) datum.

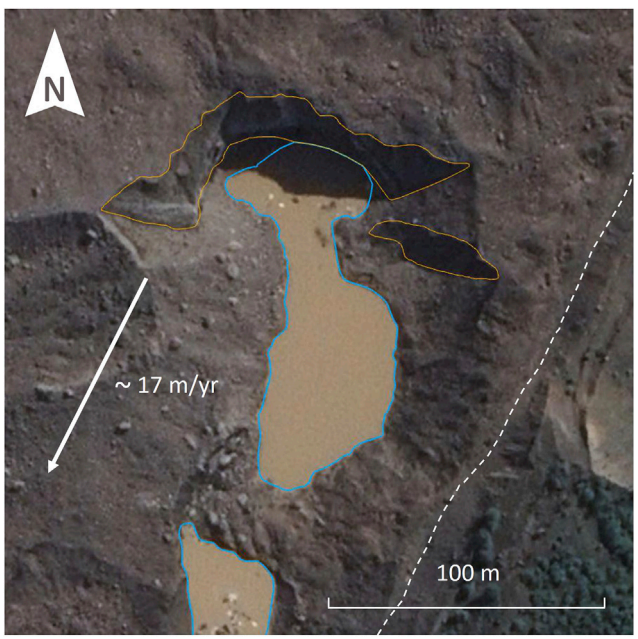

FIGURE 4 | Outlines of mapped ponds (solid blue lines) and south-facing ice cliffs (solid orange lines), from march 4, 2018. White arrow indicates local mean surface velocity, extracted from spline interpolation surface. White dashed line shows the glacier outline.

from the north on **Figure 7**), while the measured retreat was about 9 m/yr.

DISCUSSION

Ponds and Ice Cliff Distribution and Formation

Although supraglacial ponds and ice cliffs are observed across the whole elevation range, their distribution is uneven over the tongue (**Figure 3**). Four main clusters can be identified, from North to South, in particular when describing the ice cliffs distribution (**Figure 3B**). The first cluster counts few ponds and two channels of numerous ice cliffs parallel to the flowline. The formation of these ice cliffs seems to be associated with supraglacial channels visible on the upper part of the debris-covered tongue. The second and the third clusters show the largest populations of ponds and ice cliffs. A clear gap, showing no features, is visible between the first and the second clusters, which we attributed to a huge quantity of debris deposited on the tongue by a landslide or rock avalanche originated on the western flanks of the valley (**Figure 1**). A smallest gap is observed between the second and the third cluster, likely associated with a former landslide or rock avalanche, forming visible arched ridges on the glacier surface. These thick deposits of debris appear to be inhibiting the

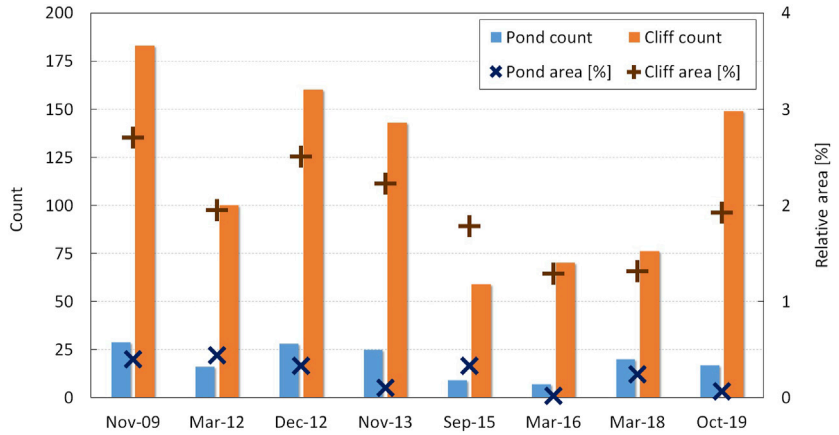

FIGURE 5 | Observed ponds and ice cliffs number and area.

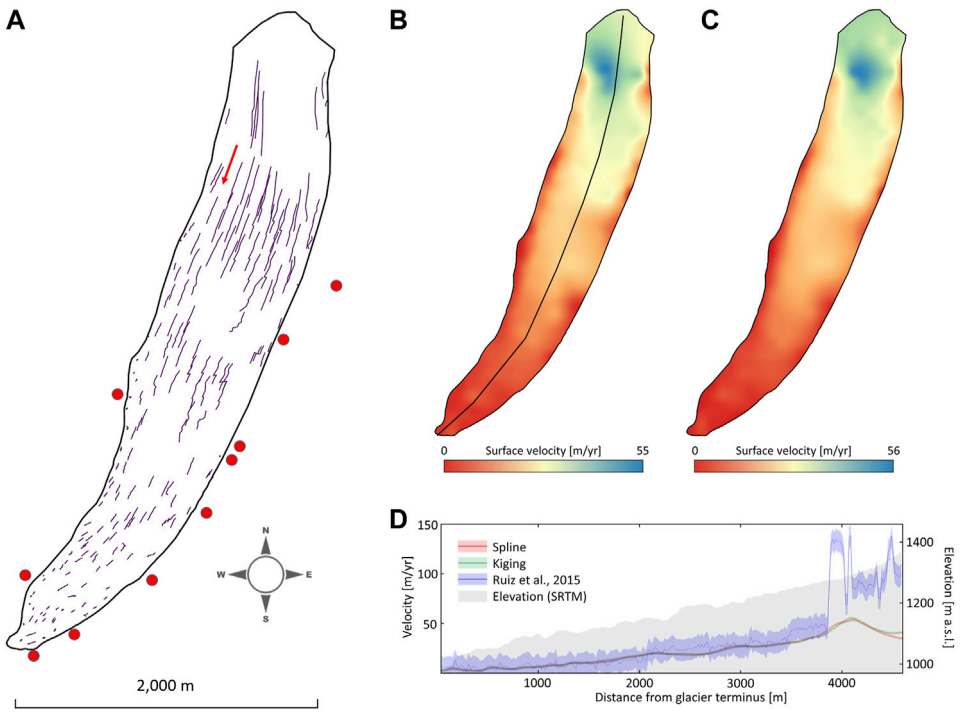

FIGURE 6 | (A) Tracked boulders on the debris-covered tongue of Verde glacier between November 2009 and October 2019. The red arrow shows the location of the boulder of **Figure 2**. Red dots mark the location of control points outside glacier area **(B, C)** Interpolated surface velocity using spline and kriging interpolation methods, respectively.**(D)** Surface velocity profiles corresponding to the black line on **(B)**. Shaded area correspond to error associated to the interpolated velocities. Blue line and light grey area show results from Ruiz et al. (2015) and the elevation along the same profile, respectively.

TABLE 3 | Main statistical characteristics of the interpolated velocity results.

	Minimum	Mean	Maximum	Standard deviation	Pearson's *r*
–	–	(m/yr)	–	–	–
Spline	0.30	12.86	55.19	12.49	0.99
Kriging	0.30	19.05	55.49	12.89	–

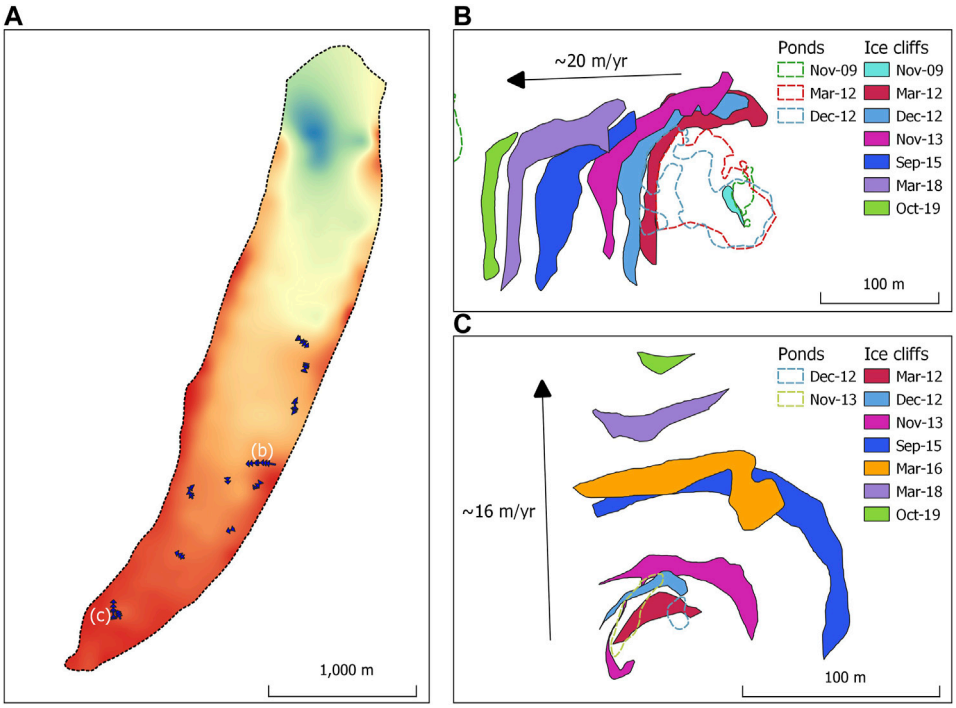

FIGURE 7 | (A) Direction and length of retreat of 11 ice cliffs on the debris-covered tongue of Verde glacier. Colormap corresponds to the spline interpolation of surface velocity of **Figure 6B**. **(B)** and **(C)** refer to the right panels showing detailed time-lapse retreat of two selected ice cliffs and the associated ponds.

formation of supraglacial ponds and ice cliffs at the glacier surface. Finally, the fourth cluster, located near the front, shows smaller density of ponds and ice cliffs, whereas reduced surface velocity and gentle slopes would be adequate for their formation (see **Figure 3**). We attributed this small amount of feature to a significant debris thickness, highlighted by the presence of trees and vegetation on the glacier surface (**Figure 1**). The lowest ponds and ice cliffs numbers in the areas with thicker debris layers is concordant with results from Steiner et al. (2019) in the Langtang catchment (Himalaya), who observed few features near the front, where the debris layer is the thickest. The absence of ponds and cliffs in areas of thick debris is likely due to suppression of ablation, as the insulation threshold might be exceeded.

All mapped ponds take place on the tongue with gradient below 10 (**Figure 8**). Above this threshold, all the available meltwater is able to drain away, as previously reported by (Reynolds, 2000) on DCGs in Bhutan. Specifically, 14, 74 and 12% of the ponds were observed on slopes <2°, between 2–6 and between 6–10, respectively. These distributions are concordant with observations made on DCGs in Himalaya (Liu et al., 2015; Chand and Watanabe, 2019).

The ice cliffs distribution shows a similar pattern with less than 1% observed on areas with gradient above 10, while 10, 73 and 16% of the mapped cliffs are located on slopes <2°, between 2–6 and between 6–10, respectively. These similar distributions of ponds and ice cliffs with respect to gradient could signify their formations are associated processes. Indeed, despite the fact that only 70 of 907 ice cliffs were in contact with a pond at the moment of their mapping, we observed that most of the backwasting ice cliffs (**Table 4**) are in contact with a pond at the initial stages of their formation (**Figures 7B,C**). Afterwards, the cliffs lose contact as they retreat and the ponds are either drained or filled with debris.

The distribution of ponds with respect to their surface area is strongly controlled by both surface gradient and surface velocity (**Figure 8**). Large ponds (>1,000 m^2) only develop on glacier surface of relatively low velocity (<17 m/yr) and low gradient (<6). This results in large ponds being constrained to the lower-half and the margins of the tongue (**Figure 3A**).

Regarding the distribution of ice cliffs with respect to their area, no clear influence of surface velocity nor surface gradient was observed (**Figure 9**). Nevertheless, it appears that large ice cliffs only develop where surface velocity is low (**Figure 9A**).

The observed high variability in ponds and ice cliff distribution and their interannual evolution seems to highlight a very dynamic behaviour of Verde glacier, which is concordant with observed high surface velocity. These observations tends to demonstrate that the supraglacial ponds do connect and disconnect with the englacial conduits as crevasses open and close, respectively.

Seasonality

No long-term trend in ponds and ice cliffs count or covered area was detected between 2009 and 2019. On the other hand, and

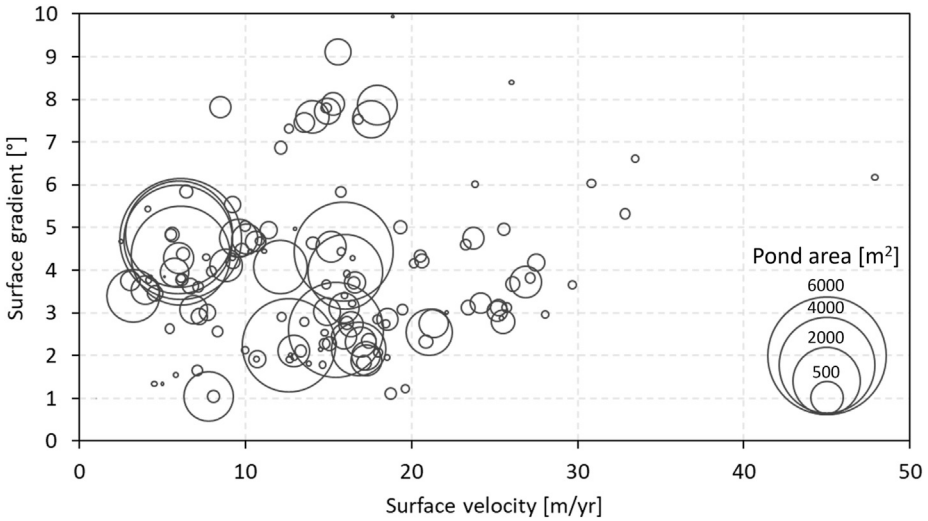

FIGURE 8 | Pond area as a function of surface gradient and interpolated velocity (derived form the spline method). Pond area is proportional to circles size.

based on the available data, we observed a seasonal signal in the number of supraglacial ponds and in the number and area of ice cliff mapped through the year (**Table 2**; **Figure 5**). We found a maximum of supraglacial ponds and ice cliffs during spring and at the beginning of summer (November 2009, December 2012, November 2013, October 2019), and a minimum of ponds and ice cliffs, at the end of summer (March 2012, March 2016, March 2018), and at the end of winter (September 2015). We suggest the number of ponds and number and area of ice-cliff might be related to the evolution of the hydrological network through the year, as previously proposed in other studies (Reynolds, 2000; Sakai et al., 2000). At the beginning of the ablation period (spring and beginning of summer), the hydrological network is not well connected yet, so meltwater accumulated into depressions and form supgraglacial ponds. This early pond formation initiates the exposure of associated ice cliffs. During the ablation season, the crevasses and englacial conduits open and enhance connectivity. Similar cycles have been observed in the Eastern Himalaya and Karakoram, with an increase in ponds number at the beginning of spring (April) and a sharp decrease in June-July (Narama et al., 2017). Authors attributed the increase to inflow of meltwater from snow and ice, and the later decrease to a enhanced connectivity to the englacial drainage network. The earlier part of the cycle was also observed in High Mountain Asia during the pre-monsoon season, and related to the observed reduction of the snow cover (Miles et al., 2017b; Chand and Watanabe, 2019).

Finally, during the beginning of the accumulation season (winter), there is no meltwater at the surface to fill the ponds. This small amount of ponds and their reduced cover in winter are concordant with results from the Everest region (Chand and Watanabe, 2019).

The smallest amount of ice cliffs at the end of summer might also be related to their fast-vanishing behaviour, as few of them have been observed to persist year to year which could also explains that no seasonality was observed regarding the ponds area.

TABLE 4 | Persistent and backwasting ice cliffs on Verde glacier, listed from north to south. The 'Pond' column indicates the presence (Y) or not (N) of a coalescent pond at any stage of the backwasting process.

Initial date	Final date	Days	Backwasting		Aspect	Pond
			(m)	(m/yr)		(Y/N)
30-03-2012	17-10-2019	2,757	128	17	NW	N
25-11-2009	17-10-2019	3,613	116	12	S	Y
30-03-2012	17-10-2019	2,757	180	24	S	Y
25-11-2009	17-10-2019	3,613	190	19	SE	Y
30-03-2012	18-11-2013	598	9	5	NW	N
26-12-2012	18-03-2016	1,178	60	19	SW	Y
25-11-2009	18-03-2016	2,305	135	21	S	Y
26-12-2012	02-09-2015	980	40	15	E	Y
25-11-2009	18-11-2013	1,454	76	19	SE	Y
30-03-2012	17-10-2019	2,757	145	19	S	Y
25-11-2009	18-11-2013	1,454	80	20	S	Y

Characteristics of Backwasting Ice Cliffs

Most of the persistent and backwasting ice cliffs were found to be south-facing (**Table 4**), which is consistent with results from Sakai et al. (2002) and Buri and Pellicciotti (2018), who found that persistent ice cliffs are mostly north-facing in the northern hemisphere. In all cases, persistent ice cliffs appear to be pole-facing. In contrast, the sun-facing ice cliffs do not have time to extent spatially, and do not survive the ablation season, as they receive the highest amount of radiations. They are thought to not contribute significantly to annual mass balance (Buri and Pellicciotti, 2018). According to Sakai et al. (2002), the difference in stability between the pole-facing and the sun-facing ice cliffs is caused by a difference in incoming radiations. Pole-facing cliffs receive mostly long-wave radiation from the surrounding debris cover, which reaches the lower portion more than the upper portion. This results in the ice cliff being steep enough to not be covered by debris and persist over time. On the other hand, sun-

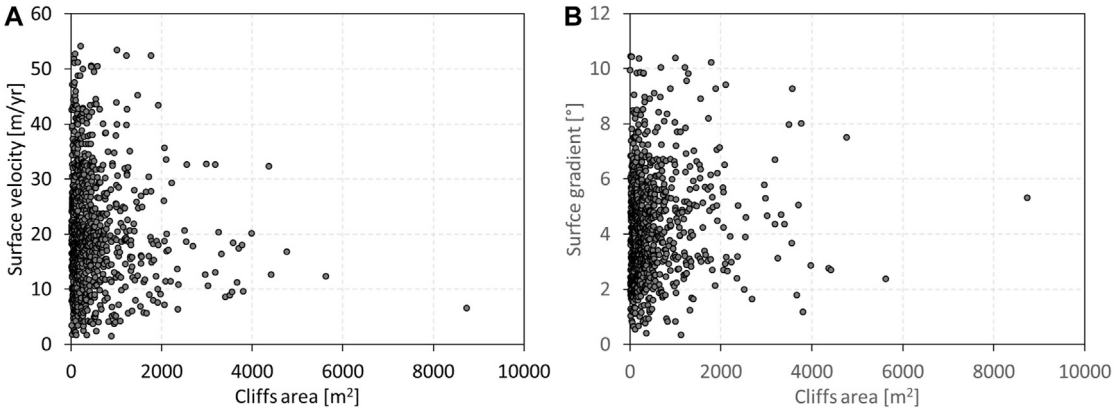

FIGURE 9 | Cliff area as a function of **(A)** surface velocity, derived from the spline interpolation, and **(B)** surface gradient, extracted from SRTM.

facing cliffs are exposed to direct and more intense short-wave radiation, which affect mainly their upper portion. These cliffs have thus shallower slope and are more likely to get covered by debris.

The growth and demise of a persistent south-facing ice cliff on glacier Verde is illustrated on **Figure 7C**. This south-facing ice cliff initially emerges as a concave feature in contact with a pond. The ice cliff then grows spatially and reach a maximal extent, before it tails off as a convex feature. In the later stages, there is no apparent pond adjacent to the persistent ice cliffs.

CONCLUSION

We have compiled a complete inventory of supraglacial ponds and ice cliffs of the debris-covered tongue of Verde glacier, in the Chilean Northern Patagonian Andes. The inventory was based on Google Earth historical imagery covering the 2009–2019 period. Coverage ranges from 0.02 to 0.44% for ponds, and from 0.51 to 2.70% for ice cliffs.

Supraglacial ponds and ice cliffs are present at every elevation range of the debris-covered tongue. Ponds distribution is controlled by surface characteristics, with large features only occurring on areas of reduced velocity and low gradient. Ice cliffs distribution is less clear and appears to be slightly controlled by surface velocity. Debris thickness appears to also play a role in the presence or not of ponds and cliffs, as areas of thicker debris covers exhibit none of the two features. Based on available data, supraglacial ponds count and ice-cliff count and area exhibit a seasonal signal, with a maximum during the beginning of the ablation season and a minimum at the end of the ablation season and through the accumulation seasons. We attribute this seasonality to the opening and closure of the hydrological network through the year. Finally, we identified eleven persistent ice cliffs, most of them south-facing (or pole-facing). Ice cliff backwasting up to 200 m was observed, which highlights that ablation processes take place on the glacier surface, contrasting with the stagnant terminus.

Further researches need to be conducted to address the role of supraglacial ponds and ice cliffs on glacier mass balance, as well as their impact on the hydrological regime of DCGs. A continuous *in-situ* monitoring of ponds and ice cliff evolution could give insights into their interannual evolution, as well as the frequency and velocity of drainage and filling.

DATA AVAILABILITY STATEMENT

The raw data supporting the conclusions of this article will be made available by the authors, without undue reservation.

AUTHOR CONTRIBUTIONS

TL gathered and prepared all data, performed all processing and calculations, and made all figures and tables. TL and LR contributed to the discussion of results, and shared the writing of the paper.

FUNDING

The Centro de Estudios Cientificos (CECs) is co-funded by the base Finance program of ANID/PIA APOYO CCTE AFB170003. LR acknowledges supports from Ministerio de Ambiente y Desarrollo Sustentable de Argentina (Inventario Nacional de Glaciares), Agencia de Promocion Cientfica (projects PICT 2010-1,438; PICT 2014-1794) and CONICET.

REFERENCES

Alifu, H., Johnson, B. A., and Tateishi, R. (2016a). Delineation of Debris-Covered Glaciers Based on a Combination of Geomorphometric Parameters and a TIR/NIR/SWIR Band Ratio. *IEEE J. Sel. Top. Appl. Earth Observations Remote Sensing* 9 (2), 781–792. doi:10.1109/jstars.2015.2500906

Alifu, H., Tateishi, R., Alsaaideh, B., and Gharechelou, S. (2016b). Multi-criteria Technique for Mapping of Debris-Covered and Clean-Ice Glaciers in the Shaksgam valley Using Landsat TM and ASTER GDEM. *J. Mountain Sci.* 13 (4), 703–714.

Anderson, R. S., Anderson, L. S., Armstrong, W. H., Rossi, M. W., and Crump, S. E. (2018). Glaciation of alpine Valleys: The Glacier - Debris-Covered Glacier - Rock Glacier Continuum. *Geomorphology* 311, 127–142. doi:10.1016/j.geomorph.2018.03.015

Aravena, J.-C., and Luckman, B. H. (2009). Spatio-temporal Rainfall Patterns in Southern South America. *Int. J. Climatol.* 29, 2106–2120. doi:10.1002/joc.1761

Ayala, A., Pellicciotti, F., MacDonell, S., McPhee, J., Vivero, S., Campos, C., et al. (2016). Modelling the Hydrological Response of Debris-free and Debris-Covered Glaciers to Present Climatic Conditions in the Semiarid Andes of central Chile. *Hydrol. Process.* 30 (22), 4036–4058. doi:10.1002/hyp.10971

Barcaza, G., Nussbaumer, S. U., Tapia, G., Valdés, J., García, J. L., Videla, Y., et al. (2017). Glacier Inventory and Recent Glacier Variations in the Andes of Chile, South America. *Ann. Glaciology* 58 (75), 166–180. doi:10.1017/aog.2017.28

Benn, D. I., Bolch, T., Hands, K., Gulley, J., Luckman, A., Nicholson, L. I., et al. (2012). Response of Debris-Covered Glaciers in the Mount Everest Region to Recent Warming, and Implications for Outburst Flood Hazards. *Earth-Science Rev.* 114 (1-2), 156–174. doi:10.1016/j.earscirev.2012.03.008

Bhushan, S., Syed, T. H., Arendt, A. A., Kulkarni, A. V., and Sinha, D. (2018). Assessing Controls on Mass Budget and Surface Velocity Variations of Glaciers in Western Himalaya. *Sci. Rep.* 8 (1), 8885–8911. doi:10.1038/s41598-018-27014-y

Bisset, R. R., Dehecq, A., Goldberg, D. N., Huss, M., Bingham, R. G., and Gourmelen, N. (2020). Reversed Surface-Mass-Balance Gradients on Himalayan Debris-Covered Glaciers Inferred from Remote Sensing. *Remote Sensing* 12 (10). doi:10.3390/rs12101563

Brock, B., Rivera, A., Casassa, G., Bown, F., and Acuña, C. (2007). The Surface Energy Balance of an Active Ice-Covered Volcano: Villarrica Volcano, Southern Chile. *Ann. Glaciol.* 45 (1), 104–114. doi:10.3189/172756407782282372

Brun, F., Wagnon, P., Berthier, E., Shea, J. M., Immerzeel, W. W., Kraaijenbrink, P. D. A., et al. (2018). Ice Cliff Contribution to the Tongue-wide Ablation of Changri Nup Glacier, Nepal, central Himalaya. *The Cryosphere* 12 (11), 3439–3457. doi:10.5194/tc-12-3439-2018

Burger, F., Ayala, A., Farias, D., Shaw, T. E., MacDonell, S., Brock, B., et al. (2019). Interannual Variability in Glacier Contribution to Runoff from a High-elevation Andean Catchment: Understanding the Role of Debris Cover in Glacier Hydrology. *Hydrological Process.* 33 (2), 214–229. doi:10.1002/hyp.13354

Buri, P., and Pellicciotti, F. (2018). Aspect Controls the Survival of Ice Cliffs on Debris-Covered Glaciers. *Proc. Natl. Acad. Sci. USA* 115 (17), 4369–4374. doi:10.1073/pnas.1713892115

Carrasco, J. F., Casassa, G., and Quintana, J. (2005). Changes of the 0°C isotherm and the equilibrium line altitude in central Chile during the last quarter of the 20th century/Changements de l'isotherme 0°C et de la ligne d'équilibre des neiges dans le Chili central durant le dernier quart du 20ème siècle. *Hydrological Sci. J.* 50 (6), 933–948. doi:10.1623/hysj.2005.50.6.933

Casassa, G., Rodríguez, J. L., and Loriaux, T. (2014). A New Glacier Inventory for the Southern Patagonia Icefield and Areal Changes 1986-2000. In Global Land Ice Measurements from Space, pages 639–660. doi:10.1007/978-3-540-79818-7_27

Chand, M. B., and Watanabe, T. (2019). Development of Supraglacial Ponds in the Everest Region, Nepal, between 1989 and 2018. *Remote Sensing* 11 (9). doi:10.3390/rs11091058

Charbonneau, A. A., and Smith, D. J. (2018). An Inventory of Rock Glaciers in the central British Columbia Coast Mountains, Canada, from High Resolution Google Earth Imagery. *Arctic, Antarctic, Alpine Res.* 50 (1). doi:10.1080/15230430.2018.1489026

Chikita, K., Jha, J., and Yamada, T. (1998). The basin Expansion Mechanism of a Supraglacial lake in the Nepal Himalaya. *J. Hokkaido Univ. Fac. Sci. Ser. VII: Geophys.* 11 (2), 501–521.

Collier, E., Maussion, F., Nicholson, L. I., Mölg, T., Immerzeel, W. W., and Bush, A. B. G. (2015). Impact of Debris Cover on Glacier Ablation and Atmosphere-Glacier Feedbacks in the Karakoram. *The Cryosphere* 9 (4), 1617–1632. doi:10.5194/tc-9-1617-2015

Condom, T., Coudrain, A., Sicart, J. E., and Théry, S. (2007). Computation of the Space and Time Evolution of Equilibrium-Line Altitudes on Andean Glaciers (10N-55S). *Glob. Planet. Change* 59 (1-4), 189–202. doi:10.1016/j.gloplacha.2006.11.021

Deline, P. (2005). Change in Surface Debris Cover on Mont Blanc Massif Glaciers after the'Little Ice Age' Termination. *The Holocene* 15, 302–309. doi:10.1191/0959683605hl809rr

Ferri, L., Dussaillant, I., Zalazar, L., Masiokas, M. H., Ruiz, L., Pitte, P., et al. (2020). Ice Mass Loss in the Central Andes of Argentina between 2000 and 2018 Derived from a New Glacier Inventory and Satellite Stereo-Imagery. *Front. Earth Sci.* 8 (December), 1–16. doi:10.3389/feart.2020.530997

Fyffe, C. L., Brock, B. W., Kirkbride, M. P., Black, A. R., Smiraglia, C., and Diolaiuti, G. (2019). The Impact of Supraglacial Debris on Proglacial Runoff and Water Chemistry. *J. Hydrol.* 576, 41–57. doi:10.1016/j.jhydrol.2019.06.023

Fyffe, C. L., Brock, B. W., Kirkbride, M. P., Mair, D. W. F., and Diotri, F. (2012). *The Hydrology of a Debris-Covered Glacier, the Miage Glacier, Italy*. BHS Eleventh National Symposium, Hydrology For a Changing World. Dundee ((January).

Garreaud, R. D., Vuille, M., Compagnucci, R., and Marengo, J. (2009). Present-day South American Climate. *Palaeogeogr. Palaeoclimatol. Palaeoecol.* 281 (3-4), 180–195. doi:10.1016/j.palaeo.2007.10.032

Hagg, W., Mayer, C., Lambrecht, A., and Helm, A. (2008). Sub-debris Melt Rates on Southern Inylchek Glacier, central Tian Shan. *Geografiska Annaler: Ser. A, Phys. Geogr.* 90 (1), 55–63. doi:10.1111/j.1468-0459.2008.00333.x

Immerzeel, W. W., Kraaijenbrink, P. D. A., Shea, J. M., Shrestha, A. B., Pellicciotti, F., Bierkens, M. F. P., et al. (2014). High-resolution Monitoring of Himalayan Glacier Dynamics Using Unmanned Aerial Vehicles. *Remote Sensing Environ.* 150, 93–103. doi:10.1016/j.rse.2014.04.025

Immerzeel, W. W., Lutz, A. F., Andrade, M., Bahl, A., Biemans, H., Bolch, T., et al. (2020). Importance and Vulnerability of the World's Water Towers. *Nature* 577 (7790), 364–369. doi:10.1038/s41586-019-1822-y

Irvine-Fynn, T. D. L., Porter, P. R., Rowan, A. V., Quincey, D. J., Gibson, M. J., Bridge, J. W., et al. (2017). Supraglacial Ponds Regulate Runoff from Himalayan Debris-Covered Glaciers. *Geophys. Res. Lett.* 44 (23), 11894–11094. doi:10.1002/2017gl075398

Iwata, S., Watanabe, O., and Fushimi, H. (1980). Surface Morphology in the Ablation Area of the Khumbu Glacier. *J. Jpn. Soc. Snow Ice* 41 (Special), 9–17. doi:10.5331/seppyo.41.special_9

Janke, J. R., Bellisario, A. C., and Ferrando, F. A. (2015). Classification of Debris-Covered Glaciers and Rock Glaciers in the Andes of central Chile. *Geomorphology* 241, 98–121. doi:10.1016/j.geomorph.2015.03.034

Jones, D. B., Harrison, S., Anderson, K., Selley, H. L., Wood, J. L., and Betts, R. A. (2018). The Distribution and Hydrological Significance of Rock Glaciers in the Nepalese Himalaya. *Glob. Planet. Change* 160 (November), 123–142. doi:10.1016/j.gloplacha.2017.11.005

Kirkbride, M. P. (1993). The Temporal Significance of Transitions from Melting to Calving Termini at Glaciers in the central Southern Alps of New Zealand. *The Holocene* 3 (3), 232–240. doi:10.1177/095968369300300305

Knight, J., Harrison, S., and Jones, D. B. (2019). Rock Glaciers and the Geomorphological Evolution of Deglacierizing Mountains. *Geomorphology* 324, 14–24. doi:10.1016/j.geomorph.2018.09.020

Liu, Q., Mayer, C., and Liu, S. (2015). Distribution and Interannual Variability of Supraglacial Lakes on Debris-Covered Glaciers in the Khan Tengri-Tumor Mountains, Central Asia. *Environ. Res. Lett.* 10 (1).

Lliboutry, L. (1998). "Glacier of Chile and Argentina," in Glaciers Of South America, *Pages 109–206*. Editors R. S. Williams and J. G. Ferrigno. edition (Washington, isgs profe: USGS).

Maurer, J. M., Rupper, S. B., and Schaefer, J. M. (2016). Quantifying Ice Loss in the Eastern Himalayas since 1974 Using Declassified Spy Satellite Imagery. *Cryosphere Discuss.* 10, 2203–2215. doi:10.5194/tc-10-2203-2016

Miles, E. S., Willis, I., Buri, P., Steiner, J. F., Arnold, N. S., and Pellicciotti, F. (2018). Surface Pond Energy Absorption across Four Himalayan Glaciers Accounts for 1/8 of Total Catchment Ice Loss. *Geophys. Res. Lett.* 45 (1910), 10464–10473. doi:10.1029/2018GL079678

Miles, E. S., Steiner, J., Willis, I., Buri, P., Immerzeel, W. W., Chesnokova, A., et al. (2017a). Pond Dynamics and Supraglacial-Englacial Connectivity on Debris-Covered Lirung Glacier, Nepal. *Front. Earth Sci.* 5 (September), 1–19. doi:10.3389/feart.2017.00069

Miles, E. S., Willis, I. C., Arnold, N. S., Steiner, J., and Pellicciotti, F. (2017b). Spatial, Seasonal and Interannual Variability of Supraglacial Ponds in the Langtang Valley of Nepal, 1999-2013. *J. Glaciol.* 63 (237), 88–105. doi:10.1017/jog.2016.120

Miles, K. E., Hubbard, B., Irvine-Fynn, T. D. L., Miles, E. S., Quincey, D. J., and Rowan, A. V. (2020). Hydrology of Debris-Covered Glaciers in High Mountain Asia. *Earth-Science Rev.* 207 (June), 103212. doi:10.1016/j.earscirev.2020.103212

Miles, K. E., Hubbard, B., Quincey, D. J., Miles, E. S., Irvine-Fynn, T. D. L., and Rowan, A. V. (2019). Surface and Subsurface Hydrology of Debris-Covered

Khumbu Glacier, Nepal, Revealed by Dye Tracing. *Earth Planet. Sci. Lett.* 513, 176–186. doi:10.1016/j.epsl.2019.02.020

Monnier, S., and Kinnard, C. (2017). Pluri-decadal (1955-2014) Evolution of Glacier-Rock Glacier Transitional Landforms in the central Andes of Chile (30-33° S). *Earth Surf. Dynam.* 5 (3), 493–509. doi:10.5194/esurf-5-493-2017

Monnier, S., and Kinnard, C. (2015). Reconsidering the Glacier to Rock Glacier Transformation Problem: New Insights from the central Andes of Chile. *Geomorphology* 238, 47–55. doi:10.1016/j.geomorph.2015.02.025

Nagai, H., Fujita, K., Sakai, A., Nuimura, T., and Tadono, T. (2016). Comparison of Multiple Glacier Inventories with a New Inventory Derived from High-Resolution ALOS Imagery in the Bhutan Himalaya. *The Cryosphere* 10 (1), 65–85. doi:10.5194/tc-10-65-2016

Narama, C., Daiyrov, M., Tadono, T., Yamamoto, M., Kääb, A., Morita, R., et al. (2017). Seasonal Drainage of Supraglacial Lakes on Debris-Covered Glaciers in the Tien Shan Mountains, Central Asia. *Geomorphology* 286, 133–142. doi:10.1016/j.geomorph.2017.03.002

Nicholson, L., and Benn, D. I. (2012). Properties of Natural Supraglacial Debris in Relation to Modelling Sub-debris Ice Ablation. *Earth Surf. Process. Landforms* 38 (5), 490–501. doi:10.1002/esp.3299

Pandey, P. (2019). Inventory of Rock Glaciers in Himachal Himalaya, India Using High-Resolution Google Earth Imagery. *Geomorphology* 340, 103–115. doi:10.1016/j.geomorph.2019.05.001

Paul, F., and Mölg, N. (2014). Hasty Retreat of Glaciers in Northern Patagonia from 1985 to 2011. *J. Glaciol.* 60 (224), 1033–1043. doi:10.3189/2014jog14j104

Pellicciotti, F., Stephan, C., Miles, E., Herreid, S., Immerzeel, W. W., and Bolch, T. (2015). Mass-balance Changes of the Debris-Covered Glaciers in the Langtang Himal, Nepal, from 1974 to 1999. *J. Glaciol.* 61 (226), 373–386. doi:10.3189/2015jog13j237

Quincey, D. J., Richardson, S. D., Luckman, A., Lucas, R. M., Reynolds, J. M., Hambrey, M. J., et al. (2007). Early Recognition of Glacial lake Hazards in the Himalaya Using Remote Sensing Datasets. *Glob. Planet. Change* 56 (1-2), 137–152. doi:10.1016/j.gloplacha.2006.07.013

Rangecroft, S., Harrison, S., Anderson, K., Magrath, J., Castel, A. P., and Pacheco, P. (2014). A First Rock Glacier Inventory for the Bolivian Andes. *Permafrost Periglac. Process.* 25 (4), 333–343. doi:10.1002/ppp.1816

Reid, T. D., and Brock, B. W. (2014). Assessing Ice-Cliff Backwasting and its Contribution to Total Ablation of Debris-Covered Miage Glacier, Mont Blanc Massif, Italy. *J. Glaciol.* 60 (219), 3–13. doi:10.3189/2014jog13j045

Reinthaler, J., Paul, F., Granados, H. D., Rivera, A., and Huggel, C. (2019). Area Changes of Glaciers on Active Volcanoes in Latin America between 1986 and 2015 Observed from Multi-Temporal Satellite Imagery. *J. Glaciol.* 65, 542–556. doi:10.1017/jog.2019.30

Reynolds, J. M. (2000). *On the Formation of Supraglacial Lakes on Debris-Covered Glaciers*. Seattle: IAHS-AISH Publication, 153–161.

Röhl, K. (2008). Characteristics and Evolution of Supraglacial Ponds on Debris-Covered Tasman Glacier, New Zealand. *J. Glaciol.* 54 (188), 867–880. doi:10.3189/002214308787779861

Ruiz, L., Berthier, E., Masiokas, M., Pitte, P., and Villalba, R. (2015). First Surface Velocity Maps for Glaciers of Monte Tronador, North Patagonian Andes, Derived from Sequential Pléiades Satellite Images. *J. Glaciol.* 61 (229), 908–922. doi:10.3189/2015jog14j134

Ruiz, L., Berthier, E., Viale, M., Pitte, P., and Masiokas, M. H. (2017). Recent Geodetic Mass Balance of Monte Tronador Glaciers, Northern Patagonian Andes. *The Cryosphere* 11 (1), 619–634. doi:10.5194/tc-11-619-2017

Sakai, A., and Fujita, K. (2010). Formation Conditions of Supraglacial Lakes on Debris- Covered Glaciers in the Himalaya. *J. Glaciology* 56 (195), 231–326. doi:10.3189/002214310791190785

Sakai, A., Nakawo, M., and Fujita, K. (2002). Distribution Characteristics and Energy Balance of Ice Cliffs on Debris-Covered Glaciers, Nepal Himalaya. *Arctic, Antarctic, Alpine Res.* 34 (1), 12–19. doi:10.1080/15230430.2002.12003463

Sakai, A., Takeuchi, N., Fujita, K., and Nakawo, M. (2000). , IAHS-AISH Publication, Seattle: IAHS-AISH Publication, pp , 119–130.Role of Supraglacial Ponds in the Ablation Process of a Debris-Covered Glacier in the Nepal Himalayas264

Salerno, F., Thakuri, S., D'Agata, C., Smiraglia, C., Manfredi, E. C., Viviano, G., et al. (2012). Glacial lake Distribution in the Mount Everest Region: Uncertainty of Measurement and Conditions of Formation. *Glob. Planet. Change* 92-93, 30–39. doi:10.1016/j.gloplacha.2012.04.001

Schmid, M.-O., Baral, P., Gruber, S., Shahi, S., Shrestha, T., Stumm, D., et al. (2015). Assessment of Permafrost Distribution Maps in the Hindu Kush Himalayan Region Using Rock Glaciers Mapped in Google Earth. *The Cryosphere* 9 (6), 2089–2099. doi:10.5194/tc-9-2089-2015

Steiner, J. F., Buri, P., Miles, E. S., Ragettli, S., and Pellicciotti, F. (2019). Supraglacial Ice Cliffs and Ponds on Debris-Covered Glaciers: Spatio-Temporal Distribution and Characteristics. *J. Glaciol.* 65 (252), 617–632. doi:10.1017/jog.2019.40

Steiner, J. F., Pellicciotti, F., Buri, P., Miles, E. S., Immerzeel, W. W., and Reid, T. D. (2015). Modelling Ice-Cliff Backwasting on a Debris-Covered Glacier in the Nepalese Himalaya. *J. Glaciol.* 61 (229), 889–907. doi:10.3189/2015jog14j194

Stevenson, J. A., Sun, X., and Mitchell, N. C. (2010). Despeckling SRTM and Other Topographic Data with a Denoising Algorithm. *Geomorphology* 114 (3), 238–252. doi:10.1016/j.geomorph.2009.07.006

Stokes, C. R., Popovnin, V., Aleynikov, A., Gurney, S. D., and Shahgedanova, M. (2007). Recent Glacier Retreat in the Caucasus Mountains, Russia, and Associated Increase in Supraglacial Debris Cover and Supra-/proglacial lake Development. *Ann. Glaciol.* 46 (5642 m), 195–203. doi:10.3189/172756407782871468

Thakuri, S., Salerno, F., Smiraglia, C., Bolch, T., D'Agata, C., Viviano, G., et al. (2014). Tracing Glacier Changes since the 1960s on the South Slope of Mt. Everest (central Southern Himalaya) Using Optical Satellite Imagery. *The Cryosphere* 8 (4), 1297–1315. doi:10.5194/tc-8-1297-2014

Thompson, S., Benn, D. I., Mertes, J., and Luckman, A. (2016). Stagnation and Mass Loss on a Himalayan Debris-Covered Glacier: Processes, Patterns and Rates. *J. Glaciol.* 62 (233), 467–485. doi:10.1017/jog.2016.37

Tielidze, L. G., Bolch, T., Wheate, R. D., Kutuzov, S. S., Lavrentiev, I. I., and Zemp, M. (2020). Supra-glacial Debris Cover Changes in the Greater Caucasus from 1986 to 2014. *The Cryosphere* 14 (2), 585–598. doi:10.5194/tc-14-585-2020

Viale, M., Bianchi, E., Cara, L., Ruiz, L., Villalba, R., Pitte, P., et al. (2019). Contrasting Climates at Both Sides of the Andes in Argentina and Chile. *Front. Environ. Sci.* 7 (May), 1–15. doi:10.3389/fenvs.2019.00069

Viale, M., and Garreaud, R. (2015). Orographic Effects of the Subtropical and Extratropical Andes on Upwind Precipitating Clouds. *J. Geophys. Res. Atmospheres* 120, 1–13. doi:10.1002/2014jd023014

Watson, C. S., King, O., Miles, E. S., and Quincey, D. J. (2018a). Optimising NDWI Supraglacial Pond Classification on Himalayan Debris-Covered Glaciers. *Remote Sensing Environ.* 217 (August), 414–425. doi:10.1016/j.rse.2018.08.020

Watson, C. S., Quincey, D. J., Carrivick, J. L., Smith, M. W., Rowan, A. V., and Richardson, R. (2018b). Heterogeneous Water Storage and thermal Regime of Supraglacial Ponds on Debris-Covered Glaciers. *Earth Surf. Process. Landforms* 43 (1), 229–241. doi:10.1002/esp.4236

Wendi, D., Liong, S.-Y., Sun, Y., and Doan, C. D. (2016). An Innovative Approach to Improve SRTM DEM Using Multispectral Imagery and Artificial Neural Network. *J. Adv. Model. Earth Syst.* 8, 691–702. doi:10.1002/2015ms000536

Wigmore, O., and Mark, B. (2017). Monitoring Tropical Debris Covered Glacier Dynamics from High Resolution Unmanned Aerial Vehicle Photogrammetry. Cordillera Blanca, Peru: The Cryosphere 11, 2463–2480. doi:10.5194/tc-11-2463-2017

Wilson, R., Glasser, N. F., Reynolds, J. M., Harrison, S., Anacona, P. I., Schaefer, M., et al. (2018). Glacial Lakes of the Central and Patagonian Andes. *Glob. Planet. Change* 162, 275–291. doi:10.1016/j.gloplacha.2018.01.004

Zalazar, L., Ferri, L., Castro, M., Gargantini, H., Gimenez, M., Pitte, P., et al. (2020). Spatial Distribution and Characteristics of Andean Ice Masses in Argentina: Results from the First National Glacier Inventory. *J. Glaciol.* 66 (260), 938–949. doi:10.1017/jog.2020.55

Zorzut, V., Ruiz, L., Rivera, A., Pitte, P., Villalba, R., and Medrzycka, D. (2020). Slope Estimation Influences on Ice Thickness Inversion Models: a Case Study for Monte Tronador Glaciers, North Patagonian Andes. *J. Glaciology* 66, 996–1005. doi:10.1017/jog.2020.64

Conflict of Interest: The authors declare that the research was conducted in the absence of any commercial or financial relationships that could be construed as a potential conflict of interest.

frontiers in Earth Science

ORIGINAL RESEARCH
published: 09 June 2021
doi: 10.3389/feart.2021.671854

Evolution of Surface Characteristics of Three Debris-Covered Glaciers in the Patagonian Andes From 1958 to 2020

Daniel Falaschi[1,2], Andrés Rivera[3], Andrés Lo Vecchio Repetto[1,2], Silvana Moragues[1,2], Ricardo Villalba[1], Philipp Rastner[4,5], Josias Zeller[4] and Ana Paula Salcedo[6]*

[1]Instituto Argentino de Nivología, Glaciología y Ciencias Ambientales, Mendoza, Argentina, [2]Departamento de Geografía, Facultad de Filosofía y Letras, Universidad Nacional de Cuyo, Mendoza, Argentina, [3]Departamento de Geografía, Universidad de Chile, Santiago, Chile, [4]Geography Department, University of Zurich, Zürich, Switzerland, [5]GeoVille Information Systems and Data Processing GmbH, Innsbruck, Austria, [6]Subgerencia Centro Regional Andino, Instituto Nacional del Agua, Mendoza, Argentina

OPEN ACCESS

Edited by:
Aparna Shukla, Ministry of Earth Sciences, India

Reviewed by:
Jakob Steiner, International Centre for Integrated Mountain Development, Nepal
Qiao Liu, Institute of Mountain Hazards and Environment, Chinese Academy of Sciences (CAS), China

***Correspondence:**
Daniel Falaschi
dfalaschi@mendoza-conicet.gob.ar

Specialty section:
This article was submitted to Cryospheric Sciences, a section of the journal Frontiers in Earth Science

Received: *24 February 2021*
Accepted: *20 May 2021*
Published: *09 June 2021*

Citation:
Falaschi D, Rivera A, Lo Vecchio Repetto A, Moragues S, Villalba R, Rastner P, Zeller J and Salcedo AP (2021) Evolution of Surface Characteristics of Three Debris-Covered Glaciers in the Patagonian Andes From 1958 to 2020. Front. Earth Sci. 9:671854. doi: 10.3389/feart.2021.671854

A number of glaciological observations on debris-covered glaciers around the globe have shown a delayed length and mass adjustment in relation to climate variability, a behavior normally attributed to the ice insulation effect of thick debris layers. Dynamic interactions between debris cover, geometry and surface topography of debris-covered glaciers can nevertheless govern glacier velocities and mass changes over time, with many glaciers exhibiting high thinning rates in spite of thick debris cover. Such interactions are progressively being incorporated into glacier evolution research. In this paper we reconstruct changes in debris-covered area, surface velocities and surface features of three glaciers in the Patagonian Andes over the 1958–2020 period, based on satellite and aerial imagery and Digital Elevation Models. Our results show that debris cover has increased from 40 ± 0.6 to 50 ± 6.7% of the total glacier area since 1958, whilst glacier slope has slightly decreased. The gently sloping tongues have allowed surface flow velocities to remain relatively low (<60 m a^{-1}) for the last two decades, preventing evacuation of surface debris, and contributing to the formation and rise of the ice cliff zone upper boundary. In addition, mapping of end of summer snowline altitudes for the last two decades suggests an increase in the Equilibrium Line Altitudes, which promotes earlier melt out of englacial debris and further increases debris-covered ice area. The strongly negative mass budget of the three investigated glaciers throughout the study period, together with the increases in debris cover extent and ice cliff zones up-glacier, and the low velocities, shows a strong linkage between debris cover, mass balance evolution, surface velocities and topography. Interestingly, the presence of thicker debris layers on the lowermost portions of the glaciers has not lowered thinning rates in these ice areas, indicating that the mass budget is mainly driven by climate variability and calving processes, to which the influence of enhanced thinning at ice cliff location can be added.

Keywords: debris-covered glacier, ice cliff, glacier velocity, Monte San Lorenzo, Patagonian Andes

INTRODUCTION

Driven by climate change, glaciers in most high mountain ranges around the globe are receding and losing mass rapidly (Jomelli et al., 2011; Davies and Glasser, 2012; Zekollari et al., 2019; Davaze et al., 2020; Hugonnet et al., 2021). Whilst glaciers steadily thin and contribute to sea level rise through increased melting (Zemp et al., 2019), another aspect of glacier change and adjustment to drier conditions is the progressive accumulation of surface debris stemming from the surrounding valley walls and lateral moraines (Scherler et al., 2011; Kirkbride and Deline, 2013; Sasaki et al., 2016; Tielidze et al., 2020). Debris cover on glacier surfaces accounts for ~7% of the mountain glacier area worldwide (Herreid and Pellicciotti, 2020), and is relevant from a surface energy balance point of view, as the distribution and thickness variability of debris layers can alter glacier melt rates (Nicholson et al., 2018; Fyffe et al., 2020). Length adjustments and overall response times of debris-covered glaciers to climate variability are often delayed compared to debris-free glaciers. This delayed signal can occur as ablation rates decrease when debris layers are thicker than the *effective thickness* (i.e. the thickness above which glacier ice is sheltered and insulated from solar radiation, commonly <0.1 m; Mattson, 2000; Mihalcea et al., 2008; Reznichenko et al., 2010). Normally, the thickness of debris layers increases toward the glacier terminus, resulting in lower or even reversed mass balance gradients (e.g. Benn et al., 2012; Rounce et al., 2018; Bisset et al., 2020).

The spatio-temporal relationship between debris cover, surface mass balance glacier dynamics is nevertheless not simple. The mass balance gradient of debris-covered glaciers may not vary in straightforward form with elevation, and debris-covered glaciers are said to react by thinning or thickening in response to climate forcing rather than terminus recession or advance due to their typically gentle slopes (Bolch et al., 2008; Pellicciotti et al., 2015). Reduced ablation on the debris-covered portions of glaciers can result in a decrease in overall slope, which subsequently favors a reduction in ice flow velocities (Rowan et al., 2015; Dehecq et al., 2019). A feedback mechanism is established whereby rising Equilibrium Line Altitudes (ELA) lead to an earlier melt out and emergence of englacial debris, extending the debris layer further up-glacier. In this way, the overall glacier slope is additionally reduced, leading to stagnation of the glacier tongues (Quincey et al., 2009; Benn et al., 2012; Haritashya et al., 2015). Surface and basal ice melt, coupled with surface lowering, culminate in the formation and expansion of supraglacial lakes, causing further enhancement of glacier ablation (Mertes et al., 2017).

In spite of the above, more than a few studies, particularly in the Himalayas, have shown that debris-covered glaciers can have surface lowering rates comparable to those of debris-free glaciers (Kääb et al., 2012; Ragettli et al., 2016; King et al., 2019). A number of causes for this uncertainty have been identified so far (see e.g. Mölg et al., 2019 and references therein), including the influence of ice cliffs. Ice cliffs are steeply inclined areas of glacier ice, usually covered only by a very thin layer of debris, that vary from sub-circular to largely elongated in shape, and are of varying size (Sakai et al., 2002; Steiner et al., 2019). The occurrence of exposed ice in otherwise predominantly debris-covered glacier surfaces in the form of cliffs and supraglacial ponds (often associated) can boost ablation in comparison to "regular" debris-covered surfaces or even debris-free areas (Sakai et al., 1998; Sakai et al., 2002; Juen et al., 2014). The influence of ice cliffs and supraglacial ponds on the evolution of debris-covered glaciers is presently well acknowledged and the mapping and monitoring of these cryokarst forms has increased in recent years (Buri et al., 2016; Watson et al., 2017; Herreid and Pellicciotti, 2018; Mölg et al., 2019; Steiner et al., 2019; Ferguson and Vieli, 2020).

Bolch et al. (2012) pointed out that understanding the interactions between debris cover, mass balance and glacier dynamics would be a major achievement for envisaging the future evolution of debris-covered glaciers in high mountain areas. Consequently, recent studies have attempted to integrate this subject by assimilating diverse glacier variables (mass balance, debris distribution, thickness and transport, flow rates) and their feedback mechanisms into numerical models (Banerjee and Shankar, 2013; Collier et al., 2015; Rowan et al., 2015; Anderson and Anderson, 2018). Although large-scale assessments on debris-covered ice worldwide distribution exist (Scherler et al., 2018), modeling efforts are currently limited by the relative scarcity of more specific debris-covered glacier data, such as debris thickness and the evolution of ice cliffs and supraglacial ponds. These parameters are available mostly for the Himalaya, Karakorum, (e.g. Han et al., 2010; Thompson et al., 2012; Brun et al., 2018; Nicholson et al., 2018; Rounce et al., 2018; Buri et al., 2021) and to a lesser degree the European Alps (Reid and Brock, 2014; Mölg et al., 2019), but are lacking for other mountain regions where debris-covered glaciers are common (Röhl, 2006). In the Andes of Argentina and Chile, specifics about the evolution of debris layers, and their influence in glacier surface morphology, overall dynamics and mass changes, is particularly limited despite the abundance of debris-covered ice in some sectors such as the Central Andes (see e.g. Bodin et al., 2010; Wilson et al., 2016a; Falaschi et al., 2018; Ferri et al., 2020). In comparison to the Central Andes, however, the Patagonian Andes show a much lower relative concentration of debris-covered glaciers (Falaschi et al., 2013; Masiokas et al., 2015), although debris-covered ice can be relevant in some specific sites. Specifically for the Río Mayer catchment, debris-covered ice accounts for ~15% of the total glacier area (IANIGLA, 2018). In addition, recent studies have detected signs of increasing proportions of debris-covered ice in the large outlet glaciers from the Patagonian Icefields in recent decades (Glasser et al., 2016).

In this study, we aim to determine the main characteristics of the morphological features of the Río Oro, Río Lácteo and San Lorenzo Sur debris-covered glaciers in the eastern (Argentinian) side of the Monte San Lorenzo massif (Southern Patagonian Andes), namely the distribution and area changes of the debris layer, ice cliffs and supraglacial ponds from 1958 to 2020. In addition, we produce the most complete glacier velocity record from freely available (mostly Landsat) satellite imagery. Whilst the mass balance evolution of these glaciers has been strongly linked to climate variability, proglacial lakes influence glacier

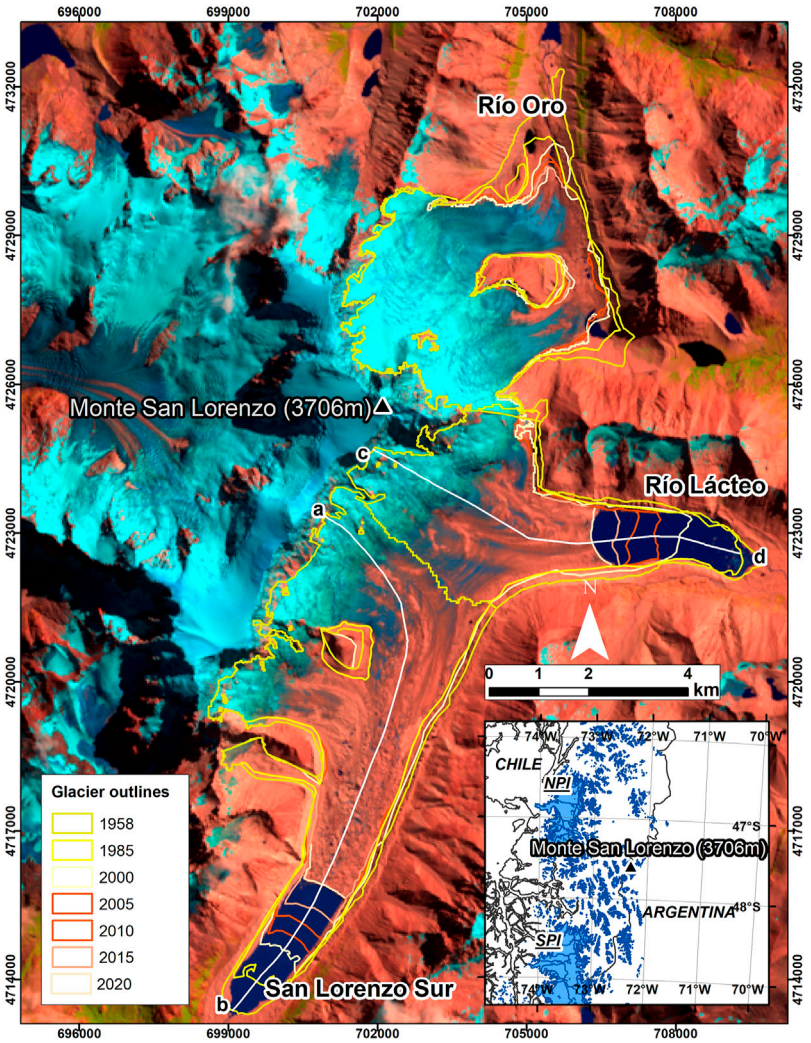

FIGURE 1 | View of the investigated glaciers in the Monte San Lorenzo and location of the study area in relation to the Northern (NPI) and Southern Patagonian Icefields (SPI). Coordinates are UTM WGS84 Zone 18 S. a–d are the surface velocity profiles detailed in **Figure 5**.

evolution to a significant extent as well (Falaschi et al., 2019). Additionally, these three glaciers have one of the longest (geodetic) mass balance records in the Southern Andes and have been studied previously in regards to their geometric evolution. Combining the newly produced datasets and mass balance and climate records previously available, we discuss the spatio-temporal interactions between surface features and glacier velocities, and the likely impact on mass balance evolution. Finally, we evaluate the possible linkage between the observed areal evolution of the debris-covered area in view of the late-summer snowline elevation and climate variability in the area.

STUDY AREA AND PREVIOUS STUDIES

Río Oro, Río Lácteo, and San Lorenzo Sur valley glaciers (**Figure 1**; **Supplementary Table S1**) lie on the Argentinian side of Monte San Lorenzo (47°35′S, 72°18′W; 3,706 m asl), the second highest peak in Southern Patagonia, ~70 km East of the southernmost tip of the Northern Patagonian Icefield. At these latitudes, the Andes act as an effective orographic barrier to the humid westerly flow (Rivera et al., 2007), producing steep meteorological gradients and a strong rain shadow effect to the east of the main water divide (Bravo et al., 2019; Sauter, 2020). In fact, whilst the Northern Patagonian Icefield has a clear maritime climatic regime and receives extreme precipitation (Lenaerts et al., 2014), the San Lorenzo area lies in a more transitional environment and receives much less precipitation (Damseaux et al., 2020).

The Monte San Lorenzo area is presently well-researched in terms of the number and area of glaciers, the hypsometrical distribution of debris-covered and debris-free ice, and the rates of glacier recession (1% a^{-1} in the last ~3.5 decades; Falaschi et al., 2013). The three glaciers investigated in this study have thinned at considerable rates since the mid- 20th century in spite of the debris cover, particularly in comparison to nearby debris-free

glaciers (Falaschi et al., 2017). A strong link between climate variability (added to the influence of calving dynamics on proglacial lakes) and glacier mass loss has been made (Falaschi et al., 2019). Sagredo et al. (2017) estimated (>1,600 m asl) paleo- and modern ELAs for the Tranquilo glacier in the northern flank of Monte San Lorenzo. There is currently, however, no detailed information about how climate change and altitudinal shifts of ELAs with time have promoted the development of debris layers and how the inception of feedback mechanisms between glacier dynamics (e.g. glacier flow velocity), morphological features (ice cliffs, supraglacial ponds) and glacier geometry have affected the evolution of these particular glaciers.

Glacier inventories in Southern Patagonia have shown that the surface of both outlet and mountain glaciers is mostly free of debris, and that the amount of debris-covered ice is usually marginal in comparison (e.g. Glasser and Jansson, 2008; Paul and Mölg, 2014; Masiokas et al., 2015; Glasser et al., 2016). In some specific areas of extremely abrupt relief, high valley walls and lateral moraines can be the source of larger quantities of supraglacial debris, and extensive debris layers and debris-covered glaciers can exist, such as in the Monte San Lorenzo massif. Río Lácteo and San Lorenzo Sur are valley glaciers lying at the very bottom of Monte San Lorenzo's >2,000 m nearly vertical East face, have lake-terminating fronts and noticeable debris layers in an otherwise largely debris-free glacier inventory in the area (Falaschi et al., 2013). On the other hand, Río Oro has a minor proportion of debris-covered area compared to Río Lácteo and San Lorenzo Sur, and its only partially calving-type.

Probably because of their relevance as contributors to sea-level rise (Dussaillant et al., 2019), much scientific research upon the impact of climate change on glaciers has been focused in the nearby Patagonian Icefields. Numerical Modeling and mapping of ELAs and Accumulation Area Ratios (AAR) from remote-sensed data has been carried out to test the mass balance sensitivity of glaciers (Barcaza et al., 2009; De Angelis, 2014). In the periphery of the Patagonian Icefields, however, there are still a vast number of smaller mountain glaciers that can provide complementary information for refining our understanding of overall glacier dynamics and glacier-climate interactions.

DATA AND METHODS

For this study we used 1) a set of orthophotos derived from archival aerial images, 2) medium resolution satellite imagery (Landsat 5, 7, 8, SPOT 5, Sentinel 2) available from various archives and 3) high spatial resolution satellite imagery (Pléiades) available from Google Earth. Unfortunately, during the commercial phase of Landsat, Thematic Mapper (TM) data for Southern Patagonia between 1984 and 1997 was not acquired beyond very few local requests (Goward et al., 2006). In general, these scenes are not suitable for glacier mapping (due to cloud cover or seasonal snow), and thus this period had to be omitted from the analysis (except for the 1985–1986 interval). The main characteristics of the implemented imagery (including spatial resolution, usage of each scene/photo is described in **Supplementary Table S2**, whereas **Supplementary Table S3** shows the time span covered on each of the specific analyses caried out in this study.

Glacier-specific geodetic mass balance values for the 1958–2018 period, as well as length and area changes for the investigated glaciers are available from Falaschi et al. (2019). These data are essential for shedding further light into the interaction of debris covers and the dynamic evolution of glaciers, and therefore incorporated to the discussion sections.

Mapping of the Debris-Covered Ice Extent

Glacier outlines for the years 1958, 1981, 2000, 2012, and 2018 were retrieved from Falaschi et al. (2019). For all the remaining survey years, we modified the glacier outlines by visual interpretation of Landsat scenes. In the 1958 and 1981 orthophotos produced by Falaschi et al. (2019), we mapped the extent of debris layers on each individual glacier by on-screen manual digitization. We considered only areas with a fairly continuous debris cover extent, discarding this way small debris patches and very thin debris covered areas. Excluding now the years 1958 and 1981, debris-covered ice area for each survey year was obtained by calculating the debris-free area on the corresponding Landsat scene (from which the glacier outline had been previously generated), using a thresholded ratio image of the NIR/SWIR band (Paul et al., 2015), and substracting the debris free mask from the total glacier area.

So far, a number of (semi) automatic methods for identifying and mapping of debris-covered ice have been proposed (e.g. Shukla et al., 2010; Racoviteanu and Williams, 2012; Rastner et al., 2014). These approaches, which combine multi-spectral and terrain analyses, are a good approximation and reduce processing time, but ultimately require additional manual corrections to produce the final glacier outlines. Paul et al. (2004) stated that after manual editing, the accuracy of the debris-covered glacier outlines can be equal to pixel resolution. We have thus calculated the uncertainty in debris-covered area by implementing ±1 pixel buffers around the debris-covered ice area. Conservatively, the uncertainty in the debris-covered area change between 1958 and 2020 ($\sigma_{dc.tot}$) was calculated by quadratically summing the uncertainties of the initial ($\sigma_{dc.i}$) and final ($\sigma_{dc.f}$) debris-covered areas:

$$\sigma_{dc.tot} = \sqrt{\sigma_{dc.i}^2 + \sigma_{dc.f}^2} \quad (1)$$

Glacier Surface Velocity

Because glaciers are constantly adjusting and redistributing ice mass in an effort to reach an equilibrium state, ice surface velocity is frequently used as an indicator of glacier mass balance conditions and dynamic state (Wilson et al., 2016b). This relationship assumes that during positive mass balance conditions ice surface velocities increase due to increased ice deformation and vice versa. Here we used Landsat 5–7, ASTER, SPOT 5, and Sentinel-2 images to automatically obtain velocity field maps of the three investigated glaciers for the 1985–1986 and 2000–2020 periods. The 1958–1981 and 1981–1985 observation periods were omitted from this analysis due to the lack of corresponding surface features in the imagery used (preventing the use of manual feature tracking techniques e.g. Mölg et al., 2019).

The optical satellite imagery was processed in the CIAS feature-tracking algorithm (Kääb and Vollmer, 2000). This algorithm calculates sub-pixel displacement and direction magnitudes by first coregistering a master (t1 or initial epoch) and slave (t2 or final epoch) images and then comparing the coordinates of the highest correlation pixel block in a search window of the slave image with those of the master pixel block. Given the relatively low speed flow expected for the Río Lácteo and San Lorenzo Sur glaciers, a time separation of ~1 year between the initial and final scenes was required to detect significant glacier flow that would surpass the total uncertainty in surface velocity (see below). For survey intervals where the initial and final images differed in spatial resolution (e.g. Landsat TM and Landsat ETM+), the highest resolution were resampled to the coarser one before coregistration (Wilson et al., 2016b). Once the CIAS output displacement vectors were generated, a correlation threshold between the initial and final pixel block of $r > 0.4$ was used to remove abnormal velocities. The resultant displacement points were upscaled to annual velocities and converted to raster grids. The final output cell size of the velocity maps was 30 × 30 and 45 × 45 m for Landsat ETM+ and Landsat TM pairs, respectively. Due to the lack of identifiable features on the debris-free ice, only some portions of the debris-covered tongue of Río Oro can be derived and velocity variations along longitudinal profiles cannot be entirely identified. This prevented a full comparison between the velocity map of Río Oro and the neighboring Río Lácteo and San Lorenzo Sur.

The total uncertainty associated with each glacier velocity map σv_{tot} was calculated for a given time interval as the quadratic sum of the systematic (σv_{sys}) and random (σv_{rand}) uncertainties, following the laws of error propagation (Berthier et al., 2003):

$$\sigma v_{tot} = \sqrt{\sigma v_{sys}^2 + \sigma v_{rand}^2} \quad (2)$$

The systematic uncertainty σv_{sys} depends on the performance quality of the image cross-correlation algorithm and typically, a ±2 pixel accuracy is expected for Landsat scenes:

$$\sigma v_{sys} = \frac{2R}{\Delta t} \quad (3)$$

where R is the pixel size and Δt the time separation between the initial and final epochs in days. In turn, the random uncertainty σv_{rand} is measured over stable terrain (off-glacier), in a buffer area around each individual glacier outline minus shadow areas and overlay steep terrain (>25°).

Identification of Ice-Cliffs and Supraglacial Ponds

Mapping of ice exposures (cliffs and supraglacial drainage channels, **Supplementary Figure S1**) has been carried out in different studies by means of object-oriented and principal components analyses in satellite and aerial imagery (Racoviteanu and Williams, 2012; Mölg et al., 2019), slope thresholding of high-resolution elevation data (Herreid and Pellicciotti, 2018), linear spectral unmixing approaches (Kneib et al., 2021), and of course, by on-screen digitizing of high resolution satellite imagery (Watson et al., 2017; Steiner et al., 2019). For the sake of simplicity, here we mapped ice cliffs and ponds by on screen digitization. We also mapped exposed ice in supraglacial drainage channels, but excluded heavily crevassed areas. The terminal portion of the San Lorenzo Sur glacier was not fully covered in the 2011 imagery available on Google Earth.

Since the ice cliffs and supraglacial ponds located on the glaciers investigated here are relatively small in size, only the highest resolution (<1 m) imagery available from our dataset was used (see **Supplementary Table S2**). The Minimum Mapping Unit (MMU) is the smallest sized object that determines whether an object can be identified and mapped in remotely sensed imagery, and needs to be four contiguous pixels in size. In this way, we mapped ice cliffs ≥4 m^2, which is the MMU of our lowest resolution data (aerial photos, 1 m resolution). On the other hand, intra-annual variations in both number and area of supraglacial ponds between seasons has shown to be significant (Steiner et al., 2019). We have minimized this potential bias by mapping ponds on images acquired from very late spring (December 10, 2009) to mid-summer (February 22, 2018).

The overall accuracy of manual mapping of ice cliffs is dependent on several sources of uncertainty, including the spatial resolution and quality of the utilized imagery (optical contrast, shadows), and the user's inherent mapping subjectivity when identifying an ice cliff and its characteristics. Some studies aiming to map ice cliff geometry exhaustively (including information regarding slope, aspect, slope area) have carried out in-depth delineation uncertainty assessments (Steiner et al., 2019), by checking ice cliff outlines and omissions made by multiple users and slope analyses derived from high resolution DEMs. Whilst such a thorough quality evaluation was not considered here, three independent operators inspected visually all individual ice-cliffs, whilst we also carried out a multiple user digitization of 50 randomly selected cliffs on each scene (Watson et al., 2017). Results of the round-robin digitizations are provided in **Supplementary Table S4** and **Supplementary Figure S2**. We observed two main sources of uncertainties in ice-cliff mapping. One source is related to inherent imagery properties, not necessarily related to spatial resolution, but rather image illumination conditions and contrast (aerial photos were the least adequate in this regard). The second source relates to ice-cliff specifics such as complexity or branchiness, preservation/degradation state and debris layer thickness on ice exposures.

In addition to the ice cliff inventory, we also investigated ice cliff evolution in terms of changes in mean size and total area, and the altitudinal distribution of ice cliffs through time. This was done by calculating the relative proportion of ice-cliff area per 50 m elevation band across each glaciers' debris-covered surface.

Snowline Altitude and Climate Records

Mapping of the Transient Snowline Altitude

We mapped the elevation of the transient snow line (SLA) and Snow Cover Ratio (SCR, defined as the snow-covered area with respect to the total glacier area) for Río Oro, Río Lácteo, and San Lorenzo Sur glaciers. To infer possible ELA changes with time for

the three surveyed glaciers, we relied on the assertion that the Snow Line Altitude at the end of the hydrological year provides an effective proxy of the equilibrium line in temperate glaciers (Rabatel et al., 2008 and references therein) for that specific year. Because differences between the theoretical annual ELA and the snowline may exist at the end of summer (due to mass additions or losses e.g. superimposed ice or atypical length of the ablation period), the term *end of summer snowline* has been coined in the Southern Hemisphere (Clare et al., 2002).

The main limitations for deriving end of summer snowlines lies in that suitable satellite imagery for snow mapping on glaciers (no cloud cover or fresh snow on glacier surfaces), DEMs and glacier outlines when dealing with a long time series are not always available for each individual year. To minimize this impact, we implemented a prototype version of the Automatic Snow Mapping on Glaciers (ASMAG) tool (Rastner et al., 2019), running now on the Google Earth Engine (GEE) platform. The algorithm currently maps SCR from Landsat and Sentinel 2 scenes, after converting digital numbers to top of atmosphere reflectance. The histogram approach of Bippus (2011) is then used within a single glacier mask to distinguish snow from ice by implementing an automatic threshold based on the Otsu (1979) thresholding algorithm to the Near Infrared (NIR) band (Rastner et al., 2019). After comparing the automatic derived snow cover area with the manual digitized ones, it became obvious that the ASMAG approach leads to systematically lower values compared to the manual derived ones (mapped on RGB true color compositions). We attribute this to the still missing topographic correction procedure not yet implemented in the GEE procedure so that we used this prototype in this study only for a straightforward selection of the satellite scene with the highest SLA for each single survey year. After knowing all the automatic derived acquisition dates with the highest SLAs (termed "SLAs" hereafter) for each period (ranging between February 1 and April 10), we manually digitized the snow cover area to retrieve SLAs based on three DEMs (SRTM-X, ALOS PALSAR and Pléiades) for three different time periods (2000–2009, 2010–2017, and 2018–2020).

End of Summer Snowline Altitude and Climate

Here we investigate the influence of temperature and precipitation on the end of summer snowline elevations (and consequently ELAs) on Río Oro, Río Lácteo, and San Lorenzo Sur glaciers. For the 2000–2020 period, we performed correlation analyses between mapped snowlines and monthly, annual and seasonal (summer, autumn, winter and spring) temperatures of the Balmaceda meteorological station (45.912°S, 71.694°W, 517 m a.s.l.), retrieved from the GISS-NASA portal. A similar analysis was carried out, relating monthly precipitations for the December and January months prior to the February-March snowline mapping. Results are presented as the individual temperature and precipitation influence on both glacier-specific and glacier-averaged SLAs, as well as the joint temperature and precipitation influence, again at both glacier-specific and glacier-averaged scale. For all statistical analyses, we used a confidence interval of 95%.

RESULTS

Debris-Covered Area Evolution

Among the three sampled glaciers, the total glacier area was $60.6 \pm 1\ km^2$ in 1958 and $46 \pm 0.8\ km^2$ in 2020. This represents an area reduction of $14.6\ km^2$ (~$0.25\ km^2$ per year) (**Figure 1**). Individually, Río Lácteo glacier had the largest (relative) area loss (29.2%; $4.7\ km^2$), followed by San Lorenzo Sur (22.8%; $5.7\ km^2$) and Río Oro (22%; $4.3\ km^2$).

The oldest dataset available for the Monte San Lorenzo region, from which the extent of the debris-covered ice can be quantified are the 1958 orthophotos. At this time, 48 ± 0.4% ($12 \pm 0.1\ km^2$), 32 ± 0.6% ($5.2 \pm 0.1\ km^2$) and 15 ± 0.5% ($3 \pm 0.1\ km^2$) of San Lorenzo Sur, Río Lácteo, and Río Oro area ($20.2 \pm 0.3\ km^2$ 40 ± 0.6% overall) respectively, were debris-covered. Later imagery reveals (**Figure 2**) that the debris-covered extent has expanded up-glacier to higher elevations on all three glaciers. By 2020, the debris cover area percentage has risen to 71 ± 6.7% on San Lorenzo Sur, 54 ± 6% on Río Lácteo and 19 ± 4.9% on Río Oro (50 ± 6.7% in total).

Linear fits of the percentage of debris-covered area as a function of time revealed a trend of progressively higher percentages of debris-covered area on Río Lácteo ($0.2\%\ a^{-1}$) and San Lorenzo Sur ($0.24\%\ a^{-1}$) glaciers up to the year 2020, whereas there is no clear trend for Río Oro (**Figure 3**). In principle, expansion of proglacial lakes affecting the lowest part of the glaciers should lead to a smaller proportion of debris-covered glacier area, yet our results show that yearly debris input has compensated the debris-cover area losses through calving. Indeed, if the yearly debris-covered area is divided by the initial 1958 total glacier area, the debris-covered area increase rates rise to $0.38\%\ a^{-1}$ (San Lorenzo Sur), $0.48\%\ a^{-1}$ (Río Lácteo), and $0.33\%\ a^{-1}$ for Río Oro. The regression analysis of debris-covered area with time for these later cases revealed statistically significant ($p < 10^{-3}$ for all glaciers), very high r values of 0.86 (Río Oro), 0.91 (Río Lácteo) and 0.96 (San Lorenzo Sur) at the 95% confidence level.

Concomitantly to the increase in debris-cover area, debris layers have progressively occupied higher elevations on glacier surfaces as well. Between 1958 and 2020, sporadic debris has appeared on accumulation areas, shifting the maximum elevation of debris-covered ice from 1,570 to 3,240 m on Río Oro, 1,515–2,840 m on Río Lácteo, and 1,700–2,840 m on San Lorenzo Sur. Considering the glacier thinning that has taken place during this time interval (Falaschi et al., 2019), mean elevation of the debris covered ice has increased ~240 m (1,130–1,370 m) on Río Oro, ~130 m (1,320–1,450 m) on Río Lácteo, and ~160 m (1,280–1,440 m) on San Lorenzo Sur.

Regarding the thickness of the debris layer on the glaciers investigated, we did not undertake *systematic in situ* surveys, nor did we estimate it from remote sensing data. Field observations on ice exposures (crevasses, ice cliffs) of Río Lácteo (**Supplementary Figure S1**), however, revealed a rough estimate of debris thickness between 1 and 2 m in proximity of the glacier terminus. In the lateral margins, boulders up to ~3 m in diameter are frequent, these possibly resulting from the degradation of the lateral moraines. Thickness of the debris layer progressively decreases in the upward direction and in the uppermost part of the debris-covered tongue,

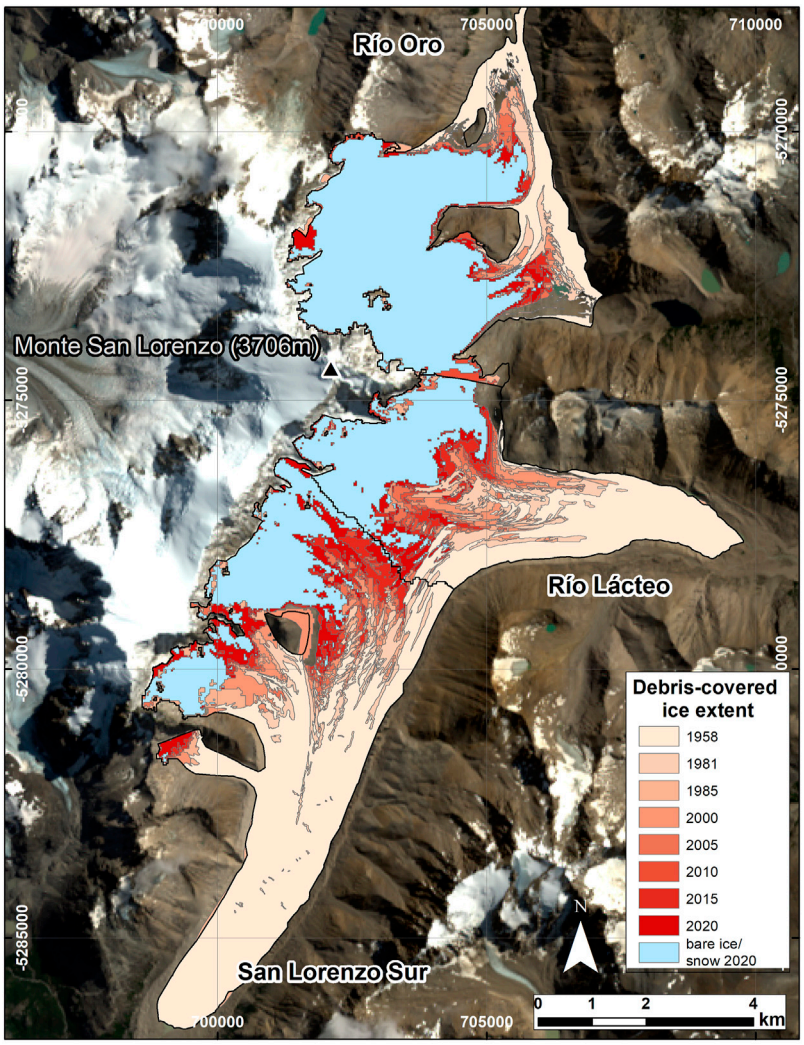

FIGURE 2 | Evolution of the debris-covered ice extent through time and the remaining bare ice and snow. Background image is a 2020 Landsat 8 RGB 654 false color composition.

close to the debris-free ice, the debris layer is pebbly in grain size, a few centimeters thick and interspersed with ~10 cm blocks.

Glacier Velocities

Glacier velocity profiles and maps and were produced for Río Lácteo and San Lorenzo Sur glaciers for the 1985–1986 and 2000–2020 periods (**Figures 1**, **4**, **5**). In terms of spatial distribution, the highest velocities for both glaciers were found at the steep icefalls located just below the vertical rock wall of Monte San Lorenzo's East Face (~90 ± 33 and ~75 ± 55 $m a^{-1}$) for Río Lácteo and San Lorenzo Sur, respectively). In the case of San Lorenzo Sur, velocities steadily decrease from these icefalls toward the terminus, where the extremely low velocities (<18 ± 29 $m a^{-1}$) indicate that the glacier terminus is practically stagnant. Aside from the icefall area, the velocity maps for Río Lácteo show higher velocities around the central flow line and a flow speed increase toward the calving front which is visible between 2012–2014 and 2018–2020 (maximum velocity of ~51 ± 34 $m a^{-1}$ in 2020) (**Figures 4**, **5**).

Overall, we found that the spatio-temporal patterns and magnitudes of ice flows at both glaciers were fairly constant during the survey period (1985–2020). For both glaciers, average velocities only fluctuated within a narrow range of ±36.5 $m a^{-1}$ along the whole length of the glaciers, and no significant trends of progressive velocity decrease were detected for the longer 1985–2020 time span (**Figure 5**). Short-term variations were detected during sub-periods (e.g. speed-ups between the years 2001 and 2007, deceleration between 2015 and 2020), however, these changes were small in magnitude and within the displacement error rate calculated for nearby stable terrain.

Inventory and Area Changes of Ice Cliffs and Supraglacial Ponds

We found that the number of ice cliffs at the individual glacier scale increased considerably during the observation period, with

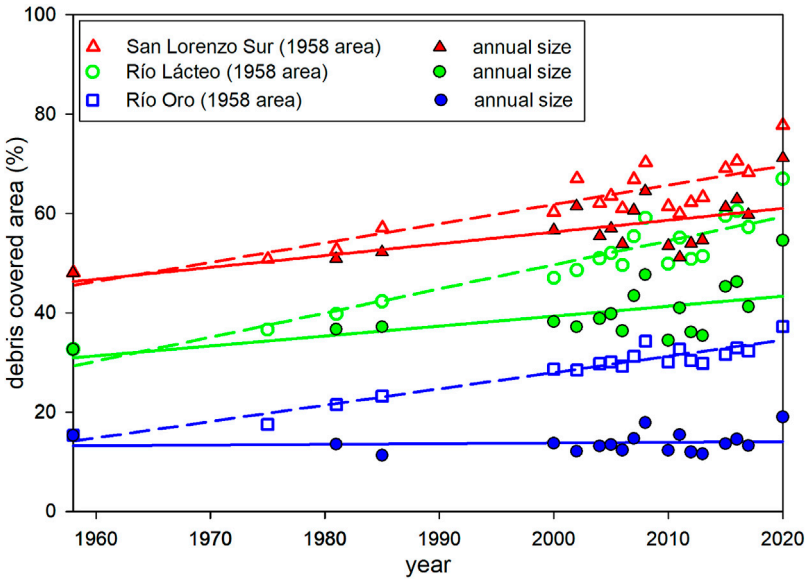

FIGURE 3 | Scatter plot showing the debris cover increase through time. The color-void (and regression dashed line) symbols show the percentual increase of debris-covered ice area considering the initial 1958 glacier area, and the color-filled symbols (regression solid lines) depicts the increase taking the actual glacier size for each survey year into account.

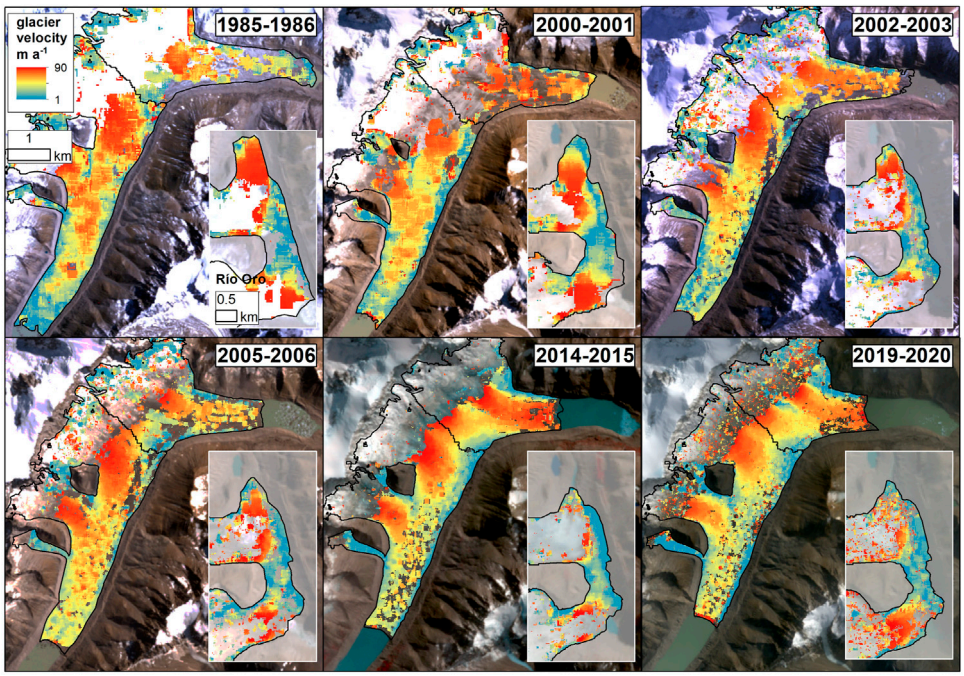

FIGURE 4 | Examples of glacier flow velocity maps selected for six survey periods.

the total count more than doubling between 1958 (639) and 2018 (1,395) (**Table 1**). This increase, however, amounts only to a relatively small change in the area occupied by ice cliffs (0.65 ± 0.07 and 0.78 ± 0.02 km^2). In absolute terms, the maximum in total ice cliff area (1.02 km^2) occurred in the year 2009. Individually, the percentage of ice-cliff area on debris-covered ice varies strongly between glaciers, from an absolute minimum of 0.3 ± 0.1% on Río Lácteo (1958) to a maximum of 7.6 ± 2% on San Lorenzo Sur (2009). Between 1958 and 2018, the overall percentage of ice-cliff area on debris-covered ice increased only

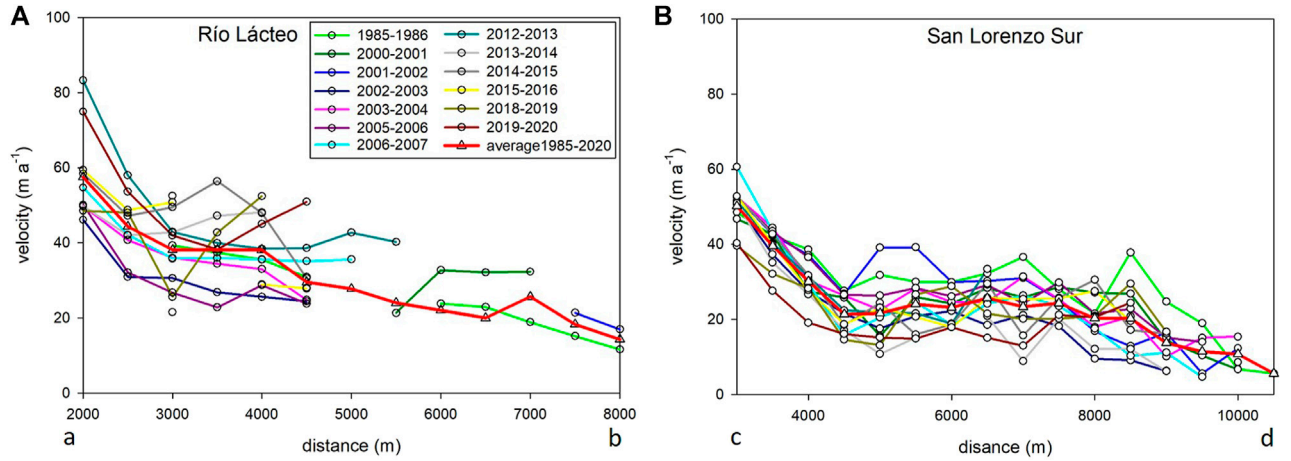

FIGURE 5 | Glacier flow velocities for longitudinal profiles on Río Lácteo **(A)** and San Lorenzo Sur **(B)**.

TABLE 1 | Glacier-specific main characteristics of ice cliffs.

	1958	1981	2009	2011	2017	2018
Río Oro						
Cliff number	123	103	163	201	128	202
Cliff area (m^2)	63,000 ± 8,000	74,000 ± 4,000	77,000 ± 2,000	68,000 ± 4,000	31,000 ± 2,600	49,000 ± 2,000
Share of debris-covered area (%)	2.1 ± 0.3	3.1 ± 0.2	3.5 ± 0.1	2.8 ± 0.2	1.4 ± 0.1	2 ± 0.1
Mean size (m^2)	512	718	471	335	221	247
Max size (m^2)	7,004	9,009	17,956	8,652	1,715	4,486
Max elevation (m)	1,151	1,158	1,178	1,136	1,143	1,191
Río Lácteo						
Cliff number	30	20	61	35	41	78
Cliff area (km^2)	13,000 ± 2,000	13,000 ± 1,000	59,000 ± 16,000	31,000 ± 2,000	19,000 ± 7,000	32,000 ± 1,000
Share of debris-covered area (%)	0.3 ± 0.1	0.3 ± 0.1	1.3 ± 0.4	0.6 ± 0.1	0.4 ± 0.1	0.6 ± 0.1
Mean size (m^2)	433	650	968	899	463	411
Max size (m^2)	3,097	3,047	17,608	5,046	3,726	7,184
Max elevation (m)	1,270	1,346	1,351	1,251	1,267	1,317
San Lorenzo Sur						
Cliff number	486	279	944	514	887	1,115
Cliff area (km^2)	571,000 ± 76,000	540,000 ± 34,000	884,000 ± 233,000	457,000[a] ± 26,000	726,000 ± 284,000	693,000 ± 28,000
Share of debris-covered area (%)	4.8 ± 0.6	4.4 ± 0.3	7.6 ± 2	4.4 ± 0.2[a]	5.8 ± 2.3	6.1 ± 0.2
Mean size (m^2)	1,174	1935	937	890	818	619
Máximum size (m^2)	50,909	83,918	50,174	25,178	18,671	13,904
Max elevation (m)	1,278	1,278	1,384	1,286	1,312	1,457
Total						
Cliff number	639	402	1,168	750[a]	1,056	1,395
Cliff area (km^2)	647,000 ± 67,000	627,000 ± 31,000	1,020,000 ± 200,000	556,000 ± 22,000[a]	776,000 ± 279,000	774,000 ± 24,000
Share of debris-covered area (%)	3.2 ± 0.3	3.1 ± 0.2	5.6 ± 1.1	3.1 ± 0.1[a]	3.9 ± 1.4	3.8 ± 0.1
Mean size (m^2)	1,012	1,559	873	741[a]	726	556

[a]*Indicates the terminal portion of San Lorenzo Sur was not surveyed for the year 2011 due to lack of coverage (see* ***Figure 6****).*

slightly from 3.2 ± 0.3 to 3.8 ± 0.1% (**Table 1**). Individually, San Lorenzo Sur showed the largest increase in ice cliff area (4.8 ± 0.6–6.1 ± 0.2%).

For all surveyed years, San Lorenzo Sur was found to have the highest concentration of ice cliffs amongst the investigated glaciers, accounting for 75–85 and 85–90% of the total cliff number and area, respectively (**Table 1**). For this glacier, the total ice-cliff area ranged between ~0.54 ± 0.06 and ~0.89 ± 0.23 km^2, whereas the average area of individual ice-cliffs varied between 670 and 1,900 m^2. Over time, glacier retreat and proglacial lake expansion removed a number of ice cliffs in the glacier lowest sections, though we still observed a number and area increase of ice cliffs. This possibly means that the relative number increase would be much more if the glaciers had land-terminating tongues. Interestingly, we also found that the maximum and mean area of ice cliffs decreased with time except for the year 1981, when the largest identified ice cliff was 83,918 m^2 on San Lorenzo Sur and caused an anomalously high mean size.

Another aspect of ice-cliff evolution is the increasing altitudinal range at which ice cliffs occur (**Table 1**). Overall, the upper limit of this range has shifted toward higher altitudes on all three glaciers. For Río Oro (1,140–1,190 m) and Río Lácteo (1,270–1,320 m) glaciers, the shift was 40–50 m. The altitudinal shift of ice cliffs is better exemplified at San Lorenzo Sur glacier, where the increase is ~180 m (1,280–1,480 m). When calculating the percentage share of ice-cliffs within debris-covered areas by elevation (considering 50 m elevation bands), we found that ice-cliffs began to form above 1,250 m at least from the year 2009 onwards, and that ice-cliff area below 1,150 m (the lowermost portion of the glacier tongue) decreased after the same year (**Figure 6**), probably as a consequence of fast glacier area removal by calving processes.

In comparison to ice-cliffs, the total area and number of supraglacial ponds was found to be consistently smaller, representing merely 0.3% of the total debris-covered area at all times among the three sampled glaciers. The total number and area of supraglacial ponds was shown to be highly variable on all three glaciers across time, with San Lorenzo Sur again hosting the highest concentration (~70–90% in number). The total pond area on this glacier varied between 0.04 and 0.06 km^2, whereas the mean size ranged between 350 and 780 m^2. Except for the two initial survey years (1958 and 1981), more than 50% of supraglacial ponds were associated with an ice-cliff (**Table 2**). For the most recent 2018 pond inventory, 38% of the ponds were situated on debris-covered ice surfaces with no relation to a cliff, 36% occur at the bottom of longitudinal or lateral cliffs, 13% are contained within a circular cliff, and a further 13% are associated with complex cliffs.

Changes in Snow Cover Ratio and Snow Line Altitude

Snow Cover Ratios and Snow Line Altitudes were calculated for Río Oro, Río Lácteo and San Lorenzo Sur glaciers. In general, Río Oro has always the greatest SCR values (mean = 0.44), whereas the (average) minimum SCR of Río Lácteo and San Lorenzo Sur are 0.23 and 0.16 respectively (**Figure 7**). Data reveal also that when the minimum SCR values for each survey year are considered, SCR appears to have diminished with time on all three glaciers. Linear fits for the SCR scatter data suggest moderate to high correlation (statistically significant with $\alpha = 0.05$) with time for Río Lácteo ($r = 0.6$; $p = 0.007$), Río Oro ($r = 0.7$; $p = 0.001$) and San Lorenzo Sur (0.76; $p = 2 \times 10^{-4}$). The maximum SLA varied strongly on a yearly basis on all glaciers, with altitudinal differences between maximum and minimum values of up to ~800 m on Río Oro and ~600 m on Río Lácteo and ~500 m San Lorenzo Sur. For the full study period, the averaged maximum SLA was 1905 ± 100 m (Río Oro), 1720 ± 85 m (Río Lácteo) and 1815 ± 165 m (San Lorenzo Sur).

Relationships Between Late-Summer Snowline and Climate Variables

At the monthly scale, March temperature is significantly related to SLAs (**Figures 8**, **9**; **Table 3**). This is not surprising, since most of5 the snow line determinations were based on satellite images collected during March. Although the correlation coefficients between March temperature and SLAs are significant for all

TABLE 2 | Number (*n*) and area of supraglacial ponds through time. The cliff % column stands for the percentage of ponds that are in contact with ice cliffs, and the debris (%) column refers to the debris-covered area share of the supraglacial ponds.

1958				1981				2009				2011				2017				2018			
n	Area (m^2)	Cliff %	Debris (%)	*n*	Area (m^2)	Cliff %	Debris (%)	*n*	Area (m^2)	Cliff %	Debris (%)	*n*	Area (m^2)	Cliff %	Debris (%)	*n*	Area (m^2)	Cliff %	Debris (%)	*n*	Area (m^2)	Cliff %	Debris (%)
Río Oro																							
3	800	0	7×10^{-3}	0	0	0	0	8	5,000	62	0.2	17	4,000	59	0.2	21	14,000	24	0.7	28	15,000	64	0.6
Río Lácteo																							
18	3,000	5	0.02	26	4,000	0	0.1	4	5,000	50	0.1	11	4,000	9	0.1	11	2000	9	<0.1	5	2000	60	<0.1
San Lorenzo Sur																							
150	60,000	29	0.5	92	39,000	30	0.3	67	52,000	58	0.5	62*	35,000*	53*	0.4	125	44,000	41	0.4	86	42,000	57	0.4
Total																							
171	63,800	26	0.3	118	43,000	30	0.2	79	62,000	58	0.3	90*	43,000*	50*	0.3	157	60,000	36	0.3	119	59,000	62	0.3

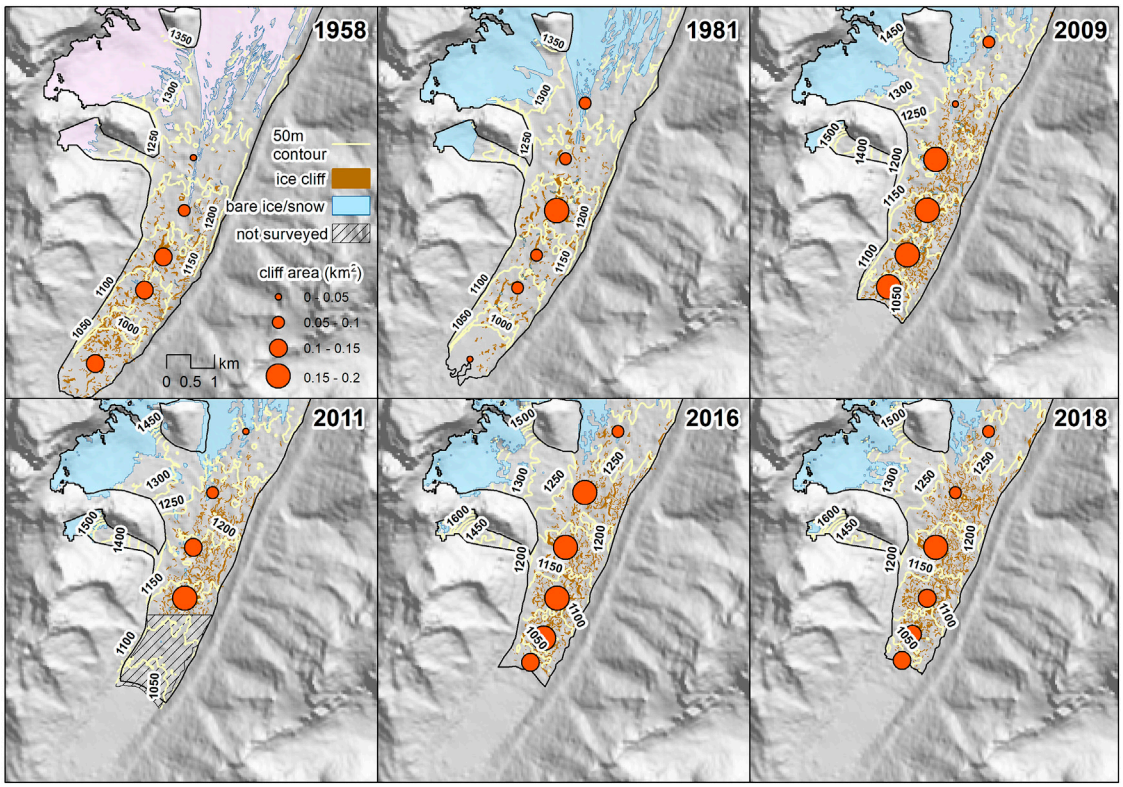

FIGURE 6 | Ice cliff and pond distribution and temporal evolution in the San Lorenzo Sur glacier.

three glaciers, the relationship is stronger when considering the glacier-averaged SLA in all three areas (r = 0.64, p < 0.01; see **Figure 8A**). Based on this result, we show that March temperature explains about 37% of the total variance of SLA in the 2000–2020 interval. The annual temperature, from December of the previous year to November preceding the SLA determination, is also significantly associated, although weaker (r = 0.58), to the SLA, indicating that SLA variations are also influenced by snowpack accumulation during the previous year.

December-January precipitation is the seasonal arrangement most significant related to SLA. Similar to temperature, the relationships improve when the comparison between December and January precipitation is based on the glacier-averaged SLAs (r = 0.68; see **Figure 8B**). The percentage of total variance in SLAs changes explained by December-January precipitation over the interval 2000–2020 is somewhat higher (R^2 around 44%) than that accounted by temperature.

The joint use of March temperature and December-January precipitation from Balmaceda as predictors of the SLAs at Mount San Lorenzo in a regression analysis shows that these climatic variables can explain more than 50% of the total variance of the glacier-averaged SLAs during the period 2000–2020 (adjusted r^2 = 55%, F(2,16) = 12.031 p < 0.00065; **Figure 8** and **Table 3**). However, we noted that each climatic variable has a distinctive impact on each of the glaciers (**Table 4**). For the Río Oro glacier, the total variance explained by both climatic variables is high (adjusted r^2 = 50%), but only December-January precipitation is a significant (p = 0.009) predictor for SLA variations in this glacier. For the Río Lácteo glacier, the explained SLA variance remains significant (adjusted r^2 = 41%) but none of the predictors are statistically significant at 95% confidence level (p = 0.054 and p = 0.085 for December-January precipitation and March temperature, respectively). Finally, the SLA variance explained for the San Lorenzo Sur glacier is adjusted r^2 = 40%, with March temperature being statistically significant (p = 0.033) as a regression predictor (**Table 5**).

DISCUSSION

Increase in Debris-Covered Area

Overall, the total extent of debris-covered ice area for the three glaciers investigated has increased from 40 ± 0.6% to 50 ± 6.7% from 1958 to 2020. Because glacier recession in this study area is significant due to calving in proglacial lakes (particularly in the cases of Río Lácteo and San Lorenzo Sur), each year a large amount of debris-covered ice is lost (Falaschi et al., 2017). The above estimate of debris-covered area increase represents thus a minimum value of the potential debris-covered ice area increase. To give a better idea of the above, it can be said that if the initial 1958 glacier area is kept for all calculations (i.e., omitting all area losses since 1958 due to calving), the increase would be from 40 to 56%. Throughout the study period, the total debris-covered ice area has increased a steady rate, and we were unable to detect any

TABLE 3 | Regression summaries for mean snowline altitudes (mean-SLA) using March temperature, December-January precipitation, and both variables as predictors.

Dependent variable: mean-SLA, independent variable Mar temp. r = 0.64, r^2 = 0.41, adjusted r^2 = 0.37, F(1,17) = 11.72	
N = 19	*p*-value
March temp	0.003
Dependent variable: mean-SLA, independent variable December-January precipitation r = 0.68, r^2 = 0.47, adjusted r^2 = 0.44, F(1,17) = 14.95	
N = 19	*p*-value
December-January precipitation	0.001
Dependent variable: mean-SLA, Independent variables: December-January precipitation, March temperature multiple r = 0.77, r^2 = 0.6, adjusted r^2 = 0.55, F(2,16) = 12.03	
N = 19	*p*-value
December-January precipitation	0.01
March temp	0.03

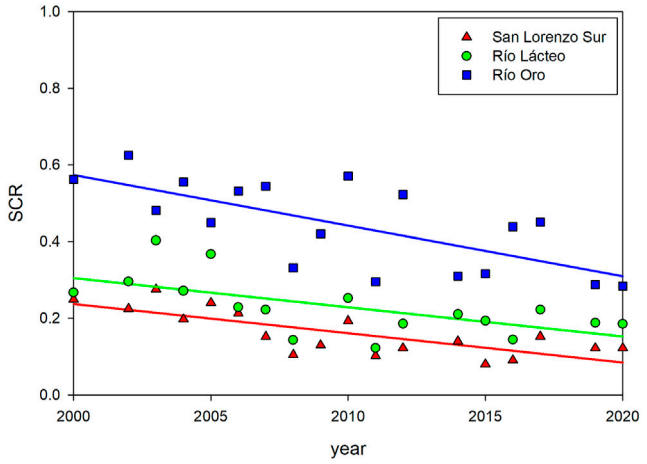

FIGURE 7 | Scatter plot showing Snow Cover Ratios (SCR) for the 2000–2020 period. Note the absence of data for years 2013 and 2018.

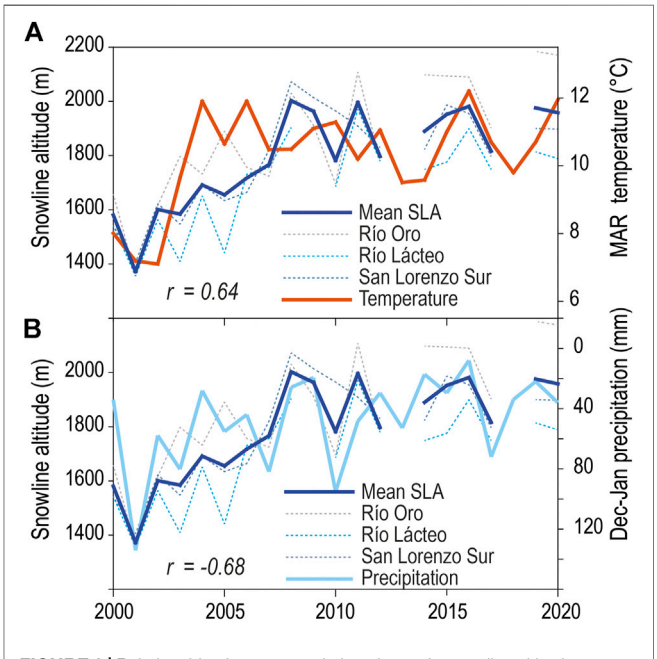

FIGURE 8 | Relationships between variations in yearly snowline altitude, March temperature **(A)** and accumulated December-January precipitation **(B)**.

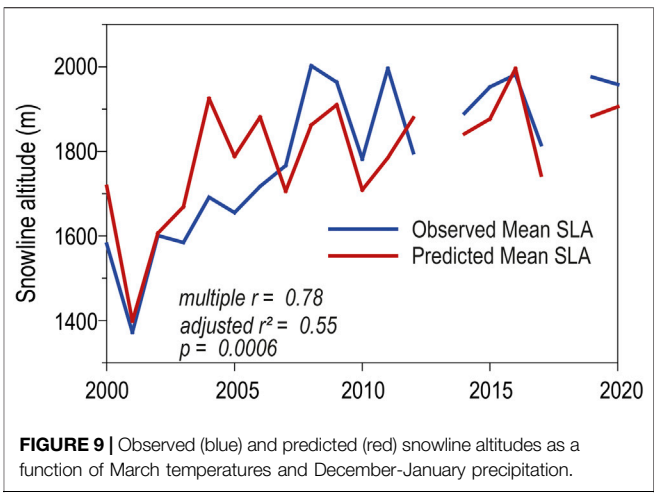

FIGURE 9 | Observed (blue) and predicted (red) snowline altitudes as a function of March temperatures and December-January precipitation.

short-term migration of the upper boundary of the debris layer toward lower elevation.

Most debris input probably originates from the headwalls of each glacier, especially the East Face of Monte San Lorenzo, where the accumulation areas of the investigated glaciers are located. Although lateral moraine degradation is relevant on the investigated glaciers (Falaschi et al., 2019), we infer from the field visit to Río Lácteo glacier that they contribute merely to the glacier margins in the form of large boulders. Incidentally, van Woerkom et al. (2019) also showed that debris supply from lateral moraines alone cannot explain thick and continuous debris layers on debris-covered glacier surfaces. On the sampled glaciers here, no large rock avalanches were detected, which would rapidly add to the debris-covered area (see e.g. Berthier and Brun, 2019).

In the nearby Northern Patagonian Icefield, Glasser et al. (2016) found an increase in the number of debris-covered glaciers and a relative increase of ~4% in debris-covered ice area between 1987 and 2015. Given the much larger size of the outlet glaciers investigated by Glasser et al. (2016) compared to the Monte San Lorenzo glaciers, this seemingly minor relative increase of ~4% is naturally much larger in terms of the total debris-covered area (139 vs. ~3 km^2 in San Lorenzo). Our findings nevertheless confirm that the trend of increasing debris-covered area is taking place not only in the large ice masses of the Patagonian

TABLE 4 | Correlation matrix between snowline altitude, temperature (March and Annual [December-November] and precipitation (December, January, joint December and January) on Balmaceda weather station. Non-significant *r* values at $p < 0.05$ are marked in [*Italics*].

Variable	Río Oro	Río Lácteo	San Lorenzo Sur	Mean SLA
Temperature-March	0.55	0.58	0.62	0.64
	N = 19	*N* = 18	*N* = 19	*N* = 19
	p = 0.014	*p* = 0.012	*p* = 0.004	*p* = 0.003
Temperature-Annual	0.55	0.57	0.46	0.58
	N = 19	*N* = 18	*N* = 19	*N* = 19
	p = 0.014	*p* = 0.014	*p* = 0.046	*p* = 0.009
Precipitation-December	–0.51	–0.47	[–0.35]	–0.5
	N = 19	*N* = 18	[*N = 19*]	*N* = 19
	p = 0.025	*p* = 0.048	[*p = 0.144*]	*p* = 0.028
Precipitation-January	–0.58	[*–0.47*]	–0.49	–0.57
	N = 19	[*N = 18*]	*N* = 19	*N* = 19
	p = 0.009	[*p = 0.051*]	*p* = 0.031	*p* = 0.011
Precipitation-December-January	–0.7	–0.6	–0.54	–0.68
	N = 19	*N* = 18	*N* = 19	*N* = 19
	p = 0.001	*p* = 0.008	*p* = 0.018	*p* = 0.001

TABLE 5 | Regression summaries for snowline altitudes at individual glaciers using March temperature and December-January precipitation as predictors. Non-significant *r* values at $p < 0.05$ are marked in [*Italics*].

Dependent variable: Río Oro snowline altitude Mutiple $r = 0.74$, $r^2 = 0.55$, adjusted $r^2 = 0.5$, F(2,16) = 9.89	
N = 19	*p*-value
December-January precipitation	0.009
March temperature	[*0.13*]
Dependent variable: Río Lacteo snowline altitude Mutiple $r = 0.7$, $r^2 = 0.48$, adjusted $r^2 = 0.41$, F(2,15) = 7.01	
N = 19	*p*-value
December-January precipitation	[*0.054*]
March temperature	[*0.09*]
Dependent variable: San Lorenzo Sur snowline altitude Mutiple $r = 0.68$, $r^2 = 0.47$, adjusted $r^2 = 0.40$, F(2,16) = 7.0411	
N = 19	*p*-value
December-January precipitation	[*0.14*]
March temperature	0.03

Icefields, but also in the smaller mountain glaciers in their periphery. In recent decades, expansion of debris-covered ice areas has also been observed in the Himalayas, Karakorum (Bolch et al., 2008; Bhambri et al., 2011; Kirkbride and Deline, 2013; Xie et al., 2020), Caucasus (Tielidze et al., 2020) and the European Alps (Mölg et al., 2019), mostly at decadal to subdecadal scale.

Interaction Between Flow Velocity, Mass Balance, Proglacial Lakes and Ice Cliff Evolution

The flow velocity time series produced here for Río Lácteo and San Lorenzo Sur glaciers is, despite its relatively shortness, the longest one available for Patagonia beyond the outlet glaciers of the Patagonian Icefields (Mouginot and Rignot, 2015). The unavailability of Landsat TM imagery acquired during the second half of the 1980's and most of the 1990's, added to the persistent cloud cover in this region, preclude a longer and high temporal resolution assessment. Whilst some studies have used large boulders visible on old aerial photos to derive isolated and sporadic velocities (e.g. Mölg et al., 2019), this was not possible in our case, as the morphology of the glacier surfaces being observed have transformed greatly between the acquisition of our 1958 and 1981 aerial photographs and the availability of the first satellite images.

A possible explanation for the differences in flow speed evolution between Río Lácteo and San Lorenzo Sur described in *Glacier Velocities* may be related to the dynamic effect originating at the glacier fronts in response to local lake water depths. Greater proglacial depths enhance calving at the snout of lake-terminating glacier tongues due to increased glacier-lake contact area subjected to subaqueous melt, accelerating flow rates and ice flux toward glacier terminus (Kirkbride and Warren, 1997; Benn et al., 2007). Acceleration of flow rates has been in fact acknowledged at the glacier terminus of several glaciers in the Himalaya (Liu et al., 2020; Pronk et al., 2021). The deceleration of San Lorenzo Sur could hence be linked to shallower lake depths, whereas the constant velocities on Río Lácteo (and even slight acceleration of the glacier front in recent years) might be connected to the presence of a deeper proglacial lake and consequently to higher calving rates.

The dynamic thinning described above is highly relevant for understanding glacier dynamics, since it has shown to exacerbate glacier retreat and thinning rates of freshwater calving glaciers compared to land-terminating ones (King et al., 2018; King et al., 2019). Ice velocities close to the front of Río Oro (small panels in **Figure 4**) are similar to the maximum values found at Río Lácteo and San Lorenzo Sur (~90 m a^{-1}), though we interpret them as a result of a higher local slope and not a dynamic acceleration due

TABLE 6 | Elevation changes (m a^{-1}) for full glacier, debris-covered ice and ice cliff areas. The values in bracket for each study period indicate the year in which the ice cliff mapping was carried out.

Glacier	1958–1981 [1981]			2000–2012 [2011]			2012–2018 [2018]		
	Full glacier area	Debris-covered area	Ice cliff area	Full glacier area	Debris-covered area	Ice cliff area	Full glacier area	Debris-covered area	Ice cliff area
Río Oro	−1	−1.77	−1.55	−0.84	−2.3	−3.29	−0.36	−1.16	−1.5
Río Lácteo	−1.41	−2.01	−2.33	−2.05	−3.13	−3.67	−2.46	−4.08	−4.55
San Lorenzo Sur	−1.39	−1.59	−1.68	−1.89	−2.12	−3.05	−2.01	−2.35	−3.13

to the presence of a proglacial lake. Falaschi et al. (2019) found a strong relation between higher rates of proglacial lake expansion and increased mass losses. In particular, the 1958–2018 thinning rates of the lake-terminating Río Lacteo and San Lorenzo Sur (1.87 and 1.94 m a^{-1}, respectively) appear to be much stronger than the land-terminating Río Oro (0.92 m a^{-1}).

When comparing average surface velocities along longitudinal profiles on Río Lácteo and San Lorenzo Sur in relation to their geodetic mass balance (as retrieved from Falaschi et al. (2019)), however, we did not find a clear correlation between mass balance and glacier flow rates. The velocity of Río Lácteo did not change significantly between the 2000–2007 and 2012–2018 periods (~33 m a^{-1} for both time intervals), whereas mass balance values shifted toward more negative conditions from −1.74 ± 0.05 to −2.09 ± 0.15 m w.e. a^{-1} for the 2000–2012 and 2012–2018 periods, respectively. Additionally, surface ice flow at San Lorenzo Sur diminished only slightly (~28–25 m a^{-1}) between 2000–2007 and 2012–2018, whilst mass balance conditions at San Lorenzo Sur remained almost equal (−1.61 ± 0.03 and −1.71 ± 0.16 m w.e. a^{-1} for 2000–2012 and 2012–2018).

Despite the above limitations in establishing a clear relation between flow speed and thinning rates, it can be argued that the overall mass balance of Río Lácteo and San Lorenzo Sur glaciers is primarily driven by climate variability and calving processes. Indeed, thinning rates increase at lower elevations at all of the investigated glaciers (Falaschi et al., 2019) in spite of the increase in debris layer thickness observed during field trips. Naturally, however, some spatial heterogeneity in the thinning patterns exist due to local variations in debris thickness, which is in turn partly linked to the occurrence of ice cliffs. To quantify the possible influence of ice cliffs on mass balance, we generated buffer zones of 35 m around the mapped ice cliffs (see Mölg et al., 2019) for three time intervals of geodetic mass balance studied in Falaschi et al. (2019). Also included within these buffer areas were supraglacial ponds, as they are closely related to ice cliffs (Watson et al., 2017; Steiner et al., 2019) and actually appear to contribute to their formation. The mean elevation change (dh/dt) in meters per year for the elevation grid cells that correspond to the buffered areas (including actual ice cliffs and ponds) effectively shows higher thinning rates compared to the debris-covered portions that are not affected by ice cliffs/ponds on nearly all glaciers and evaluated time periods (**Table 6**). This signal of increased ablation at ice cliff location might be even attenuated here, since a given ice cliff might have disappeared or migrated downglacier within each surveyed time interval. In addition, DEM differencing using 30–40 m resolution DEMs might be too coarse for the relatively small ice cliffs. High contribution to glacier ablation from ice cliffs (though seasonally variable) has also been acknowledged on several other debris-covered glacier sites like the Himalayas (e.g. Brun et al., 2016; Buri et al., 2021).

Another aspect of glacier velocity in relation to the occurrence of glacier surface features (cliffs and ponds) was brought out by Mölg et al. (2019) for the Zmuttgletscher in the Swiss Alps. These authors showed that time intervals of relatively high flow speeds hampered the emergence of ice cliffs, and concomitantly shifted the upper boundary of debris-covered area downglacier. In principle, our results for the investigated glaciers in Monte San Lorenzo agree with this assertion, since we also found a continuous increase in the debris-covered ice area and a steady shift of the upper altitudinal limit of the ice cliff area toward higher elevations during the study period. Average slopes on Río Lácteo and San Lorenzo, as retrieved from a 1958–2018 multi-sourced DEM time series (see Falaschi et al., 2019), have decreased only very slightly on the debris-covered glacier portions between 1958 and 2018 (9°–8° and 11°–9° respectively). The relatively high slopes can explain the still continually flowing glacier tongues, though velocities might be still low enough to have enabled the growth of ice cliff and supraglacial ponds areas at increasingly higher elevation with time. Watson et al. (2017) and Steiner et al. (2019), however, found no clear link between ice cliff spatial density and glacier surface velocity on debris-covered glaciers in the Everest and Langtang regions in the Himalaya, nor a preferential formation sites of ice cliffs on stagnating tongues. Also, Río Oro (3.4% max), and especially San Lorenzo Sur glacier (7.6% max), have a much higher ice cliff share of the debris-covered ice area compared to e.g. Zmuttgletscher (1.5% max), which flows at similar speed compared to San Lorenzo Sur, or a series of five valley glaciers in the Langtang Himalaya (max 3.8%) whose lowermost tongues are almost stagnant (Steiner et al., 2019). Also, the 16–18% annual survival rate of the ice cliffs in the investigated glaciers (measured for the 2009–2011 and 2017–2018 time intervals) happens to be somewhat higher than for Langtang glacier (9–13% Steiner et al., 2019) despite higher flow velocities.

Influence of Snow Line Altitude/Snow Cover Ratio Variability in Glacier Changes

Our satellite-derived SLAs were highly variable in elevation (various hundreds of meters). This is due to limitations posed

by the occasionally unavailable actual late-summer imagery to derive the highest SLA for many survey years (**Supplementary Table S2**). In fact, there was only a single suitable scene for SLA mapping in many years. Hence, images acquired earlier in the ablation season will provide a lower SLA compared to actual late-summer scenes, as long as no snowstorms hit the mountains later in the ablation season. Facing the same limitations, Barcaza et al. (2009) recorded differences of up to 300 m in satellite-derived ELAs for singe glaciers in the Northern Patagonian Icefield between 1975 and 2003.

With the restrictions imposed by the overall limited satellite imagery availability in mind, we found that SLAs have increased during the 2000–2020 time interval (**Figures 8**, **9**). Increasing SLAs are more evident before the year 2008 than for later years, coinciding with the contemporary temperature and precipitation changes during these earlier years. From 2001 to 2008, December-January monthly precipitation decreases from 120 mm to only 20 mm, whereas there is no clear trend afterward. Likewise, March mean temperature shifts from ~7°C before 2002 to ~12°C in 2004 and remained fairly stable since then.

Given that the March air temperature and December-January precipitation can explain more than 50% of the total variance of the glacier-averaged SLAs, a first, preliminary conclusion from *Changes in Snow Cover Ratio and Snow Line Altitude* is that our mapped glacier-averaged SLAs and their changes through time are fairly representative of the climate variability in the Monte San Lorenzo region. Because in the temperate ice masses of Patagonia superimposed ice is not to be expected (Cuffey and Paterson, 2010), end of summer snowlines are a good approximation of ELAs. Therefore, our findings suggest progressively lower Accumulation Area Ratios (AAR) on the investigated glaciers (**Figure 7**), which is compatible with glaciers in decidedly disequilibrium state (Bakke and Nesje, 2011). Previously, a paleoclimatic reconstruction by Sagredo et al. (2017) in the nearby Tranquilo glacier (in the northern slope of Monte San Lorenzo), estimated a 130–170 m shift in ELA since the Last Millennium Maximum. Further supportive data to this assertion comes from Glaciar de los Tres, ~200 km south of San Lorenzo (but still the closest glacier where *in-situ* measurements are available). Here, glaciological surveys have also shown rapidly increasing ELAs since the late 1990s (WGMS, 2020).

Climate data presented in Falaschi et al. (2019) indicate that there have been clear trends of diminishing annual precipitation and increasing summer air temperatures in the Monte San Lorenzo region, at least since the mid-20th century, promoting rising ELAs in the district. The observed increase in debris-covered area in the sampled glaciers may hence stem not only from the low glacier flow speeds that fail to evacuate debris from the glaciers' surface, but also from the enhanced emergence of englacial debris at higher elevations up-glacier due to higher SLAs with time. In consequence, climate forcing (by way of changes in SLAs through time) needs to be incorporated as a causing factor in the feedback interactions governing the dynamics of the investigated glaciers.

In regards to changes in SLAs and glacier mass balance, we split the 2000–2020 observation period into two sub-periods (2000–2012 and 2012–2020) to match the geodetic mass balance intervals sampled in Falaschi et al. (2019), and found a shift of time-averaged SLAs toward higher elevations on all three glaciers (~300 m on Río Oro, ~120 m on Río Lácteo and ~100 m on San Lorenzo Sur). In principle, rising SLAs (ELAs) should promote higher thinning and ablation rates, as a now larger portion of the glacier is under melting conditions and the glacier surface is exposed to higher temperatures. Given that the largest shift in SLA was found ELA for Río Oro, it is surprising that Falaschi et al. (2019) found that thinning rates of both Río Lácteo and San Lorenzo Sur) have increased between 2000–2012 and 2012–2018 (**Table 6**), yet the thinning rates of Río Oro have decreased in the last decade approximately.

CONCLUSION

In this study we have reconstructed the evolution of surface features and morphology, debris cover, and a superficial flow velocity of Río Oro, Río Lácteo, and San Lorenzo Sur glaciers in Patagonia, which, taken as a whole, covers a time span of over 60 years. Throughout the study period, glaciers showed 1) an overall debris-covered area increase from 40 ± 0.6 to 50 ± 6.7% [1958–2020] 2) slow surface flow velocities [2000–2020] 3) an increase in ice cliff area and maximum elevation [1958–2018]and 4) a shift toward higher end of summer snowlines [2000–2020].

In the last six decades approximately, summer air temperatures have increased significantly in the San Lorenzo region. Coupled with glacier dynamics linked to freshwater calving processes, this has led to strongly negative mass balance conditions throughout this period, in spite of extensive debris layers on the glaciers surface. In addition to the climate forcing and inherent calving dynamics that drive the mass changes of the sampled glaciers, here we add the abundant presence of ice cliffs as an additional factor leading to enhanced mass loss, especially in comparison to other debris free glaciers in this region. Higher summer temperatures have resulted in increased end of summer snowlines (and presumably ELAs), exposing this way bare ice and supraglacial debris at higher elevations. This has resulted in a ~10% expansion of the debris cover extent among the three glaciers. The considerably large extent and further expansion of debris cover at higher elevations might suggest an increasing importance of ice cliffs in overall glacier mass budget.

Preliminary *in situ* observations on Río Lácteo glacier indicate increasing debris layer thickness toward glacier termini, which should hamper ablation and cause a gentler or reversed mass balance gradient. Under these conditions, we hypothesize that ablation maxima at the ice cliff locations, in addition to ice speed acceleration and ice thinning toward the lowermost parts of the glacier tongues have prevented this from happening.

The overall surface flow velocity record of Río Lácteo and San Lorenzo Sur for the last two decades did not show a clear shift toward slower velocities (indicating progressive stagnation) in spite of the (slightly) reduced glacier slope. The overall low velocities might stem from the reduced ice thickness with time rather than the gentle slope of the glaciers. Nonetheless, velocities have not been fast enough to evacuate supraglacial debris, facilitating the up-glacier expansion and thickening of debris layers, nor have they prevented the growth of newly formed ice

cliffs and the occurrence of ice cliffs at increasingly higher elevation with time.

The results presented in this study, mostly based on remote sensing data and records, represents a first line approach for understanding the complex relations between climate variability, glacier dynamics, debris cover and ice cliffs of glaciers in southern Patagonia. In this regard, more specific and *in situ* surveys are necessary (such as glaciological mass balance of annual resolution, ablation and backwasting at ice cliff locations, debris cover thickness measurements) for a better understanding of these feedback mechanisms and their ingestion in larger scale assessments and numerical modeling.

DATA AVAILABILITY STATEMENT

The raw data supporting the conclusion of this article can be made available on request to the corresponding author.

AUTHOR CONTRIBUTIONS

DF designed the study, analyzed data and wrote the manuscript. AR contributed to the study design and wrote the manuscript. ALR, SM, RV, PR, JZ, and AS analyzed data. All authors contributed to the writing of the final version of the manuscript.

FUNDING

This research was funded by the Agencia Nacional de Promoción Científica y Técnica (Grants PICT 2007-0379 and PICT 2016-1282). PR acknowledges financial support from the ESA project Glaciers_cci (4000109873/14/I-NB). AR was funded by FONDECYT 1171832.

ACKNOWLEDGMENTS

SRTM-X and ALOS PALSAR DEM tiles were obtained from the Deutsches Zentrum für Luft und Raumfahrt (DLR) EOWEB, and the Alaska Satellite Facility portals. The Pléiades data used in this study was provided by the Pléiades Glacier Observatory (PGO) initiative of the French Space Agency (CNES). Pléiades data© CNES 2018, Distribution Airbus D&S. We acknowledge Frank Paul and Nico Mölg from the Geography Department at the University of Zurich for the manual mapping of snowlines and Mariano Castro for his photos and observations on the debris layer of Río Lácteo glacier. Thanks also to Pierre Pitte (IANIGLA) for his insight into ELAs at Glaciar de los Tres. Special thanks to Tobias Bolch (University of St. Andrews, Scotland) for his constructive comments and Ryan Wilson (University of Huddersfield, United Kingdom) for proofreading a previous version of the manuscript. Finally, we thank handling editor Aparna Shukla and two reviewers for their valuable comments and suggestions, which led to a much improved presentation of this study's content.

SUPPLEMENTARY MATERIAL

The Supplementary Material for this article can be found online at: https://www.frontiersin.org/articles/10.3389/feart.2021.671854/full#supplementary-material

REFERENCES

Anderson, L. S., and Anderson, R. S. (2018). Debris Thickness Patterns on Debris-Covered Glaciers. *Geomorphology* 311, 1–12. doi:10.1016/j.geomorph.2018.03.014

Bakke, J., and Nesje, A. (2011). "Equilibrium-Line Altitude (ELA)," in *Encyclopedia of Snow, Ice and Glaciers*. Editors V. Singh, V. P. Singh, and U. Haritashya (Dordrecht, Netherlands: Springer), 268–277.

Banerjee, A., and Shankar, R. (2013). On the Response of Himalayan Glaciers to Climate Change. *J. Glaciol.* 59 (215), 480–490. doi:10.3189/2013JoG12J130

Barcaza, G., Aniya, M., Matsumoto, T., and Aoki, T. (2009). Satellite-Derived Equilibrium Lines in Northern Patagonia Icefield, Chile, and Their Implications to Glacier Variations. *Arct. Antarct. Alp. Res.* 41 (2), 174–182. doi:10.1657/1938-4246-41.2.174

Benn, D. I., Bolch, T., Hands, K., Gulley, J., Luckman, A., Nicholson, L. I., et al. (2012). Response of Debris-Covered Glaciers in the Mount Everest Region to Recent Warming, and Implications for Outburst Flood Hazards. *Earth-Sci. Rev.* 114 (1–2), 156–174. doi:10.1016/j.earscirev.2012.03.008

Benn, D. I., Warren, C. R., and Mottram, R. H. (2007). Calving Processes and the Dynamics of Calving Glaciers. *Earth-Sci. Rev.* 82 (3–4), 143–179. doi:10.1016/j.earscirev.2007.02.002

Berthier, E., and Brun, F. (2019). Karakoram Geodetic Glacier Mass Balances Between 2008 and 2016: Persistence of the Anomaly and Influence of a Large Rock Avalanche on Siachen Glacier. *J. Glaciol.* 65 (251), 494–507. doi:10.1017/jog.2019.32

Berthier, E., Raup, B., and Scambos, T. (2003). New Velocity Map and Mass-Balance Estimate of Mertz Glacier, East Antarctica, Derived From Landsat Sequential Imagery. *J. Glaciol.* 49 (167), 503–511. doi:10.3189/172756503781830377

Bhambri, R., Bolch, T., Chaujar, R. K., and Kulshreshtha, S. C. (2011). Glacier Changes in the Garhwal Himalaya, India, From 1968 to 2006 Based on Remote Sensing. *J. Glaciol.* 57 (203), 543–556. doi:10.3189/002214311796905604

Bippus, G. (2011). Characteristics of Summer Snow Areas on Glaciers Observed by Means of Landsat Data. [PhD thesis]. Innsbruck (Austria): University of Innsbruck).

Bisset, R. R., Dehecq, A., Goldberg, D. N., Huss, M., Bingham, R. G., and Gourmelen, N. (2020). Reversed Surface-Mass-Balance Gradients on Himalayan Debris-Covered Glaciers Inferred From Remote Sensing. *Remote Sens.* 12 (10), 1563. doi:10.3390/rs12101563

Bodin, X., Rojas, F., and Brenning, A. (2010). Status and Evolution of the Cryosphere in the Andes of Santiago (Chile, 33.5°S.). *Geomorphology* 118 (3–4), 453–464. doi:10.1016/j.geomorph.2010.02.016

Bolch, T., Buchroithner, M., Pieczonka, T., and Kunert, A. (2008). Planimetric and Volumetric Glacier Changes in the Khumbu Himal, Nepal, Since 1962 Using Corona, Landsat TM and ASTER Data. *J. Glaciol.* 54 (187), 592–600. doi:10.3189/002214308786570782

Bolch, T., Kulkarni, A., Kaab, A., Huggel, C., Paul, F., Cogley, J. G., et al. (2012). The State and Fate of Himalayan Glaciers. *Science* 336 (6079), 310–314. doi:10.1126/science.1215828

Bravo, C., Quincey, D. J., Ross, A. N., Rivera, A., Brock, B., Miles, E., et al. (2019). Air Temperature Characteristics, Distribution, and Impact on Modeled Ablation for the South Patagonia Icefield. *J. Geophys. Res. Atmos.* 124 (2), 907–925. doi:10.1029/2018JD028857

Brun, F., Buri, P., Miles, E. S., Wagnon, P., Steiner, J., Berthier, E., et al. (2016). Quantifying Volume Loss from Ice Cliffs on Debris-Covered Glaciers Using High-Resolution Terrestrial and Aerial Photogrammetry. *J. Glaciol.* 62 (234), 684–695. doi:10.5194/tc-12-3439-201810.1017/jog.2016.54

Brun, F., Wagnon, P., Berthier, E., Shea, J. M., Immerzeel, W. W., Kraaijenbrink, P. D. A., et al. (2018). Ice Cliff Contribution to the Tongue-Wide Ablation of Changri Nup Glacier, Nepal, Central Himalaya. *The Cryosphere* 12 (11), 3439–3457. doi:10.5194/tc-12-3439-2018

Buri, P., Miles, E. S., SteinerRagettli, J. F. S., Ragettli, S., and Pellicciotti, F. (2021). Supraglacial Ice Cliffs Can Substantially Increase the Mass Loss of Debris-Covered Glaciers. *Geophys. Res. Lett.* 48 (6), e2020GL092150. doi:10.1029/2020GL092150

Buri, P., Pellicciotti, F., Steiner, J. F., Miles, E. S., and Immerzeel, W. W. (2016). A Grid-Based Model of Backwasting of Supraglacial Ice Cliffs on Debris-Covered Glaciers. *Ann. Glaciol.* 57 (71), 199–211. doi:10.3189/2016AoG71A059

Clare, G. R., Fitzharris, B. B., Chinn, T. J. H., and Salinger, M. J. (2002). Interannual Variation in End-of-Summer Snowlines of the Southern Alps of New Zealand, and Relationships With Southern Hemisphere Atmospheric Circulation and Sea Surface Temperature Patterns. *Int. J. Climatol.* 22 (1), 107–120. doi:10.1002/joc.722

Collier, E., Maussion, F., Nicholson, L. I., Mölg, T., Immerzeel, W. W., and Bush, A. B. G. (2015). Impact of Debris Cover on Glacier Ablation and Atmosphere-Glacier Feedbacks in the Karakoram. *The Cryosphere* 9 (4), 1617–1632. doi:10.5194/tc-9-1617-2015

Cuffey, K. M., and Paterson, W. S. (2010). *The Physics of Glaciers*. 4th Edn. Oxford, United Kingdom: Elsevier, Butterworth-Heinemann, 693.

Damseaux, A., Fettweis, X., Lambert, M., and Cornet, Y. (2020). Representation of the Rain Shadow Effect in Patagonia Using an Orographic-Derived Regional Climate Model. *Int. J. Climatol* 40 (3), 1769–1783. doi:10.1002/joc.6300

Davaze, L., Rabatel, A., Dufour, A., Hugonnet, R., and Arnaud, Y. (2020). Region-Wide Annual Glacier Surface Mass Balance for the European Alps From 2000 to 2016. *Front. Earth Sci.* 8, 149. doi:10.3389/feart.2020.00149

Davies, B. J., and Glasser, N. F. (2012). Accelerating Shrinkage of Patagonian Glaciers From the Little Ice Age (~AD 1870) to 2011. *J. Glaciol.* 58 (212), 1063–1084. doi:10.3189/2012JoG12J026

De Angelis, H. (2014). Hypsometry and Sensitivity of the Mass Balance to Changes in Equilibrium-Line Altitude: The Case of the Southern Patagonia Icefield. *J. Glaciol.* 60 (219), 14–28. doi:10.3189/2014JoG13J127

Dehecq, A., Gourmelen, N., Gardner, A. S., Brun, F., Goldberg, D., Nienow, P. W., et al. (2019). Twenty-First Century Glacier Slowdown Driven by Mass Loss in High Mountain Asia. *Nat. Geosci.* 12 (1), 22–27. doi:10.1038/s41561-018-0271-9

Dussaillant, I., Berthier, E., Brun, F., Masiokas, M., Hugonnet, R., Favier, V., et al. (2019). Two Decades of Glacier Mass Loss Along the Andes. *Nat. Geosci.* 12 (10), 802–808. doi:10.1038/s41561-019-0432-5

Falaschi, D., Bolch, T., Lenzano, M. G., Tadono, T., Lo Vecchio, A., and Lenzano, L. (2018). New Evidence of Glacier Surges in the Central Andes of Argentina and Chile. *Prog. Phys. Geogr. Earth Environ.* 42 (6), 792–825. doi:10.1177/0309133318803014

Falaschi, D., Bolch, T., Rastner, P., Lenzano, M. G., Lenzano, L., Lo Vecchio, A., et al. (2017). Mass Changes of Alpine Glaciers at the Eastern Margin of the Northern and Southern Patagonian Icefields Between 2000 and 2012. *J. Glaciol.* 63 (238), 258–272. doi:10.1017/jog.2016.136

Falaschi, D., Bravo, C., Masiokas, M., Villalba, R., and Rivera, A. (2013). First Glacier Inventory and Recent Changes in Glacier Area in the Monte San Lorenzo Region (47°S), Southern Patagonian Andes, South America. *Arct. Antarct. Alp. Res.* 45 (1), 19–28. doi:10.1657/1938-4246-45.1.19

Falaschi, D., Lenzano, M. G., Villalba, R., Bolch, T., Rivera, A., and Lo Vecchio, A. (2019). Six Decades (1958-2018) of Geodetic Glacier Mass Balance in Monte San Lorenzo, Patagonian Andes. *Front. Earth Sci.* 7, 326. doi:10.3389/feart.2019.00326

Ferguson, J., and Vieli, A. (2020). Modelling Steady States and the Transient Response of Debris-Covered Glaciers. *The Cryosphere* doi:10.5194/tc-2020-228

Ferri, L., Dussaillant, I., Zalazar, L., Masiokas, M. H., Ruiz, L., Pitte, P., et al. (2020). Ice Mass Loss in the Central Andes of Argentina Between 2000 and 2018 Derived From a New Glacier Inventory and Satellite Stereo-Imagery. *Front. Earth Sci.* 8, 530997. doi:10.3389/feart.2020.530997

Fyffe, C. L., Woodget, A. S., Kirkbride, M. P., Deline, P., Westoby, M. J., and Brock, B. W. (2020). Processes at the Margins of Supraglacial Debris Cover: Quantifying Dirty Ice Ablation and Debris Redistribution. *Earth Surf. Process. Landf.* 45 (10), 2272–2290. doi:10.1002/esp.4879

Glasser, N. F., Holt, T. O., Evans, Z. D., Davies, B. J., Pelto, M., and Harrison, S. (2016). Recent Spatial and Temporal Variations in Debris Cover on Patagonian Glaciers. *Geomorphology* 273, 202–216. doi:10.1016/j.geomorph.2016.07.03636

Glasser, N., and Jansson, K. (2008). The Glacial Map of Southern South America. *J. Maps* 4 (1), 175–196. doi:10.4113/jom.2008.1020

Goward, S., Arvidson, T., Williams, D., Faundeen, J., Irons, J., and Franks, S. (2006). Historical Record of Landsat Global Coverage. *Photogramm. Eng. Remote Sensing* 72 (10), 1155–1169. doi:10.14358/PERS.72.10.1155

Han, H., Wang, J., Wei, J., and Liu, S. (2010). Backwasting Rate on Debris-Covered Koxkar Glacier, Tuomuer Mountain, China. *J. Glaciol.* 56 (196), 287–296. doi:10.3189/002214310791968430

Haritashya, U. K., Pleasants, M. S., and Copland, L. (2015). Assessment of the Evolution in Velocity of Two Debris-Covered Valley Glaciers in Nepal and New Zealand. *Geogr. Ann. A Phys. Geogr.* 97 (4), 737–751. doi:10.1111/geoa.12112

Herreid, S., and Pellicciotti, F. (2018). Automated Detection of Ice Cliffs within Supraglacial Debris Cover. *The Cryosphere* 12 (5), 1811–1829. doi:10.5194/tc-12-1811-2018

Herreid, S., and Pellicciotti, F. (2020). The State of Rock Debris Covering Earth's Glaciers. *Nat. Geosci.* 13, 621–627. doi:10.1038/s41561-020-0615-0

Hugonnet, R., McNabb, R., Berthier, E., Menounos, B., Nuth, C., Girod, L., et al. (2021). Accelerated Global Glacier Mass Loss in the Early Twenty-First Century. *Nature* 592 (7856), 726–731. doi:10.1038/s41586-021-03436-z

IANIGLA (2018). Informe de la subcuenca de los lagos Nansen y Belgrano. Cuenca del río Mayer y lago San Martín. Mendoza, Argentina: IANIGLA-CONICET, Ministerio de Ambiente y Desarrollo Sustentable de la Nación. . Available at: http://www.glaciaresargentinos.gob.ar/?page_id=1056 (Accessed April 18, 2021).

Jomelli, V., Khodri, M., Favier, V., Brunstein, D., Ledru, M.-P., Wagnon, P., et al. (2011). Irregular Tropical Glacier Retreat Over the Holocene Epoch Driven by Progressive Warming. *Nature* 474 (7350), 196–199. doi:10.1038/nature10150

Juen, M., Mayer, C., Lambrecht, A., Han, H., and Liu, S. (2014). Impact of Varying Debris Cover Thickness on Ablation: A Case Study for Koxkar Glacier in the Tien Shan. *The Cryosphere* 8 (2), 377–386. doi:10.5194/tc-8-377-20144

Kääb, A., Berthier, E., Nuth, C., Gardelle, J., and Arnaud, Y. (2012). Contrasting Patterns of Early Twenty-First-century Glacier Mass Change in the Himalayas. *Nature* 488 (7412), 495–498. doi:10.1038/nature11324

Kääb, A., and Vollmer, M. (2000). Surface Geometry, Thickness Changes and Flow Fields on Creeping Mountain Permafrost: Automatic Extraction by Digital Image Analysis. *Permafr. Periglac. Process.* 11, 315–326. doi:10.1002/1099-1530(200012)11:4<315::AID-PPP365>3.0.CO;2-J

King, O., Bhattacharya, A., Bhambri, R., and Bolch, T. (2019). Glacial Lakes Exacerbate Himalayan Glacier Mass Loss. *Sci. Rep.* 9 (1), 18145. doi:10.1038/s41598-019-53733-x

King, O., Dehecq, A., Quincey, D., and Carrivick, J. (2018). Contrasting Geometric and Dynamic Evolution of Lake and Land-Terminating Glaciers in the Central Himalaya. *Glob. Planet. Change* 167, 46–60. doi:10.1016/j.gloplacha.2018.05.006

Kirkbride, M. P., and Deline, P. (2013). The Formation of Supraglacial Debris Covers by Primary Dispersal From Transverse Englacial Debris Bands. *Earth Surf. Process. Landf.* 38 (15), 1779–1792. doi:10.1002/esp.3416

Kirkbride, M. P., and Warren, C. R. (1997). Calving Processes at a Grounded Ice Cliff. *Ann. Glaciol.* 24, 116–121. doi:10.3189/S0260305500012039

Kneib, M., Miles, E. S., Jola, S., Buri, P., Herreid, S., Bhattacharya, A., et al. (2021). Mapping Ice Cliffs on Debris-Covered Glaciers Using Multispectral Satellite Images. *Remote Sens. Environ.* 253, 112201. doi:10.1016/j.rse.2020.112201

Lenaerts, J. T. M., van den Broeke, M. R., van Wessem, J. M., van de Berg, W. J., van Meijgaard, E., van Ulft, L. H., et al. (2014). Extreme Precipitation and Climate Gradients in Patagonia Revealed by High-Resolution Regional Atmospheric Climate Modeling. *J. Clim.* 27 (12), 4607–4621. doi:10.1175/JCLI-D-13-00579.1

Liu, Q., Mayer, C., Wang, X., Nie, Y., Wu, K., Wei, J., et al. (2020). Interannual Flow Dynamics Driven by Frontal Retreat of a Lake-Terminating Glacier in the Chinese Central Himalaya. *Earth Planet. Sci. Lett.* 546, 116450. doi:10.1016/j.epsl.2020.116450

Masiokas, M. H., Delgado, S., Pitte, P., Berthier, E., Villalba, R., Skvarca, P., et al. (2015). Inventory and Recent Changes of Small Glaciers on the Northeast

Margin of the Southern Patagonia Icefield, Argentina. *J. Glaciol.* 61 (227), 511–523. doi:10.3189/2015JoG14J094

Mattson, L. E. (2000). "The Influence of a Debris Cover on the Mid-Summer Discharge of Dome Glacier, Canadian Rocky Mountains," in Proceedings of a Workshop Held in Seattle, Washington, USA, September 2000, (Washington, DC: IAHS Publications), 25–33.

Mertes, J. R., Thompson, S. S., Booth, A. D., Gulley, J. D., and Benn, D. I. (2017). A Conceptual Model of Supra-Glacial Lake Formation on Debris-Covered Glaciers Based on GPR Facies Analysis. *Earth Surf. Process. Landf.* 42 (6), 903–914. doi:10.1002/esp.4068

Mihalcea, C., Mayer, C., Diolaiuti, G., D'Agata, C., Smiraglia, C., Lambrecht, A., et al. (2008). Spatial Distribution of Debris Thickness and Melting from Remote-Sensing and Meteorological Data, at Debris-Covered Baltoro Glacier, Karakoram, Pakistan. *Ann. Glaciol.* 48, 49–57. doi:10.3189/172756408784700680

Mölg, N., Bolch, T., Walter, A., and Vieli, A. (2019). Unravelling the Evolution of Zmuttgletscher and its Debris Cover Since the End of the Little Ice Age. *The Cryosphere* 13 (7), 1889–1909. doi:10.5194/tc-13-1889-2019

Mouginot, J., and Rignot, E. (2015). Ice Motion of the Patagonian Icefields of South America: 1984-2014. *Geophys. Res. Lett.* 42 (5), 1441–1449. doi:10.1002/2014GL062661

Nicholson, L. I., McCarthy, M., Pritchard, H. D., and Willis, I. (2018). Supraglacial Debris Thickness Variability: Impact on Ablation and Relation to Terrain Properties. *The Cryosphere* 12 (12), 3719–3734. doi:10.5194/tc-12-3719-2018

Otsu, N. (1979). A Threshold Selection Method From Gray-Level Histograms. *IEEE Trans. Syst. Man. Cybern.* 9 (1), 62–66. doi:10.1109/TSMC.1979.4310076

Paul, F., Bolch, T., Kääb, A., Nagler, T., Nuth, C., Scharrer, K., et al. (2015). The Glaciers Climate Change Initiative: Methods for Creating Glacier Area, Elevation Change and Velocity Products. *Remote Sens. Environ.* 162, 408–426. doi:10.1016/j.rse.2013.07.043

Paul, F., Huggel, C., and Kääb, A. (2004). Combining Satellite Multispectral Image Data and a Digital Elevation Model for Mapping Debris-Covered Glaciers. *Remote Sens. Environ.* 89 (4), 510–518. doi:10.1016/j.rse.2003.11.007

Paul, F., and Mölg, N. (2014). Hasty Retreat of Glaciers in Northern Patagonia From 1985 to 2011. *J. Glaciol.* 60 (224), 1033–1043. doi:10.3189/2014JoG14J104

Pellicciotti, F., Stephan, C., Miles, E., Herreid, S., Immerzeel, W. W., and Bolch, T. (2015). Mass-Balance Changes of the Debris-Covered Glaciers in the Langtang Himal, Nepal, From 1974 to 1999. *J. Glaciol.* 61 (226), 373–386. doi:10.3189/2015JoG13J237

Pronk, J. B., Bolch, T., King, O., Wouters, B., and Benn, D. I. (2021). Proglacial Lakes Elevate Glacier Surface Velocities in the Himalayan Region. [Preprint]. Available at: https://doi.org/10.5194/tc-2021-90 (Accessed April 20, 2021).

Quincey, D. J., Luckman, A., and Benn, D. (2009). Quantification of Everest Region Glacier Velocities Between 1992 and 2002, Using Satellite Radar Interferometry and Feature Tracking. *J. Glaciol.* 55 (192), 596–606. doi:10.3189/002214309789470987

Rabatel, A., Dedieu, J.-P., Thibert, E., Letréguilly, A., and Vincent, C. (2008). 25 Years (1981-2005) of Equilibrium-Line Altitude and Mass-Balance Reconstruction on Glacier Blanc, French Alps, Using Remote-Sensing Methods and Meteorological Data. *J. Glaciol.* 54 (185), 307–314. doi:10.3189/002214308784886063

Racoviteanu, A., and Williams, M. W. (2012). Decision Tree and Texture Analysis for Mapping Debris-Covered Glaciers in the Kangchenjunga Area, Eastern Himalaya. *Remote Sens.* 4 (10), 3078–3109. doi:10.3390/rs4103078

Ragettli, S., Bolch, T., and Pellicciotti, F. (2016). Heterogeneous Glacier Thinning Patterns Over the Last 40 Years in Langtang Himal, Nepal. *The Cryosphere* 10 (5), 2075–2097. doi:10.5194/tc-10-2075-2016

Rastner, P., Bolch, T., Notarnicola, C., and Paul, F. (2014). A Comparison of Pixel- and Object-Based Glacier Classification With Optical Satellite Images. *IEEE J. Sel. Top. Appl. Earth Obs. Remote Sens.* 7 (3), 853–862. doi:10.1109/JSTARS.2013.2274668

Rastner, P., Prinz, R., Notarnicola, C., Nicholson, L., Sailer, R., Schwaizer, G., et al. (2019). On the Automated Mapping of Snow Cover on Glaciers and Calculation of Snow Line Altitudes from Multi-Temporal Landsat Data. *Remote Sens.* 11 (12), 1410. doi:10.3390/rs11121410

Reid, T. D., and Brock, B. W. (2014). Assessing Ice-Cliff Backwasting and its Contribution to Total Ablation of Debris-Covered Miage Glacier, Mont Blanc Massif, Italy. *J. Glaciol.* 60 (219), 3–13. doi:10.3189/2014JoG13J045

Reznichenko, N., Davies, T., Shulmeister, J., and McSaveney, M. (2010). Effects of Debris on Ice-Surface Melting Rates: An Experimental Study. *J. Glaciol.* 56 (197), 384–394. doi:10.3189/002214310792447725

Rivera, A., Benham, T., Casassa, G., Bamber, J., and Dowdeswell, J. A. (2007). Ice Elevation and Areal Changes of Glaciers From the Northern Patagonia Icefield, Chile. *Glob. Planet. Change* 59 (1–4), 126–137. doi:10.1016/j.gloplacha.2006.11.037

Röhl, K. (2006). Thermo-Erosional Notch Development at Fresh-Water-Calving Tasman Glacier, New Zealand. *J. Glaciol.* 52 (177), 203–213. doi:10.3189/172756506781828773

Rounce, D. R., King, O., McCarthy, M., Shean, D. E., and Salerno, F. (2018). Quantifying Debris Thickness of Debris-Covered Glaciers in the Everest Region of Nepal Through Inversion of a Subdebris Melt Model. *J. Geophys. Res. Earth Surf.* 123 (5), 1094–1115. doi:10.1029/2017JF004395

Rowan, A. V., Egholm, D. L., Quincey, D. J., and Glasser, N. F. (2015). Modelling the Feedbacks Between Mass Balance, Ice Flow and Debris Transport to Predict the Response to Climate Change of Debris-Covered Glaciers in the Himalaya. *Earth Planet. Sci. Lett.* 430, 427–438. doi:10.1016/j.epsl.2015.09.004

Sagredo, E. A., Lowell, T. V., Kelly, M. A., Rupper, S., Aravena, J. C., Ward, D. J., et al. (2017). Equilibrium Line Altitudes Along the Andes During the Last Millennium: Paleoclimatic Implications. *The Holocene* 27 (7), 1019–1033. doi:10.1177/0959683616678458

Sakai, A., Nakawo, M., and Fujita, K. (2002). Distribution Characteristics and Energy Balance of Ice Cliffs on Debris-Covered Glaciers, Nepal Himalaya. *Arct. Antarct. Alp. Res.* 34 (1), 12–19. doi:10.1080/15230430.2002.12003463

Sakai, A., Nakawo, M., and Fujita, K. (1998). Melt Rate of Ice Cliffs on the Lirung Glacier, Nepal Himalayas, 1996. *Bull. Glaciol. Res.* 16, 57–66.

Sasaki, O., Noguchi, O., Zhang, Y., Hirabayashi, Y., and Kanae, S. (2016). A Global High-Resolution Map of Debris on Glaciers Derived from Multi-Temporal ASTER Images. *The Cryosphere Discuss.* 1–24. doi:10.5194/tc-2016-222

Sauter, T. (2020). Revisiting Extreme Precipitation Amounts Over Southern South America and Implications for the Patagonian Icefields. *Hydrol. Earth Syst. Sci.* 24 (4), 2003–2016. doi:10.5194/hess-24-2003-2020

Scherler, D., Bookhagen, B., and Strecker, M. R. (2011). Spatially Variable Response of Himalayan Glaciers to Climate Change Affected by Debris Cover. *Nat. Geosci.* 4 (3), 156–159. doi:10.1038/ngeo1068

Scherler, D., Wulf, H., and Gorelick, N. (2018). Global Assessment of Supraglacial Debris-Cover Extents. *Geophys. Res. Lett.* 45 (21), 11798–11805. doi:10.1029/2018GL080158

Shukla, A., Gupta, R. P., and Arora, M. K. (2010). Delineation of Debris-Covered Glacier Boundaries Using Optical and Thermal Remote Sensing Data. *Remote Sens. Lett.* 1 (1), 11–17. doi:10.1080/01431160903159316

Steiner, J. F., Buri, P., Miles, E. S., Ragettli, S., and Pellicciotti, F. (2019). Supraglacial Ice Cliffs and Ponds on Debris-Covered Glaciers: Spatio-Temporal Distribution and Characteristics. *J. Glaciol.* 65, 617–632. doi:10.1017/jog.2019.40

Thompson, S. S., Benn, D. I., Dennis, K., and Luckman, A. (2012). A Rapidly Growing Moraine-Dammed Glacial Lake on Ngozumpa Glacier, Nepal. *Geomorphology* 145–146, 1–11. doi:10.1016/j.geomorph.2011.08.015

Tielidze, L. G., Bolch, T., Wheate, R. D., Kutuzov, S. S., Lavrentiev, I. I., and Zemp, M. (2020). Supra-Glacial Debris Cover Changes in the Greater Caucasus From 1986 to 2014. *The Cryosphere* 14 (2), 585–598. doi:10.5194/tc-14-585-2020

van Woerkom, T., Steiner, J. F., Kraaijenbrink, P. D. A., Miles, E. S., and Immerzeel, W. W. (2019). Sediment Supply From Lateral Moraines to a Debris-Covered Glacier in the Himalaya. *Earth Surf. Dynam.* 7 (2), 411–427. doi:10.5194/esurf-7-411-2019

Watson, C. S., Quincey, D. J., Carrivick, J. L., and Smith, M. W. (2017). Ice Cliff Dynamics in the Everest Region of the Central Himalaya. *Geomorphology* 278, 238–251. doi:10.1016/j.geomorph.2016.11.017

WGMS (2020). "Global Glacier Change Bulletin No. 3 (2016-2017)," in *ISC(WDS)/IUGG(IACS)/UNEP/UNESCO/WMO*. Editors M. Zemp, I. Gärtner-Roer, S. U. Nussbaumer, J. Bannwart, P. Rastner, F. Paul, et al. (Zürich, Switzerland: World Glacier Monitoring Service).

Wilson, R., Carrión, D., and Rivera, A. (2016a). Detailed Dynamic, Geometric and Supraglacial Moraine Data for Glaciar Pio XI, the Only Surge-type Glacier of the Southern Patagonia Icefield. *Ann. Glaciol.* 57 (73), 119–130. doi:10.1017/aog.2016.32

Wilson, R., Mernild, S. H., Malmros, J. K., Bravo, C., and Carrión, D. (2016b). Surface Velocity Fluctuations for Glaciar Universidad, Central Chile, Between 1967 and 2015. *J. Glaciol.* 62 (235), 847–860. doi:10.1017/jog.2016.73

Xie, F., Liu, S., Wu, K., Zhu, Y., Gao, Y., Qi, M., et al. (2020). Upward Expansion of Supra-Glacial Debris Cover in the Hunza Valley, Karakoram, During 1990 ~ 2019. *Front. Earth Sci.* 8, 308. doi:10.3389/feart.2020.00308

Zekollari, H., Huss, M., and Farinotti, D. (2019). Modelling the Future Evolution of Glaciers in the European Alps Under the EURO-CORDEX RCM Ensemble. *The Cryosphere* 13 (4), 1125–1146. doi:10.5194/tc-13-1125-2019

Zemp, M., Huss, M., Thibert, E., Eckert, N., McNabb, R., Huber, J., et al. (2019). Global Glacier Mass Changes and Their Contributions to Sea-Level Rise From 1961 to 2016. *Nature* 568 (7752), 382–386. doi:10.1038/s41586-019-1071-0

Conflict of Interest: Author PR was partly employed by the company GeoVille Information Systems and Data Processing GmbH.

The remaining authors declare that the research was conducted in the absence of any commercial or financial relationships that could be construed as a potential conflict of interest.

frontiers in Earth Science

ORIGINAL RESEARCH
published: 13 July 2021
doi: 10.3389/feart.2021.678375

Distributed Melt on a Debris-Covered Glacier: Field Observations and Melt Modeling on the Lirung Glacier in the Himalaya

Jakob F. Steiner[1,2]*, *Philip D. A. Kraaijenbrink*[1] *and Walter W. Immerzeel*[1]

[1]Department of Physical Geography, Utrecht University, Utrecht, Netherlands, [2]International Center for Integrated Mountain Development, Kathmandu, Nepal

Debris-covered glaciers, especially in high-mountain Asia, have received increased attention in recent years. So far, few field-based observations of distributed mass loss exist and both the properties of the debris layer as well as the atmospheric drivers of melt below debris remain poorly understood. Using multi-year observations of on-glacier atmospheric data, debris properties and spatial surface elevation changes from repeat flights with an unmanned aerial vehicle (UAV), we quantify the necessary variables to compute melt for the Lirung Glacier in the Himalaya. By applying an energy balance model we reproduce observed mass loss during one monsoon season in 2013. We show that melt is especially sensitive to thermal conductivity and thickness of debris. Our observations show that previously used values in literature for the thermal conductivity through debris are valid but variability in space on a single glacier remains high. We also present a simple melt model, which is calibrated based on the results of energy balance model, that is only dependent on air temperature and debris thickness and is therefore applicable for larger scale studies. This simple melt model reproduces melt under thin debris (<0.5 m) well at an hourly resolution, but fails to represent melt under thicker debris accurately at this high temporal resolution. On the glacier scale and using only off-glacier forcing data we however are able to reproduce the total melt volume of a debris-covered tongue. This is a promising result for catchment scale studies, where quantifying melt from debris covered glaciers remains a challenge.

Keywords: debris cover, glacier melt, Himalaya, energy balance, temperature index

OPEN ACCESS

Edited by:
Lindsey Isobel Nicholson, University of Innsbruck, Austria

Reviewed by:
Akiko Sakai, Nagoya University, Japan
Rijan Bhakta Kayastha, Kathmandu University, Nepal

***Correspondence:**
Jakob F. Steiner
jakob.steiner@icimod.org

Specialty section:
This article was submitted to Cryospheric Sciences, a section of the journal Frontiers in Earth Science

Received: *09 March 2021*
Accepted: *25 June 2021*
Published: *13 July 2021*

Citation:
Steiner JF, Kraaijenbrink PDA and Immerzeel WW (2021) Distributed Melt on a Debris-Covered Glacier: Field Observations and Melt Modeling on the Lirung Glacier in the Himalaya. Front. Earth Sci. 9:678375. doi: 10.3389/feart.2021.678375

INTRODUCTION

Debris-covered glaciers are common in a number of glaciated mountain ranges, including high-mountain Asia [HMA, (Scherler et al., 2011)], the European Alps (Brock et al., 2010), the Caucasus (Lambrecht et al., 2011), the Andes of Chile (Janke et al., 2015) and Peru (Wigmore and Mark 2017), and the Russian (Barr et al., 2018), North American (Herreid and Pellicciotti 2018) and Scandinavian Arctic (Midgley et al., 2018). In HMA, they represent a considerable portion of the entire glacierized area (11%) and of the ice mass below the equilibrium line altitude (30%, Bolch et al., 2012; Kraaijenbrink et al., 2017), which is largely due steep hillslopes and high erosion rates.

Debris cover controls melt, with debris beyond a couple of centimeters in thickness inhibiting melt (Östrem, 1959; Nicholson and Benn 2006) and thinner cover increasing melt due to a decrease

in albedo. A number of recent studies found debris-covered and clean ice glacier tongues to have comparable surface lowering rates on the glacier scale (Gardelle et al., 2012; Kääb et al., 2012; Nuimura et al., 2012; Basnett et al., 2013), while point scale observational studies have documented reduced melt below a critical thickness of few centimeters of debris (Loomis 1970; Khan 1989; Kayastha et al., 2000; Nicholson and Benn 2006; Lambrecht et al., 2011; Chand et al., 2015).

A number of studies have since investigated melt of debris-covered tongues in detail. Studies in the Alps and HMA have shown that energy balance models perform well to estimate melt at the point scale. However these models are very sensitive to thickness, thermal conductivity and surface roughness of the debris layer, all of which are difficult to measure (Nicholson and Benn 2006; Reid and Brock 2010; Rounce et al., 2015). A number of studies have also observed and modeled melt of supraglacial ice cliffs (Sakai et al., 2002; Steiner et al., 2015; Brun et al., 2016; Buri et al., 2016a) and ponds (Sakai et al., 2000; Miles and Arnold, 2016; Watson et al., 2016), which are common surface features on debris-covered tongues, especially in the Himalaya. Around these features melt intensifies considerably, but they cover only a relatively small area of the total tongue (Steiner et al., 2019).

A distributed energy balance model, based on the point scale model developed on Miage Glacier by Reid and Brock (2010), has since been deployed on the same glacier in the European Alps (Fyffe et al., 2014; Shaw et al., 2016) and on a nearby partially debris-covered glacier (Reid et al., 2012). Fyffe et al. (2014) found that sub-debris melt is only sensitive to changes in temperature in the upper parts of the tongue where debris is thin, but not particularly sensitive to lapse rates of temperature or wind used to distributed these climatic variables over the complete surface. Shaw et al. (2016) also found the sub-debris melt at locations where the debris thickness is small to be sensitive to lapse rates, which corresponds to the local sensitivity to a temperature change. Both studies used an uncertain coarse debris thickness estimate derived from thermal imagery (following Foster et al., 2012) and 30 m DEMs. As a result, such studies fail to account for local variabilities of climatic variables as well as topographic controls. For example, within a 30 m DEM cell elevation differences of up to 10 m frequently occur due to the hummocky terrain characteristics of most debris-covered tongues.

Carenzo et al. (2016) proposed a simpler index model, which enables the calculation of melt below debris simply by combining temperature, solar radiation and debris thickness data. Ragettli et al. (2015) applied the same approach on Lirung Glacier for a hydrological model. Both studies lacked high resolution debris-thickness data, and accuracy of the results has not been validated with datasets of mass loss. Such index models are, however, extremely useful for application in hydrological models as they are less data intensive than energy balance approaches and computationally inexpensive.

Local investigations of surface elevation changes with satellite (Ragettli et al., 2016) and UAV imagery (Immerzeel et al., 2014a; Kraaijenbrink et al., 2016a; Wigmore and Mark 2017) show melt rates to be highly heterogeneous on debris-covered tongues, most plausibly explained by the occurrence of ice cliffs and supraglacial ponds as well as by heterogeneous debris thickness.

Here we aim to combine these two approaches, namely modeling of melt with an energy balance approach and validating the results with high resolution elevation data. We use climate data collected on the glacier in 2013 as well as data on the variability of air and surface temperatures (Steiner and Pellicciotti 2016; Kraaijenbrink et al., 2018), surface roughness (Miles et al., 2017a), debris thickness (McCarthy et al., 2017; Nicholson et al., 2018) and wind and debris properties. This allows us to run an energy balance model at high spatial (10 m) and temporal (1 h) resolution. We compare these results to downwasting rates derived from bi-annually obtained DEMs at the glacier (Kraaijenbrink and Immerzeel 2020). We specifically attempt to 1) assess the suitability of an energy balance model to represent sub-debris melt in time and space for a Himalayan glacier, 2) determine the sensitivity of such models to important, but often difficult to observe variables, including climatic variables, debris thickness and conductivity, and 3) to compare a simple temperature index model for debris-covered glaciers that is suitable for inclusion in catchment scale hydrological models with the detailed energy balance model results.

STUDY AREA AND DATA

Our study area is the Langtang catchment in the Nepalese Himalaya (28.2°N, 85.6°E), which extends over an area of 560 km^2 (upstream of the confluence with the Trisuli river), approximately 30% of which is glacierized (**Figure 1B**). Debris cover accounts for approximately 25% of the total glacierized area (Ragettli et al., 2016). This study focuses on Lirung Glacier, where most data in recent years has been collected (6.5 km^2, ~16% debris-covered, 4,044–7,130 m above sea level (a.s.l.)). The tongue is covered in continuous debris below the ELA, with a number of ice cliffs and ponds on the surface (Steiner et al., 2019). The local climate is dominated by monsoon circulation, with 68–89% of the annual precipitation falling between June and September (Immerzeel, et al., 2014b), with a very rapid decrease in temperature, humidity and precipitation from the end of August until the end of October. The up-valley winds typically transport moisture to higher altitudes resulting in condensation and overcast conditions in the afternoon. Due to the thick and dark debris cover, surface temperatures increase well beyond air temperatures during the day (Steiner and Pellicciotti 2016).

Climate Data

Meteorological measurements are available from an automatic weather station (AWS) installed on the glacier for multiple years (LIR1, 28.2349°N, 85.5613°E, 4,195 m; LIR2, 28.2326°N, 85.5621°E, 4,075 m; LIR3, 28.2396°N, 85.5571°E, 4,200 m) as well as from an off-glacier location (Kyanjing, 28.2108°N, 85.5695°E, 3,862 m, **Figure 1B**). All sensor specifications are shown in **Table 1** and measurement periods in the **Supplementary Table S1**. The locations of measurements are marked in **Figure 1A**. The surface temperature of the debris at the AWS location was derived from outgoing longwave radiation, assuming a debris emissivity of 1.

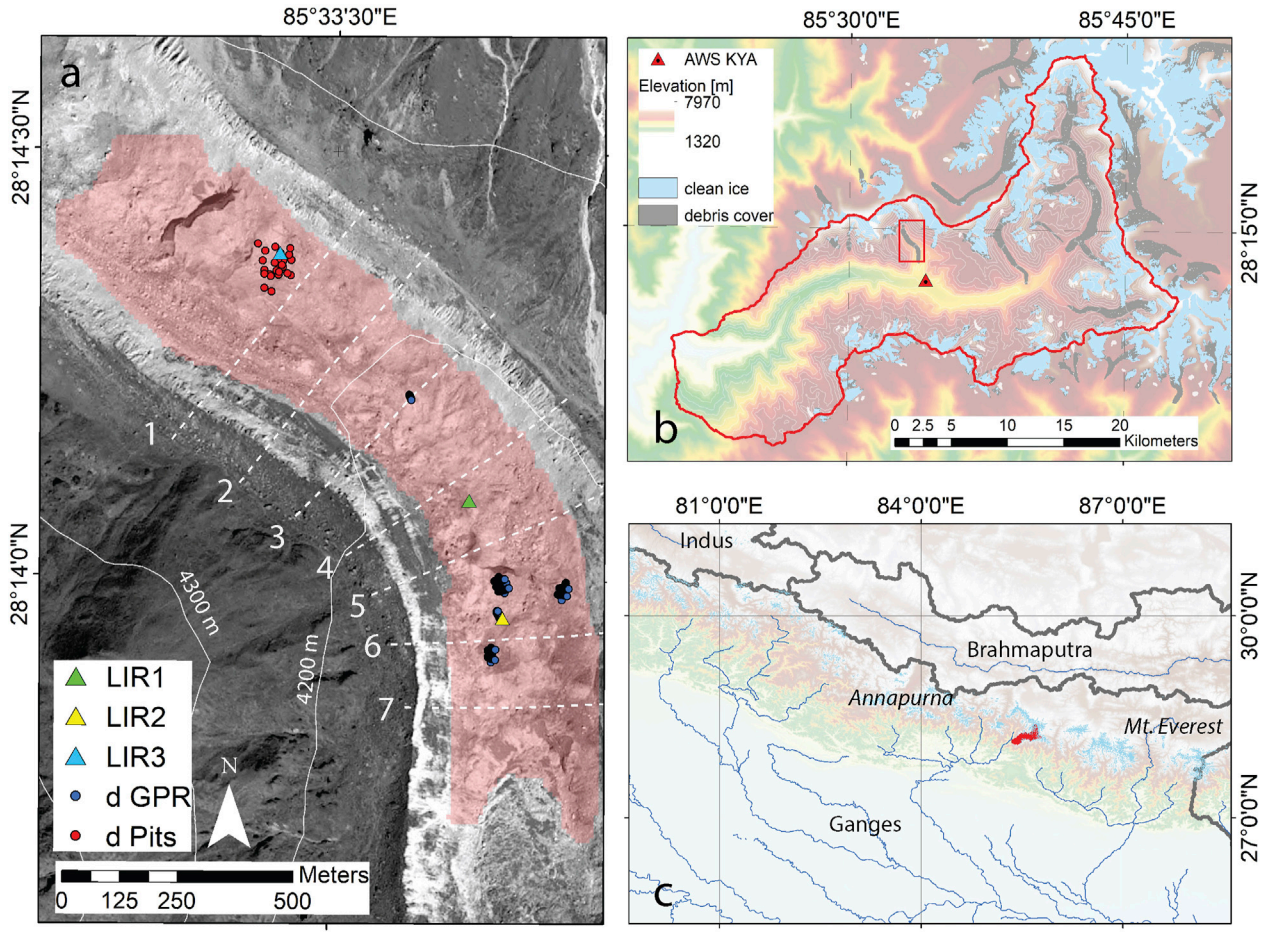

FIGURE 1 | (A) Overview map of the study site, showing the ablation tongue with the locations of atmospheric measurements (LIR1, LIR2, LIR3) as well as debris thickness measurements by GPR (d GPR) and excavation (d Pits). The red shaded area shows the model domain in 2013, where mass loss measurements are available. The image shows the part of the tongue where continuous debris is observed. The white dashed lines show the flux gates (used for the calculation of emergence velocity (see **Supplementary Material**). **(B)** Langtang catchment, with all debris-covered glaciers shaded grey, and the location of the Kyanjing AWS (AWS KYA) south of Lirung Glacier. **(C)** Location of Langtang catchment in the Central Himalaya.

TABLE 1 | Sensor specifications for the AWS off-glacier (Kyanjing) and on-glacier locations. Climate data at LIR3, used to validate the usability of off-glacier climate data, were collected with a WS500-UMB.

	Height [m]	Sensor	Manufacturer	Range	Accuracy
SW ↑↓	2	CNR4	Kipp&Zonen	305–2, 800 nm	±10% (day)
LW ↑↓	2	CNR4	Kipp&Zonen	5–50 µm	±10% (day)
RH_{air}	1.90	MP-103A	Rotronic	0–100%	±0.8%
T_{air}	1.90	MP-103A	Rotronic	−50° to +100°C	±0.1°C
u	2	WM05103	CS		±0.3 m/s
T_{deb}	Multiple	PT100/3 + HOBO U23	CS + Onset	−200–600°C/-40–70°C	±0.1°C/± 0.21°C
Surface height	1.38 m	SR-50 (UDG)	CS	−45–50°C	±1 cm/± 0.4% of distance to target

CS stands for Campbell Scientific; UDG stands for ultrasonic depth gauge.

Debris Data

Debris thickness measurements of Lirung Glacier are available from ground-penetrating radar (GPR) measurements in 2015 (McCarthy et al., 2017), as well as from 27 pit measurements between 2016 and 2017 (**Figure 1A**). These measurements are aggregated to the model resolution (10 m) and used to validate the debris thickness estimate.

Measurements of debris temperatures are available from all three locations on Lirung Glacier, covering varying depths. Debris densities, porosity and volumetric soil moisture were measured

by taking 55 samples at varying depths in the 27 pits in October 2016 and April 2017. Samples were taken with a 100 ml soil corer for the fine textured layers and were dried for 24 h and weighed and sieved in the lab.

Unmanned Aerial Vehicle Data

Elevation data of both glacier tongues are obtained from co-registered orthomosaics (0.1 m resolution) and DEMs (0.2 m) derived from multiple UAV flights with an optical camera (**Supplementary Table S1**). The DEMs were resampled to 10 m resolution and corrected for flow. From the same flights, velocities were derived which, in combination with modeled ice thickness, were used to compute emergence velocities over the glacier tongue (see Section 2 in **Supplementary Material**). We refer to previous studies on the generation of DEMs and velocity products (Immerzeel, et al., 2014a; Kraaijenbrink, et al., 2016b).

METHODS

Mass Loss Data

We derived mass loss by comparing the DEMs of two consecutive timesteps that were corrected for horizonal flow and the emergence velocity. To correct for emergence velocity, we placed fluxgates perpendicular to the flowline at approximately 500 m distance (**Figure 1**) and used modeled ice thickness data (Farinotti et al., 2019) and UAV-derived flow velocities, determined similarly as in Kraaijenbrink et al. (2016a). We then calculate emergence velocities for the resulting segments and correct the mass loss product accordingly. Average emergence over the model time period in 2013 is estimated to be small (approximately 0.07 m averaged over the model domain over the 157 days, see **Supplementary Table S2**). Using the individual DEM uncertainties (0.25 m, Immerzeel et al., 2014a; Kraaijenbrink and Immerzeel, 2020) we estimate the uncertainty of the mass loss product to be 0.35 m.

Debris Thickness

Deriving debris thickness in space is challenging and several studies have attempted this at the glacier scale. Foster et al. (2012) initially proposed to derive thickness from thermal imagery, following the logic that the energy absorption by the glacier ice underneath would be reflected more in the surface temperature of a thin than of a thick debris layer. Some studies build on this approach (Rounce and McKinney 2014; Schauwecker et al., 2015; Kraaijenbrink et al., 2017) but little validation data exists and uncertainties remain large, because the signal saturates at thicknesses over ~30 cm and other factors drive the surface temperature variation, e.g., shading, moisture and spatial variation in surface energy balance components. Secondly, Rounce et al. (2018) used the inversion of an energy balance model to derive debris thickness. Finally, it is also possible to use observed mass loss data and invert the Østrem curve (Rounce et al., 2018). While both latter approaches show promising results, inverting the Østrem curve is considerably less computationally intensive and is used in this study (**Eq. 1**). As we perform this analysis using mass loss data from 2016, while we apply the energy balance model in 2013, we are able to produce an independent debris thickness map. To create an average Østrem curve we use data from all currently published studies that include both debris thickness as well as melt rates. The following equation is solved at each individual pixel:

$$d = \left(\frac{(\dot{m}/m_c)}{a}\right)^{1/b}, \tag{1}$$

where d is the debris thickness [m], $\dot{m}$ is the UAV-derived melt rate [m yr^{-1}], m_c is the melt rate [m yr^{-1}] at critical thickness (2 cm) over the same period as the mass balance was derived and a [m^{-1}] and b [−] are parameters. While both the critical thickness and m_c can in reality be expected to vary over the glacier, we chose to calculate m_c with the measured fluxes at the AWS for the fixed critical thickness, in order to avoid introducing unquantifiable errors into our procedure. Running 100 simulations only varying parameters within their uncertainty (see Section *Debris Properties and Conductivity*) results in m_c = 0.04 m d^{-1} (σ = 0.01 m d^{-1}).

Using velocity and emergence-corrected mass balance data for the monsoon season 2016, in conjunction with the mean Østrem curve, we then derive a distributed map of debris thickness. While strictly speaking this debris thickness map only applies for a specific time step, we argue that due to the low surface velocities of Lirung Glacier (with maxima of ~2 m a^{-1}) and the resolution of the model (10 m) it is reasonable to apply it ± 3 years from the date of acquisition.

Energy Balance Model

The sub-debris melt model is based on earlier work by Reid and Brock (2010), which numerically estimates the surface temperature of the debris by considering the balance of the heat fluxes at the air-debris interface and melt is calculated by heat conduction through the debris. One advantage of this approach is that it does not require surface temperature as an input, a variable that is notoriously difficult to obtain accurately in space (Steiner and Pellicciotti 2016; Kraaijenbrink et al., 2018). The energy balance $F(T_S)$ at the air-debris interface can be written as

$$SW\downarrow - SW\uparrow + LW\downarrow - LW\uparrow(T_S) + H(T_S) + LE(T_S) + G(T_S) = 0$$
$$or\ F(T_S) = 0 \tag{2}$$

where T_s is the surface temperature, $SW\downarrow\uparrow$ is the incoming and outgoing shortwave radiation, $LW\downarrow\uparrow$ is the incoming and outgoing longwave radiation, H and LE are sensible and latent heat flux respectively and G is the ground heat flux through the debris. We ignore fluxes from precipitation in this work, as on-glacier measurements do not exist and the fluxes are often considered negligible.

We then solve T_s using a Newton-Raphson scheme

$$T_S(n+1) = T_S(n) - \frac{F(T_S)}{F'(T_S)} \tag{3}$$

where $F'(T_S)$, the derivative of the total surface flux, is calculated by the central difference method. The initial estimate for $T_S(n=0)$, is always chosen as the air temperature T_{air}, and **Eq. 2** is subsequently iterated until $T_S(n+1) - T_S(n) < 0.01$. Iterations are stopped when n reaches 100 or if the temperature gradient in the topmost debris layer exceeds 5°C cm^{-1}. This is rarely the case but ensures that the surface does not heat up to unrealistic values, which would drive sensible heat and outgoing longwave radiation fluxes to unrealistic levels.

Incoming solar radiation $SW\downarrow$ is taken from measurements and corrected for local topographic shading using the initial DEM. Shading is calculated following the approach in Buri et al. (2016b) in which the view factor is calculated, i.e. the fraction of the sky blocked by surrounding topography is calculated. Considering the actual view factor at the AWS where radiation is measured, the $SW\downarrow$ is corrected using the cell-specific view factor. Outgoing shortwave radiation $SW\uparrow$ is computed using a constant albedo α_d determined from on-glacier measurements. Incoming longwave radiation $LW\downarrow$ is taken from measurements wherever available and otherwise computed using a model developed for the Himalaya (Kok et al., 2019). Contrary to the original model, which used stability corrections based on the Richardson number, we calculate sensible and latent heat flux only using a bulk transfer coefficient (Nicholson and Benn 2006; Cuffey and Paterson 2010), which was found to be more appropriate compared to direct measurements of turbulent fluxes (Steiner et al., 2018). Since the specific humidity of the debris surface is not known, and will remain difficult to derive in space and time, it is derived based on a relation with surface temperature (Steiner et al., 2018).

Debris Properties and Conductivity

The conduction from the air-debris to the debris-ice interface can be calculated from a heat-conservation equation based on Fourier's law with the partial derivatives of temperature $T_{i,s}$

$$\rho_d c_d \frac{\delta T_{i,s}}{\delta t} = \frac{\delta}{\delta z}\left(k_d \frac{\delta T_{i,s}}{\delta z}\right) \quad (4)$$

where i denotes time t, and s denotes depth z, and ρ_d, c_d, and k_d are density, specific heat capacity and thermal conductivity of the debris, respectively, all assumed to be constant with depth and over time. The equation is solved numerically by dividing the debris layer in N layers of 1 cm each and taking the surface temperature T_s and the ice temperature T_i as boundary conditions. For cases where the debris layer is thinner than 5 cm, the number of layers is fixed to 5. For a full description of the numerical solution see (Reid and Brock 2010).

The effective thermal conductivity of debris is calculated using the density of the debris pack

$$k_d = \kappa\left(\rho_r c_r(1-\phi_d) + \left(\rho_w c_w \frac{\theta}{\theta_{sat}} + \rho_a c_a\left(1-\frac{\theta}{\theta_{sat}}\right)\right)\phi_d\right) \quad (5)$$

where κ [m^2 s^{-1}], is the apparent thermal diffusivity determined from profiles of debris temperature collected at multiple sites and times, following the same approach as described in (Conway and Rasmussen 2000). We only use measurements during the night (20:00 to 07:00) to avoid inversions. ρ_r is the density of the actual rock making up the debris [2,650 kg m^{-3}, considering the region mainly consists of metamorphic gneiss (Macfarlane et al., 1992)], c_r is the specific heat capacity of rock (890 J kg^{-1}K^{-1}) and ϕ_d is the debris porosity, which we determine from field measurements [−]. $\rho_{w/a}$ are density, and $c_{w/a}$ the specific heat capacity of water and air, respectively. θ is the soil moisture [m^3 m^{-3}]. The second term of the equation describes the conductivity through the space between the debris, and can be set to fully saturated ($\theta = \theta_{sat} = 0.2$) or completely dry ($\theta = 0$). As moisture changes in space, depth and time, it likely is the biggest driver of uncertainty for calculated conductivity.

To characterize the debris properties in depth we also determined the grain size distribution for 30 samples from different depths at the 27 pit sites around LIR3. These samples exclude rocks larger than 5 cm.

Uncertainty due to spatial and temporal variability in all of the parameters associated to the debris, most importantly the thermal conductivity, are accounted for by a Monte Carlo simulation in which multiple realizations of the model with random combinations of the input parameters are performed. The parameter space and distribution type are based on field data. All parameters and their ranges used in this study are detailed in **Table 2**. To assess the ability of the model to reproduce mass loss accurately we run a number of simulations. First, the model is run at the location of the AWS where climate data and debris thickness are well constrained and we only vary debris thermal conductivity (which is dependent on porosity, soil moisture and diffusivity), debris density and surface roughness using 1,000 random parameter sets. Secondly, for 64 locations where debris thickness has been measured 1,000 simulations are run where, in addition, debris albedo, air temperature, relative humidity of the air, wind speed and incoming longwave radiation are varied within the expected range of uncertainty. This allows us to discuss the sensitivity of the energy balance model to these variables and constrains the number of model runs required for all pixels to just 50 realizations by only varying debris thermal conductivity. Although the model is coded to run in parallel, performing 1,000 realisations on each individual pixel for Lirung Glacier for one melt season would take >2 weeks to execute on eight cores, so increasing the computational efficiency by reducing the parameter space is a helpful way forward for multi-annual and regional applications.

Index Models

A variety of index models are used in literature to calculate melt on clean ice glaciers, most commonly relying on air temperature only (Hock 1999), i.e., a temperature index model, and occasionally also considering incoming solar radiation (Pellicciotti et al., 2005), i.e., an enhanced temperature index model. The latter approach was adapted for a debris-covered glacier (Carenzo et al., 2016) and this approach has also been applied on Lirung Glacier in a catchment scale study (Ragettli et al., 2015). As energy balance studies are generally computationally more expensive and rely on more input data, we compare both approaches and test the model performance when only using

TABLE 2 | Constants used in the study and the range used for the uncertainty analysis.

Constant	Symbol	Unit	Value	Range	References
Atmospheric					
von Kármán constant	K	[–]	0.41	–	
Stefan-Boltzmann constant	Σ	[W m^{-2} K^{-4}]	5.67 10^{-8}	–	
Debris emissivity	ε_d	[–]	1	–	Steiner et al. (2018)
Roughness length of momentum*	z_0	[m]	0.03	0.005–0.5 (lognormal)	Miles et al. (2017a)
Roughness length of temperature	z_{0t}	[m]	0.05*z_0	–	–
Specific heat capacity dry air	c_{ad}	[J kg^{-1} K^{-1}]	1,005	–	–
Debris albedo*	α_d	[–]	0.13	±0.03 (normal)	this study
Debris					
Debris porosity*	ϕ_d	[–]	0.44	±0.07 (normal)	this study
Specific heat capacity rock	c_r	[J kg^{-1} K^{-1}]	890	–	Nicholson and Benn (2006)
Density of rock	ρ_r	[kg m^{-3}]	2,650	–	
Density of water	ρ_w	[kg m^{-3}]	999.7	–	
Density of air	ρ_a	[kg m^{-3}]	0.819	–	
Specific heat capacity water	c_w	[J kg^{-1} K^{-1}]	4,181.3	–	
Thermal conductivity debris*	k_d	[J kg^{-1} K^{-1}]	2.03 (wet)	0.95–3.00	this study
			0.85 (dry)	0.40–1.26	
			1.29 (all)	0.66–2.01 (normal)	
Thermal diffusivity debris	k	[m^2 s^{-1}]	6.41 10^{-7} (σ = 2.21 10^{-7})	–	this study
Debris moisture	θ	[m^3 m^{-3}]	0.09	±0.05	this study
Ice temperature	T_i	[K]	273.15	–	

*Ranges of variables marked * are directly used in the Monte-Carlo analysis of the energy balance model.*

data from an off-glacier station. In the simpler temperature index model, melt m [mm w.e. h^{-1}] is calculated as

$$m = TF\,T_{air}\left(t - lag_T * d\right) \quad (6)$$

where T_{air} [°C] is the air temperature at time $t–lag_T*d$, where d [m] is debris thickness and lag_T [h m^{-1}] is the time per unit distance it takes for the energy flux to travel through the debris pack. TF is the temperature factor calculated as

$$TF = TF_1\,d^{TF_2}, \quad (7)$$

with TF_1 and TF_2 being two free parameters to be calibrated.

To test the suitability of the model proposed in Carenzo et al. (2016), we also use

$$m = TF\,T_{air}\left(t - lag_T * d\right) + SRF\,(1-\alpha)\,SW{\downarrow}\left(t - lag_{SW} * d\right) \quad (8)$$

where SRF is the radiation factor computed as $SRF_1\,e^{SRF_2 d}$, with SRF_1 and SRF_2 being two additional free parameters. $SW{\downarrow}$ [W m^{-2}] is incoming solar radiation, α [–] albedo of debris and lag_{SW} the time lag as described above. We refer to the two equations as dTI (for the temperature index model) and dETI (for the enhanced model) respectively.

RESULTS AND DISCUSSION

Debris Properties

Debris composition is very variable across the glacier and with depth. Surface cover ranges from loose boulders to sandy patches and the surface properties do not necessarily indicate a vertical consistency in debris texture (**Figure 2**). There is a tendency for debris to become finer towards the ice (**Figure 2F**, Naylor, 1980). In some pits (**Figures 2C,E**) a water table of ~5 cm above the ice, with a very weak current of melt water with suspended sediments, was observed. Reworking by ice flow, slumping of debris due to collapsing cliffs and channels (Benn et al., 2012; Buri et al., 2016a; Miles et al., 2017b) and deposition of material eroded from the surrounding moraines (Woerkom et al., 2019) continuously alters the composition. We use point scale observations over limited periods of time to derive a reasonable range of debris thickness and debris conductivity used in the model.

Debris thickness measurements derived from GPR (McCarthy et al., 2017) and debris pits, although measured at different locations, exhibit similar mean values (0.84 and 0.82 m respectively) with minimum depths at 0.11 and 0.4 m and maximum depths at 2.3 and 1.6 m, respectively. Both distributions show a log-normal distribution, corresponding to observations of thickness on other glaciers (see Nicholson et al., 2018). Hence, for the Monte Carlo runs, we use a set of debris thicknesses that are sampled from a log-normal distribution, with a mean of 0.84 m and minimum and maximum values of 0 m and 2.7 m respectively, based on the GPR measurements.

To produce a distributed debris thickness map, we produced standardized Østrem curves from all available studies that show field measurements of ablation and debris thickness (**Figure 3A**). Assuming a critical thickness, where melt below debris is equal to bare ice melt, these curves derived in different climates can be compared. This still leaves a considerable spread, especially as the debris thickens.

The calibrated parameters for **Eq. 1** are a = 0.13 (σ = 0.002), and b = -0.52 (σ = 0.006), which is very similar to the curve used in Kraaijenbrink et al. (2017) that used a similar approach and data (including thermal Landsat bands, a = 0.11 and b = −0.51),

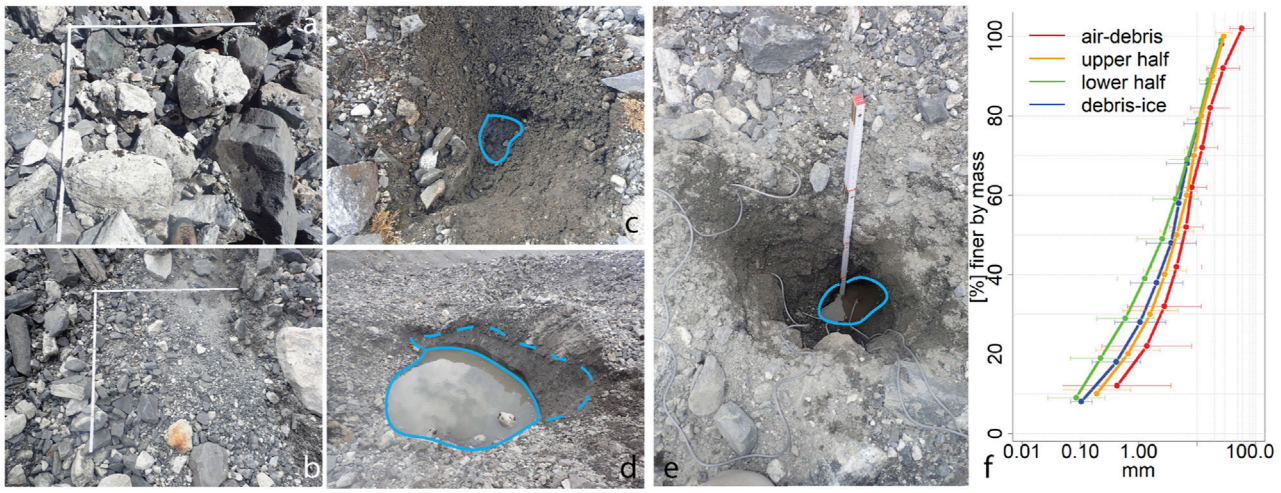

FIGURE 2 | (A) A typically coarse surface with little change between years and likely thick cover underneath, **(B)** example of short-length-scale transition between cobbles and sand. White ruler shows a 1 by 1 m area. **(C)** Surface with thin debris cover (~0.15 m) consisting of fine material, where melt water is surfacing (solid blue line). **(D)** Glacier ice (dashed blue line) appearing in a region of otherwise thick cover, with multiple pits in a 10 m radius of >1 m depth. **(E)** Melt water ponding in a deep pit (~0.65 m). **(F)** Grain size distribution of the debris pack, with samples from the debris surface, inside the debris pack (upper and lower half) and from just above the ice plotted separately.

but considerably different from two other studies that used a similar inversion but were based on local data (Ragettli et al., 2015; Rounce et al., 2018). The distributed map was produced using the difference between the DEMs in May and October 2016, corrected for emergence and aggregated to a 10 m product. All melt features not covered by debris (cliffs and ponds) as well as outliers (beyond the 5th and 95th percentile) were removed, so were pixels where mass loss was below the accuracy of the product (0.35 m) as well as individual pixels before aggregation that were thicker than 2 m. While thicknesses beyond 2 m may occur, just 0.5% of ~6,000 GPR data points and none of the pits are this deep. When aggregated to a 10 m resolution thicknesses over 2 m are hence even less likely. We then derived the thickness for the remaining pixels and interpolated over the complete domain by inverse distance weighted interpolation. Comparing the resulting map (**Figure 3C**) to point measurements (**Figure 3B**), shows an overall agreement, with no bias and an acceptable mean absolute error (MAE) of 22 cm. Debris thickness is generally thicker closer to the moraines due to a constant resupply from the moraines (Woerkom et al., 2019). It is especially thin at the terminus where bare ice appears as the tongue retreats rapidly, thickens in the lower part but thins again towards the accumulation are where it then gradually transcends into the bare ice area (**Figure 3C**). Most challenging however is that variability over relatively short length scales is high and can happen gradually or abruptly, with thickness differences in the range of 1 m over horizontal distances of 100 m on both Lirung Glacier and other field sites (see Table 2 in Nicholson et al., 2018). The uncertainty for individual pixels from the model logically remains considerable and is a result of the spread in the Østrem curves, the critical debris thickness and the uncertainty of the DEMs.

Measurements of debris temperatures at different locations and different depths provide largely similar results (**Figure 4**), suggesting that diffusivity through the debris is relatively constant in space even with differences in debris texture. Generally, temperatures are higher in the wet season, with the exception of 2013, where surface temperatures were in general higher but also sensors malfunctioned towards the end of the wet season. As a result, most data from the dry season in this year is from pre-monsoon, which is generally warmer. Measurements in the uppermost part of the debris pack also suggest that most of the diurnal variability is attenuated after 10 cm of debris. The mean peak temperature pattern at the top and bottom profiles of all years reveals that the transit time of the temperature peak is roughly similar in all profiles, ranging from 15.6 h m^{-1} in the wet season at LIR2 to 18.5 h m^{-1} in the wet season at LIR3.

From the temperature profiles we can calculate diffusivity in the wet (7.4×10^{-7} m^2 s^{-1}) and dry season (6.8×10^{-7} m^2 s^{-1}). This is similar to the values from Conway and Rasmussen (2000) (6 and 9×10^{-7} m^2 s^{-1}) and Nicholson and Benn (2013) (9.5×10^{-7} m^2 s^{-1} in the wet summer and 7×10^{-7} m^2 s^{-1} in winter) but much higher than values measured on likely drier surroundings in the range of 3–3.9 $\times 10^{-7}$ m^2 s^{-1} (Nicholson and Benn 2006; Juen et al., 2013). Recent investigations in the Everest region show similar gradients of temperature through the debris, suggesting that these profiles remain relatively stable throughout the season (Rowan et al., 2020). This space and time invariance provides some confidence in applying constant diffusivity values in distributed analysis.

Since the debris is never completely dry, its moisture content needs to be accounted for in the determination of thermal conductivity. Soil moisture measurements in a number of pits indicate a moisture content of 0.01–0.2 m^3 m^{-3} (μ = 0.09, σ = 0.05), where the maximum value corresponds to saturation of sandy soils. Highest variability can be found near the surface, due to its very variable composition (**Figures 2**, **5A**). The general distribution corresponds to typical soil moisture curves (e.g.

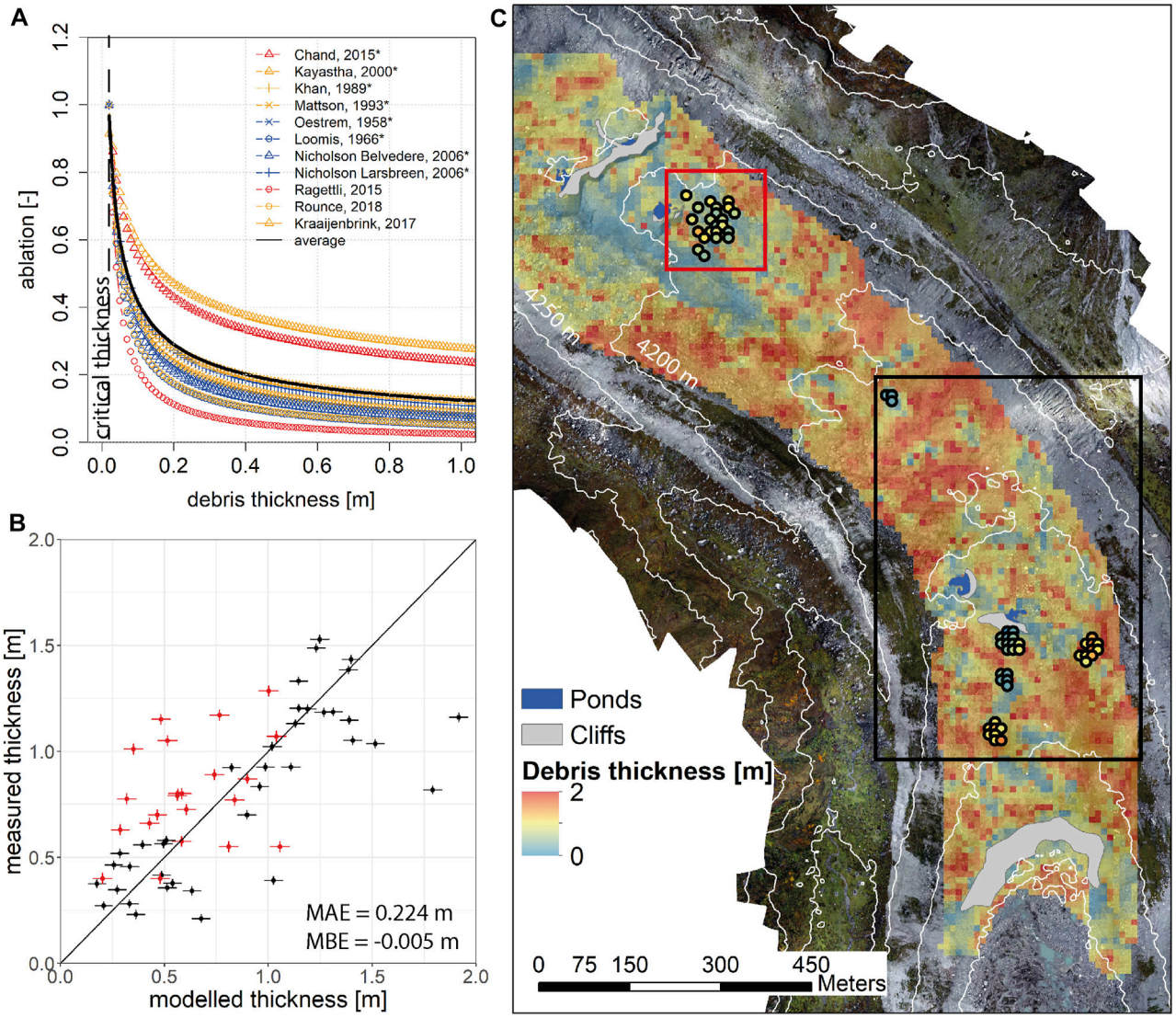

FIGURE 3 | (A) Standardized Østrem curves for all studies with field data (*) and three modeling studies. Only data from field studies was used to generate the average curve. The vertical dashed line shows the critical thickness, where melt is equal to a clean ice glacier in the same climate (2 cm). In red are studies from Lirung Glacier, yellow are from HMA, blue are studies from other regions. **(B)** Modeled compared to measured debris thickness at 10 m resolution, red are from pits and black from GPR measurements as noted by the squares in **(C)**. **(C)** Modeled debris thickness map. Points shown in the black frame are from GPR measurements, red frame denotes excavated pits.

Genuchten, 1980), with the peculiar case here that soil moisture at the bottom of the debris layer is higher due to melting ice, while close to the surface it is due to precipitation and condensation. Measured porosity on the glacier ranged from 0.30 to 0.59 (μ = 0.44, σ = 0.07), which corresponds to the only other two measurements from literature, namely a mean of 0.43 in Popovnin and Rozova, (2002) and a range between 0.19 and 0.6 in Collier et al. (2014). The actual debris density was between 1,300 and 1,950 kg m^{-3} (μ = 1,588 kg m^{-3}, σ = 175 kg m^{-3}), which corresponds well to the mean of 1,496 kg m^{-3} used in Reid and Brock (2010). Considering the large variability in space and depth, we use all diffusivity estimates and moisture data from literature and from this study to aggregate a reasonable range of conductivity for the model, shown as boxplots in **Figure 5B**. Note how assuming full saturation or complete dryness results in a very large range of conductivity values. The median conductivity of 1.29 J m^{-1} K^{-1} matches well with the few available direct measurements from our field site. Reported conductivity values are rare for specific seasons (Nicholson and Benn 2006; Nicholson and Benn 2013), but do exist for unspecified conditions (Conway and Rasmussen 2000; Reid and Brock 2010; Juen et al., 2013; Rounce et al., 2015). These reported values correspond well with the range in conductivity values that we have derived (**Figure 5B**).

Two main observations can be made from the grain size distribution (**Figure 2F**). First, the variability with depth is

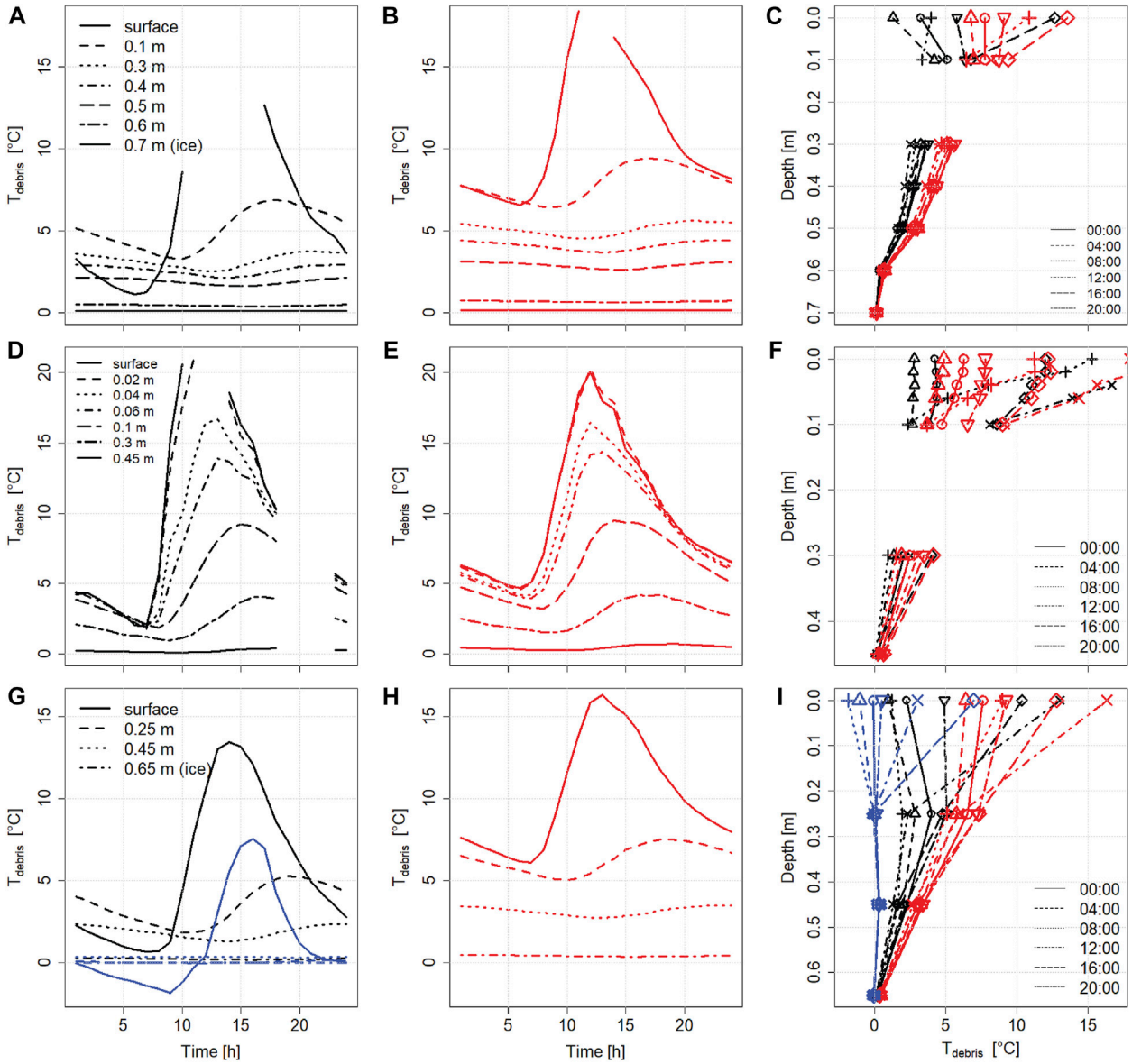

FIGURE 4 | Temperature profiles in debris measured at the AWS in 2012 [**(A–C)**, LIR1], 2013 [**(D–F)**, LIR2] and from 2017 [**(G–I)**, LIR3]. Blue is the winter season (1st January to 28th February), red the wet season (06/15 to 09/19) and black the dry seasons.

quite large, with finer sediments being more abundant in the lower part of the debris pack. Approximately 40% of the debris is sand, which results in a relatively high water retention capacity compared to gravel or small boulders. This results in an increase in conductivity compared to a drier coarse-texture debris pack by a factor of 2 (**Figure 4B**). Such considerations are essential to further drive development of more complex models that are able to incorporate moisture (Collier et al., 2014; Giese et al., 2020), but also for routing times of melt water from the glacier as melt water does not immediately become available to discharge. Second, due to this available water in the pores and relatively dense debris texture, the debris pack is largely frozen below a depth of 20 cm in winter. On Lirung Glacier this occurs specifically in winter (**Figure 4**). As temperatures become positive in spring at the surface, it takes up to a week to defrost the entire debris pack at depths of ~1 m. Although we can calculate the available energy for (re-)freezing our model cannot account for lateral or vertical transport of water within the debris and hence an appropriate quantification is impossible. However, melt estimates for the cold season are likely to overestimate actual rates, especially in spring, when this process is unaccounted for.

Climate Data and Resulting Uncertainties

Due to the heterogeneity of the debris surface, climate variables vary over the surface and errors are introduced due to the lapsing

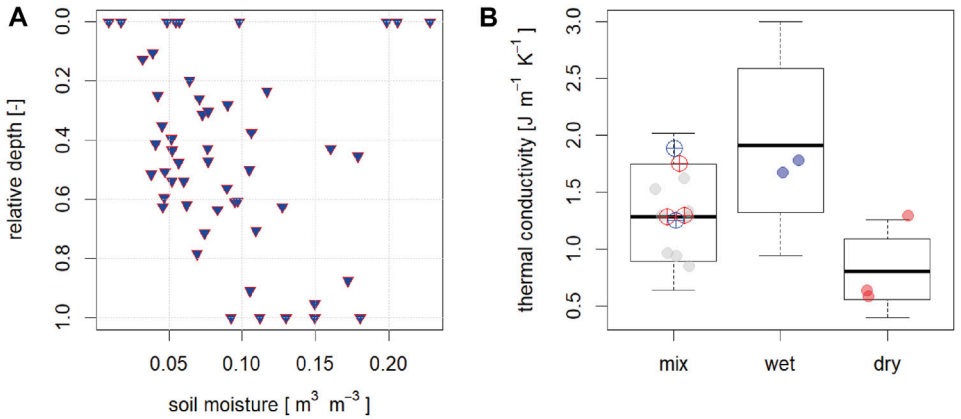

FIGURE 5 | (A) Soil moisture measurements from pits around LIR3. **(B)** Thermal conductivity calculated using temperature profiles and the moisture content. The box plots indicate the range of thermal conductivities as calculated using the range of diffusivities from literature and using the observed moisture range (mix), full saturation (wet) and completely dry debris assumptions (dry). Solid dots are values from literature, transparent crossed dots are calculated with diffusivity and debris moisture only from the observed field data (red—dry, blue—wet).

of variables from the location of weather stations to other parts of the glacier. By comparing climate data from three locations on the glacier, we assess the extent of this variability (**Figure 6**).

Variability in air temperature over debris cover was investigated for Lirung Glacier in earlier studies (Fujita and Sakai 2000; Steiner and Pellicciotti 2016). To evaluate the use of off-glacier measurements, we used a seasonally varying lapse rate (Heynen et al., 2016) up to the glacier snout combined with lapse rates for the glacier surface for the specific seasons (−0.005, −0.0066, and −0.0078°C m^{-1} for pre-monsoon, monsoon and post-monsoon respectively, Steiner and Pellicciotti, 2016). Lapsing temperature from an off-glacier station introduces an additional error on top of the spatial variability (**Figure 6**), resulting in a mean bias error (MBE) between 1 and 2°C. This is especially visible during the day and larger during the monsoon. We therefore use a conservative uncertainty range of 2°C for all air temperature values. This is especially relevant when using simpler index models that only rely on air temperature as a proxy for melt. The fact that we are able to reproduce air temperature reasonably well using this lapsing approach provides confidence in the use of a single AWS for deriving melt rates for multiple glaciers in a catchment.

While relative humidity also changes with elevation, the trend is less clear and variability is more impacted by local debris properties (Bonekamp et al., 2020). However, no measurements at different locations are available over the same period. Measurements at the off-glacier station are similar to on-glacier measurements with the exception of the monsoon season, in which the air is much more humid off-glacier at the Kyanjing station in the main valley. The root mean square error (RMSE) ranges between 10 and 20%. We use a conservative uncertainty estimate of 20% for the modeling.

Wind speed is also variable over the debris surface due to the hummocky terrain, but is approximately a factor 2 lower than at the off-glacier AWS, which is located in the exposed main valley (**Figures 1B**, **6**). While in 2012 and 2017 the AWSs were located on relatively exposed parts of the glacier, the station was situated in a depression from 2013 to 2014, resulting in a decrease of average wind speed by a factor of 3, which significantly affects the turbulent fluxes (Steiner et al., 2018). When using the on-glacier data from 2013 to drive the model, we allow wind speeds to vary by up to a factor of 2.5 to account for this variability.

Finally, incoming radiation is affected by the hummocky terrain as well. It causes parts of the surface to be shaded longer than more exposed sections and hence receive less direct incoming shortwave and longwave radiation. These sites also receive added longwave radiation from the surrounding debris. We apply the sky view factor relative to the location of the measurement of radiation for all pixels when running the energy balance. For the sensitivity analysis, we furthermore assume that the longwave radiation flux may vary by ± 50 W m^{-2} due to additional radiation emitted by the surrounding debris.

Albedo is relatively consistent between the 3 different locations on the glacier, with daily mean values between 0.12 and 0.16 during the dry seasons and values down to 0.06 on rainy days in the monsoon season, when debris is wet. The mean albedo ranges between 0.11 in 2012 and 0.13 in all other years. We therefore use a normal distribution with μ = 0.13 and the measured σ = 0.03 for the uncertainty analysis.

Energy Balance Model on the Point Scale

At the location of the AWS the energy balance can be validated accurately in 2013 as the climate data is available at that specific site and the surface elevation changes are continuously monitored during the first month. It also allows us to validate the performance of the model against measured surface temperature. **Figure 7A** shows modeled and measured mass loss at the location of the AWS. The modeled debris thickness for this location is 0.37 m, which corresponds to the 0.29 m measured at the location of the AWS and 0.45 m measured in another pit just 3 m away. This variability within a relatively small

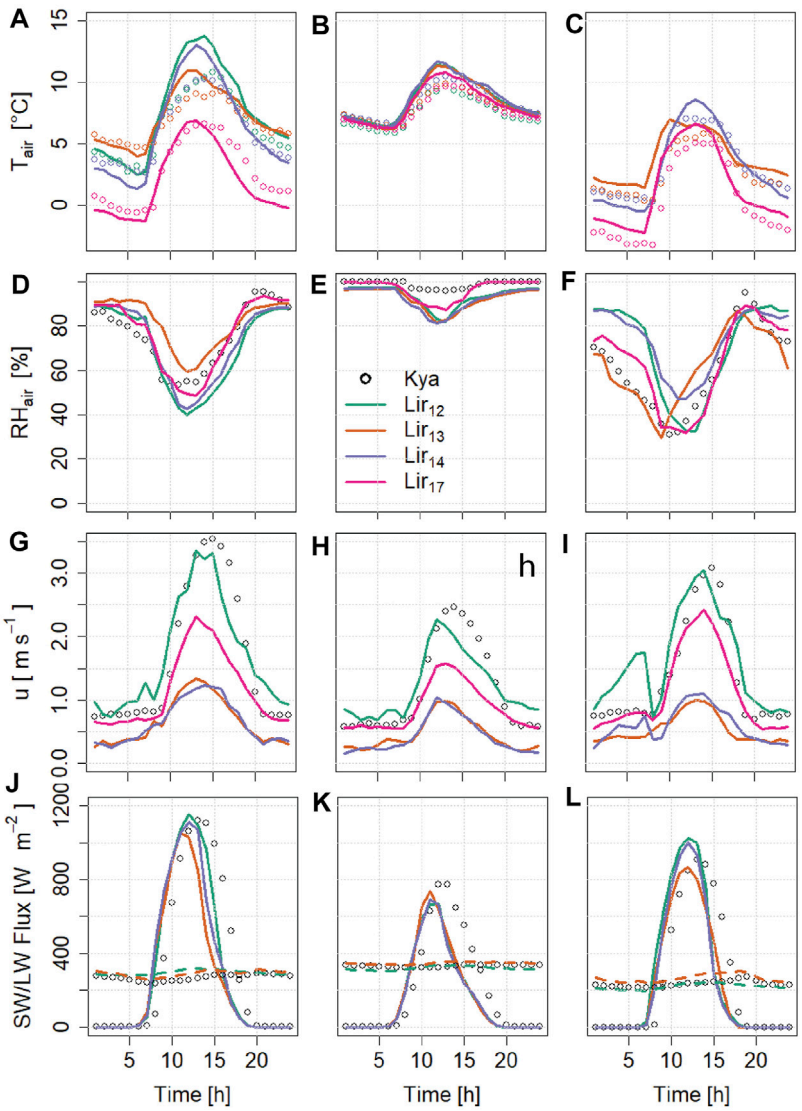

FIGURE 6 | Mean diurnal cycles for climate variables used in the energy balance, including air temperature **(A–C)**, relative humidity of the air **(D–F)**, wind speed **(G–I)** and incoming shortwave (solid lines) and longwave radiation (dashed lines, **(J–L)**). For air temperature the lapsed data from Kyanjing (Kya) to the respective on-glacier location is shown. Wind speed at Kyanjing is shown with a factor of 0.5. The three columns represent three seasons, pre-monsoon, monsoon and post-monsoon from left to right. Lir_{12-17} refers to the AWS on Lirung Glacier. Lir_{17} was operational from September 2016 to October 2018, while all other setups only measured during the monsoon in the respective year (see **Supplementary Table S1** for exact periods).

area is indicative of the spatial heterogeneity of debris thickness (Anderson and Anderson 2018; Nicholson et al., 2018).

In **Figure 7** we focus on the 25 model runs of 1,000 simulations that match observed mass loss (blue) or observed surface temperature (red) most closely. For surface temperature this was assessed by finding the time series that had the lowest combined MBE and RMSE and highest NSE. It is encouraging however, that the model also matches well with the independent measurement of surface height at the beginning of the season (**Figure 7C**). Unfortunately, the sensor also tends to tilt as debris moves which eventually caused it to fall over after June. **Figure 7B** shows the spread of the model parameters for the best performing runs. The range for conductivity values is large and the values are quite high, with an average of 1.6 W m^{-1} K^{-1}. The mean surface roughness value corresponds well with the observations from the very same location in 2014 (0.03 m) (Miles et al., 2017a). The model is relatively insensitive to debris density (**Figure 7B**).

Alternatively, model performance can also be assessed by comparing the modeled and measured surface temperature, which allows for an assessment of the model performance over time (Reid and Brock 2010). This works well for the AWS location, indicated by a mean Nash-Sutcliffe Efficiency (NSE) of 0.79 and a RMSE/MBE of 3.6°C/−0.4°C for the 25 best performing runs. While this approach is useful to evaluate the ability of the model to reproduce fluxes accurately, it depends

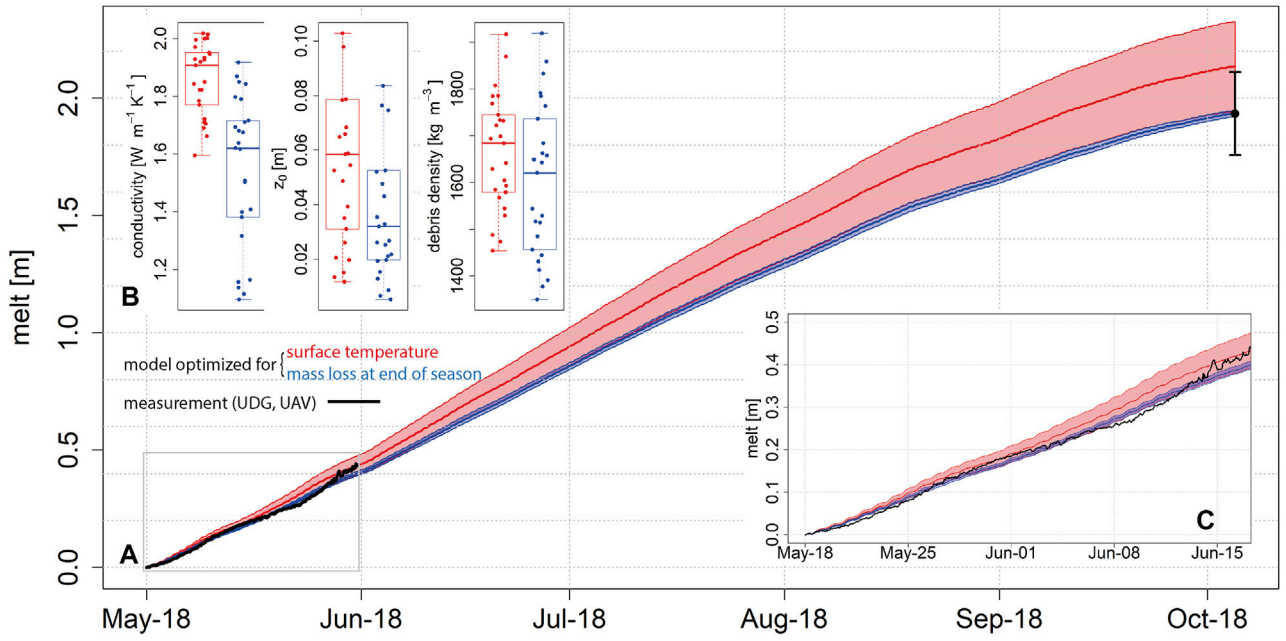

FIGURE 7 | (A) Modeled melt at the location of the AWS in 2013. The blue and red line and shaded area show the mean and standard deviation of the 25 best performing model runs (97.5th percentile) compared to the observed mass loss from the UAV and the observed surface temperature respectively. The error bar of the UAV measurement corresponds to the uncertainty of the DEM accuracy. The solid black line are hourly measurements from an ultrasonic depth gauge (UDG, **Table 1**), which only monitored for a limited time, shown in detail in **(C)**. **(B)** Conductivity, surface roughness and debris density for the 25 best performing model runs, once for optimization with UAV (blue) and once with surface temperature (red).

on the accuracy of the surface temperature measurements (Steiner and Pellicciotti 2016; Kraaijenbrink et al., 2018). The results presented here suggest that using either surface temperature or a single mass loss measurement as validation provides similar results. However, the model runs that correspond most closely to the surface temperature measurements overestimate the final mass loss (**Figure 7A**), the measurement from the local sensor (**Figure 7C**) and also tends to be on the upper end of resulting conductivity values (**Figure 7B**).

Irrespective of whether mass loss or surface temperatures are used for validation, the modeled surface temperatures agree well with the observed temperatures (NSE = 0.76/0.77, MBE = −0.2/1.1°C, **Figure 8**). However, the model fails to capture the very high peaks of surface temperature (>35°C) and overestimates temperatures on days when the observed values suddenly drop due to overcast conditions.

The net shortwave, longwave, latent and sensible heat fluxes are shown in **Figure 8**. Net shortwave radiation is the dominant flux. Net longwave radiation is consistently negative on clear days but becomes positive on overcast days. The sensible heat flux is consistently negative, while the latent heat flux is generally low and can be negative or positive. Modeled melt lags the energy peak by a couple of hours due to the delay of energy transfer through the debris. As a result, sub-debris ice also melts, when the surface energy balance is negative. This is in contrast to clean ice glaciers, where melt stops as soon as the net energy is below zero.

Energy Balance on the Distributed Scale

As a first step we applied the energy balance on all pixels where debris thickness observations were available (**Figure 9**). We selected the 25 simulations from the total of 1,000 that reproduced observed mass loss best. It is clear that the highest mass loss is observed for thin debris as expected. However, below half a meter of thickness there is a lot of variability in mass loss, as other drivers, such as moisture and debris texture become more important. Nevertheless, the model is able to reproduce the observed mass loss in nearly all cases, which indicates that all essential processes are incorporated.

The model is sensitive to all the parameters that were varied during the Monte Carlo runs, indicated by a relatively narrow range around the respective median (**Figure 9**). However, for debris density, surface albedo and surface roughness the optimal values are independent of debris thickness and therefore a constant value for all pixels can be assumed for these variables.

Of the climate variables the model is most sensitive to the potential variability in space and time of longwave radiation and slightly less sensitive to air temperature. Both these variables increase with increasing debris thickness. Relative humidity and wind speed on the other hand show no such trend and the observed value from a single location provides satisfactory results on the glacier scale.

Incoming longwave radiation from surrounding terrain plays a role since it directly adds energy to the surface. However, quantifying spatial patterns of longwave radiation on a hummocky surface is challenging. The uncertainty in observed

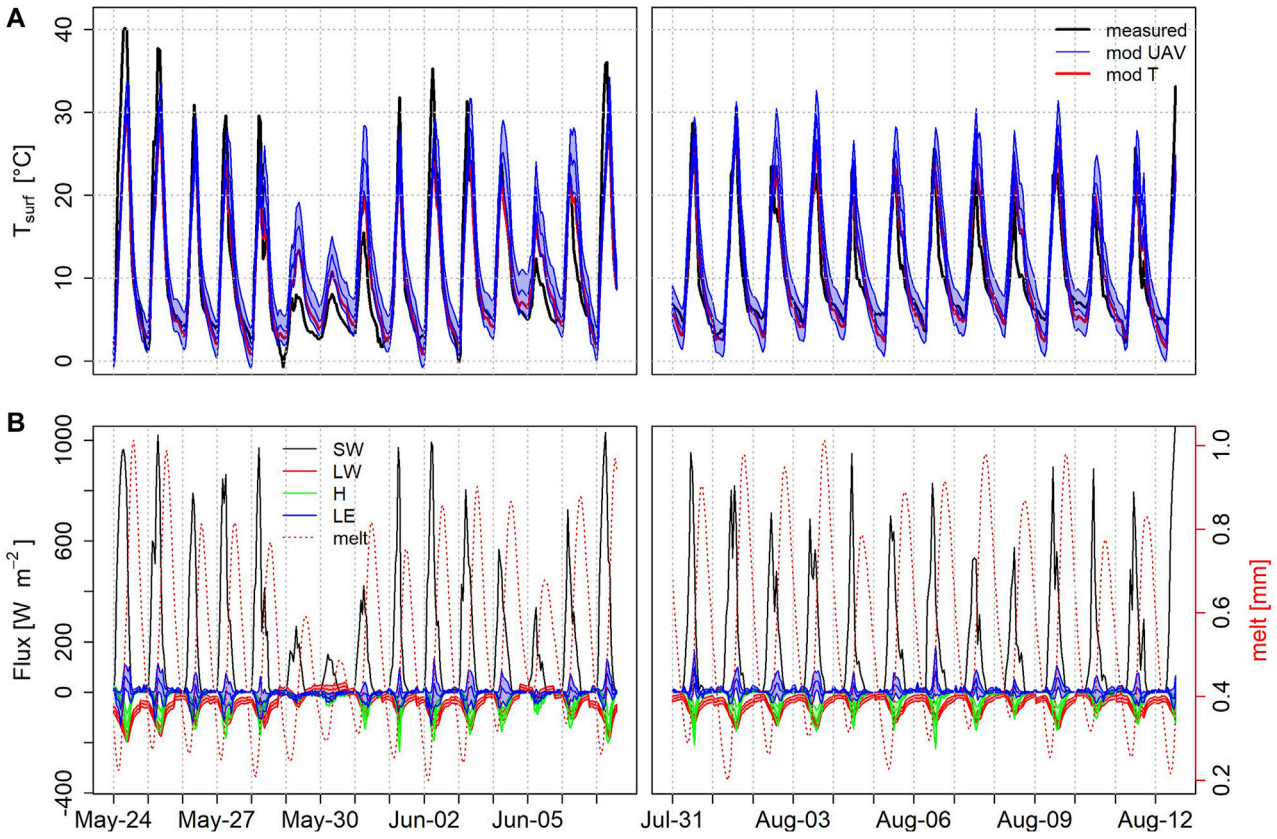

FIGURE 8 | Measured and modeled surface temperature of the debris at the AWS, with 'mod UAV' denoting the results that fit best with the UAV mass loss measurement and 'mod T' those fitting best with observed surface temperature **(A)**. Resulting (net) fluxes and melt rates based on the model **(B)**. The shaded area shows the range of results based on the 25 best performing model runs after comparison of the modeled mass loss with the measured mass loss (**Figure 7**).

surface temperatures (Kraaijenbrink et al., 2018) makes it even more difficult to quantify additional incoming longwave radiation in space.

For the fully distributed model, we only run 50 simulations per pixel in which we allow k_d to vary, the variable to which the model is particularly sensitive (**Figure 9**). Using constant parameters but a variable k_d, we model mass loss in space. We include pixels where melt was observed and where no cliffs or ponds were present at the beginning of the season.

Figure 10A shows the difference between observed and modeled melt, applying varying k_d values that fit most closely to the observed data. The blue and green boxplots in **Figure 10C** show the results aggregated for 100 m bins in distance from the terminus. The mean observed melt over the whole domain is 0.89 m (±0.76 m). Modeled melt using spatially variable conductivity is 0.77 m (±0.37 m) and using fixed conductivity is 0.88 m (±0.42 m). Observed high values cannot be reproduced by the model, which can be explained by mechanical processes of mass loss, i.e. slumping around cliffs and ponds as well as disintegration of subglacial structures. The high retreat rates at the terminus, where debris cover is present but thin and ice repeatedly collapses, are equally poorly represented. However, overall it is possible to reproduce observed melt rates well, with a RMSE and MBE of 0.29 and 0.04 cm d^{-1} respectively. The resulting k_d map (**Figure 10A**, inset) naturally follows melt patterns. Where melt is high but debris thick and surface features like cliffs and ponds are rare, k_d is high. Where melt is low, in this case the middle section of the tongue, very low k_d counter balances the energy input at the surface. Rather than reflecting actual k_d, the value here acts as a free parameter. However, these values do not only lie within the range of previously reported values for conductivity, they also have some physical merit. Thick and continuous debris can hold more moisture leading in turn to higher bulk k_d values. In the center part and the upper part of the modeled domain, debris is discontinuous and relatively thin, making the debris pack more susceptible to evaporative drying and drainage and hence decreasing the conductivity.

Distributed data of conductivity is however virtually impossible to retrieve, let alone accounting for its change in time. For practical applications, we need to assume a constant conductivity value in space and time. **Figure 10B** shows the results for the median k_d of 1.41 W m^{-1} K^{-1}. Results become less variable and as a result modeled rates in the central part are considerably higher than observed. This is notably also where observed mass loss was especially low even though a number of cliffs and ponds were present and emergence velocities are possibly higher than what we estimated. The RMSE increases

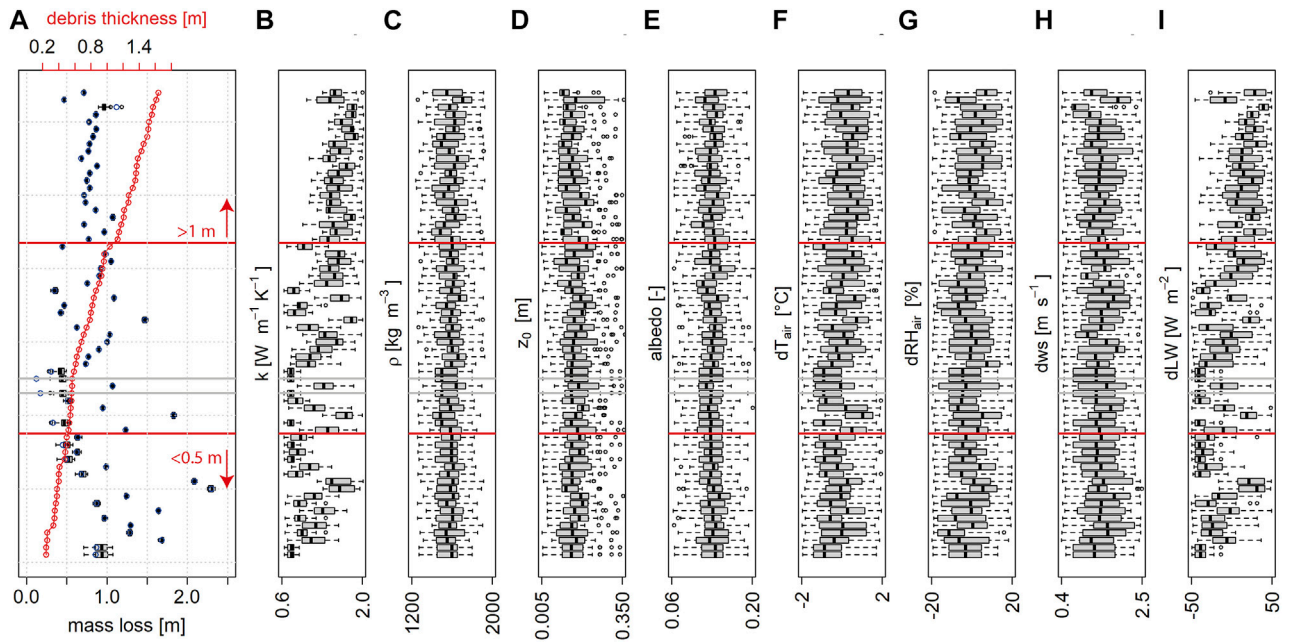

FIGURE 9 | (A) Modeled mass loss at locations where debris thickness observations are available. The boxplots cover the 25 model runs that most closely reproduce observed mass loss. **(B–I)** Range of variables (from left to right: debris conductivity, debris density, surface roughness, surface albedo, as well as uncertainty/spatial variability ranges for air temperature, relative humidity of air, wind speed and incoming longwave radiation from surrounding terrain). Grey solid horizontal lines show cases where the observed melt could not be reproduced with any parameter combination.

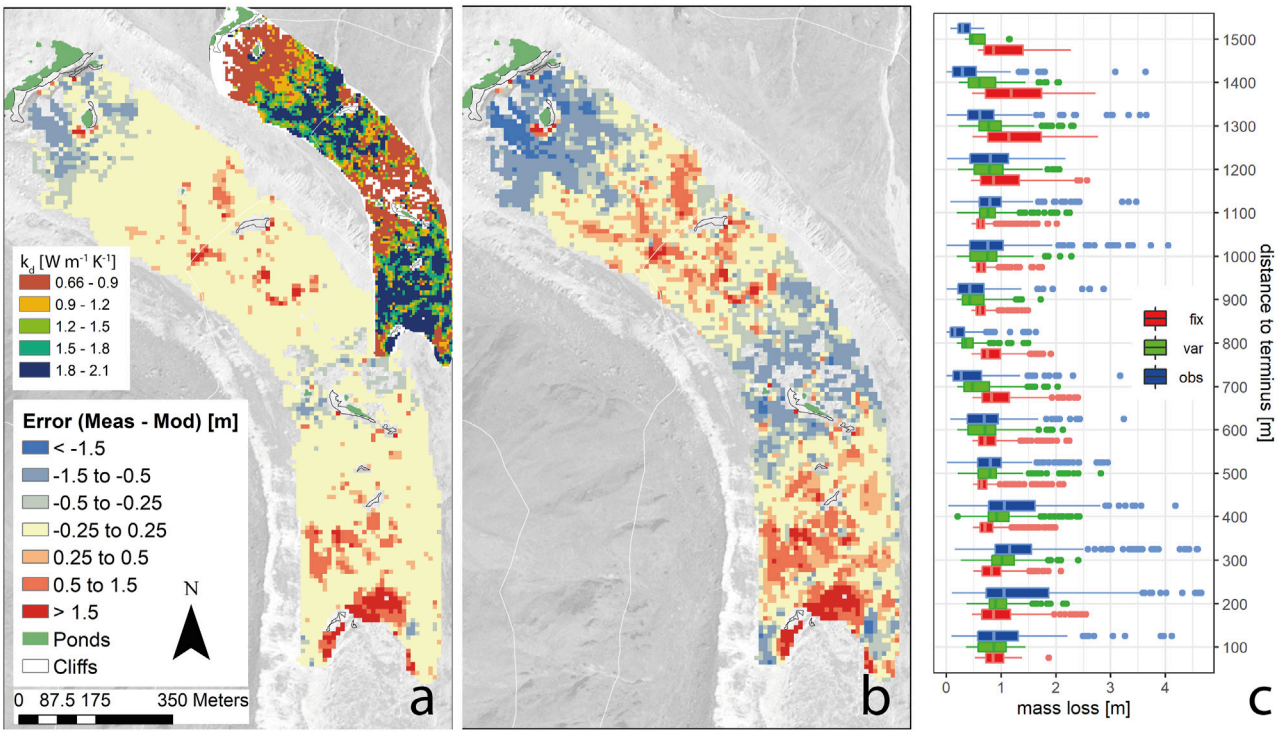

FIGURE 10 | (A) Difference between observed and modeled melt with variable (shown as an inset) and **(B)** constant conductivity k_d. **(C)** Melt over all pixels for the observed (obs), variable k_d (var) and fixed k_d (fix) case, binned in distance to the terminus.

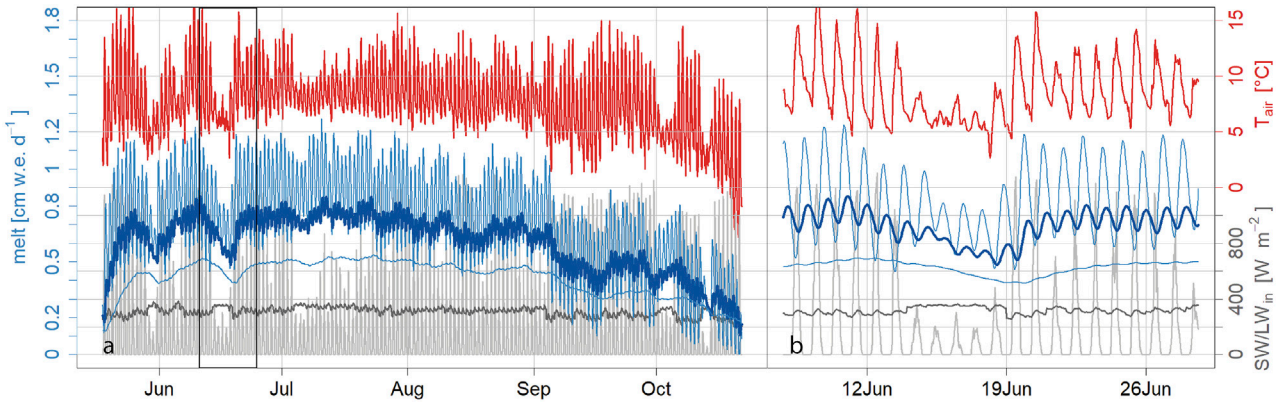

FIGURE 11 | (A) Mean hourly melt rates during the model period melt below average debris thickness (50–100 cm, thick dark blue line) as well as thick (>1 m) and thin (<0.5 m, thin light blue lines below and above). Additionally shown measured air temperature (red), incoming shortwave radiation (light grey) and incoming longwave radiation (dark grey). The black rectangle in panel a shows the boundaries of the inset of panel **(B)**.

subsequently to 0.47 cm d^{-1} but MBE remains low (−0.03 cm d^{-1}).

With the model we compute melt for all ~4,500 pixels of the debris-covered area of the glacier with a timestep of 1 h. In **Figure 11** the average melt rate below 0.5 m, between 0.5 and 1 m and above 1 m debris thickness is shown. Melt rates clearly follow the air temperature and solar radiation, albeit with a considerable lag (**Figure 11B**). Even for locations with debris thinner than 0.5 m, the melt peaks a few hours after the temperature peak. Three specific processes illustrate the effect of climatic drivers on temporal melt patterns below debris. Firstly, when there are a number of subsequent cloudy days with limited shortwave radiation (e.g. during the first half of July, **Figure 11A**), melt rates overall remain unaffected, however melt rates during the night under thinner debris surprisingly increase. This can be explained by the absence of radiative cooling during the night and the higher longwave radiation input from clouds. This results in a less negative or even positive net longwave radiation without a clear diurnal cycle (see May 30th in **Figure 8**). While the increase of longwave radiation seems small, it consistently increases the entire day, while the decrease of solar radiation only occurs during daytime. In addition, turbulent fluxes become less negative as radiative heating decreases (Steiner et al., 2018). Secondly, when air temperature and shortwave radiation decrease (**Figure 11B**) melt rates decrease everywhere, resulting in an overall decrease of meltwater output on the glacier scale. Thirdly, in the beginning of September the solar radiation remains consistently high and the daytime temperatures are similar to the monsoon. However due to the strong radiative cooling at night, temperatures drop considerably causing a decrease in melt. Nighttime temperatures therefore have an important effect on melt below debris.

We conclude that air temperature is a good indicator of both variability and magnitude of sub-debris melt rates in a monsoon climate, due to the interplay between shortwave radiation, longwave radiation and turbulent fluxes in the energy budget.

Sources of Uncertainty and Model Limitations

There remain several uncertainties and limitations that we can not address in further detail either because they play a less significant role in our field site or we lack the data to assess them reasonably. We address the issues of emergence velocity, melt at critical thickness as well as sub-debris melt under thin debris below.

The accuracy of observed melt from repeat DEMs depends on our ability to accurately estimate emergence velocity. Emergence velocity decreases towards the terminus and hence is relatively low for debris-covered tongues (Anderson and Anderson 2018; Brun et al., 2018). This is especially true for Lirung Glacier, where we only investigate the lower part of the tongue and where flow velocities are overall low and hence our confidence in melt estimates is large. Emergence velocity increases towards the ELA and hence our dependence on accurate ice thickness increases up glacier from the terminus. So far no reliable understanding of emergence velocity exists for the region that would help to judge its importance. The fact that debris-covered glaciers tend to stagnate with progressive mass loss (Dehecq et al., 2019) may however work to our advantage, as this would suggest that the relative uncertainty from emergence velocity becomes less important for accurate sub-debris melt observations in future. Our estimate of debris thickness includes a number of uncertainties, which we quantify in the **Supplementary Section S3**. We calculated melt at critical thickness m_c only for the location of the AWS where atmospheric variables are most accurately known, while technically this value varies in space and should be calculated at each individual pixel. However doing this would further cumulate uncertainties with no apparent gain in knowledge. Considering that there is no apparent bias in our modeled thickness compared to the available measurements, we believe that the simpler approach chosen here is appropriate.

On Lirung Glacier thin debris is only present at the transition to clean ice, outside of the model domain and where ice cliffs appear from under the debris. Around cliffs our model does reproduce high melt rates accurately and due to our approach to

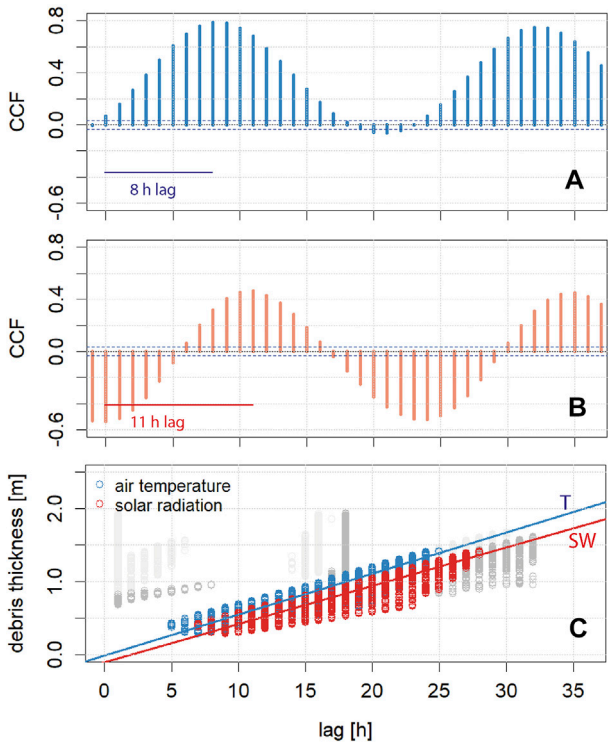

FIGURE 12 | (A) Correlogram showing the cross-correlation function (CCF) between air temperature and melt at a pixel with 51 cm debris thickness. **(B)** CCF between solar radiation and melt at the same pixel. Horizontal blue lines show the 95% confidence interval. **(C)** Lag derived from the CCF at all pixels against debris thickness. Grey values have no positive correlation and are not considered for the regression.

determine debris thickness we can not capture thin debris below the critical thickness (2 cm). In thin debris thermal conductivity and turbulent exchange likely also play a different role than what we are able to account for here based on measurements in debris of at least a few tens of centimeters. Previous studies have noted the complex processes at play in thin marginal debris (Fyffe et al., 2020) as well as around ice cliffs (Buri et al., 2016b), however more research and data will be necessary to include these aspects into distributed melt modeling.

Application of Index Models

While the energy balance model over the whole melt season (157 days) is efficient for a single pixel for a single melt season (<1 min, running on a single core, R code), it quickly becomes unmanageable when simulating melt over thousands of pixels with multiple scenarios for long periods for multiple glaciers. For inclusion in a catchment wide analysis, we rely on climate data from off-glacier stations possibly combined with remote sensing or reanalysis products. To this end the simpler and computationally lightweight index models are a more feasible approach, which we discuss below.

The *lag* parameter necessary for index models to account for the delay due to the debris on energy transport, was earlier derived using two additional free parameters (Carenzo et al., 2016). We derive it from field observations and the energy balance calculations described above as follows.

As the melt cycle follows the diurnal pattern of air temperature and solar radiation (**Figure 11B**), we calculated the cross correlation between these two variables and the melt rate at each pixel. This leaves us with correlograms for each pixel, indicating the shift between the cycle of climatic drivers and melt by calculating the time lag between 0 (when both curves would be synchronous as expected on a clean ice glacier) and the hour with the highest correlation (**Figure 12**). 20% of all pixels had lag times exceeding 36 h, all with very low correlations and high debris thickness (>1 m). For these pixels the melt is not related anymore to the daily climate cycle and we excluded them from the analysis. We then compared lag times at all remaining pixels against debris thickness (**Figure 12C**). Based on this analysis, we find lag times of 17.7 and 19.1 h m^{-1} for lag_T and lag_{SW} respectively. These values are confirmed by our direct measurement of the temperature peak delay through debris of 15.6–18.5 h m^{-1}. Carenzo et al. (2016) found higher values on Miage (lag_T = 20 and lag_{SW} = 22 h m^{-1} respectively), which could be explained by a higher conductivity in the generally wetter debris in the Himalaya. Following Carenzo et al. (2016), and to reduce the number of parameters, we only use one lag value (lag = 17.7 h m^{-1}), since this matches the direct measurements best and differentiating between the two types (SW and T) did not further improve the results. Through optimization Ragettli et al. (2015) found a considerably lower value of 14 h m^{-1} for Lirung Glacier, but this is below the observed value.

To derive the remaining parameters, we minimized RMSE and MBE and maximized the NSE (Byrd et al., 1995) against the hourly values computed with the best performing energy balance model, using the median debris conductivity of 1.41 W m^{-1} K^{-1}. Resulting parameters for the dTI are TF_1 = 0.029 and TF_2 = -0.919 and TF_1 = 0.034, TF_2 = 0.845, SRF_1 = -0.0002 and SRF_2 = −0.31 for the dETI. Additionally, we also tested the same approach for specific thickness classes, yielding different parameters for each subset, which allows for individual application on glaciers depending on their average thickness (**Supplementary Table S3**).

The dETI model does have a higher NSE (0.68 over 0.58 for the dTI) and reproduces the melt rate better for thinner debris in particular. However the optimized SRF_1 is negative, i.e. additional solar radiation would result in reduced energy for melt. While theoretically possible, it is unlikely to represent a correct reproduction of a physical process. Carenzo et al. (2016) also found that SRF_1 approaches zero towards a debris thickness of 0.5 m. It is likely that in their case it would also turn negative for even thicker debris layers. The TF factors for the dETI model correspond very closely to the values found in Ragettli et al. (2015), while their SRF factors are positive but very small. As both RMSE and MBE are not different for either approach, the only improvement from the solar radiation comes in small shifts in the diurnal cycle.

While the index models are able to accurately simulate the melt peak over different thicknesses, they over- and underestimate the low melt for thin and thick debris, respectively (**Figures 13A,B**). This can be explained by the fact that both air temperature and incoming solar radiation

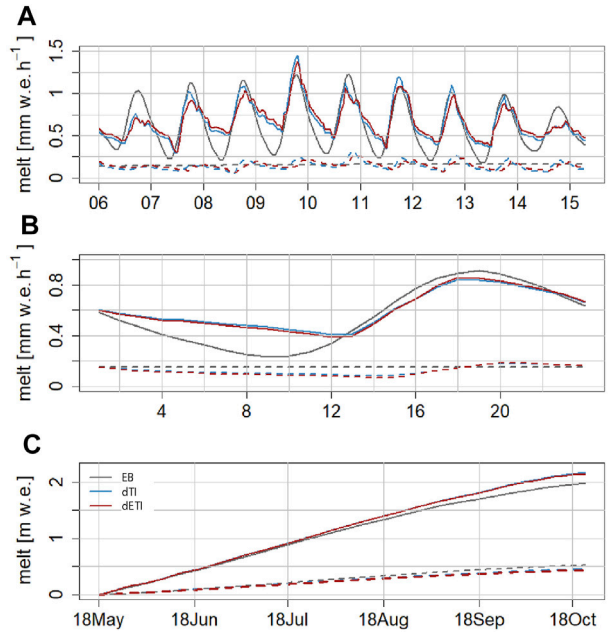

FIGURE 13 | Melt curves for two pixels with a debris thickness of 36 (solid) and 181 cm (dashed lines) respectively during nine days in June 2013 **(A)**, the diurnal cycle over the whole season **(B)** and cumulatively over the whole season **(C)**, calculated with the full energy balance model as well as the two index models.

are not a proxy for the cooling and drying process of debris. This does not have significant effects on cumulative melt neither for thick nor thin debris, however, as that is well simulated with the index models (**Figure 13C**). Index models poorly reproduce hourly melt for debris thicknesses beyond half a meter as shown here and in previous studies (Ragettli et al., 2015; Carenzo et al., 2016). Unless the interplay between atmospheric forcing and drying and wetting debris is better understood, it is unlikely that parametrizations based on temperature (and other atmospheric variables) will be further improved. On a daily or seasonal scale, the application of a temperature index model with only two free parameters provides satisfying results.

Validation in Space and Time

The mean mass loss rate based on the dTI model in 2013 over the whole domain (0.82 m ± 0.48 m) reproduced the average observed melt (0.89 m ± 0.76 m) well and the MBE is relatively small (0.07 m). However, the model performance for individual pixels is poor (NSE = −0.2, RMSE = 0.83 m), which is explained by the inaccuracy of the debris thickness as well as our lack of knowledge regarding the variability of conductivity in space.

The dTI model was calibrated with on-glacier data. In catchment scale studies over a longer period of time such datasets are often not available. Therefore we also evaluate the model using off-glacier station data. We already showed that lapsing off-glacier temperature data works reasonably well, with the caveat that warm temperatures over debris during the monsoon are underestimated (**Figure 6**). We have 4 DEM pairs from Lirung Glacier that are matched by temperature data, namely the monsoon seasons of 2013 and 2016, as well as the winter season 2015 to 2016 and 2017 to 2018 (**Supplementary Table S1**). With the exception of the last winter season, the median mass loss over the debris-covered surface is matched well by the simple dTI model using off-glacier forcing, with three important caveats; very low, very high melt rates and inter-annual trends (**Figure 14**). While the median melt rate is well reproduced for both the high (MBE of −0.03 and −0.15 m for 2013 and 2015 respectively) and the low melt season (0.06 and 0.22 for 2015 and 2017), the model has a much smaller spread, especially in the winter season. Very low observed melt rates can be explained by an underestimation of the emergence flux or when ice melt was counterbalanced by redistributed debris, which is obviously not captured separately, as well as by refreezing processes described earlier. The lowest modeled melt rate in winter is 0.5 mm day^{-1}. The very high melt rates (>8 m yr^{-1}, which correspond to a melt rate of >2 cm d^{-1}) are associated to regions around rapidly melting ice cliffs, ice below ponds and the terminus. Accounting for the mass loss on the margins of ice cliffs and along the cliff-pond interface remains challenging (Buri et al., 2016a; Miles et al., 2016) and has so far not been attempted in distributed energy balance models. Any processes related to cliffs or ponds are not captured by a simple index model, but could be incorporated in future by different surface classifications and separate parameters for these surface types.

Finally, it is obvious, that temperature alone does not seem useful to individually explain the differences in mass loss between years. While the observed mass loss decreased between the two monsoon seasons and increased between the winter seasons, the model results do not reproduce this (**Figure 14**). While temperature alone allows us to get the order of magnitude right and hence provides a valuable input for the catchment scale water balance, more knowledge of the glacier surface, including the debris properties and

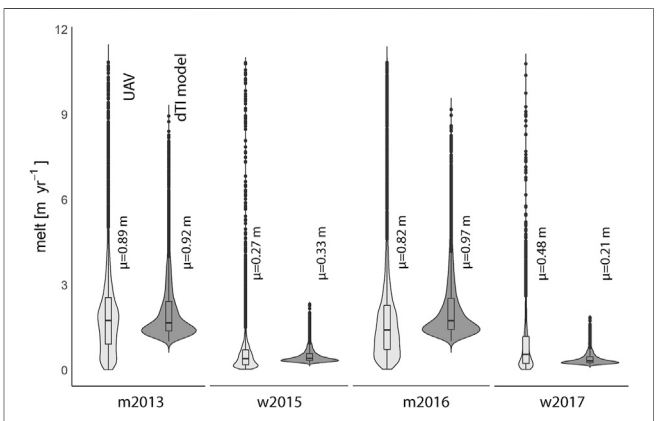

FIGURE 14 | Ice melt below debris for two monsoon (*m*) and two winter seasons (*w*, see **Supplementary Table S1** for exact time periods), measured by DEM differencing (UAV) and modeled with the dTI model.

occurrence of features like cliffs and ponds is necessary to describe the temporal evolution of melt of debris-covered glaciers.

CONCLUSION

In this study we combine modeling with a unique number of observed datasets from the debris-covered Lirung Glacier, to quantify mass loss in time and space using an energy balance model as well as two index models. The two overarching goals were to evaluate the performance of an energy balance model to reproduce melt at an hourly resolution over a debris-covered tongue, and test the applicability of a computationally fast, but simpler index model to be applied at larger scale.

As a first step we derived a debris thickness map, by inverting the Østrem curve. Comparison to *in-situ* thickness measurements show this to be a viable approach for the glacier scale, with a MAE of 0.22 m and a MBE of −0.005 m. The results reveal large spatial variability, which ultimately leads to heterogeneous sub-debris melt rates and is likely one of the factors explaining the characteristic hummocky surface morphology of the glacier.

Direct measurements of debris properties show strong variation in texture and associated moisture content with depth. We show that the debris moisture content increases from $<0.05\,m^3\,m^{-3}$ in the upper 10% of the debris to $>0.15\,m^3\,m^{-3}$ above the debris-ice interface (μ = $0.09\,m^3\,m^{-3}$), even during the drier seasons. As temperature profiles are relatively constant between different locations, we conclude that variability in thermal conductivity of the debris is mainly driven by the varying moisture content. The median thermal conductivity measured in the field ($1.29\,J\,m^{-1}\,K^{-1}$) agrees well with the calibrated conductivity range of our full energy balance model at the location of the AWS ($1.1–1.9\,J\,m^{-1}\,K^{-1}$ for the best matching simulations) as well as for the entire glacier tongue ($1.41\,J\,m^{-1}\,K^{-1}$). We conclude, however, that variability in thermal conductivity remains the single most sensitive variable in our estimates of sub-debris melt. Approaching a debris-covered glacier with lessons from unsaturated zone hydrology as well as permafrost studies could therefore advance our understanding of its mass loss processes. Future investigations should focus on incorporating the spatial (in extent as well as in depth) and temporal heterogeneity of thermal conductivity by considering convective processes and refreezing within the debris pack. For eventual melt water output the retention time of debris as a function of its variable packing density will equally be crucial before including its melt water in catchment wide streamflow.

Using direct hourly surface height change measurements at an AWS on the glacier, we are able to show that the energy balance model reproduces melt rates well over multiple days. Using UAV-derived DEMs, we also conclude that the model reproduces the overall mass loss after an entire melt season for a large part of the glacier tongue well. We also show that using only a single UAV-derived map of seasonal mass balance differences as calibration for the energy balance model produces very similar results as using continuous point-based surface temperature measurements. Moreover, this approach is less prone to temperature measurement uncertainties.

When the conductivity is calibrated in the model, we reproduce the observed mass loss over the complete glacier surface accurately (RMSE of $0.29\,cm\,d^{-1}$ and MBE of $0.04\,cm\,d^{-1}$) including its spatial patterns. Only very high melt rates that occur at the terminus and in the vicinity of supraglacial cliffs and ponds are not captured. When a constant conductivity for the whole glacier is used, the total mass loss can still be reproduced accurately, but spatial patterns are logically represented less well.

Finally, we test a temperature index model that includes the time lag required for energy to travel through the debris layer, and compare its results against the energy balance model. We show that an index model relying on air temperature (dTI) only performs similar to a model that also includes a solar radiation parameterization (dETI). While these simple models do not accurately capture diurnal melt patterns, they perform satisfactorily in quantifying total melt and we conclude that for catchment scale studies and transient simulations the dTI approach that includes the time lag is most suitable and technically feasible.

DATA AVAILABILITY STATEMENT

Datasets presented in this study can be found in online repositories. Data from AWS Kyanjing can be accessed from https://doi.org/10.26066/RDS.22464, all data collected from UAV flights can be accessed from https://zenodo.org/record/3824264#.YBz0xuA3EWo. Data from AWS and debris on the glacier can be accessed via the authors.

AUTHOR CONTRIBUTIONS

JS and WI conceptualized the study and collected data. JS executed the analysis and wrote the manuscript with the assistance of WI and PK. PK provided data from UAV flights.

FUNDING

This project was supported by funding from the European Research Council (ERC) under the European Union's Horizon 2020 research and innovation program (grant agreement no. 676819) and by the research programme VIDI with project number 016.161.308 financed by Netherlands Organisation for Scientific Research (NWO). The views and interpretations in this publication are those of the authors and they are not necessarily attributable to their organizations.

ACKNOWLEDGMENTS

We acknowledge the help of numerous people who have participated in field work that made this work possible,

including porters and Sirdars from our trekking agency that assisted in the work. We are grateful to Francesca Pellicciotti, Pascal Buri, Evan Miles and all other team members for data collected on Lirung Glacier between 2012 and 2014. We kindly acknowledge Michael McCarthy for providing the GPR data of debris thickness.

SUPPLEMENTARY MATERIAL

The Supplementary Material for this article can be found online at: https://www.frontiersin.org/articles/10.3389/feart.2021.678375/full#supplementary-material

REFERENCES

Anderson, L. S., and Anderson, R. S. (2018). Debris Thickness Patterns on Debris-Covered Glaciers. *Geomorphology*. 311, 1–12. doi:10.1016/j.geomorph.2018.03.014

Barr, I., Dokukin, M., Kougkoulos, I., Livingstone, S., Lovell, H., Małecki, J., et al. (2018). Using ArcticDEM to Analyse the Dimensions and Dynamics of Debris-Covered Glaciers in Kamchatka, Russia. *Geosciences* 8 (6), 216. doi:10.3390/geosciences8060216

Basnett, S., Kulkarni, A. V., and Bolch, T. (2013). The Influence of Debris Cover and Glacial Lakes on the Recession of Glaciers in Sikkim Himalaya, India. *J. Glaciol.* 59 (218), 1035–1046. doi:10.3189/2013JoG12J184

Benn, D. I., Bolch, T., Hands, K., Gulley, J., Luckman, A., Nicholson, L. I., et al. (2012). Response of Debris-Covered Glaciers in the Mount Everest Region to Recent Warming, and Implications for Outburst Flood Hazards. *Earth-Science Rev.* 114 (1), 156–174. doi:10.1016/j.earscirev.2012.03.008

Bolch, T., Kulkarni, A., Kääb, A., Huggel, C., Paul, F., Cogley, J. G., et al. (2012). The State and Fate of Himalayan Glaciers. *Science* 336 (6079), 310–314. doi:10.1126/science.1215828

Bonekamp, P. N. J., van Heerwaarden, C. C., Steiner, J. F., and Immerzeel, W. W. (2020). Using 3D Turbulence-Resolving Simulations to Understand the Impact of Surface Properties on the Energy Balance of a Debris-Covered Glacier. *The Cryosphere*. 14 (5), 1611–1632. doi:10.5194/tc-14-1611-2020

Brock, B. W., Mihalcea, C., Kirkbride, M. P., Diolaiuti, G., Cutler, M. E. J., and Smiraglia, C. (2010). Meteorology and Surface Energy Fluxes in the 2005-2007 Ablation Seasons at the Miage Debris-Covered Glacier, Mont Blanc Massif, Italian Alps. *J. Geophys. Res.* 115 (D9). doi:10.1029/2009JD013224

Brun, F., Buri, P., Miles, E. S., Wagnon, P., Steiner, J., Berthier, E., et al. (2016). Quantifying Volume Loss from Ice Cliffs on Debris-Covered Glaciers Using High-Resolution Terrestrial and Aerial Photogrammetry. *J. Glaciol.* 62 (234), 684–695. doi:10.1017/jog.2016.54

Brun, F., Wagnon, P., Berthier, E., Shea, J. M., Immerzeel, W. W., Kraaijenbrink, P. D. A., et al. (2018). Ice Cliff Contribution to the Tongue-wide Ablation of Changri Nup Glacier, Nepal, Central Himalaya. *The Cryosphere*. 12 (11), 3439–3457. doi:10.5194/tc-12-3439-2018

Buri, P., Miles, E. S., Steiner, J. F., Immerzeel, W. W., Wagnon, P., and Pellicciotti, F. (2016a). A Physically Based 3-D Model of Ice Cliff Evolution over Debris-covered Glaciers. *J. Geophys. Res. Earth Surf.* 121, 2471–2493. doi:10.1002/2016jf004039

Buri, P., Pellicciotti, F., Steiner, J. F., Miles, E. S., and Immerzeel, W. W. (2016b). A Grid-Based Model of Backwasting of Supraglacial Ice Cliffs on Debris-Covered Glaciers. *Ann. Glaciol.* 57 (71), 199–211. doi:10.3189/2016AoG71A059

Byrd, R. H., Lu, P., Nocedal, J., and Zhu, C. (1995). A Limited Memory Algorithm for Bound Constrained Optimization. *SIAM J. Sci. Comput.* 16 (5), 1190–1208. doi:10.1137/0916069

Carenzo, M., Pellicciotti, F., Mabillard, J., Reid, T., and Brock, B. W. (2016). An Enhanced Temperature index Model for Debris-Covered Glaciers Accounting for Thickness Effect. *Adv. Water Resour.* 94, 457–469. doi:10.1016/j.advwatres.2016.05.001

Chand, M. B., Kayastha, R. B., Parajuli, A., and Mool, P. K. (2015). Seasonal Variation of Ice Melting on Varying Layers of Debris of Lirung Glacier, Langtang Valley, Nepal. *Proc. IAHS*. 368, 21–26. doi:10.5194/piahs-368-21-2015

Collier, E., Nicholson, L. I., Brock, B. W., Maussion, F., Essery, R., and Bush, A. B. G. (2014). Representing Moisture Fluxes and Phase Changes in Glacier Debris Cover Using a Reservoir Approach. *The Cryosphere*. 8 (4), 1429–1444. doi:10.5194/tc-8-1429-2014

Conway, H., and Rasmussen, L. A. (2000). Summer Temperature Profiles within Supraglacial Debris on Khumbu Glacier, Nepal. *IAHS Proc. n.* 264, 89–97.

Cuffey, K. M., and Paterson, W. S. B. (2010). *The Physics of Glaciers*. 4th Edition. Academic Press. Available at: https://www.elsevier.com/books/the-physics-of-glaciers/cuffey/978-0-12-369461-4.

Dehecq, A. N., Gourmelen, A. S., Gardner, F., Brun, D., Goldberg, P. W., Nienow, E., et al. (2019). Twenty-First Century Glacier Slowdown Driven by Mass Loss in High Mountain Asia. *Nat. Geosci.* 12 (1), 22–27. doi:10.1038/s41561-018-0271-9

Farinotti, D., Huss, M., Fürst, J. J., Landmann, J., Machguth, H., Maussion, F., et al. (2019). A Consensus Estimate for the Ice Thickness Distribution of All Glaciers on Earth. *Nat. Geosci.* 12 (3), 168–173. doi:10.1038/s41561-019-0300-3

Foster, L. A., Brock, B. W., Cutler, M. E. J., and Diotri, F. (2012). A Physically Based Method for Estimating Supraglacial Debris Thickness from Thermal Band Remote-Sensing Data. *J. Glaciol.* 58 (210), 677–691. doi:10.3189/2012JoG11J194

Fujita, K., and Sakai, A. (2000). Air Temperature Environment on the Debris-Covered Area of Lirung Glacier, Langtang Valley, Nepal Himalayas. *IAHS Proc. n.* 264, 83–88.

Fyffe, C. L., Reid, T. D., Brock, B. W., Kirkbride, M. P., Diolaiuti, G., Smiraglia, C., et al. (2014). A Distributed Energy-Balance Melt Model of an Alpine Debris-Covered Glacier. *J. Glaciol.* 60 (221), 587–602. doi:10.3189/2014JoG13J148

Fyffe, C. L., Woodget, A. S., Kirkbride, M. P., Deline, P., Westoby, M. J., and Brock, B. W. (2020). Processes at the Margins of Supraglacial Debris Cover: Quantifying Dirty Ice Ablation and Debris Redistribution. *Earth Surf. Process. Landforms*. 45, 2272–2290. doi:10.1002/esp.4879

Gardelle, J., Berthier, E., and Arnaud, Y. (2012). Slight Mass Gain of Karakoram Glaciers in the Early Twenty-First Century. *Nat. Geosci.* 5 (5), 322–325. doi:10.1038/ngeo1450

Genuchten, M. Th. van. (1980). A Closed-form Equation for Predicting the Hydraulic Conductivity of Unsaturated Soils. *Soil Sci. Soc. America J.* 44 (5), 892–898. doi:10.2136/sssaj1980.03615995004400050002x

Giese, A., Boone, A., Wagnon, P., and Hawley, R. (2020). Incorporating Moisture Content in Surface Energy Balance Modeling of a Debris-Covered Glacier. *The Cryosphere* 14 (5), 1555–1577. doi:10.5194/tc-14-1555-2020

Herreid, S., and Pellicciotti, F. (2018). Automated Detection of Ice Cliffs within Supraglacial Debris Cover. *The Cryosphere* 12 (5), 1811–1829. doi:10.5194/tc-12-1811-2018

Heynen, M., Miles, E., Ragettli, S., Buri, P., Immerzeel, W. W., and Pellicciotti, F. (2016). Air Temperature Variability in a High-Elevation Himalayan Catchment. *Ann. Glaciol.* 57 (71), 212–222. doi:10.3189/2016AoG71A076

Hock, R. (1999). A Distributed Temperature-Index Ice- and Snowmelt Model Including Potential Direct Solar Radiation. *J. Glaciol.* 45 (149), 101–111. doi:10.3189/S0022143000003087

Immerzeel, W. W., Kraaijenbrink, P. D. A., Shea, J. M., Shrestha, A. B., Pellicciotti, F., Bierkens, M. F. P., et al. (2014a). High-Resolution Monitoring of Himalayan Glacier Dynamics Using Unmanned Aerial Vehicles. *Remote Sensing Environ.* 150, 93–103. doi:10.1016/j.rse.2014.04.025

Immerzeel, W. W., Petersen, L., Ragettli, S., and Pellicciotti, F. (2014b). The Importance of Observed Gradients of Air Temperature and Precipitation for Modeling Runoff from a Glacierized Watershed in the Nepalese Himalayas. *Water Resour. Res.* 50 (3), 2212–2226. doi:10.1002/2013WR014506

Janke, J. R., Bellisario, A. C., and Ferrando, F. A. (2015). Classification of Debris-Covered Glaciers and Rock Glaciers in the Andes of Central Chile. *Geomorphology*. 241, 98–121. doi:10.1016/j.geomorph.2015.03.034

Juen, M., Mayer, C., Lambrecht, A., Wirbel, A., and Kueppers, U. (2013). Thermal Properties of a Supraglacial Debris Layer with Respect to Lithology and Grain Size. *Geografiska Annaler: Ser. A, Phys. Geogr.* 95 (3), 197–209. doi:10.1111/geoa.12011

Kääb, A., Berthier, E., Nuth, C., Gardelle, J., and Arnaud, Y. (2012). Contrasting Patterns of Early Twenty-First-Century Glacier Mass Change in the Himalayas. *Nature*. 488 (7412), 495–498. doi:10.1038/nature11324

Kayastha, R. B., Takeuchi, Y., Nakawo, M., and Ageta, Y. (2000). Practical Prediction of Ice Melting beneath Various Thickness of Debris Cover on Khumbu Glacier, Nepal, Using a Positive Degree-Day Factor. *IAHS Proc. n.* 264, 71–81.

Khan, M. I. (1989). Ablation on Barpu Glacier, Karakoram Himalaya, Pakistan a Study of Melt Processes on a Faceted, Debris-Covered Ice Surface. MSc Thesis. Waterloo: Wilfrid Laurier University.

Kok, R. J., Steiner, J. F., Litt, M., Wagnon, P., Koch, I., Wagnon, P., et al. (2019). Measurements, Models and Drivers of Incoming Longwave Radiation in the Himalaya. *Int. J. Climatol.* 40 (2), 942–956. doi:10.1002/joc.6249

Kraaijenbrink, P. D. A., Bierkens, M. F. P., Lutz, A. F., and Immerzeel, W. W. (2017). Impact of a Global Temperature Rise of 1.5 Degrees Celsius on Asia's Glaciers. *Nature*. 549 (7671), 257–260. doi:10.1038/nature23878

Kraaijenbrink, P. D. A., and Immerzeel, W. W. (2020). Unmanned Aerial Vehicle Data of Lirung Glacier and Langtang Glacier for 2013–2018 (Version 1.0.0) [Data set]. *Zenodo*. doi:10.5281/zenodo.3824264

Kraaijenbrink, P. D. A., Shea, J. M., Litt, M., Steiner, J. F., Treichler, D., Koch, I., et al. (2018). Mapping Surface Temperatures on a Debris-Covered Glacier with an Unmanned Aerial Vehicle. *Front. Earth Sci.* 6, 1. doi:10.3389/feart.2018.00064

Kraaijenbrink, P. D. A., Meijer, S. W., Shea, J. M., Pellicciotti, F., De Jong, S. M., and Immerzeel, W. W. (2016a). Seasonal Surface Velocities of a Himalayan Glacier Derived by Automated Correlation of Unmanned Aerial Vehicle Imagery. *Ann. Glaciol.* 57 (71), 103–113. doi:10.3189/2016AoG71A072

Kraaijenbrink, P. D. A., Shea, J. M., Pellicciotti, F., Jong, S. M. d., and Immerzeel, W. W. (2016b). Object-Based Analysis of Unmanned Aerial Vehicle Imagery to Map and Characterise Surface Features on a Debris-Covered Glacier. *Remote Sensing Environ.* 186, 581–595. doi:10.1016/j.rse.2016.09.013

Lambrecht, A., Mayer, C., Hagg, W., Popovnin, V., Rezepkin, A., Lomidze, N., et al. (2011). A Comparison of Glacier Melt on Debris-Covered Glaciers in the Northern and Southern Caucasus. *The Cryosphere*. 5 (3), 525–538. doi:10.5194/tc-5-525-2011

Loomis, S. R. (1970). Morphology and Ablation Processes on Glacier Ice. *Assoc. Am. Geogr. Proc.* 2, 88–92.

Macfarlane, A. M., Hodges, K. V., and Lux, D. (1992). A Structural Analysis of the Main Central Thrust Zone, Langtang National Park, Central Nepal Himalaya. *GSA Bull.* 104 (11), 1389–1402. doi:10.1130/0016-7606(1992)104<1389:asaotm>2.3.co;2

McCarthy, M., Pritchard, H., Willis, I., and King, E. (2017). Ground-Penetrating Radar Measurements of Debris Thickness on Lirung Glacier, Nepal. *J. Glaciol.* 63 (239), 543–555. doi:10.1017/jog.2017.18

Midgley, N. G., Tonkin, T. N., Graham, D. J., and Cook, S. J. (2018). Evolution of High-Arctic Glacial Landforms during Deglaciation. *Geomorphology*. 311, 63–75. doi:10.1016/j.geomorph.2018.03.027

Miles, E. S., Pellicciotti, F., Willis, I. C., Steiner, J. F., Buri, P., and Arnold, N. S. (2016). Refined Energy-Balance Modeling of a Supraglacial Pond, Langtang Khola, Nepal. *Ann. Glaciol.* 57 (71), 29–40. doi:10.3189/2016AoG71A421

Miles, E. S., Steiner, J. F., and Brun, F. (2017a). Highly Variable Aerodynamic Roughness Length (Z 0) for a Hummocky Debris-Covered Glacier. *J. Geophys. Res. Atmos.* 122 (16), 8447–8466. doi:10.1002/2017JD026510

Miles, E. S., Steiner, J., Willis, I., Buri, P., Immerzeel, W. W., Chesnokova, A., et al. (2017b). Pond Dynamics and Supraglacial-Englacial Connectivity on Debris-Covered Lirung Glacier, Nepal. *Front. Earth Sci.* 5, 69. doi:10.3389/feart.2017.00069

Naylor, M. A. (1980). The Origin of Inverse Grading in Muddy Debris Flow Deposits; a Review. *J. Sediment. Res.* 50 (4), 1111–1116. doi:10.1306/212F7B8F-2B24-11D7-8648000102C1865D

Nicholson, L., and Benn, D. I. (2006). Calculating Ice Melt beneath a Debris Layer Using Meteorological Data. *J. Glaciol.* 52 (178), 463–470. doi:10.3189/172756506781828584

Nicholson, L., and Benn, D. I. (2013). Properties of Natural Supraglacial Debris in Relation to Modeling Sub-debris Ice Ablation. *Earth Surf. Process. Landforms.* 38 (5), 490–501. doi:10.1002/esp.3299

Nicholson, L. I., McCarthy, M., Pritchard, H. D., and Willis, I. (2018). Supraglacial Debris Thickness Variability: Impact on Ablation and Relation to Terrain Properties. *The Cryosphere*. 12 (12), 3719–3734. doi:10.5194/tc-12-3719-2018

Nuimura, T., Fujita, K., Yamaguchi, S., and Sharma, R. R. (2012). Elevation Changes of Glaciers Revealed by Multitemporal Digital Elevation Models Calibrated by GPS Survey in the Khumbu Region, Nepal Himalaya, 1992-2008. *J. Glaciol.* 58 (210), 648–656. doi:10.3189/2012JoG11J061

Östrem, G. (1959). Ice Melting under a Thin Layer of Moraine, and the Existence of Ice Cores in Moraine Ridges. *Geografiska Annaler*. 41 (4), 228–230. doi:10.1080/20014422.1959.11907953

Pellicciotti, F., Brock, B., Strasser, U., Burlando, P., Funk, M., and Corripio, J. (2005). An Enhanced Temperature-index Glacier Melt Model Including the Shortwave Radiation Balance: Development and Testing for Haut Glacier d'Arolla, Switzerland. *J. Glaciol.* 51 (175), 573–587. doi:10.3189/172756505781829124

Popovnin, V. V., and Rozova, A. V. (2002). Influence of Sub-debris Thawing on Ablation and Runoff of the Djankuat Glacier in the Caucasus. *Nordic Hydrol.* 33 (I), 75–94. doi:10.2166/nh.2002.0005

Ragettli, S., Bolch, T., and Pellicciotti, F. (2016). Heterogeneous Glacier Thinning Patterns over the Last 40 Years in Langtang Himal, Nepal. *The Cryosphere* 10 (5), 2075–2097. doi:10.5194/tc-10-2075-2016

Ragettli, S., Pellicciotti, F., Immerzeel, W. W., Miles, E. S., Petersen, L., Heynen, M., et al. (2015). Unraveling the Hydrology of a Himalayan Catchment through Integration of High Resolution *In Situ* Data and Remote Sensing with an Advanced Simulation Model. *Adv. Water Resour.* 78, 94–111. doi:10.1016/j.advwatres.2015.01.013

Reid, T. D., and Brock, B. W. (2010). An Energy-Balance Model for Debris-Covered Glaciers Including Heat Conduction through the Debris Layer. *J. Glaciol.* 56 (199), 903–916. doi:10.3189/002214310794457218

Reid, T. D., Carenzo, M., Pellicciotti, F., and Brock, B. W. (2012). Including Debris Cover Effects in a Distributed Model of Glacier Ablation. *J. Geophys. Res.* 117 (D18), a–n. doi:10.1029/2012JD017795

Rounce, D. R., King, O., McCarthy, M., Shean, D. E., and Salerno, F. (2018). Quantifying Debris Thickness of Debris-Covered Glaciers in the Everest Region of Nepal through Inversion of a Subdebris Melt Model. *J. Geophys. Res. Earth Surf.* 123 (5), 1094–1115. doi:10.1029/2017JF004395

Rounce, D. R., and McKinney, D. C. (2014). Debris Thickness of Glaciers in the Everest Area (Nepal Himalaya) Derived from Satellite Imagery Using a Nonlinear Energy Balance Model. *The Cryosphere*. 8 (4), 1317–1329. doi:10.5194/tc-8-1317-2014

Rounce, D. R., Quincey, D. J., and McKinney, D. C. (2015). Debris-covered Glacier Energy Balance Model for Imja-Lhotse Shar Glacier in the Everest Region of Nepal. *The Cryosphere*. 9 (6), 2295–2310. doi:10.5194/tc-9-2295-2015

Rowan, A. V., Nicholson, L. I., Quincey, D. J., Gibson, M. J., Irvine-Fynn, T. D. L., Watson, C. S., et al. (2020). Seasonally Stable Temperature Gradients through Supraglacial Debris in the Everest Region of Nepal, Central Himalaya. *J. Glaciol.* 67, 170. doi:10.1017/jog.2020.100

Sakai, A., Nakawo, M., and Fujita, K. (2002). Distribution Characteristics and Energy Balance of Ice Cliffs on Debris-Covered Glaciers, Nepal Himalaya. *Arctic, Antarctic, Alpine Res.* 34 (1), 12–19. doi:10.2307/155250310.1080/15230430.2002.12003463

Sakai, A., Takeuchi, N., Fujita, K., and Nakawo, M. (2000). Role of Supraglacial Ponds in the Ablation Process of a Debris-Covered Glacier in the Nepal Himalayas. *IAHS Proc.* 265, 119–130.

Schauwecker, S., Rohrer, M., Huggel, C., Kulkarni, A., Ramanathan, A., Salzmann, N., et al. (2015). Remotely Sensed Debris Thickness Mapping of Bara Shigri Glacier, Indian Himalaya. *J. Glaciol.* 61 (228), 675–688. doi:10.3189/2015JoG14J102

Scherler, D., Bookhagen, B., and Strecker, M. R. (2011). Hillslope-Glacier Coupling: The Interplay of Topography and Glacial Dynamics in High Asia. *J. Geophys. Res.* 116 (March), 1–21. doi:10.1029/2010JF001751

Shaw, T. E., Brock, B. W., Fyffe, C. L., Pellicciotti, F., Rutter, N., and Diotri, F. (2016). Air Temperature Distribution and Energy-Balance Modeling of a Debris-Covered Glacier. *J. Glaciol.* 62 (231), 185–198. doi:10.1017/jog.2016.31

Steiner, J. F., Buri, P., Miles, E. S., Ragettli, S., and Pellicciotti, F. (2019). Supraglacial Ice Cliffs and Ponds on Debris-Covered Glaciers: Spatio-Temporal Distribution and Characteristics. *J. Glaciol.* 65 (252), 617–632. doi:10.1017/jog.2019.40

Steiner, J. F., Litt, M., Stigter, E. E., Shea, J., Bierkens, M. F. P., and Immerzeel, W. W. (2018). The Importance of Turbulent Fluxes in the Surface Energy Balance of a Debris-Covered Glacier in the Himalayas. *Front. Earth Sci.* 6, 144. doi:10.3389/feart.2018.00144

Steiner, J. F., Pellicciotti, F., Buri, P., Miles, E. S., Immerzeel, W. W., and Reid, T. D. (2015). Modeling Ice-Cliff Backwasting on a Debris-Covered Glacier in the Nepalese Himalaya. *J. Glaciol.* 61 (229), 889–907. doi:10.3189/2015JoG14J194

Steiner, J. F., and Pellicciotti, F. (2016). Variability of Air Temperature over a Debris-Covered Glacier in the Nepalese Himalaya. *Ann. Glaciol.* 57 (71), 295–307. doi:10.3189/2016AoG71A066

Watson, C. S., Quincey, D. J., Carrivick, J. L., and Smith, M. W. (2016). The Dynamics of Supraglacial Ponds in the Everest Region, Central Himalaya. *Glob. Planet. Change*. 142, 14–27. doi:10.1016/j.gloplacha.2016.04.008

Wigmore, O., and Mark, B. (2017). Monitoring Tropical Debris-Covered Glacier Dynamics from High-Resolution Unmanned Aerial Vehicle Photogrammetry, Cordillera Blanca, Peru. *The Cryosphere*. 11 (6), 2463–2480. doi:10.5194/tc-11-2463-2017

Woerkom, T. van., Steiner, J. F., Kraaijenbrink, P. D. A., Miles, E. S., and Immerzeel, W. W. (2019). Sediment Supply from Lateral Moraines to a Debris-Covered Glacier in the Himalaya. *Earth Surf. Dyn.* 7 (2), 411–427. doi:10.5194/esurf-7-411-2019

Conflict of Interest: The authors declare that the research was conducted in the absence of any commercial or financial relationships that could be construed as a potential conflict of interest.

frontiers in Earth Science

ORIGINAL RESEARCH
published: 14 July 2021
doi: 10.3389/feart.2021.657440

Quantifying Patterns of Supraglacial Debris Thickness and Their Glaciological Controls in High Mountain Asia

Karla Boxall[1†], Ian Willis[1†], Alexandra Giese[2] and Qiao Liu[3†]*

[1]Scott Polar Research Institute, University of Cambridge, Cambridge, United Kingdom, [2]Department of Geography, University of Utah, Salt Lake City, UT, United States, [3]Institute of Mountain Hazards and Environment, Chinese Academy of Sciences, Chengdu, China

OPEN ACCESS

Edited by:
Lindsey Isobel Nicholson,
University of Innsbruck, Austria

Reviewed by:
Tom Holt,
Aberystwyth University,
United Kingdom
Maria Shahgedanova,
University of Reading, United Kingdom

***Correspondence:**
Karla Boxall
kb621@cam.ac.uk

†ORCID:
Karla Boxall
orcid.org/0000-0002-6574-7717
Ian Willis
orcid.org/0000-0002-0750-7088
Qiao Liu
orcid.org/0000-0002-7285-5425

Specialty section:
This article was submitted to Cryospheric Sciences, a section of the journal Frontiers in Earth Science

Received: 22 January 2021
Accepted: 08 June 2021
Published: 14 July 2021

Citation:
Boxall K, Willis I, Giese A and Liu Q (2021) Quantifying Patterns of Supraglacial Debris Thickness and Their Glaciological Controls in High Mountain Asia. Front. Earth Sci. 9:657440. doi: 10.3389/feart.2021.657440

Mapping patterns of supraglacial debris thickness and understanding their controls are important for quantifying the energy balance and melt of debris-covered glaciers and building process understanding into predictive models. Here, we find empirical relationships between measured debris thickness and satellite-derived surface temperature in the form of a rational curve and a linear relationship consistently outperform two different exponential relationships, for five glaciers in High Mountain Asia (HMA). Across these five glaciers, we demonstrate the covariance of velocity and elevation, and of slope and aspect using principal component analysis, and we show that the former two variables provide stronger predictors of debris thickness distribution than the latter two. Although the relationship between debris thickness and slope/aspect varies between glaciers, thicker debris occurs at lower elevations, where ice flow is slower, in the majority of cases. We also find the first empirical evidence for a statistical correlation between curvature and debris thickness, with thicker debris on concave slopes in some settings and convex slopes in others. Finally, debris thickness and surface temperature data are collated for the five glaciers, and supplemented with data from one more, to produce an empirical relationship, which we apply to all glaciers across the entire HMA region. This rational curve: 1) for the six glaciers studied has a similar accuracy to but greater precision than that of an exponential relationship widely quoted in the literature; and 2) produces qualitatively similar debris thickness distributions to those that exist in the literature for three other glaciers. Despite the encouraging results, they should be treated with caution given our relationship is extrapolated using data from only six glaciers and validated only qualitatively. More (freely available) data on debris thickness distribution of HMA glaciers are required.

Keywords: debris-covered glacier, debris thickness, remote sensing, high mountain asia, glaciological controls

INTRODUCTION

Debris-covered glaciers (DCGs) respond differently to clean ice glaciers under the same climatic forcing (Nicholson and Benn, 2013). The empirical relationship between debris thickness and ablation rates is well established (Östrem, 1959; Nakawo and Young, 1981; Mattson et al., 1993; Nicholson and Benn, 2006). Thin debris enhances ablation because it lowers surface albedo compared to that of clean ice, increasing absorption of solar radiation and heat transfer to the ice (Vincent et al., 2016). Thick debris, however, attenuates melt because it reduces heat conduction to the underlying ice (Nakawo and Young, 1981; Mattson et al., 1993). The critical thickness marking the boundary between enhancing and inhibiting melt is commonly ~2 cm but ranges from 2 to 10 cm depending on debris properties (Nakawo et al., 1993; Kayastha et al., 2000; Brock et al., 2010). Difficulty in obtaining high-quality debris thickness distribution is one of the principal limitations in applying melt models to DCGs (Nicholson and Benn, 2006; Zhang et al., 2011). Thus, it is important to quantify the spatial distribution of supraglacial debris thickness from the scale of glaciers to entire mountain ranges in order to understand and predict its impacts on glacial mass balance (Benn and Luhmkuhl, 2000; Mölg et al., 2020), glacier dynamics (Quincey et al., 2009a; Scherler et al., 2011a; Scherler et al., 2011b), meltwater runoff (Bajracharya and Mool, 2009; Harrison et al., 2018), local water resources (Immerzeel et al., 2010; Mark et al., 2015) and ultimately global sea level (Jacob et al., 2012; Gardner et al., 2013). This paper aims to build on previous work and contribute to improving the mapping of supraglacial debris thickness, at both a glacier and regional scale, and enhancing understanding of the glaciological controls on debris thickness distribution, at a glacier scale.

At the glacier scale, debris thickness distributions have been derived using both *in situ* (McCarthy et al., 2017; Nicholson and Mertes, 2017) and remote sensing methods. The latter rely on the strong positive relationship between debris thickness and surface temperature (Ranzi et al., 2004; Reid and Brock, 2010; Evatt et al., 2015), where debris thickness is calculated from surface temperature obtained from thermal band satellite imagery, using either an energy balance model (Foster et al., 2012; Rounce and McKinney, 2014; Schauwecker et al., 2015) or an empirically-derived relationship. Uncertainties remain regarding the best form of empirically-derived relationship to use, since different studies use different equations. A linear relationship performed best for data on Miage Glacier, Italy (Mihalcea et al., 2008a) whereas an exponential relationship was best for data collected on Baltoro Glacier, Pakistan (Mihalcea et al., 2008b). Kraaijenbrink et al. (2017) used a different form of exponential equation to derive debris thickness from satellite thermal imagery across the entire High Mountain Asia (HMA) region. McCarthy (2019) used a rational curve to calculate debris thickness from surface temperatures for Suldenferner Glacier, Italy. Therefore, the first aim of this study is to undertake a formal comparison of these four types of empirical relationship, using data from five glaciers across HMA.

Understanding how debris is distributed across glacier surfaces is important for understanding the processes by which debris arrives at the glacier surface and is subsequently redistributed. This process understanding is needed to build predictive models of how debris thickness may change across glaciers in the future. Previous studies have shown that debris thickness varies with glacier hypsometry (Anderson, 2000; Kellerer-Pirklbauer, 2008; Gibson et al., 2017), surface topography (Lawson, 1979; Moore, 2018; Nicholson et al., 2018) and ice velocity (Nakawo et al., 1986; Anderson and Anderson, 2016; Anderson and Anderson, 2018). Controls on the spatial distribution of debris thickness are numerous and complex in the way they interact but can be divided into primary and secondary debris dispersal mechanisms (Kirkbride and Deline, 2013). Primary dispersal refers to the supraglacial dispersal of debris across melting ice surfaces provided by mass movement processes from the valley sides (Scherler et al., 2011b; Dunning et al., 2015; Banerjee and Wani, 2018), englacial melt out (Evatt et al., 2015; Rowan et al., 2015), in addition to the extension/compression of debris by ice flow (Nakawo et al., 1986; Anderson and Anderson, 2016). Secondary dispersal refers to the gravitational processes that distribute debris locally, which are strongly influenced by terrain characteristics, such as slope, aspect and curvature (Lawson, 1979; Moore, 2018; Nicholson et al., 2018). Therefore, the second aim of this study is to understand the impacts of these mechanisms and the complex ways in which they interact to control glacier scale debris thickness distribution.

Regional scale knowledge of debris thickness distribution is required for modeling regional scale glacier mass balance and runoff. Calculating and predicting glacier runoff is particularly important in HMA because the region provides a net 36 ± 10 km^3 of seasonally delayed meltwater each summer (Pritchard, 2019) and the region's increased runoff in response to recent climate change comprises ~10% of the global contribution of mountain glaciers to sea level rise (Vaughan et al., 2013). To the authors' knowledge, the only published estimate of debris thickness distribution for all glaciers in the HMA region has been made by Kraaijenbrink et al. (2017). That study uses a scaling approach to derive an exponential relationship between surface temperature and debris thickness. There is a need to provide alternative estimates of glacier debris thickness distribution at a regional scale to compare with that made using the Kraaijenbrink et al. (2017) approach. The final aim of this study, therefore, is to develop the empirical extrapolation approach trialed for the five individual glaciers above and use it at a regional scale to compare with the Kraaijenbrink et al. (2017) study.

Thus, the overall aims here are threefold. First, to improve the mapping of debris thickness at a local scale by determining the most relevant form of empirical equation between surface temperature and debris thickness for use on five individual glaciers. Second, to investigate the controls on the spatial distribution of debris thickness on those glaciers through statistical analysis with topography and velocity. Third, to establish a suitable empirical equation between surface temperature and debris thickness to map the debris thickness distribution across all glaciers throughout HMA.

MATERIALS AND METHODS

Study Area

HMA encompasses ~25–45°N to 70–100°E. HMA was chosen for the study because its glaciated area is 100,693 ± 11.970 km^2

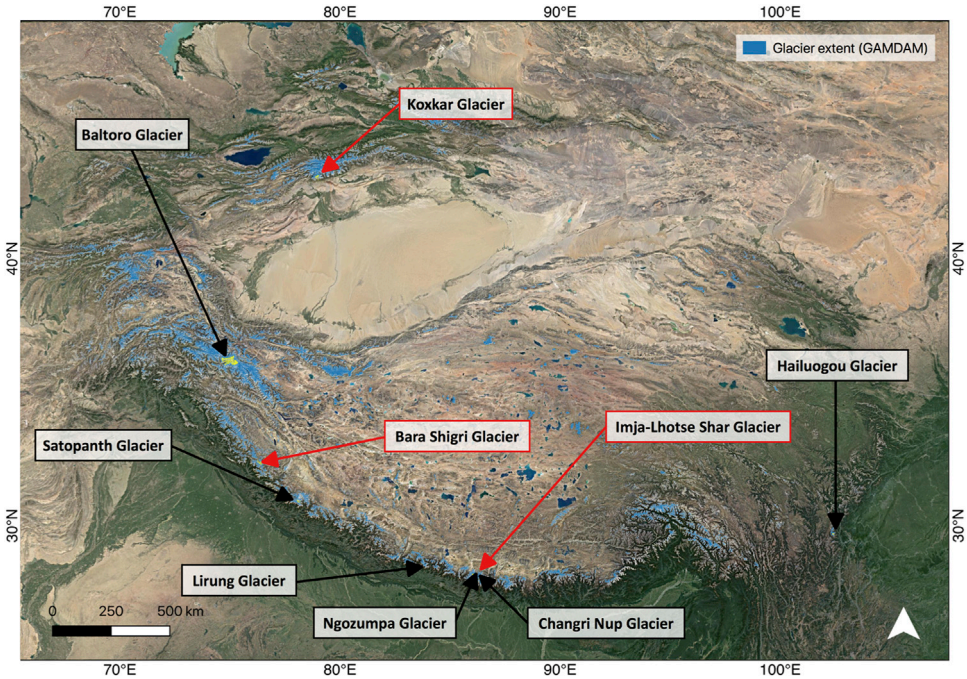

FIGURE 1 | The six studied glaciers (black outline and arrow) and the three validation glaciers (red outline and arrow), in the context of the glaciated areas of High Mountain Asia, according to the Glacier Area Mapping for Discharge from the Asian Mountains (GAMDAM) inventory (Sakai, 2019). Base map: Google Satellite Maps.

(Sakai et al., 2019), which comprises ~16% of the glaciated area globally (RGI Consortium, 2017) and represents the greatest concentration of glaciers outside of the polar regions (Dyhrenfurth, 2011; Brun et al., 2017). The region also contains the largest ice volume outside of the polar regions, 7,000 ± 1,800 km^3, ~4.4% of the global total (Farinotti et al., 2019). There is a high proportion of DCGs in the region; ~11% of its glaciers are debris-covered (Kraaijenbrink et al., 2017) and ~18% of the total ice mass is stored under a debris mantle (Bolch et al., 2012; Nuimura et al., 2012). Thus, accurate estimates of debris thickness distributions across HMA glaciers are needed to improve the accuracy of current estimates and future predictions of the response of the world's glaciers to climate (Kamp et al., 2011). This information is particularly important because glaciers in HMA provide water to more than 1.4 billion people (Immerzeel et al., 2010; Shukla and Qadir, 2016) and it is estimated they will contribute ~15 ± 10 mm to sea level rise by 2100 under RCP6.0 (Radić et al., 2014).

Six HMA glaciers were initially chosen for the focus of this study (**Figure 1**). They were chosen according to the availability of *in situ* debris thickness measurements, but they are also well distributed across the region and so are representative of a range of climatic settings (Bookhagen and Burbank, 2010; Bolch et al., 2012; Kapnick et al., 2014; Rounce et al., 2019). The glaciers are Baltoro Glacier, Karakoram (35.73°N, 76.38°E), Satopanth Glacier, Central Himalaya (30.73°N, 79.32°E), Lirung Glacier, Langtang (28.25°N, 85.51°E), Ngozumpa Glacier, Everest region (27.93°N, 86.71°E), Changri Nup Glacier, Everest region (27.98°N, 86.78°E), and Hailuogou Glacier, Hengduan Mountains (29.59°N, 101.94°E).

Deriving Debris Thickness Distribution From Surface Temperature at the Glacier Scale

A systematic comparison of the application of four different forms of the relationship between debris thickness (DT) in cm and surface temperature (T_s) in °C was undertaken. The comparison was carried out on six individual glaciers to determine which form of the equation produces the most accurate debris thickness distribution on each. The four relationships are: linear (Mihalcea et al., 2008a) (**Eq. 1**), rational curve (McCarthy, 2019) (**Eq. 2**), an exponential curve from Mihalcea et al. (2008b) (**Eq. 3**) and an exponential curve from Kraaijenbrink et al. (2017) (**Eq. 4**).

$$DT = c_1 T_s + c_2 \quad (1)$$

$$DT = \frac{T_s}{c_1 + c_2 T_s} \quad (2)$$

$$DT = e^{(c_1 T_s - c_2)} \quad (3)$$

$$DT = e^{\frac{(T_s - T_{s\,min})\ln(DT_{max})}{T_{s\,95} - T_{s\,min}}} \quad (4)$$

where c_1 and c_2 are empirically-derived coefficients, $T_{s\ min}$ is the minimum surface temperature, $T_{s\ 95}$ is the 95th percentile of surface temperature and DT_{max} is the assumed maximum debris

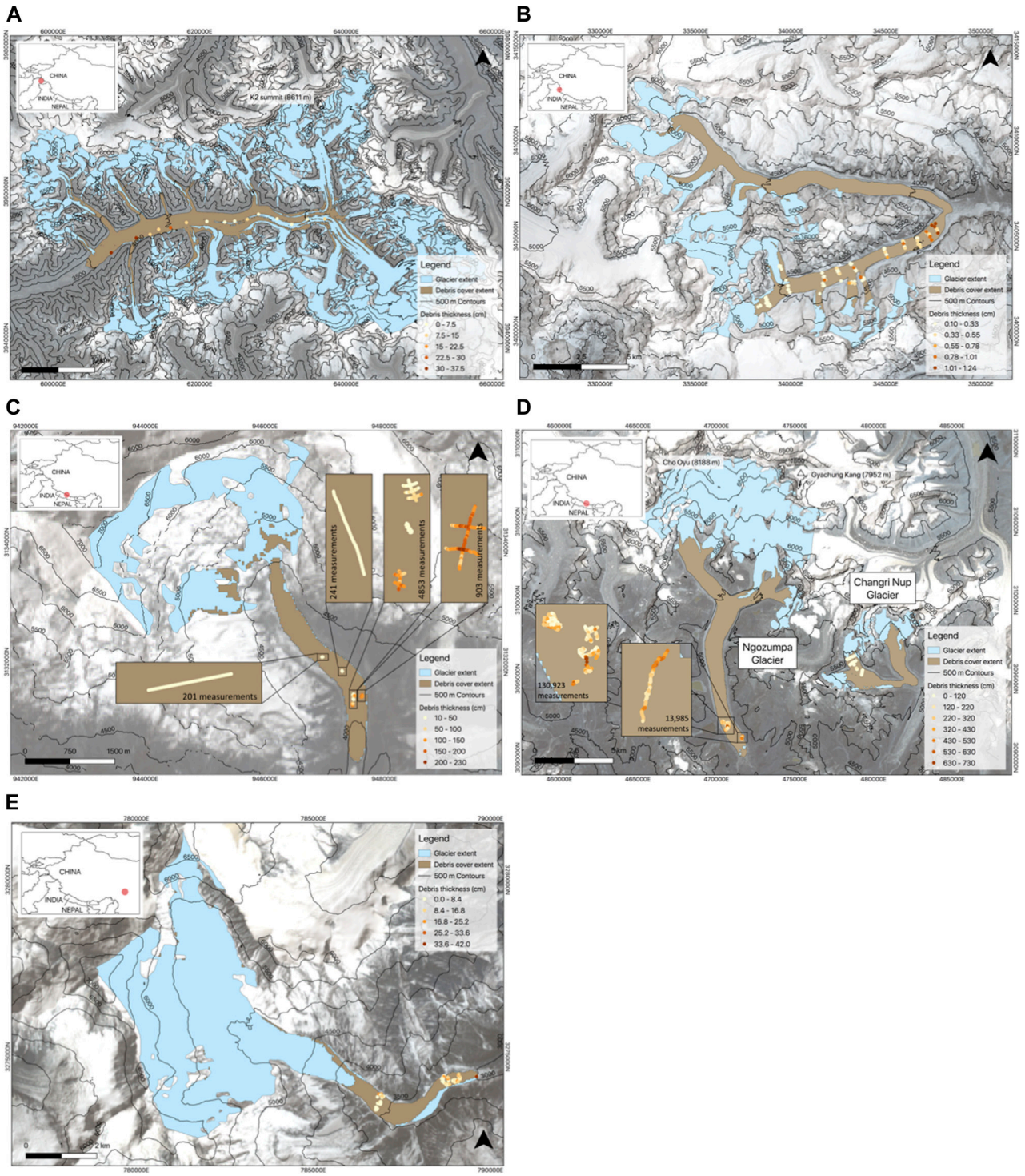

FIGURE 2 | Maps to show the distribution of *in situ* debris thickness measurements for **(A)** Baltoro (UTM 43N), **(B)** Satopanth (UTM 44N), **(C)** Lirung (UTM 45N), **(D)** Ngozumpa and Changri Nup (UTM 45N), and **(E)** Hailuogou Glaciers (UTM 47N). Glacier outlines are provided by GAMDAM (Sakai, 2019) and debris cover outlines are provided by Scherler et al. (2018). Note: Giese (2019), consistent with Miles et al. (2018) and Giese et al. (2020), defines the extent of Changri Nup within the southern of the two lobes indicated in this figure and considers the northern lobe to be a separate glacier named Changri Shar. However, for the purposes of this study the outline provided by GAMDAM (Sakai, 2019) is used, which includes both the northern and southern lobe.

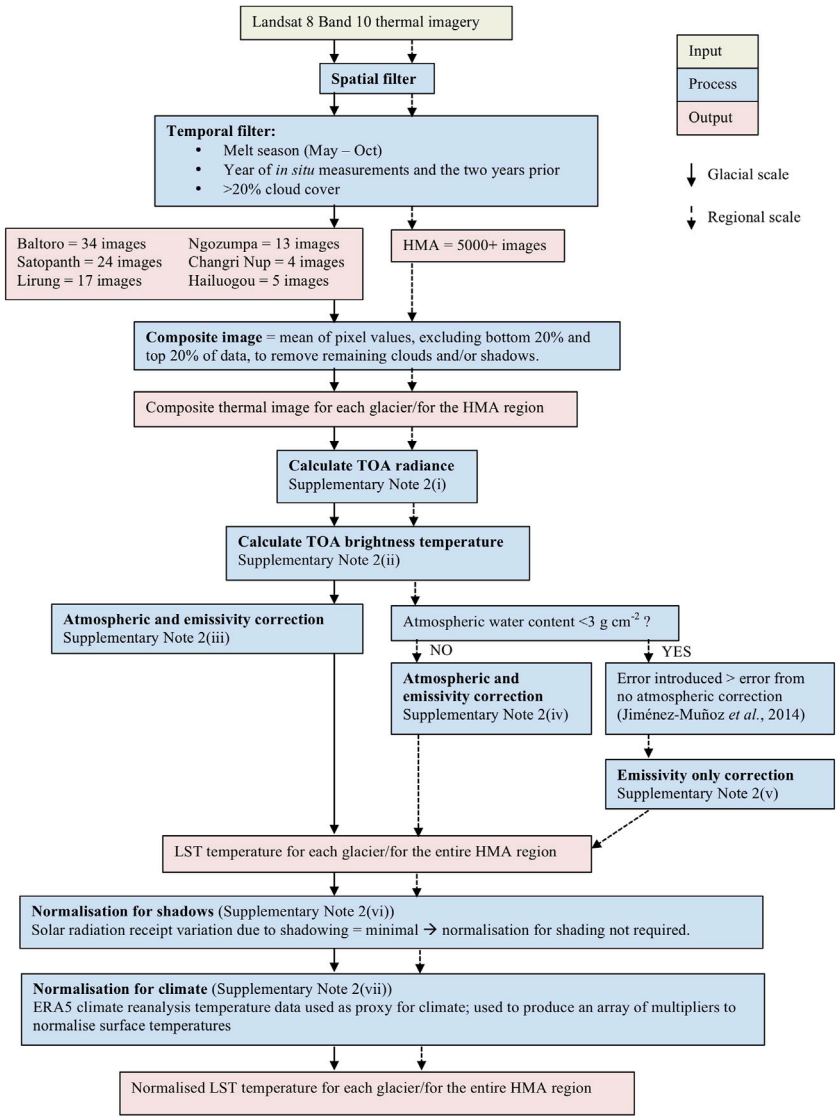

FIGURE 3 | Flowchart of methodology to calculate and normalise Land Surface Temperature from Landsat 8 thermal band imagery, within Google Earth Engine.

thickness. The exponential relationships based on Mihalcea et al. (2008b) and Kraaijenbrink et al. (2017) will henceforth be referred to as "exponential (M)" and "exponential (K)", respectively. The justification for the use of a rational curve to describe the relationship between the surface temperature and debris thickness depends on understanding the components of the surface energy balance model as multiples of either surface temperature or debris thickness. On this basis, the surface energy balance equation for a DCG surface can be rearranged by collecting the surface temperature terms to parameterise debris thickness in the form of a rational curve (**Data Sheet S1**: **Supplementary Note S1**).

The *in situ* debris thickness data were collected from published studies. Data collected using both manual excavation and Ground Penetrating Radar (GPR) were selected to ensure a wide range of debris thicknesses covering large areas of the glaciers. Data collected by manual excavation tended to cover a large proportion of the glaciers' area with discrete measurements but may have been skewed towards thinner debris, whereas data collected by GPR included thicker debris and tended to cover a smaller proportion of the glaciers' area but with dense measurements. Only data from the last decade were used, to align approximately with the availability of Landsat 8 thermal imagery (2013-present). Following these criteria, the six datasets selected were from: Baltoro Glacier (Groos et al., 2017), Satopanth Glacier (Shah et al., 2019), Lirung Glacier (McCarthy et al., 2017), Ngozumpa Glacier (Nicholson and Mertes, 2017; Nicholson, 2018), Changri Nup Glacier (Giese, 2019), and Hailuogou Glacier (Zhang et al., 2011) (**Figure 2**; **Supplementary Table S1**).

The cloud-computing platform, Google Earth Engine (GEE), was used to gather and process satellite thermal band imagery to calculate the land surface temperatures (**Figure 3**). Landsat 8 data

were chosen because they have a sufficiently high temporal and spatial resolution (16-day repeat cycle, acquired at 100 m resolution, but resampled to 30 m in the distributed data products). Landsat 8 has two thermal bands (Band 10 and Band 11), both collected by the Thermal Infrared Sensor (TIRS). Band 10 was chosen because Band 11 has a greater stray light error, resulting in a greater difference between ground-based and TIRS results (Montanaro et al., 2014). A composite thermal image was produced for each glaciated area of interest. The composite image was calculated from multiple thermal images, filtered to account for the variation caused by the variable presence of clouds and shadows, in addition to the seasonal variability of surface temperature itself. The image collection consisted of images with less than 20% cloud cover that fell within the melt season (May–October) in the year the *in situ* data were acquired, and the 2 years prior. To calculate the composite image from the image collection, the mean Digital Number, excluding the top 20% and bottom 20% of data, was calculated to remove any remaining clouds and shadows that would have exceptionally high or low pixel values, respectively.

After calculating the land surface temperature from the composite thermal imagery and correcting it for emissivity and atmospheric effects [**Data Sheet S1**: **Supplementary Note S2(i)–(v)**], the data were normalised for climate to account for differences in climate across the HMA region. To do this, a composite image of ERA5 climate reanalysis temperature data was produced for the HMA region, using all data within the melt season (May–October) over the time period in which *in situ* data were acquired (2013–2016). The average value of the composite image was calculated (287 K), and the percentage difference between the temperature of a pixel according to ERA5 composite and the average value was used to adjust the land surface temperature calculated from the thermal band imagery [**Data Sheet S1**: **Supplementary Note S2(vii)**].

Following Mihalcea et al. (2008b) and Kraaijenbrink et al. (2017), this study does not account for temperature change with elevation. The climate normalisation accounts for larger-scale spatial variations in temperature only, not for the changes in temperature with elevation at a glacier scale. Therefore, this should be acknowledged as an inherent limitation with the empirical temperature inversion method. Normalisation for shadows was also considered, but not applied because the effect was considered negligible [**Data Sheet S1**: **Supplementary Note S2(vi)**].

The normalised temperature was extracted from the relevant pixel for each debris thickness measurement to form the datasets used to derive the relationships. *K*-fold cross-validation was used to calculate the error associated with each relationship for each glacier dataset (Brenning et al., 2012). This involves randomly partitioning the dataset into k equal sized subsamples. One subsample is retained to later "test" the relationship, and the remaining subsamples are used as "training" data. The procedure is repeated k times, with each of the subsamples being used once as the "test" set. For our study, we used $k = 10$.

The median error (ME) and median absolute deviation (MAD) were calculated each time the relationship was trained and the mean of the ten ME values and of the ten MAD values were taken to produce two error values for each relationship. ME is an indicator of accuracy, while MAD is an indicator of precision. Statistics such as the root-mean-square error and the mean error were avoided because they are sensitive to the maximum debris thickness value. This is problematic because the non-linearity of three of the surface temperature/debris thickness equations results in small surface temperature errors having a much greater effect on the derived debris thickness estimates for higher surface temperatures (Evatt et al., 2015; Schauwecker et al., 2015). ME and MAD, however, are insensitive to the maximum debris thickness.

Quantifying the Relationship Between Glaciological Characteristics and Debris Thickness

Terrain characteristics that can influence the distribution of supraglacial debris include elevation, slope, aspect, and curvature (Lawson, 1979; Anderson and Anderson, 2018; Moore, 2018; Nicholson et al., 2018). Each can be extracted from Digital Elevation Models (DEMs). The preferred DEM source was the 8 m HMA DEM produced from high-resolution commercial optical satellite imagery (Shean et al., 2016; Shean et al., 2019). Its coverage is directly dependent on the availability of cloud-free optical imagery but as HMA receives 3,000 mm yr^{-1} of precipitation, cloud cover is abundant and coverage is discontinuous (Bolch et al., 2012; Yao et al., 2012; Wagnon et al., 2013; Maussion et al., 2014; Salerno et al., 2017). Thus, complete 8 m HMA DEMs were unavailable for Hailuogou Glacier and Baltoro Glacier. For these glaciers, therefore, the 1 arc second (~30 m) resolution Advanced Spaceborne Thermal Emission and Reflection Radiometer (ASTER) Global Digital Elevation Model Version 3 (GDEM 003) was used for the entire glacier, instead of the 8 m HMA DEM.

For each glacier, elevation values were extracted directly for each grid cell from the respective DEM. Slope, aspect and curvature of each grid cell were extracted using the *r.slope.aspect* tool in the GRASS QGIS toolbox. This tool compares the pixel value to the values of the adjacent pixels to calculate the slope of each pixel in degrees of inclination from horizontal and the aspect of the slopes in degrees counterclockwise from East. The cosine of aspect was taken subsequently to transform the measurements to a linear scale, from –1 (W) to 1 (E). The tool also calculates the profile curvature of the slope for each pixel, where a negative value represents a concave slope and a positive value represents a convex slope.

Glacier velocity has also been shown to influence the distribution of supraglacial debris (Rowan et al., 2015; Salerno et al., 2017; Bhushan et al., 2018). For each glacier, velocities were extracted from the NASA MEaSUREs ITS_LIVE project (Gardner et al., 2013). They are derived using the autonomous Repeat Image Feature Tracking (auto-RIFT v0.1) processing scheme applied to all Landsat 7 and 8 images acquired between August 2013 and May 2016 with 80% cloud cover or less (Gardner et al., 2018). Image pairs are searched for matching features, as defined by Normalised Cross Correlation maxima (Paragios et al., 2006). Both the terrain and velocity datasets were resampled to the grid size of the derived debris thickness datasets.

To determine statistically the relationship between debris thickness and these glaciological characteristics, two statistical tests were carried out on the dataset for each glacier. First, the non-parametric Spearman's Rank Correlation Coefficient was calculated by correlating all the derived debris thickness pixel values with each glaciological characteristic (elevation, slope, aspect, curvature, and velocity) for the corresponding pixel, for each individual glacier. A non-parametric test was chosen because none of the individual datasets were normally distributed, as determined using the Kolmogorov–Smirnov test with 99% confidence. However, it should be noted that this technique does not account for spatial autocorrelation. Furthermore, the correlation coefficients between debris thickness and each of the five glaciological variables ignore the role of any correlations between the glaciological characteristics. This covariance is high in some cases (**Supplementary Table S2**), which reduces the reliability of some of the correlation coefficients. Principal Components Analysis (PCA) diagnoses correlations among the glaciological characteristics by detecting patterns of variability that are shared between them. Second, therefore, for each glacier an unrotated PCA was carried out on datasets consisting of only the elevation, slope, aspect, curvature, and velocity data. Principal Components (PCs) were found, which are linear combinations of the glaciological characteristics that explain the directions of maximum variance in each glacier's dataset. The debris thickness data were excluded from the PCA because the glaciological characteristics describing the terrain and velocity of each glacier were treated as *a priori* controls on the spatial distribution of supraglacial debris thickness. The debris thickness data were later regressed against the PCs with an eigenvalue greater than or equal to 1, using forward stepwise regression. The regression equations were used to assess how much of the debris thickness variability could be explained by these PCs, in addition to the strength and direction of the contribution of each PC to debris thickness variability, for each glacier.

Deriving Debris Thickness Distribution at the Regional Scale

Debris thickness and surface temperature data from the six individual glaciers were collated and the four forms of empirical relationship (linear, rational, exponential (M), and exponential (K) were fitted to the combined dataset. Errors (ME and MAD) were calculated based on the results of a *k*-fold cross validation. The relationship with the smallest error was used to calculate debris thickness distribution from surface temperature over the entire HMA region.

The land surface temperature of the entire region was calculated from a composite thermal image produced for the HMA region in largely the same way as described for each glaciated area of interest (see Section *Deriving Debris Thickness Distribution From Surface Temperature at the Glacier Scale*). The only difference is the correction for the emissivity and atmospheric effects (**Figure 3**). The single-channel atmospheric correction algorithm implemented at the glacier scale [**Data Sheet S1**: **Supplementary Note S2(iii)**] could not be used at a regional scale because the parameter values vary significantly over space. The variation of these parameters can be approximated by water vapour [**Data Sheet S1**: **Supplementary Note S2(iv)**]. However, the atmospheric water content of the region is <3 g cm^{-2}, which introduces error greater than if no atmospheric correction was performed (Jiménez-Muñoz et al., 2014). Thus, an emissivity-only correction was performed [**Data Sheet S1**: **Supplementary Note S2(v)**]. The coverage of the composite thermal image was continuous over the entire HMA region due to the vast amount of Landsat imagery available over the region within the specified time period.

TABLE 1 | Correlations between the debris thickness/surface temperature datasets, for each glacier.

	Spearman's rank correlation coefficient	Significance	Sample size
Baltoro	0.72	0.003[b]	15
Satopanth	0.65	0.000[b]	180
Lirung	−0.23	0.000[b]	6,198
Ngozumpa	0.40	0.000[b]	144,908
Changri Nup	0.12	0.022[a]	380
Hailuogou	0.53	0.000[b]	140

[a]*indicates 95% confidence.*
[b]*indicates 99% confidence.*

RESULTS

Derivation of Debris Thickness at the Glacier Scale

Five of the six glacier debris thickness/surface temperature datasets show a positive correlation, while Lirung Glacier shows a negative correlation (**Table 1**). On closer inspection, the data for Lirung Glacier seem to comprise two samples, one of relatively high debris thickness values for low surface temperatures and one of relatively low thickness values for high temperatures. The two samples come from different parts of the glacier; the high thickness/low temperature group from close to the eastern margin and the low thickness/high temperature set from the central flowline and towards the western margin (**Figure 2C**). This could be a result of shading patterns, the presence of snow or interstitial ice or the unintentional bias of where debris thickness measurements were taken within the larger 30 m grids. We further note that the debris thickness measurements covered a relatively small area of the glacier compared to those on the other glaciers (the high temperature set represents just five 30 m pixels). Furthermore, the range of temperatures sampled is small (between 18 and 25°C) by comparison with the range measured across the whole glacier (0 and 29°C), whereas the range sampled on the other glaciers is more representative of their full range. For these reasons, the Lirung Glacier data set is excluded from further analysis at the glacier scale. The four forms of empirical relationship fitted to the data from the remaining five glaciers are shown in **Figure 4** and the derived constants for the relationships are given in **Table 2**.

For the five glaciers, the "best" relationship was taken to be that with the smallest ME (highest accuracy); for Baltoro and

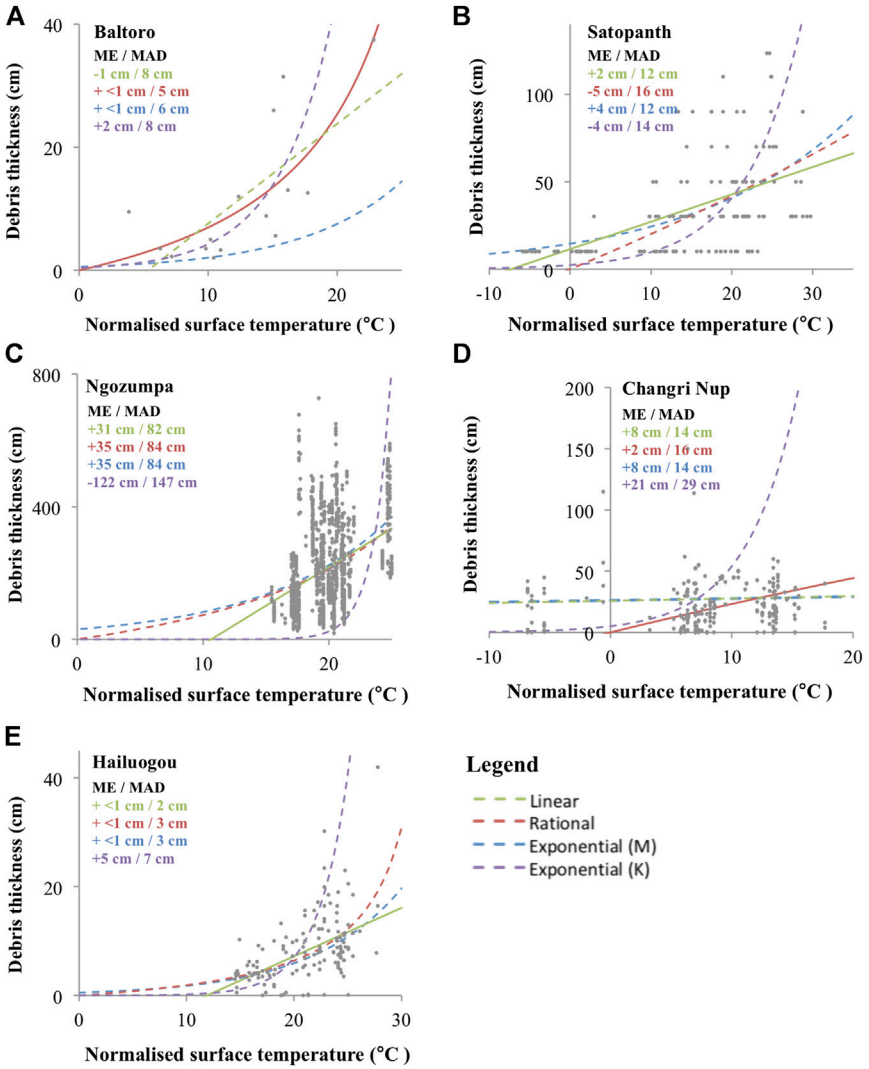

FIGURE 4 | Comparison of the errors of the linear (green), rational curve (red), exponential (M) (blue), and exponential (K) (purple) forms of the relationship between debris thickness and surface temperature for **(A)** Baltoro Glacier, **(B)** Satopanth Glacier, **(C)** Ngozumpa Glacier, **(D)** Changri Nup Glacier, and **(E)** Hailuogou Glacier. Circles represent data points, solid line indicates chosen relationship, dashed lines represent remaining relationships.

TABLE 2 | Constants derived for each of the four forms of debris thickness/surface temperature relationship [linear, rational curve, exponential (M) and exponential (K)], for all six glaciers and for the HMA region.

	Linear		Rational curve		Exponential (M)		Exponential (K)		
	c_1	c_2	c_1	c_2	c_1	c_2	$T_{s\ min}$	DT_{max}	$T_{s\ 95}$
Baltoro	1.624	−8.655	2.086	−0.065	0.13	−0.58	3.87	37.5	19.24
Satopanth	1.565	11.44	0.520	−0.002	0.052	−2.675	−5.88	123.5	27.72
Lirung	11.81	−190	1.80	−0.07	0.19	−0.10	18.75	230	25.13
Ngozumpa	23.32	−248.3	0.179	−0.004	0.10	−3.41	15.47	734	24.84
Changri Nup	0.186	25.83	0.402	0.002	0.006	−3.263	−6.83	200	15.52
Hailuogou	0.890	−10.59	7.405	−0.214	0.12	0.62	14.48	42	25.08
HMA	16.5	−123.2	0.558	−0.0198	0.07	−3.84	−6.83	734.28	23.84

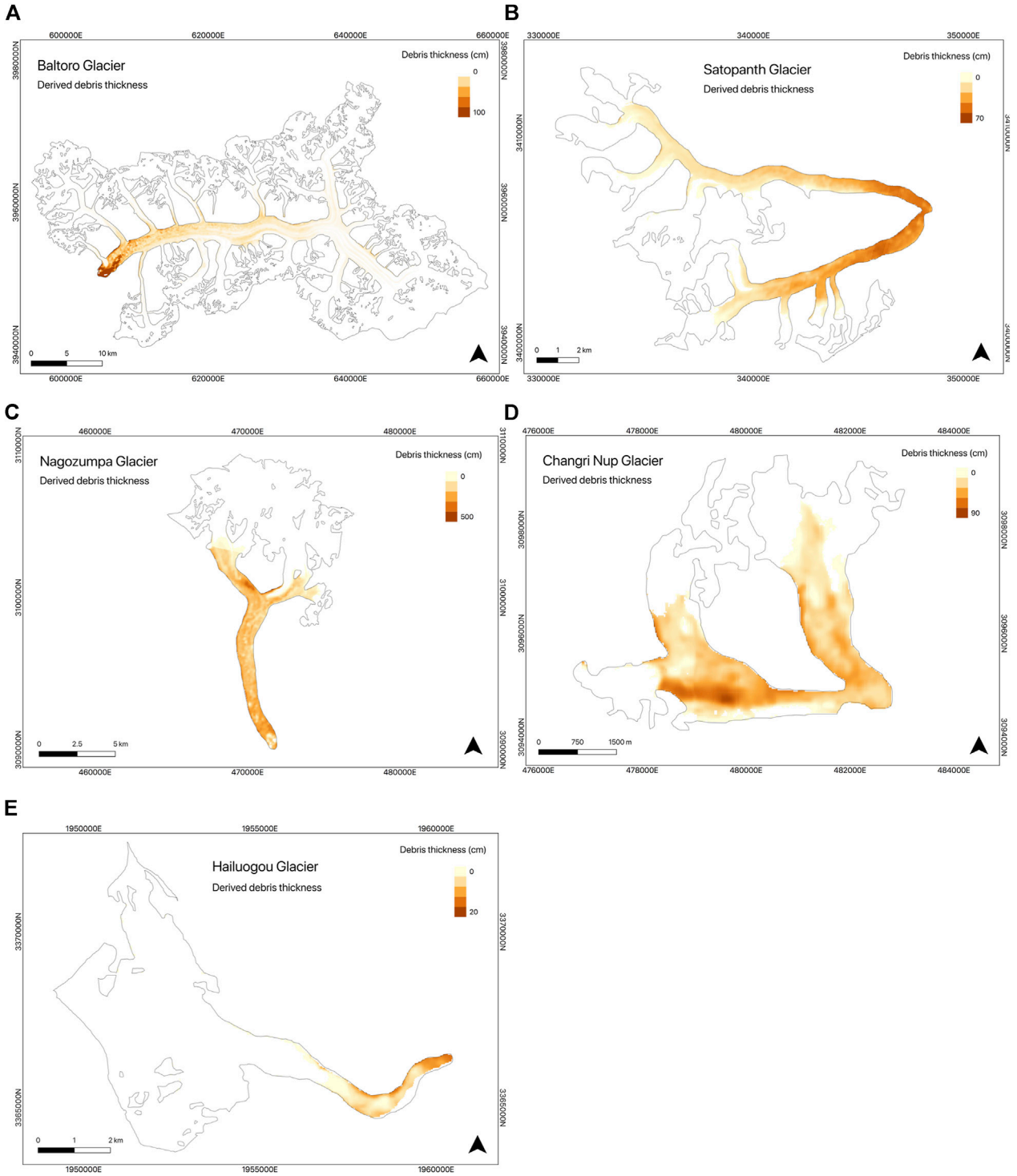

FIGURE 5 | Derived debris thickness distributions for the debris-covered parts of **(A)** Baltoro Glacier, **(B)** Satopanth Glacier, **(C)** Ngozumpa Glacier, **(D)** Changri Nup Glacier, and **(E)** Hailuogou Glacier. Glacier outlines are provided by GAMDAM (Sakai, 2019). See note in caption for **Figure 2** regarding Changri Nup Glacier outline. Note that debris thickness scales vary between glaciers.

Hailuogou Glaciers, where two relationships had similarly high accuracies, the relationship with additionally the smallest MAD (highest precision) was chosen (**Figure 4**). Different forms of relationship perform best across the five glaciers. The linear relationship performs best for three (Satopanth, Ngozumpa and Hailuogou Glaciers) and the rational curve performs best

TABLE 3 | Comparison of the measured and modeled mean (μ), median and standard deviation (σ) debris thicknesses, at a glacier scale and at a regional scale.

	Baltoro	Satopanth	Ngozumpa	Changri Nup	Hailuogou
Measured μ (cm)	11.7	28.9	208.7	27.5	8.2
Modelled glacier scale μ (cm)	16.3	22.7	163.9	26.3	4.9
Modelled regional scale μ (cm)	71.9	57.9	86.3	96.0	40.5
Measured median (cm)	8.8	10.0	172.4	20.0	7.5
Modelled glacier scale median (cm)	15.0	19.5	174.6	26.5	4.5
Modelled regional scale median (cm)	60.7	40.4	76.2	76.6	38.3
Measured σ (cm)	11.2	28.8	132.4	32.7	6.2
Modelled glacier scale σ (cm)	16.8	15.4	81.4	20.0	4.1
Modelled regional scale σ (cm)	94.6	50.3	613.1	79.4	15.4

TABLE 4 | Correlations between debris thicknesses derived at a glacier scale and selected glaciological characteristics (aspect, slope, curvature, velocity, and elevation).

	Baltoro *DT*	Satopanth *DT*	Ngozumpa *DT*	Changri Nup *DT*	Hailuogou *DT*
Sample size	320,914	29,713	22,153	7,933	2,045
Aspect	–0.19[b]	–0.01[b]	0.17[b]	0.16[b]	–0.01
Slope	–0.25[b]	0.07[b]	0.16[b]	0.05[b]	0.12[b]
Curvature	0.03[b]	–0.01[a]	–0.01	0.01	–0.10[b]
Velocity	0.08[b]	–0.27[b]	–0.29[b]	–0.28[b]	–0.28[b]
Elevation	–0.70[b]	–0.85[b]	–0.50[b]	–0.30[b]	–0.56[b]

Aspect, slope, curvature, and elevation derived from HMA 8 m DEM (Shean et al., 2019) for Satopanth, Ngozumpa and Changri Nup Glaciers, and from ASTER GDEM 003 for Baltoro and Hailuogou Glaciers. Velocities from the NASA MEaSUREs ITS_LIVE dataset (Gardner et al., 2013).

[a]*indicates 95% confidence.*

[b]*indicates 99% confidence.*

for two (Baltoro and Changri Nup Glaciers). For each glacier, the best relationship was used to derive the debris thickness distribution across its entire surface from the surface temperature measurements (**Figure 5**).

In addition to the ME and MAD values of the debris thickness relationships, the descriptive statistics of the modeled and measured debris thickness values are compared to further assess their error (**Table 3**). The modeled mean and median debris thicknesses generally correspond well to their respective measured values, particularly for Baltoro, Satopanth, Changri Nup, and Hailuogou Glaciers where the modeled and measured mean debris thicknesses vary by less than ~7 cm and the median values vary by less than ~10 cm. The difference between the modeled and the measured mean debris thicknesses is understandably greater for Ngozumpa Glacier at ~50 cm, where the ME of the surface temperature/debris thickness relationship is greater. However, the modeled and the measured median debris thicknesses correspond well for Ngozumpa Glacier. With respect to the standard deviation of the modeled and measured debris thicknesses, the values generally correspond well, particularly for Baltoro, Satopanth, Changri Nup, and Hailuogou Glaciers, but less so for Ngozumpa Glacier where the modeled standard deviation is significantly less than the measured. This is most likely a result of the model being less able to replicate the thick debris on Ngozumpa Glacier given the relationship between surface temperature and debris thickness decays with increasing debris thickness (Taschner and Ranzi, 2002).

Overall, we have confidence that the derived debris thickness maps are realistic, albeit with a centimetre to decimetre scale error. The debris thickness distributions for the five glaciers are used for further analysis to assess the controls on the spatial distribution of debris cover.

Quantification of the Relationship Between Glaciological Characteristics and Debris Thickness

The Spearman's Rank Correlation Coefficients between debris thickness and the glaciological characteristics are shown in **Table 4**. The strongest and most consistent correlation is the negative relationship between debris thickness and elevation, showing that thicker debris occurs at lower elevations. There is also a consistent negative relationship between debris thickness and velocity, suggesting that debris thickens as velocity decreases. There is a weak positive relationship between debris thickness and slope for all of the glaciers, except Baltoro. The relationship between debris thickness and aspect is mixed in both strength and direction, and the relationship with curvature is weak in most cases.

The component loadings of each PC (i.e., the correlation of each PC with a given glaciological characteristic) with an eigenvalue equal to or greater than 1 are given in **Table 5**, alongside the regression of debris thickness (*DT*) with these PCs, for each glacier. In most cases, elevation and velocity have the largest component loadings in PC1. All the

TABLE 5 | Component loadings of the Principal Components (PCs) with an eigenvalue equal to or greater than 1, and the regression equations and R^2 values (bold) of debris thickness (*DT*) with PCs as independent variables, for each glacier.

		PC1	PC2	PC3	R^2
		Component loadings	**Component loadings**	**Component loadings**	
Baltoro	Elevation	0.649	0.410	N/A (PC3 eigenvalue < 1)	
	Velocity	−0.606	0.342	N/A (PC3 eigenvalue < 1)	
	Slope	0.869	0.051	N/A (PC3 eigenvalue < 1)	
	Aspect	0.531	0.087	N/A (PC3 eigenvalue < 1)	
	Curvature	−0.175	0.852	N/A (PC3 eigenvalue < 1)	
	Regression	***DT* = 14.232 + (−8.946) PC1 + (−6.373) PC2**			**0.010**
Satopanth	Elevation	0.768	0.227	−0.057	
	Velocity	0.815	0.060	−0.076	
	Slope	−0.323	0.666	0.105	
	Aspect	0.033	0.741	0.232	
	Curvature	0.138	−0.235	0.957	
	Regression	***DT* = 23.371 + (−10.285) PC1 + (−2.571) PC2 + (1.075) PC3**			**0.505**
Ngozumpa	Elevation	0.852	0.016	0.016	
	Velocity	0.894	0.110	0.011	
	Slope	−0.577	0.223	0.183	
	Aspect	0.042	0.935	0.256	
	Curvature	0.076	−0.298	0.947	
	Regression	***DT* = 176.079 + (−26.858) PC1 + (12.106) PC2 + (3.472) PC3**			**0.178**
Changri Nup	Elevation	0.623	0.491	−0.115	
	Velocity	0.764	−0.054	0.046	
	Slope	−0.465	0.335	0.248	
	Aspect	0.171	0.796	−0.311	
	Curvature	0.109	0.246	0.910	
	Regression	***DT* = 29.999 + (−6.031) PC1 + (0.751) PC2**			**0.144**
Hailuogou	Elevation	0.808	0.220	0.079	
	Velocity	0.676	0.537	0.049	
	Slope	0.486	−0.703	0.076	
	Aspect	0.112	−0.329	0.824	
	Curvature	−0.360	0.449	0.627	
	Regression	***DT* = 6.074 + (−1.861) PC1 + (−1.239) PC2 + (−0.502) PC3**			**0.386**

regression relationships have the strongest relationship between debris thickness and PC1. This suggests that a proportion of the variation in debris thickness (as determined by the R^2 value) is principally controlled by elevation and velocity. The negative value of the relationship suggests that thicker debris is more likely on ice at low elevations with slower velocities. Baltoro Glacier is an exception to this as the largest component loadings in PC1 are the large positive values for slope and elevation, and the large negative value for velocity. The negative value of the relationship between debris thickness and PC1 on Baltoro suggests that thicker debris is more likely on ice with flatter slopes at lower elevations but with higher velocities, although the proportion of debris thickness variation explained by the PCs is very low (R^2 = 0.010).

The greatest component loadings in PC2 are slope and aspect in most cases, except for Baltoro and Hailuogou Glaciers. The relationship with PC2 is not consistent between the glaciers. Where PC2 has large, positive component loadings for slope and aspect, the relationship between PC2 and debris thickness is positive for Ngozumpa and Changri Nup, but negative for Satopanth. Therefore, on Satopanth, thicker debris is more likely on flatter, west-facing slopes, but on Ngozumpa and Changri Nup, thicker debris is more likely on steeper, east-facing slopes. Where PC2 has a large, positive component loading for curvature (Baltoro Glacier), the relationship with debris thickness is negative, suggesting that on this glacier, thicker debris is more likely on concave slopes.

The role of curvature also presides in the inclusion of PC3 in the regression relationships for Satopanth, Ngozumpa, and Hailuogou Glaciers. This suggests that thick debris is more likely on convex slopes on Satopanth and Ngozumpa Glaciers, but on concave slopes on Hailuogou Glacier. However, the contribution of curvature is not as dominant as the contribution of elevation, velocity, slope and aspect on these glaciers.

This analysis has quantified the interplay between five glaciological characteristics across five glaciers, highlighting dominant relationships between velocity and elevation, and between slope and aspect. Furthermore, it has quantified the ways in which the interaction of the characteristics explains a proportion of the variability in debris thickness across the five glaciers. In all cases, the relationship between debris thickness and PC1 is stronger than the relationship between debris thickness and PC2, suggesting that the contribution of velocity and elevation to debris thickness variability dominates over the contribution of slope and aspect for all the studied glaciers, except Baltoro where slope dominates. Moreover, this analysis reveals the small contribution of curvature on the distribution of debris thickness on four of the five glaciers.

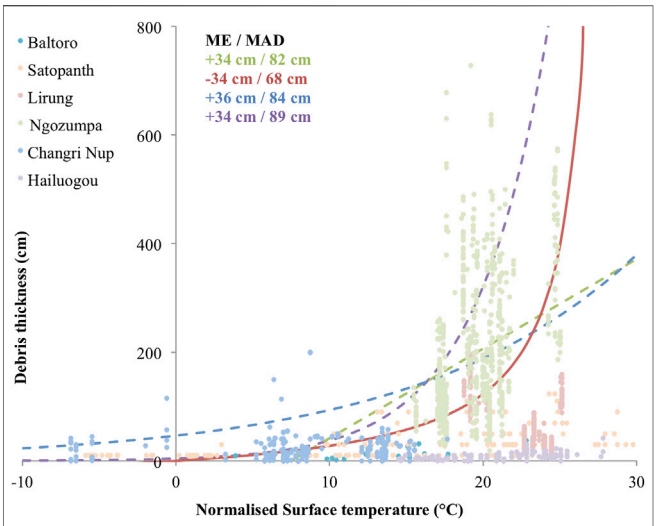

FIGURE 6 | Comparison of the errors of the linear relationship (green), rational curve (red), exponential (M) (blue), and exponential (K) (purple) forms of the relationship between debris thickness and surface temperature for the collated dataset from all six glaciers. The solid line indicates the chosen form of the relationship.

Map of Debris Thickness Distribution at the Regional Scale

To calculate the pattern of debris thickness distribution across the entire HMA, it is important to use a robust empirical relation that has been derived using data from a wide range of climate and topographical settings. The combined surface temperature/debris thickness dataset from the six glaciers has a mean debris thickness of 2.02 m, a median of 1.64 m, a standard deviation of 1.33 m, and a range spanning 0–7.34 m. This would appear to be representative of the debris thickness distribution we might expect on DCGs in the HMA region (Nicholson and Benn, 2013; Juen et al., 2014; Rounce and McKinney, 2014; Rounce et al., 2015). For the collated dataset (n = 151,821), the non-parametric Spearman's Rank Correlation Coefficient between surface temperature and debris thickness was 0.30 (99% confidence). The linear, rational curve, exponential (M) and exponential (K) relationships were fitted to this collated dataset and are graphed in **Figure 6**, with the derived constants given in **Table 2**. The Lirung Glacier data were included in this work because the possible sampling bias that was apparent at the glacier scale (**Figure 2**) was not apparent in the context of the entire dataset for all six glaciers (**Figure 6**).

The accuracies are the same for the linear relationship, the rational curve and the exponential (K) relationship, but the debris thickness is underestimated with the rational curve (ME = −34 cm) and overestimated with the linear and exponential (K) relationships (MEs = +34 cm). The rational curve has a smaller MAD (68 cm) than that for the linear and exponential (K) relationships (82 and 89 cm respectively) and is therefore the most precise. Although the MAD remains high for the rational curve, it is the best available with the given data for deriving debris thickness from surface temperature at the regional scale. We apply this relationship within the GEE platform to the debris-covered glaciated areas of the HMA region. The GEE code is available in the **Data Sheets S2, S3**.

Comparison of the debris thickness modeled using the regional scale relationship with the *in situ* debris thickness measurements available for the five glaciers analyzed above reveals that the regional scale relationship overestimates the mean and median debris thickness for glaciers with a relatively thin debris cover (Baltoro, Satopanth, Changri Nup, and Hailuogou Glaciers), but underestimates the mean and median debris thickness for glaciers with a relatively thick debris cover (Ngozumpa Glacier) (**Table 3**).

Due to the lack of *in situ* debris thickness data on other HMA glaciers, the accuracy of the relationship applied to other glaciers cannot be quantified. Thus, the method is validated by comparing qualitatively the debris thickness distributions produced by this relationship to maps of debris thickness produced using other remote sensing methods in the literature: Koxkar Glacier, Central Tien Shan (Juen et al., 2014); Imja-Lhotse Shar Glacier, Nepal Himalaya (Rounce and McKinney, 2014); and Bara Shigri Glacier, Indian Himalaya (Schauwecker et al., 2015). Their locations are in **Figure 1** and their debris thickness distributions are in **Figure 7**.

The debris thickness distribution on Koxkar Glacier produced using our method is very similar to that produced by Juen et al. (2014) (**Figure 7A**). In both cases, the debris is thicker closer to the terminus and along the eastern margin, and thinner upglacier. However, compared to the distribution produced by Juen et al. (2014), our distribution overestimates the thin debris upglacier by up to 30 cm and underestimates the thick debris near the terminus by up to 150 cm in some places. According to both our method and Rounce and McKinney (2014), on Imja-Lhotse Shar, thicker debris is present on the northern limb, particularly on the western margin and along the central flowline, while thinner debris dominates on the southern limb. On both limbs, the debris thins upglacier according to both methods (**Figure 7B**). Similarly, on Bara Shigri, both our method and Schauwecker et al. (2015) show the debris is thickest at the terminus and along the north-eastern margin and thins upglacier (**Figure 7C**). For both Imja-Lhotse Shar and Bara Shigri, however, our method tends to overestimate debris thickness by up to 50 cm for Imja-Lhotse Shar and by up to 60 cm for Bara Shigri. Both Rounce and McKinney (2014) and Schauwecker et al. (2015) comment that their methods tend to underestimate debris thickness but do not state by how much. Their underestimation would at least partly explain the differences between their modeled debris thickness values and those produced by our method.

Overall, the regional relationship performs well with regards to replicating the values and patterns of debris across all eight glaciers compared, but the depth of thin debris cover tends to be overestimated while that of thick debris cover tends to be underestimated. This is an expected result given the large ME and MAD (−34 and 68 cm, respectively) in comparison to the mean debris thickness of the region (2.02 m). Furthermore, there is a lack of independent *in situ* debris thickness data with which to validate these results. Therefore, although the patterns of debris thickness distribution determined by alternative methods are

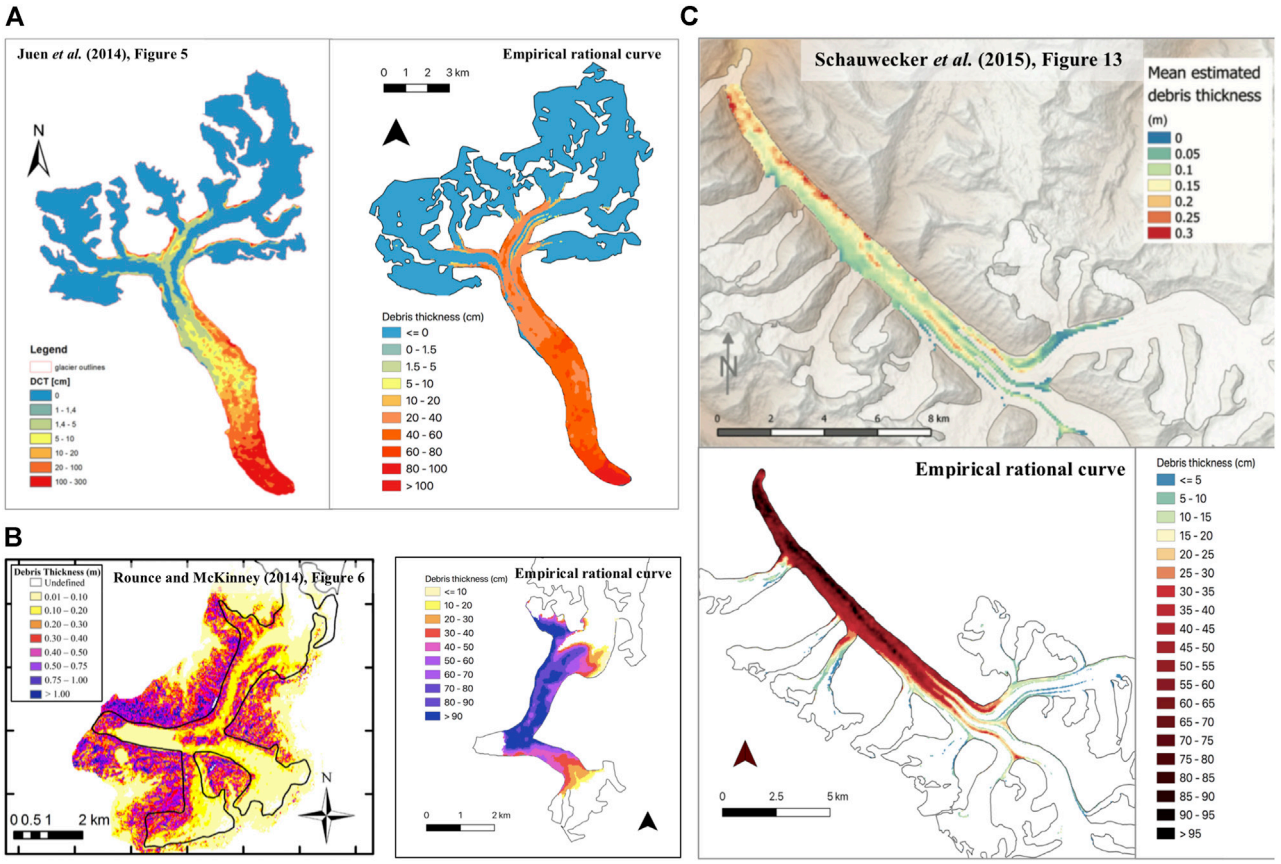

FIGURE 7 | Derived debris thickness distributions for the debris-covered parts of **(A)** Koxkar Glacier (UTM 44N), **(B)** Imja-Lhotse Shar Glacier (UTM 45N), and **(C)** Bara Shigri Glacier (UTM 44N), in comparison to published maps of derived debris thickness.

qualitatively replicated using the regional application of this empirical rational curve, its performance cannot be validated quantitatively. Thus, despite this empirical relationship improving upon the precision of the empirical relationship of Kraaijenbrink et al. (2017), the results should be treated with caution.

DISCUSSION

Debris Thickness at the Glacier Scale

For five out of the six glaciers, the derived surface temperature/debris thickness relationship produced glacier-scale debris thickness distributions with centimetre to decimetre scale errors. A rational curve was the most accurate for Baltoro and Changri Nup Glaciers, while a linear relationship was best for Satopanth, Ngozumpa and Hailuogou Glaciers. Over the range of input data, these two relationships perform similarly (**Figure 4**). The exponential (K) relationship consistently performs the worst and can be explained by the extent to which it responds to input data. The linear and rational curves are extrapolation approaches (Mihalcea et al., 2008a), whereas the exponential (K) relationship is a scaling approach (Kraaijenbrink et al., 2017). The extrapolation approaches use all input data to calculate parameters, whereas the scaling approach scales the relationship between 1 cm (assumed to be at the minimum surface temperature) and the maximum debris thickness (assumed to be at the 95th percentile of surface temperature). Thus, the extrapolation approaches are likely to produce more accurate debris thickness distributions because they are optimised using the entire dataset, whereas the scaling approach is optimised using only two data points.

For the extrapolation approaches to prove successful, the input data must be well distributed and represent the full range of debris thicknesses and surface temperatures across the glacier. This was why a realistic debris thickness/surface temperature relationship could not be derived for Lirung Glacier because its input surface temperature range was only 18–25°C, but the surface temperature of the debris-covered area reached 0°C upglacier. This represents a limitation with the distribution of the *in situ* dataset, which was focused near the glacier terminus and did not reflect the full range of surface temperatures present.

The success of the rational curve in producing the most accurate debris thickness distributions for Baltoro and Changri Nup Glaciers is important because the only non-linear relationships applied previously in published works have been

exponential forms (Mihalcea et al., 2008b; Kraaijenbrink et al., 2017). The success of the rational curve could be because it passes through the origin and so calculates clean ice to be at 0°C. The surface temperature datasets used to derive the relationships are mean values over the melt seasons, so clean ice can be assumed to be at its melting point of 0°C. Therefore, the rational curve provides a physically accurate representation of the surface temperature/debris thickness relationship. However, the rational curve does not perform best for all glaciers. It is not clear which factors, if any, cause the linear relationship to perform better. Tentatively, we suggest that debris thickness may influence whether the linear relationship or rational curve provides a better fit to the data. Satopanth and Ngozumpa Glaciers, where a linear relationship is more accurate, have thicker debris covers than Baltoro and Changri Nup, where a rational curve is more accurate. The distribution of debris thickness data used to fit the relationship is also likely a controlling factor, in addition to the potential role of glacier-specific debris sources. Due to the limited number of glaciers studied, these suggestions are only tentative, and more research is required in this regard.

The Relationship Between Glaciological Characteristics and Debris Thickness

The percentage of debris thickness variability explained by the PCs varies between 1% for Baltoro Glacier and 50% for Satopanth Glacier. The PCs represent the combined influence of surface elevation, slope, aspect, curvature and velocity. Elevation and velocity represent primary controls on debris dispersal. Elevation is a proxy for mass movement, by representing the cumulative effects of mass movement processes from the valley sides (Dunning et al., 2015), and for ablation rate, which partially controls melt out rate of englacial debris (Rowan et al., 2015). Velocity represents the influence of ice flow on the concentration of debris through horizontal compression. Slope, aspect and curvature are surrogates for factors controlling the secondary mechanisms of debris dispersal. However, mass movement processes from the valley sides and the melt out of englacial debris cannot be explained by elevation alone. Therefore, it is possible that the unexplained debris thickness variance is explained by processes related to mass movement from the valley sides or the melt out of englacial debris, but which are not fully accounted for in the PCs, such as bedrock geology.

Of particular note is the minimal proportion of debris thickness variability explained on Baltoro Glacier, where just 1% is accounted for by the PCs. **Figure 2A** highlights the presence of multiple tributary glaciers feeding Baltoro Glacier. Thus, the emergence of englacial debris at the confluence of multiple ice sources is likely to be a dominant mechanism controlling the distribution of debris thickness here (Eyles and Rogerson, 1978; Deline, 2005). This mechanism is not accounted for in the selected glaciological characteristics and provides a potential explanation as to why only 1% of the debris thickness variability is explained. Given the negligible proportion of debris thickness variability explained, the relationship between glaciological characteristics and debris thickness on Baltoro Glacier is not discussed further.

On Satopanth, Ngozumpa, Changri Nup, and Hailuogou Glaciers, results show that thicker debris is more likely to be found where elevation and velocity are both low (**Table 5**). This is an expected finding given previous observations that debris thickness tends to increase towards the terminus (Kirkbride and Warren, 1999; Anderson, 2000; Kellerer-Pirklbauer, 2008; Mihalcea et al., 2008b; Gibson et al., 2017), where ice is lower lying and slower moving (Kirkbride, 2002; Quincey et al., 2009a; Quincey et al., 2009b; Scherler et al., 2011b). Lower elevations, and therefore warmer temperatures, initially encourage the melt out of englacial debris (Kirkbride and Deline, 2013) and encourage erosion (Heimsath and McGlynn, 2008; Banerjee and Wani, 2018). Once enough debris cover has built up to inhibit ablation, the zone of maximum velocity shifts upglacier due to the decreasing thickness and slope of the debris-covered portion, resulting in a slow-flowing debris-covered tongue (Scherler et al., 2011a). The negative velocity gradient causes debris thickness to increase further due to horizontal compression, as dictated by the law of mass conservation (Nakawo et al., 1986; Anderson and Anderson, 2016).

On Satopanth Glacier, the results indicate that thicker debris is found on flatter, west-facing slopes. This relationship agrees with the literature, which states that thicker debris is more likely on flatter slopes, where the chance of debris sliding is lower (Moore et al., 2018; Nicholson et al., 2018). The incidence of sliding is also reduced on slopes with a lower receipt of solar radiation, i.e., northwest-facing slopes in the Northern Hemisphere (Hock and Noetzli, 1997), because meltwater production is lower and therefore less able to act as a lubricant for sliding. Thus, debris is more likely to build up to greater thicknesses where meltwater production is less (Lawson, 1979; Nicholson et al., 2018). Satopanth Glacier is the only glacier to corroborate previous findings in the literature with regards to the way in which velocity/elevation *and* slope/aspect control debris thickness distribution.

On the remaining glaciers (Hailuogou, Ngozumpa, and Changri Nup), debris thickness variability is principally controlled by velocity and elevation (PC1) in the same way as on Satopanth Glacier. However, for these three glaciers, slope and aspect have unexpected relationships with debris thickness. On Hailuogou Glacier, thicker debris is more likely to be found on steeper slopes and on Ngozumpa and Changri Nup Glaciers thicker debris is more likely on steeper, east-facing slopes. This contrasts to the literature, which states sliding is more likely to occur on steeper, east-facing slopes (Lawson, 1979; Moore et al., 2018; Nicholson et al., 2018), causing thinner debris to dominate in these locations.

It is possible that a methodological bias caused this unexpected relationship. The Landsat satellite has a sun-synchronous orbit and so the images used to derive debris thicknesses were taken at 10:11 (±15 min) Mean Local Time (MLT). At the time the images are taken, the sun azimuth varies between 120° and 140° and so the southeast-facing slopes receive the most direct sunlight. This could result in a bias towards greater surface temperatures, and therefore calculated thicker debris, on southeast-facing slopes. Furthermore, the sun elevation angle, at the time the images are taken, varies between 55° and 65°. Thus, slopes at this angle would receive the

sunlight most directly, compared to flatter slopes where the sunlight would be spread over a larger area. The slopes on the debris-covered surfaces have a maximum of 70°. Thus, the steeper slopes could be biased towards higher surface temperatures, and towards calculated thicker debris. Therefore, the occurrence of thicker debris on steeper, southeast-facing slopes on Hailuogou, Ngozumpa, and Changri Nup Glaciers could be due to this methodological bias.

However, because the thermal images used to calculate the land surface temperature are all acquired at the same time of day and the temperatures were normalised to take into account spatial variations in the climate of the region, this methodological bias would occur systematically, such that all steep and southeast-facing slopes would be affected. Such a bias does not seem to occur on Satopanth Glacier, where thicker debris occurs on flatter, west-facing slopes. Furthermore, when looking at the regional scale debris thickness distribution, there does not appear to be widespread evidence that glaciers with a predominantly easterly aspect have thicker debris cover than glaciers with different aspects. If the outlined bias had a notable impact, it would likely be evident on all debris thickness distributions, but it does not appear to be, so the likelihood of a methodological bias is small.

Therefore, it is suggested that the debris is, in fact, thicker on steep, east-facing slopes on Ngozumpa, Changri Nup, and Hailuogou Glaciers. However, local scale slope and aspect are not necessarily the factors controlling the prevalence of thick debris. Isolated areas of thick debris cover may result from the occurrence of localised supraglacial debris supply from mass movement from the valley sides (Dunning et al., 2015). On Ngozumpa, Changri Nup, and Hailuogou Glaciers, isolated patches of thick debris can be identified. On the southern of the two lobes comprising Changri Nup Glacier, there is a thick ridge of debris in the glacier's midline (**Figure 5D**). The debris that emerges as part of this surface ridge is eroded from a large rocky spur that generates many rockfalls (Giese, 2019). On Ngozumpa Glacier, there is an isolated area of thick debris cover near the upglacier limit of debris cover, on the northern edge of the northwestern branch (**Figure 5C**). On Hailuogou Glacier, thick debris can be identified along the entire northern edge of the debris-covered tongue (**Figure 5E**). It is possible that these areas of thick debris cover on Ngozumpa and Hailuogou Glaciers are also caused by mass movement onto the glacier surface, rather than by the gravitational reworking of debris as a result of the local slope and aspect of the surface. Images in **Data Sheet S1**: **Supplementary Note S3** show scars on the valley sides suggesting large scale mass movement onto these specific areas of Ngozumpa and Hailuogou Glaciers.

The role of valley side mass movement has not been comprehensively considered in this study; only implicitly with elevation as a proxy. To do so would involve consideration of the valley side slopes (Scherler et al., 2011b), temperatures (Nagai et al., 2013; Banerjee and Wani, 2018; Kuschel et al., 2020) and geologies (Fischer et al., 2012), all of which control the temporal and spatial occurrence of mass movement processes (Draebing and Krautblatter, 2019). The images in **Data Sheet S1**: **Supplementary Note S3** take the first steps required to investigate whether the unexpected relationships between debris thickness and slope/aspect on Ngozumpa, Changri Nup, and Hailuogou Glaciers are caused by large scale mass movement processes rather than local scale debris transfer processes, but further research is needed.

The results on Satopanth, Ngozumpa and Hailuogou Glaciers are of particular interest because the regression relationships suggest a relationship between curvature and the distribution of debris thickness. The role of curvature is less than that of velocity/elevation and slope/aspect, but to the authors' knowledge these are the first empirical relationships to have been found between curvature and debris thickness (cf. Nicholson et al., 2018). On Hailuogou Glacier, the debris is thicker where slopes have a concave profile. This agrees with the expectation that debris should become more stable in a downslope direction on concave slopes as the gradient of the slope decreases (Moore, 2018). However, on Satopanth and Ngozumpa Glaciers, the debris is thicker on slopes with a convex profile. The reasons for this are currently unknown and require further research.

Debris Thickness Distribution at the Regional Scale

To the authors' knowledge, Kraaijenbrink et al. (2017) have produced the only published estimate of glacier debris thickness distribution for the entire HMA region. However, the present study suggests that a rational curve is equally, if not more, appropriate for deriving debris thickness from surface temperature over the HMA region. The ME of the rational curve (−34 cm) is equal in magnitude to the ME of the exponential (K) relationship (+34 cm), but the exponential (K) overestimates debris thickness, while the rational curve underestimates it. The MAD associated with the rational curve (68 cm) is smaller than that associated with the exponential (K) curve (89 cm). Therefore, the use of the rational curve rather than the exponential (K) curve has the potential to derive more precise glacier debris thickness distributions across HMA. Despite this improved precision, the results should be treated with caution given the ME and MAD remain high as a proportion of the mean debris thickness of 2.02 m, at 17 and 34%, respectively.

Figure 8 displays the difference between the debris thickness derived using the rational curve and that derived using the exponential (K) relationship. The greatest difference between the two distributions occurs at the glacier termini, where debris is thickest. The exponential (K) relationship calculates debris to be >3 m thicker than that calculated by the rational curve in some cases. However, for areas with thinner debris covers, such as upglacier locations, the two relationships produce comparable results. This is because the relationships are very similar until ~10°C (~30 cm), at which point the rational curve begins to underestimate debris thickness and the exponential (K) relationship begins to overestimate debris thickness for a given surface temperature (**Figure 6**).

The application of either empirical relationship to the entire HMA region is inevitably associated with some limitations, primarily as a result of the large spatial variations in temperature that exist in the HMA region (Bookhagen and Burbank, 2010; Bolch et al., 2012; Kapnick et al., 2014; Rounce

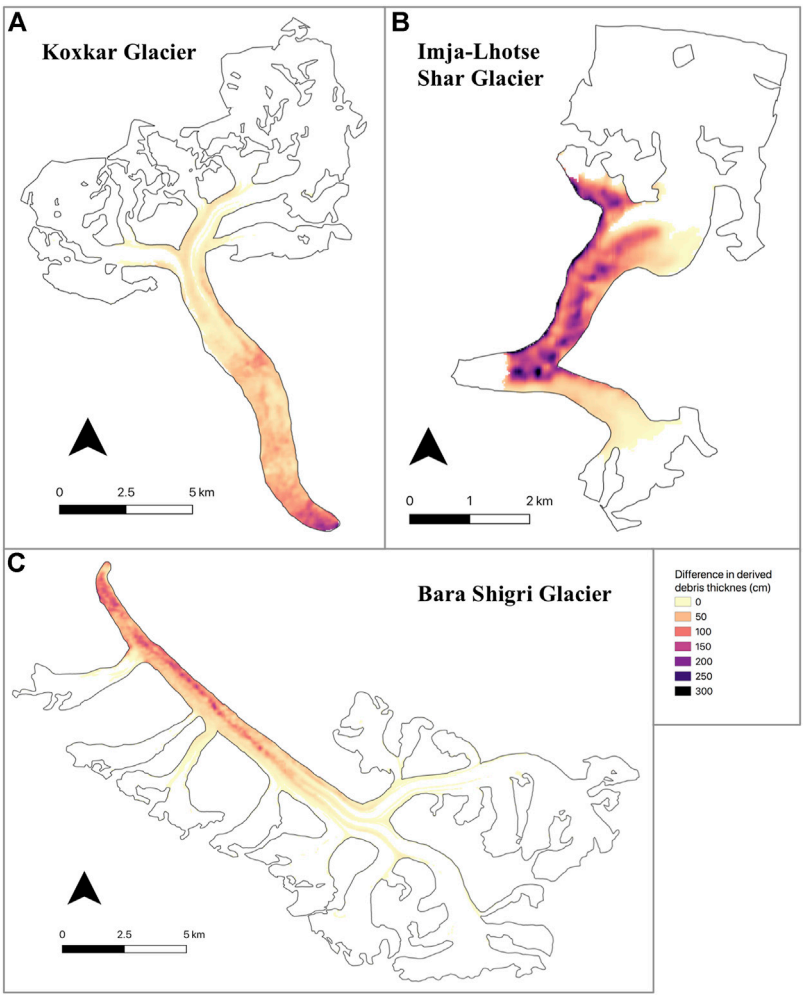

FIGURE 8 | The difference between the debris thickness calculated using rational curve and the exponential (K) form of the regional scale empirical relationship, for **(A)** Koxkar Glacier, **(B)** Imja-Lhotse Shar Glacier, and **(C)** Bara Shigri Glacier (difference calculated by subtracting rational curve debris thickness from exponential (K) debris thickness).

et al., 2019). However, the impact of this limitation has been mitigated in this study, namely though the climate normalisation applied to the thermal imagery [**Data Sheet S1**: **Supplementary Note S2(vii)**]. Furthermore, there is seasonal variability in land surface temperature. The use of composite thermal images calculated from the mean of thermal imagery over the melt season addresses this issue (**Figure 3**). The reduction of climatic influence and seasonal variation in this way increases the proportion of surface temperature controlled by debris thickness, and thus increases our confidence in the regional application of the relationship.

Limitations

There are several limitations of our approach to calculating glacier debris thickness. First, calculating land surface temperature from thermal satellite imagery inevitably means that the calculated temperature represents at best a 30 m × 30 m area (resampled from a 100 m × 100 m area). Only a single debris thickness value can be derived for a pixel area represented by a single surface temperature value. However, debris thickness varies on a scale smaller than a 30 m × 30 m area (Nicholson and Benn, 2013). In the datasets used to derive the empirical relationships, there is often a range of debris thickness measurements associated with a single surface temperature (**Figure 4**). The details of this heterogeneity are not displayed in the derived debris thickness distributions, although it does contribute to our error calculations. Thus, there is a need for future research to quantify debris thickness variability within a 30 m × 30 m area. The acquisition of more detailed *in situ* datasets would contribute towards this and allow for statistical modeling (e.g., the construction of semi-variograms) or interpolation (e.g., kriging) at finer spatial scales than the resolution of the thermal imagery.

Second, the empirical relationship between surface temperature and debris thickness is less accurate at greater debris thicknesses. This is because as debris thickness

increases, the influence of glacier ice on the surface temperature decreases, and eventually stops, due to the reduced effectiveness of heat conduction with depth (Taschner and Ranzi, 2002; Ranzi et al., 2004). Thus, a warmer surface temperature may represent a wider range of debris thicknesses than a cooler surface temperature. This exposes another limitation of this empirical method in that it performs best for thinner debris, where the relationship between surface temperature and debris thickness is stronger (Mihalcea et al., 2006; Mihalcea et al., 2008a; Mihalcea et al., 2008b). However, melt rates below a thick debris layer are generally low, and so the impact of this limitation will be negligable in the context of a melt model.

Third, the temperature inversion method does not account for variation in surface temperature with elevation. Following the work of Mihalcea et al. (2008b) and Kraaijenbrink et al. (2017), surface temperature is assumed to vary solely in response to debris thickness. Potential solutions to this problem include the derivation of empirical relationships for each elevation band of a glacier surface (Mihalcea et al., 2008a) or the use of an surface energy balance model to account for all the factors that contribute towards the surface temperature (Foster et al., 2012; Rounce and McKinney, 2014; Schauwecker et al., 2015).

Finally, limitations remain with the regional application of our empirical relationship due to the limited dataset from which the relationship was derived. There are 134,770 glaciers in the HMA region (according to GAMDAM; Sakai, 2019), and our relationship was derived using data from just six of them. The six glaciers differ in their debris thickness and distribution, incorporating some of the variation of debris thickness characteristics in the region, but our work would be improved by the inclusion of more *in situ* debris thickness datasets. More data would improve both the empirical relationship itself and provide more information for the uncertainity assessment. Our rational curve provides an alternative to the previously used exponential (K) relationship for calculating glacier debris thickness distribution across the whole of HMA but both empirically-based estimates should be treated with caution. Further work is required to compare both these estimates against other methods inverting for debris thickness using the energy balance model approach (Foster et al., 2012; Rounce and McKinney, 2014; Schauwecker et al., 2015), as well as other measurements of debris thickness using either *in situ* or airborne techniques.

CONCLUSION

The comparison of four different types of empirical relationship fitted to *in situ* debris thickness and remotely sensed surface temperature on six glaciers shows that a rational curve and a linear relationship consistently perform best. It is tentatively suggested that the linear relationship performs best for glaciers with a thicker debris cover, while the rational curve performs best for glaciers with a thinner debris cover. However, their success was dependent on the availability of well-distributed input data that represented the full range of debris thicknesses and surface temperatures.

This study also found consistently that debris thickness increases downglacier, as both elevation and velocity decrease. Debris thickness has a weaker and less consistent statistical correlation with slope and aspect: on Satopanth Glacier, thicker debris occurs on flatter, more west-facing slopes (where smaller gradients and less meltwater increase the stability of the debris at the local scale), whereas on Ngozumpa, Changri Nup, and Hailuogou Glaciers, thicker debris occurs on steeper, more east-facing slopes (possibly due to the influence of larger scale supraglacial debris supply from the valley sides). Furthermore, the first empirical evidence of a statistical correlation between debris thickness and curvature was found. On Hailuogou Glacier, thicker debris occurs on more concave slopes, but on Satopanth and Ngozumpa Glaciers, thicker debris occurs on more convex slopes. These findings will be useful in the context of modeling debris cover evolution, as the topography and dynamics of DCGs respond to climate-driven mass balance change.

Finally, a rational curve derived from the collated dataset of the six glaciers produces a debris thickness distribution over the HMA region which is as accurate as that produced using the exponential curve pioneered by Kraaijenbrink et al. (2017) and is more precise. Despite this, the MAD value remains high, so the acquisition and sharing of more *in situ* debris thickness measurements is required to further improve and validate the method.

This study contributes to a fuller understanding of the current distribution of debris thickness on DCGs in HMA, at both the glacier and the regional scale. It also points to some of the important glaciological controls on debris thickness distribution, which will be useful for training models of debris thickness evolution in response to changes in glacier surface topography and velocity. These findings should feed into future research predicting DCG response to climate change, and help improve the accuracy of future runoff projections. This is of particular importance in HMA where better estimations of local and regional water availability as well as global sea level rise will inform essential socio-economic and political decisions.

DATA AVAILABILITY STATEMENT

The original contributions presented in the study are included in the article/**Supplementary Material**, further inquiries can be directed to the corresponding author.

AUTHOR CONTRIBUTIONS

KB and IW designed the research. AG and QL provided *in situ* debris thickness data. KB analysed the data and results and wrote the initial version of the manuscript under the supervision of IW. All authors helped edit and improve the manuscript.

FUNDING

This research was undertaken while KB was in receipt of a United Kingdom Natural Environment Research Council PhD

studentship awarded through University of Cambridge Doctoral Training Partnerships (grant number: NE/S007164/1). QL is funded by the National Science Foundation of China (NSFC 41871069). AG's work on debris cover thickness supported by NSF GRF DGE-1313911 and NASA Space Grant NNX15AH79H.

ACKNOWLEDGMENTS

We acknowledge the use of the freely available Landsat imagery and ERA5 data, accessed through the Google Earth Engine cloud-computing platform. We also acknowledge the use of the freely available HMA 8 m DEM (Shean et al., 2016; Shean et al., 2019), the ASTER GDEM 003 (Hulley et al., 2015) and NASA MEaSUREs ITS_LIVE velocities (Gardner et al., 2018; Gardner et al., 2013). We also acknowledge the use of published debris thickness data: for Lirung Glacier (**Supplementary Material**, McCarthy et al., 2017); Ngozumpa Glacier (Nicholson and Mertes, 2017; Nicholson, 2018); Baltoro Glacier (**Table 3**, Groos et al., 2017); and Satopanth Glacier (digitised from **Figure 1**, Shah et al., 2019). We thank Neil Arnold for sharing the model developed by Arnold and Rees (2009) to calculate the potential solar radiation reaching glacier surfaces. Finally, we thank Mike McCarthy for his ideas and encouragement throughout the execution of this work. **Figure 7C** is reprinted from Figure 13 in Schauwecker et al. (2015), Journal of Glaciology, with permission of the International Glaciology Society and the original author. The content of this manuscript is based on the dissertation written by KB submitted for the degree of Master of Philosophy at the Scott Polar Research Institute, University of Cambridge, which is available at: https://doi.org/10.17863/CAM.58844. We are grateful to Tom Holt and Maria Shahgedanova for their detailed comments that significantly improved the quality of this paper.

SUPPLEMENTARY MATERIAL

The Supplementary Material for this article can be found online at: https://www.frontiersin.org/articles/10.3389/feart.2021.657440/full#supplementary-material

REFERENCES

Anderson, L. S., and Anderson, R. S. (2018). Debris Thickness Patterns on Debris-Covered Glaciers. *Geomorphology* 311, 1–12. doi:10.1016/j.geomorph.2018.03.014

Anderson, L. S., and Anderson, R. S. (2016). Modeling Debris-Covered Glaciers: Response to Steady Debris Deposition. *The Cryosphere* 10 (3), 1105–1124. doi:10.5194/tc-10-1105-2016

Anderson, R. S. (2000). A Model of Ablation-Dominated Medial Moraines and the Generation of Debris-Mantled Glacier Snouts. *J. Glaciol.* 46 (154), 459–469. doi:10.3189/172756500781833025

Bajracharya, S. R., and Mool, P. (2009). Glaciers, Glacial Lakes and Glacial lake Outburst Floods in the Mount Everest Region, Nepal. *Ann. Glaciol.* 50, 81–86. doi:10.3189/172756410790595895

Banerjee, A., and Wani, B. A. (2018). Exponentially Decreasing Erosion Rates Protect the High-Elevation Crests of the Himalaya. *Earth Planet. Sci. Lett.* 497, 22–28. doi:10.1016/j.epsl.2018.06.001

Benn, D. I., and Lehmkuhl, F. (2000). Mass Balance and Equilibrium-Line Altitudes of Glaciers in High-Mountain Environments. *Quat. Int.* 65, 15–29. doi:10.1016/S1040-6182(99)00034-8

Bhushan, S., Syed, T. H., Arendt, A. A., Kulkarni, A. V., and Sinha, D. (2018). Assessing Controls on Mass Budget and Surface Velocity Variations of Glaciers in Western Himalaya. *Sci. Rep.* 8, 1–11. doi:10.1038/s41598-018-27014-y

Bolch, T., Kulkarni, A., Kääb, A., Huggel, C., Paul, F., Cogley, J. G., et al. (2012). The State and Fate of Himalayan Glaciers. *Science* 336 (6079), 310–314. doi:10.1126/science.1215828

Bookhagen, B., and Burbank, D. W. (2010). Toward a Complete Himalayan Hydrological Budget: Spatiotemporal Distribution of Snowmelt and Rainfall and Their Impact on River Discharge. *J. Geophys. Res.* 115 (F3). doi:10.1029/2009JF001426

Brenning, A., Long, S., and Fieguth, P. (2012). Detecting Rock Glacier Flow Structures Using Gabor Filters and IKONOS Imagery. *Remote Sensing Environ.* 125, 227–237. doi:10.1016/j.rse.2012.07.005

Brock, B. W., Mihalcea, C., Kirkbride, M. P., Diolaiuti, G., Cutler, M. E. J., and Smiraglia, C. (2010). Meteorology and Surface Energy Fluxes in the 2005-2007 Ablation Seasons at the Miage Debris-Covered Glacier, Mont Blanc Massif, Italian Alps. *J. Geophys. Res.* 115 (D9). doi:10.1029/2009JD013224

Brun, F., Berthier, E., Wagnon, P., Kääb, A., and Treichler, D. (2017). A Spatially Resolved Estimate of High Mountain Asia Glacier Mass Balances from 2000 to 2016. *Nat. Geosci* 10 (9), 668–673. doi:10.1038/ngeo2999

Deline, P. (2005) Change in Surface Debris Cover on Mont Blanc Massif Glaciers after the'Little Ice Age' Termination, *The Holocene*, 15, 302–309. doi:10.1191/0959683605hl809rr

Draebing, D., and Krautblatter, M. (2019). The Efficacy of Frost Weathering Processes in Alpine Rockwalls. *Geophys. Res. Lett.* 46, 6516–6524. doi:10.1029/2019GL081981

Dunning, S. A., Rosser, N. J., McColl, S. T., and Reznichenko, N. V. (2015). Rapid Sequestration of Rock Avalanche Deposits within Glaciers. *Nat. Commun.* 6.(1), 1–7. doi:10.1038/ncomms8964

Dyhrenfurth, G. O. (2011). *To the Third Pole - The History of the High Himalaya*. Nielsen Press.New York, USA,

Evatt, G. W., Abrahams, I. D., Heil, M., Mayer, C., Kingslake, J., Mitchell, S. L., et al. (2015). Glacial Melt under a Porous Debris Layer. *J. Glaciol.* 61 (229), 825–836. doi:10.3189/2015JoG14J235

Eyles, N., and Rogerson, R. J. (1978). A Framework for the Investigation of Medial Moraine Formation: Austerdalsbreen, Norway, and Berendon Glacier, British Columbia, Canada. *J. Glaciol.* 20, 99–113. doi:10.3189/S0022143000021249

Farinotti, D., Huss, M., Fürst, J. J., Landmann, J., Machguth, H., Maussion, F., et al. (2019). A Consensus Estimate for the Ice Thickness Distribution of All Glaciers on Earth. *Nat. Geosci.* 12, 168–173. doi:10.1038/s41561-019-0300-3

Fischer, L., Purves, R. S., Huggel, C., Noetzli, J., and Haeberli, W. (2012). On the Influence of Topographic, Geological and Cryospheric Factors on Rock Avalanches and Rockfalls in High-Mountain Areas. *Nat. Hazards Earth Syst. Sci.* 12 (1), 241–254. doi:10.5167/uzh-6755610.5194/nhess-12-241-2012

Foster, L. A., Brock, B. W., Cutler, M. E. J., and Diotri, F. (2012). A Physically Based Method for Estimating Supraglacial Debris Thickness from thermal Band Remote-Sensing Data. *J. Glaciol.* 58 (210), 677–691. doi:10.3189/2012JoG11J194

Gardner, A. S., Moholdt, G., Cogley, J. G., Wouters, B., Arendt, A. A., and Wahr, J. (2013). A reconciled estimate of glacier contributions to sea level rise: 2003 to 2009. *Science* 340 (6134), 852–857.

Gardner, A. S., Moholdt, G., Cogley, J. G., Wouters, B., Arendt, A. A., Wahr, J., et al. (2013). A Reconciled Estimate of Glacier Contributions to Sea Level Rise: 2003 to 2009. *Science* 340, 852–857. doi:10.1126/science.1234532

Gardner, A. S., Moholdt, G., Scambos, T., Fahnstock, M., Ligtenberg, S., van den Broeke, M., et al. (2018). Increased West Antarctic and Unchanged East Antarctic Ice Discharge over the Last 7 Years. *The Cryosphere* 12 (2), 521–547. doi:10.5194/tc-12-521-2018

Gibson, M. J., Glasser, N. F., Quincey, D. J., Mayer, C., Rowan, A. V., and Irvine-Fynn, T. D. L. (2017). Temporal Variations in Supraglacial Debris Distribution on Baltoro Glacier, Karakoram between 2001 and 2012. *Geomorphology* 295, 572–585. doi:10.1016/j.geomorph.2017.08.012

Giese, A. (2019). Heat Flow, Energy Balance, and Radar Propagation: Porous media Studies Applied to the Melt of Changri Nup Glacier, Nepal Himalaya. Ph.D Thesis, Dartmouth College. Hanover, New Hampshire, USA,

Giese, A., Boone, A., Wagnon, P., and Hawley, R. (2020). Incorporating Moisture Content in Surface Energy Balance Modeling of a Debris-Covered Glacier. *The Cryosphere* 14, 1555–1577. doi:10.5194/tc-14-1555-2020

Groos, A. R., Mayer, C., Smiraglia, C., Diolaiuti, G., and Lambrecht, A. (2017). A First Attempt to Model Region-wide Glacier Surface Mass Balances in the Karakoram: Findings and Future Challenges. *Geografia fisica e dinamica quaternaria* 40 (2), 137–159. doi:10.4461/GFDQ

Harrison, S., Kargel, J. S., Huggel, C., Reynolds, J., Shugar, D. H., Betts, R. A., et al. (2018). Climate Change and the Global Pattern of Moraine-Dammed Glacial lake Outburst Floods. *The Cryosphere* 12, 1195–1209. doi:10.5194/tc-12-1195-2018

Heimsath, A. M., and McGlynn, R. (2008). Quantifying Periglacial Erosion in the Nepal High Himalaya. *Geomorphology* 97, 5–23. doi:10.1016/j.geomorph.2007.02.046

Hock, R., and Noetzli, C. (1997). Areal Melt and Discharge Modelling of Storglaciären, Sweden. *A. Glaciology.* 24, 211–216. doi:10.3189/S0260305500012192 10.1017/s0260305500012192

Hulley, G. C., Hook, S. J., Abbott, E., Malakar, N., Islam, T., and Abrams, M. (2015). The ASTER Global Emissivity Dataset (ASTER GED): Mapping Earth's Emissivity at 100 Meter Spatial Scale. *Geophys. Res. Lett.* 42, 7966–7976. doi:10.1002/2015GL065564

Immerzeel, W. W., Van Beek, L. P. H., and Bierkens, M. F. P. (2010). Climate Change Will Affect the Asian Water Towers. *Science* 328, (5984), 1382–1385. doi:10.1126/science.1183188

Jacob, T., Wahr, J., Pfeffer, W. T., and Swenson, S. (2012). Recent Contributions of Glaciers and Ice Caps to Sea Level Rise. *Nature* 482 (7386), 514–518. doi:10.1038/nature10847

Jiménez-Muñoz, J. C., Sobrino, J. A., Skokovic, D., Mattar, C., and Cristóbal, J. (2014) Land Surface Temperature Retrieval Methods from Landsat-8 thermal Infrared Sensor Data. *IEEE Geosci. Remote Sensing Lett.*, 11 (10), 1840–1843, doi:10.1109/lgrs.2014.2312032

Juen, M., Mayer, C., Lambrecht, A., Han, H., and Liu, S. (2014). Impact of Varying Debris Cover Thickness on Ablation: a Case Study for Koxkar Glacier in the Tien Shan. *The Cryosphere* 8, 377–386. doi:10.5194/tc-8-377-2014

Kamp, U., Byrne, M., and Bolch, T. (2011). Glacier Fluctuations between 1975 and 2008 in the Greater Himalaya Range of Zanskar, Southern Ladakh. *J. Mt. Sci.* 8 (3), 374–389. doi:10.1007/s11629-011-2007-9

Kapnick, S. B., Delworth, T. L., Ashfaq, M., Malyshev, S., and Milly, P. C. D. (2014). Snowfall Less Sensitive to Warming in Karakoram Than in Himalayas Due to a Unique Seasonal Cycle. *Nat. Geosci* 7 (11), 834–840. doi:10.1038/ngeo2269

Kayastha, R. B., Takeuchi, Y., Nakawo, M., and Ageta, Y. (2000). Practical Prediction of Ice Melting beneath Various Thickness of Debris Cover on Khumbu Glacier. *Nepal, using a positive degree-day factor, IAHS-AISH P* 264, 71–81.

Kellerer-Pirklbauer, A. (2008). The Supraglacial Debris System at the Pasterze Glacier, Austria: Spatial Distribution, Characteristics and Transport of Debris. *Zeit fur Geo Supp* 52, 3–25. doi:10.1127/0372-8854/2008/0052S1-0003

Kirkbride, M. P., and Deline, P. (2013). The Formation of Supraglacial Debris Covers by Primary Dispersal from Transverse Englacial Debris Bands. *Earth Surf. Process. Landforms* 38, 1779–1792. doi:10.1002/esp.3416

Kirkbride, M. P. (2002). Icelandic Climate and Glacier Fluctuations through the Termination of the "Little Ice Age". *Polar Geogr.* 26 (2), 116–133. doi:10.1080/789610134

Kirkbride, M. P., and Warren, C. R. (1999). 20th-century Thinning and Predicted Calving Retreat. *Glob. Planet. Change* 22, 1–4. doi:10.1016/S0921-8181(99)00021-1

Kraaijenbrink, P. D. A., Bierkens, M. F. P., Lutz, A. F., and Immerzeel, W. W. (2017). Impact of a Global Temperature Rise of 1.5 Degrees Celsius on Asia's Glaciers. *Nature* 549 (7671), 257–260. doi:10.1038/nature23878

Kuschel, E., Zangerl, C., Prokop, A., Bernard, E., Tolle, F., and Friedt, J.-M. (2020). "Paraglacial Adjustment of Sediment-Mantled Slopes through Landslide Processes in the Vicinity of the Austre Lovénbreen Glacier (Ny-Ålesund, Svalbard)." in Proceedings of EGU General Assembly 2020, Ny-Ålesund, Svalbard, May-2020, doi:10.5194/egusphere-egu2020-9509

Lawson, D. (1979). Semdimentological Analysis of the Western Terminus Region of the Matanuska Glacier, Alaska, Cold Regions Research and Engineering Lab. Hanover, NH: CRREL report. 79–9. Available at: https://hdl.handle.net/11681/9016.

Mark, B. G., Baraer, M., Fernandez, A., Immerzeel, W. W., Moore, R. D., and Weingartner, R. (2015). "Glaciers as Water Resources," in *The High-Mountain Cryosphere Environmental Changes and Risks*. Editors C. Huggel, M. Carey, J. J. Clague, and A. Kääb (Cambridge, UK: Cambridge University Press), 184–203. doi:10.1017/CBO9781107588653.011

Mattson, L. E., Gardner, J. S., and Young, G. J. (1993). Ablation on Debris Covered Glaciers: an Example from the Rakhiot Glacier, Punjab, Himalaya. *IAHS Publ.* 218, 289–296.

Maussion, F., Scherer, D., Mölg, T., Collier, E., Curio, J., and Finkelnburg, R. (2014). Precipitation Seasonality and Variability over the Tibetan Plateau as Resolved by the High Asia Reanalysis*. *J. Clim.* 27 (5), 1910–1927. doi:10.1175/JCLI-D-13-00282.1

McCarthy, M. (2019). Quantifying Supraglacial Debris Thickness at Local to Regional Scales, Ph.D. Thesis. Cambridge. UK: University of Cambridge,

McCarthy, M., Pritchard, H., Willis, I., and King, E. (2017). Ground-penetrating Radar Measurements of Debris Thickness on Lirung Glacier, Nepal. *J. Glaciol.* 63, 543–555. doi:10.1017/jog.2017.18

Mihalcea, C., Brock, B. W., Diolaiuti, G., D'Agata, C., Citterio, M., Kirkbride, M. P., et al. (2008a). Using ASTER Satellite and Ground-Based Surface Temperature Measurements to Derive Supraglacial Debris Cover and Thickness Patterns on Miage Glacier (Mont Blanc Massif, Italy). *Cold Regions Sci. Tech.* 52, 341–354. doi:10.1016/j.coldregions.2007.03.0043

Mihalcea, C., Mayer, C., Diolaiuti, G., D'Agata, C., Smiraglia, C., Lambrecht, A., et al. (2008b). Spatial Distribution of Debris Thickness and Melting from Remote-Sensing and Meteorological Data, at Debris-Covered Baltoro Glacier, Karakoram, Pakistan. *Ann. Glaciol.* 48, 49–57. doi:10.3189/172756408784700680

Mihalcea, C., Mayer, C., Diolaiuti, G., Lambrecht, A., Smiraglia, C., and Tartari, G. (2006). Ice Ablation and Meteorological Conditions on the Debris-Covered Area of Baltoro Glacier, Karakoram, Pakistan. *Ann. Glaciol.* 43, 292–300. doi:10.3189/172756406781812104

Miles, E. S., Willis, I., Buri, P., Steiner, J. F., Arnold, N. S., and Pellicciotti, F. (2018). Surface Pond Energy Absorption across Four Himalayan Glaciers Accounts for 1/8 of Total Catchment Ice Loss. *Geophys. Res. Lett.* 45, 10–464. doi:10.1029/2018GL079678

Mölg, N., Ferguson, J., Bolch, T., and Vieli, A. (2020). On the Influence of Debris Cover on Glacier Morphology: How High-Relief Structures Evolve from Smooth Surfaces. *Geomorphology* 357, 107092doi:10.1016/j.geomorph.2020.107092

Montanaro, M., Gerace, A., Lunsford, A., and Reuter, D. (2014). Stray Light Artifacts in Imagery from the Landsat 8 Thermal Infrared Sensor. *Remote Sensing* 6 (11), 10435–10456. doi:10.3390/rs61110435

Moore, P. L. (2018). Stability of Supraglacial Debris. *Earth Surf. Process. Landforms* 43 (1), 285–297. doi:10.1002/esp.4244

Nagai, H., Fujita, K., Nuimura, T., and Sakai, A. (2013). Southwest-facing Slopes Control the Formation of Debris-Covered Glaciers in the Bhutan Himalaya. *The Cryosphere* 7, 1303–1314. doi:10.5194/tc-7-1303-2013

Nakawo, M. (1993). Satellite Data Utilization for Estimating Ablation of Debris Covered Glaciers. *Intern. Assoc. Hydrol. Sci.* 218, 75–83.

Nakawo, M., Iwata, S., Watanabe, O., and Yoshida, M. (1986). Processes Which Distribute Supraglacial Debris on the Khumbu Glacier, Nepal Himalaya. *A. Glaciology.* 8, 129–131. doi:10.3189/S0260305500001294 10.3189/S0260305500012941 0.1017/s0260305500001294

Nakawo, M., and Young, G. J. (1981). Field Experiments to Determine the Effect of a Debris Layer on Ablation of Glacier Ice. *Ann. Glaciol.* 2, 85–91. doi:10.3189/172756481794352432

Nicholson, L. (2018). Supraglacial Debris Thickness Data from Ngozumpa Glacier, Nepal [Data Set]. *Zenodo*. doi:10.5281/zenodo.1451560

Nicholson, L., and Benn, D. I. (2006). Calculating Ice Melt beneath a Debris Layer Using Meteorological Data. *J. Glaciol.* 52 (178), 463–470. doi:10.3189/172756506781828584

Nicholson, L., and Benn, D. I. (2013). Properties of Natural Supraglacial Debris in Relation to Modelling Sub-debris Ice Ablation. *Earth Surf. Process. Landforms* 38 (5), 490–501. doi:10.1002/esp.3299

Nicholson, L. I., McCarthy, M., Pritchard, H. D., and Willis, I. (2018). Supraglacial Debris Thickness Variability: Impact on Ablation and Relation to Terrain Properties. *The Cryosphere* 12, 3719–3734. doi:10.5194/tc-12-3719-2018

Nicholson, L., and Mertes, J. (2017). Thickness Estimation of Supraglacial Debris above Ice Cliff Exposures Using a High-Resolution Digital Surface Model Derived from Terrestrial Photography. *J. Glaciol.* 63 (242), 989–998. doi:10.1017/jog.2017.68

Springer Science & Business Media,"N. Paragios, Y. Chen, and O.D. Faugeras in *Handbook of Mathematical Models in Computer Vision*, New York, USA, Springer US, doi:10.1007/0-387-28831-7

Nuimura, T., Fujita, K., Yamaguchi, S., and Sharma, R. R. (2012). Elevation Changes of Glaciers Revealed by Multitemporal Digital Elevation Models Calibrated by GPS Survey in the Khumbu Region, Nepal Himalaya, 1992-2008. *J. Glaciol.* 58 (210), 648–656. doi:10.3189/2012JoG11J061

östrem, G. (1959). Ice Melting under a Thin Layer of Moraine, and the Existence of Ice Cores in Moraine Ridges. *Geografiska Annaler* 41 (4), 228–230. doi:10.1080/20014422.1959.11907953

Pritchard, H. D. (2019). Asia's Shrinking Glaciers Protect Large Populations from Drought Stress. *Nature* 569 (7758), 649–654. doi:10.1038/s41586-019-1240-1

Quincey, D. J., Copland, L., Mayer, C., Bishop, M., Luckman, A., and Belò, M. (2009a). Ice Velocity and Climate Variations for Baltoro Glacier, Pakistan. *J. Glaciol.* 55, 1061–1071. doi:10.3189/002214309790794913

Quincey, D. J., Luckman, A., and Benn, D. (2009b). Quantification of Everest Region Glacier Velocities between 1992 and 2002, Using Satellite Radar Interferometry and Feature Tracking. *J. Glaciol.* 55 (192), 596–606. doi:10.3189/002214309789470987

Radić, V., Bliss, A., Beedlow, A. C., Hock, R., Miles, E., and Cogley, J. G. (2014). Regional and Global Projections of Twenty-First century Glacier Mass Changes in Response to Climate Scenarios from Global Climate Models. *Clim. Dyn.* 42, 1–2. doi:10.1007/s00382-013-1719-7

Ranzi, R., Grossi, G., Iacovelli, L., and Taschner, S. (2004). Use of Multispectral ASTER Images for Mapping Debris-Covered Glaciers within the GLIMS Project, in IGARSS 2004.2004 IEEE International Geoscience and Remote Sensing Symposium. Vol. 2. IEEE, Anchorage, AK, USA, (2004, September), 1144–1147. doi:10.1109/IGARSS

RGI. Consortium (2017). Randolph Glacier Inventory (RGI) – A Dataset of Global Glacier Outlines: Version 6.0 Global Land Ice Measurements from Space, Technical Report, Boulder: Colorado. USA., Digital Media, doi:10.7265/N5-RGI-60

Rounce, D. R., Hock, R., and Shean, D. E. (2019). Glacier Mass Change in High Mountain Asia through 2100 Using the Open-Source Python Glacier Evolution Model (PyGEM). *Front. Earth Sci.* 7. doi:10.3389/feart.2019.00331

Rounce, D. R., and McKinney, D. C. (2014). Debris Thickness of Glaciers in the Everest Area (Nepal Himalaya) Derived from Satellite Imagery Using a Nonlinear Energy Balance Model. *The Cryosphere* 8, 1317–1329. doi:10.5194/tc-8-1317-2014

Rounce, D. R., Quincey, D. J., and McKinney, D. C. (2015). Debris-covered Glacier Energy Balance Model for Imja-Lhotse Shar Glacier in the Everest Region of Nepal. *The Cryosphere* 9, 2295–2310. doi.org/doi:10.5194/tc-9-2295-2015

Rowan, A. V., Egholm, D. L., Quincey, D. J., and Glasser, N. F. (2015). Modelling the Feedbacks between Mass Balance, Ice Flow and Debris Transport to Predict the Response to Climate Change of Debris-Covered Glaciers in the Himalaya. *Earth Planet. Sci. Lett.* 430, 427–438. doi:10.1016/j.epsl.2015.09.004

Sakai, A. (2019). Brief Communication: Updated GAMDAM Glacier Inventory over High-Mountain Asia. *The Cryosphere* 13, 2043–2049. doi:10.5194/tc-13-2043-2019

Salerno, F., Thakuri, S., Tartari, G., Nuimura, T., Sunako, S., Sakai, A., et al. (2017). Debris-covered Glacier Anomaly? Morphological Factors Controlling Changes in the Mass Balance, Surface Area, Terminus Position, and Snow Line Altitude of Himalayan Glaciers. *Earth Planet. Sci. Lett.* 471, 19–31. doi:10.1016/j.epsl.2017.04.039

Schauwecker, S., Rohrer, M., Huggel, C., Kulkarni, A., Ramanathan, A., Salzmann, N., et al. (2015). Remotely Sensed Debris Thickness Mapping of Bara Shigri Glacier, Indian Himalaya. *J. Glaciol.* 61, 675–688. doi:10.3189/2015JoG14J102

Scherler, D., Bookhagen, B., and Strecker, M. R. (2011b). Hillslope-glacier Coupling: The Interplay of Topography and Glacial Dynamics in High Asia. *J. Geophys. Res.* 116 (F2). doi:10.1029/2010JF001751

Scherler, D., Bookhagen, B., and Strecker, M. R. (2011a). Spatially Variable Response of Himalayan Glaciers to Climate Change Affected by Debris Cover. *Nat. Geosci* 4, 156–159. doi:10.1038/ngeo1068

Scherler, D., Wulf, H., and Gorelick, N. (2018). Global Assessment of Supraglacial Debris-Cover Extents. *Geophysical Research Letters* 45 (21), 11–798.

Shah, S. S., Banerjee, A., Nainwal, H. C., and Shankar, R. (2019). Estimation of the Total Sub-debris Ablation from point-scale Ablation Data on a Debris-Covered Glacier. *J. Glaciol.* 65 (253), 759–769. doi:10.1017/jog.2019.48

Shean, D. E., Alexandrov, O., Moratto, Z. M., Smith, B. E., Joughin, I. R., Porter, C., et al. (2016). An Automated, Open-Source Pipeline for Mass Production of Digital Elevation Models (DEMs) from Very-High-Resolution Commercial Stereo Satellite Imagery. *ISPRS J. Photogrammetry Remote Sensing* 116, 101–117. doi:10.1016/j.isprsjprs.2016.03.012

Shean, D. E., Bhushan, S., Montesano, P. M., Rounce, D., Arendt, A., and Osmanoglu, B. (2019) A Systematic, Regional Assessment of High-Mountain Asia Glacier Mass Balance. *Front. Earth Sci.*, 7, p.363. doi:10.3389/feart.2019.00363

Shukla, A., and Qadir, J. (2016) Differential Response of Glaciers with Varying Debris Cover Extent: Evidence from Changing Glacier Parameters, *Int. J. Remote Sensing*, 37, 2453–2479. doi:10.1080/01431161.2016.1176272

Taschner, S., and Ranzi, R. (2002). "Comparing the Opportunities of Landsat-TM and Aster Data for Monitoring a Debris Covered Glacier in the Italian Alps within the GLIMS Project," in Proceedings of IEEE International Geoscience and Remote Sensing Symposium, Vol. 2. IEEE, Toronto, ON, Canada, (2002, June), 1044–1046. doi:10.1109/IGARSS

Vaughan, D. G., Comiso, J. C., Allison, I., Carrasco, J., Kaser, G., Kwok, R., et al. (2013). "Observations of the Cryosphere," in *Climate Change 2013: The Physical Science Basis. Contribution of Working Group I to the Fifth Assessment Report of the Intergovernmental Panel on*. Cambridge University Press, Cambridge, United Kingdom and New York, NY, USA., Editors IPCC, and W. G. I., 317–382. doi:10.5167/uzh-104510

Vincent, C., Wagnon, P., Shea, J. M., Immerzeel, W. W., Kraaijenbrink, P., Shrestha, D., et al. (2016). Reduced Melt on Debris-Covered Glaciers: Investigations from Changri Nup Glacier, Nepal. *The Cryosphere* 10, 1845–1858. doi:10.5194/tc-10-1845-2016

Wagnon, P., Vincent, C., Arnaud, Y., Berthier, E., Vuillermoz, E., Gruber, S., et al. (2013). Seasonal and Annual Mass Balances of Mera and Pokalde Glaciers (Nepal Himalaya) since 2007. *The Cryosphere* 7, 1769–1786. doi:10.5194/tc-7-1769-2013

Yao, T., Thompson, L., Yang, W., Yu, W., Gao, Y., Guo, X., et al. (2012). Different Glacier Status with Atmospheric Circulations in Tibetan Plateau and Surroundings. *Nat. Clim Change* 2 (9), 663–667. doi:10.1038/nclimate1580

Zhang, Y., Fujita, K., Liu, S., Liu, Q., and Nuimura, T. (2011). Distribution of Debris Thickness and its Effect on Ice Melt at Hailuogou Glacier, southeastern Tibetan Plateau, Using *In Situ* Surveys and ASTER Imagery. *J. Glaciol.* 57 (206), 1147–1157. doi:10.3189/002214311798843331

Conflict of Interest: The authors declare that the research was conducted in the absence of any commercial or financial relationships that could be construed as a potential conflict of interest.

frontiers in Earth Science

ORIGINAL RESEARCH
published: 27 July 2021
doi: 10.3389/feart.2021.710131

Numerical Simulation of Supraglacial Debris Mobility: Implications for Ablation and Landform Genesis

Peter L. Moore *

Department of Natural Resource Ecology and Management, Iowa State University, Ames, IA, United States

Supraglacial debris does not remain fixed atop ablating ice, but can move across the ice surface as supraglacial topography evolves. This active debris movement (distinct from passive movement due to underlying ice motion) affects landform genesis as well as the rate and spatial distribution of ablation. While observations of debris transport across evolving supraglacial topography are abundant, models of these coupled processes over timescales of decades and longer are few. Here I adapt a numerical model of coupled ablation and downslope debris transport to simulate the evolution of an idealized debris-covered glacier on the timescale of complete de-icing. The model includes ablation that depends on supraglacial debris thickness and a hillslope-scale debris transport function that scales non-linearly with slope angle. Ice thickness and debris distribution evolve with model time, allowing complete simulation of de-icing and landform construction in an idealized glacier test-section. The model produces supraglacial relief that leads to topographic inversions consistent with conceptual models of hummocky landform genesis. Model results indicate that the relief of the glacier surface and postglacial hummocks depend on the relationship between characteristic timescales for ablation and debris transport, which is defined as an index of debris mobility. When debris mobility is high, topographic inversions are rapid and supraglacial and postglacial relief are subdued. When debris mobility is low, more pronounced supraglacial relief is produced, but postglacial relief remains subdued. An intermediate mobility appears to optimize both postglacial relief and the rate of de-icingcompared with both highly-mobile and immobile debris. This enhancement of de-icing due to debris mobility could contribute to the observed anomalous rates of ablation in some debris-covered glaciers.

Keywords: debris covered glacier, ablation, hummocky moraine, debris transport, hillslope diffusion

OPEN ACCESS

Edited by:
Koji Fujita,
Nagoya University, Japan

Reviewed by:
Christoph Mayer,
Bavarian Academy of Sciences and Humanities, Germany
Joseph Michael Shea,
University of Northern British Columbia, Canada

***Correspondence:**
Peter L. Moore
pmoore@iastate.edu

Specialty section:
This article was submitted to Cryospheric Sciences, a section of the journal Frontiers in Earth Science

Received: *15 May 2021*
Accepted: *30 June 2021*
Published: *27 July 2021*

Citation:
Moore PL (2021) Numerical Simulation of Supraglacial Debris Mobility: Implications for Ablation and Landform Genesis. Front. Earth Sci. 9:710131. doi: 10.3389/feart.2021.710131

INTRODUCTION

Hummocky moraine landscapes are widespread along the margins of ancient ice sheets. A leading hypothesis for the origin of hummocky moraine invokes supraglacial debris movement during wastage of debris-covered ice (Sharp, 1949; Eyles, 1979; Clayton et al., 2008; Schomacker, 2008). According to this hypothesis, basins on the ice surface collect debris while inter-basin ridges shed debris. Once the ice is gone, thick debris from the supraglacial basins becomes hills, while areas of thin debris from surrounding ridgetops become swales and wetlands. This conversion of hills to basins during deglaciation is often called topographic inversion. At a 10^3–10^5 m scale, hummocky

moraine tracts often exhibit characteristic hummock wavelength and height (Johnson and Clayton, 2005). These characteristics must reflect the physical processes that shed or concentrate debris on an ablating, debris-covered ice surface.

Supraglacial debris not only serves as the medium for construction of distinct postglacial landforms, but also modifies ablation of the underlying glaciers. While thin (less than a few centimeters) or discontinuous debris cover can enhance melt rates compared with debris-free ice, thicker debris typically reduces ablation rates (Østrem, 1959; Nakawo and Young, 1981). The relationship between debris thickness and ablation rate is usually strong where ablation is dominated by downwasting, wherein heat for melting is transferred to the ice primarily by conduction through the debris layer. However, backwasting of ice cliffs, thermokarst-like melting from ponded and flowing supraglacial (and possibly subglacial) meltwater, and bottom melting can also contribute to ice mass loss to varying degrees (Driscoll, 1980; Schomacker, 2008; Thompson et al., 2016).

As recent climate warming has caused widespread glacier thinning and retreat, an increasing fraction of earth's glacier area is becoming debris-covered (Scherler et al., 2018), and this fraction is expected to grow in the near future (Herreid and Pellicciotti, 2020). While many studies have sought to simulate the physics of ablation on subannual timescales and local spatial scales in debris-covered glaciers, these models still perform inconsistently when scaled up to regional glacier mass balance assessments (e.g., Kääb et al., 2012). The difficulty may stem from inadequate accounting of unobserved processes such as changing extent of ponded (Thompson et al., 2016) or subsurface meltwater (Benn et al., 2017), ice dynamics (Banerjee, 2017), or elevation lapse rates (Vincent et al., 2016). However, debris mobilization can also influence the distribution of high- and low-ablation-rate areas through time, a phenomenon that has yet to be explored in detail (cf. Nicholson et al., 2018). This paper explores some of the consequences of supraglacial debris mobility for the patterns and rates of ice ablation and debris distribution over multi-annual and longer timescales.

Supraglacial Debris Movement

That supraglacial debris moves across underlying ice as the ice ablates is widely appreciated, particularly among glacial geomorphologists and sedimentologists seeking to explain the origins of ancient glacial landforms (Gravenor, 1955; Clayton, 1964; Reid, 1970; Wright, 1980; Hambrey, 1984; Attig et al., 1989; Johnson et al., 1995; Hambrey, 1997; Ham and Attig, 2001; Andersson, 2008; Krüger et al., 2010). Note that this refers to debris transport relative to underlying ice rather than passive transport atop actively-moving ice. A small but important body of work explores supraglacial debris movement processes and phenomena.

Though early descriptions of shallow slope failure and meltwater transport of supraglacial debris are abundant (Russell, 1893; Gilbert, 1904; Tarr and Martin, 1914; Sharp, 1949), not until the middle of the 20th century did researchers begin to explore the physics of debris movement (Sharp, 1949; Boulton, 1967). Although these authors discussed ideas about thresholds for debris movement and textural clues to transport mechanisms, formal mechanical descriptions of debris movement only emerged in the 1970s (Boulton and Paul, 1976; Lawson, 1979, 1982; Paul and Eyles, 1990). These authors recognized supraglacial debris flows of varying degrees of fluidity and sought explanations from frozen-ground engineering literature for failure thresholds and rates of movement. These discussions highlighted the role of meltwater pore pressure developed through "thaw consolidation" of supraglacial debris, which was reported to govern the rate and style of mass movement and the resulting sediment properties (Lawson, 1982) but was difficult to implement in practical models (Moore, 2018). Much more recently, Moore (2018) reframed the description of thresholds for debris destabilization in terms of material properties that are more readily quantified, and incorporated terrain attributes that allow prediction of the spatial distribution of unstable debris and zones of likely surface runoff. Observed relationships between supraglacial topography and debris thickness (Nicholson et al., 2018) and transient change in debris thickness across an evolving glacier surface (Westoby et al., 2020) are broadly consistent with expected areas of debris destabilization. The stability model stops short, however, of predicting debris transport rates or deposition, and this remains an area of future research need.

Rapid mass movement and glaciofluvial transport are not the only mechanisms of downslope debris movement. Individual supraglacial debris particles have been observed to migrate relatively slowly across underlying ice in either the downslope or sunward direction (Fryxell, 1933). This typically occurs when the melt reduction beneath a particle causes it to become perched on a pedestal of ice relative to the surrounding ablating surface—features like this capped with large boulders are often referred to as a "boulder tables." As the pedestal height grows and/or the girth diminishes, the particle slides or topples from the pedestal to a new position where the process may begin again. The net result over repeated cycles is a relatively slow motion that some have termed "topple-walk." Fryxell (1933) found on Teton Glacier, United States, that most of the motion occurred in the downslope direction, though for gently sloping ice surfaces (< 12°) particles acquired trajectories increasingly deflected southward (toward the sun) with decreasing ice surface slopes. Anderson (2000) adopted a similar topple-walk mechanism in a model simulation of medial moraine evolution, rationalizing that downslope particle flux should be proportional to debris particle size and ice surface slope.

A recent study by Fyffe et al. (2020) explored topple-walk transport and related phenomena using high-resolution repeat imagery on Miage Glacier, Italy. The authors documented particle transport in areas of partial debris cover on the order of a few centimeters per day down slopes ranging from 5° to 30°. In the same areas, ablation proceeded at 3–6 cm per day, suggesting that downslope debris movement in this setting is of the same order of magnitude as ablation rate. This study largely confirmed the slope and particle-size dependence of debris flux by the topple-walk mechanism, but additionally documented slope-dependent creep in areas of complete debris cover at smaller (less than 1 cm/day) but still significant rates. Details of the creep mechanism were not

investigated, but the process was an important component of the total debris flux across the ice surface.

In other terrestrial settings, creep of hillslope materials is caused by a variety of stochastic disturbances, both biotic and abiotic, which tend to slowly and intermittently displace particles downslope at rates that are sensitive to slope angle and slope curvature (Heimsath et al., 2002; Roering, 2004; Pawlik and Šamonil, 2018). Abiotic disturbances from these regimes that also act in supraglacial settings include wetting/drying cycles, freezing/thawing cycles and snow loading, among many others. Thus, while the physical processes responsible for topple-walk creep may not be sustained where supraglacial debris thickness exceeds a few clast diameters, several creep-inducing processes can be expected to be active. This remains an issue in need of further investigation.

In debris-covered glacier settings, it is important to realize that sub-debris ablation by downwasting requires debris to "settle" under the influence of gravity and perhaps an additional seepage force related to the evacuation of meltwater (Moore, 2018). Even if the circumstances of this seepage are not sufficient to surpass the stability thresholds described by Moore (2018), some downslope displacement may still occur. Much like the particle re-arrangements caused by acoustic vibrations introduced in some laboratory hillslope creep experiments (Roering et al., 2001), it is reasonable to hypothesize that the combined settling and seepage processes in supraglacial debris should promote net downslope transport that scales with slope angle (Furbish et al., 2009) and ablation rate (Houssais et al., 2021). This, too, requires future study. Nevertheless, it appears justified to proceed with a heuristic description of slow downslope debris transport until a more rigorous description, grounded in observation or theory, becomes available.

Coupled Melt-Transport Models

Evolution of debris distribution on debris-covered glaciers has been modeled in two different ways. At the scale of a full valley glacier, landsliding, debris emergence, melt-out, and passive supraglacial transport has been described by models seeking to explain. debris cover effects on glacier extent and moraine position (Shulmeister et al., 2009; Vacco et al., 2010; Anderson and Anderson, 2016; Anderson et al., 2018) or debris cover effects on mass balance and runoff (Rowan et al., 2015). In most of these models, debris is passively transported within or atop dynamic ice. A second type of model focuses on local-scale transport of debris across the ice surface as surface relief evolves through differential melting. This approach requires a description of active debris transport relative to the underlying ice, where any ice dynamics (and passive downglacier ice and debris transport) is treated separately. The local-scale coupling of ablation and debris transport in these types of models creates a complex pattern of evolving supraglacial relief that can govern both the spatial patterns of debris accumulation and the rate of ablation of the underlying ice. The present study builds on this latter type of model, so I review some key examples of this approach here.

Anderson (2000) investigated how the width and topographic expression of medial moraines evolves as one moves downglacier from their englacial debris source near the glacier equilibrium line. Ablation under debris was approximated by an exponential decay function with increasing debris thickness, neglecting the small-thickness ablation enhancement characteristic of some Østrem curves. Spatial variation in debris cover thickness led with time to creation of relief on the glacier surface. Anderson then reasoned that debris was transported across the ablating ice surface by the topple-walk mechanism, with the probability distribution of toppling steps becoming larger and more downslope with increasing slope angle. He therefore reasoned that this process could be described more generally with a slope-dependent flux of the form $q_s \sim D\nabla z$ where q_s is downslope sediment flux $[L^2T^{-1}]$, ∇z is the debris surface slope, and D is a rate parameter. Model results simulating the ablation of a glacier cross-section with vertical englacial debris bands compared favorably with the patterns of medial moraine relief and width on an Alaskan valley glacier (Anderson, 2000).

Following in part from Anderson, Fowler and Mayer (2017) explored the origins of "ice sails," which are ridges or pinnacles of debris-free ice on the order of $10^0 - 10^1$ meters high and $10^1 - 10^2$ meters long that emerge in some settings from ice otherwise covered with thin debris. Their model focused on the physics of ablation that is enhanced (compared to debris-free ice) by the presence of a thin debris layer, which results in lowering of debris covered ice relative to clean ice. The model also included a description of diffusive (slope-dependent) debris flux similar to that used by Anderson (2000), which allowed emerging ice sails to shed debris to surrounding debris-covered ice lows. Their model produced results broadly consistent with observed ice sails on a Himalayan glacier (Fowler and Mayer, 2017). These features are, however, transient and unlikely to have significant impacts on either glacier mass balance or landform genesis. Nevertheless, they demonstrate one among the diverse array of features that can arise through coupling of ablation and local-scale debris transport.

A recent study by Mölg et al. (2020) explored the evolution of debris cover originating from medial moraines similar to those described in Anderson (2000). They constructed a model similar to that of Anderson (2000) except with a hyperbolic function of debris thickness describing sub-debris melt (Anderson and Anderson, 2016). The authors used this model to help explain both the evolution of supraglacial relief with downglacier position and the influence of that relief on supraglacial and subglacial meltwater drainage. They show that the results compare favorably with the topographic features of Zmuttgletscher in the Swiss Alps. They further link the development of ice cliffs, which contribute disproportionately to ablation in some debris-covered areas, to meltwater concentration in the troughs between moraine ridges.

The studies reviewed above demonstrate the power of simple models coupling ablation and debris redistribution to improve our understanding of surface features of debris-covered glaciers. Each of these studies, however, is focused on reproducing the features of a particular glacier (Anderson, 2000; Mölg et al., 2020) or generating a particular feature (Fowler and Mayer, 2017). None explores the range of features and patterns that emerge as model parameters vary, nor do they carry simulations to complete de-icing (de-icing is used here to refer to the long-term wastage of

an ice volume of interest, independent of process or glacier dynamics). Thus, many process-form relationships remain unexplored, particularly on the longer timescales relevant to landform genesis.

In this paper, I combine some aspects of these prior studies to simulate the coupled processes of sub-debris ablation and debris transport in downwasting debris-covered glaciers. Attention is focused on the influence of initial conditions and parameter values on the coupled dynamics and consequent distribution of debris on the ice-free landscape at the end of simulations. Generality and simplicity is favored over detail and complexity in order to highlight the relationships that most strongly impact the morphological result.

MATERIALS AND METHODS

Ablation rate $\dot{m}$ under a debris layer is approximated here with a simple hyperbolic function of debris thickness, H:

$$\dot{m} = \frac{K}{\rho_i L_f} \frac{T_s}{(H + H^*)} \tag{1}$$

where K is thermal conductivity, ρ_i and L_f are the density of ice and latent heat of fusion for ice, respectively, and T_s is the debris surface temperature. The first term on the right-hand side contains thermal properties of the system, while the second approximates an average linear temperature gradient through the debris layer. While temperature gradients within debris are rarely linear at any moment in time, the assumption of linearity is a convenient simplification that has also been substantiated in real-world settings (Nicholson and Benn, 2006; Rowan et al., 2021). The ablation enhancement at small debris thickness exhibited in some Østrem curves is omitted here for simplicity, as it has been in many other studies (Anderson, 2000; Anderson and Anderson, 2016). The parameter H^* is a small reference debris thickness, which ensures that the hyperbolic function yields finite ablation rates in the limit of small H. This parameter also constrains the ablation rate for debris-free ice.

When melt releases debris from debris-bearing ice, the resulting debris production P is described as

$$P = \frac{\dot{m}c}{1 - n} \tag{2}$$

where c is volumetric debris concentration in the ice and n is the porosity of the debris once it is released.

Differential melt produces relief on the debris-covered ice surface and debris transport can take place by the various processes reviewed above. For the purposes of this analysis, transport is assumed to take place in one horizontal dimension x, governed by conservation of sediment mass:

$$\frac{\partial H}{\partial t} + \frac{\partial q_x}{\partial x} + P = 0 \tag{3}$$

where as before H is the thickness of supraglacial debris, $H = z_{surf} - z_{ice}$, and z_{surf} and z_{ice} are the elevation of the debris surface and debris-ice interface, respectively. Here, q_x is the along-slope unit-width flux of sediment in the x-direction relative to the underlying ice, which does not move or deform. This conservation of mass rule states that the change in debris thickness at any place x on the ice surface is due to a difference in flux of sediment between x and $x + \delta x$ plus any "production" of sediment P as debris is released from melting ice. In reality, the sediment flux q_x depends on several processes that aren't easily summarized in a simple transport equation. However, on the long timescales captured by a landform evolution model, a heuristic transport equation that satisfies a few basic requirements may still yield illuminating results (Dietrich et al., 2003).

A general form of nonlinear transport is used here to simulate the contributions of both slow creep and rapid mass movements to downslope debris flux. Transport rate thus increases sharply as the slope $S = \partial z_{surf}/\partial x$ approaches a threshold, S_c, above which shallow landsliding is presumed to occur:

$$q_x = -D \frac{S}{1 - \left(\frac{S}{S_c}\right)^{\alpha}} \tag{4}$$

Here, D is a transport rate parameter analogous to diffusivity that constrains the volumetric debris flux per unit width for a reference slope. The parameter α affects the nonlinearity of the slope-dependence and is often taken to be equal to 2. Relationships of this form have been used extensively in modeling the degradation of mountainous, soil-covered landscapes (e.g., Roering et al., 2001). Anderson (2000) derived an expression for D that related downslope transport rate to the topple-walk magnitude and frequency. While the rationale for such a relationship may not hold for large debris thicknesses, a functionally-similar transport coefficient may be expressed:

$$D = D_0 \left[1 - \exp\left(-H/H^*\right)\right] \tag{5}$$

where D_0 is a reference rate constant (valid for large debris thickness) and H^* remains a small reference debris thickness. When H is large compared with H^*, D approaches D_0, but for small H, D approaches zero. Like Anderson (2000), I make the simplifying assumption that gradients in debris thickness are negligible compared with slope gradients so that debris thickness change is dominated by slope curvature terms in the combined **Eqs 3–5**.

Modeling Approach

A 1D explicit finite difference model was constructed in MATLAB using **Eqs 1–5** to explore the evolution of supraglacial topography and debris re-distribution, as well as the resulting patterns of debris accumulation following complete de-icing. A conservative finite-difference scheme adapted from Perron (2011) was used in which melt and debris production were computed at nodes, while slope and debris flux were computed at midpoints between nodes. The ablation and debris transport problems were each treated in one spatial dimension, where ablation caused adjustment of the ice surface vertically (z) and

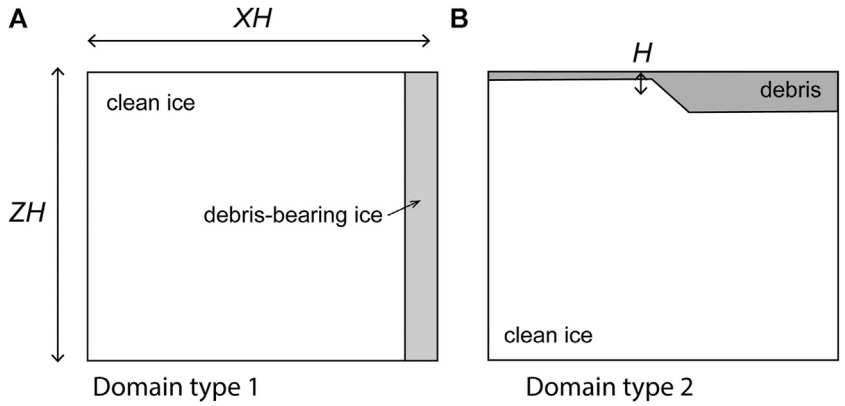

FIGURE 1 | Schematic illustration of the simplified model domains used in this study. Both types of domains represent vertical cross-sections through a glacier and have dimensions scaled to the mean supraglacial debris thickness H **(A)** Domain type 1 has one or more debris bands with debris volumetric concentration c within or at the margin of the domain **(B)** Domain type 2 has no englacial debris, but a supraglacial debris blanket with non-uniform initial thickness.

TABLE 1 | Parameter definitions, units, and simulated values for model quantities. Single values are given for quantities that were not varied, while ranges are given for those parameters varied experimentally. Note that K and D_0 have different time units (seconds and years, respectively), so computation of M in **Eq. 6** requires a time unit conversion factor.

Symbol	Meaning	units	Simulated values
K	Debris thermal conductivity	J/(s m°C)	0.5–1.5
ρ_i	Ice density	kg/m^3	900
L_f	Latent heat of fusion for ice	J/kg	334,000
T_s	Debris surface temperature	°C	1–5
H^*	Reference debris thickness	m	0.05
c	Volumetric debris concentration in ice	–	0.01–0.15
n	Debris porosity	–	0.35
D_0	Reference debris transport parameter	m^2/yr	0.1–10
S_c	Threshold slope for mass wasting	m/m	0.5–1
α	Transport nonlinearity exponent	–	2
Z	Vertical length scale	m	10–100
X	Horizontal length scale	m	10–500

debris transport could occur across the ice surface horizontally (x). In each time step, ice and debris surface elevations were adjusted vertically according to computed ablation distributions, followed by computation of debris fluxes and thickness changes. While an adaptive time-step tied to the value of D would have ensured numerical stability, for simplicity and computational efficiency, time step length was fixed for each simulation to $\Delta t = a\Delta x/2D_0$, where Δx is the grid size (1 m in all simulations) and a is a manually-adjusted parameter < 1 that was tuned by trial-and-error to maintain numerical stability. Time steps ranged from approximately 0.01–0.5 years. Ice flow was not explicitly modeled, making simulations most relevant to stagnant ice. All simulations were run until all ice was gone from the domain (Code for this model will be freely available at https://github.com/peteymoore/DCGsimulation through the author's Github site should this manuscript be accepted for publication).

The behavior of the model was investigated within two idealized domain types: 1) a rectangular glacier cross-section with one or more vertical englacial debris bands; and 2) a rectangular section with no englacial debris but a supraglacial debris blanket of non-uniform initial thickness (**Figure 1**). No-flux conditions were enforced on the left and right boundaries for both domain types, representing either barriers to transport there or a mirror-image (periodic) domain. Domain sizes and aspect ratios were varied along with parameter values to explore impacts on ablation and debris accumulation patterns. For simplicity, all parameter values were held constant during a given simulation, but varied among simulations. Parameter definitions and ranges of values used in simulations are given in **Table 1**.

Domain type 1 was first used to validate model results by comparison with results of Anderson (2000), and then to explore the effects of varying initial conditions (e.g., domain geometry and debris mobility) and physical properties on supraglacial relief and debris distribution during and after melt. In all domain 1 simulations, the englacial debris sources were arbitrarily defined to be 10 m wide. In most of these, a single debris band was located along the right-hand boundary of the domain as illustrated in **Figure 1A**. However, a few simulations were conducted with multiple englacial debris bands in the interior of the domain to explore the interactions between sources. Domain type 2,

representing debris originating from events like landslides that don't produce continuous debris sources with glacier depth, was used to further explore the effects of initial conditions and physical properties on long term melt rates and changes in debris thickness distribution. In all of the domain 2 simulations presented here, initial debris thickness ranged from 0.1 to 1.1 m, with an arithmetic mean initial thickness of 0.6 m. A smooth ramp in debris thickness spanning 10 nodes accommodated the transition between thick and thin debris ensuring that initial debris thickness gradients did not exceed 0.1. In each domain type, geometry, and parameter values were varied over reasonable ranges to explore consequences for de-icing rates and surface relief. Ranges of parameter values considered are presented in **Table 1**.

The relationships between characteristic rates of transport and melt are expected to determine how supraglacial relief evolves with time, and therefore whether debris thickness evolves toward uniform thickness or growing non-uniformity. To explore this with more generality, the length dimensions can be scaled by a characteristic length of this system. With this in mind, results are compared across model runs using scaled spatial variables normalized to the arithmetic mean debris thickness H.

Assuming that melt occurs by conduction through supraglacial debris only, the timescale t_m to melt a thickness ZH of ice under a uniform debris thickness H is $\rho_i L_f ZH^2/KT_s$. Here, H is taken to be the arithmetic mean thickness. For domain type 1, mean thickness is defined as the final debris area divided by domain width, while in domain type 2 it is the mean initial thickness. Since the evolution of debris thickness differs between these two settings, results are only compared within domain types. The timescale t_t for debris transport over a distance XH is X^2H^2/D_0, assuming that debris transport occurs primarily by creep (i.e., $S < S_c$). Define the mobility index M, as the ratio of t_m to t_t:

$$M = \frac{t_m}{t_t} = \frac{\rho L_f Z D_0}{K T_s X^2} \tag{6}$$

Since each characteristic timescale is the reciprocal of a characteristic speed, M provides a means to characterize the relative speed of debris transport compared to supraglacial relief production by differential melt. For larger values of M, transport efficiently responds to any developing supraglacial relief, while for smaller values differential melt produces relief more rapidly compared with debris transport response.

While this simple model cannot reasonably represent the full range of behaviors exhibited in supraglacial debris, it can nevertheless be used to explore the impacts of varying parameter values on surface relief and de-icing time relative to that assuming a constant static debris thickness. The results highlight the influence of debris mobility on differential ablation, surface relief, and landform genesis in debris covered glacier settings.

RESULTS

Simulations with medial moraines (domain type 1) were broadly consistent with prior model experiments (Anderson, 2000; Mölg et al., 2020). **Figure 2** summarizes two simulations with different domain lengths X, thereby representing different transport timescales. Each line within a panel represents the ice or debris surface at a moment in simulation time (an isochron), with constant intervals between isochrons given in the caption. Animations of the first simulation as well as an example simulation from domain 2 are provided as **Supplementary Material**. In both simulations illustrated in **Figure 2**, debris melt-out supplies debris cover to the surface, producing surface relief due to subsequent differential melt. As ablation proceeds, the relief between the moraine crest and remaining debris-free ice grows until debris extends across the entire domain width, representing the merging of debris covers from adjacent moraines or deposition at a lateral glacier margin. The timing of this merging affects the subsequent rate of ablation and distribution of debris.

In **Figure 2A**, the debris sources are relatively close together ($2XH$), and the debris-covered moraine slope extends to cover the full domain width early in the simulation. As a consequence, the debris thickness in the basin between moraines grows. By contrast, the debris sources in **Figure 2B** are farther apart, and ice between the widening moraine ridges completely disappears before debris extends to cover the domain fully. As a consequence, limited debris thickening occurs in the basins between moraine ridges, and ablation proceeds more rapidly (**Figure 3**). This should be no surprise, as the same volume of debris is permitted to spread over a larger area of ice surface, attaining smaller mean thicknesses. Even so, it leads to the somewhat counterintuitive result that larger volumes (wider domains) of ice disappear faster than smaller when flanked by the same single debris band. For debris band spacing exceeding that in **Figure 2B**, there is no further change in ridge relief or ablation rates since debris-free ice beyond the ridge slope has disappeared before debris advances further.

As noted in Anderson (2000), the flanks of growing medial moraine ridges quickly evolve to a nearly constant slope just sufficient to deliver downslope the debris produced by ablation at the debris band, beneath the moraine crest. Steady moraine slopes ranged from 0.35 to 0.6 (approximately 20°–30°) for high to low-mobility cases, respectively. Simulations reported here are consistent with the importance of debris supply rate (ablation rate or debris concentration) and mobility in governing the steady-state moraine-flank slope. As supply rate increases or diffusivity decreases, the slope steepens. The effect of steepening moraine-flank slopes is similar to that of increasing moraine spacing, leading to narrower moraine ridges that permit debris-free de-icing to proceed longer.

Results of several simulations with domain type 1 suggest that the postglacial moraine relief, quantified as the interquartile range of debris thickness normalized to mean debris thickness (IQRnorm), is small in most cases. This is consistent with field observations that indicate poor preservation potential for linear englacial or supraglacial features like medial moraines (Evans, 2009). Even so, the results shown here indicate that relief is greatest in settings with intermediate mobility index M. Where M is large, debris accumulation in basins between moraines is rapid relative to ablation and differential melting

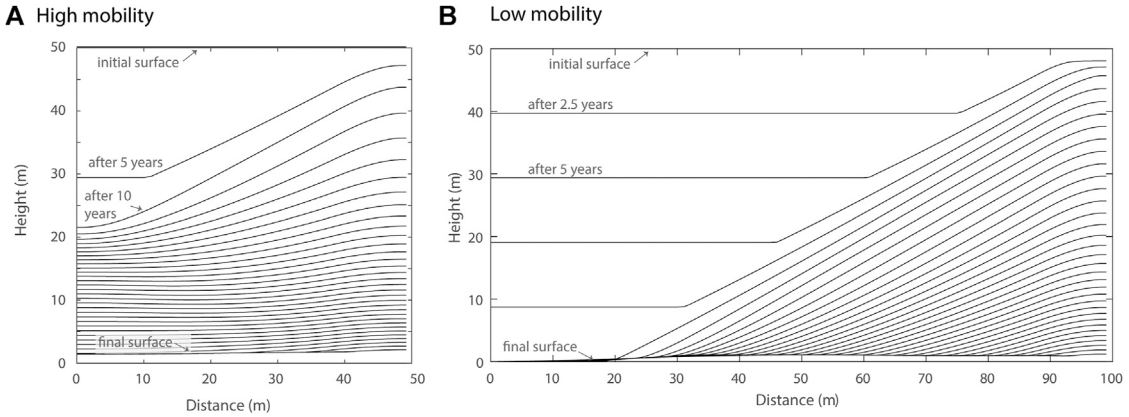

FIGURE 2 | Glacier surface isochrones from simulations in domain type 1 with debris-band width 10 m, debris concentration c = 0.1, T_s = 2°**C**, K = 1 J/(s m°**C**), and D_0 = 1m^2/yr. Each isochrone line in this figure (as well as **Figures 4**, **5**) represents the debris-covered ice surface at an instant in time, separated by constant time intervals and advancing in time from top to bottom. The simulations are classified as low- and high-mobility based on differences in the domain width **(A)** High-mobility simulation (X/Z = 1) with 5-years intervals between isochrones **(B)** Low-mobility simulation (X/Z = 2) with 2.5-years intervals between isochrones.

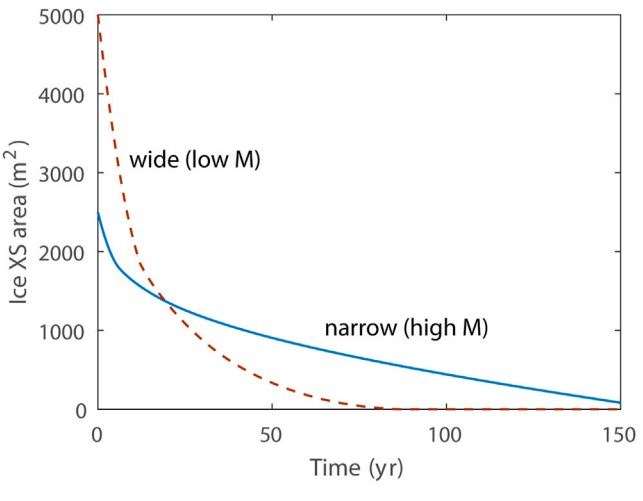

FIGURE 3 | De-icing histories for the two simulations shown in **Figure 2**. The quantity of ice remaining is represented by the cross-sectional area of ice, since ablation rate and ice lowering are non-uniform across the domain. Solid blue line corresponds to de-icing from **Figure 2A**, and dashed red line to **Figure 2B**.

leads to a reduction in moraine slope and reduced debris fluxes into these basins. Where M is small, on the other hand, debris redistribution occurs slowly compared to ablation and is distributed more uniformly at the ice-free toe of the moraine ridge as it decays.

The position of single, sustained englacial debris sources fixes the location of topographic highs, and consequently also the intervening lows where debris collects. However, when multiple bands interact, as illustrated in the three-band simulation in **Figure 4** (with bands at 100, 200, and 300 m), greater debris accumulation in topographic lows receiving debris from multiple bands suppresses ice lowering there, flattening those areas in order to shed debris to remaining topographic lows. While each band initially produces a distinct moraine ridge (like the isochron highlighted in blue), the eventual merging of ridges and suppression of melt between them leads to a convex glacier cross-section (highlighted in red). The glacier surface becomes peaked at the middle band position and steepens beyond the adjacent bands in order to deliver their added debris flux toward the lateral margins.

Interesting patterns emerge in simulations in domain type 2 as well. Here, instead of a sustained englacial debris source, all debris in the system is prescribed as a non-uniform supraglacial debris blanket in the initial conditions, akin to a rockfall or landslide deposit. **Figure 5** compares two simulations with the same initial conditions (debris thickness 1.1 m on the right half, 0.1 m on the left half) but different parameter values manifesting as different degrees of debris mobility. In the high-mobility case of panel (A), differential melt initially lowers the surface on the left-hand side of the domain where thin debris suppresses ablation less. Highly mobile debris quickly descends the resulting surface slope from right to left, accumulating on the left and suppressing ablation there. The slope reverses twice more before de-icing is complete, at which time debris is nearly uniformly distributed across the domain (IQRnorm = 0.18). In **Figure 5** panel (B), debris mobility is lower and greater relief (and a steeper slope) develops before significant transport takes place. Transport is sufficiently slow in this case that the left side of the domain is almost completely ice-free before significant debris accumulation occurs there. Subsequent debris transport accumulates much of the debris to the left side of the domain, where it remains as a higher-relief (IQRnorm = 1.19) postglacial mound following a single episode of topographic inversion.

Figure 6 illustrates the effects of debris mobility on the ablation history for the simulation in **Figure 5B**. The heavy blue line shows the loss of ice cross-sectional area (or volume per unit distance normal to the study plane) as a function of simulation time. Also shown is the steady melt predicted for the same amount of debris cover if it were static and distributed

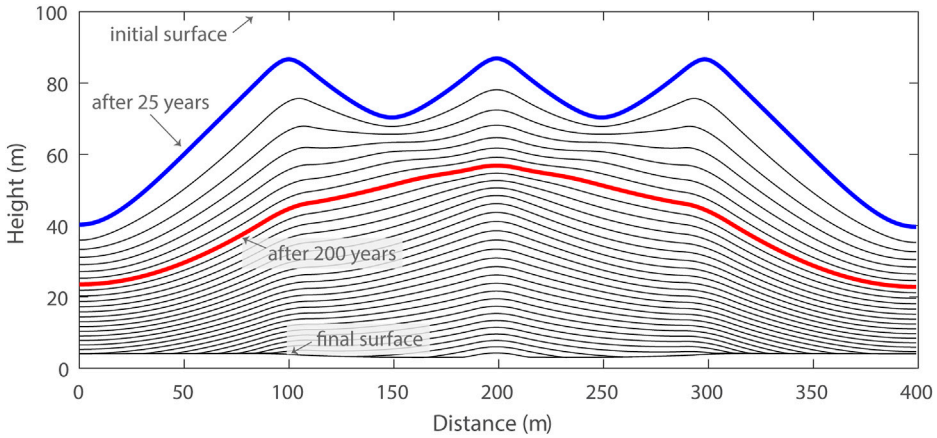

FIGURE 4 | Glacier surface isochrones at 25 years intervals from a 400-m wide, 100-m thick type 1 domain simulation with three debris bands centered at 100, 200, and 300 m distance. Band width was 10 m in each case. All other parameters were the same as the simulation shown in **Figure 2**. Blue and red isochrones highlight the differences between early surface evolution (blue) when each debris band has a prominent, separate medial moraine ridge, and later (red) when moraine ridges have merged and the ice surface has organized to shed debris to the lateral ice margins.

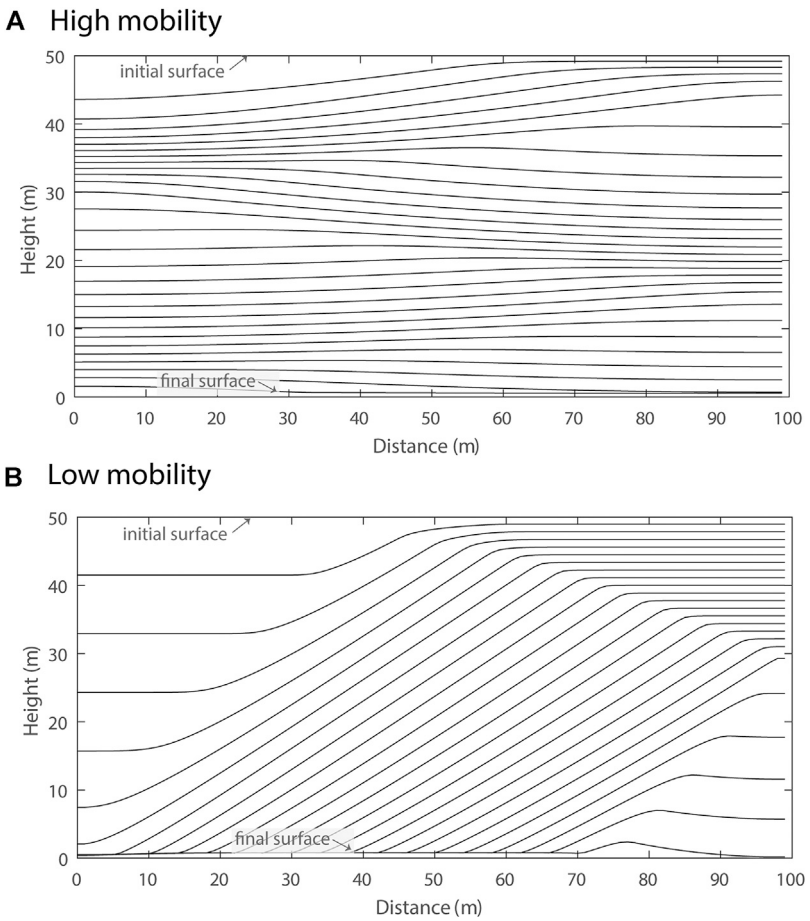

FIGURE 5 | Glacier surface isochrones (5 years interval) from simulations in domain type 2 with debris blanket ranging from 0.1 m thick on the left side to 1.1 m on the right. The simulations are classified as low- and high-mobility based on differences in debris transport parameter D_0. In both simulations, T_s = 2°***C*** and K = 1 J/(s m °***C***) **(A)** High-mobility simulation with D_0 = 5 m^2/yr and **(B)** Low-mobility simulation with D_0 = 0.75 m^2/yr.

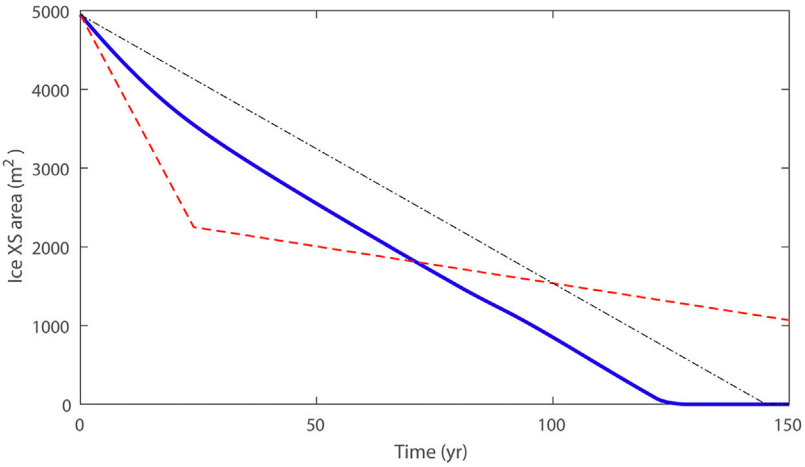

FIGURE 6 | De-icing history for the domain type 2 simulation shown in **Figure 5B** (blue) compared with immobile debris of the same initial thickness distribution (red dashed) and uniform thickness H_{mean} = 0.6 m (black dash-dot).

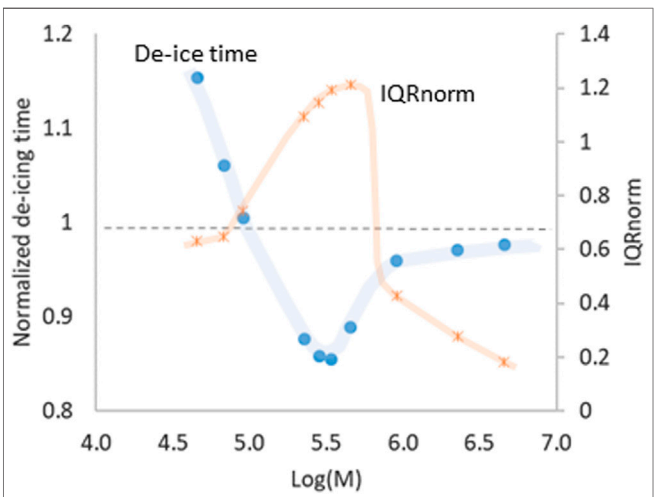

FIGURE 7 | De-icing time and postglacial moraine relief as a function of debris mobility for ten simulations in type two domains spanning two orders of magnitude in D_0. Simulated de-icing time normalized to de-icing time for uniform immobile debris is shown in blue, while moraine relief, quantified as the interquartile range (normalized to mean) of debris thickness following complete de-icing, is shown in orange. Debris mobility on the horizontal axis is expressed for convenience as the base-10 Logarithm of the mobility index *M*, given by **Eq. 6**.

uniformly over the ice surface (black dash-dot pattern line). Finally, the dashed red line shows the expected melt history if the debris was arranged according to the initial conditions of **Figure 5B** but was unable to move laterally within the domain. The simulated duration of deicing is significantly shorter for mobile debris than for either of the other immobile-debris cases. Although the initial simulated area loss rate for mobile debris is intermediate between the immobile end-member cases, the mobile debris shedding from areas that experience periods of melt suppression ensures that ice throughout the domain is subject to periods of reduced melt suppression under thinned debris.

The effect of debris mobility on total de-icing time and postglacial moraine relief in ten domain type 2 simulations is shown in **Figure 7**. De-icing time (the time required to ablate all ice from the model domain) is normalized to the time required to remove all ice under a static, uniform debris layer of thickness *H*, the arithmetic mean thickness. Note that, as indicated in the immobile, non-uniform debris case (red dashed line) in **Figure 6**, the de-icing time for low-mobility debris is greater than that of the reference uniform-thickness debris. Similarly, extremely-high mobility debris tends to produce de-icing times that are asymptotic to the uniform-thickness reference, since high-mobility tends to disperse debris more evenly across the ice surface. But an intermediate mobility leads to expedited de-icing times, reaching almost 15% shorter than the reference case in the simulation shown in **Figure 5B**.

Postglacial moraine relief is also affected by debris mobility (orange symbols in **Figure 7**). Much like the effective de-icing rate, postglacial relief is greatest for debris of intermediate mobility. Highly-mobile debris tends to become distributed more evenly across the model domain, leading to smaller differences in debris thickness. Low-mobility (but still mobile) debris doesn't homogenize like highly-mobile debris, but produces somewhat lower relief. However, it should be noted that immobile non-uniform debris with the same initial distribution as in **Figure 5** would retain an IQRnorm of 1.65, suggesting a more complex pattern of relief generation for vanishing mobility.

DISCUSSION

The model explored here greatly simplifies the physics of coupled melt and debris transport, and omits many phenomena known to be important in real debris-covered glacier settings. Even so, the simulations highlight relationships that likely contribute in real settings to ablation rates and debris accumulation patterns. A key

objective was to examine the effects of debris mobility on relief and debris accumulation patterns on downwasting ice. Simulation types representing debris release from englacial debris bands and supraglacial debris deposits allowed examination of ablation-debris transport feedbacks in two end-member scenarios common to today's debris-covered valley glaciers.

Results of simulations in type 1 domains are broadly consistent with observations of medial moraine emergence from englacial debris concentrations. Medial moraine ridges grow in relief and width as melt releases englacial debris that subsequently suppresses melt in the underlying ice. The relief thereby created promotes downslope movement of debris down the broadening medial moraine slopes by mechanisms that remain poorly understood, but that may include topple-walk mechanisms in thin debris covers. Indeed, sustaining expansion of medial moraine ridges requires a mechanism for slow transport of debris down slopes that are usually too gentle to produce rapid mass-wasting. The required transport rate should be governed by the rate of debris supply from upslope debris melt-out. While these phenomena remain poorly documented in real field settings, (Fyffe et al., 2020) described melt-season expansion of debris-covered moraine slopes over adjacent dirty ice areas where the debris wasn't evacuated by supraglacial streams.

Model results indicate that debris mobility, characterized here by M, affects the long-term de-icing rate and debris accumulation patterns in predictable ways. When manifested as differences in spacing of the debris-band sources, widely-spaced debris bands correspond (**Eq. 6**) to lower mobility than closely-spaced bands. Where bands are spaced sufficiently that much of the ice thickness in basins between moraine ridges is melted before moraine ridges merge, de-icing is efficient compared to cases where moraine ridges merge and produce thick debris accumulations between them. The optimal spacing appears to occur where the horizontal distance between debris bands normalized to ice thickness (X/Z) is just less than twice the reciprocal of the equilibrium moraine slope ($\tan\theta$, where θ is slope angle). The equilibrium slope is, in turn, a function of the debris supply rate and the transport rate parameter. Simulations with multiple interacting debris bands highlighted the influence of debris supply rate when the transport rate parameter was held fixed. When the glacier surface evolved to have a single central moraine crest (red isochrone in **Figure 4**), the glacier surface increased in slope at the position of the adjacent (100 and 300 m) debris bands, which added their contributions to debris supply, thus requiring a steeper moraine flank slope.

Domain type 2 simulations allowed additional exploration of the influence of initial conditions and debris mobility parameters on supraglacial relief and de-icing rate. High-mobility debris rapidly responds to relief production by differential melt, maintaining relatively small surface slopes, and low relief. The ice surface in these cases evolves through several reversals of topography and results in debris thickness distributions that approach uniform. Lower-mobility debris reduces the number of topographic reversals until only one reversal occurs, manifesting as complete topographic inversion.

An optimal geometry for rapid de-icing appears to exist for these simulations as well, and it may coincide with the conditions that produce a single complete topographic inversion. This arises when the debris mobility is just sufficient to allow nearly complete de-icing under thin debris before the wave of downslope-transported debris thickens debris and suppresses melt there. Not only is postglacial moraine relief greatest under these conditions, but de-icing rate is as much as 15% faster than it would be if the debris thickness was uniform. This relative acceleration of melt is presumably due to the redistribution of melt-suppressing debris to areas where ice has already been removed, as well as the nonlinearity of the sub-debris ablation function.

The extent to which debris mobility modifies time-integrated de-icing rates is likely underestimated in the present model for at least two reasons. First, retaining finite debris thicknesses is important for numerical stability in the model formulation used here. Therefore, debris thickness in the model remained at least 15–20 cm even on steeply-dipping slopes once they were covered with debris. In reality, areas of thinner debris (and therefore higher ablation rate) are under-represented in the model. A second reason to expect greater impacts from mobile debris than shown here is the neglect of the thin-debris enhancement of ablation that is sometimes documented. Since the sub-debris melt model employed here omits any such enhancement, allowance for this melt-enhancement effect when debris is thin would further elevate ablation rates on slopes steep enough to shed debris.

Another key element missing from the simulations presented here and in other published model studies is the removal of debris from the supraglacial setting by meltwater. Many recent observations highlight the importance of meltwater in maintaining high relief and steep slopes on debris-covered glaciers (e.g., Fyffe et al., 2020; Mölg et al., 2020). If meltwater removes mobile debris from the base of a debris-covered slope, accumulation and melt-suppression are inhibited there and the existing relief can be maintained or enhanced. This stands in contrast, however, to the phenomenon of topographic inversion, which is also widely documented in debris-covered glacier settings. Thus, further research is required to explore the conditions under which meltwater streams can allow topographic relief to persist on debris-covered glaciers, and where it may be unable to prevent topographic inversion.

Because the model simulations described here were idealized one-dimensional experiments, the results don't readily compare with particular field settings. Surface topography on debris-covered glaciers and ice-free supraglacial landsystems is very much two- (or three-) dimensional, and a more sophisticated 2D model would be required to generate meaningful comparisons. Even so, some of the patterns observed here can help to inform interpretations of process-landform relationships. The length-scales used in the domain set-up ($\sim 10^2$ m) are generally consistent with those observed in topographic features of modern debris-covered valley glaciers (Bartlett et al., 2020), and for simulations that produced significant postglacial relief, moraine ridges are similarly spaced. This spacing is also consistent with some observed hummocky moraine tracts (albeit in only one dimension) (Johnson and Clayton, 2005), and is inherited from the prescribed spacing of debris source non-uniformity. Even so, simulations with high mobility or extremely-low mobility yielded very little postglacial topographic relief, which is consistent with past studies of controlled moraines (Evans, 2009).

Thus, an interesting consequence is that supraglacial debris redistribution can both create and destroy relief in de-glacial and postglacial settings, depending upon mobility.

CONCLUSION

Debris mobility on debris-covered glaciers can take the form of rapid mass movements, fluid-assisted flows, or slow creep. This movement is not only essential for genesis of key landforms in the so-called supraglacial landsystem (Johnson and Clayton, 2005), but affects the magnitude and spatial distribution of ablation. The model simulations presented here examine relationships between measures of debris mobility, sub-debris ablation and the spatial distribution and redistribution of debris during and following de-icing. Among the key findings are that debris mobility can hasten ice mass loss compared to immobile debris, and that an optimum mobility exists where de-icing rate is greatest and postglacial moraine relief is high. This optimal mobility is related to the initial distribution of debris sources and the ice thickness to be melted. These results have implications for the practice of projecting mass balance in areas of debris cover, where predictions of mass loss often assume static debris or debris with minimal spatial variation in thickness. The results also inform interpretations of process-form relationships in supraglacial landsystems. Greater insights will, however, require a better understanding of the processes of slow downslope debris transport in supraglacial settings and the variables that govern them.

DATA AVAILABILITY STATEMENT

The original contributions presented in the study are included in the article/**Supplementary Material**, further inquiries can be directed to the corresponding author.

AUTHOR CONTRIBUTIONS

PM is responsible for all aspects of this paper.

FUNDING

This study was funded by the U.S. National Science Foundation under grant EAR-1225880.

ACKNOWLEDGMENTS

The author gratefully acknowledges the editor and two reviewers for their suggestions, which improved the clarity of this manuscript.

SUPPLEMENTARY MATERIAL

The Supplementary Material for this article can be found online at: https://www.frontiersin.org/articles/10.3389/feart.2021.710131/full#supplementary-material

REFERENCES

Anderson, L. S., and Anderson, R. S. (2016). Modeling Debris-Covered Glaciers: Response to Steady Debris Deposition. *The Cryosphere* 10, 1105–1124. doi:10.5194/tc-10-1105-2016

Anderson, R. S. (2000). A Model of Ablation-Dominated Medial Moraines and the Generation of Debris-Mantled Glacier Snouts. *J. Glaciol.* 46, 459–469. doi:10.3189/172756500781833025

Anderson, R. S., Anderson, L. S., Armstrong, W. H., Rossi, M. W., and Crump, S. E. (2018). Glaciation of alpine Valleys: The Glacier - Debris-Covered Glacier - Rock Glacier Continuum. *Geomorphology* 311, 127–142. doi:10.1016/j.geomorph.2018.03.015

Andersson, G. (2008). Genesis of Hummocky Moraine in the Bolmen Area, Southwestern Sweden. *Boreas* 27, 55–67. doi:10.1111/j.1502-3885.1998.tb00867.x

Attig, J. W., Mickelson, D. M., and Clayton, L. (1989). Late Wisconsin Landform Distribution and Glacier-Bed Conditions in Wisconsin. *Sediment. Geology.* 62, 399–405. doi:10.1016/0037-0738(89)90128-0

Banerjee, A. (2017). Brief Communication: Thinning of Debris-Covered and Debris-free Glaciers in a Warming Climate. *The Cryosphere* 11, 133–138. doi:10.5194/tc-11-133-2017

Bartlett, O. T., Ng, F. S. L., and Rowan, A. V. (2020). Morphology and Evolution of Supraglacial Hummocks on Debris-Covered Himalayan Glaciers. *Earth Surf. Process. Landforms* 46, 525–539. doi:10.1002/esp.5043

Benn, D. I., Thompson, S., Gulley, J., Mertes, J., Luckman, A., and Nicholson, L. (2017). Structure and Evolution of the Drainage System of a Himalayan Debris-Covered Glacier, and its Relationship with Patterns of Mass Loss. *The Cryosphere* 11, 2247–2264. doi:10.5194/tc-11-2247-2017

Boulton, G. S., and Paul, M. A. (1976). The Influence of Genetic Processes on Some Geotechnical Properties of Glacial Tills. *Q. J. Eng. Geology. Hydrogeology* 9, 159–194. doi:10.1144/GSL.QJEG.1976.009.03.03

Boulton, G. S. (1967). The Development of a Complex Supraglacial Moraine at the Margin of Sørbreen, Ny Friesland, Vestspitsbergen. *J. Glaciol.* 6, 717–735. doi:10.3189/s0022143000019961

Clayton, L., Attig, J. W., Ham, N. R., Johnson, M. D., Jennings, C. E., and Syverson, K. M. (2008). Ice-walled-lake plains: Implications for the Origin of Hummocky Glacial Topography in Middle North America. *Geomorphology* 97, 237–248. doi:10.1016/j.geomorph.2007.02.045

Clayton, L. (1964). Karst Topography on Stagnant Glaciers. *J. Glaciol.* 5, 107–112. doi:10.3189/s0022143000028628

Dietrich, W., Bellugi, D., and Sklar, L. (2003). Geomorphic Transport Laws for Predicting Landscape Form and Dynamics. *Geophysical* 135, 1–30. doi:10.1029/135GM09

Driscoll, F. G. (1980). Formation of the Neoglacial Surge Moraines of the Klutlan Glacier, Yukon Territory, Canada. *Quat. Res.* 14, 19–30. doi:10.1016/0033-5894(80)90004-6

Evans, D. J. A. (2009). Controlled Moraines: Origins, Characteristics and Palaeoglaciological Implications. *Quat. Sci. Rev.* 28, 183–208. doi:10.1016/j.quascirev.2008.10.024

Eyles, N. (1979). Facies of Supraglacial Sedimentation on Icelandic and Alpine Temperate Glaciers. *Can. J. Earth Sci.* 16, 1341–1361. doi:10.1139/e79-121

Fowler, A. C., and Mayer, C. (2017). The Formation of Ice Sails. *Geophys. Astrophysical Fluid Dyn.* 111, 411–428. doi:10.1080/03091929.2017.1370092

Fryxell, F. (1933). The Migration of Superglacial Boulders. *J. Geology.* 41, 737–747. doi:10.1086/624093

Furbish, D. J., Haff, P. K., Dietrich, W. E., and Heimsath, A. M. (2009). Statistical Description of Slope-dependent Soil Transport and the Diffusion-like Coefficient. *J. Geophys. Res.* 114, F00A05. doi:10.1029/2009JF001267

Fyffe, C. L., Woodget, A. S., Kirkbride, M. P., Deline, P., Westoby, M. J., and Brock, B. W. (2020). Processes at the Margins of Supraglacial Debris Cover: Quantifying Dirty Ice Ablation and Debris Redistribution. *Earth Surf. Process. Landforms* 45, 2272–2290. doi:10.1002/esp.4879

Gilbert, G. K. (1904). *Alaska Volume III: Glaciers and Glaciation*. New York: Doubleday, Page, & Co.

Gravenor, C. P. (1955). The Origin and Significance of Prairie mounds [alberta]. *Am. J. Sci.* 253, 475–481. doi:10.2475/ajs.253.8.475

Ham, N. R., and Attig, J. W. (2001). Minor End Moraines of the Wisconsin Valley Lobe, north-central Wisconsin, USA. *Boreas* 30, 31–41. doi:10.1080/030094801300062266

Hambrey, M. J., Huddart, D., Bennett, M. R., and Glasser, N. F. (1997). Genesis of 'hummocky Moraines' by Thrusting in Glacier Ice: Evidence from Svalbard and Britain. *J. Geol. Soc.* 154, 623–632. doi:10.1144/gsjgs.154.4.0623

Hambrey, M. J. (1984). Sedimentary Processes and Buried Ice Phenomena in the Pro-glacial Areas of Spitsbergen Glaciers. *J. Glaciol* 30.

Heimsath, A. M., Chappell, J., Spooner, N. a., and Questiaux, D. G. (2002). Creeping Soil. *Geol.* 30, 111. doi:10.1130/0091-7613(2002)030<0111:cs>2.0.co;2

Herreid, S., and Pellicciotti, F. (2020). The State of Rock Debris Covering Earth's Glaciers. *Nat. Geosci.* 13, 621–627. doi:10.1038/s41561-020-0615-0

Houssais, M., Maldarelli, C., and Morris, J. F. (2021). Athermal Sediment Creep Triggered by Porous Flow. *Phys. Rev. Fluids* 6, L012301. doi:10.1103/PhysRevFluids.6.L012301

Johnson, M. D., and Clayton, L. (2005). "Supraglacial Landsystems in lowland Terrain," in *Glacial Landsystems*. Editor D. J. A. Evans (Arnold), 228–258.

Johnson, M. D., Mickelson, D. M., Clayton, L., and Attig, J. W. (1995). Composition and Genesis of Glacial Hummocks, Western Wisconsin, USA. *Boreas* 24, 97–116. doi:10.1111/j.1502-3885.1995.tb00630.x

Kääb, A., Berthier, E., Nuth, C., Gardelle, J., and Arnaud, Y. (2012). Contrasting Patterns of Early Twenty-First-century Glacier Mass Change in the Himalayas. *Nature* 488, 495–498. doi:10.1038/nature11324

Krüger, J., Kjær, K. H., and Schomacker, A. (2010). "Dead-Ice Environments: A Landsystems Model for a Debris-Charged, Stagnant Lowland Glacier Margin, Kötlujökull," in *Developments in Quaternary Sciences*. Editors A. Schomacker, J. Krüger, and K. H. Kjær (Elsevier), 105–126. doi:10.1016/S1571-0866(09)01307-4

Lawson, D. E. (1982). Mobilization, Movement and Deposition of Active Subaerial Sediment Flows, Matanuska Glacier, Alaska. *J. Geology.* 90, 279–300. doi:10.1086/628680

Lawson, D. E. (1979). *Semdimentological Analysis of the Western Terminus Region of the Matanuska Glacier, Alaska (No. CRREL-79-9)*. Hanover, NH: Cold Regions Research and Engineering Lab.

Mölg, N., Ferguson, J., Bolch, T., and Vieli, A. (2020). On the Influence of Debris Cover on Glacier Morphology: How High-Relief Structures Evolve from Smooth Surfaces. *Geomorphology* 357, 107092. doi:10.1016/j.geomorph.2020.107092

Moore, P. L. (2018). Stability of Supraglacial Debris. *Earth Surf. Process. Landforms* 43, 285–297. doi:10.1002/esp.4244

Nakawo, M., and Young, G. J. (1981). Field Experiments to Determine the Effect of a Debris Layer on Ablation of Glacier Ice. *Ann. Glaciol.* 2, 85–91. doi:10.3189/172756481794352432

Nicholson, L., and Benn, D. I. (2006). Calculating Ice Melt beneath a Debris Layer Using Meteorological Data. *J. Glaciol.* 52, 463–470. doi:10.3189/172756506781828584

Nicholson, L. I., McCarthy, M., Pritchard, H., and Willis, I. (2018). Supraglacial Debris Thickness Variability: Impact on Ablation and Relation to Terrain Properties. *Cryosph. Discuss.* 12, 1–30. doi:10.5194/tc-2018-83

östrem, G. (1959). Ice Melting under a Thin Layer of Moraine, and the Existence of Ice Cores in Moraine Ridges. *Geografiska Annaler* 41, 228–230. doi:10.1080/20014422.1959.11907953

Paul, M. A., and Eyles, N. (1990). Constraints on the Preservation of Diamict Facies (Melt-out Tills) at the Margins of Stagnant Glaciers. *Quat. Sci. Rev.* 9, 51–69. doi:10.1016/0277-3791(90)90004-T

Pawlik, Ł., and Šamonil, P. (2018). Soil Creep: The Driving Factors, Evidence and Significance for Biogeomorphic and Pedogenic Domains and Systems - A Critical Literature Review. *Earth-Science Rev.* 178, 257–278. doi:10.1016/j.earscirev.2018.01.008

Perron, J. T. (2011). Numerical Methods for Nonlinear Hillslope Transport Laws. *J. Geophys. Res.* 116, 2021. doi:10.1029/2010JF001801

Reid, J. R., Jr. (1970). Geomorphology and Glacial Geology of the Martin River Glacier, Alaska. *Arctic* 23, 213–296. doi:10.14430/arctic3181

Roering, J. J., Kirchner, J. W., Sklar, L. S., and Dietrich, W. E. (2001). Hillslope Evolution by Nonlinear Creep and Landsliding: An Experimental Study. *Geol.* 29, 143–146. doi:10.1130/0091-7613(2001)029<0143:hebnca>2.0.co;2

Roering, J. J. (2004). Soil Creep and Convex-Upward Velocity Profiles: Theoretical and Experimental Investigation of Disturbance-Driven Sediment Transport on Hillslopes. *Earth Surf. Process. Landforms* 29, 1597–1612. doi:10.1002/esp.1112

Rowan, A. V., Egholm, D. L., Quincey, D. J., and Glasser, N. F. (2015). Modelling the Feedbacks between Mass Balance, Ice Flow and Debris Transport to Predict the Response to Climate Change of Debris-Covered Glaciers in the Himalaya. *Earth Planet. Sci. Lett.* 430, 427–438. doi:10.1016/j.epsl.2015.09.004

Rowan, A. V., Nicholson, L. I., Quincey, D. J., Gibson, M. J., Irvine-Fynn, T. D. L., Watson, C. S., et al. (2021). Seasonally Stable Temperature Gradients through Supraglacial Debris in the Everest Region of Nepal, Central Himalaya. *J. Glaciol.* 67, 170–181. doi:10.1017/jog.2020.100

Russell, I. C. (1893). Malaspina Glacier. *J. Geology.* 1, 219–245. doi:10.1086/606179

Scherler, D., Wulf, H., and Gorelick, N. (2018). Global Assessment of Supraglacial Debris-Cover Extents. *Geophys. Res. Lett.* 45, 11798–11805. doi:10.1029/2018GL080158

Schomacker, A. (2008). What Controls Dead-Ice Melting under Different Climate Conditions? A Discussion. *Earth-Science Rev.* 90, 103–113. doi:10.1016/j.earscirev.2008.08.003

Sharp, R. P. (1949). Studies of Superglacial Debris on valley Glaciers. *Am. J. Sci.* 247, 289–315. doi:10.2475/ajs.247.5.289

Shulmeister, J., Davies, T. R., Evans, D. J. A., Hyatt, O. M., and Tovar, D. S. (2009). Catastrophic Landslides, Glacier Behaviour and Moraine Formation - A View from an Active Plate Margin. *Quat. Sci. Rev.* 28, 1085–1096. doi:10.1016/j.quascirev.2008.11.015

Tarr, R., and Martin, L. (1914). *Alaskan Glacier Studies of the National Geographic Society in the Yakutat Bay, Prince William Sound and Lower Copper River Regions*. Palala Press, 750.

Thompson, S., Benn, D. I., Mertes, J., and Luckman, A. (2016). Stagnation and Mass Loss on a Himalayan Debris-Covered Glacier: Processes, Patterns and Rates. *J. Glaciol.* 62, 467–485. doi:10.1017/jog.2016.37

Vacco, D. A., Alley, R. B., and Pollard, D. (2010). Glacial advance and Stagnation Caused by Rock Avalanches. *Earth Planet. Sci. Lett.* 294, 123–130. doi:10.1016/j.epsl.2010.03.019

Vincent, C., Wagnon, P., Shea, J., and Immerzeel, W. (2016). *Reduced Melt on Debris-Covered Glaciers: Investigations from Changri Nup Glacier*. Nepal.

Westoby, M. J., Rounce, D. R., Shaw, T. E., Fyffe, C. L., Moore, P. L., Stewart, R. L., et al. (2020). Geomorphological Evolution of a Debris-Covered Glacier Surface. *Earth Surf. Process. Landforms* 45, 3431–3448. doi:10.1002/esp.4973

Wright, H. E. (1980). Surge Moraines of the Klutlan Glacier, Yukon Territory, Canada: Origin, Wastage, Vegetation Succession, lake Development, and Application to the Late-Glacial of Minnesota. *Quat. Res.* 14, 2–18. doi:10.1016/0033-5894(80)90003-4

Conflict of Interest: The authors declares that the research was conducted in the absence of any commercial or financial relationships that could be construed as a potential conflict of interest.

frontiers in Earth Science

ORIGINAL RESEARCH
published: 24 August 2021
doi: 10.3389/feart.2021.680995

The Causes of Debris-Covered Glacier Thinning: Evidence for the Importance of Ice Dynamics From Kennicott Glacier, Alaska

Leif S. Anderson[1,2,3]*, *William H. Armstrong*[1,4], *Robert S. Anderson*[1], *Dirk Scherler*[2,5] *and Eric Petersen*[6]

[1]Department of Geological Sciences and Institute of Arctic and Alpine Research, University of Colorado, Boulder, CO, United States, [2]Helmholtz Centre Potsdam, German Research Centre for Geosciences (GFZ), Potsdam, Germany, [3]Institute of Earth Surface Dynamics, University of Lausanne, Lausanne, Switzerland, [4]Department of Geological and Environmental Sciences, Appalachian State University, Boone, NC, United States, [5]Institute of Geological Sciences, Freie Universität, Berlin, Germany, [6]Geophysical Institute, University of Alaska, Fairbanks, AK, United States

The cause of debris-covered glacier thinning remains controversial. One hypothesis asserts that melt hotspots (ice cliffs, ponds, or thin debris) increase thinning, while the other posits that declining ice flow leads to dynamic thinning under thick debris. Alaska's Kennicott Glacier is ideal for testing these hypotheses, as ice cliffs within the debris-covered tongue are abundant and surface velocities decline rapidly downglacier. To explore the cause of patterns in melt hotspots, ice flow, and thinning, we consider their evolution over several decades. We compile a wide range of ice dynamical and mass balance datasets which we cross-correlate and analyze in a step-by-step fashion. We show that an undulating bed that deepens upglacier controls ice flow in the lower 8.5 km of Kennicott Glacier. The imposed velocity pattern strongly affects debris thickness, which in turn leads to annual melt rates that decline towards the terminus. Ice cliff abundance correlates highly with the rate of surface compression, while pond occurrence is strongly negatively correlated with driving stress. A new positive feedback is identified between ice cliffs, streams and surface topography that leads to chaotic topography. As the glacier thinned between 1991 and 2015, surface melt in the study area decreased, despite generally rising air temperatures. Four additional feedbacks relating glacier thinning to melt changes are evident: the debris feedback (negative), the ice cliff feedback (negative), the pond feedback (positive), and the relief feedback (positive). The debris and ice cliff feedbacks, which are tied to the change in surface velocity in time, likely reduced melt rates in time. We show this using a new method to invert for debris thickness change and englacial debris content (~0.017% by volume) while also revealing that declining speeds and compressive flow led to debris thickening. The expansion of debris on the glacier surface follows changes in flow direction. Ultimately, glacier thinning upvalley from the continuously debris-covered portion of Kennicott Glacier, caused by mass balance changes, led to the reduction of flow into the study area. This caused ice emergence rates to decline rapidly leading to the occurrence of maximum, glacier-wide thinning under thick, insulating debris.

OPEN ACCESS

Edited by:
Lindsey Isobel Nicholson, University of Innsbruck, Austria

Reviewed by:
Takayuki Nuimura, Tokyo Denki University, Japan
Andreas Vieli, University of Zurich, Switzerland

***Correspondence:**
Leif S. Anderson
leif.anderson@utah.edu

Specialty section:
This article was submitted to Cryospheric Sciences, a section of the journal Frontiers in Earth Science

Received: *15 March 2021*
Accepted: *06 August 2021*
Published: *24 August 2021*

Citation:
Anderson LS, Armstrong WH, Anderson RS, Scherler D and Petersen E (2021) The Causes of Debris-Covered Glacier Thinning: Evidence for the Importance of Ice Dynamics From Kennicott Glacier, Alaska. Front. Earth Sci. 9:680995. doi: 10.3389/feart.2021.680995

Keywords: ice cliff, stream, pond, feedback, velocity, expansion, bed, inversion

INTRODUCTION

Debris cover thicker than a few centimeters insulates the ice surface beneath it and reduces melt (Østrem, 1959; Nicholson and Benn, 2006). On debris-covered glaciers, the insulating effect of debris appears to strongly control area-averaged melt rates (Bisset et al., 2020). However, the low melt rates within debris-covered surfaces seem to conflict with the common observation that glacier-wide thinning is often highest beneath melt reducing debris (e.g., Kääb et al., 2012; Gardelle et al., 2013). This phenomenon has been referred to as the 'debris-cover anomaly' (Pellicciotti et al., 2015); it appears to occur globally and has been reported in High Mountain Asia, the European Alps (Mölg et al., 2019), and Alaska (Anderson et al., 2021).

We approach this topic hoping that the study of a single glacier in detail will effectively reveal the underlying processes that control the debris cover anomaly more generally. For this case study we consider Kennicott Glacier, a large, dynamic glacier in the Wrangell Mountains of Alaska (**Figure 1**).

To discern the fundamental controls on debris-covered glacier evolution in response to climate change we parse the issue in two: First, we consider a modern "snapshot" of Kennicott Glacier (i.e., frozen in time) to develop our understanding of causal relationships between different parts of the system. Second, we consider the glacier's evolution over multiple decades.

In order to study the complex interactions occurring on Kennicott Glacier, we attempt to establish causal relationships between various parts of the system, namely debris thickness, melt hotspots, and ice dynamics. Because debris thickness strongly controls melt, an understanding of the processes controlling debris thickness is essential for projecting the future evolution of debris covered glaciers (e.g., Banerjee, 2017). Processes that control the distribution of sediment on glaciers include the melt out of debris from within the glacier, the compression (or extension) of ice due to the pattern of ice velocity, the advection of typically thinner debris downglacier, and local sediment re-distribution (hillslope) processes (Moore, 2018; Huo et al., 2021). Anderson and Anderson (2018) showed that thin debris should be expected to occur where velocities are high and thick debris should occur where velocities are low. They suggested that debris melt out from the glacier to the surface should decline downglacier following the reduction of melt rates under thicker and thicker debris.

Melt hotspots like ice cliffs, streams, and ponds are scattered across debris-covered ice surfaces and locally increase melt rates (e.g., Miles et al., 2018; Buri et al., 2021). It has been previously shown that ice cliffs correlate with the degree to which surface flow is compressive (Benn et al., 2012; Kraaijenbrink et al., 2016). Streams on debris-covered glaciers tend to be larger where debris is thin and melt rates are high and smaller where debris is thick and melt rates are low (Iwata et al., 1980; Fyffe et al., 2019). Ponds

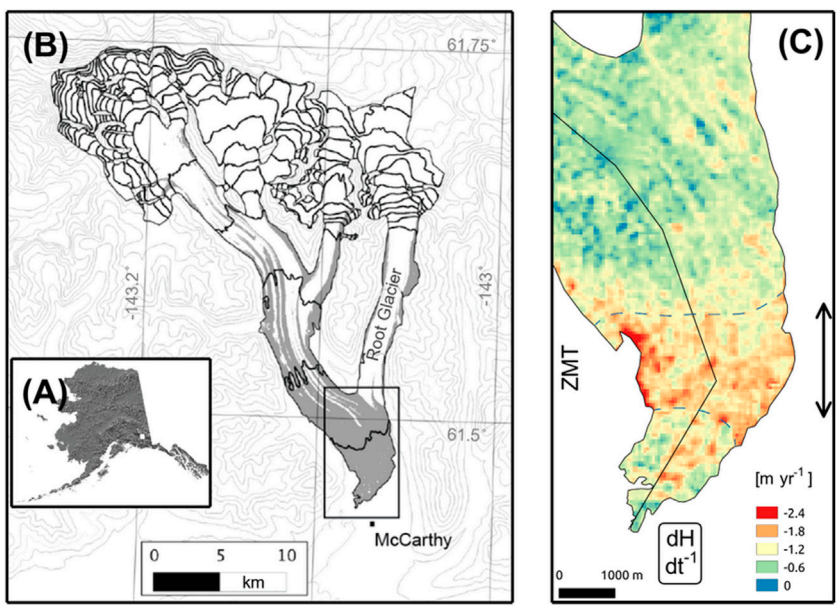

FIGURE 1 | Context and thinning maps of the study area. **(A)** Map of Alaska showing the location of panel B as a white square. **(B)** Kennicott Glacier with the extent of panel C as a black rectangle. The contour interval is 200 m. The most southerly contour on the glacier represents 600 m a.s.l. **(C)** The study area with the rate of glacier surface elevation change (dH dt^{-1}) between 1957 and 2004 (see Das et al., 2014). *ZMT* refers to the zone of maximum thinning and its extent is designated by the double headed arrow and the blue dashed lines on the glacier. The solid black line is the trace of the 1,000 m wide swath profile used to present data with distance from the terminus in later figures.

on debris-covered glaciers occur preferentially where surfaces slopes are low (e.g., Reynolds, 2000).

Previous work has revealed a striking pattern in ice cliffs and debris thickness across the debris-covered tongue of Kennicott Glacier (Anderson et al., 2021). Where ice cliffs on the modern glacier are most abundant, a rapid increase in debris thickness downglacier also occurs, suggesting that there is a common control. Here we therefore first consider: What controls the patterns of ice flow, debris, and melt hotspots on the modern Kennicott Glacier (independent of significant glacier thinning)? To address this question, we produce and compile 18 different variables from the modern debris-covered tongue of Kennicott Glacier and cross-correlate them and attempt to establish causal relationships by identifying processes that connect the correlated variables.

When considering the evolution of Kennicott Glacier over several decades, our focus is on explaining how the glacier has thinned and why melt rates appear to have declined in time. The thinning of glaciers must occur either by mass loss in place or by dynamical redistribution of mass loss occurring elsewhere on the glacier surface. To show the potential for feedbacks in the debris-covered glacier system, we highlight three fundamental equations governing the evolution of debris-covered glaciers. First, the continuity equation for ice:

$$\frac{dH}{dt} = \dot{b} - \frac{\partial \overline{u}H}{\partial x} - \frac{\partial \overline{v}H}{\partial y}, \tag{1}$$

where H is ice thickness, t is time, $\dot{b}$ is annual area-average mass balance (or loosely ablation in the ablation zone), $\overline{u}$ is depth-averaged velocity in the x-direction, and $\overline{v}$ is depth-averaged velocity in the y-direction, x-represents east-west direction, and y-represents the north-south direction. Note that $\overline{u}H$ and $\overline{v}H$ are the ice discharges (Q) in the x- and y-direction, respectively. The last two terms on the right combine to represent ice emergence velocity (or surface uplift) and represent the effect of ice dynamics on glacier thinning. Within the debris-covered zone, mass balance $\dot{b}$ is the area-averaged melt from beneath debris ($\dot{b}_{debris}$) and from melt hotspots ($\dot{b}_{hotspots}$).

Debris thickness affects the melt rate beneath debris through Østrem's curve, which can be described as a hyperbolic relationship [i.e., the Hyper-fit model of Anderson and Anderson (2016)]:

$$\dot{b}_{debris} = \dot{b}_{ice}\frac{h_*}{(h_{debris} + h_*)}, \tag{2}$$

where $\dot{b}_{ice}$, is bare-ice melt rate, h_{debris} is debris thickness, and h_* is the characteristic debris thickness.

Surface debris patterns depend on ice flow and debris thickness itself. The governing equation for the evolution of debris thickness (e.g., Nakawo et al., 1986) is

$$\frac{\partial h_{debris}}{\partial t} = \frac{C\dot{b}}{(1-\phi)\rho_r} - \frac{\partial u h_{debris}}{\partial x} - \frac{\partial v h_{debris}}{\partial y} \tag{3}$$

where C is near-surface englacial debris concentration, φ is the porosity of the debris, ρ_r is the density of the rock composing the debris, and u is surface velocity in the x-direction and v is surface velocity in the y-direction. The first term on the right-hand side of **Eq. 3** is the rate of debris melt out, the second and third terms represent the combined effects of surface compression (i.e., surface strain rate, $\partial u/\partial x + \partial v/\partial y$) and the advection of debris in the x- and y-directions.

Feedbacks within the debris-covered glacier system are abundant and are represented by the shared terms within and between **Eqs 1–3**. Feedbacks occur when a 'cause' influences the resulting 'effect' and the resulting effect loops back to influence the cause. As an example, thinning, due to rising temperatures, reduces ice flow causing melt hotspot patterns to change, which in turn affects melt rates and thinning, completing the feedback loop (**Supplementary Figure S1**). Feedbacks are positive when the effect amplifies the cause and negative when the effect lessens the cause.

The chain of process-links from boundary conditions to observables on debris-covered glacier surfaces (like thinning or ice cliff patterns) are difficult to discern because of the sheer number of possible controls. To address and simplify this issue we consider: What processes and feedbacks control the thinning of Kennicott Glacier as it thins over multiple decades?

We quantified most terms in the first three equations as they vary in space and time. All terms of the continuity equation for ice (**Eq. 1**) are quantified, including annual mass balance and ice emergence. To constrain the glacier thinning pattern we difference digital elevation models (DEMs). We quantify all terms in the debris–thickness melt relationship (**Eq. 2**) and the continuity equation for debris (**Eq. 3**) excluding the debris porosity and density. The development and inversion for this range of datasets affords us a rare view into the controls of the multi-decadal-scale evolution of a large, rapidly thinning debris-covered glacier. Analyses of debris and melt hotspots as they change in time further show how essential ice dynamics are for understanding and predicting the evolution of debris-covered glaciers.

Study Glacier

Kennicott Glacier is 42 km long and broadly faces south-southeast in the Wrangell Mountains of Alaska (**Figure 1**; 387 km^2 area). As of 2015, 20% of Kennicott Glacier was debris-covered (Anderson et al., 2021). Below the equilibrium-line altitude at about 1,500 m (Armstrong et al., 2017), nine medial moraines can be identified on the glacier surface. Debris thicknesses were measured on the glacier surface in 2011 and extrapolated across the central five medial moraines of Kennicott Glacier (Anderson et al., 2021). Debris thicknesses have also been estimated across the glacier based on remotely sensed data and modeling (Rounce et al., 2021). Above 700 m elevation debris is typically less than 5 cm thick, although, near the glacier margin debris tends to be thicker. Medial moraines coalesce 7 km from the terminus to form a debris mantle with ice cliffs, streams, and ponds scattered within an otherwise continuous debris cover. Ice cliffs are especially abundant on Kennicott Glacier (Anderson et al., 2021). The zone of maximum thinning, or the ZMT, is defined as the portion of the glacier that has thinned at a rate greater than 1.2 m yr^{-1} between 1957 and 2004 (Das et al., 2014; **Figure 1**). The ZMT has been continuously debris covered since

at least 1957 and debris expanded upglacier by 1.6 km between 1957 and 2009.

Kennicott Glacier has been the focus of outburst flood research for almost two decades. Each year the ice-marginal Hidden Creek lake drains under Kennicott Glacier increasing basal water pressures leading to a 1–2 days period of enhanced basal sliding (Rickman and Rosenkrans, 1997; Anderson et al., 2005; Walder et al., 2006; Bartholomaus et al., 2008; Armstrong and Anderson, 2020). Armstrong et al. (2016) and Armstrong et al. (2017) showed that up to half of the surface displacement in the debris-covered tongue of Kennicott Glacier occurs in the summer, due to sliding at the glacier bed.

METHODS

The data we produced fit into four categories: 1) glacier thinning; 2) ice dynamics; 3) mass balance (MB); and 4) surface features (melt hotspots and topography). All data sets were derived from remotely sensed data, except for the *in situ* measurement of the maximum height of 60 ice cliffs during the summer of 2011 (see Anderson et al., 2021).

We focus on the lower 8.5 km of Kennicott Glacier (**Figure 1**; **Supplementary Figures S2–S4**). Most of the datasets presented here are based on a 1 km wide swath profile running down the center of the glacier. Estimates of annual mass balance and ice emergence rate represent averages across the glacier surface. Our analysis of the modern glacier surface is based on datasets collected between 2011 and 2016. Although these datasets are not all from the same year, we assume that changes in the properties are negligible over this period. For temporal changes over several decades, we assemble data obtained between 1957 and 2016.

We transition between spatial scales, from 'area-averaged' to 'local' processes. We define 'area-averaged' mass balance, as the mean mass balance over the spatial scale for which the surface slope and ice thickness influence ice dynamics, roughly four times the local ice thickness (Kamb and Echelmeyer, 1986). We define 'local' as the 1–10 m spatial scale that is relevant for the control of glacier surface topography by differential ablation.

Glacier Surface Lowering From 1957 to 2016

To constrain the thinning pattern and its changes in time we differenced seven digital elevation models (DEMs) covering the period between 1957 and 2016 (**Supplementary Table S1** and **Supplementary Figure S5**). Before differencing each pair of DEMs they were co-registered relative to one another using the pc_align routine in the Ames StereoPipeline software (Shean et al., 2016). This was accomplished using the iterative point-to-point algorithm and allowing for the translation of one raster relative to another with the glacier area masked out. Uncertainties are based on the standard deviation of elevation change within common, low-sloped areas adjacent to the glacier terminus. To minimize seasonal bias, we only differenced DEMs that 1) have acquisition years more than 9 years apart or 2) were acquired with a day-of-the-year difference of less than 3 weeks (**Supplementary Table S2**).

Ice Dynamics Terms

Ice Thickness

Ice thickness is a fundamental control on the flow of glaciers but can be difficult to constrain through debris cover (Pritchard et al., 2020). To estimate ice thicknesses along the centerline, we inverted the measured early spring 2013 surface velocities from Armstrong et al. (2016) for ice thickness. Ice thickness estimates from previously published, global-scale products have unrealistic step changes in the upper portion of the study area (Farinotti et al., 2019; **Supplementary Figures S6–S8**). It is a common glaciological practice to assume that early spring and winter surface velocities result solely from internal deformation (e.g., Armstrong et al., 2016). We acknowledge that winter sliding occurs (e.g., Raymond, 1971; Amundson et al., 2006; Armstrong et al., 2016), but its magnitude cannot be quantified without borehole observations or independent knowledge of the ice thickness distribution.

We used Glen's flow law to estimate ice thickness H by assuming the flow law exponent n is equal to 3 and solving:

$$H_j = \left[\frac{2\|\vec{V}\|}{A\left(S_f \rho_{ice} g \sin\alpha_j\right)^3}\right]^{\frac{1}{4}} \quad (4)$$

in which j is the index down the glacier centerline, $\vec{V}$ is the surface velocity vector, with the magnitude of the vector indicated by double lines, A is the rate factor, S_f is the shapefactor, ρ_{ice} is ice density, assumed to be 920 kg m^{-3}, g is the acceleration due to gravity, 9.81 m s^{-2}, and α is the surface slope. We want to solve for H in **Eq. 4**, but both S_f and A are unknown, yet they have the same effect on H. By keeping the recommended value of A for temperate ice, 2.4×10^{-24} Pa^{-3}s^{-1} (Cuffey and Paterson, 2010) and using a root-mean-squared error (RMSE) metric, we found that a shapefactor of 0.9 best reproduced known ice thicknesses upglacier from the study area (**Supplementary Figure S6**). Ice thickness near the glacier center is 730 m 12 km upglacier from the terminus (Armstrong et al., 2016) and 600 m 10 km up glacier from the terminus (personal communication, Martin Truffer). We assumed that S_f is uniform through the lower 12 km of the glacier allowing for the estimation of centerline thickness in the swath profile. Uncertainty in ice thickness is estimated by varying the tuned shapefactor (±10%).

Surface Velocities

We estimated horizontal glacier surface velocity in 1991, 2005, and 2015 using Landsat 5 TM (L5) and Landsat 8 OLI (L8) imagery (available at earthexplorer.usgs.gov; **Supplementary Table S3**; **Supplementary Figure S9**). Glacier motion between images taken at different times offsets distinctive pixel "chunks", with the offset proportional to glacier speed. We utilized Fourier-space feature tracking implemented in COSI-Corr (Leprince et al., 2007) to quantitatively estimate feature offsets across Kennicott Glacier and characterize the spatial distribution of glacier surface velocity. We produced high quality annual velocity estimates ingesting snow and cloud-free single image pairs from the same worldwide reference system (WRS) path and row, with input images spaced approximately 1 year apart. Utilizing input

imagery separated by approximately 1 year minimizes seasonal effects on the velocity pattern that can arise from compositing short-term velocity estimates. Despite this long temporal baseline, the feature tracking algorithm still produced high confidence matches, indicating that the planview appearance of the glacier surface does not change substantially over this timespan.

We created our own velocity estimates rather than using existing velocity products like GO_LIVE (Fahnestock et al., 2016; Scambos et al., 2016) or ITS_LIVE (Gardner et al., 2018, Gardner et al., 2020) because site-specific tuning of processing parameters and input imagery produces higher quality results for our single site than these datasets, which are optimized for large-scale applications. The earlier L5 satellite does not have a panchromatic band, so we utilize reflectance in the green wavelengths (L5 Band 2, 0.52–0.60 μm; L8 Band 3, 0.64–0.67 μm). Reflectance in this waveband has 30 m resolution for both L5 and L8 and minimizes potential bias arising from varying spatial resolution between the missions (Dehecq et al., 2019). All feature tracking used a step between adjacent estimates of 4 pixels and a variable search window that starts as 64 × 64 pixels, then decreasing to 32 × 32 pixels. The resulting velocity estimates have a spatial resolution of 120 m (4 × 30 m). Pixels with a signal-to-noise ratio of <0.9 are removed from further analysis. Image pairs are not separated by exactly 1 year, and so displacement components are all normalized to that expected in a 1-year timespan to produce an annual velocity. We calculated apparent velocity in off-glacier pixels (**Supplementary Figure S10**) for each image pair to provide estimates of bias and random pixel matching error. We subtract the median off-glacier apparent velocity component from each image to remove systematic error due to image misregistration. After bias correction, we estimated random error (σ) for each velocity component using the interquartile range (IQR) of apparent velocity in off-glacier pixels using $\sigma = \sqrt{IQR_u^2 + IQR_v^2}$ (**Supplementary Text**; **Supplementary Table S3**; **Supplementary Figure S11**).

To evaluate potential controls on the expansion of debris on Kennicott Glacier, we also assessed the change in surface velocity direction. We interpret aerial and satellite imagery from 1957, 1978, and 2009 (**Supplementary Table S4**) to constrain changes in medial moraine shape (a proxy for flow direction and surface strain).

Driving Stress, Surface Strain Rates and Accumulated Downglacier Compression

Driving stress (or the basal shear stress, τ_b) is a fundamental control on the motion of glaciers and can be expressed as:

$$\tau_b = \rho_{ice} g H \sin\alpha \tag{5}$$

and may therefore be a control on other properties within the debris-covered glacier system.

Using the *x*- and *y*-velocities from our annual velocity fields we also calculated surface strain rate $\dot{\varepsilon}$:

$$\dot{\varepsilon} = \frac{\partial u}{\partial x} + \frac{\partial v}{\partial y}, \tag{6}$$

where this term is positive debris will tend to thicken due to compressive flow and where this term is negative, debris will thin due to extensive flow (**Supplementary Figure S12**). Strain rates are calculated across a 200 m × 200 m grid, similar patterns resulted from calculations based on 400 × 400 m grids. We also calculated the amount of strain a debris parcel would experience as it advected downglacier using the 2015 velocity field.

Ice Emergence Rates

The reduction of ice emergence rates in time can be a strong control on debris-covered glacier thinning (e.g., Vincent et al., 2016). To estimate ice emergence rates through the study area we used a mass-continuity approach following Bisset et al. (2020). We divided the glacier surface with across-flow segments approximately 2 km apart based on glacier outlines derived from thinning maps and aerial and satellite imagery. For the 2015 ice extent we used the 2009 WorldView (WV) satellite image, and a Landsat image from 2016 (**Supplementary Figure S2**). For the 1991 ice extent we used a conservative extent based on a 1978 USGS aerial photo (a 2004 ice extent produces similar results; **Supplementary Figures S3–S4**). Ice emergence rates were estimated first by calculating the ice discharge *Q*:

$$Q_m = \sum_{i=1}^{i=20} \overline{\|\dot{V}_i\|} H_i l_i \tag{7}$$

where *m* represents an entire across-flow transect, *i* the index of the cell within each across-flow transect, $\overline{\|\dot{V}_i\|}$ the depth-averaged velocity magnitude in the downglacier direction interpolated to segment *i*, H_i is the mean ice thickness of the cell, and l_i is the length of each cell. In order to estimate *H* as it varies in cross section, we followed the approach of Armstrong et al. (2016) but use a symmetrical cross section instead of an asymmetrical one defined by the tuned shapefactor of 0.9. Ice emergence rate $\dot{E}_j$ in each glacier section is then calculated following:

$$\dot{E}_j = \frac{Q_{input_j} - Q_{output_j}}{Area_j} \tag{8}$$

where *j* is the downglacier index and *Area* is the surface area between the across-flow transects.

We then propagated the error to produce uncertainties for ice emergence rates and mass balance estimates. For results presented in the main text we assumed that all ice motion is due to basal sliding following Bisset et al. (2020). Assuming that all motion is due to internal deformation has a small effect on the annual mass balance estimates (see next section for sensitivity tests).

(Annual) Mass Balance

Constraining annual mass balance is essential for understanding the causes of glacier thinning. We reorganize **Eq. 1** to estimate the mass balance in the area between each across-flow transect:

$$\dot{b}_j = \left(\frac{dH_j}{dt} - \dot{E}_j \right) \tag{9}$$

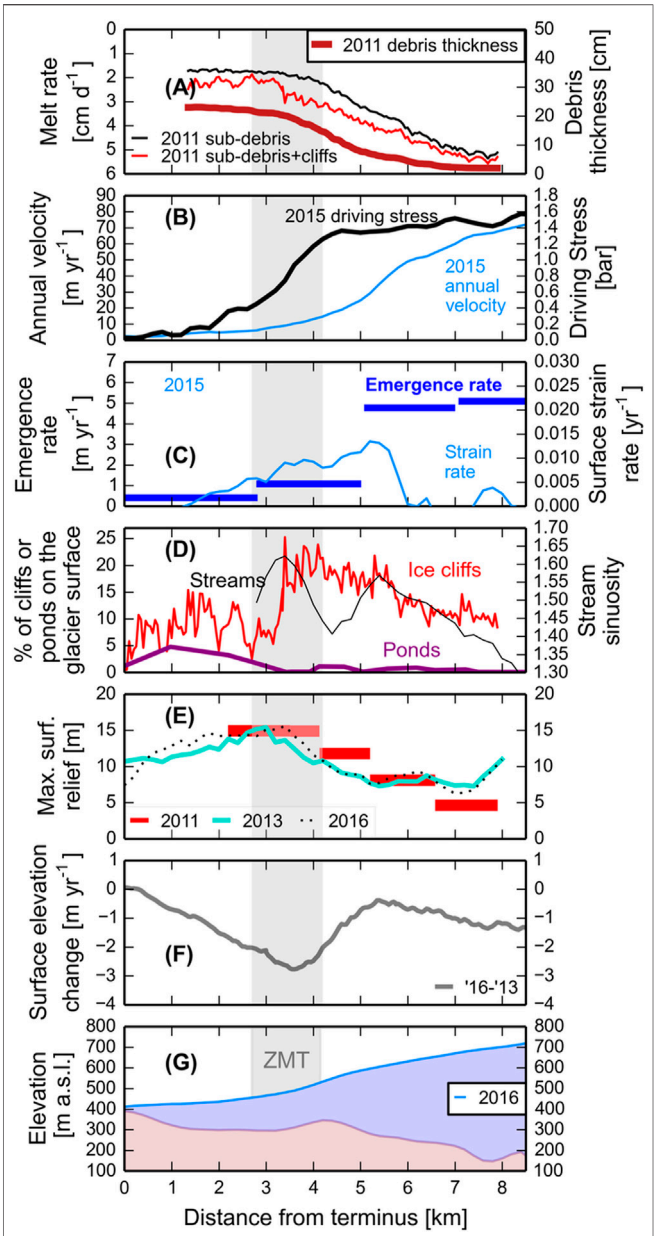

FIGURE 2 | Modern snapshot comparison. The zone of maximum thinning (ZMT) is shown with grey shading. **(A)** Surface melt rate and debris thickness patterns from the summer of 2011 (Anderson et al., 2021). **(B)** 2015 annual surface velocity pattern with the driving stress based on the surface slope and ice thickness from 2016. **(C)** The ice emergence rate averaged over approximately 2 km intervals as well as the surface strain rate from the swath profile, smoothed with a 1 km moving window. **(D)** Patterns of melt hotspots, including ice cliffs and stream sinuosity from the swath profile, as well as ponds across the glacier width. **(E)** Maximum surface relief within the swath profile taken from 2013 (turquoise) and 2016 (black dots) DEMs. Maximum measured ice cliff relief (red) from the glacier surface in 2011 is also shown. **(F)** The surface elevation change pattern based on fall 2013 and fall 2016 DEMs. **(G)** Glacier surface elevation and bed topography from 2016 down the glacier centerline.

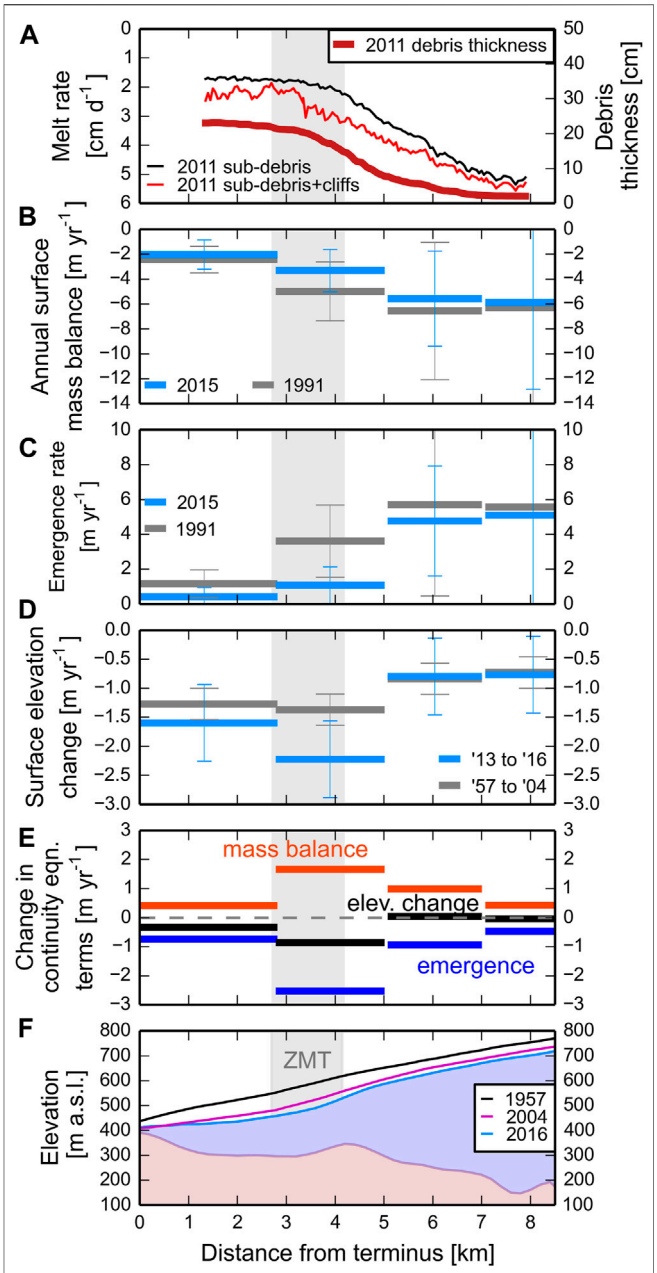

FIGURE 3 | Changes in ice continuity equation terms over multiple decades. The zone of maximum thinning (ZMT) is shown with grey shading. **(A)** Debris thickness with distance from the terminus for the 5 central medial moraines (Anderson et al., 2021). Distributed melt rate estimates from Anderson et al. (2021). **(B)** Annual surface mass balance based on 2015 annual velocities and thinning between 2013 and 2016. As well as the annual surface mass balance based on 1991 annual velocities and thinning between 1957 and 2004. **(C)** The change in ice emergence rate in time. **(D)** Glacier surface elevation change from 1957 to 2004 and from 2013 to 2016. **(E)** The change in the terms of the continuity equation between 1991 and 2015. The bars represent the difference between the bars in each of panels B, C, and D. **(F)** Surface profiles through time and the bed profile of Kennicott Glacier.

where $\dot{b}_j$ is the area-averaged mass balance in the glacier section, dH dt^{-1} is the mean ice surface elevation change. We followed the error estimation approach of Bisset et al. (2020) in which there is a 99.8% probability (±3 standard deviation window) that the mass balance estimate lies within the error envelope. These area-averaged mass balance estimates

include the contribution of surface, englacial, and subglacial melt.

We produced two estimates of annual mass balance representing the years 2015 and 1991. In both cases ice thicknesses were updated based on the thinning estimates over the intervening timespan. For the 2015 estimates we used the 2015 velocities as well as thinning data based on fall 2013 and fall 2016 DEMs. For the 1991 mass balance estimates, we used the 1991 annual surface velocity as well as the thinning data based on 1957 and 2004 DEMs. We note that this long-time interval is not ideal for estimating the mass balance in 1991, using annual velocities from 1991. We therefore provide sensitivity analyses to help reveal uncertainties.

Additional estimates of mass balance and emergence rate are provided in which we 1) assumed that all ice motion is due to internal deformation; 2) varied the tuned shapefactor; 3) assumed there is no change in thinning rate in time; 4) applied a 2004 glacier outline for the 1991 estimates; and 5) applied ITS_LIVE composite velocities (**Supplementary Figures S13–S18**). Note that in **Figures 2**, **3** surface melt rate and debris thickness estimates of Anderson et al. (2021) from the summer of 2011 are plotted for comparison.

Inversion to Estimate Debris Thickness Change and Englacial Debris Concentration

To aid in our understanding of the evolution of Kennicott Glacier in time we estimated debris thickness changes between 1991 and 2011 as well as the mean englacial debris concentration in the study area. To do this we inverted measured debris thickness, surface velocities, strain rates, and annual mass balance estimates from the swath profile.

The first step used a Monte Carlo approach to estimate 10^6 potential 1991 debris thickness patterns (e.g., Tarantola, 2005). We allow random changes in each 200 m pixel from the 2011 *in situ* debris thickness pattern to generate possible 1991 debris thickness patterns. Second, for each possible 1991 debris thickness pattern and englacial debris concentration we numerically solved **Eq. 3** in this form starting in 1991 until an estimate of 2011 debris thickness was produced:

$$\partial h_{debris} = \left(\frac{C\dot{b}\,(x)}{(1-\phi)\rho_r} - \dot{\varepsilon}\,(x) h_{debris}\,(x) - \frac{\partial h_{debris}\,(x)}{\partial x} \left\| \dot{V} \right\| (x) \right) dt \tag{10}$$

The first term on the right is the contribution of englacial debris melt out, the second term is the contribution of compression or extension, and the third term represents the advection of debris downglacier. The timestep, dt is set to 1 year h_{debris} is initially h_{debris}^{1991} and is then updated in each timestep as the debris thickness evolves. For $\dot{b}$ we used linearly interpolated annual mass balances for each year between the 1991 and 2015 estimates. For $\left\| \dot{V} \right\|$ ($\dot{\varepsilon}$) we used linearly interpolated surface velocities (strain rates) for each year between the 1991 and 2015 following the rate of change through time shown in **Supplementary Figure S9**.

For the case presented in the main text we assumed that C is uniform and does not vary in time, that porosity is 0.3 (Nicholson and Benn, 2013), and that the rock density is 2,200 kg m^{-3} (see MacKevett, 1972; MacKevett and Smith, 1972; Miles et al., 2021). Because we have no a priori knowledge of the pattern or magnitude of C, porosity, and rock density we ran 13 additional inversions in which 1) C increases downglacier linearly through the swath profile by factors of 2, 10, 100, and 1,000; 2) C decreases linearly downglacier through the swath profile by factors of 0.5, 0.1, 0.01, and 0.001; 3) porosity varies between 0.1 and 0.4; 4) rock density varies between 2000 and 2,700 kg m^{-3}; and 5) use the remotely sensed debris pattern of Rounce et al. (2021) instead of the *in situ* debris thicknesses as the 2011 evaluating dataset (**Supplementary Table S5**). The range of increase in near-surface C downglacier explored (up to 3 orders of magnitude) is comparable to the increase documented downglacier on Khumbu Glacier (Miles et al., 2021).

After we used **Eq. 10** to calculate 2011 debris thickness patterns for each of the 1991 debris pattern guesses and value of C, we evaluated the calculated 2011 debris thickness patterns against the measured *in situ* debris pattern from 2011 using the RMSE. A single best 1991 debris thickness pattern and englacial debris concentration was identified for each of the 14 inversions. Because the contributions of englacial melt out and ice dynamics were also calculated while solving **Eq. 10** we were also able to explore the role of each in controlling debris thickness change in time.

Melt Hotspots and Surface Relief

Melt hotspots are associated with surface features like ice cliffs, surface streams, and surface ponds which locally enhance melt and thinning. We used the delineated ice cliff extents from Anderson et al. (2021), who used an Adaptive Binary Threshold method applied to a 0.5 m resolution WV satellite image (from July 13, 2009; **Supplementary Table S4**).

Supraglacial Streams

Streams paths on the glacier surface were delineated using the GRASS GIS command *r.stream.extract* and a fall 2013 DEM with a 2 m spatial resolution (Porter et al., 2018; **Supplementary Table S1**). Because of the complex topography on the glacier surface, and observations of many undercut streams the filling of depressions less than 16 m^2 was required to produce viable stream paths on the glacier surface. Stream sinuosity S was then calculated along individual stream paths using TopoToolbox 2 (Schwanghart and Scherler, 2014) and the equation:

$$S = \frac{L_{channel}}{L_{straight}} \tag{11}$$

where $L_{channel}$ is the length of the channel and $L_{straight}$ is the straight-line distance downstream. An S value of 1 represents a straight stream. The higher the value of S the more sinuous the stream. Each sinuosity value was calculated over a reach of 400 m. Uncertainties in surface stream sinuosity are estimated by varying the 400 m reach by ±100 m. Because sinuosity values at either end of a stream segment are biased due to the lack of a downstream reach, stream sinuosities were not plotted or analyzed for the upper and lower 200 m of each stream. Streams at the glacier

margin were removed from the sinuosity calculations. In order to identify where streams are present at the glacier margin, we digitized their paths in QGIS using the 2009 WV image.

Supraglacial Ponds

Pond coverage was determined for two time periods. Pond extent was hand digitized from a United States Geological Survey (USGS) 1957 aerial photo and the 2009 WV image in QGIS. Ponds were searched for using a fixed grid to ensure complete coverage of the study area. Depressions on the glacier surface with exposed ice and/or ice-cut shorelines were digitized and assumed to be drained ponds.

Glacier Surface Relief

The topography of debris-covered glacier surfaces can vary widely over ten- to hundred-meter scales (Iwata et al., 1980). Relief is the difference in elevation between the highest and lowest point within a given area. In order to assess how finer scale topography has changed through time on Kennicott Glacier we estimated glacier surface relief at 50 m resolution using the Raster Terrain Analysis Plugin in QGIS for three DEMs. We measured maximum surface relief within each band of the swath profile for the 1957 (shown in the **Supplementary Figures**), as well as the fall 2013 and fall 2016 DEMs. Uncertainties in the DEMs are presented in **Supplementary Table S1**. Because the 1957 USGS DEM has an original resolution of 60 × 30 m we chose an intermediate resolution of 50 m over which to calculate glacier surface relief.

We also measured maximum relief of 60 ice cliffs in the summer of 2011 using a laser rangefinder (see Anderson et al., 2021 for locations). Uncertainty in these estimates arises from not targeting the actual location of lowest elevation at the base of the ice cliff. To reduce uncertainty five measurements were taken from possible lowest points at each ice cliff and the maximum value is reported. Error in these estimates is unlikely to exceed 1 m.

Correlation Between Variables

To guide the analysis relating ice dynamics, debris, and melt hotspots variables from a single snapshot in time (**Figure 2**), we cross-correlated 18 of the variables described above. Each variable represents the 1 km wide swath profile except for pond coverage, surface mass balance, and ice emergence which represent the full width of the glacier. The Pearson linear correlation coefficient was calculated between all variables. To explore the processes controlling the thinning pattern on Kennicott Glacier over several decades we cross-correlated each term of **Eq. 1** (thinning, annual mass balance, and ice emergence) for the modern glacier and as the terms changed between 1991 between and 2015 (**Figure 3**). All terms from **Eq. 1** represent the full width of the glacier following the discretization described in *Ice Emergence Rates* and *(Annual) Mass Balance*.

RESULTS

Glacier Thickness Distribution and Change in Time

Our bed elevation estimates show that the glacier thickens upvalley from the terminus (**Figure 2**). A transverse ridge in the bed topography is predicted just upstream from the zone of maximum thinning (ZMT) under the surface topographic bulge (at ~4 km in **Figure 2G**). Upglacier from the ridge, the bed is overdeepened (bed elevations are lower upglacier). The lowest bed elevation predicted within the study area is 150 m a.sl., 7.7 km upglacier from the terminus, where the glacier is estimated to be 550 m thick. A 10% change in the tuned shapefactor results in a 10% change in bed elevation.

Independent of the period examined, glacier thinning is highest in the ZMT (**Figure 3D** and **Supplementary Figure S5**). Surface lowering rates increased towards the present. Between 1957 and 2004 the surface lowering rate was $-1.4\ m\ yr^{-1}$ within the ZMT and between fall 2013 and fall 2016 the surface lowering rate was $-2.2\ m\ yr^{-1}$. Uncertainties for surface lowering rates used in the main text range from ±0.66 to $0.27\ m\ yr^{-1}$ (**Supplementary Table S2**).

Ice Dynamics Terms

Surface velocities decrease downglacier and towards the glacier margin. For the 2015 (1991) surface velocities, maximum annual surface velocities of 75 (105) $m\ yr^{-1}$ occur in the upper portion of the study area (**Figure 4B** and **Supplementary Figure S9**). The 2015 (1991) surface velocities become indistinguishable from noise 3 (1.8) km upglacier from the terminus.

The terminal region of Kennicott Glacier slowed substantially over the study period, with a ~40 $m\ yr^{-1}$ (~50%) velocity decrease between 1991 and 2015 (**Supplementary Figure S9**). Most of the velocity change occurred between 1991 and 2005, with only minor slowing occurring after this time. The fact that most of the slowing occurred between the early and middle time periods, which are both estimated using L5 imagery, indicates that this is not an artifact of intermission comparison, radiometric range, and spatial resolution of the sensors (Dehecq et al., 2019). Our use of a fixed spatial resolution for input images, restriction to snow-free acquisitions, and the study area being in a wide and low elevation location minimizes potential biases. For L5, velocity uncertainty is on the order of 10–15 $m\ yr^{-1}$, while it is $<3\ m\ yr^{-1}$ for L8 (**Supplementary Table S3**).

Between 1991 and 2015 surface flow directions changed substantially in the middle of the study area (**Figure 4**). Between 1957 and 2009 medial moraine boundaries on the glacier surface were also deformed. The consistent change in shape of these stripes from more linear towards increasingly "S"-shaped in some cases is also reflected in the changes in velocity vectors between 1991 and 2015. Debris on the surface of Kennicott Glacier expanded between 1957 and 2009 following these changes in ice flow direction.

Surface strain rates are highest (flow is more compressive) just above the ZMT in both 1991 and 2015 and decline towards the present across the study area (**Supplementary Figures S12, S19**). For the ice-free error check area totaling 4.05 km^2 adjacent to the terminus, where strain rates are zero, strain rate uncertainties are $\pm 0.0017\ yr^{-1}$ for the 1991 field and $\pm 0.0006\ yr^{-1}$ for the 2015 velocity field.

Averaged across the full glacier width, ice emergence rate estimates are highest at the upglacier end of the study area for both velocity fields and below $1\ m\ yr^{-1}$ below the ZMT (**Figures**

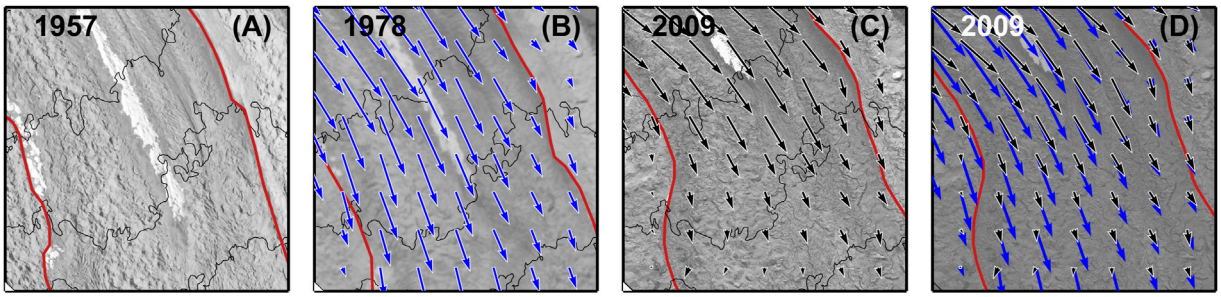

FIGURE 4 | Changes in debris extent. Each panel reflects the same 3 × 3 km area on the glacier surface (see **Figure 6**). Red lines in each panel represent the border between the same medial moraines. Note the distinct change in medial moraine boundaries through time, especially between 1978 and 2009. **(A)** 1957 aerial photo. **(B)** 1978 aerial photo with annual surface velocity vectors from 1991. The largest vector at the top of the panel has a magnitude of 105 m yr^{-1}. **(C)** 2009 WorldView image with annual surface velocity vectors from 2015. The largest vector at the top of the panel has a magnitude of 75 m yr^{-1}. Flow is compressive where debris extent has expanded. **(D)** 2009 WorldView image, with darker shade, overlaid with annual surface velocity vectors from 2015, in black with white outlines, and the annual surface velocity vectors from 1991 in blue.

2C, **3C**). Ice emergence rates declined throughout the study area from 1991 to 2015, most within the ZMT (2.4 m yr^{-1}) and within 2 km upglacier of the ZMT (1.95 m yr^{-1}). Ice emergence rates changed least below the ZMT and at the upglacier end of the study area. Uncertainties (±3 St. dev.) scale with the magnitude of the emergence rate and range from 1 to 9 m yr^{-1}. While there are significant uncertainties in the estimates of ice emergence rate, ice emergence rate is the dominant control on thinning in the ZMT for all sensitivity tests (**Supplementary Figures S13–S18**).

Annual Mass Balance

Annual surface mass balance appears to have increased from 1991 to 2015, suggesting that melt rates decreased towards the present in the study area (**Figures 3B,E**). The largest estimated reduction in annual melt rates occurred in the ZMT (+2.1 m yr^{-1}) and in an area of the glacier just upglacier from the ZMT (+1.8 m yr^{-1}). While there are significant uncertainties in the estimates of annual mass balance, the reduction in melt rate between 1991 and 2015 is present in all sensitivity tests (**Supplementary Figures S13–S18**).

Inversion to Estimate Debris Thickness Change and Englacial Debris Concentration

Figure 5 shows an estimate of how debris thickness changed in time in the study area assuming uniform englacial debris concentrations. Panels B and C show the change in debris thickness from 1991 to 2011. Panels B and C also show the absolute and relative roles of ice dynamics and debris melt out in changing debris thickness. In all 14 inversions, debris melt out occurs across the study area and decreases downglacier. This occurs because ice is melting across the study area and area-averaged melt rates decline downglacier. Ice dynamics thickens debris within and below the ZMT and tends to thin debris above the ZMT. This dynamical effect is present in all inversion scenarios and is the result of the measured patterns of surface velocity and strain rate.

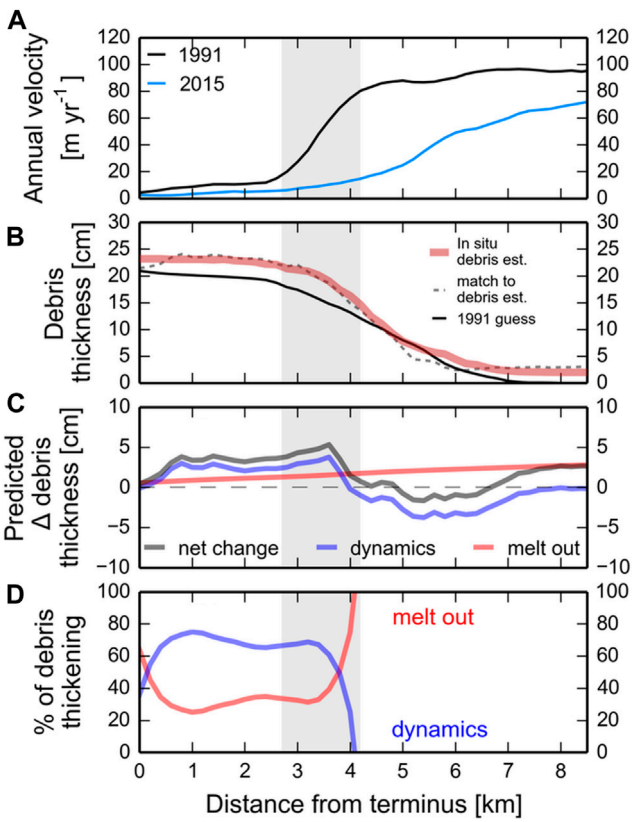

FIGURE 5 | The debris feedback expressed on the surface of Kennicott Glacier. For all panels the zone of maximum thinning (ZMT) is shown in grey. **(A)** Annual surface velocities from 1991 to 2015 from the swath profile. **(B)** *In situ* debris thickness from 2011. The best estimate of the debris pattern in 1991 is shown as well as the simulated debris thicknesses in 2011 produced from the inversion assuming a uniform englacial debris concentration. **(C)** Predicted absolute change in debris thickness from 1991 to 2011 due to dynamics and debris melt out. **(D)** The relative role of ice dynamics and debris melt out in debris thickness change. Above the ZMT debris melt out accounts for 100% of the debris thickening because flow is high and ice dynamics tends to thin debris by advection there.

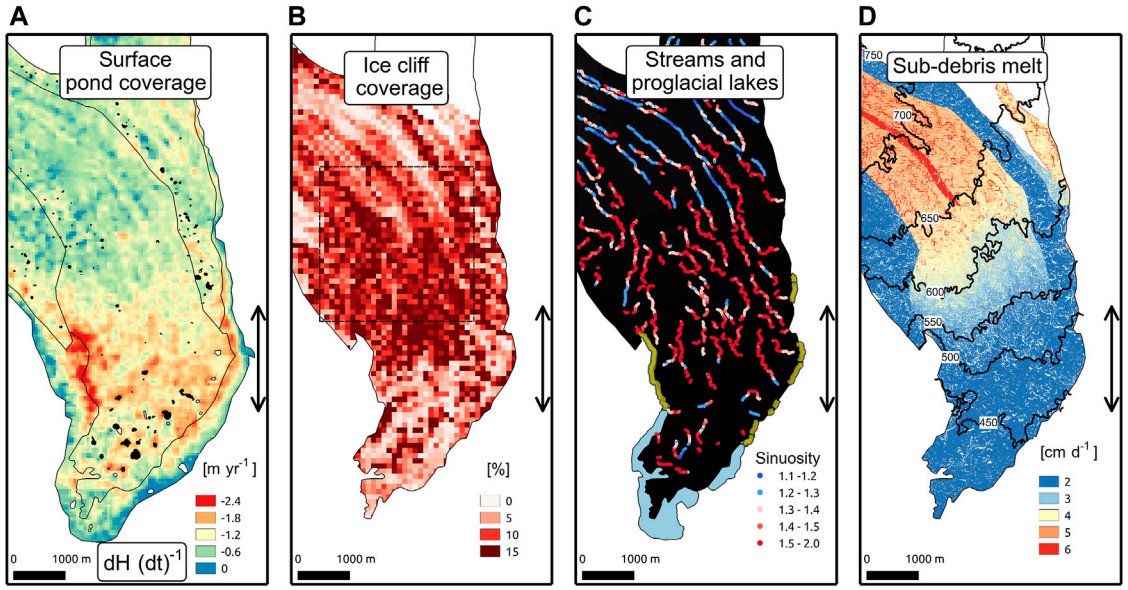

FIGURE 6 | Comparison of thinning, melt hotspots, and melt in map view. The double headed arrows indicate the extent of the zone of maximum thinning (ZMT). **(A)** Glacier surface elevation change between 1957 and 2004 and observed surface pond extent in 1957 (white) and 2009 (black). The 1957 glacier extent is shown by the extent of the thinning map. The 2015 glacier outline is shown in black, as is the boundary between the central 5 medial moraines (compare with panel D). **(B)** Ice cliff coverage in fractional area ×100 (percent) from Anderson et al. (2021) with a 100 m grid. The black box shows the extent of each panel in **Figure 4**. **(C)** Supraglacial stream extent and sinuosity across the study area. Ice marginal streams digitized from the 2009 WorldView image are shown as yellow lines. The proglacial lake in 2009 is shown in blue. **(D)** Sub-debris melt estimates from the summer of 2011 (Anderson et al., 2021). Contours are derived from a 2015 DEM.

The mean of all inversions for the average englacial debris concentration across the study area was 0.017% by volume with a standard deviation of 0.0076% (**Supplementary Table S5**). The maximum average englacial debris concentration from a single inversion run was 0.033% and the minimum was 0.007%. The estimated mean concentrations are comparable with previous near-surface measurements from other glaciers (e.g., Bozhinskiy et al., 1986; Miles et al., 2021). All 14 inversions for surface debris thickness change between 1991 and 2011 indicated that on average debris thickened in the study area. Almost all estimates indicated that debris thickened most in and downglacier from the ZMT (**Supplementary Figure S20**) where both dynamics and debris melt out contribute to debris thickening.

Melt Hotspots, Surface Slope, and Surface Relief

Area-averaged surface slopes declined below the ZMT and tended to increase in the upper portion of the ZMT and 1 km above the ZMT (**Supplementary Figure S21**). Modern maximum glacier surface relief is highest in the ZMT, remains high downglacier towards the terminus and decreases upglacier from the ZMT (**Figure 2E**). The location of maximum glacier surface relief was near the toe in 1957 and shifted into the ZMT towards the present (**Supplementary Figure S22**). In and above the ZMT maximum relief increased from 1957 to 2016. Uncertainties in the DEMs used to calculate relief range from 15 m for the 1957 DEM to less than 3 m for the ArcticDEMs (**Supplementary Table S1**).

Stream paths are longer above the ZMT than below the ZMT (**Figure 6C**). Stream sinuosity is low in the upper portion of the study area and increases downglacier until the middle of the *ZMT* (**Figures 2D**, **6C**). Streams tend to be less sinuous in the upper portion of the study area and become increasingly sinuous until the middle of the zone of maximum thinning. Field investigations in the summer of 2011 and digitization of streams on the glacier surface using the WV images suggest that streams are limited on the glacier surface below the upper portion of the ZMT (**Supplementary Figure S23**). At the transition between these domains in the middle of the ZMT the largest supraglacial streams descend into a series of moulins or flow off glacier (Anderson, 2014). A 10% change in the distance over which sinuosity is calculated changes the mean sinuosity across the study area by 2.2%.

Surface pond area is largest below the ZMT (**Figure 6A** and **Supplementary Figure S22**). Based on the 2009 WV image ponds are most abundant 1 km upglacier from the terminus and occupied about 5% of the glacier surface. Uncertainty in 2009 pond area, based on digitization by an independent operator, is ±1% of the glacier surface. Digitized 1957 pond extents show that ponds were largely present near the terminus with a maximum of about 5.5% of the glacier surface near the terminus. Uncertainty in 1957 pond area, based on digitization by an independent operator, is ±2% of the glacier surface. Pond coverage increased from 1957 to 2009 (**Figures 3D**, **6A**). Upglacier from the ZMT ponds are only abundant in medial moraines near the glacier margin, where debris tends to be thicker and ice flow slower than near the glacier center.

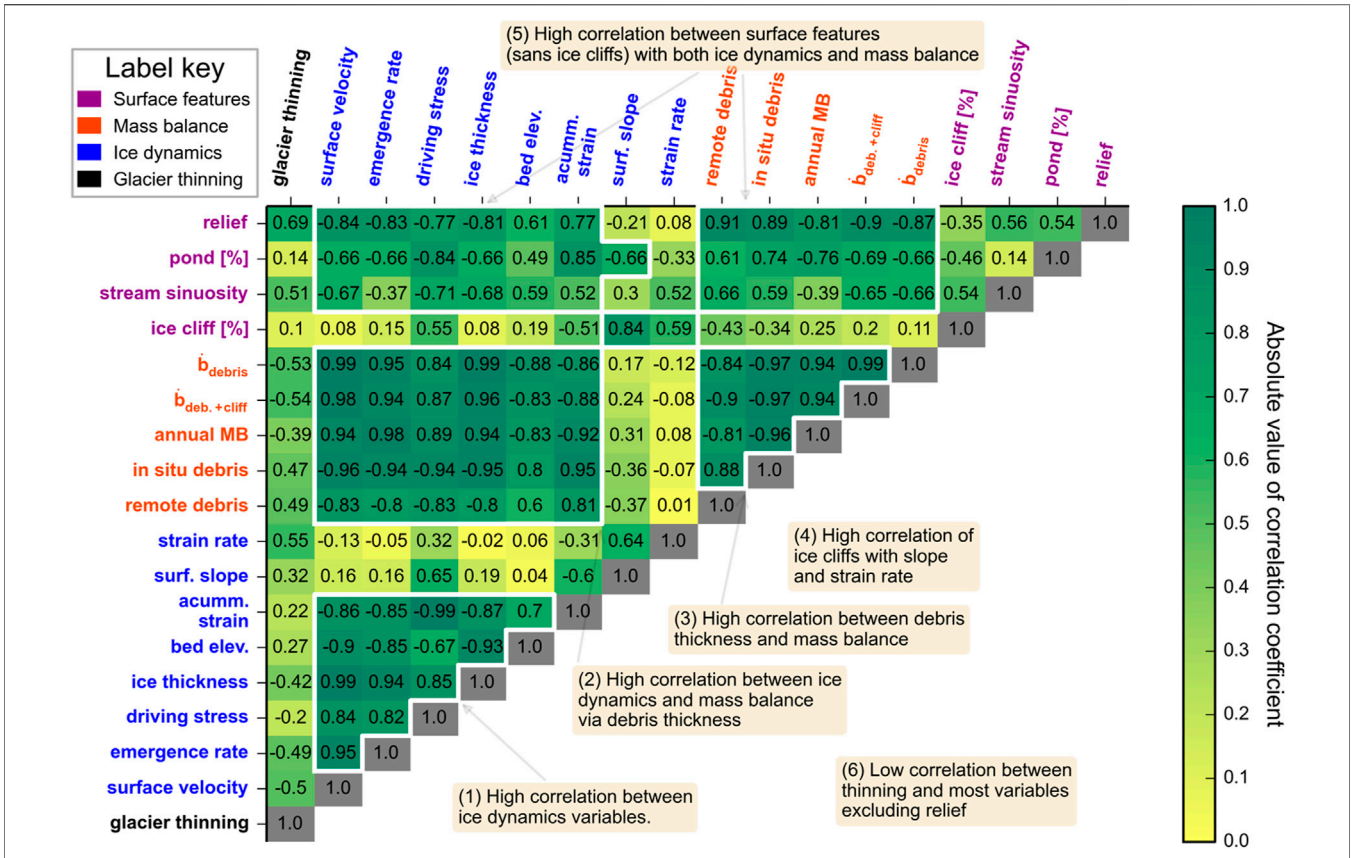

FIGURE 7 | Correlations from the modern snapshot. All datasets are derived from between 2011 and 2016. Correlations between all 18 variables are contained in this matrix. The green-yellow color bar shows the magnitude of correlation. The sign of correlation can be read from the black labels in each cell. Cells with high magnitude of correlation are outlined in white and described with annotations on the figure. The numbers in the annotations follow the chain of process links presented in the discussion. Relief for example can be correlated with all other properties by starting at the upper left and looking across the row to the relief label in the upper right. Pond (%) can be correlated with all other variables by starting with the upper left label and continuing across the row until the last cell and then looking vertically to see the correlation between pond (%) and relief. Note that increased thinning is represented by positive numbers in this figure. This contrasts with **Figure 8** where more negative surface elevation change is equivalent to more positive thinning.

Correlation Between Variables

Figure 7 shows the cross-correlation matrix for the modern snapshot. Ice dynamics variables show strong correlations with one another. Surface velocity and ice thickness are highly correlated with ice emergence rate (r = 0.99 and 0.95). Variations in ice thickness are highly correlated with bed elevation (r = −0.93) and therefore bed elevation is also strongly associated with the other ice dynamics variables.

Surface slope and strain rate are generally only weakly correlated with other dynamical terms. The surface slope plays a role in setting the ice dynamical terms through Glen's flow law, but its role is secondary to ice thickness, especially for low sloped glaciers like the Kennicott. The strain rate is determined by the gradient in surface velocity terms and therefore does not correlate with most other ice dynamics variables, which are more closely linked to velocity at a single point.

The ice dynamical terms have high magnitudes of correlation with the annual mass balance estimates from 2015 and the independent summer 2011 melt rate estimates from Anderson et al. (2021). The magnitude of correlation between ice dynamical terms and *in situ* debris thickness are all higher than 0.8. The cumulative sum of compression is highly correlated with debris thickness (r = 0.95). Debris thickness patterns on Kennicott Glacier follow the inverse of surface velocity (r = −0.94). *In situ* debris thickness is highly correlated with all mass balance estimates ($\|r\| > 0.96$).

The relief of the glacier surface is linked to *in situ* debris thickness and mass balance ($\|r\|$ greater than at least 0.81). Relief is also highly correlated with ice dynamical terms. Relief is the variable most highly correlated with glacier thinning (r = 0.69). Ice cliffs correlate highly with surface strain rates and slope (r = 0.59 and 0.84 respectively; **Supplementary Figures S19, S21**). On Kennicott Glacier, 2009 surface ponds are more abundant below the ZMT and are most strongly correlated with driving stress (r = −0.84; **Supplementary Figure S22**) and surface slope (r = −0.66).

Figure 8 is the cross-correlation matrix for glacier change over multiple decades. See **Figure 3** for the signs of individual terms in **Figure 8**. Glacier surface elevation change (1957–2016) and its change in time (1957–2004 minus 2013–2016) are both highly positively correlated (red) with the decline in ice emergence rate

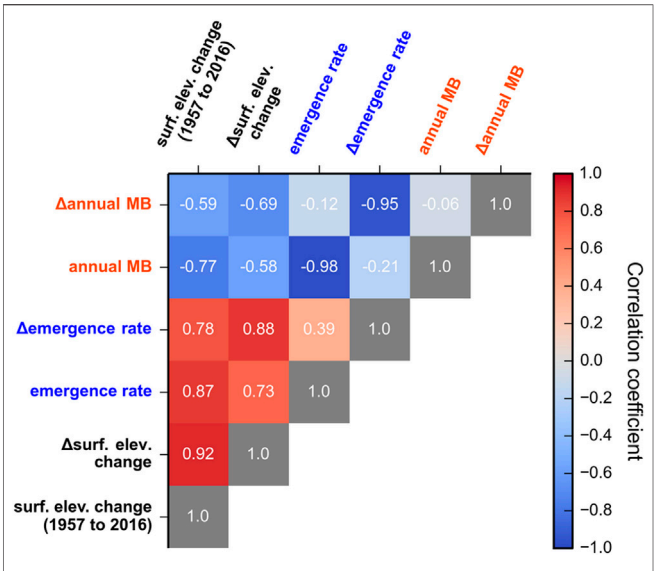

FIGURE 8 | Correlations between ice continuity terms as they change over multiple decades. Correlations between all terms in the continuity equation can be read from the matrix. As an example: A high positive correlation (red) between surface elevation change and Δemergence rate indicates that the negative surface elevation change from 1991 to 2015 is positively correlated with the negative decline in ice emergence rate in time. See **Figure 3** for the patterns and signs of each term in this figure.

in time. In other words where thinning was highest the reduction in emergence rate was also highest and where the change in thinning was highest the decline in emergence rates in time was also highest. In contrast surface elevation change and its change in time are negatively correlated with annual mass balance and its change in time. This means that where melt is high thinning tends to be low and where thinning has increased in time melt rates have decreased in time.

DISCUSSION

In the discussion we build a chain of process links evident on the modern surface of Kennicott Glacier starting from the glacier bed. We use the correlation coefficients presented in *Correlation Between Variables* and **Figure 7** to help identify processes links for the modern snapshot. Next, we delve into how these process links change over several decades including feedbacks related to changes in the terms of **Eq. 1** in *Processes Controlling Glacier Change Over Multiple Decades*.

Chain of Process Links From the Modern Snapshot

Expression of the Glacier Bed in Surface Velocity

The bed pattern explains the pattern of ice dynamics apparent across the study area. Based on Glen's flow law, glacier surface velocity varies with ice thickness to the power of 4 and surface slope to the power of 3 (**Equation 4**; e.g., Hooke, 1998). The topographic bulge on the glacier surface near the upglacier end of the ZMT likely exists due to a rise in the glacier bed beneath it. Because the glacier thins here, it must steepen to pass the same ice discharge coming from the thick ice upstream. Further geophysical surveys are needed to confirm this inference.

Surface Velocity Controls Debris Thickness and Mass Balance

Surface velocity is an important control on debris thickness patterns (**Figure 5**). Within and below the zone of maximum thinning, ice dynamics and debris melt out both tend to thicken debris. Because surface speeds are low here downglacier translation of thin debris is also low allowing debris compression to thicken debris locally. Above the ZMT ice dynamics tends to thin debris while debris melt out tends to thicken debris. High surface speeds translate debris downglacier rapidly (**Figure 5**). In other words, within a given pixel thin debris is translated from upglacier leading at an apparent thinning of debris. This dynamic thinning effect is compensated for by the rapid melt out of debris from within the glacier (**Figure 5C**).

We can expect these same general patterns on other debris covered glaciers: where velocities are high debris thicknesses will tend to be low, where velocities are low debris thickness will tend to be high. The results from Kennicott Glacier bolster the theoretical arguments laid out first by Kirkbride (2000) and later supported and expanded upon by Anderson and Anderson (2018).

The control of surface velocities on debris thickness means that area-average melt rates are also highly correlated with surface velocity and ice emergence rates. The high correlation between annual mass balance and ice emergence rate is expected because they compensate for one another *via* feedbacks between surface slope and ice thickness as is also the case for glaciers unperturbed by debris (e.g., Hooke, 1998). The co-evolution of ice dynamics and surface melt is a result of inevitable physical relationships (see **Eq. 3**) for debris-covered glaciers and should therefore be observed generally.

Thin Debris and Dynamic Thinning Control Surface Relief

Glacier surface relief correlates highly with most variables in **Figure 7**. Process controls on relief assuredly vary in space, depending on location relative to the ZMT and whether flow is rapid or slow. Where flow is high, surface roughness is linked to area-averaged debris thickness as differences in local melt rate help produce surface topography (e.g., Anderson, 2000; Moore, 2018). Because of the hyperbolic shape of Østrem's curve, where area-averaged debris thicknesses are low, small differences in debris thickness produce large differences in local melt rate that rapidly increase local surface relief. The glacier surface acts like a conveyor belt, so it follows that relief cumulatively increases downglacier above the ZMT. The further down glacier the longer differential melt has acted to increase local relief. Streams are expected to increase relief production above the ZMT as discussed in *Ice Cliff-Stream-Relief Feedback*.

Below the ZMT, where flow is low and debris is generally thick, small differences in debris thickness do not produce significant differences in melt rate, limiting relief production. Below the ZMT, tunnel collapse has an important role in relief production

(e.g., Benn et al., 2017). Interestingly, across the study area, glacier thinning is most highly correlated with surface relief. Because dynamic glacier thinning directly changes glacier surface elevations (*via* the decline in emergence rates in time) it follows that surface relief should correlate with thinning.

Debris Thickness and Ice Dynamics Control Melt Hotspots

Melt hotspots have distinctive patterns on the surface of Kennicott Glacier. A number of processes connect debris and ice dynamics with ice cliffs, streams, ponds, and relief which we describe below.

Ice Cliffs are Abundant Where Compression and Surface Slopes are High

Ice cliffs are most abundant where surface compression is high on Kennicott Glacier. A correlation between strain rate and ice cliffs also occurs on glaciers in the Himalaya (Benn et al., 2012; Kraaijenbrink et al., 2016; **Supplementary Figure S19**). But to date no clear process connecting surface compression and ice cliff coverage has been identified. One way in which surface compression could increase ice cliff abundance is if debris compression is manifested in a non-uniform fashion and localized in shear bands. This would lead to the increase of local debris thicknesses in some areas and not others, therefore allowing for differential melt, local surface slope steepening, and ice cliff formation.

An assessment of local patterns of ice emergence rate (surface uplift) is also needed to determine if dynamic steepening and ice cliff abundance correlate. Short-lived high-compression events may also play a role on Kennicott Glacier. The annual summer flood of Hidden Creek Lake produces a period of very rapid sliding (e.g., Bartholomaus et al., 2008), translating the entire ice column down glacier leading to high strain rates exactly where ice cliffs are abundant. Perhaps the shaking of the glacier surface during the summer flood encourages debris failure and cliff formation?

Ice cliffs on Kennicott Glacier are positively correlated with surface slope (**Supplementary Figure S21**). Where area-averaged surface slopes are high debris failure is more likely. Steep debris-covered slopes on the glacier surface, present due to differential melt, can be steepened even further as they are passively transported into areas with steep area-averaged slopes. This steepening effect would tend to encourage ice cliff formation and persistence. But on Kennicott Glacier area-averaged slopes tend to be low (<0.06) implying that this effect is minor. Ultimately the physical explanations for an area-average slope control on ice cliff abundance at Kennicott Glacier are less viable than the strain rate controls outlined in the paragraph above. For this reason, we assume that strain rate is the primary control on ice cliff abundance as it changes in time on Kennicott Glacier.

On less dynamic portions of debris-covered glaciers, with thick debris, thermal erosion from surface ponds can be the dominant control on ice cliff distribution (e.g., Röhl, 2008). This is not the case for most ice cliffs on Kennicott Glacier where ice cliffs and ponds are negatively correlated with one another. On debris-covered glaciers, the processes that control ice cliff distribution above the ZMT (e.g., compression) may in fact be different below the ZMT (e.g., tunnel collapse and ponds).

Stream Sinuosity Varies With Roughness and Surface Slope

Estimated stream sinuosity increases downglacier with glacier surface relief (**Figure 2D**). At the upper end of the study area troughs between medial moraines are more linear and stream sinuosity is low. As the medial moraines coalesce downglacier the troughs are occupied by increasingly chaotic topography just as streams become more sinuous. Supraglacial streams on uncovered glaciers tend to be more sinuous where slopes are steep and water discharge is high (Ferguson, 1973); observations that also appear to apply within the debris cover of Kennicott Glacier. Without further field investigations into the dynamics of supraglacial streams, it is hard to discern the degree to which rough surface topography or the physics of supraglacial stream flow itself controls stream sinuosity on debris-covered ice.

Ice Cliff-Stream-Relief Feedback

A positive feedback between ice cliffs, surface streams, and surface relief occurs on Kennicott Glacier. Streams and ice cliffs should amplify the occurrence of each other: melt from ice cliffs increases stream flow and streams maintain ice cliffs by undercutting them. Undercutting streams can create gaps between ice cliffs and the debris-covered surface below *via* thermal erosion (Reid and Brock, 2010; **Supplementary Figure S24**). This prevents ice cliff burial while still allowing debris, that trundles down the ice cliff, to accumulate across the stream.

Importantly, stream undercutting is enhanced where streams are more sinuous (Parker, 1975). As a result, the arc-shaped meander bends of streams help maintain arc-shaped ice cliffs (**Supplementary Figure S24**). The arc-shaped ice cliffs focus trundling debris into a smaller area, locally increasing debris thickness and increasing debris thickness variability in space. *Via* differential melt, local surface topography will grow in time, which can produce additional ice cliffs and increase stream sinuosity by roughening the glacier surface, therefore completing the positive feedback loop.

It is likely that this feedback will apply on other glaciers where 1) area-average debris is relatively thin (less than 20 cm), so relatively high melt rates can increase stream flow and 2) surface strain rates and slopes are high increasing ice cliff abundance. Sato et al. (2021) found a correspondence between drainage patterns and ice cliff occurrence on the more heavily debris covered Trakarding Glacier in the Nepalese Himalaya. The thicker the debris the less likely streams are to undercut ice cliffs precluding the occurrence of this feedback on heavily debris-covered portions of glaciers. Because study of the stream-ice cliff feedback is just beginning, we do not discuss it as a control on the thinning of Kennicott Glacier over multiple decades below.

Driving Stress and Ponds

On Kennicott Glacier, surface ponds are strongly negatively correlated with driving stress which is dependent on both ice thickness and surface slope (**Eq. 5**; **Supplementary Figure 22**). Ponds also occur where surface slopes are low on Kennicott Glacier, but the correlation magnitude is lower than for driving stress. A number of previous studies identified correlations between pond occurrence and low surface slopes in the Himalaya (e.g., Reynolds, 2000; Quincey et al., 2007; Sakai and

Fujita, 2010; Scherler et al., 2011; Benn et al., 2012). Driving stress could be used to predict the future expansion of ponds as it eliminates false predictions where glacier surfaces are low sloped but still fast flowing.

Summary of Process Links From the Modern Snapshot

Within the debris-covered tongue of Kennicott Glacier the bed appears to be a strong control on the pattern of ice velocity, which in turn controls the pattern of debris thickness, mass balance, and ice emergence rate. Controls on surface relief are different above and below the ZMT. The pattern of dynamic thinning is an expected control on the pattern of surface relief. Ice cliff abundance appears to best follow surface strain rate. Supraglacial stream sinuosity increases with surface roughness. The interaction between ice cliffs, sinuous streams, and relief can form a positive feedback loop in which all three are amplified. Supraglacial ponds are abundant where driving stresses are low.

Processes Controlling Glacier Change Over Multiple Decades

Primary Control of Thinning: Ice Emergence Rates Declined Strongly in the ZMT

The decline in emergence rates is the primary control on the rapid thinning under thick debris at Kennicott Glacier (**Figures 3E**, **8**). Increased mass loss upglacier of the debris cover has led to the reduction of ice flow into the debris-covered portion of the glacier reducing ice emergence rates and increasing thinning in time. Vincent et al. (2016) and Brun et al. (2018) made similar observations for the debris covered Changri Nup Glacier in Nepal. Using simple numerical glacier models and linear bed profiles, Banerjee (2017) and Ferguson and Vieli (2020) both concluded that rapid thinning under debris cover is primarily the result of the decline in ice emergence rates in time. Simulations from Crump et al. (2017) and Anderson et al. (2018) also support this conclusion. Because ice dynamics plays the primary role in controlling the location of the maximum thinning of uncovered glaciers (Nye, 1960) we should expect that it also plays a vital if not dominant role for debris-covered glaciers as well.

Melt Decreased in Time

Annual melt rates across the study area declined between 1991 and 2015 (**Figure 3E**). This occurred as positive degree-days at Kennicott Glacier increased by 8% specifically between the 1990–1991 and 2014–2015 image acquisition time periods (**Table 1**; **Supplementary Figure S25**). Within the ZMT, annual melt rates decreased by 51% between the years 1991 and 2015. This implies that the relationship between air temperature and area-averaged melt changed, for example by changes in debris thickness or ice cliff coverage.

We describe four additional feedbacks directly linking debris thickness, ice cliffs, ponds, and glacier surface roughness to thinning (**Table 1**; **Figures 9**, **10**). These feedbacks are likely to combine to explain the decrease in melt rate across the study area between 1991 and 2015. Note that we consider the pond and relief feedbacks over a longer period (1957–2009 and 1957–2016 respectively). The two negative feedbacks (the debris and ice cliff) most likely caused the reduction in melt rates in time.

Debris Feedback (Negative Feedback)

As Kennicott Glacier thinned surface velocity declined leading to debris thickening and expansion (*Surface Velocity Controls Debris Thickness and Mass Balance*), feeding back to affect thinning by reducing melt rates. Debris thickening is due to the combined effects of slowing downglacier translation of debris, continued compression of debris and the melt out of debris from within the glacier (**Figure 5**). The reduction in surface velocity (in time) reduces the downstream translation of debris in a given pixel. Because debris is moving out of the given pixel at a slower rate, the reduction of velocity downglacier (in space), which compresses the debris, is locally able to increase debris thickness. Increases in melt rates leading to enhanced debris melt out also thicken debris on debris-covered glaciers (e.g., Deline, 2005; Kirkbride and Deline, 2013). The greatest debris thickening occurs in and below the ZMT where dynamics and melt out both thicken debris. Debris expanded in the upper portion of the study area due to changing surface velocity directions, also contributing to the decrease in melt rates.

Surface velocities typically decline as glaciers thin (e.g., Quincey et al., 2009; Neckel et al., 2017; Dehecq et al., 2019). Changes in surface velocity may be an underappreciated explanation for debris thickening and expansion on debris-covered glaciers more generally (e.g., Kirkbride, 1993; Deline, 2005; Kirkbride and Deline, 2013; Gibson et al., 2017; Azzoni et al., 2018; Stewart et al., 2021). We expect that the debris feedback generally reduces melt rates in time and is occurring on most debris-covered glaciers.

Ice Cliff Feedback (Negative Feedback)

The ice cliff feedback occurs when glacier thinning leads to reduced surface compression which reduces ice cliff occurrence and therefore area-averaged melt rates, looping back to affect the thinning pattern (**Supplementary Figure S19**). The negative thinning-ice cliff feedback will occur on other glaciers where strain rates are correlated with ice cliff abundance, which will most likely occur where flow is active above the ZMT on other glaciers.

Perhaps the evolution of ice cliffs, and their effect on area-averaged melt rates in time, on individual glaciers will depend on whether ice cliff abundance is controlled predominantly by changes in strain rate (more likely above the ZMT) or by the expansion of tunnel collapse-related depressions and ponds (more likely below the ZMT). Steiner et al. (2019) found no clear trend in ice cliff area over a 41-year period across five glaciers in the Nepalese Himalaya, but most of these ice cliffs are associated with depressions on the glacier surface and not surface compression.

Ferguson and Vieli (2020) used driving stress as a proxy for ice cliff change in time. This approach will be most applicable below the ZMT where debris is thick and surface depressions dominate ice cliff occurrence. Above the ZMT their approach asserts a monotonically declining abundance of ice cliffs upglacier, which is inconsistent with Watson et al. (2016)'s analysis of 14 glaciers in the Khumbu region of Nepal and Kennicott Glacier were ice cliff occurrence peaks where flow is still active and above the ZMT. Ultimately for Kennicott Glacier

TABLE 1 | Thinning-melt rate feedbacks occurring over multiple decades at Kennicott Glacier.

Feedback	Description of feedback	Sign of feedback	Proxy/ indicator
Debris (thickness and extent)	Glacier thinning leads to velocity changes, debris thickening and expansion[a], which reduces melt and glacier thinning	–	Debris thickness
Ice cliffs (coverage)	Glacier thinning leads to lower surface compression and ice cliff reduction, which decreases melt and glacier thinning	–	Strain rate
Ponds (coverage)	Glacier thinning leads to reduced driving stress, pond expansion, which increases melt and glacier thinning	+	Pond coverage
Relief (surface area)	Glacier thinning leads to the increase in surface relief, which increases the debris-covered area susceptible to melt and glacier thinning	+	Relief
Streams (coverage)	Glacier thinning has an unknown effect on surface stream coverage in time	?	?

[a]*Also increases in debris melt out from within the glacier.*

where most ice cliffs exist above the ZMT we expect the thinning-ice cliff feedback to have reduced melt rates in time as flow became less compressive.

Pond Feedback (Positive Feedback)

The expansion of ponds upglacier in response to thinning represents a positive feedback. Thinning leads to the decrease in surface slopes, ice thickness, and driving stress, below the ZMT, allowing for the upglacier propagation of ponds. Expanding ponds locally increase melt rates, therefore increasing thinning, completing the feedback loop. The feedback between thinning and ponds has also been documented on glaciers in High Mountain Asia (Gardelle et al., 2011; Thakuri et al., 2016; Watson et al., 2016; King et al., 2020), New Zealand (Kirkbride, 1993) and now in Alaska. The expansion of ponds upglacier as debris-covered glaciers thin is therefore likely a phenomenon occurring at the global scale. For Kennicott Glacier we expect that this feedback increased melt rates in time, but not enough to overcome the melt reducing roles of the debris and ice cliff feedbacks.

Relief Feedback (Positive Feedback)

The increase in local surface relief and debris-covered surface area in response to thinning represents a positive feedback (**Figure 9E**). As the glacier thins, englacial tunnel collapse (e.g., Benn et al., 2001), differential melt (e.g., Mölg et al., 2020), and the rapid decline of ice emergence rates lead to the increase in local relief. Other studies have documented the increase in surface relief on glaciers in the Himalaya (Benn et al., 2017; King et al., 2020) and Alps (Mölg et al., 2020). Increasing relief (and local slopes) in time inherently leads to an increase in the total debris-covered area susceptible to melt as a steeper surface exposes more sub-debris ice to melt than a flat surface. When averaged across a planview pixel on the glacier this effect will increase area-average melt rates and thinning, completing the feedback loop. For Kennicott Glacier we expect that this feedback increased melt rates in time, but not enough to overcome the melt-reducing effect of the debris and ice cliff feedbacks.

Implications

This case study of Kennicott Glacier highlights how important ice dynamics are for understanding and predicting debris-covered glacier behavior. It is tempting to overlook ice dynamics where ice flow appears to currently be slow (i.e., below 20 m yr^{-1}), but neglecting it can lead to erroneous interpretations of the causes, for example, of glacier thinning or debris thickening. This is especially true considering that dynamic thinning is the dominant control on the location of maximum glacier-wide thinning for Kennicott Glacier.

The overdeepened and undulating bed under Kennicott Glacier acts as a boundary condition that strongly controls the pattern of ice flow (*Expression of the Glacier Bed in Surface Velocity*). This ice flow pattern in turn determines the distribution of debris thickness and surface melt which feeds back to affect ice flow (Anderson and Anderson, 2016; Anderson and Anderson, 2018), each component working in concert with the others. The basal geometry and slopes under debris-covered glaciers will certainly differ from the pattern inverted for under Kennicott Glacier. None-the-less this study reveals how important it can be to constrain basal topography when attempting to reveal cause and effect in the debris-covered glacier system.

We have highlighted some processes links between ice cliffs, ponds, streams, and local surface relief. Of special note is the potential role of streams as geomorphic and melt agents on debris-covered glaciers. We outlined how meandering, sinuous surface streams can influence ice cliff shape, debris thickness patterns, and local surface topography. Undercutting streams may also encourage the collapse of ice cliffs. Large streams may be effective at removing debris from the glacier surface *via* moulins and crevasses. Quantifying the role of local surface relief, ice cliffs, ponds, and streams in debris-covered glacier surface melt and evolution requires new, detailed field studies.

Out of the four thinning-ice dynamics-mass balance feedbacks discussed (debris, ice cliffs, ponds, and relief), the debris and ice cliff feedbacks appear to combine to cause in the reduction of surface melt rate in time on Kennicott Glacier as the pond and relief feedbacks work in the opposite direction and increase melt in time. Naturally these feedbacks should be

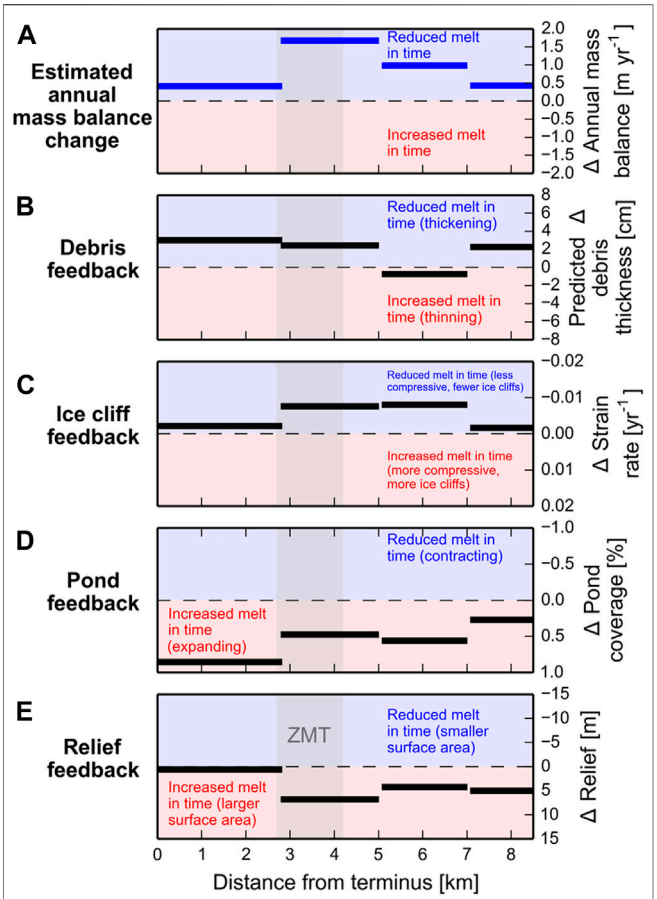

FIGURE 9 | Spatial distributions of terms indicating the sign of feedbacks. The title of each panel is on the left side. In each panel blue shading indicates the area where melt will be reduced in time. Red shading indicates the portion of each panel in which melt will be increased in time. Grey shading indicates the extent of the zone of maximum thinning (ZMT). For **(B–D)** if the black bars are in the blue area the feedback is negative. If the black bars are in the red area the feedback is positive. **(A)** Observed change in annual mass balance showing a reduction of melt in time across the study area (see **Figures 3B,E**). **(B)** Representation of the negative debris feedback using predicted change in debris thickness in time as a proxy. Debris thickens due to changes in surface velocities, strain rate, and melt out leading to a reduction of melt in time. **(C)** Representation of the negative ice cliff feedback using change in surface compression (strain rate) as a proxy. Ice cliffs are positively correlated with strain rate, meaning areas with decreased compression tend to have fewer ice cliffs. Positive values indicate increased compression and negative values decreased compression in time. **(D)** Representation of the positive pond feedback using the change in pond coverage in time as a proxy. **(E)** Representation of the relief feedback. The steepening of local slopes on the glacier increases the total area of ice subject to surface melt within and above the ZMT.

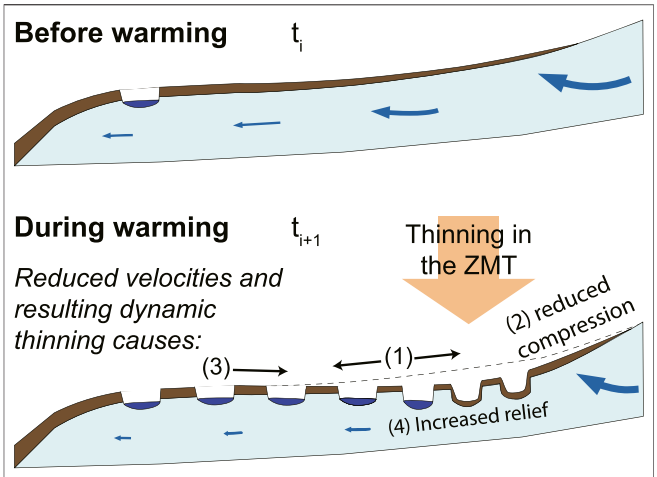

(1) **debris** thickening and expansion via compression, slowing speeds, changing flow directions, and melt out (negative feedback).

(2) **ice cliff** coverage reduction via reduced compression (negative feedback).

(3) **pond** expansion via decline in driving stress (positive feedback).

(4) **relief** and debris-covered area increase via declining emergence rates, differential melt, and tunnel collapse (positive feedback).

FIGURE 10 | Schematic explaining the feedbacks occurring on Kennicott Glacier over multiple decades. At time t_i, the glacier has not yet started to respond to warming. The blue arrows qualitatively reflect englacial flow paths. The length and width of the arrow reflects the flow velocity. At time t_{i+1} the glacier is responding to warming and thinning is localized in the zone of maximum thinning (ZMT). The downglacier portion of the ZMT shallows, while the upglacier portion of the ZMT steepens. Thinning across the glacier leads to reduced compression in time.

quantified on other debris-covered glaciers with different geometries, rock erodibilities, and climates.

CONCLUSION

Kennicott Glacier is a large, thick, and dynamically active Alaskan glacier that supports striking patterns of ice dynamics and melt hotspots on its surface. We use Kennicott Glacier as a test case to reveal causality within the debris-covered glacier system in a step-by-step fashion.

Within the debris-covered tongue of Kennicott Glacier the pattern of ice flow is dominated by an overdeepened bed. This imposed pattern of ice flow in turn strongly controls patterns of both debris thickness and area-averaged melt rate. The annual mass balance gradient in the debris-covered tongue is reversed and melt rates decline towards the terminus.

Ice dynamics are an important control on debris thickness. Surface compression dominates debris thickness where velocities are low; where velocities are high downglacier advection keeps debris thin while also allowing for the efficient melt out of debris. Using an inverse modeling approach, we show that a declining, compressive flow field downglacier from the ZMT thickened debris at a rate of 0.125 cm per year between 1991 and 2011. The mean englacial debris concentration was estimated to be 0.017% by volume. Debris expansion on the glacier surface follows the change in surface velocity direction in time.

Glacier surface relief is largest where dynamic thinning is highest. Ice cliffs correlate with the rate of compression on the

glacier surface. A new feedback is identified on the modern glacier surface leading to chaotic topography: ice cliffs and sinuous streams amplify each other and tend to enhance differential melt, and local surface roughness. Ponds are strongly negatively correlated with driving stress. Despite abundant ice cliffs, ponds, and streams scattered within the debris cover, melt rates averaged across the glacier width are primarily controlled by the melt-reducing effects of debris.

We also explore the consequences of glacier thinning over the last several decades. The zone of glacier-wide maximum thinning (ZMT) has been in a consistent location since at least 1957. Between 1991 and 2015, where the glacier thinned the most, melt rates appear to have contributed less to thinning over time despite generally rising air temperatures. We consider the role of four feedbacks related to decadal changes in melt and thinning: the debris feedback (negative), the ice cliff feedback (negative), the pond feedback (positive), and the relief feedback (positive). Of these four, the melt reducing debris and ice cliff feedbacks appear to cause the observed decline in melt rates in the ZMT. Maximum glacier wide thinning occurs under debris where melt rates are low and contributing less and less to thinning in time.

We provide evidence showing that rapid thinning under thick debris (i.e., the debris-cover anomaly) is predominately caused by dynamic thinning. Ultimately this occurs because increasingly negative mass balance upglacier of the continuous debris cover thins the glacier there and subsequently reduces ice flow, in a compounding fashion, downglacier. The reduced ice flux into the debris-covered tongue causes drastic reductions in ice emergence rates and maximum glacier-wide thinning despite the strong insulating effect of debris on melt rates.

DATA AVAILABILITY STATEMENT

The raw data supporting the conclusions of this article will be made available by the authors, without undue reservation. Data used to produce the correlation figures are available at: DOI: 10.5281/zenodo.4955563.

AUTHOR CONTRIBUTIONS

LA designed the study, composed the manuscript, and completed most analyses. WA produced the annual surface velocities and added important discussion points. RA added important discussion points and provided support throughout the effort. DS aided in the analysis of surface streams. EP added important discussion points. All authors revised the manuscript.

FUNDING

LA acknowledges support from a 2011 Muire Science and Learning Center Fellowship, NSF DGE-1144083 (GRFP), and funding from European Union's Horizon 2020 research and innovation programme under grant agreement No. 851614. LA and DS were also supported by funding from the European Research Council (ERC) under the European Union's Horizon 2020 research and innovation programme under grant agreement No 759639. RA and WA acknowledge support of NSF EAR-1239281 (Boulder Creek CZO) and NSF EAR-1123855. WA acknowledges support from NSF OPP-1821002 and the University of Colorado at Boulder's Earth Lab initiative.

ACKNOWLEDGMENTS

We thank Craig Anderson, Emily Longano, and Oren Leibson for field support. We thank Per Jenssen, Susan Fison, Ben Hudson, Patrick Tomco, Rommel Zulueta, the Wrangell-St. Elias Interpretive Rangers, the Wrangell Mountains Center, Indrani Das, and Ted Scambos (NSIDC) for logistical support and the gracious loan of equipment. We thank Lucy Tyrell for facilitating outreach efforts. We also thank Joshua Scott, Wrangell-St Elias National Park and the Polar Geospatial Center for access to satellite imagery. We thank Martin Truffer, Jack Holt, and Regine Hock for helpful conversations. LA thanks the organizers and participants of the 2010 Glaciological Summer School held in McCarthy, AK, who inspired this work. We appreciate helpful comments from David Rounce and Martin Kirkbride from an earlier version of the manuscript.

SUPPLEMENTARY MATERIAL

The Supplementary Material for this article can be found online at: https://www.frontiersin.org/articles/10.3389/feart.2021.680995/full#supplementary-material

REFERENCES

Amundson, J. M., Truffer, M., and Lüthi, M. P. (2006). Time-dependent Basal Stress Conditions beneath Black Rapids Glacier, Alaska, USA, Inferred from Measurements of Ice Deformation and Surface Motion. *J. Glaciol.* 52, 347–357. doi:10.3189/172756506781828593

Anderson, L. S., and Anderson, R. S. (2018). Debris Thickness Patterns on Debris-Covered Glaciers. *Geomorphology* 311, 1–12. doi:10.1016/j.geomorph.2018.03.014

Anderson, L. S., and Anderson, R. S. (2016). Modeling Debris-Covered Glaciers: Response to Steady Debris Deposition. *Cryosphere* 10, 1105–1124. doi:10.5194/tc-10-1105-2016

Anderson, L. S., Armstrong, W. H., Anderson, R. S., and Buri, P. (2021). Debris Cover and the Thinning of Kennicott Glacier, Alaska: *In Situ* Measurements, Automated Ice Cliff Delineation and Distributed Melt Estimates. *Cryosphere* 15, 265–282. doi:10.5194/tc-15-265-2021

Anderson, L. S. (2014). Glacier Response to Climate Change: Modeling the Effects of Weather and Debris-Cover. Available at: https://scholar.colorado.edu/geol_gradetds/90 (Accessed November 15, 2019).

Anderson, R. S. (2000). A Model of Ablation-Dominated Medial Moraines and the Generation of Debris-Mantled Glacier Snouts. *J. Glaciol.* 46, 459–469. doi:10.3189/172756500781833025

Anderson, R. S., Anderson, L. S., Armstrong, W. H., Rossi, M. W., and Crump, S. E. (2018). Glaciation of alpine Valleys: The Glacier - Debris-Covered

Glacier - Rock Glacier Continuum. *Geomorphology* 311, 127–142. doi:10.1016/j.geomorph.2018.03.015

Anderson, R. S., Walder, J. S., Anderson, S. P., Trabant, D. C., and Fountain, A. G. (2005). The Dynamic Response of Kennicott Glacier, Alaska, USA, to the Hidden Creek Lake Outburst Flood. *Ann. Glaciol.* 40, 237–242. doi:10.3189/172756405781813438

Armstrong, W. H., Anderson, R. S., Allen, J., and Rajaram, H. (2016). Modeling the WorldView-Derived Seasonal Velocity Evolution of Kennicott Glacier, Alaska. *J. Glaciol.* 62, 763–777. doi:10.1017/jog.2016.66

Armstrong, W. H., Anderson, R. S., and Fahnestock, M. A. (2017). Spatial Patterns of Summer Speedup on South Central Alaska Glaciers. *Geophys. Res. Lett.* 44, 9379–9388. doi:10.1002/2017GL074370

Armstrong, W. H., and Anderson, R. S. (2020). Ice-marginal lake Hydrology and the Seasonal Dynamical Evolution of Kennicott Glacier, Alaska. *J. Glaciol.* 66, 699–713. doi:10.1017/jog.2020.41

Azzoni, R. S., Fugazza, D., Zerboni, A., Senese, A., D'Agata, C., Maragno, D., et al. (2018). Evaluating High-Resolution Remote Sensing Data for Reconstructing the Recent Evolution of Supra Glacial Debris. *Prog. Phys. Geogr. Earth Environ.* 42, 3–23. doi:10.1177/0309133317749434

Banerjee, A. (2017). Brief Communication: Thinning of Debris-Covered and Debris-free Glaciers in a Warming Climate. *Cryosphere* 11, 133–138. doi:10.5194/tc-11-133-2017

Bartholomaus, T. C., Anderson, R. S., and Anderson, S. P. (2008). Response of Glacier Basal Motion to Transient Water Storage. *Nat. Geosci.* 1, 33–37. doi:10.1038/ngeo.2007.52

Benn, D. I., Bolch, T., Hands, K., Gulley, J., Luckman, A., Nicholson, L. I., et al. (2012). Response of Debris-Covered Glaciers in the Mount Everest Region to Recent Warming, and Implications for Outburst Flood Hazards. *Earth Sci. Rev.* 114, 156–174. doi:10.1016/j.earscirev.2012.03.008

Benn, D. I., Thompson, S., Gulley, J., Mertes, J., Luckman, A., and Nicholson, L. (2017). Structure and Evolution of the Drainage System of a Himalayan Debris-Covered Glacier, and its Relationship with Patterns of Mass Loss. *Cryosphere* 11, 2247–2264. doi:10.5194/tc-11-2247-2017

Benn, D. I., Wiseman, S., and Hands, K. A. (2001). Growth and Drainage of Supraglacial Lakes on Debris-Mantled Ngozumpa Glacier, Khumbu Himal, Nepal. *J. Glaciol.* 47, 626–638. doi:10.3189/172756501781831729

Bisset, R. R., Dehecq, A., Goldberg, D. N., Huss, M., Bingham, R. G., and Gourmelen, N. (2020). Reversed Surface-Mass-Balance Gradients on Himalayan Debris-Covered Glaciers Inferred from Remote Sensing. *Remote Sensing* 12, 1563. doi:10.3390/rs12101563

Bozhinskiy, A. N., Krass, M. S., and Popovnin, V. V. (1986). Role of Debris Cover in the Thermal Physics of Glaciers. *J. Glaciol.* 32, 255–266. doi:10.3189/s0022143000015598

Brun, F., Wagnon, P., Berthier, E., Shea, J. M., Immerzeel, W. W., Kraaijenbrink, P. D. A., et al. (2018). Ice Cliff Contribution to the Tongue-wide Ablation of Changri Nup Glacier, Nepal, central Himalaya. *Cryosphere* 12, 3439–3457. doi:10.5194/tc-12-3439-2018

Buri, P., Miles, E. S., Steiner, J. F., Ragettli, S., and Pellicciotti, F. (2021). Supraglacial Ice Cliffs Can Substantially Increase the Mass Loss of Debris-Covered Glaciers. *Geophys. Res. Lett.* 48, 1–11. doi:10.1029/2020GL092150

Crump, S. E., Anderson, L. S., Miller, G. H., and Anderson, R. S. (2017). Interpreting Exposure Ages from Ice-Cored Moraines: a Neoglacial Case Study on Baffin Island, Arctic Canada. *J. Quat. Sci.* 32, 1049–1062. doi:10.1002/jqs.2979

Cuffey, K. M., and Paterson, W. S. B. (2010). *The Physics of Glaciers*. 4th ed.. Oxford, UK: Academic Press.

Das, I., Hock, R., Berthier, E., and Lingle, C. S. (2014). 21st-century Increase in Glacier Mass Loss in the Wrangell Mountains, Alaska, USA, from Airborne Laser Altimetry and Satellite Stereo Imagery. *J. Glaciol.* 60, 283–293. doi:10.3189/2014JoG13J119

Dehecq, A., Gourmelen, N., Gardner, A. S., Brun, F., Goldberg, D., Nienow, P. W., et al. (2019). Twenty-first century Glacier Slowdown Driven by Mass Loss in High Mountain Asia. *Nat. Geosci* 12, 22–27. doi:10.1038/s41561-018-0271-9

Deline, P. (2005). Change in Surface Debris Cover on Mont Blanc Massif Glaciers after the'Little Ice Age' Termination. *Holocene* 15, 302–309. doi:10.1191/0959683605hl809rr

Fahnestock, M., Scambos, T., Moon, T., Gardner, A., Haran, T., and Klinger, M. (2016). Rapid Large-Area Mapping of Ice Flow Using Landsat 8. *Remote Sensing Environ.* 185, 84–94. doi:10.1016/j.rse.2015.11.023

Farinotti, D., Huss, M., Fürst, J. J., Landmann, J., Machguth, H., Maussion, F., et al. (2019). A Consensus Estimate for the Ice Thickness Distribution of All Glaciers on Earth. *Nat. Geosci.* 12, 168–173. doi:10.1038/s41561-019-0300-3

Ferguson, J., and Vieli, A. (2020). Modelling Steady States and the Transient Response of Debris-Covered Glaciers. *Cryosphere Discuss.*, 1–31. doi:10.5194/tc-2020-228

Ferguson, R. I. (1973). Sinuosity of Supraglacial Streams. *Geol. Soc. America Bull.* 84, 251. doi:10.1130/0016-7606(1973)84<251:soss>2.0.co;2

Fyffe, C. L., Brock, B. W., Kirkbride, M. P., Mair, D. W. F., Arnold, N. S., Smiraglia, C., et al. (2019). Do debris-covered Glaciers Demonstrate Distinctive Hydrological Behaviour Compared to Clean Glaciers?. *J. Hydrol.* 570, 584–597. doi:10.1016/j.jhydrol.2018.12.069

Gardelle, J., Arnaud, Y., and Berthier, E. (2011). Contrasted Evolution of Glacial Lakes along the Hindu Kush Himalaya Mountain Range between 1990 and 2009. *Glob. Planet. Change* 75, 47–55. doi:10.1016/j.gloplacha.2010.10.003

Gardelle, J., Berthier, E., Arnaud, Y., and Kääb, A. (2013). Region-wide Glacier Mass Balances Over the Pamir-Karakoram-Himalaya During 1999-2011. *The Cryosphere* 7, 1885–1886. doi:10.5194/tc-7-1885-2013

Gardner, A. S., Fahnestock, M. A., and Scambos, T. A. (2020). ITS_LIVE Regional Glacier and Ice Sheet Surface Velocities. Data archived at National Snow and Ice Data Center. doi:10.5067/6II6VW8LLWJ7

Gardner, A. S., Moholdt, G., Scambos, T., Fahnstock, M., Ligtenberg, S., van den Broeke, M., et al. (2018). Increased West Antarctic and Unchanged East Antarctic Ice Discharge over the Last 7 Years. *Cryosphere* 12, 521–547. doi:10.5194/tc-12-521-2018

Gibson, M. J., Glasser, N. F., Quincey, D. J., Mayer, C., Rowan, A. V., and Irvine-Fynn, T. D. L. (2017). Temporal Variations in Supraglacial Debris Distribution on Baltoro Glacier, Karakoram between 2001 and 2012. *Geomorphology* 295, 572–585. doi:10.1016/j.geomorph.2017.08.012

Hooke, R. L. (1998). *Principles of Glacier Mechanics*. New Jersey: Prentice-Hall.

Huo, D., Bishop, M. P., and Bush, A. B. (2021). Understanding Complex Debris-Covered Glaciers: Concepts, Issues and Research Directions. *Front. Earth Sci.* 9, 358. doi:10.3389/feart.2021.652279

Iwata, S., Watanabe, O., and Fushimi, H. (1980). Surface Morphology in the Ablation Area of the Khumbu Glacier. *J. Jpn. Soc. Snow Ice* 41, 9–17. doi:10.5331/seppyo.41.Special_9

Kääb, A., Berthier, E., Nuth, C., Gardelle, J., and Arnaud, Y. (2012). Contrasting Patterns of Early Twenty-First-century Glacier Mass Change in the Himalayas. *Nature* 488, 495–498. doi:10.1038/nature11324

Kamb, B., and Echelmeyer, K. A. (1986). Stress-gradient Coupling in Glacier Flow: Longitudinal Averaging of the Influence of Ice Thickness and Surface Slope. *J. Glaciol.* 32, 267. doi:10.3189/s0022143000015604

King, O., Turner, A. G. D., Quincey, D. J., and Carrivick, J. L. (2020). Morphometric Evolution of Everest Region Debris-Covered Glaciers. *Geomorphology* 371, 107422. doi:10.1016/j.geomorph.2020.107422

Kirkbride, M. P., and Deline, P. (2013). The Formation of Supraglacial Debris Covers by Primary Dispersal from Transverse Englacial Debris Bands. *Earth Surf. Process. Landforms* 38, 1779–1792. doi:10.1002/esp.3416

Kirkbride, M. P. (2000). "Ice-marginal Geomorphology and Holocene Expansion of Debris-Covered Tasman Glacier, New Zealand," in *Debris-Covered Glaciers* (Seattle, Washington: IAHS Publication), 211–217.

Kirkbride, M. P. (1993). The Temporal Significance of Transitions from Melting to Calving Termini at Glaciers in the central Southern Alps of New Zealand. *Holocene* 3, 232–240. doi:10.1177/095968369300300305

Kraaijenbrink, P. D. A., Shea, J. M., Pellicciotti, F., Jong, S. M. d., and Immerzeel, W. W. (2016). Object-based Analysis of Unmanned Aerial Vehicle Imagery to Map and Characterise Surface Features on a Debris-Covered Glacier. *Remote Sensing Environ.* 186, 581–595. doi:10.1016/j.rse.2016.09.013

Leprince, S., Ayoub, F., Klinger, Y., and Avouac, J.-P. (2007). "Co-registration of Optically Sensed Images and Correlation (COSI-Corr): An Operational Methodology for Ground Deformation Measurements," in IEEE International Geoscience and Remote Sensing Symposium, Barcelona, Spain, 23–28 July (IEEE), 1943–1946. doi:10.1109/igarss.2007.4423207

MacKevett, E. M., Jr. (1972). Geologic Map of the McCarthy C-6 Quadrangle, Alask. Geologic Quadrangle Map 979. U.S. Geological Survey.

MacKevett, E. M., Jr., and Smith, J. G. (1972). Geologic Map of the MCCarthy B-6 Quadrangle, Alaska. Geologic Quadrangle 1035. U.S. Geological Survey. doi:10.3133/gq1035

Miles, E. S., Willis, I., Buri, P., Steiner, J. F., Arnold, N. S., and Pellicciotti, F. (2018). Surface Pond Energy Absorption across Four Himalayan Glaciers Accounts for 1/8 of Total Catchment Ice Loss. *Geophys. Res. Lett.* 45 (10), 10,464–10,473. doi:10.1029/2018GL079678

Miles, K. E., Hubbard, B., Miles, E. S., Quincey, D. J., Rowan, A. V., Kirkbride, M., et al. (2021). Continuous Borehole Optical Televiewing Reveals Variable Englacial Debris Concentrations at Khumbu Glacier, Nepal. *Commun. Earth Environ.* 2, 12. doi:10.1038/s43247-020-00070-x

Mölg, N., Bolch, T., Walter, A., and Vieli, A. (2019). Unravelling the Evolution of Zmuttgletscher and its Debris Cover since the End of the Little Ice Age. *Cryosphere* 13, 1889, 1909. doi:10.5194/tc-13-1889-2019

Mölg, N., Ferguson, J., Bolch, T., and Vieli, A. (2020). On the Influence of Debris Cover on Glacier Morphology: How High-Relief Structures Evolve from Smooth Surfaces. *Geomorphology* 357, 107092. doi:10.1016/j.geomorph.2020.107092

Moore, P. L. (2018). Stability of Supraglacial Debris. *Earth Surf. Process. Landforms* 43, 285–297. doi:10.1002/esp.4244

Nakawo, M., Iwata, S., Watanabe, O., and Yoshida, M. (1986). Processes Which Distribute Supraglacial Debris on the Khumbu Glacier, Nepal Himalaya. *A. Glaciology.* 8, 129–131. doi:10.1017/s0260305500001294

Neckel, N., Loibl, D., and Rankl, M. (2017). Recent Slowdown and Thinning of Debris-Covered Glaciers in South-Eastern Tibet. *Earth Planet. Sci. Lett.* 464, 95–102. doi:10.1016/j.epsl.2017.02.008

Nicholson, L., and Benn, D. I. (2006). Calculating Ice Melt beneath a Debris Layer Using Meteorological Data. *J. Glaciol.* 52, 463–470. doi:10.3189/172756506781828584

Nicholson, L., and Benn, D. I. (2013). Properties of Natural Supraglacial Debris in Relation to Modelling Sub-debris Ice Ablation. *Earth Surf. Process. Landforms* 38, 490–501. doi:10.1002/esp.3299

Nye, J. F. (1960). The Response of Glaciers and Ice-Sheets to Seasonal and Climatic Changes. *Proc. R. Soc. Lond. A.* 256, 559–584. doi:10.1098/rspa.1960.0127

Östrem, G. (1959). Ice Melting under a Thin Layer of Moraine, and the Existence of Ice Cores in Moraine Ridges. *Geografiska Annaler* 41, 228–230. doi:10.1080/20014422.1959.11907953

Parker, G. (1975). Meandering of Supraglacial Melt Streams. *Water Resour. Res.* 11, 551–552. doi:10.1029/WR011i004p00551

Pellicciotti, F., Stephan, C., Miles, E., Herreid, S., Immerzeel, W. W., and Bolch, T. (2015). Mass-balance Changes of the Debris-Covered Glaciers in the Langtang Himal, Nepal, from 1974 to 1999. *J. Glaciol.* 61, 373–386. doi:10.3189/2015JoG13J237

Porter, C., Morin, P., Howat, I., Noh, M.-J., Bates, B., Peterman, K., et al. (2018). ArcticDEM. *Harvard Dataverse, V1.* doi:10.7910/DVN/OHHUKH

Pritchard, H. D., King, E. C., Goodger, D. J., McCarthy, M., Mayer, C., and Kayastha, R. (2020). Towards Bedmap Himalayas: Development of an Airborne Ice-Sounding Radar for Glacier Thickness Surveys in High-Mountain Asia. *Ann. Glaciol.* 61, 35–45. doi:10.1017/aog.2020.29

Quincey, D. J., Luckman, A., and Benn, D. (2009). Quantification of Everest Region Glacier Velocities between 1992 and 2002, Using Satellite Radar Interferometry and Feature Tracking. *J. Glaciol.* 55, 596–606. doi:10.3189/002214309789470987

Quincey, D. J., Richardson, S. D., Luckman, A., Lucas, R. M., Reynolds, J. M., Hambrey, M. J., et al. (2007). Early Recognition of Glacial lake Hazards in the Himalaya Using Remote Sensing Datasets. *Glob. Planet. Change* 56, 137–152. doi:10.1016/j.gloplacha.2006.07.013

Raymond, C. F. (1971). Flow in a Transverse Section of Athabasca Glacier, Alberta, Canada. *J. Glaciol.* 10, 55–84. doi:10.1017/s0022143000012995

Reid, T. D., and Brock, B. W. (2010). An Energy-Balance Model for Debris-Covered Glaciers Including Heat Conduction through the Debris Layer. *J. Glaciol.* 56, 903–916. doi:10.3189/002214310794457218

Reynolds, J. M. (2000). "On the Formation of Supraglacial Lakes on Debris-Covered Glaciers," in *Debris-Covered Glaciers* (Seattle, Washington: IAHS Publication), 153–161.

Rickman, R. L., and Rosenkrans, D. S. (1997). *Hydrologic Conditions and Hazards in the Kennicott River Basin, Wrangell-St. Elias National Park and Preserve, Alaska*. Anchorage, Alaska: U.S. Geological Survey.

Röhl, K. (2008). Characteristics and Evolution of Supraglacial Ponds on Debris-Covered Tasman Glacier, New Zealand. *J. Glaciol.* 54, 867–880. doi:10.3189/002214308787779861

Rounce, D. R., Hock, R., McNabb, R. W., Millan, R., Sommer, C., Braun, M. H., et al. (2021). Distributed Global Debris Thickness Estimates Reveal Debris Significantly Impacts Glacier Mass Balance. *Geophys. Res. Lett.* 48, 1–12. doi:10.1029/2020GL091311

Sakai, A., and Fujita, K. (2010). Formation Conditions of Supraglacial Lakes on Debris-Covered Glaciers in the Himalaya. *J. Glaciol.* 56, 177–181. doi:10.3189/002214310791190785

Sato, Y., Fujita, K., Inoue, H., Sunako, S., Sakai, A., Tsushima, A., et al. (2021). Ice Cliff Dynamics of Debris-Covered Trakarding Glacier in the Rolwaling Region, Nepal Himalaya. *Front. Earth Sci.* 9, 398. doi:10.3389/feart.2021.623623

Scambos, T. A., Fahnestock, M., Moon, T., Gardner, A., and Klinger, M. (2016). Global Land Ice Velocity Extraction from Landsat 8 (GoLIVE), Version 1. (NSIDC-0710). Boulder, Colorado, USA: NSIDC: National Snow and Ice Data Center. doi:10.7265/N5ZP442BAccessed May 16, 2019)

Scherler, D., Bookhagen, B., and Strecker, M. R. (2011). Spatially Variable Response of Himalayan Glaciers to Climate Change Affected by Debris Cover. *Nat. Geosci* 4, 156–159. doi:10.1038/ngeo1068

Schwanghart, W., and Scherler, D. (2014). Short Communication: TopoToolbox 2 - MATLAB-Based Software for Topographic Analysis and Modeling in Earth Surface Sciences. *Earth Surf. Dynam.* 2, 1–7. doi:10.5194/esurf-2-1-2014

Shean, D. E., Alexandrov, O., Moratto, Z. M., Smith, B. E., Joughin, I. R., Porter, C., et al. (2016). An Automated, Open-Source Pipeline for Mass Production of Digital Elevation Models (DEMs) from Very-High-Resolution Commercial Stereo Satellite Imagery. *ISPRS J. Photogram. Remote Sensing* 116, 101–117. doi:10.1016/j.isprsjprs.2016.03.012

Steiner, J. F., Buri, P., Miles, E. S., Ragettli, S., and Pellicciotti, F. (2019). Supraglacial Ice Cliffs and Ponds on Debris-Covered Glaciers: Spatio-Temporal Distribution and Characteristics. *J. Glaciol.* 65, 617–632. doi:10.1017/jog.2019.40

Stewart, R. L., Westoby, M., Pellicciotti, F., Rowan, A., Swift, D., Brock, B., et al. (2021). Using Climate Reanalysis Data in Conjunction with Multi-Temporal Satellite thermal Imagery to Derive Supraglacial Debris Thickness Changes from Energy-Balance Modelling. *J. Glaciol.* 67, 366–384. doi:10.1017/jog.2020.111

Tarantola, A. (2005). *Inverse Problem Theory and Methods for Model Parameter Estimation*. Philadelphia, PA, USA: Society for Industrial and Applied Mathematics.

Thakuri, S., Salerno, F., Bolch, T., Guyennon, N., and Tartari, G. (2016). Factors Controlling the Accelerated Expansion of Imja Lake, Mount Everest Region, Nepal. *Ann. Glaciol.* 57, 245–257. doi:10.3189/2016AoG71A063

Vincent, C., Wagnon, P., Shea, J., Immerzeel, W., Kraaijenbrink, P., Shrestha, D., et al. (2016). Reduced Melt on Debris-Covered Glaciers: Investigations from Changri Nup Glacier, Nepal. *Cryosphere* 15, 1845–1858. doi:10.5194/tc-10-1845-2016

Walder, J. S., Trabant, D. C., Cunico, M., Fountain, A. G., Anderson, S. P., Anderson, R. S., et al. (2006). Local Response of a Glacier to Annual Filling and Drainage of an Ice-Marginal lake. *J. Glaciol.* 52, 440–450. doi:10.3189/172756506781828610

Watson, C. S., Quincey, D. J., Carrivick, J. L., and Smith, M. W. (2016). The Dynamics of Supraglacial Ponds in the Everest Region, central Himalaya. *Glob. Planet. Change* 142, 14–27. doi:10.1016/j.gloplacha.2016.04.008

Conflict of Interest: The authors declare that the research was conducted in the absence of any commercial or financial relationships that could be construed as a potential conflict of interest.

Publisher's Note: All claims expressed in this article are solely those of the authors and do not necessarily represent those of their affiliated organizations, or those of the publisher, the editors and the reviewers. Any product that may be evaluated in this article, or claim that may be made by its manufacturer, is not guaranteed or endorsed by the publisher.

frontiers in Earth Science

DATA REPORT
published: 24 August 2021
doi: 10.3389/feart.2021.715129

Seasonal Cold-Wave Propagation Into the Near-Surface Ice of Debris-Covered Khumbu Glacier, Nepal

Katie E. Miles[1], Bryn Hubbard[1], Duncan J. Quincey[2], Evan S. Miles[3], Samuel H. Doyle[1] and Ann V. Rowan[4]*

[1]Centre for Glaciology, Department of Geography and Earth Sciences, Aberystwyth University, Aberystwyth, United Kingdom, [2]School of Geography, University of Leeds, Leeds, United Kingdom, [3]Swiss Federal Research Institute WSL, Birmensdorf, Switzerland, [4]Department of Geography, University of Sheffield, Sheffield, United Kingdom

Keywords: debris-covered glacier, ice temperature, Khumbu glacier, Himalaya, near surface, glacier borehole

OPEN ACCESS

Edited by:
Michael Lehning,
École Polytechnique Fédérale de Lausanne, Switzerland

Reviewed by:
Argha Banerjee,
Indian Institute of Science Education and Research, Pune, India
Philip D.A. Kraaijenbrink,
Utrecht University, Netherlands

****Correspondence:***
Katie E. Miles
kam64@aber.ac.uk

Specialty section:
This article was submitted to Cryospheric Sciences, a section of the journal Frontiers in Earth Science

Received: *26 May 2021*
Accepted: *03 August 2021*
Published: *24 August 2021*

Citation:
Miles KE, Hubbard B, Quincey DJ, Miles ES, Doyle SH and Rowan AV (2021) Seasonal Cold-Wave Propagation Into the Near-Surface Ice of Debris-Covered Khumbu Glacier, Nepal. Front. Earth Sci. 9:715129. doi: 10.3389/feart.2021.715129

INTRODUCTION

Meltwater from high-elevation debris-covered glaciers—particularly those located in the greater Himalaya and Andes—shapes the water supply of major rivers and nourishes substantial terrestrial, estuarine, and marine habitats (Kraaijenbrink et al., 2017; Immerzeel et al., 2020). However, the relative inaccessibility and high elevation of such glaciers results in a paucity of data relating to their fundamental physical properties and processes, limiting the information available to constrain and evaluate numerical models of their behaviour and project future change. Knowledge of the subsurface properties of such glaciers is particularly deficient because it is largely obscured to satellite and airborne remote sensing; englacial investigations therefore commonly require direct access (Miles et al., 2020). Of the physical properties of glaciers, ice temperature exerts an important control over glaciological processes, such as glacier motion, and their modelled behaviour. For example, ice viscosity is sensitive to temperature such that, under the same stress, ice approaching the melting point deforms 5–10 times more rapidly than it would at −10°C (Deeley and Woodward, 1908; Cuffey and Paterson, 2010). Basal motion depends on lubrication facilitated by the presence of meltwater at the ice-bed interface and/or within the pore space of a subglacial sediment layer. Measurements of near-surface ice temperatures are important for modelling the surface energy balance and projecting the future mass-balance response of glaciers to anticipated climate change. This is especially the case for glaciers with a thick supraglacial debris layer that insulates the underlying ice (according to debris layer thickness and lithology), reducing ablation and potentially extending glacier longevity (Nicholson and Benn, 2006; Nicholson and Benn, 2013; Anderson and Anderson, 2016).

Here, we present a one-year time series of near-surface ice temperatures, measured between 1.5 and 7.0 m below the ice surface, in a borehole drilled by hot water into the debris-covered tongue of Khumbu Glacier, Nepal.

METHODS

Field Site

Khumbu Glacier is a large debris-covered glacier in the Nepal Himalaya (**Figure 1**) with a clean-ice accumulation area in the Western Cwm of Mount Everest, from ~5,800–8,000 m a.s.l., where mean annual air temperatures are of the order of −10 to −20°C (Matthews et al., 2020). The supraglacial

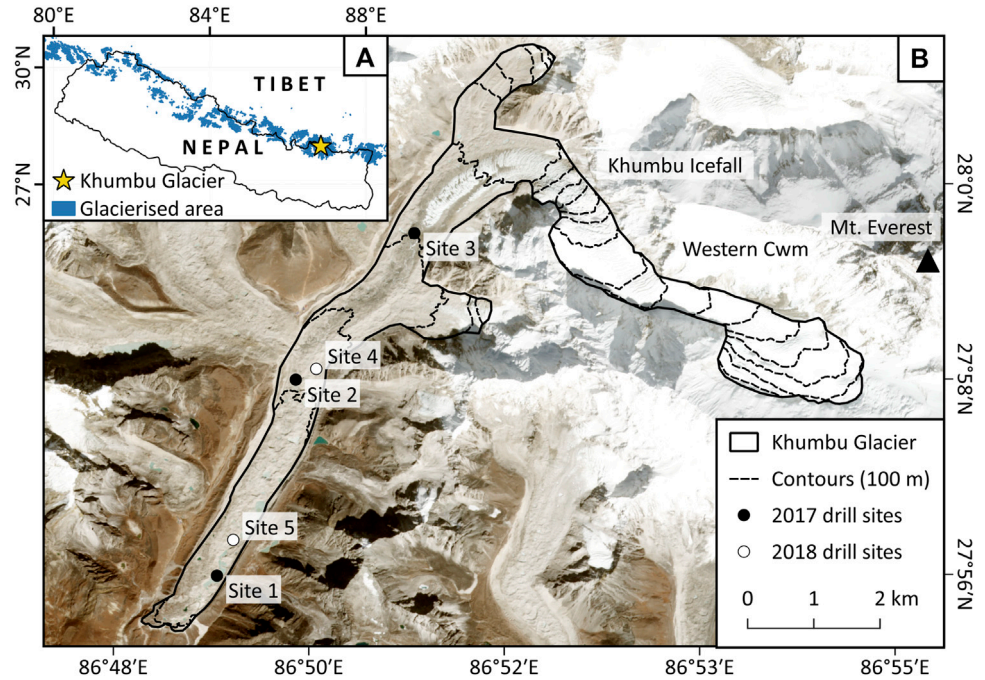

FIGURE 1 | Location of Khumbu Glacier and drill sites. **(A)** Location of Khumbu Glacier, Nepal. **(B)** Location of drill sites on the glacier in 2017 and 2018. Background is a Sentinel-2A image acquired on October 30, 2018 (Planet Team, 2017). Glacier contours are at 100 m intervals from 4,900 to 6,800 m a.s.l., created from the 2015 SETSM DEM (Noh and Howat, 2015).

debris layer begins to form just beyond the base of the Khumbu Icefall at ~5,400 m elevation, increasing in thickness to several metres at the terminus (Iwata et al., 1980; Miles et al., 2020; Miles et al., 2021). Below the depth of zero annual temperature variation (~15 m), the glacier is polythermal, based on records from deep thermistor strings across the ablation area (Sites 1–3, **Figure 1B**) (Miles et al., 2018).

Methods and Data Analysis

Twenty-seven boreholes were drilled by hot water at five sites across the debris-covered ablation area of Khumbu Glacier in 2017 and 2018 (Miles et al., 2019). Deep ice temperatures were measured at Sites 1–3 (**Figure 1B**); the first 6 months of measurements between May and October 2017 were reported in Miles et al. (2018). In this data report, we present hitherto unreported shallow ice temperature measurements from Site 4 recorded between May 2018 and May 2019. The temperature data herein were measured by a string of 12 thermistors installed at 0.5 m depth increments, from 1.5 to 7.0 m, below the ice surface at Site 4 (**Figure 1B**). Before drilling, supraglacial debris of ~0.6 m in thickness was removed from an approximately circular area of ~0.5 m diameter around the borehole location (Miles et al., 2019; Miles et al., 2021). When revisited 1 year later, the borehole was beneath a debris layer that was visually indistinguishable in thickness and character from that more generally present in the area, though the rate of reformation through englacial debris melt-out and gravitational processes is not known at this site.

Following Miles et al. (2018), Honeywell UNI-CURVE 192-502-LET-AOI thermistors were used to record ice temperatures to an accuracy of ± 0.05°C at 0°C following calibration in a distilled water and ice bath (Iken et al., 1993; Bayley, 2007; Doyle et al., 2018). Thermistor resistance was measured by a Campbell Scientific CR1000 data logger located at the glacier surface, as detailed by Miles et al. (2018). Measurements were made every 10 min between May 5, 2018 and November 14, 2018, and every hour between November 14, 2018, and May 30, 2019 to ensure memory capacity of the data loggers was not exceeded. Resistance was converted to temperature using a Steinhart and Hart (1968) polynomial fitted to the manufacturer's calibration curve, corrected using a freezing-point offset for each individual thermistor obtained from the ice-bath calibration.

CONCLUSION

The data we present herein comprise a time series of shallow ice temperatures measured between May 2018 and May 2019 at Khumbu Glacier, Nepal. Ice temperatures were recorded simultaneously by 12 thermistors installed at increments of 0.5 m below the ice surface, from 1.5 to 7.0 m depth.

The time series (**Figure 2**) captured the propagation of the cold-season cold wave into the near-surface ice of Khumbu Glacier. The thermistors froze into the borehole within 6 weeks. Beyond the settling curve, the ice temperature increased by ~0.5°C through the remainder of the warm season (to November), decreased by several degrees through the cold season, and finally began to warm again into the following warm season. The record quantified three

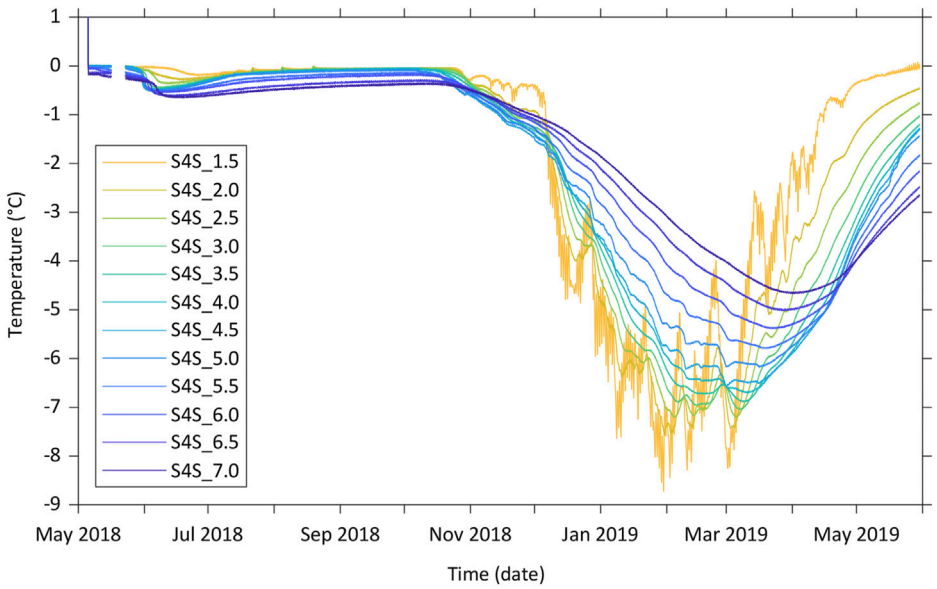

FIGURE 2 | Time series of temperature data measured by the Site 4 shallow-depth thermistor string, colour-coded by thermistor depth. Our thermistor naming convention (e.g., S4S_1.5) is comprised of the borehole site (here, "S4S" refers to "Site 4 shallow"), followed by the depth (in metres) of each thermistor below the surface (here, 1.5 m).

anticipated effects as the cold wave propagated to depth: 1) it was delayed, 2) its amplitude decreased, and 3) its high-frequency elements were progressively filtered out. Using daily mean values through the full cold season, the relationship between the rate of change of temperature and second derivative of temperature change with depth (Cuffey and Paterson, 2010) yielded a material thermal diffusivity of 1.1 m^2 s^{-1}, and hence a thermal conductivity of 2.1 m^{-1} K^{-1}. These values are typical of glacier ice close to its melting point (Cuffey and Paterson, 2010).

The dataset could be relevant to:

- Comparing shallow englacial temperatures, and interannual variability in them, with air temperatures from AWS data (e.g., Sherpa et al., 2017).
- Investigating near-surface ice mechanics and fracture (e.g., Podolskiy et al., 2018) and constraining thermo-mechanical models of glacier ice deformation (e.g., Gilbert et al., 2020).
- Investigating englacial liquid water availability and microbiology (e.g., Hotaling et al., 2017).
- Extending models of energy transfer through supraglacial debris into the underlying ice (e.g., Nicholson and Benn, 2006; Evatt et al., 2015), possibly including known debris temperature gradients (e.g., Rowan et al., 2021).
- Estimating the timing of the onset and end of the ablation season.
- Estimating the shallow ice temperature gradient along the glacier, and thus its equilibrium line altitude.

DATA AVAILABILITY STATEMENT

The datasets presented in this study can be found in online repositories. The names of the repository/repositories and accession number(s) can be found below: https://doi.org/10.6084/m9.figshare.14673837.

AUTHOR CONTRIBUTIONS

DQ, AR, and BH led the EverDrill research project. KM, BH, and SD designed and assembled the thermistor strings. KM, DQ, EM, BH, and AR participated in the fieldwork, including borehole drilling and thermistor string installation. KM led manuscript writing, to which BH, DQ, EM, AR, and SD contributed.

FUNDING

This research was supported by the "EverDrill" Natural Environment Research Council Grant awarded to the Universities of Leeds, Sheffield (NE/P00265X) and Aberystwyth (NE/P002021). Support for equipment also came from HEFCW Capital Equipment Grant awarded to BH at Aberystwyth University. KM was funded by an Aberystwyth University AberDoc PhD Scholarship.

ACKNOWLEDGMENTS

We thank Himalayan Research Expeditions for organising logistics and fieldwork permits, and Mahesh Magar for invaluable assistance in the field. We also thank Emily Potter, Tenzing Chogyal Sherpa, and Dawa Tshering Sherpa, who provided support during drilling. We gratefully acknowledge the Sagarmatha National Park authorities for their assistance in granting access and permits.

REFERENCES

Anderson, L. S., and Anderson, R. S. (2016). Modeling Debris-Covered Glaciers: Response to Steady Debris Deposition. *The Cryosphere* 10, 1105–1124. doi:10.5194/tc-10-1105-2016

Bayley, O. D. R. (2007). *Temperature of a "Temperate" alpine Glacier*. [PhD Thesis]. Switzerland: Glacier de Tsanfleuron.

Cuffey, K., and Paterson, W. S. B. (2010). *The Physics of Glaciers*. 4th edition. Burlington, MA, USA: Butterworth-Heinemann.

Deeley, R. M., and Woodward, H. (1908). The Viscosity of Ice. *Proc. R. Soc. Lond. Ser. A.* 81, 250–259.

Doyle, S. H., Hubbard, B., Christoffersen, P., Young, T. J., Hofstede, C., Bougamont, M., et al. (2018). Physical Conditions of Fast Glacier Flow: 1. Measurements from Boreholes Drilled to the Bed of Store Glacier, West Greenland. *J. Geophys. Res. Earth Surf.* 123, 324–348. doi:10.1002/2017JF004529

Evatt, G. W., Abrahams, I. D., Heil, M., Mayer, C., Kingslake, J., Mitchell, S. L., et al. (2015). Glacial Melt under a Porous Debris Layer. *J. Glaciol.* 61, 825–836. doi:10.3189/2015JoG14J235

Gilbert, A., Sinisalo, A., Gurung, T. R., Fujita, K., Maharjan, S. B., Sherpa, T. C., et al. (2020). The Influence of Water Percolation through Crevasses on the thermal Regime of a Himalayan Mountain Glacier. *The Cryosphere* 14, 1273–1288. doi:10.5194/tc-14-1273-2020

Hotaling, S., Hood, E., and Hamilton, T. L. (2017). Microbial Ecology of Mountain Glacier Ecosystems: Biodiversity, Ecological Connections and Implications of a Warming Climate. *Environ. Microbiol.* 19, 2935–2948. doi:10.1111/1462-2920.13766

Iken, A., Echelmeyer, K. A., Harrison, W., and Funk, M. (1993). Mechanisms of Fast Flow in Jakobshavns Isbræ, West Greenland: Part I. Measurements of Temperature and Water Level in Deep Boreholes. *J. Glaciol.* 39, 15–25. doi:10.1017/S0022143000015689

Immerzeel, W. W., Lutz, A. F., Andrade, M., Bahl, A., Biemans, H., Bolch, T., et al. (2020). Importance and Vulnerability of the World's Water Towers. *Nature* 577, 364–369. doi:10.1038/s41586-019-1822-y

Iwata, S., Watanabe, O., and Fushimi, H. (1980). Surface Morphology in the Ablation Area of the Khumbu Glacier. *J. Jpn. Soc. Snow Ice* 41, 9–17. doi:10.5331/seppyo.41.Special_9

Kraaijenbrink, P. D. A., Bierkens, M. F. P., Lutz, A. F., and Immerzeel, W. W. (2017). Impact of a Global Temperature Rise of 1.5 Degrees Celsius on Asia's Glaciers. *Nature* 549, 257–260. doi:10.1038/nature23878

Matthews, T., Perry, L. B., Koch, I., Aryal, D., Khadka, A., Shrestha, D., et al. (2020). Going to Extremes: Installing the World's Highest Weather Stations on Mount Everest. *Am. Meteorol. Soc.* 101, E1870–E1890. doi:10.1175/BAMS-D-19-0198.1

Miles, K. E., Hubbard, B., Irvine-Fynn, T. D. L., Miles, E. S., Quincey, D. J., and Rowan, A. V. (2020). Hydrology of Debris-Covered Glaciers in High Mountain Asia. *Earth-Science Rev.* 207, 103212. doi:10.1016/j.earscirev.2020.103212

Miles, K. E., Hubbard, B., Miles, E. S., Quincey, D. J., Rowan, A. V., Kirkbride, M., et al. (2021). Continuous Borehole Optical Televiewing Reveals Variable Englacial Debris Concentrations at Khumbu Glacier, Nepal. *Commun. Earth Environ.* 2, 1–9. doi:10.1038/s43247-020-00070-x

Miles, K. E., Hubbard, B., Quincey, D. J., Miles, E. S., Sherpa, T. C., Rowan, A. V., et al. (2018). Polythermal Structure of a Himalayan Debris-Covered Glacier Revealed by Borehole Thermometry. *Sci. Rep.* 8, 1–9. doi:10.1038/s41598-018-34327-5

Miles, K. E., Miles, E. S., Hubbard, B., Quincey, D. J., Rowan, A. V., and Pallett, M. (2019). Instruments and Methods: Hot-Water Borehole Drilling at a High-Elevation Debris-Covered Glacier. *J. Glaciol.* 65, 822–832. doi:10.1017/jog.2019.49

Nicholson, L., and Benn, D. I. (2006). Calculating Ice Melt beneath a Debris Layer Using Meteorological Data. *J. Glaciol.* 52, 463–470. doi:10.3189/172756506781828584

Nicholson, L., and Benn, D. I. (2013). Properties of Natural Supraglacial Debris in Relation to Modelling Sub-debris Ice Ablation. *Earth Surf. Process. Landforms* 38, 490–501. doi:10.1002/esp.3299

Noh, M.-J., and Howat, I. M. (2015). Automated Stereo-Photogrammetric DEM Generation at High Latitudes: Surface Extraction with TIN-Based Search-Space Minimization (SETSM) Validation and Demonstration over Glaciated Regions. *GIScience & Remote Sensing* 52, 198–217. doi:10.1080/15481603.2015.1008621

Planet Team (2017). "Planet Application Program Interface," in *Space for Life on Earth* (San Fr. CA). Available at: https://api.planet.com.

Podolskiy, E. A., Fujita, K., Sunako, S., Tsushima, A., and Kayastha, R. B. (2018). Nocturnal Thermal Fracturing of a Himalayan Debris-Covered Glacier Revealed by Ambient Seismic Noise. *Geophys. Res. Lett.* 45, 9699–9709. doi:10.1029/2018GL079653

Rowan, A. V., Nicholson, L. I., Quincey, D. J., Gibson, M. J., Irvine-Fynn, T. D. L., Watson, C. S., et al. (2021). Seasonally Stable Temperature Gradients through Supraglacial Debris in the Everest Region of Nepal, Central Himalaya. *J. Glaciol.* 67, 170–181. doi:10.1017/jog.2020.100

Sherpa, S. F., Wagnon, P., Brun, F., Berthier, E., Vincent, C., Lejeune, Y., et al. (2017). Contrasted Surface Mass Balances of Debris-free Glaciers Observed between the Southern and the Inner Parts of the Everest Region (2007-15). *J. Glaciol.* 63, 637–651. doi:10.1017/jog.2017.30

Steinhart, J. S., and Hart, S. R. (1968). Calibration Curves for Thermistors. *Deep Sea Res. Oceanographic Abstr.* 15, 497–503. doi:10.1016/0011-7471(68)90057-0

Conflict of Interest: The authors declare that the research was conducted in the absence of any commercial or financial relationships that could be construed as a potential conflict of interest.

The reviewer AB is currently organizing a Research Topic with one author DJQ.

frontiers in Earth Science

ORIGINAL RESEARCH
published: 30 August 2021
doi: 10.3389/feart.2021.681059

What Can Thermal Imagery Tell Us About Glacier Melt Below Rock Debris?

Sam Herreid *

Independent Researcher, Bradley Beach, NJ, United States

Rock debris on the surface of a glacier can dramatically reduce the local melt rate, where the primary factor governing melt reduction is debris layer thickness. Relating surface temperature to debris thickness is a recurring approach in the literature, yet demonstrations of reproducibility have been limited. Here, I present the results of a field experiment conducted on the Canwell Glacier, Alaska, United States to constrain how thermal data can be used in glaciology. These datasets include, 1) a measured sub-daily "Østrem curve" time-series; 2) a time-series of high resolution thermal images capturing several segments of different debris thicknesses including the measurements from 1); 3) a thermal profile through a 38 cm debris cover; and 4) two Advanced Spaceborne Thermal Emission and Reflection Radiometer (ASTER) satellite thermal images acquired within 2 and 3 min of a field-based thermal camera image. I show that, while clear sky conditions are when space-borne thermal sensors can image a glacier, this is an unfavorable time, limiting the likelihood that different thicknesses of debris will have a unique thermal signature. I then propose an empirical approach to estimate debris thickness and compare it to two recently published methods. I demonstrate that instantaneous calibration is essential in the previously published methods, where model parameters calibrated only 1 h prior to a repeat thermal image return diminished debris thickness estimates, while the method proposed here remains robust through time and does not appear to require re-calibration. I then propose a method that uses a time-series of surface temperature at one location and debris thickness to estimate bare-ice and sub-debris melt. Results show comparable cumulative melt estimates to a recently published method that requires an explicit/external estimate of bare ice melt. Finally, I show that sub-pixel corrections to ASTER thermal imagery can enable a close resemblance to high resolution, field-based thermal imagery. These results offer a deeper insight into what thermal data can and cannot tell us about surface debris properties and glacier melt.

Keywords: thermal infrared, glacier melt modeling, ASTER thermal infrared, debris covered glaciers, cryosphere, mountain glaciers, thermal image processing

OPEN ACCESS

Edited by:
Lindsey Isobel Nicholson, University of Innsbruck, Austria

Reviewed by:
Peter Moore, Iowa State University, United States
Rosie Bisset, University of Edinburgh, United Kingdom

***Correspondence:**
Sam Herreid
samherreid@gmail.com

Specialty section:
This article was submitted to Cryospheric Sciences, a section of the journal Frontiers in Earth Science

Received: *15 March 2021*
Accepted: *10 August 2021*
Published: *30 August 2021*

Citation:
Herreid S (2021) What Can Thermal Imagery Tell Us About Glacier Melt Below Rock Debris?. Front. Earth Sci. 9:681059. doi: 10.3389/feart.2021.681059

1 INTRODUCTION

Most large-scale glacier models consider a glacier to be composed solely of ice and snow. However, eroded rock debris from surrounding bedrock can enter a glacier and is either sequestered within the ice or rafts on the glacier surface (Goodsell et al., 2005). A layer of rock debris at the surface causes a modulation of the net atmospheric energy flux that reaches the sub-debris ice surface. A debris layer that is less than a few centimeters thick can enhance the local melt rate, while a debris layer with a thickness greater than a few centimeters causes an exponential decrease in the local melt rate, scaling with increasing debris thickness (Østrem, 1959; Mattson, 1993; Evatt et al., 2015). Englacial debris is exhumed to the surface through glacier melt causing an increased accumulation of surface debris towards the terminus of a glacier where melt rates would be the highest in a debris-free setting (Anderson, 2000).

Earth's mountain glaciers are 7.3% debris-covered (Herreid and Pellicciotti, 2020), yet estimates of debris thickness, the key variable governing sub-debris melt rates, are only now being derived at large scales (Kraaijenbrink et al., 2017; Rounce et al., 2021) and their accuracy will benefit from further validation. Debris thickness can be derived from a high density network of excavation point measurements (e.g., Anderson et al., 2021), naturally occurring cross sections (e.g., Nicholson and Mertes, 2017) or ground penetrating radar (e.g., Nicholson et al., 2018); however, these methods are time and resource intensive and impractical at large spatial scales. Proposed methods to derive debris thickness at wider spatial scales are 1) empirical relations between debris thickness and satellite thermal data (e.g., Ranzi et al., 2004; Mihalcea et al., 2008a; Kraaijenbrink et al., 2017); 2) debris thickness derived from satellite thermal data as the residual of a physically-based surface temperature inversion (Foster et al., 2012; Rounce and McKinney, 2014; Schauwecker et al., 2015); 3) a sub-debris melt inversion (Ragettli et al., 2015; Rounce et al., 2018); and 4), a combination of both a sub-debris melt inversion and a surface temperature inversion (Rounce et al., 2021). While studies using moderate/coarse resolution thermal data acquired from satellites is common, the use of field-based oblique or airborne/unmanned aerial vehicle (UAV) acquired high resolution thermal data is surprisingly rare in glaciology (Hopkinson et al., 2010; Aubry-Wake et al., 2015, 2018; Herreid and Pellicciotti, 2018; Kraaijenbrink et al., 2018), and none of these studies used their thermal data to explicitly solve for debris thickness and/or glacier melt rates.

A thermal data approach to derive debris thickness is based on a relation first described by Lougeay (1974). Lougeay (1974) established the shallow, ~0.5 m, debris thickness detection limit as the surface temperature signal from thick debris cover decouples from the cooling effect of the ice below. This limitation persists through modern methods, yet thermal data remain a recurring central component of new methods to derive debris thickness. While debris thicknesses that exceed 0.5 m are common, an argument can be made that the required debris thickness estimate accuracy decreases as the debris thickness increases and the sub-debris melt rate asymptotically approaches 0, or a low rate of melt (Kraaijenbrink et al., 2017). Because debris thickness is a relatively stable quantity over short timescales (months to years), scientists can, optimally, be selective with the acquisition timing of the data used to derive a debris thickness estimate. More realistically, the data acquisition will be limited by satellite pass frequency, snow cover and cloud cover constraints. Mihalcea et al. (2008a) considered the strength of the relation between debris thickness and in-field surface temperature data as a function of time of day. Their results suggested the early morning hours optimize the correlation, while the weakest correlation was observed in the afternoon. To my knowledge, this experiment has not been repeated and a deeper understanding of the variable meteorological conditions and diurnal/seasonal timing of data acquisition would help optimize debris thickness estimate methodologies as well as better inform what information can be feasibly extracted from thermal data. Here, I use a high spatiotemporal resolution time-series of thermal imagery over variable debris thicknesses to consider the time of day and meteorological conditions that are most favorable for acquiring an optimal thermal image to derive debris thickness.

The stability of debris thickness over months to years also posits the main challenge for researchers attempting to derive debris thickness from surface temperature measurements: a constantly changing independent variable needs to repeatedly return a constant dependent variable. While solving for debris thickness is a nontrivial challenge in its own right, apart from mountain erosion rate problems and the study of peri/supraglacial landforms, the explicit volume of rock debris rafting on a glacier is a largely inconsequential quantity. For research centered around water resources and sea level rise, it is strictly the impact this layer of rock has on sub-debris melt rates that is significant. To this point, a debris thickness estimate that succeeds in extracting a constant and correct value from surface temperature data is also removing information coupled to the energy flux that is driving sub-debris melt. While a thermal image time-series of bare-glacier ice at the pressure-melting point will reveal nothing about the melt rate occurring in frame, a thermal time-series of neighboring supraglacial debris that is sufficiently thick to thermally decouple from a melting ice heat sink below, or possibly a thermal time-series of a local valley wall that can be considered a debris cover of infinite thickness, can presumably be used to derive the melt rate at both bare glacier ice locations and below a debris cover of any thickness. In this study, I explore both of these propositions: 1) can a simple function relate variable surface temperatures to stable debris thicknesses while retaining model stability through time where parameter calibration is not required for each thermal image? And 2), can surface temperature collected at a location with thick debris, or of a neighboring glacier valley wall, be used to solve for glacier melt below any known thickness of debris?

To evaluate these questions, I use data from a carefully orchestrated field experiment that includes an Østrem curve time-series (sub-debris melt rates collected at neighboring locations of variable debris thickness at a sub-daily interval) that is coincident in time with, and captured within the frame of, a high resolution thermal camera time-series. This enables a

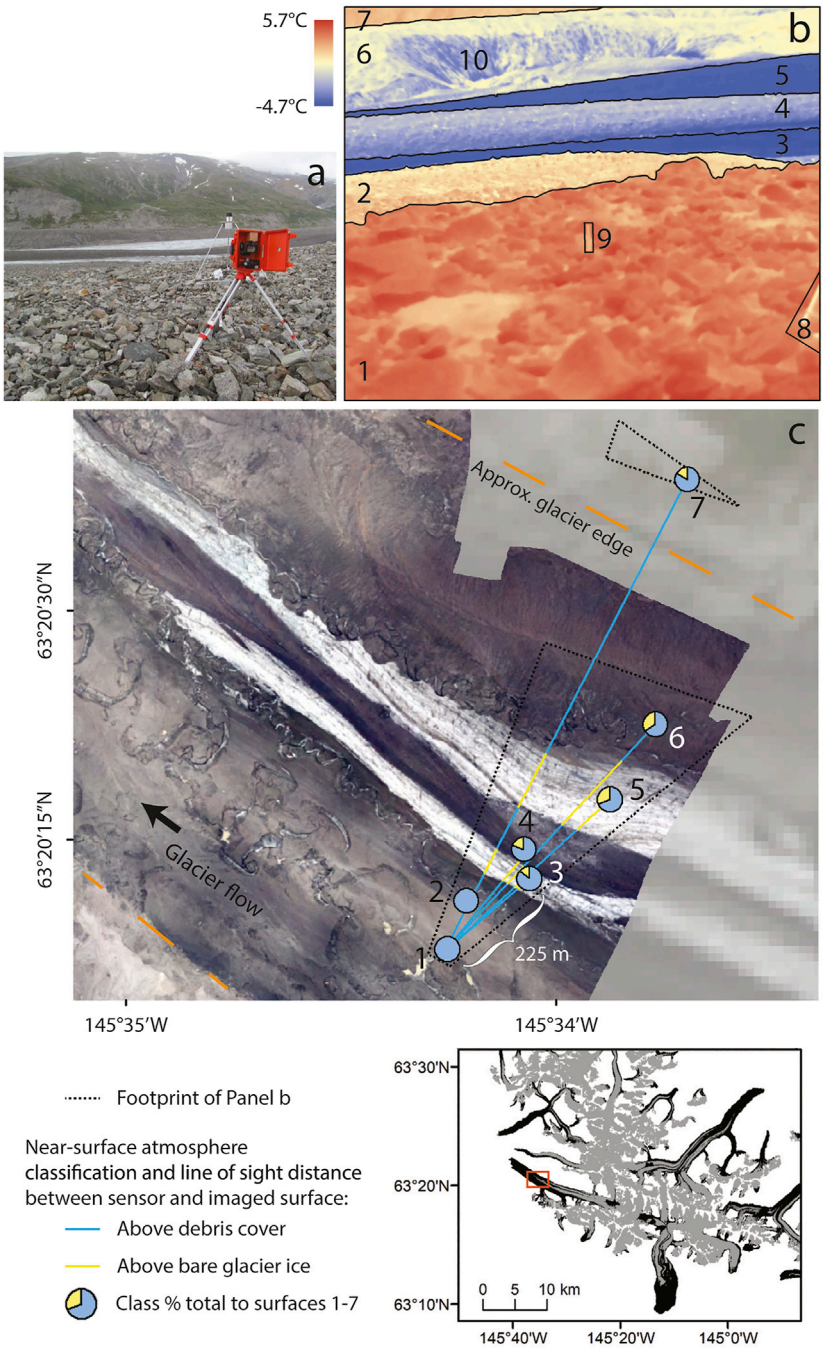

FIGURE 1 | (A) thermal camera in position to capture **(B)**. **(B)** one (unprocessed) frame of the thermal time-series with black lines defining image segments (1–7) described in **Section 3.1**. (8) is the corner of a weather station structure and (9) is an aluminum ablation stake, both were cut out of each thermal image to not influence segment statistics. (10) is the side of a medial moraine with a thinly debris-covered, or proto, ice cliff visible. The nadir footprint of **(B)** is shown in **(C)** and one to seven correspond to their respective image segments. The line of sight distance is shown between the thermal camera [10 m away from (1)] and the seven segments. Ablation was measured at (1)–(5) where the atmospheric classification pie is centered over the ablation measurement location.

field-based derivation of the mirrored relation between surface temperature and sub-debris melt rates as a function of debris thickness that has been established through modeling (Nicholson et al., 2018). While this analysis relies on a carefully chosen field site and data that are not feasibly acquired at wide scales, I present a set of methods where each field-based thermal image can essentially be treated as if it were a moderate resolution thermal satellite image. Following these methods, input data to solve for debris thickness and sub-debris melt can be extracted from the thermal image itself with an optional alternative input

from a thermistor deployed at the surface of local and thick debris cover. I quantify the success of the proposed methods and consider factors that cause method failure, specifically, by indirectly solving for debris layer saturation. I then compare these results to two recently proposed/published methods from Rowan et al. (2021) and Rounce et al. (2021).

Finally, to further bridge the gap between fine-scale, in-field studies and moderate-scale satellite based methodologies, I propose a sub-pixel signal correction for satellite thermal data. I evaluate this correction using two Advanced Spaceborne Thermal Emission and Reflection Radiometer (ASTER) satellite images, one acquired during the day and one at night, where both were acquired within minutes of high resolution field-based thermal images.

2 STUDY SITE

Canwell Glacier (**Figure 1**) is a 60 km^2 glacier in the Delta Mountains, a sub-range of the eastern Alaska Range (63°19.8′N, 145°32′W). The lower-middle ablation zone of Canwell Glacier was a carefully selected field site for the experiment conducted in this study, meeting a specific set of conditions packed tightly into one location. Several prior field seasons were spent developing and testing field methods and surveying debris thicknesses for an ideal field site and thermal camera vantage point (**Supplementary Figure S1**). Looking orthogonal to glacier flow, from the higher elevation and more thickly debris-covered southern half of the ablation zone, there are seven swaths of near-homogeneous surface types in one field of view. Medial moraine bands at different stages of englacial exhumation and/or with different source-point erosion rates are visible, either as a discrete band surrounded by bare glacier ice, or connected to neighboring moraines as they coalesce down glacier, while still retaining their near-homogeneous rock composition and thickness (**Supplementary Figure S1**). The presence of relatively thick (~38 cm) debris cover next to swaths of thinner debris cover and bare ice provides an ideal natural setting to measure the Østrem curve, normalized to bare glacier melt rates, under effectively homogeneous meteorological conditions, as well as allowing this field experiment to be conducted with only one thermal camera. Further, the off-glacier valley wall is also within the frame of view adding one more potentially useful point of reference that I explore further in this study.

3 DATA AND METHODS

3.1 Field-Based Thermal Infrared Camera Data

Between July 30, 2016 23:42 AKDT (Alaska daylight time) and August 30, 2016 20:14 AKDT, a field experiment monitoring sub-debris glacier melt and temperature at an array of locations was conducted (data gaps will limit different experiments in this study to subsets of this time range). Using a FLIR T620 camera (uncooled microbolometer, 640 × 480 resolution, spectral range 7.5–14.0 μm, accuracy ±2°C, thermal sensitivity <0.04°C at 30°C), surface temperature was monitored at a 15 min interval for 164 h, broken into six observations periods under different meteorological conditions. Due to data gaps, there were 102 h, split between four observation periods (1 August 11:42 AKDT to 3 August 10:57; 3 August 3:45 to 4 August 16:13; 10 August 21:47 to 11 August 8:02; and, 16 August 23:15 to 17 August 19:45) where measurements from all data sources were collected simultaneously. The thermal camera was mounted on a surveying tripod and deployed at the same coordinate location for each of the six periods. Emissivity was set to one and distance set to 0 to facilitate post-processing. Within each oblique thermal image, seven distinct image segments were captured, each with a near-homogeneous debris thickness (**Supplementary Figure S1**). The segments, ordered in distance from the thermal camera and corresponding to locations shown in **Figure 1**, are:

1. 38 cm (average) debris thickness (10 m from sensor)
2. 8 cm debris thickness (110 m)
3. Debris-free glacier ice (225 m)
4. 4 cm debris thickness (275 m)
5. Debris-free glacier ice (490 m)
6. 10 cm debris thickness (620 m)
7. Off glacier, southwest facing valley wall (1,000 m)

3.2 Meteorological Data to Process Thermal Imagery

Air temperature and relative humidity are required input to solve for surface temperature from a thermal image. Measurements of 1.5 m air temperature and relative humidity were collected at a 10 min interval throughout the duration of this study at site 1 (on top of structure 8) labeled in **Figure 1**. The measurements were made using an ONSET HOBO U23 Pro v2 Temperature/Relative Humidity Data Logger housed in a radiation shield. A second, identical structure and sensor configuration was deployed to the same debris-covered location as well as a bare ice location (**Figure 1**, site 5) in 2012 spanning the same period of time as the data collected in 2016 (31 July 23:42 AKDT to 30 August 20:14 AKDT). These 2012 data are used in this study to amend a 2016 sensor deployment deficiency, providing hourly correction factors to quantify the difference in air temperature over debris cover and bare ice which is notably different (**Supplementary Figure S2**). To provide context to analysis of debris saturation, precipitation was also measured at site 1 (on top of structure 8) labeled in **Figure 1**, using a HOBO tipping bucket Rain Gauge Data Logger.

3.3 Solving for Surface Temperature

Thermal infrared cameras are often sold along with integrated software packages that facilitate post processing. There is nothing inherently wrong with using proprietary software packages, but given the complexities and scales that glacier research is conducted on, it is helpful to have oversight/control of the equations used to decompose the several entangled signals present in at-sensor radiance values. In contrast to other geophysical applications of thermal imagery, e.g., volcanology

where dramatic thermal anomalies (+100s of degrees) are the signal of interest (Spampinato et al., 2011), applications in glaciology mainly use absolute temperature values that have a relatively low deviation (~10–30°C over varying debris thicknesses), thus further increasing the importance of careful image processing. Here, I present a method to process field-based, oblique time-lapse thermal imagery which poses unique difficulties from, 1) variable atmospheric attenuation that can be present in one frame imaging several surfaces at different distances (in this study, ranging from a few meters to a kilometer away from the sensor); 2) variable atmospheric attenuation through time; and 3), image shift and rotation from both imaging an unstable landscape and, in the case of this study, acquiring the image time-series from an unstable location on the glacier surface. The method uses Thermimage (Tattersall, 2017) to automate the extraction of raw values from FLIR images and (TŸč and Gohlke, 2015) to co-register images in the series. This processing routine was developed specifically for a glacier setting by including atmospheric corrections accounting for variability in near-surface conditions over bare and debris-covered ice surfaces present along the line of sight distance from the thermal camera sensor to the target surface. Aside from this correction, which can be omitted, the image processing routine is suitable for any Earth science application with a few meters to a few kilometers line of sight surface to sensor distance. The code uses both R and *Python* packages combined in one open-source Jupyter Notebook available at (https://github.com/samherreid/ThermalTimelapse).

The value assigned to each pixel in a thermal image is a quantization of the net radiant intensity, W_{tot} (Wm^{-2}), received at the sensor within a set, sensor specific, spectral range (7.5–14.0 μm for the camera used in this study). Following the formulation from Usamentiaga et al. (2014), the surface temperature of an object, T_s (K), can be calculated by:

$$T_s = \sqrt[4]{\frac{W_{tot} - (1-\varepsilon_{obj}) * \tau_{atm} * \sigma * (T_{refl})^4 - (1-\tau_{atm}) * \sigma * (T_{atm})^4}{\varepsilon_{obj} * \tau_{atm} * \sigma}} \quad (1)$$

where ε_{obj} is the emissivity of the object, τ_{atm} is the transmittance of the atmosphere between the sensor and the object, σ is the Stefan-Boltzmann constant (5.67×10^{-8} $Wm^{-2}K^{-4}$), T_{refl} (K) is the reflected temperature and T_{atm} (K) is the temperature of the atmosphere.

None of these quantities (apart from σ) are constant in time or space. However, variability in ε_{obj} through time, e.g., from rock surfaces becoming wet, was assumed to be negligible. In this study, ε_{obj} was varied in space based on site specific values extracted from an ASTER image, acquired on August 30th, 2016 at 13:25 AKDT, that was processed to estimate surface emissivity (AST05) (following Gillespie et al., 1998; Abrams et al., 2002). These values averaged to a debris cover emissivity of 0.94 and an ice emissivity of 0.97. T_{refl} was assigned for each thermal image by extracting the mean temperature of the aluminum poles of the weather station structure visible in the field of view of each image (**Figure 1**). This loosely follows the reflector method described in Usamentiaga et al. (2014); however, variation from vectors normal to a smooth cylindrical aluminum surface rather than normal to a complex, randomly oriented crumpled and then flattened aluminum surface (a more favorable configuration) was not quantified. Atmospheric temperature (T_{atm}, **Section 3.2**) measurements coincident in time with each thermal image were extracted, and a correction (derived from local data collected 4 years earlier in 2012) was applied to account for air temperature variability for the portions of each thermal image that were debris-free. A set of correction factors were computed for each hour of the day by finding the difference between hourly averaged 1.5 m air temperature collected at location **Figure 1** 1) and the same measurement recorded at location **Figure 1** 5) (**Supplementary Figure S2**).

The final parameter needed to solve **Eq. 1**, τ_{atm}, can be formulated as the product of the two main quantities that cause signal attenuation received at the thermal camera,

$$\tau_{atm} = \tau_m \tau_s, \quad (2)$$

where τ_m is molecular absorption by constituent gases and τ_s is scattering by particles in the atmosphere (Gaussorgues, 1994). Following Gaussorgues (1994), τ_m is simplified to account for the two dominant constituent gases of the atmosphere, water vapor and gaseous carbon dioxide:

$$\tau_m = \tau_{H_2O} \tau_{CO_2}. \quad (3)$$

As electromagnetic radiation travels through the atmosphere from the target glacier surface to the infrared sensor, some of the radiation is absorbed by atmospheric water vapor molecules (Gaussorgues, 1994). Discrete volumes of interest requiring a solution for atmospheric water vapor content can be approximated as a solid angle or ellipse-based cone, where the point of the cone is at the sensor and the ellipse base approximates the glacier surface radiation source area surrounding each (rectangular) pixel in a thermal image. The number of water vapor molecules present within this cone is a function of the local partial pressure of water vapor and the presences of gaseous water vapor molecules (Gaussorgues, 1994). These quantities are governed both by predictable factors (e.g., elevation, diurnal and seasonal cycles) and chaotic factors (e.g., wind and weather systems). Considering these factors, τ_{H_2O} cannot be considered static even at sub-hourly time scales. For this study, the volume of the ellipse-based cone was simplified to a one-dimensional distance, x, from the object surface to the infrared sensor. This is a practical simplification even in an oblique setting because objects that are close to the sensor have a sufficiently disproportionate pixel resolution to the length of x scale ratio of millimeters to meters and objects imaged in the distance have a scale ratio of centimeters to 100s of meters. The quantity of water vapor along x is most commonly expressed as a height of precipitable water, which is the amount of liquid water that would result from the condensation of all of the present water vapor molecules (Gaussorgues, 1994). Precipitable water, h, can be expressed as

$$h = \int_0^x q_v \rho dx, \quad (4)$$

where q_v (dimensionless) is specific humidity, the mass mixing ratio of water vapor to the total mass of the moist air along x, and ρ (kg m^{-3}) is the density of the moist air. h has units of kg m^{-2} which is equal to a one-dimensional height of water in *mm*. h is frequently solved for over a vertical column from the ground to the top of the atmosphere. Many parameterizations exist for this quantity (e.g., Maghrabi and Al Dajani, 2013), but are not applicable to a horizontal x with a variable length and also where pressure and temperature profiles cannot be approximated as simple functions of elevation. h is therefore estimated using measured relative humidity, RH (dimensionless), T_{atm} (K) and sensor to surface distance, x (m).

The longest x over which h was solved for was 1 km with variable ground-surface types (alternating between debris cover and bare glacier ice, **Figure 1C**) where RH and T_{atm} cannot be assumed constant. For this study, the landscape imaged repeatedly was broken into segments where each segment contains area with a near constant debris thickness (**Supplementary Figure S1**) and a similar ground to sensor distance, x (**Figure 1**; 1–7). For each segment, h is approximated from the quadrature of **Eq. 4** by

$$h = q_{v_{ice}}\rho_{ice}x_{ice} + q_{v_{deb}}\rho_{deb}x_{deb}, \quad (5)$$

where the distance, x, is the sum of two components accounting for variability in the atmosphere above two distinct surfaces, bare ice, x_{ice}, and debris cover, x_{deb} (**Figure 1**). Using a set of standard equations, T_{atm} and RH can be used to solve for q_v and ρ over bare ice ($q_{v_{ice}}$, ρ_{ice}) and over debris cover ($q_{v_{deb}}$, ρ_{deb}) (**Supplementary Appendix**). With a solution for h from **Eq. 5**, spectral transmittance through the atmosphere considering molecular absorption of water vapor, τ_{H_2O}, can be estimated as a function of wavelength (λ, μm) (Passman and Larmore, 1956; Gaussorgues, 1994) (**Supplementary Appendix**). Numerical integration of $\tau_{H_2O}(\lambda)$ over the specific thermal camera spectral range (in this study 7.5–14.0 μm) enables a solution of τ_{H_2O}.

Solving for spectral transmittance through the atmosphere considering molecular absorption of gaseous carbon dioxide, τ_{CO_2} and signal attenuation from scattering by particles in the atmosphere, τ_s, can be estimated more simply as functions of λ and sensor to object distance, x (Gaussorgues, 1994) (**Supplementary Appendix**). Together, these calculations of τ_{H_2O}, τ_{CO_2} and τ_s enable an estimate of τ_{atm} for each image segment that accounts for the specifications of the thermal camera, the physical setting of the experiment and the instantaneous near-surface atmosphere.

The unique setting of imaging a glacier surface with simultaneous measurements of non-zero melt means that bare glacier ice can be expected to be at the pressure melting point. While small impurities are present on even bare ice surfaces with the potential to raise the surface temperature slightly above 0°C, I used this setting of a known, in-frame temperature to identify and correct an assumed linear −2°C sensor bias for all of the images used in this study.

The procedure described here forms the basis of a thermal image processing routine that considers variable surface types, variable line of sight distances and variable near-surface atmosphere along the line of sight distance within a single thermal image. This routine was applied to 684 images acquired over a total span of 164 h. This process was fully automated including automated rotation, translation and scaling data shifts (TŸč and Gohlke, 2015) to co-register images to match manually defined image segments (black lines in **Figure 1B**). Locations in the image where unnatural objects were present (e.g., an ablation stake and the corner of a weather station) were removed to not disrupt the mean, median and percentile values computed for each segment.

3.4 Sub-daily Ablation Measurements

Contemporaneous with the thermal image time-series, sub-daily melt measurements were made within four of the seven segments defined in **Figure 1**: Segments 1, 2, 4, and 5 with debris thicknesses 38, 8, 4, and 0 cm, respectively. Melt measurements were made using a "glacier selfie stick" approach where a graduated, rigid aluminum ablation stake was drilled into bare, or sub-debris ice with a visible spectrum time-lapse camera loosely attached and floating on the surface to photograph the progressive exposure of graduations 5 times per day (**Figure 2**, **Supplementary Video S1**). For the ablation stake located closest to the thermal camera [**Figure 1** (8), 38 cm debris thickness], the visible spectrum time-lapse camera was fixed to the floating meteorological station. These measurements enabled a sub-daily measurement of melt and were validated against periodic, field-based manual measurements. The presence of the camera assembly at the ablation stake also impacted melt, which was most visible at the bare ice location. Instances where the camera assembly caused clear excess lowering were corrected for by adding back the height of an unnatural (few cm) trench, yet these instances were rare and the assembly remained largely flush with the visible surrounding surface (**Supplementary Video S1**). Each of the four image time-series were post-processed to derive melt rates by manually measuring the graduation exposure rate. While the cameras acquired five images per day, the frequency of melt measurements were also a function of melt. If the melt rate between images was low, e.g., for the locations with a thicker debris cover, measurements intervals were lengthened until a discernible change could be confidently measured. This makes selecting a meaningful common dt for the computed melt rate difficult. For the purposes of the modeling effort described in **Section 3.6** below, where high frequency (10 or 15 min) measurements were downsampled to a 1 h frequency, these melt measurements were resampled to 1 h. This resampling produces error in the melt model validation, but preserves the diurnal variation in the melt rate below thin debris cover and at bare ice. This diurnal variation is a unique signal since most melt measurements of bare glacier ice or sub-debris melt are averaged over days to weeks or months. The bare ice ablation stake, with the highest melt rate, needed to be occasionally re-drilled to maintain a continuous record. These disruptions to the melt record and subsequent post processing proved difficult to mitigate, where disruptions to the melt rate only causes obvious momentary unrealistic values, while a large and more subtle error can accrue in the cumulative melt signal. Large

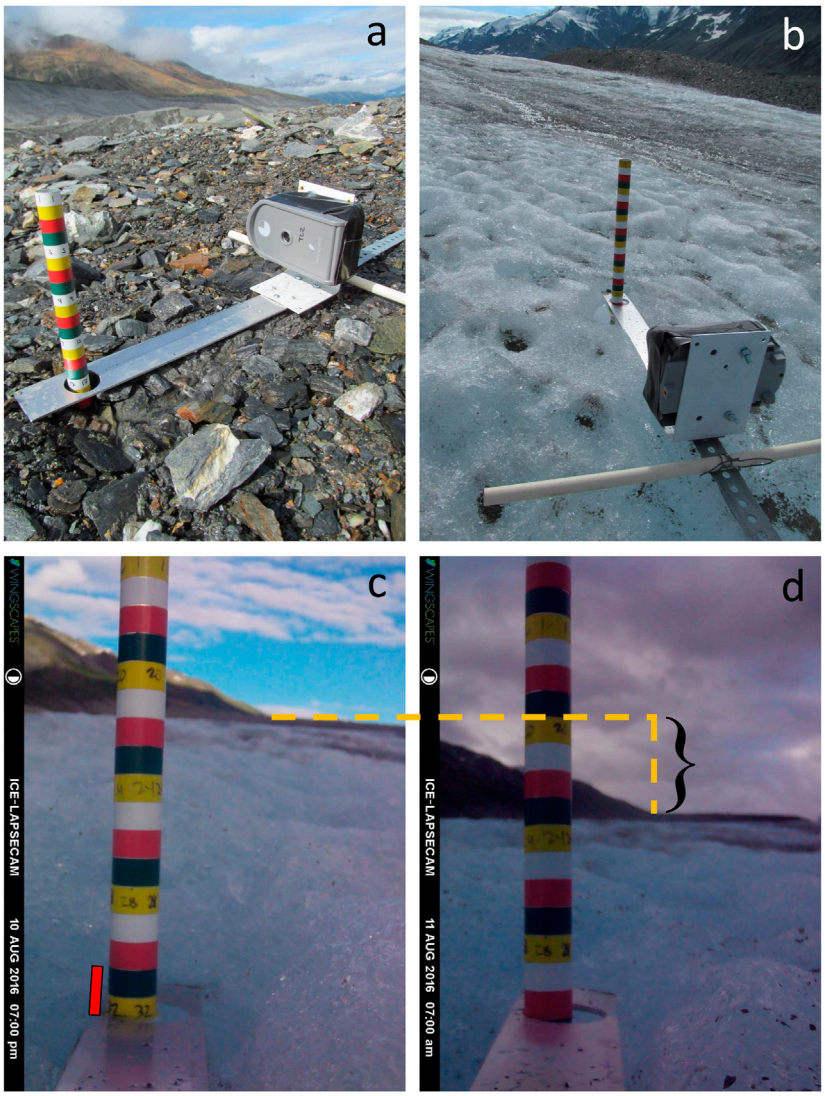

FIGURE 2 | (A,B) glacier selfie stick configuration used to collect a sub-daily record of surface lowering at locations (2), (4), and (5) in **Figure 1**. Location (1) had its ablation time-lapse camera fixed to the floating weather station structure. Errors in this style of measurement can be estimated by observing offset in the surrounding landscape compared with the melt signal. **(C,D)** an example of a particularly large camera movement between two successive images (the camera was set to turn off during the night) where a simple reading of the graduations exposed would suggest glacier accumulation (red bar) but is clearly an error of upward camera rotation based on the lowering of the background landscape. An additional advantage of this method to record ablation is the background imaging of the local sky and cloud fraction.

errors were manually smoothed by taking an average between the surrounding days melt measurements at the same time of day. Finally, to have all of the ablation records begin at the same time, linear regression was used to solve for melt over the hours needed to be subtracted from earlier emplaced ablation stakes to align with the initial measurement of the last emplaced ablation stake.

Melt measurement error was estimated at 0.12 cm per measurement, which sums to 0.6 cm per day if all five images were suitable for use. This value is the result of watching the landscape shift in the background of each image which is caused by movement of the camera assembly unrelated to melt-driven surface lowering. **Figures 2C,D** shows an extreme shift event where the camera tilted backwards overnight giving the impression of glacier accumulation. While the distance to the background landscape is unknown as well as the angle of rotation, it is still a clear indication of when the measurement will contain an error, requiring a correction factor that will carry through the remaining melt measurements when solving for cumulative melt. A video (**Supplementary Video S1**) of the complete visible time-lapse datasets from the four locations shows that while events like the one shown in **Figures 2C,D** do occur, through much of the time-series, the camera position (and background landscape) remains stable, facilitating meaningful melt measurements.

3.5 Thermal Diffusivity

For the three locations of measured ablation with debris cover [**Figure 1**(1,2,4)], temperatures were recorded within the debris layer in 4 cm increments from the debris-ice interface to the surface. These measurements were collected using ONSET U23 Pro v2 External Temperature Data Loggers at a 10 min increment (resampled to 1 h for the modeling effort, described in **Sections 3.4**, **3.6**). At the location of the thickest debris cover [**Figure 1**(1), 38 cm debris thickness], further analysis was conducted to investigate the energy transfer within the debris layer concurrently with the ablation and thermal time-lapse measurements. Thermal diffusivity, in a strictly conductive energy transfer setting, can be solved for using the finite-difference method to approximate the Biot-Fourier diffusion equation,

$$\frac{\partial T}{\partial t} = \kappa_c \frac{\partial^2 T}{\partial h_d^2} \tag{6}$$

where T is temperature (°C), h_d is depth (mm), t is time and κ_c is thermal diffusivity ($mm^2 s^{-1}$) (Hinkel et al., 1990; Conway et al., 2000; Rowan et al., 2021). The subscript, c, denotes the exclusion of any heat transfer mechanism besides conduction.

A second approach was used to solve for thermal diffusivity from diurnal amplitude decay with depth, incorporating all heat transfer mechanisms. In order to automate the selection of diurnal maximum and minimums, a Savitzky-Golay filter was applied (polynomial order 3, window length 51) to smooth the jagged nature of a surface, or near-surface temperature profile as clouds pass overhead. Considering the change in temperature amplitude with depth for each day, amplitude derived thermal diffusivity, κ_a can be calculated,

$$\kappa_a = \frac{\omega (h_1 - h_2)^2}{2(\ln(A(h_1)) - \ln(A(h_2)))^2} \tag{7}$$

where $A(h_1)$ and $A(h_2)$ are temperature amplitudes at depths h_1 and h_2, respectively Wang et al. (2020). ω is the radial frequency,

$$\omega = \frac{2\pi}{\phi} \tag{8}$$

where ϕ is the period of the diurnal cycle set to 86,400 s (24 h).

Using the smoothed temperature profiles, phase shift was calculated at each measurement depth by finding the lag in time between the maximum temperature at depth and the maximum temperature at the surface for each day. The slope of phase shift with depth is also proportional to thermal diffusivity (Anderson, 1998).

3.6 Methods to Estimate Debris Thickness and Sub-debris Melt

The simultaneous hourly measurements of sub-debris melt under variable debris thicknesses and the corresponding surface temperatures offer an ideal framework to evaluate, and possibly improve upon, methods to solve for debris thickness and sub-debris melt.

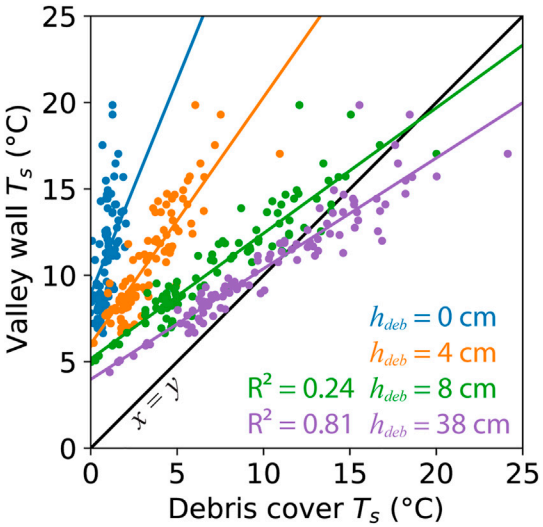

FIGURE 3 | Thermal camera derived surface temperatures over the observation period shown in **Figure 5**. Debris cover surface temperatures approach the warm valley wall temperature as debris thickness increases. Where debris is sufficiently thick, it is possible surface temperature from these two surfaces could be used interchangeably to force a model of local sub-debris melt, giving preference to whichever is easier to collect in a given field setting. Model coefficients should be able to accommodate any valley wall aspect. Imaging rock surfaces, preferably till, rather than vegetation is likely critical to maintain a similar emissivity. These data suggest an off-plot, non-zero convergence, likely due to differences in emissivity/aspect/surface angle, or the temperature at the surface of a 38 cm debris cover may not be entirely free from close proximity temperature modulation from glacier ice below.

Exponential scaling is often used to describe the nonlinear relation between surface temperature and debris thickness (e.g., Mihalcea et al., 2008b), yet local variability intrinsic to the relation are embedded within the model parameters, limiting transferability. Here, I propose a method similar to Kraaijenbrink et al. (2017) that draws on information present in the same thermal image used to estimate debris thickness to constrain the exponential scaling. The approach here differs from Kraaijenbrink et al. (2017) by 1) introducing one model parameter that I hypothesize will be stable through time and for other locations on Earth; and 2) looking both within the glacier domain as well as outside the glacier domain, to the local valley walls, to constrain a realistic relation between debris thickness and surface temperature even if there is no thick debris cover present within a thermal image (or no debris cover at all).

I define T_s^* as the "warmest local temperature" extracted from the thermal image. T_s^* is used as a reference surface temperature representing the local radiative forcing without heat sinks. For any location with little or no prior knowledge of the setting, for example, a routine iterating through all glaciers on Earth, T_s^* can be defined as $T_s^* = \max(\max(T_s), \max(T_{sbuffer}))$, where T_s is surface temperature across the glacier domain and $T_{sbuffer}$ is off-glacier surface temperature within a set buffer distance outside of the glacier domain to capture the local valley walls.

The assumption behind looking off-glacier is that the maximum temperature in close proximity, and at a similar elevation, will be from a rock surface with a similar emissivity and surface roughness to a thick debris cover that is decoupled from heat sinks regardless of whether there is thick, thin or no supraglacial debris present at that location. The maximum function is used to discard less ideal, e.g., vegetated, surfaces that will likely be cooler than till or bedrock. Measurements from this study show the surface temperature of thick debris cover can exceed even south facing valley wall temperature, but the two quantities, thick debris T_s and valley wall T_s, are correlated (**Figure 3**). Since the field experiment presented here is conducted with the knowledge that there is thick debris cover, T_s^* is set to $\max(T_s)$ which, for this time-series, is equivalent to T_s at the 38 cm debris thickness segment. If using only $\max(T_s)$ or $\max(T_{sbuffer})$, it is possible for T_s to exceed T_s^* which can be accommodated by using a piecewise function. Where available, T_s^* is taken from the thermal camera data. For the sub-debris melt analysis expanding beyond the thermal camera observation windows, T_s^* is set to the temperature measured by the contact thermistor at the top of the thermal profile at the 38 cm debris thickness segment (**Section 3.5**).

With T_s^* established, a relation to solve for debris thickness, h_{deb}, can be expressed as,

$$h_{deb}(T_s) = \begin{cases} \min\left(a_9 \exp\left(\frac{T_s^*}{T_s^* - T_s}\right), h_{max}\right), & 0 \le T_s < T_s^* \\ h_{max}, & T_s \ge T_s^* \end{cases} \tag{9}$$

where a_9 is the single model coefficient (subscript referring to the equation number in this paper, subsequently developed model coefficients, a_x, b_x and c_x, will follow the same, subscript to the equation number, notation) that I hypothesize will be stable through space and time because much of the local and regional variability, both in terms of micrometeorology and broad geographical/orographical effects, will be captured in T_s^*. h_{max} is a user defined value of "thick" debris cover where associated sub-debris melt rates can be assumed to have asymptotically approached a stable, low value. Here, I set h_{max} to 40 cm. While an exponential function is generally successful at capturing the relation between surface temperature and debris thickness for debris thicknesses around 40 cm or less, towards thicker debris cover, it is unrealistic that small, incremental increases in surface temperature should return exponentially thicker debris cover. Lacking data to support, for example, a third-order polynomial fit that would smoothly transition to a constant debris thickness while surface temperature continues to increase, I have opted to flat-line debris thickness to make clear that what can be safely resolved is that the debris is thick, but the model is unable to predict an absolute thickness. This method also cannot predict debris thicknesses when temperatures are below freezing.

I compare this approach to two recently proposed/published methods from Rowan et al. (2021) and Rounce et al. (2021). Analysis by Rowan et al. (2021) shows a power-law relation between debris thickness and near-surface temperature which they invoke to suggest solving for sub-debris melt from surface temperature data. Following this framework, I evaluate the inverse of the power-law from (Rowan et al., 2021, Figure 7A), where

$$h_{deb}(T_s) = a_{10} {T_s}^{b_{10}}. \tag{10}$$

I also evaluate the approach used by Rounce et al. (2021) where debris thickness is estimated using the Hill equation,

$$h_{deb}(T_s) = \left(\frac{T_s {b_{11}}^{c_{11}}}{a_{11} - T_s}\right)^{\frac{1}{c_{11}}}. \tag{11}$$

With h_{deb} either known or estimated from one of the methods described above, it becomes feasible to estimate sub-debris melt rate, $\dot{b}$. For the method I propose here, I continue to use T_s^* as defined above, but now use it to first solve for debris cover surface temperature. This may sound redundant, since T_s^* was derived from distributed surface temperature data. However, the above method was developed to solve for stable (over the timescale considered here) debris thickness. To solve for debris thickness, especially over large spatial scales, there are at best a few suitable (cloud and snow free) satellite-based thermal images acquired per year. To force a method to derive $\dot{b}$, T_s^* is not discovered, as above, but rather measured (or derived) continuously from a fixed location. For this study, T_s^* is again set to T_s at the "thick" 38 cm debris thickness segment from thermal camera data where available, and from the contact thermistor at the debris surface for the longer time-scale analysis. In future applications, T_s^* can be measured from either a contact thermistor at the surface of thick debris (which is an exceptionally easy sensor to deploy in the field) or by taking repeat thermal images below as much of the cloud canopy as possible which could be possible from a vantage point off-glacier where a power source might be more readily available.

Using T_s^* and one model coefficient, distributed debris surface temperature, T_s, can be estimated at the same temporal interval as T_s^* where debris thickness is known,

$$T_s(T_s^*, h_{deb}) = T_s^* - (T_s^* \exp(-a_{12} h_{deb})). \tag{12}$$

With distributed T_s derived through time, $\dot{b}$ can be estimated as,

$$\dot{b}(T_s^*, h_{deb}) = \begin{cases} a_{13}(1 - b_{13})(T_s^* - T_s(T_s^*, h_{deb})) + a_{13} b_{13} T_s^*, & T_s^* \ge 0 \\ 0, & T_s^* < 0 \end{cases} \tag{13}$$

where $a_{13} = \dot{b}_0 / T_s^*$, the ratio of bare ice melt rate, $\dot{b}_0$, and T_s^*. This term scales the relation to melt. I hypothesize a_{13} will remain relatively stable through space and time because it is a ratio of two physically related quantities. If true, this would mean that $\dot{b}_0$ would not need to be explicitly derived from other melt modeling methods to solve for bare ice and sub-debris melt rates. a_{13} will likely need to be recalibrated between geographic regions where the energy balance terms are not similarly weighted and the hypothesis may be rejected where the weighting is locally variable, e.g., where turbulent fluxes are an important component of the

energy balance (Steiner et al., 2018). b_{13} is a term that accounts for the thermal inertia of a debris cover, where melt below thick debris is forced by energy transfer occurring over a period longer than the 24 h diurnal cycle. Here, I parameterize b_{13} as b_{13} = median($\dot{b}_{38}$)/median($\dot{b}_0$), where $\dot{b}_{38}$ is the melt rate below a "thick" 38 cm debris cover (note $\dot{b}_{38}$ is a melt rate, while b_{13} is a model parameter). This ratio is the empirical middle value of a fairly difficult to obtain set of measurements. It scales the empirical asymptotic convergence of the full (in time) melt rate dataset collected for this study and is possibly stable through space and time. If stable, this would facilitate transferability and reduce the frequency these cumbersome measurements would need to be repeated. With the two model parameters expressed in their expanded ratio form and explicitly solved for (meaning without taking the median values), the last term of **Eq. 13** reduces from $\frac{\dot{b}_0}{T_s^*}\frac{\dot{b}_{38}}{\dot{b}_0}T_s^*$, to $\dot{b}_{38}$. This sets the melt rate for the region of the curve after the exponential decay approaches the asymptote. Because the parameterized form is scaled by T_s^*, melt will not continue throughout the winter as surface temperature drops to 0°C, or below, from the piecewise case of sub-freezing temperatures.

While **Eq. 12** has the same arguments as **Eq. 13** and could thus be easily written into **Eq. 13**, it is worthwhile to consider it as a separate step because surface temperature measurements are easier to obtain than sub-debris melt measurements for the purposes of method validation.

The analysis presented in this study is over a small portion of one glacier where factors like elevation dependent temperature lapse rates can be neglected. In order to derive distributed results from the new methods presented here, T_s^* will need to be extracted at elevation bins to solve for h_{deb}, and corrected for elevation to solve for $\dot{b}$.

Finally, I evaluate the method proposed above against the approach used by Rounce et al. (2021) where $\dot{b}$ is estimated using a second-order reaction rate equation,

$$\dot{b}(\dot{b}_0, h_{deb}) = \frac{\dot{b}_0}{1 + a_{14}\dot{b}_0 h_{deb}.} \tag{14}$$

While Rounce et al. (2021) used an energy balance model to solve for $\dot{b}_0$ and a_{14}, for this study, I simply fit **Eq. 14** to measured $\dot{b}_0$, thus evaluating the expression as if bare ice melt was externally modeled perfectly (under the assumption that my bare ice melt measurements are correct). To evaluate the methods used in this study, the coefficient of determination was found between instantaneous measurements (debris thickness, surface temperature or glacier melt rates) and the respective instantaneous modeled values.

3.7 Sub-pixel Correction for ASTER Thermal Data

Three ASTER thermal images were acquired under clear sky conditions that were coincident in space and time (2 min, 3 min, and 3 h separation) with the terrestrial based, high resolution thermal images collected within this study. Of the two ASTER images with a separation of minutes, one was acquired during the night (August 28, 2016 23:16 AKDT) and the other during the day (August 30, 2016 13:25 AKDT) about 1.5 days later. These images were processed on-demand by NASA to surface kinetic temperature (AST08) which has a spatial resolution of 90 m and a temperature accuracy and precision of about 1.5 K (Gillespie et al., 1998; Abrams et al., 2002).

Due to the high spatial variability in surface characteristics that can occur over very short length scales within a debris cover (Kraaijenbrink et al., 2018), a correction was applied to the ASTER thermal pixels that were coincident with this study. While acknowledging the ASTER processing algorithm is not linear, the most simplistic approach to applying any correction at all is through linear spatial averaging. Using the high resolution, manually digitized bare glacier ice and ice cliff map used as a validation dataset in Herreid and Pellicciotti (2018), the fraction of bare glacier ice within each ASTER pixel was found. Assuming the temperature value assigned to the ASTER pixel is an area weighted average of the true temperature distribution within the pixel area and assuming the area mapped as bare ice or ice cliff has a surface temperature of 273.15 K, the surface temperature of the remaining debris-covered fraction of the pixel can be computed. This debris area only temperature, T_{scor}, can be defined as

$$T_{scor} = \frac{T_{ssat}{L_{sat}}^2 - (273.15\beta_{ice}{L_{sat}}^2)}{(1-\beta_{ice}){L_{sat}}^2} \tag{15}$$

where T_{ssat} (K) is the raw satellite temperature for the whole pixel, L_{sat} is the length of one edge of a satellite pixel (90 m for ASTER) and β_{ice} is the fraction of a pixel that can be assumed to have a surface temperature of 273.15 K.

4 RESULTS AND DISCUSSION

The field data collected in this study provide an Østrem curve time-series, capturing the diurnal variation in melt rates below different thicknesses of debris cover, which are all spatially contained within the field of view of a high resolution thermal image time-series. A record of temperature within a 38 cm thick debris layer is also coincident in time and space. These data are best shown as a video time-series (**Supplementary Video S2**).

4.1 Optimal Timing for Thermal Image Acquisition

For each thermal image segment with a near-homogeneous debris thickness (**Figure 1**, **Supplementary Figure S1**), median and percentile statistics were computed (**Figure 4**). The time-evolution of the median and spread of temperatures within each segment illustrate when it is most feasible to automate the differentiation of these segments and assign a debris thickness. The ideal setting is when there is near-homogeneous temperatures within a segment (narrow individual ranges, **Figure 4F**), heterogeneous temperatures across segments (high stacked spread, **Figure 4G**) and even, un-clustered distribution of the spread (swaths equal in magnitude, **Figure 4H**).

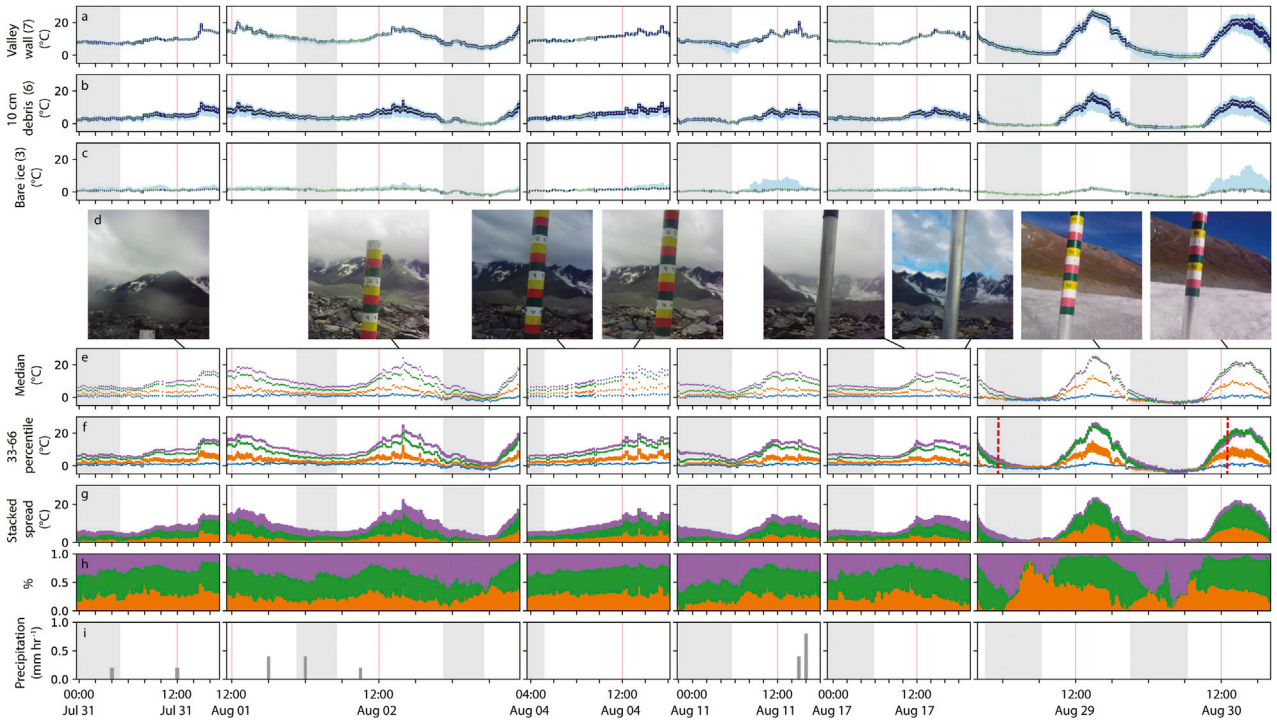

FIGURE 4 | (A–C) segments where glacier melt was not measured. Location from **Figure 1** is given on the *y*-axis label. Light and dark blue are the 10–90 and 33–66 percentile temperature range, respectively. The green dot is the segment median temperature. **(D)** select images from the glacier selfie sticks. Ignoring the ablation stake in the center frame, cloudiness and the local weather can be observed. Segment median temperature **(E)** and 33–66 percentile range **(F)** for the four segments where ablation was measured. The colors correspond to: blue, bare glacier ice at **Figure 1** location (5); orange, 4 cm debris thickness (4); green, 8 cm debris thickness (2); and purple, 38 cm debris thickness (1). **(G)** spread of median values for segments in **(E)** by stacking the gap, in °C, between two neighboring segments. The difference swath is assigned the color of the upper segment. **(H)** same as **(G)**, normalized to 100%. **(I)** precipitation of liquid water. Solid red vertical lines show noon of each day, and grey swaths show the local night (corrected for local latitude). The two vertical red dashed lines in **(F)** show the timing of two ASTER thermal images that were acquired concurrently with this time-series.

While satellites can only acquire surface temperature data when the surface is not obstructed by clouds, **Figure 4** suggests that the two cloud-free days (August 29 and August 30) were the least optimal of the collected time-series. During these clear sky conditions, the percentile spread in individual segments is high, and the spread between segments is uneven to nonexistent. The warmest two segments (with debris thicknesses of 38 and 8 cm) became nearly isothermic during the peak heat of the day. On the contrary, it appears that overcast days without precipitation offer the most ideal conditions for deriving debris thickness from surface temperature (some rain occurred during this time-series but no major rain events were recorded). While this could be useful for small scale studies using terrestrial or airborne/UAV imaging platforms that can operate under a cloud ceiling, it adds to the challenge of using thermal satellite data to derive debris thickness.

There are reasonable arguments to use thermal data from both night and day-time imagery to derive debris thickness. During the night the near-isothermic state described above would be avoided, and, drawing on the stored heat signal of a thick debris cover, or its absence for a thin debris cover, the surface temperature may scale well with debris thickness. On the other hand, during the day, direct short-wave radiation will warm thick debris cover surfaces while thin layers remain cool, even under direct incoming short-wave radiation. Both approaches seem reasonable and possibly a combination will be most successful. The key circumstances to avoid are a night isothermic state when debris cover of all thicknesses cool off, or during peak heat of a clear day when most rock surfaces are heated to a high temperature and decouple from a predictable relation with the ice below. Within the data acquired in this study, there is evidence of all four states: an optimal night setting, an optimal daytime setting, isothermic nights and isothermic days. Both isothermic states (for all segments at night and the two segments with the thickest debris cover during the day) occur during the clear sky days, August 29 and 30. The remaining measurement days have variable degrees of spread but differentiation seems feasible at any time of day. Based solely on the spread of the full thermal histogram over the observation period (**Supplementary Video S2**), daytime offers a more broad spectrum of temperature to discretize.

4.2 Solving for Debris Thickness From Surface Temperature Data

Three empirical equations relating surface temperature to debris thickness were evaluated using the same input data over the same

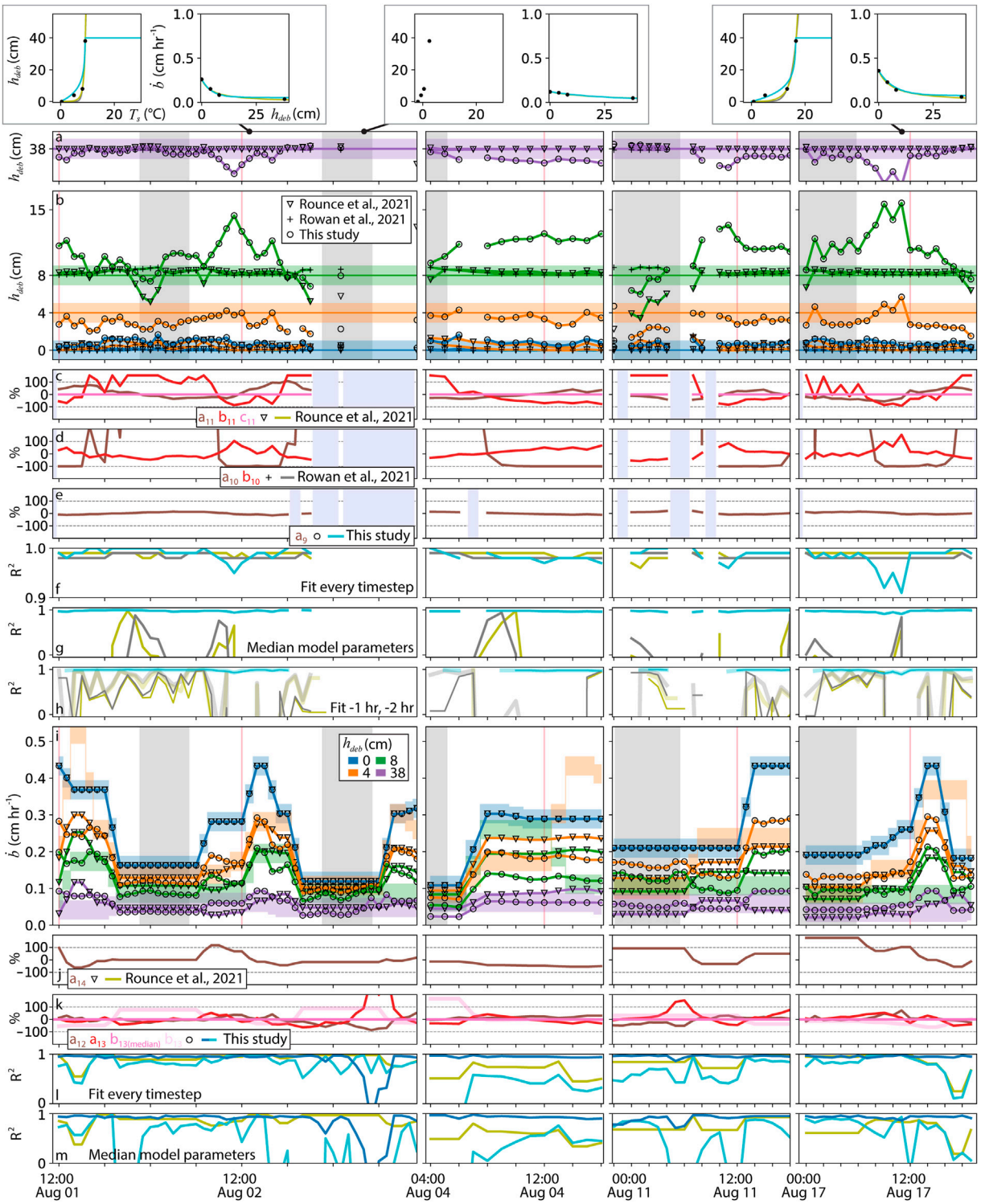

FIGURE 5 | (A,B) measured debris thickness, solid flat lines with a ±1 cm error buffer; and modeled debris thickness, forced with T_s from thermal camera segment medians over the measured debris thicknesses. Model coefficients were calibrated for every timestep. A successful model would match the flat line debris thickness of the same color for every timestep. Different models are denoted by shape at each timestep. Debris thickness colors are the same as **(I)** and **Figures 3**, **4**, **6**: blue, bare glacier ice at **Figure 1** location (5); orange, 4 cm debris thickness (4); green, 8 cm debris thickness (2); and purple, 38 cm debris thickness (1). Solid red vertical lines show noon of each day, and grey swaths show the local night [same in **(I)**]. **(C–E)** Normalized [(*x* –median(*x*))/median(*x*)] variability in model coefficients calibrated at every timestep for the three methods used. Legend gives the model coefficient name, subscript with equation number, and color coded to the plot of its variability through time.

(*Continued*)

FIGURE 5 | Dashed lines are ±100% deviation from the median value. Vertical lavender swaths are where the model failed, e.g., log of a negative. **(F–H)** R^2 for each model, color defined in legends **(C–E)**, where: **(F)** calibrated at every timestep; **(G)** constant median model coefficients, derived over this time-series **(C–E)**, applied at every timestep; and **(H)** using model coefficients calibrated 1 h prior (wide, transparent line) and 2 h prior (thin solid line). **(I)** same figure configuration as **(A,B)** but for bare ice and sub-debris melt, comparing only two methods. Measurements are colored swaths, model results are solid lines. For this experiment, both methods were prescribed measured bare ice melt and therefore match it perfectly. **(J,K)** same figure configuration as **(C–E)** but for sub-debris melt. $b_{13(median)}$ is derived from median melt data spanning the whole time-series in **Figure 6** and used for the calculations here and in **Figure 6**. b_{13}, light pink, is the same data ratio but using the explicit solution for each timestep, not medians, to show its relative stability, it is not used elsewhere. **(L,M)** R^2 for each model, color defined in legends **(J,K)** where dark blue is **Eq. 12**, solving for surface temperature; and light blue is **Eq. 13**, solving for sub-debris melt. **(L)** calibrated at every timestep; **(M)** constant median model coefficients, derived over this time-series **(J,K)**, applied at every timestep. Three timestep examples are shown at the top of the Figure illustrating **(A,B,I)**. Model color coding follows the legends in **(C–E)**; measurements are black dots.

102 h of observation (**Figure 5**). Each approach was evaluated in four ways: 1) the number of required model coefficients and their stability through time; 2) the optimal performance of the method where a new set of model coefficients were calibrated for each hourly instance in the 102 h time-series; 3) method performance when holding the model coefficients stable through time as the median values of the model coefficient set derived in 2); and 4) using the model coefficients that were best fit one and 2 h prior.

General results from this analysis show that the methods from Rowan et al. (2021) and Rounce et al. (2021) (**Eqs. 10**, **11**, respectively) easily translate variable surface temperatures through time into stable and correct debris thicknesses when calibrated at every timestep (**Figures 5A,B**). A notable exception for both methods is an under estimation of debris that is 4 cm thick, both methods returned a near-zero debris thickness for every timestep. The method presented here (**Eq. 9**), is notably less stable, especially at 8 cm debris thickness, where, at its worst, the debris thickness estimate is off by nearly a factor of 2. A visible advantage of this method is the ability to better estimate the 4 cm thick debris cover. Given these visible shortcomings and advantages, when calibrated at every timestep, all three methods have a high (>0.90) coefficient of determination for every timestep (**Figure 5F**).

The equations from Rowan et al. (2021) and Rounce et al. (2021) produce a nearly identical curve (**Supplementary Video S3**, frame examples at the top of **Figure 5**), yet **Eq. 11** from Rounce et al. (2021) requires one additional model coefficient (c_{11}) that appears to remain constant and does not absorb any temporal variability (**Figure 5C**). The remaining two model coefficients in **Eq. 11** (a_{11} and b_{11}) and the two in **Eq. 10** from Rowan et al. (2021) (a_{10} and b_{10}) show considerable variability through time with varying adherence to a diurnal pattern (**Figures 5C,D**). The two parameter sets are most stable during mid-day on August 4th, which for **Eq. 11**, means the values are constrained within the ±100% deviation from median bounds, which is still considerable variability. For the rest of the series, both approaches deviate outside of these bounds to absorb the surface temperature variability. While these two methods are very accurate when instantaneously calibrated, their coefficients of determination are rarely above zero when the median model coefficient values were used (**Figure 5G**, **Supplementary Table S1**). Rounce et al. (2021) implemented a clever methodology to derive, and optimize a parameter set for each surface temperature instance within a dataset covering all mountain glaciers on Earth. In this case, temporal transferability is not necessarily relevant, but even a short *dt* between neighboring thermal images might cause a depreciation of results. To explore this, I used each method to solve for debris thickness with the current timestep surface temperature, but used the best fit model coefficients from one and 2 h prior (**Figure 5H**). Results from this experiment show a dramatic loss of performance, where R^2 averaged across the time-series decreased from 0.99 (no lag), 0.53 (−1 h) and 0.37 (−2 h) for **Eq. 11** (Rounce et al., 2021); and 0.98 (no lag), 0.54 (−1 h) and 0.41 (−2 h) for **Eq. 10** (Rowan et al., 2021).

While the method proposed here, **Eq. 9**, carries more variability than the other two methods when calibrated at every timestep, it has some key advantages when used in less ideal conditions. Nearly all of the local variability in surface temperature is accounted for by T_s^*, which means the single model coefficient is simply scaling a physical relation and not needing to vary itself to accommodate different thermal distributions. The parameter stability apparent in **Figure 5E** carries through both experiments, of a constant median value and −1 and −2 h, with a notably high coefficient of determination. For the hours lag experiment, average R^2 remains constant at 0.98 (no lag), 0.98 (−1 h) and 0.98 (−2 h). While these results show more variability from **Eq. 9** around the 8 cm debris thickness, it is a quantifiable variability. Because evidence suggest the method is stable, an appropriate error can be assigned and assumed also stable enabling confident and constrained estimates of debris thickness through time.

4.3 Solving for Bare Ice and Sub-debris Melt from Surface Temperature Data

Following the same framework used to evaluate debris thickness methods above, I propose a method to solve for bare ice and sub-debris melt from debris thickness and surface temperature and compare it to the method from Rounce et al. (2021). The method used by Rounce et al. (2021) (**Eq. 14**) is not forced by surface temperature, but is a similar simple parameterization of sub-debris melt. For the 102 h time-series, where hourly sub-debris melt is known, measured bare ice melt, $\dot{b}_0$, and constant, known debris thicknesses were used as input to **Eq. 14** and a least squares fit was used to optimized a_{14}, the single model coefficient, for each timestep. Similarly, the 102 h time-series was used to fit the sub-debris melt method presented in this study for each timestep, but instead of melt data, **Eq. 12**, solving for debris surface temperature, was forced with thermal camera derived surface temperature over thick debris (T_s^*) and the same constant, known debris thicknesses. The model coefficient, a_{12}, was fit using thermal camera derived surface temperature for the known

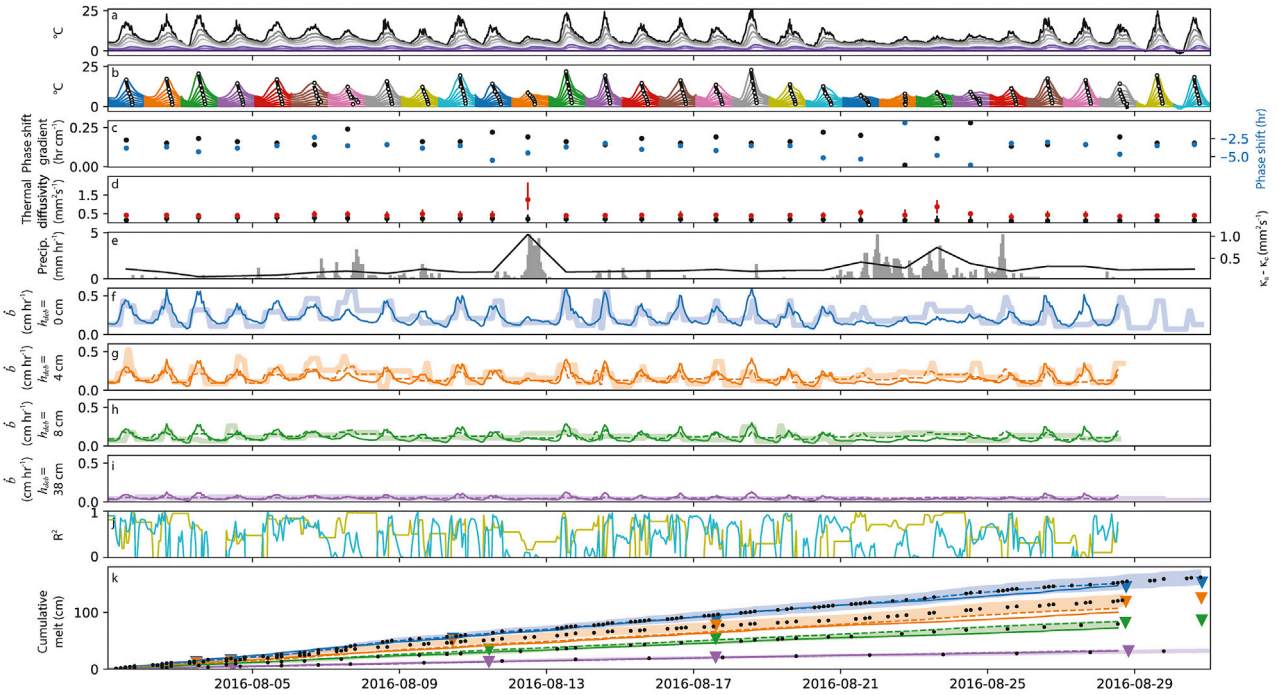

FIGURE 6 | Time-series showing data and model results at locations (1)–(5) in **Figure 1**. **(A)** raw temperature profile data where each line is a temperature record from within the debris cover (4 cm spacing). Black is the surface and dark purple is the debris-ice interface. **(B)** same as **(A)** but smoothed to automate the selection of diurnal maxima and amplitude values. The series is segmented per day (colors). The phase shift gradient is shown: white dots are diurnal maxima and the black line is a least squares linear fit of these points. These gradients are plotted in temperature over time space, but due to the linear spacing of the sensors, is proportional to the time over debris depth gradient **(C)** (black dots). Blue dots in **(C)** are the maximum phase shift in hours between the top surface layer and the bottom of the debris layer. Both values in **(C)** are computed for each day. **(D)** median (dot) and 33–66 percentile range (bar) of apparent thermal diffusivities calculated for each day from two methods: diurnal amplitudes (κ_a, red) and the Biot-Fourier diffusion equation considering only conductive heat transfer (κ_c, black). **(E)** local precipitation rate (grey vertical bars) measured at location (8) in **Figure 1**. The black line scaled by the second *y*-axis is the difference between κ_a and κ_c. **(F–I)** ablation modeled from **Eq. 13** (this study) solid lines; and from **Eq. 14** (Rounce et al., 2021) dashed lines. Measured melt is wide transparent. Colors are the same as **Figures 3–5**: blue, bare glacier ice at **Figure 1** location (5); orange, 4 cm debris thickness (4); green, 8 cm debris thickness (2); and purple, 38 cm debris thickness (1). **(J)** R^2 between the measured and modeled Østrem curve for each time step; turquoise, this study; yellow-green, Rounce et al. (2021). The model following Rounce et al. (2021) was forced with measured bare ice melt and is therefore omitted from **(F)** and not included in the R^2 calculation **(J)**. **(K)** cumulative melt. Selfie stick sub-daily measurements are shown as black dots. Error bounds around measured melt are colored, transparent; and traditional, manual ablation stake measurements are shown as colored triangles. Model results are shown as a solid line (this study), and dashed (Rounce et al., 2021). All colors in **(K)** match **(F–I)**.

debris thicknesses. This solution of debris surface temperature was then used in **Eq. 13** to solve for sub-debris melt where a_{13} was set to the ratio of b_0 and T_s^*, adjusted for each timestep, and b_{13} was set to the ratio of median melt rate measured below 38 cm of debris and median melt rate of bare ice (both medians computed from the entire time-series in this study, shown in **Figure 6**). This means that for this limited 102 h time-series, both methods are prescribed measured bare ice melt rates and will fit the (identical) bare ice validation time-series perfectly. This enables the evaluation of how each method resolves sub-debris melt starting from a perfect solution of bare ice melt, and enables an evaluation of model coefficient stability.

The general results of this experiment are shown in **Figure 5I** and the **Supplementary Video S3** (where three frames are shown at the top of **Figure 5**. Error within the melt measurements make model validation less robust. I do not have complete confidence that instances of notable deviation, for example, measured sub-debris melt being higher below 8 cm of debris than below 4 cm of debris in the morning of August 4th, are correct. Still, both methods preform reasonably well with average R^2 values of 0.85 for **Eq. 14** (Rounce et al., 2021) and 0.71 for **Eq. 13** (**Figure 5L**). Repeating the experiment with the median model coefficient, average R^2 reduces to 0.77 for **Eq. 14** and is 0.50, notably less for **Eq. 13** (**Figure 5M**). Using median model coefficients seems to cause **Eq. 13** to fail dramatically during nights when melt is nearly shut off for all debris thicknesses. Interestingly, these nighttime failures are not necessarily caused by a failure of the surface temperature estimates from **Eq. 12**, which remain stable and accurate for most of the time-series (**Figures 5L,M**). During the night of August 3rd, R^2 of estimated surface temperature crashes, but appears independent of when sub-debris melt is unable to be resolve, for example, the evening of August 1st, afternoon of August 2nd (preceding the surface temperature crash) and the morning of August 11th. Model coefficients appear to remain mostly stable for both methods (**Figures 5J,K**), which is encouraging for the method presented here because this means that the ratios contained within a_{13} and b_{13} are stable, physical relations that can now be prescribed as constants,

TABLE 1 | Cumulative melt ($\sum \dot{b}\Delta t$) from August 1st 2:00 AKDT to August 28th 13:00 AKDT 2016. Difference, in parentheses, is the difference relative to the nearest (±) error bound, where "(0)" means the sum fell within the error bounds.

Location (Figure 1)	h_{deb} (cm)	Measurement		Modeled (This study)			Modeled (Following Rounce et al., 2021)		
		$\sum \dot{b}\Delta t$ (cm)	% of $\sum \dot{b}_0\Delta t$	$\sum \dot{b}\Delta t$ (cm)	Diff. from true (cm)	Diff. |% of true|	$\sum \dot{b}\Delta t$ (cm)	Diff. from true (cm)	Diff. |% of true|
5	0	152 ± 11	100	147	−5 (0)	3	—	—	—
4	4	121 ± 10	80	100	−21 (−11)	17 (10)	107	−14 (−4)	11 (4)
2	8	80 ± 4	53	72	−8 (−4)	10 (5)	84	+4 (0)	5
1	38	31 ± 2	20	32	+1 (0)	3	33	+2 (0)	6

eliminating the need for an explicit solution of $\dot{b}_0$, which **Eq. 14** will always need. By prescribing these ratios as constants, I next apply both approaches to a wider time-series of measurements and evaluate the loss of performance from my method forced with surface temperature and debris thickness alone, against **Eq. 14** forced with measured $\dot{b}_0$.

For the time interval August 1st 2:00 AKDT to August 28th 13:00 AKDT 2016, thermal camera images were not continuously collected, so T_s^* was set to contact thermistor data collected at the surface of the 38 cm debris cover temperature profile (**Sections 3.5**, **3.6**). Using T_s^*, debris thickness and median values of a_{12}, a_{13}, and b_{13} derived above (**Supplementary Table S1**), **Eqs. 12**, **13** were used to estimate sub-debris melt below 0, 4, 8 and 38 cm of debris, where sub-debris was simultaneously measured for validation (**Figures 6F–I**; **Supplementary Video S4**). Forced with measured $\dot{b}_0$ and the median value of a_{14} derived above, **Eq. 14** was also used to estimate sub-debris melt, but only below 4, 8, and 38 cm of debris since melt at 0 cm ($\dot{b}_0$) was used as model input. **Eq. 14** from Rounce et al. (2021) out performs the method presented here (**Figure 6J**) with averaged R^2 values of 0.50 and 0.38 for the two methods, respectively. While the instantaneous fit to Østrem curve measurements have a relatively low R^2, estimated melt summed over the 28 days observation period was close to the measured value (**Figure 6K**; **Table 1**). The largest error was modeled melt falling 11 cm below the lower error bound for summed measured melt at 4 cm debris thickness. Summed melt at the lower error bound was 111 cm, indicating the least accurate melt measurement from the method presented in this study had a 10% error. The bare ice estimate was off by only 5 cm, indicating 3% error from the middle measured value (the estimate fell within the error bounds). Some instances where one, or both, methods performed poorly appear to be non-random, correlating with rainfall (**Figures 6E,J**). The next section considers moisture entering the system and how it could disrupt sub-debris melt estimates.

4.4 Solving for Debris Layer Saturation to Isolate a Source of Sub-debris Melt Estimate Failure

For a statistical glacier melt model framework emphasizing simplicity, minimal input and transferability, there will always be a trade off in performance relative to more sophisticated approaches with more comprehensive input data. Still, it is worthwhile to consider additional data when available to look for patterns of when the simple method fails and if there might be a simple fix, or an approach to infer method confidence as a function of some variable. From the melt modeling experiment conducted in this study, there are numerous instances where the method fails, yet there is an apparent pattern of failure around rain events (**Figures 6E,J**). Evaporative cooling of the debris and interstitial water modifying the thermal properties of the debris layer (Collier et al., 2014) are two possible explanations for the phase shift gradient variability visible in **Figures 6B,C**. While at least one rainy day shows a phase shift gradient that is reduced to near zero, it seems more common that introducing moisture into the debris layer causes more thermal resistance, a more gradual phase shift gradient and an increase in the number of hours it takes diurnal surface warming to reach a depth of 38 cm. During days of heavy rain, apparent thermal diffusivity formulated to include all energy transfer mechanisms, κ_a, spikes while apparent thermal diffusivity considering only conduction, κ_c remains essentially static (**Figure 6D**). Drawing on this observation, the difference between κ_a and κ_c appears to have the potential to be a proxy measure of precipitation, where relative precipitation rate may even be inferred (**Figure 5E**). Emphasizing again a methodology favoring simplicity and minimal field sensor deployment, it might be advantageous to establish a network of surface and sub-debris thermistor strings rather than one or two costly and cumbersome weather stations.

4.5 Improving ASTER Thermal Data for Wide-scale Applications

While I provide evidence in **Section 4.1** suggesting clear days are the least favorable for deriving debris thickness from thermal data (**Figure 4**, August 28 to August 30), it was during these days that two ASTER scenes were acquired concurrently within minutes (a third within hours) of a high resolution, field-based thermal image. The timing of the ASTER images are shown in **Figure 4F** (red dashed vertical lines) and show that the August 28th acquisition narrowly missed the nighttime isothermic state, and captured the August 30th warming limb of the diurnal cycle. The sub-pixel bare ice correction described in **Section 3.7** was applied to each image

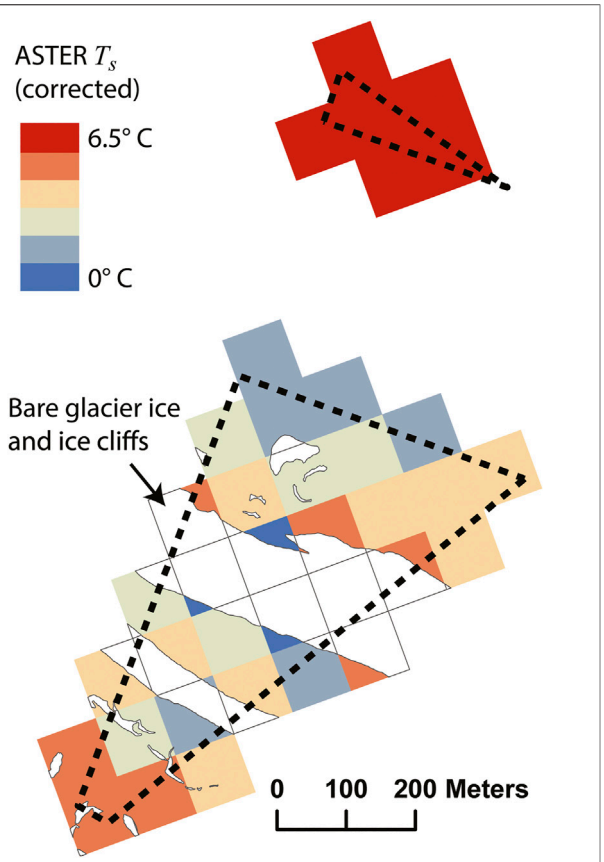

FIGURE 7 | Example of the linear spatial averaging (**Eq. 15**) applied to ASTER surface temperature data. The sub-pixel area and thermal signal of locations known to be bare glacier ice, or ice cliff area, are removed. The dashed line outlines the study site (**Figure 1C**).

(**Figure 7**) and a comparison between ASTER and field-based thermal camera surface temperature data is shown in **Figure 8** where the ASTER data is draped over a local DEM [from Herreid and Pellicciotti (2018)] and obliquely angled to mimic the field of view of the field-based thermal image. While acquired under less favorable conditions, the relation between the ASTER pixels contained within the field of view of the field-based thermal camera image agree with R^2 values of 0.70 and 0.78 for the nighttime August 28 and daytime August 30 images, respectively. The near isothermic state during the night is apparent, yet a thermal delineation can still be made between the near-field 38 cm thick debris cover and the adjacent 8 cm thick debris (segment boundaries are shown in **Figure 1**). The ability of these two ASTER images to replicate high resolution field-based data during less than ideal conditions is promising for satellite based methodologies to derive debris thickness.

5 CONCLUSION

Thermal imagery, particularly from field-based or airborne sensors, have been under utilized in glaciology. In an effort to bring attention to thermal image applications, I have established a series of methods and field experiments using surface temperature data to solve for glacier melt below rock debris in a mountain glacier setting. I begin with a decomposition of the many factors that are entangled within a raw thermal image and describe a method to solve for surface temperature from a field-based, oblique thermal image time-series. My hope is that, instead of appearing discouragingly complicated, future glaciolgists can use this paper, and the accompanying annotated Jupyter notebook as a way to bypass industry focused literature that rarely addresses the specific problems (environmental factors, line of sight distances) encountered in glacier, or more generally, Earth science applications.

The series of field experiments explored in this study build upon one another with standalone methods and results. The first used the tight (dt = 15 min) time-series of thermal imagery, encompassing seven segments with different debris thicknesses, to determine the ideal time of day and meteorological conditions to acquire a thermal image for the purpose of deriving debris thickness. This is a relevant question when designing a field campaign that will collect thermal imagery, in a situation where it is possible to task a satellite or when it would be helpful to know what information can be extracted from the one good image that exists over a particularly cloudy field site. Results from this analysis suggest thermal images acquired below a cloud cover at most times of day, apart from cold nights when all surfaces become isothermal, are best suited to derive high confidence debris thickness estimates. The least favorable time appears to be clear sunny days with cool nights, which is unfortunately the late ablation season conditions when satellite data is the most useful for many applications in glaciology. The closing section of this paper, however, applies a sub-pixel correction to two ASTER thermal images that fall within this least favorable window and the resulting images are promisingly similar to high resolution field-based thermal imagery captured within minutes of the satellite data.

Building on the conceptual framework of when a thermal image would be best suited to derive debris thickness, I applied two methods, and proposed a third, to solve for debris thickness from surface temperature, validated against known debris thickness segments. This approach makes use of the unique, low and consistent dt (relative to satellite data) between thermal images to evaluate how the three methods mitigate diurnal and meteorological variability in order to return a stable-through-time debris thickness output. The method I propose treats part of the thermal image like a model coefficient that is able to absorb the temperature variability and allow the one model coefficient to remain stable through time. The other two established methods perform well when calibrated for each instance, yet have diminished results, by almost 50%, if the set of model coefficients used were optimized only 1 h earlier. Where instantaneous calibration is feasible, all of the methods can confidently capture the relation between an instance of surface temperature and stable debris thicknesses, however, the stability demonstrated in the method proposed here opens new avenues for easy transferability in space and time.

Finally, I build on the application of surface temperature data in glaciology by solving for one of the key unknowns remaining in

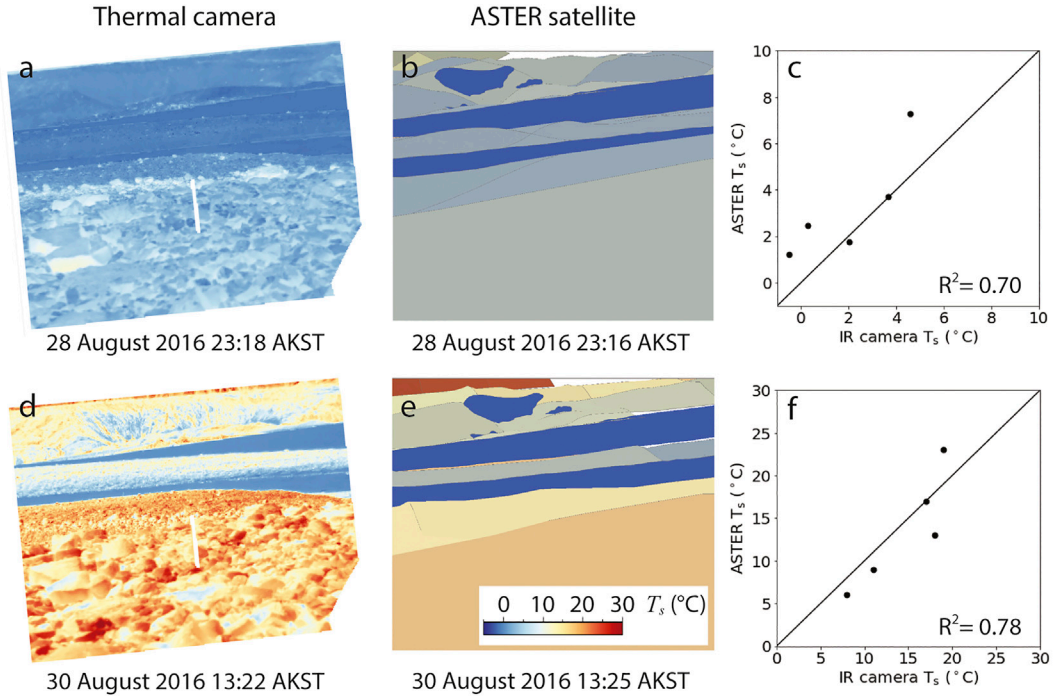

FIGURE 8 | Two image pairs of oblique field-based thermal camera data coupled with space-borne ASTER thermal data that are coincident in time. The ASTER data is draped over a DEM and displayed obliquely to match the view angle of the thermal camera image. The image pair **(A,B)** are coincident in time by 2 min and **(D,E)** are coincident in time by 3 min. Surface temperatures were averaged over the image segments shown in **Figure 1A,B**; regression is shown between the infrared (here shortened to "IR") camera and ASTER thermal data. Bare ice segments were excluded from the regression because the ASTER values were unnaturally set to 0°C from **Eq. 15**. The 1:1 line is plotted for reference. **(C)** corresponds to image pair **(A,B)**; **(F)** corresponds to image pair **(D,E)**. Temperatures in **(A,B,D,E)** are all scaled to the temperature scale in **(E)**.

mountain glacier research, sub-debris melt rates. For this analysis, I partially diverge from using thermal imagery in order to consider a wider time interval where data were available. I use a contact thermistor at the surfaces of a "thick" debris cover and known distributed debris thickness to solve for both bare ice and sub-debris melt. While the sensor is different, the key quantity remains surface temperature which can be measured using either approach. Debris thicknesses were prescribed from measurements, but in future applications at wider scales or where less prior knowledge is available, debris thickness can be derived from one of the methods described in this paper. The method was evaluated alongside an alternative parameterization of sub-debris melt forced, in part, with externally modeled bare ice melt rates, or, for the controlled method evaluation experiment conducted in this study, forced with directly measured bare ice melt rates. Both methods were evaluated against a time-series of sub-daily Østrem curve measurements. While the approach described here using only surface temperature and debris thickness as input was outperformed by the method forced with bare ice melt measurements, this is fairly predictable trade-off of performance for simplicity, and, perhaps surprisingly, the divergence between the two methods and the measured validation data was on the order of a few to 10 cm for summed melt values over a 28 days observation period, equivalent to a maximum error of 10%. Further development and evaluation of this, or a similar approach will likely be able to reduce this error term further. As first steps towards this, I present some approaches to identify instances of debris cover saturation where a temporary alternative parameterization of sub-debris might better fit the apparent altered energy transfer state.

The methods proposed in this study can be implemented at any location on Earth with one good satellite thermal image to derive debris thickness and one local time-series of surface temperature collected at either a location of "thick" debris or a neighboring valley wall. The surface temperature data can be collected either *via* thermal camera or a contact thermistor which is a notably cheap, small and easy sensor to deploy in the field, relative to a traditional weather station, and runs a very low risk of being damaged from wind, bears or other factors that hamper glacier data collection. Further, by burying a thermistor string within the debris layer, it may be possible to solve indirectly for precipitation from apparent thermal diffusivity calculations which further simplifies field sensor deployment. For the next few implementations, model coefficients should be again empirically derived from a network of coincident measurements of debris thickness, surface temperature and sub-debris melt, but if the set of model coefficients prove to remain stable and transferable, especially at different locations on Earth, this will support wider application in space and time with fewer validating measurements.

The methods and comparative results presented in this study offer a new evaluation of what thermal imagery and surface temperature measurements can tell us about a glacier setting. Future studies may be better equipped to make informed methodological choices and have a greater understanding of what information can and possibly cannot be extracted from surface temperature measurements. This study emphasizes simplistic, empirical methods that require minimal input and field data. The intent is to bring method stability and constrained confidence to large-scale problems. Next steps would be to successfully distribute these methods accounting for elevation and constraining a field sensor array that is minimal but adequate. With several well resolved full glaciers, it would become easier to evaluate new and existing methods to derive debris thickness and sub-debris melt from remote sensing data alone and arrive at confident global scale solutions that will aid water resource management and reduce error in glacier sourced eustatic sea level rise estimates.

DATA AVAILABILITY STATEMENT

The raw data supporting the conclusion of this article will be made available by the author, without undue reservation.

AUTHOR CONTRIBUTIONS

The author confirms being the sole contributor of this work and has approved it for publication.

FUNDING

This project, including the publishing fee, was self-funded. A successful proposal to the University of Alaska Fairbanks Technology Advisory Board written during my undergraduate in 2012 provided funding for the FLIR thermal camera. An earlier version of this study was included in my PhD thesis at Northumbria University.

ACKNOWLEDGMENTS

I would like to thank Rebekah Tsigonis Helkenn for her invaluable help in the field and Francesca Pellicciotti for her helpful suggestion on how to appropriately use 2012 data to make up for a 2016 field data deficiency. I would also like to thank Liza Ershova, Lauren Moulder and Ned Rozell for their support of this work. Two reviewers and the Editor, LN, provided very constructive feedback that helped me bring this work to its potential. Finally, I would like to thank Maeberrie Market in Avon-By-The-Sea, New Jersey for providing me with gainful employment as a barista during the pandemic which enabled me to write this paper.

SUPPLEMENTARY MATERIAL

The Supplementary Material for this article can be found online at: https://www.frontiersin.org/articles/10.3389/feart.2021.681059/full#supplementary-material

REFERENCES

Abrams, M., Hook, S., and Ramachandran, B. (2002). Aster User Handbook, Version 2. *Jet propulsion Lab.* 4800, 135.

Anderson, L. S., Armstrong, W. H., Anderson, R. S., and Buri, P. (2021). Debris Cover and the Thinning of Kennicott Glacier, alaska: *In Situ* Measurements, Automated Ice Cliff Delineation and Distributed Melt Estimates. *The Cryosphere* 15, 265–282. doi:10.5194/tc-15-265-2021

Anderson, R. S. (2000). A Model of Ablation-Dominated Medial Moraines and the Generation of Debris-Mantled Glacier Snouts. *J. Glaciol.* 46, 459–469. doi:10.3189/172756500781833025

Anderson, R. S. (1998). Near-surface thermal Profiles in alpine Bedrock: Implications for the Frost Weathering of Rock. *Arctic Alpine Res.* 30, 362–372. doi:10.2307/1552008

Aubry-Wake, C., Baraer, M., McKenzie, J. M., Mark, B. G., Wigmore, O., Hellström, R. Å., et al. (2015). Measuring Glacier Surface Temperatures with Ground-Based thermal Infrared Imaging. *Geophys. Res. Lett.* 42, 8489–8497. doi:10.1002/2015GL065321

Aubry-Wake, C., Zéphir, D., Baraer, M., McKenzie, J. M., and Mark, B. G. (2018). Importance of Longwave Emissions from Adjacent Terrain on Patterns of Tropical Glacier Melt and Recession. *J. Glaciol.* 64, 49–60. doi:10.1017/jog.2017.85

Collier, E., Nicholson, L. I., Brock, B. W., Maussion, F., Essery, R., and Bush, A. B. G. (2014). Representing Moisture Fluxes and Phase Changes in Glacier Debris Cover Using a Reservoir Approach. *The Cryosphere* 8, 1429–1444. doi:10.5194/tc-8-1429-2014

Conway, H., Rasmussen, L., and Nakawo, M. (2000). *Summer Temperature Profiles within Supraglacial Debris on Khumbu Glacier*. Nepal: IAHS PUBLICATION, 89–98.

Evatt, G. W., Abrahams, I. D., Heil, M., Mayer, C., Kingslake, J., Mitchell, S. L., et al. (2015). Glacial Melt under a Porous Debris Layer. *J. Glaciol.* 61, 825–836. doi:10.3189/2015jog14j235

Foster, L. A., Brock, B. W., Cutler, M. E. J., and Diotri, F. (2012). A Physically Based Method for Estimating Supraglacial Debris Thickness from thermal Band Remote-Sensing Data. *J. Glaciol.* 58, 677–691. doi:10.3189/2012jog11j194

Gaussorgues, G. (1994). *Infrared Thermography*. Berlin/Heidelberg, Germany: Springer.

Gillespie, A., Rokugawa, S., Matsunaga, T., Cothern, J. S., Hook, S., and Kahle, A. B. (1998). A Temperature and Emissivity Separation Algorithm for Advanced Spaceborne thermal Emission and Reflection Radiometer (Aster) Images. *IEEE Trans. Geosci. Remote Sensing* 36, 1113–1126. doi:10.1109/36.700995

Goodsell, B., Hambrey, M. J., and Glasser, N. F. (2005). Debris Transport in a Temperate valley Glacier: Haut Glacier d'Arolla, Valais, Switzerland. *J. Glaciol.* 51, 139–146. doi:10.3189/172756505781829647

Herreid, S., and Pellicciotti, F. (2018). Automated Detection of Ice Cliffs within Supraglacial Debris Cover. *The Cryosphere* 12, 1811–1829. doi:10.5194/tc-12-1811-2018

Herreid, S., and Pellicciotti, F. (2020). The State of Rock Debris Covering Earth's Glaciers. *Nat. Geosci.* 13, 621–627. doi:10.1038/s41561-020-0615-0

Hinkel, K. M., Outcalt, S. I., and Nelson, F. E. (1990). Temperature Variation and Apparent thermal Diffusivity in the Refreezing Active Layer, Toolik lake, alaska. *Permafrost Periglac. Process.* 1, 265–274. doi:10.1002/ppp.3430010306

Hopkinson, C., Barlow, J., Demuth, M., and Pomeroy, J. (2010). Mapping Changing Temperature Patterns over a Glacial Moraine Using Oblique thermal Imagery and Lidar. *Can. J. Remote Sensing* 36, S257–S265. doi:10.5589/m10-053

Kraaijenbrink, P. D. A., Bierkens, M. F. P., Lutz, A. F., and Immerzeel, W. W. (2017). Impact of a Global Temperature Rise of 1.5 Degrees Celsius on Asia's Glaciers. *Nature* 549, 257–260. doi:10.1038/nature23878

Kraaijenbrink, P. D. A., Shea, J. M., Litt, M., Steiner, J. F., Treichler, D., Koch, I., et al. (2018). Mapping Surface Temperatures on a Debris-Covered Glacier with an Unmanned Aerial Vehicle. *Front. Earth Sci.* 6, 64. doi:10.3389/feart.2018.00064

Lougeay, R. (1974). "Detection of Buried Glacial and Ground Ice with thermal Infrared Remote Sensing," in *Advanced Con-Cepts and Techniques in the Study of Snow and Ice Resources* (Washington, DC, USA: National Academy of Sciences).

Maghrabi, A., and Al Dajani, H. M. (2013). Estimation of Precipitable Water Vapour Using Vapour Pressure and Air Temperature in an Arid Region in central saudi arabia. *J. Assoc. Arab Universities Basic Appl. Sci.* 14, 1–8. doi:10.1016/j.jaubas.2012.11.001

Mattson, L. (1993). Ablation on Debris Covered Glaciers: an Example from the Rakhiot Glacier, punjab, Himalaya. *Intern. Assoc. Hydrol. Sci.* 218, 289–296.

Mihalcea, C., Brock, B. W., Diolaiuti, G., D'Agata, C., Citterio, M., Kirkbride, M. P., et al. (2008a). Using Aster Satellite and Ground-Based Surface Temperature Measurements to Derive Supraglacial Debris Cover and Thickness Patterns on Miage Glacier (Mont Blanc Massif, italy). *Cold Regions Sci. Tech.* 52, 341–354. doi:10.1016/j.coldregions.2007.03.004

Mihalcea, C., Mayer, C., Diolaiuti, G., D'Agata, C., Smiraglia, C., Lambrecht, A., et al. (2008b). Spatial Distribution of Debris Thickness and Melting from Remote-Sensing and Meteorological Data, at Debris-Covered Baltoro Glacier, Karakoram, pakistan. *Ann. Glaciol.* 48, 49–57. doi:10.3189/172756408784700680

Nicholson, L. I., McCarthy, M., Pritchard, H. D., and Willis, I. (2018). Supraglacial Debris Thickness Variability: Impact on Ablation and Relation to Terrain Properties. *The Cryosphere* 12, 3719–3734. doi:10.5194/tc-12-3719-2018

Nicholson, L., and Mertes, J. (2017). Thickness Estimation of Supraglacial Debris above Ice Cliff Exposures Using a High-Resolution Digital Surface Model Derived from Terrestrial Photography. *J. Glaciol.* 63, 989–998. doi:10.1017/jog.2017.68

Østrem, G. (1959). Ice Melting under a Thin Layer of Moraine, and the Existence of Ice Cores in Moraine Ridges. *Geografiska Annaler* 41, 228–230. doi:10.1080/20014422.1959.11907953

Passman, S., and Larmore, L. (1956). *Atmospheric Transmission*. Santa Monica, CA: Tech. rep., Rand Corp Santa Monica CA.

Ragettli, S., Pellicciotti, F., Immerzeel, W. W., Miles, E. S., Petersen, L., Heynen, M., et al. (2015). Unraveling the Hydrology of a Himalayan Catchment through Integration of High Resolution *In Situ* Data and Remote Sensing with an Advanced Simulation Model. *Adv. Water Resour.* 78, 94–111. doi:10.1016/j.advwatres.2015.01.013

Ranzi, R., Grossi, G., Iacovelli, L., and Taschner, S. (2004). "Use of Multispectral Aster Images for Mapping Debris-Covered Glaciers within the Glims Project," in *Geoscience and Remote Sensing Symposium, 2004. IGARSS'04. Proceedings. 2004 IEEE International* (IEEE), 1144–1147.

Rounce, D., and McKinney, D. (2014). Debris Thickness of Glaciers in the everest Area (nepal Himalaya) Derived from Satellite Imagery Using a Nonlinear Energy Balance Model. *The Cryosphere* 8, 1317–1329. doi:10.5194/tc-8-1317-2014

Rounce, D. R., Hock, R., McNabb, R. W., Millan, R., Sommer, C., Braun, M. H., et al. (2021). Distributed Global Debris Thickness Estimates Reveal Debris Significantly Impacts Glacier Mass Balance. *Geophys. Res. Lett.* 48, e2020GL091311. doi:10.1029/2020GL091311

Rounce, D. R., King, O., McCarthy, M., Shean, D. E., and Salerno, F. (2018). Quantifying Debris Thickness of Debris-Covered Glaciers in the everest Region of nepal through Inversion of a Subdebris Melt Model. *J. Geophys. Res. Earth Surf.* 123, 1094–1115. doi:10.1029/2017JF004395

Rowan, A. V., Nicholson, L. I., Quincey, D. J., Gibson, M. J., Irvine-Fynn, T. D. L., Watson, C. S., et al. (2021). Seasonally Stable Temperature Gradients through Supraglacial Debris in the everest Region of nepal, central Himalaya. *J. Glaciol.* 67, 170–181. doi:10.1017/jog.2020.100

Schauwecker, S., Rohrer, M., Huggel, C., Kulkarni, A., Ramanathan, A., Salzmann, N., et al. (2015). Remotely Sensed Debris Thickness Mapping of Bara Shigri Glacier, Indian Himalaya. *J. Glaciol.* 61, 675–688. doi:10.3189/2015jog14j102

Spampinato, L., Calvari, S., Oppenheimer, C., and Boschi, E. (2011). Volcano Surveillance Using Infrared Cameras. *Earth-Science Rev.* 106, 63–91. doi:10.1016/j.earscirev.2011.01.003

Steiner, J. F., Litt, M., Stigter, E. E., Shea, J., Bierkens, M. F. P., and Immerzeel, W. W. (2018). The Importance of Turbulent Fluxes in the Surface Energy Balance of a Debris-Covered Glacier in the Himalayas. *Front. Earth Sci.* 6, 144. doi:10.3389/feart.2018.00144

Tattersall, G. (2017). *Thermimage: Thermal Image Analysis*.

TŸč, M., and Gohlke, C. (2015). *Imreg Dft*.

Usamentiaga, R., Venegas, P., Guerediaga, J., Vega, L., Molleda, J., and Bulnes, F. (2014). Infrared Thermography for Temperature Measurement and Non-destructive Testing. *Sensors* 14, 12305–12348. doi:10.3390/s140712305

Wang, J., Lee, W. F., and Ling, P. P. (2020). Estimation of thermal Diffusivity for Greenhouse Soil Temperature Simulation. *Appl. Sci.* 10, 653. doi:10.3390/app10020653

Conflict of Interest: The author declares that the research was conducted in the absence of any commercial or financial relationships that could be construed as a potential conflict of interest.

frontiers in Earth Science

ORIGINAL RESEARCH
published: 01 October 2021
doi: 10.3389/feart.2021.709957

Debris Emergence Elevations and Glacier Change

Joseph M. Shea[1]*, *Philip D. A. Kraaijenbrink*[2], *Walter W. Immerzeel*[2] and *Fanny Brun*[3]

[1]Department of Geography, Earth, and Environmental Science, University of Northern British Columbia, Prince George, BC, Canada, [2]Department of Physical Geography, Utrecht University, Utrecht, Netherlands, [3]Université Grenoble Alpes, CNRS, IRD, Grenoble, France

Debris-covered glaciers represent potentially significant stores of freshwater in river basins throughout High Mountain Asia (HMA). Direct glacier mass balance measurements are extremely difficult to maintain on debris-covered glaciers, and optical remote sensing techniques to evaluate annual equilibrium line altitudes (ELAs) do not work in regions with summer-accumulation type glaciers. Surface elevation and glacier velocity change have been calculated previously for debris-covered glaciers across the region, but the response of debris cover itself to climate change remains an open question. In this research we propose a new metric, i.e. the debris emergence elevation (Z_{DE}), which can be calculated from a combination of optical and thermal imagery and digital elevation data. We quantify Z_{DE} for 975 debris-covered glaciers in HMA over three compositing periods (1985–1999, 2000–2010, and 2013–2017) and compare Z_{DE} against median glacier elevations, modelled ELAs, and observed rates of both mass change and glacier velocity change. Calculated values of Z_{DE} for individual glaciers are broadly similar to both median glacier elevations and modelled ELAs, but slightly lower than both. Across the HMA region, the average value of Z_{DE} increased by 70 +/− 126 m over the study period, or 2.7 +/− 4.1 m/yr. Increases in Z_{DE} correspond with negative mass balance rates and decreases in glacier velocity, while glaciers and regions that show mass gains and increases in glacier velocity experienced decreases in Z_{DE}. Regional patterns of Z_{DE}, glacier mass balance, and glacier velocities are strongly correlated, which indicates continued overall increases in Z_{DEE} and expansion of debris-covered areas as glaciers continue to lose mass. Our results suggest that Z_{DE} is a useful metric to examine regional debris-covered glacier changes over decadal time scales, and could potentially be used to reconstruct relative mass and ELA changes on debris-covered glaciers using historical imagery or reconstructed debris cover extents.

Keywords: glacier, debris cover, mass balance, velocity, High Mountain Asia

OPEN ACCESS

Edited by:
Aparna Shukla,
Ministry of Earth Sciences, India

Reviewed by:
William Armstrong,
Appalachian State University, United States
David Rounce,
Carnegie Mellon University, United States

***Correspondence:**
Joseph M. Shea
joseph.shea@unbc.ca

Specialty section:
This article was submitted to Cryospheric Sciences, a section of the journal Frontiers in Earth Science

Received: *14 May 2021*
Accepted: *16 September 2021*
Published: *01 October 2021*

Citation:
Shea JM, Kraaijenbrink PDA, Immerzeel WW and Brun F (2021) Debris Emergence Elevations and Glacier Change. Front. Earth Sci. 9:709957. doi: 10.3389/feart.2021.709957

INTRODUCTION

Glacier changes in High Mountain Asia (HMA; **Figure 1**) have been quantified through *in situ* glaciological measurements (Vincent et al., 2013; Wagnon et al., 2013; Azam et al., 2016), surface elevation differencing (Bolch et al., 2011; Gardelle et al., 2012; Wang et al., 2014; Kääb et al., 2015; Maurer et al., 2016; Brun et al., 2017; Maurer et al., 2019; Shean et al., 2020), models of glacier mass balance (Braun et al., 1993; Collier et al., 2013; Shea et al., 2015; Engelhardt et al., 2017), and changes in glacier velocity (Dehecq et al., 2019). Annual equilibrium line altitudes (ELAs), the elevation where annual mass balance (b_a) equals zero, are highly correlated with annual net glacier

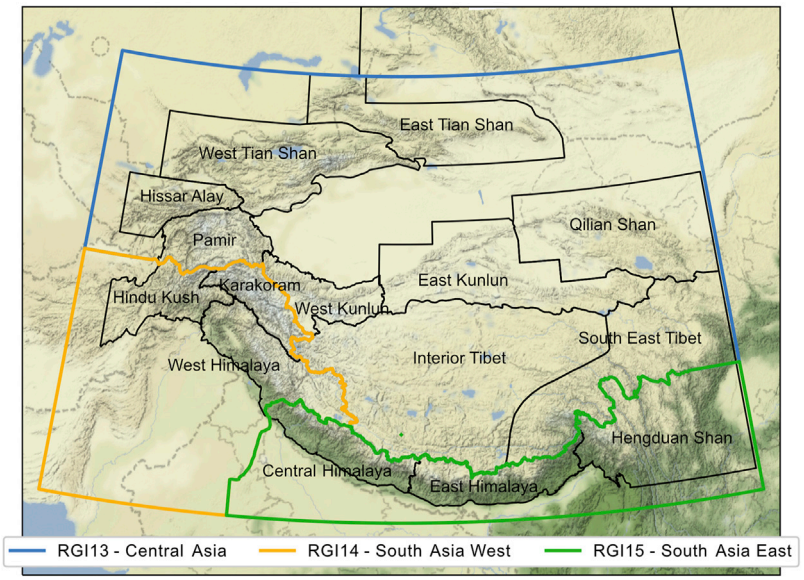

FIGURE 1 | Study area map with Randolph Glacier Inventory regions **(Table 1)** and High Mountain Asia sub-regions **(Table 2)**.

mass balance (B_a; (Yinsheng et al., 1998; Benn and Lehmkuhl, 2000; Rabatel et al., 2017), and are also a key indicator of the glacier status.

On temperate mid-latitude glaciers, ELAs can be inferred from the elevation of the transient snowline at the end of the ablation season (Rabatel et al., 2005; Rabatel et al., 2013; Shea et al., 2013) or glacier reflectivity (Brun et al., 2015). In tropical/subtropical regions where accumulation and ablation occur simultaneously, the transient snowline is not correlated to the ELA (Ageta and Higuchi, 1984; Brun et al., 2015). Median glacier elevations (Z_{med}) are highly correlated with glaciologically determined ELAs (Carrivick and Brewer, 2004; Machguth et al., 2012), though the exact relation varies with glacier type and region (Braithwaite, 1984) and the presence of debris cover (Owen and Benn, 2005; Robson et al., 2016).

Debris-covered glaciers are defined as glaciers with a layer of supraglacial debris that covers some portion of their tongue (Cogley et al., 2011). They are common in many mountain regions (Alaska, European Alps, New Zealand, Coast Ranges of British Columbia, and the Andes), and in High Mountain Asia it is estimated that 10% of the total glacierized area is covered by debris (Scherler et al., 2011; Kraaijenbrink et al., 2017; Scherler et al., 2018). Debris is introduced to the glacier through either mass movements onto the glacier surface from adjoining rock walls or lateral moraines (rockfall, debris flow), or subglacial erosion (Kirkbride, 2011). Supraglacial or englacial debris is then transported down-glacier and becomes thickest at lower elevations where ablation rates are typically highest for debris-free glaciers (Benn and Ballantyne, 1994; van Woerkom et al., 2019). Changes in debris-covered area have been used to infer relative glacier status (Herreid et al., 2015) within HMA, but as glaciological mass balance measurements on debris-covered glaciers are notoriously difficult to maintain, there are few direct estimates of ELAs and glacier mass balance on debris-covered glaciers.

Observational and modelling studies demonstrate that the presence of a debris cover leads to longer glacier lengths and lower accumulation area ratios (AAR; (Scherler, Bookhagen and Strecker, 2011; Anderson and Anderson, 2016; Banerjee, 2017). In a warming climate, increased melt and decreased accumulation will lead to higher ELAs and transient decreases in AAR, reduced ice transport and glacier velocities, and increased ice ablation and mass loss (Shea and Immerzeel, 2016; Dehecq et al., 2019). We hypothesize that debris-covered glaciers with increased mass loss would experience accelerated debris melt-out and locally enhanced ablation rates. This will lead to an up-glacier expansion of the debris-covered area, and Z_{DE} should increase. Conversely, debris-covered glaciers experiencing mass gain (Sakai and Fujita, 2017; de Kok et al., 2018; Farinotti et al., 2020) would exhibit increased ice transport from higher elevations and decreases in Z_{DE}.

Expansion or contraction of Z_{DE} will likely occur over decadal time scales (Anderson and Anderson, 2016) and changes in Z_{DE} could thus be used to infer long-term trends in glacier mass balance as an alternative or complementary approach to geodetic methods based on DEM differencing. Using existing glacier inventories (Pfeffer et al., 2014) and a method for debris cover delineation (Kraaijenbrink et al., 2017), we construct composites of debris cover for three time periods and extract values of Z_{DE} for individual debris-covered glaciers in HMA. We then examine relations between Z_{DE}, median glacier elevations, modelled ELAs, and observed mass balances and velocity changes.

DATA AND METHODS

To examine changes in debris cover and Z_{DE}, debris masks were calculated for three different time periods (1985–1999;

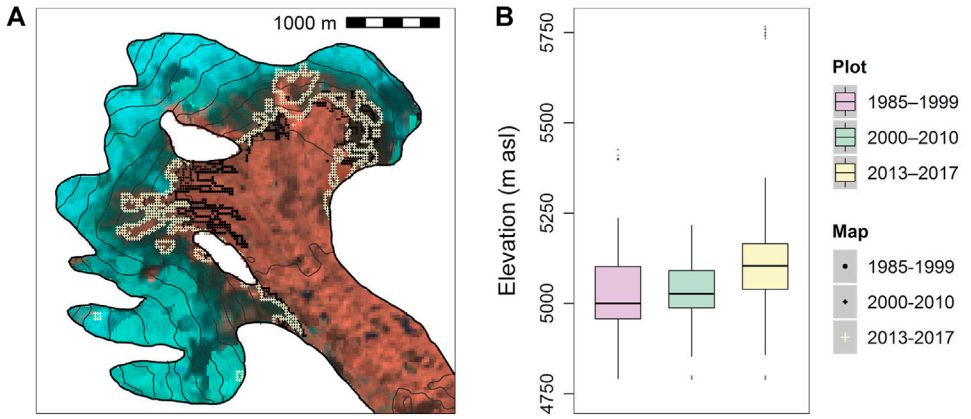

FIGURE 2 | Example of a debris-covered glacier (RGI50-15.02637, 90.51N, 28.04E), with **(A)** two delineations of ice/debris, and **(B)** boxplots of extracted elevations.

2000–2010; 2013–2017) using both optical and thermal imagery. Elevation data from the Shuttle Radar Topography Mission (SRTM, collected in 2000) was then used to calculate elevation statistics for debris-covered portions of each HMA glacier in the Randolph Glacier Inventory (Pfeffer et al., 2014). Modelled (Kraaijenbrink et al., 2017) and observed mass balance rates (Brun et al., 2017) and trends in glacier velocity (Dehecq et al., 2019) for individual debris-covered glaciers were used to independently evaluate the trends in Z_{DE}. While the total number of debris-covered glaciers in HMA is over 7,000, our analysis includes only 1) debris-covered glaciers larger than 5 km^2 to match the analysis of Dehecq et al., (2018), and 2) glaciers that have more than 10% of their area below the median elevation covered by debris.

Debris Cover Masks

Debris cover masks were mapped for all HMA glaciers using RGI glacier extents and a normalized difference snow index (NDSI; Hall et al., 1995) calculated from multi-year composites of Landsat imagery (www.usgs.gov). We preferentially select pixels with the highest surface brightness temperatures to construct the NDSI mosaics, which will reduce classification errors due to clouds, shadows, or the presence of snow. An NDSI threshold of 0.25 was then used to classify pixels within RGI glacier extents as either snow/ice (NDSI>0.25) or debris (NDSI<0.25). The classification procedure was performed in Google Earth Engine (GEE) and full details on the classification algorithm and accuracy are given in Kraaijenbrink et al. (2017; https://doi.org/10.5281/zenodo.2548690). Glacier IDs were assigned to each debris-covered glacier in the analysis using the Randolph Glacier Inventory (RGI V5; RGI Consortium, 2017), and a resulting geodatabase was created and populated with data from this analysis and from other sources (see below). The average date and day of year (DOY) of acquisition for each glacier was also extracted from GEE and assigned to the geodatabase (**Supplementary Figures S1, S2**), and used to assess temporal trends in Z_{DE} and the possibility of bias related to the DOY of acquisition.

Median Glacier Elevation, Debris Emergence Elevation, and Modelled ELA

For each glacier retained in the analysis, a median glacier elevation (Z_{med}) was extracted from the gap-filled, 90 m resolution SRTM V3.0 elevation data that was collected in February 2000 (Farr et al., 2007). While SRTM accuracy decreases with increasing slope angle (Mukul et al., 2017), the debris-covered glaciers we focus on typically have lower angle slopes. To estimate Z_{DE}, the boundary between debris-free and debris-covered ice was mapped as a polyline, and the median elevation of this contour was extracted from SRTM data (**Figure 2**). Taking this conservative approach ensures that narrow medial moraines which can extend far up-glacier (or conversely, bare ice patches that extend downglacier) do not affect the determination of Z_{DE}. Alternative approaches for estimation of Z_{DE} (such as using percentiles of elevation for debris-covered pixels) were tested but these produced a wider range of possible values (**Supplementary Material**), and did not correspond to other ELA metrics (see below). A modelled ELA (ELA_{mod}) for each glacier, based on mass balance gradient constructed from a degree-day climatology, gridded precipitation (Kraaijenbrink et al., 2017), and the SRTM data, is included as a comparison against median glacier elevations and Z_{DE}. Values of Z_{med}, Z_{DE}, and ELA_{mod} were assigned to each debris-covered glacier in the geodatabase.

Rates of Change: Z_{DE}

Rates of Z_{DE} change (dZ_{DE}/dt; m yr^{-1}) were calculated for each glacier using a linear regression between the glacier-averaged dates of acquisition for the debris cover composites and the corresponding value of Z_{DE}. Positive values of dZ_{DE}/dt indicate an increase in Z_{DE} and are likely associated with increased ELAs, more negative net mass balances, and decreased glacier velocities (Dehecq et al., 2019). Negative values of dZ_{DE}/dt indicate decreased ELAs and positive mass balances or glacier surges. To exclude both surge-type glaciers and other outliers from affecting our analysis, dZ_{DE}/dt values greater than or less than

two standard deviations from the mean (5% of all glaciers) were removed prior to analysis and plotting.

Rates of Change: Glacier Mass Balance

Rates of mass change between 2000 and 2016 have been calculated previously for 6,350 glaciers in the HMA region using time series of digital elevation models constructed from re-processed ASTER imagery (Brun et al., 2017). Linear regressions of surface elevation against time were performed for each 30-m glacierized pixel, and outliers were excluded to calculate trends in surface elevation (m yr^{-1}). For each glacier, surface elevation trends were aggregated to 100 m elevation bands, and then converted to net glacier mass change with an assumed density of 850 kg m^{-3} (Huss, 2013). Net glacier mass balances calculated by Brun et al. (2017) were then merged with the debris-covered database of this study on the RGI V5 glacier ID.

Rates of Change: Glacier Velocity

For each debris-covered glacier in our database, we assign a change in glacier velocity using the dataset produced by Dehecq et al. (2019). Systematic surface feature tracking was applied to a database of Landsat-7 pairs between 1999 and 2017 to estimate gridded annual surface velocities at a grid resolution of 240 m. Trends in glacier velocity were then calculated from the annual velocity estimates, and extrapolated to the year 2000 to establish an initial velocity field. The median percent change in glacier velocity from 2000 to 2016 for each RGI glacier was then extracted from all grid points below the median glacier elevation, and we merge this final dataset with our geodatabase on the RGI ID. Full details on the calculation of glacier velocity changes and their uncertainties can be found in Dehecq et al. (2019).

Analyses

The total number of debris covered glaciers mapped for this analysis is $N = 7{,}457$. We exclude debris-covered glaciers less than 5 km^2 to match the glacier velocity inventory of Dehecq et al. (2018), and we also exclude glaciers where the debris covered area is less than 10% of the area below the ELA, which leaves $N = 976$. RGI regions 13 (South Asia East), 14 (South Asia West) and 15 (Central Asia) are used to broadly classify the studied glaciers, and reflect substantial differences in climate and topography (**Figure 1**). We first examine distributions of Z_{med}, Z_{DE}, and ELA_{mod}. Rates of Z_{DE} change are then compared with observed rates of mass change within each region. We also compare the spatial pattern of dZ_{DE}/dt with the spatial pattern of geodetic mass balances (Brun et al., 2017) and trends in glacier velocity (Dehecq et al., 2019). We then subdivide the RGI regions into smaller sub-regions based on mountain ranges identified in Kraaijenbrink et al. (2017) and compare sub-regional means.

RESULTS

Median Glacier Elevation, Debris Emergence Elevation, and Modelled ELA

Distributions of Z_{med}, Z_{DE}, and ELA_{mod} (**Figure 3**) show strong similarities within all three RGI regions, which supports the use of dZ_{DE}/dt as a metric of glacier change. Differences between regions highlight the climatic and geomorphic factors that determine glacier size and shape (**Table 1**). The highest values for all three metrics are found in South Asia (East), which contains some of the highest elevation mountains in the world. Continental glaciers on the colder and drier Tibetan Plateau and in the Tien Shan mountains (Central Asia) have the lowest values for all three metrics. Bi-modal distributions of Z_{med}, Z_{DE}, and ELA_{mod} are also found in Central Asia, which may indicate strong climatic differences (e.g. mountain vs. plateau) within the region. South Asia (West), which includes the Pamir and Karakoram ranges, is influenced by both the monsoon and westerly disturbances in winter. Elevations of Z_{med}, Z_{DE}, and ELA_{mod} for debris-covered glaciers in South Asia (West) are between the values found for Central Asia and South Asia (East).

Values of Z_{DE} are systematically lower than both ELA_{mod} and Z_{med} (**Table 1**) by approximately 150–250 m. Standard deviations of the regional Z_{DE} averages ranged between 361 and 571 m, which is consistent with the standard deviations in mean Z_{med} (370–560 m) and ELA_{mod} (403–559 m).

Changes in Z_{DE}

In all RGI regions, the average value of Z_{DE} increased from early to late periods (**Table 1**; **Figure 4**). To further quantify changes in Z_{DE} through time for each debris-covered glacier, we calculate 1) simple differences in Z_{DE} between periods (early to middle, and middle to late), and 2) the linear trend through time (dZ_{DE}/dt; with units of m/yr) over all three compositing periods, using the average acquisition dates and the observed changes in Z_{DE} at each glacier. In Central Asia, an average Z_{DE} increase of 49 m was observed between the composite midpoints 1990 and 2014. In South Asia (West) and South Asia (East), average Z_{DE} increases of 39 and 110 m were observed, respectively, over the same period. In South Asia (West), average values of Z_{DE} increased 65 m between early and middle periods, and decreased 26 m between the 2005 and 2014 midpoints. This decrease in Z_{DE} corresponds with the decadal scale mass changes and corresponding decreases in temperature and increases in precipitation observed in the region by Hugonnet et al. (2021).

Changes in Z_{DE} between compositing periods (**Figure 4A**) show a range of debris-covered glacier responses. For Central Asia and South Asia (East), changes in Z_{DE} are more positive between the middle and late periods. A clear decrease in Z_{DE} can be seen in South Asia (West) in the later period, which suggests either increased ice fluxes or decreased ablation on the glacier termini. Glaciers in this region, which includes the Karakoram and Kunlun Shan ranges, have well-documented anomalous mass gains or neutral mass balances (Hewitt, 2005; Brun et al., 2017; de Kok et al., 2018; Shean et al., 2020). As South Asia (West) contains a large number of surging glaciers (Hewitt, 2005; Quincey et al., 2011) it is also possible that our filtering process does not eliminate surging glaciers completely from the analysis. A glacier surge phase would likely affect Z_{DE} and would be interpreted as a mass gain and velocity acceleration at the terminus.

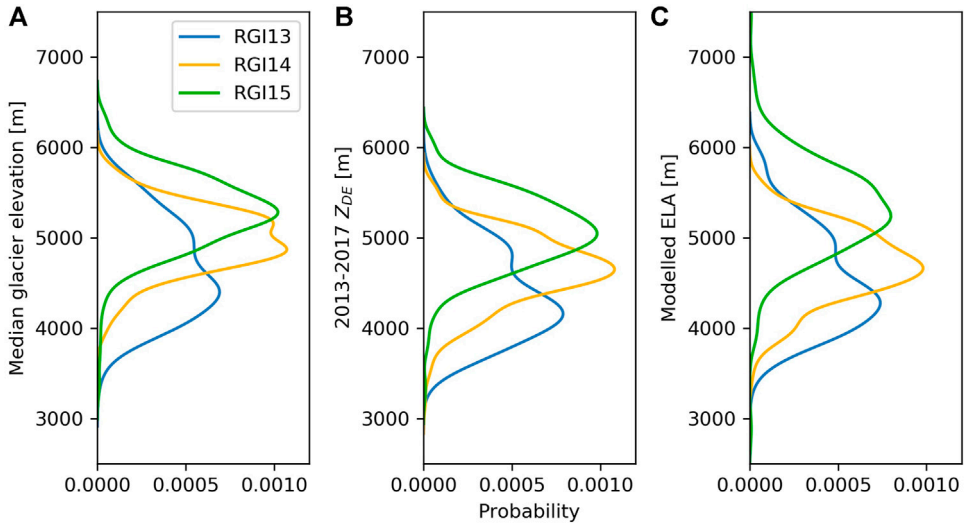

FIGURE 3 | Distributions of **(A)** median glacier elevation derived from SRTM data, **(B)** median elevation of Z_{DE} 2013–2017, and **(C)** modelled equilibrium line altitude (Kraaijenbrink et al., 2017) for three RGI regions in HMA.

TABLE 1 | Average ($\underline{x}$), standard deviation (σ), and sample size (N) of Z_{med}, ELA_{mod}, and Z_{DE} for three different composite periods, stratified by RGI region. Median glacier elevation is based on the 2000 SRTM data, and ELA_{mod} is based on 1996–2014 climatology.

	Z_{med} (m)	ELA_{mod} (m)	Z_{DE} (m)			N
	$\underline{x}$ (σ)	$\underline{x}$ (σ)	1985–1999 $\underline{x}$ (σ)	2001–2010 $\underline{x}$ (σ)	2013–2017 $\underline{x}$ (σ)	
Central Asia (RGI13)	4667 (502)	4535 (532)	4342 (502)	4369 (478)	4392 (496)	358
South Asia West (RGI14)	4976 (350)	4976 (399)	4601 (388)	4678 (359)	4643 (390)	349
South Asia East (RGI15)	5274 (418)	5274 (418)	4930 (460)	5029 (413)	5065 (400)	267

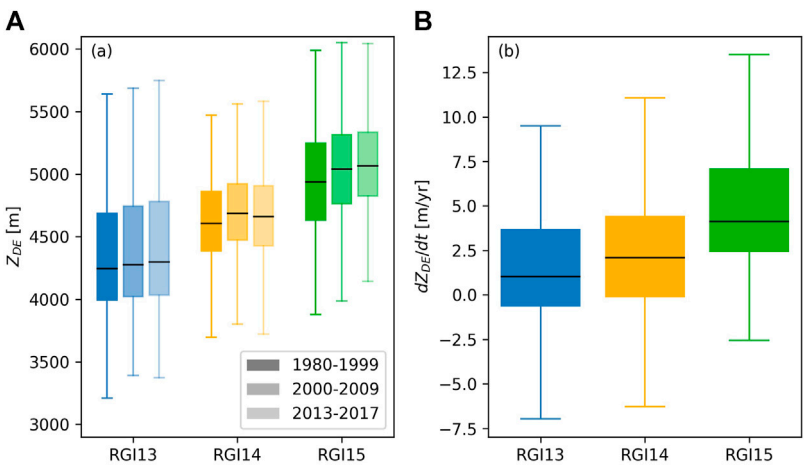

FIGURE 4 | (A) boxplots of Z_{DE} by RGI region and compositing period, and **(B)** boxplots of debris emergence elevation trends (dZ_{DE}/dt; m yr^{-1}) by RGI region over the period 1980–2017.

Median values of dZ_{DE}/dt are positive (increasing Z_{DE} over time) in all three HMA regions, with the greatest rates observed in South Asia East (**Figure 4B**). Values of dZ_{DE}/dt for individual glaciers range between −10 and +20 m/yr. These trends are in agreement with observed and projected rates of changes in both ELA and seasonal snowline elevations (Pandey et al., 2013; Hasson et al., 2014; Huss and Hock, 2015; Shea et al., 2015; Viste and Sorteberg, 2015; Pieczonka et al., 2018)

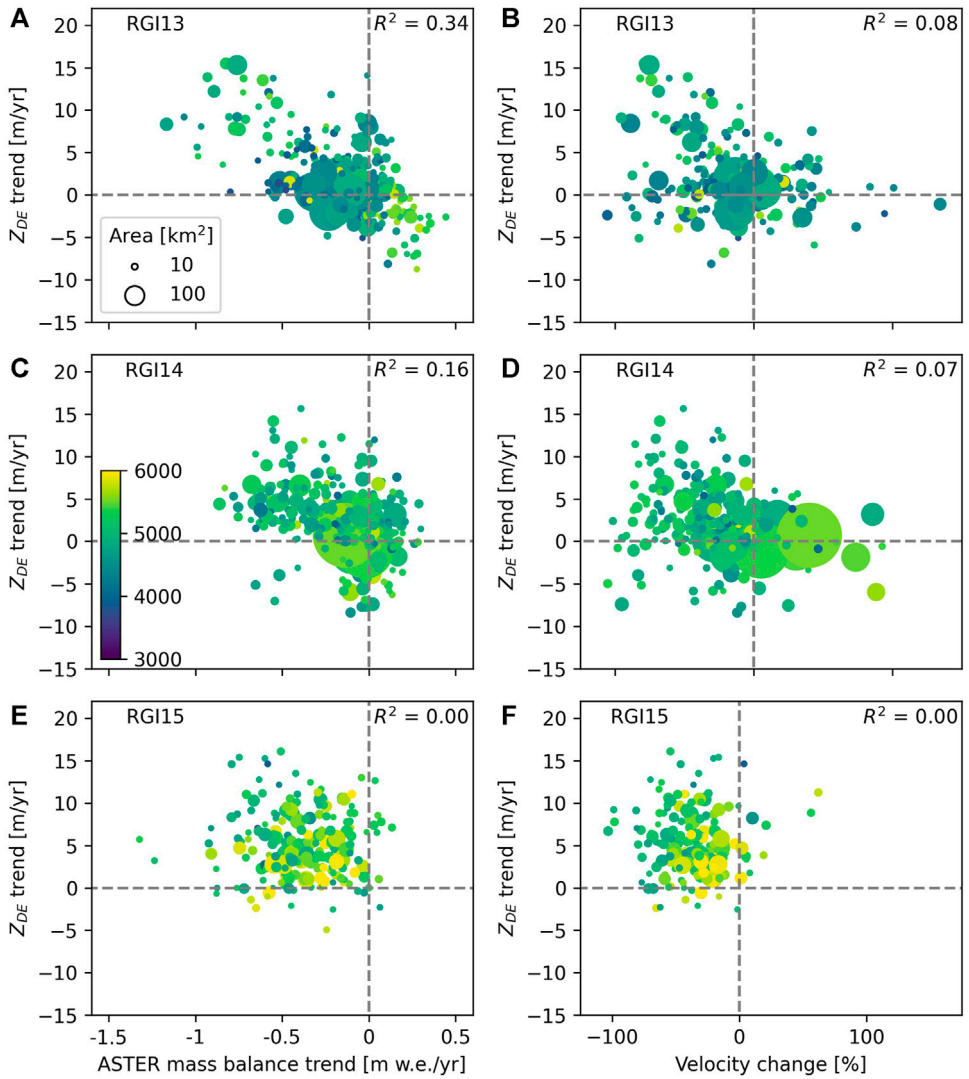

FIGURE 5 | Left column: calculated rates of changes in Z_{DE} (m yr^{-1}) vs. ASTER mass balance trends (m w.e. yr^{-1}; from Brun et al., 2017) for **(A)** Central Asia (RGI13), **(C)** South Asia West (RGI14), and **(E)** South Asia East (RGI15). Right column: calculated rates of changes in Z_{DE} (m yr^{-1}) vs. median change in glacier surface velocity from 2000 to 2016 (%; from Dehecq et al., 2019). Points are scaled to the area of the individual glaciers, and coloured by the median glacier elevation.

Mass Balance, Glacier Velocity, and Z_{DE}

Changes in Z_{DE} should relate directly to changes in glacier mass balances and glacier velocities, as ice flux and ablation control the melt out and emergence of englacial debris. Increased mass loss and a corresponding decrease in glacier velocity would concentrate englacial debris at the surface at the upper limit of the debris-covered area and lead to increases in Z_{DE}. To test this hypothesis, we compare individual rates of Z_{DE} change with observed geodetic glacier mass balances and changes in glacier velocity (**Figure 5**) in each RGI region.

Glaciers in Central Asia and South Asia (West) exhibit statistically significant relations between net mass balance and Z_{DE} trends (R^2 = 0.18–0.35), but this relation is weak or non-existent in South Asia (East; R^2 = 0.00; **Figure 5**). Median glacier elevation and glacier area do not appear to affect the relation between dZ_{DE}/dt and net mass balance. Similar relations are observed between Z_{DE} and changes in glacier velocity (**Figure 5**), though velocity changes and Z_{DE} are not as closely linked as mass balance (R^2 = 0.08 for both Central Asia and South Asia West). Debris-covered glaciers that are stable or gaining mass typically show decreases in Z_{DE}, and a mixed velocity response.

Glaciers in South Asia (East) have considerably thinned and retreated in recent decades, and have relatively fewer glaciers that exhibit mass gains. The lack of significant relations between mass balance and Z_{DE} and glacier velocity and Z_{DE} may simply indicate a sampling bias, or the fact that debris-covered glaciers in advanced state of recession will tend to have more variable changes in Z_{DE}. Alternatively, the debris cover mask in South Asia (East) may be less reliable due to monsoon cloud cover which dominates South Asia (East) more than the other regions.

TABLE 2 | Regional and sub-regional trends in Z_{DE}, mass balance, and velocity for debris covered glaciers with a total area greater than 5 km^2. Values given are mean +/– standard deviation.

Region	ID	Subregion	*N*	dZ_{DE}/dt (m yr^{-1})	mass balance (m w.e. yr^{-1})	change in velocity (%)
Central Asia (RGI13)			343	1.73 ± 4.0	-0.14 ± 0.26	-15.6 ± 44.1
RGI13	WKL	Kunlun Shan W	29	–2.8 ± 2.8	0.22 ± 0.10	0.9 ± 39.3
RGI14	EKL	Kunlun Shan E	10	–0.5 ± 2.5	0.11 ± 0.09	–25.6 ± 0
RGI13	SET	South and East Tibet	41	8.4 ± 3.7	–0.58 ± 0.26	–47.4 ± 10.5
RGI13	INT	Interior Tibet	3	1.3 ± 1.5	–0.32 ± 0.11	7.2 ± 14.3
RGI13	ETS	Tien Shan E	5	3.4 ± 2.6	–0.40 ± 0.13	–47.4 ± 10.5
RGI13	WTS	Tien Shan W	93	1.0 ± 2.8	–0.17 ± 0.17	–1.8 ± 57.7
RGI13	QSH	Qilian Shan	0	-	-	-
RGI13	PAM	Pamir Alay	140	1.6 ± 2.9	–0.10 ± 0.16	–20.5 ± 35.4
RGI14	HIA	Hissar Alay	22	–0.1 ± 2.0	–0.06 ± 0.10	–23.4 ± 15.9
South Asia (West) RGI14			342	2.2 ± 3.9	–0.17 ± 0.24	–28.5 ± 39.5
RGI14	KRK	Karakoram	180	0.7 ± 3.6	–0.02 ± 0.12	–18.1 ± 46.6
RGI14	HKU	Hindu Kush	43	3.0 ± 2.4	–0.13 ± 0.15	–18.1 ± 23.7
RGI14	WHL	Himalaya W	121	4.2 ± 3.7	–0.42 ± 0.19	–45.0 ± 25.8
South Asia East (RGI15)			242	4.9 ± 3.7	–0.38 ± 0.24	–36.6 ± 23.9
RGI15	EHL	Himalaya E	85	3.5 ± 2.9	–0.38 ± 0.18	–31.7 ± 18.2
RGI15	CHL	Himalaya C	110	5.8 ± 3.6	–0.31 ± 0.18	–31.9 ± 22.0
RGI15	HSH	Hengduan Shan	45	5.3 ± 4.5	–0.55 ± 0.34	–60.3 ± 26.2
ALL			928	2.7 ± 4.1	–0.22 ± 0.26	–26.5 ± 44.1

Regional and Sub-Regional Trends

At the sub-regional scale (**Supplementary Figures S4, S5**, **Table 2**), relations between dZ_{DE}, glacier mass balance, and glacier velocity for individual glaciers exhibit a greater degree of variability, yet the same basic relations exist. Sub-regions with positive net mass balances and increasing glacier velocities (Karakoram and Kunlun Shan W) notably have stable or decreasing Z_{DE} through time. All other regions, which exhibit mass losses and velocity decreases, show increases in Z_{DE}. When sub-regional means are calculated, strong links between Z_{DE}, glacier mass balance, and glacier velocity are observed (**Figure 6**).

Spatial patterns of Z_{DE}, glacier mass change, and glacier velocity (**Figure 7**) further demonstrate the linkages between these metrics. The observed trends in mass balance, velocity, and Z_{DE} are nearly identical across the region, and demonstrate the potential use of Z_{DE} to map historical patterns of glacier change. The most negative mass balance rates and the greatest increases in Z_{DE} are seen in the eastern Himalayas. Regions of anomalous mass gain (Kunlun Shan and Karakoram) that have been identified previously (Hewitt, 2005; Gardelle et al., 2013; Kääb et al., 2015; Brun et al., 2017) coincide with regions of decreases in Z_{DE}. Regional changes in Z_{DE} thus provide a broad indication of glacier mass change, and there are very few outliers to this regional pattern.

Previous work has shown that there are no significant differences in the mass balance of debris-covered and debris-free glaciers in the region (Brun et al., 2019). While debris insulates ice from melt, this is countered by low slope angles, low velocities, and low emergence velocities observed on debris-covered tongues (Brun et al., 2018). And though the glaciological ELA will respond to annual climate fluctuations, the terminus response times of debris-covered glaciers is substantially longer (Banerjee and Shankar, 2013). Thus, both the debris-covered area and changes in Z_{DE} will lag behind annual variations in climate.

DISCUSSION

Debris covered glaciers in the HMA region represent a potentially significant source of meltwater on decadal/century time scales (Kraaijenbrink et al., 2017; Scherler et al., 2018; Herreid and Pellicciotti, 2020). The few studies that have examined the temporal evolution of debris cover have pointed out that a stable debris-covered area corresponds to a neutral or positive mass balance (Herreid et al., 2015).

This work demonstrates that the elevation of the debris-ice transition (Z_{DE}) has a similar distribution to both median glacier elevations and modelled equilibrium line altitudes (**Table 1**; **Figure 3**). As the ELA responds to annual variation in climate, we focus on how Z_{DE} changes through time and compare this with published mass balance and velocity trends. Our discussion here focuses on the implications of our results, the limitations of the research, and opportunities for future research.

Debris covered glacier extents can be difficult to map with remotely sensed imagery (Frey et al., 2012). However, the transition between debris and clean glacier ice can be reliably estimated from cloud-free optical imagery (Rounce et al., 2021). While the elevation of this debris-ice transition will vary over individual glaciers (e.g. **Figure 2**), the median value of the transition elevation extracted here as Z_{DE} has very similar distributions to both median glacier elevations and modelled ELAs (**Figure 3**). Limitations to our approach include the use of a static DEM and the duration of the compositing period used to construct debris cover maps. In the absence of accurate DEMs for each composite period, we have relied on SRTM elevations (ca.

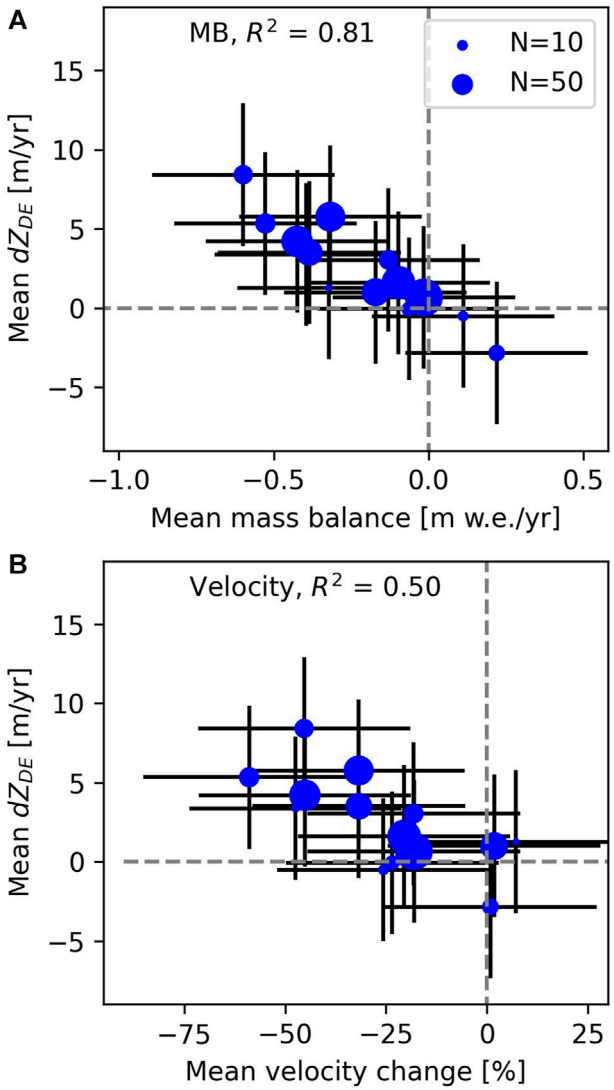

FIGURE 6 | Sub-region means of Z_{DE} versus mass balance rate (top panel) and Z_{DE} vs. change in glacier velocity. Error bars are standard deviations for each sub-region and metric, as in **Table 2**, and points are scaled to the sample size.

2000) for all estimates of Z_{DE}. If we assume that the majority of glaciers in the region have been experiencing mass loss and surface lowering, our use of SRTM data for all periods may result in overestimates of Z_{DE} in the 2013–2017 period, and underestimates in the 1981–2000 period. Nevertheless, we do not expect the reliance on a static DEM to affect our conclusions substantially, as these errors are likely small near the ELA (which is slightly higher in elevation than Z_{DE}, **Figure 3**). This study relies on compositing periods that cover 7–15 years periods, in order to obtain sufficient snow-free imagery to map the full extent of debris cover accurately. Changes in Z_{DE} at shorter timescales would likely not be detectable with reasonable accuracy, and given the absence of annual mass balance or velocity trends there is no need for finer temporal resolutions.

Sub-regional means of Z_{DE} exhibit clear negative relations with mass balance and velocity trends (**Figure 7**), with negative mass balances and velocity slowdowns associated with increased elevations of debris emergence. However, we do not find strong evidence for these relations at the scale of individual glaciers (**Figures 6**, **7**). Glaciers in Central Asia (Tien Shan, Kunlun Shan, Pamir, and Tibetan ranges) appear to have the strongest links between these three glacier metrics, while the relation is weaker in South Asia (West) and South Asia (East). These differences are possibly the result of sampling bias, the relative health of glaciers in a region, the date of imagery acquisition, debris supply rates, and the density of lake-terminating debris-covered tongues.

As there are no debris-covered glaciers in South Asia (West) or South Asia (East) that are gaining mass, the first issue is sampling bias: we are only able to sample glaciers that are losing mass. This bias is further related to the general health of glaciers in a given region. Sustained negative mass balances in South Asia (West) and South Asia (East) have produced debris-covered glaciers that are in an advanced state of decline, and in some cases are being cut off from their accumulation areas (Naito et al., 2000; Shea et al., 2015; Pieczonka et al., 2018) and in transition to becoming rock glaciers (Anderson et al., 2018). As a result, Z_{DE} will have an upper limit.

Our analysis of the dates of acquisition shows that imagery is typically collected in early August in most regions and composites (**Supplementary Figure S1**). However, we find a slight bias towards a later average glacier acquisition DOY for RGI15 in the 2013–2017 composite. While debris emergence elevations are expected to change on annual/decadal timescales in response to mass balance forcings, the timing of image acquisition could potentially affect the delineation of debris cover due to snow. Our compositing procedure preferentially selects pixels with the highest brightness temperatures to help minimize this bias. The average date of acquisition also varies between glaciers (**Supplementary Figure S2**). In using glacier-averaged composite dates for the trend calculations we find greater trend magnitudes than if the arithmetic mid-point of the composites is used.

Additionally, our calculated Z_{DE} metric extends beyond the time periods of the mass balance and velocity data. Looking only at the absolute change in Z_{DE} between the last two debris-cover masks, we observe a similar, albeit weaker, pattern in all three regions (**Supplementary Figure S4**). Glaciers that experience mass loss and decreases in velocity tend to show increases in Z_{DE}. As debris-covered glaciers thin, there is the possibility of increased debris supply from unstable and de-buttressed lateral moraines (van Woerkom et al., 2019) which would act to increase Z_{DE}. Finally, South Asia (West) and South Asia (East) contain a greater density of lake-terminating debris-covered glaciers (King et al., 2019), which have accelerated rates of mass loss relative to land-terminating glaciers. These factors all introduce some uncertainty in the relation between mass balance and Z_{DE}.

This research is unable to resolve a mechanism for changes in Z_{DE}, though enhanced ablation at the boundary between ice and debris, and a positive albedo feedback (warmer temperatures leading to increased ablation, melt out of entrained debris,

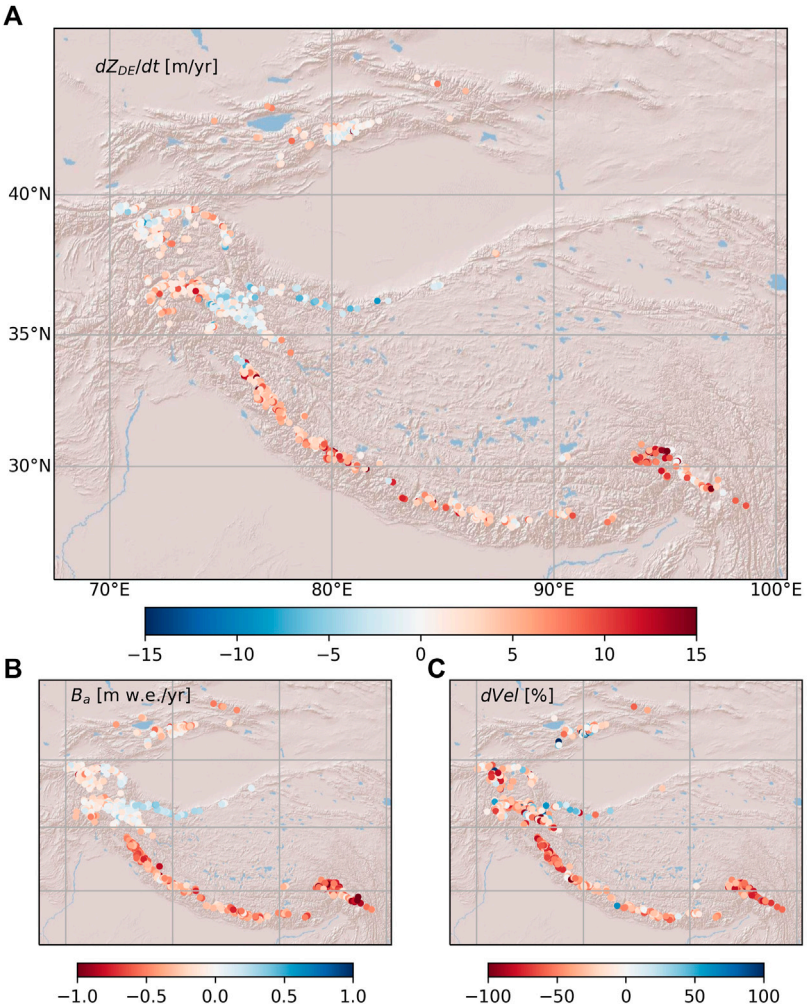

FIGURE 7 | Spatial distributions of dZ_{DE}/dt **(A)**, mass balance **(B)**, and change in velocity **(C)** for debris covered glaciers >5 km^2 in HMA. Mass balance data and velocity data from (Brun et al., 2017; Dehecq et al., 2018), respectively.

decreased surface albedo, and enhanced melt) is our working hypothesis. Detailed energy balance modelling work at a regional scale would help test this hypothesis. A reduction in ice flux would point towards reduced debris transport, so the correlation between reduced ice fluxes and increase in Z_{DE} may simply be due to the previously observed relations between mass balance and velocity (Dehecq et al., 2019).

The conceptual model of supraglacial debris given by (Anderson and Anderson, no date) and (Bozhinskiy et al., 1986) suggest that englacial debris emergence at the surface is governed by the local ablation rate and the concentration of the debris within the ice. When debris begins to emerge and concentrate at the surface, ablation rates are reduced at debris thicknesses greater than 0.05–0.10 m, which leads to an increase in local relief of the emerging medial moraine. The increase in surface slopes promotes dispersal of the debris, and so increased mass loss promotes increased debris emergence.

As the velocity is due primarily to the driving stress (with glacier thinning and mass loss leading to reduced driving stress and reduced velocities), the link between changes in velocity and Z_{DE} may be coincidental, and not causal. Put another way, the rise in Z_{DE} and the reduction in horizontal velocities are consequences of the same mechanism but are not directly linked. The rise in Z_{DE} can be seen as the consequence of an increased ELA, which leaves a larger area with positive vertical velocity (downglacier of the ELA), and thus leads to debris cover expansion up-glacier. The rise in ELA leads to more thinning and thus a reduced driving stress, as highlighted in Dehecq et al (2019).

Debris-covered glaciers respond to ELA shifts at decadal or century-scale timescales (Banerjee, 2017). Given the importance of larger debris-covered glaciers to local water supplies (Fegel et al., 2016), we split the dataset in each RGI region according to glacier size (greater than or less than 10 km^2) and re-calculate the mean rates of Z_{DE} change to determine if glacier size affects the rate of Z_{DE} change. In RGI13, larger glaciers have a slightly higher Z_{DE} rate of change (+3.23 m yr^{-1}, N = 81) than smaller glaciers (+2.68 m yr^{-1}, N = 104), though the standard deviations on these estimates are large (5.90 and 4.86 m yr^{-1}, respectively). In South

Asia (West) and South Asia (East), smaller debris-covered glaciers have higher rates of Z_{DE} change (3.15 and 6.23 m yr^{-1}, respectively) than larger debris-covered glaciers (2.69 and 5.24 m yr^{-1}, respectively). Again, large uncertainties prevent any meaningful conclusions about the role of glacier area in the rate of Z_{DE} response.

In light of these discussion points, our work indicates that changes in Z_{DE} derived from historical airborne or spaceborne imagery could be used as indicators of past glacier change. Historical regional inventories of Z_{DE} derived from Corona/Hexagon imagery (Maurer et al., 2016; Bolch et al., 2017) would provide additional information for the development and testing of models of glacier dynamics and the response times of debris-covered glaciers to climatic change. Extension of this work also includes the potential for refinements to reconstructions of debris-cover extents and ELAs from the Last Glacial Maximum (Owen et al., 2002) or early Holocene (Fernández-Fernández et al., 2017) from geomorphological evidence.

CONCLUSION

Debris-covered glaciers are common in High Mountain Asia, and represent a potentially important long term source of meltwater. In this study, we map the elevation of the debris-ice transition zone (Z_{DE}) for debris-covered glaciers in High Mountain Asia over three different compositing periods, identify trends and changes in Z_{DE} between periods, and compare rates of glacier mass change and velocity change with changes in Z_{DE}. Over decadal timescales and sub-regional spatial scales, Z_{DE} is closely related to both glacier mass balance and glacier velocity. Glacier mass loss and reductions in velocity are coincident with increases in Z_{DE}, and we hypothesize that this is likely a result of increased ablation at the debris-ice transition leading to increased melt-out of englacial debris. Rates of increases in Z_{DE} are of the same magnitude as modelled and observed increases in ELA. Our results provide an avenue for mapping the relative health of debris-covered glaciers from historical imagery, which can be used to improve debris-covered glacier models and projections of future meltwater availability.

DATA AVAILABILITY STATEMENT

The raw data supporting the conclusion of this article will be made available by the authors, without undue reservation.

AUTHOR CONTRIBUTIONS

JS, WI, PK, and FB designed the study. JS and PK conducted the analyses and prepared the figures, and all authors contributed to the writing.

FUNDING

JS is funded by an NSERC Discovery Grant and was supported by Global Water Futures and the University of Saskatchewan during the inception of this study. PK and WI are financially supported by the Strategic Priority Research Program of the Chinese Academy of Sciences within the Pan-Third Pole Environment framework (grant agreement number XDA20100300), by the European Research Council (ERC) under the European Union's Horizon 2020 research and innovation programme (grant agreement number 676819), and by the Netherlands Organization for Scientific Research under the Innovational Research Incentives Scheme VIDI (grant agreement 016.181.308).

ACKNOWLEDGMENTS

We gratefully acknowledge Amaury Dehecq for providing the glacier velocity change database, and the constructive comments and feedback from the reviewers.

SUPPLEMENTARY MATERIAL

The Supplementary Material for this article can be found online at: https://www.frontiersin.org/articles/10.3389/feart.2021.709957/full#supplementary-material

REFERENCES

Ageta, Y., and Higuchi, K. (1984). Estimation of Mass Balance Components of a Summer-Accumulation Type Glacier in the Nepal Himalaya. *Geografiska Annaler: Ser. A, Phys. Geogr.* 66 (3), 249–255. doi:10.2307/52069810.1080/04353676.1984.11880113

Anderson, L. S., and Anderson, R. S. (2016). Modeling Debris-Covered Glaciers: Response to Steady Debris Deposition. *The Cryosphere* 10 (3), 1105–1124. doi:10.5194/tc-10-1105-2016

Anderson, R. S., Anderson, L. S., Armstrong, W. H., Rossi, M. W., and Crump, S. E. (2018). Glaciation of alpine Valleys: The Glacier - Debris-Covered Glacier - Rock Glacier Continuum. *Geomorphology* 311, 127–142. doi:10.1016/j.geomorph.2018.03.015

Azam, M. F., Ramanathan, A., Wagnon, P., Vincent, C., Linda, A., Berthier, E., et al. (2016). Meteorological Conditions, Seasonal and Annual Mass Balances of Chhota Shigri Glacier, Western Himalaya, India. *Ann. Glaciol.* 57 (71), 328–338. doi:10.3189/2016AoG71A570

Banerjee, A. (2017). Brief Communication: Thinning of Debris-Covered and Debris-free Glaciers in a Warming Climate. *The Cryosphere* 11 (1), 133–138. doi:10.5194/tc-11-133-2017

Banerjee, A., and Shankar, R. (2013). On the Response of Himalayan Glaciers to Climate Change. *J. Glaciol.* 59 (215), 480–490. doi:10.3189/2013JoG12J130

Benn, D. I., and Ballantyne, C. K. (1994). Reconstructing the Transport History of Glacigenic Sediments: a New Approach Based on the Co-variance of Clast Form Indices. *Sed. Geol.* 91 (1), 215–227. doi:10.1016/0037-0738(94)90130-9

Benn, D. I., and Lehmkuhl, F. (2000). Mass Balance and Equilibrium-Line Altitudes of Glaciers in High-Mountain Environments. *Quat. Int.* 65-66, 15–29. doi:10.1016/S1040-6182(99)00034-8

Bolch, T., Pieczonka, T., and Benn, D. I. (2011). Multi-decadal Mass Loss of Glaciers in the Everest Area (Nepal Himalaya) Derived from Stereo Imagery. *The Cryosphere* 5 (2), 349–358. doi:10.5194/tc-5-349-2011

Bolch, T., Pieczonka, T., Mukherjee, K., and Shea, J. (2017). Brief Communication: Glaciers in the Hunza Catchment (Karakoram) Have Been Nearly in Balance since the 1970s. *The Cryosphere* 11, 531–539. doi:10.5194/tc-11-531-2017

Bozhinskiy, A. N., Krass, M. S., and Popovnin, V. V. (1986). Role of Debris Cover in the Thermal Physics of Glaciers. *J. Glaciol.* 32 (111), 255–266. doi:10.3189/S0022143000015598

Braithwaite, R. J. (1984). Can the Mass Balance of a Glacier Be Estimated from its Equilibrium-Line Altitude. *J. Glaciol.* 30 (106), 364–368. doi:10.3189/S0022143000006237

Braun, L. N., Grabs, W., and Rana, B. (1993). "Application of a Conceptual Precipitation- Runoff Model in the Langtang Kfaola Basin,". Editor G. J. Young, Proceedings of the Kathmandu Symposium, Nepal Himalaya, November 16–21, 1992 (Wallingford, United Kingdom: IAHS), 221–237.

Brun, F., Berthier, E., Wagnon, P., Kääb, A., and Treichler, D. (2017). A Spatially Resolved Estimate of High Mountain Asia Glacier Mass Balances from 2000 to 2016. *Nat. Geosci* 10 (9), 668–673. doi:10.1038/NGEO2999

Brun, F., Dumont, M., Wagnon, P., Berthier, E., Azam, M. F., Shea, J. M., et al. (2015). Seasonal Changes in Surface Albedo of Himalayan Glaciers from MODIS Data and Links with the Annual Mass Balance. *The Cryosphere* 9, 341–355. doi:10.5194/tc-9-341-2015

Brun, F., Wagnon, P., Berthier, E., Jomelli, V., Maharjan, S. B., Shrestha, F., et al. (2019). Heterogeneous Influence of Glacier Morphology on the Mass Balance Variability in High Mountain Asia. *J. Geophys. Res. Earth Surf.* 124, 1331–1345. doi:10.1029/2018JF004838

Brun, F., Wagnon, P., Berthier, E., Shea, J. M., Immerzeel, W. W., Kraaijenbrink, P. D. A., et al. (2018). Ice Cliff Contribution to the Tongue-wide Ablation of Changri Nup Glacier, Nepal, central Himalaya. *The Cryosphere* 12, 3439–3457. doi:10.5194/tc-12-3439-2018

Carrivick, J. L., and Brewer, T. R. (2004). Improving Local Estimations and Regional Trends of Glacier Equilibrium Line Altitudes. *Geografiska Annaler: Ser. A, Phys. Geogr.* 86 (1), 67–79. doi:10.1111/j.0435-3676.2004.00214.x

Cogley, J. G., Hock, R., Rasmussen, L. A., Arendt, A. A., Bauder, A., Braithwaite, R. J., et al. (2011). *'Glossary of Glacier Mass Balance and Related Terms, IHP-VII Technical Documents in Hydrology No. 86, IACS Contribution No. 2*. Paris: UNESCO-IHP. doi:10.5167/uzh-53475

Collier, E., Mölg, T., Maussion, F., Scherer, D., Mayer, C., and Bush, A. B. G. (2013). High-resolution Interactive Modelling of the Mountain Glacier-Atmosphere Interface: an Application over the Karakoram. *The Cryosphere* 7 (3), 779–795. doi:10.5194/tc-7-779-2013

de Kok, R. J., Tuinenburg, O. A., Bonekamp, P. N. J., and Immerzeel, W. W. (2018). Irrigation as a Potential Driver for Anomalous Glacier Behavior in High Mountain Asia. *Geophys. Res. Lett.* 45 (4), 2047–2054. doi:10.1002/2017GL076158

Dehecq, A., Gourmelen, N., Gardner, A. S., Brun, F., Goldberg, D., Nienow, P. W., et al. (2019). Twenty-first century Glacier Slowdown Driven by Mass Loss in High Mountain Asia. *Nat. Geosci* 12 (1), 22–27. doi:10.1038/s41561-018-0271-9

Engelhardt, M., Leclercq, P., Eidhammer, T., Kumar, P., Landgren, O., and Rasmussen, R. (2017). Meltwater Runoff in a Changing Climate (1951-2099) at Chhota Shigri Glacier, Western Himalaya, Northern India. *Ann. Glaciol.* 58 (75), 47–58. doi:10.1017/aog.2017.13

Farinotti, D., Immerzeel, W. W., de Kok, R. J., Quincey, D. J., and Dehecq, A. (2020). Manifestations and Mechanisms of the Karakoram Glacier Anomaly. *Nat. Geosci.* 13 (1), 8–16. doi:10.1038/s41561-019-0513-5

Farr, T. G., Rosen, P. A., Caro, E., Crippen, R., Duren, R., Hensley, S., et al. (2007). The Shuttle Radar Topography mission. *Rev. Geophys.* 45 (2). doi:10.1029/2005rg000183

Fegel, T. S., Baron, J. S., Fountain, A. G., Johnson, G. F., and Hall, E. K. (2016). The Differing Biogeochemical and Microbial Signatures of Glaciers and Rock Glaciers. *J. Geophys. Res. Biogeosci.* 121 (3), 919–932. doi:10.1002/2015jg003236

Fernández-Fernández, J. M., Palacios, D., García-Ruiz, J. M., Andrés, N., Schimmelpfennig, I., Gómez-Villar, A., et al. (2017). Chronological and geomorphological investigation of fossil debris-covered glaciers in relation to deglaciation processes: A case study in the Sierra de La Demanda, northern Spain. *Quat. Sci. Rev.* 170, 232–249. doi:10.1016/j.quascirev.2017.06.034

Frey, H., Paul, F., and Strozzi, T. (2012). Compilation of a Glacier Inventory for the Western Himalayas from Satellite Data: Methods, Challenges, and Results. *Remote Sensing Environ.* 124, 832–843. doi:10.1016/j.rse.2012.06.020

Gardelle, J., Berthier, E., Arnaud, Y., and Kääb, A. (2013). Region-wide Glacier Mass Balances over the Pamir-Karakoram-Himalaya during 1999-2011. *The Cryosphere* 7 (4), 1263–1286. doi:10.5194/tc-7-1263-2013

Gardelle, J., Berthier, E., and Arnaud, Y. (2012). Slight Mass Gain of Karakoram Glaciers in the Early Twenty-First century. *Nat. Geosci* 5, 322–325. doi:10.1038/ngeo1450

Hall, D. K., Riggs, G. A., and Salomonson, V. V. (1995). Development of Methods for Mapping Global Snow Cover Using Moderate Resolution Imaging Spectroradiometer Data. *Remote Sensing Environ.* 54 (2), 127–140. doi:10.1016/0034-4257(95)00137-P

Hasson, S., Lucarini, V., Khan, M. R., Petitta, M., Bolch, T., and Gioli, G. (2014). Early 21st century Snow Cover State over the Western River Basins of the Indus River System. *Hydrol. Earth Syst. Sci.* 18 (10), 4077–4100. doi:10.5194/hess-18-4077-2014

Herreid, S., Pellicciotti, F., Ayala, A., Chesnokova, A., Kienholz, C., Shea, J., et al. (2015). Satellite Observations Show No Net Change in the Percentage of Supraglacial Debris-Covered Area in Northern Pakistan from 1977 to 2014. *J. Glaciol.* 61 (227), 524–536. doi:10.3189/2015JoG14J227

Herreid, S., and Pellicciotti, F. (2020). The State of Rock Debris Covering Earth's Glaciers. *Nat. Geosci.* 13 (9), 621–627. doi:10.1038/s41561-020-0615-0

Hewitt, K. (2005). The Karakoram Anomaly? Glacier Expansion and the 'Elevation Effect,' Karakoram Himalaya. *Mountain Res. Develop.* 25, 332–340. doi:10.1659/0276-4741(2005)025[0332:tkagea]2.0.co;2

Hugonnet, R., McNabb, R., Berthier, E., Menounos, B., Nuth, C., Girod, L., et al. (2021). Accelerated Global Glacier Mass Loss in the Early Twenty-First century. *Nature* 592 (7856), 726–731. doi:10.1038/s41586-021-03436-z

Huss, M. (2013). Density Assumptions for Converting Geodetic Glacier Volume Change to Mass Change. *The Cryosphere* 7 (3), 877–887. doi:10.5194/tc-7-877-2013

Huss, M., and Hock, R. (2015). A New Model for Global Glacier Change and Sea-Level Rise. *Front. Earth Sci.* 3, 54. doi:10.3389/feart.2015.00054

Kääb, A., Treichler, D., Nuth, C., and Berthier, E. (2015). Brief Communication: Contending Estimates of 2003-2008 Glacier Mass Balance over the Pamir-Karakoram-Himalaya. *The Cryosphere* 9 (2), 557–564. doi:10.5194/tc-9-557-2015

King, O., Bhattacharya, A., Bhambri, R., and Bolch, T. (2019). Glacial Lakes Exacerbate Himalayan Glacier Mass Loss. *Sci. Rep.* 9 (1), 18145. doi:10.1038/s41598-019-53733-x

Kirkbride, M. P. (2011). "Debris-Covered Glaciers," in *Encyclopedia of Snow, Ice and Glaciers*. Editors V. P. Singh, P. Singh, and U. K. Haritashya (Dordrecht: Springer Netherlands), 180–182. doi:10.1007/978-90-481-2642-2_622

Kraaijenbrink, P. D. A., Bierkens, M. F. P., Lutz, A. F., and Immerzeel, W. W. (2017). Impact of a Global Temperature Rise of 1.5 Degrees Celsius on Asia's Glaciers. *Nature* 549 (7671), 257–260. doi:10.1038/nature23878

Machguth, H., Haeberli, W., and Paul, F. (2012). Mass-balance Parameters Derived from a Synthetic Network of Mass-Balance Glaciers. *J. Glaciol.* 58 (211), 965–979. doi:10.3189/2012JoG11J223

Maurer, J. M., Rupper, S. B., and Schaefer, J. M. (2016). Quantifying Ice Loss in the Eastern Himalayas since 1974 Using Declassified Spy Satellite Imagery. *The Cryosphere* 10 (5), 2203–2215. doi:10.5194/tc-10-2203-2016

Maurer, J. M., Schaefer, J. M., Rupper, S., and Corley, A. (2019). Acceleration of Ice Loss across the Himalayas over the Past 40 Years. *Sci. Adv.* 5, eaav7266. doi:10.1126/sciadv.aav7266

Mukul, M., Srivastava, V., Jade, S., and Mukul, M. (2017). Uncertainties in the Shuttle Radar Topography Mission (SRTM) Heights: Insights from the Indian Himalaya and Peninsula. *Sci. Rep.* 7, 41672. doi:10.1038/srep41672

Naito, N., Nakawo, M., and Kadota, T. (2000). "Numerical Simulation of Recent Shrinkage of Khumbu Glacier, Nepal Himalayas," in *Debris Covered Glaciers*, Proceedings of the Seattle Symposium. Editors M. Nakawo, C. Raymond, and A. Fountain (Wallingford, Oxfordshire: IAHS), 245–254.

Owen, L. A., and Benn, D. I. (2005). Equilibrium-line Altitudes of the Last Glacial Maximum for the Himalaya and Tibet: an Assessment and Evaluation of Results. *Quat. Int.* 138-139, 55–78. doi:10.1016/j.quaint.2005.02.006

Owen, L. A., Finkel, R. C., and Caffee, M. W. (2002). A Note on the Extent of Glaciation throughout the Himalaya during the Global Last Glacial Maximum. *Quat. Sci. Rev.* 21 (1), 147–157. doi:10.1016/S0277-3791(01)00104-4

Pandey, P., Kulkarni, A. V., and Venkataraman, G. (2013). Remote Sensing Study of Snowline Altitude at the End of Melting Season, Chandra-Bhaga basin, Himachal Pradesh, 1980-2007. *Geocarto Int.* 28 (4), 311–322. doi:10.1080/10106049.2012.705336

Pfeffer, W. T., Arendt, A. A., Bliss, A., Bolch, T., Cogley, J. G., Gardner, A. S., et al. (2014). The Randolph Glacier Inventory: a Globally Complete Inventory of Glaciers. *J. Glaciol.* 60 (221), 537–552. doi:10.3189/2014JoG13J176

Pieczonka, T., Bolch, T., Kröhnert, M., Peters, J., and Liu, S. (2018). Glacier branch Lines and Glacier Ice Thickness Estimation for Debris-Covered Glaciers in the Central Tien Shan. *J. Glaciol.* 64 (247), 835–849. doi:10.1017/jog.2018.75

Quincey, D. J., Braun, M., Glasser, N. F., Bishop, M. P., Hewitt, K., and Luckman, A. (2011). Karakoram Glacier Surge Dynamics. *Geophys. Res. Lett.* 38 (18), a–n. doi:10.1029/2011GL049004

Rabatel, A., Dedieu, J.-P., and Vincent, C. (2005). Using Remote-Sensing Data to Determine Equilibrium-Line Altitude and Mass-Balance Time Series: Validation on Three French Glaciers, 1994-2002. *J. Glaciol.* 51 (175), 539–546. doi:10.3189/172756505781829106

Rabatel, A., Letréguilly, A., Dedieu, J.-P., and Eckert, N. (2013). Changes in Glacier Equilibrium-Line Altitude in the Western Alps from 1984 to 2010: Evaluation by Remote Sensing and Modeling of the Morpho-Topographic and Climate Controls. *The Cryosphere* 7 (5), 1455–1471. doi:10.5194/tc-7-1455-2013

Rabatel, A., Sirguey, P., Drolon, V., Maisongrande, P., Arnaud, Y., Berthier, E., et al. (2017). Annual and Seasonal Glacier-wide Surface Mass Balance Quantified from Changes in Glacier Surface State: A Review on Existing Methods Using Optical Satellite Imagery. *Remote Sensing* 9 (5), 507. doi:10.3390/rs9050507

RGI Consortium (2017). *Randolph Glacier Inventory–A Dataset of Global Glacier Outlines: Version 6.0: Technical Report, Global Land Ice Measurements from Space*. Colorado, United States: Digital Media. doi:10.7265/N5-RGI-60

Robson, B., Hölbling, D., Nuth, C., Strozzi, T., and Dahl, S. (2016). Decadal Scale Changes in Glacier Area in the Hohe Tauern National Park (Austria) Determined by Object-Based Image Analysis. *Remote Sensing* 8 (1), 67. doi:10.3390/rs8010067

Rounce, D. R., Hock, R., McNabb, R. W., Millan, R., Sommer, C., Braun, M. H., et al. (2021). Distributed Global Debris Thickness Estimates Reveal Debris Significantly Impacts Glacier Mass Balance. *Geophys. Res. Lett.* 48 (8), e2020GL091311. doi:10.1029/2020GL091311

Sakai, A., and Fujita, K. (2017). Contrasting Glacier Responses to Recent Climate Change in High-Mountain Asia. *Sci. Rep.* 7 (1), 13717. doi:10.1038/s41598-017-14256-5

Scherler, D., Bookhagen, B., and Strecker, M. R. (2011). Spatially Variable Response of Himalayan Glaciers to Climate Change Affected by Debris Cover. *Nat. Geosci* 4, 156–159. doi:10.1038/ngeo1068

Scherler, D., Wulf, H., and Gorelick, N. (2018). Global Assessment of Supraglacial Debris-Cover Extents. *Geophys. Res. Lett.* 45 (21), 11798–11805. doi:10.1029/2018gl080158

Shea, J. M., and Immerzeel, W. W. (2016). An Assessment of basin-scale Glaciological and Hydrological Sensitivities in the Hindu Kush-Himalaya. *Ann. Glaciol.* 57, 308–318. doi:10.3189/2016AoG71A073

Shea, J. M., Immerzeel, W. W., Wagnon, P., Vincent, C., and Bajracharya, S. (2015). Modelling Glacier Change in the Everest Region, Nepal Himalaya. *The Cryosphere* 9, 1105–1128. doi:10.5194/tc-9-1105-2015

Shea, J. M., Menounos, B., Moore, R. D., and Tennant, C. (2013). An Approach to Derive Regional Snow Lines and Glacier Mass Change from MODIS Imagery, Western North America. *The Cryosphere* 7, 667–680. doi:10.5194/tc-7-667-2013

Shean, D. E., Bhushan, S., Montesano, P., Rounce, D. R., Arendt, A., and Osmanoglu, B. (2020). A Systematic, Regional Assessment of High Mountain Asia Glacier Mass Balance. *Front. Earth Sci.* 7, 363. doi:10.3389/feart.2019.00363

van Woerkom, T., Steiner, J. F., Kraaijenbrink, P. D. A., Miles, E. S., and Immerzeel, W. W. (2019). Sediment Supply from Lateral Moraines to a Debris-Covered Glacier in the Himalaya. *Earth Surf. Dynam.* 7 (2), 411–427. doi:10.5194/esurf-7-411-2019

Vincent, C., Ramanathan, A., Wagnon, P., Dobhal, D. P., Linda, A., Berthier, E., et al. (2013). Balanced Conditions or Slight Mass Gain of Glaciers in the Lahaul and Spiti Region (Northern India, Himalaya) during the Nineties Preceded Recent Mass Loss. *The Cryosphere* 7 (2), 569–582. doi:10.5194/tc-7-569-2013

Viste, E., and Sorteberg, A. (2015). Snowfall in the Himalayas: an Uncertain Future from a Little-Known Past. *The Cryosphere* 9 (3), 1147–1167. doi:10.5194/tc-9-1147-2015

Wagnon, P., Vincent, C., Arnaud, Y., Berthier, E., Vuillermoz, E., Gruber, S., et al. (2013). Seasonal and Annual Mass Balances of Mera and Pokalde Glaciers (Nepal Himalaya) since 2007. *The Cryosphere* 7 (6), 1769–1786. doi:10.5194/tc-7-1769-2013

Wang, P., Li, Z., Li, H., Wang, W., and Yao, H. (2014). Comparison of Glaciological and Geodetic Mass Balance at Urumqi Glacier No. 1, Tian Shan, Central Asia. *Glob. Planet. Change* 114, 14–22. doi:10.1016/j.gloplacha.2014.01.001

Yinsheng, Z., Koji, F., Ageta, Y., and Nakawo, M. (1998) 'The response of glacier ELA to climate fluctuations on High Asia', *Bull. Glac. Res.*, 16 (1), 1–11. doi:10.1142/9789812839718_0001

Conflict of Interest: The authors declare that the research was conducted in the absence of any commercial or financial relationships that could be construed as a potential conflict of interest.

Publisher's Note: All claims expressed in this article are solely those of the authors and do not necessarily represent those of their affiliated organizations, or those of the publisher, the editors and the reviewers. Any product that may be evaluated in this article, or claim that may be made by its manufacturer, is not guaranteed or endorsed by the publisher.

frontiers in Earth Science

ORIGINAL RESEARCH
published: 14 October 2021
doi: 10.3389/feart.2021.710276

The Concept of Steady State, Cyclicity and Debris Unloading of Debris-Covered Glaciers

Christoph Mayer and Carlo Licciulli*

Bavarian Academy of Sciences and Humanities, Geodesy and Glaciology, Munich, Germany

It can easily be expected that debris-covered glaciers show a different response on external forcing compared to clean-surface glaciers. The supra-glacial debris cover acts as an additional transfer layer for the energy exchange between atmosphere and ice. The related glacier reaction is the integral of local effects, which changes strongly between enhanced melt for thin debris layers and considerably reduced melt for thicker debris. Therefore, a realistic feedback study can only be performed, if both the ice flow and the debris-influenced melt is treated with a high degree of detail. We couple a full Stokes representation of ice dynamics and the most complete description of energy transfer through the debris layer, in order to describe the long-term glacier reaction in the coupled system. With this setup, we can show that steady-state conditions are highly unlikely for glaciers, in case debris is not unloaded from the surface. For continuous and complete debris removal from the lowermost glacier tongue, however, a balance of the debris budget and the glacier conditions are possible. Depending on displacement and removal processes, our results demonstrate that debris-covered glaciers have an inherent tendency to switch to an oscillating state. Then, glacier mass balance and debris balance are out of phase, such that glacier advance periods end with the separation of the heavily debris-loaded lowermost glacier tongue, at time scales of decades to centuries. As these oscillations are inherent and happen without any variations in climatic forcing, it is difficult to interpret modern observations on the fluctuation of debris-covered glaciers on the basis of a changing climate only.

Keywords: glacier dynamics, debris cover, steady state, glacier-debris feedback, long-term glacier evolution

OPEN ACCESS

Edited by:
Koji Fujita,
Nagoya University, Japan

Reviewed by:
Leif S. Anderson,
The University of Utah, United States
Peter Moore,
Iowa State University, United States

****Correspondence:***
Christoph Mayer
christoph.mayer@keg.badw.de

Specialty section:
This article was submitted to Cryospheric Sciences, a section of the journal Frontiers in Earth Science

Received: *15 May 2021*
Accepted: *16 September 2021*
Published: *14 October 2021*

Citation:
Mayer C and Licciulli C (2021) The Concept of Steady State, Cyclicity and Debris Unloading of Debris-Covered Glaciers. Front. Earth Sci. 9:710276. doi: 10.3389/feart.2021.710276

1 INTRODUCTION

The knowledge about debris-covered glaciers advanced considerably during the last two decades. This development was driven by the recognition that debris-covered glaciers represent considerable parts of the cryosphere in many mountain regions, especially in High Mountain Asia (HMA), but also other mountain ranges.

Especially three features of debris-covered glaciers came into the focus of scientific investigations: the effect of debris thickness and other inherent parameters on melt rates, the distribution of debris cover across individual glaciers and glaciated mountain ranges and the different morphological expressions of debris-covered glaciers like ice cliffs, melt ponds and surface debris redistribution. The effect of debris cover on the glacier evolution, however, attracted much less attention, even though the interaction between a surface mass balance influenced debris cover and ice dynamics fundamentally determines the extent and distribution of debris-covered glaciers. Here we

introduce four key papers, in order to demonstrate some important issues in the development of modelling debris-covered glaciers.

A first numerical description of a coupled ice/debris glacier system was presented by Konrad and Humphrey (2000). They used a simplified force balance approach with shear stress as the single driver for describing ice dynamics along a two-dimensional (2-D) flow line, assuming parallel ice flow and a constant surface slope of the glacier. Debris input was prescribed as constant and restricted to the ELA, while debris transport was solely through downward advection of ice. However, the additional effect of the debris load on the shear stress was accounted for. Their linear mass balance function was affected by the existence of surface debris, which reduces ice melt exponentially to the respective debris thickness. This model predicts an infinite glacier length for steady-state conditions. Higher debris input leads to a thinner mean debris layer, due to an increase in ice velocity, while a steepening of the mass balance gradient leads to lower ice thicknesses, because the higher mass transport reduces debris thickness and thus increases ice melt. However, the limitations of the model (constant surface slope, simple mass balance parameterisation, singular debris source) only allow very general conclusions.

In a more practical approach, Rowan et al. (2015) used a higher-order shallow-ice (SIA) model, including longitudinal and transverse stress gradients, as well as a simple description of basal sliding to simulate the evolution of debris-covered Khumbu Glacier in the Himalaya. The effect of debris on ice melt was described by an exponential function, which reduces ablation from the clean-ice value to 50% at 0.5 m debris thickness and prescribes diminishing ablation rates for debris thicknesses exceeding 1 m. Debris is transported from the accumulation region (with a constant input concentration) by advection along flow paths to either the surface or the bed (in case of basal melting) in the ablation zone. Simulations were initialised for Late Holocene conditions in order to reconstruct a steady-state maximum extent. This served as a base for investigating the glacier evolution towards its present state and into the future, where the elevation of the ELA was the climatic driver. Experiments for clean-ice conditions and reduced ice melt resulted in a present glacier extent much smaller than currently observed (16% of the modern volume for the clean-ice case) compared to the existence of glacial debris. The results demonstrate that only the implementation of debris-related processes enable reliable simulations of debris-covered glaciers and support the observations that mass loss at such glaciers is mainly by surface lowering compared to frontal ice melt.

A further development was made by Anderson and Anderson (2016), who also used a 2-D numerical flow line model (SIA, coupled with longitudinal stress gradients) to investigate the role of englacial and supraglacial advection of debris and its impact on the mass balance for glacier evolution. They used a hypothetical clean-ice steady state on a linear bed as initial condition and perturbing it with step functions of debris deposition. The prescribed altitudinal mass balance gradient is modified by the effect of the debris cover, which assumes a hyperbolic decline of ice melt with debris thickness, neglecting enhanced ice melt for very thin debris cover. Debris loss occurs by introducing a terminal wedge, which allows the definition of a discharge debris flux. All experiments were driven to a steady state, where the integrated glacier mass balance disappeared and a balance was reached between debris deposition and debris loss from the terminus. It appeared that the final glacier length strongly depends on the magnitude of debris deposition and the relation between melt rate and debris thickness. Also, the location of debris deposition strongly influences the glacier geometry, because a deposition near the ELA has a more sustained effect on the mass balance. The observation of a reduced AAR for debris-covered glaciers in comparison with clean-ice glaciers could be confirmed by these experiments.

Ferguson and Vieli (2021) extended these investigations with the aim of defining the role of the debris cover on the glaciers transient behaviour, but also analysed the effect of cryokarst features in such a system. The methods are strongly based on Anderson and Anderson (2016), but now include the formation of supra-glacial lakes and ice cliffs for a stagnant glacier tongue. Debris concentration is uniform in the glacier and thus ice melt produces a constant contribution of supra-glacial debris. The existence of supra-glacial debris reduces ice melt according to an inverse relationship with debris thickness (Nicholson and Benn, 2006). Debris slides off the terminus if a threshold ice thickness is reached, resulting in a permanent exposition of ice at a frontal cliff. With this configuration, the authors are capable of simulating steady states, where surface mass balance and debris balance are both zero. Based on these conditions, the effect of a changing climate on the glacier evolution is investigated by abrupt changes as well as introducing white noise on the changes. They found that debris cover influences the geometric evolution of glaciers and especially the length response to warming periods is delayed. This characteristic is mitigated by contrasting melt enhancement, if cryokarst features are included in the simulations.

These examples demonstrate that the general feedback mechanisms of glacial debris can be reproduced by using simplified ice-dynamics models, coupled with a debris model of varying complexity. We also do not aim on explaining the full dynamic response of debris-covered glaciers. In particular, we do not delve into details like cryokarst phenomena or variability of englacial debris distribution, even though this likely has relevant consequences on the general glacier evolution (e.g., Wirbel et al. (2018), Miles et al. (2021)). We rather want to point out some crucial fundamental conditions, which might help to understand the complex behaviour of such glaciers. Therefore, we first raise the well-known question about the steady state of debris-covered glaciers, which seems straightforward but turned out to be rather complex. Then, we investigate the problem of debris unloading at the glacier terminus, which turns out to be crucial when it comes to potential steady-state conditions. Finally, we investigate the possibility of recurring glacier advances due to a hysteresis in the ice flux—ice melt balance of the glacier terminus.

Our experiments are based on two sophisticated models, which apply extensive physical theories to ice melt under a

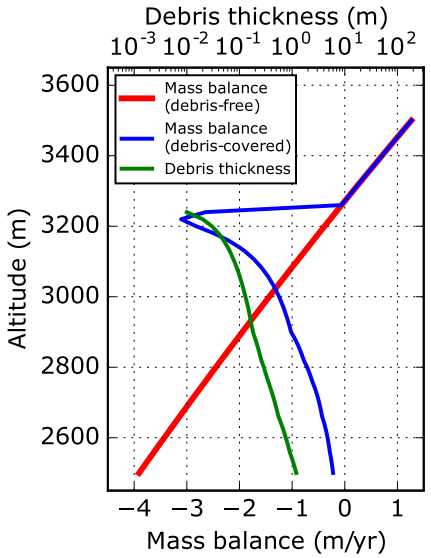

FIGURE 1 | Mass balance gradient used in the basic experiments for clean-ice conditions (red) compared with an example mass balance gradient from a debris-covered glacier (blue). The green curve indicates the corresponding example debris thickness profile.

debris cover (Evatt et al., 2015) and the detailed evolution of glacier geometry by solving the full Stokes equations for ice deformation using Elmer/Ice (Gagliardini et al., 2013). In doing so, we ensure that the complex relation between debris thickness and ice melt is represented across the entire thickness scale based on physical principles, including enhanced melt rates for thin debris layers in the upper part of the ablation region. Considering that we simulate small-scale glaciers, the full Stokes approach ensures that we can rely on a most realistic geometry of the glacier terminus and frontal dynamics, which is crucial for our debris discharge experiments and evolution of the whole system.

2 MODEL DESCRIPTION

2.1 Surface Mass Balance

Ice melt beneath a supra-glacial debris cover is rather complex, due to the interaction of different energy fluxes and the usually inhomogeneous composition of the debris column. The first issue can be tackled by applying a sophisticated physical model, which includes all important fluxes. The highly variable structure of the debris layer is rather location dependent and cannot be solved in detail for larger areas, because of unknown initial conditions and rather random variability in debris composition (e.g., Nicholson et al., 2018; Fyffe et al., 2020). However, for our application the assumption of homogeneous conditions is justified, because we focus on long-term and general glacier evolution, not aiming on resolving localised melt variability. Therefore, we decided to use an ablation model, which is capable of describing the melt rate for all debris thicknesses by including turbulent fluxes within the upper debris cover (Evatt et al., 2015). This formulation resolves the enhanced melt rates for a thin debris cover as well as the decreasing melt rates for thickening debris above a threshold of typically less than 10 cm (e.g., Östrem, 1959; Nicholson and Benn, 2006). As forcing, we use artificial and constant climate conditions, which are based on annual mean values of the required variables in dependence of altitudinal gradients (see the selected parameter set in **Supplementary Table S1**). Thus, we simulate a climate, which enables the existence of glaciers and their steady state in the model domain, comparable to alpine conditions with glaciers of several kilometers in length, extending across an elevation range between 2,800 m and 3,500 m. **Figure 1** shows an example of the surface mass balance model in case of a clean-ice and a debris-covered glacier simulation.

2.2 Ice Dynamics

The key goal is to investigate the effect of debris cover on glacier dynamics, which we approach by deploying a full Stokes flow-line model. The gravity-driven ice flow is solved by considering momentum balance and mass conservation. We treat ice as an incompressible fluid with constant density $\rho_{ice} = 910\text{kg m}^{-3}$ and assume viscous flow according to Glen's law with exponent $n = 3$ to relate deviatoric stresses and strain (Greve and Blatter, 2009). Since we focus on the effect of debris cover on glacier evolution, we switch off englacial thermodynamical processes and assume constant climate forcing. The temperature dependent flow rate factor $A(T)$ is kept constant and derived from an Arrhenius-type law (Cuffey and Paterson, 2010) with pre-exponential factor $A_0 = 1.916 \times 10^3 \text{s}^{-1}\,\text{Pa}^{-3}$, activation energy $Q = 139\,\text{kJ mol}^{-1}\,\text{K}^{-1}$ and a constant englacial temperature, set to $T = -3^{\circ}\text{C}$.

The coupling between the debris layer and the underlying ice is twofold. Debris coverage has an effect on the glacier flow via its strong influence on the surface mass balance. This, in turn, influences the debris distribution itself, since debris transport depends on the flow field. In our modelling approach we simplify these feedback mechanisms. In particular we did not consider 1) the change in the momentum balance due to additional debris-induced stress on the ice surface and 2) the effect of englacial debris on the rheology of the debris/ice mixture. Further, the exclusion of englacial thermodynamical processes implies that 3) we do not capture temperature changes within the glacier derived from the debris-perturbed surface thermal boundary condition. These simplifications, however, do not compromise the suitability of our model setup to investigate the fundamental dynamical behaviour of debris-covered glaciers, because we do not expect these processes to considerably alter the basic feedback mechanisms.

The modelled ice/debris glacier system is forced by changes in surface mass balance in response to the evolving debris coverage, despite the constant climatic boundary condition at the debris/ice surface and thus a constant clean-ice surface mass balance distribution (**Figure 1**). The resulting glacier geometry variations are governed by the free-surface equation (Greve and Blatter, 2009), which calculates surface elevation changes due to down-slope transport of ice and local mass

balance. Moreover, we investigate the response of the system to different basal sliding conditions. We calculate basal flow velocities using a simple linear relation between the basal velocity component parallel to the bedrock $v_{b\parallel}$ and the corresponding basal stress component $\tau_{b\parallel}$:

$$v_{b\parallel} = \beta^2 \tau_{b\parallel}, \tag{1}$$

where β^2 is the friction coefficient. The basal velocity component perpendicular to the bedrock is set to zero ($v_{b\perp} = 0$) in order to avoid ice penetration into the bedrock. For the simulations without basal sliding, the entire basal velocity vector is set to zero (no-slip condition).

2.2.1 Debris Source and Transport

Debris is generally deposited on glaciers due to avalanches or rockfalls, but it can also be incorporated in the ice column by lateral or basal erosion (Wirbel et al., 2018). If this happens in the accumulation zone, debris submerges into the ice, is transported within the ice body and re-emerges in the ablation zone. There, debris remains on the glacier surface and is transported passively down-valley towards the terminus (neglecting any redistribution processes). Even though several studies (e.g., Miles et al., 2021; Wirbel et al., 2018) demonstrate the importance of spatial variations of englacial debris concentration, we do not include processes for debris input to the glacier, nor debris transport within the ice. Although the variability in such processes certainly influences the glacier reaction on the climatic boundary conditions, we focus on the fundamental debris-glacier-climate feedback at the glacier surface. Therefore, we only consider an englacial debris concentration ζ which is constant in time and space, as a result from debris deposition and transport. Based on the analysis of ice flux gradients in our experiments, we consider this constraint as a further but potentially minor limitation of the coupling between debris cover and glacier dynamics, since extensive or compressive flow will not alter the debris concentration before emergence. We define ζ as the ratio between the height of the debris column within the debris/ice mixture and the total height of the debris/ice mixture and use different prescribed debris concentrations to explore its influence on the glacier dynamics.

In the modelling approach, debris is only considered, if it emerges at the glacier surface. As this is only the case for melt conditions, a supra-glacial debris cover is limited to the ablation zone. Therefore, an emerging debris height dD results from ice melt $\dot{b}$ over a specific time interval dt at a specific location x and the prescribed debris concentration ζ:

$$dD(x,t) = \dot{b}(x,t)\,\zeta\,dt. \tag{2}$$

The newly emerged debris dD is added to the already existing local debris height D.

The debris layer is transported with the ice flow downstream towards the glacier terminus. This debris advection is governed by the calculated surface flow field and therefore includes compressive or extensive flow and thus dynamic thickening or thinning of the debris cover. We calculate debris advection only at the glacier surface, which reduces the problem in our 2-D glacier geometry to a 1-D advection problem. The advection of the debris column D by a known 1-D velocity (i.e., the horizontal surface velocity component v_x) is:

$$\frac{\partial D}{\partial t} = D_s - v_x \frac{\partial D}{\partial x} - D\frac{\partial v_x}{\partial x}, \tag{3}$$

where D_s is the debris source from melting ice, which is calculated by integrating **Eq. 2**.

2.2.2 Debris Displacement and Removal

A major issue in investigating long-term glacier evolution is related to the fate of supra-glacial debris, when it reaches the glacier terminus, because melt conditions at the lowermost part of the glacier are crucial for the dynamics of the whole system. At least for debris covers of several tens of centimeters (which is usually the case for well developed debris covered glaciers), debris loss by completely melting the underlying ice is very small compared to downstream debris transport rates. Thus, any substantial debris removal from the glacier requires an active process. The observational basis for developing appropriate mechanisms is weak and theoretical approaches are few (Moore, 2018). We do not aim on providing an elaborated theory about debris mobilisation and removal from the terminus. We rather established some very simple algorithms, which mimic complicated debris migration processes in a general way and thus allow us to investigate the glacier response.

One way to deal with the debris layer on the terminus is to consider only the surface velocity field and neglect any active debris migration. Because the ice velocity approaches zero at the terminus, supra-glacial debris will then accumulate to very large and finally unrealistic debris thicknesses. In reality, it is reasonable that in presence of steep slopes, as it is often the case at the glacier front, single rocks are mobilised or an entire debris layer may abruptly slide down, and thus leave the system. We implemented mechanisms in the model, which lead to displacement or removal of debris. These mechanisms can be switched on separately or in a combined form, allowing us to investigate the consequences in detail.

Purely slope-triggered removal sets in, where the slope of the ice surface exceeds a prescribed threshold $\tilde{\alpha}$. All debris downstream of this location is removed from the system. Debris transport from upstream and debris melt out can rebuild the debris layer, if the surface slope drops again below $\tilde{\alpha}$. Another mechanism of abrupt debris removal considers the driving stress τ_d of the debris layer:

$$\tau_d = \rho_d g D \sin\alpha, \tag{4}$$

where ρ_d is the density of the bulk debris layer (i.e., accounting for porosity in the layer), g the gravitational acceleration, D the thickness of the debris layer and α the surface slope. If the driving stress exceeds a defined yield stress $\tilde{\tau}$, i.e., the maximum shear stress that the debris layer can execute on the ice surface without sliding, the debris layer collapses and is eliminated from the system. This is certainly a simplified representation of a more complex failure mechanism, which is

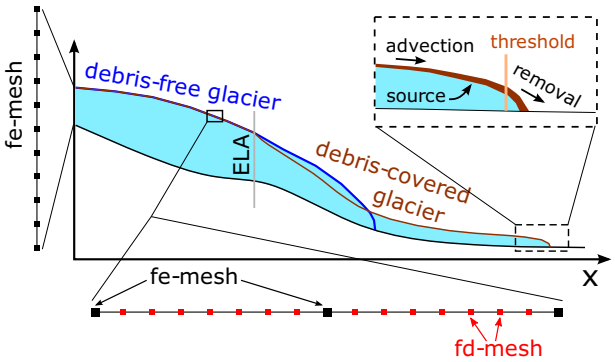

FIGURE 2 | Ice/debris glacier system as implemented in our modelling approach. The bedrock geometry is pre-defined, while glacier evolution is determined by external forcing. Debris emerges below the ELA in consequence of ice melt and is advected down-valley. Different mechanisms determine the fate of terminal debris. Ice dynamics is calculated on an fe-mesh (black squares), whereas debris advection requires a finer fd-mesh (red squares).

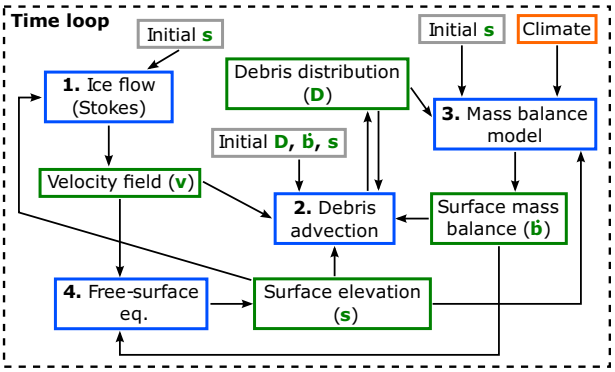

FIGURE 3 | Schematic representation of our modelling approach. Blue boxes indicate essential equations (with order of execution). Important state variables are in green. Grey boxes indicate variables requiring an initialisation. Climate forcing is kept constant (orange box).

based on the assumption that the debris column in itself is more stable than the debris/ice interface. We also assume that a thicker debris layer increases the potential for failure at the debris/ice interface, neglecting possible stabilisation mechanisms of thicker debris layers (Moore, 2018). Our approach is supported by recent laboratory experiments on limestone–ice–limestone samples, showing that at temperatures close to melting conditions normal stresses exceeding a certain threshold lower the coefficient of friction at rock-ice interfaces (Mamot et al., 2018). This behavior is ascribed to an enhanced pressure melting effect at higher normal stresses.

In addition to these complete removal conditions, we also implemented algorithms to describe step-wise gravitational debris displacement along the glacier surface in the terminus area. This mechanism resembles slumping of parts of the debris layer along steep ice slopes and can involve the whole debris column or a fraction f only. This approach is motivated by observations of sediment flow on glaciers (Lawson, 1982), but is parameterised in a more general fashion as a partial failure due to a slope dependent instability. The fraction of displaced debris is linearly dependent on the surface slope α. Moreover, displacement sets in only if the surface is steeper than a threshold slope α_t, while f is defined as:

$$f = \begin{cases} 0 & , \text{if } \alpha \le \alpha_t \\ \alpha M + C & , \text{if } \alpha_t < \alpha < (1 - C)/M \\ 1 & , \text{if } \alpha \ge (1 - C)/M \end{cases}, \qquad (5)$$

where M and C are arbitrary parameters. **Eq. 5** ensures that f is constrained within the interval [0, 1] and is valid in case $\alpha_t < (1 - C)/M$. For $\alpha_t \ge (1 - C)/M$, **Eq. 5** reduces to a step function of α_t, where the entire debris column is removed for surface slopes above the threshold. Note that the surface slope α in **Eq. 5** must be expressed in terms of surface gradient (not in percentage and not in degree).

Tumbling of rocks and thus granular movement of the debris column depends on several contingencies, like e.g., the shape of single rocks and the meter-scale topography of the debris layer. Therefore, as an alternative to the deterministic calculation of f, the model contains also a stochastic approach. In this case f is a random number, which is uniformly distributed within the slope-dependent interval $(\alpha M + C - \delta, \alpha M + C + \delta)$, where δ is an arbitrary parameter. We also ensure for the stochastic approach that f is within the interval [0, 1] deploying a formulation that is analogous to **Eq. 5**.

2.3 Numerical Implementation

The numerical model is implemented using the finite-element software package Elmer/Ice (Gagliardini et al., 2013). The ice-flow component of the model is based on established tools and is briefly described in **section 2.3.1**. On the other side, all debris-related components are completely new and are described in more detail in **section 2.3.2**. The basic modelling approach is illustrated in **Figure 2**, whereas a more detailed schematic overview is provided in **Figure 3**.

2.3.1 Stokes Flow

We solve the Stokes equations on a 2-D flow line geometry and use a synthetic bedrock topography, which is inclined at higher altitudes and rather flat in the lower part (see **Figure 4**). This is the only geometrical input of the model, representing a mountain slope with a horizontal length of 4.5 km. The finite-element mesh was generated using *gmsh* (Geuzaine and Remacle, 2009). We opted for a structured mesh with quadrilateral elements. The mesh has a horizontal resolution of 10 m and it counts eleven evenly-distributed layers in the vertical direction. All simulations run with a time step of one year, which implies that all involved physical quantities (e.g., mass balance) are yearly-averaged quantities.

Using the finite-element method reduces the solution of the Stokes system to a linear system. We tackle this, deploying the direct Unsymmetric-pattern MultiFrontal method for sparse systems (*UMFPACK*; Davis, 2004), which ensures robustness

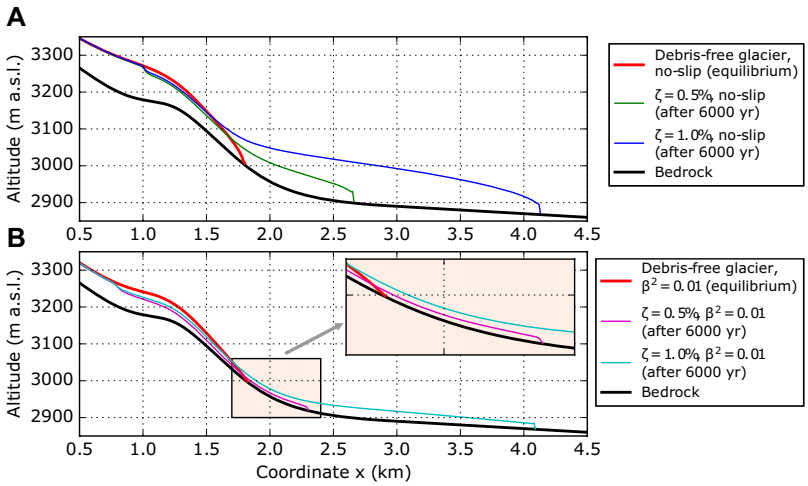

FIGURE 4 | Modelled evolution of glacier geometry for clean and debris-covered glaciers in case of **(A)** no-slip and **(B)** sliding conditions at the glacier base. Clean-ice equilibrium states (red) are compared with debris-covered states after 6,000 years (not in equilibrium). Glaciers with higher debris concentration (ζ = 1.0%) are longer (blue and cyan). On the other side, basal sliding reduces the mean glacier thickness (magenta and cyan).

to the solving procedure. For solving the free-surface equation we use the BiConjugate GradientStabilised method (*BiCGStab*; Kelley, 1995) and apply transient stabilisation (Akin and Tezduyar, 2004), which is necessary to smooth the glacier front and avoid that the ice piles up instead of advancing. Stability of the simulations is improved by adding an artificial ice layer of thickness H_{min} to ice-free bedrock areas (Wirbel and Jarosch, 2020).

2.3.2 Debris Advection

Obtaining stable solutions of the advection equation requires, in general, higher grid resolution and shorter time steps (Courant et al., 1928), compared to the Stokes system. On the other hand, the single solution of the Stokes system is computationally much more expensive compared to the advection equation. We calculate debris advection within the finite-element frame of Elmer/Ice. In contrast to the main simulation, advection is solved on a 1-D finite-differences scheme with an ad-hoc finer mesh (fd-mesh) and shorter time step. This approach proved to be very convenient, as it combines stability and computational efficiency. We refine the finite-element mesh (fe-mesh) by inserting equi-distributed sub-nodes (see **Figure 2**). If the fe-mesh has N nodes and grid size ΔX, the fd-mesh has $n = (N-1) \times (r+1) + 1$ sub-nodes and sub-grid size $\Delta x = \Delta X/(r+1)$, where r is the refinement factor, i.e., the number of sub-nodes between two nodes of the fe-mesh. Similarly, the reduced time step size Δt is a fraction of the original time step size ΔT, such that $\Delta t = \Delta T/s$ (both r and s are integers).

We discretise the advection equation using an upwind scheme, where derivatives are calculated considering sub-nodal values in the direction of the flow origin. This approach avoids oscillations in the advected debris distribution:

$$D_i^{j+1} = D_i^j - \frac{v_{x,i}^j \Delta t}{\Delta x}\left(D_i^j - D_{i-1}^j\right) - \frac{D_i^j \Delta t}{\Delta x}\left(v_{x,i}^j - v_{x,i-1}^j\right), \quad (6)$$

where i is the sub-node index and j the time sub-step index. Debris source D_s is added to the existing debris coverage before the advection step (i.e., not after each time sub-step). Fe- and fd-mesh communicate via shared nodes. Each $(r+1)^{th}$ sub-node coincides with an fe-mesh node and all fe-nodes are shared nodes. Sub-grid variables required to solve **Eq. 6** (e.g., ice velocity) are linearly interpolated between nodal values of the fe-mesh. After completing all time sub-steps within a main time step, the advected debris distribution is communicated to the fe-mesh. This happens by copying shared sub-nodal values to the fe-mesh. All sub-nodal debris values (shared and non-shared) are not modified by the Stokes solver and are used as initial condition for the next advection step (after adding again D_s from the mass balance equation).

Solving the advection equation according to **Eq. 6** is not volume-conserving. Therefore, we calculate the volume integral over the whole debris layer before and after the advection step. The ratio ψ_a between the two integrals quantifies the artificial debris volume change due to the applied solution scheme. We multiply the whole debris distribution by ψ_a, in order to compensate for this artifact.

In addition, **Eq. 6** produces small artificial changes in the spatial distribution of the advected scalar quantity, which are superimposed to real changes due to gradients in the advection velocity. In particular, it tends to flatten edges and adds long and thin tails at the downstream end of the advected distribution. These artifacts have, in general, only a small influence on the model evolution. However, in our study, these thin tails impact the simulation results, since thin debris layers create the highest ice ablation (see **section 2.1** and **Figure 1**). We tackle this issue by cutting off those tails (i.e., setting them to zero debris thickness) at the node (fe-mesh), where debris thickness is less than 0.1 m and less than 50% of the previous (uphill) node. Sub-nodal values uphill from the first adjusted node are not modified, in order not to alter the successive advection step. This procedure works,

TABLE 1 | Overview of performed simulations. Runs with debris-free glaciers (ID 01 and 02) end when the glaciers reach steady state. All other simulations run for 6,000 years. The last three columns report glacier states after those simulation times. Non-equilibrium states may change running the model over longer time periods.

Run ID	ζ (%)	β^2	H_{min} (m)	Removal mechanism	Removal Parameters	Final state	Final length (m)	Final D (m)
01	0.0	no-slip	4.9	none	None	equilibrium	1,800	–
02	″	0.01	1.0	″	″	″	1,820	–
03	0.5	no-slip	4.9	″	″	advancing	2,660	7.2
04	″	0.01	1.0	″	″	oscillating	2,300	2.1
05	1.0	no-slip	4.9	″	″	advancing	4,130	7.5
06	″	0.01	1.0	″	″	″	4,190	10.0
07	″	no-slip	4.9	slope	$\tilde{\alpha} = 35°$	equilibrium	1,910	0.7
08	″	″	″	″	$\tilde{\alpha} = 39°$	″	1,990	0.8
09	″	″	″	″	$\tilde{\alpha} = 42°$	″	2,080	0.9
10	″	″	″	″	$\tilde{\alpha} = 45°$	″	2,160	1.0
11	″	″	″	″	$\tilde{\alpha} = 50°$	″	2,400	1.4
12	″	″	″	driving stress	$\tilde{\tau} = 20$ kPa	″	2,160	1.0
13	″	″	″	″	$\tilde{\tau} = 40$ kPa	″	2,750	2.1
14	″	″	″	″	$\tilde{\tau} = 60$ kPa	advancing	3,330	3.4
15	″	″	″	″	$\tilde{\tau} = 80$ kPa	″	3,570	4.1
16	″	″	″	″	$\tilde{\tau} = 100$ kPa	″	3,710	4.5
17	″	″	″	deterministic[a]	$C = -0.50$	adv. and oscill	3,910	5.1
18	″	″	″	″	$C = -0.20$	″	3,780	4.7
19	″	″	″	″	$C = 0.00$	″	3,820	4.8
20	″	″	″	″	$C = 0.20$	″	3,580	4.0
21	″	″	″	random[a]	$C = -0.50$	″	3,890	5.0
22	″	″	″	″	$C = -0.20$	″	3,810	4.8
23	″	″	″	″	$C = 0.00$	″	3,830	4.9
24	″	″	″	″	$C = 0.20$	″	3,590	4.2
25	″	″	″	deterministic[b]	$f = 0$	advancing	3,570	4.1
26	″	″	″	″	$f = 1$	adv. and oscill	3,530	3.9

[a]*With* $\alpha_t = 35°$, $\tilde{\tau} = 80$ *kPa and* M = *1*
[b]*With* $\alpha_t = 35°$ *and* $\tilde{\tau} = 80$ *kPa*

since the thickness of the debris coverage steadily increases down-valley and rapidly drops only at the glacier terminus, where the tails occur. We compensate the debris losses due to this correction by applying a scaling factor ψ_t to the remaining advection distribution, which is analogous to the previously introduced factor ψ_a.

Our model does not include periglacial moraine mechanics for debris migration and generation of terminal moraines, as this is far out of scope of this paper. Therefore, debris deposited on bedrock after a frontal retreat is completely removed. If the glacier retreats and ice thickness drops below $\tilde{H}_{min} \gtrsim H_{min}$, all downstream-located nodal and sub-nodal debris is set to zero. Otherwise, in case of a new glacier advance, the advancing ice would migrate underneath this basal/terminal moraine and produce an artifact.

2.3.3 Model Structure

We simulate the ice/debris glacier system combining the governing equations described above as shown in **Figure 3**. First we deploy the Stokes solver to calculate the ice velocity field according to the current glacier geometry (i.e., provided as initial condition or from the previous time step). The velocity field together with information about the current debris distribution, surface mass balance (required to determine the debris source term) and surface topography (needed for debris displacement and removal mechanisms, if active) is used to solve the advection equation on the fd-mesh and determine the new debris distribution. After returning to the fe-mesh, the new debris distribution is used to calculate the new mass balance profile. This, together with the velocity field, is used by the free-surface equation to calculate surface evolution, which is the starting point for the next time iteration.

3 DESCRIPTION OF EXPERIMENTS

Even though the effect of debris cover on ice melt is investigated in high detail on a large number of glaciers, it is difficult to relate this local information to the general glacier evolution. Also, exploiting satellite imagery gives only a rather limited insight into the ongoing changes, because the evolution of debris-covered glaciers covers a much larger time scale then the satellite era. Therefore, the application of suitable models is required to shed light on the fundamental and long term glacier behaviour.

In order to investigate the general feedback mechanisms, we run a suite of experiments with different, but temporally constant englacial debris concentrations and various debris unloading schemes, as well as for different basal conditions. The bandwidth of parameter variations should provide a broad coverage of potential glacier configurations and thus allow insight into the general evolution characteristics of debris-covered glaciers. An overview of all performed simulation runs is given in **Table 1**.

We decided to run the experiments for a maximum of 6,000 years, because our results show that this time is sufficient for the glaciers to show their characteristic dynamical behaviour. It turned out that changes over the final 1,000 years of the 6,000 years simulation period are small and do not alter characteristic variables significantly (if we consider e.g., advancing rates or oscillation periods).

3.1 Experiments Without Gravitational Removal of Debris

One of the principal questions about debris-covered glaciers is concerning the potential existence of steady state, despite a continuous supply of debris to the glacier surface by melt out (Anderson and Anderson, 2016; Ferguson and Vieli, 2021). For the sake of simplicity, we assume an englacial debris concentration, which is constant in space and time, because we are interested in the basic glacier feedback, not in specific scenarios. Ice flux in the ablation zone generally decreases towards low values along the flow of a glacier, equalling surface ablation at the snout in the case of steady state. If debris piles up on the glacier terminus over time (due to compressive flow and melt out), melt rates approach zero and so does also ice flux. This results in negligible horizontal transport of supra-glacial debris, which prohibits debris transport across the terminus (if no gravitational removal is allowed) and leads to debris accumulation in the terminus region and thus a further reduction in melt. As a consequence, the mass balance turns positive and ice flux leads to a glacier advance and thus increases the ablation region. As long as debris is not removed from the glacier surface, this feedback will lead to a continuous length growth in the model, while on a real glacier differential melt and dirty-ice areas at the margin of the debris cover might change its geometry and thus also mobilisation of debris (Fyffe et al., 2020). To investigate this hypothesis of indefinite glacier growth for accumulating debris, we run a sequence of experiments with different, but temporally constant englacial debris concentrations. We expect the results to provide insight into the temporal evolution, characteristic time scales and a potential approximation of steady conditions of a debris-covered glacier in the case of no debris loss from the glacier front. These experiments are partly motivated by the observation of debris-covered and more or less stagnant glacier termini, which lack any evidence of widespread debris removal (e.g., Baltoro Glacier in the Karakoram, Inylcheck Glacier in the Tian Shan).

3.1.1 The Effect of Different Debris Concentrations

Englacial debris concentration probably has a strong influence on the time scales of glacier evolution, because the melt out of englacial debris directly influences the surface mass balance conditions. Therefore, we test this influence by running otherwise identical setups with englacial debris concentrations of $\zeta = 0.5\%$ and 1.0%. These values represent a reasonable range compared to recent *in-situ* observations at a heavily debris-covered glacier (Miles et al., 2021). All simulations start from the same steady-state debris-free geometry, which is reached by applying the surface mass balance conditions described in the model setup (see **section 2.1** and **Supplementary Table S1**) to our standard bedrock geometry until a constant clean-glacier volume is reached. Debris advection is calculated on an fd-grid setting $r = 7$ and $s = 10$ (see **section 2.3.2**). The amount of emerging debris for each grid cell results directly from the ice melt. The artificial debris mass loss, connected to the advection algorithm, is quantified and compensated. Also, the thin debris tail at the downstream end of the advected debris distribution is removed and the mass loss compensated. The minimum ice thickness is set to $H_{min} = 4.9$ m. In case of a retreating glacier front, all debris located downstream of the terminus (first sub-node with ice thickness below H_{min} down-glacier from the equilibrium line) is removed from the system. This is a considerable simplification compared to real conditions, because periglacial moraine deposits probably influence the dynamics of a recurrent glacier advance. However, taking into account such deposits (and developing a suitable deformation model) would have complicated the numerical setup too much, without providing essential insight due to the poor knowledge of the required physics.

3.1.2 The Effect of Basal Sliding

The above described experiments are performed under conditions of a frozen bed. Basal sliding has an important impact on the glacier evolution and very likely many of the debris-covered glaciers show temperate conditions at least below the equilibrium line. The investigation of glacier reaction for different basal conditions aims mainly on the time scales involved and the differences in glacier geometry in the context of debris cover and debris accumulation. Therefore, the same experiments as above are conducted with the sliding parameter β^2 set to 0.01 (see **Eq. 1**). The initial state of the simulations is a debris-free equilibrium state calculated setting $\beta^2 = 0.01$ as well. Compared to the no-slip case, switching on sliding results in higher flow velocities, lower ice thickness, but similar glacier lengths. Because of the reduced glacier thickness, we reduce the minimum ice thickness to $H_{min} = 1$ m.

3.2 Experiments With Gravitational Removal of Debris

The above condition of indefinite debris accumulation only serves as an idealised fundamental feedback system of debris-covered glaciers. The more realistic case is a removal of debris from the glacier terminus in one or another way. Here, we investigate the consequences of several basic mechanisms of debris removal on glacier response. The experiments are conducted on glaciers with englacial debris concentration $\zeta = 1.0\%$ and no-slip basal conditions.

3.2.1 Abrupt Removal

First we implement the abrupt removal of debris after reaching a defined threshold at a specific location (see **section 2.2.2**). Debris downstream of this location is entirely removed. The threshold can be a critical surface slope $\tilde{\alpha}$ or a critical driving stress of the debris layer (the yield stress $\tilde{\tau}$). For the slope-only

criterion, debris is removed as soon as the slope downstream of a single sub-node exceeds $\tilde{\alpha}$. We ran the model for several critical slopes ranging from 35° to 50°(70–120%). For the yield stress experiments it is necessary that the average driving stress over ca. 10 m (7 sub-nodes) is higher than the yield stress $\tilde{\tau}$. We used stresses between 20 and 100 kPa as limits for debris discharge from the system.

3.2.2 Continuous Debris Displacement and Abrupt Removal

Instead of an instantaneous complete removal of debris from the terminus, it often can be observed that supra-glacial debris slides down steep slopes in a more continuous way, if the slope is not too steep. We maintain an abrupt removal mechanism (for a yield stress of $\tilde{\tau}$ = 80kPa). However, this is combined with the continuous debris displacement mechanism described in **section 2.2.2**. The fraction f of the debris column of a sub-node is displaced (not removed) to the neighboring downstream sub-node according to **Eq. 5**. Debris is displaced, if the surface slope is higher than $\alpha_t = 35°$ (70%). We test different values of C between −0.50 and 0.20, whereas we always set $M = 1$. We also consider the limit cases $f = 0$ and $f = 1$. The calculation of f is either deterministic or random (within a deterministic range). In the latter case we set $\delta = 0.10$.

4 RESULTS

4.1 Equilibrium State of the Clean-Ice Case

First, we present model runs for clean-ice conditions, which we further use as initial state for all subsequent experiments with englacial debris concentrations. Due to the constant climate forcing, the model reached steady-state conditions for both no-slip and basal sliding conditions. With the chosen bedrock topography and the prescribed surface mass balance (indeed the calculated surface mass balance changes according to variations in surface elevation), the glacier developed from ice-free conditions and equilibrium was reached after 600 years for the no-slip case. Based on this state, and switching on basal sliding results in additional ca. 200 years to reach a new equilibrium state for $\beta^2 = 0.1$ and another 200 years to reach equilibrium with $\beta^2 = 0.01$. The model results show almost the same final glacier length of about 1.8 km (see **Figure 4**). However, the ice thickness distribution is rather different. The no-slip glacier shows a maximum ice thickness of about 95 m almost exactly half-way downstream, while for the sliding case the maximum results to about 63 m at the same distance (see **Supplementary Figure S1**). As a consequence, the surface elevation is more than 30 m lower in the region of the equilibrium line for sliding conditions, while the 2-D "volume" is about 30% smaller. Also the glacier velocities are considerably different, with a vertically-averaged horizontal velocity maximum of 10 m/yr for the sliding case and 5.5 m/yr for the no-slip case, respectively (**Supplementary Figure S2**). Due to the bedrock geometry, the maximum ice velocities are observed a few hundred meters downstream of the equilibrium line.

4.2 Equilibrium-State Experiments Without Debris Removal

The initial motivation for these experiments was to test the hypothesis that debris-covered glaciers cannot reach or approximate a steady state if the emerging debris remains on the glacier. In the case of close-to-balanced conditions, the unloading of debris might be difficult, because of vanishing ice velocities at the front.

Figure 4 shows glacier geometries for debris concentrations of ζ = 0.5% and 1.0% and different basal conditions spanning 6,000 years of evolution. Starting from a debris-free glacier, the increasing debris cover protects the underlying ice and the glaciers start to advance. The growth of the glacier depends on the debris concentration and results in a more than doubled glacier length and an increase of the glacier volume by over 150% for a debris concentration of 1.0%. In case of smaller englacial debris concentrations, glacier length and volume changes are more moderate, indicating convergence to conditions of clean-ice glaciers.

Basal conditions do not significantly influence the glacier length, but have a strong impact on the glacier thickness. Compared to the initial debris-free geometry, ice thicknesses just downstream of the equilibrium line reduce in the case of basal sliding by about 15–20 m (**Supplementary Figure S1**) and this thinning extends further upstream across the equilibrium line. The lower parts of the glaciers beyond the clean-ice terminus are also thinner in case of sliding, with thicknesses reduced by 60–75% compared to the no-sliding case (about 25 m compared to about 90 m for ζ = 1.0%). This also leads to a migration of the equilibrium line of about 200 m further upstream and a reduction of the accumulation area by about 20%.

Maximum ablation rates are observed just downstream of the equilibrium line with values exceeding −3 m/yr, while ablation approaches zero towards the terminus, in accordance with the expected effect of the varying debris thicknesses. Higher flow velocities due to sliding enlarge the size of the thin-debris and high-melt area (see **Supplementary Figures S3, S4**). This effect leads to a stronger reduction of ice volume for sliding conditions, but also increases the melt-out rate of englacial debris. After 6,000 years of model evolution we observe a mean debris thickness of 10 m in case of basal sliding and 7.5 m for the corresponding no-slip experiment for ζ = 1.0%, while unrealistic values of almost 40 m of debris are reached close to the terminus. The change to ζ = 0.5% reduces the mean debris thickness to 7.2 m (see **Table 1**).

All simulations without debris removal show an ongoing glacier advance even after 6,000 years evolution, except for the ζ = 0.5% sliding case (**Figure 5**). The glacier advance in case of ζ = 1.0% and basal sliding conditions is faster compared to the no-slip case for the first few millennia. However, after 5,500 years, the non-sliding glacier surpasses the sliding glacier in length, indicating a stronger imbalance compared to the sliding case. However, none of the experiments seem to approach steady-state conditions.

The experiment with ζ = 0.5% and sliding conditions is characterised by erratic length oscillations with amplitudes of

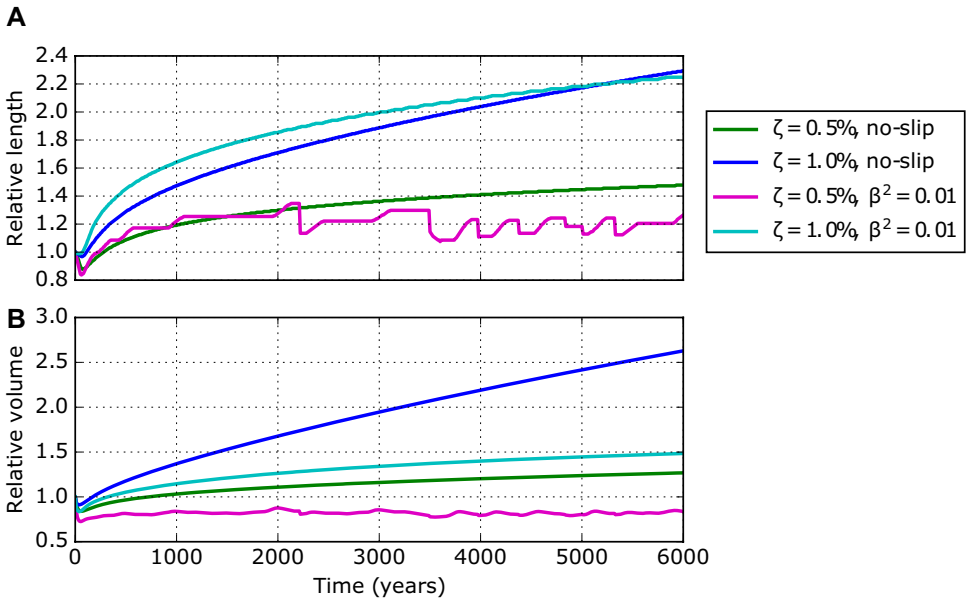

FIGURE 5 | (A) Glacier length and **(B)** volume evolution of simulated debris-covered glaciers for different englacial debris concentrations (ζ = 0.5% and 1.0%) and different basal conditions (no-slip or sliding with β^2 = 0.01). Lengths and volumes are relative to the corresponding clean-ice equilibrium state. After 6,000 years evolution none of the systems is in equilibrium. The system with ζ = 0.5% and β^2 = 0.01 (magenta) is in an erratically oscillating state. The other three systems are in an advancing state.

a few hundred meters. The model approaches repeatedly a close-to-balance state, but collapses afterwards. **Figures 6** and **7** illustrates details of such a cycle (for further details on the debris budget see **Supplementary Figure S5A**). First, the glacier advances as in the other experiments (green profile in **Figure 7**). However, due to a continuous slow down across the glacier tongue, ice loss by ablation surpasses mass gain from ice flux (see red areas in **Figure 6**, e.g., at $t \approx$ 2,100 years). This imbalance results in a slow reduction of ice thickness (blue profile in **Figure 7**), which intensifies towards the equilibrium line with its thinner debris cover. The surface slope of the glacier tongue flattens even more and ice flux decreases further (cyan profile). Finally, the lower tongue separates from the main glacier within about a century (magenta profile) and the mass balance of the remaining glacier (15% shorter) turns positive, leading to an advance of the new terminus. The cyclicity in our experiments ranges from a few centuries up to about 1,000 years. During such periods the remaining dead-ice body with about 10 m depth will disappear even for rather small ablations rates before the re-advancing glacier will cover it. Periods of close-to-balance conditions last up to 1,000 years. However, the red stripes in **Figure 6** (e.g., between t = 1,000 and 2,000 years) indicate that the glacier undergoes dynamical changes, despite the constant length and apparent quiescence. Regions with net mass loss are evident, but the imbalance is not strong enough to trigger a separation and the ice column above the low-flux area thickens and adjusts the flux budget.

These results indicate that glaciers will not reach a final steady state for the chosen boundary conditions. The glaciers rather continue to advance or turn into an oscillating state with a periodicity of several centuries and up to millennia. By extending the simulation time to more than 6,000 years, it is an open question whether the glaciers would approach steady state, keep growing or advance until detaching the frontal part and enter an oscillating state. However, such time scales of at least several millennia exceed most evolution scales of mountain glaciers anyway.

4.3 Equilibrium-State Experiments With Debris Removal

The experiments with a continuous accumulation of supra-glacial debris already demonstrate that this condition is not realistic for large time scales. Even though, some glaciers like e. g. Baltoro Glacier show very stable frontal conditions with no obvious debris transport into the flood plain, for more than a century. But also here some debris is removed at the basal water outlet through slumping from the steep cliff above. In the case of a steep glacier front and/or a thick frontal debris layer, the loss of debris from the glacier system is very likely. Our experiments for slope-only and driving stress induced debris mobilisation (see **section 2.2.2**) will investigate possible glacier reactions to such processes. In these experiments, debris at the glacier front is removed from the system as soon as the threshold conditions are met, resulting in a clean-ice glacier front which adapts its geometry to the prevalent melting conditions. Supra-glacial debris, which is advected across the upstream boundary of this region, is again removed, if the glacier geometry still meets the threshold conditions. The same is valid for emerging debris, which reaches the surface of the glacier front in consequence of ice melt.

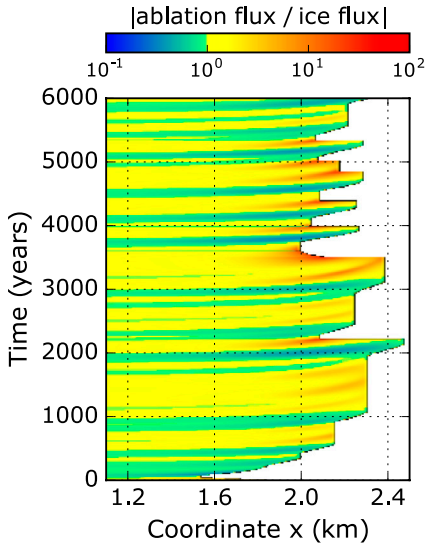

FIGURE 6 | Evolution of the ratio between ablation flux and ice flux for the oscillating experiment (magenta curve in **Figure 5**) with $\zeta = 0.5\%$ and $\beta^2 = 0.01$, calculated at each node. The ablation flux results from integrating from the current node to the downstream end of the glacier. The ice flux is calculated by integrating the ice flow through a vertical line at the current node. The ratio increases when the glacier advances, due to an increase of the ablation area. A clear divergence is evident at locations where the glacier collapses. The collapse reduces the length of the ablation area, which results in values of the flux ratio below one (green to blue), which initiates a new advance phase.

Glacier length in these experiments with complete debris removal depends strongly on either of the parameters $\tilde{\alpha}$ and $\tilde{\tau}$. Note that we investigate both discharge mechanisms separately with dedicated model runs (see **Table 1**). For a steeper sliding angle, as well as a higher yield stress for debris mobilisation, the glacier length increases. Melt rates are enhanced at the steep glacier front, if debris is removed more easily (lower threshold) from the glacier terminus. In these cases, the glacier reaches close-to-balanced conditions earlier and with a shorter length. In our setup the final glacier length increases up to 30% (total length between 1.9 and 2.4 km) with respect to the clean-ice glacier for variations of the critical sliding angle $\tilde{\alpha}$ in the range of 35°–50°(see **Figure 8A**). For a realistic, but low bandwidth of yield stresses $\tilde{\tau}$ in the range 20–40 kPa the glaciers converge to steady states, which are 20–50% longer with respect to the starting clean-ice glacier (see **Figure 8B**). Experiments using higher, but still common yield stresses in the range 60–100 kPa produce glaciers, which still grow after 6,000 years evolution (85–105% length increase after this time). Moreover, the thresholds $\tilde{\alpha}$ and $\tilde{\tau}$ influence the inclination of the glacier front in the final state. For both mechanisms it shows that, the lower the threshold, the flatter is the glacier front. The likely reason is that, if the discharge condition is met, frontal nodes are exposed to more ablation and reduce their elevation until the inclination of the glacier front is low enough to stop further debris discharge. The ongoing complete removal of supra-glacial debris from the terminus allows the establishment of a steady state for the glacier mass balance, as well as the debris flux. It can be expected that experiments with $\tilde{\tau}$ in range 60–100 kPa would reach a balanced state as well, if the simulation time is longer.

A more episodic debris transport across the glacier front, where only a certain proportion of the debris is completely removed is probably the more realistic case. The supra-glacial debris column at the unstable node is distributed across the neighboring downstream nodes in dependence of the frontal slope, before it finally leaves the system. This condition resembles a glacier front with different slope angles, where parts of the glacier front are ice-free, while neighboring regions still are debris-covered and changing surface angles will continuously modify the debris cover. The corresponding experiments reveal that a steady state is not established under such conditions.

The amount of transient supra-glacial debris on the glacier front depends on the parameter C in **Eq.5**. **Figure 8C** shows the effect of C on the temporal evolution of debris-covered glaciers (see **Figure 8D** for a zoomed view of **Figure 8C**). We test C in the range −0.50 to 0.20. The resulting differences are small between using the deterministic and the random mechanism. For lower (negative) C, the fraction f of displaced debris (we always set $M = 1$) becomes smaller and vice versa. If $f = 0$, debris displacement is zero and the simulation reduces to the example with $\tilde{\tau} = 80$ kPa (the blue profiles in **Figures 8B, 8C** are equal). In the limiting case $f = 1$, the whole debris column is transferred to the next downstream located sub-node, as soon as the surface slope exceeds the threshold $\alpha_t = 35°$.

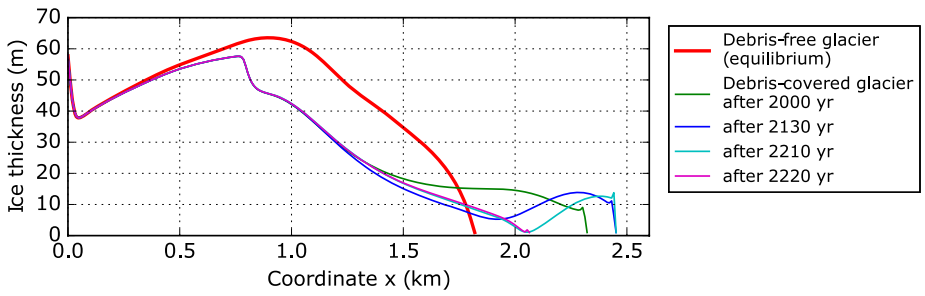

FIGURE 7 | Illustration of glacier conditions for the erratic oscillation state of the glacier system with $\zeta = 0.5\%$ and $\beta^2 = 0.01$. Four typical phases are captured: frontal advance (green), further frontal advance and thinning in the low-flux area (blue), glacier state just before the collapse (cyan), new geometry just after the collapse (magenta).

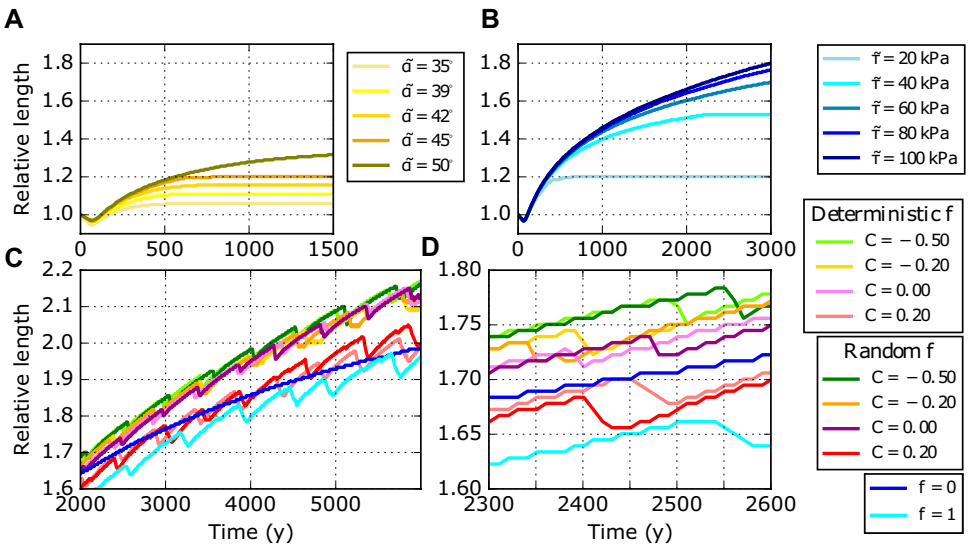

FIGURE 8 | Glacier length evolution for different debris removal and displacement mechanisms. **(A)** Slope-triggered debris removal; **(B)** driving-stress triggered debris removal; **(C)** deterministic and random slope-induced debris displacement combined with abrupt driving-stress triggered debris removal. Panel **(D)** is a zoom of **(C)**. Whereas in **(A)** and **(B)** the glaciers can reach steady state if $\tilde{\alpha}$ or $\tilde{\tau}$ are sufficiently low, in **(C)** the glaciers enter an oscillating state, which is superimposed to an advancing state. The larger the fraction of displaced debris (larger C or, equivalently, $f \rightarrow 1$), the more enhanced are the oscillations.

Within the simulation period of 6,000 years the glaciers advance and are far from steady state, although the rate of growth decreases with time. The growth is periodically interrupted by short retreat periods (ca. every 500 years). These phases last a few decades and result in glacier length reduction of some tens of meters. **Figure 9** reveals details of those oscillations in case $C = 0.20$ (further details in **Supplementary Figure S5B**). Since f is close to one, the fraction of displaced debris is large and nodes become almost debris-free, as soon as surface slope exceeds α_t. The high melt rates influence the slope of the glacier front, which is lowered below α_t. Because of the less inclined front, a thicker frontal debris layer is required to exceed $\tilde{\tau}$. Therefore, the height of the frontal debris layer can become thicker than in experiments without debris displacement. The abrupt collapse of the thick debris layer after reaching the yield stress $\tilde{\tau}$ produces a strong ice flux imbalance with respect to ablation and results in a strong glacier retreat. Ice-free nodes rapidly reduce their elevation, thus steepening upstream located surface segments and determining further debris removal or displacement. The glacier length reduces until the ice flux is high enough to compensate the lowering of the debris-free surface and the mean slope of the front starts decreasing. This allows debris to accumulate and the glacier to grow again. Lower values of C imply a smaller fraction f of displaced debris. Thus a better protected front induces larger glacier lengths, but do not alter the dynamical behaviour of the system. In comparison, switching off the unloading mechanisms produces even longer glacier states (see blue profile in **Figure 5**) because of the thicker and more protective debris layer.

The main difference between experiments with debris displacement and experiments with debris removal without displacement is the steeper slope of the terminus in the latter case. Unloading events are therefore more frequent, but the amount of removed debris is small. It follows that the induced imbalance is moderate. It can be promptly compensated by the ice flux from above and by the formation of a new debris layer. The imbalance is too gentle to generate visible length oscillations. It remains an open question whether the combination of debris displacement and removal could stop glacier growth after 6,000 years simulation time and whether the glaciers would enter an oscillating state.

5 DISCUSSION

We tried to design simple experiments, which nevertheless represent characteristic settings of debris-covered glaciers and thus form the basis for investigating fundamental glacier reactions. We did not intend to simulate all complex feedback mechanisms, which would just distract from the principal relationships between mass balance, debris cover and ice dynamics. However, we used a full Stokes model and small grid dimensions in order to obtain a realistic glacier geometry as far as possible. Another difference to earlier studies is the implementation of enhanced met rates for thin debris covers combined with a more physically based melt function.

Based on simple mass conservation considerations it seems obvious, that debris-covered glaciers cannot reach a steady state, unless the accumulated volume of supra-glacial debris on the glacier tongue also is in equilibrium with the melt-out conditions. Konrad and Humphrey (2000) argued that a debris-covered glacier in steady state must be infinitely long. This is in principle true: if debris is not allowed to leave the system, it accumulates and reduces ablation at the terminus almost to

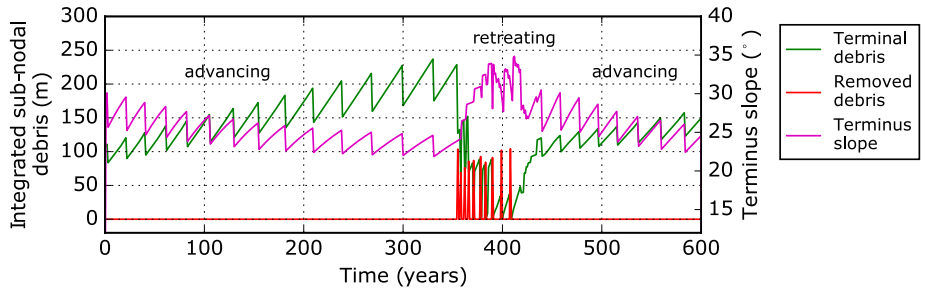

FIGURE 9 | Evolution of debris coverage and slope of the terminus in case of deterministic debris displacement and removal for $C = 0.20$. Terminal debris is the sum of sub-nodal debris loads across the last five nodes (green). Removed debris is calculated from sub-nodal values as well (red). Terminus slope is calculated considering the last five nodes (magenta). Note that the last five nodes migrate in flow direction in case of an advancing glacier. Just after advancing to the next node, the last glacier node has very low debris cover and surface elevation. This bias is responsible for the observed saw tooth behavior.

zero. Still, continuous glacier volume growth is expected in case of ongoing accumulation of supra-glacial debris on the glacier tongue, even though the growth rates monotonically approach zero. However, our experiments indicate that the time scales under such conditions are in the order of centuries to millennia even for moderate glacier sizes (see e.g., the example with $\zeta = 0.5\%$ and without sliding in **Figure 5**). A comparable glacier evolution in the real world will be strongly superposed by climatic fluctuations, which are not included in our experiments. But even by including glacier response to moderate climate variations, it might be impossible to discriminate between close-to-steady conditions under the dominating climate and minimal growth rates due to long-term debris accumulation. A glacier with a moderate mean englacial debris concentration ($\zeta \approx 0.5\%$) can therefore evolve over many centuries in a rather continuous way with only small debris accumulation rates on the lower tongue, adding up to several meters in total debris thickness. During the usual observation intervals of a few years up to some decades, no significant change in glacier geometry will be observed for such glaciers, while climate sensitivity will be greatly reduced over the centuries, due to the build-up of a thick debris cover on the lower terminus.

However, it is clear that an indefinite growth of debris thickness is impossible and certain removal mechanisms gain importance over time. Our results show that, without unloading mechanisms, the debris coverage of the lowermost glacier tongue may reach unrealistic values of up to 40 m (see **Supplementary Figure S3, S4**). Recent studies introduced debris down-wasting mechanisms to overcome this apparent unrealistic behavior of indefinite glacier growth. Anderson and Anderson (2016) implemented a triangular terminal wedge parameterisation, which enables debris flux into the foreland and provides conditions for the glacier to reach steady state. Ferguson and Vieli (2021) followed a more pragmatic approach, removing debris if the ice thickness falls below a critical value. This condition permits the glacier to reach steady state as well. Those simplified approaches reflect a different focus of those studies with respect to ours, aiming on more general conclusions.

One possibility of overcoming the problem of continuous glacier growth results from the inversion of the vertical mass balance gradient in the case of debris-covered glaciers (see **Figure 1**), which shows decidedly higher melt rates towards the equilibrium line compared to the lower glacier tongue. This strong gradient leads to a reduction in surface slope across the glacier tongue over time (see **Figure 4**), because of the higher melt rates upstream. In consequence, the mass flux through the tongue will be reduced.

The simulation run with englacial debris concentration $\zeta = 0.5\%$ and basal sliding conditions shows that the feedback between reduced flux and high melt rates can potentially lead to a separation of the lower tongue from the main glacier. If this happens, the loss of a considerable part of the ablation zone (ca. 25%) and a subsequent accumulation of supra-glacial debris on the new terminus leads to a new advance of the remaining glacier. The dead ice body very likely melts down, before being covered by the advancing ice. This cyclic behaviour is only evident in the experiment with basal sliding and low debris concentration, because glaciers with basal sliding conditions are thinner and more likely to collapse. Moreover, they have shorter reaction times, such that temporary flux imbalances turn into rapid geometry changes, which can enforce the imbalance and induce a collapse.

We are aware that very thick debris columns might compromise our assumption about the additional debris-induced stress on the ice surface, which we neglect in the momentum balance. Including the weight of the debris layer in the momentum balance will have an impact on the dynamics of the system similar to enhanced sliding and thus enforce the oscillation mechanism to a small degree.

The glacier separations of our idealised setup are difficult to observe in nature, because natural climate fluctuations, the non-continuous englacial debris concentration and additional processes of debris redistribution and melt hot spots on the glacier tongue likely modify the evolution of the modelled cycles. On the other hand, observed elevated glacier beds with clearly expressed lateral and terminal moraines, where frontal debris cannot easily be transported off the glacier (e.g., Khumbu Glacier, Ngozumpa Glacier, Nepal) might be the result of subsequent terminus collapses in the past.

Our simulations show that glacier oscillations are suppressed, if we increase the englacial debris concentration ζ to 1.0% or impose no-slip basal conditions (both changes modify the glacier

states towards less ablation and larger ice volumes). In these cases the generated glacier systems advance over the whole simulation period of 6,000 years. We do not know how the glaciers would behave, if we would further extend the simulation in time: they could keep growing, reach a steady state (at least asymptotically) or enter an oscillating state. The glacier system with $\zeta = 0.5\%$ and no-slip conditions and the system with $\zeta = 1.0\%$ and $\beta^2 = 0.01$ show very small growth rates at the end of the simulation time. This indicates close-to-balance conditions, but on time scales in the order of millennia.

In the view of a dynamic debris budget, Anderson and Anderson (2016) broadly investigated consequences of varying the location of debris input in the accumulation area and considered englacial debris transport. Ferguson and Vieli (2021) explored the effect of debris coverage on glacier response time in reaction to climatic variation. Our investigation of different debris discharge mechanisms in relation to the question about the steady state of debris-covered glaciers is connected to the conceptual examination given in Konrad and Humphrey (2000) relative to debris-induced terminus dynamics. In particular, the authors considered an advancing terminus with debris resting on top of the ice, which is exposed to high ablation rates on the clean down-glacier side. The enhanced melt lowers the terminus surface, which becomes steeper. Debris starts ravelling down the face of the glacier and accumulates at the base. Piled debris protects the advancing ice face, which overrides the fallen debris. Debris removal mechanisms that we implemented shed light on Konrad and Humphrey (2000)'s conceptual model. However, two major issues still hamper its full numerical realisation: 1) the realistic representation of terminus geometry evolution; 2) modelling debris pile-up at the base of the ice front and the overriding of the debris pile. The first issue requires careful treatment of the surface evolution. In case of an advancing glacier front, we observe that the calculated free surface is characterised by small irregularities in the terminus region (see the little spikes just above the steep glacier fronts in **Figure 4**, e.g., green profile). Wirbel and Jarosch (2020) pointed out similar instability issues in case of inequality-constrained free-surface evolution and showed that full Stokes representations of glacier dynamics are able to reproduce realistic geometries, when treating the free-surface problem with appropriate stabilisation techniques. In our case, instabilities are minor and appear in experiments without debris removal, where front advance is fast and the terminus geometry is not decisive for the glacier evolution, because it doesn't govern the debris mass balance. We are therefore convinced that the observed minor numerical instabilities at the glacier front do not impact our results. On the other hand, off-glacier debris dynamics and the overriding of periglacial deposits could be tackled with additional physics. However, the coupling with the frontal glacier dynamics is not yet solved.

Episodic or continuous removal of frontal debris depositions is a pre-requisite for a long-lasting debris balance. Otherwise the accumulation of debris in front of the glacier will prevent further debris migration from the glacier. Therefore, either melt water events, erosion by river flow or other processes need to remove the unloaded debris from the region in front of the glacier terminus. An equilibrium between debris melt out and its removal can likely be established, if such external conditions exist. This might then lead to a steady-state glacier geometry in case of constant climate conditions. We only focused on the on-glacier processes and glacier length under such conditions depends on the critical surface angle for debris migration or the related critical stress conditions. The glaciers then reach equilibrium states with lengths of up to 1.5 times the clean-ice glacier equilibrium length, which is 1.8 km in our model setup. For critical driving stresses between 60 and 100 kPa the observed length increase is up to 105% after 6,000 years simulation. Those are non-equilibrium states, but it is likely that a balanced state would be reached, running the simulation over longer time periods.

Because such an ongoing complete debris removal across the entire frontal zone is not realistic, we also investigated continuous debris displacement mechanisms combined with removal events. Under such conditions, the glacier shows a cyclic behaviour, which is superimposed to a general advancing trend (see **Figure 8C**). The retreating phases are short (few decades), of small amplitude (less than 50 m) and occur every ca. 500 years. Small fluctuations of debris-covered glaciers, which are observed today (e.g., Scherler et al. (2011), Banerjee and Shankar (2013)), therefore, could result from the complicated interaction between ice and debris dynamics, decoupled from the climatic superposition.

Excluding the question about steady state, fundamental results of our investigation are consistent with previous modelling studies, where comparable. We observe that debris input increases the glacier length and reduces the AAR. Moreover, as pointed out in Anderson and Anderson (2016), when approaching the terminus, the presence of debris coverage reduces gradients of thickness, surface velocity and ice flux (see **Supplementary Figures S1, S2**). As in Ferguson and Vieli (2021), we could validate that the debris layer delays the glacier length response with respect to the volume response, especially in the retreating case. We observe this e. g. in the experiment without debris removal with oscillations ($\zeta = 1.0\%$ and $\beta^2 = 0.01$) where, after reaching the maximum extension, volume loss sets in, before the glacier length starts decreasing (see **Figures 5**, **6**). The retreat is massive, only after the collapse of the stagnant terminus. Our results show that debris-covered glaciers quickly converge to steady state, if debris is allowed to leave the system. In particular (as Anderson and Anderson (2016) also show), a faster unloading mechanism and thus lower thresholds $\tilde{\alpha}$ and $\tilde{\tau}$ results in a glacier reaching earlier a steady state. As a consequence of the low ablation rates, we observe that flow paths in the lower ablation zone are almost parallel to surface, as Konrad and Humphrey (2000) also observed. The effect of basal sliding on the thickness of the debris layer is twofold. On the one side we could confirm results of previous studies, referring that basal sliding conditions and the related higher ice-flow velocities imply a thinner debris coverage. We observe this in the thin-debris area just below the ELA, which is larger in case of basal sliding conditions compared to no-slip (see red areas in **Supplementary Figures S3, S4**, panels **A** and **C**). On the other side, according to our model construction, larger thin-debris areas due to sliding determine higher melt rates and a larger debris input. This additional debris amount accumulates in the near-terminus area and generates (in those areas and on

average over the whole ablation area) a thicker debris coverage for basal sliding conditions (see violet areas in **Supplementary Figures S3, S4**, panels **A** and **C**, and compare run IDs 05 and 06 in **Table 1**). Related to this, as in Konrad and Humphrey (2000), we found out that a larger debris input (larger ζ) does not necessarily imply a proportionally thicker debris coverage (see **Table 1** and compare run IDs 03 and 05). Indeed, a larger debris input may influence the glacier evolution increasing its thickness and flow velocity (see **Supplementary Figures S1, S2**), thus reducing the thickness of the debris layer (at least on a first evolution step). Finally, maximum debris thicknesses calculated for the different scenarios are impossible to compare with results from previous studies, because they depend on glacier-specific properties (like the flow velocity) and are tightly connected to the implemented discharge mechanisms, which distinguish our study.

6 CONCLUSIONS

The existence of supra-glacial debris considerably complicates the energy exchange between glaciers and the atmosphere. Several additional physical processes play a role and, together with the wide range of debris properties, makes it unlikely, that ice ablation can be calculated on a local scale across extended glacier regions. Furthermore, the feedback mechanisms between ice dynamics, debris dynamics and surface energy balance influence and might obscure the glacier reaction to climatic variations. Therefore, we focused this study on the relation between the glacier response on debris thickness variations only and used an appropriate numerical setup to ensure the most realistic dynamic glacier response. Our results show that the glacier-debris interaction leads to long periods of adaptation, which can reach even millennia also for medium-sized glaciers. Therefore, the glaciers' climate response can be superposed by the ongoing adaptation to the changing debris cover on any time scale.

Moreover, we demonstrated that debris-covered glaciers have an inherent ability to shed supra-glacial debris by separating the highly debris-covered tongue region from the main glacier in case of continuous accumulation of debris. As a consequence, the glacier loses a part of its volume and the changed mass balance conditions initiate a subsequent glacier advance. If debris on the lowermost tongue is directly removed, the glacier develops a steady state, depending on the continuity and conditions of the debris removal. Given that all arriving debris is continuously and fully expelled from the glacier, it is possible to reach a balance between debris melt-out and removal. In consequence, such a system also develops a steady state with regard to the ice mass balance. However, such a continuous and complete debris removal, without any modifying effect on the exposed ice areas at the terminus, is not realistic. A more transient debris evacuation, where debris displacement on the glacier surface (without leaving the glacier system) is allowed, leads again to an oscillating reaction of the glacier, where debris balance and ice balance are slightly shifted in time. For our chosen model setup, these oscillations are superimposed to a predominant advancing phase: periods of few hundred years with ca. 100 m length increase (for our setup) and short retreating phases of few decades, where the glaciers lose tens of meters of length.

Our parameterisations of the physical processes of debris evacuation are rather simple, but demonstrate that debris-covered glaciers will show inherent fluctuations on a broad time scale even without changes in the forcing. In a next step it is necessary to work on a more accurate treatment of the dominating processes, including a more advanced representation of glacier fronts and a proper description of periglacial debris dynamics. This also includes the implementation of debris load in glacier dynamics, which might affect regions with very thick debris cover and small ice thicknesses. Such experiments will provide important details about the periodicity and the magnitude of the glacier response. In addition, the interaction between climate variations and the inherent glacier-debris response needs to be investigated, in order to reveal potential feed-back reactions, which determine the ongoing and future glacier evolution. However, even our basic experiments demonstrate, that the evolution of debris-covered glaciers under a changing climate very likely are underlain by long-periodic responses to the glacial debris mass budget, which complicate the interpretation of the climatic impact.

DATA AVAILABILITY STATEMENT

The original contributions presented in the study are publicly available. This data can be found here: https://github.com/carlolic/DebrisExp. Further inquiries can be directed to the corresponding author.

AUTHOR CONTRIBUTIONS

CM designed the study. CL conducted the numerical experiments. Both authors wrote the manuscript.

FUNDING

This research was funded by institutional funding of the Bavarian Academy of Sciences and Humanities.

ACKNOWLEDGMENTS

We highly appreciate the thorough reviews by LA and PM, which helped to improve the manuscript.

SUPPLEMENTARY MATERIAL

The Supplementary Material for this article can be found online at: https://www.frontiersin.org/articles/10.3389/feart.2021.710276/full#supplementary-material

REFERENCES

Akin, J. E., and Tezduyar, T. E. (2004). Calculation of the Advective Limit of the SUPG Stabilization Parameter for Linear and Higher-Order Elements. *Comput. Methods Appl. Mech. Eng.* 193, 1909–1922. doi:10.1016/j.cma.2003.12.050

Anderson, L. S., and Anderson, R. S. (2016). Modeling Debris-Covered Glaciers: Response to Steady Debris Deposition. *Cryosphere* 10, 1105–1124. doi:10.5194/tc-10-1105-2016

Banerjee, A., and Shankar, R. (2013). On the Response of Himalayan Glaciers to Climate Change. *J. Glaciol.* 59, 480–490. doi:10.3189/2013jog12j130

Courant, R., Friedrichs, K., and Lewy, H. (1928). Uber die partiellen Differenzengleichungen der mathematischen Physik. *Math. Ann.* 100, 32–74. doi:10.1007/bf01448839

Cuffey, K. M., and Paterson, W. S. B. (2010). *The Physics of Glaciers*. 4th Edition. Cambridge, Massachussetts, US: Academic Press.

Davis, T. A. (2004). A Column Pre-ordering Strategy for the Unsymmetric-Pattern Multifrontal Method. *ACM Trans. Math. Softw.* 30, 165–195. doi:10.1145/992200.992205

Evatt, G. W., Abrahams, I. D., Heil, M., Mayer, C., Kingslake, J., Mitchell, S. L., et al. (2015). Glacial Melt under a Porous Debris Layer. *J. Glaciol.* 61, 825–836. doi:10.3189/2015jog14j235

Ferguson, J. C., and Vieli, A. (2021). Modelling Steady States and the Transient Response of Debris-Covered Glaciers. *Cryosphere* 15, 3377–3399. doi:10.5194/tc-15-3377-2021

Fyffe, C. L., Woodget, A. S., Kirkbride, M. P., Deline, P., Westoby, M. J., and Brock, B. W. (2020). Processes at the Margins of Supraglacial Debris Cover: Quantifying Dirty Ice Ablation and Debris Redistribution. *Earth Surf. Process. Landforms* 45, 2272–2290. doi:10.1002/esp.4879

Gagliardini, O., Zwinger, T., Gillet-Chaulet, F., Durand, G., Favier, L., de Fleurian, B., et al. (2013). Capabilities and Performance of Elmer/Ice, a New-Generation Ice Sheet Model. *Geosci. Model. Dev.* 6, 1299–1318. doi:10.5194/gmd-6-1299-2013

Geuzaine, C., and Remacle, J.-F. (2009). Gmsh: A 3-D Finite Element Mesh Generator with Built-In Pre- and post-processing Facilities. *Int. J. Numer. Meth. Engng.* 79, 1309–1331. doi:10.1002/nme.2579

Greve, R., and Blatter, H. (2009). *Dynamics of Ice Sheets and Glaciers*. Springer, Dordrecht, Heidelberg, London. New York. Science & Business Media. doi:10.1007/978-3-642-03415-2

Kelley, C. T. (1995). *Iterative Methods for Linear and Nonlinear Equations*. Philadelphia:SIAM.

Konrad, S. K., and Humphrey, N. F. (2000). *Steady-state Flow Model of Debris-Covered Glaciers (Rock Glaciers)*. Wallingford:Iahs Publication, 255–266.

Lawson, D. E. (1982). Mobilization, Movement and Deposition of Active Subaerial Sediment Flows, Matanuska Glacier, alaska. *J. Geol.* 90, 279–300. doi:10.1086/628680

Mamot, P., Weber, S., Schröder, T., and Krautblatter, M. (2018). A Temperature- and Stress-Controlled Failure Criterion for Ice-Filled Permafrost Rock Joints. *Cryosphere* 12, 3333–3353. doi:10.5194/tc-12-3333-2018

Miles, K. E., Hubbard, B., Miles, E. S., Quincey, D. J., Rowan, A. V., Kirkbride, M., et al. (2021). Continuous Borehole Optical Televiewing Reveals Variable Englacial Debris Concentrations at Khumbu Glacier, nepal. *Commun. Earth Environ.* 2, 1–9. doi:10.1038/s43247-020-00070-x

Moore, P. L. (2018). Stability of Supraglacial Debris. *Earth Surf. Process. Landforms* 43, 285–297. doi:10.1002/esp.4244

Nicholson, L., and Benn, D. I. (2006). Calculating Ice Melt beneath a Debris Layer Using Meteorological Data. *J. Glaciol.* 52, 463–470. doi:10.3189/172756506781828584

Nicholson, L. I., McCarthy, M., Pritchard, H. D., and Willis, I. (2018). Supraglacial Debris Thickness Variability: Impact on Ablation and Relation to Terrain Properties. *Cryosphere* 12, 3719–3734. doi:10.5194/tc-12-3719-2018

östrem, G. (1959). Ice Melting under a Thin Layer of Moraine, and the Existence of Ice Cores in Moraine Ridges. *Geografiska Annaler* 41, 228–230. doi:10.1080/20014422.1959.11907953

Rowan, A. V., Egholm, D. L., Quincey, D. J., and Glasser, N. F. (2015). Modelling the Feedbacks between Mass Balance, Ice Flow and Debris Transport to Predict the Response to Climate Change of Debris-Covered Glaciers in the Himalaya. *Earth Planet. Sci. Lett.* 430, 427–438. doi:10.1016/j.epsl.2015.09.004

Scherler, D., Bookhagen, B., and Strecker, M. R. (2011). Spatially Variable Response of Himalayan Glaciers to Climate Change Affected by Debris Cover. *Nat. Geosci.* 4, 156–159. doi:10.1038/ngeo1068

Wirbel, A., and Jarosch, A. H. (2020). Inequality-constrained Free-Surface Evolution in a Full Stokes Ice Flow Model (Evolve_glacier v1.1). *Geosci. Model. Dev.* 13, 6425–6445. doi:10.5194/gmd-13-6425-2020

Wirbel, A., Jarosch, A. H., and Nicholson, L. (2018). Modelling Debris Transport within Glaciers by Advection in a Full-Stokes Ice Flow Model. *Cryosphere* 12, 189–204. doi:10.5194/tc-12-189-2018

Conflict of Interest: The authors declare that the research was conducted in the absence of any commercial or financial relationships that could be construed as a potential conflict of interest.

Publisher's Note: All claims expressed in this article are solely those of the authors and do not necessarily represent those of their affiliated organizations, or those of the publisher, the editors and the reviewers. Any product that may be evaluated in this article, or claim that may be made by its manufacturer, is not guaranteed or endorsed by the publisher.

frontiers in Earth Science

ORIGINAL RESEARCH
published: 04 November 2021
doi: 10.3389/feart.2021.740160

Ablation Patterns of the Debris Covered Tongue of Halong Glacier Revealed by Short Term Unmanned Aerial Vehicle Surveys

Wanqin Guo[1], Xiaojun Guo[1], Yushuo Liu[1], Jing Li[1], Donghui Shangguan[1], Liqun Chen[1] and Jin Ga[2]*

[1]State Key Laboratory of Cryospheric Science, Northwest Institute of Eco-Environment and Resources, Chinese Academy of Science, Lanzhou, China, [2]Mgolok Nationalities Senior High School, Maqin, China

Debris-covered glaciers are an important glacier type and have attracted more and more attention. This study presents the results of ablation patterns of debris-covered tongue of the Halong Glacier in the northeastern Tibetan Plateau, by using two repeated unmanned aerial vehicle (UAV) surveys performed on August 11 and September 15, 2019. The results show that the tongue of Halong Glacier has experienced strong ablation during the surveyed period, with an overall ice loss amount to 4.17×10^5 metric tons. Among all the briefly classified surface types, supraglacial debris has the largest area (80.9%) and also mass losses (58.6%) comparing to others. However, ice cliffs show the strongest and the most significant ablation rates (averagely 1.36 and 1.22 m w.e. for supraglacial and lateral ice cliffs, respectively), followed by clean ice regions (1.01 m w.e.). The backwastes of ice cliffs also resulted in up to 7.8 m horizontal back-off at different parts of Halong Glacier, lead to fast terminal retreat and narrowing down of the glacier tongue, and may result in the break off of Halong Glacier tongue into separated parts in the future. The surface ablation rates show a clear negative exponential relationship with the measured debris thicknesses, well in accordance with previous studies. Regions in cutting and flushing by supraglacial and lateral rivers have the largest surface elevation decreases but are not significant due to their limited area and the relatively lower quality of UAV digital surface models (DSMs) in those covered regions.

Keywords: Halong Glacier, debris covered glacier, ablation pattern, unman aerial vehicle, ice cliff

OPEN ACCESS

Edited by:
Aparna Shukla,
Ministry of Earth Sciences, India

Reviewed by:
Raaj Ramsankaran,
Indian Institute of Technology Bombay, India
Qiao Liu,
Institute of Mountain Hazards and Environment (CAS), China

****Correspondence:***
Wanqin Guo
guowq@lzb.ac.cn

Specialty section:
This article was submitted to Cryospheric Sciences, a section of the journal Frontiers in Earth Science

Received: *12 July 2021*
Accepted: *07 October 2021*
Published: *04 November 2021*

Citation:
Guo W, Guo X, Liu Y, Li J, Shangguan D, Chen L and Ga J (2021) Ablation Patterns of the Debris Covered Tongue of Halong Glacier Revealed by Short Term Unmanned Aerial Vehicle Surveys. Front. Earth Sci. 9:740160. doi: 10.3389/feart.2021.740160

INTRODUCTION

Debris-covered glaciers are one of the major types of glaciers worldwide, which are covered by varying extents and thicknesses of debris formed by different sources of sediments with diverse grain sizes (Bozhinskiy et al., 1986). Although almost all mountain glaciers are covered by at least thin or sparsely distributed surface debris, only parts of them with distinctive debris covers can be recognized by remote sensing, and thus were classified as debris-covered glaciers. A recent study by Herreid and Pellicciotti (2020) has revealed that about 44% of the world's mountain glaciers are debris-covered, which was identified through Landsat imagery, while the debris-covered glacier area only accounts for 7.3% of all mountain glacier area.

Global warming during the last decades has caused significant mass losses on global glaciers (e.g., Marzeion et al., 2018; Wouters et al., 2019; Vargo et al., 2020). Previous studies found that different thicknesses of debris covers have distinctive effects on glacier ablation, in which thin debris (<0.5–2 cm) can strengthen the ice ablation while thicker debris will provide some protection to the ablation processes (Østrem, 1959; Mattson et al., 1993). However, like clean-ice glaciers, it was proved that debris-covered glaciers also experienced dramatic mass losses in response to the warming climate (e.g., Glasser et al., 2016; Pratibha and Kulkarni, 2018). Moreover, some studies have further illustrated that the debris-covered glaciers have a similar magnitude of mass loss with adjacent clean-ice glaciers, leading to a so-called "debris-cover anomaly" (Pellicciotti et al., 2015; Vincent et al., 2016; Salerno et al., 2017). Therefore, large discrepancies still exist in the knowledge acquired on the evolutions of debris-covered glaciers and their disparities with clean-ice glaciers, in which the limited accuracies and large inconsistencies of the data (*in-situ* observations versus remote sensing techniques) used in those studies is one major reason.

The fast developments of unmanned aerial vehicle (UAV) survey techniques during the last 2 decades have provided new opportunities to the glacier monitoring works (Pajares, 2015; Gaffey and Bhardwaj, 2020). The major advantages of UAV measurements include the accuracy and spatial resolution (Gindraux et al., 2017), and also flexibility in operation time. Therefore, the application of UAV on glacier monitoring has developed quickly during the last decades; more and more researchers have used this technique in glacier change studies, such as glacier topography (Bliakharskii et al., 2019; Ewertowski et al., 2019), mass balance (Wigmore and Mark, 2017; Bash and Moorman, 2020; Che et al., 2020), surface features (Crocker et al., 2012; Fugazza et al., 2015; Kraaijenbrink P. et al., 2016; Florinsky and Bliakharskii, 2019), velocities (Kraaijenbrink P. D. A. et al., 2016; Benoit et al., 2019; Jouvet et al., 2020), and temperatures (Kraaijenbrink et al., 2018).

Some researchers applied the UAV survey to debris-covered glacier change studies. Kraaijenbrink P. et al. (2016) have used UAV imagery to map the surface features on a debris-covered glacier, which can result in a 6 cm spatial resolution. Wigmore and Mark (2017) monitored the glacier dynamics via repeated UAV surveys and found highly heterogeneous patterns of glacier change in the Cordillera Blanca, Peru. Kraaijenbrink et al. (2018) further used a UAV vehicle that carried a thermal infrared sensor to measure the surface temperature of a debris-covered glacier in the New Zealand Alps. Che et al. (2020) used orhtomosaic and DEM from two repetitive UAV surveys to study the summer mass balance of Baishui River Glacier No.1 in Southern China. Therefore, the UAV survey technique has been proved to have great potential for debris-covered glacier monitoring and their change studies.

This study used two repetitive surveys via a UAV device with a 1-month interval in 2019, to study the ablation patterns of the debris-covered tongue of the Halong Glacier. The major objectives of this study are to understand the short-term ablation patterns of Halong Glacier among different surface types, investigate their relationships with the debris thickness and surface topography of Halong Glacier, and provide more knowledge on the temporal and spatial evolutions of debris-covered glaciers.

The Halong Glacier is located on the Anye Machen Mountain (also called Amney Machen Mountain; see Paul, 2019) in the northeastern Tibetan Plateau. According to the second Chinese glacier inventory (Guo et al., 2015), there were 74 glaciers on Anye Machen, with a total area of 102.7 km^2 in 2009 (see **Figure 1B**). Halong Glacier is the largest glacier in this region, with an area of 20.06 km^2 in 2017. It consists of two major branches, of which the south branch is longer and has a length of ~7.8 km (**Figure 1C**). The records of an automatic weather station (AWS) installed at a site (4,437 m a.s.l; LT-GCP3 in **Figure 1C**) on the end moraine of Halong Glacier in 2014 show that the recent mean annual temperature near the glacier terminus is −3.1°C. The precipitation observation at the AWS site since 2017 also shows that this region has up to 750 mm annual precipitation, indicating that the Halong Glacier has a relatively large accumulation and ablation rate. About the lowest 3 km of the tongue of Halong Glacier is covered by debris (1.70 km^2 in total) with variant thickness and abundant typical surface features of normal debris-covered glaciers, e.g., ice cliffs, supraglacial ponds, etc. (**Figure 2A**).

Yang et al. (2003) have studied the glacier change of Anye Machen during 1965-2000, which revealed that glaciers in this region has shrunk 17.3% in that period. Glaciers in this region can be regarded as in unstable status since the Halong Glacier has advanced or surged between 1965 and 2000 (Yang et al., 2003) and the nearby Yehelong Glacier also surged during 2000-2013 (Jiang et al., 2018). Another glacier has even repeatedly collapsed which was caused by surges and led to a certain level of hazards (Paul, 2019). The study by Jiang et al. (2018) further illustrated that the glaciers of Anye Machen had a negative mass balance during 2000-2013, the surface elevation of Halong Glacier has averagely decreased 8.73 ± 3.70 m, which proved that Halong Glacier was in strong melt in the last decades.

DATA AND METHODS

UAV Used and its Camera Settings

The UAV used in this study is the Phantom 4 Pro V2.0 manufactured by DJ-Innovations (DJI), which was a reliable low-cost consumer-level drone and widely used in UAV-based studies (e.g., Che et al., 2020; Hsu et al., 2020; Pearce et al., 2020; Fraser et al., 2021). It carries a 24 mm/F2.8, 20 megapixel single-lens digital camera, corresponding to 2.5–3 cm ground resolution at 50 m flight height. One battery of the Phantom 4 Pro V2.0 can support ~15 min of flight at 4,500 m a.s.l. in summer, which can cover ~1.8×10^5 m^2 ground area at the flight height of 50 m with ~80% overlapping rate for captured photos.

UAV Flights and Ground Control Points Measurements

Two UAV surveys were scheduled and performed in 2019, one on August 11 and another on September 15. UAV survey on August

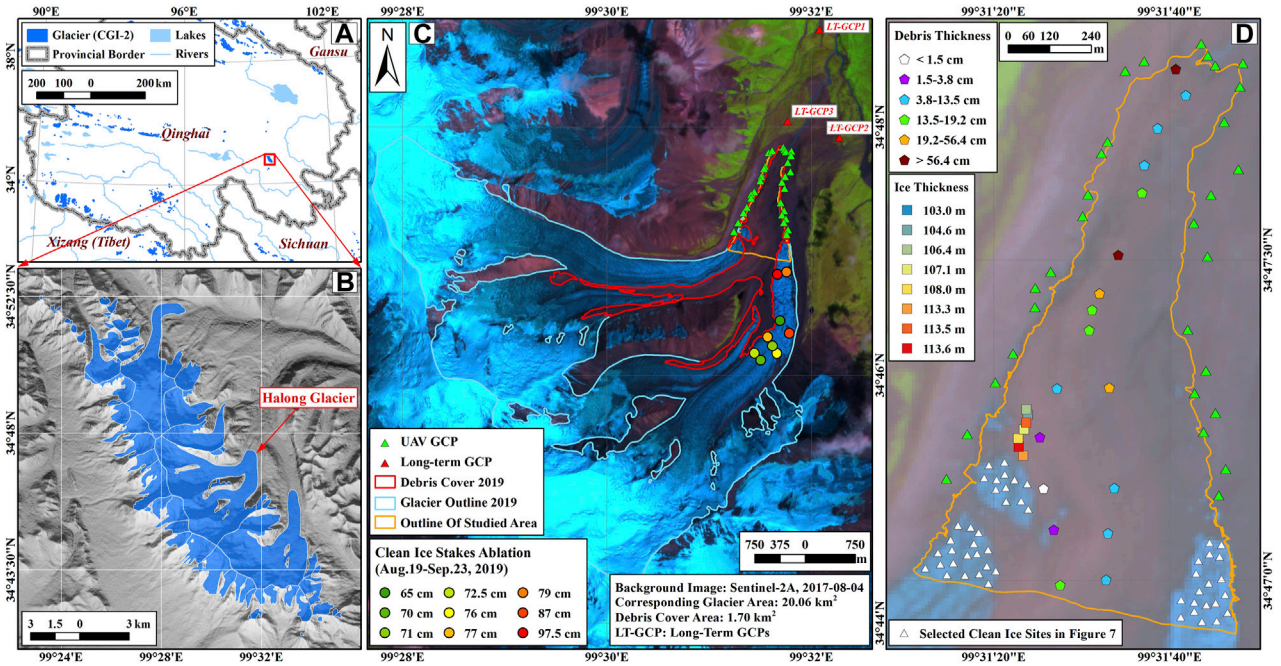

FIGURE 1 | Location of Halong Glacier **(A,B)**, distribution of UAV GCPs and ablations of installed stakes in clean ice region **(C)**, and distribution of measured debris (on May 24, 2019) and ice (on October 2, 2016; only at selected sites) thickness **(D)**.

11 has 10 flights, while September 15 has 9 flights, to cover the lower ablation area of the Halong Glacier. The camera angles were set to nadir view (90°) in all flights. The drone heights were all set to 50 m at each take-off point to make sure the drone obtaining sufficient spatial resolution.

On August 11, 30 GCPs (see **Figures 2C–F** for their collections) used in UAV surveying were painted and their coordinates simultaneously measured. To make sure they could be used for a longer time, sites were chosen on relatively stable locations, i.e., on boulders or larger stones located outside the active region of Halong Glacier (see **Figures 1C,D**). The marks of control points are circles (~30 cm diameter) with a cross inside and lacquered by oil paint (See **Figure 2D**), which means they could be easily found in the UAV photos (**Figures 2E,F**) and existed for more than 1 year.

The coordinates of the GCPs were measured by a HUACE I70 Real-Time Kinematic Global Navigation Satellite System (RTK/GNSS; **Figure 2C**). The system includes two GNSS antennas, one fixed as the base station and another as the mobile measuring station. The RTK/GNSS survey was referred to and rigorously adjusted by three long-term GCPs surveyed and fixed deep in the ground during 2013-2015 (see **Figure 1C** for locations, LT-GCP1 to LT-GCP3). The coordinates of the long-term GCPs were rigorously determined by polygonometrical geodetic surveying method via static GNSS measurements by six HUACE T5 GNSS antennas. The horizontal and vertical coordinates for the three long-term GCPs were rigorously resolved. The positioning errors are less than ±10 mm horizontally and ±15 mm vertically, which can result in sufficient precision for all new UAV GCPs.

Digital Surface Model Generation and Ablation Pattern Retrieval

The Pix4D® photogrammetry software was used to process all the UAV photos following the typical procedures. The ground resolutions was set to 3 cm for the output DSMs, which can best reflect ground resolution at the flight height of ~50 m for both UAV surveys. Before the fully automatic processing of Pix4D, all 30 GCPs were firstly stung onto the related photos by finding the cross center of each painted mark on UAV photos, which may only have a relative horizontal error of ~±2 cm because of the high resolution and narrow width of the painted ground marks (**Figure 2D**). **Figures 3A,B** show the final mosaicked UAV images on August 11 and September 15, respectively, and **Figure 3C** shows the generated DSM (shaded) on September 15.

To better describe the ablation pattern of different surface types and provide an overview on the influences of different surface types on the glacier ablation, we performed a brief image classification on the mosaicked UAV image obtained on September 15 by using image segmentation algorithm in ERDAS Imagine®. The basic logic of image segmentation is to divide the image into sub-regions with similar reflectance (pixel values). We used the default parameters suggested by ERDAS Imagine® in this step, i.e. minimal pixel value differences of 15 and variance factor of 3.5. The segmented image was then vectorized and intensively manually edited referring to the

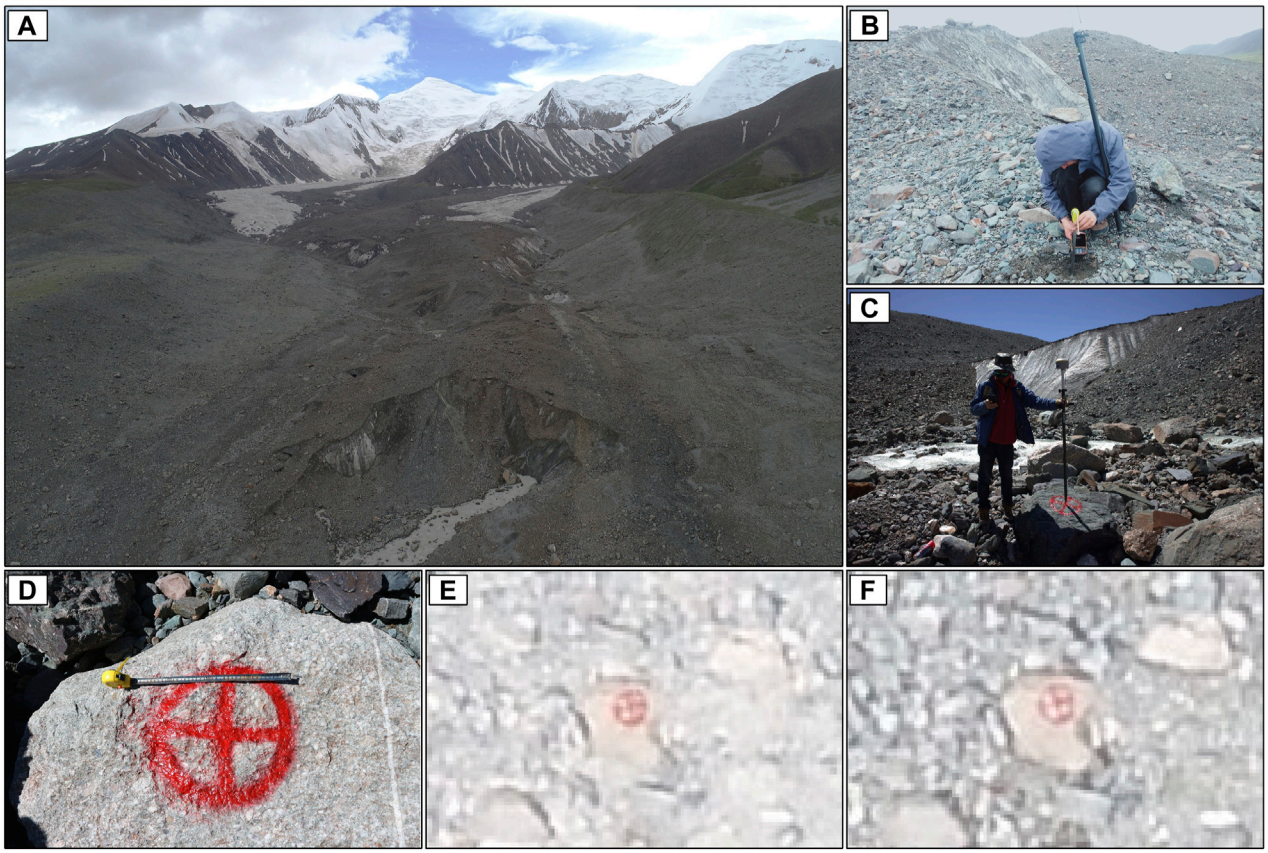

FIGURE 2 | Field photos of Halong Glacier **(A)**, measurements of debris thickness **(B)** and UAV GCP **(C)** and their painting **(D)**, as well as the same point photoed by UAV at ~50 m height on August 11 **(E)** and September 15 **(F)**.

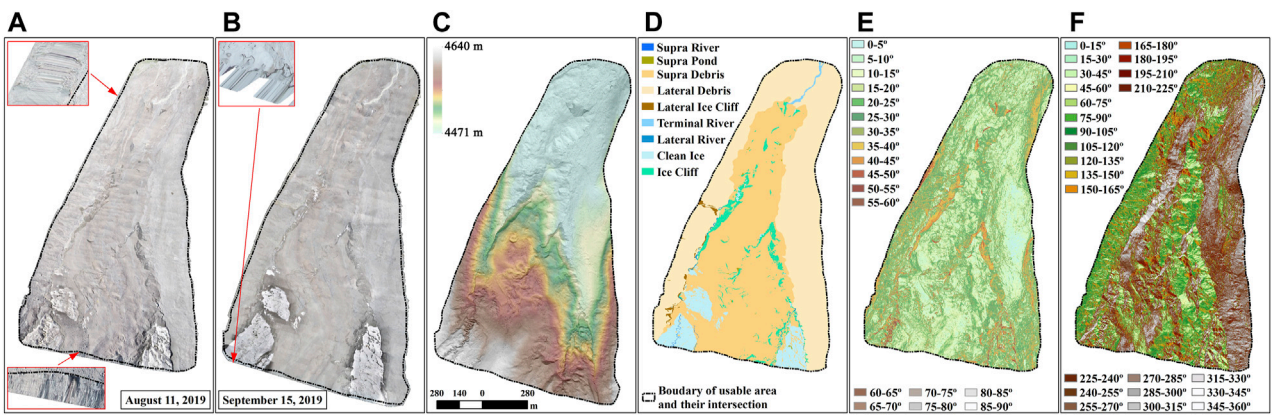

FIGURE 3 | The mosaicked UAV images on August 11 **(A)** and September 15 **(B)**, and the shaded DSM **(C)**, vectorized and manually modified surface classification **(D)**, slope **(E)**, and aspect **(F)** classes, all from image and DSM on September 15. Insets in A and B show the artifacts exist along the edges of the UAV surveyed region which were excluded from the studied area by the manually digitized boundaries (dash-dot lines).

UAV image on September 15, by merging small embedded patches into surrounding larger ones. All the image segments were attributed into nine surface types, i.e. clean ice, ice cliff, supra debris, supra river, supra pond, lateral debris, lateral river, lateral ice cliff, and terminal river. The lateral debris refers to those slope surfaces on the paleo lateral moraine aside the active glacier margin (the left and right side steep slopes in **Figure 2A**), which are mostly separated from the active

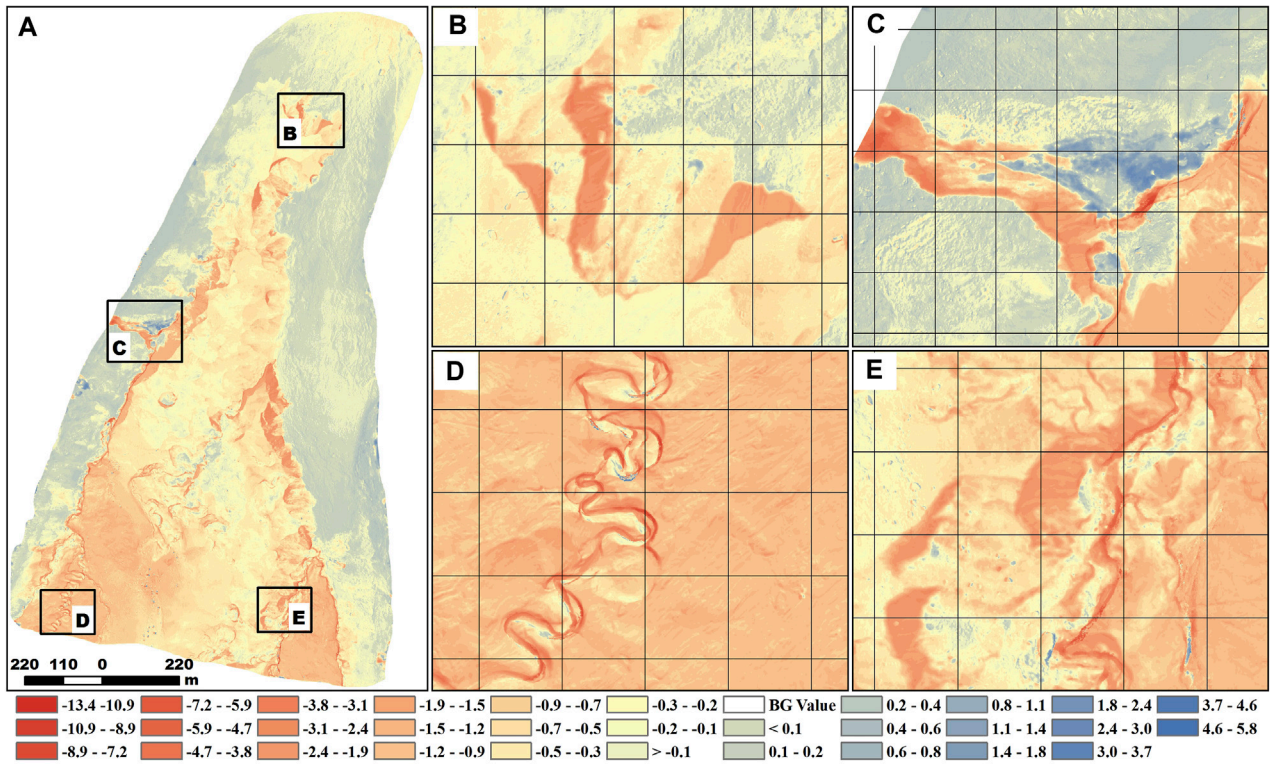

FIGURE 4 | Elevation difference subtracted by DSMs on September 15 minus August 11, with spatial resolution in 3 cm. Rectangles in **(A)** mark the locations of glacier terminus **(B)**, region with the largest surface uplift **(C)**, supraglacial river channels in **(D)** and aside **(E)** clean ice regions. All gridlines shown as scale reference are in 30 m intervals..

glacier by lateral rivers or ice cliffs. Although there are possibly some inactive buried ices under the surface of the lateral debris, especially those regions on the two sides of the glacier tongue which are illustrated by DSM difference in **Figure 4A**, they cannot be identified through UAV photos or even by on-site investigations. The lateral ice cliff represents those apparently exposed ice cliffs that mainly appear on the southeast facing left side of Halong Glacier. The final classification was shown in **Figure 3D**.

Conversion From the Vertical Surface Lowering Into Horizontal Retreat

To better illustrate the horizontal surface change of Halong Glacier, we used the following formulas to convert the vertical elevation differences into equivalent X and Y retreats on steep terrain (slope >45°), by using simple geometric transformation based on terrain slopes and aspects calculated from DSM on September 15.

$$\Delta x = \frac{\Delta h}{\tan(\alpha)} \cdot \cos(90° - \beta) \quad (1)$$

$$\Delta y = \frac{\Delta h}{\tan(\alpha)} \cdot \sin(90° - \beta) \quad (2)$$

$$|D| = \sqrt{\Delta x^2 + \Delta y^2} \quad (3)$$

Where Δh is the elevation difference between DSMs on two dates; α and β are surface slope and aspect in degree, respectively; Δx and Δy are the glacier surface retreats along x (east-west) and y (north-south) direction, respectively; and $|D|$ is the absolute retreat distance of the glacier surface. **Eqs 1, 2** firstly convert the vertical difference (Δh) into horizontal displacement by dividing it with the tangent value of surface slope (α), then decompose the horizontal displacement into X and Y direction components (Δx and Δy) by multiplying the cosine and sine values of the east-start anti-clockwise aspect in a Cartesian coordinate system (converted from the clockwise north-start aspect by $90° - \beta$).

Debris Thickness Measurements

Simultaneous debris thickness measurement was not performed in 2019. Since the debris thickness will not have significant change annually (Bozhinskiy et al., 1986), we briefly measured the debris thickness on May 24, 2021 (see **Figure 2B**, and **Supplementary Figure S1** for samples of debris thickness at several sites) at 23 sites on the debris-covered tongue of Halong Glacier, to study the influences of debris thickness on the ablations of the debris-covered tongue of Halong Glacier. The debris thicknesses varied significantly along the ablation area of

TABLE 1 | The statistics of surface elevation change and corresponding ice loss for different surface types.

Surface type	Area and percentage		Mean elevation differences/m	STD of elevation differences/m	Ice loss and percentage	
	Area/m^2	Percentage (%)			Ice loss (ton w.e.)	Percentage (%)
Clean Ice	90562.3	11.4	−1.19	0.49	−91419.0	21.9
Ice Cliff	49941.6	6.3	−1.60	0.64	−67980.0	16.3
Supra Debris	640680.7	80.9	−0.45	0.33	−244352.4	58.6
Supra Pond	1075.5	0.1	−0.76	0.69	−695.5	0.2
Supra River	1428.9	0.2	−2.27	1.32	−2753.7	0.7
Lateral Ice Cliff	6141.0	0.8	−1.43	0.80	−7439.3	1.8
Lateral River	1645.9	0.2	−1.80	1.41	−2517.5	0.6
Total	791475.9	100	−0.62	0.38	−417157.5	100.0

the Halong Glacier tongue (see **Figure 1D**), where the minimum measured thickness is only 1.5 cm, while the underlying ice at two of the sites cannot be uncovered even after 1 m of digging. The location of these digging sites was also measured by HUACE I70 GNSS at the same time to precisely correlate them with the ablation rates retrieved.

Error Assessment

We employed the cross-validation method to briefly assess the accuracy of the generated DSMs, in which the three-dimensional mismatches of the final processed UAV results were checked using the coordinates of the 30 GCPs by calculating the difference between the coordinates of those GCPs measured by RTK/GNSSS and on corresponding UAV images and DSMs. The results show that the mean coordinate differences and standard deviations on August 11 are 1.19 cm/±8.12 cm for X, 0.83 cm/±2.40 cm for Y, and −3.74 cm/±4.52 cm for Z. The same values on September 15 are 0.24 cm/±5.45 cm for X, 0.37 cm/±5.37 cm for Y, and −1.12 cm/±6.55 cm for Z. Although the standard deviations of elevations (Z value), which can be regarded as the error of the generated DSMs (Zhilin, 1988; Fisher, 1998), are slightly larger than the image spatial resolution used (3 cm), the centimeter-scale error will not have significant influences on the meter-scale surface elevation change as well the retrieved ablation patterns.

RESULTS

General Ablation Pattern Revealed by Elevation Differences From Two DSMs

Figure 4 shows the elevation difference subtracted by two mosaicked DSMs (September 15 min August 11). It clearly illustrated the strong ablation of Halong Glacier between August 11 and September 15, 2019. The maximum elevation decrease of all surveyed regions can reach up to 13.4 m, while some regions also show certain levels of uplift up to 5.8 m. From the smaller zoomed maps in **Figure 4**, we can clearly identify that the largest elevation lowering happens on the ice cliffs aside the glacier tongue and also the lateral ice cliffs outside the margin of the active glacier.

Table 1 shows the average elevation differences for different surface types as well the corresponding ice losses by supposing an ice density of 850 kg/m^3 (Huss, 2013). From **Table 1**, we can read that the total glacier area (exclude periglacial area covered by lateral debris and terminal river in **Figure 3D**) covered commonly by both UAV surveys is 0.79 km^2, in which the major part (80.9%) was covered by supraglacial debris, while the rest of the area was mainly covered by clean ice (11.4%) and ice cliffs (6.3%). Our study shows that the overall mass loss between August 11 and September 15 in 2019 among the surveyed region of Halong Glacier is 417,158 tons w. e., in which 58.6%, 21.9%, 16.3% happened on regions covered by debris, clean ice, and ice cliffs, respectively. Although the supraglacial debris covered more than 4/5 of the surveyed surface, its contribution to total ice loss is much smaller (less than 3/5), in contrast to ice cliff and clean ice, which only cover very few areas (totally 17.7%) but contributed large part (totally 38.2%) of the ice loss.

The mean elevation differences denote the ablation intensities of different surface types, and can clearly describe the brief ablation pattern of different surface types. The lateral and supra river have the two biggest average elevation differences, which illustrate these two surface types have the most intensive ice loss during the studied period. By contrast, the supra debris has the smallest average elevation differences, which indicates the strong protecting effects of surface debris cover on glacier ablation. The lateral ice cliff and ice cliff aside the glacier show larger average elevation differences too, while clean ice shows intermediate ablation intensity.

The standard deviation (STD) of elevation difference describes the variations of glacier ablation in each surface type. The large STD denotes the lesser dependence of the ablation rate on the surface type, which means the surface type may have an ablation rate with large differences. The strongest variation happens on the two kinds of rivers (supra and lateral), which may be caused by variant supraglacial runoff flux, terrain slope (see below), or by the lower quality of the UAV DSMs on deep channels (see Discussion). The smaller STDs, which were mainly presented by supra debris, indicate that the ablation rate on debris-covered areas are more evenly distributed. The intermediate STD of clean ice and two ice cliff type should be caused by large differences in terrain slope and aspect (see below).

The glacier ablation observations on nine stakes installed in the upper clean ice region of the south branch of the Halong Glacier (**Figure 1D**) were provided as a comparison to this study. The ablation of those clean ice stakes was in the range of 65–97.5 cm from August 19 to September 23, 2019. The maximum ablation of 97.5 cm appeared on the lowest site

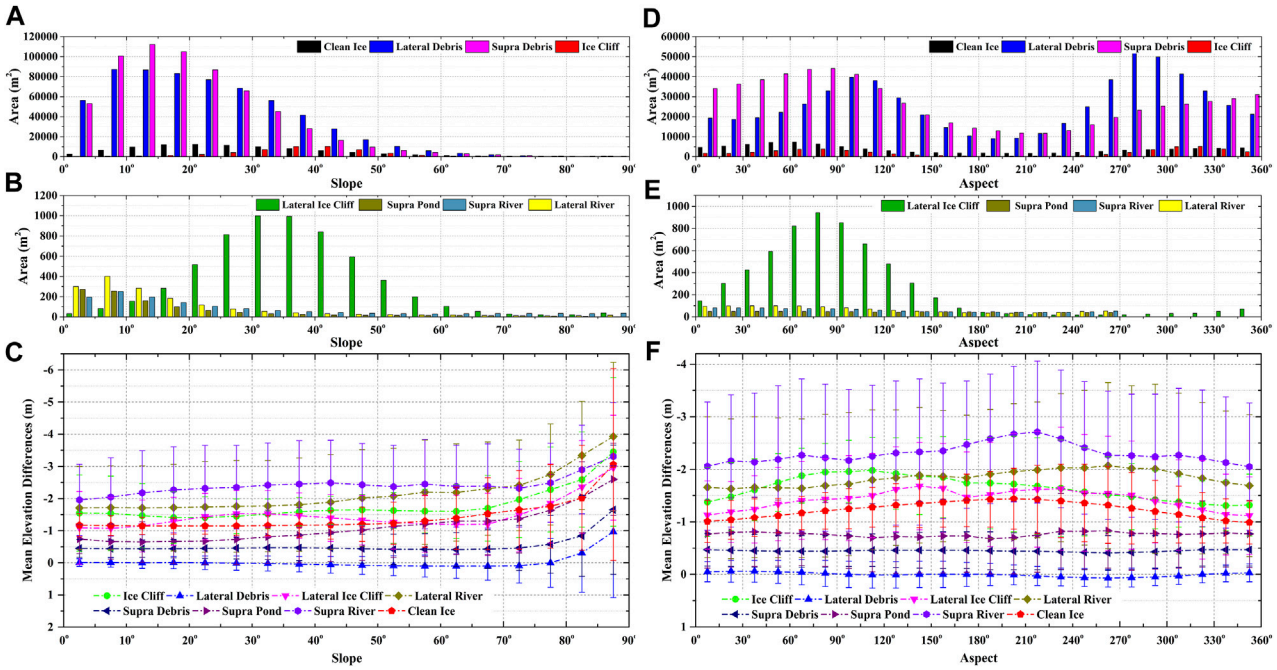

FIGURE 5 | The total area of different surface types within different slope **(A)** and **(B)**, in 5° interval) and aspect **(D)** and **(E)**, in 15° interval) ranges, and the relationships between elevation differences and surface slope **(C)** as well as aspect **(F)** within different surface types. The error bar represents the standard deviation of elevation differences in the surface type within different slope and aspect ranges.

close to the margin of the study area, in good accordance with the elevation differences revealed by this study in a nearby region (lower left clean ice region in **Figure 4A**).

The Effects of Slope and Aspect on Intensities of Surface Ablation

We calculated the mean elevation differences of different surface types on different slopes and aspects by intersecting the surface type with slope (in 5° interval) and aspect (in 15° interval) range classes to better understand the influences of terrain slope/aspect on the ablation rate over different surface type. **Figure 5** shows the results of these analyses, in which the lateral debris-covered region was also included in this figure. **Figures 5A,B,D,E** show clearly that the dominants of two debris-covered regions, i.e. supraglacial and lateral debris, whose major portions were located on a surfaces with a slope smaller than 40° and with mostly east-, north-, and west-facing aspects. Two ice cliff types, i.e. the lateral ice cliff and ice cliff aside the glacier, are mainly distributed upon the surface with a slope greater than 15° and less than 60°. Supraglacial ice cliffs were mostly orientated toward northeast and northwest, but lateral ice cliffs are mostly facing east. The clean ice area was distributed more evenly on surfaces with different slopes but was also mostly orientated toward north, northeast, and northwest. Two river types (supraglacial and lateral) were located on more flat terrains (<20°) but evenly on most aspect ranges.

Figures 5C,F show the relationships between the mean elevation changes of different surface types on terrains with different slopes and aspects. The larger variances (range of error bar) of supra rivers and ponds as well lateral rivers are likely caused by incorrect inclusion of pixels surrounding or embedding into those surface types due to the highly patched surface features (see **Supplementary Figure S2**). Those features with a slope above 70° are not very representative due to the minimal area of each surface type on this kind of terrain (~0.9% in total) but can describe some characteristics of the glacier ablation on those regions. **Figures 5C,F** clearly shows that the supraglacial debris has the minimum ablation rates among all supraglacial surface types. The ablation rates were near uniformly distributed along different slopes and aspects on all debris-covered surfaces except those with a slope steeper than 70°. This phenomenon further illustrates the strong protections of debris cover on ice ablation by comparing to the clean ice, whose ablation rates show near-linear increase with slopes larger than 40°. Furthermore, the changes of mean elevation differences of supraglacial debris along increasing slopes show a slightly decreasing trend below 70°. This can be explained by the falling and subsequent deposition of larger unstable debris (with a grain size of 10^{-2}–10^{-1} m) along the edge of ice cliff or melted out from ice cliffs, as well as the downslope creeping of melt-water soaked muddy debris (with a grain size of 10^{-6}–10^{-2} m). The falling of larger debris happens on steeper slopes (greater than ca. 70°) but were blocked by the downslope depositions accumulated before on the gentler slope (i.e. 40°–70°; see **Supplementary Figure S3A**, some of larger patches were also classified as debris cover in this study), and should be the major causes of such depositions on steep terrain. The deposition

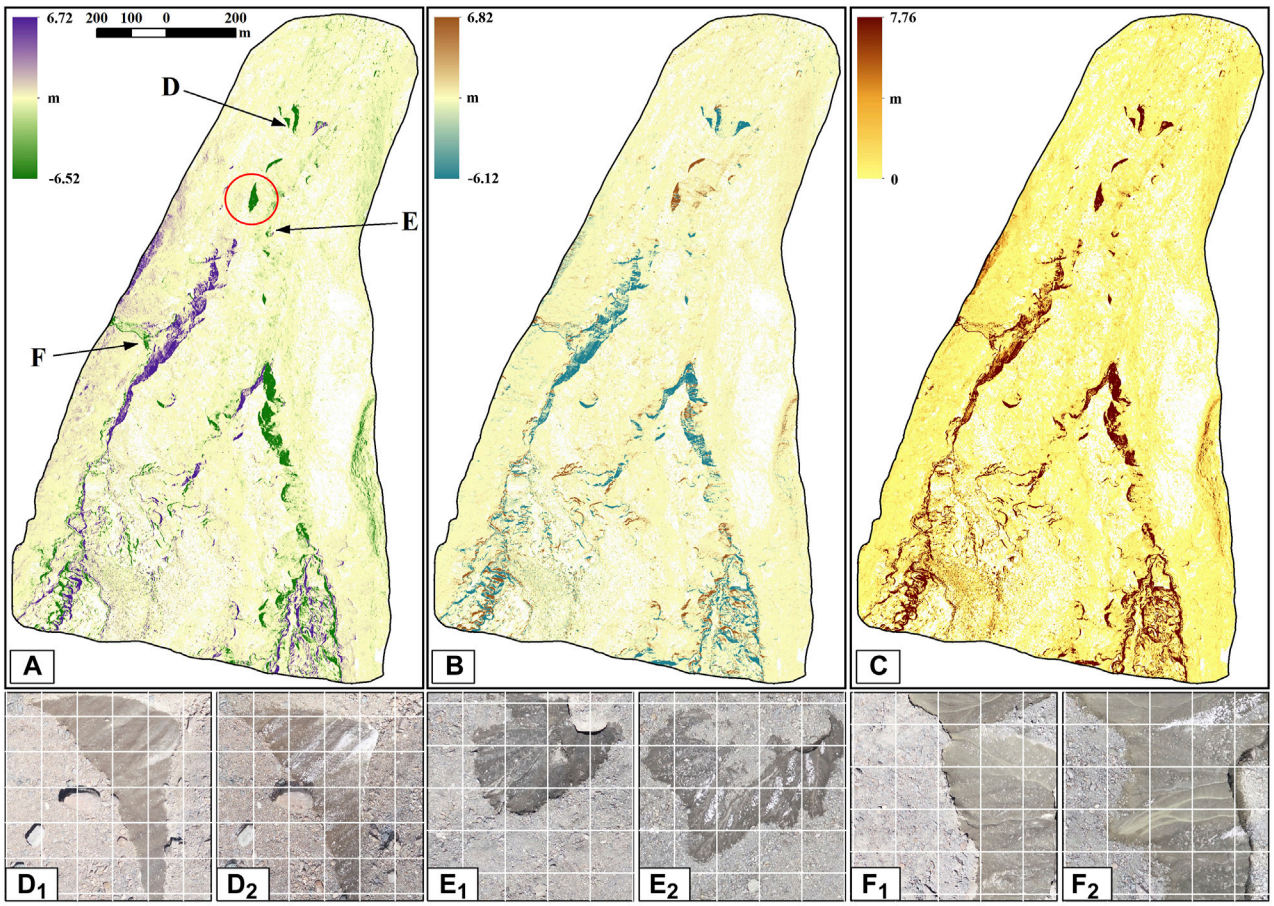

FIGURE 6 | The X **(A)**; positive to east) and Y **(B)**; positive to north) components as well as the integrated absolute distance **(C)** of horizontal ice cliff retreats for regions with a slope greater than 45°. Small maps below are the samples of fast backwasting ice cliff illustrated by UAV images on August 11 (subscript 1) and September 15 (subscript 2) for three locations **(D–F)** marked in A, with all the gridlines in 5 m interval. The red circle in A marks the bigger backwaste toward the left side of the glacier.

of creeping muddy debris happens on gentler slopes (**Supplementary Figure S3B**).

By contrast, **Figure 5C** also shows that the clean ices have a nearly tripled ablation rate compared to the debris-covered area on all slope classes. Besides, unlike supra debris, its ablation rates show a recognizable increasing trend with larger slopes, especially those larger than 40°, indicating the strong influences of the flushing as well as the heat release of melted water on ice ablation among this surface type (Pitcher and Smith, 2019). The slightly larger ablation (~0.5 m) of south- than north-facing clean ice (and also supraglacial river channels) in **Figure 5F** can be explained by more solar radiation being received, but also may partly be induced by the influences of glacier movement on ablation patterns retrieved by the elevation differencing method (see DISCUSSION).

Supraglacial ice cliff has a larger ablation rate than clean ice. The ice cliffs with lower mean slopes (<25°) may be caused by the fast change of ice cliffs between August 11 and September 15 (e.g., the under-slope regions were turned into flatter terrain due to ice cliff retreats), or by incorrect inclusion of image classification due to highly patched surface features (see **Supplementary Figure S2C**). The elevation decrease of supraglacial ice cliffs with a slope above 25° show another slight increasing tendency toward larger slopes, especially those above 65°, also indicating the enhanced effects of melted water flushing and heat-releasing on the surface ice ablation. The east- and south-facing ice cliffs in **Figure 5F** show larger ablation rates than other orientations because of the stronger solar radiations received in these two directions. The lowering down of ablation rate for lateral ice cliff in slope ranges between 35°-70° may be caused by similar debris deposition effects because of the plentiful sources of erosion on the upper slope regions above lateral ice cliff (see **Supplementary Figure S3B**).

Fast Backwasting of Ice Cliff revealed by DSM Elevation Differences and Slopes

Although the elevation differences in **Figure 4** can be used to represent the ice losses as a whole, they can only describe

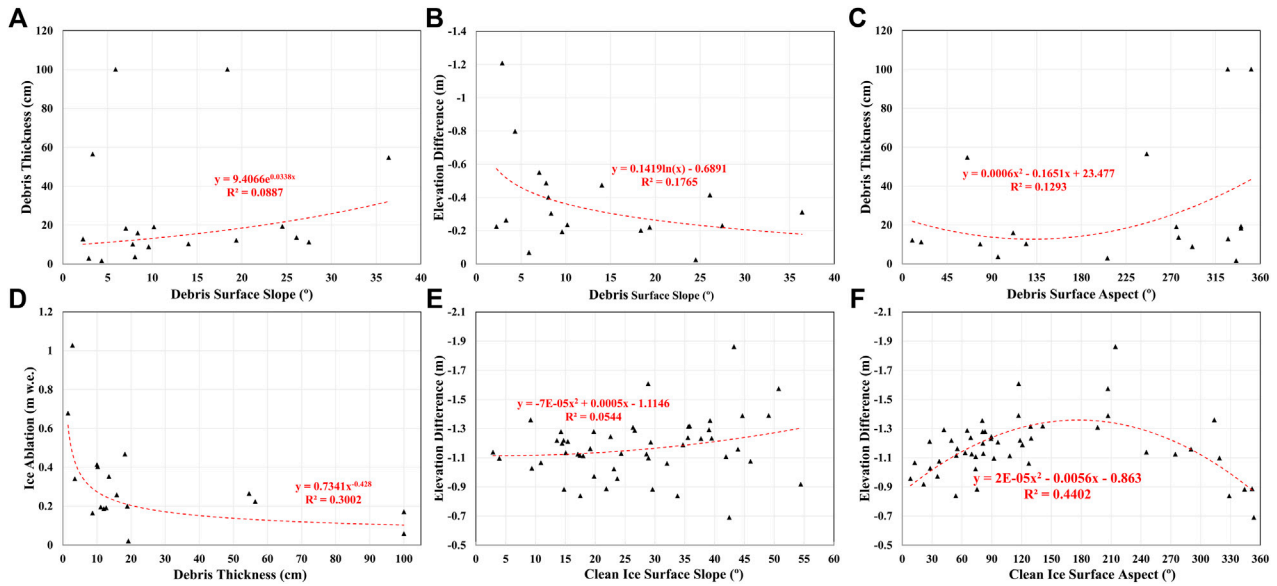

FIGURE 7 | Relationships of surface slope, aspects, debris thickness, and elevation differences/ice ablations on measured sites compared to 50 randomly selected sites on clean ice.

the changes in ice surface height. They cannot illustrate the retreat of steep ice cliffs caused by intensive backward ablations. To solve this problem, we converted the vertical elevation differences to horizontal retreats on steep terrains (slopes greater than 45°) by using **Eqs 1–3**, the results are shown in **Figure 6**. From this figure, we can easily distinguish the dramatic backwastes of all ice cliffs and also other regions with steep terrains. The largest absolute horizontal backwaste reached nearly 7.8 m (**Figure 6C**), indicating that the surface retreats caused by backwastes can easily reach 20 m over the whole ablation season (from early May to later October in recent years according to our monitoring works) since this is only a 1-month observation. Although the glacier terminus also shows significant retreat (region D in **Figure 6**; with a median and maximum retreat of 2.1 and 4.2 m respectively), the largest retreats appeared in the middle part of the surveyed region where a larger area of ice cliffs exist. Besides, the backwasting directions of all large supraglacial ice cliffs in debris-covered regions (See **Figure 3D**) are generally toward the centerline of the Halong Glacier and also the upper glacier direction, but the ice cliffs on regions right above the glacier terminus were wasting ice toward the left margin (marked by a red circle in **Figure 6A**). It indicates that this region is in strong narrowing which may cause the break off of the Halong Glacier at this point in the near future. This can also be proved by the shaded DSM on September 15 (**Figure 3C**) and elevation differences showing in **Figure 4A**.

The clean ice regions of Halong Glacier also show a relatively larger backwasting rate. Those regions have very rugged terrains (see **Figure 4D**) caused by the cutting effects of supraglacial rivers. The downslope flushing of melted water toward the river channels gradually caused the widening and deepening of glacier surface depressions and channels, further increasing the evolvements of the rugged terrain as well as the strong backwasting effects.

The Influence of Debris Thickness on Ice Ablation Compared to Clean Ice

We extracted the slopes, aspects, and elevation differences of all the sites with measured debris thicknesses to study the relationships between debris cover thickness and surface slope/aspects, and also the influence of debris thickness on glacier ablations. We also randomly selected 50 clean-ice sites (see **Figure 1D**) and extracted their slope, aspects, and elevation differences for comparison. The results (**Figure 7**) show that there are some relationships between supraglacial debris thickness with terrain slope, aspect, and also the elevation differences (converted to ice ablation in **Figure 7D** to better compare with other studies). Although only the debris thicknesses on surfaces with slope below 40° were measured, they show certain insignificant relationships with terrain slope over all sites (**Figure 7A**), which may result from similar mechanisms mentioned before, i.e. the larger deposition rates on gentler than steeper slopes. Correspondingly, the ablation rate of all measured sites has insignificant nonlinear relationships with terrain slopes (**Figure 7B**) and debris thicknesses (**Figure 7D**). The relationship between debris thickness and surface aspect (**Figure 7C**) shows that east- and south-facing slopes have thinner debris than north- and west-facing ones, illustrating that the formation of debris cover may also be slightly controlled by terrain orientations.

The significance of the exponential relationship between debris thickness and ice ablation (**Figure 7D**) is much higher than the

relationship between elevation difference and surface slope (R^2 0.3002 vs. 0.1765). The ablation rate drops dramatically for debris thinner than 3 cm, then slowly decreases toward zero, in good accordance with previous studies which show strong protection effects of thicker debris (>2 cm) on glacier ablation (Østrem, 1959; Mattson et al., 1993). However, since the number of measured sites is very limited in this study, these relationships and the influences of thinner debris (<2 cm) on glacier ablation need to be further confirmed in the future.

Figure 7E shows an increasing but insignificant trend of clean ice ablations with increasing slopes, which is consistent with the phenomenon illustrated by **Figure 5C** that can be explained by heat releasing and flushing of upper slope melt-waters. The larger ablation rates of south-facing clean ice in **Figure 7F** further proved the influence of stronger solar radiation and also the impacts of glacier movements on ablation patterns retrieved by elevation differencing (see DISCUSSION).

DISCUSSION

Influences of River Channels and Supraglacial Ponds on Glacier Ablation

From **Table 1** and **Figure 5**, we can read that two river surface types, i.e. the supra and lateral rivers, have the largest elevation changes among all glacial and periglacial surface types, although they only covered ~3100 m^2 surface area. Both surface river types are mainly located on regions with slopes less than 20°. The mean elevation differences for these two types during the studied period are −2.27 m and −1.80 m, respectively, which are the first- and second-largest values over all surface types, indicating the strong cutting and flushing effects of river flow on strengthening the ablation of bilateral and underneath ices. Furthermore, regions covered by the supra river have larger elevation lowering on surfaces with slope <75° than the lateral river. The possible reason for this phenomenon is that supra rivers mostly appear on clean ice regions (**Figure 3D**), where the role of meltwater flushing is the most effective. However, such analysis in this study may not be comprehensive because of the limitations of the nadir view angle UAV survey discussed below.

Theoretically, the supraglacial ponds should have enhancing effects on the ablation of the glacier ice beneath because of the large absorption of energy and thus higher temperature of water in the pond than the underlying ice (Sakai et al., 2000; Miles et al., 2016; Miles et al., 2018). However, our results astonishingly show that the areas covered by supra ponds have an ablation rate only slightly greater than supraglacial debris (see **Table 1** and **Figure 5C**). This may be because the accumulating meltwater pouring into those turbid ponds has caused their expansions and thus uplifts of surface elevation. Besides, the supraglacial ponds on Halong Glacier are all very small and shallow, which may not have bigger effects on enhancing glacier melt (see **Supplementary Figure S4**).

Influences of Glacier Movements on Glacier Ablation Pattern Retrieval

Flow is one of the representative features of glaciers, characterizing the active region of a glacier. Surface displacements caused by glacier flow should have significant influences on glacier surface ablation patterns extracted by elevation differencing. We manually measured the amplitude of the surface displacements of Halong Glacier at several locations, and briefly investigated their influences on the ablation pattern retrieved. The most active regions of the upper surveyed glacier area, i.e. two regions of clean ice and the nearby debris-covered region between them (regions coded as B-D in **Figure 8A**), have surface displacements ~0.50 m during the studied period (see **Figures 8B–D** subscripted with 1 and 2). Due to the glacier surface movement, the surface inclining backward to glacier flow direction (south to southwest in **Figure 8**) has a much larger elevation difference than actual ablation, compared with those inclining toward glacier flow (mainly north), which have smaller elevation differences lower than the real ablation (**Figures 8B–D** with subscript 4). The displacements of narrow river channels caused by surface movements further amplified these discrepancies. This can also be proved by **Figure 5F** and **Figure 7F**, which shows that the south-facing clean ices and supraglacial river channels have larger elevation differences than other directions. On the other hand, the larger boulders on the debris-covered glacier surface are not only moving together with glacier ice but also rolling toward the downslope direction caused by differentiated surface ablations, further enlarging the inconsistencies between the elevation differences and the real surface ablations (**Figure 8C**). Such influences should have caused some changes in the statistics of the ablation pattern in **Figure 5**, particularly for the area covered by clean ice which has the most complex terrain. Therefore, it's better to eliminate the influences of glacier movements when intending to retrieve the ablation patterns more precisely. However, it's beyond the scope of this study and will try to be solved in future works.

Besides, the glacier flow during the studied period must have caused some inputs of glacier ice from the upper regions of both major branches of the Halong Glacier. These inputted ices were also melting together with the existing glacier ice, and therefore should be counted into the total mass loss. The ice thickness measurements on Halong Glacier performed in October 2016 via Canadian EKKO-PRO Ground Penetrating Radar (Guo and Wu, 2019) showed that mean ice thickness on the upper debris-covered region right below clean ice of the north branch (see **Figure 1D** for the distribution and ice thickness of measured sites) was about ~109 m (102–114 m). If using 100 m as the mean ice thickness (in regard to the surface ablation during 2016–2019) for both branches, multiplying with their total width of ~900 m and mean estimated surface displacement of ~0.5 m, the ice inputs from the upper glacier during the studied period can amount to 4.5×10^4 m^3 (3.83×10^4 m^3 w. e.). By considering this contribution, the total mass loss of the studied area from August 11 to September 15 will reach up to 4.55×10^5 m^3 w. e., i.e. the contribution of ice inputs from the upper glacier will be ~8% of the total mass loss. However, this is only a very rough estimation. The accurate estimation needs very detailed measurements on the ice thickness along the upper edge of the studied area, as well as the well-distributed glacier surface velocity that should be extracted by feature tracking methods (e.g., Leprince et al.,

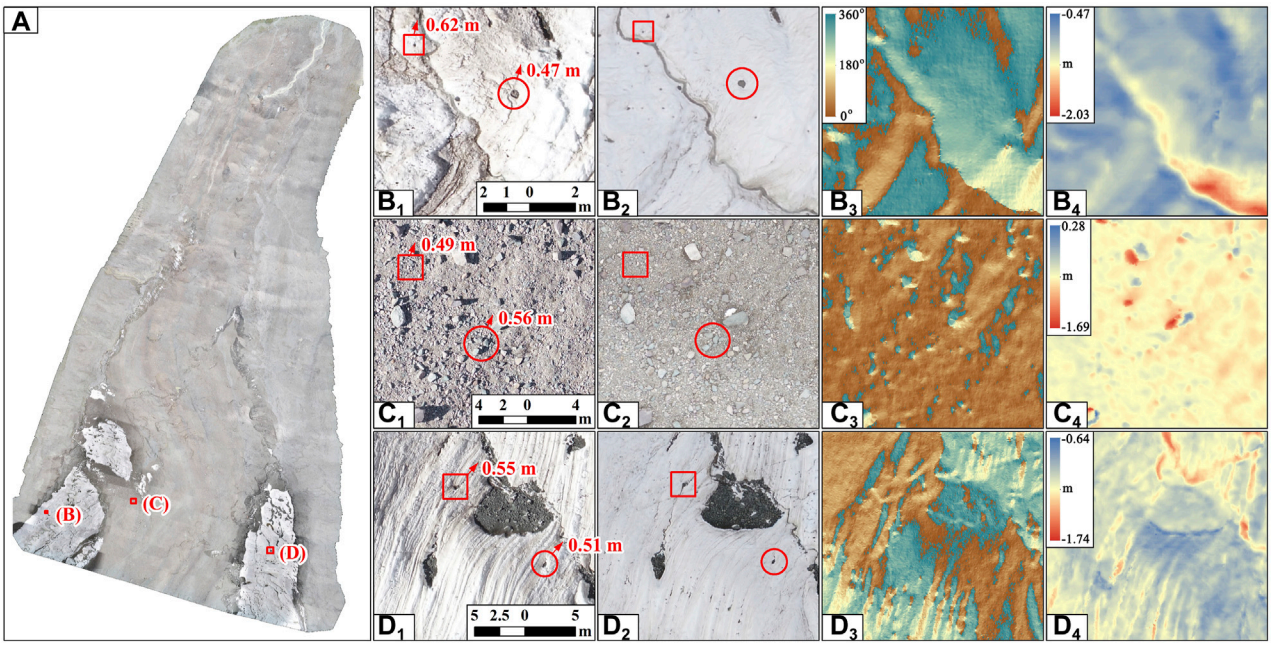

FIGURE 8 | Examples illustrating the influences of glacier surface movements on retrieved ice ablation. **(B)**, **(C)**, and **(D)** correspond to three regions in **(A)**. Subscripts 1–4 denote the UAV images on August 11 and September 15, the surface aspects from DSM on September 15, and the derived elevation differences, respectively. Rectangles and circles in one and two represent the apparent features that can be read on both images, and arrows and marked numbers are the corresponding moving directions and distances.

2007; Messerli and Grinsted, 2015), and also the vertical profile of ice velocity below glacier surface, which are all beyond the scope of this study.

Further Potentials of UAV Survey in Detecting Buried Ice and Geomorphologic Evolvements

Aside from the ablation patterns of Halong Glacier, the precise and high-resolution elevation difference used in this study also obtained extra information on the additional ice storage of Halong Glacier, i.e. the existence of large amounts of buried inactive ice beyond the active glacier margin, which show clear changes during the surveyed period. Such kinds of buried ice cannot be distinguished from the single-phase UAV photos with the highest spatial resolution (~3 cm), or even by on-site visual inspection. The difference of DEMs generated by two short-term UAV surveys in this study distinctively illustrated the existence of some of the buried ice outside the active margin of Halong Glacier, which means the buried inactive ice can be partially distinguished by this kind of method. However, such application is only confined to those regions with exposed ice cliffs or buried ice with significant ablations. The ice buried under thick debris or other kinds of sediments outside the glacier margin still cannot be distinguished because of their negligible surface lowering rate.

The analysis in **Figure 5** included the lateral debris which also shows distinctive elevation changes in some regions, especially the left side and upper lateral regions on both sides (see **Figure 4**). From the curve of lateral debris in **Figure 5C**, we can see that the lateral debris with a slope below 30° generally remains unchanging. However, those between 35°-70° show slightly increased positive elevation changes, while those above 75° show large and quickly increased negative elevation differences. This may indicate that the larger erosion rate of debris-covered slopes on steep terrain which caused a large lowering down of surface elevation, while the eroded debris subsequently deposited onto the downslope gentler terrain, causing the raise in elevation of those surfaces. This means that the repetitive UAV survey with higher spatial resolutions and accuracies can be used to study the geomorphologic dynamics of periglacial slopes even over short time periods.

Limitations of Current Works

Although the DJI Phantom 4 Pro V2.0 has good performance in generating high-resolution DSMs with sufficient accuracies, it has some intrinsic limitations due to the single view angle camera it carried. Such a camera configuration has resulted in many artifacts on regions with reversed or steep terrain slope, e.g. the inward tilted surfaces (**Figures 9A,B**), steep ice cliffs, and the deep narrow river channels (**Figures 9C,D**). Those artifacts may have caused some problems in the retrieved ablation patterns. One solution for this by using the same device is to perform an oblique survey with tripled flights on a region, in which one uses the same nadir view angle, and another two use forward and backward view angles, respectively. However, this will drastically increase the time and workloads on surveying a

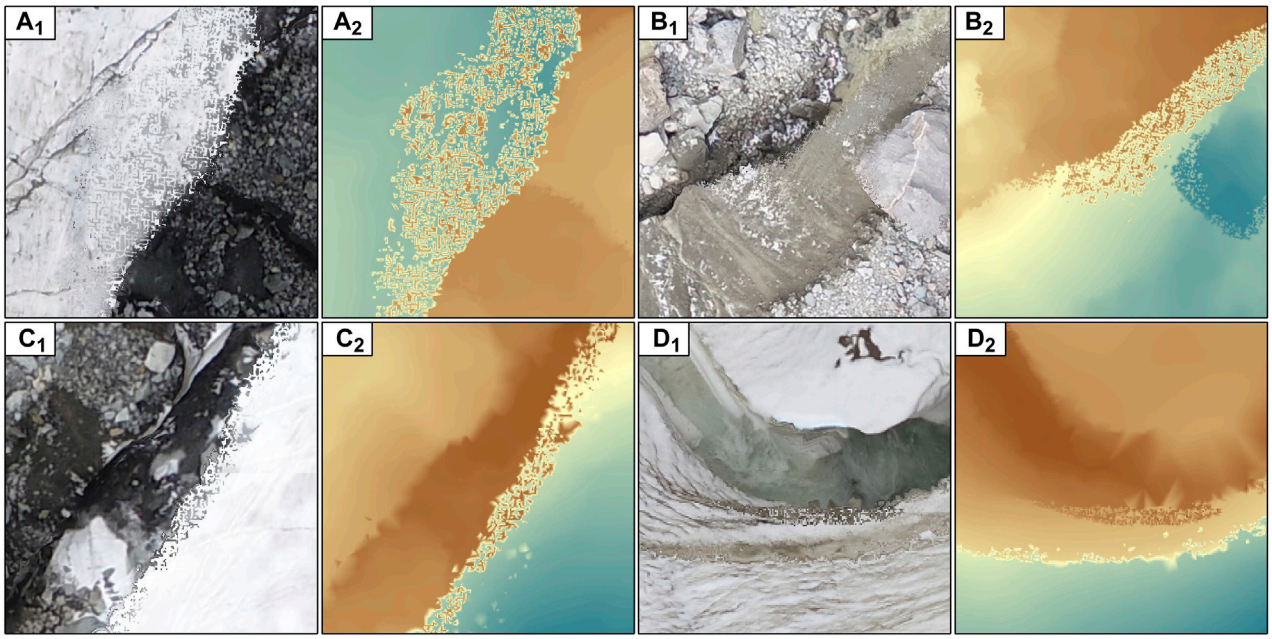

FIGURE 9 | Examples of the limitations of nadir view UAV survey in DSM generation on steep terrains, e.g. lateral river aside clean ice **(A)** and ice cliff **(B)**, as well as supra river aside **(C)** and on **(D)** clean ice. Subscript 1 is UAV image and two is DSM.

small region but could be tested on the Halong Glacier in future works.

Additionally, this study only aimed to reveal the overall patterns of glacier ablation related to nine brief surface types. We only used one of the pixel-wise classification algorithms, i.e. image segmentation, to classify the UAV image on September 15, and disregarded the fast changes in the glacier surface between the two surveyed dates. The classification results were further simplified by merging small surface patches into surrounding larger ones to illustrate the overall patterns. Since such pixel-wise classification algorithms were proved to have very limited accuracies on high-resolution images (Myint et al., 2011), plus with the larger simplification on the classified surface types, our current results can only describe the conceptual rather than rigorous patterns of glacier ablations related to surface features. To retrieve precise and detailed relationship between surface types and glacier ablation as well as their own changes of those defined surface types, high complexity classification algorithms with higher accuracies, such as object-oriented (Johnson and Xie, 2013) or deep neural networks (Jozdani et al., 2019), should be used for both UAV images in future work.

CONCLUSION

Through two repeated UAV surveys, we studied the short-term ablation pattern of the tongue of Halong Glacier between August 11 and September 15, 2019. The results clearly show that Halong Glacier has experienced strong ablation during the studied period. The average surface lowering of the studied area was 0.62 m, with a corresponding overall mass loss of 4.17×10^5 tons w. e.

Supraglacial debris cover is the dominant surface type in the studied area (80.9%), while clean ice and ice cliffs cover the major parts of the rest of the area. Different surface types have distinctive elevation lowering as well as their contribution to total ice loss. Although debris-covered regions have the minimum surface lowering (0.45 m, 0.38 m w. e.), they contributed 58.6% to total ice loss because they comprise the largest area. The regions covered by the lateral and supraglacial rivers have the largest but insignificant surface lowering rate (1.8 and 2.27 m, respectively) because of their minimal area and also the lower qualities of DSMs on those steep terrains.

Two types of ice cliff covered region, i.e. the supraglacial and lateral ice cliffs, have significant surface lowering of 1.60 m (1.36 m w. e.) and 1.43 m (1.22 m w. e.), respectively, and contributed in total 18.1% to the total ice loss, compared to their small area coverage of only 7.1%. The clean ice covered 11.4% of the studied area and has a moderate surface lowering (1.19 m, 1.01 m w. e.). However, it also contributed to 21.9% of total ice loss during the studied period. The supraglacial ponds only covered 0.1% of the whole studied area. They have insignificant surface lowering (0.76 m, 0.65 m w. e.) compared to other studies, and contributed only 0.2% to total ice loss.

Our study also revealed the fast backwastes of ice cliffs and other steep terrains. The horizontal surface retreats caused by backwasting are evenly distributed among all the ice cliff covered regions, with the maximimum retreat amount to 7.8 m. This indicates the fast changes of Halong Glacier from another aspect, which is represented by notable terminus retreat and also the glacier tongue narrowing down. The fast backwaste

of ice cliffs right above the glacier terminus may further cause the break off of Halong Glacier into separated parts in the near future.

Our study proved that a low-cost UAV has large potentials for monitoring fast changes of both debris-covered and clean ice glaciers. Although the single nadir view UAV survey used in this study has some limitations on steep terrain, it can be overcome in the future through performing multiple flights using different view angles.

DATA AVAILABILITY STATEMENT

The original contributions presented in the study are included in the article/**Supplementary Material**, further inquiries can be directed to the corresponding author.

AUTHOR CONTRIBUTIONS

WG designed and organized this study, XG is the operator and data processor of the UAV surveys. YL provided some technical suggestions and advice on this UAV-based study. JL, LC, and JG are the assistants of related field works. DS provides part of the financial support for this study.

FUNDING

The study is supported by National Natural Science Foundation of China (grant No. 41201068, 41671075 and 42171148), Light of West China Program of CAS, the Strategic Priority Research Program of CAS (grant No. XDA19050702), and the Natural Science Foundation of Gansu Province (grant No. 18JR3RA394).

ACKNOWLEDGMENTS

We give thanks for the long and continuous support provided by local residents and officials of Anye Machen Mountain on the monitoring works of the glaciers in this region. We also offer thanks for all the precious works done by Dr. Junfeng Wei, Dr. Weijia Bao, Dr. Zhen Wu, and other colleagues in building the glacier monitoring networks of this region.

SUPPLEMENTARY MATERIAL

The Supplementary Material for this article can be found online at: https://www.frontiersin.org/articles/10.3389/feart.2021.740160/full#supplementary-material

REFERENCES

Bash, E. A., and Moorman, B. J. (2020). Surface Melt and the Importance of Water Flow - an Analysis Based on High-Resolution Unmanned Aerial Vehicle (UAV) Data for an Arctic Glacier. *The Cryosphere* 14 (2), 549–563. doi:10.5194/tc-14-549-2020

Benoit, L., Gourdon, A., Vallat, R., Irarrazaval, I., Gravey, M., Lehmann, B., et al. (2019). A High-Resolution Image Time Series of the Gorner Glacier - Swiss Alps - Derived from Repeated Unmanned Aerial Vehicle Surveys. *Earth Syst. Sci. Data* 11 (2), 579–588. doi:10.5194/essd-11-579-2019

Bliakharskii, D. P., Florinsky, I. V., and Skrypitsyna, T. N. (2019). Modelling Glacier Topography in Antarctica Using Unmanned Aerial Survey: Assessment of Opportunities. *Int. J. Remote Sensing* 40 (7), 2517–2541. doi:10.1080/01431161.2019.1584926

Bozhinskiy, A. N., Krass, M. S., and Popovnin, V. V. (1986). Role of Debris Cover in the thermal Physics of Glaciers. *J. Glaciol.* 32 (111), 255–266. doi:10.3189/s0022143000015598

Che, Y., Wang, S., Yi, S., Wei, Y., and Cai, Y. (2020). Summer Mass Balance and Surface Velocity Derived by Unmanned Aerial Vehicle on Debris-Covered Region of Baishui River Glacier No. 1, Yulong Snow Mountain. *Remote Sensing* 12 (20), 3280. doi:10.3390/rs12203280

Crocker, R. I., Maslanik, J. A., Adler, J. J., Palo, S. E., Herzfeld, U. C., and Emery, W. J. (2012). A Sensor Package for Ice Surface Observations Using Small Unmanned Aircraft Systems. *IEEE Trans. Geosci. Remote Sensing* 50 (4), 1033–1047. doi:10.1109/tgrs.2011.2167339

Ewertowski, M. W., Tomczyk, A. M., Evans, D. J. A., Roberts, D. H., and Ewertowski, W. (2019). Operational Framework for Rapid, Very-High Resolution Mapping of Glacial Geomorphology Using Low-Cost Unmanned Aerial Vehicles and Structure-From-Motion Approach. *Remote Sensing* 11 (1), 65. doi:10.3390/rs11010065

Fisher, P. (1998). Improved Modeling of Elevation Error with Geostatistics. *GeoInformatica* 2 (3), 215–233. doi:10.1023/a:1009717704255

Florinsky, I. V., and Bliakharskii, D. P. (2019). Detection of Crevasses by Geomorphometric Treatment of Data from Unmanned Aerial Surveys. *Remote Sensing Lett.* 10 (4), 323–332. doi:10.1080/2150704x.2018.1552809

Fraser, R. H., Pouliot, D., and van der Sluijs, J. (2021). UAV and High Resolution Satellite Mapping of Forage Lichen (Cladonia spp.) in a Rocky Canadian Shield Landscape. *Can. J. Remote Sensing*. doi:10.1080/07038992.2021.1908118

Fugazza, D., Senese, A., Azzoni, R. S., Smiraglia, C., Cernuschi, M., Severi, D., et al. (2015). High-resolution Mapping of Glacier Surface Features. The UAV Survey of the Forni Glacier (Stelvio National Park, Italy). *Geografia Fisica E Dinamica Quaternaria* 38 (1), 25–33. doi:10.4461/GFDQ.2015.38.03

Gaffey, C., and Bhardwaj, A. (2020). Applications of Unmanned Aerial Vehicles in Cryosphere: Latest Advances and Prospects. *Remote Sensing* 12 (6), 948. doi:10.3390/rs12060948

Gindraux, S., Boesch, R., and Farinotti, D. (2017). Accuracy Assessment of Digital Surface Models from Unmanned Aerial Vehicles ' Imagery on Glaciers. *Remote Sensing* 9 (2), 186. doi:10.3390/rs9020186

Glasser, N. F., Holt, T. O., Evans, Z. D., Davies, B. J., Pelto, M., and Harrison, S. (2016). Recent Spatial and Temporal Variations in Debris Cover on Patagonian Glaciers. *Geomorphology* 273, 202–216. doi:10.1016/j.geomorph.2016.07.036

Guo, W., Liu, S., Xu, J., Wu, L., Shangguan, D., Yao, X., et al. (2015). The Second Chinese Glacier Inventory: Data, Methods and Results. *J. Glaciol.* 61 (226), 357–372. doi:10.3189/2015jog14j209

Guo, W., and Wu, Z. (2019). 2016 Halong Glacier Subglacieal Topography Dataset. *Natl. Cryosphere Desert Data Cent.* Available at: http://www.ncdc.ac.cn/portal/metadata/eb849170-0cc0-469c-9d77-f684588944f4.

Herreid, S., and Pellicciotti, F. (2020). The State of Rock Debris Covering Earth's Glaciers. *Nat. Geosci.* 13 (9), 621–627. doi:10.1038/s41561-020-0615-0

Hsu, A. J., Kumagai, J., Favoretto, F., Dorian, J., Martinez, B. G., and Aburto-Oropeza, O. (2020). Driven by Drones: Improving Mangrove Extent Maps Using High-Resolution Remote Sensing. *Remote Sensing* 12 (23), 3986. doi:10.3390/rs12233986

Huss, M. (2013). Density Assumptions for Converting Geodetic Glacier Volume Change to Mass Change. *The Cryosphere* 7 (3), 877–887. doi:10.5194/tc-7-877-2013

Jiang, Z., Liu, S., Guo, W., Li, J., Long, S., Wang, X., et al. (2018). Recent Surface Elevation Changes of Three Representative Glaciers in Anyemaqen Mountains,source Region of Yellow River. *J. Glaciology Geocryology* 40 (2), 231–237.

Johnson, B., and Xie, Z. (2013). Classifying a High Resolution Image of an Urban Area Using Super-object Information. *ISPRS J. Photogrammetry Remote Sensing* 83, 40–49. doi:10.1016/j.isprsjprs.2013.05.008

Jouvet, G., van Dongen, E., Lüthi, M. P., and Vieli, A. (2020). *In Situ* measurements of the Ice Flow Motion at Eqip Sermia Glacier Using a Remotely Controlled Unmanned Aerial Vehicle (UAV). *Geosci. Instrum. Method. Data Syst.* 9 (1), 1–10. doi:10.5194/gi-9-1-2020

Jozdani, S. E., Johnson, B. A., and Chen, D. (2019). Comparing Deep Neural Networks, Ensemble Classifiers, and Support Vector Machine Algorithms for Object-Based Urban Land Use/Land Cover Classification. *Remote Sensing* 11 (14), 1713. doi:10.3390/rs11141713

Kraaijenbrink, P. D. A., Shea, J. M., Litt, M., Steiner, J. F., Treichler, D., Koch, I., et al. (2018). Mapping Surface Temperatures on a Debris-Covered Glacier with an Unmanned Aerial Vehicle. *Front. Earth Sci.* 6, 64. doi:10.3389/feart.2018.00064

Kraaijenbrink, P. D. A., Shea, J. M., Pellicciotti, F., Jong, S. M. d., and Immerzeel, W. W. (2016b). Object-based Analysis of Unmanned Aerial Vehicle Imagery to Map and Characterise Surface Features on a Debris-Covered Glacier. *Remote Sensing Environ.* 186, 581–595. doi:10.1016/j.rse.2016.09.013

Kraaijenbrink, P., Meijer, S. W., Shea, J. M., Pellicciotti, F., De Jong, S. M., and Immerzeel, W. W. (2016a). Seasonal Surface Velocities of a Himalayan Glacier Derived by Automated Correlation of Unmanned Aerial Vehicle Imagery. *Ann. Glaciol.* 57 (71), 103–113. doi:10.3189/2016aog71a072

Leprince, S., Ayoub, F., Klinger, Y., and Avouac, J. P. (2007). Co-Registration of Optically Sensed Images and Correlation (COSI-Corr): an Operational Methodology for Ground Deformation Measurements. *IGARSS 2007 IEEE Int. Geosci. Remote Sensing Symp.* 1–12, 1943–1946. doi:10.1109/igarss.2007.4423207

Marzeion, B., Kaser, G., Maussion, F., and Champollion, N. (2018). Limited Influence of Climate Change Mitigation on Short-Term Glacier Mass Loss. *Nat. Clim Change* 8 (4), 305–308. doi:10.1038/s41558-018-0093-1

Mattson, L. E., Gardner, J. S., and Young, G. J. (1993). Ablation on Debris Covered Glaciers: an Example from the Rakhiot Glacier, Punjab, Himalaya. *IAHS Publ.* 218, 289–296.

Messerli, A., and Grinsted, A. (2015). Image Georectification and Feature Tracking Toolbox: ImGRAFT. *Geosci. Instrum. Method. Data Syst.* 4 (1), 23–34. doi:10.5194/gi-4-23-2015

Miles, E. S., Willis, I., Buri, P., Steiner, J. F., Arnold, N. S., and Pellicciotti, F. (2018). Surface Pond Energy Absorption across Four Himalayan Glaciers Accounts for 1/8 of Total Catchment Ice Loss. *Geophys. Res. Lett.* 45 (19), 10464–10473. doi:10.1029/2018GL079678

Miles, E. S., Pellicciotti, F., Willis, I. C., Steiner, J. F., Buri, P., and Arnold, N. S. (2016). Refined Energy-Balance Modelling of a Supraglacial Pond, Langtang Khola, Nepal. *Ann. Glaciol.* 57 (71), 29–40. doi:10.3189/2016aog71a421

Myint, S. W., Gober, P., Brazel, A., Grossman-Clarke, S., and Weng, Q. (2011). Per-pixel vs. Object-Based Classification of Urban Land Cover Extraction Using High Spatial Resolution Imagery. *Remote Sensing Environ.* 115 (5), 1145–1161. doi:10.1016/j.rse.2010.12.017

Østrem, G. (1959). Ice Melting under a Thin Layer of Moraine, and the Existence of Ice Cores in Moraine Ridges. *Geografiska Annaler* 41 (4), 228–230. doi:10.1080/20014422.1959.11907953

Pajares, G. (2015). Overview and Current Status of Remote Sensing Applications Based on Unmanned Aerial Vehicles (UAVs). *Photogram Engng Rem Sens* 81 (4), 281–330. doi:10.14358/pers.81.4.281

Paul, F. (2019). Repeat Glacier Collapses and Surges in the Amney Machen Mountain Range, Tibet, Possibly Triggered by a Developing Rock-Slope Instability. *Remote Sensing* 11 (6), 708. doi:10.3390/rs11060708

Pearce, S., Ljubicic, R., Pena-Haro, S., Perks, M., Tauro, F., Pizarro, A., et al. (2020). An Evaluation of Image Velocimetry Techniques under Low Flow Conditions and High Seeding Densities Using Unmanned Aerial Systems. *Remote Sensing* 12 (2), 232. doi:10.3390/rs12020232

Pellicciotti, F., Stephan, C., Miles, E., Herreid, S., Immerzeel, W. W., and Bolch, T. (2015). Mass-balance Changes of the Debris-Covered Glaciers in the Langtang Himal, Nepal, from 1974 to 1999. *J. Glaciol.* 61 (226), 373–386. doi:10.3189/2015jog13j237

Pitcher, L. H., and Smith, L. C. (2019). Supraglacial Streams and Rivers. *Annu. Rev. Earth Planet. Sci.* 47, 421–452. doi:10.1146/annurev-earth-053018-060212

Pratibha, S., and Kulkarni, A. V. (2018). Decadal Change in Supraglacial Debris Cover in Baspa basin, Western Himalaya. *Curr. Sci.* 114 (4), 792–799. doi:10.18520/cs/v114/i04/792-799

Sakai, A., Takeuchi, N., Fujita, K., and Nakawo, M. (2000). "Role of Supraglacial Ponds in the Ablation Process of a Debris-Covered Glacier in the Nepal Himalayas," in *Debris-Covered Glaciers* (Seattle, Washington, USA: IAHS Publ), 264.

Salerno, F., Thakuri, S., Tartari, G., Nuimura, T., Sunako, S., Sakai, A., et al. (2017). Debris-covered Glacier Anomaly? Morphological Factors Controlling Changes in the Mass Balance, Surface Area, Terminus Position, and Snow Line Altitude of Himalayan Glaciers. *Earth Planet. Sci. Lett.* 471, 19–31. doi:10.1016/j.epsl.2017.04.039

Vargo, L. J., Anderson, B. M., Dadić, R., Horgan, H. J., Mackintosh, A. N., King, A. D., et al. (2020). Anthropogenic Warming Forces Extreme Annual Glacier Mass Loss. *Nat. Clim. Chang.* 10 (9), 856–861. doi:10.1038/s41558-020-0849-2

Vincent, C., Wagnon, P., Shea, J. M., Immerzeel, W. W., Kraaijenbrink, P., Shrestha, D., et al. (2016). Reduced Melt on Debris-Covered Glaciers: Investigations from Changri Nup Glacier, Nepal. *The Cryosphere* 10 (4), 1845–1858. doi:10.5194/tc-10-1845-2016

Wigmore, O., and Mark, B. (2017). Monitoring Tropical Debris-Covered Glacier Dynamics from High-Resolution Unmanned Aerial Vehicle Photogrammetry, Cordillera Blanca, Peru. *The Cryosphere* 11 (6), 2463–2480. doi:10.5194/tc-11-2463-2017

Wouters, B., Gardner, A. S., and Moholdt, G. (2019). Global Glacier Mass Loss during the GRACE Satellite Mission (2002-2016). *Front. Earth Sci.* 7, 96. doi:10.3389/feart.2019.00096

Yang, J., Ding, Y., Liu, S., Lu, A., and Chen, R. (2003). Glacier Change and Ist Effect on Surface Runoff in the Source Regions of the Yangtze and Yellow Rivers. *J. Nat. Resour.* 18 (5), 595–602.

Zhilin, L. (1988). On the Measure of Digital Terrain Model Accuracy. *Photogrammetric Rec.* 12 (72), 873–877. doi:10.1111/j.1477-9730.1988.tb00636.x

Conflict of Interest: The authors declare that the research was conducted in the absence of any commercial or financial relationships that could be construed as a potential conflict of interest.

frontiers in Earth Science

ORIGINAL RESEARCH
published: 16 December 2021
doi: 10.3389/feart.2021.706312

Influence of Supraglacial Debris Thickness on Thermal Resistance of the Glaciers of Chandra Basin, Western Himalaya

Lavkush Kumar Patel[*†], *Parmanand Sharma, Ajit Singh, Sunil Oulkar, Bhanu Pratap and Meloth Thamban*

National Centre for Polar and Ocean Research, Ministry of Earth Sciences, Government of India, Vasco-da-Gama, India

A large number of glaciers in the Hindu-Kush Himalaya are covered with debris in the lower part of the ablation zone, which is continuously expanding due to enhanced glacier mass loss. The supraglacial debris transported over the melting glacier surface acts as an insulating barrier between the ice and atmospheric conditions and has a strong influence on the spatial distribution of surface ice melt. We conducted *in-situ* field measurements of point-wise ablation rate, supraglacial debris thickness, and debris temperature to examine the thermal resistivity of the debris pack and its influence on ablation over three glaciers (Bara Shigri, Batal, and Kunzam) in Chandra Basin of Western Himalaya during 2016–2017. Satellite-based supraglacial debris cover assessment shows an overall debris covered area of 15% for Chandra basin. The field data revealed that the debris thickness varied between 0.5 and 326 cm, following a spatially distributed pattern in the Chandra basin. The studied glaciers have up to 90% debris cover within the ablation area, and together represent ~33.5% of the total debris-covered area in the basin. The supraglacial debris surface temperature and near-surface air temperature shows a significant correlation ($r = > 0.88$, $p = < 0.05$), which reflects the effective control of energy balance over the debris surface. The thermal resistivity measurements revealed low resistance (0.009 ± 0.01 $m^{2\circ}C\,W^{-1}$) under thin debris pack and high resistance (0.55 ± 0.09 $m^{2\circ}C\,W^{-1}$) under thick debris. Our study revealed that the increased thickness of supraglacial debris significantly retards the glacier ablation due to its high thermal resistivity.

Keywords: supraglacial debris, glacier, thermal resistance, Chandra basin, Western Himalaya, debris-cover

OPEN ACCESS

Edited by:
Duncan Joseph Quincey, University of Leeds, United Kingdom

Reviewed by:
Yong Zhang, Hunan University of Science and Technology, China
Morgan Jones, Aberystwyth University, United Kingdom

****Correspondence:***
Lavkush Kumar Patel
lavkushpatel@ncpor.res.in

†ORCID ID:
Lavkush Kumar Patel, orcid.org/0000-0002-8131-9587

Specialty section:
This article was submitted to Cryospheric Sciences, a section of the journal Frontiers in Earth Science

Received: *07 May 2021*
Accepted: *10 November 2021*
Published: *16 December 2021*

Citation:
Patel LK, Sharma P, Singh A, Oulkar S, Pratap B and Thamban M (2021) Influence of Supraglacial Debris Thickness on Thermal Resistance of the Glaciers of Chandra Basin, Western Himalaya. Front. Earth Sci. 9:706312. doi: 10.3389/feart.2021.706312

INTRODUCTION

In the Hindu Kush Himalayan (HKH) region, about 13% of the glacierized area and ~40% of the ablation area is debris-covered (Scherler et al., 2011; Bolch et al., 2012), which is expanding annually due to accelerated glacier mass loss (Shukla and Qadir, 2016). The increased debris cover over the glaciers has a significant impact on the thermodynamics of the glaciers in the high Himalaya (Banerjee and Shankar, 2013; Rowan et al., 2020). Debris cover influences the ablation rate by regulating the heat flux from surface to glacier ice, thus influencing the glacier response to climate change (Nicholson et al., 2018). Recent studies on the impact of supraglacial debris cover on ablation have shown very contrasting results like higher melting (Pellicciotti et al., 2015;

Steiner et al., 2019), no influence (Muhammad et al., 2020), and lower melting (Pratap et al., 2015; Patel et al., 2016; Sharma et al., 2016; Nicholson et al., 2018). Findings of enhanced melt have been attributed to the formation of supraglacial ponds, ice cliffs, and englacial hydrological processes (Benn et al., 2012; Fyffe et al., 2014; Buri et al., 2016). Debris cover accelerates water ponding and ice cliff (thermokarst erosion) formation over the glacier surface (Röhl, 2008) and can enhance heat transfer at the water-ice interface. However, several researchers have observed reduced melting and explained a reduction in heat transfer from thick debris (Pratap et al., 2015; Patel et al., 2016; Sharma et al., 2016; Nicholson et al., 2018). The heat transfer from debris surface to debris ice interface zone largely depends upon the thermal characteristics of the debris pack (Mihalcea et al., 2006; Lambrecht et al., 2011; Rowan et al., 2017) and atmospheric conditions (Collier et al., 2015). The thermal characteristics of the debris pack mainly depends on debris composition, its thickness, and its moisture content and is explained in terms of thermal resistance and conductivity. The thermal resistance is defined as the ratio of debris thickness and thermal conductivity of a debris layer. Thermal resistance is an important index to understand the evolution of several glaciers (Nakawo and Young, 1982; Suzuki et al., 2007; Lambrecht et al., 2011; Chand and Sharma, 2015). This index is obtained from surface temperature and heat balance within the debris layers. Since it is difficult to determine the thermal resistance of a layer of unknown material directly in the field, it was suggested that the surface temperature of the debris layer may be used for estimating the thermal resistance (Suzuki et al., 2007).

However, the thickness of a debris pack is crucial for controlling the impact of atmospheric warming and energy flux to the ice through debris (Nicholson and Benn, 2006). Sensitivity experiments have shown that an increase in debris thickness by 0.035 m can offset about 1°C of atmospheric warming (Fyffe et al., 2014), highlighting the importance of debris pack for protection of glacier ice. A thick debris pack with high moisture content effectively reduces the ablation by lowering the heat transmission by reducing the thermal diffusivity of the saturated debris layers (Juen et al., 2013; Collier et al., 2014). It is therefore imperative to investigate debris composition, moisture content and thickness, and quantify their effect on the resulting energy flux of the debris layer.

Analyzing the energy balance and ablation pattern of debris-covered glaciers has been a point of debate since 1980s' where a simplified model was used for estimating the ablation pattern under thick debris by using thermal properties and meteorological parameters (Nakawo and Young, 1981; Nakawo and Takahashi, 1982; Nakawo and Young, 1982). Later, several researchers have modified these models by incorporating degree day factors or debris surface temperatures (Haidong et al., 2006; Mihalcea et al., 2006). The DEB-Model (Reid and Brock, 2014) and Crocus-DEB (Lejeune et al., 2013) are the only melt models that attempt a process-resolving simulation of energy fluxes at a debris-covered ice surface. Most of the studies were conducted over a smaller area and for shorter periods. Some satellite observations were also used to define the thermal resistance or characteristics of the debris-covered glaciers (Suzuki et al., 2007; Zhang et al., 2011; Foster et al., 2012; Rounce et al., 2015), which have emphasized the need for improved understanding of debris temperature and thermal properties. There are very few field data available on debris cover, thickness, and associated behavior. The debris pack surface, subsurface temperature, and thermal resistance variability are important to understand the underlying processes and debris behavior.

In this study, the thermal characteristics of supraglacial debris over three debris-covered glaciers in the Chandra basin (Western Himalaya) were examined using *in-situ* field observations. The surface temperature and ablation data were collected alongside debris thicknesses, at various altitudinal zones, during the period 2016-17. The thermal resistance of the debris pack was estimated using the debris cover surface temperature and ablation rate. The aim of the study is to analyze the diurnal and seasonal variability in surface temperature and thermal resistance of debris cover to understand the control of supraglacial debris on melting in the extensive debris-covered glaciers of the Western Himalaya. This type of analysis is useful for the empirical parameterisation of numerical models that may focus on predicting the ongoing and future climate changes in the HKH region.

STUDY AREA AND SELECTED GLACIERS

In this study, *in-situ* observations were carried out over three glaciers (Bara Shigri, Batal, and Kunzam) in the Chandra basin of Western Himalaya. It is a major sub-basin of the Indus river basin, and lies within the central crystalline axis of the PirPanjal range in Lahaul-Spiti, Himachal Pradesh, India (**Figure 1**). The Chandra basin has 201 glaciers (Sangewar and Shukla, 2009), spread over an area of 2,440 km^2, and about 15% of glacier area is covered by debris with varying thicknesses (**Figure 1**). It represents a highly rugged terrain with high mountains and deeply dissected valleys (Patel et al., 2017). The basin is influenced by the Indian monsoon in summer and westerlies in winter (Bookhagen and Burbank, 2006). The Bara Shigri is the largest glacier (113.8 km^2) in the basin, and is also one of the biggest glaciers in the Indian Himalaya. This glacier has an average slope of 12° and flows towards the NW direction. The Batal Glacier covers an area of 4.35 km^2 with a flowing direction towards the NE and the average slope of the glacier is 15°. The Kunzam Glacier covers an area of 0.48 km^2 with a mean slope of 15° and it flows towards the N. Together, these three glaciers are the major debris-covered glaciers of the Chandra basin and represent almost ~21.1% of overall glacier area and ~33.5% of the debris-covered glacierized region of the basin. The debris layer comprises soil, rock fragments, pebbles, cobbles and big boulders with a hummocky [Unified Soil Classification System, USCS (ASTM D2487)] glacier surface.

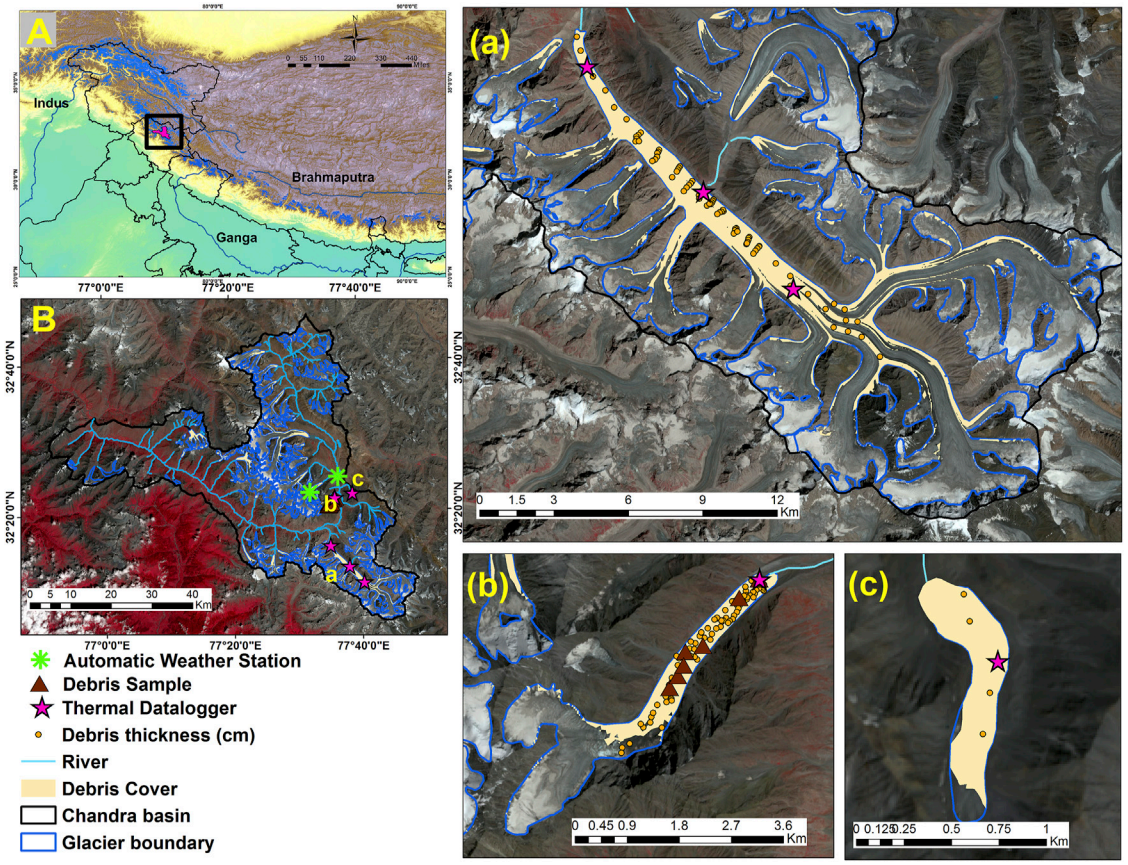

FIGURE 1 | (A) Location map of Chandra basin **(B)** Glacierized terrain, debris cover, studied glaciers, automatic weather stations and various observational sites. The distribution of debris cover using remote sensing data (yellow shade) and *in-situ* debris sample points (brown dots) over the studied glaciers are marked along with thermal data logger sites installed at **(a)** Bara Shigri, **(b)** Batal, and **(c)** Kunzam Glaciers. (Background for inset map A is SRTM DEM and others are Sentinel 2B satellite image).

DATA COLLECTION AND METHODOLOGY

Debris-Cover Mapping, Thickness, and Geological Characteristics

To analyze the thermal characteristics of the glacial debris over a glacierized basin, it was important to understand its spatial extent, hypsometry, thickness, and geological characteristics in the basin. The spatial extent and hypsometry were extracted by using Landsat 8 Operational Land Imager (OLI) satellite data and Advanced Spaceborne Thermal Emission and Reflection Radiometer, Global Digital Elevation Model Version 2 (ASTER GDEM V2), and the thickness and geological characteristics were explored by field observations and laboratory analysis. Detailed debris thickness measurements were carried out over the studied glaciers (Bara Shigri, Batal, and Kunzam) and additionally limited studies were undertaken over the Samudra Tapu, Sutri Dhaka, and Gepang Gath glaciers of Chandra basin (**Supplementary Figure S1**). The debris cover for the Chandra basin was mapped using Landsat 8 scene of the year 2016 acquired from the USGS website (https://earthexplorer.usgs.gov/). The Landsat scenes were pre-processed (atmospheric correction) converting the raw DN values to the top of atmosphere reflectance by using band multiplicative, additive rescaling factors and cosine corrections provided in the associated metadata file of the scene. Similarly, the brightness temperatures, were also converted from the thermal band (10) using band specific conversion constants (K1 and K2) from associated meta data file.

The corrected satellite datasets were used for the debris cover extraction using a semi-automated method. The semi-automated method uses band ratios (NIR, SWIR, and TIR bands) and the manually extracted glacier boundaries (Shukla et al., 2009; Alifu et al., 2015). Landsat 8 OLI scenes are 170 km by 183 km and consist of nine spectral bands (from visible through to SWIR) with a spatial resolution of 30 m (Bands 1 to 7 and 9). The spatial resolution for the panchromatic (Band 8) is 15 m, and for thermal bands (10 and 11), spatial resolution is 100 m. The ASTER GDEM V2 provides a comparable resolution, at 30 m, and with a quantified accuracy of ±2.3 m in the horizontal and ± 10 m in the vertical (Tachikawa, 2011). The manually extracted boundaries of 129 glaciers (566 km^2

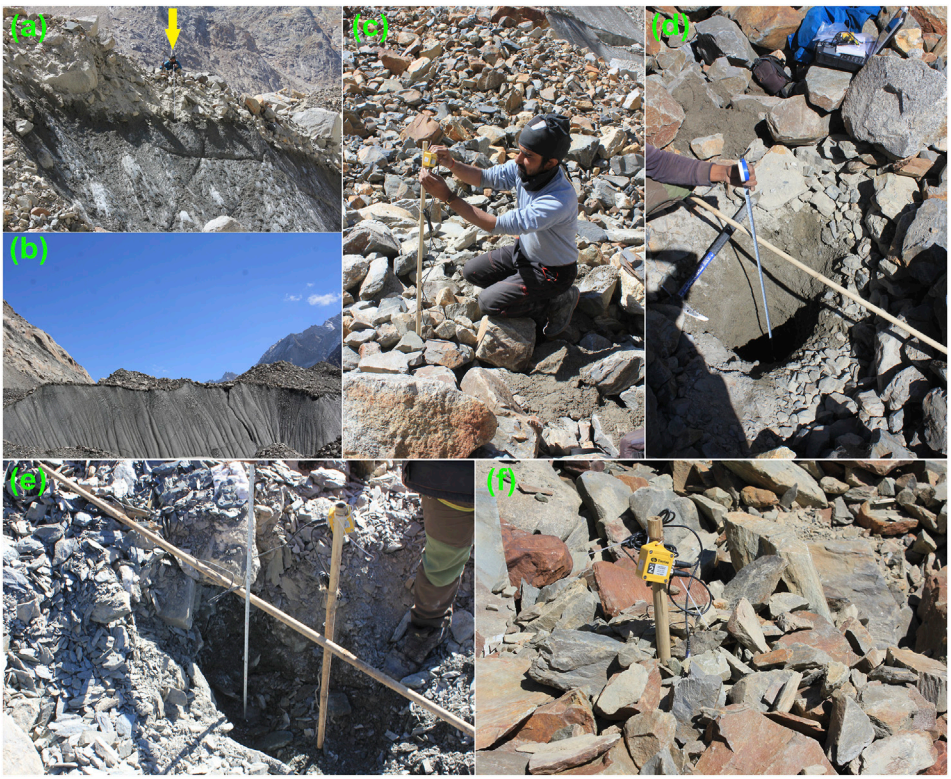

FIGURE 2 | Field photographs of the observations on debris cover and installation of the thermal dataloggers over the debris-covered glaciers of Chandra Basin. **(A)** debris cover measurement over a ice cliff in Bara Shigri Glacier, **(B)** a big and wide (~ 200 m long and ~ 35 m thick) ice cliff depicting the debris -covered region and the thickness at the lower ablation zone of Bara Shigri Glacier, **(C)** installation of Tinytag thermal dataloggers at a fixed bamboo stake over Bara Shigri Glacier, **(D)** debris thickness measurement and sample collection, where the debris pack composition (boulders, cobbles, pebbles, at the upper layer while fine to coarse level sand at the lower layer) is clearly visible. **(E)** debris thickness measurement and sample collection over Kunzam Glacier, **(F)** Tinytag thermal data logger installation over Batal Glacier.

glacier area) from Chandra basin were used for debris extent estimation. The similar spectral response of the non-glacier surface and debris-covered glacier surface makes it difficult to delineate between the glacier and non-glacier area. In this situation, the thermal band helps to separate the periglacial and supraglacial debris (Alifu et al., 2015; Patel et al., 2017). The spectral response (i.e. reflectance) of supraglacial debris cover is low for the bands NIR, and SWIR compared to the clean ice. The hypsometry of glacier area and debris cover over the Chandra basin was extracted from the distribution of the debris cover and DEM. To accurately represent the complete debris cover of the Chandra basin, debris thickness was manually measured at more than 250 locations over the glaciers by removing the debris cover from the glacier surface to the ice-debris interface zone from 4,000 m asl to 5,000 m asl (**Figure 2**). There was some minor debris presence above 5,000 m asl, especially along the glacier margins, but this was not measured as the glacier flanks were visibly unstable. The big boulders and glaciers' edges were avoided. The debris samples from the studied glaciers were also collected and analyzed for the identifying geological characteristics of the debris pack (**Figures 1**, **2**). The debris sample/rock type sizes (**Figures 2A–F**) were classified based on the USCS and major minerals were identified by the petrographic study of the thin sections using a standard Petrological Microscope.

In-Situ Debris-Cover Temperature Measurements

To study the debris cover surface temperature, five thermal data loggers with sensors (Gemini Tinytag thermal data loggers model TGP 4520 and probe PB 5001) were installed over supraglacial debris along the central flowline. They were attached with bamboo stakes, and they continuously logged temperature data at 30 min intervals between September 2016 and October 2017 (**Table 1**). Many studies have used the same thermistor probes and dataloggers for temperature profiling for similar investigations of debris-covered glaciers in the Nepal Himalaya (Mihalcea et al., 2006; Brock et al., 2010; Nicholson and Benn, 2013; Rowan et al., 2021). The Tinytag datalogger (TGP 4520) has an accuracy of ± 0.4°C at 0°C, and two thermal probes can be connected into the logger unit. We fixed one probe at the debris surface and the second one at the debris-ice interface zone. To check the consistency of the

TABLE 1 | Details of the spatial characteristics for the thermistor data loggers, and debris samples (DS) collected from selected glaciers of the Chandra Basin.

ID (sensor/ debris sample)	Glacier	Location/elevation	Observation period	Debris description	Minerology/lithology
TG 1 + DS	Batal (Surface)	32.36334 N, 77.60043E	September 11, 2016–September 14, 2017	Large boulders, cobbles, gravels with coarse to medium sand matrix	Sandstone
	30 cm below the surface	4,300 m asl	June 19, 2017–September 14, 2017		
TG 2 + DS	Kunzam	32.37291 N, 77.64613 E 5,200 m asl	September 10, 2016– August 16, 2017	Cobbles, gravels with medium to fine sand matrix	Sandstone
TG 3 + DS	Bara Shigri	32.25766 N, 77.58685 E 4,100 m asl	September 09, 2016–September 04, 2017	Large boulders, cobbles, gravels with medium to fine sand matrix	Sandstone, Phyllite
TG 4 + DS	Bara Shigri	32.21105 N, 77.63526 E 4,550 m asl	Stopped	Large cobbles, gravels with medium to coarsesand matrix	Sandstone, Granite mixed with sedimentary material
TG 5 + DS	Bara Shigri	32.17964 N, 77.6791 E 4,800 m asl	September 30, 2016	Cobbles, and medium to coarse gravels with coarse sand	Quartz, Biotite, Schist, Mica
DS1	Batal	32.36333 N, 77.60036 E 4,300 m asl	August 24, 2015	Large boulders, cobbles, gravels with medium to fine sand matrix	Phyllite
DS2	Batal	32.36047 N, 77.59664 E 4,300 m asl	August 24, 2015	Large boulders, cobbles, gravels with medium to fine sand matrix	Quartz Biotite Schist
DS3	Batal	32.35233 N, 77.5865 E 4,600 m asl	August 24, 2015	Large cobbles, gravels with coarse to medium sand matrix	Sandstone, Phyllite
DS4	Batal	32.34678 N, 77.58344 E 4,650 m asl	August 24, 2015	Large cobbles, gravels with coarse to medium sand matrix	Quartz Biotite Schist
DS5	Batal	32.34856 N, 77.58503 E 4,650 m asl	August 24, 2015	Large cobbles, gravels with coarse to medium sand matrix	Quartz Biotite Schist Sandstone
DS7	Batal	32.35019 N, 77.58611 E 4,600 m asl	August 24, 2015	Large cobbles, gravels with coarse to medium sand matrix	Sandstone
DS10	Batal	32.35317 N, 77.58972 E 4,600 m asl	August 24, 2015	Large cobbles, gravels with coarse to medium sand matrix	Sandstone

loggers, pre-installation tests were conducted at the base camp (Himansh station, Lahaul-Spiti, Himachal Pradesh) and near the installation site over the glacier. Firstly, all the thermal data loggers were fixed within a 2 × 2 m plot for 30 min at the base camp Himansh station. Secondly, for each thermal data logger, before installation at supraglacial debris, the temperature data in the air were also checked for both the probes. In both cases, between sensor variability was less than 0.5°C. Three thermal data loggers and probes were installed over Bara Shigri, one at Batal and one at Kunzam Glacier. (**Table 1**; **Figures 1**, **2**). In the Bara Shigri Glacier (5,200 m asl), both thermistor probes were at the debris surface due to thin debris (5 cm). In the Batal Glacier, during the ablation season (June 2017–September 2017), one of the probes of the Tinytag thermistor was fixed at the middle (~30 cm) of the debris pack for subsurface temperature observations. The installed data loggers were retreived at the end of the ablation season (October 2017). One of the dataloggers (TG 4) was damaged (due to mutilation of probe wire) and malfunctioned. In addition, surface temperature (ice surface and bare ground) data were also collected from infrared sensors (Apogee SI-111) integrated at two installed Automatic Weather Stations (AWS) in this Chandra basin (**Figure 1**) and used for comparison and statistical analysis. The AWS data were also used for the meteorological analysis of the study area.

Thermal Resistance and Debris Thickness

The energy transfer in debris layers depends on the physical properties of the debris like grain size, lithology, and water content (Collier et al., 2014). Under the assumption of uniform debris conditions, heat transfer is controlled by thermal resistance. The thermal resistance of the debris cover is defined as the ratio between surface temperature (T_s) and ablation rate in dependence of latent heat of fusion (L_s) and ice density (ρ_i)(Nakawo and Young, 1981; 1982; Lambrecht et al., 2011):

$$R = \frac{T_s}{L_s . \rho_i . \alpha} \quad (1)$$

where thermal resistance R was estimated for the entire period with 30 min intervals by using the recorded (T_s) and latent heat of fusion (L_s) and ablation rate (α). The ablation rate (α) was estimated by stake observations for the study period (measurements at time t_0 and t_1). The ablation rate for a specific point was estimated using the direct glaciological method (Cuffey and Paterson, 2010). A network of bamboo stakes was established using a Heucke steam drill system. Twenty-three bamboo stakes were installed over the glacier surface at representative locations based on aspect, slope angle and debris cover to obtain melt rates on the glacier. The stakes heights and debris thicknesses were measured after installation and subsequently, the stakes measurements were continued

TABLE 2 | The details of the AWS (Himansh station, Chandra Basin) sensors used in the study.

Sensor type/parameter	Measurement range	Accuracy
Campbell HC2S3/Air Temperature	–50°C to +60°C	± 0.1°C
Campbell HC2S3/Relative Humidity	0–100% RH	±0.8% RH
Campbell 05103/Wind Speed & Wind Direction	0 to 100 ms^{-1}	±0.3 ms^{-1} and ±3° Direction
Campbell SI-111/Surface Temperature	–55 to 80°C	± 0.5°C at –40 to 70°C
Kipp&Zonen CNR4/Solar Radiation	0 to 2000 Wm^{-2}	±10%$^{-day}$ total
OTT Pluvio^2/Precipitation	12–1,800 mm/h	±0.05 mm

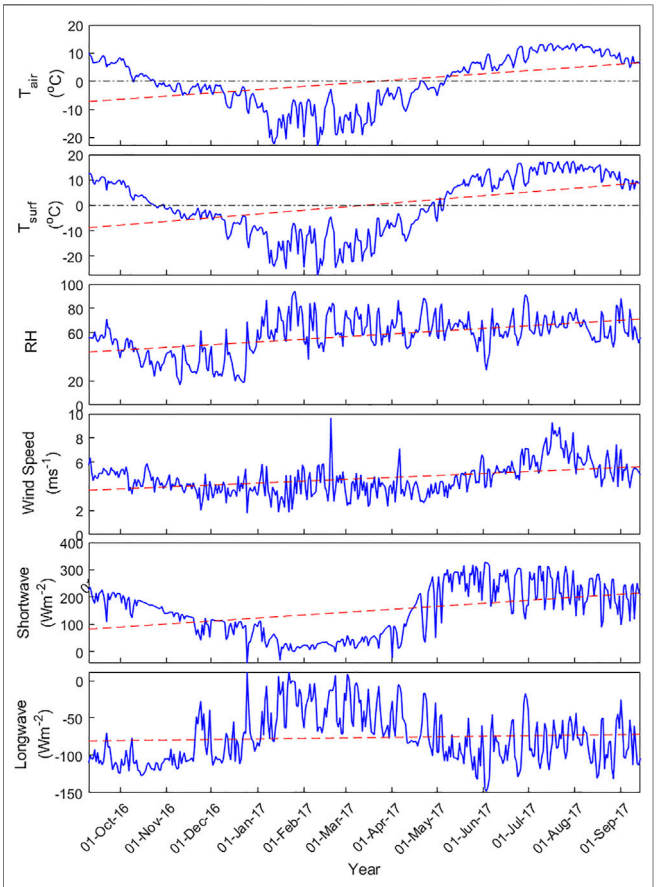

FIGURE 3 | Daily mean meteorological (temperature, RH, Wind speed, Surface temperature) and radiation (Longwave and shortwave) parameters at Himansh station AWS for 2016-17. The dotted red line indicates the trend for the selected parameters within the observation period.

throughout the ablation season (Patel et al., 2016; Sharma et al., 2016). The glacier melt rate was estimated using **Eq. 2**:

$$\frac{dh}{dt} = \frac{(h_{t1} - h_{t0})}{\Delta t} \quad (2)$$

Where h_{t0} and h_{t1} are the exposed stake lengths at different periods and dh/dt represents the melt rate for a particular location. The obtained melt rates were multiplied by an ice density of 900 kg/m^3 to obtain meters water equivalent (m.w.e.). Snow cover was not accounted for owing to its very limited impact in these debris-covered areas.

Meteorological Observations

Apart from the measurements made over debris-covered surfaces, Meteorological data were collected at the Himansh station (4,052 m asl) and over Sutri Dhaka Glacier (4,864 m asl) (**Figure 1**). The AWS of the Himansh station is installed over flat open ground (off-glacier) with NE aspect (**Figure 1**) while the Sutri Dhaka AWS is located over clean ice in the upper ablation zone of Sutri Dhaka Glacier. Thus the glacier ice surface temperature (T_{ice}) data was obtained from the AWS located above the glacier surface at Sutri Dhaka and all meteorological datasets were taken from the AWS located at Himansh station. The Himansh station is within 4 km of Batal and Kunzam Glaciers, and approximately 18 km from Bara Shigri Glacier (**Figure 1**). The AWSs were equipped with (Campbell Scientific CR 1000) dataloggers and precise sensors for continuously recording (10 min intervals) meteorological variables like air temperature, humidity, wind speed, wind direction, incoming and outgoing solar radiation, precipitation, and surface temperature. The detailed description and accuracy of the sensors are provided in **Table 2**. These meteorological datasets for the year 2016-17 were used to represent the atmospheric conditions and also for the statistical tests with air and debris surface temperature. **Figure 3** shows mean meteorological and radiation flux data for Himansh station AWS for 2016-17. The daily air temperature and surface temperature during 2016–17 fluctuated with maximum values of 14.4 and 18.7°C and a minimum values of –22.9 and –27.6°C with a mean of 2.1 and 3.1°C, respectively. Daily relative humidity varied from 16 to 94%, with a mean value of 59%. The daily mean wind speed varied between 3.4 and 9.6 ms^{-1} with a mean speed of 5.1 ms^{-1} during the study period. The net shortwave radiation varied from 42 to 322^{-2} Wm^{-2} with a mean of 181 Wm^{-2} for the study period. Net longwave radiation varied in summer months between –8.9 and –148 Wm^{-2}, with an overall mean of -84 Wm^{-2} for study the period. A simple regression (R^2) was carried out with the air temperature (T_{air}), debris surface temperature (T_s) at each site, ice-debris interface temperature (T_d), and bare ground temperature (T_{soil}) to analyze the significant heat source for the supraglacial debris pack. For this analysis, the T_{air} at each debris surface temperature site was determined by applying standard lapse rate (6.5°C/km) (**Supplementary Figure S2**) and T_{soil} was taken from the Himansh AWS data. Additionally Spearman's rank correlation cofficient (ρ) with Nash–Sutcliffe model efficiency coefficient (NSE) were also

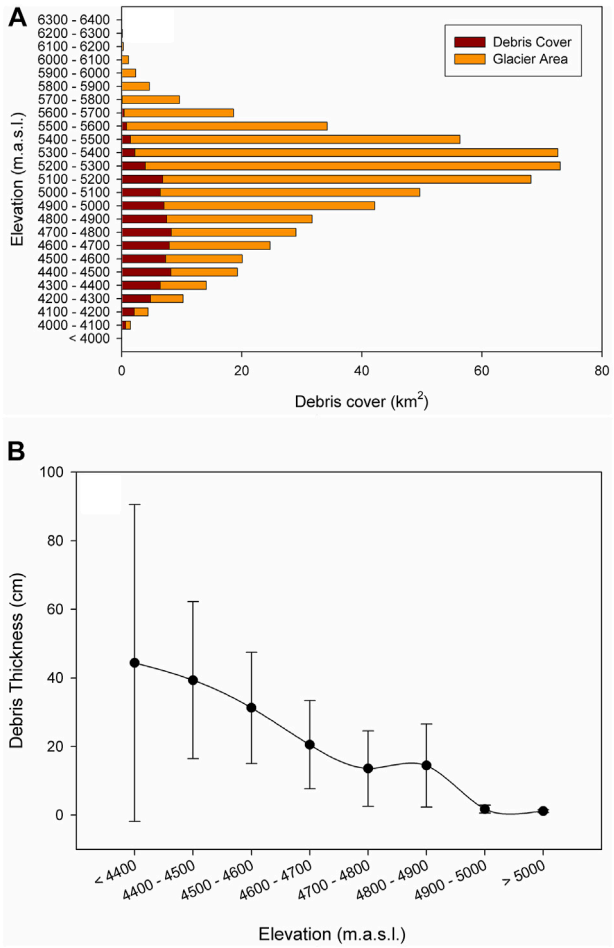

FIGURE 4 | Distribution of the debris cover over the Chandra basin glaciers. **(A)** Hypsometric distribution of debris covers and glacier area. The major debris-covered glacierized region located <5,200 m asl **(B)** the debris thickness (mean ± SD) versus the altitude. Higher debris thickness >20 cm observed <4,700 m asl while thin debris layer >4,700 m asl.

determined to assess the significance with these non parameteric datasets.

RESULTS

Debris Cover Extent, Thickness, and Geological Characteristics

The semi-automated analysis of Landsat 8 data showed that a significant area (~15% of glacier area) of the 129 glaciers from Chandra basin is debris-covered. Also, most of the debris-covered area (~13%) lies below 5,200 m asl and only a small fraction lies above 5,200 m asl (**Figures 1**, **4A**). Among the studied glaciers, 22.9% (26 km^2) of Bara Shigri Glacier is debris-covered while 39.5% (1.72 km^2) of Batal and 79.2% (0.38 km^2) of Kunzam Glaciers is debris-covered. However, the ablation area of these glaciers is almost 90% debris-covered (**Figure 1**). The field observations over the major glaciers of the Chandra basin showed that the lower ablation zone and area near to lateral moraines of these glaciers are covered by thick debris (~100 cm). The debris thickness over the Chandra basin glaciers was varying from 0.5 to 326 cm (**Figure 5** and **Supplementary Figure S1**). The mean debris thickness (mean ± STD) was 48.4 ± 27.4 cm for the region below 4,400 m asl, 46.4 ± 19.5 cm at 4,400–5,000 m asl, and 1.2 ± 0.4 cm above 5,000 m asl (**Figure 4B**). Debris thickness followed a similar trend (thicker debris being found at lower elevations) over all the studied glaciers. The Bara Shigri Glacier showed a range of 0.5–200 cm debris thickness with a mean debris thickness of 32 ± 30 cm. The Batal Glacier had a mean debris thickness of 25 ± 25 cm, varying from 5 to 100 cm, and the Kunzam Glacier had a mean debris thickness of 51 ± 25 cm varying from 5 to 163 cm. These measurements fitted well with the summary of the debris thickness provided by Rounce et al. (2021) for world wide glaciers.

The debris size over the glacier surfaces ranged from poorly sorted sand particles to large boulders, distributed throughout the surface and mainly concentrated along medial and lateral moraines. Based on the Unified Soil Classification System, USCS (ASTM D2487), the composition of the debris pack was similar in most locations. The surface of the debris pack was dominated by boulders, cobbles and gravels, while at the ice-debris interface zone coarse to fine sand was observed. There were much fewer large boulders and cobbles and fine sand at the higher altitudinal locations (TG2, TG5, DS 4, DS 5, and DS 7) (**Table 1**). Similar glacier composition (size) has been also reported for the Khumbu Glacier, Nepal Himalaya (Gibson et al., 2018). The debris samples collected from the glacier were a mixture of the different rocks and sediment. Details of the debris samples, thickness and rock types at various glaciers (including data logger points) are given at **Table 1**. Petrographic studies revealed that the major rock types of glacier debris are granite, sandstone, phyllite, and schist, whereas major minerals were quartz, alkali feldspar, plagioclase, mica, and clays.

Spatio-Temporal Variability in Surface Temperature of Debris

The summary of the debris surface temperature (T_s) is provided in the **Table 3**. The time series datasets of the debris surface temperature (T_s) including ice-surface temperature (T_{ice}) were compared to each other and also with the estimated T_{air} for each location (**Table 3**). The statistical correlation analysis and efficiency test results are presented in the **Table 4**. The Spearman rank correlation coefficient (r) values were <0.70 for all of the observation locations (including ice surface temperaure), while the Nash–Sutcliffe efficiency coefficient (E) was poor for most locations (**Table 4**). The statistical analysis highlighted the significant influence of similar weather over the debris surface temperature (T_s) including ice-surface temperature (T_{ice}). The ice-debris interface temperature (T_d) data is not included in the analysis due to the subzero (≤0°C) temperature conditions of this interface throughout the observation period.

The mean values for all the T_s was varying from −2.3 to −9.1°C while the mean T_{ice} was −12.3 ± 8.6°C (**Figure 6**).

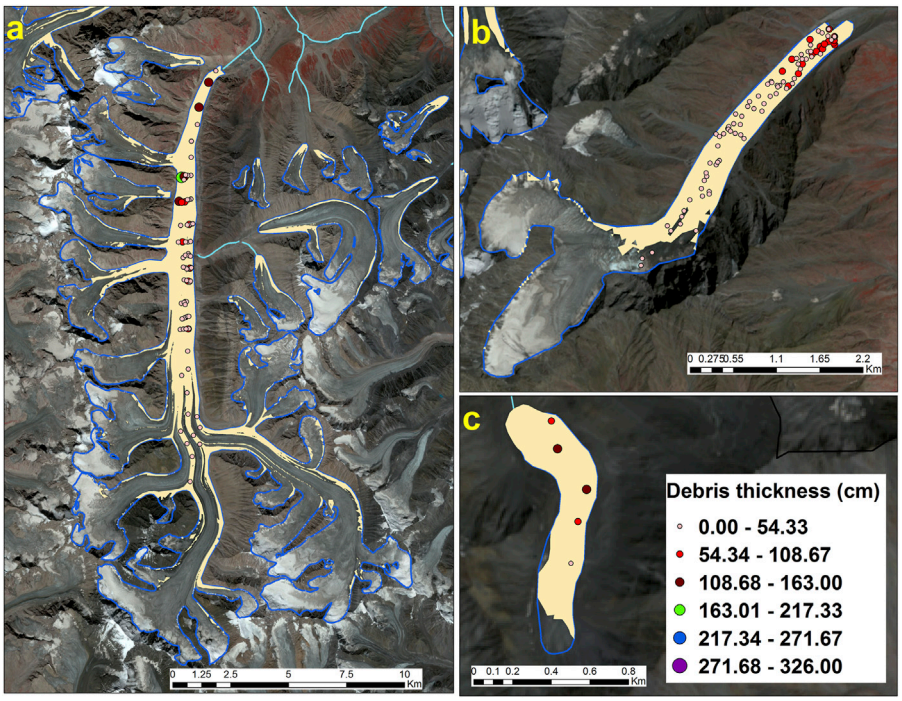

FIGURE 5 | Debris cover (yellow shade) and debris thickness (circles) over the Bara Shigri **(A)**, Batal **(B)** and Kunzam **(C)** glaciers, Chandra basin, Western Himalaya (Background satellite image: Sentinel 2B). The entire ablation zone (>75%) of the studied glaciers is covered with the debris and the thick debris over the lower ablation zone.

TABLE 3 | Spatial and seasonal debris surface temperature (T_s)variability at different altitudes of glaciers in Chandra basin, Western Himalaya.

Glacier sites	Altitude (m asl)	Debris surface temperature ˚C					
		Annual		Monsoon (JJAS)	Post monsoon (ON)	Winter (DJF)	Pre-monsoon (MAM)
Bara Shigri (TG 3)	4,100	Mean	0.2	8.7	0.9	−6.6	−2.6
		Std	6.7	3.0	3.7	2.2	3.6
Batal (TG 1)	4,300	Mean	0.9	11.3	−1.1	−7.3	−2.0
		Std	9.4	8.4	5.5	3.7	3.4
Bara Shigri (TG 5)	4,800	Mean	−4.9	0.3	−3.3	−8.4	−4.4
		Std	3.9	1.7	3.5	2.0	3.1
Kunzam (TG 2)	5,200	Mean	-6.7	0.0	−6.4	−12.2	−9.3
		Std	6.0	3.4	5.1	2.5	0.4

TABLE 4 | The Spearman rank correlation coefficient (r) and Nash–Sutcliffe efficiency coefficient (E) matrix for each observation location (half hourly raw data) debris surface temperature and Ice surface temperature (4,700 m asl) timeseries.

		Spearman rank correlation coefficient (r)				
Nash– Sutcliffe efficiency coefficient (E)	ID	4,100	4,300	4,700	4,800	5,200
	4,100	**1.00**	0.90	0.73	0.93	0.87
	4,300	*0.51*	**1.00**	0.78	0.95	0.90
	4,700	*0.54*	0.93	**1.00**	0.78	0.71
	4,800	*0.48*	*0.48*	*0.16*	**1.00**	0.90
	5,200	*−1.09*	*−0.40*	*0.60*	0.98	**1.00**

Sometimes T_s values were found below 0˚C due to snow cover over (winter season) debris. The maximum T_s was 25.5˚C at 4,300 m asl while the minimum T_s was – 19.3˚C at 5,200 m asl. The maximum T_{ice} was within the theoretical limit (0˚C) of ice surface temperature. The high correlation between all the T_s timeseries datasets highlighted the high periodic and seasonal

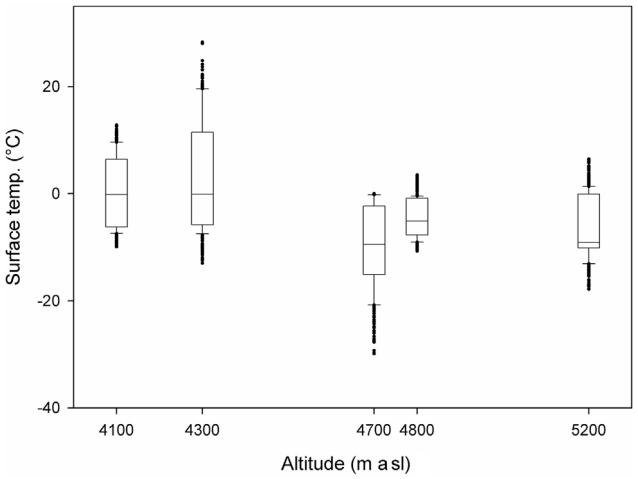

FIGURE 6 | The box plot distribution and variability for the surface temperature data collected at selected altitudinal debris cover locations of the studied glaciers (Bara Shigri, Batal, and Kunzam) and ice surface temperature (4,700 m asl) from the Sutri Dhaka Glacier.

similarity (**Table 4**) which is depicted in **Figures 7A,B**. The highest mean T_s (0.9 ± 9.4°C) was observed at 4,100 m asl (TG 3; Bara shigri) followed by 4,300 m asl (TG 1; Batal) (0.2 ± 6.7°C), 4,800 m asl (TG 5; Bara Shigri) (−4.8 ± 3.9°C), and 5,200 m asl (TG 2; Kunzam) (−6.7 ± 6.0°C), respectively (**Figure 7** and **Table 3**).

During the ablation season (May – September) the mean T_s at 4,300 m asl and 4,100 m asl were above 0°C while mean T_s was below 0°C at 5,200 and 4,800 m asl. However, the mean T_s during the accumulation season (October - April) at each location were below 0°C (**Figure 7**). The datasets were were further analyzed for summer monsoon (JJAS), post-monsoon (ON), winter (DJF), and pre-monsoon (MAM) periods. The highest mean T_s was 11.3°C during the summer monsoon while the lowest mean T_s was −12.2°C during the winter season (**Table 3**). The spatial and temporal variability were observed at all locations for the summer monsoon. Specifically during summer monsoon, the mean T_s for 4,300 and 4,100 m asl was above 0°C during both day and night, while at 4,800 and 5,200 m asl it was above 0°C during days and below 0°C during nights (**Table 3**; **Figures 7A,B**). We examined the collected T_s data collected from different sites to estimate the total duration with positive T_s to determine the ablation period. Results show that positive daily mean T_s were at a maximum at 4,100 m asl (180 days), followed by 4,300 m asl (175 days), 4,800 m asl (116 days), and 5,200 m asl (73 days) during the entire observation period.

Figure 7 shows the diurnal variability in T_s for annual, ablation, and accumulation periods. The ablation (July-September) and accumulation (October-may) periods were defined based on the reported observations for western Himalaya (Bhutiyani 2007). The data revealed that the debris pack was warm during the daytime (6:00 to 18:00 h) and the major T_s variability was recorded between 12:00 to

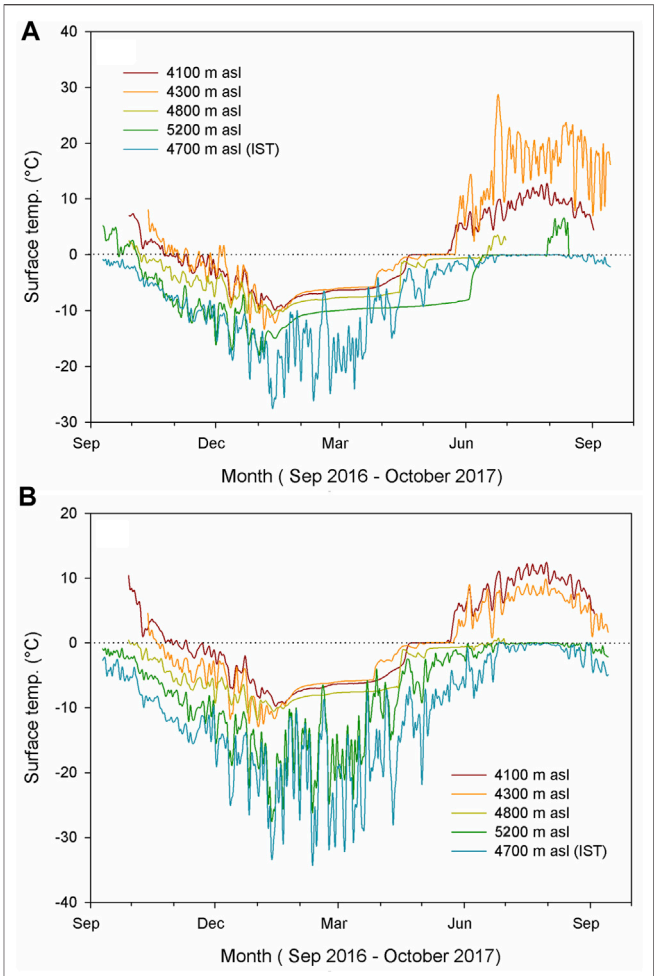

FIGURE 7 | The temporal and spatial variability of the daily mean debris surface temperature and ice surface temperature (IST) during **(A)** the day and **(B)** night at the selected locations of the Chandra basin, Western Himalaya. The daily mean day and night temperature over the debris covered location was >0°C from June to October months.

18:00 h at all the locations (**Figure 8A**). During the ablation season the T_s at 4,300 and 4,100 m asl were above 0°C throughout the day and night. However, at 4,800, and 5,200 m asl, and at the ice surface (4,700 m asl) the average T_s was close to 0°C only during the daytime. During the ablation season, the higher average T_s was 6.9 ± 1.7°C at 4,100 m asl. For the accumulation season, the average T_s at all locations was <0°C and the lowest was recorded at 5,200 m asl (**Figure 8C**).

Further analysis was undertaken to understand the relationship between surface and subsurface temperature variability at Batal Glacier. The results showed a linear reduction in the temperature from T_s (12.1 ± 7.6°C) to subsurface temperature (T_{sub}: 7.2 ± 2.8°C) that was measured at 30 cm below the surface (**Figure 9A**). T_s showed a significant correlation (r = 0.60; n = 89; p = < 0.05) with the T_{sub}. The diurnal results showed the maximum difference in T_s and T_{sub} temperature (~10.0°C) during daytime (06:00 to 18:00).

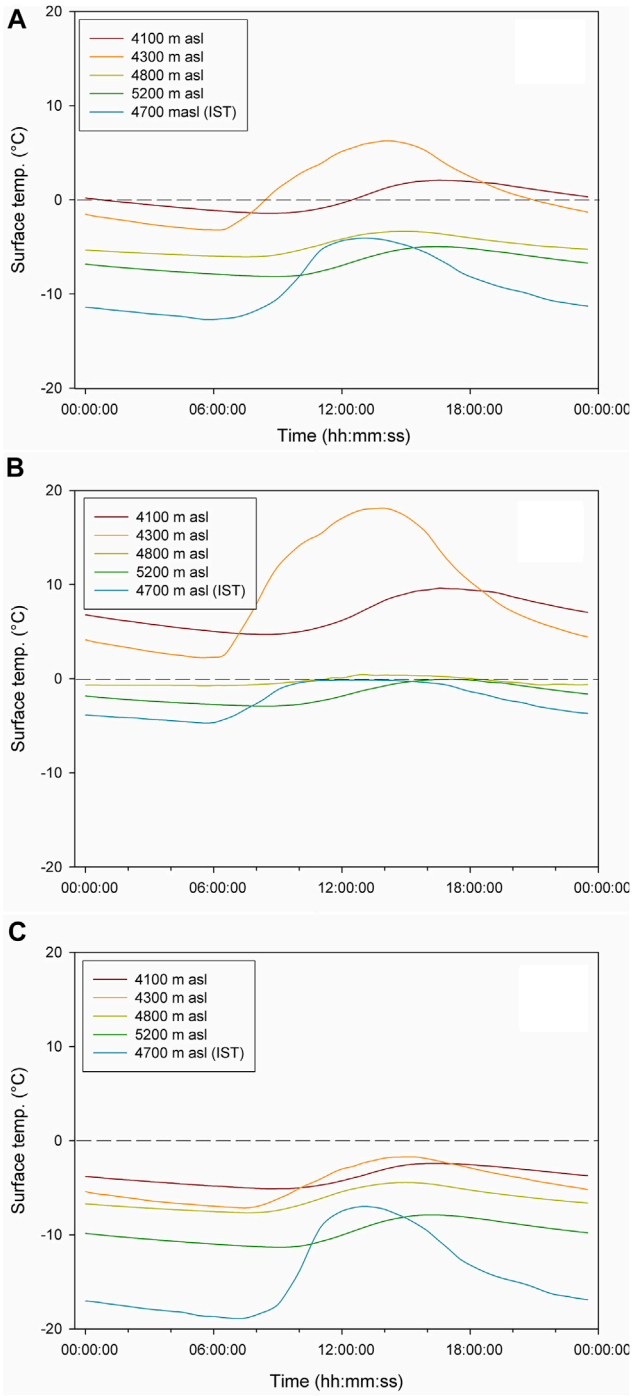

FIGURE 8 | Diurnal variability for the debris surface temperature during **(A)** annual **(B)** ablation, and **(C)** accumulation periods in Chandra basin, Western Himalaya. The mean debris surface temperature was >0°C throughout the ablation months and the peaks were observed between 12:00–16:00 Hrs.

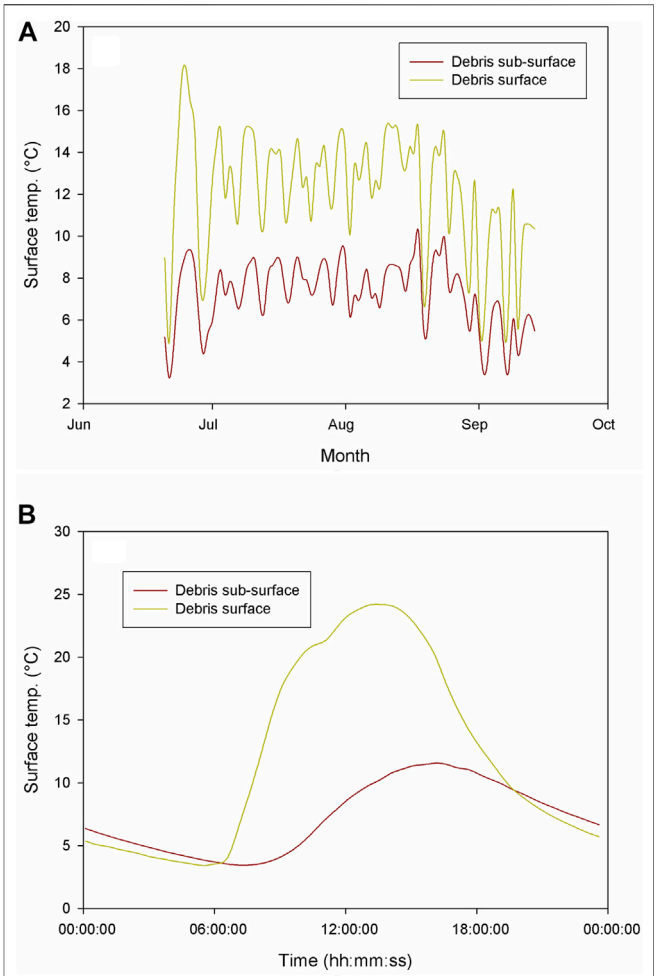

FIGURE 9 | Debris surface and subsurface temperature variability at the Batal Glacier (4,300 m asl), during **(A)** ablation season and **(B)** diurnal variability. There was a linear trend with the surface and sub surface temperature, and the surface temperature was higher during day time while subsurface was higher during nights.

However, during night, the temperature difference between the T_s and T_{sub} debris layers were comparatively negligible (0.41°C) (**Figure 9B**).

Data from the ablation stakes showed a higher cumulative loss (−8.3 m we) over the clean ice surface (4,700 m asl) during the observational period (2016-17). Among the debris covered locations, 4,300 m asl has showed the highest loss (−1.8 m we), followed by 4,800 m asl (−1.3 m we), 4,100 m asl (−1.2 m we), and 5,200 m asl (−0.6 m we) during 2016–17 (**Figure 10A**). The melt rate at Batal (4,300 m asl) and Kunzam (5,200 m asl) were 0.46 cm/day and 0.18 cm/day respectively. However, the melt rates at other selected locations (Bara Shigri) were within 0.37–0.39 cm/day (**Figure 10B**). The altitudinal variation and debris thickness were the major factors for the observed difference in the melt rates.

The estimated annual thermal resistance R_{avg} was highest (0.55 ± 0.1 $m^2°CW^{-1}$) at 4,100 m asl (Bara Shigri) and lowest R_{avg} (0.009 ± 0.01 $m^2°CW^{-1}$) was at 5,200 m asl (Kunzam; **Figure 11**). Similar variability was observed during the ablation and accumulation seasons, high (0.42 ± −0.28; 0.53 ± 0.3 $m^2°CW^{-1}$) at 4,100 m asl and low (0.002 ± 0.01; 0.006 ±

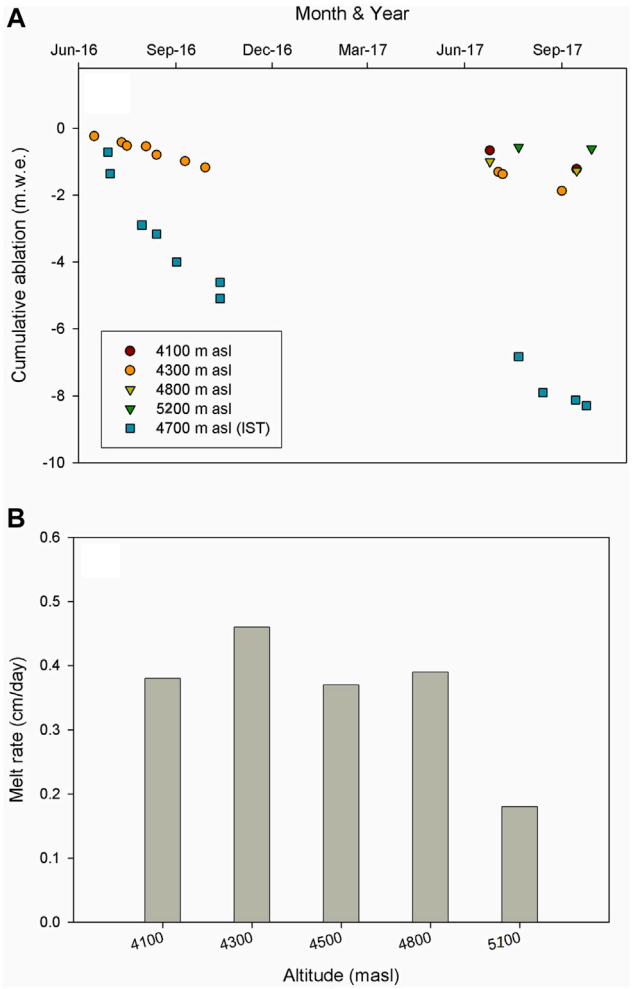

FIGURE 10 | Cumulative ablation **(A)** and melt rates **(B)** during 2016-17 at different altitudes of the selected locations of glaciers in Chandra basin, Western Himalaya. The highest ablation was observed at the 4,700 m asl while lowest ablation at 5,200 m asl. However the melt rate at the debris covered location, at 4,300 m asl it was higher and lower at 5,200 m asl.

0.02 $m^2°CW^{-1}$) at 5,200 m asl. The obtained datasets were close to the reported thermal resistance values for glaciers of the Nepal and Bhutan Himalaya (Suzuki et al., 2007; Zhang et al., 2011; Foster et al., 2012; Rounce et al., 2015). During the ablation season (June to October), a linear trend in the R_{avg} was observed as per the increasing altitude. The observations showed the highest values (0.42 ± 0.28 $m^2°CW^{-1}$) at 4,100 m asl, where R_{avg}varied from 1.13 to −0.004 $m^2°CW^{-1}$ (**Table 5** and **Supplementary Figure S3**). The lowest R_{avg} was observed at 5,200 m asl (0.002 ± 0.01 $m^2°CW^{-1}$), with a range from 0.01 to −0.01 $m^2°CW^{-1}$ (**Table 5**; **Figure 11**, and **supplementary Figure S3**). At 4,100 m asl, for a day (24 h) the R_{avg} was 0.42 ± 0.11 $m^2°CW^{-1}$, with a range from 0.59 to 0.27 $m^2°CW^{-1}$. In day time (6:00 am - 6:00 pm) the R_{avg} was 0.40 ± 0.13 $m^2°CW^{-1}$, with a range from 0.60 to 0.27 $m^2°CW^{-1}$, while during night time the R_{avg} was 0.43 ± 0.09 $m^2°CW^{-1}$, with a range from 0.59 to 0.29 $m^2°CW^{-1}$.

DISCUSSION

The glacier mapping revealed that the ablation zones of most glaciers in the Chandra basin are debris-covered, and more extensively over the lower part of the ablation zones. The large debris-covered area over the ablation zones compared to the accumulation zones indicated the glacial transportation (englacial, subglacial, and supraglacial) of rocks and sediment from the higher to the lower zones, melting and glacial erosion, and hillslope processes (Banerjee and Wani, 2018). Some of the satellite observations have reported increasing debris cover over the Chandra basin glaciers and reported increasing glacier retreat as the major factor (Gaddam et al., 2016; Pratibha and Kulkarni, 2018). The increasing debris cover has also been reported for the Bhaga and Baspa river basins of the Western Himalaya (Pratibha and Kulkarni, 2018; Das and Sharma, 2019). The compositon (boulders, cobbels, gravels, and coarse to fine sand matrix) of the debris pack was also similar as per the increasing altitude for the all of the studied glacier. The debris over the Batal and Kunzam glaciers is dominantly composed of sandstone, while in Bara Shigari, only the lower portion (<4,500 m asl) is majorily dominated by sandstone while the upper portion (<5,000 m asl) is more variable, comprising quartz, biotite and schist. The major sources for the debris over the glacier catchments are rockfall and avalanche deposits from the mountain sides and physical weathering is the dominant process for the evolution of supraglacial debris (Banerjee and Shankar, 2013). This was also confirmed with the lithological analysis, where, the lithology of the debris material was found to be similar to the lithology of the surrounding mountains (Singh et al., 2017). The debris thickness and extent over the glacier surfaces are increasing annually which has shown to have potential control over the ablation rate over the glaciers. Some studies have also reported that the >50 cm thick debris

TABLE 5 | The interrelation between the altitude, thermal resistance, melt rate and debris thickness duing the ablation season (June–October).

Altitude (m asl)	Thermal resistance				Melt rate (cm/day)	Debris thickness (cm)
	Average	STD	Max	Min		
4,100	0.425	0.281	1.133	−0.004	0.38	100
4,300	0.017	0.023	0.092	−0.001	0.46	60
4,800	−0.020	0.076	0.191	−0.164	0.39	5
5,200	−0.002	0.008	0.015	−0.014	0.18	70

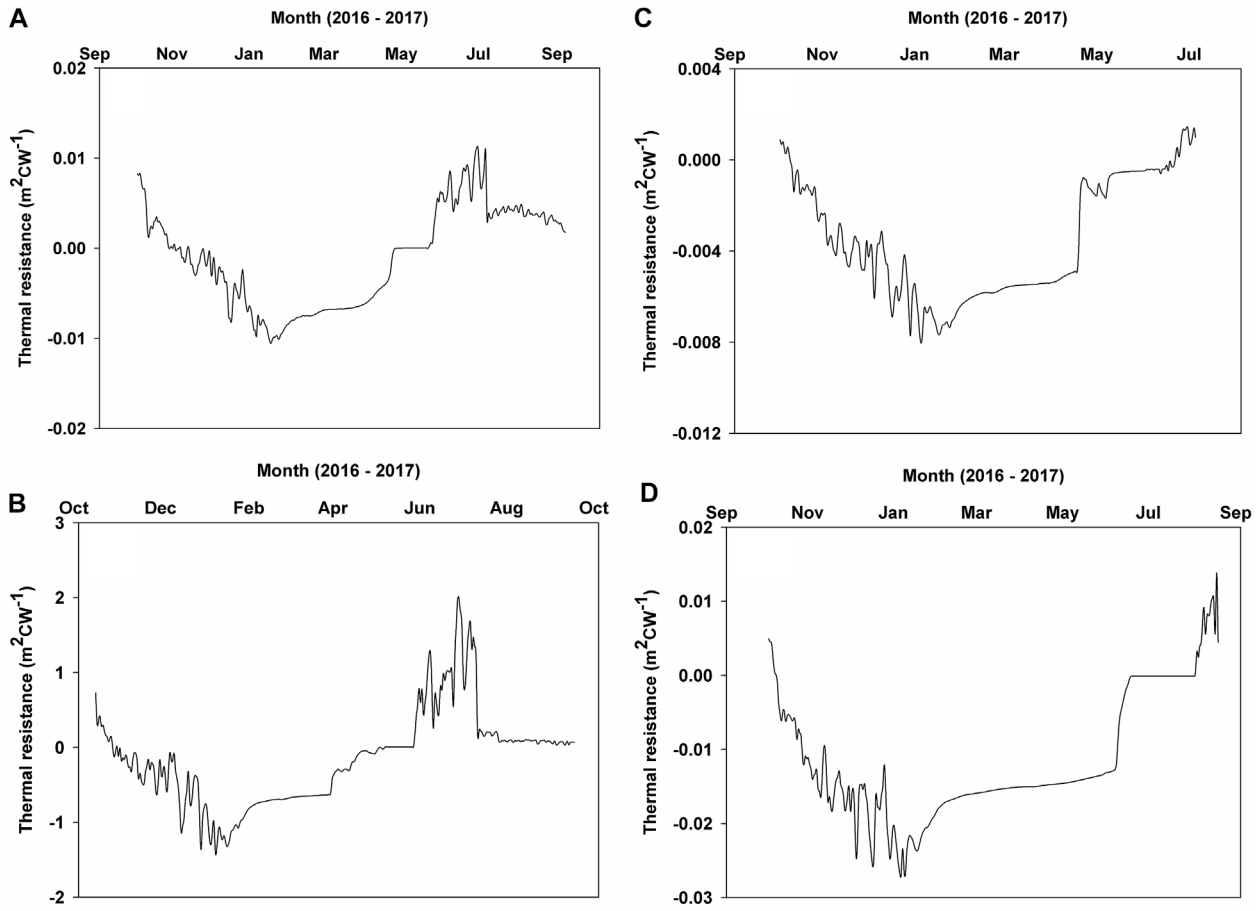

FIGURE 11 | Annual spatial variability of thermal resistance over the debris-covered glaciers of Chandra basin during ablation season [4,100 m asl: TG 3 **(A)**, 4,300 m asl: TG 1 **(B)**, 4,800 m asl: TG 4 **(C)**, and 5,200 m asl: TG 2 **(D)**].

can reduce the ablation by nearly 10 times compared to the clean glaciers in Chandra basin (Patel et al., 2016).

Factors Controlling the Debris Surface Temperature Over Glaciers

In the T_s data, seasonal and diurnal patterns were recognized at all observation locations during 2016-17. Seasonally, the T_s was higher during the initial period of the ablation season, and after mid-August, it started to decline. Diurnally, day time highest mean temperature (≥ 4.3°C) was observed between 12:00 pm to 3:00 pm, thereafter the T_s started dropping. During the observation period, the T_s data have showed higher positive temperature days at 4,100 m asl (180 days), followed by 4,300 m asl (175 days), 4,800 m asl (116 days), and 5,200 m asl (73 days). The reason for these fluctuations at different locations is most likely due to the differences in altitudes. Studies at the Everest region and specifically at Kumbhu Glacier, Nepal Himalaya have also reported a similar diurnal pattern, however, seasonally the dropping T_s has been reported after the end of June (Gibson et al., 2018; Rowan et al., 2020).

The temperature datasets (T_s, T_{air}, T_{soil}, and T_d) showed a similar trend for the entire observation period. The mean T_s was comparatively higher than the mean T_{air} and the significant correlation (r = 0.88; 0.84; 0.81; and 0.80 respectively; p = <0.05) with the debris surface temperature (T_s) of all observation sites revealed the strong connection between debris surface and air temperatures. Additionally, a significant correlation (r = 0.83; p = 0.05) between outgoing longwave radiation (L_{up}) and T_{air} supported such observations. Several studies from the Nepal Himalaya have also reported the strong control of surface temperature on air temperature variability (Foster et al., 2012; Steiner and Pellicciotti, 2016). The high correlation [Pearson (r = >0.8; p = <0.05) and Spearman rank (**Table 4**)] obtained between T_s of all locations highlighted the major control of the solar insolation on air temperature and debris surface temperature. The high correlation of daily surface temperature with all observation locations revealed the region is influenced by similar meteorological conditions. In the diurnal

data, most of T_s observation locations showed high correlation (r = >0.8; p = <0.05), but some locations showed comparatively low correlation (<0.60; p = <0.05). The low correlation in some locations highlighted the influence of local weather and topographic (aspect, shadow) conditions.

At the Batal Glacier, the linear reduction in the T_{sub} and a significant correlation between T_s and T_{sub}(r = 0.60; p = <0.05) highlights the decreasing amplitude in T_s. The observation showed a linear trend for the surface temperature with a lag time of 3–4 h to warm the debris surface below 30 cm (**Figure 9B**). The heat conduction from the surface to debris has time lags (Nicholson and Benn, 2006), which will also depend on the debris subsurface conditions. The debris subsurface conditions like moisture content, pores, and lithology play a significant role in the energy transmission and maintaining the temperature and heat conduction into the debris pack (Collier et al., 2014; Evatt et al., 2015).

The surface temperature datasets for the studied debris-covered glaciers indicated that the incoming solar radiation warms the debris surface and regulates the heat flow. The main insolation period for the debris surface warming is ablation season, especially the summer monsoon (JJAS), where the daytime (6:00 to 18:00 h) is the contributor to increasing debris surface temperature. It was also observed that the thinner debris at higher altitudes experiences enhanced warming, thus increasing the ice melt rate. Although the thicker debris surface at lower elevations is warmer, the ice beneath it undergoes less ablation.

Relationship Between Supraglacial Debris and Thermal Resistance

The measured R_{avg} data showed a decreasing trend with decreasing debris thickness over all of the studied locations (**Table 5**; **Supplementry Figure S3**). The thermal resistance reduced with decreasing debris thickness and increasing altitude. Such a trend was also observed in the melt rate, which was higher beneath thin debris (**Table 5**). Zhang et al. (2011) reported similar results of low thermal resistance for thin debris and high thermal resistance for thick debris at southeastern Tibetan Plateau. A comparison during the 2017 ablation season highlighted that R_{avg} was higher at 4,100 m asl than it was at 4,800 m asl. In our study, at 4,300 m asl R_{avg} was lower than at 4,100 m asl, due to lower debris thickness and higher melt (**Table 5**, and **Supplementry Figure S3**). During the ablation season, the thermal resistance showed a significant correlation (r = > 0.70; p =< 0.5) for most of the observation sites. The spatial and seasonal variability found in the coefficient of determination for daily R_{avg} highlighted the impact of the thickness and moisture content of the supraglacial debris pack. Our study highlights the strong control of debris thickness in defining the thermal resistance of supraglacial debris. Further, the higher thermal resistance of the thick supraglacial debris is found to attenuate the heat flow from debris surface to ice thus reducing the ablation.

CONCLUSION

In this study, *in-situ* observations of supraglacial debris cover, its thickness and thermal properties were carried out over three major debris-covered glaciers of the Chandra basin in Western Himalaya during 2016-2017. An extensive debris cover over the lower ablation zone highlighted the glacial transportation processes and observed lithology of the debris samples marked the major debris sources from surrounding mountains. The debris surface temperature data showed that significant warming of surface debris occurs during the ablation period (June to September). Observed debris surface temperature (T_s) showed a decreasing trend with altitude, and a linear relationship with sub-surface temperature. Our observations highlighted the inverse relationship of melt rate with altitude and debris thickness. The variable correlations (daily and diurnal) between the T_s of each observational site revealed a significant control of local meteorology on debris surface warming. The high thermal resistance (R_{avg}) over the thick debris and lower R_{avg} at thin debris highlighted the efficient control of debris thickness on the downward heat flow from the surface to the ice interface. Our study provides the first detailed characterization of supraglacial debris over glaciers of Chandra basin, which revealed that the thick supraglacial debris cover effectively controls the ablation to the glacier ice due to its high thermal resistivity. The study provides a record of debris thickness and surface temperature observations, which can be useful for debris thickness modelling and analysing the metereological control on the debris covered glaciers of HKH region.

DATA AVAILABILITY STATEMENT

The datasets presented in this study can be found in online repositories. The names of the repository/repositories and accession number(s) can be found below: https://pdc.ncpor.res.in/himalaya/DebrisSurfaceTempData_ChandraBasin.xls.

AUTHOR CONTRIBUTIONS

LKP, PS, and MT devised the study. LKP, PS, and AS conducted the field survey for thermal data logger installation, temperature data collection, mass balance, debris thickness measurement, and debris sampling for the study. LKP analyzed the datasets and wrote the initial draft. SO has helped in the processing of the surface temperature and meteorological datasets. LKP, PS, BP, and MT contributed to finalizing the manuscript. All authors contributed to the data interpretation and discussion of the manuscript.

FUNDING

This work is funded under the Project PACER - Cryosphere and Climate by the Ministry of Earth Sciences (MoES), Government of India.

ACKNOWLEDGMENTS

We are thankful to the Director, National Centre for Polar and Ocean Research (NCPOR) for his support. Raghuram (Senior Geologist, Geological Survey of India) is gratefully acknowledged for analyzing the lithology and mineralogy of the collected debris samples. The U. S. Geological Survey (USGS) is acknowledged for the Landsat 8 data and ASTER GDEM V2 digital elevation model. The help and support provided by the logistic support personnel at the Himansh Station are duly acknowledged. This is the NCPOR contribution no. J-60/2021-22.

SUPPLEMENTARY MATERIAL

The Supplementary Material for this article can be found online at: https://www.frontiersin.org/articles/10.3389/feart.2021.706312/full#supplementary-material

Supplementary Figure S1 | The debris cover and thickness of the additional glaciers **(A)** SamudraTapu, **(B)** Sutri Dhaka, and **(C)** Gepang Gath from Chandra basin, Western Himalaya.

Supplementary Figure S2 | The estimated mean air temperature at the selected altitudinal observation sites over the debris-covered glaciers.

Supplementary Figure S3 | The inter-relationship between Thermal resistances, debris thickness, and melt rate during ablation season of 2016-2017 observation periods.

REFERENCES

Alifu, H., Tateishi, R., and Johnson, B. (2015). A New Band Ratio Technique for Mapping Debris-Covered Glaciers Using Landsat Imagery and a Digital Elevation Model. *Int. J. Remote Sensing* 36 (8), 2063–2075. doi:10.1080/2150704X.2015.1034886

Banerjee, A., and Shankar, R. (2013). On the Response of Himalayan Glaciers to Climate Change. *J. Glaciol.* 59 (215), 480–490. doi:10.3189/2013JoG12J130

Banerjee, A., and Wani, B. A. (2018). Exponentially Decreasing Erosion Rates Protect the High-Elevation Crests of the Himalaya. *Earth Planet. Sci. Lett.* 497, 22–28. doi:10.1016/j.epsl.2018.06.001

Benn, D. I., Bolch, T., Hands, K., Gulley, J., Luckman, A., Nicholson, L. I., et al. (2012). Response of Debris-Covered Glaciers in the Mount Everest Region to Recent Warming, and Implications for Outburst Flood Hazards. *Earth-Science Rev.* 114 (1), 156–174. doi:10.1016/j.earscirev.2012.03.008

Bhutiyani, M. R., Kale, V. S., and Pawar, N. J. (2007). Long-term Trends in Maximum, Minimum and Mean Annual Air Temperatures across the Northwestern Himalaya during the Twentieth century. *Climatic Change* 85, 159–177. doi:10.1007/s10584-006-9196-1

Bolch, T., Kulkarni, A., Kääb, A., Huggel, C., Paul, F., Cogley, J. G., et al. (2012). The State and Fate of Himalayan Glaciers. *Science* 336 (6079), 310–314. doi:10.1126/science.1215828

Bookhagen, B., and Burbank, D. W. (2006). Topography, Relief, and TRMM-Derived Rainfall Variations along the Himalaya. *Geophys. Res. Lett.* 33 (8), 1–5. doi:10.1029/2006GL026037

Brock, B. W., Mihalcea, C., Kirkbride, M. P., Diolaiuti, G., Cutler, M. E. J., and Smiraglia, C. (2010). Meteorology and Surface Energy Fluxes in the 2005-2007 Ablation Seasons at the Miage Debris-Covered Glacier, Mont Blanc Massif, Italian Alps. *J. Geophys. Res.* 115 (D9), 1–16. doi:10.1029/2009JD013224

Buri, P., Miles, E. S., Steiner, J. F., Immerzeel, W. W., Wagnon, P., and Pellicciotti, F. (2016). A Physically Based 3-D Model of Ice Cliff Evolution over Debris-covered Glaciers. *J. Geophys. Res. Earth Surf.* 121 (12), 2471–2493. doi:10.1002/2016JF004039

Chand, P., and Sharma, M. C. (2015). Glacier Changes in the Ravi basin, North-Western Himalaya (India) during the Last Four Decades (1971-2010/13). *Glob. Planet. Change* 135, 133–147. doi:10.1016/j.gloplacha.2015.10.013

Collier, E., Maussion, F., Nicholson, L. I., Mölg, T., Immerzeel, W. W., and Bush, A. B. G. (2015). Impact of Debris Cover on Glacier Ablation and Atmosphere-Glacier Feedbacks in the Karakoram. *The Cryosphere* 9 (4), 1617–1632. doi:10.5194/tc-9-1617-2015

Collier, E., Nicholson, L. I., Brock, B. W., Maussion, F., Essery, R., and Bush, A. B. G. (2014). Representing Moisture Fluxes and Phase Changes in Glacier Debris Cover Using a Reservoir Approach. *The Cryosphere* 8 (4), 1429–1444. doi:10.5194/tc-8-1429-2014

Cuffey, K. M., and Paterson, W. S. B. (2010). *The Physics of Glaciers*. Cambridge, Massachusetts: Academic Press.

Das, S., and Sharma, M. C. (2019). Glacier Changes between 1971 and 2016 in the Jankar Chhu Watershed, Lahaul Himalaya, India. *J. Glaciol.* 65 (249), 13–28. doi:10.1017/jog.2018.77

Evatt, G. W., Abrahams, I. D., Heil, M., Mayer, C., Kingslake, J., Mitchell, S. L., et al. (2015). Glacial Melt under a Porous Debris Layer. *J. Glaciol.* 61 (229), 825–836. doi:10.3189/2015JoG14J235

Foster, L. A., Brock, B. W., Cutler, M. E. J., and Diotri, F. (2012). A Physically Based Method for Estimating Supraglacial Debris Thickness from thermal Band Remote-Sensing Data. *J. Glaciol.* 58 (210), 677–691. doi:10.3189/2012JoG11J194

Fyffe, C. L., Reid, T. D., Brock, B. W., Kirkbride, M. P., Diolaiuti, G., Smiraglia, C., et al. (2014). A Distributed Energy-Balance Melt Model of an alpine Debris-Covered Glacier. *J. Glaciol.* 60 (221), 587–602. doi:10.3189/2014JoG13J148

Gaddam, V. K., Sharma, P., Patel, L. K., Thamban, M., and Singh, A. (2016). "Spatio-temporal Changes Observed in Supra-glacial Debris Cover in Chenab Basins, Western Himalaya," in *Remote Sensing of the Oceans and Inland Waters: Techniques, Applications, and Challenges* (Bellingham, Washington, United States: International Society for Optics and Photonics), 98781F. doi:10.1117/12.2227993

Gibson, M. J., Irvine-Fynn, T. D. L., Wagnon, P., Rowan, A. V., Quincey, D. J., Homer, R., et al. (2018). Variations in Near-Surface Debris Temperature through the Summer Monsoon on Khumbu Glacier, Nepal Himalaya. *Earth Surf. Process. Landforms* 43, 2698–2714. doi:10.1002/esp.4425

Haidong, H., Yongjing, D., and Shiyin, L. (2006). A Simple Model to Estimate Ice Ablation under a Thick Debris Layer. *J. Glaciol.* 52 (179), 528–536. doi:10.3189/172756506781828395

Juen, M., Mayer, C., Lambrecht, A., Wirbel, A., Kueppers, U., Lambrecht, A., et al. (2013). Thermal Properties of a Supraglacial Debris Layer with Respect to Lithology and Grain size. A Comparison of Glacier Melt on Debris-Covered Glaciers in the Northern and Southern Caucasus. *Geografiska Annaler: Ser. A, Phys. Geography. Cryosphere* 955 (3), 197525–209538. doi:10.5194/tc-5-525-2011

Lejeune, Y., Bertrand, J.-M., Wagnon, P., and Morin, S. (2013). A Physically Based Model of the Year-Round Surface Energy and Mass Balance of Debris-Covered Glaciers. *J. Glaciol.* 59 (214), 327–344. doi:10.3189/2013JoG12J149

Mihalcea, C., Mayer, C., Diolaiuti, G., Lambrecht, A., Smiraglia, C., and Tartari, G. (2006). Ice Ablation and Meteorological Conditions on the Debris-Covered Area of Baltoro Glacier, Karakoram, Pakistan. *Ann. Glaciol.* 43, 292–300. doi:10.3189/172756406781812104

Muhammad, S., Tian, L., Ali, S., Latif, Y., Wazir, M. A., Goheer, M. A., et al. (2020). Thin Debris Layers Do Not Enhance Melting of the Karakoram Glaciers. *Sci. Total Environ.* 746, 141119. doi:10.1016/j.scitotenv.2020.141119

Nakawo, M., and Takahashi, S. (1982). *A Simplified Model for Estimating Glacier Ablation under a Debris Layer*. United Kingdom: International Association of Hydrological Sciences.

Nakawo, M., and Young, G. J. (1982). Estimate of Glacier Ablation under a Debris Layer from Surface Temperature and Meteorological Variables. *J. Glaciol.* 28 (98), 29–34. doi:10.3189/S002214300001176X

Nakawo, M., and Young, G. J. (1981). Field Experiments to Determine the Effect of a Debris Layer on Ablation of Glacier Ice. *Ann. Glaciol.* 2, 85–91. doi:10.3189/172756481794352432

Nicholson, L., and Benn, D. I. (2006). Calculating Ice Melt beneath a Debris Layer Using Meteorological Data. *J. Glaciol.* 52 (178), 463–470. doi:10.3189/172756506781828584

Nicholson, L., and Benn, D. I. (2013). Properties of Natural Supraglacial Debris in Relation to Modelling Sub-debris Ice Ablation. *Earth Surf. Process. Landforms* 38 (5), 490–501. doi:10.1002/esp.3299

Nicholson, L. I., McCarthy, M., Pritchard, H. D., and Willis, I. (2018). Supraglacial Debris Thickness Variability: Impact on Ablation and Relation to Terrain Properties. *The Cryosphere* 12 (12), 3719–3734. doi:10.5194/tc-12-3719-2018

Patel, L. K., Sharma, P., Laluraj, C. M., Thamban, M., Singh, A., and Ravindra, R. (2017). A Geospatial Analysis of Samudra Tapu and Gepang Gath Glacial Lakes in the Chandra Basin, Western Himalaya. *Nat. Hazards* 86 (3), 1275–1290. doi:10.1007/s11069-017-2743-4

Patel, L. K., Sharma, P., Thamban, M., Singh, A., and Ravindra, R. (2016). Debris Control on Glacier Thinning-A Case Study of the Batal Glacier, Chandra basin, Western Himalaya. *Arab J. Geosci.* 9 (4), 309. doi:10.1007/s12517-016-2362-5

Pellicciotti, F., Stephan, C., Miles, E., Herreid, S., Immerzeel, W. W., and Bolch, T. (2015). Mass-balance Changes of the Debris-Covered Glaciers in the Langtang Himal, Nepal, from 1974 to 1999. *J. Glaciol.* 61 (226), 373–386. doi:10.3189/2015JoG13J237

Pratap, B., Dobhal, D. P., Mehta, M., and Bhambri, R. (2015). Influence of Debris Cover and Altitude on Glacier Surface Melting: a Case Study on Dokriani Glacier, central Himalaya, India. *Ann. Glaciol.* 56 (70), 9–16. doi:10.3189/2015AoG70A971

Pratibha, S., and Kulkarni, A. V. (2018). Decadal Change in Supraglacial Debris Cover in Baspa basin, Western Himalaya. *Curr. Sci.* 114 (4), 792. doi:10.18520/cs/v114/i04/792-799

Reid, T. D., and Brock, B. W. (2014). Assessing Ice-Cliff Backwasting and its Contribution to Total Ablation of Debris-Covered Miage Glacier, Mont Blanc Massif, Italy. *J. Glaciol.* 60 (219), 3–13. doi:10.3189/2014JoG13J045

Röhl, K. (2008). Characteristics and Evolution of Supraglacial Ponds on Debris-Covered Tasman Glacier, New Zealand. *J. Glaciol.* 54 (188), 867–880. doi:10.3189/002214308787779861

Rounce, D. R., Hock, R., McNabb, R. W., Millan, R., Sommer, C., Braun, M. H., et al. (2021). Distributed Global Debris Thickness Estimates Reveal Debris Significantly Impacts Glacier Mass Balance. *Geophys. Res. Lett.* 48, e2020GL091311. doi:10.1029/2020GL091311

Rounce, D. R., Quincey, D. J., and McKinney, D. C. (2015). Debris-covered Glacier Energy Balance Model for Imja-Lhotse Shar Glacier in the Everest Region of Nepal. *The Cryosphere* 9 (6), 2295–2310. doi:10.5194/tc-9-2295-2015

Rowan, A. V., Nicholson, L., Collier, E., Quincey, D. J., Gibson, M. J., Wagnon, P., et al. (2017). Multiannual Observations and Modelling of Seasonal thermal Profiles through Supraglacial Debris in the Central Himalaya. *Cryosphere Discuss.* 2017, 1–39. doi:10.5194/tc-2017-239

Rowan, A. V., Nicholson, L. I., Quincey, D. J., Gibson, M. J., Irvine-Fynn, T. D. L., Watson, C. S., et al. (2021). Seasonally Stable Temperature Gradients through Supraglacial Debris in the Everest Region of Nepal, Central Himalaya. *J. Glaciol.* 67 (261), 170–181. doi:10.1017/jog.2020.100

Sangewar, C. V., and Shukla, S. P. (2009). *Inventory of the Himalayan Glaciers: A Contribution to the International Hydrological Programme. Special Publication No.34.* Kolkata, West Bengal, India: Geological Survey of India.

Scherler, D., Bookhagen, B., and Strecker, M. R. (2011). Spatially Variable Response of Himalayan Glaciers to Climate Change Affected by Debris Cover. *Nat. Geosci.* 4 (3), 156–159. doi:10.1038/ngeo1068

Sharma, P., Patel, L. K., Ravindra, R., Singh, A., K, M., and Thamban, M. (2016). Role of Debris Cover to Control Specific Ablation of Adjoining Batal and Sutri Dhaka Glaciers in Chandra Basin (Himachal Pradesh) during Peak Ablation Season. *J. Earth Syst. Sci.* 125 (3), 459–473. doi:10.1007/s12040-016-0681-2

Shukla, A., Gupta, R. P., and Arora, M. K. (2009). Estimation of Debris Cover and its Temporal Variation Using Optical Satellite Sensor Data: a Case Study in Chenab basin, Himalaya. *J. Glaciol.* 55 (191), 444–452. doi:10.3189/002214309788816632

Shukla, A., and Qadir, J. (2016). Differential Response of Glaciers with Varying Debris Cover Extent: Evidence from Changing Glacier Parameters. *Int. J. Remote Sensing* 37 (11), 2453–2479. doi:10.1080/01431161.2016.1176272

Singh, A. T., Laluraj, C. M., Sharma, P., Patel, L. K., and Thamban, M. (2017). Export Fluxes of Geochemical Solutes in the Meltwater Stream of Sutri Dhaka Glacier, Chandra basin, Western Himalaya. *Environ. Monit. Assess.* 189 (11), 555. doi:10.1007/s10661-017-6268-9

Steiner, J. F., Buri, P., Miles, E. S., Ragettli, S., and Pellicciotti, F. (2019). Supraglacial Ice Cliffs and Ponds on Debris-Covered Glaciers: Spatio-Temporal Distribution and Characteristics. *J. Glaciol.* 65 (252), 617–632. doi:10.1017/jog.2019.40

Steiner, J. F., and Pellicciotti, F. (2016). Variability of Air Temperature over a Debris-Covered Glacier in the Nepalese Himalaya. *Ann. Glaciol.* 57 (71), 295–307. doi:10.3189/2016AoG71A066

Suzuki, R., Fujita, K., and Ageta, Y. (2007). Spatial Distribution of thermal Properties on Debris-Covered Glaciers in the Himalayas Derived from ASTER Data. *Bull. Glaciological Res.* 24, 13–22.

Tachikawa, T., Hato, M., Kaku, M., and Iwasaki, A. (2011). "Characteristics of ASTER GDEM Version 2," in Proceedings of the 2011 IEEE International Geoscience and Remote Sensing Symposium, July 24–29, 2011 (Vancouver, BC: IEEE explorer), 3657–3660. doi:10.1109/igarss.2011.6050017

Zhang, Y., Fujita, K., Liu, S., Liu, Q., and Nuimura, T. (2011). Distribution of Debris Thickness and its Effect on Ice Melt at Hailuogou Glacier, southeastern Tibetan Plateau, Using *In Situ* Surveys and ASTER Imagery. *J. Glaciol.* 57 (206), 1147–1157. doi:10.3189/002214311798843331

Conflict of Interest: The authors declare that the research was conducted in the absence of any commercial or financial relationships that could be construed as a potential conflict of interest.

Publisher's Note: All claims expressed in this article are solely those of the authors and do not necessarily represent those of their affiliated organizations, or those of the publisher, the editors and the reviewers. Any product that may be evaluated in this article, or claim that may be made by its manufacturer, is not guaranteed or endorsed by the publisher.

frontiers in Earth Science

HYPOTHESIS AND THEORY
published: 21 December 2021
doi: 10.3389/feart.2021.662695

The Challenge of Non-Stationary Feedbacks in Modeling the Response of Debris-Covered Glaciers to Climate Forcing

Lindsey Nicholson[1]*, *Anna Wirbel*[1], *Christoph Mayer*[2] and *Astrid Lambrecht*[2]

[1]Department of Atmospheric and Cryospheric Sciences, University of Innsbruck, Innsbruck, Austria, [2]Commission for Geodesy and Glaciology, Bavarian Academy of Sciences, Munich, Germany

Ongoing changes in mountain glaciers affect local water resources, hazard potential and global sea level. An increasing proportion of remaining mountain glaciers are affected by the presence of a surface cover of rock debris, and the response of these debris-covered glaciers to climate forcing is different to that of glaciers without a debris cover. Here we take a back-to-basics look at the fundamental terms that control the processes of debris evolution at the glacier surface, to illustrate how the trajectory of debris cover development is partially decoupled from prevailing climate conditions, and that the development of a debris cover over time should prevent the glacier from achieving steady state. We discuss the approaches and limitations of how this has been treated in existing modeling efforts and propose that "surrogate world" numerical representations of debris-covered glaciers would facilitate the development of well-validated parameterizations of surface debris cover that can be used in regional and global glacier models. Finally, we highlight some key research targets that would need to be addressed in order to enable a full representation of debris-covered glacier system response to climate forcing.

Keywords: debris-covered glacier, review, climate change, modelling, glacier system

OPEN ACCESS

Edited by:
Shin Sugiyama,
Hokkaido University, Japan

Reviewed by:
Ann V Rowan,
The University of Sheffield, United Kingdom
Pascal Buri,
Swiss Federal Institute for Forest, Snow and Landscape Research (WSL), Switzerland

***Correspondence:**
Lindsey Nicholson
Lindsey.Nicholson@uibk.ac.at

Specialty section:
This article was submitted to Cryospheric Sciences, a section of the journal Frontiers in Earth Science

Received: *01 February 2021*
Accepted: *04 November 2021*
Published: *21 December 2021*

Citation:
Nicholson L, Wirbel A, Mayer C and Lambrecht A (2021) The Challenge of Non-Stationary Feedbacks in Modeling the Response of Debris-Covered Glaciers to Climate Forcing. Front. Earth Sci. 9:662695. doi: 10.3389/feart.2021.662695

1 INTRODUCTION

Glaciers respond sensitively to climate variability with attendant impacts on melt water production, sea-level rise and geomorphic hazards (e.g. Watanabe et al., 1994; Kääb et al., 2005; Kaser et al., 2010; Bolch et al., 2011; Huss, 2011; Leclercq et al., 2011; Immerzeel et al., 2012; Marzeion et al., 2012). Therefore, understanding how glaciers worldwide will continue to respond to current and future climatic conditions is important for increasing our holistic understanding of glaciated mountain landsystems and the ecosystems and societies they impact. Understanding the glacier-climate relationship is also prerequisite to using geomorphic evidence of past glacier states as a proxy for former climate conditions (e.g. Osmaston, 2005).

All glacier systems contain sediment, but some mountain glaciers support a continuous cover of rock debris across a substantial part of the ablation zone, defining them as debris-covered glaciers (Kirkbride, 2011). The propensity for a glacier to become debris-covered is contingent on the relative proportions of snow/ice and debris in the system (Kirkbride, 1989). Hence, they are more likely to be prevalent *1*) in tectonically active, high-relief orogenic belts, where denudation supplies abundant rock debris to the glacier surface, and *2*) during periods of glacier recession, when inputs of snow and ice are reduced relative to the rock supply, and more ice mass is removed from the system. It has long been recognized that

surface debris alters ice ablation rate (e.g. Østrem, 1959) and that debris-covered glaciers response to climate forcing is distinctly different to that of clean ice glaciers (e.g. Clark et al., 1994). Nevertheless, and despite of an upsurge of interest in the last decade, the details of the response of debris-covered glaciers to climate forcing, especially with respect to underlying glaciological theory, remain relatively little studied compared to that of clean ice glaciers.

Although regional model studies of glacier evolution and runoff show markedly different results if debris cover is accounted for or neglected (e.g. Shea et al., 2015; Ragettli et al., 2016; Rounce et al., 2020), global-scale projections of glacier change do not yet explicitly account for the role of surface debris in projections (e.g. Hock et al., 2019), and only one study has assessed the impact of the present distribution of surface debris at a global scale (Rounce et al., 2021). There are a number of reasons why neglecting debris cover in future projections of glacier behavior could be problematic. Firstly, in some regions a substantial proportion of the glacierized area is affected by surface debris cover, and this is projected to increase as glaciers continue to experience negative mass balance conditions. A recent global estimate based on automated mapping procedures suggests that about 4.4% (26,000 km^2) of the global glacier area (excluding the Greenland and Antarctic ice sheets) is debris-covered (Scherler et al., 2018), while a study using detailed manual correction to the mapping datasets revised this upward to 7.3% (Herreid and Pellicciotti, 2020), highlighting that debris cover exceeding 1 km^2 in area is found on 15% of global glaciers larger than 2 km^2. Debris cover is found on more than 10% of the glacierized area in eight of the 18 Randolph Glacier Inventory (RGI) regions, and exceeds 15% of glacierized area in North Asia, Central Europe, Caucasus and Middle East, South Asia East and New Zealand (Herreid and Pellicciotti, 2020). The global distribution of mountain glaciers with regionally high concentrations of glaciers adds to the fact that more than half of all debris-covered ice is found in Alaska (38.6%), Southwest Asia (12.6%) and Greenland (12.0%). Individual studies highlight the prominence of debris cover in specific mountain ranges (e.g. Stokes et al., 2007; Hagg et al., 2008; Scherler et al., 2011a; Kääb et al., 2012), and globally the proportion of debris-covered ice is expected to increase as mountain glacier volumes diminish in coming decades (Stokes et al., 2007; Bolch et al., 2008a; Shukla et al., 2009; Lambrecht et al., 2011; Herreid and Pellicciotti, 2020; Tielidze et al., 2020). Secondly, satellite studies show glacier-wide ice mass loss from these debris-covered glaciers tongues over recent decades is substantial and increasing (e.g. Berthier et al., 2007; Bolch et al., 2008b, 2011). Together, these two points imply that understanding the role of surface debris on meltwater production will be prerequisite to correctly forcasting the volume and timing of glacier meltwater contributions to local hydrological resources and global sea level rise in the coming decades and centuries. Thirdly, mass loss of debris-covered glaciers is closely associated with the formation of ice-contact and moraine-dammed lakes that are likely to pose an increasing local hazard potential in the context of future climate projections (Benn et al., 2012).

In this paper we review the fundamentals of how supraglacial debris cover influences the climate response of mountain glaciers and identify some priorities for furthering our understanding of these systems. We provide a brief description of the principles and key metrics of glacier-climate interaction in **section 2**, and identify the salient features of debris-covered glacier systems and their observed response to climate forcing in **section 3**. In **section 4** we use simple glacier models to examine the terms that control the extent and thickness of a supraglacial debris cover, and show the inherent non-stationarity of debris cover development and attendant consequences on traditional approaches to quantifying glacier response to climate. In **section 5** we discuss how existing modeling approaches account for supraglacial debris and highlight the case for developing a complex system model of debris-covered glaciers capable of incorporating the time-evolving impact of the debris on the glacier system. In **section 6** we identify some of the outstanding challenges of including the role of supraglacial debris in glacier system models. We conclude with summary comments on the nature of the problem and the potential ways forward.

2 PRINCIPLES OF GLACIER-CLIMATE INTERACTION

Glacier mass balance is the key property linking the glacier system to climate, and is authoritatively described in Cuffey and Paterson (2010) and Cogley et al. (2011). Here we briefly cover some aspects and terminology of glacier response to climate forcing that we use within this paper.

The annual climatic glacier mass balance B is the sum of snow/ice accumulation and ice mass loss by ablation over the whole glacier surface A, usually expressed as the mass balance rate $\dot{b}$ over the period of a hydrological year.

$$B = \int \dot{b}\, dA \tag{1}$$

The surface mass balance rate, typically increases systematically with elevation, which is referred to as the mass balance gradient. Mountain glaciers continuously redress this unequal mass distribution pattern *via* downstream transfer of ice by deformation and basal sliding. The driving stress for ice flow is a function of gravitational acceleration, slope, and ice thickness, with the local distribution of ice thickness being influenced by the mass balance gradient.

Conditions that favour more snowfall and less ice ablation result in $B > 0$, while conditions favouring less snowfall and more ice ablation result in $B < 0$. If $B > 0$ the glacier will tend to thicken and advance, while if $B < 0$, the glacier will tend to thin and retreat.

Ice flow and mass balance rate together determine the geometry of the glacier, following the continuity equation:

$$\frac{\partial H}{\partial t} = \dot{b} - \nabla \cdot \mathbf{q}, \tag{2}$$

Where H is the ice thickness and $\mathbf{q}$ is the ice flux. If $\dot{b}$ is constant in time under a theoretically constant climate forcing, the glacier attains a steady state geometry. This equilibrium state balances accumulation, ice transport and ablation over a constant-in-time glacier geometry, such that at multi-annual timescales:

$$\frac{\partial H}{\partial t} = 0, \quad \dot{b} = \nabla \cdot \mathbf{q} \tag{3}$$

The concept of a glacier achieving a steady state geometry underpins the method of quantifying glacier response to a prescribed climate forcing, and is widely used in glacier modeling. Analysing the length and/or volume change between two glacier steady states due to two different climate states reveals *1*) the glacier change that will result from a defined step-change in climate, and conversely, *2*) the equivalent step-change climate forcing signal that can be extracted from a known glacier geometry change. In reality, a glacier is expected to only rarely achieve a quasi steady state because stochastic variability even within statistically unchanging climate conditions cause glacier length fluctuations of up to several kilometers (Roe, 2011). Furthermore, although over sufficiently long timescales glacier models converge to a single geometry regardless of the initial state (Eis et al., 2019), over the shorter term, the cumulative climate history recorded in the glacier will also impact its response. Nevertheless, the concept of a steady state glacier remains a valuable idealization for quantifying and comparing system sensitivity, and is considered to be roughly achievable if climate changes are small and slow compared to the glacier response time (Cogley et al., 2011).

While the equilibrium response time of a glacier is valuable for quantifying system sensitivity and developing paleoclimatic proxies, studies for planning and policy purposes are generally more interested in the transient glacier response, specifically forward in time from the current state. Climate analysis based on, and projections of, the transient response of glaciers requires numerical modeling. The climate forcing is expressed through a regional mass balance condition, and is applied to an initial glacier geometry to force a coupled numerical model of mass exchange across the glacier boundaries, and mass redistribution within them, to quantify how the glacier system, as defined by the model constraints, is expected to evolve over time (e.g. Mackintosh et al., 2002; Jouvet et al., 2009, 2011; Clarke et al., 2015; Seguinot et al., 2018).

Historically, glacier-climate interactions have been viewed as relatively direct proxies of climate conditions because the mass change of a glacier is primarily governed directly by atmospheric conditions (the amount of solid precipitation, and the amount of atmospheric energy supplied to the glacier surface), and because the mass redistribution by ice flow and sliding is constrained by physical laws. However, glacier geometry can also be influenced by internal instability, such as surging behavior (e.g. Benn et al., 2019), or mass exchanges that are not solely governed by climate, such as iceberg calving (e.g. Benn et al., 2007) or modification of climatic ablation rate by surface debris (e.g. Vacco et al., 2010).

3 OBSERVATIONS OF DEBRIS-COVERED GLACIER BEHAVIOR

3.1 Sub-Debris Ablation and Ablation Gradient Modifications

The foremost effect of supraglacial debris is to alter the ablation rate of underlying ice (e.g. Østrem, 1959). Thin debris cover enhances ablation by absorbing more solar radiation compared to "clean" ice and transmitting this additional energy efficiently to the ice beneath. However, energy absorbed by thicker debris in the daytime is re-emitted to the atmosphere at night rather than being transmitted to the ice beneath (Reznichenko et al., 2010). As a result, beyond a critical debris thickness, ablation is inhibited compared to that of exposed ice and beyond this thickness, ablation rate decreases with increasing debris thickness. This relationship, here termed the Østrem curve, has a shape that is relatively poorly understood within the ascending limb of the relationship (e.g. Adhikary et al., 2000; Evatt et al., 2015; Fyffe et al., 2020), but well-represented by a reciprocal function in the falling limb part of the curve (Anderson and Anderson, 2016). Field (e.g. Mattson et al., 1993; Nicholson and Benn, 2013; Rowan et al., 2021), laboratory (Reznichenko et al., 2010) and modeling (e.g. Nakawo and Young, 1981; Nicholson and Benn, 2006; Reid and Brock, 2010; Evatt et al., 2015) studies demonstrate that debris thickness is the primary determinant of how sub-debris ice ablation rate differs to that of clean ice, with other properties of the debris layer, such as lithology, porosity and moisture content playing only secondary roles (e.g. Reznichenko et al., 2010; Nicholson and Benn, 2013; Collier et al., 2014).

There is a systematic tendency for supraglacial debris cover thickness to increase downglacier (e.g. Zhang et al., 2011; Nicholson and Benn, 2013). This is because melt out of englacial material can only occur in the ablation zone of the glacier, and debris is continually conveyed downglacier with ice flow (Kirkbride, 2000), and is concentrated towards the glacier terminus by ice flow deceleration towards the glacier front (Anderson et al., 2018). Further to the impact of compressional flow towards the terminus, the spatial distribution of extensional or compressional flow across the glacier will also impact the debris thickness distribution, for example, thinning the debris cover over piedmont glacier terminus, and tending to thicken debris towards slow-flowing glacier margins. Due to the progressive downglacier increase in debris thickness, the downglacier pattern in ablation rate of a debris-covered glacier has a zone of enhanced ice ablation rate associated with the thin or patchy debris at the upper end of the supraglacial debris cover (Adhikary et al., 2000), and below this zone, ablation is progressively reduced towards the terminus as a function of increasing debris thickness (e.g. Benn and Lehmkuhl, 2000; Benn et al., 2012). This is in stark contrast to the monotonic increase in ablation rate with decreasing elevation towards the terminus of a clean ice glacier.

Superimposed on the systematic spatial variation of debris thickness, local debris thickness variability (e.g. Reid and Brock, 2014; Nicholson and Mertes, 2017) leads to strong small-scale inhomogeneity in ablation rate, which can form pronounced surface relief, which facilitates ice cliff exposure by debris slumping (Moore, 2018), and the formation of supraglacial meltwater ponds within closed surface basins (Watanabe et al., 1986). These features form "hotspots" of ablation (e.g. Sakai et al., 1998, 2000; Buri et al., 2016; Miles et al., 2016; Nicholson et al., 2018), that have been shown to contribute disproportionately to glacier-wide ablation (e.g. Sakai et al., 1998; Immerzeel et al., 2014; Juen et al., 2014; Thompson et al., 2016).

3.2 Geometric Response to Climate/Debris Forcing

Numerous studies have shown a prevalence of debris-covered glaciers losing mass by thinning (e.g. Lundstrom et al., 1993; Bolch et al., 2008b; Deline et al., 2015; Ragettli et al., 2016; Purdie et al., 2018; King et al., 2020; Anderson et al., 2021), in contrast to the characteristic terminus retreat of clean ice glaciers. This can be explained by the ablation gradient of debris-covered glaciers, whereby *1*) enhanced ablation at the upper limit of the debris cover, if not adequately compensated by ice influx from upglacier, results in a flattening of the surface along the flow direction (e.g. Benn et al., 2012; Rowan, 2017; Salerno et al., 2017) and *2*) inhibition of ablation means that debris-covered glacier termini can survive at much lower elevations than neighbouring clean ice glaciers, and maintain stable terminus locations over long periods of volume loss (e.g. Mayer et al., 2006; Scherler et al., 2011b; Lambrecht et al., 2014). Declining surface gradient and mean ice thickness during negative mass balance phases both act to reduce the driving stress and ice flow within the debris-covered tongue, typically causing progressive stagnation (e.g. Bolch et al., 2008b; Quincey et al., 2009; Thompson et al., 2016).

Some debris-covered glaciers form large, impounding latero-terminal moraine complexes, as are prevalent in the eastern Nepalese Himalaya (e.g. Benn and Owen, 2002; Hambrey et al., 2008). Other present-day debris-covered glaciers terminate in outwash plains without substantial terminal moraines (e.g. Kirkbride, 1989; Mayer et al., 2006; Anderson et al., 2021), although in some cases aggradation of the outwash plain contributes to the terminus location being overdeepened with respect to the forefield (e.g. Bennett and Evans, 2012). If there are impounding glacier moraines, these affect the englacial water table, pinning it at the lowest exit point of the moraine. In negative mass balance conditions, as the glacier surface lowers towards the water table determined by the moraine, supraglacial ponds can coalesce to form large ice-contact lakes, triggering the onset of ablation by calving of ice into water (Benn et al., 2012). These hydrological states appear to be strongly tied to the surface slope angle (e.g. Reynolds, 2000) and the total amount of surface lowering that has occurred (Sakai and Fujita, 2010). If there are no impounding moraines, terminal lakes can only form by external geomorphic processes such as water being impounded by advances of neighbouring glaciers, or slope failures damming the valley downstream.

While some glaciers in the Karakoram have experienced slightly positive mass balance in recent decades (e.g. Gardelle et al., 2012), observations of glaciers under positive climatic mass balance conditions is scant and interpreting debris-covered glacier behavior in response to this is complicated by widespread surging behavior in the region (e.g. Quincey et al., 2011). Kirkbride (2000) offers a conceptual framework describing how alternating cycles of "ablation dominant" (negative mass balance) and "transport dominant" (positive mass balance) conditions serve to expand and contract the extent of the debris-covered area respectively, while also contributing to progressive downglacier thickening of the debris cover.

Individual glacier advances can be triggered by large rock avalanches onto glacier surfaces. For example, following a large rock avalanche in 1920, the Brenva glacier advanced 490 m between 1920 and 1941, whereas neighboring glaciers in the Mont Blanc massif (European Alps) retreated from the mid-1920s (Deline et al., 2015). In other cases the impacts of rockfall onto glaciers are more ambiguous (e.g. Shugar et al., 2012; Berthier and Brun, 2019), but large rockfall events have been proposed as mechanisms for forming anomalously distal moraine deposits (e.g. Tovar et al., 2008; Shulmeister et al., 2009).

While it is apparent that the modification of the surface mass balance drives a different glacier behavior, the conceptual understanding gleaned from these observations does not reveal the relevant process timescales or controls that dictate how debris-covered glaciers can be formed and evolve over time. To explore these aspects requires numerical modeling, but, before reviewing the existing modeling approaches, we describe the basic governing processes.

4 ILLUSTRATING THE FUNDAMENTAL BEHAVIOR OF SUPRAGLACIAL DEBRIS

In this section we examine the first principles of how supraglacial debris cover filters the climate forcing, as a function of its extent and thickness, and how this effect develops over time. The fundamental glacier-scale processes controlling surface debris distribution are *1*) melt out of englacial debris and *2*) redistribution of debris with ice flow, by both passive advection and thinning/thickening of debris due to extensional/compressional flow of the underlying ice. We use a simple glacier geometry to study the individual effects of melt out and ice flow redistribution in turn, to isolate how these processes individually, and together, contribute to the spatio-temporal variations in the surface debris distribution.

In our analysis we specifically neglect the local-scale, site-specific processes related to avalanching, rockfall deposits, reworking of debris by gravity or meltwater, as well as the local ablation modification associated with exposed ice cliffs, supraglacial ponds or englacial conduits. This is justified insofar as the significance of all these components varies from glacier to glacier, and we wish to highlight generalized behaviors.

To describe how the fundamental processes govern the distribution of debris on the glacier surface we employ the following continuity equation along a glacier flowline:

$$\frac{\partial h_\mathrm{d}}{\partial t} = u_\mathrm{s}\frac{\partial h_\mathrm{d}}{\partial x} + h_\mathrm{d}\frac{\partial u_\mathrm{s}}{\partial x} + m_\mathrm{d}, \tag{4}$$

Where u_s is the ice surface velocity, h_d is the debris layer thickness and m_d represents any debris sources or sinks. Similar forms of this equation have been used previously to represent the transport of debris on the glacier surface (e.g. Anderson and Anderson, 2016), however often in a modified form (e.g. Vacco et al., 2010), where a diffusion term is added in order to account for gravitational mass movements. The first term represents the advection of thicker or thinner debris from upglacier; the

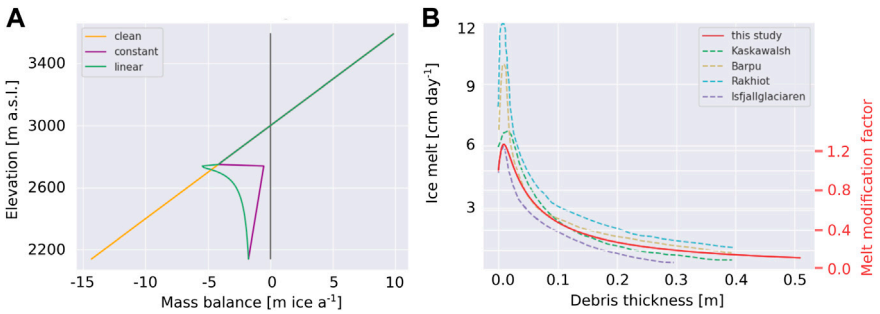

FIGURE 1 | (A) The vertical mass balance profile for clean ice (orange), and how it is modified by a debris layer of constant 0.5 m thickness below 2750 m (purple) and by a debris layer that increases linearly in thickness from 0 m at 2750–0.5 m at the lower limit of glaciation at 2140 m (green). **(B)** Østrem curves from Mattson et al. (1993) compared to the one used in this study, for which we also show the melt modification factor (f_{debris}) that we apply to the clean ice ablation gradient.

second represents thickening or thinning of a debris layer due to compressional or extensional ice flow; and in our study the source term m_d represents melt out of englacial debris, and we do not treat direct surface deposition nor any processes of debris removal at the terminus. Surface deposition and debris evacuation processes are certainly important to the development of a debris-covered glacier system, and would be an essential component of a transient system model, but given that we *1*) do not perform transient simulations, and *2*) wish to highlight the known systematic effects of debris on the glacier, we neglect these processes as they are complex, site-specific, and lacking well constrained physical relationships (*see* **Section 6** for further discussion). The melt out term will add debris mass to the glacier surface whenever there is ice ablation, at a rate determined by the prescribed englacial debris concentration, local climatic ablation rate and modification of ice ablation rate imposed by the existing debris cover at any point, whereas ice flow will cause a redistribution of surface debris.

4.1 Alteration of Debris Thickness by Ice Ablation

First, we look at the vertical profile of surface mass balance and investigate how it is modified by the presence of supraglacial debris cover. For this, we consider a regional surface mass balance rate with a gradient of −15 kg m^{-2} km^{-1} and an equilibrium line altitude (ELA) of 3000 m a.s.l., and assume the glacier elevation range spans 2140–3600 m (*see* **Figure 1A**, where the annual mass balance is plotted in units of ice equivalent in order to be consistent with later glacier surface evolution calculations). In this illustrative study we have assumed that the reference (clean ice) mass balance gradient is linear. This is an unrealistic representation of the real world condition in which *1*) the positive part of the mass balance profile frequently shows only slight variation with elevation as snowfall is more weakly related to elevation, and *2*) the negative part of the mass balance profile is often non-linear due to the influence of the gradual rise of the snowline over the ablation season. Lower elevations have longer ice ablation seasons and, as ice albedo is lower than that of snow, ablation rates are enhanced towards the terminus. Nevertheless for our illustrations we use the linear reference mass balance gradient in order to simplify and generalize the visualisation of the effect of debris, as the non-linearity in mass balance for an individual glacier is strongly dependent on its specific climate. To this, we can apply two example debris cover distributions that affect the glacier ablation below 2750 m: *1*) a debris cover of constant thickness of 0.5 m, and *2*) a debris cover that increases linearly with elevation from 0 m at 2750–0.5 m at the lower limit of glaciation at 2140 m (*see* **Figure 2A**).

We generate an Østrem curve to describe the modification of ice melt beneath supraglacial debris cover as a function of its thickness, using the approach presented in Evatt et al. (2015). We selected a combination of meteorological parameters (incoming shortwave radiation (500 W m^{-2}), incoming longwave radiation (100 W m^{-2}), wind speed (1.5 m s^{-1}), humidity (10%), and air temperature (275 K)) such that the resulting curve best mimics those measured in the field and presented in Mattson et al. (1993) (**Figure 1A**). This Østrem curve is converted into a melt modification factor (f_{debris}) expressing the sub-debris ablation as a function of clean ice ablation, shown on the secondary axis of **Figure 1A**, and we calculate sub-debris ablation by multiplying the clean ice ablation by this factor for the respective debris layer thickness. While the relationships in **Figure 1A** are based only on ablation season measurements, we apply the ablation modification factor to the reference mass balance gradient directly as the debris affects the whole snow-free ablation period. As such is independent of any inherent non-linearity of the real-world clean ice mass balance gradient inherited from the progressive decrease in the snow-free ablation season with elevation. Considering the mass balance profiles for the two different debris thickness distributions; in scenario *1*) sub-debris ablation rate is always substantially less than the ablation rate of clean ice (*see* **Figure 1B**, purple), while in scenario *2*) the upglacier part of the debris cover is thin enough to enhance the ablation compared to that of clean ice, and, with increasing debris thickness the ablation rate rapidly decreases and becomes significantly lower than that of clean ice (*see* **Figure 1B**, green).

Accumulation and thickening of debris by melt out at the surface progressively shifts the respective sub-debris ablation rate to values further along x-axis of the Østrem curve. We first consider this process of debris melt out alone, as if it were the only

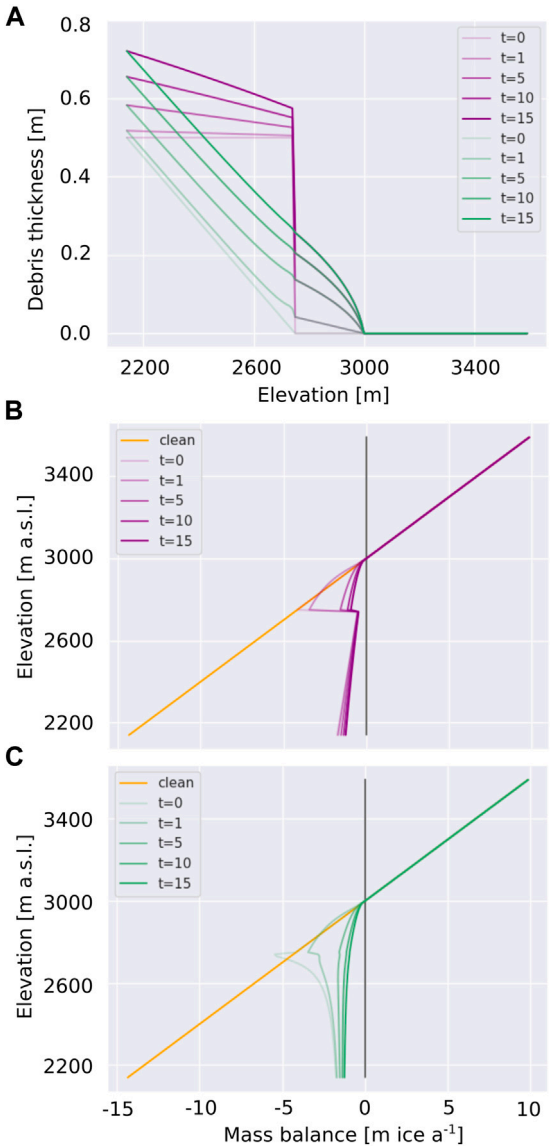

FIGURE 2 | (A) The two prescribed initial debris distributions of constant (purple) or linearly increasing (green) debris thickness, and their changes over time (t in years), as a result of melt out alone (m_d in **Eq. 4**). The modification of the ablation gradient as a result of progressive debris accumulation by melt out alone, while neglecting all other processes, is shown over time (t in years) in **(B,C)** for an initially constant (purple) and linearly increasing (green) debris thickness respectively, alongside the vertical mass balance profile for clean ice (orange).

factor affecting the debris thickness distribution, in order to isolate how this process influences the ablation gradient over the course of time. Treating this process in isolation from the dynamic glacier system is a strong abstraction of reality, but it is useful for a first principles understanding of the feedback between ablation and debris melt out over time. We consider the simplest case with a constant climate and uniform englacial debris concentration of 1% by volume, so that the debris thickness accumulated at the surface is simply a function of the debris-thickness-dependent ablation rate. This englacial concentration is within the range of those found within the Khumbu glacier (0.1–6.5%, although in reality debris is not evenly distributed within the ice (Miles et al., 2021)). As a result of the mass balance gradient, over time the initially constant debris layer thickness develops into a layer that thickens downglacier (**Figure 2A**, purple). This highlights how ablation, and melt out of debris, contributes to the systematic downglacier thickening of debris over the glacier surface. For the case of an initial debris thickness distribution that increases linearly with distance downglacier, the maximum debris thickening over 15 years occurs at the upper limit of the initial debris cover extent (**Figure 2A**, green). In both of our prescribed scenarios, above the upper limit of the initial debris cover debris melt out forms a thin debris layer extending up to the ELA. The debris layer thickness in this newly debris-covered area varies with the linear ablation gradient in the first time step, and, as it is thin, causes enhanced ablation over a relatively wide elevation range. This debris accumulation is initially rapid but, slows down due to the negative feedback on ablation rate imposed by increasingly thick debris cover. As the Østrem curve is non-linear, the newly accumulated debris layer develops a convex-downglacier variation in thickness, even with the linear mass balance gradient as forcing. This example shows how, in the absence of other factors modifying debris thickness, continual exhumation of debris causes the ablation regime of the glacier to change over time even if the climate is constant, thereby revealing the fundamental manner in which the temporal evolution of the sub-debris ablation is partially decoupled from climate forcing.

We can also illustrate a second way in which supraglacial debris cover decouples the glacier ablation gradient from a prescribed climate forcing by considering how the perturbation by the existing debris cover. In this case, we perturb the regional clean ice surface mass balance condition in four example ways: By increasing and decreasing the ELA by 100 m while maintaining the same mass balance gradient (**Figure 3B**), and by retaining the ELA but modifying the mass balance gradient by ± 2 kg m^{-2} km^{-1} (**Figure 3D**).

Upward/downward migration of the ELA for our linear clean ice mass balance gradient produces uniform negative/positive change in the mass balance profile for clean ice glaciers (orange lines in **Figure 3A**). However, the resulting change in mass balance is not uniform with elevation if a debris cover is present (purple and green lines in **Figure 3A**). Beneath a thick debris layer, the effect of a shift in ELA on the surface mass balance is greatly reduced. Beneath the 0.5 m thick debris cover the change in ablation associated with an upward shift in ELA is reduced to the order of 20% of that experienced by a clean ice glacier surface, while beneath the thin debris, the upward shift in ELA causes a local increase in ablation that is the order of 30% more than that experienced by clean ice in the same portion of the glacier (**Figure 3A**). As in the case of ELA migration, the effect of perturbing the linear mass balance gradient (orange lines in **Figure 3C**)), is strongly damped beneath the debris layer of constant thickness (purple lines in **Figure 3C**), and shows strong non-linearity beneath the debris cover that increases in thickness linearly with decreasing elevation (green lines in **Figure 3C**). These simple illustrations show how the surface

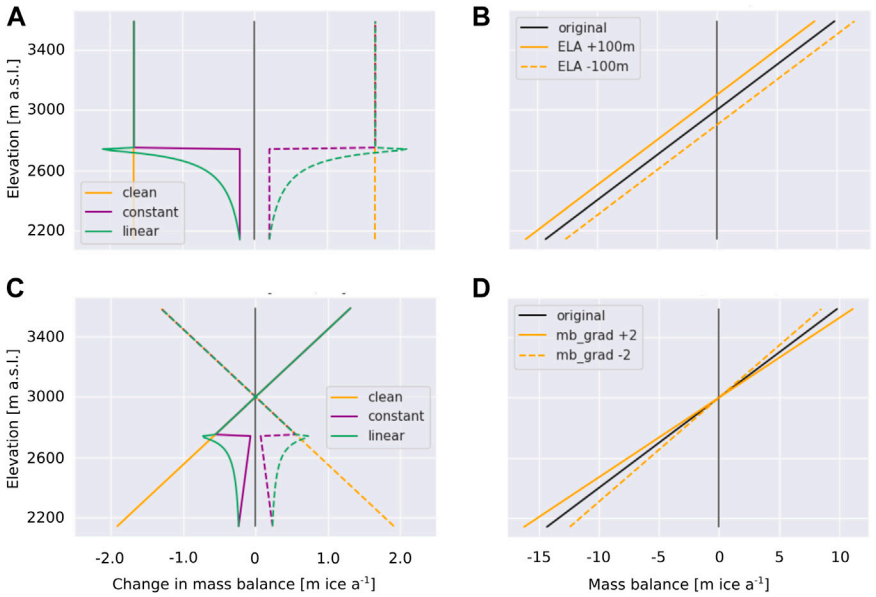

FIGURE 3 | Illustrating how an existing debris cover modifies the glacier ablation response to a climate forcing, where the climate forcing is represented as an alteration to the clean ice mass balance gradient: **(A)** shows the change of the mass balance profile experienced by shifting the ELA of the regional clean ice mass balance gradient by ± 100 m **(B)**, and how this affects the mass balance gradient for an initially constant (purple) and linearly increasing (green) debris thickness respectively; **(C)** shows the effect of altering the mass balance gradient by ± 2 kg m^{-2} km^{-1} **(D)**. Positive perturbations to the ELA and mass balance gradient are shown in solid and negative changes in dashed lines. All actual and differences in mass balance gradients are shown converted into units of ice surface height change.

mass balance forcing experienced by a glacier in response to changing climate conditions, varies depending on the existence and distribution of surface debris. The likely pattern of debris cover thickness on a glacier implies that over most of a debris-covered zone the expression of the climate shift on the surface mass balance rate is damped compared to that experienced by a clean ice glacier surface.

4.2 Alteration of Debris Thickness by Ice Flow

The effects of melt out as illustrated in the previous section are of course not the whole picture, as other factors affecting the surface debris distribution have been neglected; the most important of which is the effect of ice flow. To see how the fundamental processes of advection of upstream debris, and thickening or thinning of the overlying debris due to compressional or extensional ice flow play out in the case of a plausible glacier geometry, we compute a steady state geometry for a simple clean ice glacier long profile. This initial glacier geometry is constrained for a bed with a constant slope of 4.5° and ice flow is computed using an open-source flux-limited Shallow Ice Approximation (SIA) model (Jarosch et al. (2013), https://github.com/alexjarosch/sia-fluxlim). The same prescribed time-invariant mass balance gradient as used in the previous section (−15 kg m^{-2} km^{-1}) and an ELA of 3000 m is applied until a steady state geometry is achieved (*see* **Figure 4A**). For this steady-state clean-ice glacier longitudinal profile, we compute a velocity field with an open-source full-Stokes ice flow model (icetools, Jarosch (2008), https://github.com/alexjarosch/icetools). These computations are performed with a no-slip condition at the glacier bed and zero velocity in the flow direction (x-direction) is imposed at the upper margin. We use a full-Stokes model here to resolve the vertical distribution of ice velocities, from which we extract the surface velocities required. By considering only the variation down a flowline, we neglect any cross-glacier effects due to compressional flow at the lateral margins of the glacier. The initial debris thickness conditions for **Eq. 4**, are defined so that the lower part of the glacier ablation area ($\leq$2750 m) is debris-covered. The prescribed debris cover thicknesses are *1*) constant 0.5 m, *2*) linear increase with decreasing elevation *3*) linear increase with downglacier distance (*see* **Figure 4B**).

In the case of an initially constant debris thickness distribution *1*), the advection term in **Eq. 4** does not lead to a change of debris thickness, except that the upper margin of the debris layer will migrate downstream, which causes a change from debris to no debris cover at that location. Therefore the result for this debris distribution is not shown quantitatively in **Figure 4C**, as its magnitude is dependent on the model discretization. For the case of both variable debris thickness distributions, the advection term causes a local decrease of debris thickness throughout **Figure 4C**. For case *2*) applied to our glacier geometry (blue line in **Figure 4A**), the steep elevation change at the glacier terminus creates strong gradients in debris thickness resulting in more pronounced advective thinning towards the glacier front.

For our simple glacier geometry, surface ice velocities within the ablation zone decrease monotonically towards the glacier terminus, causing convergence of the debris layer (*see* **Figure 4D**). This process causes compressional thickening of debris cover for all three initial debris

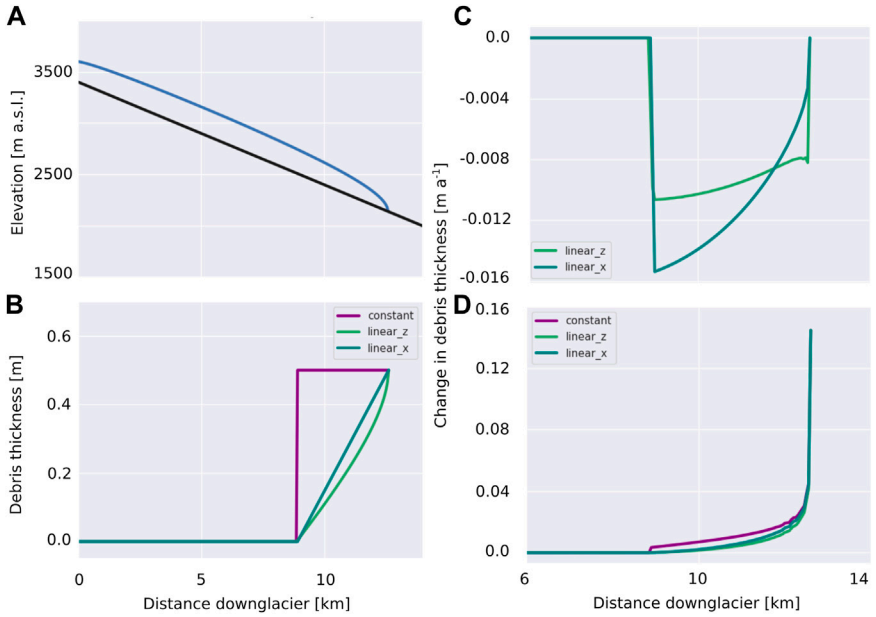

FIGURE 4 | Configuration of the illustrative example discussed in the text. **(A)** the 2D longitudinal glacier profile generated using a SIA model on a constant slope, **(B)** the three initial debris covers prescribed below 2750 m with *1*) constant thickness (purple), *2*) linear increase in thickness with decreasing elevation (green) and *3*) linear increase in thickness with downglacier distance (blue) debris thickness, **(C)** the downglacier pattern of debris advection with ice flow (first term in **Eq. 4**) and **(D)** the downglacier pattern of thickening or thinning of the debris layer due to compressional or extensional ice flow (second term in **Eq. 4**).

thickness distributions over time, at a rate that increases downglacier and is especially pronounced close to the glacier terminus where ice velocities decelerate rapidly to zero. Thus, at any given point along the glacier long profile, the processes of advection is generally acting to thin the debris cover, while compressional ice flow is serving to thicken debris, although a more complex downglacier bedslope could lead to sections of extensional ice flow. In this analysis, it should be noted that though we examine the behavior of the terms in **Eq. 4**, we do not perform transient simulations.

4.3 Can a Steady State Geometry Be Achieved?

In order to meet the conditions of steady state given by **Eq. 3**, the mass balance gradient, including the part influenced by debris cover, would need to be maintained constant in space and time, which in turn would require a solution for **Eq. 4** that can sustain a specific debris thickness distribution that is constant in space and time.

If we revisit **Eq. 2**, in the case of debris-covered glaciers, this formulation changes to:

$$\frac{\partial H}{\partial t} = \dot{b}(h_\mathrm{d}) - \nabla \cdot \mathbf{q}, \quad \dot{b}(h_\mathrm{d}) = \dot{b} f_{\mathrm{debris}}(h_\mathrm{d}(\mathbf{x}, t, \mathbf{u}, m_\mathrm{d})) \tag{5}$$

Where the clean ice mass balance rate $\dot{b}$ is now modified to become a debris aware mass balance rate $\dot{b}(h_\mathrm{d})$ that is a function of debris cover thickness, for simplicity here expressed *via* the thickness-dependent ablation modification factor f_{debris} (*see* **Figure 1A**). Hence, in order to achieve a steady state geometry, the divergence of ice flux would have to balance the debris-dependent mass balance rate, so that:

$$\frac{\partial H}{\partial t} = 0, \quad \nabla \cdot \mathbf{q} = \dot{b} f_{\mathrm{debris}}(h_\mathrm{d}(\mathbf{x}, t, \mathbf{u}, m_\mathrm{d})) \tag{6}$$

However, following **Eq. 4**, debris cover thickness is not constant in time, but a function of ice velocity and the melt out of englacial debris, which is determined by the mass balance rate and the englacial debris concentration. These interdependencies highlight that it is very unlikely that the divergence of ice flux can, over an extended period of time, balance the debris-dependent mass balance rate, as this itself is a function of ice velocity and mass balance rate, constantly evolving with time.

Posed another way, the question is whether ongoing melt out of englacial debris could be exactly offset by debris thickness redistribution by ice flow to sustain the initial debris distribution in the context of our plausible glacier mass balance and flow field conditions. The melt out and ice flow terms are plotted together in **Figure 5** to examine the relative scale of their combined effects along the glacier longitudinal profile. We emphasise that the relationships shown in **Figure 5** are not the result of transient simulations but show a representation of the processes at work for the given configuration of prescribed debris thickness distributions, glacier geometry and mass balance rate as a snapshot in time, and as such gives only a first order indication of the interplay between these processes. By plotting

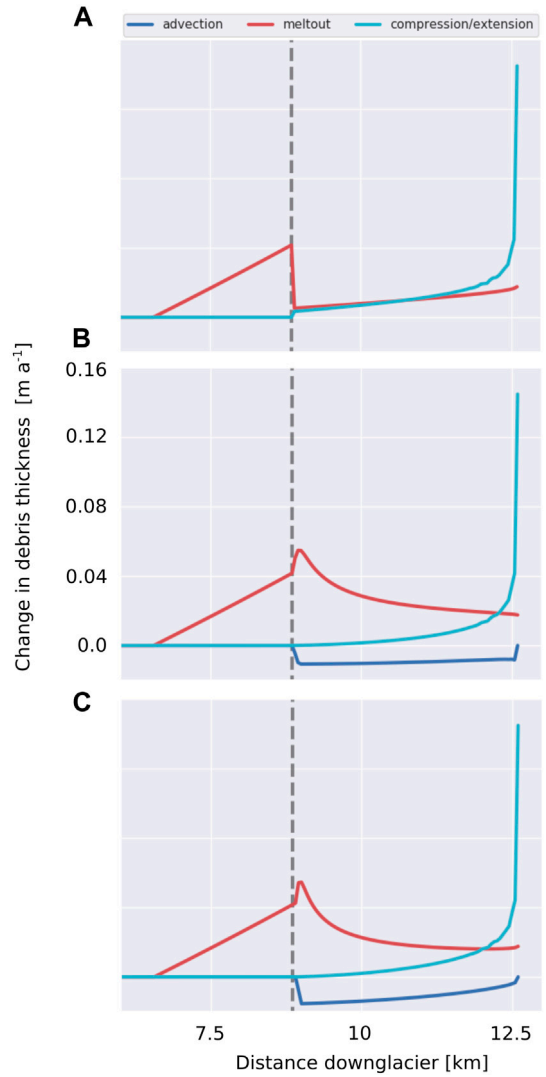

FIGURE 5 | The effect of *1*) meltout of englacial debris (red, (third term in **Eq. 4**)), *2*) advection (dark blue, second term in **Eq. 4**) and *3*) extensional/compressional ice flow (light blue, (second term in **Eq. 4**) as a result of three initial boundary conditions **(A)** constant, **(B)** linearly increasing with decreasing elevation and **(C)** linearly increasing with downglacier distance debris thickness distribution. Note that these are showing the instantaneous state for the initial boundary conditions, without time dependency. The grey dashed line indicates the upper limit of the initial debris cover distributions. In **(A)** we do not plot the advection term, which is zero everywhere except at the onset of the debris cover, where it is locally strongly negative and would cause the upper margin of the debris cover to shift downglacier.

these together, we wish to highlight how the downglacier variation of the three processes of *1*) debris meltout, *2*) advection of debris with ice flow and *3*) debris thickening/thinning due to compressional or extensional ice flow flow, result in a debris thickness change that cannot be easily offset by a glacier flowfield to maintain the constant surface geometry as specified by the steady state condition given in **Eq. 3**.

For an initially constant debris thickness *1*), the melt out of englacial debris is stronger further downglacier and the deceleration of ice flow causes convergence of the debris layer (**Figure 5A**). This leads to an increase of debris thickness along glacier that is stronger further downglacier and hence, the initially constant debris thickness will not be sustained. In the case of an initially varying debris thickness *2*) and *3*), there is an obvious incompatibility of monotonic downglacier variation of debris thickening with strongly non-linear melt out, so that these terms cannot cancel each other out to sustain a constant debris thickness distribution downglacier (*see* **Figures 5B,C**). These illustrative figures highlight that, as also indicated by considering **Eqs 5**, **6**, that a constant debris thickness is unlikely to be sustained for a prescribed set of constant climate conditions even for the simplest glacier cases.

5 NUMERICAL MODELING OF DEBRIS-COVERED GLACIER BEHAVIOR

The simple illustrations of the fundamental properties of debris-covered glaciers presented in the previous sections, show that *1*) the impact of supraglacial debris cover on the glacier mass balance is controlled by linked processes that are time-dependent, and themselves related to the temporal changes in supraglacial debris extent and thickness, *2*) these time-dependent processes and the related thresholds and feedbacks between them together determine the climate response of debris-covered glaciers and *3*) the conditions of steady state are unlikely to be achievable for a debris-covered glacier, even with idealized constant climate forcing. In short; even when considering only the fundamental governing processes in the simplest configuration, surface debris cover, and therefore the spatial pattern of surface ablation, is continually changing as a result of the dynamic coupled processes of debris melt out and alteration by ice flow. This pose challenges to understanding both the transient and equilibrium responses of debris-covered glaciers, even for highly idealized glacier cases. Numerical model representations of debris-covered glaciers in the literature differ in the level of detail they include, and the processes they represent, so in the following section we briefly describe how existing modeling approaches have dealt with these specific challenges, summarize the key lessons learned, and suggest a path forward.

5.1 Previous Numerical Modeling Studies

Two decades ago, Konrad and Humphrey (2000) suggested that under steady state climate conditions, a debris-covered glacier terminus has to constantly advance. While a provocative concept, their model effectively forces this behavior by prescribing a constant surface supply of debris >1 m thick at the equilibrium line of a vertically resolved flowline model. This means that ablation over the whole glacier is abruptly driven down to 0–10% of the bare ice ablation, while their boundary conditions continually add mass in the glacier accumulation zone. These model boundary conditions are not a good analogy for a gradually developing supraglacial debris cover as observed on present-day glaciers, which involves stages of development with sizeable expanses of clean ice below the

ELA, and debris thickness much less than 1 m at the upper margin of the debris cover. Similarly structured studies, using shallow ice approximation flowline models, and applying thick debris as single events to represent large rockfalls onto glacier ablation zones (e.g. Vacco et al., 2010; Menounos et al., 2013), illustrate instantaneously thick debris cover could cause glaciers to advance, but the advance is not sustained in the absence of continuous debris supply.

Naito et al. (2000) present a more complete process-representation of an evolving debris-covered glacier tongue. To recreate the evolution of the Khumbu glacier tongue from 1978 to 1999 they used a reconstructed climate series based on local measurements, prescribed upstream ice influx based on a 1976 estimate. They then applied a debris-modified mass balance initially constructed on the basis of the residual lowering after accounting for ice flux divergence based on the continuity equation of Kadota et al. (2000) for a glacier longitudinal profile, accounting for lateral drag *via* a shape factors assuming the glacier tongue has a trapezoidal cross-section. This mass balance was allowed to evolve gradually over time as a function of debris thickening by melt out and underlying ice flow convergence. The inputs to this scheme were simple, and uncertain, but the observed surface lowering up to 1999 was quite well captured.

A number of subsequent published modeling studies tended to move away from the coupled, time-evolving debris flux and mass balance representations of Naito et al. (2000). Banerjee and Shankar (2013), for example, compared the response of idealized clean and debris-covered glaciers to climate forcing using a shallow ice approximation flowline model in conjunction with simplified, unchanging, linearized glacier mass balance gradient forcing. By applying a fixed mass balance condition, which can neither evolve with further debris meltout, nor with redistribution of debris by ice flow, the model can achieve steady state geometries. The first conclusion of this study is that debris-covered glaciers show a longer response time, but greater sensitivity, in terms of equilibrium length change, to a given climate forcing than clean ice glaciers. The second conclusion is that debris-covered glacier response comprises two stages with two different timescales: Firstly, a stagnation timescale related to the rate at which changes propagate downglacier, and secondly, a separation timescale related to the ice thickness at the upper margin of the debris cover that controls when the debris-covered terminus becomes detached from the active glacier upstream. The pattern of these responses differs in advance and retreat, indicating that hysteresis inherent in glacier response could be amplified in the case of debris-covered glaciers. The authors explicitly highlight the need to compare their results to those of a coupled debris/ice model in order to test the robustness of their simplified model, and to determine how the mass balance profile evolves with the development of a dynamically coupled debris cover.

Jouvet et al. (2011) incorporated simple representations of surface debris into a 3D full-Stokes ice flow model that solves for an evolving glacier surface using a volume of fluid approach. This study reported difficulties in constraining an empirical representation of the rate of debris cover expansion as a function of melt-rate and a parameterized spreading function for medial moraines (Anderson, 2000). Instead they present a sensitivity analysis in which the effect of debris cover on the glacier evolution was demonstrated by prescribing several estimates of a factor simulating spreading of supraglacial debris, and reducing the ablation rate by 40% wherever there is debris cover. These simulations for different spreading rates of supraglacial debris cover highlight that the debris will substantially alter the glacier length response compared to that of a clean ice glacier, while the difference in volume response was found to be smaller. The timing of the maximum difference in glacier geometry response between the clean and debris-covered cases was dependent on the parameterization of lateral debris spreading.

Rowan et al. (2015) studied the evolution of Khumbu glacier in Nepal including a representation of the feedbacks between ice dynamics, glacier mass balance, the effect of surface debris cover and debris transport in a return to more fully coupled model systems. In this study, the impact of debris on ice melt was represented by an exponentially decaying function for increasing debris thickness, neglecting the enhancing effect of thin debris layers. Debris is supplied constantly across the whole accumulation zone, and is subsequently modified by ice flow and ablation. Debris transport is treated as an advection problem, and a higher-order shallow ice model, ISOSIA (Egholm et al., 2011), is used to simulate ice flow. ISOSIA computes depth averaged velocity components, hence the required 3D velocity field for the debris transport is computed as a post-processing step based on several assumptions. Their optimized model could recreate debris accumulation at the glacier margins and terminus, and capture the general behavior of Khumbu glacier, but neighbouring glaciers were markedly less well reproduced. Their simulations are run to steady state, although the definition of steady state is not reported. The study highlighted the importance of coupling of the debris and glacier evolution as fixed ablation reduction could not represent the present-day glacier.

Anderson and Anderson (2016) also developed a debris-covered glacier model that accounts for debris transport and melt out. They examine the sensitivity of the modelled glacier to the specific location of debris input within the system. Their model represents a 2D vertical glacier flowline, by including parameters for the longitudinal stress gradient, lateral drag, and generating vertically-resolved velocity profile from the continuity equation. Debris is transported through the glacier by ice flow and, once it has emerged on the surface, is advected with the ice surface velocity and modified by the downglacier surface velocity gradients. Debris is evacuated at the terminus according to a parameterization linked to the terminus melt rate. In keeping with expectations based on theoretical glacier flowlines, their study highlights that the system is most sensitive to debris inputs near the equilibrium line. This is because deposits in the upper accumulation zone are buried and transported at greater depth within the glacier body and so are exhumed by ablation lower down in the ablation zone. They find a convex-to-concave curvature of downglacier debris thickness which is a result of the

dominance of ablation (decelerating ice velocity) in the upper (lower) zones of the debris cover. This model can achieve a glacier steady state as debris inputs are in the form of constant supply at a single location, rather than debris distributed through the ice body, and debris removal at the terminus is stipulated at a rate that offsets the addition of debris to the surface, which together mean that a solution can be found to convey this stripe of debris through the glacier in a stable form.

More recently, a study used a shallow ice approximation flowline model to explore the impact of debris on the transient response of glaciers over centennial timescales (Ferguson and Vieli, 2021). This model neglects the possibility of enhanced ablation under thin debris, and evacuates debris from the system *via* a terminal ice cliff, whose position is a function of an ice thickness threshold. An interesting feature is the introduction of a parameterisation for ablation associated with thermokarst features into the surface mass balance forcing. The results suggest that the distinctive debris-covered glacier geometry is related to the fact that they "remember cold periods more than warm."

5.2 Lessons From, and Limitations of, Existing Numerical Modeling

Some general lessons can be drawn from reviewing the existing numerical modeling studies. Firstly, regardless of the climate conditions, increased debris influx to a glacier results in a longer glacier, with a flatter, and therefore, slower flowing terminus. Secondly, model outputs robustly demonstrate that the geometrical response of the debris-covered glacier system is sensitive to the location at which surface debris emerges (e.g. Anderson and Anderson, 2016), highlighting need to account for the location at which debris is delivered, or emerges. Thirdly, the response times of retreating debris-covered glaciers are generally shown to be longer than those for clean ice glaciers, and there may be a pronounced asymmetry in response and response rate between positive and negative mass balance phases (Banerjee and Shankar, 2013; Ferguson and Vieli, 2021).

However, there are also a number of distinct limitations of the existing numerical modeling studies of the response of debris-covered glaciers to climate forcing:

- A common feature of these numerical model studies with the exception of Naito et al. (2000) is that the existence of enhanced ablation caused by thin debris is overlooked. Instead, ablation reduction caused by debris has been prescribed as a fixed value (Jouvet et al., 2011), a linearly decreasing ablation gradient with elevation (Banerjee and Shankar, 2013) or an exponentially decreasing ablation rate (Anderson, 2000; Ferguson and Vieli, 2021), but no analysis of the impact of neglecting the role of enhanced ablation has been performed.
- The chosen model dimension also limits the processes that can be represented. For example, representing the glacier as a 1D flowline necessarily neglects the potentially important processes of debris accumulation in medial moraines and at lateral margins as well as neglecting the 2D pattern of ice surface velocities and how they redistribute debris laterally as well as longitudinally within the ablation zone.
- The time-dependent nature of the developing debris cover is often neglected, by applying time-invariant modifications to the surface mass balance forcing (e.g. Konrad and Humphrey, 2000; Banerjee and Shankar, 2013). A proposed simple model of debris expansion rates, could not be sufficiently well constrained to allow transient modeling of debris cover (Jouvet et al., 2011).
- Although steady state can be achieved in model simulations through specific formulations of the debris ablation modification, transport and evacuation problems (e.g. Banerjee and Shankar, 2013; Anderson and Anderson, 2016; Ferguson and Vieli, 2021), the underlying assumptions that allow this to be achieved have not been rigorously tested. Our analysis in this paper suggests that this warrants further investigation.
- Simple modeling suggests that debris cover alters both the response time and total volume response of a glacier (e.g. Banerjee and Shankar, 2013), and more physical modeling suggests that response times are related to the rate of debris removal (Anderson and Anderson, 2016). In both cases, untested simplifications in the models used means that it remains unclear to what extent the response times might reflects real-world short and long term glacier meltwater contribution to rising sea levels.
- In general, simplifications and assumptions used in these model formulations are not evaluated against reality, so the model study findings should be assessed critically in the light of the specific model capacities.

5.3 Coupled System Modeling to Tackle Time-Dependency and Benchmarking

Conceptually, the individual components required to represent debris within a glacier system are known (**Figure 6**). However, the details of how to quantify the variation in space and time of these individual processes and their interactions remain elusive. Given that the long-term debris-covered glacier response is strongly influenced by the interaction between two time-dependent processes: dynamic debris evolution and climate variability, and as it seems improbable that the traditional conception of glacier equilibrium can apply in the case of distributed englacial debris melting out to form a surface debris cover, climate response investigations for these systems is reliant on transient system modeling. The main limitation to interpreting the results of numerical models presented in the previous section is that the models have not been, and maybe cannot be, validated at the centennial and upward timescales relevant for the development of debris-covered glaciers. Thus, it is questionable if existing model studies will improve the accuracy of projections or just offer a different way of indicating the model uncertainty associated with debris cover.

The numerical implementation deployed within a model can be verified using appropriate rigorous testing, for example

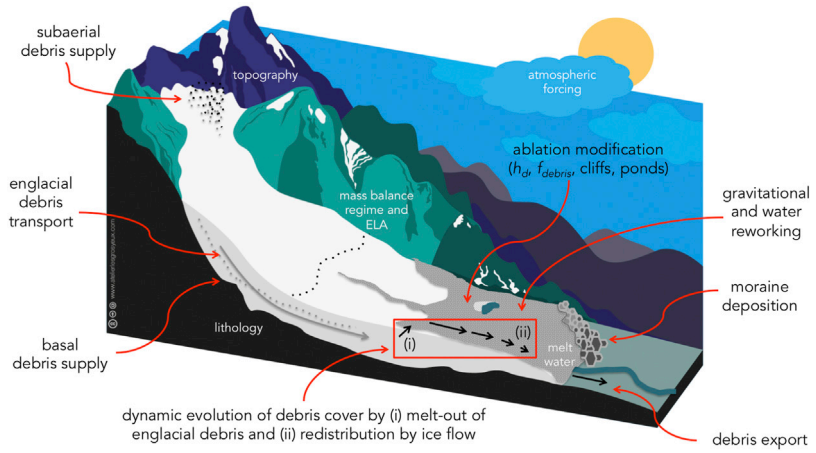

FIGURE 6 | Illustration of the processes of debris flux through a mountain glacier, that ultimately govern the surface debris cover distribution and therefore the way that surface ablation is modified by the debris cover. CC-BY-SA Lindsey Nicholson, adapted from CC-BY-SA Anne Maussion, Atelier les Gros Yeux (http://atelierlesgrosyeux.com).

comparison to exact solutions (Bueler et al., 2005). As an example, the implementation of englacial debris transport, computed as advection of a scalar quantity in an incompressible flow field in Wirbel et al. (2018), was tested by reproducing the results of a "rotating three body problem" (*see* e.g. de Frutos et al., 2014) where the initial shapes are recovered after flow displacement. However, what is further needed is model validation against a representation of reality (Bueler et al., 2005). Unfortunately, the decadal/centennial/millenial timescales involved in the development and evolution of debris-covered glaciers inhibit real-world validation as past behavior of debris-covered glaciers cannot yet be unambiguously reconstructed from the geomorphic record. Given this, a viable alternative solution could be the development of a "surrogate world" model sufficiently complex to capture the coupled, time-evolving, processes operating on debris-covered glaciers.

In addition to representing the total debris flux through the glacier system, a debris-covered glacier system model would need to represent the development of the surface debris cover over time and how it feeds back into other glacier processes, shown schematically in **Figure 7**. Specifically, in order to understand the systematic response of the glacier, even over relatively short timescales, it is crucial to accurately include the partial climate decoupling caused by how supraglacial debris modifies the spatial distribution of ice ablation, and furthermore, the knock-on effects this ablation modification has on *1*) subsequent meltout rate of englacial debris, *2*) the development of the glacier surface geometry and, consequently, *3*) the large-scale debris redistribution by ice flow. Coupling these feedbacks is made difficult by the fact that there is embedded non-stationarity within stages of the development of surface debris cover. The effect and importance of processes linked to ablation (transition from enhancement to inhibition), dynamics (transition from flowing to stagnant) and hydrology (transition from drainage to storage), themselves change in space and time with the development of the whole glacier system. Treating these embedded, non-stationary processes, operating at multiple spatio-temporal scales, poses a substantial challenge for time-dependent modeling of debris-covered glaciers systems. Added to this it is not clear to what extent treatment of non-systematic impacts of site-specific features such as localized avalanche and rockfall inputs, variable bedforms, impounding terminal moraines, gravitational reworking of surface debris and additional ablation hotspots associated with cliffs and ponds, is required in order to satisfactorily reproduce glacier behavior.

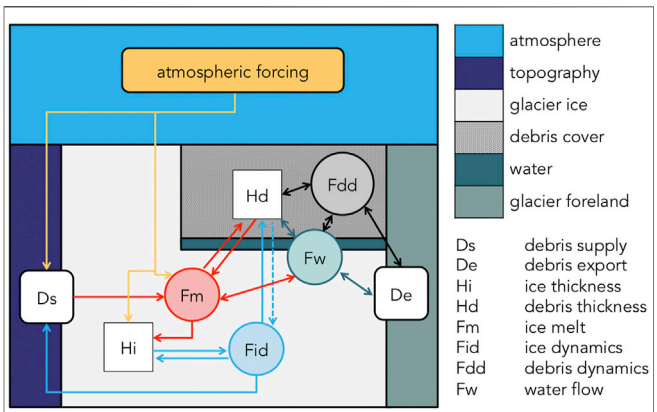

FIGURE 7 | Schematic of the processes interacting (in circles) between forcing variables (rounded boxes) governing the state of a debris-covered glacier system given by the thickness distribution of ice and debris (square boxes), placed in the colour-coded domain of the glacier system where they operate (cf. **Figure 6**).

Clearly the complexity of such a proposed model renders it not applicable to regional and global problems due to restrictions related to computer power and suitable input data. Nevertheless, the development of a time-dependent system model for debris-covered glaciers would offer a crucial tool to evaluate simpler

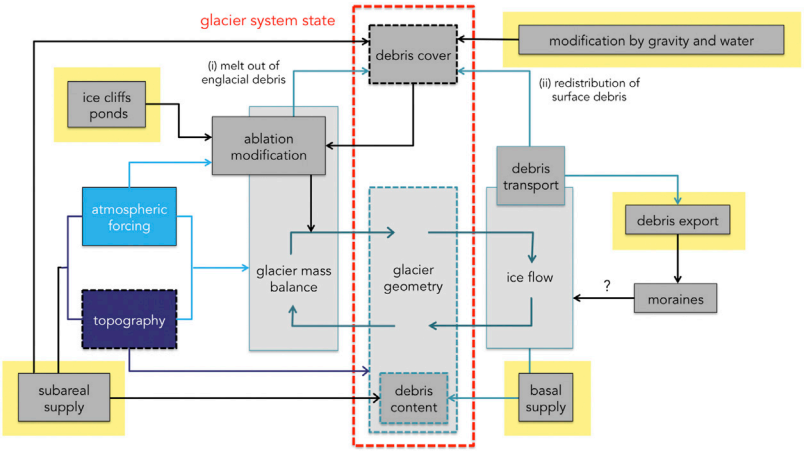

FIGURE 8 | Flowchart of a suggested model structure for a transient, coupled "surrogate world" numerical model of a debris-covered glacier system in order to determine the glacier state (within the red dashed box) at any point in time. The processes represented in solid boxes all vary in space and time, and their interactions represented by the connecting arrows operate on different spatial and temporal scales, that must be handled by the model. We highlight in yellow the components that currently pose significant open challenges to quantify within a numerical model framework: rates and processes of debris supply (subareal and basal), integration of small-scale processes (e.g. cliffs, ponds, gravitational and water re-working) and rates and processes of debris evacuation and deposition.

model representations that could then be incorporated into larger scale modeling efforts. Alternatively, sensitivity testing with a surrogate world model could form the basis of identifying robust statistical representations of the impact of surface debris so that it can be reliably incorporated as a parameterized term in regional and global models used to predict runoff supply, contributions to sea level rise and longer-term histories and projections of glacier-climate interaction (e.g. OGGM (Maussion et al., 2019) and PyGEM (Rounce et al., 2020)).

6 OPEN CHALLENGES

Developing a coupled, time-dependent, system model of debris-covered glaciers would require overcoming a number of significant obstacles, related to poorly constrained inputs, scale bridging, and dealing robustly with (differing) time-dependency in various components of the system. While some system processes have clear quantifiable process-representation developed through previous work, we highlight problematic components in the following sections, and indicate where they lie within a proposed structure of a coupled debris-covered glacier landsystem model in **Figure 8**. Regardless of the process-understanding for individual components, it remains a challenge to couple these at meaningful spatio-temporal scales, and to generate a model that offers quantifiable uncertainty and predictive power.

6.1 Debris Supply

Space- and time-variant supraglacial debris supply, both subaeral and basal (**Figure 8**), is difficult to constrain and implement realistically in a numerical modeling framework, which is problematic as previous studies suggest that the timing and location of debris inputs is critical to their ultimate impact on the glacier. Debris supply may consist of both semi-continuous small-scale inputs and episodic large deposits, necessitating some treatment of both. Applying debris continuously or episodically will influence the debris concentration distribution throughout the glacier at any point in time (Wirbel et al., 2018), and both this and the specific location and intensity of debris delivery determines location and pattern of subsequent debris emergence (e.g. Anderson and Anderson, 2016). Although it is understood that lithology and weathering rates will affect debris supply (Matsuoka and Sakai, 1999; Nagai et al., 2013; Scherler, 2014), debris source and deposition areas, volumes, frequency and rates remain poorly constrained (Benn and Evans, 2010). Estimates of denudation rates from headwall retreat (Heimsath and McGlynn, 2008; Seong et al., 2009), given in units per century or per millennium are difficult to integrate with a glacier system model that requires representation of episodic, discrete debris supply events (Scherler and Egholm, 2020). Measurements of rock volumes from individual events (e.g. Deline, 2009; Hewitt, 2009; Reznichenko et al., 2011) are relatively scarce and therefore not readily generalized. Gravitational movement of debris onto glaciers is expected to be at least partly a function of climate conditions, glacier debutressing and the changing expanse of exposed rockwall, though the nature of this relationship remains contentious. Thus, debris supply rate is also a non-stationary component of a climatically-forced glacier simulation, making it difficult to accurately know the englacial debris distribution at any specific point in time (Scherler and Egholm, 2020). Supply rate estimates based on more readily observable properties such as lithology or projected climate conditions would be helpful, but debris supply will likely continue to be associated with large uncertainties. Therefore it would be valuable to incorporate the findings of sensitivity studies as a means to bracket glacier response to a variety of possible debris supply regimes. In a subsequent step, the valuable experiments of glacier response to

different debris supply regimes in Anderson and Anderson (2016), could be built upon by performing sensitivity studies using high resolution models, that can capture the specifics of englacial debris transport and emergence (Wirbel et al., 2018; Scherler and Egholm, 2020) in the required detail to predict the thickness at the point of emergence (Kirkbride and Deline, 2013). Quantifying rates of basal debris incorporation is dependent on detailed knowledge of the basal properties, which are usually unknown, and as a result prescribed by simple assumptions and parameterizations in glacier models.

6.2 Complex Surface Processes, Operating at Multiple Scales

In addition to the systematic downglacier thickening of surface debris, as soon as debris emerges at the surface, gravitational and meltwater reworking of the supraglacial debris (**Figure 8**), potentially conditioned by differential ablation rates, modifies the spatial distribution of debris thickness (Anderson, 2000; Kirkbride and Deline, 2013). The resultant local debris thickness variability and presence of bare ice cliffs and ponded water (**Figure 8**) can all create ablation hotspots that can significantly alter the ablation and runoff regime of debris-covered glaciers (Irvine-Fynn et al., 2017). Therefore, some treatment of these effects is required in a transient modeling framework. Numerous careful field and model studies at specific glaciers have assessed the impact of ice cliffs and ponds on local and glacier-wide ablation (e.g Reid and Brock, 2014; Steiner et al., 2015; Miles et al., 2016). Although some studies suggest governing relationships might be found, for example relating local variability of debris thickness to the time elapsed since the debris formation (e.g Nicholson et al., 2018); ice cliff formation to debris stability (e.g Moore, 2018); ice cliff persistence to aspect (e.g. Buri and Pellicciotti, 2018); pond formation to the glacier surface profile flattening and the degree of net downwasting (Reynolds, 2000; Sakai and Fujita, 2010), these relationships and their effect on net ablation over time is not yet routinely incorporated into glacier scale simulations. One potential way to include these aspects would be to first robustly evaluate these proposed relationships against either field observations or detailed physically-based numerical models, and then develop statistical relationships to represent their impact at the glacier scale (c.f. Ferguson and Vieli, 2021).

6.3 Debris Evacuation and Moraine Formation

Both the process of debris removal from the system, the conditions under which large impounding moraines are formed and the impact of such moraines remain open questions (**Figure 8**). The rate of debris loss from the system will affect both timescale and length response of a glacier, yet a clear way of handling debris removal processes within numerical models of glacier evolution is still lacking. Relationships mimicking debris offloading have been implemented (Anderson and Anderson, 2016; Ferguson and Vieli, 2021), but these have not been rigorously validated, and in general the mechanism connecting the glacier debris load and marginal deposition is unclear. At unconstrained debris-covered glacier termini, debris can readily exit the glacier onto the forefield, but if impounding latero-terminal moraines are formed, debris cannot readily be exported to the proglacial area. Developing an understanding of how and why such large impounding moraines are formed is prerequisite to including their effects on glacial water storage, upstream ice dynamics and subsequent glacier geometry in both retreat and advance phases. Improved understanding of how debris cover affects glacier behavior and associated deposition will help clarify the paleoclimatic significance of former glacier geometries that may have been influenced by surface debris. At present, this remains complicated because: Debris-covered glaciers are difficult to identify unambiguously in the sedimentary record (e.g. Fernández-Fernández et al., 2017); the proxy climate interpretation of the moraine position is not well constrained (e.g. Clark et al., 1994; Jansson and Fredin, 2002).

6.4 Initial State, Timescales of Response and Regime Switching

As is the case with all glaciers, the transient response of a glacier to a prescribed climate forcing is in part dependent on its state when the forcing is applied. In the case of debris-covered glaciers this requires knowing, both initially and throughout time, whether (in the framework of the listed citations) the debris-covered glacier system state is *1*) currently transport- or ablation-dominant (Kirkbride, 2000), *2*) enhancing or inhibiting ablation relative to clean ice (Østrem, 1959), *3*) close to the threshold between downwasting behaviour and the separation of the active glacier from the former glacier terminus (Banerjee and Shankar, 2013), *4*) close to the hydrological thresholds of pond formation, coalescence, or onset of calving retreat (Benn et al., 2012). The onset of calving retreat is related to rapid terminus retreat, and more negative mass balances compared to similar glaciers without a terminus lake (e.g King et al., 2019), and model studies have highlighted that neglecting the transition from land to lake terminating glaciers will result in inaccurately simulated glacier recession and mass balance (e.g Sutherland et al., 2020). All the processes represented in **Figure 8**, vary in both space and time and furthermore, interactions represented by the connecting arrows operate on different spatial and temporal scales, that must be handled by the model. Some feedbacks are expected to be approximately instantaneous, such as the modification of debris cover by progressive melt out of englacial debris, while others, connected to the rate of ice throughput, such as debris transport by ice flow, and glacier geometry adjustments will involve time lags of decadal to centennial scales, and possibly longer. Finally, as evidence points towards longer response times for debris-covered glaciers it is increasingly likely that multiple timescales of forcing are involved in the observed response, including long inertial phases which might exceed the duration of a given climate perturbation, making it even more difficult to untangle a climate signal from these glaciers.

7 CONCLUSION

We have presented a back-to-basics approach to isolate and explore the fundamental processes by which supraglacial debris thickness is controlled by englacial melt out and redistribution by ice flow. In doing so, we demonstrated *1*) the key ways in which surface debris decouples a glacier system from a climate forcing and *2*) that if debris is distributed throughout the glacier, then steady state may be unattainable for a debris-covered glacier, because melt out and redistribution of debris by ice flow cannot offset each other even under constant climate forcing. As a result, classical analysis of equilibrium glacier response to climate is unlikely to be an appropriate approach for debris-covered glaciers, even with constant climate forcing. Added to which, the expected long (and possibly multiple) timescales of debris-covered glacier response to climate forcing increase the likelihood that response time exceeds the duration of the climate forcing. Recent progress in developing and applying numerical glacier system models that capture the co-evolution of debris, ice and landscape, still contain numerous untested assumptions and increasing understanding of individual components of the system, won through detailed field investigations and remote sensing investigations, remains difficult to ingest into a coupled understanding of the whole system. While it is not realistic to represent all local features correctly, we argue that understanding the response of these glaciers in a meaningful way is likely to require "surrogate world" numerical process modeling in order to validate simpler representations. The effort to include robust treatment of the full system complexity would furthermore offer the possibility to perform *1*) the validation required for existing simplified model schemes, as well as *2*) the sensitivity testing required to develop robust, yet tractable, simplified representations of debris cover that are needed to implement the long term effect of supraglacial debris in regional and global glacier modeling.

DATA AVAILABILITY STATEMENT

The original contributions presented in the study are included in the article, further inquiries can be directed to the corresponding authors.

AUTHOR CONTRIBUTIONS

LN conceived the paper, and all authors brainstormed the scope and content of the paper together. LN prepared the manuscript and AW performed computations and prepared the figures. All authors contributed to the final version of the manuscript and the design of the schematic figures.

FUNDING

This work was supported by Austrian Science Fund (FWF) Grants V309 and P28521.

ACKNOWLEDGMENTS

Thanks to Argha Banerjee and James Ferguson for stimulating discussions on a poster version of this paper, and Alexander H. Jarosch for giving input on how to frame the paper.

REFERENCES

Adhikary, S., Nakawo, M., Seko, K., and Shakya, B. (2000). Dust Influence on the Melting Process of Glacier Ice: Experimental Results from Lirung Glacier, Nepal Himalayas. *Debris-Covered Glaciers: Proceedings of an International Workshop*. Seattle, WA: International Association of Hydrological Science, 43–52.

Anderson, L. S., and Anderson, R. S. (2016). Modeling Debris-Covered Glaciers: Response to Steady Debris Deposition. *Cryosphere* 10, 1105–1124. doi:10.5194/tc-10-1105-2016

Anderson, R. S., Anderson, L. S., Armstrong, W. H., Rossi, M. W., and Crump, S. E. (2018). Glaciation of Alpine Valleys: The Glacier - Debris-Covered Glacier - Rock Glacier Continuum. *Geomorphology* 311, 127–142. doi:10.1016/j.geomorph.2018.03.015

Anderson, L. S., Armstrong, W. H., Anderson, R. S., and Buri, P. (2021). Debris Cover and the Thinning of Kennicott Glacier, Alaska: In Situ Measurements, Automated Ice Cliff Delineation and Distributed Melt Estimates. *Cryosphere* 15, 265–282. doi:10.5194/tc-15-265-2021

Anderson, R. S. (2000). A Model of Ablation-Dominated Medial Moraines and the Generation of Debris-Mantled Glacier Snouts. *J. Glaciol.* 46, 459–469. doi:10.3189/172756500781833025

Banerjee, A., and Shankar, R. (2013). On the Response of Himalayan Glaciers to Climate Change. *J. Glaciol.* 59, 480–490. doi:10.3189/2013jog12j130

Benn, D. I., and Evans, D. J. (2010). *Glaciers and Glaciation*. Hodder Arnold Publication.

Benn, D. I., and Lehmkuhl, F. (2000). Mass Balance and Equilibrium-Line Altitudes of Glaciers in High-Mountain Environments. *Quat. Int.* 65-66, 15–29. doi:10.1016/s1040-6182(99)00034-8

Benn, D. I., and Owen, L. A. (2002). Himalayan Glacial Sedimentary Environments: A Framework for Reconstructing and Dating the Former Extent of Glaciers in High Mountains. *Quat. Int.* 97–98, 3–25. doi:10.1016/s1040-6182(02)00048-4

Benn, D. I., Warren, C. R., and Mottram, R. H. (2007). Calving Processes and the Dynamics of Calving Glaciers. *Earth Sci. Rev.* 82, 143–179. doi:10.1016/j.earscirev.2007.02.002

Benn, D. I., Bolch, T., Hands, K., Gulley, J., Luckman, A., Nicholson, L. I., et al. (2012). Response of Debris-Covered Glaciers in the Mount Everest Region to Recent Warming, and Implications for Outburst Flood Hazards. *Earth Sci. Rev.* 114, 156–174. doi:10.1016/j.earscirev.2012.03.008

Benn, D. I., Fowler, A. C., Hewitt, I., and Sevestre, H. (2019). A General Theory of Glacier Surges. *J. Glaciol.* 65, 701–716. doi:10.1017/jog.2019.62

Bennett, G. L., and Evans, D. J. A. (2012). Glacier Retreat and Landform Production on an Overdeepened Glacier Foreland: The Debris-Charged Glacial Landsystem at Kvíárjökull, Iceland. *Earth Surf. Process. Landforms* 37, 1584–1602. doi:10.1002/esp.3259

Berthier, E., and Brun, F. (2019). Karakoram Geodetic Glacier Mass Balances Between 2008 and 2016: Persistence of the Anomaly and Influence of a Large Rock Avalanche on Siachen Glacier. *J. Glaciol.* 65, 494–507. doi:10.1017/jog.2019.32

Berthier, E., Arnaud, Y., Kumar, R., Ahmad, S., Wagnon, P., and Chevallier, P. (2007). Remote Sensing Estimates of Glacier Mass Balances in the Himachal Pradesh (Western Himalaya, India). *Remote Sensing Environ.* 108, 327–338. doi:10.1016/j.rse.2006.11.017

Bolch, T., Buchroithner, M., Pieczonka, T., and Kunert, A. (2008a). Planimetric and Volumetric Glacier Changes in the Khumbu Himal, Nepal, Since 1962 Using Corona, Landsat Tm and Aster Data. *J. Glaciol.* 54, 592–600. doi:10.3189/002214308786570782

Bolch, T., Buchroithner, M. F., Peters, J., Baessler, M., and Bajracharya, S. (2008b). Identification of Glacier Motion and Potentially Dangerous Glacial Lakes in the

Mt. Everest Region/Nepal Using Spaceborne Imagery. *Nat. Hazards Earth Syst. Sci.* 8, 1329–1340. doi:10.5194/nhess-8-1329-2008

Bolch, T., Pieczonka, T., and Benn, D. I. (2011). Multi-decadal Mass Loss of Glaciers in the Everest Area (Nepal Himalaya) Derived from Stereo Imagery. *Cryosphere* 5, 349–358. doi:10.5194/tc-5-349-2011

Bueler, E., Lingle, C. S., Kallen-Brown, J. A., Covey, D. N., and Bowman, L. N. (2005). Exact Solutions and Verification of Numerical Models for Isothermal Ice Sheets. *J. Glaciol.* 51, 291–306. doi:10.3189/172756505781829449

Buri, P., and Pellicciotti, F. (2018). Aspect Controls the Survival of Ice Cliffs on Debris-Covered Glaciers. *Proc. Natl. Acad. Sci. USA* 115, 4369–4374. doi:10.1073/pnas.1713892115

Buri, P., Miles, E. S., Steiner, J. F., Immerzeel, W. W., Wagnon, P., and Pellicciotti, F. (2016). A Physically Based 3-D Model of Ice Cliff Evolution Over Debris-covered Glaciers. *J. Geophys. Res. Earth Surf.* 121, 2471–2493. doi:10.1002/2016jf004039

Clark, D. H., Clark, M. M., and Gillespie, A. R. (1994). Debris-covered Glaciers in the Sierra Nevada, California, and Their Implications for Snowline Reconstructions. *Quat. Res.* 41, 139–153. doi:10.1006/qres.1994.1016

Clarke, G. K. C., Jarosch, A. H., Anslow, F. S., Radić, V., and Menounos, B. (2015). Projected Deglaciation of Western Canada in the Twenty-First Century. *Nat. Geosci.* 8, 372–377. doi:10.1038/ngeo2407

Cogley, J., Arendt, A., Bauder, A., Braithwaite, R., Hock, R., Jansson, P., et al. (2011). "Glossary of Glacier Mass Balance and Related Terms. *IHP-VII Technical Documents in Hydrology No. 86, IACS Contribution No. 2*. Paris: UNESCO-IHP.

Collier, E., Nicholson, L., Brock, B., Maussion, F., Essery, R., and Bush, A. (2014). Representing Moisture Fluxes and Phase Changes in Glacier Debris Cover Using a Single-Reservoir Approach. *Cryosphere Discuss.* 8, 1589–1629. doi:10.5194/tc-8-1429-2014

Cuffey, K., and Paterson, W. (2010). *The Physics of Glaciers*. Academic Press.

de Frutos, J., García-Archilla, B., John, V., and Novo, J. (2014). An Adaptive SUPG Method for Evolutionary Convection-Diffusion Equations. *Comput. Methods Appl. Mech. Eng.* 273, 219–237. doi:10.1016/j.cma.2014.01.022

Deline, P., Akçar, N., Ivy-Ochs, S., and Kubik, P. W. (2015). Repeated Holocene Rock Avalanches onto the Brenva Glacier, Mont Blanc Massif, Italy: A Chronology. *Quat. Sci. Rev.* 126, 186–200. doi:10.1016/j.quascirev.2015.09.004

Deline, P. (2009). Interactions Between Rock Avalanches and Glaciers in the Mont Blanc Massif During the Late Holocene. *Quat. Sci. Rev.* 28, 1070–1083. doi:10.1016/j.quascirev.2008.09.025

Egholm, D. L., Knudsen, M. F., Clark, C. D., and Lesemann, J. E. (2011). Modeling the Flow of Glaciers in Steep Terrains: The Integrated Second-Order Shallow Ice Approximation (iSOSIA). *J. Geophys. Res. Earth Surf.* 116, F02012. doi:10.1029/2010jf001900

Eis, J., Maussion, F., and Marzeion, B. (2019). Initialization of a Global Glacier Model Based on Present-Day Glacier Geometry and Past Climate Information: An Ensemble Approach. *Cryosphere* 13, 3317–3335. doi:10.5194/tc-13-3317-2019

Evatt, G. W., Abrahams, I. D., Heil, M., Mayer, C., Kingslake, J., Mitchell, S. L., et al. (2015). Glacial Melt Under a Porous Debris Layer. *J. Glaciol.* 61, 825–836. doi:10.3189/2015jog14j235

Ferguson, J. C., and Vieli, A. (2021). Modelling Steady States and the Transient Response of Debris-Covered Glaciers. *Cryosphere* 15, 3377–3399. doi:10.5194/tc-15-3377-2021

Fernández-Fernández, J. M., Palacios, D., García-Ruiz, J. M., Andrés, N., Schimmelpfennig, I., Gómez-Villar, A., et al. (2017). Chronological and Geomorphological Investigation of Fossil Debris-covered Glaciers in Relation to Deglaciation Processes: A Case Study in the Sierra de la Demanda, Northern Spain. *Quat. Sci. Rev.* 170, 232–249. doi:10.1016/j.quascirev.2017.06.034

Fyffe, C. L., Woodget, A. S., Kirkbride, M. P., Deline, P., Westoby, M. J., and Brock, B. W. (2020). Processes at the Margins of Supraglacial Debris Cover: Quantifying Dirty Ice Ablation and Debris Redistribution. *Earth Surf. Process. Landforms* 45, 2272–2290. doi:10.1002/esp.4879

Gardelle, J., Berthier, E., and Arnaud, Y. (2012). Slight Mass Gain of Karakoram Glaciers in the Early Twenty-First Century. *Nat. Geosci.* 5, 322–325. doi:10.1038/ngeo1450

Hagg, W., Mayer, C., Lambrecht, A., and Helm, A. (2008). Sub-debris Melt Rates on Southern Inylchek Glacier, Central Tian Shan. *Geografiska Annaler: Ser. A Phys. Geogr.* 90, 55–63. doi:10.1111/j.1468-0459.2008.00333.x

Hambrey, M. J., Quincey, D. J., Glasser, N. F., Reynolds, J. M., Richardson, S. J., and Clemmens, S. (2008). Sedimentological, Geomorphological and Dynamic Context of Debris-Mantled Glaciers, Mount Everest (Sagarmatha) Region, Nepal. *Quat. Sci. Rev.* 27, 2361–2389. doi:10.1016/j.quascirev.2008.08.010

Heimsath, A. M., and McGlynn, R. (2008). Quantifying Periglacial Erosion in the Nepal High Himalaya. *Geomorphology* 97, 5–23. doi:10.1016/j.geomorph.2007.02.046

Herreid, S., and Pellicciotti, F. (2020). The State of Rock Debris Covering Earth's Glaciers. *Nat. Geosci.* 13, 621–627. doi:10.1038/s41561-020-0615-0

Hewitt, K. (2009). Rock Avalanches that Travel onto Glaciers and Related Developments, Karakoram Himalaya, Inner Asia. *Geomorphology* 103, 66–79. doi:10.1016/j.geomorph.2007.10.017

Hock, R., Bliss, A., Marzeion, B., Giesen, R. H., Hirabayashi, Y., Huss, M., et al. (2019). GlacierMIP - A Model Intercomparison of Global-Scale Glacier Mass-Balance Models and Projections. *J. Glaciol.* 65, 453–467. doi:10.1017/jog.2019.22

Huss, M. (2011). Present and Future Contribution of Glacier Storage Change to Runoff from Macroscale Drainage Basins in Europe. *Water Resour. Res.* 47, W07511. doi:10.1029/2010wr010299

Immerzeel, W. W., Van Beek, L. P. H., Konz, M., Shrestha, A. B., and Bierkens, M. F. P. (2012). Hydrological Response to Climate Change in a Glacierized Catchment in the Himalayas. *Climatic change* 110, 721–736. doi:10.1007/s10584-011-0143-4

Immerzeel, W. W., Kraaijenbrink, P. D. A., Shea, J. M., Shrestha, A. B., Pellicciotti, F., Bierkens, M. F. P., et al. (2014). High-resolution Monitoring of Himalayan Glacier Dynamics Using Unmanned Aerial Vehicles. *Remote Sensing Environ.* 150, 93–103. doi:10.1016/j.rse.2014.04.025

Irvine-Fynn, T. D., Porter, P. R., Rowan, A. V., Quincey, D. J., Gibson, M. J., Bridge, J. W., et al. (2017). Supraglacial Ponds Regulate Runoff from Himalayan Debris-Covered Glaciers. *Geophys. Res. Lett.* 44, 11–894. doi:10.1002/2017gl075398

Jansson, P., and Fredin, O. (2002). Ice Sheet Growth under Dirty Conditions: Implications of Debris Cover for Early Glaciation Advances. *Quat. Int.* 95-96, 35–42. doi:10.1016/s1040-6182(02)00025-3

Jarosch, A. H., Schoof, C. G., and Anslow, F. S. (2013). Restoring Mass Conservation to Shallow Ice Flow Models over Complex Terrain. *Cryosphere* 7, 229–240. doi:10.5194/tc-7-229-2013

Jarosch, A. H. (2008). Icetools: A Full Stokes Finite Element Model for Glaciers. *Comput. Geosci.* 34, 1005–1014. doi:10.1016/j.cageo.2007.06.012

Jouvet, G., Huss, M., Blatter, H., Picasso, M., and Rappaz, J. (2009). Numerical Simulation of Rhonegletscher from 1874 to 2100. *J. Comput. Phys.* 228, 6426–6439. doi:10.1016/j.jcp.2009.05.033

Jouvet, G., Huss, M., Funk, M., and Blatter, H. (2011). Modelling the Retreat of Grosser Aletschgletscher, Switzerland, in a Changing Climate. *J. Glaciol.* 57, 1033–1045. doi:10.3189/002214311798843359

Juen, M., Mayer, C., Lambrecht, A., Han, H., and Liu, S. (2014). Impact of Varying Debris Cover Thickness on Ablation: A Case Study for Koxkar Glacier in the Tien Shan. *Cryosphere* 8, 377–386. doi:10.5194/tc-8-377-2014

Kääb, A., Huggel, C., Fischer, L., Guex, S., Paul, F., Roer, I., et al. (2005). Remote Sensing of Glacier- and Permafrost-Related Hazards in High Mountains: An Overview. *Nat. Hazards Earth Syst. Sci.* 5, 527–554. doi:10.5194/nhess-5-527-2005

Kääb, A., Berthier, E., Nuth, C., Gardelle, J., and Arnaud, Y. (2012). Contrasting Patterns of Early Twenty-First-Century Glacier Mass Change in the Himalayas. *Nature* 488, 495–498. doi:10.1038/nature11324

Kadota, T., Seko, K., Aoki, T., Iwata, S., and Yamaguchi, S. (2000). *Shrinkage of the Khumbu Glacier, East Nepal from 1978 to 1995*. IAHS-AISH Publication, 235–243.

Kaser, G., Grosshauser, M., and Marzeion, B. (2010). Contribution Potential of Glaciers to Water Availability in Different Climate Regimes. *Proc. Natl. Acad. Sci.* 107, 20223–20227. doi:10.1073/pnas.1008162107

King, O., Bhattacharya, A., Bhambri, R., and Bolch, T. (2019). Glacial Lakes Exacerbate Himalayan Glacier Mass Loss. *Sci. Rep.* 9, 18145–18149. doi:10.1038/s41598-019-53733-x

King, O., Bhattacharya, A., Ghuffar, S., Tait, A., Guilford, S., Elmore, A. C., et al. (2020). Six Decades of Glacier Mass Changes Around Mt. Everest Are Revealed by Historical and Contemporary Images. *One Earth* 3, 608–620. doi:10.1016/j.oneear.2020.10.019

Kirkbride, M. P., and Deline, P. (2013). The Formation of Supraglacial Debris Covers by Primary Dispersal from Transverse Englacial Debris Bands. *Earth Surf. Process. Landforms* 38, 1779–1792. doi:10.1002/esp.3416

Kirkbride, M. (1989). About the Concepts of Continuum and Age. *Boreas* 18, 87–88. doi:10.1111/j.1502-3885.1989.tb00376.x

Kirkbride, M. P. (2000). "Ice-marginal Geomorphology and Holocene Expansion of Debris-Covered Tasman Glacier, New Zealand," in Debris-covered Glaciers: Proceedings of an International Workshop Held at the University of Washington in Seattle, Seattle, Washington, USA, 13–15 September, 2000 (IAHS), 211–218.

Kirkbride, M. P. (2011). "Debris-covered Glaciers," in *Encyclopedia of Snow, Ice and Glaciers*. Editors V. P. Singh, P. Singh, and U. K. Haritashya (Dordrecht: Springer Netherlands), 180–182. doi:10.1007/978-90-481-2642-2_622

Konrad, S. K., and Humphrey, N. F. (2000). "Steady-state Flow Model of Debris-Covered Glaciers (Rock Glaciers)," in Debris-covered Glaciers: Proceedings of an International Workshop Held at the University of Washington in Seattle, Seattle, Washington, USA, 13–15 September, 2000 (IAHS), 255–266.

Lambrecht, A., Mayer, C., Hagg, W., Popovnin, V., Rezepkin, A., Lomidze, N., et al. (2011). A Comparison of Glacier Melt on Debris-Covered Glaciers in the Northern and Southern Caucasus. *Cryosphere* 5, 525–538. doi:10.5194/tc-5-525-2011

Lambrecht, A., Mayer, C., Aizen, V., Floricioiu, D., and Surazakov, A. (2014). The Evolution of Fedchenko Glacier in the Pamir, Tajikistan, During the Past Eight Decades. *J. Glaciol.* 60, 233–244. doi:10.3189/2014jog13j110

Leclercq, P. W., Oerlemans, J., and Cogley, J. G. (2011). Estimating the Glacier Contribution to Sea-Level Rise for the Period 1800-2005. *Surv. Geophys.* 32, 519–535. doi:10.1007/s10712-011-9121-7

Lundstrom, S. C., McCafferty, A. E., and Coe, J. A. (1993). Photogrammetric Analysis of 1984-89 Surface Altitude Change of the Partially Debris-Covered Eliot Glacier, Mount Hood, Oregon, U.S.A. *A. Glaciol.* 17, 167–170. doi:10.1017/s0260305500012787

Mackintosh, A. N., Dugmore, A. J., and Hubbard, A. L. (2002). Holocene Climatic Changes in Iceland: Evidence from Modelling Glacier Length Fluctuations at Sólheimajökull. *Quat. Int.* 91, 39–52. doi:10.1016/s1040-6182(01)00101-x

Marzeion, B., Jarosch, A. H., and Hofer, M. (2012). Past and Future Sea-Level Change from the Surface Mass Balance of Glaciers. *Cryosphere* 6, 1295–1322. doi:10.5194/tc-6-1295-2012

Matsuoka, N., and Sakai, H. (1999). Rockfall Activity from an Alpine Cliff During Thawing Periods. *Geomorphology* 28, 309–328. doi:10.1016/s0169-555x(98)00116-0

Mattson, L., Gardner, J., and Young, G. (1993). "Ablation on Debris Covered Glaciers: An Example from the Rakhiot Glacier, Punjab, Himalaya," in Snow and Glacier Hydrology: Proceedings of the Kathmandu Symposium (IAHS), 289–296.

Maussion, F., Butenko, A., Champollion, N., Dusch, M., Eis, J., Fourteau, K., et al. (2019). The Open Global Glacier Model (OGGM) v1.1. *Geosci. Model. Dev.* 12, 909–931. doi:10.5194/gmd-12-909-2019

Mayer, C., Lambrecht, A., Belò, M., Smiraglia, C., and Diolaiuti, G. (2006). Glaciological Characteristics of the Ablation Zone of Baltoro Glacier, Karakoram, Pakistan. *Ann. Glaciol.* 43, 123–131. doi:10.3189/172756406781812087

Menounos, B., Clague, J. J., Clarke, G. K. C., Marcott, S. A., Osborn, G., Clark, P. U., et al. (2013). Did Rock Avalanche Deposits Modulate the Late Holocene Advance of Tiedemann Glacier, Southern Coast Mountains, British Columbia, Canada? *Earth Planet. Sci. Lett.* 384, 154–164. doi:10.1016/j.epsl.2013.10.008

Miles, E. S., Pellicciotti, F., Willis, I. C., Steiner, J. F., Buri, P., and Arnold, N. S. (2016). Refined Energy-Balance Modelling of a Supraglacial Pond, Langtang Khola, Nepal. *Ann. Glaciol.* 57, 29–40. doi:10.3189/2016aog71a421

Miles, K. E., Hubbard, B., Miles, E. S., Quincey, D. J., Rowan, A. V., Kirkbride, M., et al. (2021). Continuous Borehole Optical Televiewing Reveals Variable Englacial Debris Concentrations at Khumbu Glacier, Nepal. *Commun. Earth Environ.* 2, 1–9. doi:10.1038/s43247-020-00070-x

Moore, P. L. (2018). Stability of Supraglacial Debris. *Earth Surf. Process. Landforms* 43, 285–297. doi:10.1002/esp.4244

Nagai, H., Fujita, K., Nuimura, T., and Sakai, A. (2013). Southwest-facing Slopes Control the Formation of Debris-Covered Glaciers in the Bhutan Himalaya. *Cryosphere* 7, 1303–1314. doi:10.5194/tc-7-1303-2013

Naito, M., Nakawo, M., Kadoata, T., and Raymond, C. (2000). "Numerical Simulation of Recent Shrinkage of Khumbu Glacier, Nepal Himalayas," in Debris-covered Glaciers: Proceedings of an International Workshop Held at the University of Washington in Seattle, Seattle, Washington, USA, 13–15 September, 2000 (IAHS), 245–254.

Nakawo, M., and Young, G. J. (1981). Field Experiments to Determine the Effect of a Debris Layer on Ablation of Glacier Ice. *Ann. Glaciol.* 2, 85–91. doi:10.3189/172756481794352432

Nicholson, L., and Benn, D. I. (2006). Calculating Ice Melt beneath a Debris Layer Using Meteorological Data. *J. Glaciol.* 52, 463–470. doi:10.3189/172756506781828584

Nicholson, L., and Benn, D. I. (2013). Properties of Natural Supraglacial Debris in Relation to Modelling Sub-debris Ice Ablation. *Earth Surf. Process. Landforms* 38, 490–501. doi:10.1002/esp.3299

Nicholson, L., and Mertes, J. (2017). Thickness Estimation of Supraglacial Debris above Ice Cliff Exposures Using a High-Resolution Digital Surface Model Derived from Terrestrial Photography. *J. Glaciol.* 63, 989–998. doi:10.1017/jog.2017.68

Nicholson, L. I., McCarthy, M., Pritchard, H. D., and Willis, I. (2018). Supraglacial Debris Thickness Variability: Impact on Ablation and Relation to Terrain Properties. *Cryosphere* 12, 3719–3734. doi:10.5194/tc-12-3719-2018

Osmaston, H. (2005). Estimates of Glacier Equilibrium Line Altitudes by the Area×Altitude, the Area×Altitude Balance Ratio and the Area×Altitude Balance Index Methods and Their Validation. *Quat. Int.* 138-139, 22–31. doi:10.1016/j.quaint.2005.02.004

Østrem, G. (1959). Ice Melting Under a Thin Layer of Moraine, and the Existence of Ice Cores in Moraine Ridges. *Geografiska Annaler* 41, 228–230. doi:10.1080/20014422.1959.11907953

Purdie, H., Anderson, B., Mackintosh, A., and Lawson, W. (2018). Revisiting Glaciological Measurements on Haupapa/Tasman Glacier, New Zealand, in a Contemporary Context. *Geografiska Annaler: Ser. A Phys. Geogr.* 100, 351–369. doi:10.1080/04353676.2018.1522958

Quincey, D. J., Luckman, A., and Benn, D. (2009). Quantification of Everest Region Glacier Velocities Between 1992 and 2002, Using Satellite Radar Interferometry and Feature Tracking. *J. Glaciol.* 55, 596–606. doi:10.3189/002214309789470987

Quincey, D., Braun, M., Glasser, N. F., Bishop, M., Hewitt, K., and Luckman, A. (2011). Karakoram Glacier Surge Dynamics. *Geophys. Res. Lett.* 38, L18504. doi:10.1029/2011gl049004

Ragettli, S., Immerzeel, W. W., and Pellicciotti, F. (2016). Contrasting Climate Change Impact on River Flows from High-Altitude Catchments in the Himalayan and Andes Mountains. *Proc. Natl. Acad. Sci. USA* 113, 9222–9227. doi:10.1073/pnas.1606526113

Reid, T. D., and Brock, B. W. (2010). An Energy-Balance Model for Debris-Covered Glaciers Including Heat Conduction Through the Debris Layer. *J. Glaciol.* 56, 903–916. doi:10.3189/002214310794457218

Reid, T. D., and Brock, B. W. (2014). Assessing Ice-Cliff Backwasting and its Contribution to Total Ablation of Debris-Covered Miage Glacier, Mont Blanc Massif, Italy. *J. Glaciol.* 60, 3–13. doi:10.3189/2014jog13j045

Reynolds, J. M. (2000). *On the Formation of Supraglacial Lakes on Debris-Covered Glaciers*, 153–164.

Reznichenko, N., Davies, T., Shulmeister, J., and McSaveney, M. (2010). Effects of Debris on Ice-Surface Melting Rates: An Experimental Study. *J. Glaciol.* 56, 384–394. doi:10.3189/002214310792447725

Reznichenko, N. V., Davies, T. R. H., and Alexander, D. J. (2011). Effects of Rock Avalanches on Glacier Behaviour and Moraine Formation. *Geomorphology* 132, 327–338. doi:10.1016/j.geomorph.2011.05.019

Roe, G. H. (2011). What Do Glaciers Tell Us about Climate Variability and Climate Change? *J. Glaciol.* 57, 567–578. doi:10.3189/002214311796905640

Rounce, D. R., Hock, R., and Shean, D. E. (2020). Glacier Mass Change in High Mountain Asia through 2100 Using the Open-Source Python Glacier Evolution Model (PyGEM). *Front. Earth Sci.* 7, 331. doi:10.3389/feart.2019.00331

Rounce, D. R., Hock, R., McNabb, R. W., Millan, R., Sommer, C., Braun, M. H., et al. (2021). Distributed Global Debris Thickness Estimates Reveal Debris Significantly Impacts Glacier Mass Balance. *Geophys. Res. Lett.* 48, e2020GL091311. doi:10.1029/2020GL091311

Rowan, A. V., Egholm, D. L., Quincey, D. J., and Glasser, N. F. (2015). Modelling the Feedbacks Between Mass Balance, Ice Flow and Debris Transport to Predict the Response to Climate Change of Debris-Covered Glaciers in the Himalaya. *Earth Planet. Sci. Lett.* 430, 427–438. doi:10.1016/j.epsl.2015.09.004

Rowan, A. V., Nicholson, L. I., Quincey, D. J., Gibson, M. J., Irvine-Fynn, T. D. L., Watson, C. S., et al. (2021). Seasonally Stable Temperature Gradients Through Supraglacial Debris in the Everest Region of Nepal, Central Himalaya. *J. Glaciol.* 67, 170–181. doi:10.1017/jog.2020.100

Rowan, A. V. (2017). The 'Little Ice Age' in the Himalaya: A Review of Glacier advance Driven by Northern Hemisphere Temperature Change. *Holocene* 27, 292–308. doi:10.1177/0959683616658530

Sakai, A., and Fujita, K. (2010). Formation Conditions of Supraglacial Lakes on Debris-Covered Glaciers in the Himalaya. *J. Glaciol.* 56, 177–181. doi:10.3189/002214310791190785

Sakai, A., Nakawo, M., and Koji, F. (1998). Melt Rate of Ice Cliffs on the Lirung Glacier, Nepal Himalayas, 1996. *Bull. Glacier Res.* 16, 57–66.

Sakai, A., Takeuchi, N., Fujita, K., and Nakawo, M. (2000). "Role of Supraglacial Ponds in the Ablation Process of a Debris-Covered Glacier in the Nepal Himalayas," in Debris-covered Glaciers: Proceedings of an International Workshop Held at the University of Washington in Seattle, Seattle, Washington, USA, 13–15 September, 2000 (IAHS), 119–132.

Salerno, F., Thakuri, S., Tartari, G., Nuimura, T., Sunako, S., Sakai, A., et al. (2017). Debris-covered Glacier Anomaly? Morphological Factors Controlling Changes in the Mass Balance, Surface Area, Terminus Position, and Snow Line Altitude of Himalayan Glaciers. *Earth Planet. Sci. Lett.* 471, 19–31. doi:10.1016/j.epsl.2017.04.039

Scherler, D., and Egholm, D. (2020). Production and Transport of Supraglacial Debris: Insights from Cosmogenic ^{10}Be and Numerical Modeling, Chhota Shigri Glacier, Indian Himalaya. *J. Geophys. Res. Earth Surf.* 125, e2020JF005586. doi:10.1029/2020jf005586

Scherler, D., Bookhagen, B., and Strecker, M. R. (2011a). Hillslope-glacier Coupling: The Interplay of Topography and Glacial Dynamics in High Asia. *J. Geophys. Res. Earth Surf.* 116, F02019. doi:10.1029/2010jf001751

Scherler, D., Bookhagen, B., and Strecker, M. R. (2011b). Spatially Variable Response of Himalayan Glaciers to Climate Change Affected by Debris Cover. *Nat. Geosci.* 4, 156–159. doi:10.1038/ngeo1068

Scherler, D., Wulf, H., and Gorelick, N. (2018). Global Assessment of Supraglacial Debris-Cover Extents. *Geophys. Res. Lett.* 45, 11–798. doi:10.1029/2018gl080158

Scherler, D. (2014). Climatic Limits to Headwall Retreat in the Khumbu Himalaya, Eastern Nepal. *Geology* 42, 1019–1022. doi:10.1130/g35975.1

Seguinot, J., Ivy-Ochs, S., Jouvet, G., Huss, M., Funk, M., and Preusser, F. (2018). Modelling Last Glacial Cycle Ice Dynamics in the Alps. *Cryosphere* 12, 3265–3285. doi:10.5194/tc-12-3265-2018

Seong, Y. B., Owen, L. A., Caffee, M. W., Kamp, U., Bishop, M. P., Bush, A., et al. (2009). Rates of basin-wide rockwall Retreat in the K2 Region of the Central Karakoram Defined by Terrestrial Cosmogenic Nuclide 10Be. *Geomorphology* 107, 254–262. doi:10.1016/j.geomorph.2008.12.014

Shea, J. M., Immerzeel, W. W., Wagnon, P., Vincent, C., and Bajracharya, S. (2015). Modelling Glacier Change in the Everest Region, Nepal Himalaya. *Cryosphere* 9, 1105–1128. doi:10.5194/tc-9-1105-2015

Shugar, D. H., Rabus, B. T., Clague, J. J., and Capps, D. M. (2012). The Response of Black Rapids Glacier, Alaska, to the Denali Earthquake Rock Avalanches. *J. Geophys. Res. Earth Surf.* 117, F01006. doi:10.1029/2011jf002011

Shukla, A., Gupta, R. P., and Arora, M. K. (2009). Estimation of Debris Cover and its Temporal Variation Using Optical Satellite Sensor Data: A Case Study in Chenab Basin, Himalaya. *J. Glaciol.* 55, 444–452. doi:10.3189/002214309788816632

Shulmeister, J., Davies, T. R., Evans, D. J. A., Hyatt, O. M., and Tovar, D. S. (2009). Catastrophic Landslides, Glacier Behaviour and Moraine Formation - A View from an Active Plate Margin. *Quat. Sci. Rev.* 28, 1085–1096. doi:10.1016/j.quascirev.2008.11.015

Steiner, J. F., Pellicciotti, F., Buri, P., Miles, E. S., Immerzeel, W. W., and Reid, T. D. (2015). Modelling Ice-Cliff Backwasting on a Debris-Covered Glacier in the Nepalese Himalaya. *J. Glaciol.* 61, 889–907. doi:10.3189/2015jog14j194

Stokes, C. R., Popovnin, V., Aleynikov, A., Gurney, S. D., and Shahgedanova, M. (2007). Recent Glacier Retreat in the Caucasus Mountains, Russia, and Associated Increase in Supraglacial Debris Cover and Supra-/proglacial lake Development. *Ann. Glaciol.* 46, 195–203. doi:10.3189/172756407782871468

Sutherland, J., Carrivick, J., Gandy, N., Shulmeister, J., Quincey, D., and Cornford, S. (2020). Proglacial Lakes Control Glacier Geometry and Behavior during Recession. *Geophys. Res. Lett.* 47, e2020GL088865. doi:10.1029/2020gl088865

Thompson, S., Benn, D. I., Mertes, J., and Luckman, A. (2016). Stagnation and Mass Loss on a Himalayan Debris-Covered Glacier: Processes, Patterns and Rates. *J. Glaciol.* 62, 467–485. doi:10.1017/jog.2016.37

Tielidze, L. G., Bolch, T., Wheate, R. D., Kutuzov, S. S., Lavrentiev, I. I., and Zemp, M. (2020). Supra-glacial Debris Cover Changes in the Greater Caucasus from 1986 to 2014. *Cryosphere* 14, 585–598. doi:10.5194/tc-14-585-2020

Santamaria Tovar, D., Shulmeister, J., and Davies, T. R. (2008). Evidence for a Landslide Origin of New Zealand's Waiho Loop Moraine. *Nat. Geosci* 1, 524–526. doi:10.1038/ngeo249

Vacco, D. A., Alley, R. B., Pollard, D., and Reusch, D. B. (2010). Numerical Modeling of Valley Glacier Stagnation as a Paleoclimatic Indicator. *Quat. Res.* 73, 403–409. doi:10.1016/j.yqres.2009.09.006

Watanabe, O., Iwata, S., and Fushimi, H. (1986). Topographic Characteristics in the Ablation Area of the Khumbu Glacier, Nepal Himalaya. *A. Glaciol.* 8, 177–180. doi:10.1017/s0260305500001415

Watanabe, T., Ives, J. D., and Hammond, J. E. (1994). Rapid Growth of a Glacial lake in Khumbu Himal, Himalaya: Prospects for a Catastrophic Flood. *Mountain Res. Develop.* 14, 329–340. doi:10.2307/3673729

Wirbel, A., Jarosch, A. H., and Nicholson, L. (2018). Modelling Debris Transport Within Glaciers by Advection in a Full-Stokes Ice Flow Model. *Cryosphere* 12, 189–204. doi:10.5194/tc-12-189-2018

Zhang, Y., Fujita, K., Liu, S., Liu, Q., and Nuimura, T. (2011). Distribution of Debris Thickness and its Effect on Ice Melt at Hailuogou Glacier, Southeastern Tibetan Plateau, Using In Situ Surveys and ASTER Imagery. *J. Glaciol.* 57, 1147–1157. doi:10.3189/002214311798843331

Conflict of Interest: The authors declare that the research was conducted in the absence of any commercial or financial relationships that could be construed as a potential conflict of interest.

The reviewer AR declared a past co-authorship with one of the authors LN to the handling editor.

Publisher's Note: All claims expressed in this article are solely those of the authors and do not necessarily represent those of their affiliated organizations, or those of the publisher, the editors and the reviewers. Any product that may be evaluated in this article, or claim that may be made by its manufacturer, is not guaranteed or endorsed by the publisher.

frontiers in Earth Science

ORIGINAL RESEARCH
published: 23 December 2021
doi: 10.3389/feart.2021.748107

Spatiotemporal Dynamics and Geodetic Mass Changes of Glaciers With Varying Debris Cover in the Pangong Region of Trans-Himalayan Ladakh, India Between 1990 and 2019

Ulfat Majeed[1], *Irfan Rashid*[1]*, *Nadeem Ahmad Najar*[1] and *Nafeeza Gul*[2]

[1]Department of Geoinformatics, University of Kashmir, Srinagar, India, [2]Department of Earth Sciences, University of Kashmir, Srinagar, India

Glaciers across the Himalayan arc are showing varying signs of recession. Glaciers in the eastern and western parts of the Himalayan arc are retreating more rapidly as compared to other regions. This differential retreat is often attributed to climatic, topographic, and geologic influences. The glaciers in the Trans-Himalayan region of Ladakh are believed to be relatively stable as compared to other parts of the western Himalaya. The present study ascertained the area changes and frontal retreat of 87 glaciers in the Pangong Region between 1990 and 2019 using satellite data. The geodetic mass changes were also assessed using SRTM and TanDEM-X digital elevation models of 2000 and 2012 respectively. Besides, the glacier outlines were delineated manually and compared with existing regional and global glacier inventories that are available over the region. The GlabTop model was used to simulate the glacier-bed overdeepenings of four glaciers that are associated with a proglacial lake. The study also analyzed the impact of topographic influences and varying debris cover on glacier recession. This analysis indicated deglaciation of 6.7 ± 0.1% (0.23% a^{-1}) from 1990 to 2019 over the Pangong Region with clean-ice glaciers showing a higher retreat (8.4 ± 0.28%) compared to the debris-covered glaciers (5.7 ± 0.14%). However, the overall recession is lower compared to other parts of northwestern Himalayas. The glacier recession showed a positive correlation with mean glacier slope (r = 0.3) and debris cover (r = 0.1) with bigger size glaciers having retreated at a lesser pace compared to smaller ones. This underpins the need for *in-situ* data about debris thickness to precisely ascertain the role of debris on glacier recession in the Trans-Himalayan Ladakh where debris thickness data is absent. The mean glacier elevation did not indicate any influence on glacier recession. From 2000 to 12, the glaciers lost an ice mass amounting to 0.33 ± 0.05 m we. per year. The formation of four new proglacial lakes, although small (<6 ha), need to be monitored using remote sensing data while the infrastructure development activities should not be permitted given glacial lake outburst flood risk.

Keywords: glacier recession, geodetic mass changes, glacier inventories, remote sensing, pangong lake, ladakh himalaya

OPEN ACCESS

Edited by:
Aparna Shukla,
Ministry of Earth Sciences, India

Reviewed by:
Martin Truffer,
University of Alaska Fairbanks, United States
Atanu Bhattacharya,
University of Zurich, Switzerland

***Correspondence:**
Irfan Rashid
irfangis@gmail.com
irfangis@kashmiruniversity.ac.in

Specialty section:
This article was submitted to Cryospheric Sciences, a section of the journal Frontiers in Earth Science

Received: *28 July 2021*
Accepted: *22 November 2021*
Published: *23 December 2021*

Citation:
Majeed U, Rashid I, Najar NA and Gul N (2021) Spatiotemporal Dynamics and Geodetic Mass Changes of Glaciers With Varying Debris Cover in the Pangong Region of Trans-Himalayan Ladakh, India Between 1990 and 2019. Front. Earth Sci. 9:748107. doi: 10.3389/feart.2021.748107

INTRODUCTION

Glaciers are important indicators of climate change (Haeberli and Hoelzle, 1995; Roe, 2011) and have significant impacts on water availability (Immerzeel et al., 2009). Changes in the glacier extent (Bolch et al., 2012; Kulkarni and Karyakarte, 2014; Rashid et al., 2017) and mass (Brun et al., 2017; Bandyopadhyay et al., 2019) have been very well documented in many parts of the Himalayas, but comparatively little attention has been paid to glacier monitoring in the Ladakh Region (Chudley et al., 2017; Schmidt and Nüsser, 2017), which besides being at a high altitude happens to be a rain-shadow region (Abdullah et al., 2020). For these reasons, it is also known as a cold desert (Romshoo et al., 2020). Owing to the remoteness of the area (Azam et al., 2018), there is only one field-based glaciological study (Soheb et al., 2020) that reported a negative mass balance of the neighbouring Stok Glacier between 1978 and 2019.

Remote sensing data products have been widely used to monitor the alpine cryosphere (Dar et al., 2014; Pratibha and Kulkarni, 2018; Chand and Watanabe, 2019; Liu et al., 2019; Sujakhu et al., 2019). Various approaches include automatic classification (Paul et al., 2002, 2004; Zhang et al., 2019; Lu et al., 2020), semi-automatic classification (Shukla et al., 2010; Rastner et al., 2014; Sahu and Gupta, 2018; Robson et al., 2020), object-based image algorithms, and manual digitization (Ye et al., 2006; Bhambri et al., 2011; Rashid and Majeed, 2020) have been widely used by remote sensing glaciologists. Manual digitization has been documented to be the most reliable since it takes the cognitive inputs from the analyst (Paul et al., 2013), however, it is time-consuming and subjective to the skill of the analyst. Besides areal changes, remote sensing has a capacity to map volumetric changes; the most important being the DEM products that are mostly stereo-products (Cogley, 2009; Gaddam et al., 2021). Owing to the lack of field data, rugged topography, and remote locations, the geodetic mass change assessments offer the easiest choice to estimate volume changes. However, such estimates are associated with uncertainties, which need to be quantified for reporting an accurate estimate.

While glacier recession is primarily attributed to atmospheric warming (Wang et al., 2017; Cook et al., 2019) and an increase in the anthropogenic footprint in the glacier and peri-glacier environments (Wang et al., 2019; Huggel et al., 2020), there could be several topographic and geological factors (Garg et al., 2017; Patel et al., 2018) that could affect glacier health. The variable debris cover on the glaciers could be a controlling factor (Barrand and Murray, 2006; Shukla and Qadir, 2016; Salerno et al., 2017), however, a recent study on the Karakoram (Muhammad et al., 2020) negates the role of thin debris cover on glacier recession.

The long-term records of the hydro-meteorological data are almost absent, which hampers quantifying any historic changes in the glaciers of the region. Although the use of gridded climate datasets for glaciohydrological assessments has been documented (Bhattacharya et al., 2021), such datasets need bias correction (Hussain et al., 2017; Kanda et al., 2020). The prevalent warming temperatures over the western Himalayas aid in glacier recession and also result in the formation of numerous proglacial lakes and expansion of already existing ones (Worni et al., 2013; Wang et al., 2015). These lakes are growing in both area and number (Nie et al., 2017; Rashid and Majeed, 2018). One of the most dangerous hazards that these proglacial lakes pose is that of a glacial lake outburst flood (Vuichard and Zimmermann, 1987; Liu et al., 2013; Allen et al., 2019). This calls for increased attention, as they can prove to be fatal in case of a sudden outburst. There are just a few studies (Govindha Raj, 2010; Mir et al., 2018; Rashid and Majeed, 2018) of these proglacial lakes in the region. This necessitates a need for continuous monitoring and detailed risk assessment for precisely quantifying the risk that these lakes pose to the downstream communities and infrastructure. To our knowledge, there is only one detailed study that reconstructed a GLOF event in the Ladakh region (Majeed et al., 2021). The receding glaciers and the damming of water behind the moraines could alter the hydrological regimes (Singh and Bengtsson, 2004; Immerzeel et al., 2010, 2012) in the region and cause water availability issues (Miller et al., 2012). This could have serious implications on the socio-economy of the region and threaten food security (Misra, 2014; Bocchiola et al., 2019).

This study aims to map the glaciers of the Pangong region, Trans-Himalaya Ladakh. Multi-temporal satellite datasets were used to assess the area changes and frontal retreat of the glaciers in the region. A qualitative comparison was carried out by comparing the glacier outlines delineated in this study with three existing global and regional glacier inventories. The topographic characteristics and debris cover were correlated with glacier area changes. The geodetic mass changes were quantified using multi-date DEMs of 2000 and 2012. In addition, the GlabTop model was used to simulate the proglacial lake expansion utilizing information about glacier bed overdeepenings.

STUDY AREA

This study focused on the glaciers of the Pangong Mountain Range (PMR), in the northern region of Ladakh. The PMR runs parallel to the Ladakh Range (Godwin-Austen, 1867) ~100 km northwest from Chushul. The highest elevation in the range is 6,700 m and the northern slopes are heavily glaciated. This area is situated on the left bank of Pangong Lake but lies at an elevation of 1,400 m above the lake. Pangong Lake is an endorheic lake in the Himalayas (Rathour et al., 2020) situated at a height of about 4,350 m. It is 134 km long and extends from India to China. Approximately 60% of the length of the lake lies in China. The lake is 5 km wide at its broadest point and covers a total area of 604 km^2. Geographically, it is not a part of the Indus River basin area and is a separate land-locked river basin without any outlet. While the total area of the watershed is 844 km^2, the glaciated area is ~60 km^2 which amounts to a total of just ~7%. There are a total of 87 glaciers with a cumulative area of 59.45 ± 6.86 km^2 as mapped from satellite data of 1990. These glaciers are relatively small with an average size of 0.8 km^2. The smallest glacier has an

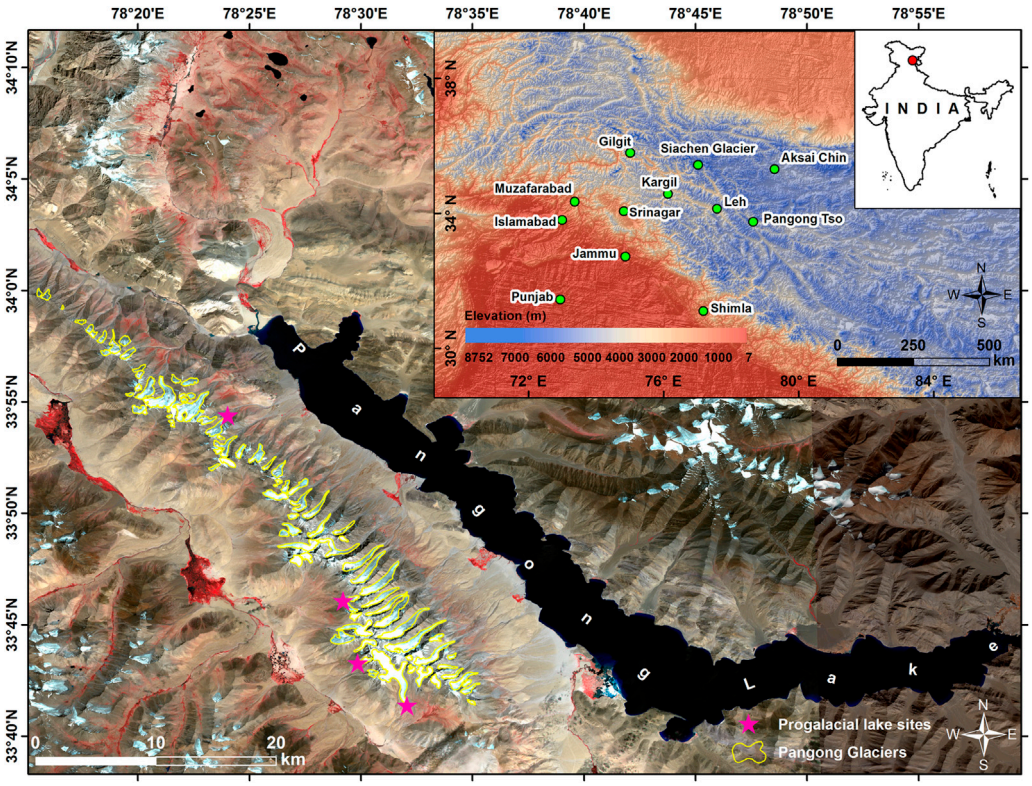

FIGURE 1 | Location of the study area. Glaciers (yellow outlines) and proglacial lakes (pink stars) of the Pangong Mountain Range draped on the Sentinel 2A image (August 28, 2017). Inset image: Major locations around Pangong Region draped on 30-arc second GTOPO DEM. Red dot in the India map indicates Pangong Region.

TABLE 1 | Details of the datasets used in this study.

Dataset	Scene/product/path and row ID	Spatial resolution (m)	Date of acquisition	Source	Usage of datasets
Satellite data					
Landsat TM	LT05_L1TP_146,037_19900802_20170129_01_T1	30	August 02, 1990	http://www.earthexplorer.usgs.gov	Boundary delineation (1990)
Planet labs	20190919_052142_83_1066_3B_AnalyticMS.tif 20190919_051248_1,105_3B_AnalyticMS.tif 20190919_051246_1,105_3B_AnalyticMS.tif 20190919_051247_1,105_3B_AnalyticMS.tif 20190919_035516_1,020_3B_AnalyticMS.tif 20190919_035515_1,020_3B_AnalyticMS.tif 20190919_035514_1,020_3B_AnalyticMS.tif	3	September 19, 2019	https://www.planet.com/	Boundary delineation (2019)/Glacier dynamics, debris mapping, proglacial lake mapping
Topographic data					
SRTM	SRTM3N33E078V1 SRTM3N34E078V1	30	February 2000	http://www.earthexplorer.usgs.gov	Geodetic mass balance, topographic characterization
TanDEM-X	N33E078 N34E078	90	2012	https://download.geopservice.dlr.de/TDM90/	Geodetic mass balance
ALOS	AP_08149_FBD_F0660_RT1	12.5	2011	https://asf.alaska.edu/	GlabTop analysis

area of 0.29 ± 0.01 km^2 while the largest has an area of 4.31 ± 0.35 km^2. Most of the glaciers are debris-covered. The watershed lies between latitudes 33°36′ N—34°2′ N and longitudes 78°14′ E—78°39′ E (**Figure 1**). The mean elevation of the watershed is 5,109 m. The summers are mild, while the winters are extreme in the region (Srivastava

et al., 2020). The lake freezes completely in winters. Pangong receives winter precipitation mostly by Mediterranean influences.

MATERIALS AND METHODS

Data

A repository of satellite data and DEMs were used to carry out this study. The snow-free images from 1990 to 2019 were used for areal changes of the glaciers while two different DEMs were used for quantifying the mass changes. The details of these datasets are provided in **Table 1**.

Methods

Glacier Changes

The standard geometric correction (Jensen, 2005) was used to coregister the images. The images from 1990 to 2019 were coregistered to arrive at an accuracy of one pixel. The glaciers were manually digitized at a scale of 1:30,000. Mountain shadows, cloud cover, and debris cover limit the accuracy of the glacier mapping. However, alternate images from ±2 years were used to overcome this. All the glacier boundaries were validated using high-resolution Google Earth data. Proglacial lakes are also mapped from the same images. The precision of the glacier boundary delineation is within half a pixel (Bolch et al., 2010; Paul et al., 2013). For the 1990s outlines, we assumed a mapping inaccuracy of half a pixel (~15 m) for Landsat TM data and one pixel (~3 m) for Planet Cubesat data (Pieczonka and Bolch, 2015; Bhattacharya et al., 2016).

The uncertainties related to the area changes (E_{AC}) was calculated considering the law of error propagation as (Hall et al., 2003):

$$E_{AC} = \sqrt{E_{A1}^2 + E_{A2}^2} \quad (1)$$

where E_{AC} is the uncertainty related to the change in the area between two time periods, E_{A1} is the uncertainty of glacier area at one point in time and E_{A2} is the uncertainty of glacier area at the second point in time.

The uncertainties related to snout changes between two times (E_{SC}) is given by the following formula (Hall et al., 2003):

$$E_{SC} = \sqrt{\lambda_1^2 + \lambda_2^2} \quad (2)$$

where E_{SC} is the uncertainty in snout change, λ1 and λ2 are the spatial resolutions of the two images used for calculating the snout changes.

Glacier Debris and Topographic Parameters

The supraglacial debris was manually delineated from the high-resolution Planet Cubesat images for the year 2019. Besides high-resolution Google Earth imagery was used to validate the debris cover. The topographic parameters that include slope, elevation, and southerly aspect of the glaciers were estimated using TanDEM-X in a GIS environment. The topographic parameters and debris cover were co-related with glacier recession rates to arrive at trends.

Geodetic Mass Balance

The glaciological method to estimate mass loss is a challenging task given the costs involved and also the remoteness of glaciers (Rashid et al., 2021). Many glaciers in the Jammu and Kashmir region are inaccessible for direct measurements due to the ruggedness of the terrain (Immerzeel et al., 2009; Bolch et al., 2019). It is pertinent to mention that long-term glaciological mass balance measurements in the trans-Himalayan region of Ladakh do not exist, however, there have been some initiatives very recently that attempt to establish long-term field-based glacial mass balance records in Stok Kangri (Soheb et al., 2020) and Zanskar regions (Mehta et al., 2021). On the contrary, the geodetic mass balance assessment is a quick method to access mass losses in the glaciers. It simply involves the DEMs of two times and differencing to arrive at thickness changes (Braithwaite, 2002). This thickness change can be converted to corresponding mass loss using

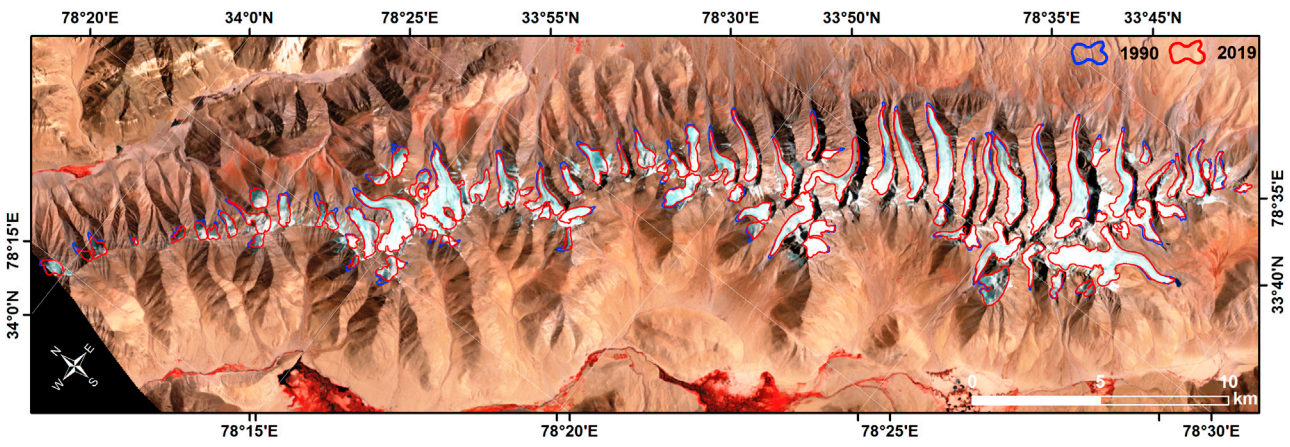

FIGURE 2 | Area changes and frontal retreat of Pangong group of glaciers from 1990 to 2019. Background image: Sentinel 2A of August 28, 2017.

TABLE 2 | Area and frontal changes of Pangong Group of glaciers from 1990 to 2019.

GLIMS id	T.S id	Area 1990 (ha)	Area 2019 (ha)	Debris 2019 (ha)	Area change (2019–1990)	Snout change (m)	M.G.E	Aspect	Frontal slope(°)	Overall slope(°)	Mean surface lowering (ma^{-1})
G33706E78579N	1	21.92	19.16	0	−2.76	−135	5914	NE	16	22.4	0.11
G33708E78575N	2	86.31	79.04	7.28	−7.27	−80	6234	NE	19	17.8	0.29
G33712E78568N	3	38.78	37.93	0.25	−0.85	−108	6286	N	16.8	21	0.14
G33708E78556N	4	46.03	40.31	0	−5.72	−54	5906	SE	17.8	28.9	0.52
G33717E78538N	5	20.5	20.62	0	0.12	−4	5963	SE	19.5	25.7	0.26
G33715E78523N	6	357.5	353.43	0.82	−4.07	−150	5898	SE	13.2	17.6	0.43
G33736E78504N	7	51.64	50.75	1.12	−0.89	−26	6012	W	11.8	23.3	0.25
G33723E78503N	8	35.89	31.67	3.3	−4.22	−200	5746	W	21.7	25.9	0.69
G33758E78524N	9	169.26	166.45	0.85	−2.81	−57	5849	NE	11.5	15.3	0.50
G33763E78492N	10	30.08	28.14	0	−1.95	−106	6072	N	14.5	24.6	0.42
G33764E78519N	11	91.42	83.23	3.58	−8.19	−57	5863	NE	13.8	17.2	0.46
G33771E78515N	12	98.76	94.09	1.32	−4.67	−106	5838	NE	12.6	15.2	0.62
G33782E78514N	13	194.31	180.08	1.03	−14.23	−148	6155	NE	14.8	15.1	0.48
G33797E78499N	14	125.07	125.53	0.71	0.46	−110	5818	NE	6.5	13.8	0.45
G33809E78456N	15	119.32	117.29	0	−2.03	−9	6141	SW	13.8	18	0.21
G33807E78481N	16	124.8	119.94	5.55	−4.85	−98	6244	E	10.7	17.1	0.45
G33821E78487N	17	45.37	41.75	0.72	−3.62	−128	6534	NE	17.5	26.2	0.49
G33822E78449N	18	60.48	56.85	0	−3.63	−100	5740	N	17.4	19.6	0.36
G33831E78449N	19	28.09	23.8	0	−4.29	−60	5969	W	14.3	20	0.17
G33837E78466N	20	83.31	78.52	4.39	−4.79	−48	6007	NE	16.3	18.4	0.45
G33870E78431N	21	27.06	24.25	8.02	−2.81	−143	5953	NW	11.7	19.3	0.61
G33877E78423N	22	79.26	72.51	3.12	−6.75	−283	5692	NW	17.1	23	0.44
G33880E78410N	23	42.63	35.98	0	−6.66	−110	5846	NE	14.1	18.2	0.35
G33897E78392N	24	97.72	92.19	20.9	−5.53	−372	5764	NW	18.5	23.9	0.45
G33912E78372N	25	255.96	243.44	8.13	−12.52	−56	5802	NE	16	17.8	0.52
G33920E78352N	26	241.82	233.28	2.22	−8.55	−136	5659	N	17.3	19.4	0.38
G33926E78341N	27	110.71	105.75	0	−4.96	−60	6039	NW	21.1	24.1	0.25
G33900E78359N	28	9.14	7.46	0	−1.68	−100	6068	SE	30.3	39	0.69
G33918E78368N	29	13.34	11.86	0	−1.47	−156	6000	N	15.5	22.8	0.55
G33921E78371N	30	36.63	31.68	0.31	−4.95	−42	6055	NE	25.9	25.2	0.78
G33726E78568N	31	19.49	16.05	0	−3.44	0	5997	N	19.8	22.3	0.28
G33911E78356N	32	6.27	5.66	0	−0.6	−148	5960	SW	18.6	18.2	0.20
G33903E78384N	33	51.47	51.83	0	0.36	−64	5742	NE	16.6	22.8	0.48
G33713E78546N	34	97.75	86.03	0	−11.72	−56	5777	S	15.3	19.5	0.26
G33757E78496N	35	33.49	28.53	0	−4.95	−192	6000	SW	28.6	29.4	0.14
G33725E78536N	36	13.37	12.67	0	−0.7	−557	6096	E	32.3	32.3	0.17
G33883E78398N	37	91.91	84.74	3.59	−7.17	−53	6098	NE	10.4	16.9	0.71
G33853E78444N	38	39.44	31.23	0.96	−8.21	−108	6059	NE	18.2	27.6	0.28
G33853E78454N	39	65.88	59.72	0	−6.15	−171	6187	NE	18.4	20.9	0.24
G33748E78531N	40	195.02	182.93	3.78	−12.1	−225	6107	NE	13.3	13.8	0.40
G33791E78505N	41	148.19	143.79	0.63	−4.4	−95	6197	NE	12.1	13.6	0.58
G33842E78455N	42	89.87	82.32	0.55	−7.54	−60	6093	NE	11	19	0.45
G33747E78498N	43	129.21	125.83	0	−3.38	−148	6016	SW	15.2	14.1	0.25
G33847E78436N	44	89.01	81.47	0	−7.54	−170	6055	NW	18.6	20.8	0.07
G33719E78564N	45	30.68	29.34	1.08	−1.35	−79	6025	NE	16.7	22.5	0.28
G33727E78553N	46	127.14	120.37	0	−6.77	−174	5997	N	13.8	16.9	0.22
G33865E78438N	47	62.05	58.47	0	−3.58	−82	5959	NE	13	26.5	0.51
G33872E78401N	48	45.44	42.98	0.6	−2.47	−92	6099	NE	14.8	16.6	0.24
G33737E78537N	49	210.9	206.95	2.04	−3.95	−50	6053	NE	9.9	14	0.26
G33822E78468N	50	59.37	57.62	0.54	−1.76	−63	5800	NW	7.7	19.6	0.30
G33953E78326N	51	52.16	45.26	1.28	−6.9	−86	5867	N	19.4	22.9	0.34
G33958E78316N	52	66.01	61.76	0.5	−4.25	−61	5811	N	11.3	30.5	0.32
G33965E78307N	53	34.31	30.46	1.62	−3.85	−230	5793	NE	21.8	28.6	0.37
G34005E78247N	54	40.41	37.51	0.2	−2.9	−434	5814	NW	28.3	28.3	0.03
G33937E78335N	55	28.65	23.97	0	−4.67	−65	5773	E	18.8	24.3	0.50
G33942E78335N	56	31.56	23.7	0.71	−7.86	−356	5925	NE	23.9	30.9	0.77
G33933E78361N	57	26.62	24.21	0	−2.41	−57	5763	N	25.7	31.5	0.09
G33932E78372N	58	56.48	47.92	0	−8.56	−178	5834	N	28.2	28.6	0.50
G33962E78323N	59	46.51	44.43	0	−2.08	−178	5798	N	29.2	30.5	0.19
G33971E78297N	60	27.63	22.98	1.1	−4.65	−63	5745	N	26.5	31.9	0.17
G33996E78265N	61	37.29	31.16	2.76	−6.14	−178	5907	NE	29.5	38.5	0.46

(Continued on following page)

TABLE 2 | (*Continued*) Area and frontal changes of Pangong Group of glaciers from 1990 to 2019.

GLIMS id	T.S id	Area 1990 (ha)	Area 2019 (ha)	Debris 2019 (ha)	Area change (2019–1990)	Snout change (m)	M.G.E	Aspect	Frontal slope(°)	Overall slope(°)	Mean surface lowering (ma^{-1})
G33740E78486N	62	112.54	106.79	0	−5.75	−254	5949	NW	26.4	35.7	0.27
G33740E78557N	63	36.65	34.18	0	−2.47	−202	5880	NE	32.4	30.4	0.37
G33819E78442N	64	32.75	27.98	0	−4.76	−202	5763	NW	31	34.8	0.13
G33814E78487N	65	16.9	15.91	0	−0.99	−35	5870	E	25.7	34.4	0.72
G33857E78438N	66	13.51	11.06	0	−2.44	−122	6133	E	29.1	35.4	0.47
G33880E78393N	67	15.71	15.21	0	−0.5	−58	5917	NE	15.8	31.7	0.48
G33967E78300N	68	19.29	17.01	0.5	−2.28	−77	5710	NE	31.8	32.5	0.60
G33977E78291N	69	20.46	17.6	0	−2.86	−280	5905	N	27.2	34.4	0.28
G33987E78277N	70	4.79	3.49	0	−1.3	−62	5722	NE	24.5	35.1	0.45
G33998E78260N	71	19.42	14.63	1.18	−4.79	−310	5820	N	31.2	40	0.23
G33954E78309N	72	24.42	21.62	0	−2.8	−70	5802	NW	32.9	34.7	0.01
G33909E78339N	73	8.9	8.37	0	−0.53	−172	5878	SE	30	40.9	0.58
G33906E78357N	74	8.61	6.71	0	−1.89	−148	5736	W	29	28.2	0.03
G33854E78436N	75	6.56	3.7	0	−2.86	−60	5889	NW	10.2	25.6	0.00
G33798E78452N	76	50.97	49.36	0	−1.61	−24	5645	S	39.9	39	0.58
G33801E78459N	77	41.65	40.09	0	−1.56	−43	5775	E	13.6	33.2	0.43
G33714E78509N	78	31.19	28.74	0	−2.45	−20	5773	NW	23.1	34.8	0.13
G33692E78583N	79	13.12	11.51	0	−1.61	−258	5727	E	25.3	26.4	0.31
G33868E78390N	80	21.15	17.56	0	−3.59	−14	5773	W	23.9	35.5	0.04
G33890E78395N	81	10.78	10.21	4.06	−0.56	−52	5647	NE	29.8	33.7	0.39
G33927E78334N	82	18.98	17.14	0	−1.84	−170	5731	E	29.4	32.2	0.60
G33922E78327N	83	14.48	10.18	0	−4.29	−136	5875	NW	30.4	39.8	0.45
G33702E78581N	84	48.14	41.49	0.92	−6.65	−41	6170	NE	18.3	29.9	0.36
G33911E78334N	85	55.56	46.44	0	−9.12	−98	5716	NW	19.7	31.8	0.09
G33770E78494N	86	26.11	22.55	0	−3.56	−70	5613	W	18.2	19.3	0.29
G33902E78358N	87	10.06	7.99	0	−2.07	−229	5931	W	28.4	30.4	0.16

glacier area and density assumptions (Cogley, 2009; Muhammad et al., 2019; Rashid and Majeed, 2020). For quantifying the geodetic mass changes over the Pangong region, SRTM C band DEM of 2000 and TanDEM-X of 2012 were used. A correction factor of 3.4 m for SRTM C band penetration in glacier ice was used as suggested by Gardelle et al. (2013). TanDEM-X is a stacked product with data acquired over multiple seasons/years. Hence, a uniform radar penetration is unlikely. The potential radar penetration of the X band was ignored due to its high frequency and non-uniform penetration across different seasons (Huber et al., 2020). The DEMs were coregistered using the universal co-registration algorithm (Nuth and Kääb, 2011). Further, the outliers in the off-glacier (**Supplementary Figure S1**) and on-glacier elevation (**Supplementary Figure S3**) were identified and removed using the inter-quartile range approach suggested by Barbato et al. (2011) and adopted by Huber et al. (2020). The DEM differencing results were interpolated using Inverse Distance Weighted (IDW) algorithm over the voided areas (13.49%) of SRTM DEM. The elevation-dependent outliers in the on-glacier DEM difference image were ignored since the glaciers lie in a homogenous topographic zone (Mean glacier elevation: 5,613–6,534 m asl).

The uncertainty in geodetic mass balance (∇M) related to glacier area (A), ice density (ρ) assumed to be 850 ± 60 kg m^{-3}, and surface elevation change (h) is expressed as (Ramsankaran et al., 2019):

$$\frac{\nabla M}{M} = \sqrt{\left(\frac{\nabla \overline{dh}}{dh}\right)^2 + \left(\frac{\nabla \rho_{ice}}{\rho_{ice}}\right)^2 + \left(\frac{\nabla A}{A}\right)^2} \quad (3)$$

where ∇ represents the uncertainty in estimates.

The uncertainty in elevation change ($\sigma_{\Delta h}$) is calculated based on the following formula Huber et al. (2020):

$$\sigma_{\Delta H} = \sqrt{\sigma_{dem}^2 + \sigma_{void\,fill}^2 + \sigma_{TDXdate}^2} \quad (4)$$

where σ_{em} is the uncertainty in DEM, $\sigma_{voidfill}$ is the uncertainty introduced by the void-filling approach, and $\sigma_{TDXdate}$ is the date uncertainty of TanDEM-X and estimated to be ± 2 times the change of elevation per year. The uncertainty in the void filling was assumed negligible since the observed and predicted values for non-voided areas showed an insignificant bias (0.02 m).

The σ_{dem} was calculated after the approach suggested by McNabb et al. (2019) as:

$$\sigma_{dem} = \frac{\sqrt{(\sigma_{\Delta z}\, A)^2 + (\sigma_{area}\, \Delta z)^2}}{A} \quad (5)$$

where $\sigma_{\Delta z}$ is the mean of glacier difference between the two DEMs after coregistration, A is the glacier area, σ_{area} is the uncertainty in glacier area and ΔZ is the mean elevation difference of on-glacier pixels.

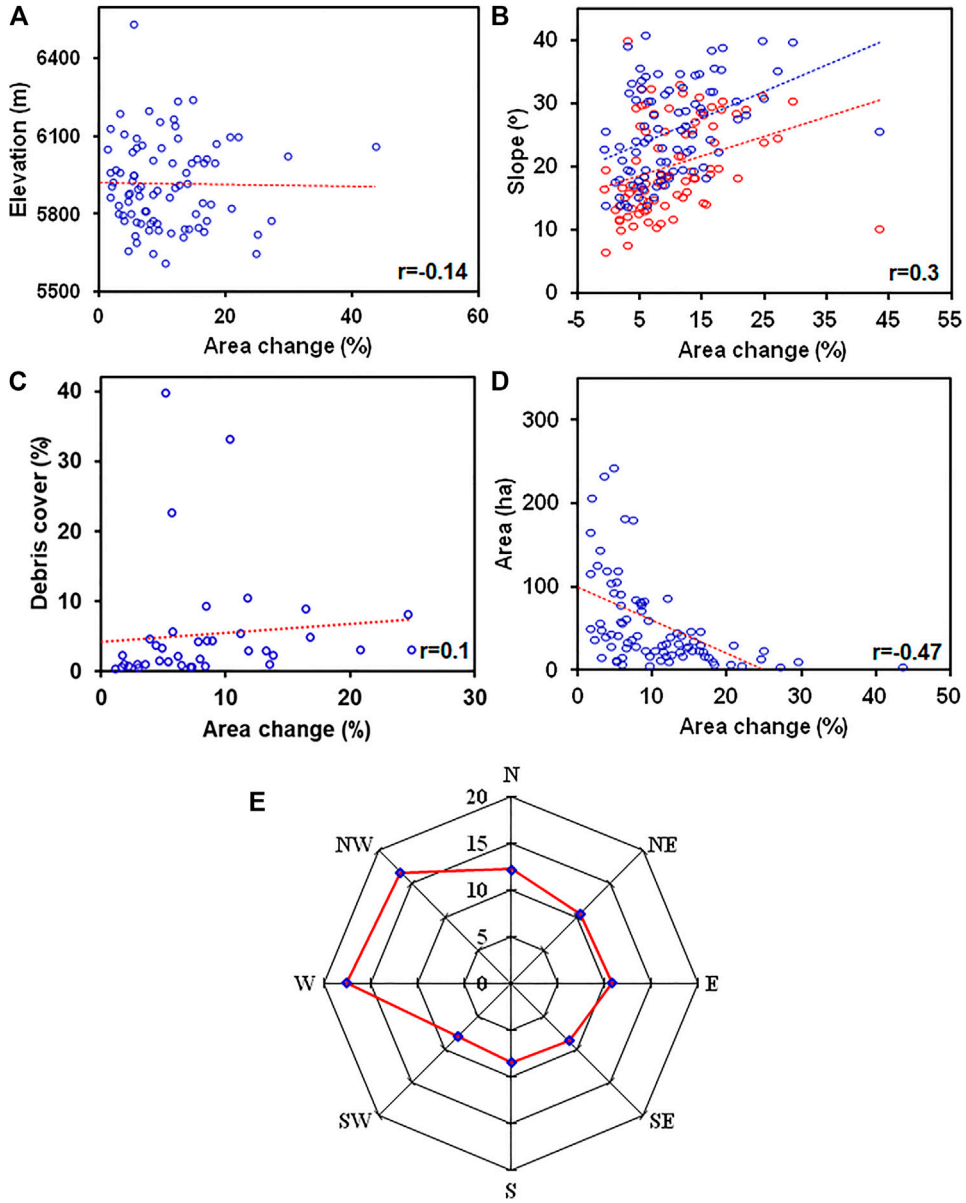

FIGURE 3 | Correlation of glacier area changes with **(A)** Mean glacier elevation, **(B)** Mean glacier slope, **(C)** Debris cover, **(D)** Glacier area, and **(E)** Slope-aspect.

Glacier Bed Overdeepenings

Glacier-bed overdeepenings and ice thickness were estimated for four glaciers associated with proglacial lakes in the Pangong region using the GlabTop model to check the possibility of expansion of existing proglacial lakes in the future. The input parameters to the model are glacier outlines, DEM, and the glacier flowlines. In this study, the glacier outlines and flowlines were manually delineated from the satellite data and also using a 3D perspective from Google Earth. The glacier bed overdeepenings were modeled using glacier outlines and flowlines and ALOS PALSAR DEM. The model has been extensively used for predicting ice thickness and glacier bed overdeepenings in the Himalayas with an uncertainty of 30% (Linsbauer et al., 2016; Rashid and Majeed, 2020; Sattar et al., 2021), however, the uncertainty in the ice thickness estimates could be reduced to 17% using better quality DEMs and improved shape factor (Ramsankaran et al., 2018; Majeed et al., 2021). The model assumes constant basal stress along the central flowline of a glacier (Linsbauer et al., 2012) and quantifies ice-thickness using a slope-dependent approach (Haeberli and Hoelzle, 1995).

Comparison With Existing Glacier Inventories

The various glacier inventories available for this region include the Randolph Glacier Inventory (RGI), Glacier Area Mapping for Discharge from the Asian Mountains (GAMDAM), and

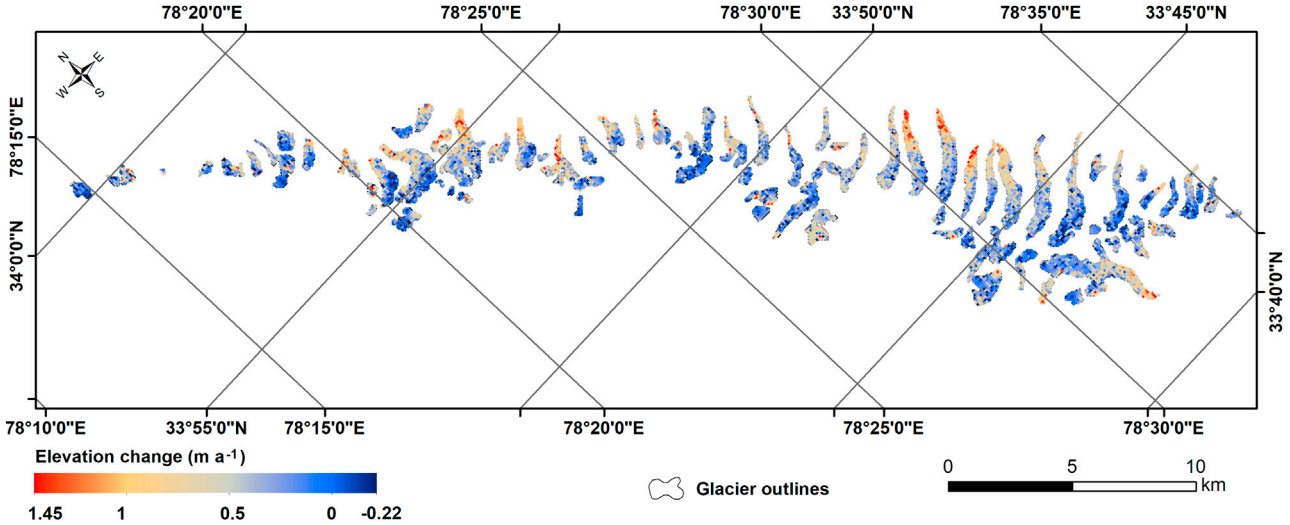

FIGURE 4 | Geodetic mass changes of glaciers in Pangong region from 2000–2012.

International Council for Integrated Mountain Development (ICIMOD) Glacier Inventories. A comparative analysis is made between these inventories and the glacier inventory generated in this study.

RESULTS

Glacier Area and Frontal Changes

Satellite data revealed a total of 87 glaciers in the study area covering an area of 54.8 ± 2.53 km^2 in 1990. The glacier cover reduced to 51.1 ± 1.03 km^2 by 2019 indicating a 6.7 ± 0.1% area loss at a rate of 0.23% a^{-1} (**Figure 2**; **Table 2**). While the clean-ice glaciers retreated by 8.4 ± 0.28% (1.6 km^2), the debris-covered glaciers lost 5.7 ± 0.14% (2.03 km^2) at a rate of 0.29% a^{-1} and 0.2% a^{-1} respectively. The glacier size varies between 3.5 and 353.4 ha with an average size of 58.8 ha. The snout recession, with an uncertainty of ± 30.1 m, varied between 0 m (GLIMS Id G33717E78538N) to 557 m (GLIMS Id G33725E78536N) at an average of 126 m (4.3 m a^{-1}).

The mean glacier elevation for all the glaciers is more than 5,600 m asl ranging from 5,613 m asl to 6,534 m asl. Analysis of glacier area changes does not show any significant correlation (r = -0.14) with the mean glacier elevation (**Figure 3A**). The mean glacier slope varied between 13.6° and 40.9°. The mean glacier slope showed a positive correlation (r = 0.3) with glacier recession (**Figure 3B**) which was further researched by ascertaining the frontal slope of each glacier. The frontal slope was calculated for the 400 m area from the snout of each glacier. The mean frontal slope for the glaciers of the Pangong Region varied between 6.5° and 39.9°. The frontal slope also showed a similar positive correlation (r = 0.31) with glacier recession.

Based on the debris cover, the glaciers were categorized into clean-ice and debris-covered glaciers (**Figure 3C**). This analysis indicated 48 (~55%) out of 87 glaciers were clean-ice glaciers and 39 (45%) were debris-covered with debris-cover varying from 0.2–39.8%. This analysis indicated that glacier recession has a slightly positive correlation with debris cover (r = 0.1) which needs to be further investigated. The glacier area showed an inverse relation (r = -0.47) with glacier recession (**Figure 3D**) indicating smaller glaciers recede faster than larger ones. Moreover, the role of slope-aspect was correlated with glacier recession (**Figure 3E**). Analysis of slope-aspect indicated that glaciers having west and northwest-facing slopes lose area slightly faster compared to south-facing glaciers.

Geodetic Mass Balance

DEM differencing indicated that the Pangong group of glaciers, on average, lost 4.59 ± 0.64 m at a rate of 0.38 ± 0.05 m a^{-1} between 2000 and 2012 with the highest thickness loss of 1.45 m a^{-1} and the highest gain of 0.22 m a^{-1} (**Figure 4**). While the surface of clean-ice glaciers lowered by 0.28 m a^{-1} the ice loss for debris-covered glaciers was estimated to be 0.43 m a^{-1}. Glacier-wise the highest mean surface lowering of 0.78 m a^{-1} was observed in TS ID 30 (GLIMS ID G33921E78371N) and the highest surface gain of 0.002 m a^{-1} was observed for TS ID 75 (GLIMS ID G33854E78436N). The mass loss corresponding to surface lowering for these glaciers is calculated to be 199.48 Mt from 2000 to 2012. This is indicative of ice loss at the rate of 16.62 Mt a^{-1}. The equivalent water loss is estimated to be 3.9 ± 0.54 m we. at a rate of 0.33 m w. e. per year. For clean-ice glaciers, the estimated equivalent water loss is 0.24 m we. per year. However, for debris-covered glaciers, the equivalent water loss is 0.37 m we. per year.

Glacier Thickness and Bed Overdeepenings

Out of the total 87 glaciers mapped in the Pangong Region, four glaciers (GLIMS ID: G33715E78523N, G33723E78503N,

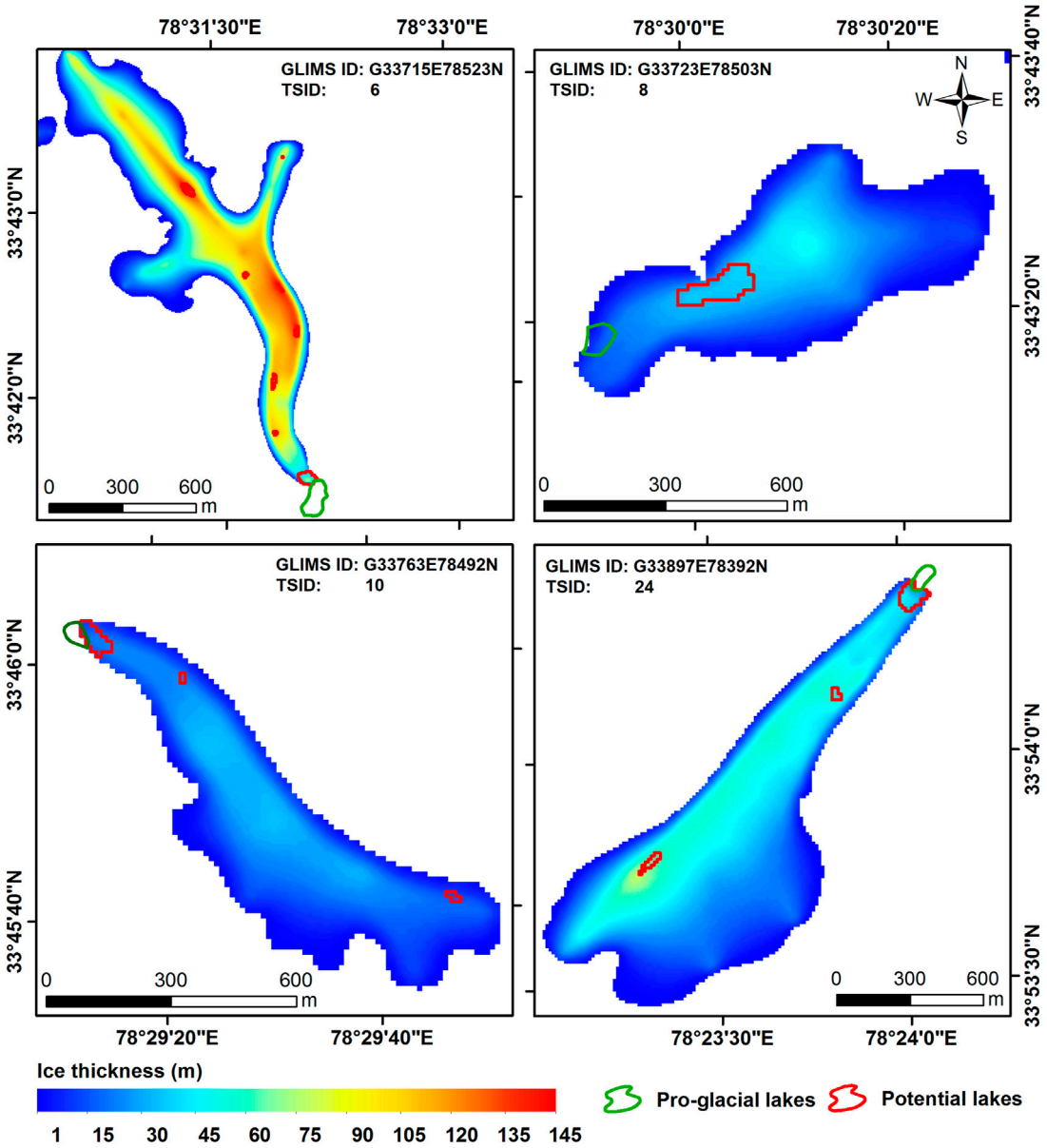

FIGURE 5 | GlabTop model simulations indicating ice-thickness and glacier-bed overdeepenings.

G33763E78492N, and G33897E78392N) are associated with a proglacial lake. These lakes have an area of 5.74 ± 0.16 ha, 0.42 ± 0.04 ha, 0.23 ± 0.03 ha and 0.56 ± 0.05 ha, respectively, GlabTop model analysis simulated a mean glacier ice thickness of 58 m with a maximum and minimum thickness of 1 and 145 m, respectively (**Figure 5**). It further indicated that the proglacial lake associated with G33715E78523N can further grow by 1.72 ha reaching a maximum area of 7.46 ha. The model suggests the formation of eight additional glacier bed overdeepenings for the glacier most of which lie in the upper ablation zone with areas less than a hectare. For G33723E78503N the ice thickness varies between 1 and 48 m with a mean thickness of 19 m. The model does not simulate any expansion of the proglacial lake, however, it predicted the formation of a new lake with an area of 1.06 ha around the middle of the ablation zone of the glacier. For G33763E78492N the ice thickness varies between 1 and 34 m with a mean of 17 m. The model predicted expansion of the existing proglacial lake by 0.36 ha reaching a maximum area of 0.59 ha. The model indicated the formation of two more bed overdeepenings with an area of 0.03 and 0.06 ha in

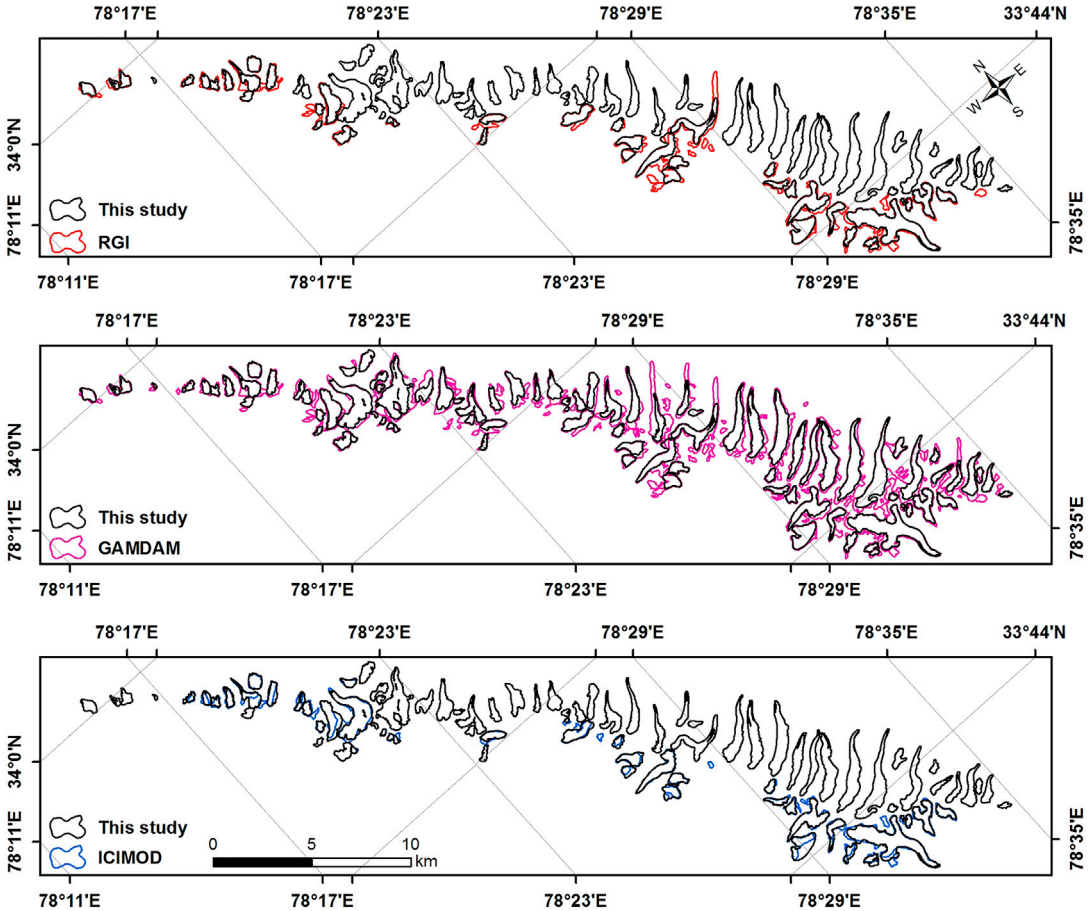

FIGURE 6 | Comparison of glacier outlines delineated in this study with Randolph Glacier Inventory (RGI), GAMDAM glacier inventory, and ICIMOD glacier inventory.

the upper ablation zone. For G33897E78392N the ice thickness varies between 1 and 75 m with a mean of 31 m. The model pointed to the expansion of the existing proglacial lake by 0.87 ha reaching a maximum area of 1.43 ha. Further, the model predicted three additional bed overdeepenings in the upper ablation zone.

Comparison With Existing Glacier Inventories

There is a huge uncertainty concerning the total number of glaciers in the Himalayas (Bolch et al., 2012; Azam et al., 2021), the objective of comparison of existing global and regional inventories was made with the inventory generated in this study. Of the three glacier inventories—CIMOD, GAMDAM, and RGI—available for the region, GAMDAM glacier inventory captured all the glaciers that were delineated in this study (**Figure 6**; **Table 3**). The total number of glaciers in the GAMDAM inventory for the Pangong Region is 132 which cover an area of 72.7 km^2 indicating an overestimation by 51% (45 glaciers) in the number of glaciers and 42.3% (21.6 km^2) in glacier area. The smallest glacier area mapped in this study has an area of 3.49 ha compared to 1.03 ha mapped in the GAMDAM inventory. Similarly, the largest glacier area mapped in this study is 353.4 ha compared to 418.5 ha in GAMDAM. The other two inventories, ICIMOD and RGI, grossly underestimate the total number of glaciers and total glacier area in the Pangong Region. The ICIMOD glacier inventory suggests 44 glaciers spread over 19.9 km^2 indicating an underestimation of 49.4% (43 glaciers) total number of glaciers and 61.1% (31.3 km^2) in the glacier area. The RGI suggests 50 glaciers spread over 26.6 km^2 indicating an underestimation of 42.5% (37 glaciers) total number of glaciers and 61.1% (24.6 km^2) in the glacier area.

DISCUSSION

This analysis indicated that the glaciers in Pangong Region have been retreating like the other glaciated basins in northwestern Himalaya. However, the rate of retreat is lower since the study

TABLE 3 | Comparison of the present inventory (TS) with the existing inventories (RGI, ICIMOD and GAMDAM).

GLIMS ID	Area (ha)				TS-RGI	TS-ICIMOD	TS-GAMDAM
	RGI	ICIMOD	GAMDAM	This Study (TS)			
G33987E78277N	NA	NA	3.19	3.49	X	X	0.30
G33854E78436N	NA	7.44	4.27	3.70	X	−3.74	−0.57
G33911E78356N	NA	NA	4.89	5.66	X	X	0.77
G33906E78357N	NA	NA	10.41	6.71	X	X	−3.70
G33900E78359N	NA	12.83	NA	7.46	X	−5.36	X
G33902E78358N	15.02	8.17	15.02	7.99	−7.03	−0.18	−7.03
G33909E78339N	NA	7.23	NA	8.37	X	1.14	X
G33922E78327N	43.2	NA	43.25	10.18	−33.01	X	−33.07
G33890E78395N	NA	NA	9.83	10.21	X	X	0.38
G33857E78438N	NA	NA	17.66	11.06	X	X	−6.60
G33692E78583N	NA	NA	11.67	11.51	X	X	−0.16
G33918E78368N	NA	NA	12.59	11.86	X	X	−0.73
G33725E78536N	NA	NA	11.91	12.67	X	X	0.76
G33998E78260N	24.44	NA	24.44	14.63	−9.81	X	−9.81
G33880E78393N	NA	NA	NA	15.21	X	X	X
G33814E78487N	NA	NA	15.13	15.91	X	X	0.78
G33726E78568N	NA	NA	27.74	16.05	X	X	−11.69
G33967E78300N	20.51	16	20.51	17.01	−3.49	1.01	−3.50
G33927E78334N	43.25	18.14	43.25	17.14	−26.11	−1.00	−26.11
G33868E78390N	21.6	NA	21.6	17.56	−4.04	X	−4.04
G33977E78291N	20	10.39	20	17.60	−2.40	7.21	−2.40
G33706E78579N	NA	NA	14.03	19.16	X	X	5.13
G33717E78538N	20.85	22.89	20.85	20.62	−0.23	−2.27	−0.23
G33954E78309N	21.11	NA	21.11	21.62	0.51	X	0.51
G33770E78494N	29	25.67	35.5	22.55	−6.45	−3.11	−12.95
G33971E78297N	31.47	17.59	31.47	22.98	−8.49	5.39	−8.49
G33942E78335N	NA	21.68	NA	23.70	X	2.02	X
G33831E78449N	29.7	13.25	31.41	23.80	−5.89	10.55	−7.61
G33937E78335N	NA	28.5	70.89	23.97	X	−4.53	−46.92
G33933E78361N	NA	24.33	25.06	24.21	X	−0.12	−0.85
G33870E78431N	NA	NA	47.53	24.25	X	X	−23.28
G33819E78442N	28.6	12.68	28.6	27.98	−0.61	15.30	−0.62
G33763E78492N	44.51	27.6	48.21	28.14	−16.37	0.54	−20.07
G33757E78496N	29.81	32.29	29.81	28.53	−1.27	−3.75	−1.28
G33714E78509N	48.12	18.9	38.02	28.74	−19.38	9.84	−9.28
G33719E78564N	NA	NA	58.34	29.34	X	X	−29.00
G33965E78307N	37.28	33.42	37.28	30.46	−6.82	−2.96	−6.82
G33996E78265N	35.5	NA	35.5	31.16	−4.34	X	−4.34
G33853E78444N	NA	NA	45.32	31.23	X	X	−14.09
G33723E78503N	41.27	23.8	41.27	31.67	−9.60	7.87	−9.60
G33921E78371N	NA	NA	42.56	31.68	X	X	−10.88
G33740E78557N	NA	NA	34.39	34.18	X	X	−0.21
G33880E78410N	NA	NA	66	35.98	X	X	−30.02
G34005E78247N	44.18	NA	44.18	37.51	−6.67	X	−6.67
G33712E78568N	NA	NA	86.01	37.93	X	X	−48.08
G33801E78459N	40.08	34.75	38.12	40.09	0.01	5.34	1.97
G33708E78556N	42.68	42.86	42.68	40.31	−2.37	−2.55	−2.37
G33702E78581N	NA	NA	44.78	41.49	X	X	−3.29
G33821E78487N	NA	NA	79.55	41.75	X	X	−37.80
G33872E78401N	59.74	49.38	59.74	42.98	−16.76	−6.40	−16.76
G33962E78323N	43.48	40.82	43.48	44.43	0.95	3.61	0.95
G33953E78326N	68.57	41.2	68.57	45.26	−23.31	4.06	−23.31
G33911E78334N	61.73	NA	61.73	46.44	−15.29	X	−15.29
G33932E78372N	NA	NA	50.64	47.92	X	X	−2.72
G33798E78452N	48.41	36.2	45.8	49.36	0.95	13.16	3.56
G33736E78504N	68.83	58.62	73.76	50.75	−18.08	−7.87	−23.01
G33903E78384N	NA	NA	95.94	51.83	X	X	−44.11
G33822E78449N	76.21	52.2	76.21	56.85	−19.36	4.64	−19.36
G33822E78468N	NA	NA	189.54	57.62	X	X	−131.92
G33865E78438N	NA	NA	82.82	58.47	X	X	−24.35
G33853E78454N	NA	NA	87.39	59.72	X	X	−27.67
G33958E78316N	94.55	31.4	89.36	61.76	−32.79	30.36	−27.60
G33877E78423N	NA	NA	95.11	72.51	X	X	−22.60

(Continued on following page)

TABLE 3 | (*Continued*) Comparison of the present inventory (TS) with the existing inventories (RGI, ICIMOD and GAMDAM).

GLIMS ID	Area (ha)				TS-RGI	TS-ICIMOD	TS-GAMDAM
	RGI	ICIMOD	GAMDAM	This Study (TS)			
G33837E78466N	NA	NA	110.28	78.52	X	X	−31.76
G33708E78575N	NA	NA	112.74	79.04	X	X	−33.70
G33847E78436N	99.5	77.08	99.51	81.47	−18.03	4.39	−18.04
G33842E78455N	NA	NA	127.82	82.32	X	X	−45.50
G33764E78519N	NA	NA	342.11	83.23	X	X	−258.88
G33883E78398N	NA	NA	139.96	84.74	X	X	−55.22
G33713E78546N	102.16	96.13	102.16	86.03	−16.13	−10.10	−16.13
G33897E78392N	NA	NA	140.23	92.19	X	X	−48.04
G33771E78515N	NA	NA	126.69	94.09	X	X	−32.60
G33926E78341N	126.01	74.03	126.23	105.75	−20.26	31.72	−20.48
G33740E78486N	112.47	54.33	112.47	106.79	−5.68	52.46	−5.68
G33809E78456N	161.37	118.4	117.28	117.29	−44.08	−1.11	0.00
G33807E78481N	190.62	NA	193.66	119.94	−70.68	X	−73.72
G33727E78553N	NA	NA	192.75	120.37	X	X	−72.38
G33797E78499N	NA	NA	190.88	125.53	X	X	−65.35
G33747E78498N	170.56	143.82	173.61	125.83	−44.73	−17.97	−47.78
G33791E78505N	NA	NA	201.91	143.79	X	X	−58.12
G33758E78524N	NA	NA	342.11	166.45	X	X	−175.66
G33782E78514N	NA	NA	240.01	180.08	X	X	−59.93
G33748E78531N	NA	NA	255.31	182.93	X	X	−72.39
G33737E78537N	NA	NA	306.17	206.95	X	X	−99.22
G33920E78352N	NA	242.96	281.62	233.28	X	−9.68	−48.34
G33912E78372N	NA	NA	325.47	243.44	X	X	−82.03
G33715E78523N	399.63	358.08	418.51	353.43	−46.19	−4.65	−65.08

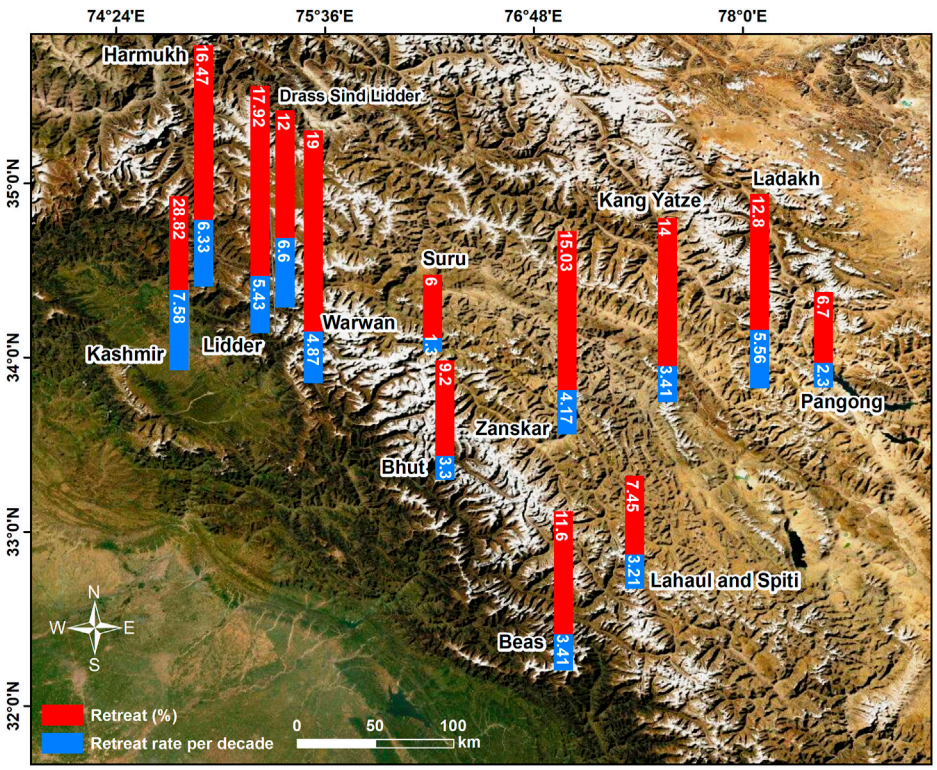

FIGURE 7 | Comparison of glacier retreat of Pangong region with neighbouring areas in western Himalaya. Red bar indicates total loss (as %) and blue bar indicates loss per decade (as %).

area is located in the *Trans*-Himalayan Ladakh region-a rain shadow area (Raj and Sharma, 2013; Kumar et al., 2017). Based on the existing knowledge and compared to other Trans-Himalayan glaciated regions, the area experienced the second-lowest retreat (**Figure 7**, **Supplementary Table S1**). The frontal changes of glaciers in the Pangong Region, also on the lower side, are consistent with the previously documented studies over the region (Majeed et al., 2021).

The glacier recession in Pangong was correlated with topographic parameters and debris cover to better understand the influence of these parameters on glacier melt. This analysis indicated that the mean glacier elevation does not have any impact on the recession at higher elevations. It is pertinent to mention that the mean glacier elevation of the Pangong group of glaciers lies above ~5,600 m asl. Analysis of mean glacier slope shows a positive correlation with glacier recession. This anomalous behavior was further analyzed by taking into consideration the frontal slope of each glacier which was generally flatter than the mean glacier slope indicating that the glaciers with flatter frontal slopes retreated faster. Analysis of debris cover indicated a weak positive correlation with glacier melt. Although there are no *in-situ* debris thickness data the visual analysis generally indicated a thin debris layer on the Pangong group of glaciers. It is pertinent to mention that Muhammad et al. (2020) also suggested that the thin debris layers do not influence the melting of glaciers in the high-altitude Karakoram. Glacier area showed a negative correlation with glacier recession which has been established by many previous studies (Ceballos et al., 2006; Debnath et al., 2019; Zhao et al., 2020).

While this analysis indicated that the Pangong group of glaciers thinned at a rate of 0.38 ± 0.05 m a^{-1} between 2000 and 2012, Abdullah et al. (2020) report a similar retreat of 0.46 m a^{-1} for the Pangong region. The uncertainty estimates of surface lowering and mass change in this study are higher given the fact that the ice loss is lower. Some other mass balance studies over the region suggest comparatively lesser mass changes. For instance, a study by Brun et al. (2017), who used ASTER stereo pairs for estimating the mass changes of the glaciers, suggested a loss of ~0.5 m a^{-1} of glacier ice. A relatively older study by Kääb et al. (2012) also puts the ice loss estimate for this region at ~0.5 m a^{-1}. Vijay and Braun (2018) have put up similar estimates for the glaciers located towards the eastern part of the Pangong region. The differences in the ice loss estimates could be a manifestation of the different DEMs, analysis techniques and the time period for which the mass changes were estimated.

GlabTop model simulations indicate that out of the four glaciers associated with a proglacial lake, three lakes could expand. While the proglacial lake associated with G33723E78503N might not expand, there is a formation of a 1.06 ha lake in the midst of the ablation zone also evident on satellite data and Google Earth imagery of August 2013 and June 2016. It is pertinent to mention that the model has been tested in different glaciated regions of the European Alps (Linsbauer et al., 2012; Magnin et al., 2020) and Himalayas (Linsbauer et al., 2016; Pandit and Ramsankaran, 2020) including Trans-Himalayan Ladakh (Rashid and Majeed, 2018; Majeed et al., 2021) for ice-thickness and glacier-bed overdeepenings. Given the prevailing glacier melt scenario over the seismically-active Jammu and Kashmir region, the development of new proglacial lakes and the formation of already existing ones would pose a significant glacial lake outburst (GLOF) risk to the downstream communities and infrastructure. Studies indicate that there have already been a few incidences of GLOF (Schmidt et al., 2020) and cloudburst (Kumar et al., 2012) in the Trans-Himalayan Ladakh.

Another important aspect of this study was to compare the glacier inventory generated in this study with the existing global and regional inventories. This analysis indicated that only the GAMDAM glacier inventory captured all the glaciers that were delineated in the current effort. This could be attributed to the fact that while ICIMOD and RGI inventories have been synthesized by automatic and semiautomatic methods, the glaciers in GAMDAM inventory have been delineated manually which allows for cognitive inputs from the analyst, unlike automated methods. The overestimation in both area and number of glaciers in GAMDAM glacier inventory could be attributed to the mapping of smaller seasonal or perennial snowpacks without any proper ablation and accumulation zones having been delineated as glaciers in the region.

CONCLUSION

This analysis utilized remote sensed data including satellite images and DEMs to quantify glacier recession, frontal retreat, and geodetic mass changes of the Pangong group of glaciers in Trans-Himalayan Ladakh. Satellite data analysis revealed that the glaciers retreated conservatively at 0.23% per year between 1990 and 2019 as compared to other regions of the western Himalaya. The geodetic mass change estimates for the selected glaciers indicated a surface lowering of 0.38 ± 0.05 m a^{-1}. While clean-ice and debris-covered glaciers respectively lost 8.4 and 5.7% of the area, the surface lowering was more for debris-covered glaciers (0.43 m a^{-1}) compared to clean-ice glaciers (0.28 m a^{-1}). However, this needs to be researched further through extensive ground surveys aimed at collecting debris thickness measurements in the study area. It is pertinent to mention that debris-thickness measurements are absent in Trans-Himalayan Ladakh and scanty in the Indian Himalaya. Further, glacier recession was correlated with topographic parameters and debris cover which indicated that mean glacier elevation does not influence recession patterns in the Pangong region owing to the relatively higher elevation of glaciers (~5,600 asl) in the study area. There is an inverse relation between glacier size and recession which has been widely reported in previous studies. The mean glacier slope showed a positive correlation with glacier recession indicating that the glaciers with flatter tongues are retreating faster compared to steeper ones. The glacier outlines mapped manually in this study were compared with the existing three regional/global glacier inventories (ICIMOD, GAMDAM,

and RGI). Although GAMDAM glacier inventory captured most of the glaciers it overestimated the glacier area and number owing to the fact that smaller snowpacks were delineated as glaciers. The GlabTop model simulations indicated expansion of three proglacial lakes and formation of a new periglacial lake which could be potential lake outburst hotspots given that the region is experiencing a temperature warming scenario and the glaciers lie in a seismically active area. There is a potential for catastrophic glacial floods and any infrastructure development in the downstream areas should not proceed without a detailed land-use plan.

DATA AVAILABILITY STATEMENT

The raw data supporting the conclusion of this article will be made available by the authors, without undue reservation.

AUTHOR CONTRIBUTIONS

IR conceptualized and designed the study. UM, IR, NN, and NG performed data analysis. IR wrote the first draft of the manuscript. UM and NN wrote sections of the manuscript. All authors contributed to manuscript revision, read, and approved the submitted version.

ACKNOWLEDGMENTS

The authors are thankful to USGS for making the Landsat data freely available to users. The authors also express gratitude to Andreas Linsbauer, University of Zurich for providing the GlabTop model. The first author also acknowledges the support of Department of Science and Technology, Government of India (DST, GoI) for INSPIRE fellowship (Grant Number: IF180682) for pursuing Ph.D. The comments and suggestions from the two reviewers greatly improved the manuscript structure and content.

SUPPLEMENTARY MATERIAL

The Supplementary Material for this article can be found online at: https://www.frontiersin.org/articles/10.3389/feart.2021.748107/full#supplementary-material

REFERENCES

Abdullah, T., Romshoo, S. A., and Rashid, I. (2020). The Satellite Observed Glacier Mass Changes over the Upper Indus Basin during 2000-2012. *Sci. Rep.* 10, 14285. doi:10.1038/s41598-020-71281-7

Allen, S. K., Zhang, G., Wang, W., Yao, T., and Bolch, T. (2019). Potentially Dangerous Glacial Lakes across the Tibetan Plateau Revealed Using a Large-Scale Automated Assessment Approach. *Sci. Bull.* 64, 435–445. doi:10.1016/j.scib.2019.03.011

Azam, M. F., Kargel, J. S., Shea, J. M., Nepal, S., Haritashya, U. K., Srivastava, S., et al. (2021). Glaciohydrology of the Himalaya-Karakoram. *Science* 373, eabf3668. doi:10.1126/SCIENCE.ABF3668

Azam, M. F., Wagnon, P., Berthier, E., Vincent, C., Fujita, K., and Kargel, J. S. (2018). Review of the Status and Mass Changes of Himalayan-Karakoram Glaciers. *J. Glaciol.* 64, 61–74. doi:10.1017/jog.2017.86

Bandyopadhyay, D., Singh, G., and Kulkarni, A. V. (2019). Spatial Distribution of Decadal Ice-Thickness Change and Glacier Stored Water Loss in the Upper Ganga basin, India during 2000-2014. *Sci. Rep.* 9, 16730. doi:10.1038/s41598-019-53055-y

Barbato, G., Barini, E. M., Genta, G., and Levi, R. (2011). Features and performance of some outlier detection methods. *J. Appl. Stat.* 38, 2133–2149. doi:10.1080/02664763.2010.545119

Barrand, N. E., and Murray, T. (2006). Multivariate Controls on the Incidence of Glacier Surging in the Karakoram Himalaya. *Arctic, Antarctic, Alpine Res.* 38, 489–498. doi:10.1657/1523-0430(2006)38[489:mcotio]2.0.co;2

Bhambri, R., Bolch, T., and Chaujar, R. K. (2011). Mapping of Debris-Covered Glaciers in the Garhwal Himalayas Using ASTER DEMs and thermal Data. *Int. J. Remote Sensing* 32, 8095–8119. doi:10.1080/01431161.2010.532821

Bhattacharya, A., Bolch, T., Mukherjee, K., King, O., Menounos, B., Kapitsa, V., et al. (2021). High Mountain Asian Glacier Response to Climate Revealed by Multi-Temporal Satellite Observations since the 1960s. *Nat. Commun.* 12, 4133. doi:10.1038/s41467-021-24180-y

Bhattacharya, A., Bolch, T., Mukherjee, K., Pieczonka, T., Kropáček, J., and Buchroithner, M. F. (2016). Overall Recession and Mass Budget of Gangotri Glacier, Garhwal Himalayas, from 1965 to 2015 Using Remote Sensing Data. *J. Glaciol.* 62 (236), 1115–1133. doi:10.1017/jog.2016.96

Bocchiola, D., Brunetti, L., Soncini, A., Polinelli, F., and Gianinetto, M. (2019). Impact of Climate Change on Agricultural Productivity and Food Security in the Himalayas: A Case Study in Nepal. *Agric. Syst.* 171, 113–125. doi:10.1016/j.agsy.2019.01.008

Bolch, T., Kulkarni, A., Kääb, A., Huggel, C., Paul, F., Cogley, J. G., et al. (2012). The State and Fate of Himalayan Glaciers. *Science* 336, 310–314. doi:10.1126/science.1215828

Bolch, T., Menounos, B., and Wheate, R. (2010). Landsat-based Inventory of Glaciers in Western Canada, 1985-2005. *Remote Sensing Environ.* 114, 127–137. doi:10.1016/j.rse.2009.08.015

Bolch, T., Shea, J. M., Liu, S., Azam, F. M., Gao, Y., Gruber, S., et al. (2019). "Status and Change of the Cryosphere in the Extended Hindu Kush Himalaya Region," in *The Hindu Kush Himalaya Assessment* (Springer International Publishing), 209–255. doi:10.1007/978-3-319-92288-1_7

Braithwaite, R. J. (2002). Glacier Mass Balance: The First 50 Years of International Monitoring. *Prog. Phys. Geogr. Earth Environ.* 26, 76–95. doi:10.1191/0309133302pp326ra

Brun, F., Berthier, E., Wagnon, P., Kääb, A., and Treichler, D. (2017). A Spatially Resolved Estimate of High Mountain Asia Glacier Mass Balances from 2000 to 2016. *Nat. Geosci* 10, 668–673. doi:10.1038/ngeo2999

Ceballos, J. L., Euscátegui, C., Ramírez, J., Cañon, M., Huggel, C., Haeberli, W., et al. (2006). Fast Shrinkage of Tropical Glaciers in Colombia. *Ann. Glaciol.* 43, 194–201. doi:10.3189/172756406781812429

Chand, M. B., and Watanabe, T. (2019). Development of Supraglacial Ponds in the Everest Region, Nepal, between 1989 and 2018. *Remote Sensing* 11, 1058. doi:10.3390/rs11091058

Chudley, T. R., Miles, E. S., and Willis, I. C. (2017). Glacier Characteristics and Retreat between 1991 and 2014 in the Ladakh Range, Jammu and Kashmir. *Remote Sensing Lett.* 8, 518–527. doi:10.1080/2150704X.2017.1295480

Cook, A. J., Copland, L., Noël, B. P. Y., Stokes, C. R., Bentley, M. J., Sharp, M. J., et al. (2019). Atmospheric Forcing of Rapid marine-terminating Glacier Retreat in the Canadian Arctic Archipelago. *Sci. Adv.* 5, eaau8507. doi:10.1126/sciadv.aau8507

Dar, R. A., Rashid, I., Romshoo, S. A., and Marazi, A. (2014). Sustainability of winter Tourism in a Changing Climate over Kashmir Himalaya. *Environ. Monit. Assess.* 186, 2549–2562. doi:10.1007/s10661-013-3559-7

Debnath, M., Sharma, M. C., and Syiemlieh, H. J. (2019). Glacier Dynamics in Changme Khangpu Basin, Sikkim Himalaya, India, between 1975 and 2016. *Geosciences* 9, 259. doi:10.3390/GEOSCIENCES9060259

Gaddam, V. K., Kulkarni, A. V., Bjornsson, H., Gullapalli, S., and Ballina, M. (2021). Applications of SPOT-7 Tri-stereo Imagery in Deriving the Surface Topography and Mass Changes of Glaciers in Indian Himalaya. *Geocarto Int.* 36 (13), 1512–1532. doi:10.1080/10106049.2019.1648567

Gardelle, J., Berthier, E., Arnaud, Y., and Kääb, A. (2013). Region-wide Glacier Mass Balances over the Pamir-Karakoram-Himalaya during 1999-2011. *The Cryosphere* 7 (4), 1263–1286. doi:10.5194/tc-7-1263-2013

Garg, P. K., Shukla, A., and Jasrotia, A. S. (2017). Influence of Topography on Glacier Changes in the central Himalaya, India. *Glob. Planet. Change* 155, 196–212. doi:10.1016/j.gloplacha.2017.07.007

Godwin-Austen, H. H. (1867). Notes on the Pangong lake District of Ladakh, from a Journal Made during a Survey in 1863. *J. R. Geographical Soc. Lond.* 37, 343–363. doi:10.2307/1798534

Govindha Raj, K. B. (2010). Remote Sensing Based hazard Assessment of Glacial Lakes: a Case Study in Zanskar basin, Jammu and Kashmir, India. *Geomatics, Nat. Hazards Risk* 1, 339–347. doi:10.1080/19475705.2010.532973

Graham Cogley, J. (2009). Geodetic and Direct Mass-Balance Measurements: Comparison and Joint Analysis. *Ann. Glaciol.* 50, 96–100. doi:10.3189/172756409787769744

Haeberli, W., and Hoelzle, M. (1995). Application of Inventory Data for Estimating Characteristics of and Regional Climate-Change Effects on Mountain Glaciers: a Pilot Study with the European Alps. *Ann. Glaciol.* 21, 206–212. doi:10.3189/s0260305500015834

Hall, D. K., Bayr, K. J., Schöner, W., Bindschadler, R. A., and Chien, J. Y. L. (2003). Consideration of the Errors Inherent in Mapping Historical Glacier Positions in Austria from the Ground and Space (1893-2001). *Remote Sensing Environ.* 86, 566–577. doi:10.1016/S0034-4257(03)00134-2

Huber, J., McNabb, R., and Zemp, M. (2020). Elevation Changes of West-central Greenland Glaciers from 1985 to 2012 from Remote Sensing. *Front. Earth Sci.* 8, 35. doi:10.3389/feart.2020.00035

Huggel, C., Carey, M., Emmer, A., Frey, H., Walker-Crawford, N., and Wallimann-Helmer, I. (2020). Anthropogenic Climate Change and Glacier lake Outburst Flood Risk: Local and Global Drivers and Responsibilities for the Case of lake Palcacocha, Peru. *Nat. Hazards Earth Syst. Sci.* 20, 2175–2193. doi:10.5194/nhess-20-2175-2020

Hussain, S., Song, X., Ren, G., Hussain, I., Han, D., and Zaman, M. H. (2017). Evaluation of Gridded Precipitation Data in the Hindu Kush-Karakoram-Himalaya Mountainous Area. *Hydrological Sci. J.* 62 (14), 2393–2405. doi:10.1080/02626667.2017.1384548

Immerzeel, W. W., Droogers, P., de Jong, S. M., and Bierkens, M. F. P. (2009). Large-scale Monitoring of Snow Cover and Runoff Simulation in Himalayan River Basins Using Remote Sensing. *Remote Sensing Environ.* 113, 40–49. doi:10.1016/j.rse.2008.08.010

Immerzeel, W. W., Van Beek, L. P. H., and Bierkens, M. F. P. (2010). Climate Change Will Affect the Asian Water Towers. *Science* 328, 1382–1385. doi:10.1126/science.1183188

Immerzeel, W. W., van Beek, L. P. H., Konz, M., Shrestha, A. B., and Bierkens, M. F. P. (2012). Hydrological Response to Climate Change in a Glacierized Catchment in the Himalayas. *Climatic Change* 110, 721–736. doi:10.1007/s10584-011-0143-4

Jensen, J. R. (2005). *Introductory Digital Image Processing: A Remote Sensing Perspective*. Saddle River, NJ: Prentice Hall.

Kääb, A., Berthier, E., Nuth, C., Gardelle, J., and Arnaud, Y. (2012). Contrasting Patterns of Early Twenty-First-century Glacier Mass Change in the Himalayas. *Nature* 488, 495–498. doi:10.1038/nature11324

Kanda, N., Negi, H. S., Rishi, M. S., and Kumar, A. (2020). Performance of Various Gridded Temperature and Precipitation Datasets over Northwest Himalayan Region. *Environ. Res. Commun.* 2 (8), 085002. doi:10.1088/2515-7620/ab9991

Kulkarni, A. V., and Karyakarte, Y. (2014). Observed Changes in Himalayan Glaciers. *Curr. Sci.* 106, 237–244.

Kumar, A., Srivastava, P., and Meena, N. K. (2017). Late Pleistocene Aeolian Activity in the Cold Desert of Ladakh: A Record from Sand Ramps. *Quat. Int.* 443, 13–28. doi:10.1016/J.QUAINT.2016.04.006

Linsbauer, A., Frey, H., Haeberli, W., Machguth, H., Azam, M. F., and Allen, S. (2016). Modelling Glacier-Bed Overdeepenings and Possible Future Lakes for the Glaciers in the Himalaya-Karakoram Region. *Ann. Glaciol.* 57, 119–130. doi:10.3189/2016AoG71A627

Linsbauer, A., Paul, F., and Haeberli, W. (2012). Modeling Glacier Thickness Distribution and Bed Topography over Entire Mountain Ranges with GlabTop: Application of a Fast and Robust Approach. *J. Geophys. Res.* 117, a–n. doi:10.1029/2011JF002313

Liu, J.-j., Tang, C., and Cheng, Z.-l. (2013). The Two Main Mechanisms of Glacier Lake Outburst Flood in Tibet, China. *J. Mt. Sci.* 10, 239–248. doi:10.1007/s11629-013-2517-8

Liu, Y., Wang, N., Zhang, J., and Wang, L. (2019). Climate Change and its Impacts on Mountain Glaciers during 1960-2017 in Western China. *J. Arid Land* 11, 537–550. doi:10.1007/s40333-019-0025-6

Lu, Y., Zhang, Z., and Huang, D. (2020). Glacier Mapping Based on Random Forest Algorithm: A Case Study over the Eastern Pamir. *Water* 12, 3231. doi:10.3390/w12113231

Magnin, F., Haeberli, W., Linsbauer, A., Deline, P., and Ravanel, L. (2020). Estimating Glacier-Bed Overdeepenings as Possible Sites of Future Lakes in the De-glaciating Mont Blanc Massif (Western European Alps). *Geomorphology* 350, 106913. doi:10.1016/j.geomorph.2019.106913

Majeed, U., Rashid, I., Sattar, A., Allen, S., Stoffel, M., Nüsser, M., et al. (2021). Recession of Gya Glacier and the 2014 Glacial lake Outburst Flood in the Trans-himalayan Region of Ladakh, India. *Sci. Total Environ.* 756, 144008. doi:10.1016/j.scitotenv.2020.144008

McNabb, R., Nuth, C., Kääb, A., and Girod, L. (2019). Sensitivity of Glacier Volume Change Estimation to DEM Void Interpolation. *The Cryosphere* 13, 895–910. doi:10.5194/tc-13-895-2019

Mehta, M., Kumar, V., Garg, S., and Shukla, A. (2021). Little Ice Age Glacier Extent and Temporal Changes in Annual Mass Balance (2016-2019) of Pensilungpa Glacier, Zanskar Himalaya. *Reg. Environ. Change* 21, 38. doi:10.1007/s10113-021-01766-2

Miller, J. D., Immerzeel, W. W., and Rees, G. (2012). Climate Change Impacts on Glacier Hydrology and River Discharge in the Hindu Kush-Himalayas. *Mountain Res. Develop.* 32, 461–467. doi:10.1659/mrd-journal-d-12-00027.1

Mir, R. A., Jain, S. K., Lohani, A. K., and Saraf, A. K. (2018). Glacier Recession and Glacial lake Outburst Flood Studies in Zanskar basin, Western Himalaya. *J. Hydrol.* 564, 376–396. doi:10.1016/j.jhydrol.2018.05.031

Misra, A. K. (2014). Climate Change and Challenges of Water and Food Security. *Int. J. Sustain. Built Environ.* 3, 153–165. doi:10.1016/j.ijsbe.2014.04.006

Muhammad, S., Tian, L., Ali, S., Latif, Y., Wazir, M. A., Goheer, M. A., et al. (2020). Thin Debris Layers Do Not Enhance Melting of the Karakoram Glaciers. *Sci. Total Environ.* 746, 141119. doi:10.1016/j.scitotenv.2020.141119

Muhammad, S., Tian, L., and Khan, A. (2019). Early Twenty-First century Glacier Mass Losses in the Indus Basin Constrained by Density Assumptions. *J. Hydrol.* 574, 467–475. doi:10.1016/j.jhydrol.2019.04.057

Nie, Y., Sheng, Y., Liu, Q., Liu, L., Liu, S., Zhang, Y., et al. (2017). A Regional-Scale Assessment of Himalayan Glacial lake Changes Using Satellite Observations from 1990 to 2015. *Remote Sensing Environ.* 189, 1–13. doi:10.1016/j.rse.2016.11.008

Nuth, C., and Kääb, A. (2011). Co-registration and Bias Corrections of Satellite Elevation Data Sets for Quantifying Glacier Thickness Change. *The Cryosphere* 5, 271–290. doi:10.5194/tc-5-271-2011

Pandit, A., and Ramsankaran, R. (2020). Identification of Potential Sites for Future Lake Formation and Expansion of Existing Lakes in Glaciers of Chandra Basin, Western Himalayas, India. *Front. Earth Sci.* 8, 382. doi:10.3389/feart.2020.500116

Patel, L. K., Sharma, P., Fathima, T. N., and Thamban, M. (2018). Geospatial Observations of Topographical Control over the Glacier Retreat, Miyar basin, Western Himalaya, India. *Environ. Earth Sci.* 77, 190. doi:10.1007/s12665-018-7379-5

Paul, F., Barrand, N. E., Baumann, S., Berthier, E., Bolch, T., Casey, K., et al. (2013). On the Accuracy of Glacier Outlines Derived from Remote-Sensing Data. *Ann. Glaciol.* 54, 171–182. doi:10.3189/2013AoG63A296

Paul, F., Huggel, C., and Kääb, A. (2004). Combining Satellite Multispectral Image Data and a Digital Elevation Model for Mapping Debris-Covered Glaciers. *Remote Sensing Environ.* 89, 510–518. doi:10.1016/j.rse.2003.11.007

Paul, F., Kääb, A., Maisch, M., Kellenberger, T., and Haeberli, W. (2002). The New Remote-Sensing-Derived Swiss Glacier Inventory: I. Methods. *Ann. Glaciol.* 34, 355–361. doi:10.3189/172756402781817941

Pieczonka, T., and Bolch, T. (2015). Region-wide Glacier Mass Budgets and Area Changes for the Central Tien Shan between ~1975 and 1999 Using Hexagon KH-9 Imagery. *Glob. Planet. Change* 128, 1–13. doi:10.1016/j.gloplacha.2014.11.014

Pratibha, S., and Kulkarni, A. V. (2018). Decadal Change in Supraglacial Debris Cover in Baspa basin, Western Himalaya. *Curr. Sci.* 114, 792–799. doi:10.18520/cs/v114/i04/792-799

Raj, A., and Sharma, P. (2013). Is Ladakh a "Cold Desert". *Curr. Sci.* 104, 687–688.
Ramsankaran, R., Pandit, A., and Azam, M. F. (2018). Spatially Distributed Ice-Thickness Modelling for Chhota Shigri Glacier in Western Himalayas, India. *Int. J. Remote Sensing* 39, 3320–3343. doi:10.1080/01431161.2018.1441563
Ramsankaran, R., Pandit, A., and Parla, A. (2019). "Decadal Estimates of Surface Mass Balance for Glaciers in Chandra basin, Western Himalayas, India-A Geodetic Approach," in *Climate Change Signals and Response* (Singapore: Springer), 109–125. doi:10.1007/978-981-13-0280-0_7
Rashid, I., Majeed, U., Najar, N. A., and Bhat, I. A. (2021). Retreat of Machoi Glacier, Kashmir Himalaya between 1972 and 2019 Using Remote Sensing Methods and Field Observations. *Sci. Total Environ.* 785, 147376. doi:10.1016/j.scitotenv.2021.147376
Rashid, I., and Majeed, U. (2018). Recent Recession and Potential Future lake Formation on Drang Drung Glacier, Zanskar Himalaya, as Assessed with Earth Observation Data and Glacier Modelling. *Environ. Earth Sci.* 77, 429. doi:10.1007/s12665-018-7601-5
Rashid, I., and Majeed, U. (2020). Retreat and Geodetic Mass Changes of Zemu Glacier, Sikkim Himalaya, India, between 1931 and 2018. *Reg. Environ. Change* 20, 125. doi:10.1007/s10113-020-01717-3
Rashid, I., Romshoo, S. A., and Abdullah, T. (2017). The Recent Deglaciation of Kolahoi valley in Kashmir Himalaya, India in Response to the Changing Climate. *J. Asian Earth Sci.* 138, 38–50. doi:10.1016/j.jseaes.2017.02.002
Rastner, P., Bolch, T., Notarnicola, C., and Paul, F. (2014). A Comparison of Pixel- and Object-Based Glacier Classification with Optical Satellite Images. *IEEE J. Sel. Top. Appl. Earth Observations Remote Sensing* 7, 853–862. doi:10.1109/JSTARS.2013.2274668
Rathour, R., Gupta, J., Mishra, A., Rajeev, A. C., Dupont, C. L., and Thakur, I. S. (2020). A Comparative Metagenomic Study Reveals Microbial Diversity and Their Role in the Biogeochemical Cycling of Pangong lake. *Sci. Total Environ.* 731, 139074. doi:10.1016/j.scitotenv.2020.139074
Robson, B. A., Bolch, T., MacDonell, S., Hölbling, D., Rastner, P., and Schaffer, N. (2020). Automated Detection of Rock Glaciers Using Deep Learning and Object-Based Image Analysis. *Remote Sensing Environ.* 250, 112033. doi:10.1016/j.rse.2020.112033
Roe, G. H. (2011). What Do Glaciers Tell Us about Climate Variability and Climate Change. *J. Glaciol.* 57, 567–578. doi:10.3189/002214311796905640
Romshoo, S. A., Bashir, J., and Rashid, I. (2020). Twenty-first century-end Climate Scenario of Jammu and Kashmir Himalaya, India, Using Ensemble Climate Models. *Climatic Change* 162, 1473–1491. doi:10.1007/s10584-020-02787-2
Sahu, R., and Gupta, R. D. (2018). Conceptual Framework of Combined Pixel and Object-Based Method for Delineation of Debris-Covered Glaciers. *ISPRS Ann. Photogramm. Remote Sens. Spat. Inf. Sci.* IV-5, 173–180. doi:10.5194/isprs-annals-IV-5-173-2018
Salerno, F., Thakuri, S., Tartari, G., Nuimura, T., Sunako, S., Sakai, A., et al. (2017). Debris-covered Glacier Anomaly? Morphological Factors Controlling Changes in the Mass Balance, Surface Area, Terminus Position, and Snow Line Altitude of Himalayan Glaciers. *Earth Planet. Sci. Lett.* 471, 19–31. doi:10.1016/j.epsl.2017.04.039
Sattar, A., Haritashya, U. K., Kargel, J. S., Leonard, G. J., Shugar, D. H., and Chase, D. V. (2021). Modeling lake Outburst and Downstream hazard Assessment of the Lower Barun Glacial Lake, Nepal Himalaya. *J. Hydrol.* 598, 126208. doi:10.1016/j.jhydrol.2021.126208
Schmidt, S., Nüsser, M., Baghel, R., and Dame, J. (2020). Cryosphere Hazards in Ladakh: the 2014 Gya Glacial lake Outburst Flood and its Implications for Risk Assessment. *Nat. Hazards* 104, 2071–2095. doi:10.1007/s11069-020-04262-8
Schmidt, S., and Nüsser, M. (2017). Changes of High Altitude Glaciers in the Trans-himalaya of Ladakh over the Past Five Decades (1969-2016). *Geosciences* 7, 27. doi:10.3390/GEOSCIENCES7020027
Shukla, A., Arora, M. K., and Gupta, R. P. (2010). Synergistic Approach for Mapping Debris-Covered Glaciers Using Optical-thermal Remote Sensing Data with Inputs from Geomorphometric Parameters. *Remote Sensing Environ.* 114, 1378–1387. doi:10.1016/j.rse.2010.01.015
Shukla, A., and Qadir, J. (2016). Differential Response of Glaciers with Varying Debris Cover Extent: Evidence from Changing Glacier Parameters. *Int. J. Remote Sensing* 37, 2453–2479. doi:10.1080/01431161.2016.1176272
Singh, P., and Bengtsson, L. (2004). Hydrological Sensitivity of a Large Himalayan basin to Climate Change. *Hydrol. Process.* 18, 2363–2385. doi:10.1002/hyp.1468
Soheb, M., Ramanathan, A., Angchuk, T., Mandal, A., Kumar, N., and Lotus, S. (2020). Mass-balance Observation, Reconstruction and Sensitivity of Stok Glacier, Ladakh Region, India, between 1978 and 2019. *J. Glaciol.* 66, 627–642. doi:10.1017/jog.2020.34
Sravana Kumar, M., Shekhar, M. S., Rama Krishna, S. S. V. S., Bhutiyani, M. R., and Ganju, A. (2012). Numerical Simulation of Cloud Burst Event on August 05, 2010, over Leh Using WRF Mesoscale Model. *Nat. Hazards* 62, 1261–1271. doi:10.1007/S11069-012-0145-1
Srivastava, P., Kumar, A., Singh, R., Deepak, O., Kumar, A. M., Ray, Y., et al. (2020). Rapid lake Level Fall in Pangong Tso (lake) in Ladakh, NW Himalaya: a Response of Late Holocene Aridity. *Curr. Sci.* 119 (2), 219–231. doi:10.18520/cs/v119/i2/219-231
Sujakhu, N. M., Ranjitkar, S., He, J., Schmidt-Vogt, D., Su, Y., and Xu, J. (2019). Assessing the Livelihood Vulnerability of Rural Indigenous Households to Climate Changes in Central Nepal, Himalaya. *Sustainability* 11, 2977. doi:10.3390/su11102977
Vijay, S., and Braun, M. (2018). Early 21st century Spatially Detailed Elevation Changes of Jammu and Kashmir Glaciers (Karakoram-Himalaya). *Glob. Planet. Change* 165, 137–146. doi:10.1016/j.gloplacha.2018.03.014
Vuichard, D., and Zimmermann, M. (1987). The 1985 Catastrophic Drainage of a Moraine-Dammed lake, Khumbu Himal, Nepal: Cause and Consequences. *Mountain Res. Develop.* 7, 91–110. doi:10.2307/3673305
Wang, P., Li, Z., Li, H., Wang, W., Zhou, P., and Wang, L. (2017). Characteristics of a Partially Debris-Covered Glacier and its Response to Atmospheric Warming in Mt. Tomor, Tien Shan, China. *Glob. Planet. Change* 159, 11–24. doi:10.1016/j.gloplacha.2017.10.006
Wang, S., Du, J., Li, S., He, H., and Xu, W. (2019). Impact of Tourism Activities on Glacial Changes Based on the Tourism Heat Footprint (THF) Method. *J. Clean. Prod.* 215, 845–853. doi:10.1016/j.jclepro.2019.01.120
Wang, W., Xiang, Y., Gao, Y., Lu, A., and Yao, T. (2015). Rapid Expansion of Glacial Lakes Caused by Climate and Glacier Retreat in the Central Himalayas. *Hydrol. Process.* 29, 859–874. doi:10.1002/hyp.10199
Worni, R., Huggel, C., and Stoffel, M. (2013). Glacial Lakes in the Indian Himalayas - from an Area-wide Glacial lake Inventory to On-Site and Modeling Based Risk Assessment of Critical Glacial Lakes. *Sci. Total Environ.* 468-469, S71–S84. doi:10.1016/j.scitotenv.2012.11.043
Ye, Q., Kang, S., Chen, F., and Wang, J. (2006). Monitoring Glacier Variations on Geladandong Mountain, central Tibetan Plateau, from 1969 to 2002 Using Remote-Sensing and GIS Technologies. *J. Glaciol.* 52, 537–545. doi:10.3189/172756506781828359
Zhang, J., Jia, L., Menenti, M., and Hu, G. (2019). Glacier Facies Mapping Using a Machine-Learning Algorithm: The Parlung Zangbo Basin Case Study. *Remote Sensing* 11, 452. doi:10.3390/rs11040452
Zhao, X., Wang, X., Wei, J., Jiang, Z., Zhang, Y., and Liu, S. (2020). Spatiotemporal Variability of Glacier Changes and Their Controlling Factors in the Kanchenjunga Region, Himalaya Based on Multi-Source Remote Sensing Data from 1975 to 2015. *Sci. Total Environ.* 745, 140995. doi:10.1016/J.SCITOTENV.2020.140995

Conflict of Interest: The authors declare that the research was conducted in the absence of any commercial or financial relationships that could be construed as a potential conflict of interest.

Publisher's Note: All claims expressed in this article are solely those of the authors and do not necessarily represent those of their affiliated organizations, or those of the publisher, the editors and the reviewers. Any product that may be evaluated in this article, or claim that may be made by its manufacturer, is not guaranteed or endorsed by the publisher.

frontiers in Earth Science

METHODS
published: 24 December 2021
doi: 10.3389/feart.2021.725394

Seasonal Evolution of Supraglacial Lakes on Baltoro Glacier From 2016 to 2020

Anna Wendleder[1], Andreas Schmitt[2], Thilo Erbertseder[1], Pablo D'Angelo[3], Christoph Mayer[4] and Matthias H. Braun[5]*

[1]German Remote Sensing Data Center, Earth Observation Center, German Aerospace Center, Weßling, Germany, [2]IInstitute for Applications of Machine Learning and Intelligent Systems, Munich, Germany, [3]Remote Sensing Technology Institute, Earth Observation Center, German Aerospace Center, Weßling, Germany, [4]Geodesy and Glaciology, Bavarian Academy of Sciences and Humanities, Munich, Germany, [5]Friedrich-Alexander-Universität Erlangen-Nürnberg (FAU), Institut für Geographie, Erlangen, Erlangen, Germany

The existence of supraglacial lakes influences debris-covered glaciers in two ways. The absorption of solar radiation in the water leads to a higher ice ablation, and water draining through the glacier to its bed leads to a higher velocity. Rising air temperatures and changes in precipitation patterns provoke an increase in the supraglacial lakes in number and total area. However, the seasonal evolution of supraglacial lakes and thus their potential for influencing mass balance and ice dynamics have not yet been sufficiently analyzed. We present a summertime series of supraglacial lake evolution on Baltoro Glacier in the Karakoram from 2016 to 2020. The dense time series is enabled by a multi-sensor and multi-temporal approach based on optical (Sentinel-2 and PlanetScope) and Synthetic Aperture Radar (SAR; Sentinel-1 and TerraSAR-X) remote sensing data. The mapping of the seasonal lake evolution uses a semi-automatic approach, which includes a random forest classifier applied separately to each sensor. A combination of linear regression and the Hausdorff distance is used to harmonize between SAR- and optical-derived lake areas, producing consistent and internally robust time series dynamics. Seasonal variations in the lake area are linked with the Standardized Precipitation Index (SPI) and Standardized Temperature Index (STI) based on air temperature and precipitation data derived from the climate reanalysis dataset ERA5-Land. The largest aggregated lake area was found in 2018 with 5.783 km^2, followed by 2019 with 4.703 km^2, and 2020 with 4.606 km^2. The years 2016 and 2017 showed the smallest areas with 3.606 and 3.653 km^2, respectively. Our data suggest that warmer spring seasons (April–May) with higher precipitation rates lead to increased formation of supraglacial lakes. The time series decomposition shows a linear increase in the lake area of 11.12 ± 9.57% per year. Although the five-year observation period is too short to derive a significant trend, the tendency for a possible increase in the supraglacial lake area is in line with the pronounced positive anomalies of the SPI and STI during the observation period.

Keywords: supraglacial lake, ice-dammed lake, Baltoro Glacier, remote sensing, summertime series, multi-sensor, multi-temporal

OPEN ACCESS

Edited by:
Duncan Joseph Quincey, University of Leeds, United Kingdom

Reviewed by:
Adina Elena Racoviteanu, University of Exeter, United Kingdom
Qiao Liu, Institute of Mountain Hazards and Environment (CAS), China

****Correspondence:***
Anna Wendleder
anna.wendleder@dlr.de

Specialty section:
This article was submitted to Cryospheric Sciences, a section of the journal Frontiers in Earth Science

Received: *15 June 2021*
Accepted: *19 November 2021*
Published: *24 December 2021*

Citation:
Wendleder A, Schmitt A, Erbertseder T, D'Angelo P, Mayer C and Braun MH (2021) Seasonal Evolution of Supraglacial Lakes on Baltoro Glacier From 2016 to 2020. Front. Earth Sci. 9:725394. doi: 10.3389/feart.2021.725394

1 INTRODUCTION

Glaciers with an extensive debris cover respond in a more complex way to changes in climate than those that are debris-free. The glacier response depends on debris thickness and its spatial distribution (Benn et al., 2012). A thin debris cover of only a few centimeters leads to enhanced ablation compared to clean ice due to increased absorption of solar radiation (Ostrem, 1959; Nicholson and Benn, 2006). A debris cover with greater thickness has an insulating effect on the energy transfer to the glacier ice from atmospheric energy sources and reduces ice ablation. With respect to mass balance calculations, various properties of debris cover need to be considered, such as thickness, slope, aspect, and lithology (Mihalcea et al., 2008). Mass balance models can include such debris-dependent surface properties, but due to a lack of empirical data, it is difficult to readily include their impact on glacier melt rates. The ablation of debris-covered glaciers is very heterogeneous with minimal lowering beneath thick debris near the terminus and maximal downwasting in the upper ablation zone near the equilibrium line where thin debris dominates (Benn et al., 2017). Additionally, ice cliffs may contribute up to 25% to ice ablation despite their small area share of 7–8% (Brun et al., 2018; Buri et al., 2021) and supraglacial lakes can be heated by incoming solar radiation and thus can be responsible for considerable subaqueous melting. Previous studies have indicated that lakes could be responsible for 1/8 of total ice loss in the Langtang Valley, Nepal (Miles et al., 2018; Miles et al., 2020).

Only a handful of studies focused on modeling the response of debris-covered glaciers to climatic changes have included a heterogeneous debris thickness distribution in their approach. These studies have found that supraglacial debris delays glacier response to warming and leads to surface lowering and ice cliff backwasting rather than frontal recession (Rowan et al., 2015; Thompson et al., 2016; Brun et al., 2018). Both the surface debris flux and the relationship between debris thickness and the sub-debris melt rate appear to positively affect the glacier length (Anderson and Anderson, 2019), and if a uniform debris thickness value is used rather than one that is spatially variable, the sub-debris ablation rate can be underestimated by 11–30% (Nicholson et al., 2018). The positive interaction between debris thickness, surface ponding, and ice ablation is therefore complex and non-linear and influences glacier dynamics, geometry, and surface properties (Huo et al., 2021). With an up-glacier expansion of the debris cover, these effects will be intensified with time (Mölg et al., 2020; Xie et al., 2020).

Supraglacial lakes mainly form on debris-covered glaciers with a surface inclination of $\leq 2^{o}$ (Reynolds, 2006) and surface velocities of ≤10 m per year. Most of the lakes develop towards the terminus, which is characterized by the lowest surface velocities (Quincey et al., 2007; Sakai, 2012; Kraaijenbrink et al., 2016; Miles K. E. et al., 2017). They form as rain or meltwater accumulates in depressions of the debris cover in early spring. In late summer, many of the lakes drain, while some lakes persist. If the water is able to drain to the glacier bed, it can support basal sliding and hence higher glacier velocities (Sakai and Fujita, 2006; Sakai, 2012; Watson et al., 2016; Benn et al., 2017; Miles E. S. et al., 2017; Miles et al., 2020). Higher precipitation tends to intensify both lake filling and drainage. Stronger spring precipitation leads to increased filling of supraglacial lakes, while stronger winter precipitation causes higher glacier velocities leading to crevasse development and therefore increased pathways for the drainage of lake water (Wendleder et al., 2018). Additionally, warmer springs lead to greater lake drainage later in the same year as more meltwater causes redevelopment of the subsurface drainage system (Liu et al., 2015).

Previous multi-temporal studies mapped the supraglacial lakes in Tian Shan and Himalaya based on optical data. Liu et al. (2015) used an object-based image analysis (OBIA) on Landsat imagery for the months of August and September from 1990 to 2011 to analyze the distribution and seasonal variability of lakes in the Khan Tengri-Tumor Mountains, Tian Shan. Watson et al. (2016) also implemented an OBIA to examine the spatiotemporal dynamics of 9,340 supraglacial ponds located on nine glaciers in the Everest region of Nepal for the period 2000 to 2015. Miles K. E. et al. (2017) combined the Normalized Difference Water Index (NDWI) with two further band ratios to Landsat 5 and 7 imagery on the Langtang Valley, Nepal, to study lake dynamics from 1999 to 2013. Miles et al. (2018) also applied the NDWI, additionally using Otsu's method to semi-automatically establish an appropriate classification threshold, applied to a dense time series of PlanetScope and RapidEye imagery. An optimized NDWI was introduced by Watson et al. (2018) to account for under- and overestimation of lake areas when using coarser-resolution imagery, using Himalayan debris-covered glaciers with Pleiades, Sentinel-2, and Landsat data to show a proof of concept.

However, to better understand the seasonal evolution of supraglacial lakes and the relationship between lake growth and climate, a continuous time series covering a period of several years is essential. In this study, we combine optical and Synthetic Aperture Radar (SAR) data in order to create such a dense temporal coverage of glacial lake evolution. As SAR signals are able to penetrate clouds, they provide relevant information during the rainy seasons and especially during the period of lake onset. Previous studies have tended to use only optical data and hence have been unable to monitor lake dynamics during the cloudy and rainy seasons. Our multi-sensor approach combining optical and SAR data is a novelty in this application area and could bridge this gap.

We present a semi-automatic approach based on a random forest classifier for the monitoring of supraglacial lake evolution. We apply it to the Baltoro Glacier, located in Karakoram, Pakistan, for the years 2016–2020. The approach uses a multi-temporal and multi-sensor summertime series comprising optical data from Sentinel-2 with a regular acquisition of 5 days and PlanetScope with a very high temporal resolution of 3–5 days and SAR data from Sentinel-1 and TerraSAR-X, both with a regular acquisition of 12 and 11 days, respectively. For the sake of simplicity, we implemented the random forest classifier for all four sensors but with different classification classes and training data. Our aim was to answer the following research questions: 1) What are the characteristic filling and the drainage periods? 2) In what way does the lake area change over the years? 3) What does

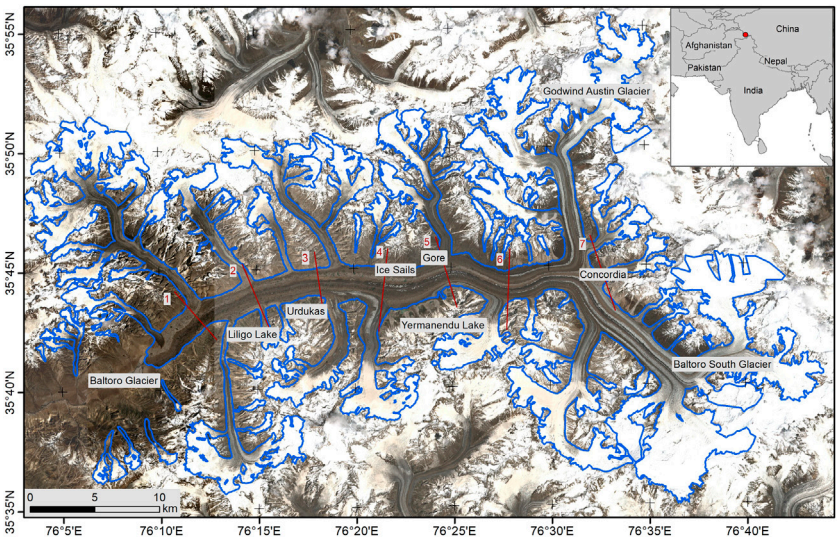

FIGURE 1 | Overview of Baltoro Glacier, Pakistan, with the glacier boundaries (blue) and the sectors (red) used for the supraglacial lake area analyzed in Sections 4.2 and 4.3. Important place names are indicated. The background image is a Sentinel-2 RGB (B2, B3, B4) composite acquired on July 22, 2019. The glacier boundaries are derived from a Landsat-7 scene acquired on July 12, 2010, based on the Normalized Difference Snow index and manual editing.

the spatial lake distribution look like? 4) How does the seasonal evolution vary over the years?

2 STUDY SITE

For our study of glacial lake dynamics, we selected the Baltoro Glacier in the eastern Karakoram. In 2012, the Karakoram region had a glacierized area of 18,000 km^2 (Collier et al., 2015; Bolch et al., 2012), and approximately 18–22% of it was covered with supraglacial debris (Collier et al., 2015; Scherler et al., 2011; Hewitt, 2011). The Baltoro Glacier is situated in the northern part of Pakistan near the border to India and China (**Figure 1**). In 2016 the glacier had a total length of 63 km and together with its tributaries covered an area of approximately 524 km^2 (Mayer et al., 2006). The two major tributaries are the Godwin Austin Glacier and the Baltoro South Glacier, which join at Concordia (4,600 m a.s.l.) to form the main glacier. This main trunk flows in the east-west direction and terminates at 3,410 m a.s.l. The surface velocities derived from SAR data from 1992 to 2017 ranged from 180 to 240 m per year (summer) and 100–140 m per year (winter) between Concordia and Urdukas and decreased to 10–40 m per year near the terminus (Wendleder et al., 2018). Approximately 38% of the Baltoro Glacier is debris-covered, which exceeds the average debris coverage in the Karakoram (Scherler et al., 2011). At Concordia, the debris cover is thin (5–15 cm), increasing in thickness at Urdukas (30–40 cm) and reaching a maximum at the terminus of about 1 m (Mayer et al., 2006; Quincey et al., 2009). Debris-covered glaciers are characterized by the presence of ice sails (Mayer et al., 2006; Evatt et al., 2017), ice cliffs, and supraglacial lakes. On the Baltoro Glacier, ice sails are found in a region from about 6 km downstream to 2 km upstream of Gore (**Figure 1**) and ice cliffs predominate between the terminus and Gore. Supraglacial lakes are located from the terminus up to Concordia. The majority of those lakes are supraglacial lakes located on the main glacier. There are also two ice-dammed lakes located south of the main trunk, namely, Liligo and Yermanendu Lakes.

The Karakoram climate is characterized by cold winters and mild summers and is dominated by three different systems: 1) the winter westerly disturbances with dominant snowfall in winter and spring, contributing up to two-thirds of the yearly snowfall at high altitudes (Dobreva et al., 2017), 2) the Indian summer monsoon incursion that can lead to higher precipitation, temperatures, and cloud coverage during summer, contributing to snow accumulation in the higher reaches of the glacier (Bookhagen and Burbank, 2006; Thayyen and Gergan, 2010), and 3) the predominantly stable Tibetan Anticyclone that, in the case of an irregular weakening, provokes an incursion of the Indian summer monsoon with large amounts of precipitation (Dobreva et al., 2017). The mean annual precipitation is approximately 1,600 mm per year at 5,300 m a.s.l. (Godwin Austen region) and at 5,500 m a.s.l. (Baltoro South region). As the mean daytime temperature during summer is close to the freezing point at 5,400 m a.s.l., most of the precipitation deposits as snow above this elevation (Mayer et al., 2006).

3 METHODOLOGY

3.1 Data

We used a multi-sensor time series with an acquisition every two to four days based on optical data from PlanetScope and Sentinel-2 and SAR data from Sentinel-1 and TerraSAR-X. The sensor

TABLE 1 | Overview of the sensor characteristics and acquisition parameters. In the case of Sentinel-2, only the used spectral bands are listed. The pass directions of the SAR sensors are abbreviated as A for ascending and D for descending. Eineder and Fritz (2009), Vincent et al. (2019), PlanetScope (2020), Gatti and Bertolini (2013).

	Sentinel-2	PlanetScope	Sentinel-1	TerraSAR-X
Mode	Multispectral instrument (MSI)	Analytic ortho scene products	Interferometric wide swath (IW)	ScanSAR (SC)
Spectral bands/Frequency	B: 439–535 nm G: 537–582 nm R: 646–685 nm NIR: 767–908 nm SWIR: 1,539–1,681 nm	B: 455–515 nm G: 500–590 nm R: 590–670 nm NIR: 780–860 nm —	C-Band (5.4 GHz)	X-Band (9.65 GHz)
Polarization	—	—	VV (2016) VV/VH (2017–2020)	HH —
Ground sampling	10 m (VIS, NIR), 20 m (SWIR)	3 m	10 m	18 m
Scene extent	100 × 100 km	24.6 × 16.4 km	250 × 180 km	110 × 110 km
Orbit	5 (T43SFV)	—	27/34	98/151
Pass direction	D	—	A/D	A/D
Incidence angle	—	—	35°/35°	35°/35°
Repeat orbit	5 days (2016–2017)	1–7 days	12 days	11 days
—	10 days (2018–2020)	—	—	—
Observation period	2016–2020	2017–2020	2016–2020	2019–2020
Acquisitions per summer	7/11/28/28/20	30/25/30/34	13/23/24/23/26	18/24

characteristics and acquisition parameters are summarized in **Table 1** and the data availability is visualized in **Figure 2**. All four sensor systems are characterized by frequent and consistent coverage. Sentinel-2 has a repeat orbit of 5 days (Gatti and Bertolini, 2013) and provides a continuous and stable time series with relevant information about glacier surface cover like debris, ice, snow, and lakes. The time series is complemented by the high temporal sampling of PlanetScope data. The PlanetScope satellite constellation of about 130 small satellites called "Doves" gathers information every two to five days during cloud-free periods (Miles K. E. et al., 2017; PlanetScope, 2020). The SAR data of Sentinel-1 (Vincent et al., 2019) and TerraSAR-X (Eineder and Fritz, 2009) bridge the gaps of the optical data, which are brought about by cloud cover during the westerly disturbances in April and the monsoon season from the end of May until the end of July. We used data acquired between April and September for the years 2016–2020, and the number and timing of images differed for each season of study, depending on data availability (**Table 1**).

For the semi-automated classification, the data needed to be atmospherically corrected, radiometrically calibrated, and orthorectified. Therefore, the Sentinel-2 Multi-Spectral Instrument (MSI) orthorectified Level-1C Top-Of-Atmospheric products were atmospherically corrected to L2A products using MAJA (MACCS ATCOR Joint Algorithm, release 4.2). MAJA is a processor for cloud detection and atmospheric correction and is specifically designed to process optical time series (Hagolle et al., 2017). The PlanetScope Analytic Ortho Scene Products (Level 3B) were already downloaded as orthorectified and atmospherically corrected Surface Reflectance (SR) data. Sentinel-1 Interferometric Wide Swath C-band and TerraSAR-X ScanSAR X-band data were processed to normalized radar backscatter Analysis Ready Data (ARD) using the Multi-SAR System (Schmitt et al., 2015; Schmitt et al., 2020). For the orthorectification, the 3-arcsecond Copernicus-DEM (GLO-90) (Airbus, 2020) was used as it had the best geometric correspondence to Sentinel-2 and PlanetScope data.

The relationship between supraglacial lake evolution and meteorological conditions was analyzed using the corresponding monthly averaged air temperature at 2 m above the surface and total precipitation data of the climate reanalysis dataset ERA5-Land (Hersbach and Bell, 2020). The data are available on a 0.1° by 0.1° grid and were downloaded from the Copernicus Climate Change Service (C3S) Climate Data Store (CDS) (Muñoz-Sabater, 2019).

3.2 Random Forest Classification

We used a random forest approach in classification mode (Breiman, 2001) and applied it to Sentinel-2, PlanetScope,

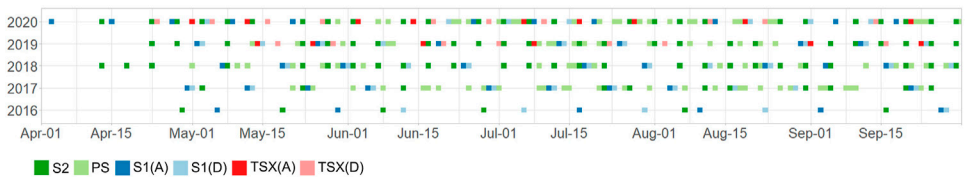

FIGURE 2 | Data availability for the summertime series from 2016 to 2020 with respect to Sentinel-2 (S2), PlanetScope (PS), Sentinel-1 (S1), and TerraSAR-X (TSX). "A" and "D" in parentheses denote the passing direction, i.e., ascending or descending.

TABLE 2 | Overview of the used classes, features, and training data for the random forest classifier. NDI stands for normalized difference index, GLCM for gray level co-occurrence matrix, and ROI for region of interest.

	Sentinel-2	PlanetScope	Sentinel-1	TerraSAR-X
Classes	Lakes, dry debris, wet debris, ice, snow, shadow, clouds	Lake, dry debris, wet debris, ice	Dry, wet	Dry, wet
Features	B, NIR, SWIR, NDI_{NIR-R}, NDI_{B-R}, NDI_{G-NIR}	B, NIR, NDI_{NIR-R}, NDI_{B-R}, NDI_{G-NIR}	VV amplitude with GLCM image (2016), VV and VH amplitude with GLCM images (2017–2020)	HH amplitude with GLCM image
Training data	200 ROI for each class (50 ROI each from spring and summer in 2018 and 2019)	50 ROI each class	200 ROI for each class from 2019 to 2020	200 ROI for each class from 2019 to 2020
Peculiarity	ROIs from spring and late summer to reflect different water turbidity	Individual training data of images with the same acquisition date	Separation of the lake and wet glacier surface with optical data	Separation of the lake and wet glacier surface with optical data

Sentinel-1, and TerraSAR-X images separately in order to detect the supraglacial lakes. Random forest is a common and robust machine learning classification algorithm. It combines the results of many different random decision trees taking the majority votes for each decision tree. Due to the different spectral resolution and the radiometric calibration of Sentinel-2 and PlanetScope, the random forests differed in the number of classes, feature spaces, and training data (**Table 2**). Training and validation datasets (80: 20 ratio) were manually created. Classification and subsequent processing steps were implemented in the open-source software RStudio.

3.2.1 Sentinel-2

For the Sentinel-2 data, we used the same training dataset for all 5 years. The classification results reflect the dominant glacier surface cover types: "dry debris," "wet debris," "lakes," "snow," and "ice." As the cloud mask produced by the MAJA algorithm frequently misclassified glacier ice as cloud, we created our own cloud and shadow mask by adding the two classes "shadow" and "clouds." These masks were generated after the classification in three subsequent steps: 1) since cloud rims were often wrongly classified as water, lake pixels with a distance of 20 m to clouds were deleted; 2) lakes that existed only three to five times in the summertime series were removed (with the exact threshold varying depending on the number of optical data per summertime series); 3) scenes with a cloud coverage over the glacier surface of more than 80% were automatically omitted. For a better distinction of shadows and clouds from lakes, we added the blue and shortwave infrared bands. Shadows showed high absorption in both bands, with lower rates in the shortwave infrared. Clouds showed a high reflection compared to the surrounding area with highest rates in the blue band (Roth, 2019). In order to cover seasonal and annual variations of the water turbidity, the training data were collected in spring and late summer in 2018 and 2019. These 2 years were selected as they had the lowest cloud cover.

3.2.2 PlanetScope

The radiometric quality of PlanetScope data is known to be inconsistent between each of the "Doves" (Houborg and McCabe, 2016; Cooley et al., 2017), which leads to different reflectances between the sensors and prevents the use of a single training dataset as we did for Sentinel-2. For this reason, we chose the random forest approach with individual training data derived from scenes with the same acquisition date. The training data were selected from the classification results of an index approach. Therefore, we introduced the Supraglacial Lake Index (SGLI), a modification of the Normalized Difference Water Index (McFeeters, 1996), specially designed for debris-covered glaciers. The three-step approach is based on two normalized difference indices, one calculated with green and near-infrared and the other with near-infrared and red (**Figure 3A**). Using this approach, it was possible to discriminate between the classes "debris," "ice," and "lake." For every scene, an individual threshold for the differentiation between the reflectance of "ice" and "lake" was automatically calculated using the unimodal threshold determination (Rosin, 2001). The threshold was defined as the point with the maximum distance between the histogram and line of maximum and minimum peak (**Figure 3B**). In the final classification, snow was classified as ice because of its spectral similarity, and "shadow" and "cloud" classes were both omitted since all of the PlanetScope imagery we selected was cloud-free. Overall, the random forest yielded an improved classification compared to the index approaches alone, which tend to underestimate the lake area.

As the access to PlanetScope data is restricted to a specific download quota per month, only cloud-free data were selected. Therefore, it was not necessary to include the classes "shadow" and "cloud." Additionally, the data have no shortwave infrared bands, which impedes cloud detection anyway.

3.2.3 Sentinel-1 and TerraSAR-X

The random classifier was executed separately on the ascending and descending orbits of the Sentinel-1 and TerraSAR-X datasets. Due to the similar SAR backscatter of rough debris cover and ice, we could only define the two classes "dry" and "wet." The discrimination of lake and wet objects is based on the maximal lake extent map of the corresponding year produced by Sentinel-2 data (Miles K. E. et al., 2017). The

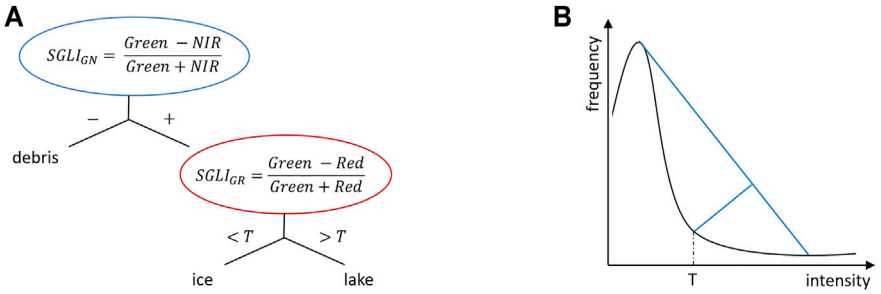

FIGURE 3 | (A) Decision tree of the Supraglacial Lake Index (SGLI). "T" stands for threshold derived with the unimodal threshold determination (Rosin, 2001). **(B)** Method of the unimodal threshold determination (Rosin, 2001). The line between maximum and minimum peak and the maximum distance between histogram and line are displayed in blue.

classification was performed on amplitude and texture information. Therefore, the SAR amplitudes were filtered using a 3 × 3 median filter. The median filter size was a trade-off between the reduction of speckle noise and preserving the supraglacial lake shape (Davies, 2005). Additionally, a gray level co-occurrence matrix (GLCM) texture derived with a 3 × 3 kernel filters in the 0°direction was added to the feature space (Haberäcker, 1987). The use of a single (or combination) of kernel filter(s) in the other three directions (45°, 90°, 135°) had no influence on the classification results.

3.3 Harmonization of SAR-Derived Lake Area

Due to the side-looking radar and the undulating glacier surface, the SAR signal could not map the lake area completely. The SAR-derived lake areas were underestimated and had to be harmonized in order to achieve a consistent lake area time series. The correction was calculated with a linear regression using lake areas derived from optical and SAR data with the same acquisition date. The SAR data were individually corrected depending on their sensor and their pass direction. The linear regression was calculated for each lake separately. In the case of persistent lakes, we used measurements from their complete lifetime rather than just a single year. Pearson's correlation coefficients before linear regression of all measurements for Sentinel-1 and TerraSAR-X were between 0.89 and 0.93, showing strong evidence of a linear relationship between the two variables. The residual standard error of all linear regressions was between 1,397 m^2 and 1923 m^2 and the p-value was between 0.029 and 0.037 (95% confidence level), indicating a significant correlation.

3.4 Multi-Sensor Summertime Series

The classification results of all supraglacial lakes were combined and smoothed to yield a consistent summertime series (de Jonge and van der Loo, 2013). Detected outliers and data gaps were filled with interpolated values. During the harmonization of the lake area, not all SAR-derived areas were corrected due to the absence of any significant associations between the predictor and the outcome variables. The outliers were characterized by their local minimum in the time series and could be detected with the Hausdorff distance (Hausdorff, 1914). This metric is defined as the maximum distance between the original curve and a simplified line between preceding and subsequent measurements. We calculated two simplified lines where the first line is defined by the two previous measurements and the second line by the two following measurements. According to our definition, a negative distance indicated a local minimum. The outlier detection was performed on each lake separately. Missing data were linearly interpolated based on the lake area of the previous and subsequent acquisition. Using the neighboring water level change for interpolation was not possible because each lake had its own characteristic pattern of water level rise and fall, and in addition, cloud coverage often affected large parts of the scene and thus also the neighboring lakes. Based on the summertime series, we analyzed the number of lakes, their total area, the date of maximum area, distribution and duration of water coverage, and the seasonal evolution during the 5 years.

3.5 Seasonal and Trend Components

To examine the seasonal evolution, the time series of the lake area Y_t was analyzed with the multicomponent model following Weatherhead et al. (1998):

$$Y_t = \mu + S_t + \frac{1}{12}\omega + N_t, \quad (1)$$

where μ is the constant term, S_t is the seasonal component, ω represents the linear trend per year, and N_t is the residual variability. The seasonal component was assumed to be stationary and was modeled as a sinusoid where eight superimposed harmonics are fitted. The uncertainty of the linear trend component was derived as follows:

$$\sigma_\omega = \frac{\sigma_r}{n^{3/2}}\sqrt{\frac{1+\varphi}{1-\varphi}}, \quad (2)$$

TABLE 3 | Number of lakes, cumulative area of lakes in km^2, percentage of seasonal and permanent lakes at the end of the ablation season, and date and area in km^2 at maximum lake area for each summer season from 2016 to 2020. The number and cumulative area of lakes are divided into two categories: lakes with an area smaller and larger than 0.01 km^2.

	Number of lakes (<1 ha/> 1 ha)	Percentage of seasonal and permanent lakes	Cumulative area (km^2) (<1 ha/> 1 ha)	Date of max. area (max. area in km^2)
2016	553 (485/67)	63%/37%	3.606 (1.725/1.881)	08.06. (2.166 km^2)
2017	412 (329/81)	54%/46%	3.563 (1.342/2.221)	28.07. (1.945 km^2)
2018	501 (351/148)	62%/38%	5.783 (1.592/4.191)	23.07. (2.587 km^2)
2019	498 (365/131)	33%/67%	4.703 (1.700/3.003)	08.07. (2.437 km^2)
2020	379 (243/136)	30%/70%	4.606 (1.212/3.939)	12.07. (2.002 km^2)

TABLE 4 | Accuracy assessment with absolute and relative Root Squared Error (RSE) for Sentinel-2 (S2), PlanetScope (PS), TerraSAR-X (TSX), and Sentinel-1 (S1) for the multi-sensor time series (TS) based on manually digitized reference dataset derived of PlanetScope data from 2019. The lake area referred to the total classified lake area covered by the reference data set of PlanetScope. The coverage of the reference data set was given as distance along the centerline.

Date	Sensor	Lake area (km^2)	Coverage (km)	RSE$_{abs}$ (km^2)	RSE$_{rel}$ (%)
July 07, 2019	S2	1.061	15.7–35.5	0.016	1.5
July 22, 2019	S2	1.286	2.4–18.0	0.025	1.9
August 01, 2019	S2	0.610	18.5–35.5	0.011	1.7
August 06, 2019	S2	1.400	2.3–23.7	0.024	1.7
August 21, 2019	S2	0.592	0–11.8	0.013	2.1
July 07, 2019	PS	0.748	15.7–35.5	0.021	2.8
July 22, 2019	PS	0.683	2.4–18.0	0.069	10.0
August 01, 2019	PS	0.417	18.5–35.5	0.020	4.7
August 06, 2019	PS	0.889	2.3–23.7	0.055	6.1
August 21, 2019	PS	0.333	0–11.8	0.048	14.1
July 08, 2019	TSX (A)	0.607	2.3–20.0	0.018	3.0
July 23, 2019	TSX (D)	0.539	14.0–35.6	0.013	2.5
July 13, 2019	S1 (A)	0.651	11.8–35.6	0.020	3.0
July 14, 2019	S1 (D)	0.736	2.3–20.0	0.015	2.1
July 07, 2019	TS	1.157	15.7–35.5	0.038	3.4
July 22, 2019	TS	1.392	2.4–18.0	0.026	2.0
August 01, 2019	TS	0.724	18.5–35.5	0.034	5.1
August 06, 2019	TS	1.558	2.3–23.7	0.029	2.0
August 21, 2019	TS	0.697	0–11.8	0.023	3.4
July 08, 2019	TS	0.943	2.3–20.0	0.028	3.0
July 23, 2019	TS	0.925	14.0–35.6	0.020	2.3
July 13, 2019	TS	0.954	11.8–35.6	0.036	3.9
July 14, 2019	TS	1.322	2.3–20.0	0.042	3.4

with σ_r being the standard deviation of the de-trended residuals, n the number of months, and φ the first-order autocorrelation of the residuals.

3.6 Accuracy Assessment of Supraglacial Lake Area

For the accuracy assessment, a reference dataset was manually mapped based on the RGB composite and the NDWI (McFeeters, 1996) calculated with the green and near-infrared band of PlanetScope data. The reference datasets varied in their spatial coverage (**Table 4**; **Supplementary Figure S1**) but were consistently selected from 2019, as this year had the lowest cloud coverage and the highest number of coincident pairs between PlanetScope and Sentinel/TerraSAR-X. In order to reflect the accuracy at different turbidity levels and thus the seasonal accuracy, we chose five validation dates for the optical data distributed over the whole summer. Since SAR sensors distinguish only between wet and dry and thus are not sensitive to seasonal turbidity variations, we selected one validation date for each SAR sensor and each pass direction. The PlanetScope data used for the accuracy assessment were omitted in the summertime series. The accuracy was assessed by the comparison of the classified area with the reference area. The classification error was referred to the total area and quantified with the absolute and relative Root Squared Error (RSE) (Liang et al., 2012):

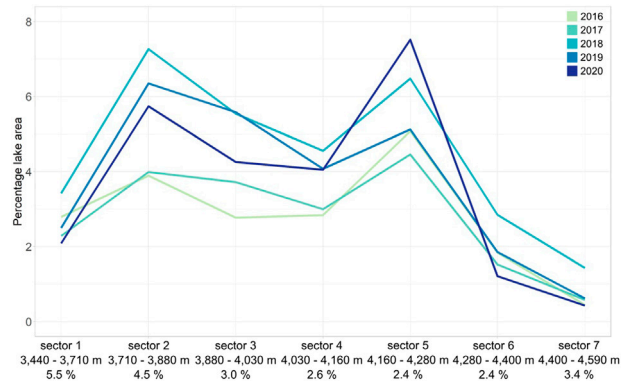

FIGURE 4 | Percentage of lake area to the surface area of the main glacier for 2016 to 2020. The glacier was divided into seven sectors from glacier terminus to Concordia Place. Each sector is specified by its altitude range (m a.s.l.) and mean slope (%).

$$RSE_{abs} = \sqrt{\sum (area_{cla} - area_{ref})^2}, \quad (3)$$

$$RSE_{rel} = \frac{RSE_{abs}}{\sum area_{cla}}. \quad (4)$$

4 RESULTS

4.1 Annual Area Fluctuations

Based on the multi-temporal time series, we calculated the total number and the cumulative area of supraglacial lakes on the main trunk of Baltoro Glacier. We further derived the date of the maximum lake area for each summer season from 2016 to 2020 (**Table 3**). The cumulative lake area denotes the maximum norm over all lakes during the summer period, whereas the maximum lake area includes all lake areas at a certain point in time. The number of lakes varied from year to year without any clear trend, with a minimum of 379 in 2020 and a maximum of 553 in 2016 (**Table 3**). The total lake area was lowest in 2017 (3.563 km^2) and the highest values in 2018 (5.783 km^2). The number and area of lakes larger than 0.01 km^2 have increased constantly since 2016 with a distinct rise from 2018 onwards. Thus, larger lakes comprised a larger percentage of the total lake area through time. The date of the maximum water level varied between mid-June in 2016 and the end of July in 2017 and 2018. The peak lake area ranged between 1.945 km^2 in 2017 and 2.587 km^2 in 2018. **Table 3** shows the percentage of ephemeral and permanent lakes at the end of the ablation season. As a reference, we used the classification results from September and October. From 2016 to 2019, the proportion of seasonal lakes was between 54 and 64% and fell to 30 and 33% in 2019 and 2020.

4.2 Percentage of Lake Area

Figure 4 shows the percentage of lake area compared to total glacier area for each sector (**Figure 1** for the definition of the sectors). The lowest lake area was consistently detected above 4,280 m a.s.l. Lake areas were consistently lowest in 2016 and highest in 2018 and 2019. The lowermost sector (3,440–3,710 m a.s.l.) shows the least variation with time, whereas the second sector (3,710–3,880 m a.s.l.) shows the greatest variation, with a total relative area increase of 3.3% between 2017 and 2018. The third (3,880–4,030 m a.s.l.), fourth (4,030–4,160 m a.s.l.), and fifth (4,160–4,280 m a.s.l.) sectors showed an increase of 1.82%, 1.56%, and 2.03%, respectively. However, patterns across the glacier and through time were highly non-linear.

4.3 Size and Altitude Distribution

The number of lakes with altitude (**Figure 5**) followed a similar distribution to that shown by the percentage of lake area (**Figure 4**). The sixth and seventh (higher-elevation) sectors consistently had the lowest number of lakes (<50). The second, third, and fourth sectors had the greatest number of lakes, with a maximum number in the second sector (100–120) and a decrease towards the fourth sector (60–90). Lake numbers in the fifth sector varied over the observation period: the highest number was found in 2016 (117) and the lowest number was found in 2017 (60). The years 2018–2020 had between 70 and 90 lakes in this sector. The distribution of the lake area is shown in **Figure 5B**. The lake area ranged between 500 m^2 to 440, 000 m^2. The number of lakes with a size of 1,000–2,000 m^2 ranged between 15 and 57, whereas those between 2,000 and 3,000 m^2 varied from 80 to120; otherwise, as the lake size increased, the number of lakes decreased, with the exception of a peak in the size bin of 10,000–20,000 m^2. The overall number of lakes was less in 2016 and 2017, with maxima in 2018 and 2020 across the glacier surface. There were very few lakes observed in the largest lake classes (20,000–30,000 m^2).

The spatial distribution of lakes (**Figure 6**; **Supplementary Figures S2,S3**) was highly variable between each of the observation periods. Additionally, the mapping of the inundated area gives an indication of the lake bathymetry, as shown in **Figures 6D,E** for the Yermanendu Lake in 2018 and 2020.

4.4 Seasonal Evolution

The seasonal evolution of the maximum area of all supraglacial lakes (including Yermanendu and Liligo Lakes) for each summer season from 2016 to 2020 is displayed in **Figure 7**. The equivalent disaggregated data for Yermanendu and Liligo Lakes can be found in **Supplementary Figure S4**. The lake area evolution can be divided into three distinct stages: 1) in 2016 and 2017, the total lake area remains below 2 km^2 with a maximum in early June and end-July, respectively, followed by a consistent decrease from early and mid-August onward, 2) 2018 and 2019 were characterized by larger water areas of about 2.5 km^2 from mid-June to mid-July and a steeper decrease from end-July onward, and 3) in 2020, the lake area peaks at 2.62 km^2 in early June with a following decrease until mid-August and a short increase from mid-August to mid-September. A consistent characteristic for all 5 years is the rapid lake expansion at the beginning of the ablation season. In 2018, 2019, and 2020, the lake onset had started in mid-April with a continuous increase until mid-June. The years 2016 and 2017 were characterized by a delayed lake onset, starting 1 month later in mid-May. In 2020, the increase in lake area between mid-April and

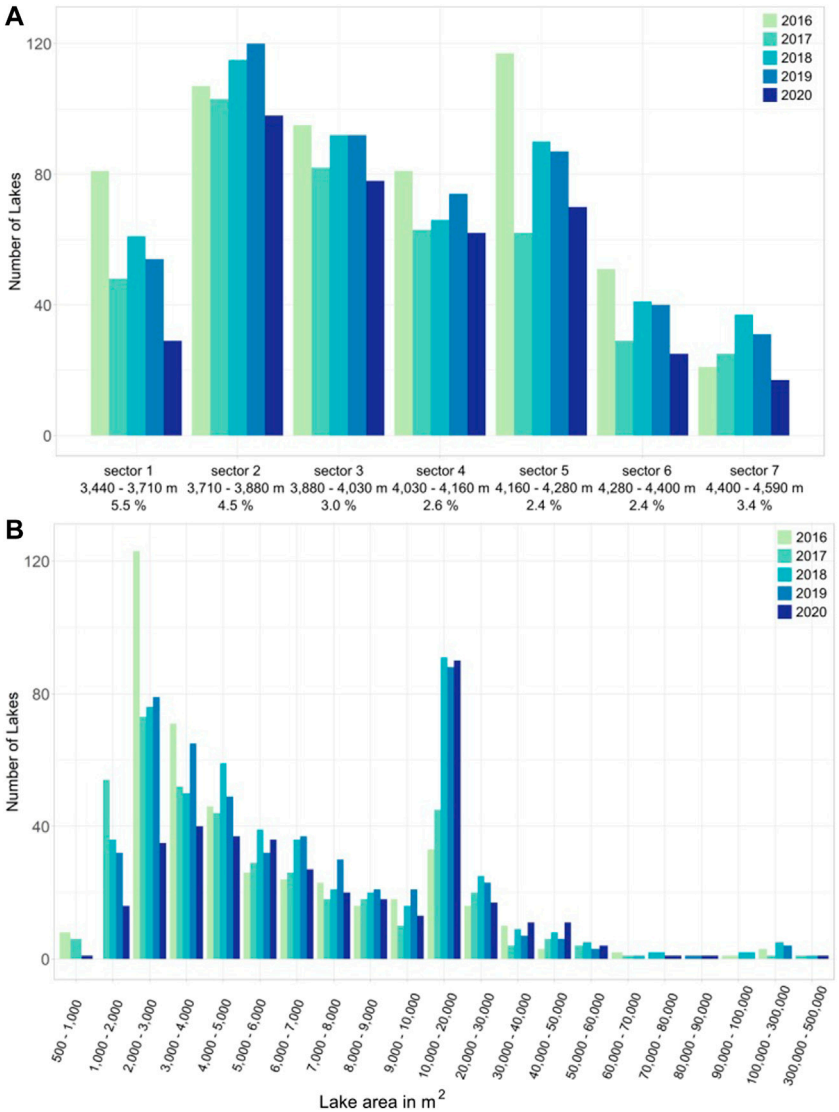

FIGURE 5 | (A) Distribution of the number of lakes along the altitude divided into seven sectors. Each sector is specified by its altitude range (m a.s.l.). **(B)** Distribution of the number of lakes according to their area in m^2.

early June is similar in 2018 and 2019, but instead of a constant lake area until mid-July, it decreased. The peak in the lake area from early September to mid-September corresponds well with the dynamics of Yermanendu Lake (**Supplementary Figures S4A,B**). Data availability reduced the number of observations available in 2016. Consequently, the seasonal evolution could not be sampled with the same high temporal resolution as it was possible for the other years (**Supplementary Figure S5**).

4.5 Probability Density

Figure 8 shows the distribution of lake areas through time and depicts median, interquartile range, and probability density values. The rise of the median lake area from 1.2 in 2016 to 1.7–1.9 in 2018–2020 is clearly visible. The interquartile ranges of 2016 and 2018 showed a larger variation of lake areas than in 2020. The probability density represents the distribution of lake areas and differs each year. The lake area of 2016 was symmetrically distributed, meaning a relatively high variance. In contrast, the lake areas of 2017 and 2019 were bimodal with a more pronounced shape in 2017. The probability density of 2019 had a negative skew indicating that most of the lake areas were larger than the median. In 2020, most of the lake areas were concentrated around the median value. Overall, the probability density data reinforce the observation of there being great year-to-year variability.

4.6 Seasonal and Trend Components

The seasonal variability in the lake area (**Figure 9**) largely reflects the pattern depicted in **Figure 7**, with a yearly maximum being identified in June/July. It is positively skewed, indicating a quick

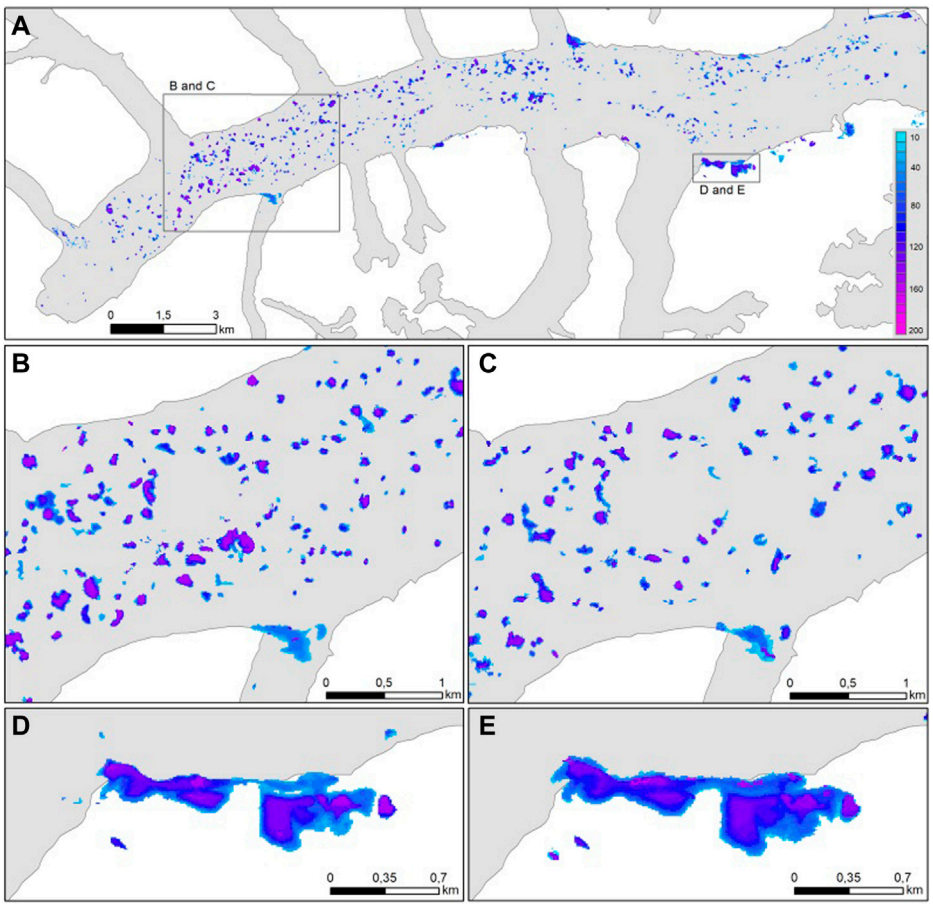

FIGURE 6 | Distribution of lakes and duration of water coverage for the complete glacier in 2018 **(A)**, for the second sector (3,710–3,880 m a.s.l.) in 2018 **(B)** and in 2020 **(C)**, and for the Yermanendu Lake (4,160–4,280 m a.s.l.) in 2018 **(D)** and in 2020 **(E)**. The color represents the duration of water coverage in days. Pink color means that the pixel was covered with water for 120 days, whereas blue means coverage of 40–50 days. All figures have the same legend shown in **(A)**.

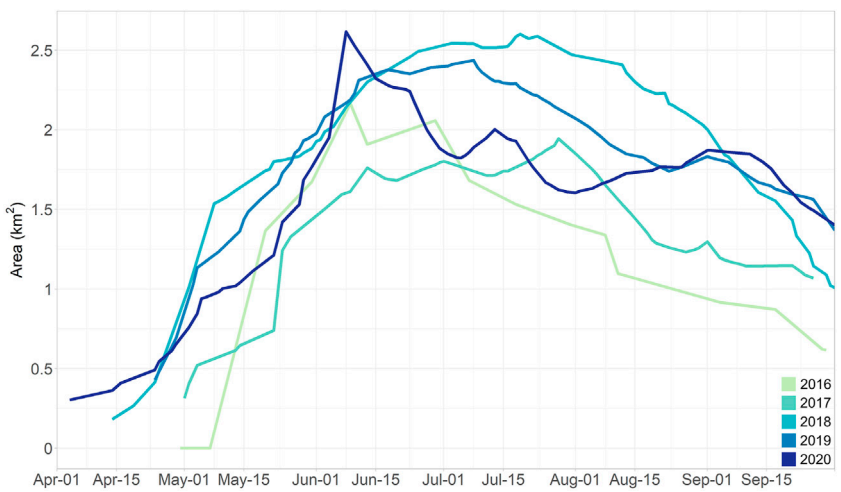

FIGURE 7 | Seasonal evolution of the total supraglacial lake area in km^2 from April to September for 2016 to 2020.

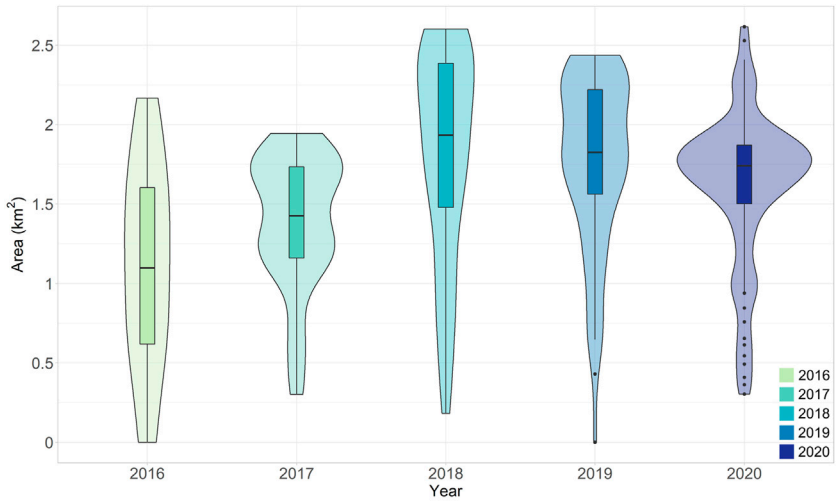

FIGURE 8 | Median, interquartile ranges, and probability density of the lake areas of the summertime series for the 5 years presented in a violin plot.

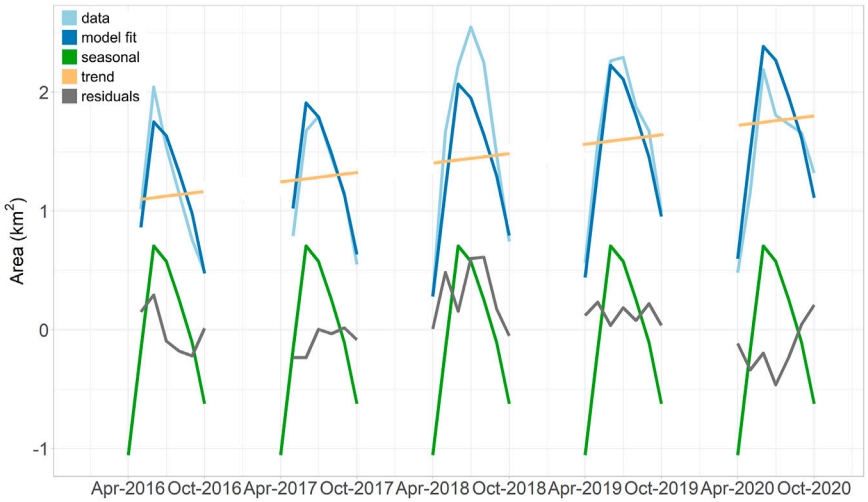

FIGURE 9 | Monthly means of the total lake area (data), model fit, seasonal components, linear trend, and residuals for 2016 to 2020. The seasonal component and the residuals are plotted in relative units.

onset of lake formation in spring and slower drainage in the lake area towards autumn. The linear trend component was quantified to 0.16 ± 0.14 km^2 per year, which corresponds to an increase in the supraglacial lake area of 11.12 ± 9.57% per year. Considering the uncertainty of the linear trend component and the degrees of freedom defined by the number of months of the times series, the linear trend is not significant at the 95% level (p-value 0.125) (Weatherhead et al., 1998; Santer et al., 2000).

4.7 Precipitation and Temperature

Figure 10 represents the precipitation and temperature in the Standardized Precipitation Index (SPI) and the Standardized Temperature Index (STI) for the period from 2016 to 2020 (McKee et al., 1993). The advantage of using indices (rather than raw data) is the better representation of anomalies. We aggregated both variables over a period of 3 months, as this reflects seasonal-scale deficit and surpluses (Winkler et al., 2017; Wendleder et al., 2018). A significant increase for both indices above 1.0 is observed from 2016 to 2018 and in summer 2019, which represents moderate surpluses. A direct connection between supraglacial lake evolution and climate could not be identified, even though the climate data show a tendency to greater precipitation and higher temperatures in terms of amplitude and time.

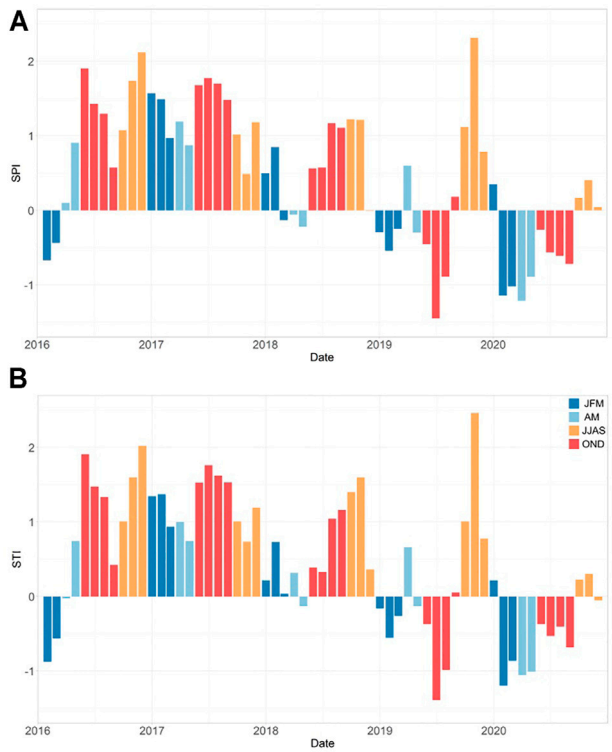

FIGURE 10 | SPI **(A)** and STI **(B)** from 2016 to 2020 for the monthly precipitation and temperature, color-coded for the seasonal distribution: January, February, and March (JFM) in dark blue, April and May (AM) in light blue, June to September (JJAS) in orange, and October to December (OND) in red. The index values range from −2 to +2, whereas −0.99 to +0.99 indicate near normal, +1.0 to +1.4 moderate surpluses, +1.5 to +1.99 very high surpluses, −1.0 and −1.49 moderate deficits, and −1.5 to −1.99 and < −2.0 severe deficits.

5 ACCURACY OF SUPRAGLACIAL LAKE AREAS

Table 4 lists the RSE for all sensors and the multi-temporal time series. Variability in image coverage impeded a direct comparison of the classification accuracy from optical imagery of different dates. It is notable that the reference datasets of July 7, August 6, and August 21 (all 2019) had a higher RSE. These scenes covered the Liligo Lake (7 km) with an area of 0.06 km^2 (July 22, 2019). From mid-July, Liligo Lake was fed by the meltwater of the Liligo Glacier and hence, the turbidity increased. As turbid water and ice had similar spectral reflectance, the Liligo Lake was consistently misclassified as ice. In the case of the SAR sensors, the classifications derived from descending passes, i.e., glacier velocity parallel to the SAR line of sight, provided better results. However, the mean relative RSE of the multi-temporal time series was at 1.0% (total area of 9.151 km^2 with an absolute RSE of 0.0945 km^2) and showed better accuracy than the mean relative RSE of Sentinel-2, PlanetScope, TerraSAR-X, and Sentinel-1 with 7.1% (total area of 7.483 km^2 with an absolute RSE of 0.054 km^2). Our classification errors are comparable with the error of 2.7% in Liang et al. (2012), 4.5% in Sundal et al. (2009), and 4.0% in Selmes et al. (2011).

6 DISCUSSION

6.1 Comparison With Existing Methods for Supraglacial Lake Classifications

Two previous studies have classified the supraglacial lakes on the Baltoro Glacier, but only for one to three scenes per year. Wendleder et al. (2018) calculated the NDWI based on the green and the near-infrared band for the Landsat-8 Operational Land Imager (OLI) Level-2 data. The threshold for the water detection was empirically determined to be 0.1. Misclassifications like ice-covered surfaces of the tributaries Yermanendu and Biarchedi Glacier and ice sails were manually removed. They detected a total lake area of 2.28 km^2 on June 04, 2016, 1.83 km^2 on June 20, 2016, 1.45 km^2 on September 08, 2016, and 2.09 km^2 on June 23, 2017. The results of this study differ by −0.28 km^2, +0.16 km^2, −0.52 km^2, and −0.37 km^2, respectively. The acquisition dates of the time series do not correspond to the Landsat-8 dates; hence, we linearly interpolated to the lake area for better comparison. Since the lake dynamics are highly variable, the linear interpolation could produce differences. Furthermore, the coarser spatial resolution of Landsat-8 of 30 m could lead to a higher lake area (Watson et al., 2018). The greatest discrepancy of +0.52 km^2 is due to there being only two Sentinel-2 scenes between July and September 2016, neither of which are completely cloud-free, and there being no image pairs of Sentinel-1 and 2 acquired on the same date, which is needed for the calculation of the linear regression. Consequently, the SAR area harmonization employed in the current study could not be applied for all lakes, only for persistent lakes, and the missing lake areas could not be interpolated based on Sentinel-2. Hence, the classification results on September 08, 2016, derived from Sentinel-1 are lower. On the other hand, the lake dynamics shown in 2016 in the previous study, with a high lake area in early June followed by a decrease in lake area, corresponds with our current observation.

The second study mapping supraglacial lakes on Baltoro Glacier used a U-Net model with EfficientNet backbone based on PlanetScope data (Qayyum et al., 2020). Qayyum et al. (2020) classified lake areas of 2.25 km^2 on July 14, 2017, 1.96 km^2 on July 27, 2017, 1.83 km^2 on August 7, 2017, 2.22 km^2 on July 14 and 15, 2018, and 2.61 km^2 on July 12–16, 2019. For complete coverage of the glacier surface in 2018 and 2019, they used PlanetScope data acquired within a period of 2 or 4 days. Since the total lake area was constant at both times, the classification results do not contain any seasonal variations. Our results differ by −0.51, −0.02, −0.18, +0.3, and −0.3 km^2. The differences in the classification results can most likely be accounted for by the different ground samplings. In particular, the data of the multi-sensor time series in our study were sampled to 10 m, whereas the study of Qayyum et al. (2020) was based on the ground sampling of 3 m.

6.2 Relationship Between Supraglacial Lake Evolution and Climate

According to SPI and STI, the years 2016–2017 were influenced by stronger precipitation and higher air

temperatures in April and May compared to 2018, 2019, and 2020. As the seasonal lake evolution shows a larger area for 2018, 2019, and 2020, a connection between lake evolution and climate cannot be identified, even though the climate data show a tendency to larger precipitation and higher temperatures in terms of amplitude and time. Satellite images and classification results revealed that newly created supraglacial lakes were mostly fed by precipitation, either directly by rain or delayed via snowmelt in the depressions. The ice-dammed lakes were additionally filled by snowmelt of the adjacent slopes and glacier meltwater. The greater the contribution of glacier meltwater, the more turbid the lake, as is the case at Liligo Lake around the middle or end of July. It appears then that the stronger and earlier precipitation in 2018–2020 caused an increase in the lake area. In 2018, the glacier downstream of Gore and the north exposed slopes near Liligo Lake and Urdukas were unusually snow-free by mid-April. This was 2–4 weeks in advance of other years. Hence, 2018 was affected by higher temperatures leading to an intensified contribution of snow and glacier meltwater at an altitude of about 4,400 m a.s.l. The period July until September 2020 was cloudier than usual, which could indicate a stronger Indian summer monsoon. Therefore, the undulating patterns in **Figure 7** can be explained by higher precipitation resulting in short-term lake fluctuations. This observation is supported by several other studies that monitored an intensification of the westerlies, hence leading to an increase of precipitation for the Karakoram (Cannon et al., 2015; Mölg et al., 2017; de Kok et al., 2020). On the other hand, the frequency and duration of heatwaves in Pakistan also increased, mostly affecting the central and southeast regions and less the Himalayan and the Karakoram (Khan et al., 2019). However, for March and April, 2018, high temperatures were recorded as well for Skardu (World Meteorological Organization, 2021). It seems that the heat waves affected the Karakoram, which would be consistent with our observation of an early snowmelt in spring 2018.

7 OPPORTUNITIES AND LIMITATIONS

7.1 Multi-Temporal and Multi-Sensor Time Series

The advantage of the presented approach is the usage of a dense multi-temporal and multi-sensor summertime series. Each sensor has advantages and disadvantages, which can be compensated by integrating them into a combined approach. Sentinel-2 provides a continuous, radiometrically stable time series but without daily or sub-daily imaging capability; this can be filled by the high temporal sampling of PlanetScope data. During periods of cloud cover, SAR data provide important information and in view of the amplification of the winter westerlies and the Indian summer monsoon, its usage will likely become essential. In contrast, the disadvantages of the SAR data, i.e., lake area underestimates and missing data from side-looking radar geometry and undulating glacier surface topographies, can be compensated using optical data acquired on the same day. Due to the east-west orientation of the Baltoro Glacier and the broad glacier valley with a width of 3.5 km, the main glacier was not influenced by layover or radar shadow effects in the SAR images. As both ascending and descending acquisitions were acquired with the same incidence angle of 35°, we cannot determine which incidence angle would be more suitable. The images acquired in the descending orbit, i.e., with the SAR line of sight parallel to the glacier flow, mapped the lake shapes better, which confirms the accuracy improvement by 1% (**Table 3**).

7.2 Semi-Automatic Approach for Supraglacial Lake Detection

Our study shows that optical and SAR data can be used synergistically to monitor the seasonal evolution of supraglacial lakes on debris-covered glaciers. The approach works semi-automatically without the need for manual cloud removal. Manual interaction is only needed to select the Sentinel-1 and 2 and TerraSAR-X training data for the random forest classifier and the adaption of the threshold for the detection of pixel clusters that were misclassified as water. As the threshold was mostly adjusted for the summertime series in 2016 and 2017 with less imagery, this step will become unnecessary with increased data availability. The classification of the PlanetScope data was completely automatic as the selection of the training data was based on the SGLI results. For the Sentinel-2 data, the MAJA atmospheric correction was used. The main feature of MAJA is the use of multi-temporal information contained in the time series to better estimate aerosol optical thickness and correct atmospheric effects (Hagolle et al., 2017). This enables the comparability within the data and potentially supports the use of our training data for supraglacial lake detection on other debris-covered glaciers. However, for a simple supraglacial lake classification based on the classes “debris,” “ice,” and “lake,” the SGLI, presented for the first time in this study, could be applied on cloud-free Sentinel-2 and PlanetScope data without any previous knowledge.

8 CONCLUSION

To study the variability of supraglacial lakes on the Baltoro Glacier, we developed a semi-automatic approach based on multi-sensor and multi-temporal summertime series from 2016 to 2020 acquired by the optical sensors Sentinel-2 and PlanetScope and the SAR sensors Sentinel-1 and TerraSAR-X. Our study showed that the supraglacial lakes filled between mid-April to mid-June and drained between mid-June to mid-September. In all cases, lake areas expanded faster than they contracted. The five-year study period showed that the total lake area varied from year to year, with the largest total lake area in 2018 (5.783 km^2) and the smallest lake area in 2017 (3.563 km^2). Variations in the total number of lakes were not recognizable, though there was a tendency towards creating larger lakes (>0.04 km^2) over time. The local distribution of the lakes densified, especially in the glacier section between

3,710 m and 3,880 m a.s.l. The percentage of lake area (as a component of overall glacier area) rose by 3.3% between 2017 and 2018. The supraglacial lakes were mostly fed by precipitation either directly with rainfall or time delayed via snowmelt in the hummocks. The ice-marginal lakes (Yermanendu and Liligo) were additionally filled by snowmelt derived from adjacent slopes and glacier meltwater. A linear trend of 11.12 ± 9.57% per year was derived that indicates a possible increase in the lake area. This is supported by pronounced positive anomalies of the SPI and STI during the observation period. However, we conclude that the time series need to be extended in order to identify significant signals. In addition, the connection to climate parameters and oscillations demands further process-based analysis. We anticipate that the rising trend of the supraglacial lake area will continue due to climate change and the accompanying rise in air temperature and intensification of precipitation, which underlines the importance of evaluating continuous time series and thus the use of semi-automated processors.

DATA AVAILABILITY STATEMENT

The original contributions presented in the study are included in the article/**Supplementary Material**; further inquiries can be directed to the corresponding author.

AUTHOR CONTRIBUTIONS

AW, AS, CM, and MB designed the research. AW analyzed the data and results and wrote the manuscript. AS helped with the methodology. TE calculated the seasonal and trend components and wrote Section 3.5 and Section 4.6. PD processed the MAJA corrected Sentinel-2 data. All authors helped to edit and to improve the manuscript.

ACKNOWLEDGMENTS

The authors acknowledge the use of TerraSAR-X data (©DLR 2019-2020), Sentinel-1 and 2 data (©ESA 2019-2020) provided by DLR PAC/LTA, PlanetScope data (©Planet 2019-2020), and ERA5-Land provided by Copernicus Climate Change Service (C3S) Climate Data Store (CDS). We would like to thank Duncan Quincey, Adina Elena Racoviteanu, and Qiao Liu for their corrections that helped to strengthen the manuscript.

SUPPLEMENTARY MATERIAL

The Supplementary Material for this article can be found online at: https://www.frontiersin.org/articles/10.3389/feart.2021.725394/full#supplementary-material

REFERENCES

Airbus (2020). *Copernicus Digital Elevation Model Product Handbook RFP/RFI-No.: AO/1-9422/18/I-LG, Version: 2.1*. https://spacedata.copernicus.eu/documents/20126/0/GEO1988-CopernicusDEM-SPE-002_ProductHandbook_I1.00.pdf/082dd479-f908-bf42-51bf-4c0053129f7c?t=1586526993604.

Anderson, L. S., and Anderson, R. S. (2019). Modeling Debris-Covered Glaciers: Response to Steady Debris Deposition. *Cryosphere* 10, 1105–1124. doi:10.5194/tc-10-1105-2016

Benn, D. I., Bolch, T., Hands, K., Gulley, J., Luckman, A., Nicholson, L. I., et al. (2012). Response of Debris-Covered Glaciers in the Mount everest Region to Recent Warming, and Implications for Outburst Flood Hazards. *Earth Sci. Rev.* 114, 156–174. doi:10.1016/j.earscirev.2012.03.008

Benn, D. I., Thompson, S., Gulley, J., Mertes, J., Luckman, A., and Nicholson, L. (2017). Structure and Evolution of the Drainage System of a Himalayan Debris-Covered Glacier, and its Relationship with Patterns of Mass Loss. *Cryosphere* 11, 2247–2264. doi:10.5194/tc-11-2247-2017

Bolch, T., Kulkarni, A., Kääb, A., Huggel, C., Paul, F., Cogley, J. G., et al. (2012). The State and Fate of Himalayan Glaciers. *Science* 336, 310–314. doi:10.1126/science.1215828

Bookhagen, B., and Burbank, D. W. (2006). Topography, Relief, and TRMM-Derived Rainfall Variations along the Himalaya. *Geophys. Res. Lett.* 33, 1–5. doi:10.1029/2006GL026037

Breiman, L. (2001). Random Forests. *Machine Learn.* 45, 5–32. doi:10.1023/A:1010933404324

Brun, F., Wagnon, P., Berthier, E., Shea, J. M., Immerzeel, W. W., Kraaijenbrink, P. D. A., et al. (2018). Ice Cliff Contribution to the Tongue-wide Ablation of Changri Nup Glacier, nepal, central Himalaya. *Cryosphere* 12, 3439–3457. doi:10.5194/tc-12-3439-2018

Buri, P., Miles, E. S., Steiner, J. F., Ragettli, S., and Pellicciotti, F. (2021). Supraglacial Ice Cliffs Can Substantially Increase the Mass Loss of Debris-Covered Glaciers. *Geophys. Res. Lett.* 48, 1–11. doi:10.1029/2020gl092150

Cannon, F., Carvalho, L. M. V., Jones, C., and Bookhagen, B. (2015). Multi-annual Variations in winter westerly Disturbance Activity Affecting the Himalaya. *Clim. Dyn.* 44, 441–455. doi:10.1007/s00382-014-2248-8

Collier, E., Maussion, F., Nicholson, L. I., Mölg, T., Immerzeel, W. W., and Bush, A. B. G. (2015). Impact of Debris Cover on Glacier Ablation and Atmosphere-Glacier Feedbacks in the Karakoram. *Cryosphere* 9, 1617–1632. doi:10.5194/tc-9-1617-2015

Cooley, S., Smith, L., Stepan, L., and Mascaro, J. (2017). Tracking Dynamic Northern Surface Water Changes with High-Frequency Planet Cubesat Imagery. *Remote Sensing* 9, 1306–1321. doi:10.3390/rs9121306

Davies, E. R. (2005). "Basic Image Filtering Operations," in *Signal Processing and its Applications*. Editor E. Davies. Third Edition (Burlington: Morgan Kaufmann), 47–101. doi:10.1016/b978-012206093-9/50006-x

de Jonge, E., and van der Loo, M. (2013). *An Introduction to Data Cleaning with R*. The Hague: Statistics Netherlands.

de Kok, R. J., Kraaijenbrink, P. D. A., Tuinenburg, O. A., Bonekamp, P. N. J., and Immerzeel, W. W. (2020). Towards Understanding the Pattern of Glacier Mass Balances in High Mountain Asia Using Regional Climatic Modelling. *Cryosphere* 14, 3215–3234. doi:10.5194/tc-14-3215-2020

Dobreva, I., Bishop, M., and Bush, A. (2017). Climate-Glacier Dynamics and Topographic Forcing in the Karakoram Himalaya: Concepts, Issues and Research Directions. *Water* 9, 405–429. doi:10.3390/w9060405

Eineder, M., and Fritz, T. (2009). TerraSAR-X Ground Segment Basic Product Specification Document; Doc: TX-GS-DD-3302. Wessling, Germany: German Aerospace Center (DLR). https://tandemx-science.dlr.de/pdfs/TX-GS-DD-3302_Basic-Products-Specification-Document_V1.9.pdf.

Evatt, G. W., Mayer, C., Mallinson, A., Abrahams, I. D., Heil, M., and Nicholson, L. (2017). The Secret Life of Ice Sails. *J. Glaciol.* 63, 1049–1062. doi:10.1017/jog.2017.72

Gatti, A., and Bertolini, A. (2013). Sentinel-2 Product Specification Document 14, 510.

Haberäcker, P. (1987). *Digitale Bildverarbeitung; Grundlagen und Anwendungen*. Muenchen, Wien: Hanser.

Hagolle, O., Huc, M., Desjardins, C., Auer, S., and Richter, R. (2017). Maja Algorithm Theoretical Basis Document. *Stochastic Environ. Res. Risk Assess.* Version 1.0, 1–40. doi:10.5281/zenodo.1209633

Hausdorff, F. (1914). *Grundzüge der Mengenlehre*. Leipzig: Veit.

Hersbach, H., Bell, B., Berrisford, P., Hirahara, S., Horányi, A., Muñoz-Sabater, J., et al. (2020). The Era5 Global Reanalysis. *Q.J.R. Meteorol. Soc.* 146, 1999–2049. doi:10.1002/qj.3803

Hewitt, K. (2011). Glacier Change, Concentration, and Elevation Effects in the Karakoram Himalaya, Upper Indus basin. *Mountain Res. Develop.* 31, 188–200. doi:10.1659/MRD-JOURNAL-D-11-00020.1

Houborg, R., and McCabe, M. (2016). High-resolution Ndvi from Planet's Constellation of Earth Observing Nano-Satellites: A New Data Source for Precision Agriculture. *Remote Sensing* 8, 1–19. doi:10.3390/rs8090768

Huo, D., Bishop, M. P., and Bush, A. B. G. (2021). Understanding Complex Debris-Covered Glaciers: Concepts, Issues, and Research Directions. *Front. Earth Sci.* 9, 358. doi:10.3389/feart.2021.652279

Khan, N., Shahid, S., Ismail, T., Ahmed, K., and Nawaz, N. (2019). Trends in Heat Wave Related Indices in pakistan. *Stoch Environ. Res. Risk Assess.* 33, 287–302. doi:10.1007/s00477-018-1605-2

Kraaijenbrink, P., Meijer, S. W., Shea, J. M., Pellicciotti, F., De Jong, S. M., and Immerzeel, W. W. (2016). Seasonal Surface Velocities of a Himalayan Glacier Derived by Automated Correlation of Unmanned Aerial Vehicle Imagery. *Ann. Glaciol.* 57, 103–113. doi:10.3189/2016AoG71A072

Liang, Y.-L., Colgan, W., Lv, Q., Steffen, K., Abdalati, W., Stroeve, J., et al. (2012). A Decadal Investigation of Supraglacial Lakes in West greenland Using a Fully Automatic Detection and Tracking Algorithm. *Remote Sensing Environ.* 123, 127–138. doi:10.1016/j.rse.2012.03.020

Qiao, L., Mayer, C., and Liu, S. (2015). Distribution and Interannual Variability of Supraglacial Lakes on Debris-Covered Glaciers in the Khan Tengri-Tumor Mountains, central Asia. *Environ. Res. Lett.* 10, 014014. doi:10.1088/1748-9326/10/1/014014

Mayer, C., Lambrecht, A., Belò, M., Smiraglia, C., and Diolaiuti, G. (2006). Glaciological Characteristics of the Ablation Zone of Baltoro Glacier, Karakoram, pakistan. *Ann. Glaciol.* 43, 123–131. doi:10.3189/172756406781812087

McFeeters, S. K. (1996). The Use of the Normalized Difference Water Index (NDWI) in the Delineation of Open Water Features. *Int. J. Remote Sensing* 17, 1425–1432. doi:10.1080/01431169608948714

McKee, T. B., Doesken, N. J., and Kleist, J. (1993). "The Relationship of Drought Frequency and Duration to Time Scales," in Proceedings of the 8th Conference on Applied Climatology. Anaheim, January 17-22, 1993, 179–183.

Mihalcea, C., Mayer, C., Diolaiuti, G., D'Agata, C., Smiraglia, C., Lambrecht, A., et al. (2008). Spatial Distribution of Debris Thickness and Melting from Remote-Sensing and Meteorological Data, at Debris-Covered Baltoro Glacier, Karakoram, pakistan. *Ann. Glaciol.* 48, 49–57. doi:10.3189/172756408784700680

Miles, E. S., Willis, I. C., Arnold, N. S., Steiner, J., and Pellicciotti, F. (2017a). Spatial, Seasonal and Interannual Variability of Supraglacial Ponds in the Langtang Valley of Nepal, 1999-2013. *J. Glaciol.* 63, 88–105. doi:10.1017/jog.2016.120

Miles, K. E., Willis, I. C., Benedek, C. L., Williamson, A. G., and Tedesco, M. (2017b). Toward Monitoring Surface and Subsurface Lakes on the greenland Ice Sheet Using sentinel-1 Sar and Landsat-8 Oli Imagery. *Front. Earth Sci.* 5, 58. doi:10.3389/feart.2017.00058

Miles, E. S., Willis, I., Buri, P., Steiner, J. F., Arnold, N. S., and Pellicciotti, F. (2018). Surface Pond Energy Absorption across Four Himalayan Glaciers Accounts for 1/8 of Total Catchment Ice Loss. *Geophys. Res. Lett.* 45, 10464–10473. doi:10.1029/2018GL079678

Miles, K. E., Hubbard, B., Irvine-Fynn, T. D. L., Miles, E. S., Quincey, D. J., and Rowan, A. V. (2020). Hydrology of Debris-Covered Glaciers in High Mountain Asia. *Earth Sci. Rev.* 207, 103212. doi:10.1016/j.earscirev.2020.103212

Mölg, T., Maussion, F., Collier, E., Chiang, J. C. H., and Scherer, D. (2017). Prominent Midlatitude Circulation Signature in High Asia's Surface Climate during Monsoon. *J. Geophys. Res. Atmos.* 122, 12702–12712. doi:10.1002/2017JD027414

Mölg, N., Ferguson, J., Bolch, T., and Vieli, A. (2020). On the Influence of Debris Cover on Glacier Morphology: How High-Relief Structures Evolve from Smooth Surfaces. *Geomorphology* 357 (12), 702–712. doi:10.1002/2017JD027414

Muñoz-Sabater, J. (2019). Era5-land Hourly Data from 1981 to Present. Copernicus Climate Change Service (C3s) Climate Data Store (Cds). doi:10.24381/cds.e2161bac

Nicholson, L., and Benn, D. I. (2006). Calculating Ice Melt beneath a Debris Layer Using Meteorological Data. *J. Glaciol.* 52, 463–470. doi:10.3189/172756506781828584

Nicholson, L. I., McCarthy, M., Pritchard, H. D., and Willis, I. (2018). Supraglacial Debris Thickness Variability: Impact on Ablation and Relation to Terrain Properties. *Cryosphere* 12, 3719–3734. doi:10.5194/tc-12-3719-2018

Ostrem, G. (1959). Ice Melting under a Thin Layer of Moraine, and the Existence of Ice Cores in Moraine Ridges. *Geografiska Annaler* 41, 228–230. doi:10.1080/20014422.1959.11907953

PlanetScope (2020). *Planet Imagery Product Specification*. San Francisco, CA: Planet Labs, Inc. https://assets.planet.com/docs/Planet_Combined_Imagery_Product_Specs_letter_screen.pdf.

Qayyum, N., Ghuffar, S., Ahmad, H., Yousaf, A., and Shahid, I. (2020). Glacial Lakes Mapping Using Multi Satellite Planetscope Imagery and Deep Learning. *ISPRS Int. J. Geo. Inform.* 9, 1–23. doi:10.3390/ijgi9100560

Quincey, D. J., Richardson, S. D., Luckman, A., Lucas, R. M., Reynolds, J. M., Hambrey, M. J., et al. (2007). Early Recognition of Glacial lake Hazards in the Himalaya Using Remote Sensing Datasets. *Glob. Planet. Change* 56, 137–152. doi:10.1016/j.gloplacha.2006.07.013

Quincey, D. J., Copland, L., Mayer, C., Bishop, M., Luckman, A., and Belò, M. (2009). Ice Velocity and Climate Variations for Baltoro Glacier, pakistan. *J. Glaciol.* 55, 1061–1071. doi:10.3189/002214309790794913

Reynolds, J. M. (2006). Role of Geophysics in Glacial hazard Assessment. *First Break* 24, 61–66. doi:10.3997/1365-2397.24.8.27068

Rosin, P. L. (2001). Unimodal Thresholding. *Pattern Recognition* 34, 2083–2096. doi:10.1016/S0031-3203(00)00136-9

Roth, A. (2019). Methoden zur Schattendetektion und -entfernung zur Verbesserten Landbedeckungsklassifikation im Untersuchungsgebiet Berchtesgadener Land anhand von Sentinel-2 Daten. Bachelorarbeit. Hochschule München-Kartographie, Geomedientechnik.

Rowan, A. V., Egholm, D. L., Quincey, D. J., and Glasser, N. F. (2015). Modelling the Feedbacks between Mass Balance, Ice Flow and Debris Transport to Predict the Response to Climate Change of Debris-Covered Glaciers in the Himalaya. *Earth Planet. Sci. Lett.* 430, 427–438. doi:10.1016/j.epsl.2015.09.004

Sakai, A., and Fujita, K. (2010). Formation Conditions of Supraglacial Lakes on Debris-Covered Glaciers in the Himalaya. *J. Glaciol.* 56, 177–181. doi:10.3189/002214310791190785

Sakai, A. (2012). Glacial Lakes in the Himalayas: a Review on Formation and Expansion Processes. *Glob. Environ. Res.*, 23–30.

Santer, B. D., Wigley, T. M. L., Boyle, J. S., Gaffen, D. J., Hnilo, J. J., Nychka, D., et al. (2000). Statistical Significance of Trends and Trend Differences in Layer-Average Atmospheric Temperature Time Series. *J. Geophys. Res.* 105, 7337–7356. doi:10.1029/1999JD901105

Scherler, D., Bookhagen, B., and Strecker, M. R. (2011). Spatially Variable Response of Himalayan Glaciers to Climate Change Affected by Debris Cover. *Nat. Geosci.* 4, 156–159. doi:10.1038/NGEO1068

Schmitt, A., Wendleder, A., and Hinz, S. (2015). The Kennaugh Element Framework for Multi-Scale, Multi-Polarized, Multi-Temporal and Multi-Frequency SAR Image Preparation. *ISPRS J. Photogram. Remote Sensing* 102, 122–139. doi:10.1016/j.isprsjprs.2015.01.007

Schmitt, A., Wendleder, A., Kleynmans, R., Hell, M., Roth, A., and Hinz, S. (2020). Multi-source and Multi-Temporal Image Fusion on Hypercomplex Bases. *Remote Sensing* 12, 943–2096. doi:10.3390/rs12060943

Selmes, N., Murray, T., and James, T. D. (2011). Fast Draining Lakes on the greenland Ice Sheet. *Geophys. Res. Lett.* 38, 1–5. doi:10.1029/2011GL047872

Sundal, A. V., Shepherd, A., Nienow, P., Hanna, E., Palmer, S., and Huybrechts, P. (2009). Evolution of Supra-glacial Lakes across the greenland Ice Sheet. *Remote Sensing Environ.* 113, 2164–2171. doi:10.1016/j.rse.2009.05.018

Thayyen, R. J., and Gergan, J. T. (2010). Role of Glaciers in Watershed Hydrology: a Preliminary Study of a "Himalayan Catchment". *Cryosphere* 4, 115–128. doi:10.5194/tc-4-115-2010

Thompson, S., Benn, D. I., Mertes, J., and Luckman, A. (2016). Stagnation and Mass Loss on a Himalayan Debris-Covered Glacier: Processes, Patterns and Rates. *J. Glaciol.* 62, 467–485. doi:10.1017/jog.2016.37

Vincent, P., Bourbigot, M., Johnsen, H., and Piantanida, R. (2019). Sentinel-1 Product Specification.

Watson, C. S., Quincey, D. J., Carrivick, J. L., and Smith, M. W. (2016). The Dynamics of Supraglacial Ponds in the everest Region, central Himalaya. *Glob. Planet. Change* 142, 14–27. doi:10.1016/j.gloplacha.2016.04.008

Watson, C. S., King, O., Miles, E. S., and Quincey, D. J. (2018). Optimising Ndwi Supraglacial Pond Classification on Himalayan Debris-Covered Glaciers. *Remote Sensing Environ.* 217, 414–425. doi:10.1016/j.rse.2018.08.020

Weatherhead, E. C., Reinsel, G. C., Tiao, G. C., Meng, X.-L., Choi, D., Cheang, W.-K., et al. (1998). Factors Affecting the Detection of Trends: Statistical Considerations and Applications to Environmental Data. *J. Geophys. Res.* 103, 17149–17161. doi:10.1029/98jd00995

Wendleder, A., Friedl, P., and Mayer, C. (2018). Impacts of Climate and Supraglacial Lakes on the Surface Velocity of Baltoro Glacier from 1992 to 2017. *Remote Sensing* 10, 1681. doi:10.3390/rs10111681

Winkler, K., Gessner, U., and Hochschild, V. (2017). Identifying Droughts Affecting Agriculture in Africa Based on Remote Sensing Time Series between 2000-2016: Rainfall Anomalies and Vegetation Condition in the Context of ENSO. *Remote Sensing* 9, 831–927. doi:10.3390/rs9080831

World Meteorological Organization (2021). Available at: https://public.wmo.int/en/media/news/march-3rd-warmest-record-many-contrasts (Accessed 05 29, 2021).

Xie, F., Liu, S., Wu, K., Zhu, Y., Gao, Y., Qi, M., et al. (2020). Upward Expansion of Supra-Glacial Debris Cover in the Hunza Valley, Karakoram, during 1990 ~ 2019. *Front. Earth Sci.* 8, 308. doi:10.3389/feart.2020.00308

Conflict of Interest: The authors declare that the research was conducted in the absence of any commercial or financial relationships that could be construed as a potential conflict of interest.

Publisher's Note: All claims expressed in this article are solely those of the authors and do not necessarily represent those of their affiliated organizations, or those of the publisher, the editors and the reviewers. Any product that may be evaluated in this article, or claim that may be made by its manufacturer, is not guaranteed or endorsed by the publisher.

frontiers | Frontiers in Earth Science

ORIGINAL RESEARCH
published: 11 April 2022
doi: 10.3389/feart.2021.767317

Recent Evolution of Glaciers in the Manaslu Region of Nepal From Satellite Imagery and UAV Data (1970–2019)

Adina E. Racoviteanu[1,2], Neil F. Glasser[1], Benjamin A. Robson[3], Stephan Harrison[2], Romain Millan[4], Rijan B. Kayastha[5] and Rakesh Kayastha[5]*

[1]Department of Geography and Earth Sciences, Aberystwyth University, Aberystwyth, United Kingdom, [2]Department of Geography, University of Exeter, Exeter, United Kingdom, [3]Department of Earth Science, University of Bergen, Bergen, Norway, [4]Institut de Géosciences de L'Environnement, Grenoble, France, [5]Department of Environmental Science and Engineering, Kathmandu University, Dhulikhel, Nepal

Glacierized mountain ranges such as the Himalaya comprise a variety of glacier types, including clean and debris-covered glaciers. Monitoring their behaviour over time requires an assessment of changes in area and elevation along with surface features and geomorphology. In this paper we quantify the surface evolution of glacier systems in the Manaslu region of Nepal over the last five decades using 2013/2019 multi-sensor imagery and elevation data constructed from 1970 declassified Corona imagery and 1970 declassified Corona imagery. We investigate area changes, glacier thickness, geodetic glacier mass balance and surface velocity changes at regional scales and focus on the Ponkar Glacier and Thulagi Glacier and Lake for an in-depth assessment of surface geomorphology and surface feature dynamics (ponds, vegetation and ice cliffs). The time series of surface elevation changes for the lower ablation area of Ponkar Glacier is extended using 2019 UAV-based imagery and field-based ablation rates measured over the period 2016–2019. Glaciers in the Manaslu region experienced a mean area loss of $-0.26 \pm 0.0001\%\ a^{-1}$ between 1970 and 2019. The mean surface lowering was $-0.20 \pm 0.02\ m a^{-1}$ over the period 1970 to 2013, corresponding to a regional geodetic mass balance of -0.17 ± 0.03 m w. e.a^{-1}. Overall, debris-covered glaciers had slightly higher thinning rates compared to clean ice glaciers; lake-terminating glaciers had double thinning rates compared to land-terminating glaciers. Individual glacier mass balance was negatively controlled by glacier slope and mean glacier elevation. During the period 1970 to 2013, Ponkar Glacier had a geodetic mass balance of -0.06 ± 0.01 m w. e.a^{-1}, inversely correlated with parts of the central trunk thickening. Between 2013 and 2019 there was a nine-fold increase in the thinning rates over the lower parts of the glacier tongue relative to the period 1970–2013. Ice-surface morphology changes between 1970 and 2019 on Ponkar Glacier include a decrease in ogives and open crevasses, an increase in ice cliffs and ponds and the expansion of the supraglacial debris and ice-surface vegetation. These changes point to reduced ice-dynamic activity and are commensurate with the observed recession and negative glacier mass balance over the last five decades.

Keywords: Himalayan glaciers, Manaslu region, geodetic mass balance, debris cover, geomorphology, Corona/RapidEye

OPEN ACCESS

Edited by:
Argha Banerjee, Indian Institute of Science Education and Research, India

Reviewed by:
Levan Tielidze, Victoria University of Wellington, New Zealand
Rachel Joanne Carr, Newcastle University, United Kingdom

****Correspondence:***
Adina E. Racoviteanu
a.racoviteanu@exeter.ac.uk

Specialty section:
This article was submitted to Cryospheric Sciences, a section of the journal Frontiers in Earth Science

Received: *30 August 2021*
Accepted: *17 November 2021*
Published: *11 April 2022*

Citation:
Racoviteanu AE, Glasser NF, Robson BA, Harrison S, Millan R, Kayastha RB and Kayastha R (2022) Recent Evolution of Glaciers in the Manaslu Region of Nepal From Satellite Imagery and UAV Data (1970–2019). Front. Earth Sci. 9:767317. doi: 10.3389/feart.2021.767317

INTRODUCTION

Supraglacial debris cover is a prominent feature of glaciers in high, rugged relief orogenic belts including the Hindu Kush Himalaya (Kääb et al., 2012), the Tien Shan (Hagg et al., 2008), Caucasus (Stokes et al., 2007; Tielidze et al., 2020), Alaska (Berthier et al., 2010), New Zealand (Anderson and Mackintosh, 2012; Anderson B. et al., 2021) and to a smaller extent in parts of the Andes (Racoviteanu et al., 2008) and the European Alps (Smiraglia et al., 2000; Deline, 2005). Globally, however, supraglacial debris cover only accounts for a small percentage (~4–7%) of the global glacierized area (Scherler et al., 2018; Herreid and Pellicciotti, 2020). Debris material generally originates from rock and snow avalanches from the steep surrounding valley slopes, melt-out of englacial debris due to subglacial erosion processes (Jansson and Fredin, 2002), or collapsing lateral or terminal moraines (Hambrey et al., 2008; Kirkbride and Deline, 2013; Rowan et al., 2015). The high denudation rates characteristic of rugged environments favour the accumulation and transport of large quantities of rock debris to the glacier surface (Kirkbride, 2011), creating debris-covered glacier tongues up to a few tens of kilometres long such as Baltoro Glacier (62 km) in the Karakoram (Mihalcea et al., 2006) or Ngozumpa Glacier (~20 km) in Nepal Himalaya (Rowan et al., 2020). Despite its small global extent, supraglacial debris plays an important role in the mass balance of glaciers and their future behaviour, and for this reason it has gained increasing attention in recent decades. One area of concern is currently the fast development of supraglacial lakes in certain areas of the Himalaya, and the potential implications of this for water resources and glacier hazards, notably glacier lake outburst floods (GLOFs).

Supraglacial debris cover controls the ice melt underneath the debris layer (Benn and Evans, 1998; Kayastha et al., 2000; McCarthy et al., 2017) i.e. a thin debris layer initially increases rates of ice-surface melt (Østrem, 1975) but for a thick debris layer, the insulating effect dominates (Nicholson and Benn, 2006). Understanding the ablation rates associated with debris-covered glaciers is important for predicting the melt rates from glacierized regions and estimating their contribution to sea-level rise with climate change (Scherler et al., 2011; Shannon et al., 2019; Immerzeel et al., 2020). Recent studies based on satellite imagery have shown an upwards expansion of the supraglacial debris cover upwards in several regions (Mölg et al., 2019; Tielidze et al., 2020; Xie et al., 2020), associated with the stagnation of the glacier fronts and glacier surface velocity slowdown (Dehecq et al., 2019). Furthermore, in the last decade, several studies reported similar thinning rates and mass loss for debris-covered and clean ice glaciers (Bolch et al., 2012; Gardelle et al., 2012; Kääb et al., 2012; Brun et al., 2017). At the glacier scale, ephemeral features such as bare ice cliffs and supraglacial ponds play an important role in the ablation of debris-covered glaciers by enhancing local ablation (Brun et al., 2016; Miles et al., 2018b; Irvine-Fynn et al., 2017). However, field-based studies reveal important local variability in the role of these supraglacial features for ice melt rates. For example, the insulating effect still dominates on many debris-covered glaciers such as Changri Nup Glacier in Nepal Himalaya) (Vincent et al., 2016; Brun et al., 2018; Anderson et al., 2021). These supraglacial features are also extremely dynamic. Ice cliffs are high–relief, bare-ice areas that are commonly visible as vertical or near-vertical 'scars' on the surface of debris-covered glaciers (Sakai et al., 2002; Steiner et al., 2015; Buri et al., 2016; Buri et al., 2021). Supraglacial ponds are seasonal, i.e., they emerge during the monsoon season (Miles et al., 2018a); some can disappear through intra-glacial conduits (Gulley et al., 2009) or re-emerge in the same location (Taylor et al., 2021). Others persist between seasons and coalesce to form larger supraglacial lakes which may evolve into fully-formed proglacial ice and/or moraine-dammed lakes (Benn et al., 2012; Thompson et al., 2012) with a potential to create GLOF events (Richardson and Reynolds, 2000; Komori, 2008; Benn et al., 2012; Reynolds, 2014; GAPHAZ, 2017). Increasing trends of pond development of 17–52% a^{-1} have been reported for the last few decades, for example in the Khumbu region of Nepal Himalaya (Watson et al., 2016; Chand and Watanabe, 2019). Such trends are consistent with the reported proglacial lake and supraglacial pond increase and over the entire Himalaya (Nie et al., 2017). Quantifying the evolution of these features has been the focus of several studies (Watson et al., 2016; Watson et al., 2017a; Miles et al., 2017; Steiner et al., 2019), but these remain biased towards well-studied regions such as the Khumbu and Langtang regions in the Nepal Himalaya.

The role of glacier morphology in controlling glacier behaviour has been demonstrated in recent Himalayan studies (Salerno et al., 2017; Brun et al., 2019), but features such as supraglacial vegetation on debris-covered glaciers have not received much attention. It has been shown that supraglacial vegetation has been expanding on the surface of debris-covered glaciers (Fickert et al., 2007; Tampucci et al., 2016; Anderson et al., 2020), but studies on this topic remain scarce. Comprehensive assessments of surface geomorphology, supraglacial pond coverage, moraine characteristics and vegetation are still needed. Understanding the fluctuations of these surface characteristics is important, as they may indicate the transition from a debris-covered glacier to a rock glacier which has been hypothesised as an evolutionary response for at least some glaciers under climate change (Shroder et al., 2000; Monnier and Kinnard, 2017; Jones et al., 2019; Knight et al., 2019). With the exception of a few studies (Watson et al., 2016; Watson et al., 2017a; Watson et al., 2017b; Miles et al., 2017; Steiner et al., 2019; Taylor et al., 2021), significant gaps remain with respect to the evolution of these supraglacial features, particularly over decadal time scales. Despite the increasing emergence of remote sensing large-scale studies, automated workflows and big data (Brun et al., 2017; Dehecq et al., 2020; Rounce et al., 2021), small scale studies that combine remote sensing with field observations remain crucial and complementary for understanding the intra-regional variability in the behaviour of debris-covered glaciers.

The aim of our study is to fill the gap in a poorly studied area of the Nepal Himalaya—the Manaslu region of the central Himalaya, comprising both clean and debris-covered glaciers. In a previous study, Robson et al. (2018) investigated area and elevation changes

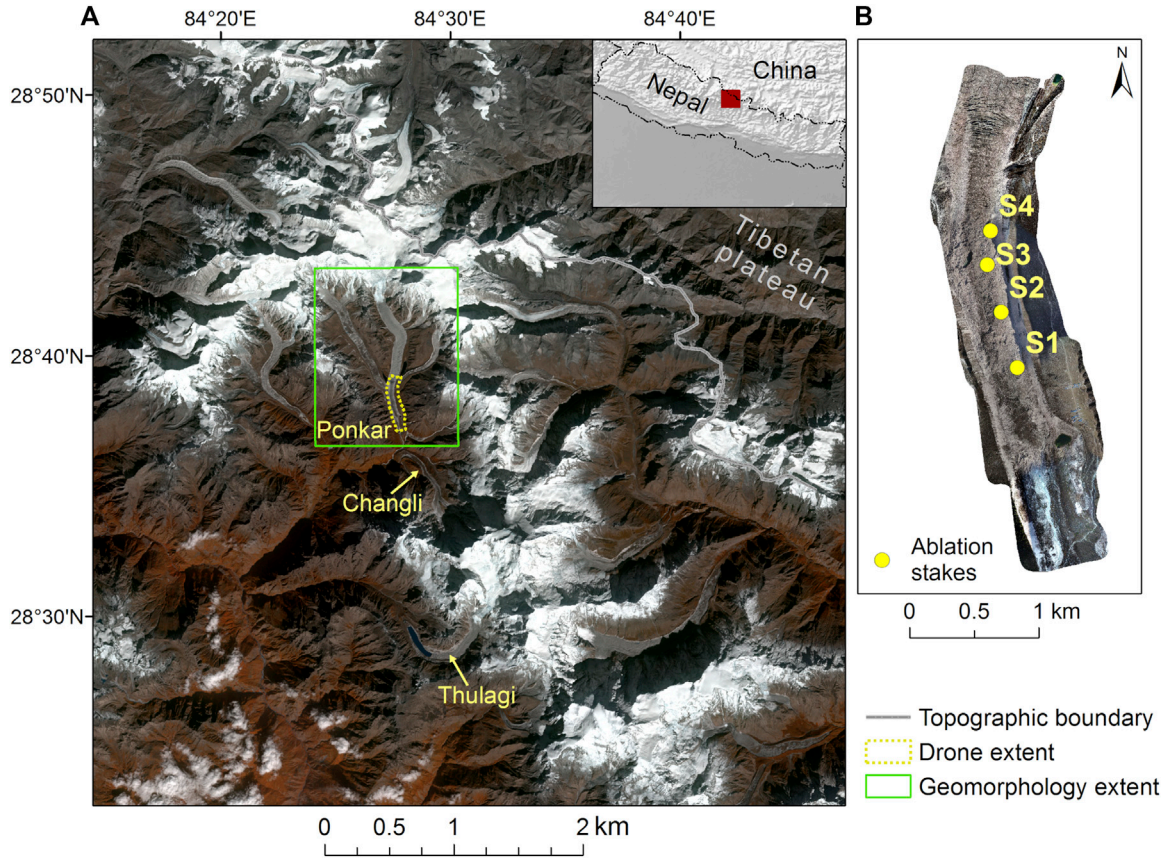

FIGURE 1 | Location map of the Manaslu study area, located in the Gandaki Province of Nepal **(A)** False colour composite (bands 5,4,3) of RapidEye satellite image acquired on November 20th, 2019 showing the glaciers discussed in the text; **(B)** Orthophoto from of the UAV survey (dashed yellow polygon in **(A)**). The green rectangle shows the extent of the geomorphology analysis on Ponkar Glacier (see **Figure 8**).

in this region from 1962 to 2013 using Corona declassified imagery and medium resolution Landsat data (30 m). In this study, we use new, freely available high-resolution Planet images (3–5 m), a better coverage of Corona 1970 data and 2019 UAV data acquired in the field to update and expand the existing study and to characterize the surface and evolution of glaciers in the Manaslu region over the last five decades. This complements the existing Robson et al. (2018) study by providing higher quality datasets to investigate area and surface elevation changes, geodetic glacier mass balance, surface velocity changes, and structural changes. We illustrate these changes at the local scale by comparing and contrasting the evolution of two debris-covered glaciers in this region: Ponkar Glacier, which has been studied in the field since 2016 (Shrestha et al., 2020) and Thulagi Glacier and Lake, which have been described in the context of GLOFs (Pant and Reynolds, 2000; Haritashya et al., 2018). Field-based ablation measurements on Ponkar Glacier provide opportunities for validating the remote sensing methods. By combining various methodologies and data sources, our study complements and expands the existing records on these glaciers and assesses the spatial representativeness of the dynamics observed on these two glaciers. Our study provides an example of an integrated assessment of a glacier system, and how it can be nested within a regional scale analysis.

STUDY AREA

Our study focuses on the Manaslu region (1,971 km^2), situated in the headwaters of the Dudh Khola in the Manang district, Gandaki Province of Nepal (**Figure 1**). The study area is located in the central Himalaya region as defined in previous studies (Bolch et al., 2012). Climatically, this region is located at the boundary between the Indian summer monsoon in the south west and the drier areas of the Tibetan plateau in the north (Yanai et al., 1992; Benn and Owen, 1998). The last major glacier advance in this area was probably in the Little Ice Age (LIA) (Rowan, 2017), with the peak of moraine building between 1,300 and 1600 CE, slightly earlier than the coldest period of the Northern Hemisphere (Rowan, 2017) and earlier than several regions in the Southern Hemisphere (Solomina et al., 2015). The area comprises various types of glaciers, with a mix of clean

TABLE 1 | Satellite data used in this study and their characteristics.

Image/data	Date	Sensor	Product	Bands	Type	Focal length	Nominal resolution
DS1112-1007DA183 DS1112-1007DA184 DS1112-1007DA185	1970–11-19	Corona KH4	Scanned film	panchromatic	Stereo (after)	24	7.5 m
DS1112-1007DF178 DS1112-1007DF179 DS1112-1007DF180					Stereo (forward)		
20191120_042852_4552403 to 455240620191120_042856_4552303 to 455230620191120_042904_4552203 to 4,55220420191120_042904_4552103 to 455210620191120_042904_4452127 to 4452327	2019–11-20	RapidEye	Analytic 3A	Blue 440–510 nm Green 520–590 nm Red 630–685 nm Red edge 690–730 nm NIR 760–850 nm			5 m
HMA DEM	2013	WorldView 2	Elevation				8 m

glaciers, debris-covered glaciers, lake-terminating glaciers (Robson et al., 2018) and rock glaciers. A small number of glaciers in our study area are located across the topographic divide in Tibet and are discussed separately in the text. The southern part of our study area (627 km^2) was investigated in a previous study (Robson et al., 2018). The study area also comprises Thulagi Glacier and Thulagi Lake. The latter is a proglacial moraine-dammed lake surveyed in the field as well as by remote sensing with regards to its hazard potential (Haritashya et al., 2018).

For the study of in-depth geomorphology and glacier surface changes with UAV measurements, we focused on the largest glacier system in the study area, Ponkar Glacier (28°37′49″ N; 84°28′14″ E). The glacier has three tributaries (Kechakyu Khola, Ponkar and Salpudanda) (**Figure 1A**) (Sapkota et al., 2016; Shrestha et al., 2020). The estimated average glacier thickness is ~134 m (Bajracharya et al., 2014), with a median elevation of 5,872 m a.s.l. and a terminus elevation of 3,651 m a.s.l. in 2019. The lower part of the tongue comprises large patches of mature supraglacial vegetation. We chose this glacier due to the relatively easy accesses as well as the field measurements initiated in the last 8 years in this area.

METHODOLOGY

Satellite Data

Our analysis spans the periods 1970–2013 and 2013–2019, corresponding to two spatial scales (regional/local). Satellite data used for the various time steps are summarized in **Table 1**. For the 1970s decade, we obtained declassified imagery from the Corona KH-4B mission (Dashora et al., 2007). Corona KH-4B satellites acquired data from September 1967 and May 1972 using a pair of counter-rotating panoramic cameras with a 30° separation angle (one camera tilted 15° forward and one 15° backwards), yielding stereo imagery (Dashora et al., 2007). We obtained three stripes of stereo images from the mission 1,112 acquired on Nov 19, 1970. This date corresponds to the end of the ablation season in this part of the Himalaya (Oct/Nov). Image stripes were scanned at 7 microns directly from the original film stripes and USGS; the digital scans were obtained at no cost from the US Geological Survey (https://earthexplorer.usgs.gov). The scenes were cloud-free over the glaciers.

For the recent time period, we obtained high-resolution images stripes at 5 m from Planet's RapidEye constellation (Planet_Labs, 2021). RapidEye consists of multispectral data (five spectral bands in the visible and near infrared) with a spatial resolution of 6.5 m on the ground and a positional accuracy of <10 m (**Table 1**) (Planet Labs, 2016). We used Level 3A data, which consist in stripes of multispectral, radiometrically corrected orthotiles processed at 5 m spatial resolution. These represent surface reflectance computed using at-sensor radiance based on the 6S radiative transfer model (Vermote et al., 1997) and MODIS data, which accounts for atmospheric effects (Planet Labs, 2021). We mosaicked these using nearest neighbour to output a single image covering our study area (**Figure 1A**). The Nov 20, 2019 image was cloud-free and was acquired at the same time of the year as the Corona data (Nov 19, 1970) and a few days after our field campaign (Nov 12–16th, 2019). The 2019 image had some seasonal snow outside the glaciers in some areas, so we used a second scene from Oct 20, 2015 to refine the glacier extents around rock outcrops and debris cover, and to eliminate seasonal snow.

The High Mountain Asia (HMA) DEM at 8 m spatial resolution (Shean, 2017) was chosen as reference to represent the modern glacier surface for the 2010s decade. The HMA DEM tiles are generated from very high-resolution satellite imagery from Digital Globe Inc., from 2002 to 2016, processed using the NASA AMES Stereo Pipeline as described in Shean et al. (2016). We obtained six DEM tiles derived from along-track Worldview two imagery from the NSIDC DAAC High Mountain Asia (HMA) collection (https://nsidc.org/data/highmountainasia) with dates ranging from November 16, 2013 to November 25, 2013. Although DEM tiles were available from subsequent years, the coverage of the study area was incomplete and in particular large voids were present over some of the glacier accumulation areas. The geolocation accuracy of the HMA DEM is estimated at < 5 m, with relative vertical errors of 1–2 m. Larger uncertainties occur due to clouds, steep slopes image saturation and/or correlation failures (Shean et al., 2016). We also obtained the ALOS Global Digital Surface Model (AW3D30) version 2.2

(30 m) (JAXA, 2019), constructed from data acquired from 2006 to 2011. The vertical accuracy of this dataset is estimated at ~10 m in Eastern Nepal (Tadono et al., 2014). The AW3D30 DEM was used as regional elevation reference for ground control points in the Corona DEM extraction process (see section *Corona DEM Generation and Co-Registration*).

Field Data

In November 2019, we conducted a UAV survey of the lower ablation area of Ponkar Glacier (~4 km^2, 3,646–4,238 m a.s.l.) (**Figure 1B**) using two DJI Phantom four Pro UAVs, with an 80% forward and 70% side overlap, covering an area of 3.36 km^2. A total of 1,110 images were orthorectified using nine ground control points (GCPs) and were processed using a dense stereo matching algorithm in Pix4D Mapper software to produce a 0.50 m orthoimage and 1 m DEM. The accuracy of the orthorectification process was estimated as 1 m horizontally and <1.5 m vertically (2 and 3 times the ground sampling distance, respectively). Both the orthoimages and the resulting DEM were used to refine the geomorphological mapping (see section *Mapping of Supraglacial and Geomorphological Features*).

The lower ablation area of Ponkar Glacier has been surveyed in the field for mass balance and hydro-geochemical studies since 2016 (Shrestha et al., 2021). Ice ablation measurements on the lower area of Ponkar Glacier have been carried out yearly from 2016 to 2019. A Kovacs hand driller was used to drill the debris-covered ice up to 2.5 m to install the ablation stake at four locations under different debris thicknesses ranging from 11 to 20 cm. Four stakes (Stakes 1–4) were installed in March 2016 and resurveyed in different dates during field trips from 2016 to 2019. Their locations are shown on **Figure 1B** and their are characteristics listed in **Table 2**.

Glacier Mapping and Auxiliary Data

Glacier outlines for the year 1970, including debris cover, were delineated using on-screen manual digitization complemented with image thresholding from the Corona panchromatic image. Shaded relief terrain derived from the 1970 Corona DEM was used to identify rock outcrops. The low contrast of the black and white Corona image made it difficult to distinguish ice from snow in a few areas. Therefore, Corona outlines were compared with the ICIMOD inventory (Mool et al., 2002), which was constructed by manual mapping on topographic maps at 1: 50,000 scale published in the 1950s–1970s by the Survey of India (Survey of India, 2005). The latest glacier inventory in this area is the GAMDAM glacier inventory (Sakai, 2019), constructed based on semi-automated mapping from Landsat imagery and manual editing. However, most of the GAMDAM glacier outlines in our study area dated from 1994, except for those in the northern part (China) which dated from 2010, and were thus not suitable for analysis. For the year 2019, glacier outlines were derived by manual digitization on the RapidEye image; areas of seasonal snow were removed manually. When glaciers disconnected or disintegrated, we counted them as special glacier entities as per guidelines established by the Global Land Ice Measurements from Space community (Raup and Khalsa, 2007; Racoviteanu et al., 2009). Debris-covered glacier sections were cross-checked visually against high-resolution SPOT imagery from Oct 24, 2019 visible on the Google Earth platform. For both the 1970 and 2019 time steps, ice divides were constructed on the basis of the AW3D30 DEM complemented with the HMA DEM using the buffer method (Granshaw and Fountain, 2006; Bolch et al., 2010). These were kept constant for the two time steps to facilitate the glacier change detection analysis and to minimize uncertainties related to differences in the upper part of the accumulation area. Rock outcrops were delineated for 1970 and 2019 separately.

We calculated glacier surface slope, mean altitude, and altitudinal range for all the glaciers in the study area based on the AW3D30 DEM (for the regional trends) and the HMA DEM (for the in-depth study on Ponkar Glacier). We also calculated glacier surface velocities in the Manaslu region using a combination of Sentinel-2 and Landsat-8 imagery, following Millan et al. (2019). The ice velocity maps were calculated using a feature tracking algorithm on all possible image pairs, with repeat cycles ranging from the sensor nominal repeat cycle (i.e., 5 days for Sentinel-2, 16 days for Landsat-8) up to more than a year (Millan et al., 2019). Ice velocity mosaics are finally assembled at a sampling resolution of 50 m, by computing a pixel-by-pixel weighted average (Millan et al., 2019). We also obtained yearly velocity data from 2000 to 2017, generated using auto-RIFT (Gardner et al., 2018) and provided by the NASA MEaSUREs ITS_LIVE project (Gardner et al., 2019).

TABLE 2 | Location of the ablation stakes on the lower part of the Ponkar Glacier, shown on **Figure 1B**.

	Elevation (m)	Latitude (°)	Longitude (°)	Debris thickness (cm)
S1	3,780	28.63717	84.46619	20
S2	3,830	28.64102	84.46481	15
S3	3,881	28.64432	84.46365	11
S4	3,924	28.64669	84.46384	20

Corona DEM Generation and Co-registration

The Corona image stripes were set up as a single block file in ERDAS IMAGINE Photogrammetry Suite (ERDAS, 2010) using the UTM projection system (zone 45N), with WGS84 vertical and horizontal datums. Since Corona parameters are not available, we used a non-metric camera model based on the actual flying height, focal length and the nominal scale of the photos (**Table 1**). The interior and exterior orientation of the stripes were solved in the aerial triangulation step using Ground Control Points (GCPs) and Tie Points (TPs). For the northern part of the study area (four stereo image stripes), TPs were generated automatically in ERDAS IMAGINE Photogrammetry and were complemented with manually generated points. This resulted in a total of 3,047 TPs with a mean uncertainty of 6.6 m and a standard deviation of 9.1 m. A total of 255 GCPs were manually digitized on stable terrain from the RapidEye scene and identified on each of the stereo image stripes. Elevations of the ground control points were extracted from the AW3D30 DEM. The total root mean square error for the triangulation

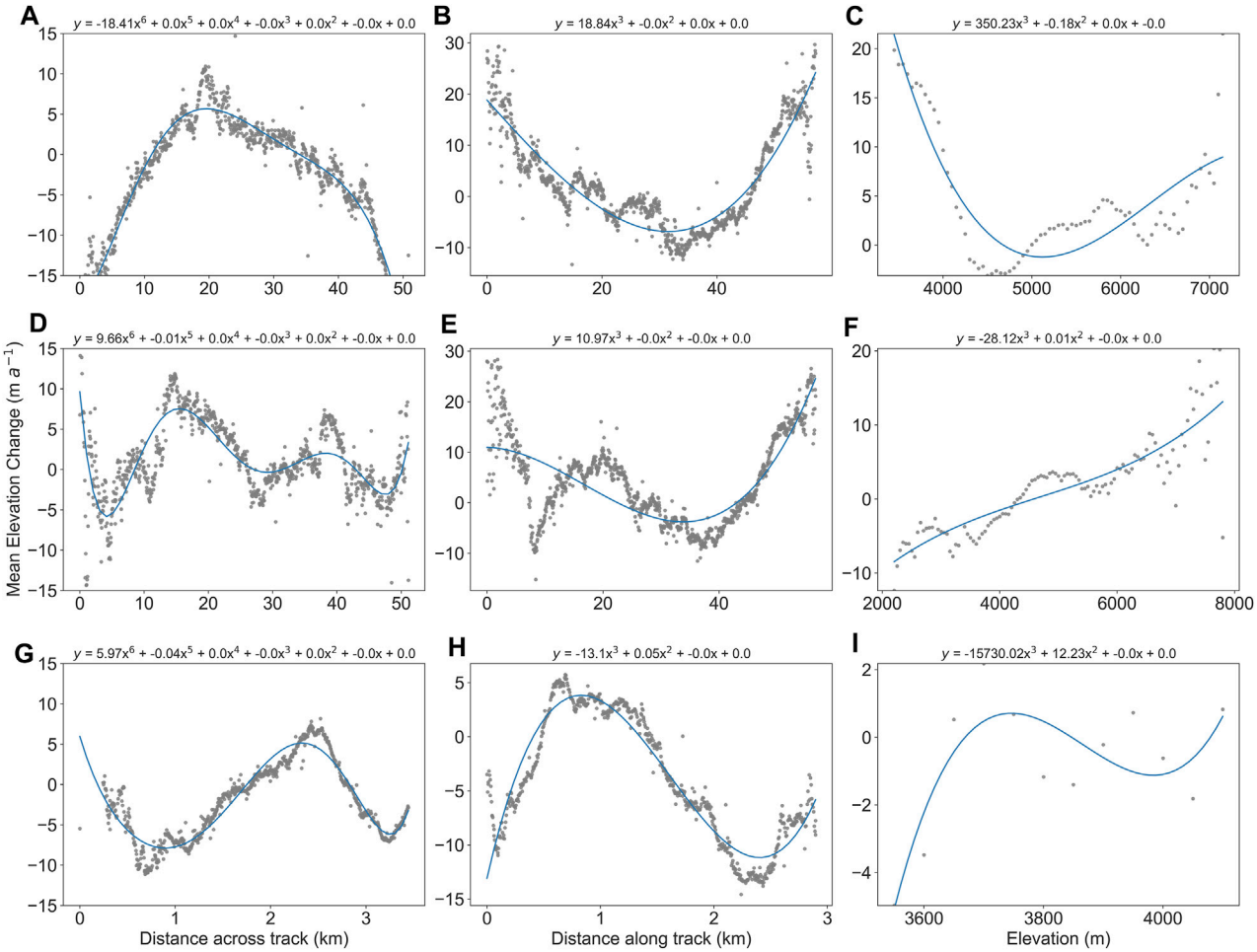

FIGURE 2 | Non-linear elevation biases over stable (non-glacierized) terrain. The top two rows show biases between the 2013 HMA DEM and the 1970 Corona DEM for the Northern DEM **(A–C)** and the Southern DEM **(D–F)**. The bottom row shows the elevation biases between the 2019 UAV DEM and the 2013 HMA DEM for the lower part of Ponkar Glacier **(G–I)**. From left to right, graphs represent: across track biases, along track biases and vertical biases, respectively. The blue lines show the polynomials used to remove non-linear co-registration biases (sixth-order for the across-track, and third-order for along-track and elevation biases.

(RMSE) was 1.9 pixels, with ground x, y and z accuracy of 14.9, 11.2 and 19.3 m, respectively. Point clouds were generated using the Dense Point Matching with the Enhanced Automatic Terrain Extraction (eATE) in ERDAS Imagine Photogrammetry module using the Normalized Cross-Correlation routine with a 9 × 9 window size, spike interpolation setting to remove extreme values and a point threshold of 2.5 (number of points for interpolation). No filtering was applied to the point clouds. For the southern part of the study area where Thulagi Glacier is located, two 1970 image stripes had been processed similarly in a previous study (Robson et al., 2018) using 75 GCPs and 1837 tie points with a RMSEz <5 m. To extract the DEMs, we utilised both the eATE routine in ERDAS and PCI Geomatica. Each DEM was extracted as a point cloud which was then gridded using a finite difference interpolation method with 10 iterations within Geomatica Banff (PIC Geomatics Inc., 2020).

Two DEMs were produced: one for the northern stereo pairs, and one for the southern stereo pairs. Each DEM was co-registered independently before being mosaiced together. The DEM co-registration was performed in a two-step process using the Numpy and ArcPy python packages. Linear co-registration biases were removed using the method outlined by Nuth and Kääb (2011) which minimizes the root mean square residuals of the elevation bias over stable (i.e non-glacial) terrain. Terrain with slope values less than 10° and greater than 40° was excluded. The co-registration was repeated iteratively until the mean elevation bias over stable terrain decreased by <2%. In both cases, this led to the process being run 8 times. Corona imagery contains significant

TABLE 3 | Summary of the co-registration shifts for the northern and southern parts of the study area, corresponding to the Corona stripes and the UAV DEM.

DEM	Co-registration shift X (m)	Co-registration shift Y (m)	Co-registration shift Z (m)
Northern	5.28	−0.81	−25.78
Southern	−6.23	8.57	−21.84
UAV	1.20	−3.75	−114.82

TABLE 4 | Criteria used in geomorphological mapping to identify ice-surface and proglacial landforms. Adapted from Glasser et al. (2005).

Landform/ feature	Identification criteria		Possible identification errors	Glaciological significance
	Morphology	Colour/structure/texture		
Contemporary glaciers	Bare ice, snow and debris. Surface structures (e.g., crevasses) may be visible	White to light blue Surface smooth to rough	Minor over-estimate in glacier extent possible where confused with snow cover	Foci for ice discharge
Terminal and lateral moraines	Prominent cross-valley single or multiple ridges with positive relief. Linear, curved, sinuous or saw-toothed in plan. Lateral moraines follow glacier margins	Shadowing due to change in relief and change in colour where moraines are vegetated	Possible, but unlikely, confusion with trimlines where moraines have low relative height	Moraines mark the former terminal and lateral position of glaciers
Sandur/outwash sediment	Valley floor accumulations of sediment, commonly dissected by a braided stream pattern	Flat, mainly grey areas where there is thin vegetation cover. Erosional scars and sharp boundaries with surrounding terrain	Possible, but unlikely, confusion with deltas or ice-contact deposits	Marks major drainage routes from contemporary glaciers and other glacier-fed streams

panoramic lens distortions which can result in non-linear elevation biases of up to 20 m (Bolch et al., 2011; Robson et al., 2018). These elevation biases were removed by fitting a sixth order polynomial for along track and third order for across track and elevation to the stable terrain elevation biases (**Figure 2**). A summary of the co-registration shifts is given in **Table 3**. The process was iterated a total of six times until no noticeable trend in stable ground polynomials was visible. The co-registered surface elevation rasters were then mosaicked together to one file. The same co-registration routine was applied to co-register the 2019 UAV data to the 2013 DEM with the linear-co-registration being repeated four times and the non-linear co-registration repeated three times.

Geodetic Methods

Surface elevation changes and the resulting geodetic mass balance were computed at two time steps for the two spatial domains using the geodetic (DEM differencing) method (Berthier et al., 2004). For the large spatial domain (Manaslu region), we used the 1970 Corona DEM and the 2013 HMA DEM. For the smaller domain (the lower area of Ponkar Glacier), we used the 2013 HMA DEM and the 2019 UAV data. DEMs were subtracted on a cell-by-cell basis for each of the time periods. For both periods, the elevation difference rasters resulting from the co-registration and mosaicking were cleaned using the method set out by Gardelle et al. (2013) where the mean surface elevation change per 50 m altitudinal band was calculated. Any pixels that were not within three standard deviations of the mean value were excluded. Voids were filled by fitting third-order polynomials to the mean elevation change per 50 m altitudinal band, after McNabb et al. (2019). A uniform glacier ice density of 850 ± 60 kg m^{-3} (cf. Huss, 2013) was used to convert volume changes into mass changes for the geodetic mass balance calculation.

Mapping of Supraglacial and Geomorphological Features

We mapped the glacier surface features and associated geomorphology in 1970 and 2019 at the local scale (Ponkar Glacier). Ice-surface features mapped included glacier flow units, crevasses and ogives; mapped landforms included terminal and lateral moraines and large areas of outwash which complement the glacier extents. These were mapped manually using on-screen digitization on the Corona and RapidEye images on the basis of standard criteria for identifying and mapping ice-structural and glacial landforms (adapted from Glasser et al., 2005) and Goodsell et al. (2005)) (**Table 4**). Surface features (ice cliffs, supraglacial ponds and ice-surface vegetation) were mapped from Corona and RapidEye scenes using an image segmentation workflow implemented in the ENVI Feature Extraction Module (Harris Geospatial, 2017). This consisted in applying an edge algorithm to identify the pond, ice cliffs and vegetation segments using a texture kernel size of 3 pixels. Segments were merged manually to prevent over-segmenting and to combine different segments into one pond, ice cliff or vegetation patch.

Uncertainty Estimates

The uncertainty of the elevation change was calculated based on the method set out by Falaschi et al. (2019). The uncertainty of the volume change ($E\Delta v_i$) (in m^3) was determined by summing up the standard error ($E\Delta h_i$) per 50 m altitudinal band, multiplied by the area of each altitudinal band (A_i) in order to account for the hypsometry:

$$E\Delta v_i = \sum_i^n E\Delta h_i \times A_i \quad (1)$$

Where the standard error ($E\Delta h_i$) is derived from the standard deviation over stable ground (σ_{stable}), divided by the effective number of observations (N):

$$E\Delta h_i = \frac{\sigma_{stable}}{\sqrt{N}} \quad (2)$$

N is calculated using the number of pixels (N_{tot}) in the DEM differencing, the pixel size (PS), and the distance of spatial autocorrection, which following Bolch et al. (2011) we took to be equal to 20 pixels:

$$N = \frac{N_{tot} \times PS}{2d} \quad (3)$$

TABLE 5 | Summary of area changes (1970–2019) and elevation changes (1970–2013) over the entire domain for all the glaciers and for the various types of glaciers.

Sample	# Glaciers	Area change (% a^{-1})	# Glaciers	Mean elevation change (ma^{-1})	Mean mass balance (m w.e. a^{-1})
	1970/2019	1970–2019		1970–2013	
All glaciers	212/274	−0.26 ± 0.01	136	−0.20 ± 0.02	−0.17 ± 0.03
Debris-covered glaciers	35/35	−0.23 ± 0.01	30	−0.22 ± 0.02	−0.18 ± 0.03
Clean glaciers	177/239	−0.24 ± 0.01	106	−0.17 ± 0.02	−0.14 ± 0.02
Lake-terminating glaciers	3/3	−0.25 ± 0.01	3	−0.41 ± 0.04	−0.35 ± 0.06

In addition to $E\Delta v_i$ we also considered the uncertainties relating to the volume to mass conversion (E_ρ), which following Huss (2013) was taken to be ±60 kg m^{-3} and the error in delineating the glacier outline (E_a) which was assumed to be 5%. $E\Delta v_i$ was combined with E_ρ and E_a to derived the total uncertainty, $E\Delta v_{tot}$:

$$E\Delta v_{tot} = E^2\Delta v_i + E_\rho^2 + E_a^2 + E_r^2 \quad (4)$$

Surface elevation change raster data tends to contain data voids over steep or shadowed terrain, as well in areas of low image contrast. The polynomial fit used to interpolate each glacier was inspected, and any glacier where the fit was poor was not included in the analysis of surface change. In the absence of comparable *in-situ* data, we estimated DEM uncertainties in the based on the literature combined with biases measured over the stable terrain using a conservative approach. Magnusson et al. (2016) demonstrated that such techniques typically overestimate uncertainties as they neglect the spatial dependence of DEM errors.

Uncertainties in the 1970 and 2019 glacier areas and geomorphology units were determined using the buffer method (Granshaw and Fountain, 2006; Pekel et al., 2016; Paul et al., 2017). This consists of applying a buffer inside and outside the glacier polygons and calculating the standard deviation as an uncertainty estimate. Following the method of Granshaw and Fountain (2006), we used ~½ of the RMSE of the geolocation errors of both images for the size of the buffer (5 m buffer for RapidEye and 6.5 m buffer for Corona). Geolocation errors were calculated as the RMSE of each satellite image orthorectification. The uncertainty of the area change analysis was estimated as the RMSE of the two error uncertainties (1970 and 2019). The error of the supraglacial vegetation was estimated using a ½ pixel buffer (1 and 2.5 m for Corona and RapidEye images, respectively). For ice cliffs and ponds mapping, we used uncertainty values from Steiner et al. (2019) study also based on manual digitization of high resolution imagery. The uncertainty in the glacier terminus recession was estimated using two RapidEye 2 pixels and 5 Corona pixels.

RESULTS

Regional Glacier Changes in the Manaslu Region

Area Changes 1970–2019

Mapping of the 1970 glacier extents from Corona imagery yielded 212 glaciers (177 clean ice glaciers and 35 debris-covered glaciers), ranging in area from 0.005 ± 0.0001 km^2 to 49.5 ± 1.0 km^2, with a total area of 610.1 ± 12.8 km^2 (**Table 5**). For 2019, based on RapidEye imagery, we mapped 274 glaciers (239 clean ice and 35 debris-covered glaciers), ranging in area from 0.002 ± 0.0001 km^2 to 46.7 ± 1.3 km^2 and a total area of 531.6 ± 14.4 km^2. Some glaciers fragmented or detached from the main glacier by 2019, resulting in a higher number of glacier entities in 2019. Of the total glacierized area, 35 glaciers had debris cover in the lower part of their ablation areas. In 2019, the area of the supraglacial debris cover was 73 ± 2 km^2 (13.6% of the total glacierized area), which is 3.5 km^2 larger than the area obtained based on the Herreid and Pellicciotti (2020) dataset for the same extent. Out of the 35 debris-covered glacier entities mapped, 24 overlapped with Herreid and Pellicciotti (2020); we mapped 11 additional debris-covered glacier entities based on the RapidEye image.

The total glacierized area in the Manaslu region reduced by 78.5 ± 2.7 km^2 (−12.9 ± 0.4%) from 1970 to 2019, at a mean rate of −1.6 ± 0.05 km^2 a^{-1} (−0.26 ± 0.01% a^{-1}). The 35 debris-covered glaciers lost 46.1 ± 1.6 km^2 (−11.4 ± 0.4%) of their area from 1970 to 2019 (a mean rate of −0.23 ± 0.01% a^{-1}). The remaining clean ice glaciers (177 glaciers in 1970 and 239 in 2019) lost 22.9 ± 0.8 km^2 (−11.6 ± 0.4% of their area), at a rate of −0.24 ± 0.01% a^{-1}, similar to that of debris-covered glaciers. We identified three glaciers that terminated in a proglacial lake both in 1970 and 2019. The glacierized area of these glaciers reduced by 12% from 1970 to 2019 (−0.25 ± 0.01% a^{-1}). The 19 glaciers located north of the topographic divide (on the Tibetan plateau) lost 10.1 ± 0.3 km^2 from 1970 to 2019 (−12 ± 0.4% of the glacierized area, or −0.24 ± 0.01% a^{-1}). All of these glaciers except two are clean glaciers, and they exhibit rates of area loss similar to the entire domain. Glacier median elevation over the entire domain shifted from 5,729 m a.s.l in 1970 to 5,800 m. a.s.l. in 2019, a rise of +72 m over five decades. Similarly, the elevation of glacier termini rose from 3,118 m a.s.l to 3,265 m a.s.l in 2019, a +147 m upward shift. The maximum elevation of glaciers in the domain was 8,057 m a.s.l. in 2019.

Surface Elevation Changes and Mass Balance (1970–2013)

Here we present surface elevation changes for the 136 glaciers (a surface of 512.2 km^2, or 84% of the 1970 glacierized area) which had sufficient elevation change data to determine geodetic mass balances and mean surface lowering rates. A total of 76 glaciers were excluded from the surface change analysis due to data voids. Glaciers in the Manaslu region exhibited a mean surface lowering of −0.20 ± 0.02 ma^{-1} between 1970 and 2013 (**Table 5** and **Figure 3**), corresponding to a mean geodetic mass balance of −0.17 ± 0.03 m w. e.a^{-1}. On average, debris-covered tongues thinned at the rate of −0.22 ± 0.02 ma^{-1} (−0.18 ± 0.03 m w. e.a^{-1}), a slightly

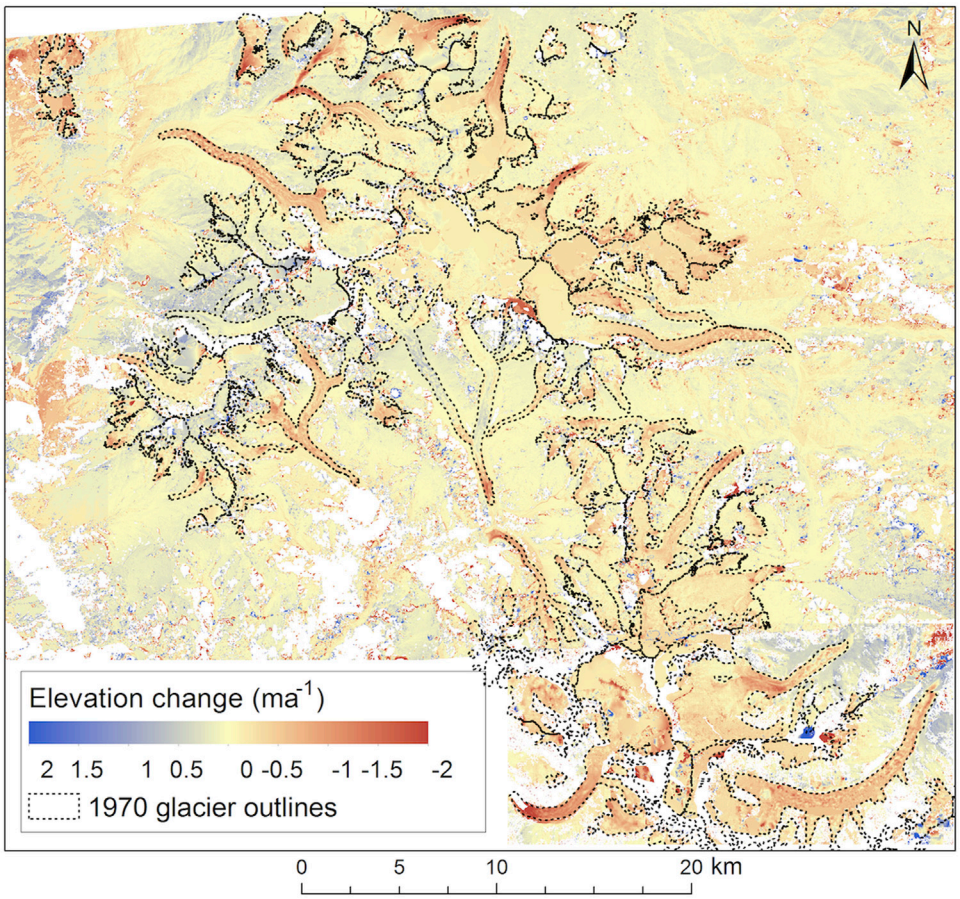

FIGURE 3 | Surface elevation changes for all glaciers over the full domain (Manaslu region) from 1970 to 2013.

higher rate than clean ice glaciers (−0.17 ± 0.02 ma^{-1}, −0.14 ± 0.02 m w. $e.a^{-1}$) (**Table 5**). The three lake-terminating glaciers had a double thinning rate and mass balance (−0.41 ± 0.04 ma^{-1}, −0.35 ± 0.06 m w. $e.a^{-1}$) compared to the regional average (**Table 5**). Individual average thinning rates and mass balance of the clean ice glacier sample (n = 106) and debris-covered glaciers (n = 30) were statistically significant based on the two independent sample Welch's *t*-test (Welch, 1947) (90% confidence level, *p*-value < 0.10). Individual glacier mass balances ranged from −0.56 ± 0.16 m w. $e.a^{-1}$ to +0.35 ± 0.07 m w. $e.a^{-1}$. Thirty glaciers had positive or approximately in balance geodetic mass balances between 1970 and 2013, all of which were situated at high elevations (>6,000 m a.s.l.). Mean glacier-by-glacier average thinning rates exhibit a slight southwest to northeast pattern, with negative thinning rates increasing at the rate of 0.003 ma^{-1} per 1 km in the longitude direction and 0.002 ma^{-1} per 1 km in the latitude direction.

Changes at Glacier Scale: Ponkar and Thulagi Glaciers

Area and Elevation Change 1970–2013–2019

The largest individual glacier system was Ponkar Glacier, with 38.0 ± 1.0 km^2 clean ice and 13.3 ± 0.4 km^2 debris-covered ice in 2019. Counting the three branches, its total area reduced from 54.7 ± 1.1 km^2 in 1970 to 51.2 km^2 in 2019, a loss of 3.5 ± 0.1 km^2 (−6.4 ± 0.1% of its area, or −0.13 ± 0.003% a^{-1}). The rate of area loss of Ponkar Glacier is about half of the average area loss experienced by debris-covered glaciers over the entire domain (−0.23 ± 0.01% a^{-1}). The terminus of Ponkar Glacier receded by 890 ± 10 m from 1970 to 2019, based on our estimates from the Corona and RapidEye imagery. Supraglacial debris cover expanded from 11.9 ± 0.2 km^2 in 1970 to 13.3 ± 0.4 km^2 in 2019 (+11.7 ± 0.4%). The area of the debris-covered Thulagi Glacier in the southern part of our study area reduced from 24.5 ± 0.5 km^2 in 1970 to 22.3 ± 0.6 km^2 in 2019, a loss of 2.2 ± 0.1 km^2 (−8.78 ± 0.4% of its area, or −0.18 ± 0.008% a^{-1}). The area loss of Thulagi Glacier is 0.05% a^{-1} larger than that of Ponkar Glacier, and the recession of its tongue (−1,500 m, or ~30 ma^{-1}) was 40% larger compared to that of Ponkar Glacier (−890 m, ~18 ma^{-1}) between 1970 and 2019. While the proglacial Thulagi Lake has doubled in size from 0.46 ± 0.01 km^2 in 1970 to 0.92 ± 0.02 km^2 in 2019, Ponkar Glacier on the contrary did not develop a proglacial lake at its terminus.

During the period 1970 to 2013, Ponkar Glacier had a slight negative geodetic mass balance of −0.06 ± 0.01 m w. $e.a^{-1}$. The western and eastern trunks were approximately stable, and losses

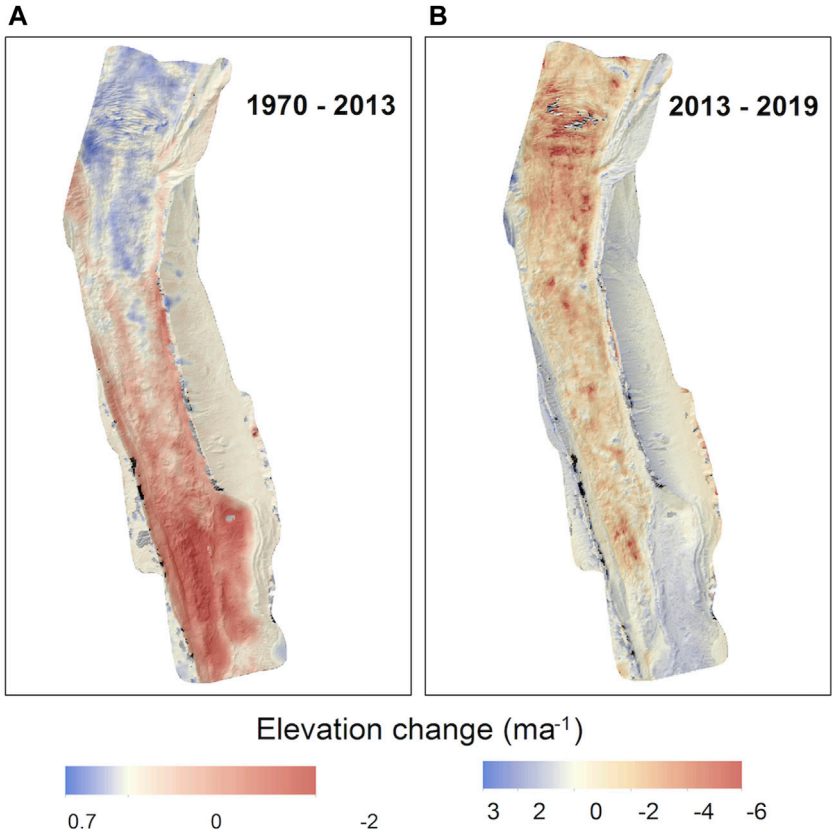

FIGURE 4 | Surface elevation changes on the lower ablation part of Ponkar Glacier from **(A)** 1970 to 2013 and **(B)** 2013 to 2019.

concentrated on the eastern trunk (ranging from −0.3 to −0.8 ma^{-1}) (**Figure 3**). Surface thinning was concentrated around the terminus, with surface lowering rates of ~ −1.3 ma^{-1}, while otherwise losses are found at elevations of ~5,500–6,000 m a.s.l. Parts of the central trunk of Ponkar Glacier have been thickening by ~0.1–0.3 ma^{-1} during this period (**Figure 3**). In contrast, Thulagi Glacier had a mean geodetic mass balance of −0.45 ± 0.08 m w. e.a^{-1}. Parts of its terminus have been thinning at rates > −2.5 ma^{-1}, which are amongst the highest in the study area and 10.9 times more than that of the land-terminating Ponkar Glacier.

For the lower section of the central trunk of Ponkar Glacier surveyed with the UAV (**Figure 1B**), surface elevation changes averaged −0.21 ± 0.11 ma^{-1} from 1970 to 2013 (**Figure 4A**) and −1.88 ± 0.30 ma^{-1} (**Figure 4B**) from 2013 to 2019. The thinning for the recent period represents a ~ nine-fold increase over the 1970–2013 period, suggesting an accelerated mass loss for this part of the glacier. The largest increases in glacier thinning occurred at the upper part of the area surveyed with the UAV (4,000–4,200 m a.s.l), where rates increased from −0.07 ma^{-1} between 1970 and 2013 to −1.6–2.4 ma^{-1} between 2013 and 2019 (**Figures 4A,B**). The highest thinning rates (−2.5 ma^{-1}) were observed at elevations around 4,100 m a.s.l and otherwise decrease both up- and downglacier (**Figure 5**). The rate of thinning at the terminus (~3,700 m a.s.l) based on elevation data was −1.83 ma^{-1}. Field-based measurements in this area of the glacier show that Stake 1 lowered by −6.95 m, Stake two lowered by −6.46 m and Stake 3 lowered by −6.61 m between March 2016 and November 2019. Stake four does not have the whole period of ablation data. On average, the lower part of the glacier thinned by nearly −6.67 m in that period (**Figure 6**), a mean rate of −1.78 ma^{-1}. Assuming an average ice thickness of 50 m over the lower 1.5 km section surveyed with the UAV (cf. Farinotti et al. (2019) and a surface velocity of ~10 ma^{-1} based on the velocity data from Millan et al., 2022 (see section *Glacier Velocity Patterns and Changes* below), we calculated an emergence velocity of ~0.3 ma^{-1}. Taking into account the emergence velocity, we estimated the total surface lowering over the lower part of the glacier as ~ −2.21 ± 0.30 ma^{-1}. The mean thinning rates of −1.88 ± 0.30 ma^{-1} obtained from remote sensing are therefore consistent with direct measurements from the lower three ablation stakes installed on Ponkar Glacier (see **Figure 1** and **Table 2**). Debris thickness measured in the field averaged 16.5 cm for the four stake measurement sites.

Glacier Velocity Patterns and Changes

Based on the recent dataset from 2017/2018 (Millan et al., 2022), we observe rather low surface velocities for the majority of glaciers in the Manaslu region, with median surface velocities ranging from ~0 to 20 ma^{-1} (**Figure 7A**). However, we observe

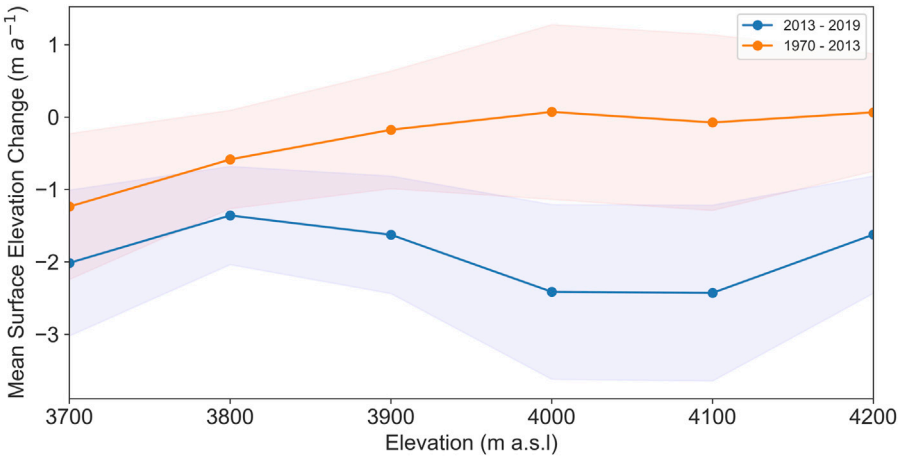

FIGURE 5 | Comparison of mean annual change in surface elevation over the lower part of the ablation area of Ponkar Glacier (3,700 m a s l. to 4,200 m a s l.) between 1970 and 2013 (orange line) and 2013 and 2019 (blue line). The shaded uncertainty intervals correspond to one standard deviation per elevation bin. On average, surface elevation changes were approximately nine times more negative between 2013–2019 compared with 1970–2013 with the entire terminus now undergoing thinning.

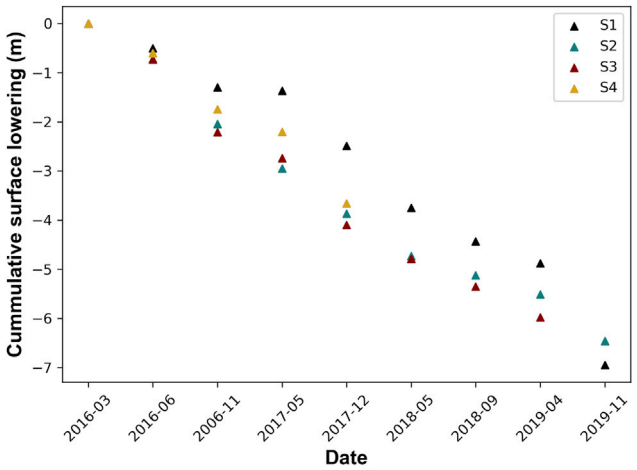

FIGURE 6 | Cumulative surface lowering measured from March 2016 to November 2019 at four stakes installed on the lower part of Ponkar Glacier (locations are shown on **Figure 1B** and their characteristics listed in **Table 2**). Ablation measurements were not available from the highest stake (S4) for 2017 and 2018.

some exceptions to this on a glacier-by-glacier basis. The Ponkar tributary and the neighbouring Larkya Glacier have median velocities in the range of 20–30 ma^{-1}. Suti Glacier in the northern part of the region and HimalChuli Glaciers in the southern part have median velocities between 30 and 40 ma^{-1}. The fastest flowing glacier is the clean ice Purdi Glacier located east of Changli Glacier, with a median surface speed in the range of 60–70 ma^{-1} (**Figure 7A**). The debris-covered parts of the three branches of the Ponkar Glacier complex display different velocity patterns (**Figure 7B**). The upper part of the centre branch (Ponkar) displays high velocities (300–600 ma^{-1}). Velocities decrease to 50–100 ma^{-1} over most of the centre part and to 5–10 ma^{-1} at the terminus and some stagnating areas towards the lateral moraine. The western part (Kechakyu Khola) displays moderate velocities (10–20 ma^{-1}) over most of its area, with several pockets of higher velocities (20–50 ma^{-1}) in the middle of the tongue and lower velocities towards the confluence with the main branch. The eastern branch of Ponkar Glacier complex (Salpudanda) has an overall low median surface velocity, similar to the majority of glaciers in the region, with very low velocities of 0–5 ma^{-1} over the lower half of the debris-covered tongue (**Figure 7B**).

The re-analysis of velocity data generated using auto-RIFT (Gardner et al., 2018) and provided by the NASA MEaSUREs ITS_LIVE project (Gardner et al., 2019) shown in **Figure 8** gives an insight into changes in surface flow velocity over the studied period. Over the western, slow-moving branch of Ponkar (**Figure 8A**), the ITS_LIVE dataset indicates a clear slowdown from ~30 ma^{-1} to ~16 ma^{-1} from 1990 to 2017. For the eastern branch, only the lower part of the glacier of the ice tongue (downstream of the ice fall) can be used for the analysis, as the ice fall and neighbouring regions are not captured by the feature tracking algorithm. This branch shows a large slowdown in velocity between 1990 and 2000, from 90 ma^{-1} to 50 ma^{-1}, with an acceleration to 70 ma^{-1} between 2000 and 2010 (**Figure 8B**). For the period 2010–2017, the velocity of this branch decreased again, consistent with what can be observed on the western branch of Ponkar Glacier. The latest available ITS_LIVE mosaic from 2018 does not show any significant changes compared to 2017 on either branch. The analysis of this dataset should, however, be considered carefully, since the sampling resolution of ITS_LIVE is 240 m, and the glacier has a relatively narrow tongue (~500–800 m), which can induce large uncertainties in the image matching algorithm [e.g., wrong correlation, see Millan et al. (2019)].

Geomorphological Changes on Ponkar Glacier

Geomorphological maps of Ponkar Glacier based on Corona and RapidEye imagery show clear changes in the overall configuration of the different flow units of Ponkar Glacier between 1970 and 2019.

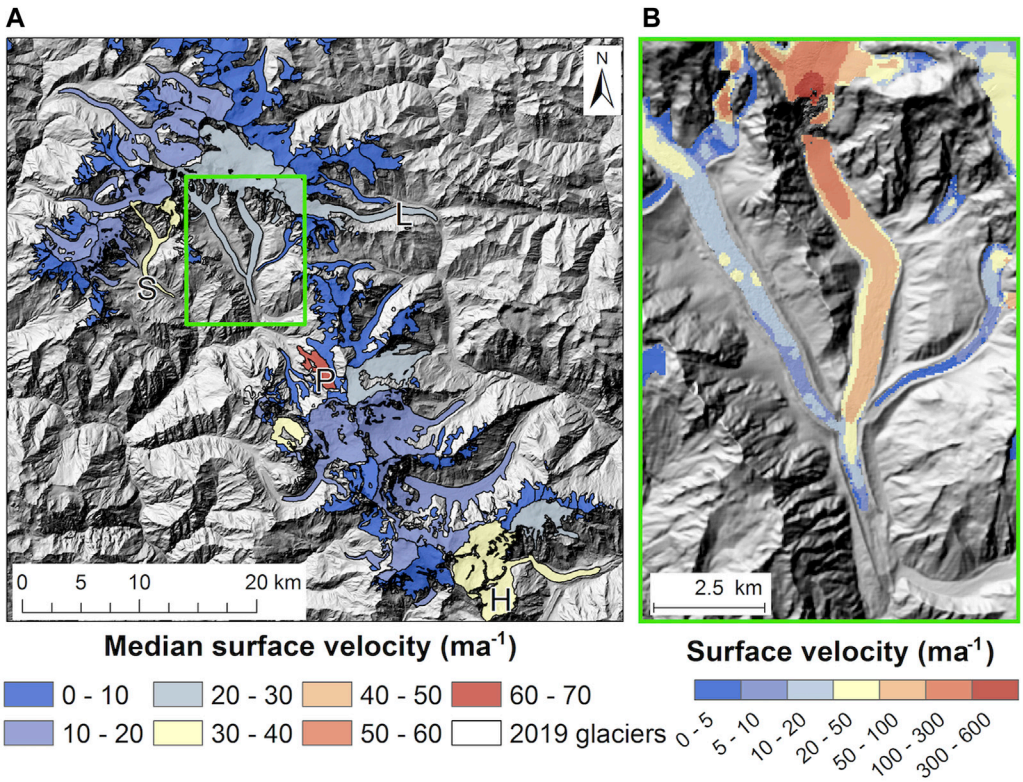

FIGURE 7 | Surface flow velocity of glaciers in the Manaslu region between 2017 and 2018 color coded from blue **(low velocity)** to red **(high velocity)**: **(A)** Median surface velocity calculated over the 2019 glacier boundaries with glaciers discussed in the text: S—Suti Glacier, L—Larkya Glacier; H—HimalChuli Glaciers and P—Purdi Glacier; the green rectangle represents the extent of Ponkar Glacier complex from **Figure 9**; **(B)** Zoom on the surface flow velocity map of the Ponkar Glacier overlaid on AW3D30 and HMA DEM shaded relief. Missing velocity data at the upper part of the middle tributary in (b) correspond to areas where the velocity was not captured by the feature tracking algorithm (Millan et al., 2019).

For example, the ice-flow contribution from Flow Unit 1 to the main trunk (Flow Unit 2) decreased from 3.92 ± 0.1 km^2 in 1970 to 3.62 ± 0.1 km^2 in 2019, a decrease of 7.7%. This can also be inferred from the change in the size, shape and continuity of the flow-unit boundary where the two glaciers meet (**Figure 9**). Flow Unit 3 was already more or less detached from the main trunk (Flow Unit 2) in 1970, so there has been no change in its overall contribution. There is generally more glacial outwash present around the glacier in 2019 (2.63 ± 0.1 km^2) than in 1970 (0.18 ± 0.005 km^2) (**Figure 9**).

Ogives were present on the main Ponkar Glacier trunk on both 1970 and 2019 images (**Figures 9A,B**), but they extended ~100 m further down-glacier in 1970 (4,203 m a.s.l.) compared to 2019 (4,321 m a.s.l.). Similarly, crevasses are visible near the three-way glacier confluence on both 1970 and 2019 images (**Figures 9A,B**). We mapped a total of 236 crevasses on the 1970 image (**Figure 9A**); in 2019 only 76 crevasses were visible on the RapidEye image (**Figure 9B**).

We identified 265 ice cliffs on the surface of the glacier in 1970 image, covering an area of 0.12 ± 0.02 km^2 (0.21% of the glacier area or 1.00% of the debris-covered area). For the year 2019, we mapped 156 ice cliffs with a total area of 0.18 ± 0.03 km^2 (0.35% of the glacier area or 1.35% of the debris-covered area in 2019). The number of ice cliffs decreased but the total area increased by 0.05 km^2 in 2019 compared to 1970.

Supraglacial ponds increased in number and area from 56 ponds with a total area of 0.03 ± 0.007 km^2 in 1970 (0.05% of the glacier area; 0.25% of the debris-covered area) to 123 ponds in 2019 with a total area of 0.06 ± 0.01 km^2 (0.12% of the glacier area or 0.45% of the debris-covered area).

Ice-surface vegetation is clearly visible on several areas of the glacier surface in both 1970 and 2019 (**Figures 9A,B**). Its area increased from 0.72 ± 0.07 km^2 (1.3% of the glacier area; 6% of the debris-covered area) to 1.9 ± 0.16 km^2 (3.8% of the glacier area; 14.5% of the debris-cover area) in 2019.

Uncertainties in Area and Elevation Changes

Remote sensing estimates of glacier area, area changes, and geomorphological features are subject to the quality of the images as well as the accuracy of the glacier delineation procedure (Paul et al., 2013). Using the buffer method, we obtained a glacier area uncertainty of 2.7% for the RapidEye imagery and 2.1% for the Corona imagery. While Corona imagery is panchromatic and is likely to have more uncertainty, the total error is slightly less than RapidEye because the buffer method takes into account the higher spatial resolution of Corona compared to RapidEye. The uncertainty of the area change analysis,

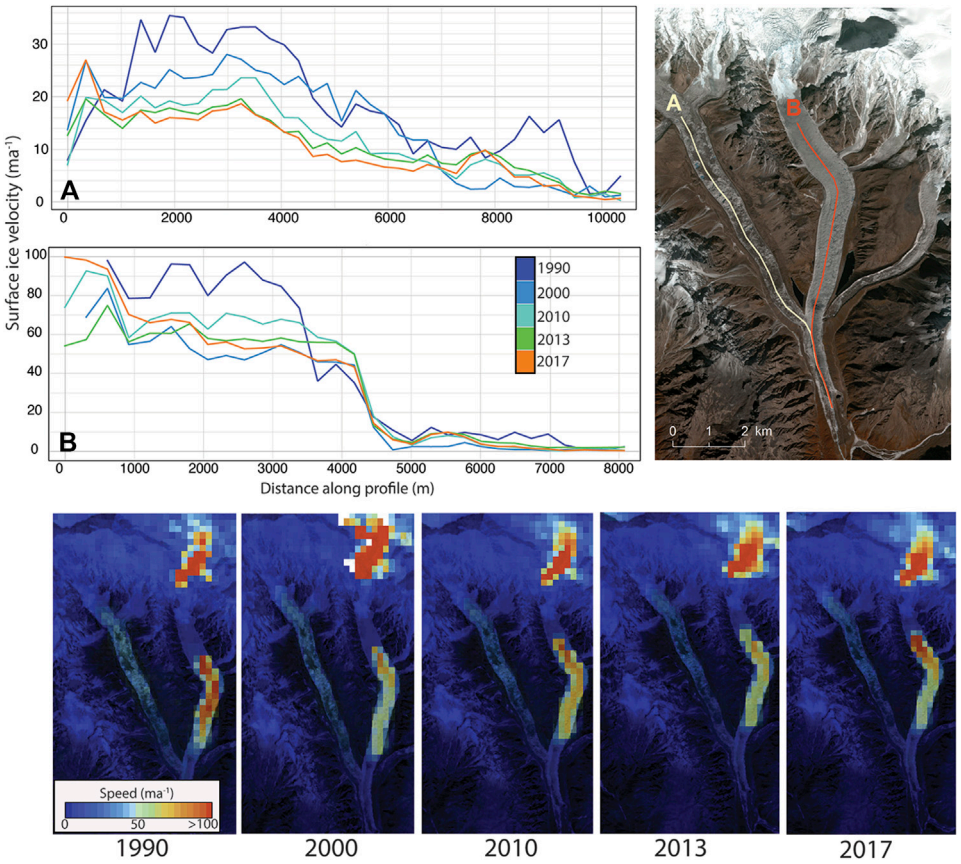

FIGURE 8 | Ice velocity changes of the Ponkar Glacier between 1990 and 2017. Panel **(A)** and **(B)** represent velocity profiles along the flowline of the two branches of Ponkar Glacier (light yellow and red solid lines, respectively, overlayed on The RapidEye imagery from 2019. The bottom panels show the ice velocity mosaics color coded on a linear scale from blue (low velocity) to red (velocity >100 ma^{-1}).

estimated as the RMSE uncertainties of the two dates was 3.4%. The uncertainty in the glacier terminus recession was estimated at 10 m (i.e., two RapidEye pixels and 5 Corona pixels). The error of the supraglacial vegetation amounted to 9.7 and 8.2% for 1970 and 2019, respectively. Supraglacial pond and ice cliffs were difficult to identify on the Corona image as they sometimes mixed with shadow and lithology. We used uncertainty values of 26 and 21% respectively (cf. Steiner et al., 2019). The feature detection routine helped mitigate some of this challenge and helped automate the delineation of supraglacial ponds and ice cliffs, but we remain cautious about the area estimates for these two features.

With regards to surface elevation changes, all of our regional mass balance estimates, along with 89% of the individual glacier mass balance estimates, and 94% of the surface lowering estimates were significantly different from zero. The non-linear co-registration biases (**Figure 2**) show that there were deviations from the polynomial of up to 5 m. These biases are also visible on **Figure 4**, and predominantly occur on steep slopes as well as areas of low-image contrast, such as shadows. In most cases, the surfaces of the glaciers in the study area had good image contrast, especially over the debris-covered surfaces. As such, our error estimates of mass balance are conservative. At the glacier scale, the removal of the non-linear co-registration biases on the UAV data was complicated by the lack of stable terrain in the dataset. The only terrain that could be used to identify the biases was on the steeply sloped eastern side of the terminus of Ponkar Glacier. As such we cannot be confident that the polynomials used to remove the biases are equally applicable across the entire study area; this most likely explains the 0.2–0.5 ma^{-1} elevation bias that can be observed on the lateral moraine of Ponkar Glacier in **Figure 4**. Nevertheless, the changes visible on the glacier surface are greater than the biases remaining on the stable ground so we are confident that the elevation change patterns observed are reliable.

DISCUSSION

Glacier Behaviour in the Manaslu Region

In this study, we find that glaciers in the Manaslu region of Nepal have been receding and losing mass over the last five decades. The region-wide mean rate of area loss (−0.23% a^{-1}, 1970–2013) is slightly lower than those reported for the Everest area over the last four decades (Thakuri et al., 2014: −0.27 ± 0.06% a^{-1}, 1962–2011; King et al., 2020: −0.39 ± 0.13 m a^{-1}, 1962–2018). The area changes over the entire period 1970 to 2019 is much lower than the area loss over recent periods reported in the same

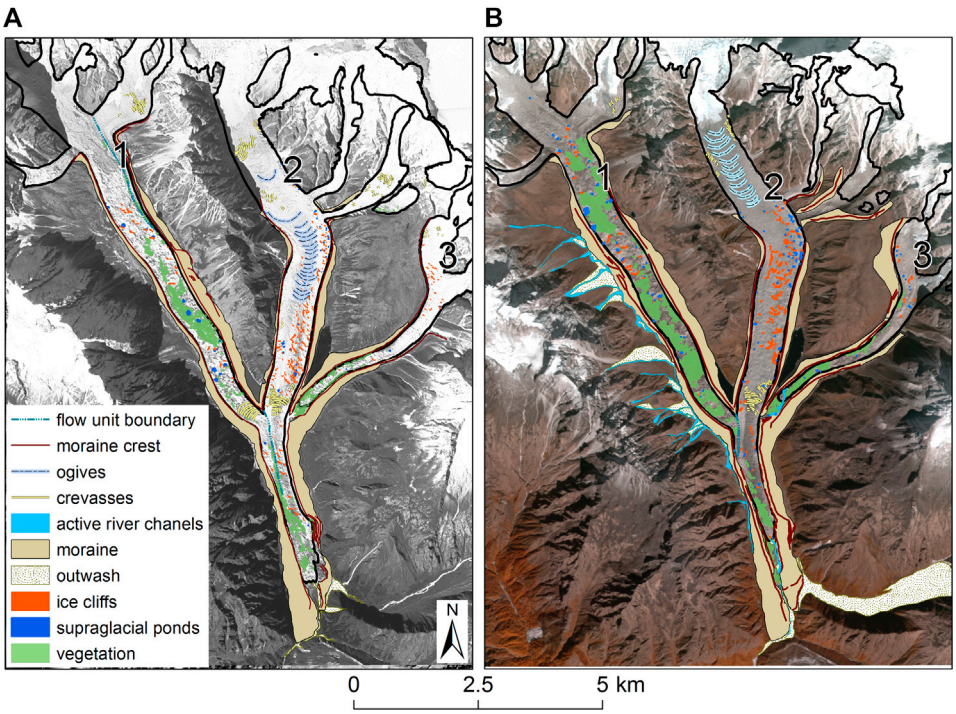

FIGURE 9 | Geomorphology and ice-surface changes for the Ponkar Glacier system for period 1970 to 2019: **(A)** interpretation based on the Corona 1970 panchromatic image; **(B)** interpretation based on RapidEye 2019 false colour composite bands 543.

area in a previous study (Robson et al., 2018: −1.2% a^{-1}, 2001–2005; −0.4 a^{-1}, 2005–2013). This suggests an accelerated area loss in the last decade, also noted in other areas of the Himalaya (Ren et al., 2006; Thakuri et al., 2014; King et al., 2020). However, we interpret the difference in rates of area change between our study and Robson et al. (2018) with caution, because of the different glacier mapping methods used. Regional area change estimates going back to the 1960s and 1970s remain limited in the Himalaya, making it difficult to directly compare the behaviour of glaciers in the Manaslu region to other regions. Here we compare our findings with existing remote sensing studies for similar timescales.

For the period 1970 to 2013, our estimated mean geodetic mass balance (−0.17 ± 0.03 m w. e.a^{-1}) for the Manaslu region is lower than the larger central-west Himalaya domain where are study area is located (King et al., 2019: an average of ~ −0.25 ± 0.11 w. e.a^{-1} from ~1974–2015), as well as than Himalaya-wide estimates (Maurer et al., 2019: −0.31 ± 0.13 m w. e. a^{-1}, 1975–2016). Both cited studies used similar methodology to ours (declassified Hexagon KH-9 imagery combined with SRTM and ASTER DEMs, respectively). However, the slight differences in the size of the domains, the time span of ±3 years and the type of imagery used may account for some of the differences between our study and the cited studies. With respect to temporal evolution of the mass balance, the rate of mass loss over the period 1970–2013 in the Manaslu area is lower than rates reported for the last decade (2000–2015/2016) in the central Himalaya (Brun et al., 2017: −0.28 ± 0.08 m w. e. a^{-1}; King et al., 2019: −0.26 ± 0.11 m w. e a^{-1}). This suggests an acceleration of mass loss in this area in the last decade compared to the previous decades, which is consistent with findings from other studies (Maurer et al., 2019; Hugonnet et al., 2021).

In addition to mass loss, our study shows that glaciers are slowing down as they experience negative mass balance, a general pattern noted in other studies across the Himalaya. Dehecq et al. (2019) reported a slowdown of glaciers in High Mountain Asia for the period 2000–2016. For instance, in the Manaslu region, glaciers experience moderate thinning along with moderate glacier velocities compared to other regions such as Nyainqntanglha and Lahaul Spiti regions (Dehecq et al., 2019). Coupled with the low supraglacial pond and ice cliff coverage in this region (Racoviteanu et al., 2021), this indicates that glaciers in this area might be in the initial phase of retreat, characterized by melting and slow downwasting associated with slowly retreating glacier termini (Kirkbride, 1993). The presence of only three lake-terminating glaciers out of 213/274 glaciers in 1970/2019 indicates that the third phase in the evolution of a glacier, marked by the development of deepening proglacial lakes (Kirkbride, 1993; Benn et al., 2012) is not under way in this area. This is different than the eastern Himalaya, for example Sikkim, which is characterized by accelerated growth of supraglacial and proglacial lakes (Basnett et al., 2013; Racoviteanu et al., 2015; Shukla et al., 2018).

Clean vs. Debris-Covered Glaciers

Previous studies reported higher rates of area loss of clean ice glaciers compared to debris-covered glaciers in various parts of

TABLE 6 | Correlation matrix for morphology controls on glacier surface change for the Manaslu region for the 135 valid glaciers with positive correlations shown in green and negative correlations in red. Statistically significant correlations are marked with "**"and "*" for 95 and 90% confidence level, respectively. Variables are expressed as average slope, aspect and elevation, median velocity and percent debris. Elevation changes are expressed as ma^{-1} for the period 2013–2017.

	Surface change	Glacier area	Percent debris	Elevation	Slope	Aspect	Velocity
Surface change	1						
Glacier area	0.01	1					
Percent debris	0.00	0.20**	1				
Elevation	−0.12*	0.07	−0.34**	1			
Slope	−0.25**	−0.24**	−0.32**	0.20**	1		
Aspect	0.04	−0.05	0.00	0.00	−0.04	1	
Velocity	−0.09	0.47**	0.20*	−0.08	0.00	0.13	1

the Himalaya such as Khumbu in the Central Himalaya (Bolch et al., 2008; Nuimura et al., 2012; Thakuri et al., 2014), Sikkim to the east (Racoviteanu et al., 2015), or the Garwhal Himalayas in the west (Bhambri et al., 2011). Low rates of glacier surface area loss and even stable or slowly receding glacier termini were reported over the entire Himalaya (Scherler et al., 2011). We did not notice such patterns in the Manaslu region, where clean and debris-covered glaciers lost area at similar rates from 1970 to 2013 (−0.23 ± 0.01% and −0.24 ± 0.01% a^{-1}, respectively). Clean glaciers on the north side of the divide on the Tibetan plateau receded at almost the same rate as the entire region. This region is in a monsoon shadow and is drier than the southern slopes, with fewer debris-covered tongues. Furthermore, in this study we find that debris-covered glaciers in this area exhibited slightly higher thinning rates and mass loss compared to clean ice glaciers. This is consistent with similar patterns noted in two other regional studies (King et al., 2019; Maurer et al., 2019). However, this is in contrast with previous studies that had found similar thinning rates for clean and debris-covered glaciers (Gardelle et al., 2012; Kääb et al., 2012; Brun et al., 2017). In our study, with a few exceptions, both debris-coved glaciers and clean ice glaciers exhibit most thinning at their termini, with the highest reaches of the glaciers remaining approximately stable, or thickening. These trends are clearly visible for some of the debris-covered glaciers including Ponkar and Thulagi Glaciers discussed in more detail below; other glaciers exhibit more homogenous thinning rates over the entire debris cover area, up to the transition with clean ice.

In terms of debris control on glacier surface changes, we did not find any correlation between extent of the debris and surface elevation changes for the glaciers in the Manaslu region (**Table 6**). Debris cover extent had a significant negative correlation with mean glacier elevation and slope (**Table 6**), i.e., steeper glaciers situated at higher altitudes have less debris cover, and these tend to be rather clean glaciers. In general, debris-covered glaciers extend to lower altitudes, and display an inverted mass-balance regime compared to clean ice glaciers, notably larger ablation rates in the middle ablation area (Benn and Lehmkuhl, 2000; King et al., 2017). These general findings hold for some, but not all, glaciers in our study area.

Lake-Terminating vs. Land-Terminating Glaciers

In this study, we found that lake-terminating glaciers retreat at a slightly higher rate than land-terminating glaciers; however, our sample only includes three lake-terminating glaciers. Other studies showed that proglacial lakes accelerate glacier area change in the Himalayas and elsewhere (Basnett et al., 2013; Bajracharya et al., 2014; Racoviteanu et al., 2015; King et al., 2018; King et al., 2019; Sutherland et al., 2020). The mass loss of −0.35 ± 0.06 m w. e a^{-1} of lake-terminating glaciers found in this study is consistent with findings from King et al. (2019) for the central-western Himalaya region where our study area is located (an average of −0.34 ± 0.11 ma^{-1} from ~1974 to 2015) as well as Himalaya-wide estimates from Maurer et al. (2019) (−0.40 ± 0.07 ma^{-1} from ~1975 to 2016). It has been shown that lake-terminating Himalayan glaciers retreated and exhibited maximum thinning near the glacier termini at almost double rates compared to land-terminating glaciers (King et al., 2018; King et al., 2019). The lake-terminating glaciers in our study area including Thulagi Glacier conform to this pattern. While these recent studies showed that land-terminating glaciers all decelerated and thinned most in their middle reaches, our results do not support this finding, i.e. we found high thinning rates at glacier termini for both types of glaciers.

Effect of Topography

Glaciers in the Manaslu region exhibit rather homogenous slope patterns, with a regional average of 26° and a standard deviation of 7°. Ponkar and Thulagi Glaciers have similar average slopes (21 and 27°, respectively). The slightly higher slope average for Thulagi might partly explain its different behaviour compared to Ponkar, i.e., the growth of a proglacial lake. We found a significant negative correlation between surface elevation change and glacier slope ($r = -0.25$, $p < 0.05$) (**Table 6**), suggesting that glaciers with lower surface slopes have larger surface elevation changes. These results are consistent with findings from Salerno et al. (2017), who reported that surface slopes along with and supraglacial pond coverage were the main factors controlling the behaviour of glaciers in the Khumbu region of Nepal. Similarly, over the entire High Mountain Asia, Brun et al. (2019) reported that for most of the regions, the slope of the ablation area and the mean glacier elevation were the main predictors of glacier mass balances. In this study we found a significant negative correlation between surface change and mean glacier elevation (**Table 6**), although the correlation was rather weak ($r = -0.12$, $p < 0.10$). This suggests that glaciers in the Manaslu region conform to the patterns noted elsewhere in the Himalaya, i.e., glaciers situated at lower elevations exhibit greater surface thinning.

Supraglacial Pond and Ice Cliff Coverage

Supraglacial ponds are typical of debris-covered glaciers, and are a result of differential ablation patterns (Sakai et al., 2000; Buri et al., 2016; Miles et al., 2016; Miles et al., 2018b). Supraglacial ponds develop on stagnating areas on the ablation areas of glaciers with negative mass balance and surface angles lower than 2° (Reynolds, 2000; Quincey et al., 2007; Sakai and Fujita, 2010), and rarely exist or survive where the glacier is actively flowing. Supraglacial pond density was found to be the second most important factor controlling glacier behaviour in two studies (Salerno et al., 2017; Brun et al., 2019). In a previous study (Racoviteanu et al., 2021), we reported an overall pond coverage of ~2% of the debris-covered glacier areas in the Manaslu region based on spectral unmixing of Landsat 8 imagery (30 m) for 2015. Other studies reported 0.3–7% pond coverage in the Khumbu based on high-resolution Pléiades data (Salerno et al., 2012; Watson et al., 2017a; Kneib et al., 2020; Racoviteanu et al., 2021). However, due to the differences in spatial resolution of the sensors used, these results cannot be compared directly.

Ice cliffs are exposed on a glacier either as a consequence of redistribution of ice-surface debris during ablation, or the collapse of the roof of a water channel, but the processes responsible for their formation and persistence are largely unknown (Kirkbride, 1993; Sakai et al., 2000). This has consequences for glacier ablation, since these features greatly enhance local ablation (Sakai et al., 1998; Buri et al., 2021). Previous studies in the Himalaya have shown that ice cliffs enhance the overall surface lowering of debris-covered glaciers and contribute to up to 15% of the total ice melt on a glacier (Reid and Brock, 2014; Brun et al., 2016; Ragettli et al., 2016; Buri et al., 2021). The increase in ice cliff area on Ponkar Glacier conforms to the surface thinning patterns at this glacier. While our datasets do not include regional coverage of ice cliffs, we note that the increase in ice cliff area on Ponkar Glacier in the last decades is consistent with observations in other areas of the Nepal Himalaya (Iwata et al., 2000).

Vegetation Development

Ice-surface vegetation is generally rare on glaciers (Fickert et al., 2007; Tampucci et al., 2016; Anderson et al., 2020), but it can develop where the glacier surface is stable over periods of decades. Conversely, it cannot exist or survive where the glacier is actively flowing. In the Manaslu area, we observe the development of supraglacial vegetation on debris-covered tongues with low velocity rates and strong thinning rates such as Ponkar Glacier and the glaciers nearby. In a previous study (Racoviteanu et al., 2021) supraglacial vegetation was estimated at ~ 4% of the debris-covered glacier areas in the Manaslu region based on spectral unmixing of Landsat 8 imagery for the year 2015. The vegetation coverage is higher in the Manaslu region compared to the Khumbu and Bhutan Himalaya further east. However, at regional scales, the controls on vegetation development remain unclear. At local scales, thinning trends coupled with glacier slowdown are particularly visible on Flow Unit 3 of Ponkar Glacier (Salpundanda Glacier), where ~ half of the lower area exhibits low velocities, ranging from 0 to 5 ma^{-1} (**Figure 7B**). As shown on **Figure 9**, this branch of the glacier has detached from the main body by 2019, has become stagnant and is associated with the development of extensive supraglacial vegetation. Similarly, the lower parts of Flow Unit 1 (Kechakyu Khola Glacier) exhibit similar tendencies of vegetation expansion in the lower part. Flow Unit 3 is a good example of part of a glacier which has evolved towards a "vegetated" tongue as we observed in the field on the nearby Changli Glacier (**Supplementary Figure S1**). We infer that such transitions occurred over the last five decades as a consequence of slow velocities and negative mass balance and may continue in the future.

Contrasting debris-covered glacier behaviour: the example of Ponkar and Thulagi Glaciers

While the area and elevation change in the Manaslu region are moderate compared to other regions, and rather homogenous (clean vs. debris-covered glaciers), differences exist on a glacier-by-glacier basis. The influence of supraglacial debris on glacier area and surface changes in the Himalayas has been addressed in recent studies (Brun et al., 2017; Dehecq et al., 2019; Shean et al., 2020). In this discussion, we focus on the contrasted behaviour of the lake-terminating Thulagi Glacier and the land-terminating Ponkar Glacier and we infer links between surface morphology (supraglacial pond and ice cliff coverage, slope, and debris cover), surface velocity and mass balance of these two glaciers.

These glaciers are both covered with debris but behave differently with respect to area and elevation losses. The lake-terminating Thulagi Glacier had higher area loss, terminus retreat and thinning rates compared to the non-lake terminating Ponkar Glacier from 1970 to 2013/2019. The proglacial Thulagi Lake, previously identified as a hazardous glacial lake, has doubled in size since the 1970s based on our estimates. The growth of Thulagi Lake occurred concomitantly with the thinning of Thulagi Glacier noted in this study as well as in previous studies (Pant and Reynolds, 2000; Robson et al., 2018; Maskey et al., 2020; Watson et al., 2020). Ponkar Glacier, in contrast, did not develop a proglacial lake at its terminus. In terms of surface elevation changes, Ponkar Glacier stands out as an exception to the regional pattern noted earlier (i.e. thinning towards the terminus with stable or thickening trends in the upper areas, vs. consistent thinning across the debris-covered part for most of the glaciers in the region). The thickened upper ablation zone shown in **Figures 3**, **4** is probably best explained by the velocity data in **Figures 7**, **8**, which indicates that this part of the glacier is still dynamically active. The simplest explanation is therefore that there is still some ice actively flowing from the accumulation area into the upper ablation area but that the glacier is then more or less dynamically inactive below this (i.e. in the middle and lower ablation zone). We infer that the recent prolonged period of negative mass balance led to reduced ice velocities and enhanced ice-surface lowering, especially near the glacier terminus.

Using the example of Ponkar Glacier, we note that changes in the ice-surface morphology based on satellite imagery are commensurate with the recession and thinning of the glacier between 1970 and 2013/2019. For example, we note an increase in the area of ice-surface vegetation over the 1970–2019 period. This

supports the idea that Ponkar Glacier is currently in a stagnation phase, in comparison with Thulagi Glacier which is at the stage of lake development and calving. Furthermore, the ice-flow contribution from Flow Unit 1 to the main trunk (Flow Unit 2) decreased by 2019. Ogives, which form beneath icefalls on glacier surfaces indicate active glacier flow; crevasses generally open and form beneath actively-flowing ice. The decrease in number and extent of both of these ice-surface features, coupled with an increase in the size of lateral moraines and expanded outwash plains further indicate that Ponkar Glacier is currently less dynamically active than in 1970. Crevasses in Flow Unit 1 are only visible on that section of the glacier in the 1970 image and some crevasses appear to have closed up by 2019. While this can be a function of glacier recession (i.e., glacier recession means there is more available space for outwash plains to expand on the valley floor), the expansion of outwash plains could also indicate an increase in ablation and associated fluvial activity between 1970 and 2019.

The large lateral moraines present along the glacier margins in 1970 indicate that glacier thinning was already underway five decades ago. Moraines expanded in size between 1970 and 2019 as the glacier continued to thin and recede during this period. The most conspicuous change observed is near the snout in the "embayment" area, on the true left-hand side near the terminus, where moraines can be seen actively forming at the 1970 ice margin. By 2019, these moraines separated from the glacier itself and a new lateral lake had formed within the moraines in the embayment area (**Figure 9B**).

On Ponkar Glacier, supraglacial ponds covered a small percent of the debris-covered glacier area in both 1970 and 2019 (0.25% and 0.45% of the debris-covered area, respectively). Ice cliffs covered 1–1.35% of the debris-covered area. The low supraglacial pond coverage is a pattern over the entire Manaslu area as noted in a previous study (Racoviteanu et al., 2021). With respect to regional ice cliff coverage, we cannot compare directly the local estimates with the regional ones due to the difference in the spatial resolution of the data used in the cited study vs. this study (30 vs 5 m). However, we note that the pond and ice cliff coverage that we obtained for the post-monsoon (dry) season in 1970 and 2019 is about half that of the area reported from other glaciers in the Nepal Himalaya for the same season. For example, Steiner et al. (2019) reported 2.5% ice cliff coverage and 0.9% pond coverage relative to the debris-cover area of five glaciers in the Langtang valley, about 115 km east of our study area in October 2015. Brun et al. (2018) found a 7–8% ice cliff coverage on the Changri Nup Glacier in the Khumbu Himalaya during the dry season, east of our study area, based on Pléiades imagery (2 m). This is ~7 times larger than the ice cliff coverage we estimated on Ponkar Glacier for the dry season (November 1970 and 2019). The increased number of ice cliffs from 1970 to 2019 on Ponkar Glacier appears to be consistent with the thinning patterns we noted earlier (see section *Changes at Glacier Scale: Ponkar and Thulagi Glaciers*). The doubling of the number and surface area of supraglacial ponds on Ponkar Glacier from 1970 to 2019 also supports the idea that the glacier was less dynamically active in 2019 than it was in 1970. The slight increase in the number of ice cliffs on this glacier suggest that ice cliffs are in the "development" phase as defined by Sakai et al. (2002). Ponkar Glacier represents a good example of the relationship between glacier mass balance, glacier dynamics and changes in supraglacial debris cover for a glacier which has not reached the transition to the calving stage. In terms of local ablation, we found that surface elevation changes between 2013 and 2019 were noticeably higher within the vicinity of supraglacial ponds and exposed ice (up to $-4.5\,ma^{-1}$) (**Figure 4B**), with implications for the future behaviour of this glacier. Other studies in the Himalaya clearly showed that while these surface features cover only several percent of the total ablation area of glaciers (Steiner et al., 2019), they can enhance local ablation rates by up to three times (Brun et al., 2016; Irvine-Fynn et al., 2017; Miles et al., 2018b; Buri et al., 2021).

Future Outlook of Debris-Covered Glaciers

In this study, we have shown that glaciers in the Manaslu region have undergone thinning and frontal recession in recent decades in response to regional climate change. During this period, the glacier ablation zones have accumulated debris at an increased rate. Debris naturally accumulates in a supraglacial position during surface lowering of glaciers in mountain areas such as the Himalaya for two main reasons. First, material falls onto the ice surface from the collapsing inner faces of the surrounding lateral moraines (Hambrey et al., 2008). These moraines are progressively de-stabilised during ice-surface lowering as the supporting ice is removed. This is especially the case near the terminus of glaciers, where ice velocity is low or where the ice is stagnant and therefore supraglacial material cannot be evacuated. Second, there is a tendency for an increase in supraglacial debris cover simply because debris becomes concentrated on the ice surface during ablation (i.e., as the proportion of ice in an ice-rock mixture decreases during ablation, the proportion of debris increases). The ~12% increase in supraglacial debris cover from 1970 to 2019 noted in this study is consistent with the increase in debris cover reported in other studies in the Himalaya and the Alps (Mölg et al., 2019; Xie et al., 2020). Again, this is especially the case near glacier termini where velocities tend to be low during periods of negative mass balance (Benn and Evans, 1998).

The regional pattern of surface lowering leads to an increase in debris cover for the two main reasons noted above, which in turn reduces ablation. This accounts for the large and increasing number of debris-covered glaciers in the Himalaya (Scherler et al., 2018; Herreid and Pellicciotti, 2020). *This poses the question: how will this, and other glaciers in the region, evolve as climate warming continues?* There are perhaps two obvious answers to this question: first, all the glaciers could melt and lose mass through the rest of this century and beyond, leaving behind small niche glaciers at high altitudes and plateau icefields on broad mountain tops; second, debris-covered glaciers such as Ponkar Glacier might

undergo a transition to a rock glacier as debris cover accumulates and glacier snouts reorganize and undergo increased downslope creep (Harrison et al., 2021). This transition process has been hypothesized to occur in the arid Andes (e.g. Monnier and Kinnard, 2015), in the Himalayas (Jones et al., 2019) and elsewhere globally (Knight et al., 2019).

If Ponkar Glacier does undergo a future transition to a rock glacier then we would envisage this to occur in two stages. In Stage 1, climate change leads to increased air temperature and associated reduction in solid precipitation, which influences ice flow and drives glacier recession. While few long-term climate datasets exist in the high mountain region of western Nepal, there are data from valley locations in the region that show a recent rise in temperature in the area allied to a reduction in precipitation (Basnet et al., 2020; Paudel, 2020). If these trends exist at high altitudes, we would expect these to induce negative mass balance of the glacier. As a result, the glacier thins and accumulates surface debris via rockfalls from valley sides, mass-wasting of lateral moraines and transport of debris from subglacial and englacial sources (Benn and Owen, 2002; Knight and Harrison, 2009; Kirkbride and Deline, 2013; van Woerkom et al., 2019). In Stage 2, accumulation of surface debris occurs to the extent that mass balance of the terminus becomes more positive as ice melt is reduced. In conjunction, basal shear stress increases as does internal deformation of the terminus ice mass as debris load increases. This induces flow and deformation of the terminus which transitions to an ice-cored rock glacier. However, the processes outlined in Stage 2 have clearly not occurred on Ponkar Glacier, where the terminus area shows low velocities rather than the increased velocity hypothesised in this transition model (see **Figure 8B**), despite the clear increase in supraglacial debris in this zone.

SUMMARY AND FURTHER WORK

In this study, we found that the glacierized area in the Manaslu region of Nepal Himalaya reduced at the mean rate of $-0.26 \pm 0.0001\%\ a^{-1}$ from 1970 to 2019, with slightly higher rates for debris-covered glaciers. For a sample of 135 glaciers, we found thinning trends of $-0.20 \pm 0.03\ m a^{-1}$ between 1970 and 2013, corresponding to a mean geodetic mass balance of -0.17 ± 0.03 m w. e. a^{-1}. Surface elevation changes were negatively influenced to some extent by the mean slope of the glacier and mean glacier elevations, pointing to increasingly negative mass balance for gentle-sloped glaciers situated at lower elevations. Stronger thinning rates and negative mass balance were observed for lake-terminating glaciers such as Thulagi Glacier, compared to the land-terminating Ponkar Glacier. Overall, glaciers in this area exhibit low supraglacial pond and ice cliff coverage compared to other regions in the eastern Himalaya such as Khumbu. Using the example of the largest glacier system in the region (Ponkar Glacier), the geomorphology analysis shows an increase in pond and ice cliff coverage concomitant with a reduction in ogives and crevasses. This indicates that the glacier was more active in 1970 compared to the present day, and that it is currently undergoing a stagnation phase marked by ice-surface vegetation growth and a significant expansion of the supraglacial debris cover. Coupled with increased thinning trends for the recent years (2013–2019) compared to 1970 to 2013 period and the relatively low glacier surface velocities, such trends indicate that glaciers in the Manaslu region might be in the initial transitional phase characterized by rather slowly receding glacier termini. Remaining work will focus on expanding the geomorphology analysis used in this study to map the evolution of ice cliffs, ponds and vegetation over the entire region in order to understand the consequences of slow velocities and negative mass balance at the regional scale.

DATA AVAILABILITY STATEMENT

The datasets presented in this study can be found in online repositories. ITS_LIVE velocity data are found at: https://its-live.jpl.nasa.gov/. Planet imagery are available from Planet Labs (www.planet.com). Corona images are available from the USGS EarthExplorer at https://earthexplorer.usgs.gov. The geodetic mass balance produced in this study can be found at the zenodo repository: http://10.5281/zenodo.5700932.

AUTHOR CONTRIBUTIONS

AR designed the study, processed the Corona and RapidEye images, refined geomorphology mapping using the RapidEye image, prepared figures and led the paper. NG provided geomorphology expertise for manual mapping of geomorphology features and supervised the study. BR produced the Corona DEMs, computed the geodetic mass balance, prepared figures and helped edit the paper. SH provided climate expertise and paper edits. RM provided glacier velocity data, processed the ITS_Live data, provided figures and helped edit the paper. RBK and RK provided the field-based ablation measurements and supported the UAV field campaign.

FUNDING

AR was supported by a Fellowship from the European Union's Horizon 2020 research and innovation programme under the Marie Skłodowska-Curie COFUND Ser Cymru II scheme (Grant agreement No 663830). Financial support for travel and field logistics for NFG and AR was provided by a GCRF (Global Challenges Research Fund) Agility Grant through CIDRA (Center for International Research Development at Aberystwyth University). SH was supported by funding from College of Life and Environmental Sciences, University of Exeter. BR was supported by a University of Bergen stipend between 2017 and 2020. The participation of Nepalese and Indian students to the fieldwork training at Ponkar Glacier was

supported financially by the UNESCO IGCP Project 672. The UAV survey was conducted by a pilot team from Nepal Flying Labs.

ACKNOWLEDGMENTS

We thank all fieldwork participants for their hard work and enthusiasm. We acknowledge the Himalayan Research Expeditions in Nepal for organizing fieldwork logistics on Ponkar Glacier. RapidEye images were provided at no cost using an API from Planet Labs (https://www.planet.com). Ice velocity were processed by Romain Millan thanks to a post-doctoral fellowship from the French Centre National d'Etudes Spatiales (CNES) and the CNES MaiSON project.

SUPPLEMENTARY MATERIAL

The Supplementary Material for this article can be found online at: https://www.frontiersin.org/articles/10.3389/feart.2021.767317/full#supplementary-material

Supplementary Figure S1 | The vegetated debris-covered tongue of Changli Glacier as viewed from Yak Kharka on the way to Ponkar Glacier. Photo credit: N.F. Glasser.

REFERENCES

Anderson, B., and Mackintosh, A. (2012). Controls on Mass Balance Sensitivity of Maritime Glaciers in the Southern Alps, New Zealand: The Role of Debris Cover. *J. Geophys. Res.* 117 (F1), a–n. doi:10.1029/2011JF002064

Anderson, B., Mackintosh, A. N., Dadić, R., Oerlemans, J., Zammit, C., Doughty, A., et al. (2021). Modelled Response of Debris-Covered and lake-calving Glaciers to Climate Change, Kā Tiritiri O Te Moana/Southern Alps, New Zealand. *Glob. Planet. Change* 205, 103593. doi:10.1016/j.gloplacha.2021.103593

Anderson, K., Fawcett, D., Cugulliere, A., Benford, S., Jones, D., and Leng, R. (2020). Vegetation Expansion in the Subnival Hindu Kush Himalaya. *Glob. Change Biol.* 26 (3), 1608–1625. doi:10.1111/gcb.14919

Anderson, L. S., Armstrong, W. H., Anderson, R. S., and Buri, P. (2021). Debris Cover and the Thinning of Kennicott Glacier, Alaska: *In Situ* Measurements, Automated Ice Cliff Delineation and Distributed Melt Estimates. *The Cryosphere* 15 (1), 265–282. doi:10.5194/tc-15-265-2021

Bajracharya, S. R., Maharjan, S. B., and Shrestha, F. (2014). The Status and Decadal Change of Glaciers in Bhutan from the 1980s to 2010 Based on Satellite Data. *Ann. Glaciol.* 55 (66), 159–166. doi:10.3189/2014AoG66A125

Basnet, K., Shrestha, A., Joshi, P. C., and Pokharel, N. (2020). Analysis of Climate Change Trend in the Lower Kaski District of Nepal. *Himalayan J. Appl. Sci. Engin.* 1, 11–22. doi:10.3126/hijase.v1i1.33536

Basnett, S., Kulkarni, A. V., and Bolch, T. (2013). The Influence of Debris Cover and Glacial Lakes on the Recession of Glaciers in Sikkim Himalaya, India. *J. Glaciol.* 59 (218), 1035–1046. doi:10.3189/2013jog12j184

Benn, D. I., Bolch, T., Hands, K., Gulley, J., Luckman, A., Nicholson, L. I., et al. (2012). Response of Debris-Covered Glaciers in the Mount Everest Region to Recent Warming, and Implications for Outburst Flood Hazards. *Earth-Science Rev.* 114 (1), 156–174. doi:10.1016/j.earscirev.2012.03.008

Benn, D. I., and Evans, D. J. A. (1998). *Glaciers and Glaciations*. New York: John Wiley & Sons.

Benn, D. I., and Lehmkuhl, F. (2000). Mass Balance and Equilibrium-Line Altitudes of Glaciers in High-Mountain Environments. *Quat. Int.* 65-66, 15–29. doi:10.1016/s1040-6182(99)00034-8

Benn, D. I., and Owen, L. A. (2002). Himalayan Glacial Sedimentary Environments: a Framework for Reconstructing and Dating the Former Extent of Glaciers in High Mountains. *Quat. Int.* 97-98, 3–25. doi:10.1016/S1040-6182(02)00048-4

Benn, D. I., and Owen, L. A. (1998). The Role of the Indian Summer Monsoon and the Mid-latitude Westerlies in Himalayan Glaciation: Review and Speculative Discussion. *J. Geol. Soc.* 155 (2), 353–363. doi:10.1144/gsjgs.155.2.0353

Berthier, E., Arnaud, Y., Baratoux, D., Vincent, C., and Remy, F. (2004). Recent rapid thinning of the "Mer de Glace" glacier derived from satellite optical images. *Geophys. Res. Lett.* 31 (17). doi:10.1029/2004gl020706

Berthier, E., Schiefer, E., Clarke, G. K. C., Menounos, B., and Rémy, F. (2010). Contribution of Alaskan Glaciers to Sea-Level Rise Derived from Satellite Imagery. *Nat. Geosci* 3, 92–95. doi:10.1038/ngeo737

Bhambri, R., Bolch, T., Chaujar, R. K., and Kulshreshtha, S. C. (2011). Glacier Changes in the Garhwal Himalaya, India, from 1968 to 2006 Based on Remote Sensing. *J. Glaciol.* 57 (203), 543–556. doi:10.3189/002214311796905604

Bolch, T., Buchroithner, M., Pieczonka, T., and Kunert, A. (2008). Planimetric and Volumetric Glacier Changes in the Khumbu Himal, Nepal, since 1962 Using Corona, Landsat TM and ASTER Data. *J. Glaciol.* 54 (187), 592–600. doi:10.3189/002214308786570782

Bolch, T., Kulkarni, A., Kääb, A., Huggel, C., Paul, F., Cogley, J. G., et al. (2012). The State and Fate of Himalayan Glaciers. *Science* 336 (6079), 310–314. doi:10.1126/science.1215828

Bolch, T., Menounos, B., and Wheate, R. (2010). Landsat-based Inventory of Glaciers in Western Canada, 1985-2005. *Remote Sensing Environ.* 114, 127–137. doi:10.1016/j.rse.2009.08.015

Bolch, T., Pieczonka, T., and Benn, D. I. (2011). Multi-decadal Mass Loss of Glaciers in the Everest Area (Nepal Himalaya) Derived from Stereo Imagery. *The Cryosphere* 5 (2), 349–358. doi:10.5194/tc-5-349-2011

Brun, F., Berthier, E., Wagnon, P., Kääb, A., and Treichler, D. (2017). A Spatially Resolved Estimate of High Mountain Asia Glacier Mass Balances from 2000 to 2016. *Nat. Geosci* 10, 668–673. doi:10.1038/ngeo2999

Brun, F., Buri, P., Miles, E. S., Wagnon, P., Steiner, J., Berthier, E., et al. (2016). Quantifying Volume Loss from Ice Cliffs on Debris-Covered Glaciers Using High-Resolution Terrestrial and Aerial Photogrammetry. *J. Glaciol.* 62 (234), 684–695. doi:10.1017/jog.2016.54

Brun, F., Wagnon, P., Berthier, E., Jomelli, V., Maharjan, S. B., Shrestha, F., et al. (2019). Heterogeneous Influence of Glacier Morphology on the Mass Balance Variability in High Mountain Asia. *J. Geophys. Res. Earth Surf.* 124 (6), 1331–1345. doi:10.1029/2018JF004838

Brun, F., Wagnon, P., Berthier, E., Shea, J. M., Immerzeel, W. W., Kraaijenbrink, P. D. A., et al. (2018). Ice Cliff Contribution to the Tongue-wide Ablation of Changri Nup Glacier, Nepal, central Himalaya. *The Cryosphere* 12 (11), 3439–3457. doi:10.5194/tc-12-3439-2018

Buri, P., Miles, E. S., Steiner, J. F., Immerzeel, W. W., Wagnon, P., and Pellicciotti, F. (2016). A Physically Based 3-D Model of Ice Cliff Evolution over Debris-covered Glaciers. *J. Geophys. Res. Earth Surf.* 121 (12), 2471–2493. doi:10.1002/2016JF004039

Buri, P., Miles, E. S., Steiner, J. F., Ragettli, S., and Pellicciotti, F. (2021). Supraglacial Ice Cliffs Can Substantially Increase the Mass Loss of Debris-Covered Glaciers. *Geophys. Res. Lett.* 48 (6), e2020GL092150. doi:10.1029/2020GL092150

Chand, M. B., and Watanabe, T. (2019). Development of Supraglacial Ponds in the Everest Region, Nepal, between 1989 and 2018. *Remote Sensing* 11 (9), 1058. doi:10.3390/rs11091058

Dashora, A., Lohani, B., and Malik, J. N. (2007). A Repository of Earth Resource Information-CORONA Satellite Programme. *Curr. Sci.* 92 (7).

Dehecq, A., Gardner, A. S., Alexandrov, O., McMichael, S., Hugonnet, R., Shean, D., et al. (2020). Automated Processing of Declassified KH-9 Hexagon Satellite Images for Global Elevation Change Analysis since the 1970s. *Front. Earth Sci.* 8, 516. doi:10.3389/feart.2020.566802

Dehecq, A., Gourmelen, N., Gardner, A. S., Brun, F., Goldberg, D., Nienow, P. W., et al. (2019). Twenty-first century Glacier Slowdown Driven by Mass Loss in High Mountain Asia. *Nat. Geosci* 12 (1), 22–27. doi:10.1038/s41561-018-0271-9

Deline, P. (2005). Change in Surface Debris Cover on Mont Blanc Massif Glaciers after the 'Little Ice Age' Termination. *The Holocene* 15 (2), 302–309. doi:10.1191/0959683605hl809rr

ERDAS (2010). *LPS Project Manager User's Guide*. Norcross, GA 30092-2500 USA.

Falaschi, D., Lenzano, M. G., Villalba, R., Bolch, T., Rivera, A., and Lo Vecchio, A. (2019). Six Decades (1958-2018) of Geodetic Glacier Mass Balance in Monte San Lorenzo, Patagonian Andes. *Front. Earth Sci.* 7, 326. doi:10.3389/feart.2019.00326

Farinotti, D., Huss, M., Fürst, J. J., Landmann, J., Machguth, H., Maussion, F., et al. (2019). A Consensus Estimate for the Ice Thickness Distribution of All Glaciers on Earth. *Nat. Geosci.* 12 (3), 168–173. doi:10.1038/s41561-019-0300-3

Fickert, T., Friend, D., Grüninger, F., Molnia, B., and Richter, M. (2007). Did Debris-Covered Glaciers Serve as Pleistocene Refugia for Plants? A New Hypothesis Derived from Observations of Recent Plant Growth on Glacier Surfaces. *Arctic, Antarctic, Alpine Res.* 39 (2), 245–257. doi:10.1657/1523-0430(2007)39[245:ddgsap]2.0.co;2

Gaphaz (2017). in *Assessment of Glacier and Permafrost Hazards in Mountain Regions – Technical Guidance Document*. *Standing Group on Glacier and Permafrost Hazards in Mountains (GAPHAZ) of the International Association of Cryospheric Sciences (IACS) and the International Permafrost Association (IPA)*. Editors S. Prepared by Allen, H. Frey, and C. Huggel (Zurich, Switzerland/Lima, Peru).

Gardelle, J., Berthier, E., Arnaud, Y., and Kääb, A. (2013). Region-wide Glacier Mass Balances over the Pamir-Karakoram-Himalaya during 1999-2011. *The Cryosphere* 7 (4), 1263–1286. doi:10.5194/tc-7-1263-2013

Gardelle, J., Berthier, E., and Arnaud, Y. (2012). Slight Mass Gain of Karakoram Glaciers in the Early Twenty-First century. *Nat. Geosci.* 5, 322–325. doi:10.1038/ngeo1450

Gardner, A. S., Fahnestock, M. A., and Scambos, T. A. (2019). *ITS_LIVE Regional Glacier and Ice Sheet Surface Velocities*. Data archived at National Snow and Ice Data Center. doi:10.5067/6II6VW8LLWJ7

Gardner, A. S., Moholdt, G., Scambos, T., Fahnstock, M., Ligtenberg, S., van den Broeke, M., et al. (2018). Increased West Antarctic and Unchanged East Antarctic Ice Discharge over the Last 7 Years. *The Cryosphere* 12 (2), 521–547. doi:10.5194/tc-12-521-2018

Glasser, N. F., Jansson, K. N., Harrison, S., and Rivera, A. (2005). Geomorphological Evidence for Variations of the North Patagonian Icefield during the Holocene. *Geomorphology* 71, 263–277. doi:10.1016/j.geomorph.2005.02.003

Goodsell, B., Hambrey, M. J., Glasser, N. F., Nienow, P., and Mair, D. (2005). The Structural Glaciology of a Temperate Valley Glacier: Haut Glacier d'Arolla, Valais, Switzerland. *Arctic, Antarctic, Alpine Res.* 37 (2), 218–232. doi:10.1657/1523-0430(2005)037[0218:tsgoat]2.0.co;2

Granshaw, F. D., and G. Fountain, A. (2006). Glacier Change (1958-1998) in the North Cascades National Park Complex, Washington, USA. *J. Glaciol.* 52 (177), 251–256. doi:10.3189/172756506781828782

Gulley, J. D., Benn, D. I., Screaton, E., and Martin, J. (2009). Mechanisms of Englacial Conduit Formation and Their Implications for Subglacial Recharge. *Quat. Sci. Rev.* 28 (19), 1984–1999. doi:10.1016/j.quascirev.2009.04.002

Hagg, W., Mayer, C., Lambrecht, A., and Helm, A. (2008). Sub-debris Melt Rates on Southern Inylchek Glacier, central Tian Shan. *Geografiska Annaler: Ser. A, Phys. Geogr.* 90, 55–63. doi:10.1111/j.1468-0459.2008.00333.x

Hambrey, M. J., Quincey, D. J., Glasser, N. F., Reynolds, J. M., Richardson, S. J., and Clemmens, S. (2008). Sedimentological, Geomorphological and Dynamic Context of Debris-Mantled Glaciers, Mount Everest (Sagarmatha) Region, Nepal. *Quat. Sci. Rev.* 27 (25-26), 2361–2389. doi:10.1016/j.quascirev.2008.08.010

Haritashya, U., Kargel, J., Shugar, D., Leonard, G., Strattman, K., Watson, C., et al. (2018). Evolution and Controls of Large Glacial Lakes in the Nepal Himalaya. *Remote Sensing* 10, 798. doi:10.3390/rs10050798

Harris Geospatial (2017). *ENVI Feature Extraction Module*. Available at: https://www.l3harrisgeospatial.com/Portals/0/pdfs/HG_ENVI_FX_module_data-sheet_WEB.pdf (Accessed 04 25, 2021).

Harrison, S., Jones, D., Anderson, K., Shannon, S., and Betts, R. A. (2021). Is Ice in the Himalayas More Resilient to Climate Change Than We Thought? *Geografiska Annaler: Ser. A, Phys. Geogr.* 103 (1), 1–7. doi:10.1080/04353676.2021.1888202

Herreid, S., and Pellicciotti, F. (2020). The State of Rock Debris Covering Earth's Glaciers. *Nat. Geosci.* 13 (9), 621–627. doi:10.1038/s41561-020-0615-0

Hugonnet, R., McNabb, R., Berthier, E., Menounos, B., Nuth, C., Girod, L., et al. (2021). Accelerated Global Glacier Mass Loss in the Early Twenty-First century. *Nature* 592 (7856), 726–731. doi:10.1038/s41586-021-03436-z

Huss, M. (2013). Density Assumptions for Converting Geodetic Glacier Volume Change to Mass Change. *The Cryosphere* 7 (3), 877–887. doi:10.5194/tc-7-877-2013

Immerzeel, W. W., Lutz, A. F., Andrade, M., Bahl, A., Biemans, H., Bolch, T., et al. (2020). Importance and Vulnerability of the World's Water Towers. *Nature* 577 (7790), 364–369. doi:10.1038/s41586-019-1822-y

Irvine-Fynn, T. D. L., Porter, P. R., Rowan, A. V., Quincey, D. J., Gibson, M. J., Bridge, J. W., et al. (2017). Supraglacial Ponds Regulate Runoff from Himalayan Debris-Covered Glaciers. *Geophys. Res. Lett.* 44 (2311), 11894–11904. doi:10.1002/2017GL075398

Iwata, S., Aoki, T., Kadota, T., Seko, K., and Yamaguchi, S. (2000). "Morphological Evolution of the Debris Cover on Khumbu Glacier, Nepal, between 1978 and 1995," in *Debris-covered Glaciers*. Editors M. Nakawo, C. F. Raymond, and A. Fountain.

Jansson, P., and Fredin, O. (2002). Ice Sheet Growth under Dirty Conditions: Implications of Debris Cover for Early Glaciation Advances. *Quat. Int.* 95-96, 35–42. doi:10.1016/s1040-6182(02)00025-3

JAXA (2019). *ALOS Global Digital Surface Model*. ALOS World 3D- 30m.

Jones, D. B., Harrison, S., and Anderson, K. (2019). Mountain Glacier-To-Rock Glacier Transition. *Glob. Planet. Change* 181, 102999. doi:10.1016/j.gloplacha.2019.102999

Kääb, A., Berthier, E., Nuth, C., Gardelle, J., and Arnaud, Y. (2012). Contrasting Patterns of Early Twenty-First-century Glacier Mass Change in the Himalayas. *Nature* 488, 495–498. doi:10.1038/nature11324

Kayastha, R. B., Takeuchi, Y., Nakawo, M., and Ageta, Y. (2000). "Practical Prediction of Ice Melting beneath Various Thickness of Debris Cover on Khumbu Glacier, Nepal, Using a Positive Degree-Day Factor," in *Debris-Covered Glaciers*. Editors C. F. Raymond, M. Nakawo, and A. Fountain (Wallingford, UK: IAHS), 71–81.

King, O., Bhattacharya, A., Bhambri, R., and Bolch, T. (2019). Glacial Lakes Exacerbate Himalayan Glacier Mass Loss. *Sci. Rep.* 9 (1), 18145. doi:10.1038/s41598-019-53733-x

King, O., Bhattacharya, A., Ghuffar, S., Tait, A., Guilford, S., Elmore, A. C., et al. (2020). Six Decades of Glacier Mass Changes Around Mt. Everest Are Revealed by Historical and Contemporary Images. *One Earth* 3 (5), 608–620. doi:10.1016/j.oneear.2020.10.019

King, O., Dehecq, A., Quincey, D., and Carrivick, J. (2018). Contrasting Geometric and Dynamic Evolution of lake and Land-Terminating Glaciers in the central Himalaya. *Glob. Planet. Change* 167, 46–60. doi:10.1016/j.gloplacha.2018.05.006

King, O., Quincey, D. J., Carrivick, J. L., and Rowan, A. V. (2017). Spatial Variability in Mass Loss of Glaciers in the Everest Region, central Himalayas, between 2000 and 2015. *The Cryosphere* 11 (1), 407–426. doi:10.5194/tc-11-407-2017

Kirkbride, M. P. (2011). "Debris-Covered Glaciers," in *Encyclopedia of Snow, Ice and Glaciers*. Editors V. P. Singh, P. Singh, and U. K. Haritashya (Dordrecht: Springer Netherlands), 180–182. doi:10.1007/978-90-481-2642-2_622

Kirkbride, M. P., and Deline, P. (2013). The Formation of Supraglacial Debris Covers by Primary Dispersal from Transverse Englacial Debris Bands. *Earth Surf. Process. Landforms* 38 (15), 1779–1792. doi:10.1002/esp.3416

Kirkbride, M. P. (1993). The Temporal Significance of Transitions from Melting to Calving Termini at Glaciers in the central Southern Alps of New Zealand. *The Holocene* 3 (3), 232–240. doi:10.1177/095968369300300305

Kneib, M., Miles, E. S., Jola, S., Buri, P., Herreid, S., Bhattacharya, A., et al. (2021). Mapping Ice Cliffs on Debris-Covered Glaciers Using Multispectral Satellite Images. *Remote Sensing Environ.* 253, 112201. doi:10.1016/j.rse.2020.112201

Knight, J., Harrison, S., and Jones, D. B. (2019). Rock Glaciers and the Geomorphological Evolution of Deglacierizing Mountains. *Geomorphology* 324, 14–24. doi:10.1016/j.geomorph.2018.09.020

Knight, J., and Harrison, S. (2009). Periglacial and Paraglacial Environments: a View from the Past into the Future. *Geol. Soc. Lond. Spec. Publications* 320 (1), 1–4. doi:10.1144/SP320.1

Komori, J. (2008). Recent Expansions of Glacial Lakes in the Bhutan Himalayas. *Quat. Int.* 184 (1), 177–186. doi:10.1016/j.quaint.2007.09.012

Magnússon, E., Muñoz-Cobo Belart, J., Pálsson, F., Ágústsson, H., and Crochet, P. (2016). Geodetic Mass Balance Record with Rigorous Uncertainty Estimates Deduced from Aerial Photographs and Lidar Data - Case Study from Drangajökull Ice Cap, NW Iceland. *The Cryosphere* 10 (1), 159–177. doi:10.5194/tc-10-159-2016

Maskey, S., Kayastha, R. B., and Kayastha, R. (2020). Glacial Lakes Outburst Floods (GLOFs) Modelling of Thulagi and Lower Barun Glacial Lakes of Nepalese Himalaya. *Prog. Disaster Sci.* 7, 100106. doi:10.1016/j.pdisas.2020.100106

Maurer, J. M., Schaefer, J. M., Rupper, S., and Corley, A. (2019). Acceleration of Ice Loss across the Himalayas over the Past 40 Years. *Sci. Adv.* 5 (6), eaav7266. doi:10.1126/sciadv.aav7266

McCarthy, M., Pritchard, H., Willis, I., and King, E. (2017). Ground-penetrating Radar Measurements of Debris Thickness on Lirung Glacier, Nepal. *J. Glaciol.* 63 (239), 543–555. doi:10.1017/jog.2017.18

McNabb, R., Nuth, C., Kääb, A., and Girod, L. (2019). Sensitivity of Glacier Volume Change Estimation to DEM Void Interpolation. *The Cryosphere* 13 (3), 895–910. doi:10.5194/tc-13-895-2019

Mihalcea, C., Mayer, C., Diolaiuti, G., Lambrecht, A., Smiraglia, C., and Tartari, G. (2006). Ice Ablation and Meteorological Conditions on the Debris-Covered Area of Baltoro Glacier, Karakoram, Pakistan. *Ann. Glaciol.* 43, 292–300. doi:10.3189/172756406781812104

Miles, E. S., Pellicciotti, F., Willis, I. C., Steiner, J. F., Buri, P., and Arnold, N. S. (2016). Refined Energy-Balance Modelling of a Supraglacial Pond, Langtang Khola, Nepal. *Ann. Glaciol.* 57 (71), 29–40. doi:10.3189/2016AoG71A421

Miles, E. S., Watson, C. S., Brun, F., Berthier, E., Esteves, M., Quincey, D. J., et al. (2018a). Glacial and Geomorphic Effects of a Supraglacial lake Drainage and Outburst Event, Everest Region, Nepal Himalaya. *The Cryosphere* 12, 3891–3905. doi:10.5194/tc-12-3891-2018

Miles, E. S., Willis, I., Buri, P., Steiner, J. F., Arnold, N. S., and Pellicciotti, F. (2018b). Surface Pond Energy Absorption across Four Himalayan Glaciers Accounts for 1/8 of Total Catchment Ice Loss. *Geophys. Res. Lett.* 45 (1910), 10464–10473. doi:10.1029/2018GL079678

Miles, E. S., Willis, I. C., Arnold, N. S., Steiner, J., and Pellicciotti, F. (2017). Spatial, Seasonal and Interannual Variability of Supraglacial Ponds in the Langtang Valley of Nepal, 1999-2013. *J. Glaciol.* 63 (237), 88–105. doi:10.1017/jog.2016.120

Millan, R., Mouginot, J., Rabatel, A., Jeong, S., Cusicanqui, D., Derkacheva, A., et al. (2019). Mapping Surface Flow Velocity of Glaciers at Regional Scale Using a Multiple Sensors Approach. *Remote Sensing* 11 (21), 2498. doi:10.3390/rs11212498

Millan, R., Mouginot, J., Rabatel, A., and Morlighem, M. (2022). Ice Velocity of the World's Glaciers : Reconciling Ice Thickness Distribution with Glacier Dynamics, Nature Geosciences. *Nat. Geosciences* 15, 124–129.

Mölg, N., Bolch, T., Walter, A., and Vieli, A. (2019). Unravelling the Evolution of Zmuttgletscher and its Debris Cover since the End of the Little Ice Age. *The Cryosphere* 13 (7), 1889–1909. doi:10.5194/tc-13-1889-2019

Monnier, S., and Kinnard, C. (2017). Pluri-decadal (1955-2014) Evolution of Glacier-Rock Glacier Transitional Landforms in the central Andes of Chile (30-33° S). *Earth Surf. Dynam.* 5 (3), 493–509. doi:10.5194/esurf-5-493-2017

Monnier, S., and Kinnard, C. (2015). Reconsidering the Glacier to Rock Glacier Transformation Problem: New Insights from the central Andes of Chile. *Geomorphology* 238, 47–55. doi:10.1016/j.geomorph.2015.02.025

Mool, P. K., Bajracharya, S. R., Joshi, S. P., Sakya, K., and Baidya, A. (2002). *Inventory of Glaciers, Glacial Lakes and GLOF Monitoring Nepal*. Nepal: International Center for Integrated Mountain Development.

Nicholson, L., and Benn, D. I. (2006). Calculating Ice Melt beneath a Debris Layer Using Meteorological Data. *J. Glaciol.* 52 (178), 463–470. doi:10.3189/172756506781828584

Nie, Y., Sheng, Y., Liu, Q., Liu, L., Liu, S., Zhang, Y., et al. (2017). A Regional-Scale Assessment of Himalayan Glacial lake Changes Using Satellite Observations from 1990 to 2015. *Remote Sensing Environ.* 189, 1–13. doi:10.1016/j.rse.2016.11.008

Nuimura, T., Fujita, K., Yamaguchi, S., and Sharma, R. R. (2012). Elevation Changes of Glaciers Revealed by Multitemporal Digital Elevation Models Calibrated by GPS Survey in the Khumbu Region, Nepal Himalaya, 1992-2008. *J. Glaciol.* 58 (210), 648–656. doi:10.3189/2012jog11j061

Østrem, G. (1975). Erts Data in Glaciology-An Effort to Monitor Glacier Mass Balance from Satellite Imagery. *J. Glaciol.* 15 (73), 403–415. doi:10.3189/S0022143000034511

Pant, S. R., and Reynolds, J. M. (2000). Application of Electrical Imaging Techniques for the Investigation of Natural Dams: an Example from the Thulagi Glacier Lake, Nepal. *J. Nepal Geol. Soc.* 22. doi:10.3126/jngs.v22i0.32348

Paudel, U. (2020). Trends of Temperature and Rainfall in Pokhara. *Prithvi Acad. J.* 3, 22–32. doi:10.3126/paj.v3i0.29556

Paul, F., Barrand, N. E., Baumann, S., Berthier, E., Bolch, T., Casey, K., et al. (2013). On the Accuracy of Glacier Outlines Derived from Remote-Sensing Data. *Ann. Glaciol.* 54 (63), 171–182. doi:10.3189/2013AoG63A296

Paul, F., Bolch, T., Briggs, K., Kääb, A., McMillan, M., McNabb, R., et al. (2017). Error Sources and Guidelines for Quality Assessment of Glacier Area, Elevation Change, and Velocity Products Derived from Satellite Data in the Glaciers_cci Project. *Remote Sensing Environ.* 203, 256–275. doi:10.1016/j.rse.2017.08.038

Pci_Geomatics_Inc (2020). *Geomatica Banff*. Markham, Ontario.

Pekel, J.-F., Cottam, A., Gorelick, N., and Belward, A. S. (2016). High-resolution Mapping of Global Surface Water and its Long-Term Changes. *Nature* 540 (7633), 418–422. doi:10.1038/nature20584

Planet Labs (2021). *Planet Imagery Product Specifications*.

Planet Labs (2016). RapidEye Imagery Produce Specification Version 6.1. Available: https://www.planet.com/products/satellite-imagery/files/160625-RapidEye%20Image-Product-Specifications.pdf (Accessed 0805, 2021).

Quincey, D. J., Richardson, S. D., Luckman, A., Lucas, R. M., Reynolds, J. M., Hambrey, M. J., et al. (2007). Early Recognition of Glacial lake Hazards in the Himalaya Using Remote Sensing Datasets. *Glob. Planet. Change* 56 (1 - 2), 137–152. doi:10.1016/j.gloplacha.2006.07.013

Racoviteanu, A. E., Arnaud, Y., Williams, M. W., and Manley, W. F. (2015). Spatial Patterns in Glacier Characteristics and Area Changes from 1962 to 2006 in the Kanchenjunga-Sikkim Area, Eastern Himalaya. *The Cryosphere* 9 (2), 505–523. doi:10.5194/tc-9-505-2015

Racoviteanu, A. E., Arnaud, Y., Williams, M. W., and Ordoñez, J. (2008). Decadal Changes in Glacier Parameters in the Cordillera Blanca, Peru, Derived from Remote Sensing. *J. Glaciol.* 54 (186), 499–510. doi:10.3189/002214308785836922

Racoviteanu, A. E., Nicholson, L., and Glasser, N. F. (2021). Surface Composition of Debris-Covered Glaciers across the Himalaya Using Linear Spectral Unmixing of Landsat 8 OLI Imagery. *The Cryosphere* 15 (9), 4557–4588. doi:10.5194/tc-2020-37210.5194/tc-15-4557-2021

Racoviteanu, A., Paul, F., Raup, B., Khalsa, S. J. S., and Armstrong, R. (2009). Challenges and Recommendations in Mapping of Glacier Parameters from Space: Results of the 2008 Global Land Ice Measurements from Space (GLIMS) Workshop, Boulder, Colorado, USA. *Ann. Glaciology* 50 (53). doi:10.3189/172756410790595804

Ragettli, S., Bolch, T., and Pellicciotti, F. (2016). Heterogeneous Glacier Thinning Patterns over the Last 40 Years in Langtang Himal, Nepal. *The Cryosphere* 10, 2075 - 2097. doi:10.5194/tc-10-2075-2016

Raup, B. H., and Khalsa, S. J. S. (2007). GLIMS Analysis Tutorial . GLIMS. Available: http://www.glims.org/MapsAndDocs/assets/GLIMS_Analysis_Tutorial_a4.pdf (Accessed 01 10, 2007 2007).

Reid, T. D., and Brock, B. W. (2014). Assessing Ice-Cliff Backwasting and its Contribution to Total Ablation of Debris-Covered Miage Glacier, Mont Blanc Massif, Italy. *J. Glaciol.* 60 (219), 3–13. doi:10.3189/2014JoG13J045

Ren, J., Jing, Z., Pu, J., and Qin, X. (2006). Glacier Variations and Climate Change in the central Himalaya over the Past Few Decades. *Ann. Glaciol.* 43, 218–222. doi:10.3189/172756406781812230

Reynolds, J. M. (2014). Assessing Glacial Hazards for Hydropower Development in the Himalayas, Hindu Kush and Karakoram. *Int. J. Hydropower Dams* 21 (1), 60–65.

Reynolds, J. M. (2000). "On the Formation of Supraglacial Lakes on Debris-Covered Glaciers," in *Debris-covered Glaciers*. Editors M. Nakawo, C. F. Raymond, and A. Fountain (Wallingsford: IAHS, published online by Cambridge University Press), 153–161.

Richardson, S. D., and Reynolds, J. M. (2000). An Overview of Glacial Hazards in the Himalayas. *Quat. Int.* 65-66, 31–47. doi:10.1016/s1040-6182(99)00035-x

Robson, B. A., Nuth, C., Nielsen, P. R., Girod, L., Hendrickx, M., and Dahl, S. O. (2018). Spatial Variability in Patterns of Glacier Change across the Manaslu

Range, Central Himalaya. *Front. Earth Sci.* 6, 12. doi:10.3389/feart.2018.00012

Rounce, D. R., Hock, R., McNabb, R. W., Millan, R., Sommer, C., Braun, M. H., et al. (2021). Distributed Global Debris Thickness Estimates Reveal Debris Significantly Impacts Glacier Mass Balance. *Geophys. Res. Lett.* 48 (8), e2020GL091311. doi:10.1029/2020GL091311

Rowan, A. V., Egholm, D. L., Quincey, D. J., and Glasser, N. F. (2015). Modelling the Feedbacks between Mass Balance, Ice Flow and Debris Transport to Predict the Response to Climate Change of Debris-Covered Glaciers in the Himalaya. *Earth Planet. Sci. Lett.* 430, 427–438. doi:10.1016/j.epsl.2015.09.004

Rowan, A. V., Nicholson, L. I., Quincey, D. J., Gibson, M. J., Irvine-Fynn, T. D. L., Watson, C. S., et al. (2020). Seasonally Stable Temperature Gradients through Supraglacial Debris in the Everest Region of Nepal, Central Himalaya. *J. Glaciol.* 67, 170–181. doi:10.1017/jog.2020.100

Rowan, A. V. (2017). The 'Little Ice Age' in the Himalaya: A Review of Glacier advance Driven by Northern Hemisphere Temperature Change. *The Holocene* 27 (2), 292–308. doi:10.1177/0959683616658530

Sakai, A. (2019). Brief Communication: Updated GAMDAM Glacier Inventory over High-Mountain Asia. *The Cryosphere* 13 (7), 2043–2049. doi:10.5194/tc-13-2043-2019

Sakai, A., and Fujita, K. (2010). Formation Conditions of Supraglacial Lakes on Debris-Covered Glaciers in the Himalaya. *J. Glaciol.* 56 (195), 177–181. doi:10.3189/002214310791190785

Sakai, A., Nakawo, M., and Fujita, K. (2002). Distribution Characteristics and Energy Balance of Ice Cliffs on Debris-Covered Glaciers, Nepal Himalaya. *Arctic, Antarctic, Alpine Res.* 34 (1), 12–19. doi:10.1080/15230430.2002.12003463

Sakai, A., Nakawo, M., and Fujita, K. (1998). Melt Rate of Ice Cliffs on the Lirung Glacier, Nepal Himalayas, 1996. *Bull. Glacier Res.* 16 (57 - 66).

Sakai, A., Takeuchi, N., Fujita, K., and Nakawo, M. (2000). Role of Supraglacial Ponds in the Ablation Process of a Debris-Covered Glacier in the Nepal Himalayas. *Int. Assoc. Hydrological Sci.* 264, 119–130.

Salerno, F., Thakuri, S., D'Agata, C., Smiraglia, C., Manfredi, E. C., Viviano, G., et al. (2012). Glacial lake Distribution in the Mount Everest Region: Uncertainty of Measurement and Conditions of Formation. *Glob. Planet. Change* 92-93, 30–39. doi:10.1016/j.gloplacha.2012.04.001

Salerno, F., Thakuri, S., Tartari, G., Nuimura, T., Sunako, S., Sakai, A., et al. (2017). Debris-covered Glacier Anomaly? Morphological Factors Controlling Changes in the Mass Balance, Surface Area, Terminus Position, and Snow Line Altitude of Himalayan Glaciers. *Earth Planet. Sci. Lett.* 471, 19–31. doi:10.1016/j.epsl.2017.04.039

Sapkota, A., Kayastha, R., Kafle, K., and Thapa, A. (2016). "Geomorphological Mapping of Lower Part of Ponkar Glacier, Bhimthang, Manang," in National Symposium on Hydrology and Metereology, Kathmandu, Nepal. doi:10.13140/RG.2.2.34880.33287

Scherler, D., Bookhagen, B., and Strecker, M. R. (2011). Spatially Variable Response of Himalayan Glaciers to Climate Change Affected by Debris Cover. *Nat. Geosci* 4 (3), 156–159. doi:10.1038/ngeo1068

Scherler, D., Wulf, H., and Gorelick, N. (2018). Global Assessment of Supraglacial Debris-Cover Extents. *Geophys. Res. Lett.* 45 (2111), 11798–11805. doi:10.1029/2018GL080158

Scott Watson, C., Quincey, D. J., Carrivick, J. L., and Smith, M. W. (2017a). Ice Cliff Dynamics in the Everest Region of the Central Himalaya. *Geomorphology* 278 (C), 238–251. doi:10.1016/j.geomorph.2016.11.017

Shannon, S., Smith, R., Wiltshire, A., Payne, T., Huss, M., Betts, R., et al. (2019). Global Glacier Volume Projections under High-End Climate Change Scenarios. *The Cryosphere* 13 (1), 325–350. doi:10.5194/tc-13-325-2019

Shean, D. E., Alexandrov, O., Moratto, Z. M., Smith, B. E., Joughin, I. R., Porter, C., et al. (2016). An Automated, Open-Source Pipeline for Mass Production of Digital Elevation Models (DEMs) from Very-High-Resolution Commercial Stereo Satellite Imagery. *ISPRS J. Photogrammetry Remote Sensing* 116, 101–117. doi:10.1016/j.isprsjprs.2016.03.012

Shean, D. E., Bhushan, S., Montesano, P., Rounce, D. R., Arendt, A., and Osmanoglu, B. (2020). A Systematic, Regional Assessment of High Mountain Asia Glacier Mass Balance. *Front. Earth Sci.* 7, 363. doi:10.3389/feart.2019.00363

Shean, D. E. (2017). *HMA 8-meter DEM Mosaics Derived from Optical Imagery, V1*. NSIDC DAAC: NSIDC Distributed Active Archive Center.

Shrestha, R., Kayastha, R. B., and Kayastha, R. (2020). Effect of Debris on Seasonal Ice Melt (2016-2018) on Ponkar Glacier, Manang, Nepal. *Sci. Cold Regions* 12 (5), 261–271. doi:10.3724/SP.J.1226.2020.00272

Shrestha, S., Bhandari, R., Bashyal, A., and Shrestha, N. (2021). A Comparative Study of Physico-Chemical Parameter in Glacial Melt Water, Ponkar Glacier, Nepal. *OALib* 08, 1–10. doi:10.4236/oalib.1107160

Shroder, J. F., Bishop, M. P., Copland, L., and Sloan, V. F. (2000). Debris-covered Glaciers and Rock Glaciers in the Nanga Parbat Himalaya, pakistan. *Geografiska Annaler: Ser. A, Phys. Geogr.* 82 (1), 17–31. doi:10.1111/j.0435-3676.2000.00108.x

Shukla, A., Garg, P. K., and Srivastava, S. (2018). Evolution of Glacial and High-Altitude Lakes in the Sikkim, Eastern Himalaya over the Past Four Decades (1975-2017). *Front. Environ. Sci.* 6, 81. doi:10.3389/fenvs.2018.00081

Smiraglia, C., Diolaiuti, G., Casati, D., and Kirkbride, M. P. (2000). "Recent Areal and Altimetric Variations of Miage Glacier (Monte Bianco Massif, Italian Alps)," in *Debris-covered Glaciers*. Editors M. Nakawo, C. F. Raymond, and A. Fountain (Wellingsford: IAHS, published online by Cambridge University Press), 227–233.

Solomina, O. N., Bradley, R. S., Hodgson, D. A., Ivy-Ochs, S., Jomelli, V., Mackintosh, A. N., et al. (2015). Holocene Glacier Fluctuations. *Quat. Sci. Rev.* 111, 9–34. doi:10.1016/j.quascirev.2014.11.018

Steiner, J. F., Buri, P., Miles, E. S., Ragettli, S., and Pellicciotti, F. (2019). Supraglacial Ice Cliffs and Ponds on Debris-Covered Glaciers: Spatio-Temporal Distribution and Characteristics. *J. Glaciol.* 65 (252), 617–632. doi:10.1017/jog.2019.40

Steiner, J. F., Pellicciotti, F., Buri, P., Miles, E. S., Immerzeel, W. W., and Reid, T. D. (2015). Modelling Ice-Cliff Backwasting on a Debris-Covered Glacier in the Nepalese Himalaya. *J. Glaciol.* 61, 889–907. doi:10.3189/2015JoG14J194

Stokes, C. R., Popovnin, V., Aleynikov, A., Gurney, S. D., and Shahgedanova, M. (2007). Recent Glacier Retreat in the Caucasus Mountains, Russia, and Associated Increase in Supraglacial Debris Cover and Supra-/proglacial lake Development. *Ann. Glaciol.* 46, 195–203. doi:10.3189/172756407782871468

Survey of India (2005). National Map Policy. Survey of India. Available: http://www.surveyofindia.gov.in/tenders/nationalmappolicy/nationalmappolicy.pdf (Accessed October 24, 2010).

Sutherland, J. L., Carrivick, J. L., Gandy, N., Shulmeister, J., Quincey, D. J., and Cornford, S. L. (2020). Proglacial Lakes Control Glacier Geometry and Behavior during Recession. *Geophys. Res. Lett.* 47 (19), e2020GL088865. doi:10.1029/2020GL088865

Tadono, T., Ishida, H., Oda, F., Naito, S., Minakawa, K., and Iwamoto, H. (2014). Precise Global DEM Generation by ALOS PRISM. *ISPRS Ann. Photogramm. Remote Sens. Spat. Inf. Sci.* II-4, 71–76. doi:10.5194/isprsannals-II-4-71-2014

Tampucci, D., Citterio, C., Gobbi, M., and Caccianiga, M. (2016). Vegetation Outlines of a Debris-Covered Glacier Descending below the Treeline. *Plant Sociol.* 53, 43–52. doi:10.7338/pls2016531/03

Taylor, C. J., Carr, J. R., and Rounce, D. R. (2021). Spatiotemporal Supraglacial Pond and Ice Cliff Changes in the Bhutan-Tibet Border Region from 2016 to 2018. *J. Glaciol.*, 1–13. doi:10.1017/jog.2021.76

Thakuri, S., Salerno, F., Smiraglia, C., Bolch, T., D'Agata, C., Viviano, G., et al. (2014). Tracing Glacier Changes since the 1960s on the South Slope of Mt. Everest (central Southern Himalaya) Using Optical Satellite Imagery. *The Cryosphere* 8, 1297 - 1315. doi:10.5194/tc-8-1297-2014

Thompson, S. S., Benn, D. I., Dennis, K., and Luckman, A. (2012). A Rapidly Growing Moraine-Dammed Glacial lake on Ngozumpa Glacier, Nepal. *Geomorphology* 145-146, 1–11. doi:10.1016/j.geomorph.2011.08.015

Tielidze, L. G., Bolch, T., Wheate, R. D., Kutuzov, S. S., Lavrentiev, I. I., and Zemp, M. (2020). Supra-glacial Debris Cover Changes in the Greater Caucasus from 1986 to 2014. *The Cryosphere* 14, 585–598. doi:10.5194/tc-14-585-2020

van Woerkom, T., Steiner, J. F., Kraaijenbrink, P. D. A., Miles, E. S., and Immerzeel, W. W. (2019). Sediment Supply from Lateral Moraines to a Debris-Covered Glacier in the Himalaya. *Earth Surf. Dynam.* 7 (2), 411–427. doi:10.5194/esurf-7-411-2019

Vermote, E. F., Tanre, D., Deuze, J. L., Herman, M., and Morcette, J.-J. (1997). Second Simulation of the Satellite Signal in the Solar Spectrum, 6S: an Overview. *IEEE Trans. Geosci. Remote Sensing* 35 (3), 675–686. doi:10.1109/36.581987

Vincent, C., Wagnon, P., Shea, J. M., Immerzeel, W. W., Kraaijenbrink, P., Shrestha, D., et al. (2016). Reduced Melt on Debris-Covered Glaciers: Investigations from Changri Nup Glacier, Nepal. *The Cryosphere* 10 (4), 1845–1858. doi:10.5194/tc-10-1845-2016

Watson, C. S., Kargel, J. S., Shugar, D. H., Haritashya, U. K., Schiassi, E., and Furfaro, R. (2020). Mass Loss from Calving in Himalayan Proglacial Lakes. *Front. Earth Sci.* 7, 342. doi:10.3389/feart.2019.00342

Watson, C. S., Quincey, D. J., Carrivick, J. L., and Smith, M. W. (2016). The Dynamics of Supraglacial Ponds in the Everest Region, central Himalaya. *Glob. Planet. Change* 142 (Suppl. C), 14–27. doi:10.1016/j.gloplacha.2016.04.008

Watson, C. S., Quincey, D. J., Smith, M. W., Carrivick, J. L., Rowan, A. V., and James, M. R. (2017b). Quantifying Ice Cliff Evolution with Multi-Temporal point Clouds on the Debris-Covered Khumbu Glacier, Nepal. *J. Glaciol.* 63 (241), 823–837. doi:10.1017/jog.2017.47

Welch, B. L. (1947). The Generalization of 'Student's' Problem when Several Different Population Varlances Are Involved. *Biometrika* 34 (1-2), 28–35. doi:10.1093/biomet/34.1-2.28

Xie, F., Liu, S., Wu, K., Zhu, Y., Gao, Y., Qi, M., et al. (2020). Upward Expansion of Supra-glacial Debris Cover in the Hunza Valley, Karakoram, during 1990 ~ 2019. *Front. Earth Sci.* 8 (308). doi:10.3389/feart.2020.00308

Yanai, M., Li, C., and Song, Z. (1992). Seasonal Heating of the Tibetan Plateau and its Effects on the Evolution of the Asian Summer Monsoon. *J. Meteorol. Soc. Jpn.* 70, 319–351. doi:10.2151/jmsj1965.70.1b_319

Conflict of Interest: The authors declare that the research was conducted in the absence of any commercial or financial relationships that could be construed as a potential conflict of interest.

frontiers | Frontiers in Earth Science

ORIGINAL RESEARCH
published: 24 August 2022
doi: 10.3389/feart.2022.796877

Modelling Debris-Covered Glacier Ablation Using the Simultaneous Heat and Water Transport Model. Part 1: Model Development and Application to North Changri Nup

Alex Winter-Billington[1]*, *Ruzica Dadić*[2], *R. D. Moore*[1], *Gerald Flerchinger*[3], *Patrick Wagnon*[4] and *Argha Banerjee*[5]

[1]Department of Geography, University of British Columbia, Vancouver, BC, Canada, [2]Antarctic Research Center Te Puna Patiotio, Victoria University of Wellington Te Herenga Waka, Wellington, New Zealand, [3]Northwest Watershed Research Center, Agriculture Research Service, U.S. Department of Agriculture, Boise, ID, United States, [4]Univ. Grenoble Alpes, CNRS, IRD, IGE, Grenoble, France, [5]Department of Earth Sciences, Indian Institute of Science Education and Research, Pune, India

OPEN ACCESS

Edited by:
Martina Barandun,
Eurac Research, Italy

Reviewed by:
Pascal Buri,
Swiss Federal Institute for Forest, Snow and Landscape Research (WSL), Switzerland
Thomas Loriaux,
Centro de Estudios Científicos, Chile

***Correspondence:**
Alex Winter-Billington
winter-billington@alumni.ubc.ca

Specialty section:
This article was submitted to Cryospheric Sciences, a section of the journal Frontiers in Earth Science

Received: 17 October 2021
Accepted: 09 May 2022
Published: 24 August 2022

Citation:
Winter-Billington A, Dadić R, Moore RD, Flerchinger G, Wagnon P and Banerjee A (2022) Modelling Debris-Covered Glacier Ablation Using the Simultaneous Heat and Water Transport Model. Part 1: Model Development and Application to North Changri Nup. Front. Earth Sci. 10:796877. doi: 10.3389/feart.2022.796877

Modelling ablation of glacier ice under a layer of mineral debris is increasingly important, because the extent of supraglacial debris is expanding worldwide due to glacier recession. Physically based models have been developed, but the uncertainty in predictions is not yet well constrained. A new one-dimensional model of debris-covered ice ablation that is based on the Simultaneous Heat and Water transfer model is introduced here. SHAW-Glacier is a physically based, vertically integrated, fully coupled, water and energy balance model, which includes the advection of heat by rainwater and lateral flow. SHAW-Glacier was applied to North Changri Nup, a high elevation alpine glacier in the monsoon-dominated Central Himalaya. Simulations were compared with observed debris temperature profiles, snow depth, and ablation stake measurements for debris 0.03–0.41 m thick, in a 2500 m^2 study area. Prediction uncertainty was estimated in a Monte Carlo analysis. SHAW-Glacier simulated the characteristic pattern of decreasing ablation with increasing debris thickness. However, the observations of ablation did not follow the characteristic pattern; annual ablation was highest where the debris was thickest. Recursive partitioning revealed a substantial, non-linear sensitivity to the snow threshold air temperature, suggesting a sensitivity to the duration of snow cover. Photographs showed patches of snow persisting through the ablation season, and the observational data were consistent with uneven persistence of snow patches. The analyses indicate that patchy snow cover in the ablation season can overwhelm the sensitivity of sub-debris ablation to debris thickness. Patchy snow cover may be an unquantified source of uncertainty in predictions of sub-debris ablation.

Keywords: glacier, debris, ablation, model, SHAW, physically based, Changri Nup

1 INTRODUCTION

Glacier meltwater is an important resource in densely populated areas such as the Himalayan foothills (Immerzeel et al., 2020). Meltwater is used in hydro-electricity and agricultural production, and it can be particularly important during prolonged periods without rain (Pritchard, 2019). Melting of alpine glaciers can also give rise to hazards affecting mountain communities, including mass movement events and flooding (Quincey et al., 2005; Dussaillant et al., 2010; Hewitt, 2014; Ragettli et al., 2016; Williams and Koppes, 2019; Molden et al., 2022), and glacier meltwater is contributing to global sea level rise (Hock et al., 2019). Models of glacier melt are used to make predictions that help resource managers evaluate and plan for the risks associated with glacier change. However, predictions are inherently uncertain. An accurate assessment of the uncertainty in predictions can be key to the success of management decisions (Lutz et al., 2014; Koppes et al., 2015; Ragettli et al., 2015; Marzeion et al., 2020).

Rock debris is found on the surface of an estimated 44% of the glaciers on Earth (Herreid and Pellicciotti, 2020); 4.4% to more than 30% of the glacier surface area in some regions has been found to be completely covered by a layer of unconsolidated material (Sasaki et al., 2016; Scherler et al., 2018). Both theory and observations indicate that the thickness and extent of supraglacial debris cover is increasing as glaciers recede (Bhambri et al., 2011), yet the role of debris has rarely been included in regional glacier melt models. Supraglacial debris can enhance or reduce melt rates (Rounce et al., 2021): observations have shown that ablation decreases exponentially as debris thickness increases beyond a few centimetres, in a relation that is known as the 'Østrem Curve'. Furthermore, unlike snow and bare ice surfaces, the temperature of supraglacial debris can rise above 0°C. Therefore, traditional glacier surface ablation models are not immediately transferable to debris-covered glaciers.

Both empirical and physically based models have been developed and applied to predict sub-debris glacier melt (e.g. Giese et al., 2020; Winter-Billington et al., 2020). A challenge with empirical models is that parameter values estimated for specific sites or periods may not be applicable under different geographic or climatic conditions. Physically based models should be more robust for application to a range of geographical contexts and under scenarios of climatic change. Major challenges in applying physically based models pertain to the typically limited availability of detailed meteorological data to drive surface mass and energy fluxes, as well as uncertainty regarding hydraulic and thermal properties of the debris layer. When applying predictive models, it is important to understand the sensitivity of model predictions to these sources of uncertainty.

The acquisition of data for physically based modelling at regional scale can require substantial resources; simplifying the representation of physical processes can reduce both the data load and computational expense. Predictions of glacier volume and area made by Giesen and Oerlemans (2013) with a simplified energy balance model were found to have the smallest uncertainties by comparison with five empirical models in a global glacier mass balance model intercomparison (Hock et al., 2019). Such simplifications can be robust for debris-free glaciers because, although the global population of glaciers remains undersampled (Mernild et al., 2013), the processes of surface ablation have been observed, and parameter uncertainty evaluated, at a relatively wide range of sites and scales (e.g. Dadić et al., 2013; Fitzpatrick et al., 2017; Marzeion et al., 2020). Fewer studies have been conducted on debris-covered glaciers; uncertainty introduced by neglecting some mass and energy fluxes in simplified models, or by using assumed parameter values, has not been assessed at a wide range of sites. To advance this area of research, the International Association of Cryospheric Sciences Working Group on Debris-Covered Glaciers has led the Debris-Covered Glacier Model Intercomparison Project, the results of which are currently in preparation. Analyses of process based, point scale models of sub-debris ablation in a range of geographies will also contribute to the aim of accurately quantifying the uncertainty in regional scale predictions of glacier ablation.

Existing physically based models of sub-debris glacier melt simulate surface energy exchanges and conductive heat fluxes through the debris layer and in a layer of ice below the debris. **Table 1** presents a compilation of physically based models reported in peer-reviewed literature that were developed to predict melt on debris-covered glaciers. To our knowledge, only one model computes full energy and water balances in the debris-glacier column. That model includes heat advection by the percolation of rain or meltwater, but heat advection was deemed to be negligible in the one study in which the model was introduced and applied (Giese et al., 2020). While existing models that neglect vertical heat advection have been found to perform reasonably well at individual sites when supported by local weather data, there is evidence that processes associated with monsoon precipitation contribute to sub-debris ablation at some sites, and could affect the sensitivity of ablation to debris thickness (Winter-Billington et al., 2020).

This paper introduces a new physically based model for predicting sub-debris ice melt that aims to provide the most complete set of process representations to date. The model is based on the Simultaneous Heat and Water (SHAW) transport model for predicting the water and energy balances of soils affected by processes of freeze/thaw, snow cover and/or vegetation at a point-scale (Flerchinger, 1987). SHAW has been widely validated at sites around the world (e.g. Flerchinger et al., 1996; Wang et al., 2010; Flerchinger et al., 2012; Li et al., 2012; Sun et al., 2016; Langford et al., 2020) and is maintained by the United States Department of Agriculture (USDA). SHAW is capable of predicting variables including the depth of soil freezing, latent heat fluxes associated with the phase change of water, snow accumulation and evolution, soil and ice temperatures, and the advection of heat by unfrozen water.

A new version of SHAW, SHAW-Glacier, was developed for this study. It incorporates all of the processes represented within the original model. In addition, SHAW-Glacier simulates energy and moisture fluxes within solid glacier ice, as well as lateral water transport above a solid ice surface and in a porous surface layer of ice.

TABLE 1 | Physically based models that have been applied to predict ablation of glacier ice under a debris layer. At a minimum, the models listed compute vertical heat conduction through the debris layer. Additional processes involved in melting of glacier ice under a debris layer that are represented in each model have been summarised under the heading *Innovations*. Groups of models having the same physical representations are listed against a number from 1 to 15, in order of increasing physical completeness. In each of the 15 groups, studies in which the models were applied are listed chronologically by the date of publication. Some of the models were named by their authors, in which case their name is given in bold font under the heading *Models*.

Model	Innovations	Scale	Study area	References
1. *Simplified energy balance*	The energy used to melt ice under a debris layer is estimated from a simplified surface energy balance.	Point	Peyto Glacier	Nakawo and Young (1981)
		Point	Lirung Glacier	Rana et al. (1998)
		Point	Lirung Glacier	Nakawo and Rana (1999)
		Point	Baltoro glacier	Mihalcea et al. (2006)
		Glacier*	Baltoro glacier	Mihalcea et al. (2008)
		Glacier*	Hailuogou Glacier	Zhang et al. (2011)
		Basin*	Hailuogou Glacier	Zhang et al. (2012)
		Basin*	Hailuogou Glacier	Zhang et al. (2015)
2. *Simplified energy balance*	The evolution of debris thickness due to melt out of particles from the glacier ice and external supply of debris is simulated.	Point	Djankuat Glacier	Bozhinskiy and Krass (1986)
3. *Simplified energy balance*	The heat used for melting ice under the debris layer is implicitly integrated into calculations of the surface energy balance; heat storage in the debris layer is implicitly simulated by extension of the time step to 24 h.	Point	Ghiacciaio del Belvedere & Larsbreen	Nicholson and Benn (2006)
		Point	Franz Joseph Glacier	Hagg et al. (2014)
4. *Simplified energy balance*	Vertically heterogeneous debris properties are accommodated; non-linear thermal profiles in the debris layer are simulated.	Point	Koxkar Glacier	Haidong et al. (2006)
5. *Simplified energy balance*	Stability correction applied to the transfer coefficient used to calculate the turbulent heat fluxes in the surface energy balance.	Point	Villarico Volcano	Brock et al. (2007)
6. **DEB-Model** *Simplified energy balance*	Hourly changes of heat storage in the debris layer are calculated explicitly.	Point	Miage Glacier	Reid and Brock (2010)
		Glacier*	Haut Glacier d'Arolla	Reid et al. (2012)
		Glacier*	Miage Glacier	Fyffe et al. (2014)
		DC area*	Miage Glacier	Reid and Brock (2014)
		Point	Imja-Lhotse Shar	Rounce et al. (2015)
		Glacier*	Miage Glacier	Shaw et al. (2016)
7. **Crocus-DEB** *Simplified water and energy balances*	A conductive heat flux is simulated in the snow/glacier layers, permitting the snow/ice temperature to fall below 0°C; changes in the liquid water content of the uppermost debris layer in response to rainfall are accommodated.	Point	DC snow, Col de Porte, France	Lejeune et al. (2013)
8. **CMB-RES** *Simplified water and energy balances*	The refreezing of melt water is included in calculations of the mass balance; latent heat fluxes associated with melting and refreezing of interstitial moisture are included in calculations of the energy balance.	Point	Miage Glacier	Collier et al. (2014)
		Region*	Karakoram	Collier et al. (2015)
9. *Simplified energy balance*	The wetness of the debris surface is estimated using an empirical relation with thermal resistance.	Basin*	Trambau Glacier	Fujita and Sakai (2014)
10. *Simplified energy balance*	Observed debris temperatures are used to calculate a non-linear thermal gradient approximation factor.	DC area*	Imja-Lhotse Shar	Rounce and McKinney (2014)
12. **WEB-DHM-S** *Simplified water and energy balances*	Sensible heat contributed by rain is included in calculations of the ground heat flux term in the surface energy balance.	Basin*	Hunza River	Shrestha et al. (2015)
13. *Simplified energy balance*	Accommodates either debris surface temperature or meteorological data as upper boundary condition.	Point	Venerocola Glacier	Bocchiola et al. (2015)
14. *Fully coupled water and energy balances*	Simulation of air movement in interconnected pore spaces, used to calculate turbulent fluxes of sensible and latent heat within debris.	Point	—	Evatt et al. (2015)
15. **ISBA-DEB** *Fully coupled water and energy balances*	A fully integrated atmosphere-surface-debris layer-glacier profile. Representations include: liquid water runoff; surface deposition; vapour diffusion in the debris layer; thermal and hydraulic properties of the debris layer coupled with the equations for moisture content and phase; explicit, distributed heat storage term; partial snow coverage of the simulation grid cell.	Point	West Changri Nup	Giese et al. (2020)

**1-dimensional models aggregated over the area of a glacier, basin, debris cover or region.*

The specific aims of this study were to 1) demonstrate the extended functionality of SHAW-Glacier using on-site input data from the debris-covered glacier North Changri Nup, 2) assess the sensitivity of predicted sub-debris ablation to uncertainty in the physical parameters, 3) quantify uncertainty in the predictions of sub-debris ablation and debris temperatures, and 4) enhance understanding of sub-debris ablation on North Changri Nup using simulations of the physical processes from SHAW-Glacier.

This manuscript begins with a description of the original SHAW model and its development for application to debris-covered glaciers. Details of the study site and observational data are presented in **Section 3**. **Section 4** outlines the approaches used to test the numerical stability of SHAW-Glacier. Procedures applied to evaluate the sensitivity of predicted ablation to physical parameters, calculate prediction uncertainty, and assess simulations of physical processes made using SHAW-Glacier are outlined in **Section 5**. **Section 6** begins with metrics used to determine a numerically stable model configuration. The simulations of sub-debris ablation are then included with results of the sensitivity and uncertainty analyses, and a selection of output variables with corresponding observations are presented. **Section 7** considers the functionality of SHAW-Glacier, and draws insight from the simulations and observations of ablation on North Changri Nup. **Section 8** summarises implications of the findings in the context of regional glacier ablation modelling, and finally, suggests new research directions indicated by the findings.

This is the first of a two-part series introducing SHAW-Glacier with its application to North Changri Nup. Part 1 is focused on the overall functionality of SHAW-Glacier with respect to the prediction of sub-debris ablation, and the uncertainty in predicted ablation introduced by the uncertainty in the physical parameter values. The second part of this work will apply SHAW-Glacier to North Changri Nup to explore the influence of patchy snow cover on the variability of sub-debris ablation, with an analysis of heat and water balances simulated under scenarios of wind redistribution (manuscript currently in preparation).

2 THE SIMULTANEOUS HEAT AND WATER MODEL

The Simultaneous Heat and Water model, SHAW, is an integrated, one-dimensional surface-subsurface model that was designed to simulate periodically snow-covered and/or frozen soil, with or without vegetation, including permafrost. The energy and water balances are fully coupled, and the atmospheric and sub-surface mass and energy fluxes are fully integrated in the surface mass and energy balance calculations. The physics underlying SHAW and the mathematical representation of the physics are detailed by Flerchinger (1987). For a complete outline of the physics without the mathematical detail, readers are directed to the technical document Flerchinger (2017a) and user manual Flerchinger (2017b).

Since the release of the open-source code, SHAW has been used in applied and academic settings, and it has been validated in studies of continental, maritime, arid and alpine climates in North America, the Tibetan Plateau, North-Central and North-East Asia and western Scandinavia, as well as waste management landfill and laboratory studies. A full list of the publications that report the development, validation and application of SHAW is maintained by the USDA (USDA, 2020).

2.1 Key Features of the Original SHAW Model

SHAW uses meteorological data to simulate the energy, water and solute balances in a 1 m^2 column of soil. The column is divided into a maximum of 100 layers. Each layer is assigned a thickness and a set of physical parameter values. The physical parameters represent the characteristics of porous sediment, interstitial air, water and ice, vegetation and vegetation residue if they are present, and snow. The parameters assigned to each layer are fixed within a single run of the model. Computations occur at nodes located at the centre of each layer.

The upper boundary of the simulation is defined by continuous time series of meteorological data. Rain and snow amounts are calculated on the basis of total precipitation, air temperature and relative humidity. The lower boundary is a time series of the moisture content and temperature at the bottom-most node in the simulation profile. The lower boundary for temperature can optionally be estimated by the model as a function of the annual average temperature of the profile at that depth, which is input by the user. The lower boundary condition for soil moisture can optionally be defined as a unit gradient (i.e. gravity flow) beyond the boundary. The initial and final conditions are defined by the moisture content and temperature set by the user for every node in the vertical dimension.

Heat flow within the soil is computed using the solution to the energy balance equation with terms for phase transition for freezing water, advective heat transfer by liquid, and latent heat transfer by vapour. The equation is expressed as:

$$C_s\frac{\partial T_d}{\partial t} - \rho_i L_f \frac{\partial \theta_i}{\partial t} = \frac{\partial}{\partial z}\left[k_s \frac{\partial T_d}{\partial z}\right] - \rho_l c_l \frac{\partial q_l T_d}{\partial z} - L_v\left(\frac{\partial q_v}{\partial z} + \frac{\partial \rho_v}{\partial t}\right) \quad (1)$$

where C_s and T_d are the volumetric heat capacity (J kg^{-1} $°C^{-1}$) and the temperature (°C) of the soil, ρ_i is the density of ice (kg m^{-3}), θ_i is the volumetric ice content (m^3 m^{-3}), k_s is the soil thermal conductivity (W m^{-1} $°C^{-1}$), z is the positive downward depth from the soil surface, ρ_l is the density of water (kg m^{-3}), c_l is the specific heat capacity of water (J kg^{-1} $°C^{-1}$), q_l is the liquid water flux (m s^{-1}), q_v is the water vapour flux (kg m^{-2} s^{-1}), and ρ_v is the vapour density (kg m^{-3}) within the soil. The volumetric heat capacity is computed from the sum of the volumetric heat capacities of the soil constituents, i.e., soil minerals, organic matter, water, ice, and air. SHAW uses the De Vries (1963) approach for computing thermal conductivity.

Water transfer within the soil is solved using the mixed form of the Richards equation with terms for soil freezing, matric-

TABLE 2 | SHAW-Glacier input data requirements and outputs. Optional outputs relating to vegetation and solute transport are not listed.

INPUT DATA	
T_a	Air temperature (°C)
WS	Wind speed (m s^{-1})
RH	Relative humidity (%)
P^*	Total precipitation (mm)
$Q_S \downarrow$	Incoming shortwave radiation (W m^{-2})
OUTPUTS	
Surface energy balance (W m^{-2})	
Q_S^*	Net shortwave radiation
$Q_S \uparrow$	Reflected shortwave radiation
$Q_L \downarrow$	Incoming longwave radiation
$Q_L \uparrow$	Outgoing longwave radiation
Q_H	Sensible heat flux, including sensible heat from rain
Q_E	Latent heat flux
Q_G	Ground heat flux
Water balance (mm w.e.)	
S	Snow melt
V	Evaporation
R	Runoff
a	Glacier ice loss
ΔS_g	Change in storage - soil moisture
ΔS_s	Change in storage - snow pack
O	Ponding
ϵ	Water balance error
Vertically distributed variables	
h_s	Snow thickness (mm)
SWE	Snow water equivalent (mm)
T_s	Temperature of snow layers (°C)
T_d	Temperature of debris layers (°C)
T_g	Temperature of glacier ice layers (°C)
θ	Moisture content (m^3 m^{-3})
θ_i	Ice content (m^3 m^{-3})
θ_l	Water content (m^3 m^{-3})
ψ	Matric potential (m)
q_l	Vertical water flux (mm)
q_{lat}	Lateral water flux (mm)
Q_C	Conductive heat flux (W m^{-2})
Q_A	Advective heat flux (W m^{-2})
Q_E	Latent heat flux (W m^{-2})

potential-based water flow, vapour transport, and lateral flow exiting the soil column:

$$\frac{\partial \theta_l}{\partial t} + \frac{\rho_i}{\rho_l}\frac{\partial \theta_i}{\partial t} = \frac{\partial}{\partial z}\left[K\left(\frac{\partial \psi}{\partial z} + 1\right)\right] + \frac{1}{\rho_l}\frac{\partial q_v}{\partial z} - q_{lat} + U \quad (2)$$

where K is the unsaturated hydraulic conductivity (m s^{-1}), ψ is the soil matric potential (m), q_{lat} is the lateral water flow exiting the soil column (m^3 m^{-3} s^{-1}), and U is a source/sink term for water flux (m^3 m^{-3} s^{-1}) that may include lateral inflow and/or root water extraction. Lateral flow exiting the soil column is considered only under saturated conditions (i.e., $\psi \geq 0$) and is computed from the slope of the ground surface and the lateral saturated conductivity, K_L (m s^{-1}). Unsaturated conductivity within SHAW is reduced linearly with ice content and assumed to be zero when available porosity falls below 0.13 m^3 m^{-3}. SHAW provides the option of selecting alternative formulations of the water release curve, but the Campbell equation was used in this study:

$$\psi = \psi_e\left(\frac{\theta_l}{\theta_s}\right)^{-b} \quad (3)$$

where θ_s is saturated water content (m^3 m^{-3}), ψ_e is air entry matric potential (cm), and b is a pore-size distribution parameter.

As presented in **Table 2**, SHAW predicts state, flux, and storage terms at the end of every time step of, optionally, 1 hour to 24 h, and at every node. The flux equations are solved in the form of finite differences by an iterative Newton-Raphson technique, with a maximum of 11 iterations per time step. In the case that the equations cannot be solved within the error tolerance, the time step is halved, and the computations are reinitiated within sub-time steps. Time steps are halved for a maximum of 128 sub-time steps per hourly time step.

2.2 New Representations in SHAW-Glacier

SHAW-Glacier uses the soil layers in SHAW as the basis for the representation of supraglacial debris in SHAW-Glacier. The debris layers are stacked upon one or more layers that have been assigned parameter values representing the characteristics of solid ice (**Figure 1**). SHAW-Glacier simulates heat transfer at the debris surface, and above and below a debris-ice interface, including an advective heat flux associated with the percolation of liquid water through pore spaces, latent heat exchanges associated with glacier melt and refreezing, and energy transfer between solid glacier ice layers. Lateral flow is calculated during both infiltration and redistribution, so that the lateral flow of water that encounters a barrier, such as a less permeable layer or solid ice, is simulated. Thus, it accounts for downslope lateral flow in a saturated layer perched above the debris-ice interface, and in a porous surface layer of ice.

There are 293 physical parameters in SHAW-Glacier. A user is required to define the value of 28 of those parameters, 30 if snow cover is present upon initialisation. An additional 48 parameters can be user-defined if the simulation is to include plants, plant residue and solute transport. Constants can be changed in the Fortran source code if necessary. There is a complete list of the physical parameters in SHAW in an Appendix to the Technical Document (Flerchinger, 2017a) and of the user-defined parameters in the User's Manual (Flerchinger, 2017b).

As with SHAW, the maximum number of layers within SHAW-Glacier is 100. The thickness of each debris and glacier ice layer is user-defined, and each layer can be assigned a different thickness. A minimum of two debris or soil layers overlaying the glacier layers is required; the extent of glacier ice below the bottom layer is assumed to be unlimited.

Equations (1)–(3) for heat and water flow through a laterally homogeneous, porous medium are assumed applicable to the glacier layers with slight modifications. The mineral bulk density, ρ_b (kg m^{-3}), is set to a value from 0.0 (translating to a porosity of 1.0) to 0.1 (i.e. ice with rock mineral content). To maintain the glacier ice layers, a user-defined minimum ice content, $\theta_{i,\min}$, is specified. As the glacier ice melts, and the ice content of an ice layer falls below $\theta_{i,\min}$, the ice content is reset to $\theta_{i,\min}$, and an equivalent amount of water is added to θ_l to

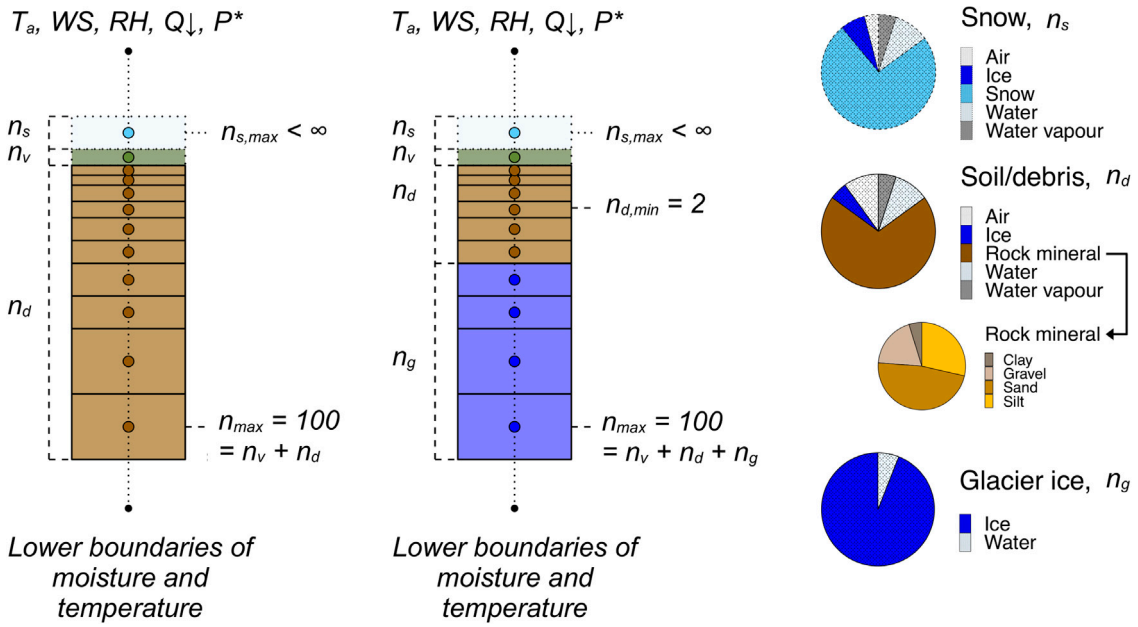

FIGURE 1 | A schematic of the simulation domain and process representations in SHAW and SHAW-Glacier. Labels n_s, n_v, n_d and n_g are the number of snow, vegetation, debris and glacier ice layers, respectively. Vegetation layers are included under SHAW-Glacier to indicate the model's functionality, but are not used in this study and therefore, are not included in the detail. Dotted lines in the stacks indicate layers that are time dependent while solid lines represent layers that are constant within a model run. The pie charts show the constituents of the layers; stippling indicates constituents that are time dependent while solid areas are constant. The portions allocated to each constituent in the schematic are for example only.

maintain the water balance in the layer. In so doing, it is assumed that the surface of the glacier recedes downward, and the glacier ice beneath the lower boundary is moved upward into the simulation domain.

A maximum water holding capacity, $\theta_{l,\max}$, is defined for the glacier layers. A low value assigned to $\theta_{l,\max}$ minimises the quantity of liquid water that can be stored in the glacier ice layers despite low values of K_S and K_L. Within the glacier layers, the value of $K_{(i,t)}$ is independent of changes in $\theta_{i(i,t)}$. When $\theta_{l(i,t)} \geq \theta_{l,\max}$, $K_{(i,t)}$ is set to K_S, and lateral flow from the layer is allowed.

Ablation of the glacier ice, $\hat{a}$ (mm w.e.), is computed by summing the ice added to each layer to maintain $\theta_{i,\min}$ and the liquid water fluxes exiting the simulated domain:

$$\hat{a} = q_{l(NS)} - q_{l(ind)} + \sum_{i=ind}^{NS-1} \left(\frac{\rho_i}{\rho_l} \left(\theta_{i,min} - \theta_i \right) + q_{lat(i)} \right) \Delta z_i \qquad (4)$$

where $q_{l(NS)}$ and $q_{l(ind)}$ are the liquid water fluxes exiting the bottom and entering the top of the glacier, NS is the total number of debris and ice layers in the simulated profile, ind is an index indicating the first solid ice layer, and $\Delta z_{(i)}$ is the thickness of ice layer i. Occasionally, ablation of the glacier can be negative as liquid water, $q_{l(ind)}$, enters the top of layer ind and has the opportunity to freeze, adding to the total ice and water content of the ice layers.

Meltwater that is generated at ice layer ind becomes a source of moisture to be drawn into the debris by capillary action. Meltwater that does not soak into the debris is allowed to exit layer ind laterally, as computed by q_l, when the water content exceeds $\theta_{l,\max}$. Refreezing of meltwater can occur in both debris and ice layers, and is included in the water and energy balances.

A weathering crust at the top of the glacier ice can be simulated by setting the water release curve parameters for layer ind to values that are appropriate for a porous material. To the best of the authors' knowledge, there have been no reports of a weathering crust below a layer of debris, and theoretically, without direct shortwave radiation penetrating below the ice surface, a weathering crust is unlikely to form. However, melt water channels may form under a debris layer, and this feature of SHAW-Glacier may facilitate future studies into the effect of the formation of runnels on sub-debris melt.

In the original SHAW model, the mineral density, ρ_m (kg m^{-3}), mineral specific heat, c_m (J kg^{-1}), and mineral thermal conductivity, k_m (W m^{-1} °C^{-1}), for the sand and rock fractions of the soil are constants that are approximately equal to the average for quartz. In SHAW-Glacier, they take user-defined values, which allows the user to evaluate the sensitivity of sub-debris melt to the values of those parameters–e.g. to explore the effect of geology on ablation rates. An option has also been included for the outputs of the energy balance to be calculated by transfer

mechanism. The conductive and advective heat fluxes are calculated as the net thermal energy transferred between layers with a reference temperature of 0°C, to allow non-conductive heat sources to be evaluated.

Finally, the maximum number of sub-hourly time steps has been increased from 128 to 512 to assist in numerical convergence. SHAW-Glacier is sensitive to initial and terminal boundary conditions and to the spatial and temporal discretisation scheme, which is discussed below.

2.3 Input Requirements

The input data required to drive SHAW and SHAW-Glacier are the same. Daily or hourly meteorological input data are required to define the upper boundary of a simulation. The input variables are air temperature, relative humidity, wind speed, incoming solar radiation and precipitation. The user can specify rainfall and snowfall amounts separately; alternatively, if only total precipitation data are available, SHAW-Glacier can partition total precipitation into rain and snow amounts based on air temperature and relative humidity.

Albedo of the dry debris surface is an input parameter, α_d. SHAW-Glacier calculates the effective surface albedo, α, at every time step to account for wetting of the debris, cloud cover, accumulation of snow, and for the evolution of snow as it ages and melts. Thus, reflected and net shortwave radiation are outputs that are computed.

Initial and terminal thermal and hydraulic boundary conditions must be defined by the user. Observational data can be used to initialise SHAW-Glacier, or in the case that observational data are not available, the simulation can be buffered with a spin-up period to simulate realistic initial profiles of temperature and moisture. The length of the spin-up period required for a given simulation depends on the particular configuration and how well the conditions used to initialise the spin-up reflect reality. The terminal conditions are required to be defined in the input files so that SHAW-Glacier can estimate the temperature and moisture content of the lower boundary if the time series that defines the lower boundary is incomplete.

3 FIELD SITE AND DATA

3.1 North Changri Nup Glacier

North Changri Nup glacier is a debris-covered alpine valley glacier in the Dudh Koshi basin, Nepal, in the Randolph Glacier Inventory v6.0 (RGI6) region 15, South Asia East (GLIMS ID G086808E28006N and RGI 6.0 ID RGI60–15.03734). North Changri Nup is one of a number of glaciers flowing from the Sagarmatha/Mt Everest massif. The massif has been estimated to be rising at an average of $2\,mm\,yr^{-1}$ due to tectonic uplift (Liang et al., 2013) and eroding at up to $4\,mm\,yr^{-1}$ (Godard et al., 2014). With plentiful granitic and metamorphic sediment supplied by erosive processes of mass movement from the valley walls (Nakawo et al., 1986), many of the glaciers in the region are debris-covered.

North Changri Nup has an approximate length of 4 km and surface area of $2.7\,km^2$ (Vincent et al., 2016), of which approximately 50%, in the ablation zone, is covered by debris (Herreid and Pellicciotti, 2020). The location of North Changri Nup is illustrated in **Figure 2**.

3.2 Meteorological Input Data

All observational data used in this study were collected within the framework of the global glacier observatory GLACIOCLIM (https://glacioclim.osug.fr/). An automatic weather station, NCN-AWS, was installed in November 2014 and was operational until February 2017 (**Figure 3A**). The AWS was installed on the debris, at 27.9925° latitude, 86.7799° longitude, 5470 m a.s.l., close to the upper extent of the debris-covered area. Data from the 2016 hydrological year were used, defined as 28 November 2015 to 28 November 2016. A Campbell Scientific CR 1000 datalogger system was installed on the AWS; details of the sensors are listed in **Supplementary Table S1**. Data from a second AWS that was located on West Changri Nup, WCN-AWS, were used to fill gaps and to correct errors in the data from NCN-AWS. The locations of the two AWS are illustrated in **Figure 2**, and corrections made to the input data are included in **Supplementary Table S1**. The data used for the simulations of ablation on North Changri Nup are presented in **Figure 4**.

3.3 Glaciological Ablation Data

Point surface mass balance was measured at ten ablation stakes that were installed in an approximately $2500\,m^2$ area around NCN-AWS (**Supplementary Figure S1**). This "stake farm" was established on 29 November 2014 to observe sub-debris ablation as a function of debris thickness under controlled conditions. The natural debris layer was around 0.08–0.10 m thick, gently undulating, with randomly distributed boulders across the surface. To install each stake, a 2 m diameter patch of debris was excavated and a 4 m long bamboo pole was drilled into the ice at the centre of the patch. Debris of the desired thickness was distributed evenly in the patch around the stake, using naturally occurring material taken from nearby. A photograph of one of the stakes is presented in **Figure 3B**. The first year of data are described in Vincent et al. (2016). Repeat measurements of the emergence of the stakes were made on 28 November 2015, 1 May 2016 and 10 November 2016. The coordinates, elevation and debris thickness at each stake are listed in **Table 3**.

3.4 Observed Debris Temperature

From November 2015, the temperature of the debris layer was recorded at two sites approximately 2 m from NCN-AWS. Two pits were dug into the debris layer, Pit 1 and Pit 2. Thermistors were inserted into the walls of the pits, distributed in profile with as little disturbance to the fabric of the sediments as possible, and the pits were back-filled. The debris in Pit 1 had a thickness, h, of 0.10 m and the thermistors were installed at depths, d, of 0.01, 0.05 and 0.10 m. Pit 2 was 0.08 m thick and thermistors were

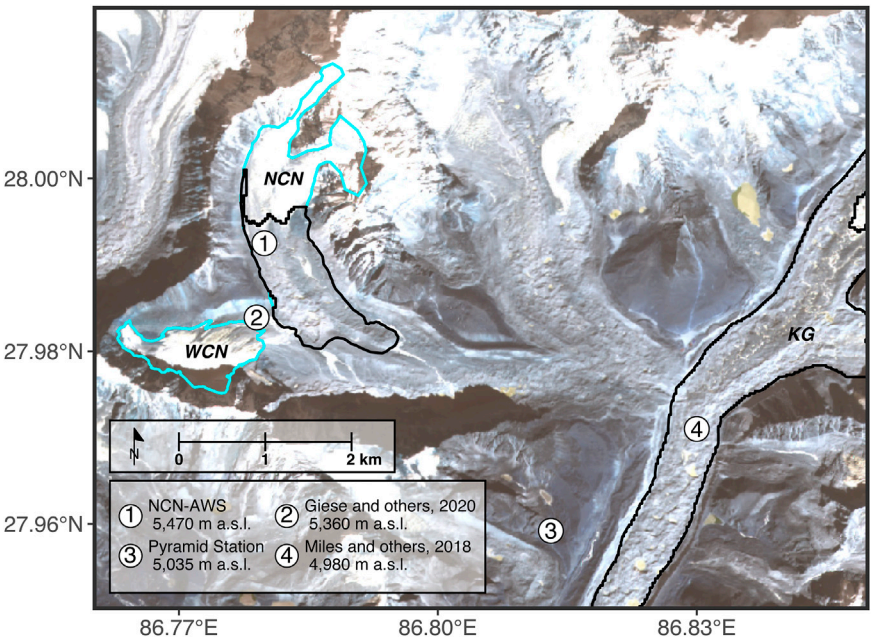

FIGURE 2 | Map of the study area. The acronyms WCN, NCN and KG stand for West Changri Nup, North Changri Nup and Khumbu Glacier. The sites where observational data were collected are numbered. The light blue and dark blue polygons are the outlines of the debris-free and debris-covered parts of the glaciers, respectively. The background image is a true colour composite of a Sentinel-2 Product level 1C image that was taken on 27 January 2021.

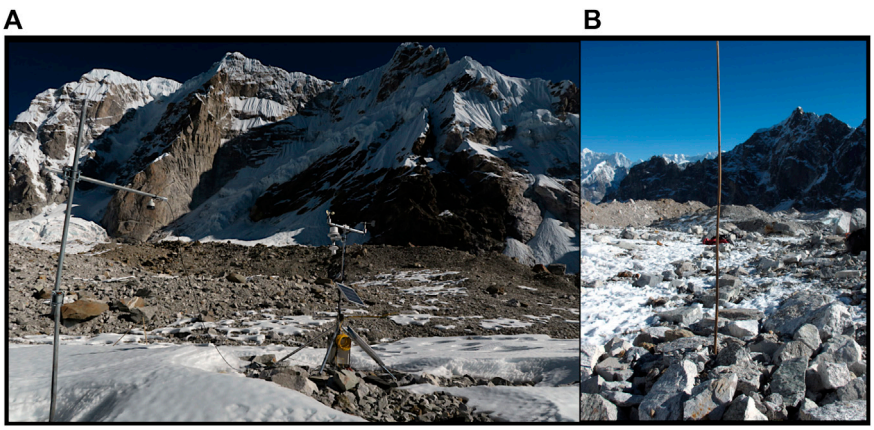

FIGURE 3 | (A) NCN-AWS. The photograph shows the relative positions of the sonic ranger and other meteorological instruments, the tilt in the tripod supporting the sonic ranger, and patchy snow cover. **(B)** One ablation stake in the "stake farm", showing the natural debris surface. Note the elevated patch of debris around the stake, and patchy snow cover. The photographs were taken on 10 November 2016.

installed at $d = 0.01$ m and $d = 0.08$ m. The thermistor model was TCA PT100, which has an uncertainty of 0.1°C.

3.5 Physical Parameter Values

The physical parameters that allow SHAW-Glacier to simulate solid ice layers were assigned constant values and excluded from the sensitivity and uncertainty analysis. The mineral bulk density, ρ_b (kg m^{-3}), was set to zero, $\theta_{i,\min}$ to 0.92 m^3 m^{-3} and $\theta_{l,\max}$ to 0.05 m^3 m^{-3}. The remaining terms in **Eq. (3)**, ψ_e and b, were assigned values of -0.01 cm and 1.5, respectively, to minimise accumulation of water in the ice. The hydraulic conductivity of the ice layers was fixed at a value of 0 cm h^{-1} to preclude vertical transfer of liquid water between the ice layers.

Physical parameters that were well constrained were also excluded from the analyses of sensitivity and uncertainty: measured values of latitude and elevation were used for the site of each ablation stake, while the solar noon hour,

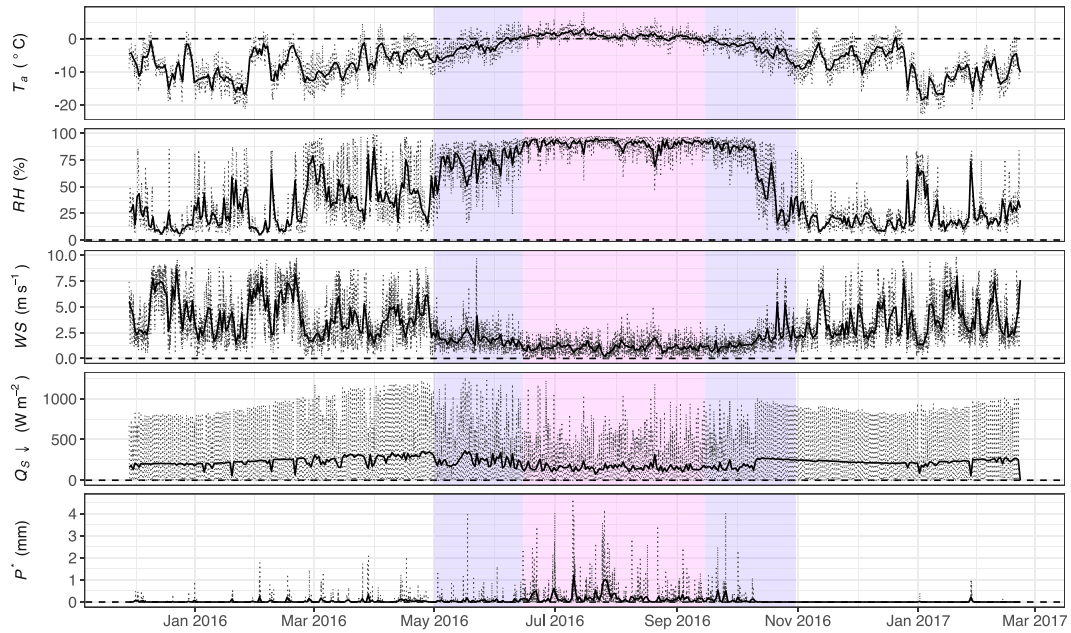

FIGURE 4 | Meteorological data used in the modelling study. The dotted lines are hourly values and the solid black lines are daily average values. These data were collected from instruments installed 2 m above the debris surface at NCN-AWS. The background colours indicate the season, as defined by Government of Nepal (2021): white is winter, pink is monsoon, and blue is both pre-monsoon and post-monsoon.

TABLE 3 | The locations of ablation stakes installed around NCN-AWS, and point surface mass balance measurements for the period 28 November 2015 to 10 November 2016.

ID	Latitude (°)	Longitude (°)	Elevation (m a.s.l.)	Debris thickness (m)	Point surface mass balance (mm w.e.)
CNBL29-14	27.992403	86.779946	5467	0.01	729
CNBL33-14	27.992399	86.780106	5466	0.03	1022
CNBL21-14	27.992532	86.779872	5468	0.06	1073
CNBL23-14	27.992452	86.779805	5467	0.11	974
CNBL28-14	27.992639	86.779855	5468	0.13	816
CNBL25-14	27.992518	86.779983	5468	0.14	859
CNBL27-14	27.992600	86.779638	5468	0.18	1009
CNBL30-14	27.992607	86.779814	5468	0.20	768
CNBL22-14	27.992514	86.779783	5468	0.33	936
CNBL26-14	27.992559	86.779734	5468	0.41	1174

estimated from the time zone, was held constant at 12:30. Slope (10%) and aspect (160°) were estimated using the data from the HMA 8 m DEM (Shean, 2017).

A feasible range of values was required for each of the remaining 18 parameters to test the ability of SHAW-Glacier to predict melt given the best available information, and to calculate prediction uncertainty. On-site measurements were not available for any of the parameters, but three measurements from neighbouring glaciers were considered to be applicable to North Changri Nup. Additional observational data were compiled from published studies to define the range that each remaining parameter could reasonably take. The parameters that were varied and the range of values used in the uncertainty analysis are presented in **Table 4**. The provenance of the values used to define a feasible range for each parameter is detailed in the Supplementary Material, and references for the values obtained from published studies are provided in **Supplementary Table S2**.

4 MODEL STABILITY AND CONFIGURATION

4.1 Boundary Conditions

Observations of the temperature of the debris in Pit 1 were used to set the initial and terminal thermal conditions. Nodes corresponding to measurement depths were assigned the

TABLE 4 | The parameters in SHAW-Glacier that were included in the sensitivity and uncertainty analysis. The minima and maxima correspond to ±10% of measured values and the lower and upper quartiles of values compiled from published studies. The provenance of the values is expanded upon in the Supplementary Material.

	Symbol	Minimum	Maximum	Source
Average annual soil temperature (°C)	$\bar{T}_i$	–3.3	–2.7	Measured
Maximum temperature at which precipitation is snow (°C)	T_p	-0.4	1.0	Literature
Wind-profile roughness parameter for momentum transfer with snow cover (cm)	$z_{0,s}$	0.01	0.19	Literature
Wind-profile roughness parameter for momentum transfer for the soil surface (cm)	$z_{0,d}$	0.59	1.92	Literature
Percent by weight of the sand, silt and clay in soil layer *i* that was sand (% of fines)	f_1	75	100	Literature
Percent by weight of sand, silt and clay in soil layer *i* that was silt (% of fines)	f_2	0	25	Literature
Percent by weight of sand, silt and clay in soil layer *i* that was clay (% of fines)	f_3	0	5	Literature
Percent by weight of the soil material in layer *i* that was rock or gravel (% of debris)	g	10	80	Literature
Albedo of dry soil	α_d	0.18	0.22	Measured
Exponent for calculating the albedo of moist soil	a_α	1.0	3.5	SHAW
Debris porosity	ϕ	0.34	0.40	Measured
Mineral thermal conductivity (W m^{-1} $°C^{-1}$)	k_m	2.62	3.68	Literature
Mineral specific heat (J kg^{-1} K^{-1})	c_m	710	880	Literature
Mineral density (kg m^{-3})	ρ_m	2084	2547	Measured
Saturated hydraulic conductivity for soil layer *i* (cm hr^{-1})	K_S	6.66 x 10^{-3}	1.80	Literature
Lateral hydraulic conductivity for soil layer *i* (cm hr^{-1})	K_L	6.66 x 10^{-3}	1.80	Literature
Air entry potential for soil layer *i* (m)	ψ_e	–0.20	–0.02	SHAW
Campbell's pore-size distribution index	b	1.5	5.0	Literature

temperatures recorded in Pit 1 at the dates and times of initialisation and termination. The topmost node of the profile was assigned a temperature that was calculated as the 2-week average of the air temperature recorded at NCN-AWS, and the bottom-most node was assigned a temperature of −3°C, from the data published in Miles et al. (2018). The temperature at the intervening nodes was linearly interpolated between those values.

No data were available with which to define the initial or terminal moisture content of the debris, so assumed values were used. The debris nodes were set to 0.3 m^3 m^{-3}, and the glacier ice nodes to 0.92 m^3 m^{-3} to represent solid glacier ice with a density of 0.92 relative to water. Moisture at the lower boundary was estimated by SHAW-Glacier.

The simulation was buffered with periods of dynamic equilibrium spin-up and spin-down (Lamontagne-Hallé et al., 2020) to ensure the predictions would not be biased by the assumed boundary conditions. Tests for numerical stability, detailed in the following section, were used to determine an appropriate spin-up period.

4.2 Determination of a Stable Discretisation Scheme

The stability of SHAW-Glacier was evaluated by performing 100-years runs with different initial thermal conditions and otherwise identical inputs. The 2016 meteorological data from NCN-AWS were looped 100 times to create the input time series. The model configuration was deemed to be stable if the 100-years time series of annual glacier ice mass loss that were predicted using different initial conditions converged to a unique solution, within a reasonable margin of error. Three initial conditions were tested, as follows:

1) Observational: 2-week mean air temperature for the node at the upper boundary, observed debris temperatures at the nodes corresponding to observation depths, and −3°C at the lower boundary, interpolated linearly to intervening nodes.
2) Isothermal: 3°C at every node from the upper to lower boundaries.
3) Observational debris and isothermal ice: 2-week mean air temperature for the node at the upper boundary, observed debris temperatures at the nodes corresponding to observation depths, interpolated to intervening debris nodes, and −3°C at every glacier ice node.

Following standard practice, the time step, Δt, depth interval, L, the maximum number of iterations at each sub-time step, I, and error tolerance, η, were adjusted to identify stable configurations. A total of 144 100-yr simulations were performed, testing every combination of the initial conditions and configuration parameters.

The first 25 years and last 1 year of each run were discarded to account for spin-up and spin-down. The remaining 74 years of predicted annual glacier ice loss of each simulation, $\hat{A}$, were used to evaluate stability. A configuration was deemed to be numerically stable if the standard deviation, s, of $\hat{A}$ predicted in three simulations with different initial conditions but the same configuration parameters (222 values in total) was ≤5 mm w. e. The criteria that were used to select a single configuration to use in the study of North Changri Nup were the magnitude of s and the annual water balance error, ϵ, and the stability of $\hat{A}$, s and ϵ.

The configuration parameter values that were tested are listed in **Supplementary Table S3**. The simulated profiles were assigned a total thickness of 50 m, and the depth intervals, L, in the top 1 m of the profile were varied among the tests. The coarsest values of L that were tested, 0.01 and 0.02 m, were distributed evenly. Then, in order to test the effect of L = 0.02 m when the thickness of the debris layer was not divisible by 2, an additional combination was tested in which the topmost layer was assigned a value of L = 0.01 m and the

remaining layers in the top 1 m of the profile were assigned L = 0.02 m; this configuration is called 'L = 0.01 and 0.02 m' in the analysis below. The remaining 49 m of the profile were divided into layers of increasing thickness with increasing depth, and were the same in every simulation.

5 SENSITIVITY AND UNCERTAINTY ANALYSIS

All data processing and analyses were performed using the R programming language, in RStudio. The packages that were used in addition to base R are listed at the end of the manuscript.

5.1 Monte Carlo Analysis for Physical Parameters

A Monte-Carlo approach was used to assess the sensitivity of predictions of ablation to uncertainty in the physical parameter values, and to estimate parameter uncertainty in $\hat{A}$ with different debris thicknesses. SHAW-Glacier was run n times for each value of h using a different set of parameters for every run. The parameter values were selected at random from the predefined ranges in **Table 4** using the *runif* function in base R.

For h = 0.03 m and h = 0.41 m, n was set to 10,000. A smaller number of model runs might have been adequate; for example, Machguth et al. (2008) used n = 5,000 in a Monte Carlo evaluation of the mass balance of Morteratsch Glacier. Machguth et al. (2008) found that the standard deviation of the predictions, and the standard deviation of the standard deviations, stabilised after only 1,000 model runs, and therefore, deemed n = 5, 000 to be robust. In the current study, n was set to 10,000 for the highest and lowest values of h to thoroughly sample the parameter space, and n = 2,000 for 0.03 m $< h <$ 0.41 m, to minimise computational expense.

5.2 Recursive Partitioning Based on Predicted Ablation

Recursive partitioning was used to explore modes in the distribution of $\hat{A}$ with respect to the distribution of values assigned to the physical parameters. Also known as regression tree analysis, recursive partitioning has been used to address a range of problems in hydrology and glaciology. For example, McGrath et al. (2018) used a recursive partitioning algorithm to model snow distribution on two Alaskan glaciers, where interactions between the terrain parameters that were used as proxies for deposition and redistribution, such as curvature and aspect, produced clusters in the response. Additional examples can be found in Elder et al. (1998), Panday et al. (2011), Bulley et al. (2013), Biddle (2015), McMahon and Moore (2017) and Trubilowicz and Moore (2017).

The recursive partitioning analysis was performed using the *rpart* function in the **rpart** R package (Therneau and Atkinson, 2019). To avoid overfitting the models, the partition trees were pruned with the complexity parameter set to 0.1. Values of annual ablation simulated for the Monte Carlo analysis were grouped according to the results of the recursive partitioning analysis. Prediction uncertainty, $U_{h,b}$, was estimated as the difference between the 10th and 90th percentiles of the n values of $\hat{A}$ on each branch, b, of the partition trees, nested in each value of h.

5.3 Interpretation of Debris Temperature Observations

Observed temperature at d = 0.01 m in Pits 1 and 2, $T_{0.01,1}$ and $T_{0.01,2}$, respectively, was used to infer the presence of snow cover. Positive values of $T_{0.01}$ and/or distinct diel fluctuations were assumed to indicate an absence of snow, while $T_{0.01} \leq 0^{\circ}$C coupled with muted diel fluctuations was assumed to indicate the presence of snow.

Snow depth, h_s, was calculated using changes in surface height recorded by the sonic ranger at the site of NCN-AWS. It can be seen in **Figure 3A** that a tilt had developed in the tripod supporting the sonic ranger after the equipment was serviced in May 2016. The tilt would have made the apparent snow depth greater than the true snow depth. The tilt must have developed after 26 July 2016 because there was no net change in h_s before that date. Therefore, the values of h_s from 01 May to 26 July were taken to be accurate. The magnitude of values of h_s from 26 July were disregarded; however, the timing and direction of changes after 26 July were consistent with T_a and $P^{\star}$ (**Figure 4**) and were used to inform the analysis.

An additional 2,000 Monte Carlo simulations were conducted for h = 0.08 m and h = 0.10 m, representing the pits in which thermistors were installed. Predicted snow depth, $\hat{h}_s$, was compared with T_d and h_s to aid interpretation of sources of uncertainty in predicted ablation. Recursive partitioning of $\hat{A}$ was performed on these model runs, and the corresponding time series of simulated debris temperature, $\hat{T}_d$, were subset on the basis of the grouping of $\hat{A}$.

A routine was tested in which the parameter for the maximum air temperature at which precipitation can fall as snow, T_p, was varied monthly on the basis of h_s. However, agreement between $\hat{h}_s$ and h_s was not improved, and those results are not discussed further.

The sensitivity of $\hat{T}_d$ to uncertainty in the parameter values was assessed by comparing the observed and simulated time series. The bottom-most thermistors were installed at the interface of the debris and ice, giving $T_{0.10,1}$ and $T_{0.08,2}$. SHAW-Glacier is structured as a stack of layers with the predictions calculated at the depth of vertically-centred nodes. Therefore, $\hat{T}_{0.10,1}$ and $\hat{T}_{0.08,2}$ were estimated by linearly interpolating between the values predicted for the two adjacent nodes, where the two adjacent nodes represented the bottom-most debris layer and top-most ice layer.

Uncertainties were estimated for $\hat{T}_d$ using the following formula:

$$U_{d,p} = 0.5 \cdot \frac{1}{n} \sum_{t=1}^{n} \left(\hat{T}90_{d,p,t} - \hat{T}10_{d,p,t} \right) \quad (5)$$

where $\hat{T}10_{d,p,t}$ and $\hat{T}90_{d,p,t}$ are the 10th and 90th percentiles of $\hat{T}_d$ at depth in the debris layer, d (m), one of the two pits, p, and time step, t, and n is the number of time steps in the series.

Representative examples of the heat and water budgets simulated for h = 0.08 m and h = 0.10 m were used to explore sensitivity in the predicted fluxes. The examples were taken from model runs that produced the median value of $\hat{A}$ in the subsets of the Monte Carlo simulations, grouped according to the results of the recursive partitioning analysis, that most accurately reproduced T_d.

6 RESULTS

6.1 Numerical Stability, Model Configuration and Performance

The numerical stability of SHAW-Glacier was sensitive to all of the configuration parameters that were tested. Numerical stability generally increased with an increase in L, an increase in the maximum number of iterations at each time step, I, and a decrease in the error tolerance, η. The distribution of $\hat{A}$ and error terms for each model configuration are plotted in **Supplementary Figure S2**.

Simulations using values of L < 0.01 m consistently suffered fatal non-convergence and were deemed to be unstable. Values of s calculated for $\hat{A}$ predicted using L = 0.01 m and $\eta = 1 \times 10^{-4}$ did not meet the criteria for stability with respect to the initial conditions or with respect to I. The range of values of $\hat{A}$ predicted using L = 0.01 m was reduced by decreasing the error tolerance to 1×10^{-5}, but the distribution of $\hat{A}$ remained unstable with respect to I. Therefore, all configurations with L = 0.01 m were also deemed to be unstable.

Using the coarser vertical discretisation schemes, L = 0.02 m and L = 0.01 and 0.02 m, in combination with the relaxed error tolerance of $\eta = 1 \times 10^{-4}$, the distribution of values of $\hat{A}$ did not stabilise with respect to I. In contrast, both of the coarser vertical discretisation schemes met the criteria for stability with respect to the initial conditions using $\eta = 1 \times 10^{-5}$, for all values of I. In both cases, the values of s were lowest with I = 11, but stabilised across higher values of I. The water balance error, ϵ, was highest with I = 11, and lowest with I = 100. Therefore, the configurations with I = 100 were deemed to be most accurate.

Diagnostic statistics for the two stable configurations are presented in **Supplementary Table S4**. Configuration 1, with L = 0.02 m, was used for profiles where h was a multiple of 0.02, and Configuration 2, with L = 0.01 and 0.02 m, was used for profiles where h was not a multiple of 0.02. It is notable that, although both configurations met the criteria for numerical stability, they produced significantly different values of $\hat{A}$. The mean values of $\hat{A}$ differed by approximately 3%, and the water balance error accounted for only approximately 1% of that.

In the stable 100-yr runs with different initial conditions, $\hat{A}$ converged within 5 years of initialisation and did not diverge approaching termination. Therefore, the simulations of ablation at North Changri Nup were run for 7 years, with the 2016 input data looped seven times. The outputs for the sixth year were extracted as independent predictions for 2016, and the outputs for the remaining years were discarded.

6.2 Sensitivity of Predicted Ablation to Model Parameters

The values of annual ablation predicted in the Monte Carlo simulations followed a multi-modal distribution for every value of h. The recursive partitioning analysis indicated that T_p was the most significant parameter determining branches at both first and second order. The structure of the partition trees was similar among the values of h; the recursive partition tree for h = 0.03 m is presented in **Figure 5** (equivalent plots for h = 0.06–0.41 m have been included in **Supplementary Figures S3–S11**). The first order partition values of T_p that were calculated for each value of h, $T1_p$, ranged from 0.03°C to 0.10°C, with apparently random variation around a mean of 0.06°C. The second order values, $T2_p$, ranged from 0.42°C to 0.62°C, with a mean of 0.53°C (**Table 5**). At third order, the percent gravel in the debris layer, g, was a significant parameter in addition to T_p for h > 0.03 m. However, the reduction in recursive partitioning error terms was consistently an order of magnitude greater with first order partitioning than it was at higher orders.

Grouping the values of $\hat{A}$ on the basis of the values used to partition branches 1b, 2a and 2b, $T_p^{\star}$, resolved the multimodal predictions into three approximately normally distributed clusters (**Figure 6A-I**). Higher values of T_p corresponded with lower values of $\hat{A}$ and a decrease in the range of $\hat{A}$ overall.

The characteristic inverse sensitivity of $\hat{A}$ to h was clearly represented in the predictions. Annual ablation of up to 2,500 mm w.e. was simulated using h = 0.03 m, while no more than 500 mm w.e. was simulated using h = 0.41 m. In some of the model runs with h = 0.03 m, ablation occurred as early as January; with increasing values of h, ablation was simulated to begin later in the year and to cease earlier (**Figure 6J–R**). A temporary abatement of ablation, which was simulated to have occurred near the beginning of July in all of the model runs, lasted longer with increasing values of h. Still more markedly, the duration of this mid-season event tended to be greater in the simulations on branch 2a, followed by branches 2b and 1b.

6.3 Uncertainty in Predictions Associated With Uncertainty in the Parameter Values

Absolute uncertainties were negatively correlated with h (**Figure 7**). Relative uncertainties increased linearly with debris thickness, from 16% to 40% on branch 2a, 16% to 33% on branch 2b, and 17% to 31% on branch 1b (**Supplementary Figure S12**).

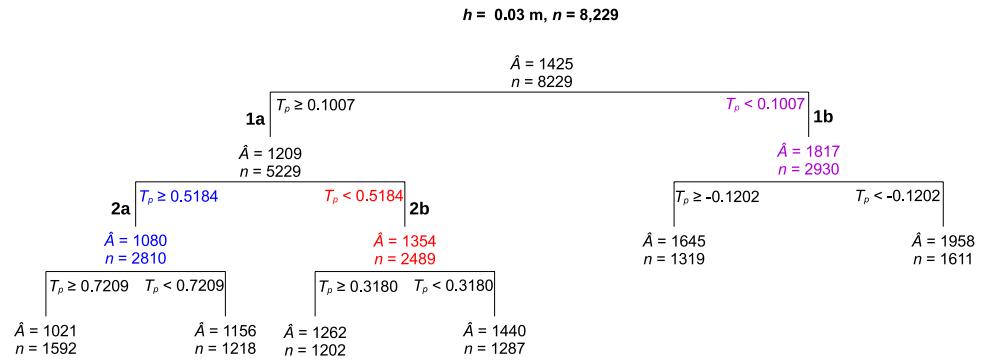

FIGURE 5 | Recursive partition tree of annual ablation predicted in the Monte Carlo simulations with debris thickness of 0.03 m. The median values of $\hat{A}$, and the number of predictions in each cluster, *n*, are printed together as a leaf at the end of the branches of the tree. The partitioning parameters and partition values are printed below the branches. Colours and labels identify clusters of parameter sets that were used in further analysis; numbers indicate the order of a branch, and letters indicate the relative direction of a limb.

TABLE 5 | The first and second order partitioning values fitted for the values of *h* used in the Monte Carlo simulations of ablation at the sites of the ablation stakes and debris pits.

h (m)	$T1_p$ (°C)	$T2_p$ (°C)
0.03	0.1007	0.5184
0.06	0.0868	0.5258
0.08	0.0435	0.5957
0.10	0.0336	0.4601
0.11	0.0885	0.4991
0.13	0.0275	0.4208
0.14	0.0810	0.5412
0.18	0.0636	0.5198
0.20	0.0448	0.5060
0.33	0.0431	0.5883
0.41	0.0893	0.6192

It can be seen in **Figure 7** that the difference between the median values on branches 2a and 1b was greater than the range of values on each branch. Therefore, the uncertainty due solely to T_p was greater than the uncertainty due to all of the other parameters, combined.

6.4 Characteristics of the Østrem Curve at North Changri Nup

Annual ablation predicted using SHAW-Glacier followed the characteristic pattern of decreasing magnitude and sensitivity with increasing debris thickness (**Figure 7**). However, while $\hat{A}$ was of similar magnitude to observed *A* for values of *h* from 0.03 to 0.14 m, the observed values did not conform to the limits of uncertainties calculated for a single branch of the regression trees–i.e., a consistent value of the T_p parameter. Further, the four observations for values of *h* from 0.18 to 0.41 m consistently plotted outside the uncertainty bounds for predicted ablation, and tended to increase with increasing debris thickness, contrary to the concept of an Østrem Curve as predicted by SHAW-Glacier.

6.5 Simulated and Observed Snow Cover

The sensors that recorded $T_{0.01,1}$, $T_{0.01,2}$ and h_s were located within meters of one another; however, the inferred time series of snow cover were not in agreement. Accumulation occurred simultaneously at the three sites, but complete ablation tended to be asynchronous. Periods with distinct snow cover characteristics, and accumulation events, are labelled P1 - P3 and E1 - E4, respectively, in **Figure 8**. **Table 6** shows that the number of days of snow cover at each site differed during those events. Photographs, such as those presented in **Figure 3**, showed that snow was distributed in patches in the vicinity of NCN-AWS at the end of the ablation season. The inferred time series were consistent with patchy snow cover.

Snow depths predicted using SHAW-Glacier are plotted in **Figure 8D**. In periods P1 and P3, a positive change in $\hat{h}_s$ coincided, exactly or closely, with a positive change in h_s in all cases but one, and only one of the accumulation events that was simulated was entirely absent from the observational records (that which occurred in December 2015). The magnitude of the change in h_s was closely matched by $\hat{h}_s$ in 6 of 10 accumulation events during P1. Furthermore, complete ablation of snow cover at the sites of the pits between E3 and E4 was accurately simulated. However, nine accumulation events were simulated during P2, a period over which the observations consistently indicated persistent snow-free conditions. Furthermore, the over-prediction of snow depth on 26 and 27 July, of 97 mm, is a lower limit for the actual difference between the true and simulated snow depths, because the true snow depth may have been less than h_s, due to the tilted sensor, but could not have been greater.

6.6 Sensitivity of Predicted Debris Temperature to Model Parameters

The recursive partition trees for the Monte Carlo simulations with $h = 0.08$ m and $h = 0.10$ m had the same structure as the partition trees for the sites of the ablation stakes; the parameter T_p was the most significant at both first and second orders, and

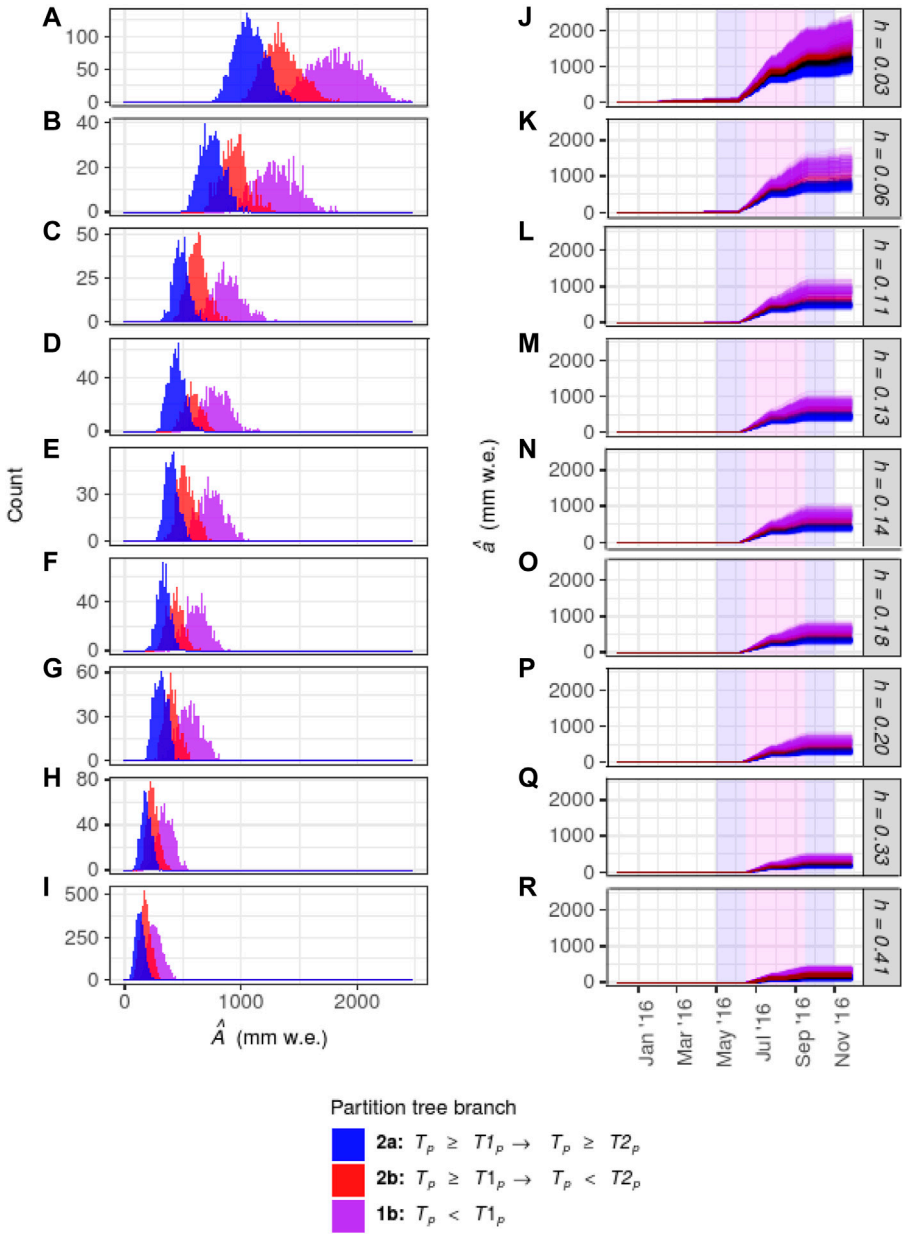

FIGURE 6 | Left column: Histograms of predicted annual ablation in 2016, $\hat{A}$, made in 10,000 (h = 0.03 m and h = 0.41 m) and 2,000 (h = 0.06 m to h = 0.33 m) Monte Carlo simulations. Right column: cumulative time series of daily ablation, $\hat{a}$, simulated in the Monte Carlo analysis. The data were subset using partition values calculated in recursive partition analysis, represented by colours. The background colours in the second column indicate the season, as defined by Government of Nepal (2021): white is winter, pink is monsoon, and blue is both pre- and post-monsoon.

g was significant at third order (**Supplementary Figure S13, S14**). The time series of $\hat{T}_d$ on branch 2a ($T_p \geq 0.49$°C) were used to calculate the uncertainty in $\hat{T}_d$. Uncertainties calculated for predicted debris temperature at each depth in the debris layer ranged from 0.40°C to 0.69°C (**Supplementary Table S5**).

The time series of $T_{d,1}$ and $\hat{T}_{d,1}$, grouped according to the corresponding partition tree for $\hat{A}$, are plotted in **Figure 9** (see **Supplementary Figure S15** for an equivalent graph for Pit 2). In general, the simulations accurately reproduced the seasonal signal: high magnitude diel fluctuations in winter, ranging from −20°C to > 20°C, a steady increase in daily minima and maxima through the pre-monsoon period, reduced maxima coupled with a lower limit of 0°C at the start of the monsoon, and a gradual return to high magnitude diel fluctuations the following winter. The simulations also reproduced, approximately, the magnitude of attenuation of the diel range of T_d with increasing depth in the debris layer.

The simulations on branch 2a of $\hat{T}_{d,1}$ and $\hat{T}_{d,2}$ correspond to the time series of $\hat{h}_s$ plotted in **Figure 8D**. It can be seen that $\hat{T}_d$

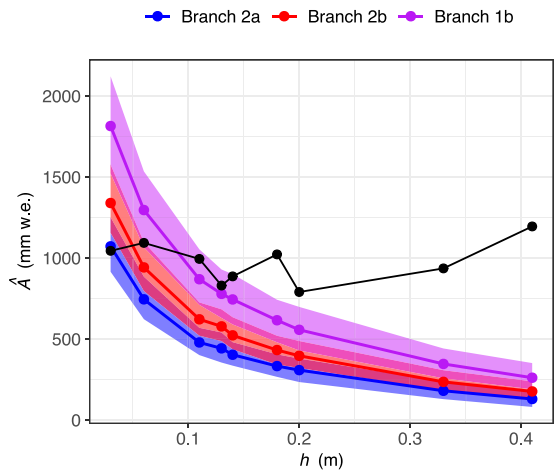

FIGURE 7 | Predicted (blue, branch 2a, red, branch 2b, and purple, branch 1b) and observed (black) sub-debris glacier ice ablation for the 2016 hydrological year, plotted against debris thickness. The coloured symbols and lines represent the median values, and the coloured ribbons represent uncertainty bounds based on the 10th and 90th percentiles around the medians.

reflects $\hat{h}_s$: when snow cover was simulated to be present, $\hat{T}_d$ was negative, and the amplitude of diel fluctuations was reduced. The accuracy of $\hat{h}_s$ affected agreement between $\hat{T}_d$ and T_d. For example, snow-free conditions were accurately simulated at the beginning of January and the beginning of March, and the range of $\hat{T}_d$ encompassed T_d, at all depths in both pits, on those occasions. When $\hat{h}_s$ was positive but no snow was observed, $\hat{T}_d$ underpredicted the range of values in T_d, and when h_s was positive but $\hat{h}_s$ was not, $\hat{T}_d$ overpredicted the range of values observed in T_d.

Grouping the predictions on the basis of $T_p^\star$ most noticeably affected the range of temperatures predicted at the start of event E2, period P3. The constant isothermal condition of T_d during E2 was reproduced in $\hat{T}_d$ on branches 2a and 2b, but not on branch 1b, because no snow cover was simulated using the values of T_p on branch 1b. The length of E2 was accurately reproduced in the simulations on branch 2a, reflecting a correspondence between the inferred and simulated presence of snow. Snow was predicted at the onset of E4 given all values of T_p, i.e. on all three branches of the partition tree, and all of the simulations accurately reproduced the return to constant isothermal conditions at that time.

6.7 Ablation Represented in the Simulated Heat and Water Budgets

The simulated heat and water budgets corresponding with the predicted snow cover plotted in **Figure 8** have been included in the **Supplementary Figures S16, S17**. Simulated glacier ice ablation began in June and ended in September for both h = 0.08 m and h = 0.10 m. Through June and July, the magnitude of $\hat{a}$ steadily increased, mirroring the magnitude of the ground heat flux, Q_G. Ablation ceased when snow cover was simulated; the magnitude of the energy fluxes at the debris surface was minor at those times. Suppression of $\hat{a}$ during accumulation events was simulated to have occurred ten times over the ablation season. The most prominent event, corresponding with E2, was reflected as a change in storage of moisture in the snow pack, ΔS_s, of more than 15 mm w. e. and a 4 week hiatus of $\hat{a}$.

Simulated ice ablation occurred only after the snowpack was fully melted. During the pre-monsoon period, snow meltwater, S, was removed by runoff, R, and percolation into the debris, where it contributed to the ground moisture storage term, ΔS_g. There was no change in storage of moisture in the debris layer during E2; R closely mirrored S, suggesting the debris had reached field capacity. Once the snowpack had been removed, S_g was reduced by evaporation, and positive values of $\hat{a}$ were simulated from the following day.

TABLE 6 | The number of days of snow cover, during selected events, at the sites of the sonic ranger (h_s), Pit 1 ($T_{0.01,1}$) and Pit 2 ($T_{0.01,2}$). The events E1 - E4 are highlighted in **Figure 8**.

Event	Period	h_s	$T_{0.01,1}$	$T_{0.01,2}$
—	28 November 2015–26 Mar	89	8	21
E1	26 March–16 Apr	22	5	8
E2	27 July–20 Aug	NA	25	25
E3	26 August–12 Sep	NA	11	20
E4	22 September–28 Nov	NA	20	54

7 DISCUSSION

7.1 The Functionality and Performance of SHAW-Glacier

To the authors' knowledge, SHAW-Glacier is the most complete physical representation of glacier ice ablation under a layer of rock debris. SHAW-Glacier is open-source. A graphical user interface can be used for simple studies, and template input files are available if greater control of the configuration and inputs is required. In this study, the compiled Fortran code was called by scripts written in the R programming language, and run on the terminal through RStudio. On an Apple Macbook Air laptop computer, the length of time to complete a 7 year simulation at hourly resolution varied from 20 s to more than five minutes, depending on the number of outputs being written to file. Manipulating the output comma separated text files was straightforward using functions in *base* R. Nineteen physical parameters were included in the Monte Carlo analysis, which produced 34,000 water balance and 4,000 temperature profile output files. Using R to open and reformat the 38,000 output files in RStudio, on a system with 2TB RAM, took approximately 14 days.

SHAW-Glacier is sensitive to the configuration of the simulation domain and computation parameters. The frequency of non-convergences was higher when one or more layers was completely frozen. When sediments are near 0°C, small changes in the moisture content and temperature can have an especially large impact on the energy and water balances, because of the interrelated effects of phase changes, latent heat fluxes, permeability and hydraulic conductivity, moisture transport and content. Numerically

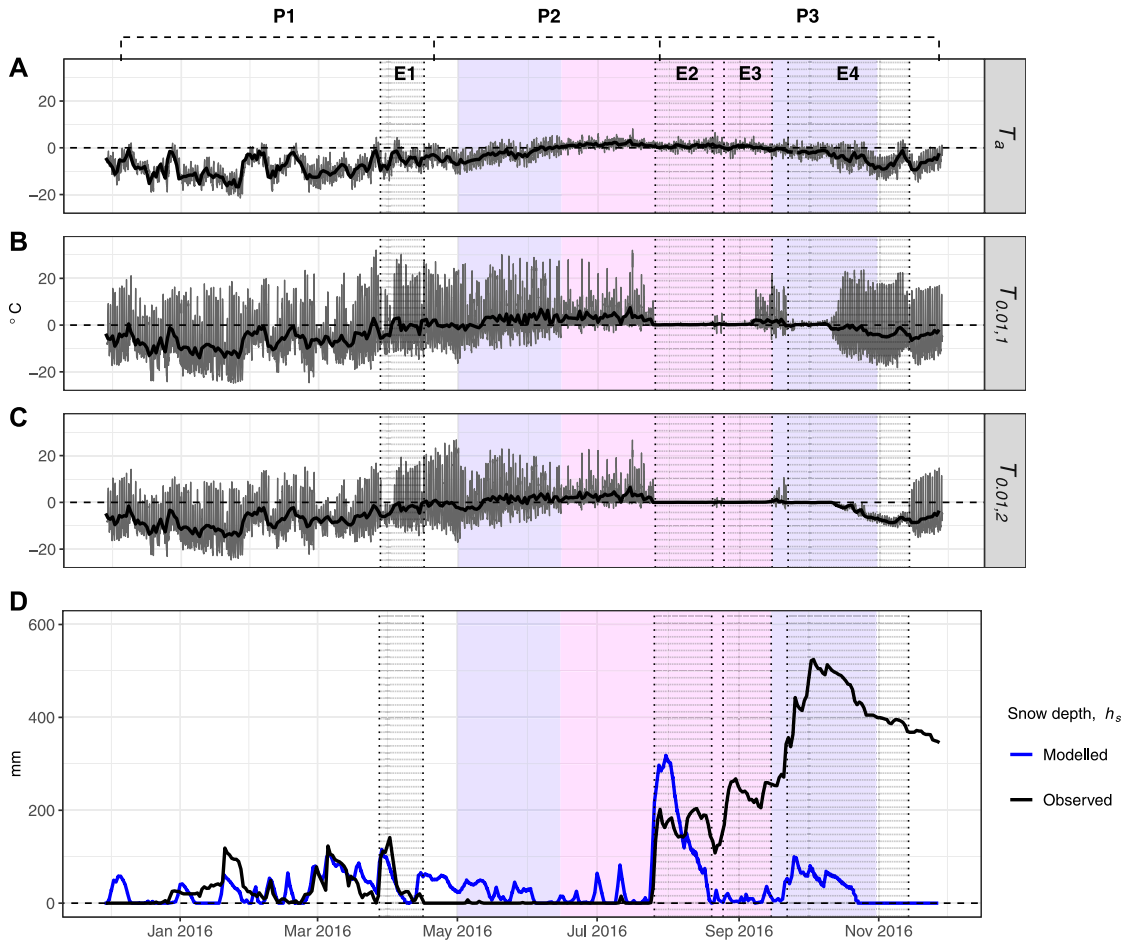

FIGURE 8 | (A) Observed air temperature **(B)** and **(C)** observed debris temperature at 0.01 m depth in Pits 1 and 2. Grey lines are hourly data and black lines are daily averages. **(D)** Daily snow depth from the sonic ranger at NCN-AWS (black), and predicted using SHAW-Glacier (blue). Events that are discussed in the text are highlighted with stippling and labelled E1 - E4; labels P1 - P3 refer to periods with distinct snow cover characteristics. The background colours indicate the seasons, as defined by Government of Nepal (2021): white is winter, pink is monsoon, blue is both pre- and post-monsoon.

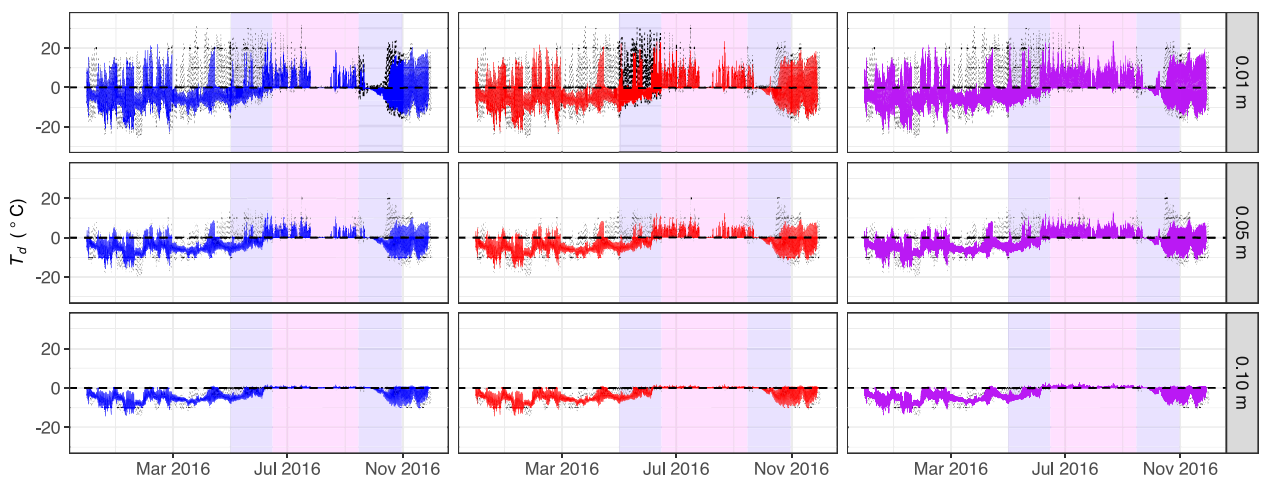

FIGURE 9 | Observed debris temperature, T_d, at depths $d = 0.01$, 0.05 and 0.10 m in Pit 1 (stipped black line). Monte Carlo simulations of the same ($n = 2{,}000$) have been grouped to second order, with the colour blue used for branch 2a, red for branch 2b and purple for branch 1b.

representing those processes in adjacent saturated and unsaturated layers due to infiltration and percolation of liquid water, freezing and thawing, is a known challenge (Zhang et al., 2010; Lamontagne-Hallé et al., 2020). Non-convergence issues in the current analysis were resolved by increasing the number of computational iterations and decreasing the error tolerance. The configuration required for numerical stability of SHAW-Glacier is likely to vary with the conditions of the study site, such as the meteorological volatility and frequency of sub-surface phase changes, meaning that the flexibility of the discretisation scheme and computing time will vary among studies.

A minimum of two debris layers is required to run SHAW-Glacier. At the current study site, the minimum debris thickness that could be simulated was 0.03 m, because layers assigned values of $L <$ 0.02 m compromised numerical stability. Therefore, it was not possible to evaluate the sensitivity of ablation to debris thinner than 0.03 m at North Changri Nup, nor whether fine debris enhanced ablation rates, i.e. the rising limb of the Østrem Curve. However, it has been estimated that, globally, the median thickness of supraglacial debris cover is 0.15 m (Rounce et al., 2021), meaning that SHAW-Glacier should be functional at the majority of sites world-wide.

SHAW-Glacier successfully modelled the inverse relationship between ablation and debris thickness that defines the falling limb of the Østrem Curve, and the response of $\hat{A}$ to variation of the physical parameters was consistent with the underlying physical relations. Clustering of $\hat{A}$ according to the values of T_p was unanticipated, but was also consistent with the underlying physical relations and with the characteristics of the meteorological data (expanded below).

Simulated snow cover could not be validated because the snow cover around NCN-AWS was uneven (discussed below); however, the simulation of debris temperatures showed that SHAW-Glacier accurately represented snow-free and snow-covered conditions (**Figure 9**). The simulations captured observed diel variation of T_d and its attenuation with depth during snow-free conditions. Periods in which snow cover was simulated were identifiable using $\hat{T}_{0.01}$ by the same criteria for identifying snow cover on the basis of $T_{0.01}$, and the time series of T_d and $\hat{T}_d$ were in fair agreement when snow cover was both observed and predicted. The simulation of the effects of spatially variable snow distribution and patchy snow cover is the focus of Part 2 of this study.

The option to include vegetation could be useful in future studies of debris-covered glaciers that have been colonised by plants. For example, communities of trees are established on a lobe of the terminus of Miage Glacier in the Italian Alps (Pelfini et al., 2012). In addition, Satopanth bamak in the Garhwal Himalaya, India, is sparsely vegetated in the lower ablation zone (Singh et al., 2019), first colonisers have been observed on the debris cover of Lirung glacier, Nepal (Kraaijenbrink et al., 2018), and established vegetation has been observed on the terminus of Malaspina Glacier in Alaska (Truffer, 2021). To the best of our knowledge, the impact of plants on sub-debris ablation has not been evaluated, and SHAW-Glacier could be used for this purpose.

7.2 Prediction Uncertainty due to Uncertainty in the Physical Parameter Values

The values of ablation predicted in the Monte Carlo simulations varied by a factor of two to three for each value of h. Uncertainty in the value of T_p contributed more to total uncertainty than all of the remaining parameters, combined, signifying the decisive sensitivity of sub-debris ablation to snow cover.

The non-linear sensitivity of $\hat{A}$ to T_p reflects the monsoon climate and a relation between the occurrence of precipitation and air temperature in 2016: the most intense precipitation events occurred with T_a between −0.25°C and 0.5°C, and within that subset, the most intense events occurred with T_a between −0.2°C and 0.1°C. Therefore, values of T_p corresponding to the first and second order partitioning values determined whether notable snow cover was simulated.

Ranges of predicted ablation, accounting for uncertainty, did not consistently overlap with observed ablation, indicating that at least one important process was not accurately represented by the parameter values, the structure of the model and/or input data. The uncertainties that were calculated for $\hat{T}_d$ did not account for the observations during periods that the simulation of snow cover was inaccurate. Giese et al. (2020) reported a similar finding: simulations made using the physically based model ISBA-DEB on West Changri Nup were inaccurate when snow cover was not accurately reproduced. In the current study there was evidence that the snow cover had accumulated or ablated unevenly, due to processes that cannot be represented in a 1-dimensional simulation (discussed further below). Neglecting uncertainty relating to uneven deposition or ablation of snow can account for underestimation of the uncertainty in debris temperatures, and may account for the observations of ablation; this hypothesis will be explored in the second part of this study.

Previous research has suggested that sources of uncertainty in predicted sub-debris ablation include properties such as mineral thermal conductivity (e.g. Bocchiola et al., 2015; Evatt et al., 2015), albedo (e.g. Fujita and Sakai, 2014), porosity (e.g. Juen et al., 2013) and surface roughness (e.g. Rounce et al., 2015; Miles et al., 2017; Giese et al., 2020). However, the relative importance of these characteristics is not consistent among studies. In addition to the sensitivity of $\hat{A}$ to T_p, the recursive partitioning analysis revealed sensitivity to g, the percent gravel in the diamict, for $h >$ 0.03 m (**Supplementary Figures S3-S11**). The value of g affects the rate of heat transmission by influencing the bulk thermal and hydrological properties of the debris layer. The sensitivity of $\hat{A}$ to g varied depending on the values of the remaining parameters. These results suggest that interactions between processes can produce variability in the sensitivity of sub-debris ablation to debris properties.

7.3 The Sensitivity of Sub-debris Ablation to Snow and Implications of Patchy Snow Cover

The observational data used in this study were unusual, in that ablation was not inversely related to debris thickness (**Figure 7**).

That can be explained by the presence of patchy snow cover during the ablation season. Photographs, as well as the snow depth and debris temperature data, show that there were periods throughout the year when snow was distributed in patches with length scales on the order of centimetres to meters. With some patches of debris covered by snow and others exposed, ablation amounts would be closely related to the duration of the snow, and if patchiness were persistent or frequent, the sensitivity of ablation to debris thickness could be entirely confounded.

Wind redistribution is a feasible mechanism for the development of patchy snow cover at the study site. Patchy snow cover can also form by differential melting and sublimation, but it is deemed unlikely that heat sources varied considerably within the 2500 m^2 study area because differences in surface slope, aspect and shading were minor (**Supplementary Figure S1**). Conversely, micro-topographic features and light winds, which were in evidence, are adequate to cause snow scour and redeposition (Radok, 1977; Dadić et al., 2010). Furthermore, the method used to control the thickness of the debris around each ablation stake produced micro-relief related inversely to debris thickness. That might explain why the sensitivity of observed ablation to debris thickness had the appearance of having been offset systematically. Patches of debris required to be thinner than the naturally occurring debris field were excavated, and thus, depressed relative to the surrounding surface. Patches where the debris was required to be thicker than the natural debris were built up, and thus, elevated relative to the surrounding surface. It is feasible that preferential wind scour occurred where the debris was thick, and preferential deposition where it was thin, producing patches of snow with depths related inversely to debris thickness.

Most glacier melt models operate with grid resolutions of tens to hundreds of meters, and do not simulate sub-grid variability of snow distribution. The results of this study suggest that the variability of snow cover had a stronger influence on ablation than variations in debris thickness. Therefore, development of patchy snow cover during the ablation season could be a source of error in predicted ablation that has not previously been recognized.

Patchy snow cover could be significant over a substantial area. Glacier surface ablation is affected by snow cover during seasonal transitions, around the snowline, and across the ablation zone of summer-accumulation type glaciers. Over 30% of all glaciers outside the polar regions (Braithwaite, 2002) and more than half in High Mountain Asia (HMA) are summer-accumulation type (Ageta and Higuchi, 1984; Sakai et al., 2015). Some proportion of the 10% of glaciers in HMA that are debris-covered (Scherler et al., 2018) lies within the summer-accumulation region. Uneven ablation of fresh snow in the ablation zone could occur routinely on glaciers in that area.

Glaciers in the Sagarmatha/Everest region have all lost mass in the past century. However, projections of the rate of glacier mass loss in the region vary (Sherpa et al., 2017). Summer-accumulation type debris-free glaciers have been found to be more sensitive to air temperature than winter-accumulation type glaciers, because air temperature affects the accumulation and duration of snow during the ablation season (Fujita, 2008; Sakai et al., 2015). In the current study, simulated precipitation phase was more sensitive to T_a during summer, when T_a fluctuated around T_p, than winter, when T_a rarely rose above T_p. It can thus be inferred that $\hat{A}$ was sensitive to T_a beyond the contribution of T_a to the turbulent heat and longwave radiative fluxes, suggesting that heightened sensitivity to air temperature is also a characteristic of summer-accumulation type debris-covered glaciers. Improved estimation of uncertainties due to the threshold temperature for partitioning rain and snow, as well as uneven ablation of snow cover, could help to constrain projections of glacier change in the Sagarmatha/Everest region and elsewhere.

8 CONCLUSION

This paper has introduced a new physically based model of sub-debris ablation, SHAW-Glacier, which is based on the Simultaneous Heat and Water transport model (SHAW). To the authors' knowledge, SHAW-Glacier is the most comprehensive physical representation of the processes of sub-debris ablation that has been reported to date, including transfer of rain, meltwater and vapour through the snow-debris-ice column, advection of heat by water, heat fluxes associated with processes of freezing and thawing in the debris, and lateral flow of water through the debris layers and a porous surface layer of ice. The comprehensive representation of physical processes makes SHAW-Glacier useful for evaluating the sensitivity and uncertainty of sub-debris ablation to physical parameters and interactions among them.

In this study, the sensitivity and uncertainty of sub-debris ablation associated with debris thickness and physical parameter values were evaluated by applying SHAW-Glacier to the debris-covered glacier North Changri Nup. Nineteen parameters were varied in a Monte Carlo analysis, and predicted ablation followed the characteristic Østrem Curve. Uncertainties calculated within groups based on the parameter for the maximum air temperature at which precipitation falls as snow increased from 16% to 40% as debris thickness increased from 0.03 m to 0.41 m.

Recursive partitioning revealed that predicted sub-debris ablation was most sensitive to snow cover associated with monsoon precipitation during the ablation season, which has not been previously reported. Indeed, the sensitivity of predicted ablation to snow cover exceeded its sensitivity to debris thickness. Observations of ablation on North Changri Nup, which were unlike any that have been published to date, had no apparent sensitivity to debris thickness. Observed snow cover was patchy during the ablation season, which could have confounded the signal of the sensitivity of ablation to debris thickness by effectively altering the length of the ablation season among the ablation stakes.

Patchy snow cover develops through the redistribution of snow by wind, which is not routinely represented in glacier-melt models at the sub-grid scale. Wind redistribution of snow and patchy snow cover could be sources of uncertainty in regional predictions of ablation, particularly those that encompass high elevation debris-covered glaciers in the monsoon-influenced climate regions of High Mountain Asia.

Further studies to improve understanding of the processes and effects of wind redistribution of snow on sub-debris ablation will be important to constrain the uncertainty introduced to predictions by patchy snow cover. The second part of this

study will begin to address that by quantifying the uncertainty introduced to ablation predicted using SHAW-Glacier given scenarios of wind redistribution. In addition, analyses to estimate the geographic extent affected by patchy snow cover during the ablation season, estimate the uncertainty introduced to glacier- and regional-scale predictions of sub-debris ablation by patchy ablation season snow cover, and evaluate the sensitivity of sub-debris ablation to changes in air temperature and precipitation at sites where patchy snow cover occurs, would also be useful to improve projections of debris-covered glacier change.

9 R PACKAGES USED

dplyr (Wickham et al., 2021), **here** (Müller, 2020), **ggforce** (Pedersen, 2021), **ggplot2** (Wickham, 2016), **ggplotify** (Yu, 2021), **ggpubr** (Kassambara, 2020), **ggspatial** (Dunnington, 2021), **ggsn** (Santos Baquero, 2019), **grDevices** (R Core Team, 2021), **grid** (R Core Team, 2021), **gridExtra** (Auguie, 2017), **magrittr** (Bache and Wickham, 2020), **raster** (Hijmans, 2021), **rgdal** (Bivand et al., 2021), **rpart** (Therneau and Atkinson, 2019), **RStoolbox** (Leutner et al., 2019), **rstudioapi** (Ushey et al., 2020), **sf** (Pebesma, 2018).

DATA AVAILABILITY STATEMENT

Publicly available datasets were analyzed in this study. The data can be found here: https://glacioclim.osug.fr/IACS-working-group-on-debris-covered-glaciers-Data-from-West-and-North-Changri.

AUTHOR CONTRIBUTIONS

SHAW-Glacier was designed and coded by GF. The observational data were collected on field campaigns conducted by PW. The research questions and methodology were designed by AW, RM, RD, GF and AB. AW performed the data analyses. GF drafted **Section 2.1**. AW drafted all other sections of the manuscript. Editing was performed by RM, RD, PW, GF and AB. All figures were made by AW except the photographs, which were taken by PW.

FUNDING

Data collection on Changri Nup Glacier has been supported by the French Service d'Observation GLACIOCLIM (part of IR OZCAR), the French National Research Agency (ANR) through ANR-13-SENV-0005-04/05-PRESHINE, and by a grant from Labex OSUG@2020 (Investissements d'avenir–ANR10 LABX56).

ACKNOWLEDGMENTS

This study was carried out within the framework of the Ev-K2-CNR Project in collaboration with the Nepal Academy of Science and Technology and Tribhuvan University (JEAI HIMALICE). Thank you to the Associate Editor Martina Barandun, and two anonymous Reviewers, whose feedback and suggestions greatly improved the quality of the manuscript. We appreciate the USDA for maintaining the SHAW model and making it available with supporting documentation. Thanks also to Te Puna Pātiotio Antarctic Research Center, VUW, for supporting AW with visitor access to departmental resources.

SUPPLEMENTARY MATERIAL

The Supplementary Material for this article can be found online at: https://www.frontiersin.org/articles/10.3389/feart.2022.796877/full#supplementary-material

REFERENCES

Ageta, Y., and Higuchi, K. (1984). Estimation of Mass Balance Components of a Summer-Accumulation Type Glacier in the Nepal Himalaya. *Geogr. Ann. Ser. A, Phys. Geogr.* 66, 249–255. doi:10.1080/04353676.1984.11880113

Auguie, B. (2017). gridExtra: Miscellaneous Functions for 'Grid' Graphics. *R. package version 2.3.* Available at: https://CRAN.R-project.org/package=gridExtra.

Bache, S. M., and Wickham, H. (2020). Magrittr: A Forward-Pipe Operator for R. *R. package version 2.0.1*. Available at: https://CRAN.R-project.org/package=magrittr.

Bhambri, R., Bolch, T., Chaujar, R. K., and Kulshreshtha, S. C. (2011). Glacier Changes in the Garhwal Himalaya, India, from 1968 to 2006 Based on Remote Sensing. *J. Glaciol.* 57, 543–556. doi:10.3189/002214311796905604

Biddle, D. (2015). Mapping Debris-Covered Glaciers in the Cordillera Blanca, Peru : an Object-Based Image Analysis Approach. MSc Thesis (Louisville, KY: University of Louisville). doi:10.18297/etd/2220

Bivand, R., Keitt, T., and Rowlingson, B. (2021). Rgdal: Bindings for the 'Geospatial' Data Abstraction Library. *R. package version 1.5-23.* Available at: https://CRAN.R-project.org/package=rgdal.

Bocchiola, D., Senese, A., Mihalcea, C., Mosconi, B., D'Agata, C., Smiraglia, C., et al. (2015). An Ablation Model for Debris-Covered Ice: The Case Study of Venerocolo Glacier (Italian Alps). *Geogr. Fis. Din. Quat.* 38, 113–128. doi:10.4461/GFDQ.2015.38.11

Bozhinskiy, A. N., Krass, M. S., and Popovnin, V. V. (1986). Role of Debris Cover in the Thermal Physics of Glaciers. *J. Glaciol.* 32, 255–266. doi:10.3189/s0022143000015598

Braithwaite, R. J. (2002). Glacier Mass Balance: the First 50 Years of International Monitoring. *Prog. Phys. Geogr. Earth Environ.* 26, 76–95. doi:10.1191/0309133302pp326ra

Brock, B., Rivera, A., Casassa, G., Bown, F., and Acuña, C. (2007). The Surface Energy Balance of an Active Ice-Covered Volcano: Villarrica Volcano, Southern Chile. *Ann. Glaciol.* 45, 104–114. doi:10.3189/172756407782282372

Bulley, H. N. N., Bishop, M. P., Shroder, J. F., and Haritashya, U. K. (2013). Integration of Classification Tree Analyses and Spatial Metrics to Assess Changes in Supraglacial Lakes in the Karakoram Himalaya. *Int. J. Remote Sens.* 34, 387–411. doi:10.1080/01431161.2012.705915

Collier, E., Maussion, F., Nicholson, L. I., Mölg, T., Immerzeel, W. W., and Bush, A. B. G. (2015). Impact of Debris Cover on Glacier Ablation and Atmosphere-Glacier Feedbacks in the Karakoram. *Cryosphere* 9, 1617–1632. doi:10.5194/tc-9-1617-2015

Collier, E., Nicholson, L. I., Brock, B. W., Maussion, F., Essery, R., and Bush, A. B. G. (2014). Representing Moisture Fluxes and Phase Changes in Glacier Debris Cover Using a Reservoir Approach. *Cryosphere* 8, 1429–1444. doi:10.5194/tc-8-1429-2014

Dadić, R., Mott, R., Lehning, M., and Burlando, P. (2010). Wind Influence on Snow Depth Distribution and Accumulation over Glaciers. *J. Geophys. Res.* 115, F01012. doi:10.1029/2009JF001261

Dadić, R., Mott, R., Lehning, M., Carenzo, M., Anderson, B., and Mackintosh, A. (2013). Sensitivity of Turbulent Fluxes to Wind Speed over Snow Surfaces in Different Climatic Settings. *Adv. Water Resour.* 55, 178–189. doi:10.1016/j.advwatres.2012.06.010

De Vries, D. A. (1963). "Thermal Properties of Soil," in *Physics of the Plant Environment*. Editor W. R. Van Wijk (Amsterdam: North-Holland Publishing). chap. 7.

Dunnington, D. (2021). Ggspatial: Spatial Data Framework for Ggplot2. *R. package version 1.1.5*. Available at: https://CRAN.R-project.org/package=ggspatial.

Dussaillant, A., Benito, G., Buytaert, W., Carling, P., Meier, C., and Espinoza, F. (2010). Repeated Glacial-Lake Outburst Floods in Patagonia: an Increasing Hazard? *Nat. Hazards* 54, 469–481. doi:10.1007/s11069-009-9479-8

Elder, K., Rosenthal, W., and Davis, R. E. (1998). Estimating the Spatial Distribution of Snow Water Equivalence in a Montane Watershed. *Hydrol. Process.* 12, 1793–1808. doi:10.1002/(sici)1099-1085(199808/09)12:10/11<1793::aid-hyp695>3.0.co;2-k

Evatt, G. W., Abrahams, I. D., Heil, M., Mayer, C., Kingslake, J., Mitchell, S. L., et al. (2015). Glacial Melt under a Porous Debris Layer. *J. Glaciol.* 61, 825–836. doi:10.3189/2015JoG14J235

Fitzpatrick, N., Radić, V., and Menounos, B. (2017). Surface Energy Balance Closure and Turbulent Flux Parameterization on a Mid-latitude Mountain Glacier, Purcell Mountains, Canada. *Front. Earth Sci.* 5, 1–20. doi:10.3389/feart.2017.00067

Flerchinger, G. N., Baker, J. M., and Spaans, E. J. A. (1996). A Test of the Radiative Energy Balance of the SHAW Model for Snowcover. *Hydrol. Process.* 10, 1359–1367. doi:10.1002/(sici)1099-1085(199610)10:10<1359::aid-hyp466>3.0.co;2-n

Flerchinger, G. N., Reba, M. L., and Marks, D. (2012). Measurement of Surface Energy Fluxes from Two Rangeland Sites and Comparison with a Multilayer Canopy Model. *J. Hydrometeorol.* 13, 1038–1051. doi:10.1175/JHM-D-11-093.1

Flerchinger, G. N. (1987). Simultaneous Heat and Water Model of a Snow-Residue-Soil System. PhD Thesis (Pullman, WA: Washington State University). Available at: https://www.proquest.com/dissertations-theses/simultaneous-heat-water-model-snow-residue-soil/docview/303504656/se-2?accountid=14656.

Flerchinger, G. N. (2017a). The Simultaneous Heat and Water (SHAW) Model: Technical Documentation, in *Tech. Rep* (Boise, ID: NWRC 2000-09, Northwest Watershed Research Center, USDA Agricultural Research Service). Available at: https://www.ars.usda.gov/ARSUserFiles/20520000/shawdocumentation.pdf.

Flerchinger, G. N. (2017b). The Simultaneous Heat and Water (SHAW) Model: User's Manual. Version 3.0.X. *Tech. Rep.* (Boise, ID: NWRC 2017-01.2, Northwest Watershed Research Center, USDA Agricultural Research Service). Available at: https://www.ars.usda.gov/ARSUserFiles/20520500/SHAW/ShawUsers.30x.pdf.

Fujita, K. (2008). Influence of Precipitation Seasonality on Glacier Mass Balance and its Sensitivity to Climate Change. *Ann. Glaciol.* 48, 88–92. doi:10.3189/172756408784700824

Fujita, K., and Sakai, A. (2014). Modelling Runoff from a Himalayan Debris-Covered Glacier. *Hydrol. Earth Syst. Sci.* 18, 2679–2694. doi:10.5194/hess-18-2679-2014

Fyffe, C. L., Reid, T. D., Brock, B. W., Kirkbride, M. P., Diolaiuti, G., Smiraglia, C., et al. (2014). A Distributed Energy-Balance Melt Model of an Alpine Debris-Covered Glacier. *J. Glaciol.* 60, 587–602. doi:10.3189/2014JoG13J148

Giese, A., Boone, A., Wagnon, P., and Hawley, R. (2020). Incorporating Moisture Content in Surface Energy Balance Modeling of a Debris-Covered Glacier. *Cryosphere* 14, 1555–1577. doi:10.5194/tc-14-1555-2020

Giesen, R. H., and Oerlemans, J. (2013). Climate-model Induced Differences in the 21st Century Global and Regional Glacier Contributions to Sea-Level Rise. *Clim. Dyn.* 41, 3283–3300. doi:10.1007/s00382-013-1743-7

Godard, V., Bourlès, D. L., Spinabella, F., Burbank, D. W., Bookhagen, B., Fisher, G. B., et al. (2014). Dominance of Tectonics over Climate in Himalayan Denudation. *Geology* 42, 243–246. doi:10.1130/G35342.1

Government of Nepal (2021). *Monsoon Onset and Withdrawal Date Information*. Babarmahal, Kathmandu: Ministry of Energy, Water Resource and Irrigation, Department of Hydrology and Meteorology, Climate Division (Climate Analysis Section). Available at: https://www.dhm.gov.np/uploads/climatic/79118284monsoon%20onset%20n%20withdrawal%20English%20final.pdf.

Hagg, W., Brook, M., Mayer, C., and Winkler, S. (2014). A Short-Term Field Experiment on Sub-debris Melt at the Highly Maritime Franz Josef Glacier, Southern Alps, New Zealand. *J. Hydrol.* 53, 157–165. Available at: https://62397185-821a-4cdf-b4f7-8cc2999495c6.usrfiles.com/ugd/623971_db45e7e64e614163b8b4ed4d055197c5.pdf.

Haidong, H., Yongjing, D., and Shiyin, L. (2006). A Simple Model to Estimate Ice Ablation under a Thick Debris Layer. *J. Glaciol.* 52, 528–536. doi:10.3189/172756506781828395

Herreid, S., and Pellicciotti, F. (2020). The State of Rock Debris Covering Earth's Glaciers. *Nat. Geosci.* 13, 621–627. doi:10.1038/s41561-020-0615-0

Hewitt, K. (2014). "Glaciers of the Karakoram Himalaya" in *Glacial Environments, Processes, Hazards and Resources* (Cham, Switzerland: Springer International Publishing Switzerland). doi:10.1007/978-94-007-6311-1

Hijmans, R. J. (2021). Raster: Geographic Data Analysis and Modeling. *R. package version 3.4-10*. Available at: https://CRAN.R-project.org/package=raster.

Hock, R., Bliss, A., Marzeion, B., Giesen, R. H., Hirabayashi, Y., Huss, M., et al. (2019). GlacierMIP - A Model Intercomparison of Global-Scale Glacier Mass-Balance Models and Projections. *J. Glaciol.* 65, 453–467. doi:10.1017/jog.2019.22

Immerzeel, W. W., Lutz, A. F., Andrade, M., Bahl, A., Biemans, H., Bolch, T., et al. (2020). Importance and Vulnerability of the World's Water Towers. *Nature* 577, 364–369. doi:10.1038/s41586-019-1822-y

Juen, M., Mayer, C., Lambrecht, A., Wirbel, A., and Kueppers, U. (2013). Thermal Properties of a Supraglacial Debris Layer with Respect to Lithology and Grain Size. *Geogr. Ann. Ser. A, Phys. Geogr.* 95, 197–209. doi:10.1111/geoa.12011

Kassambara, A. (2020). Ggpubr: 'ggplot2' Based Publication Ready Plots. *R. package version 0.4.0*. Available at: https://CRAN.R-project.org/package=ggpubr.

Koppes, M., Rupper, S., Asay, M., and Winter-Billington, A. (2015). Sensitivity of Glacier Runoff Projections to Baseline Climate Data in the Indus River Basin. *Front. Earth Sci.* 3, 1–14. doi:10.3389/feart.2015.00059

Kraaijenbrink, P. D. A., Shea, J. M., Litt, M., Steiner, J. F., Treichler, D., Koch, I., et al. (2018). Mapping Surface Temperatures on a Debris-Covered Glacier with an Unmanned Aerial Vehicle. *Front. Earth Sci.* 6, 64. doi:10.3389/feart.2018.00064

Lamontagne-Hallé, P., McKenzie, J. M., Kurylyk, B. L., Molson, J., and Lyon, L. N. (2020). Guidelines for Cold-Regions Groundwater Numerical Modeling. *WIRES Water* 7, 1–26. doi:10.1002/wat2.1467

Langford, J. E., Schincariol, R. A., Nagare, R. M., Quinton, W. L., and Mohammed, A. A. (2020). Transient and Transition Factors in Modeling Permafrost Thaw and Groundwater Flow. *Groundwater* 58, 258–268. doi:10.1111/gwat.12903

Lejeune, Y., Bertrand, J.-M., Wagnon, P., and Morin, S. (2013). A Physically Based Model of the Year-Round Surface Energy and Mass Balance of Debris-Covered Glaciers. *J. Glaciol.* 59, 327–344. doi:10.3189/2013JoG12J149

Leutner, B., Horning, N., and Schwalb-Willmann, J. (2019). RStoolbox: Tools for Remote Sensing Data Analysis. *R. package version 0.2.6*. Available at: https://CRAN.R-project.org/package=RStoolbox.

Li, Z., Ma, L., Flerchinger, G. N., Ahuja, L. R., Wang, H., and Li, Z. (2012). Simulation of Overwinter Soil Water and Soil Temperature with SHAW and RZ-SHAW. *Soil Sci. Soc. Am. J.* 76, 1548–1563. doi:10.2136/sssaj2011.0434

Liang, S., Gan, W., Shen, C., Xiao, G., Liu, J., Chen, W., et al. (2013). Three-Dimensional Velocity Field of Present-Day Crustal Motion of the Tibetan Plateau Derived from GPS Measurements. *J. Geophys. Res. Solid Earth* 118, 5722–5732. doi:10.1002/2013JB010503

Lutz, A. F., Immerzeel, W. W., Shrestha, A. B., and Bierkens, M. F. P. (2014). Consistent Increase in High Asia's Runoff Due to Increasing Glacier Melt and Precipitation. *Nat. Clim. Change* 4, 587–592. doi:10.1038/NCLIMATE2237

Machguth, H., Purves, R. S., Oerlemans, J., Hoelzle, M., and Paul, F. (2008). Exploring Uncertainty in Glacier Mass Balance Modelling with Monte Carlo Simulation. *Cryosphere* 2, 191–204. doi:10.5194/tc-2-191-2008

Marzeion, B., Hock, R., Anderson, B., Bliss, A., Champollion, N., Fujita, K., et al. (2020). Partitioning the Uncertainty of Ensemble Projections of Global Glacier Mass Change. *Earth's Future* 8, 1–25. doi:10.1029/2019EF001470

McGrath, D., Sass, L., O'Neel, S., McNeil, C., Candela, S. G., Baker, E. H., et al. (2018). Interannual Snow Accumulation Variability on Glaciers Derived from Repeat, Spatially Extensive Ground-Penetrating Radar Surveys. *Cryosphere* 12, 3617–3633. doi:10.5194/tc-12-3617-2018

McMahon, A., and Moore, R. D. (2017). Influence of Turbidity and Aeration on the Albedo of Mountain Streams. *Hydrol. Process.* 31, 4477–4491. doi:10.1002/hyp.11370

Mernild, S. H., Lipscomb, W. H., Bahr, D. B., Radić, V., and Zemp, M. (2013). Global Glacier Changes: A Revised Assessment of Committed Mass Losses and Sampling Uncertainties. *Cryosphere* 7, 1565–1577. doi:10.5194/tc-7-1565-2013

Mihalcea, C., Mayer, C., Diolaiuti, G., D'Agata, C., Smiraglia, C., Lambrecht, A., et al. (2008). Spatial Distribution of Debris Thickness and Melting from Remote-Sensing and Meteorological Data, at Debris-Covered Baltoro Glacier, Karakoram, Pakistan. *Ann. Glaciol.* 48, 49–57. doi:10.3189/172756408784700680

Mihalcea, C., Mayer, C., Diolaiuti, G., Lambrecht, A., Smiraglia, C., and Tartari, G. (2006). Ice Ablation and Meteorological Conditions on the Debris-Covered Area of Baltoro Glacier, Karakoram, Pakistan. *Ann. Glaciol.* 43, 292–300. doi:10.3189/172756406781812104

Miles, E. S., Steiner, J. F., and Brun, F. (2017). Highly Variable Aerodynamic Roughness Length (z_0) for a Hummocky Debris-Covered Glacier. *J. Geophys. Res. Atmos.* 122, 8447–8466. doi:10.1002/2017JD026510

Miles, K. E., Hubbard, B., Quincey, D. J., Miles, E. S., Sherpa, T. C., Rowan, A. V., et al. (2018). Polythermal Structure of a Himalayan Debris-Covered Glacier Revealed by Borehole Thermometry. *Sci. Rep.* 8, 16825–16829. doi:10.1038/s41598-018-34327-5

Molden, D. J., Shrestha, A. B., Immerzeel, W. W., Maharjan, A., Rasul, G., Wester, P., et al. (2022). "The Great Glacier and Snow-dependent Rivers of Asia and Climate Change: Heading for Troubled Waters," in *Water Security under Climate Change*. Editors A. K. Biswas and C. Tortajada (Singapore: Springer Singapore), 223–250. doi:10.1007/978-981-16-5493-0_12

Müller, K. (2020). Here: A Simpler Way to Find Your Files. *R. package version 1.0.1*. Available at: https://CRAN.R-project.org/package=here.

Nakawo, M., Iwata, S., Watanabe, O., and Yoshida, M. (1986). Processes Which Distribute Supraglacial Debris on the Khumbu Glacier, Nepal Himalaya. *Ann. Glaciol.* 8, 129–131. doi:10.3189/s0260305500001294

Nakawo, M., and Rana, B. (1999). Estimate of Ablation Rate of Glacier Ice under a Supraglacial Debris Layer. *Geogr. Ann. A* 81, 695–701. doi:10.1111/j.0435-3676.1999.00097.x

Nakawo, M., and Young, G. J. (1981). Field Experiments to Determine the Effect of a Debris Layer on Ablation of Glacier Ice. *Ann. Glaciol.* 2, 85–91. doi:10.3189/172756481794352432

Nicholson, L., and Benn, D. I. (2006). Calculating Ice Melt beneath a Debris Layer Using Meteorological Data. *J. Glaciol.* 52, 463–470. doi:10.3189/172756506781828584

Panday, P. K., Bulley, H., Haritashya, U., and Ghimire, B. (2011). "Supraglacial Lake Classification in the Everest Region of Nepal Himalaya," in *Geospatial Tech. Manag. Environ. Resour.* Editors J. K. Thakur, S. K. Singh, A. L. Ramanathan, M. B. K. Prasad, and W. Gossel (New Delhi: Springer India), 86–99. chap. 6. doi:10.1007/978-94-007-1858-6_6

Pebesma, E. (2018). Simple Features for R: Standardized Support for Spatial Vector Data. *R J.* 10, 439–446. doi:10.32614/RJ-2018-009

Pedersen, T. L. (2021). Ggforce: Accelerating 'ggplot2'. *R. package version 0.3.3*. Available at: https://CRAN.R-project.org/package=ggforce.

Pelfini, M., Diolaiuti, G., Leonelli, G., Bozzoni, M., Bressan, N., Brioschi, D., et al. (2012). The Influence of Glacier Surface Processes on the Short-Term Evolution of Supraglacial Tree Vegetation: The Case Study of the Miage Glacier, Italian Alps. *Holocene* 22, 847–856. doi:10.1177/0959683611434222

Pritchard, H. D. (2019). Asia's Shrinking Glaciers Protect Large Populations From Drought Stress. *Nature* 569, 649–654. doi:10.1038/s41586-019-1240-1

Quincey, D. J., Lucas, R. M., Richardson, S. D., Glasser, N. F., Hambrey, M. J., and Reynolds, J. M. (2005). Optical Remote Sensing Techniques in High-Mountain Environments: Application to Glacial Hazards. *Prog. Phys. Geogr. Earth Environ.* 29, 475–505. doi:10.1191/0309133305pp456ra

R Core Team (2021). *R: A Language and Environment for Statistical Computing*. Vienna, Austria: R Foundation for Statistical Computing. Available at: https://www.R-project.org/.

Radok, U. (1977). Snow Drift. *J. Glaciol.* 19, 123–139. doi:10.3189/S0022143000215591

Ragettli, S., Immerzeel, W. W., and Pellicciotti, F. (2016). Contrasting Climate Change Impact on River Flows from High-Altitude Catchments in the Himalayan and Andes Mountains. *Proc. Natl. Acad. Sci. U.S.A.* 113, 9222–9227. doi:10.1073/pnas.1606526113

Ragettli, S., Pellicciotti, F., Immerzeel, W. W., Miles, E. S., Petersen, L., Heynen, M., et al. (2015). Unraveling the Hydrology of a Himalayan Catchment through Integration of High Resolution *In Situ* Data and Remote Sensing with an Advanced Simulation Model. *Adv. Water Resour.* 78, 94–111. doi:10.1016/j.advwatres.2015.01.013

Rana, B., Nakawo, M., Ageta, Y., and Seko, K. (1998). "Glacier Ablation under Debris Cover: Field Observations on Lirung Glacier, Nepal Himalayas," in *International Conference on Ecohydrology of High Mountain Areas*. Editors S. Chalise, A. Herrmann, and N. Khanal (Kathmandu: AGRIS), 393–403. Available at: https://lib.icimod.org/record/23011.

Reid, T. D., and Brock, B. W. (2010). An Energy-Balance Model for Debris-Covered Glaciers Including Heat Conduction through the Debris Layer. *J. Glaciol.* 56, 903–916. doi:10.3189/002214310794457218

Reid, T. D., and Brock, B. W. (2014). Assessing Ice-Cliff Backwasting and its Contribution to Total Ablation of Debris-Covered Miage Glacier, Mont Blanc Massif, Italy. *J. Glaciol.* 60, 3–13. doi:10.3189/2014JoG13J045

Reid, T. D., Carenzo, M., Pellicciotti, F., and Brock, B. W. (2012). Including Debris Cover Effects in a Distributed Model of Glacier Ablation. *J. Geophys. Res.* 117 (D18105), 1–15. doi:10.1029/2012JD017795

Rounce, D. R., Hock, R., McNabb, R. W., Millan, R., Sommer, C., Braun, M. H., et al. (2021). Distributed Global Debris Thickness Estimates Reveal Debris Significantly Impacts Glacier Mass Balance. *Geophys. Res. Lett.* 48 (e2020GL09131), 1–12. doi:10.1029/2020gl091311

Rounce, D. R., and McKinney, D. C. (2014). Debris Thickness of Glaciers in the Everest Area (Nepal Himalaya) Derived from Satellite Imagery Using a Nonlinear Energy Balance Model. *Cryosphere* 8, 1317–1329. doi:10.5194/tc-8-1317-2014

Rounce, D. R., Quincey, D. J., and McKinney, D. C. (2015). Debris-Covered Glacier Energy Balance Model for Imja-Lhotse Shar Glacier in the Everest Region of Nepal. *Cryosphere* 9, 2295–2310. doi:10.5194/tc-9-2295-2015

Sakai, A., Nuimura, T., Fujita, K., Takenaka, S., Nagai, H., and Lamsal, D. (2015). Climate Regime of Asian Glaciers Revealed by GAMDAM Glacier Inventory. *Cryosphere* 9, 865–880. doi:10.5194/tc-9-865-2015

Santos Baquero, O. (2019). Ggsn: North Symbols and Scale Bars for Maps Created with 'ggplot2' or 'ggmap'. *R. package version 0.5.0*. Available at: https://CRAN.R-project.org/package=ggsn.

Sasaki, O., Noguchi, O., Zhang, Y., Hirabayashi, Y., and Kanae, S. (2016). A Global High-Resolution Map of Debris on Glaciers Derived from Multi-Temporal ASTER Images. *Cryosphere Disc.* 2016, 1–24. doi:10.5194/tc-2016-222

Scherler, D., Wulf, H., and Gorelick, N. (2018). Global Assessment of Supraglacial Debris-Cover Extents. *Geophys. Res. Lett.* 45, 11,798–11,805. doi:10.1029/2018GL080158

Shah, S. S., Banerjee, A., Nainwal, H. C., and Shankar, R. (2019). Estimation of the Total Sub-Debris Ablation from Point-Scale Ablation Data on a Debris-Covered Glacier. *J. Glaciol.* 65, 759–769. doi:10.1017/jog.2019.48

Shaw, T. E., Brock, B. W., Fyffe, C. L., Pellicciotti, F., Rutter, N., and Diotri, F. (2016). Air Temperature Distribution and Energy-Balance Modelling of a Debris-Covered Glacier. *J. Glaciol.* 62, 185–198. doi:10.1017/jog.2016.31

Shean, D. (2017). "High Mountain Asia 8-meter DEM Mosaics Derived from Optical Imagery, Version 1," in *Dataset, National Snow and Ice Data Center Distributed Active Archive Center, US National Aeronautics and Space Administration*. doi:10.5067/KXOVQ9L172S2 Accessed April 20, 2021).

Sherpa, S. F., Wagnon, P., Brun, F., Berthier, E., Vincent, C., Lejeune, Y., et al. (2017). Contrasted Surface Mass Balances of Debris-Free Glaciers Observed between the Southern and the Inner Parts of the Everest Region (2007-15). *J. Glaciol.* 63, 637–651. doi:10.1017/jog.2017.30

Shrestha, M., Koike, T., Hirabayashi, Y., Xue, Y., Wang, L., Rasul, G., et al. (2015). Integrated Simulation of Snow and Glacier Melt in Water and Energy Balance-Based, Distributed Hydrological Modeling Framework at Hunza River Basin of Pakistan Karakoram Region. *J. Geophys. Res. Atmos.* 120, 4889–4919. doi:10.1002/2014JD022666

Sun, Z., Wang, Q., Batkhishig, O., and Ouyang, Z. (2016). Relationship between Evapotranspiration and Land Surface Temperature under Energy- and Water-Limited Conditions in Dry and Cold Climates. *Adv. Meteorology* 2016, 1–9. doi:10.1155/2016/1835487

Therneau, T., and Atkinson, B. (2019). Rpart: Recursive Partitioning and Regression Trees. *R. package version 4.1-15*. Available at: https://CRAN.R-project.org/package=rpart.

Trubilowicz, J. W., and Moore, R. D. (2017). Quantifying the Role of the Snowpack in Generating Water Available for Run-Off during Rain-On-Snow Events from Snow Pillow Records. *Hydrol. Process.* 31, 4136–4150. doi:10.1002/hyp.11310

Truffer, M. (2021). Malaspina Glacier: July 2020 Campaign. Available at: https://glacieradventures.blogspot.com/2021/08/malaspina-glacier-july-2020-campaign.html.

USDA (2020). *SHAW-Related Publications*. Boise, ID: ARS User Files, Agricultural Research Service, United States Department of Agriculture. Available at: https://www.ars.usda.gov/ARSUserFiles/20520500/SHAW/302/SHAWReferences.pdf.

Ushey, K., Allaire, J., Wickham, H., and Ritchie, G. (2020). Rstudioapi: Safely Access the RStudio API. *R. package version 0.13*. Available at: https://CRAN.R-project.org/package=rstudioapi.

Vincent, C., Wagnon, P., Shea, J. M., Immerzeel, W. W., Kraaijenbrink, P., Shrestha, D., et al. (2016). Reduced Melt on Debris-Covered Glaciers: Investigations from Changri Nup Glacier, Nepal. *Cryosphere* 10, 1845–1858. doi:10.5194/tc-10-1845-2016

Wang, H., Flerchinger, G. N., Lemke, R., Brandt, K., Goddard, T., and Sprout, C. (2010). Improving SHAW Long-Term Soil Moisture Prediction for Continuous Wheat Rotations, Alberta, Canada. *Can. J. Soil. Sci.* 90, 37–53. doi:10.4141/CJSS08084

Wickham, H., François, R., Henry, L., and Müller, K. (2021). Dplyr: A Grammar of Data Manipulation. *R. package version 1.0.6*. Available at: https://CRAN.R-project.org/package=dplyr.

Wickham, H. (2016). *Ggplot2: Elegant Graphics for Data Analysis*. New York: Springer-Verlag. Available at: https://ggplot2.tidyverse.org.

Williams, H. B., and Koppes, M. N. (2019). A Comparison of Glacial and Paraglacial Denudation Responses to Rapid Glacial Retreat. *Ann. Glaciol.* 60, 151–164. doi:10.1017/aog.2020.1

Winter-Billington, A., Moore, R. D., and Dadić, R. (2020). Evaluating the Transferability of Empirical Models of Debris-Covered Glacier Melt. *J. Glaciol.* 66, 978–995. doi:10.1017/jog.2020.57

Yu, G. (2021). Ggplotify: Convert Plot to 'grob' or 'ggplot' Object. *R. package version 0.0.7*. Available at: https://CRAN.R-project.org/package=ggplotify.

Zhang, Y., Carey, S. K., Quinton, W. L., Janowicz, J. R., Pomeroy, J. W., and Flerchinger, G. N. (2010). Comparison of Algorithms and Parameterisations for Infiltration into Organic-Covered Permafrost Soils. *Hydrol. Earth Syst. Sci.* 14, 729–750. doi:10.5194/hess-14-729-2010

Zhang, Y., Fujita, K., Liu, S., Liu, Q., and Nuimura, T. (2011). Distribution of Debris Thickness and its Effect on Ice Melt at Hailuogou Glacier, Southeastern Tibetan Plateau, Using *In Situ* Surveys and ASTER Imagery. *J. Glaciol.* 57, 1147–1157. doi:10.3189/002214311798843331

Zhang, Y., Hirabayashi, Y., Liu, Q., and Liu, S. (2015). Glacier Runoff and its Impact in a Highly Glacierized Catchment in the Southeastern Tibetan Plateau: Past and Future Trends. *J. Glaciol.* 61, 713–730. doi:10.3189/2015JoG14J188

Zhang, Y., Hirabayashi, Y., and Liu, S. (2012). Catchment-Scale Reconstruction of Glacier Mass Balance Using Observations and Global Climate Data: Case Study of the Hailuogou Catchment, South-Eastern Tibetan Plateau. *J. Hydrology* 444-445, 146–160. doi:10.1016/j.jhydrol.2012.04.014

Conflict of Interest: The authors declare that the research was conducted in the absence of any commercial or financial relationships that could be construed as a potential conflict of interest.

Publisher's Note: All claims expressed in this article are solely those of the authors and do not necessarily represent those of their affiliated organizations, or those of the publisher, the editors and the reviewers. Any product that may be evaluated in this article, or claim that may be made by its manufacturer, is not guaranteed or endorsed by the publisher.

Advantages of publishing in Frontiers

OPEN ACCESS
Articles are free to read for greatest visibility and readership

FAST PUBLICATION
Around 90 days from submission to decision

HIGH QUALITY PEER-REVIEW
Rigorous, collaborative, and constructive peer-review

TRANSPARENT PEER-REVIEW
Editors and reviewers acknowledged by name on published articles

Frontiers
Avenue du Tribunal-Fédéral 34
1005 Lausanne | Switzerland

Visit us: www.frontiersin.org
Contact us: frontiersin.org/about/contact

REPRODUCIBILITY OF RESEARCH
Support open data and methods to enhance research reproducibility

DIGITAL PUBLISHING
Articles designed for optimal readership across devices

FOLLOW US
@frontiersin

IMPACT METRICS
Advanced article metrics track visibility across digital media

EXTENSIVE PROMOTION
Marketing and promotion of impactful research

LOOP RESEARCH NETWORK
Our network increases your article's readership